

Paulo Garrido
Filomena Soares
António Paulo Moreira
Editors

CONTROLO 2016

Proceedings of the 12th Portuguese
Conference on Automatic Control

Lecture Notes in Electrical Engineering

Volume 402

Board of Series editors

Leopoldo Angrisani, Napoli, Italy
Marco Arteaga, Coyoacán, México
Samarjit Chakraborty, München, Germany
Jiming Chen, Hangzhou, P.R. China
Tan Kay Chen, Singapore, Singapore
Rüdiger Dillmann, Karlsruhe, Germany
Haibin Duan, Beijing, China
Gianluigi Ferrari, Parma, Italy
Manuel Ferre, Madrid, Spain
Sandra Hirche, München, Germany
Faryar Jabbari, Irvine, USA
Janusz Kacprzyk, Warsaw, Poland
Alaa Khamis, New Cairo City, Egypt
Torsten Kroeger, Stanford, USA
Tan Cher Ming, Singapore, Singapore
Wolfgang Minker, Ulm, Germany
Pradeep Misra, Dayton, USA
Sebastian Möller, Berlin, Germany
Subhas Mukhopadhyay, Palmerston, New Zealand
Cun-Zheng Ning, Tempe, USA
Toyoaki Nishida, Sakyo-ku, Japan
Bijaya Ketan Panigrahi, New Delhi, India
Federica Pascucci, Roma, Italy
Tariq Samad, Minneapolis, USA
Gan Woon Seng, Nanyang Avenue, Singapore
Germano Veiga, Porto, Portugal
Haitao Wu, Beijing, China
Junjie James Zhang, Charlotte, USA

About this Series

“Lecture Notes in Electrical Engineering (LNEE)” is a book series which reports the latest research and developments in Electrical Engineering, namely:

- Communication, Networks, and Information Theory
- Computer Engineering
- Signal, Image, Speech and Information Processing
- Circuits and Systems
- Bioengineering

LNEE publishes authored monographs and contributed volumes which present cutting edge research information as well as new perspectives on classical fields, while maintaining Springer’s high standards of academic excellence. Also considered for publication are lecture materials, proceedings, and other related materials of exceptionally high quality and interest. The subject matter should be original and timely, reporting the latest research and developments in all areas of electrical engineering.

The audience for the books in LNEE consists of advanced level students, researchers, and industry professionals working at the forefront of their fields. Much like Springer’s other Lecture Notes series, LNEE will be distributed through Springer’s print and electronic publishing channels.

More information about this series at <http://www.springer.com/series/7818>

Paulo Garrido · Filomena Soares
António Paulo Moreira
Editors

CONTROLO 2016

Proceedings of the 12th Portuguese
Conference on Automatic Control

Editors

Paulo Garrido
School of Engineering
University of Minho
Guimarães
Portugal

António Paulo Moreira
Faculty of Engineering
University of Porto
Porto
Portugal

Filomena Soares
School of Engineering
University of Minho
Guimarães
Portugal

ISSN 1876-1100 ISSN 1876-1119 (electronic)
Lecture Notes in Electrical Engineering
ISBN 978-3-319-43670-8 ISBN 978-3-319-43671-5 (eBook)
DOI 10.1007/978-3-319-43671-5

Library of Congress Control Number: 2016947380

© Springer International Publishing Switzerland 2017

This work is subject to copyright. All rights are reserved by the Publisher, whether the whole or part of the material is concerned, specifically the rights of translation, reprinting, reuse of illustrations, recitation, broadcasting, reproduction on microfilms or in any other physical way, and transmission or information storage and retrieval, electronic adaptation, computer software, or by similar or dissimilar methodology now known or hereafter developed.

The use of general descriptive names, registered names, trademarks, service marks, etc. in this publication does not imply, even in the absence of a specific statement, that such names are exempt from the relevant protective laws and regulations and therefore free for general use.

The publisher, the authors and the editors are safe to assume that the advice and information in this book are believed to be true and accurate at the date of publication. Neither the publisher nor the authors or the editors give a warranty, express or implied, with respect to the material contained herein or for any errors or omissions that may have been made.

Printed on acid-free paper

This Springer imprint is published by Springer Nature
The registered company is Springer International Publishing AG Switzerland

Preface

The biennial CONTROLO conferences are the main events promoted by the Portuguese Association for Automatic Control—APCA, national member organization of the International Federation of Automatic Control—IFAC.

The CONTROLO 2016—12th Portuguese Conference on Automatic Control, Guimarães, Portugal, September 14–16, was organized by Algorithm, School of Engineering, University of Minho, in partnership with INESC TEC.

This edition of the conference has been approved for co-sponsorship by IFAC.

The conference had three partners: CEA—Comité Español de Automática, SPEE—the Portuguese Association for Education Engineering, and SPR—the Portuguese Association for Robotics.

We would like to thank the support of the Organizing Committee and the invaluable contributions of the Scientific Committee members, External Reviewers, Invited Speakers and Session Chairs. Last but not least, we want to thank the authors, for whom and by whom this event was made to happen.

We would also like to acknowledge EasyChair for their conference management system, which was freely used for managing the paper submission and evaluation process. Special thanks are due to the people in Springer.

Papers submitted to the conference were anonymously peer-reviewed by the Scientific Committee with a distribution operated by the EasyChair reviewer assignment algorithm. Based on the reviewers' ratings, 81 submissions were accepted conditionally to reviewers' recommendations being implemented.

A wide range of topics are covered by the 74 papers published in this volume cover. Of them 30, of a more theoretical nature, are distributed among the first five parts: Control Theory; Optimal and Predictive Control; Fuzzy, Neural and Genetic Control; Modeling and Identification; Sensing and Estimation.

Of a more applied nature, 44 papers are presented in the following eight parts: Robotics; Mechatronics; Manufacturing Systems and Scheduling; Vibration Control; Applications in Agricultural Systems; Power Systems Applications; General Applications; Education.

We believe that the papers in this volume, from cutting-edge theoretical research to innovative control applications, show expressively how automatic control can be used to increase the well-being of people.

Guimarães, Portugal
Guimarães, Portugal
Porto, Portugal

Paulo Garrido
Filomena Soares
António Paulo Moreira

Organization

General Chair

Paulo Garrido, EEUM/Departamento de Electrónica Industrial—Centro Algoritmi

Vice-Chair

Filomena Soares, EEUM/Departamento de Electrónica Industrial—Centro Algoritmi

Organizing Committee

António Paulo Moreira, FEUP/Departamento de Engenharia Eletrotécnica e de Computadores—INESC TEC

Aparício Fernandes, EEUM/Departamento de Electrónica Industrial—Centro Algoritmi

Celina P. Leão, EEUM/Departamento de Produção e Sistemas—Centro Algoritmi

Cristina Santos, EEUM/Departamento de Electrónica Industrial—Centro Algoritmi

Estela Bicho Erlhagen, EEUM/Departamento de Electrónica Industrial—Centro Algoritmi

Fernando Ribeiro, EEUM/Departamento de Electrónica Industrial—Centro Algoritmi

Filomena Soares, EEUM/Departamento de Electrónica Industrial—Centro Algoritmi

Jaime Fonseca, EEUM/Departamento de Electrónica Industrial—Centro Algoritmi

João Sena Esteves, EEUM/Departamento de Electrónica Industrial—Centro Algoritmi

José Boaventura Da Cunha, UTAD/Departamento de Engenharias (Engenharia Electrotécnica)—INESC TEC

José Machado, EEUM/Departamento de Engenharia Mecânica—Centro Metrics

Paulo Garrido, EEUM/Departamento de Eletrónica Industrial—Centro Algoritmi
 Pedro Costa, FEUP/Departamento de Engenharia Eletrotécnica e de Computadores
 —INESC TEC
 Sérgio Monteiro, EEUM/Departamento de Eletrónica Industrial—Centro Algoritmi
 Vitor Carvalho, IPCA—Centro Algoritmi

Scientific Committee

Adina Astilean, Universitatii Tehnice din Cluj-Napoca, Romania
 Adriano Ferreira, Instituto Politécnico de Bragança, Portugal
 Alberto Isidori, Sapienza Università di Roma, Italy
 Ana Antunes, Instituto Politécnico de Setúbal, Portugal
 Ana Catarina Carapito, Universidade da Beira Interior, Portugal
 André Conceição, Universidade Federal da Bahia, Brazil
 Aníbal Matos, Universidade do Porto, Portugal
 Antonio Barreiro Blas, Universidade de Vigo, Spain
 António Mendes Lopes, Universidade do Porto, Portugal
 António Pascoal, IST Universidade de Lisboa, Portugal
 António Pedro Aguiar, Universidade do Porto, Portugal
 António Ruano, Universidade do Algarve, Portugal
 Antonio Sala, Universitat Politècnica de València, Spain
 Bruno Ferreira, Universidade do Porto, Portugal
 Calim Ciufudean, Universitatea Stefan cel Mare Suceava, Romania
 Camelia Avram, Universitatea Tehnica din Cluj-Napoca, Romania
 Carlos Cardeira, IST Universidade de Lisboa, Portugal
 Carlos Henrique Santos, Universidade Estadual do Oeste do Paraná, Brazil
 Carlos Silvestre, IST Universidade de Lisboa, Portugal
 Cesar Prada Moraga, Universidad de Valladolid, Spain
 Claudio Melchiori, Università di Bologna, Italy
 Constantino Lagoa, the Pennsylvania State University, USA
 Damir Vrancic, Institut Jožef Stefan, Slovenia
 Dariuz Sedziak, Politechnika Poznańska, Poland
 Eduardo Perondi, Universidade Federal do Rio Grande do Sul, Brazil
 Erika Ottaviano, Università degli Studi di Cassino e del Lazio Meridionale, Italy
 Erwin-Christian Lovasz, Universitatea Politehnica Timișoara, Romania
 Esteban Arroyo, Helmut-Schmidt-Universität, Germany
 Fátima Silva Leite, Universidade de Coimbra, Portugal
 Felipe Pait, Universidade de São Paulo, Brazil
 Fellippe Souza, Universidade da Beira Interior, Portugal
 Fernando Fontes, Universidade do Porto, Portugal
 Fernando Silva, IST Universidade de Lisboa, Portugal
 Francisco Rubio, Universidad de Sevilla, Spain
 Frank Allgower, Universität Stuttgart, Germany
 Gabor Sziebig, Høgskolen i Narvik, Norway

Gerardo Acosta, Universidad del Centro Provincia de Buenos Aires, Argentina
Gerhard Jank, Rheinisch-Westfälische Technische Hochschule Aachen, Germany
Germano Veiga, Universidade do Porto, Portugal
Gil Lopes, Universidade do Minho, Portugal
Giovanni Indiveri, Università del Salento, Italy
Giuseppe Notarstefano, Università del Salento, Italy
Guilherme Kunz, Universidade Estadual do Oeste do Paraná, Brazil
Hisham Abou-Kandil, École Normale Supérieure de Cachan, France
Hubert Roth, Julius-Maximilians-Universität Würzburg, Germany
Husi Géza, Debreceni Egyetem, Hungary
Isabel Brás, Universidade de Aveiro, Portugal
Javier Sanchis Sáez, Universitat Politècnica de València, Spain
João Calado, Instituto Politécnico de Lisboa, Portugal
João Hespanha, University of California, USA
João Miguel Sousa, IST Universidade de Lisboa, Portugal
João Miranda Lemos, IST Universidade de Lisboa, Portugal
João Paulo Coelho, Instituto Politécnico de Bragança, Portugal
Joaquim Ferreira, Universidade de Aveiro, Portugal
Job von Amerongen, Universiteit Twente, the Netherlands
John Fasoulas, Τεχνολογικό Εκπαιδευτικό Ίδρυμα Κρήτης, Greece
Jonas Sjöberg, Chalmers Tekniska Högskola, Sweden
Jorge Ferreira, Universidade de Aveiro, Portugal
Jorge Sá Silva, Universidade de Coimbra, Portugal
José Barbosa, Instituto Politécnico de Bragança, Portugal
José Boaventura Cunha, Universidade de Trás-os-Montes e Alto Douro, Portugal
José Machado, Universidade do Minho, Portugal
José Moreno, Universidad Nacional de Educación a Distancia, Spain
José Ragot, Université de Lorraine, France
José Tenreiro Machado, Instituto Politécnico do Porto, Portugal
José Vieira, Instituto Politécnico de Castelo Branco, Portugal
Jurek Sasiadek, Carleton University, Canada
Justina Trojanowska, Politechnika Poznańska, Poland
Katarina Zakova, Slovenská Technická Univerzita v Bratislave, Slovakia
Klaus Schilling, Julius-Maximilians-Universität Würzburg, Germany
Krzysztof Kozłowski, Politechnika Poznańska, Poland
Leonardo Honório, Universidade Federal de Juiz de Fora, Brazil
Luís Gomes, Universidade Nova de Lisboa, Portugal
Luís Paulo Reis, Universidade do Minho, Portugal
Luiz de Siqueira Martins Filho, Universidade Federal do ABC, Brazil
Manuel Braz César, Instituto Politécnico do Bragança, Portugal
Manuel Domínguez Gonzalez, Universidad de León, Spain
Manuel Fernando Silva, Instituto Politécnico do Porto, Portugal
Marcelo Petry, Universidade Federal de Santa Catarina, Brazil
Maria do Rosário Pinho, Universidade do Porto, Portugal
Maria Graça Ruano, Universidade do Algarve, Portugal

Miguel Ayala Botto, IST Universidade de Lisboa, Portugal
Miguel Bernal, Instituto Tecnológico de Sonora, Mexico
Mikulas Huba, Slovenská Technická Univerzita v Bratislave, Slovakia
Morgado Dias, Universidade da Madeira, Portugal
Oscar Barambones, Euskal Herriko Unibertsitatea, Spain
Paula Malonek, Universidade do Porto, Portugal
Paulo Costa, Universidade do Porto, Portugal
Paulo Jorge Oliveira, IST Universidade de Lisboa, Portugal
Paulo Lopes dos Santos, Universidade do Porto, Portugal
Paulo Oliveira, Universidade de Trás-os-Montes e Alto Douro, Portugal
Paulo Salgado, Universidade de Trás-os-Montes e Alto Douro, Portugal
Pedro Albertos, Universitat Politècnica de València, Spain
Pedro Peres, Universidade Estadual de Campinas, Brazil
Ramiro Barbosa, Instituto Politécnico do Porto, Portugal
Ramon Vilanova, Universitat Autònoma de Barcelona, Spain
Rolf Johansson, Lunds Universitet, Sweden
Rui Araújo, Universidade de Coimbra, Portugal
Rui Neves-Silva, Universidade Nova de Lisboa, Portugal
Sahin Yildirim, Erciyes Üniversitesi, Turkey
Sebastian Dormido, Universidad Nacional de Educación a Distancia, Spain
Sílvia Botelho, Universidade Federal do Rio Grande, Brazil
Sónia Pinto, IST Universidade de Lisboa, Portugal
Susana Vieira, IST Universidade de Lisboa, Portugal
Teresa Perdicoulis, Universidade de Trás-os-Montes e Alto Douro, Portugal

Contents

Part I Control Theory

Input-State-Output Representations of Concatenated 2D Convolutional Codes	3
Diego Napp, Raquel Pinto and Rita Simões	
MDP Periodically Time-Varying Convolutional Codes	13
Ricardo Pereira, Paula Rocha and Diego Napp	
Periodic Event-Triggered Swing-Up Control of the Inverted Pendulum	23
E. Aranda-Escolástico, F. Gordillo, M. Guinaldo and S. Dormido	
A Simplified Control Approach for the Neuromuscular Blockade Level	37
Juliana Almeida, Teresa Mendonça and Paula Rocha	
Disturbance Rejection Improvement for the Sliding Mode Smith Predictor Based on Bio-inspired Tuning	45
Josnalde Oliveira, José Boaventura-Cunha and Paulo Moura Oliveira	
Quadruple Real Dominant Pole Tuning of a Filtered PID Controller	59
Mikuláš Huba and Pavol Bisták	
Smith Predictor Tuned Through Fuzzy Fractional PID Controller	71
Isabel S. Jesus and Ramiro S. Barbosa	
The Model-Based Disturbance Rejection with MOMI Tuning Method for PID Controllers	81
Damir Vrančić, Paulo Moura Oliveira and Jan Cvejn	
Systemic Coordination Through Numeraires: Initial Simulation Results	93
Paulo Garrido and Pedro Osório	

Wormhole Approach to Control in Distributed Computing Has Direct Relation to Physics	105
Nicolás F. Lori and Victor Alves	
A New Robust Control Scheme for LTV Systems Using Output Integral Discrete Synergetic Control Theory	117
Saeid Rastegar, Rui Araújo, Alireza Emami and Abdelhamid Iratni	
Part II Optimal and Predictive Control	
Drug Administration Design for Cancer Gompertz Model Based on the Lyapunov Method	131
B. Andrade Costa and J.M. Lemos	
Sampled–Data Model Predictive Control Using Adaptive Time–Mesh Refinement Algorithms	143
Luís Tiago Paiva and Fernando A.C.C. Fontes	
Efficient Operations at Intermodal Terminals Using a Multi-agent System	155
Tomás Hipólito, João Lemos Nabais and Miguel Ayala Botto	
Model Predictive Control Applied to a Supply Chain Management Problem	167
Tatiana M. Pinho, João Paulo Coelho, António Paulo Moreira and José Boaventura-Cunha	
Optimal Control for an Irrigation Problem with Several Fields and Common Reservoir	179
Sofia O. Lopes and Fernando A.C.C. Fontes	
Mechanical Multi-agent Maneuvering Using Noncooperative DMPC	189
José Igreja, Filipe A. Barata and Carla Viveiros	
A Parametrized NMPC Strategy for Pressure Reducing Valves	201
Carlos Felipe Ilha Pereira, André Murilo, Anderson Quadros and Walter de Britto Vidal Filho	
Part III Fuzzy, Neural and Genetic Control	
Fuzzy Kalman Filter Black Box Modeling Approach for Dynamic System with Partial Knowledge of States	215
Danúbia Soares Pires and Ginalber Luiz de Oliveira Serra	
Neural Network Control Strategies Applied to a DC Motor with a Nonlinear Load	227
Luís M.M. Ferreira and Ramiro S. Barbosa	

Grey Wolf, Gravitational Search and Particle Swarm Optimizers: A Comparison for PID Controller Design 239
 Paulo Moura Oliveira and Damir Vrančić

Part IV Modeling and Identification

Construction of Confidence Sets for Markov Chain Model 253
 Dmitry Zavalishchin and Galina Timofeeva

Monitoring and Simulation of Gas Pipelines Through Quadripole Models 265
 S.T. Baltazar, T.-P. Azevedo Perdicoulis and P. Lopes dos Santos

Data Based Modeling of a Large Scale Water Delivery System 275
 Marta Fernandes, Paulo Oliveira, Susana Vieira, Luís Mendonça, João Lemos Nabais and Miguel Ayala Botto

PDE Model for Leakage Detection in High Pressure Gas Networks 285
 T.-P. Azevedo Perdicoulis, R. Almeida, P. Lopes dos Santos and G. Jank

Part V Sensing and Estimation

Sensorless Nonlinear Control of Fed-Batch *Escherichia coli* Cultivation Bioprocess Using the State-Dependent Approach 299
 Abdelhamid Iratni, Rui Araújo, Saeid Rastegar and Mohammed Mostefai

Velocity and Brightness Control in Prototype for Blood Type Determination 311
 Ana Ferraz, Vítor Carvalho and José Machado

Development of Soft Sensors Based on Analytical and Spectral Data on a Real Small Size Wastewater Treatment Plant 323
 C. Leitão, L. Fernandes, R. Ribeiro, M.C. Almeida, C.I.C. Pinheiro and H.M. Pinheiro

Solar Pyramidal Sensor 335
 Paulo Salgado, Beatriz Pereira, Lara Félix and Paulo Afonso

Actuator Fault Detection and Isolation Based on Multiple-Model Adaptive Estimation (MMAE) 345
 Diogo Monteiro, Paulo Rosa, Paulo Oliveira and Carlos Silvestre

Part VI Robotics

Wheels for Staircases 361
 Fátima Silva Leite, Jorge Batista, Krzysztof Krakowski, André Carvalho, Tiago Cruz, Eduardo Domingues, André Lizardo and Gonçalo Saraiva

<i>Imitate Me!</i>—Preliminary Tests on an Upper Members Gestures Recognition System	373
Vinícius Silva, Pedro Leite, Filomena Soares, João Sena Esteves and Sandra Costa	
Happiness and Sadness Recognition System—Preliminary Results with an <i>Intel RealSense</i> 3D Sensor	385
Vinícius Silva, Filomena Soares, João Sena Esteves, Joana Figueiredo, Cristina Santos and Ana Paula Pereira	
A Simple Control Approach for Stereotactic Neurosurgery Using a Robotic Manipulator	397
Carlos Faria, Carolina Vale, Manuel Rito, Wolfram Erlhagen and Estela Bicho	
Motion Control of Mobile Autonomous Robots Using Non-linear Dynamical Systems Approach	409
Fernando Ribeiro, Gil Lopes, Tiago Maia, Hélder Ribeiro, Pedro Osório, Ricardo Roriz and Nuno Ferreira	
Autonomous UAV Outdoor Flight Controlled by an Embedded System Using Odroid and ROS	423
João Pedro Carvalho, Marco Aurélio Jucá, Alexandre Menezes, Leonardo Rocha Olivi, André Luis Marques Marcatto and Alexandre Bessa dos Santos	
Tracking of Physiotherapy Exercises Using Image Processing Techniques	439
Tiago Martins, Vítor Carvalho and Filomena Soares	
Inside Pipe Inspection: A Review Considering the Locomotion Systems	449
Everson Brum Siqueira, Rodrigo Zelir Azzolin, Silvia Silva da Costa Botelho and Vinícius Menezes de Oliveira	
Part VII Mechatronics	
SmartBath: A New Bathing Concept for Disabled People	461
Karolina Bezerra, José Machado, Filomena Soares, Vítor Carvalho and Demétrio Matos	
A New Approach for Dynamic Analysis of Overhead Crane Systems Under Moving Loads	471
Şahin Yildirim and Emir Esim	

CMOS Transducer with Linear Response Using Negative Capacity that Can Be Used in Mechatronic Systems for Force Measurement in Human Walking Analysis and in the Future in MEMS and NEMS Applications 483
 Anghel Constantin and Gheorghe I. Gheorghe

Behavior of the Elastomers Used in Prehension Systems for Small Cylindrical Objects 495
 Vlad Cârlescu, Mihai Adrian Rusu, Gheorghe Prisăcaru, Emanuel Miron, José Machado and Dumitru Olaru

Part VIII Manufacturing Systems and Scheduling

Collaborative Portal for Supporting Manufacturing Resources Selection in a Global Market 509
 Vaibhav Shah, Maria Leonilde Rocha Varela and Goran D. Putnik

A Simulation Platform Prototype for Evaluating Alternative Scenarios of Members Integration in Virtual Organizations 521
 António Arrais-Castro, Gaspar Vieira, Maria Leonilde Rocha Varela, Goran D. Putnik and José Machado

Formal Analysis of an Urban Road Traffic Model 533
 Camelia Avram, Eduardo Valente, Adina Aștilean, José Machado and Dan Radu

Part IX Vibration Control

Brain Emotional Learning Based Control of a SDOF Structural System with a MR Damper 547
 Manuel Braz César, José Gonçalves, João Coelho and Rui Carneiro de Barros

Pendulum TMD's in Building Vibration Control 559
 Rui Carneiro de Barros and Catarina M.A. Sousa

Fuzzy Based Control of a Vehicle Suspension System Using a MR Damper 571
 Kellie F. Oliveira, Manuel Braz César and José Gonçalves

Milling Parameters Optimization for Surface Quality 583
 Tânia Dias, Nuno Paulo, Luís Queijo, Hernâni Reis Lopes, Manuel Braz César and João Eduardo Ribeiro

Part X Applications in Agricultural Systems

Automation and Control in Greenhouses: State-of-the-Art and Future Trends 597
 Josenalde Oliveira, José Boaventura-Cunha and Paulo Moura Oliveira

A New Plant Growth System Rig Based on Thermodynamic Solar Energy: A Study for Energy Efficiency Assessment	607
João Paulo Coelho, José Gonçalves, Manuel Braz César and José Dias	
Model Predictive Control of a Conveyor-Based Drying Process Applied to Cork Stoppers	617
Pedro Tavares, Tatiana M. Pinho, José Boaventura-Cunha and António Paulo Moreira	
Robust Control of Agroindustrial Drying Process of Grains Based on Sliding Modes and Gravitational Search Algorithm	629
Josenalde Oliveira, José Boaventura-Cunha and Paulo Moura Oliveira	
Part XI Power Systems Applications	
Model Predictive Current Control of a Slow Battery Charger for Electric Mobility Applications	643
Delfim Pedrosa, Ricardo Gomes, Vitor Monteiro, José A. Afonso and João L. Afonso	
Comprehensive Analysis and Comparison of Digital Current Control Techniques for Active Rectifiers	655
Vitor Monteiro, João C. Ferreira, Delfim Pedrosa, M.J. Sepúlveda, J.C. Aparício Fernandes and João L. Afonso	
Digital Control of a Novel Single-Phase Three-Port Bidirectional Converter to Interface Renewables and Electric Vehicles with the Power Grid	667
Vitor Monteiro, José A. Afonso, Delfim Pedrosa, Júlio S. Martins and João L. Afonso	
Model Predictive Control of an On-Board Fast Battery Charger for Electric Mobility Applications	679
Delfim Pedrosa, Ricardo Gomes, Vitor Monteiro, J.C. Aparício Fernandes, João Monteiro and João L. Afonso	
Family Houses Energy Consumption Forecast Tools for Smart Grid Management	691
F. Rodrigues, C. Cardeira, J.M.F. Calado and R. Melício	
Renewable Energy System for an Isolated Sustainable Social Centre	701
J.G. Pinto, Fábio Fernandes, Bruno Exposto, Vitor Monteiro and João L. Afonso	
Evaluation of the Introduction of Electric Vehicles in the Power Grid—A Study for the Island of Maio in Cape Verde	713
Vitor Monteiro, M.J. Sepúlveda, J.C. Aparício Fernandes, J.G. Pinto and João L. Afonso	

OpenADR—Intelligent Electrical Energy Consumption Towards Internet-of-Things 725
 João Ferreira, Hugo Martins, Manuel Barata, Vítor Monteiro and João L. Afonso

Part XII General Applications

A Low-Cost ZigBee-Based Wireless Industrial Automation System 739
 Pedro Castro, João L. Afonso and José A. Afonso

Comparative Analysis of Gain-Scheduled Wheel Slip Reset Controllers with Different Reset Strategies in Automotive Brake Systems 751
 Miguel Cerdeira-Corujo, Adriana Costas, Emma Delgado and Antonio Barreiro

Design and Development of Control System for Railway Cable Laying. 763
 Valentín Cañas, Andrés García, Javier de las Morenas and Jesús Blanco

Mobile Sensing System for Cycling Power Output Control 773
 José A. Afonso, Filipe J. Rodrigues, Delfim Pedrosa and João L. Afonso

Automatic Control of Madeira Wine Aging Process 785
 Carlos M. Faria, Darío Baptista, José Carlos Marques and Fernando Morgado-Dias

Study of Quality Service in AIS Gateway System 797
 Mário Assunção and Luis Mendonça

Realization of PID Controllers in Analog Reconfigurable Hardware. 809
 Paulo J.R. Fonseca and Ramiro S. Barbosa

Speed Control of an Experimental Pneumatic Engine 821
 João Pardelhas, Miguel Silva, Luis Mendonça and Luis Baptista

Design and Implementation of a PI Controller for a Metal Casting Machine 831
 Bruno R. Mendes, Manuel F. Silva and Ramiro S. Barbosa

Part XIII Education

Control Engineering Learning by Integrating App-Inventor Based Experiments 845
 Filomena Soares, Paulo Moura Oliveira and Celina P. Leão

**Inverted Pendulum Controlled by an Analog PID Controller:
A Framework for a Laboratorial Experiment 857**
Luís Dias, José Ferreira, Filomena Soares, Gil Lopes,
João Sena Esteves, M.J. Sepúlveda and Paulo Garrido

**Online Control of TOS1A Thermo-Optical Plant
Using OpenModelica 869**
Katarína Žáková

DC Motor Educational Kit: A Teaching Aid in Control Theory. 879
António Paulo Moreira, Paulo Costa, José Gonçalves
and Brígida M. Faria

Part I
Control Theory

Input-State-Output Representations of Concatenated 2D Convolutional Codes

Diego Napp, Raquel Pinto and Rita Simões

Abstract In this paper we investigate a novel model of concatenation of a pair of two-dimensional (2D) convolutional codes. We consider finite-support 2D convolutional codes and choose the so-called Fornasini-Marchesini input-state-output (ISO) model to represent these codes. More concretely, we interconnect in series two ISO representations of two 2D convolutional codes and derive the ISO representation of the obtained 2D convolutional code. We provide necessary condition for this representation to be minimal. Moreover, structural properties of modal reachability and modal observability of the resulting 2D convolutional codes are investigated.

1 Introduction

Codes derived by combining two codes (an inner code and an outer code) form an important class of error-correcting codes called concatenated codes. This class, originally introduced by David Forney in 1965, became widely used in communications due to fact that they can achieve excellent performance with reasonable complexity. Although the first construction of concatenated codes used block codes, NASA started to use a short-constraint-length (64-state) convolutional code as an inner code, decoded by the optimal Viterbi algorithm, because it had been realized that convolutional codes are superior to block codes from the point of view of performance versus complexity. Indeed, it was in 1993 that the field of coding theory was revolutionized by the invention of turbo codes (concatenation of two convolutional codes) by Berrou et al.

D. Napp · R. Pinto · R. Simões (✉)
CIDMA—Center for Research and Development in Mathematics and Applications,
Department of Mathematics, University of Aveiro, Campus Universitário de Santiago,
3810-193 Aveiro, Portugal
e-mail: ritasimoes@ua.pt

D. Napp
e-mail: diego@ua.pt

R. Pinto
e-mail: raquel@ua.pt

Roughly speaking one dimensional (1D) convolutional codes can be seen as a generalization of block codes in the sense that a block code is a convolutional code with no delay, i.e., block codes are basically 0D convolutional codes. In this way, two-dimensional (2D) convolutional codes extend the 1D convolutional codes. These codes have a practical potential in applications as they are very suitable to encode data recorded in 2 dimensions, e.g., pictures, storage media, wireless applications, etc. However, in comparison to 1D convolutional codes, little research has been done in the area of 2D convolutional codes.

In this paper the authors further investigate the concatenation properties of 2D convolutional codes, and therefore extend their previous results presented in [1]. In this case we study a new type of concatenation that has not been analysed before in the context of 2D convolutional codes. In particular, we derive conditions for the minimality of an input-state-output representation of the concatenated code. Furthermore, we show that this concatenation of two 2D convolutional codes results in another 2D convolutional code and we explicitly compute an ISO representation. Finally, we investigate under which conditions fundamental properties such as modal observability and reachability of ISO representations of two 2D convolutional codes carry over after serial concatenation.

2 Preliminaries

Denote by $\mathbb{F}[z_1, z_2]$ the ring of polynomials in two indeterminates with coefficients in \mathbb{F} , by $\mathbb{F}(z_1, z_2)$ the field of fractions of $\mathbb{F}[z_1, z_2]$ and by $\mathbb{F}[[z_1, z_2]]$ the ring of formal powers series in two indeterminates with coefficients in \mathbb{F} .

In this section we start by giving some preliminaries on matrices over $\mathbb{F}[z_1, z_2]$.

Definition 1 A matrix $G(z_1, z_2) \in \mathbb{F}[z_1, z_2]^{n \times k}$, with $n \geq k$ is,

1. unimodular if $n = k$ and $\det(G(z_1, z_2)) \in \mathbb{F} \setminus \{0\}$;
2. right factor prime (*rFP*) if for every factorization

$$G(z_1, z_2) = \overline{G}(z_1, z_2)T(z_1, z_2),$$

- with $\overline{G}(z_1, z_2) \in \mathbb{F}[z_1, z_2]^{n \times k}$ and $T(z_1, z_2) \in \mathbb{F}[z_1, z_2]^{k \times k}$, $T(z_1, z_2)$ is unimodular;
3. right zero prime (*rZP*) if the ideal generated by the $k \times k$ minors of $G(z_1, z_2)$ is $\mathbb{F}[z_1, z_2]$.

A matrix is *left factor prime* (*lFP*)/*left zero prime* (*lZP*) if its transpose is *rFP*/*rZP*, respectively. Moreover, zero primeness implies factor primeness, but the contrary does not happen. The following lemmas give characterizations of right factor primeness and right zero primeness that will be needed later.

Lemma 1 ([2, 3]) *Let $G(z_1, z_2) \in \mathbb{F}[z_1, z_2]^{n \times k}$, with $n \geq k$. Then the following are equivalent:*

1. $G(z_1, z_2)$ is right factor prime;
2. for all $\hat{u}(z_1, z_2) \in \mathbb{F}[z_1, z_2]^k$, $G(z_1, z_2)\hat{u}(z_1, z_2) \in \mathbb{F}[z_1, z_2]^n$ implies that $\hat{u}(z_1, z_2) \in \mathbb{F}[z_1, z_2]^k$.
3. the $k \times k$ minors of $G(z_1, z_2)$ have no common factor.

Lemma 2 ([2, 3]) *Let $G(z_1, z_2) \in \mathbb{F}[z_1, z_2]^{n \times k}$, with $n \geq k$. Then the following are equivalent:*

1. $G(z_1, z_2)$ is right zero prime;
2. $G(z_1, z_2)$ admits a polynomial left inverse;
3. $G(\lambda_1, \lambda_2)$ is full column rank, for all $\lambda_1, \lambda_2 \in \bar{\mathbb{F}}$, where $\bar{\mathbb{F}}$ denotes the algebraic closure of \mathbb{F} .

It is well known that given a full column rank polynomial matrix $G(z_1, z_2)$ in $\mathbb{F}[z_1, z_2]^{n \times k}$, there exists a square polynomial matrix $V(z_1, z_2) \in \mathbb{F}[z_1, z_2]^{k \times k}$ and a rFP matrix $\bar{G}(z_1, z_2) \in \mathbb{F}[z_1, z_2]^{n \times k}$ such that

$$G(z_1, z_2) = \bar{G}(z_1, z_2)V(z_1, z_2).$$

The following lemma will be needed in the sequel. Let $G(z_1, z_2) \in \mathbb{F}[z_1, z_2]^{n \times k}$, $H(z_1, z_2) \in \mathbb{F}[z_1, z_2]^{(n-k) \times n}$, $n > k$, c_i the i th column of $H(z_1, z_2)$ and r_j the j th row of $G(z_1, z_2)$. We say that the full size minor of $H(z_1, z_2)$ constituted by the columns $c_{i_1}, \dots, c_{i_{n-k}}$ and the full size minor of $G(z_1, z_2)$ constituted by the rows r_{j_1}, \dots, r_{j_k} are corresponding maximal order minors of $H(z_1, z_2)$ and $G(z_1, z_2)$, if $\{i_1, \dots, i_{n-k}\} \cup \{j_1, \dots, j_k\} = \{1, \dots, n\}$ and $\{i_1, \dots, i_{n-k}\} \cap \{j_1, \dots, j_k\} = \emptyset$.

Lemma 3 ([4]) *Let $G(z_1, z_2) \in \mathbb{F}[z_1, z_2]^{n \times k}$ and $H(z_1, z_2) \in \mathbb{F}[z_1, z_2]^{(n-k) \times n}$ be a rFP and a ℓ FP matrices, respectively, such that $H(z_1, z_2)G(z_1, z_2) = 0$. Then the corresponding maximal order minors of $H(z_1, z_2)$ and $G(z_1, z_2)$ are equal, modulo a unit of the ring $\mathbb{F}[z_1, z_2]$.*

Next we give preliminaries on 2D linear systems, which we will use to construct 2D finite support convolutional codes. In particular we consider the Fornasini-Marchesini state space model representation of 2D systems ([5]). In this model a first quarter plane 2D linear system, denoted by $\Sigma = (A_1, A_2, B_1, B_2, C, D)$, is given by the updating equations

$$\begin{aligned} x(i+1, j+1) &= A_1x(i, j+1) + A_2x(i+1, j) + B_1u(i, j+1) + B_2u(i+1, j) \\ y(i, j) &= Cx(i, j) + Du(i, j), \end{aligned} \quad (1)$$

where $A_1, A_2 \in \mathbb{F}^{\delta \times \delta}$, $B_1, B_2 \in \mathbb{F}^{\delta \times k}$, $C \in \mathbb{F}^{(n-k) \times \delta}$, $D \in \mathbb{F}^{(n-k) \times k}$, $\delta, n, k \in \mathbb{N}$, $n > k$ and with past finite support of the input and of the state and zero initial conditions (i.e., $u(i, j) = x(i, j) = 0$ for $i < 0$ or $j < 0$ and $x(0, 0) = 0$). We say that $\Sigma = (A_1, A_2, B_1, B_2, C, D)$ has dimension δ , local state $x(i, j)$, input $u(i, j)$ and output $y(i, j)$, at (i, j) .

The input, state and output 2D sequences (trajectories), $\{u(i, j)\}_{(i, j) \in \mathbb{N}^2}$, $\{x(i, j)\}_{(i, j) \in \mathbb{N}^2}$, $\{y(i, j)\}_{(i, j) \in \mathbb{N}^2}$, respectively, can be represented as formal power series,

$$\begin{aligned}\hat{u}(z_1, z_2) &= \sum_{(i, j) \in \mathbb{N}^2} u(i, j) z_1^i z_2^j \in \mathbb{F}[[z_1, z_2]]^k \\ \hat{x}(z_1, z_2) &= \sum_{(i, j) \in \mathbb{N}^2} x(i, j) z_1^i z_2^j \in \mathbb{F}[[z_1, z_2]]^\delta \\ \hat{y}(z_1, z_2) &= \sum_{(i, j) \in \mathbb{N}^2} y(i, j) z_1^i z_2^j \in \mathbb{F}[[z_1, z_2]]^{n-k}\end{aligned}$$

We will use the sequence and the corresponding series interchangeably. Given an input trajectory $\hat{u}(z_1, z_2)$ with corresponding state $\hat{x}(z_1, z_2)$ and output $\hat{y}(z_1, z_2)$ trajectories obtained from (1), the triple $(\hat{x}(z_1, z_2), \hat{u}(z_1, z_2), \hat{y}(z_1, z_2))$ is called an *input-state-output trajectory* of $\Sigma = (A_1, A_2, B_1, B_2, C, D)$. The set of input-state-output trajectories of Σ is given by

$$\ker_{\mathbb{F}[[z_1, z_2]]} X(z_1, z_2) = \{\hat{r}(z_1, z_2) \in \mathbb{F}[[z_1, z_2]]^{n+\delta} \mid X(z_1, z_2) \hat{r}(z_1, z_2) = 0\}$$

where

$$X(z_1, z_2) = \begin{bmatrix} I_\delta - A_1 z_1 - A_2 z_2 & -B_1 z_1 - B_2 z_2 & 0 \\ & -C & I_{n-k} \end{bmatrix}. \quad (2)$$

Next we present the modal reachability and observability properties of such systems.

Definition 2 ([1, 5]) Let $\Sigma = (A_1, A_2, B_1, B_2, C, D)$ be a 2D linear system with dimension δ .

1. Σ is *modally reachable* if the matrix $\begin{bmatrix} I_\delta - A_1 z_1 - A_2 z_2 & B_1 z_1 + B_2 z_2 \end{bmatrix}$ is ℓFP . Moreover Σ is modally reachable if and only if the corresponding matrix $X(z_1, z_2)$ defined in (2) is ℓFP .
2. Σ is *modally observable* if the matrix $\begin{bmatrix} I_\delta - A_1 z_1 - A_2 z_2 \\ C \end{bmatrix}$ is rFP .

3 Input-State-Output Representations of 2D Finite Support Convolutional Codes

Definition 3 ([6]) A 2D (finite support) convolutional code C of rate k/n is a free $\mathbb{F}[z_1, z_2]$ -submodule of $\mathbb{F}[z_1, z_2]^n$, where k is the rank of C . A full column rank matrix $G(z_1, z_2) \in \mathbb{F}[z_1, z_2]^{n \times k}$ whose columns constitute a basis for C , i.e., such that

$$\mathcal{C} = \text{Im}_{\mathbb{F}[z_1, z_2]} G(z_1, z_2) = \{ \hat{v}(z_1, z_2) = G(z_1, z_2) \hat{u}(z_1, z_2) \mid \hat{u}(z_1, z_2) \in \mathbb{F}[z_1, z_2]^k \},$$

is called an encoder of \mathcal{C} . The elements of \mathcal{C} are called codewords.

Two full column rank matrices $G(z_1, z_2)$ and $\tilde{G}(z_1, z_2)$ in $\mathbb{F}[z_1, z_2]^{n \times k}$ are *equivalent encoders* if they generate the same 2D convolutional code, i.e., if

$$\text{Im}_{\mathbb{F}[z_1, z_2]} G(z_1, z_2) = \text{Im}_{\mathbb{F}[z_1, z_2]} \tilde{G}(z_1, z_2),$$

which happens if and only if there exists a unimodular matrix $U(z_1, z_2)$ in $\mathbb{F}[z_1, z_2]^{k \times k}$ such that $G(z_1, z_2)U(z_1, z_2) = \tilde{G}(z_1, z_2)$ (see [6]).

Note that the fact that two equivalent encoders differ by unimodular matrices also implies that the primeness properties of the encoders of a code are preserved, i.e., if \mathcal{C} admits a *rFP* (*rZP*) encoder then all its encoders are *rFP* (*rZP*). A 2D finite support convolutional code \mathcal{C} that admits *rFP* encoders is called *noncatastrophic* and is named *basic* if all its encoders are *rZP*. Moreover, if \mathcal{C} admits an encoder

$$G(z_1, z_2) = \begin{bmatrix} I_k \\ \tilde{G}(z_1, z_2) \end{bmatrix}, \text{ up to a row permutation, } \mathcal{C} \text{ is called } \textit{systematic}.$$

Let us now consider a first quarter plane 2D linear system Σ defined in (1). For $(i, j) \in \mathbb{N}^2$, define

$$v(i, j) = \begin{bmatrix} y(i, j) \\ u(i, j) \end{bmatrix} \in \mathbb{F}^n$$

to be the *code vector*. We will only consider the finite support input-output trajectories, $(v(i, j))_{(i, j) \in \mathbb{N}^2}$ of (1). We will not consider such trajectories with corresponding state trajectory $\hat{x}(z_1, z_2)$ having infinite support, since this would make the system remain indefinitely excited. Thus, we will restrict ourselves to finite support input-output trajectories $(\hat{u}(z_1, z_2), \hat{y}(z_1, z_2))$ with corresponding state $\hat{x}(z_1, z_2)$ also having finite support. We call such trajectories $(\hat{u}(z_1, z_2), \hat{y}(z_1, z_2))$ *finite-weight input-output trajectories* and the triple $(\hat{x}(z_1, z_2), \hat{u}(z_1, z_2), \hat{y}(z_1, z_2))$ *finite-weight trajectories*. Note that not all finite support input-output trajectories have finite weight. The following result asserts that the set of finite-weight trajectories of (1) forms a 2D finite support convolutional code.

Theorem 1 ([7]) *The set of finite-weight input-output trajectories of (1) is a 2D finite support convolutional code of rate k/n .*

We denote by $C(A_1, A_2, B_1, B_2, C, D)$ the 2D finite support convolutional code whose codewords are the finite-weight input-output trajectories of the 2D linear system $\Sigma = (A_1, A_2, B_1, B_2, C, D)$. Moreover, Σ is called an *input-state-output (ISO) representation* of $C(A_1, A_2, B_1, B_2, C, D)$ (see [7]).

Next theorem shows how the modal reachability and observability properties of ISO representations reflect on the structure of the corresponding code.

Theorem 2 ([1, 7]) *Let $\Sigma = (A_1, A_2, B_1, B_2, C, D)$ be a 2D linear system.*

1. *If Σ is modally observable then $C(A_1, A_2, B_1, B_2, C, D)$ is noncatastrophic and its codewords are the finite support input-output trajectories of Σ .*
2. *Assume that Σ is modally reachable then Σ is modally observable if and only if $C(A_1, A_2, B_1, B_2, C, D)$ is noncatastrophic.*

In the 1D case, ISO representations of a convolutional code of minimal dimension are usually used to define the code. This is due the fact that they have good structural properties that provide important tools in the analysis of the code. Such representation are called *minimal* and they are completely characterized. However it does not exist a characterization of minimal representations for 2D convolutional codes. Next theorem gives a sufficient condition for minimality.

Theorem 3 ([7]) *Let $\Sigma = (A_1, A_2, B_1, B_2, C, D)$ be a modally reachable 2D linear system with k inputs, $n - k$ outputs and dimension δ . Suppose that $X(z_1, z_2)$, defined in (2), has a $(\delta + n - k) \times (\delta + n - k)$ minor with degree δ , computed by picking up necessarily its first δ columns. Then Σ is a minimal ISO representation of $C(A_1, A_2, B_1, B_2, C, D)$.*

4 Input-State-Output Representations of Concatenated 2D Convolutional Codes

In this section we will study 2D convolutional codes that result from a series interconnection of two systems representations of other 2D convolutional codes. We will consider the second interconnection model defined in [8] for 1D systems.

Let

$$\Sigma_1 = \left(A_1^{(1)}, A_2^{(1)}, B_1^{(1)}, B_2^{(1)}, C^{(1)}, D^{(1)} \right)$$

and

$$\Sigma_2 = \left(A_1^{(2)}, A_2^{(2)}, B_1^{(2)}, B_2^{(2)}, C^{(2)}, D^{(2)} \right)$$

be two ISO representations of the 2D convolutional codes C_1 and C_2 , of rate k/m and $(m - k)/(n - k)$, respectively. Represent by $u^{(1)}$ and $u^{(2)}$ the input vectors of Σ_1 and Σ_2 , by $x^{(1)}$ and $x^{(2)}$ the state vectors of Σ_1 and Σ_2 and by $y^{(1)}$ and $y^{(2)}$ the output vectors of Σ_1 and Σ_2 , respectively. Let us consider the series interconnection of Σ_1 and Σ_2 by feeding the output vectors $y^{(1)}$ of Σ_1 as inputs of Σ_2 as represented in Fig. 1.

Theorem 4 *Let consider $C_1 = C \left(A_1^{(1)}, A_2^{(1)}, B_1^{(1)}, B_2^{(1)}, C^{(1)}, D^{(1)} \right)$ and $C_2 = C \left(A_1^{(2)}, A_2^{(2)}, B_1^{(2)}, B_2^{(2)}, C^{(2)}, D^{(2)} \right)$ two 2D convolutional codes of rate k/m and $(m - k)/(n - k)$, respectively.*

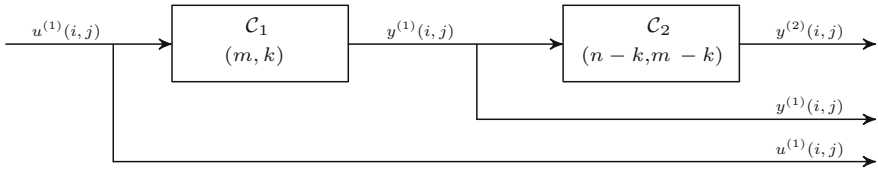


Fig. 1 Series concatenation of C_1 and C_2

Then the series interconnection of $\Sigma_1 = (A_1^{(1)}, A_2^{(1)}, B_1^{(1)}, B_2^{(1)}, C^{(1)}, D^{(1)})$ and $\Sigma_2 = (A_1^{(2)}, A_2^{(2)}, B_1^{(2)}, B_2^{(2)}, C^{(2)}, D^{(2)})$ by considering the inputs of Σ_2 to be the output vectors of Σ_1 and with code vector $v = \begin{bmatrix} y^{(2)} \\ v^{(1)} \end{bmatrix}$, where $v^{(1)}$ is the code vector of Σ_1 , is a 2D convolutional code with ISO representation $\Sigma = (A_1, A_2, B_1, B_2, C, D)$, given by

$$A_1 = \begin{bmatrix} A_1^{(2)} & B_1^{(2)} C^{(1)} \\ 0 & A_1^{(1)} \end{bmatrix}, \quad A_2 = \begin{bmatrix} A_2^{(2)} & B_2^{(2)} C^{(1)} \\ 0 & A_2^{(1)} \end{bmatrix}, \quad B_1 = \begin{bmatrix} B_1^{(2)} D^{(1)} \\ B_1^{(1)} \end{bmatrix},$$

$$B_2 = \begin{bmatrix} B_2^{(2)} D^{(1)} \\ B_2^{(1)} \end{bmatrix}, \quad C = \begin{bmatrix} C^{(2)} & D^{(2)} C^{(1)} \\ 0 & C^{(1)} \end{bmatrix}, \quad D = \begin{bmatrix} D^{(2)} D^{(1)} \\ D^{(1)} \end{bmatrix}.$$

The next theorem gives conditions to ensure the modal observability of the code obtained by concatenation. We will not present the proof here for lack of space. The proof follows a similar reasoning than Theorem IV.2. of [1].

Theorem 5 Consider two 2D systems $\Sigma_1 = (A_1^{(1)}, A_2^{(1)}, B_1^{(1)}, B_2^{(1)}, C^{(1)}, D^{(1)})$ and $\Sigma_2 = (A_1^{(2)}, A_2^{(2)}, B_1^{(2)}, B_2^{(2)}, C^{(2)}, D^{(2)})$ of dimension δ_1 and δ_2 , respectively. If Σ_1 and Σ_2 are modally observable, then the series interconnection of Σ_1 and Σ_2 (defined as in Theorem 4) is modally observable.

The next example shows that it is not sufficient that the 2D linear systems Σ_1 and Σ_2 are modally reachable to get the system obtained by series interconnection also modally reachable.

Example 1 Let α be a primitive element, with $\alpha^3 + \alpha + 1 = 0$, of the Galois field $\mathbb{F} = GF(8)$. Consider the 2D linear systems $\Sigma_1 = (A_1^{(1)}, A_2^{(1)}, B_1^{(1)}, B_2^{(1)}, C^{(1)}, D^{(1)})$ and $\Sigma_2 = (A_1^{(2)}, A_2^{(2)}, B_1^{(2)}, B_2^{(2)}, C^{(2)}, D^{(2)})$, where

$$A_1^{(1)} = A_2^{(1)} = [0], \quad B_1^{(1)} = B_2^{(1)} = [1], \quad C^{(1)} = [\alpha^4], \quad D^{(1)} = [\alpha^3],$$

$$A_1^{(2)} = A_2^{(2)} = [\alpha], \quad B_1^{(2)} = B_2^{(2)} = [1], \quad C^{(2)} = [\alpha^4], \quad D^{(2)} = [1].$$

Then Σ_1 and Σ_2 are modally reachable. In fact, it is easy to see that the matrices $[I_1 - A_1^{(1)}z_1 - A_2^{(1)}z_2 \quad B_1^{(1)}z_1 + B_2^{(1)}z_2]$ and $[I_1 - A_1^{(2)}z_1 - A_2^{(2)}z_2 \quad B_1^{(2)}z_1 + B_2^{(2)}z_2]$ are ℓFP .

Let $\Sigma = (A_1, A_2, B_1, B_2, C, D)$ be the 2D system obtained by series interconnection of Σ_1 and Σ_2 as defined in Theorem 4; then

$$A_1 = A_2 = \begin{bmatrix} \alpha & \alpha^4 \\ 0 & 0 \end{bmatrix}, \quad B_1 = B_2 = \begin{bmatrix} \alpha^3 \\ 1 \end{bmatrix}, \quad C = \begin{bmatrix} \alpha^4 & \alpha^4 \\ 0 & \alpha^4 \end{bmatrix}, \quad D = \begin{bmatrix} \alpha^3 \end{bmatrix}$$

The matrix $[I_2 - A_1z_1 - A_2z_2 \quad B_1z_1 + B_2z_2]$ is not ℓFP . In fact, there exists

$$\hat{u}(z_1, z_2) = \frac{1}{1 + \alpha(z_1 + z_2)} [1 + \alpha^2(z_1 + z_2) \quad \alpha + (1 + \alpha^2)(z_1 + z_2)]$$

which is not polynomial, such that $\hat{u}(z_1, z_2) [I_2 - A_1z_1 - A_2z_2 \quad B_1z_1 + B_2z_2]$ is polynomial. Then $[I_2 - A_1z_1 - A_2z_2 \quad B_1z_1 + B_2z_2]$ is not ℓFP , which means that Σ is not modally reachable.

The following theorem gives conditions on Σ_1 and Σ_2 to obtain the corresponding series interconnection modally reachable.

Theorem 6 Consider two 2D systems $\Sigma_1 = (A_1^{(1)}, A_2^{(1)}, B_1^{(1)}, B_2^{(1)}, C^{(1)}, D^{(1)})$ and $\Sigma_2 = (A_1^{(2)}, A_2^{(2)}, B_1^{(2)}, B_2^{(2)}, C^{(2)}, D^{(2)})$ of dimension δ_1 and δ_2 , respectively. If Σ_1 is modally reachable and the matrix $I_{\delta_2} - A_1^{(2)}z_1 - A_2^{(2)}z_2$ is unimodular, then the series interconnection of Σ_1 and Σ_2 (defined as in Theorem 4) is modally reachable.

Proof Assume that Σ_1 is modally reachable and the matrix $I_{\delta_2} - A_1^{(2)}z_1 - A_2^{(2)}z_2$ is unimodular. Attending to Definition 2, we have to prove that the matrix

$$T(z_1, z_2) = \begin{bmatrix} I_{\delta_2} - A_1^{(2)}z_1 - A_2^{(2)}z_2 & -B_1^{(2)}C^{(1)}z_1 - B_2^{(2)}C^{(1)}z_2 & B_1^{(2)}D^{(1)}z_1 + B_2^{(2)}D^{(1)}z_2 \\ 0 & I_{\delta_1} - A_1^{(1)}z_1 - A_2^{(1)}z_2 & B_1^{(1)}z_1 + B_2^{(1)}z_2 \end{bmatrix}$$

is ℓFP .

Let $\hat{u}(z_1, z_2) \in \mathbb{F}(z_1, z_2)^{1 \times (\delta_1 + \delta_2)}$ be such that $\hat{u}(z_1, z_2)T(z_1, z_2) \in \mathbb{F}[z_1, z_2]^{1 \times (\delta_1 + \delta_2 + k)}$. Suppose that $\hat{u}(z_1, z_2) = [\hat{u}_2(z_1, z_2)^T \hat{u}_1(z_1, z_2)^T]$ with $\hat{u}_2(z_1, z_2) \in \mathbb{F}(z_1, z_2)^{\delta_2}$. Then

$$\hat{u}_2(z_1, z_2)^T [I_{\delta_2} - A_1^{(2)}z_1 - A_2^{(2)}z_2] \in \mathbb{F}[z_1, z_2]^{1 \times \delta_2}$$

and, since $I_{\delta_2} - A_1^{(2)}z_1 - A_2^{(2)}z_2$ is unimodular, $\hat{u}_2(z_1, z_2) \in \mathbb{F}[z_1, z_2]^{\delta_2}$.

On the other hand,

$$\begin{aligned} & \hat{u}_2(z_1, z_2)^T \left[-B_1^{(2)}C^{(1)}z_1 - B_2^{(2)}C^{(1)}z_2 \quad B_1^{(2)}D^{(1)}z_1 + B_2^{(2)}D^{(1)}z_2 \right] \\ & + \hat{u}_1(z_1, z_2)^T \left[I_{\delta_1} - A_1^{(1)}z_1 - A_2^{(1)}z_2 \quad B_1^{(1)}z_1 + B_2^{(1)}z_2 \right] \in \mathbb{F}[z_1, z_2]^{1 \times (\delta_1 + k)} \end{aligned}$$

which implies that

$$\hat{u}_1(z_1, z_2)^T \left[I_{\delta_1} - A_1^{(1)}z_1 - A_2^{(1)}z_2 \quad B_1^{(1)}z_1 + B_2^{(1)}z_2 \right] \in \mathbb{F}[z_1, z_2]^{1 \times (\delta_1 + k)}$$

and, since Σ_1 is modally reachable, $\hat{u}_1(z_1, z_2) \in \mathbb{F}[z_1, z_2]^{\delta_1}$.

Therefore $\hat{u}(z_1, z_2)$ is in $\mathbb{F}[z_1, z_2]^{1 \times (\delta_1 + \delta_2)}$ and, by Lemma 1, $T(z_1, z_2)$ is ℓFP and thus Σ is modally reachable.

Remark 1 Note that if the matrix $I_{\delta_2} - A_1^{(2)}z_1 - A_2^{(2)}z_2$ is unimodular then Σ_2 is modally reachable. Moreover, this means that the code C_2 admits an encoder of the form $\begin{bmatrix} I \\ \tilde{G}(z_1, z_2) \end{bmatrix}$ and therefore is systematic.

We will now consider the concatenation of a 2D convolutional code C_1 of rate $1/2$ and degree δ_1 with a 2D convolutional code C_2 of rate $1/(n-1)$ and degree δ_2 and we will derive conditions on the ISO representations of C_1 and C_2 that will produce a minimal representation of concatenation code of C_1 and C_2 .

Theorem 7 Let $\Sigma_1 = (A_1^{(1)}, A_2^{(1)}, B_1^{(1)}, B_2^{(1)}, C^{(1)}, D^{(1)})$ be a ISO system with 1 input and 1 output and degree δ_1 and let $\Sigma_2 = (A_1^{(2)}, A_2^{(2)}, B_1^{(2)}, B_2^{(2)}, C^{(2)}, D^{(2)})$ be a ISO system with 1 input and $n-2$ outputs and degree δ_2 such that

$$A_1^{(1)} = \text{diag}(a_1, \dots, a_{\delta_1}), A_2^{(1)} = \text{diag}(b_1, \dots, b_{\delta_1}), B_1^{(1)} = \begin{bmatrix} p_1 \\ \vdots \\ p_{\delta_1} \end{bmatrix}, B_2^{(1)} = \begin{bmatrix} m_1 \\ \vdots \\ m_{\delta_1} \end{bmatrix}$$

$$A_1^{(2)} = \text{diag}(c_1, \dots, c_{\delta_2}), A_2^{(2)} = \text{diag}(d_1, \dots, d_{\delta_2}), B_1^{(2)} = \begin{bmatrix} s_1 \\ \vdots \\ s_{\delta_2} \end{bmatrix}, B_2^{(2)} = \begin{bmatrix} t_1 \\ \vdots \\ t_{\delta_2} \end{bmatrix}$$

with $a_i, b_i, p_i, m_i, c_k, d_k, s_k, t_k \in \mathbb{F} \setminus \{0\}$ and

- (a) $a_i b_j = a_j b_i$, $a_i \neq a_j$ and $b_i \neq b_j$, for $i \neq j$,
- (b) $c_k d_l = c_l d_k$, $c_k \neq c_l$ and $d_k \neq d_l$, for $k \neq l$,
- (c) $a_i d_k = b_i c_k$, $a_i \neq c_k$ and $b_i \neq d_k$, for all i and for all k ,
- (d) $a_i m_i = b_i l_i$, for all i ,
- (e) $c_k t_k = d_k s_k$, for all k ,

with $i, j \in \{1, \dots, \delta_1\}$, $k, l \in \{1, \dots, \delta_2\}$. Then Σ_1 and Σ_2 are a minimal representation of C_1 and C_2 , respectively, and the series interconnection Σ of Σ_1 and Σ_2 is a minimal representation of the concatenation code of C_1 and C_2 .

Proof Consider $X_1(z_1, z_2)$, $X_2(z_1, z_2)$ and $X(z_1, z_2)$ the matrices defined in (2) for the 2D linear systems Σ_1 , Σ_2 and Σ , respectively, and let

$$Y_1(z_1, z_2) = \begin{bmatrix} I_{\delta_1} - A_1^{(1)}z_1 - A_2^{(1)}z_2 & -B_1^{(1)}z_1 - B_2^{(1)}z_2 \end{bmatrix}.$$

Conditions (a) and (d) imply that $Y_1(\lambda_1, \lambda_2)$ is full row rank for all $\lambda_1, \lambda_2 \in \overline{\mathbb{F}}$. Thus $Y_1(z_1, z_2)$ is ℓZP , which implies that $X_1(z_1, z_2)$ is ℓFP . Applying the same reasoning, we show that $X_2(z_1, z_2)$ and $X(z_1, z_2)$ are also ℓFP . Moreover, it is easy to see that $\det \left(I_{\delta_i} - A_1^{(i)}z_1 - A_2^{(i)}z_2 \right)$ has degree δ_i , $i = 1, 2$, and $\det \left(I_{\delta_1+\delta_2} - A_1z_1 - A_2z_2 \right)$ has degree $\delta_1 + \delta_2$. The result follows from Theorem 3.

The distance of a code determines its robustness in terms of error correction. It can be shown that the code obtained by the concatenation of two convolutional codes C_1 and C_2 defined as in Theorem 7 has higher distance than C_2 . More investigation must be done to determine at what extent this distance can be improved.

Acknowledgments The three authors were supported by Portuguese funds through the *Center for Research and Development in Mathematics and Applications* (CIDMA), and *The Portuguese Foundation for Science and Technology* (FCT—Fundação para a Ciência e a Tecnologia), within project UID/MAT/04106/2013.

References

1. Climent, J.-J., Napp, D., Pinto, R., Simões, R.: Series concatenation of 2D convolutional codes. In: Proceedings IEEE 9th International Workshop on Multidimensional (nD) Systems (nDS) (2015)
2. Lévy, B.C.: 2d-polynomial and rational matrices and their applications for the modelling of 2-d dynamical systems. Ph.D. Dissertation, Department of Electrical Engineering, Stanford University, Stanford, CA (1981)
3. Rocha, P.: Structure and representation of 2-d systems. Ph.D. Dissertation, University of Groningen, Groningen, The Netherlands (1990)
4. Fornasini, E., Valcher, M.E.: Algebraic aspects of two-dimensional convolutional codes. *IEEE Trans. Inf. Theory* **40**(4), 1068–1082 (1994)
5. Fornasini, E., Marchesini, G.: Structure and properties of two-dimensional systems. In: Tzafestas, S.G. (ed.) *Multidimensional Systems, Techniques and Applications*, pp. 37–88 (1986)
6. Valcher, M.E., Fornasini, E.: On 2D finite support convolutional codes: an algebraic approach. *Multidimension. Syst. Signal Process.* **5**, 231–243 (1994)
7. Napp, D., Perea, C., Pinto, R.: Input-state-output representations and constructions of finite support 2D convolutional codes. *Adv. Math. Commun.* **4**(4), 533–545 (2010)
8. Climent, J.-J., Herranz, V., Perea, C.: A first approximation of concatenated convolutional codes from linear systems theory viewpoint. *Linear Algebra Appl* **425**, 673–699 (2007)

MDP Periodically Time-Varying Convolutional Codes

Ricardo Pereira, Paula Rocha and Diego Napp

Abstract In this paper we use some classical ideas from linear systems theory to analyse convolutional codes. In particular, we exploit input-state-output representations of periodic linear systems to study periodically time-varying convolutional codes. In this preliminary work we focus on the column distance of these codes and derive explicit necessary and sufficient conditions for an $(n, 2, 1)$ periodically time-varying convolutional code to have Maximum Distance Profile (MDP).

Keywords Convolutional codes · Periodically codes · MDP codes

1 Introduction

Convolutional codes [1] are an important type of error correcting codes that can be represented as a time-invariant discrete linear system over a finite field [2]. They are used to achieve reliable data transfer, for instance, in mobile communications, digital video and satellite communications [3]. In particular, maximum distance profile (MDP) convolutional codes are relevant in applications since they have the potential to correct a maximal number of errors per time interval.

In contrast to block codes, the mathematical theory for the construction of good convolutional codes is not fully exploited. In fact, most convolutional codes used in practice have been found by systematic computer search and their distance properties must be also computed by full search. In recent years a great deal of effort has been

R. Pereira (✉) · D. Napp

CIDMA—Center for Research and Development in Mathematics and Applications,
Department of Mathematics, University of Aveiro, Aveiro, Portugal
e-mail: ricardopereira@ua.pt

D. Napp

e-mail: diego@ua.pt

P. Rocha

SYSTEC, Faculty of Engineering, University of Porto, Porto, Portugal
e-mail: mprocha@fe.up.pt

dedicated to develop constructions of non-binary convolutional codes having good distance [4, 5].

The idea of considering time-varying and, in particular, periodically time-varying convolutional codes has attracted the attention of several researchers [6, 7]. One of the advantages of this type of codes is that they can have better distance properties than the best time-invariant convolutional code of the same rate and total encoder memory [8, 9].

In this paper we start by presenting the necessary concepts about convolutional code within a input-state-output approach. Then we introduce periodically time-varying convolutional codes and find necessary and sufficient conditions on the subcodes to obtain a $(n, 2, 1)$ MDP time-varying convolutional code combining (possibly) non MDP subcodes.

2 Definitions and Basic Properties

Let \mathbb{F} be a finite field. Let n, k and δ be positive integers with $k < n$. Following [10], a rate k/n convolutional code C of degree δ can be described by the linear system governed by the equations:

$$\begin{cases} x_{t+1} = Ax_t + Bu_t \\ y_t = Cx_t + Du_t \\ v_t = \begin{pmatrix} y_t \\ u_t \end{pmatrix}, \quad x_0 = 0 \end{cases}, \quad t = 0, 1, 2, \dots, \quad (1)$$

where $A \in \mathbb{F}^{\delta \times \delta}$, $B \in \mathbb{F}^{\delta \times k}$, $C \in \mathbb{F}^{(n-k) \times \delta}$ and $D \in \mathbb{F}^{(n-k) \times k}$. Moreover we assume that the pair (A, B) is controllable and the pair (A, C) is observable. We call $x_t \in \mathbb{F}^\delta$ the *state vector*, $u_t \in \mathbb{F}^k$ the *information vector*, $y_t \in \mathbb{F}^{n-k}$ the *parity vector* and $v_t \in \mathbb{F}^n$ the *code vector*. The associated code consists of all the finite sequences of code vectors, called *codewords*, produced by (1). We will refer to such a code as an (n, k, δ) -code and (A, B, C, D) is its input-state-output representation.

The *Hamming weight* of a vector $v \in \mathbb{F}^n$ is defined to be the number of nonzero components of v and is denoted by $\text{wt}(v)$. The weight of a codeword is the sum of the Hamming weights of all the code vectors that form that word.

It follows from our assumptions that in this paper we are concerned only with finite-weight codewords. These are defined as follows:

Definition 1 A sequence $\{v_t = \begin{pmatrix} y_t \\ u_t \end{pmatrix} \in \mathbb{F}^n | t = 0, 1, 2, \dots\}$ represents a finite-weight codeword if

1. Eq. (1) is satisfied for all $t = 0, 1, 2, \dots$;
2. There exists an integer j such that $u_t = 0$ for $t \geq j + 1$.

Due to the observability of (A, C) , this definition implies that $y_t = 0$ for $t \geq j + 1$ and $x_{j+1} = 0$; the codeword, therefore, has finite weight.

Important distance measures of a code are the *free distance* and the *column distance*. They are defined in the sequel as in [11] by means of this input-state-output approach.

Definition 2 The free distance of the code C described by (1) is defined as

$$d_{free}(C) = \min \left\{ \sum_{t=0}^{\infty} \text{wt}(u_t) + \sum_{t=0}^{\infty} \text{wt}(y_t) \right\},$$

where the minimum weight is to be taken over all nonzero codewords.

Rosenthal and Smarandache [12] showed that the free distance of an (n, k, δ) convolutional code is upper bounded by

$$d_{free}(C) \leq (n - k) \left(\left\lfloor \frac{\delta}{k} \right\rfloor + 1 \right) + \delta + 1.$$

This bound is called the *generalized Singleton bound*.

In this paper we focus on the following more local distance measure.

Definition 3 The j th column distance of the code C described by (1) is defined as

$$d_j^c(C) = \min_{u_0 \neq 0} \left\{ \sum_{t=0}^j \text{wt}(u_t) + \sum_{t=0}^j \text{wt}(y_t) \right\},$$

where the minimum weight is to be taken among all the codewords that start with a nonzero information vector.

The column distances satisfy

$$d_0^c \leq d_1^c \leq \dots \leq \lim_{j \rightarrow \infty} d_j^c = d_{free}(C),$$

and have the following upper bounds [11].

Proposition 1 For every $j \in \mathbb{N}_0$, we have

$$d_j^c(C) \leq (n - k)(j + 1) + 1.$$

It can be shown [5] that if the upper bound is attained for a certain j , then it is attained for all the preceding ones. Moreover, since no column distance can exceed the generalized Singleton bound, the largest integer j for which the previous bound can be attained is for $j = L$, with

$$L = \left\lfloor \frac{\delta}{k} \right\rfloor + \left\lfloor \frac{\delta}{n-k} \right\rfloor.$$

Definition 4 An (n, k, δ) -convolutional code C is said to have *maximum distance profile (MDP)* if

$$d_L^c(C) = (n-k)(L+1) + 1, \quad L = \left\lfloor \frac{\delta}{k} \right\rfloor + \left\lfloor \frac{\delta}{n-k} \right\rfloor.$$

MDP convolutional codes are characterized by the property that their initial column distances increase as rapidly as possible for as long as possible and therefore they are very important since they have the potential to correct a maximal number of errors per time interval [11]. Existence and characterizations of these codes in terms of the matrices (A, B, C, D) can be found in [11]. Here we present necessary and sufficient conditions for the periodically time-varying convolutional codes introduced in the next section to be MDP.

3 Periodically Time-Varying Convolutional Codes

In this section we start by defining periodically time-varying convolutional codes. Assume now that the matrices A_t, B_t, C_t and D_t at time t are of sizes $\delta \times \delta$, $\delta \times k$, $(n-k) \times \delta$ and $(n-k) \times k$, respectively. A time-varying convolutional code can be defined by means of the system

$$\begin{cases} x_{t+1} = A_t x_t + B_t u_t \\ y_t = C_t x_t + D_t u_t \\ v_t = \begin{pmatrix} y_t \\ u_t \end{pmatrix}, \quad x_0 = 0 \end{cases}, \quad t = 0, 1, 2, \dots, \quad (2)$$

If the matrices change periodically with periods τ_A, τ_B, τ_C and τ_D respectively, (that is $A_{\tau_A+t} = A_t, B_{\tau_B+t} = B_t, C_{\tau_C+t} = C_t$ and $D_{\tau_D+t} = D_t$ for all t) then we have a *periodically time-varying convolutional code* of period $\tau = \text{lcm}(\tau_A, \tau_B, \tau_C, \tau_D)$. For each fixed $t_0 \in \{0, 1, \dots, \tau-1\}$ the code represented by $(A_{t_0}, B_{t_0}, C_{t_0}, D_{t_0})$ is called a *subcode* of the time-varying convolutional code (2) [13]. Note that, contrary to what the name seems to indicate, the codewords generated by the ‘‘subcode’’ do not constitute a subset of the time-varying code.

Our aim is to find necessary and sufficient conditions on the subcodes to obtain a MDP time-varying convolutional code, combining (possibly) non MDP subcodes. The $(n, 1, 1)$ case was already studied in [13]. Here we present the $(n, 2, 1)$ case.

3.1 MDP ($n, 2, 1$) Convolutional Codes

In this section we assume that our convolutional codes are over a finite field \mathbb{F} with a large enough number of elements. Consider a periodically time-varying code of period τ . Then we have the matrices

$$A_t = [a_t], \quad B_t = [b_{t,1} \ b_{t,2}], \quad C_t = \begin{bmatrix} c_{t,1} \\ c_{t,2} \\ \vdots \\ c_{t,n-2} \end{bmatrix},$$

$$D_t = \left[\begin{array}{c|c} d_{t,11} & d_{t,12} \\ d_{t,21} & d_{t,22} \\ \vdots & \vdots \\ d_{t,(n-2)1} & d_{t,(n-2)2} \end{array} \right] =: [D_{t,1} | D_{t,2}],$$

with $t = 0, 1, \dots, \tau - 1$.

According to Definition 4, since

$$L = \left\lfloor \frac{\delta}{k} \right\rfloor + \left\lfloor \frac{\delta}{n-k} \right\rfloor = \left\lfloor \frac{1}{2} \right\rfloor + \left\lfloor \frac{1}{n-2} \right\rfloor = \begin{cases} 0, & n > 3 \\ 1, & n = 3 \end{cases},$$

this convolutional code is MDP if

$$d_0^c(C) = (n-2)(0+1) + 1 = n-1$$

when $n > 3$ and

$$d_1^c(C) = (3-2)(1+1) + 1 = 3$$

when $n = 3$.

- Suppose first that $n > 3$. By Definition 3 and Eq. (2) we have

$$\begin{aligned} d_0^c(C) &= \min_{u_0 \neq 0} \{ \text{wt}(u_0) + \text{wt}(y_0) \} \\ &= \min_{u_0 \neq 0} \{ \text{wt}(u_0) + \text{wt}(C_0 x_0 + D_0 u_0) \}, \quad x_0 = 0 \\ &= \min_{u_0 \neq 0} \left\{ \text{wt} \left(\begin{bmatrix} u_{0,1} \\ u_{0,2} \end{bmatrix} \right) + \text{wt} (D_{0,1} u_{0,1} + D_{0,2} u_{0,2}) \right\}, \end{aligned}$$

where $u_0 = \begin{bmatrix} u_{0,1} \\ u_{0,2} \end{bmatrix}$.

Since the minimum is taken over $u_0 \neq 0$ then $\text{wt}(u_0)$ can be either 1 or 2. We study these two cases separately.

If $\text{wt}(u_0) = 1$, assume without loss of generality that $u_{0,1} \neq 0$ and $u_{0,2} = 0$. If $D_{0,1}$ has a zero element, then $\text{wt}(D_{0,1}u_{0,1}) \leq n - 3$,

$$\text{wt}(u_0) + \text{wt}(D_{0,1}u_{0,1}) \leq 1 + n - 3 = n - 2 < n - 1,$$

and the code is not MDP. The same happens for $D_{0,2}$. This implies that all entries of the matrix D_0 must be nonzero. In this case $\text{wt}(D_{0,1}u_{0,1}) = n - 2$ and hence $\text{wt}(u_0) + \text{wt}(y_0) = 1 + n - 2 = n - 1$.

If $\text{wt}(u_0) = 2$, $\text{wt}(D_{0,1}u_{0,1}) = \text{wt}(D_{0,2}u_{0,2}) = n - 2$, but adding both terms can provoke cancellations and the weight decreases. A necessary condition to obtain the desired result is the following. If

$$d_{0,l1}d_{0,m2} - d_{0,l2}d_{0,m1} \neq 0, \forall l, m = 1, \dots, n - 2, l \neq m,$$

at most one component of $D_{0,1}u_{0,1} + D_{0,2}u_{0,2}$ can be zero and so its weight is greater or equal than $n - 3$. Thus, $\text{wt}(u_0) + \text{wt}(y_0) \geq 2 + n - 3 = n - 1$.

This shows that for $n > 3$, $d_0^c(C) = n - 1$, i.e., the convolutional code is MDP.

- Suppose now that $n = 3$. Again by Definition 3 and Eq. (2) we have

$$\begin{aligned} d_1^c(C) &= \min_{u_0 \neq 0} \left\{ \sum_{i=0}^1 \text{wt}(u_i) + \sum_{i=0}^1 \text{wt}(y_i) \right\} \\ &= \min_{u_0 \neq 0} \{ \text{wt}(u_0) + \text{wt}(u_1) + \text{wt}(y_0) + \text{wt}(y_1) \} \\ &= \min_{u_0 \neq 0} \{ \text{wt}(u_0) + \text{wt}(u_1) + \text{wt}(C_0x_0 + D_0u_0) + \text{wt}(C_1x_1 + D_1u_1) \}, x_0 = 0 \\ &= \min_{u_0 \neq 0} \left\{ \text{wt} \left(\begin{bmatrix} u_{0,1} \\ u_{0,2} \end{bmatrix} \right) + \text{wt} \left(\begin{bmatrix} u_{1,1} \\ u_{1,2} \end{bmatrix} \right) + \text{wt} (d_{0,11}u_{0,1} + d_{0,12}u_{0,2}) \right. \\ &\quad \left. + \text{wt} (c_{1,1}(b_{0,1}u_{0,1} + b_{0,2}u_{0,2}) + d_{1,11}u_{1,1} + d_{1,12}u_{1,2}) \right\} \end{aligned}$$

We want to establish conditions such that $d_1^c(C) = 3$. Since the minimum is taken over $u_0 \neq 0$ then $\text{wt}(u_0)$ can be either 1 or 2 and therefore $\text{wt}(u_0) + \text{wt}(u_1) \in \{1, 2, 3, 4\}$.

If $\text{wt}(u_0) + \text{wt}(u_1)$ is 3 or 4, obviously $\text{wt}(u_0) + \text{wt}(u_1) + \text{wt}(y_0) + \text{wt}(y_1) \geq 3$.

If $\text{wt}(u_0) + \text{wt}(u_1) = 1$, then $\text{wt}(u_1) = 0$ and $\text{wt}(u_0) = 1$ and assume without loss of generality that $u_{0,1} \neq 0$ and $u_{0,2} = 0$. Then, it is easy to check that

$$\text{wt}(u_0) + \text{wt}(u_1) + \text{wt}(y_0) + \text{wt}(y_1) = 1 + 0 + 1 + 1 = 3,$$

if and only if the elements $b_{0,1}, c_{1,1}$ and $d_{0,11}$ are nonzero. Note that, if $u_{0,1} = 0$ and $u_{0,2} \neq 0$, the previous condition holds when the elements $b_{0,2}, c_{1,1}$ and $d_{0,12}$ are nonzero.

When $\text{wt}(u_0) + \text{wt}(u_1) = 2$, two different situations can occur which will be studied separately. If $\text{wt}(u_0) = \text{wt}(u_1) = 1$, analogously to the previous cases it follows that $\text{wt}(u_0) + \text{wt}(u_1) + \text{wt}(y_0) + \text{wt}(y_1) \geq 3$.

If $\text{wt}(u_0) = 2$ and $\text{wt}(u_1) = 0$, then

$$\begin{aligned} & \text{wt}(u_0) + \text{wt}(u_1) + \text{wt}(y_0) + \text{wt}(y_1) \\ &= 2 + \text{wt}(d_{0,11}u_{0,1} + d_{0,12}u_{0,2}) + \text{wt}(c_{1,1}(b_{0,1}u_{0,1} + b_{0,2}u_{0,2})). \end{aligned}$$

In this situation we need that at least one of these weights be nonzero, which implies that

$$d_{0,11}b_{0,2} - d_{0,12}b_{0,1} \neq 0, \quad c_{1,1} \neq 0.$$

This leads to the following result.

Theorem 1 *The $(n, 2, 1)$ periodically time-varying convolutional code (2) is MDP if and only if*

(a) *When $n > 3$, all the entries of the matrix D_0 are nonzero and*

$$d_{0,l}d_{0,m2} - d_{0,l2}d_{0,m1} \neq 0, \quad \forall l, m = 1, \dots, n-2, \quad l \neq m.$$

(b) *When $n = 3$, all the entries of matrices B_0, C_1 and D_0 are nonzero and*

$$d_{0,11}b_{0,2} - d_{0,12}b_{0,1} \neq 0.$$

Example 1 Let C be a time-varying code of period $\tau = 2$ over the finite field \mathbb{F}_7 constituted by the $(3, 2, 1)$ subcodes

$$C_0 = (A_0, B_0, C_0, D_0), \quad C_1 = (A_1, B_1, C_1, D_1)$$

where

$$A_0 = A_1 = [1], \quad B_0 = [1 \ 2], \quad B_1 = [2 \ 3],$$

$$C_0 = C_1 = [1], \quad D_0 = [2 \ 1], \quad D_1 = [4 \ 6].$$

By Proposition 1. (b) this code is MDP since

$$d_{0,11}b_{0,2} - d_{0,12}b_{0,1} = 2 \times 2 - 1 \times 1 \neq 0.$$

However, the subcode C_1 is not MDP, since by Definition 4 we have that $L = 1$ but $d_1^c(C_1) < 3$. Indeed, considering the inputs $u_0 = \begin{bmatrix} 2 \\ 1 \end{bmatrix}$ and $u_1 = \begin{bmatrix} 0 \\ 0 \end{bmatrix}$, we have that

$$\begin{aligned}
& \text{wt}(u_0) + \text{wt}(u_1) + \text{wt}(y_0) + \text{wt}(y_1) \\
&= \text{wt}(u_0) + \text{wt}(u_1) + \text{wt}(C_1x_0 + D_1u_0) + \text{wt}(C_1x_1 + D_1u_1), \quad x_0 = 0 \\
&= 2 + 0 + \text{wt}(D_1u_0) + \text{wt}(C_1B_1u_0) = 2 + 0 + 0 + 0 = 2.
\end{aligned}$$

The previous example showed that it is possible to obtain an MDP time-varying convolutional combining time-invariant subcodes which are not all MDP.

4 Conclusions

In this paper we used input-state-output representations of periodic linear systems to study periodically time-varying convolutional codes. In particular, we derived explicit necessary and sufficient conditions for an $(n, 2, 1)$ periodically time-varying convolutional code to have Maximum Distance Profile (MDP). The extension of these results to codes with other rates is under investigation.

Acknowledgments This work was supported in part by the Portuguese Foundation for Science and Technology (FCT—Fundação para a Ciência e a Tecnologia), through CIDMA—Center for Research and Development in Mathematics and Applications, within project UID/MAT/04106/2013. This work was financially supported by: Project POCI-01-0145-FEDER-006933—SYSTEC—Research Center for Systems and Technologies—funded by FEDER funds through COMPETE 2020—Programa Operacional Competitividade e Internacionalização (POCI)—and by national funds through FCT—Fundação para a Ciência e a Tecnologia.

References

1. Johannesson, R., Zigangirov, K.S.: *Fundamentals of Convolutional Coding*. IEEE press, New York (1999)
2. Rosenthal, J.: Connections between linear systems and convolutional codes. In: Marcus B., Rosenthal, J. (eds.) *Codes, Systems, and Graphical Models*, vol. 123, pp. 39–66. Springer, New York (2001)
3. Viterbi, A.J.: Convolutional codes and their performance in communication systems. *IEEE Trans. Commun. Technol.* **19**(5), 751–772 (1971)
4. Almeida, P., Napp, D., Pinto, R.: A new class of superregular matrices and MDP convolutional codes. *Linear Algebra Appl.* **439**(7), 2145–2147 (2013)
5. Gluesing-Luerssen, H., Rosenthal, J., Smarandache, R.: Strongly-MDS convolutional codes. *IEEE Trans. Inf. Theory* **52**(2), 584–598 (2006)
6. Climent, J.-J., Herranz, V., Perea C., Tomás, V.: A systems theory approach to periodically time-varying convolutional codes by means of their invariant equivalent. In: Bras-Amorós, M., Høholdt, T. (eds.) *Applied Algebra, Algebraic Algorithms and Error-Correcting Codes*, vol. 5527, pp. 73–82. Springer, Heidelberg (2009)
7. Hu, Q., Perez, L.C.: Some periodic time-varying convolutional codes with free distance achieving the Heller bound. In: *Proceedings of the IEEE International Symposium on Information Theory*, p. 247 (2001)
8. Lee, P.J.: There are many good periodically time-varying convolutional codes. *IEEE Trans. Inf. Theory* **35**(2), 460–463 (1989)

9. Mooser, M.: Some periodic convolutional codes better than any fixed code. *IEEE Trans. Inf. Theory* **29**(5), 750–751 (1983)
10. Rosenthal, J., Schumacher, J.M., York, E.V.: On behaviors and convolutional codes. *IEEE Trans. Inf. Theory* **42**(6), 1981–1991 (1996)
11. Hutchinson, R., Rosenthal, J., Smarandache, R.: Convolutional codes with maximum distance profile. *Syst. Control Lett.* **54**(1), 53–63 (2005)
12. Rosenthal, J., Smarandache, R.: Maximum distance separable convolutional codes. *Appl. Algebra Eng. Commun. Comput.* **10**, 15–32 (1999)
13. Tomás, V.: Complete-MDP convolutional codes over the erasure channel. PhD Thesis, University of Alicante (2010)

Periodic Event-Triggered Swing-Up Control of the Inverted Pendulum

E. Aranda-Escolástico, F. Gordillo, M. Guinaldo and S. Dormido

Abstract In this paper, a novel strategy for swinging up an inverted pendulum is proposed. The strategy combines an energy-based control law with an event triggering condition to minimize transmissions, protect actuators and save energy. In addition, the strategy is periodic event-triggered, which provides two main advantages: An analytical way to determine a priori the sampling period to guarantee the appropriate behavior and an easy implementation in real prototypes.

1 Introduction

The inverted pendulum is an interesting system due to its peculiar behavior. Its non-linear nature has made the pendulum to be used as a common benchmark in the Control Theory. In the last decades, different strategies have been proposed to swing-up and to stabilize the inverted pendulum [2, 5, 15, 16]. One of the most famous was developed by Åström and Furuta [1], in which the control signal to balance the system to the upright position is computed based on the energy of the pendulum. However, these control laws are designed for continuous systems without consider-

This work was supported by Spanish Ministry of Economy and Competitivity under projects DPI2012-31303 and DPI2011-27818-C02-02.

E. Aranda-Escolástico (✉) · M. Guinaldo · S. Dormido
Department of Computer Science and Automatic Control, Universidad Nacional de Educación a Distancia (UNED), Madrid, Spain
e-mail: earandae@bec.uned.es

M. Guinaldo
e-mail: mguinaldo@dia.uned.es

S. Dormido
e-mail: sdormido@dia.uned.es

F. Gordillo
Department of Systems Engineering and Automatic Control,
Universidad de Sevilla, Sevilla, Spain
e-mail: gordillo@us.es

ing that discrete implementations are the most common in digital platforms. In such situations, it is generally assumed that the sampling period is small enough so that the behavior of the discrete system approaches fairly well the continuous case [3]. Moreover, the way many control engineers choose the sampling period is based on the rule of thumb that says that the sampling frequency should be at least ten times the closed loop bandwidth. In this regard, to the best of our knowledge, there are no analytical results to set the value of the sampling period in a general case.

Over the past decades, the growth of communication technologies attracted the interest of the control community. The use of a shared network to connect decentralized control elements promised improvements in terms of more flexible architectures, reduced installation costs and higher reliability than traditional communication technologies. The problems associated to such a change of paradigm also proved to be challenging [14]. Indeed, communication through a shared network is imperfect and may be affected by bandwidth limitations, delays, packet dropouts, or quantization [11]. For this reasons, sampling appears as a problem of the channel. A correct choice of the sampling instants will help to maximize the available bandwidth in those cases. In this regard, event-based control has been shown to be a good alternative to periodic control since helps to save network and computational resources [10, 13, 17, 18]. The main idea of event-based control systems is that the information is exchanged in the control loop only when a condition of the state is violated.

In this work, a novel event-based control strategy for the inverted pendulum is proposed. In mechanical system such as the inverted pendulum, event-based control not only helps to reduce the communication in the control loop, but also protects actuators from frequent wear and tear [7]. In addition, this strategy allows to take the advantages of on-off control laws but without falling into chattering. The designed sampling strategy, unlike what is showed in [4], is periodic event-triggered [9], that is, the event condition is only checked at instances of time given by a fix rate, and the plant will be sampled only at a subset of those instances, when the event condition is violated. The advantages of this periodic event-triggered strategy are twofold. On the one hand, it facilitates the design and the implementation, since it provides an analytical way of determining the sampling period for the system. On the other hand, in a networked framework, the knowledge of the minimum inter-event time gives an idea of the network delays tolerated by the system [8, 12]. Hence, the main contributions of this work can be summarized in: (i) An improvement of the control law in terms of waste of energy and communication resources, and protection of the elements of the plant, while chattering is avoided. (ii) A theoretical criteria to decide the sampling period which guarantees the desired behavior of the system.

The rest of the paper is organized as follows: In Sect. 2, the event-based control and the control law for the inverted pendulum are presented. Section 3 describes a periodic event-triggering strategy for the swing-up. In Sect. 4, an application example is presented. Finally, Sect. 5 provides the conclusions.

2 Preliminaries

2.1 Event-Based Control

Consider the dynamical system $\dot{x}(t) = f(x(t), u(t))$, where $x \in \mathbb{R}^n$ is the state and $u \in \mathbb{R}^m$ is the input signal. The input signal $u = g(x(t))$ is designed to allow the system to reach the desired control objective. The idea of the event-based control consists in transmitting the signal to the plant only if a certain condition is verified:

$$\epsilon(x(t), x(t_k)) \leq 0, \quad (1)$$

being t_k the time instants at which the events have been generated. Hence, $\dot{x}(t) = f(x(t), u(t_k))$, $\forall t \in [t_k, t_{k+1})$, being $t_{k+1} = \min(t > t_k | \epsilon(x(t), x(t_k)) \leq 0)$.

Now consider that the controller is implemented on a digital platform and the measurements are sent to the controller only at certain instants ℓh , being h the sampling period. As consequence, the set of instants t_k results a subset of the sampling instants. Then, the condition (1) turns into:

$$\epsilon(x(\ell h), x(t_k)) \leq 0 \quad (2)$$

and $t_{k+1} = \min(\ell h > t_k | \epsilon(x(\ell h), x(t_k)) \leq 0)$. The conjunction of a condition of the form (2) with the following control law provides the periodic-event triggering scheme.

2.2 Swing-Up Control Law

Let us consider the following simple pendulum model:

$$\ddot{x}_1 = \frac{mgl}{J} \sin x_1 - \frac{ml}{J} u \cos x_1, \quad \dot{x}_1 = x_2, \quad (3)$$

where m is the mass of the pendulum, l is the length of the pendulum, J is the momentum of inertia of the pendulum, g is the gravitational acceleration and u is the acceleration of the pivot. x_1 and x_2 are the states variables of the plant and correspond to the angular position and velocity of the pendulum, respectively. The energy of the system is

$$E = J \frac{x_2^2}{2} + mgl (\cos x_1 - 1), \quad (4)$$

where the origin is the zero of potential energy. The Lyapunov function candidate can be chosen such as $V = E^2/2$. Its derivative is $\dot{V} = E\dot{E} = E(Jx_2\dot{x}_2 - mgl\dot{x}_1 \sin x_1) = -mlEx_2u \cos x_1$, which is negative (except for $x_2 = 0$ or $x_1 = \pm\frac{\pi}{2}$, where it is 0) with the following control law

$$u = \lambda E \text{sign}(x_2 \cos x_1). \quad (5)$$

The pendulum approaches to the homoclinic orbit [6] following an spiral during the swing-up movement until the unstable equilibrium position [1].

A simpler control law, that however it may cause chattering [1], is

$$u = u_{\max} \text{sign}(Ex_2 \cos x_1). \quad (6)$$

3 Main Results

3.1 Event-Based Swing-Up Strategy

An event-based strategy can be followed to reduce the communication with the actuators while control law (5) is used to avoid the chattering. As explained in Sect. 1, the Lyapunov function decreases as long as the sign of the input signal is equal to $\text{sign}(x_2 \cos x_1)$. Hence, consider simply the triggering condition:

$$u(t)u(t_k) \leq 0, \quad (7)$$

where $u(t)$ is input signal computed at the current time and $u(t_k)$ is the input signal at the last event occurrence. Then, the following theorem can be stated.

Theorem 1 *Given system (3) and for any initial condition different from the downward position, the energy (4) tends to the energy value of the origin with control law (5) and under the triggering condition (7).*

Proof If $u = u(t)$ given by (5) is replaced with $u(t_k)$ in \dot{V} , it follows straightforward that (7) makes $\dot{V}(t) < 0$ for $x_2(t) \neq 0$ and $\cos x_1(t) \neq 0$ because $\text{sign}(x_2(t) \cos x_1(t)) = \text{sign}(x_2(t_k) \cos x_1(t_k))$ and the sign of the energy remains negative if the pendulum is in the homoclinic orbit. Since the pendulum cannot maintain the horizontal position and using LaSalle arguments it can be concluded that the only possibility is that the energy reaches the desired value. \square

The triggering condition produces a behavior similar to (6) since its value does not alter until it changes its sign, but with the difference that its absolute value does vary in each commutation due to the change in the value of the energy.

3.2 Discrete Implementation

In this case, the triggering condition is checked only at certain instants:

$$u(\ell h)u(t_k) \leq 0, \quad (8)$$

where h is the sampling period with $\ell \in \mathbb{N}$. As before, the control signal remains constant between two samplings. However, the control signal will not change its sign abruptly in the points $x_2 = 0$ and $x_1 = \pm \frac{\pi}{2}$ as it is desired. This produces that if it is updated with a sampling period, then there are intervals where the Lyapunov function is increasing. Logically, if the sampling period is small, then the pathological intervals will be small and the behavior will approximate to the continuous case. In this work, a theoretical criteria is proposed to choose the sampling period proving that the Lyapunov function is decreasing in each swing of the pendulum. First of all, the following assumptions are made:

Assumption 1 The control signal is saturated by $|u| \leq u_{\max}$.

Assumption 2 The initial condition is not the downward equilibrium. This is a common assumption in the swing-up strategies regardless of the event-based strategy or the discrete-time implementation. In addition, if the pendulum is sufficiently separated from the downward position, we can guarantee that at least one commutation is produced in a semi-period (we consider a semi-period the interval between two states with velocity $x_2 = 0$).

Assumption 3 The pendulum does not need to reach completely the homoclinic orbit since the control law can be switched to a linear feedback law for the stabilization once the state is close enough to the origin.

Assumption 4 Initial conditions outside the region limited by the homoclinic orbit are not considered since the pendulum is supposed to start near to the downward position.

Considering the following definitions:

$$\Delta V_1 := (2m^2 g l^2) \Delta x_2 u_{\max} h \quad (9)$$

$$\Delta V_2 := (m^2 g l^2) \Delta x_2 u_{\max} h = \frac{\Delta V_1}{2} \quad (10)$$

$$\Delta V_3 := \left(m^2 g l^2 \left(\cos \left(\frac{\pi}{2} - \Delta x_1 \right) + 1 \right) \right) \bar{x}_2 h \quad (11)$$

where \bar{x}_2 is a parameter to be determined later and being \bar{E} (\bar{E}) the minimum (maximum) energy allowed for the initial conditions.

Theorem 2 *Given an initial set of initial conditions $\Omega = \{E \in [E, \bar{E}]\}$, the system (3) tends to the homoclinic orbit at least until it gains energy \bar{E} with control law (5) and triggering condition (8), if the sampling period satisfies:*

$$\begin{aligned} |\Delta V| - \Delta V_1 &> 0 \\ |\Delta V| - \Delta V_2 - 2\Delta V_3 &> 0 \quad \forall x \in \Omega, \end{aligned} \tag{12}$$

being $|\Delta V|$ the decrease of V in a semi-period and $V_{1,2,3}$ defined in (9)–(11).

Proof The idea of the proof is to show that the maximum increase of the Lyapunov function in the pathological intervals is canceled out by the decrease during the rest of the semi-period in which they are included.

Let us observe the phase map of the pendulum. First of all, since the phase map is symmetric respect to the velocity, only positive velocities may be considered. Thus, there are two main possibilities in each semi-period: (i) The pendulum does not reach $\pm \frac{\pi}{2}$ and there is one commutation in a semi-period (Figs. 1, 2) considering

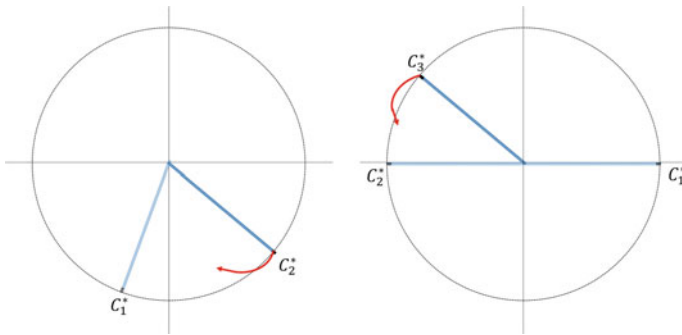


Fig. 1 *Left* Ideal case with one commutation. In C_1^* the pendulum has $x_2 = 0$. It advances until C_2^* , where a new semi-period starts. *Right* Ideal case with three commutations. The pendulum crosses $\pi/2$ (C_1^*), then it crosses $-\pi/2$ (C_2^*) and finally it ends with $x_2 = 0$ (C_3^*)

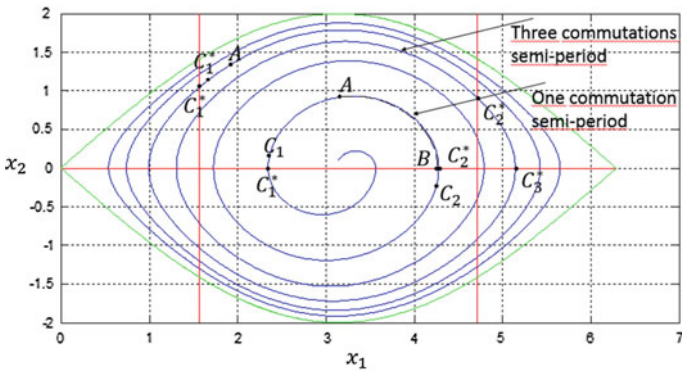


Fig. 2 *Blue* Trajectory of the pendulum. *Red* Ideal commutations. *Green* Homoclinic orbit. $C_{1,2}$ are the actual commutations. $C_{1,2,3}^*$ are the ideal commutations. A is the point that the pendulum crosses after the actual commutation C_1 . B is the fictitious ideal commutation if the control signal would be computed in A

that the pendulum is sufficiently far from the point $(\pi, 0)$ to have time to produce the commutation. This implies that the minimum energy \underline{E} should be larger than $E(\pi, 0) = -2mgl$. The computation of this distance is detailed later. (ii) The pendulum crosses $\pm\frac{\pi}{2}$ and there are three commutations in a semi-period (Figs. 1, 2). In the worst case, these commutations produce that during a whole sampling period, the Lyapunov function increases. A possible third case could occur: Two commutations in the semi-period. However, it is less conservative than the previous ones and the study is not necessary. The last plausible situation is that the pendulum crosses the homoclinic orbit and the energy becomes positive. This case will be discussed at the end of the proof.

The first part is to bound this increase. From (3):

$$\begin{aligned} |\dot{x}_2| &\leq \frac{mgl}{J} + \frac{ml}{J}u_{\max} \Rightarrow \Delta x_2 \leq \left(\frac{mgl}{J} + \frac{ml}{J}u_{\max} \right) h \\ |\dot{x}_1| = |x_2| &\Rightarrow \Delta x_1 \leq |\bar{x}_2| h. \end{aligned} \quad (13)$$

The value of $|\bar{x}_2|$ can be bounded considering that the pendulum is moving inside the homoclinic orbit and its velocity is then bounded by the velocity of the pendulum in the homoclinic when it crosses $x_1 = \pi$, i.e.,

$$x_2 \leq 2\sqrt{\frac{mgl}{J}} + \Delta x_2 = \bar{x}_2. \quad (14)$$

Hence, the bound of $|\dot{V}|$ can be computed from $|mIE_{\max}x_{2\max}(\cos x_1)_{\max}u_{\max}|$:

$$\begin{aligned} |\dot{V}| &\leq (2m^2gl^2) \Delta x_2 u_{\max} = \frac{\Delta V_1}{h} \text{ for the commutation in } x_2 = 0 \text{ for (i)} \\ |\dot{V}| &\leq (m^2gl^2) \Delta x_2 u_{\max} = \frac{\Delta V_2}{h} \text{ for the commutation in } x_2 = 0 \text{ for (ii)}. \end{aligned} \quad (15)$$

In both cases Δx_2 bounds the maximum velocity noting that the pendulum crosses $x_2 = 0$ in the sampling period of the commutation. The energy is bounded in the case (i) by the maximum absolute value of the energy. However, in the case (ii) the angle is limited in the interval $[\frac{\pi}{2}, -\frac{\pi}{2}]$. Similarly to (15) we bound the maximum energy, velocity, cosine and input signal taking into account that we are in the neighborhood of $x_1 = \pm\pi/2$.

$$|\dot{V}| \leq \left(m^2gl^2 \left(\cos \left(\frac{\pi}{2} - \Delta x_1 \right) + 1 \right) \right) \bar{x}_2 \cos \left(\frac{\pi}{2} - \Delta x_1 \right) u_{\max} = \frac{\Delta V_3}{h} \quad (16)$$

for the commutation in $x_1 = \pm\frac{\pi}{2}$. Now, the decrease of the Lyapunov function in the semi-period (12) can be computed. To do it, we use the largest trajectory, where we can guarantee that \dot{V} is always negative. This region is bounded by C_1 and C_2^* (Fig. 2) for the two cases. The decrease between these the actual commutation C_1 and the ideal commutation C_2^* can be computed from $\Delta E_k = \int_{C_1}^{C_2^*} \mathbf{F} \cdot d\mathbf{r} = \int_{C_1}^{C_2^*} \boldsymbol{\tau} \cdot d\boldsymbol{\theta} = J \int_{C_1}^{C_2^*} \dot{x}_2 dx_1$. Note that this integral can be solved analytically thanks to the fact that

the input signal remains constant between C_1 and C_2^* , and \dot{x}_2 depends only on x_1 . Hence,

$$E_k(C_2^*) - E_k(C_1) = \frac{1}{2}m(x_2^2(C_2^*) - x_2^2(C_1)) = mgl \cos x_1(C_1) + mlu_k \sin x_1(C_1) - mgl \cos x_1(C_2^*) - mlu_k \sin x_1(C_2^*). \quad (17)$$

The main complication is due to the pathological intervals bring the pendulum to unknown positions. Thus, the actual commutation C_1 and, consequently, the actual input signal differs from the ideal situation. To solve it, the point A is defined as a known point which the pendulum should necessarily cross after the actual commutation in C_1 in the case (i) and (ii) and the point B is defined as the fictitious ideal commutation if the input signal would be computed in A . \dot{V} should be negative in any case in A . That is, at least an actual commutation should be produced in each semi-period. To ensure it, $\pi - x_1(C_1^*) > \Delta x_1$. The states in B can be obtained replacing C_1 and C_2^* by A and B in (17), respectively. Then, we study both cases:

(i) There is one commutation in a semi-period. Then $x_2(C_1^*) = x_2(C_2^*) = 0$. The pendulum has to cross necessarily $x_1 = \pi$, so that $A = (\pi, x_2(A))$ can be chosen. The constraint $\pi - x_1(C_1^*) > \Delta x_1$ gives a first bound to the minimum initial separation of the pendulum from the downward position to ensure the decrease of the Lyapunov function. Nevertheless, it can be not enough. Thus, the minimum $x_2(A)$ which satisfies $V(A) - V(B) \geq \Delta V_1$ is found. Now, if the pendulum is impulsed to separate it from the down equilibrium position an angle larger than $\alpha_1 := \min\{\pi - \Delta x_1, \arccos((Jx_2^2(A) - mgl)/mgl)\}$, then the Lyapunov function decreases in each semi-period with one commutation. That is, the minimum energy \underline{E} of the set of initial condition is $\underline{E} = mgl(\cos \alpha_1 - 1)$.

(ii) There are three commutations in a semi-period. Then $x_1(C_1^*) = -x_1(C_2^*) = \frac{\pi}{2}$. The point A is $A = (\frac{\pi}{2} + \Delta x_1, x_2(A))$. The objective is to find the maximum $x_2(A)$ such that:

$$V(A) - V(B) \geq \Delta V_2 + 2\Delta V_3. \quad (18)$$

Finally, we can guarantee that the pendulum reaches an angle equal to $\alpha_2 := \arccos((Jx_2^2(A) + mgl \cos(\pi/2 + \Delta x_1))/mgl)$. That is, the maximum energy \bar{E} of the set of initial condition is $\bar{E} = mgl(\cos \alpha_2 - 1)$. However, it is still necessary to prove that $V(C_1) - V(C_2^*) \geq V(A) - V(B)$. Since the commutation has been produced in C_1 and \dot{V} has been negative from C_1 to A , then $V(C_1) \geq V(A)$. Thus, it also holds that $|E(C_1)| \geq |E(A)|$, and consequently, $u_k = u(C_1) \geq u(A)$ by (5). Hence, it can be seen from (17) that the energy in C_2^* increases if the input signal does it. As the pendulum crosses A , it holds that $V(C_2^*) \leq V(B)$.

To finalize, we deal with the possible situation when the pendulum crosses the homoclinic orbit. The pendulum does not make it while \dot{V} is negative, because $|E| \rightarrow 0$. Hence, it could occur only during a pathological interval. If this pathological is in the neighborhood of $x_2 = 0$, then there is no problem because x_1 is also close to zero and the feedback controller takes over. If the pathological interval is in the

neighborhood of $x_1 = \pm \frac{\pi}{2}$, then the Lyapunov can be increased at most ΔV_3 . After that, the Lyapunov function decreases until a new commutation. In the worst case, there is a new increase of ΔV_3 before to cross $x_2 = 0$. So we can conclude that the separation of the homoclinic orbit in this case is less conservative than (18) and we can limit our study to the first two cases. \square

Remark 1 The theorem may be trivially reformulated such that given a fixed sampling period, determine the set of initial conditions.

Remark 2 The theorem may be extended to the case of the on-off control law with the only consideration that the input signal should be either u_{\max} or $-u_{\max}$.

4 Application Example

Consider the normalized pendulum:

$$\ddot{x}_1 = \sin x_1 - u \cos x_1, \quad \dot{x}_1 = x_2. \quad (19)$$

The maximum input signal is $1 \text{ rad} \cdot \text{s}^{-2}$. The gain in (5) is $\lambda = 0.5$.

The procedure can be addressed from the two points of view provided in Theorem 1 and the subsequent remark. On one hand, the sampling period is fixed and the set of initial conditions Ω is obtained from it. On the other hand, the maximum and minimum desired bounds \underline{E} and \bar{E} can be chosen and then a maximum sampling period is computed to satisfy these bounds. In any case, the main aim is to obtain a sampling period which guarantees that the Lyapunov function decreases in each semi-period and, consequently, the pendulum approaches to the upright position. As example, the sampling period may be fixed to $h = 0.02 \text{ s}$. Thus, from (13): $\Delta x_2 \leq 2h \leq 0.04 \text{ rad} \cdot \text{s}^{-1}$. Applying (14), the maximum velocity is $\bar{x}_2 = 2 + \Delta x_2 = 2.04 \text{ rad} \cdot \text{s}^{-1}$. Consequently, $\Delta x_1 \leq 0.0408 \text{ rad}$. Now, the bounds can be computed using (15)–(16), being $\Delta V_1 = 2V_2 = 2\Delta x_2 u_{\max} h = 0.0016 \text{ J}^2$ and $\Delta V_3 = \left(\cos \left(\frac{\pi}{2} - \Delta x_1 \right) + 1 \right) \bar{x}_2 \cos \left(\frac{\pi}{2} - \Delta x_1 \right) u_{\max} h = 0.0017 \text{ J}^2$. Finally, equation (12) is used to obtain the velocities which establish Ω . For the case (i), the Lyapunov function decreases enough to be over the bound for any initial velocity larger than 0 (See Fig. 3) but we have to ensure that an actual commutation is produced. This implies that if the energy of the initial condition is larger than $\underline{E} = E(\alpha = \pi - \Delta\alpha, \dot{\alpha} = 0) = -1.999 \text{ J}$, then the Lyapunov function decreases until the pendulum enters in the case (ii). For it, the minimum angle which the pendulum reaches is 0.26 rad , i.e., we can guarantee that swing-up control law with the event-based strategy can bring the pendulum to the upright position with a maximum separation of 0.26 rad . To obtain this value, the maximum possible velocity in A which satisfies that the Lyapunov function decreases in a semi-period is computed (Fig. 4) and then $\bar{E} = -0.0336 \text{ J}$ is got. Finally, we compute the nearest angle to the upright position with this energy.

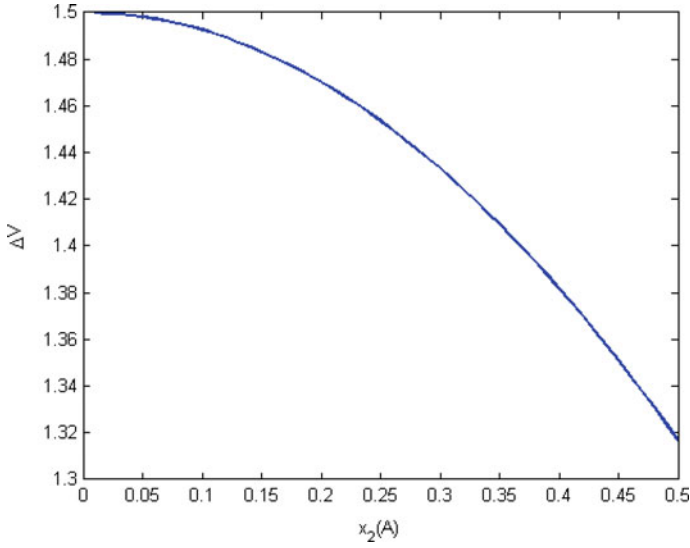


Fig. 3 Decrease of the Lyapunov function from A to C_2^* with one commutation. The *curve* is always larger than ΔV_1

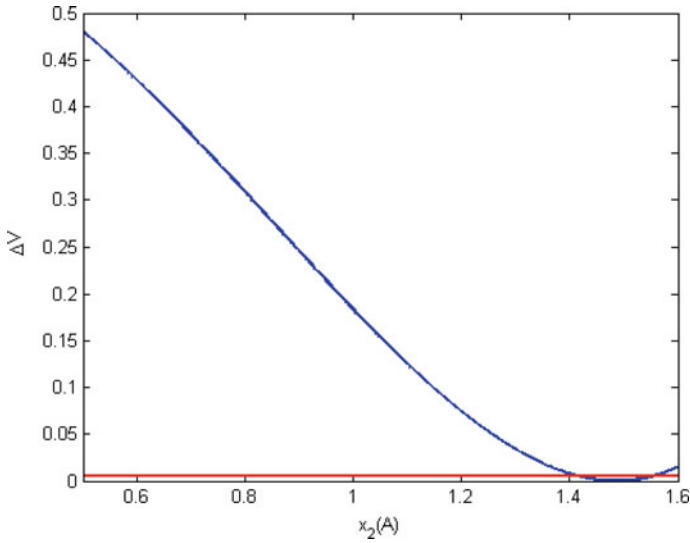


Fig. 4 *Blue* Decrease of the Lyapunov function from A to C_2^* with three commutation. *Red* Bound $\Delta V_2 + 2\Delta V_3$

As a test of the theoretical results, the system (19) has been successfully simulated. In Figs. 5, 6, we can observe that the pendulum tends to the homoclinic orbit. In addition, Fig. 7 shows that the Lyapunov function goes to zero and the energy does

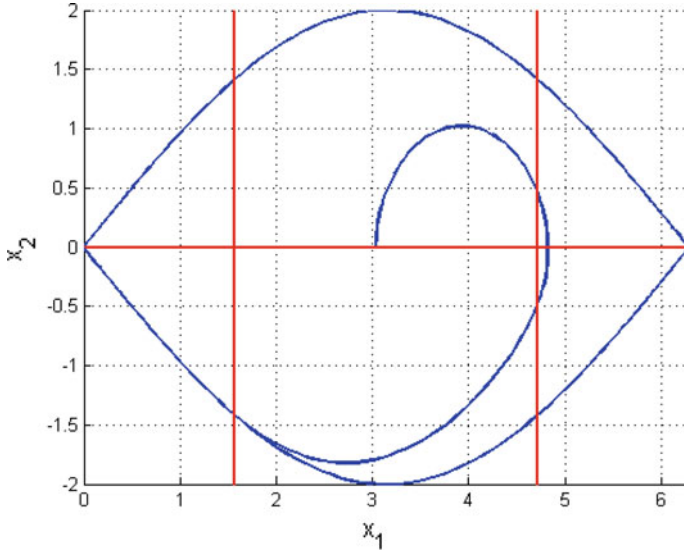


Fig. 5 Phase map of the system under the periodic event-based strategy

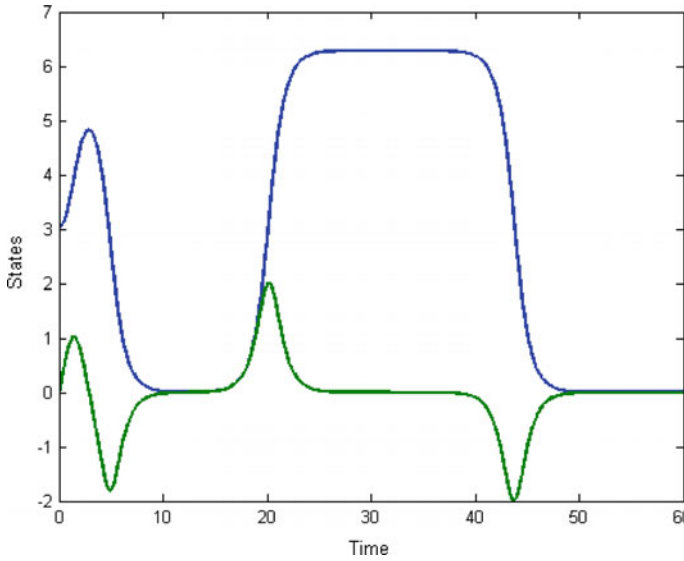


Fig. 6 Evolution of the states: *Blue* Angular position. *Green* Angular velocity

it as well. The input signal (Fig. 8) has step behavior due to the triggering of each event. Only 13 events are generated. This implies an average inter-event time of 4.61 s, being a clear reduction respect to any periodic control.

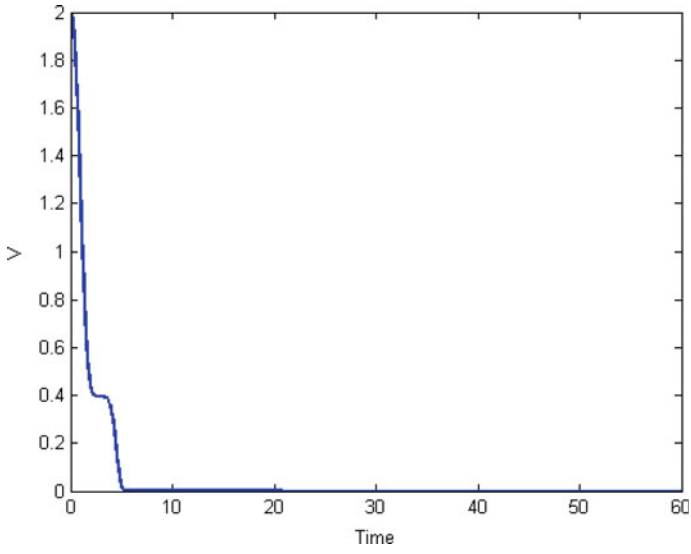


Fig. 7 Evolution of the Lyapunov function with the time

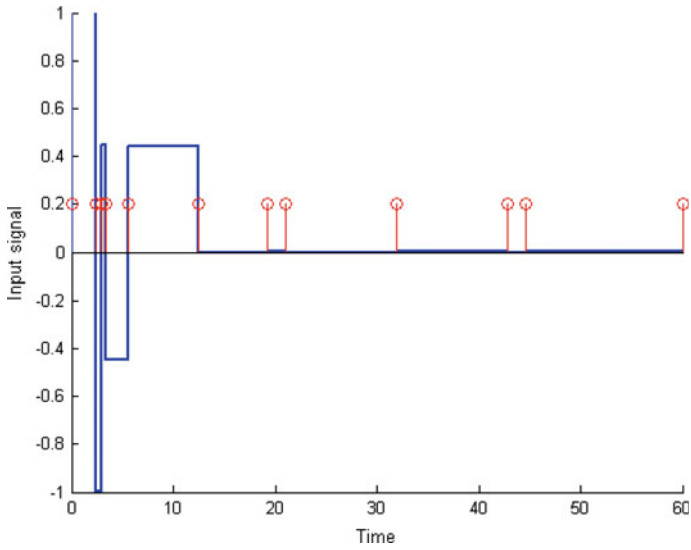


Fig. 8 Evolution of the input signal with the time. In red the events generated

5 Conclusions

In this paper a periodic event-triggered control scheme has been designed for the swing-up movement of the inverted pendulum. The design provides an analytical way to obtain a value for the sampling period of the system while the desired specifications are satisfied. This supposes a novelty in respect to the previous swing-up control laws studied in the literature. In addition, the implementation of the event-based strategy with the energy-based control law supplies advantages like as reducing transmissions, avoiding excessive changes in the actuators, limiting the voltage variations or eluding the chattering.

The numerical example for a normalized inverted pendulum provides the specific steps to determine the sampling period and shows that the number of transmissions may be clearly reduced respect to the periodic control.

The future work could be focused on the implementation in experimental plants and on the search of less conservative bounds respect to the sampling period. In addition, it could be interesting the extension to more general systems.

References

1. Åström, K.J., Furuta, K.: Swinging up a pendulum by energy control. *Autom.* **36**, 278–285 (2000)
2. Bettayeb, M., Boussalem, C., Mansouri, R., Al-Saggaf, U.: Stabilization of an inverted pendulum-cart system by fractional pi-state feedback. *ISA Trans.* **53**(2), 508–516 (2014)
3. Bugeja, M.: Non-linear swing-up and stabilizing control of an inverted pendulum system. In: *EUROCON 2003. Computer as a Tool. The IEEE Region*, vol. 8, pp. 437–441 (2003)
4. Durand, S., Guerrero-Castellanos, J.F., Marchand, N., Guerrero-Sanchez, W.F.: Event-based control of the inverted pendulum: swing up and stabilization. *J. Control Eng. Appl. Inform.* **15**(3), 96–104 (2013)
5. Gordillo, F., Acosta, J.A., Aracil, J.: A new swing-up law for the Furuta pendulum. *Int. J. Control* **76**(8), 836–844 (2003)
6. Guckenheimer, J., Holmes, P.: *Nonlinear Oscillations, Dynamical Systems, and Bifurcations of Vector Fields*. Springer Science & Business Media (1983)
7. Guinaldo, M., Lehmann, D., Sanchez, J., Dormido, S., Johansson, K.H.: Reducing communication and actuation in distributed control systems. In: *IEEE Conference on Decision and Control*, pp. 5288–5293 (2013)
8. Guinaldo, M., Lehmann, D., Sánchez, J., Dormido, S., Johansson, K.H.: Distributed event-triggered control for non-reliable networks. *J. Frankl. Inst.* **351**(12), 5250–5273 (2014)
9. Heemels, W., Donkers, M., Teel, A.: Periodic event-triggered control for linear systems. *IEEE Trans. Autom. Control* **58**(4), 847–861 (2013)
10. Heemels, W., Sandee, J., den Bosch, P.V.: Analysis of event-driven controllers for linear systems. *Int. J. Control* **81**(4), 571–590 (2008)
11. Hespanha, J.P., Naghshtabrizi, P., Xu, Y.: A survey of recent results in networked control systems. *Proc. IEEE* **95**(1), 138–162 (2007)
12. Lehmann, D., Lunze, J.: Event-based control with communication delays and packet losses. *Int. J. Control* **85**(5), 566–577 (2012)
13. Lunze, J., Lehmann, D.: A state-feedback approach to event-based control. *Autom.* **46**, 211–215 (2010)

14. Murray, R.M., Astrom, K.J., Boyd, S.P., Brockett, R.W., Stein, G.: Future directions in control in an information-rich world. *IEEE Control Syst. Mag.* **23**(2), 20–33 (2003)
15. Muskinja, N., Tovornik, B.: Swinging up and stabilization of a real inverted pendulum. *IEEE Trans. Ind. Electron.* **53**(2), 631–639 (2006)
16. Park, M.S., Chwa, D.: Swing-up and stabilization control of inverted-pendulum systems via coupled sliding-mode control method. *IEEE Trans. Ind. Electron.* **56**(9), 3541–3555 (2009)
17. Tabuada, P.: Event-triggered real-time scheduling of stabilizing control tasks. *IEEE Trans. Autom. Control* **52**(9), 1680–1685 (2007)
18. Wang, X., Lemmon, M.: On event design in event-triggered feedback systems. *Autom.* **47**(10), 2319–2322 (2011)

A Simplified Control Approach for the Neuromuscular Blockade Level

Juliana Almeida, Teresa Mendonça and Paula Rocha

Abstract In this paper a new simplified control scheme for the neuromuscular blockade level that only requires the knowledge of one model parameter is proposed. The control law is designed to track a desired target neuromuscular blockade level. Furthermore, an identification procedure to obtain the necessary model parameter is implemented. The results were validated by simulations based on real data collected during surgeries.

Keywords Positive control law · Neuromuscular level · General anesthesia

1 Introduction

The impact of automatic control and system identification techniques on devices and applications in the field of biomedicine has recently been growing. One example of application of control to biomedical systems is the automatic control of anesthetics during general surgery. In this case, several signals are taken into account to monitor the patient. One of these signals is the neuromuscular blockade (NMB) level, which gives information about the patients state regarding muscle paralysis, induced to allow the intubation and other clinical procedures. The degree of the neuromuscular

J. Almeida (✉) · P. Rocha
Faculdade de Engenharia, Universidade do Porto, Rua Dr. Roberto Frias, s/n,
4200-465 Porto, Portugal
e-mail: almeidajfc@gmail.com

P. Rocha
e-mail: mprocha@fe.up.pt

T. Mendonça
Faculdade de Engenharia, Universidade do Porto, Rua do Campo Alegre, s/n,
4169-007 Porto, Portugal
e-mail: tmendo@fe.up.pt

J. Almeida · T. Mendonça · P. Rocha
Research Center for Systems and Technologies (SYSTEC),
Rua Dr. Roberto Frias, s/n, 4200-465 Porto, Portugal

blockade can be assessed by applying a train-of-four of supramaximal twitch stimulus to the hand peripheral nerve. The NMB level corresponds to the first response measured and varies between 100 % (normal muscle activity) and 0 % (full paralysis). To achieve an adequate NMB level muscle relaxants are administered, e.g. *rocuronium* or *atracurium*. Mathematically, the relation between the drug dose and its effect can be modelled by a pharmacokinetic/pharmacodynamic (PK/PD) model. The pharmacokinetic model describes the time course of the drug concentration in the plasma whereas the pharmacodynamic model studies the relation between the drug concentration and its effect. This latter relates the effect concentration with the response by a nonlinear equation known as Hill equation, [1]. However, PK/PD models have the drawback of needing a large number of parameters to characterize the patient. In order to overcome this drawback a new simplified SISO Wiener model proposed in [2] is used in this paper. This model involves a number minimal of patientdependent parameters. More concretely, it has one parameter in the linear part of the model and another one in the nonlinear part. Here, a new simplified control law that only requires knowledge of the parameter associated to the nonlinear model is proposed. This control law is based on the one proposed in [3], which has already been applied to control the NMB level, using the two model parameters [4], [5]. In order to implement our law, an estimation procedure for the only parameter on which it depends is also proposed.

This paper is organized as follows. In Sect. 2 the SISO Wiener model and the new control law are described. The main results are shown in Sect. 3, and the conclusions are drawn in Sect. 4.

2 One Patient-Dependent Parameter Control Law

This section presents our new positive control law for the NMB level that uses a simplified description of the system. The underlying SISO Wiener NMB model is first introduced.

2.1 SISO Wiener Model

The NMB model proposed in [2] for the description of the effect of the muscle relaxant in the human body consists of one linear model followed by a nonlinear static equation.

The linear dynamics is modeled by

$$C_e(s) = \frac{k_1 k_2 k_3 \alpha^2}{(s + k_1 \alpha) (s + k_2 \alpha) (s + k_3 \alpha)} U(s), \quad (1)$$

where $C_e(s)$ is the Laplace transform of the effect concentration $c_e(t)$; $U(s)$ is the Laplace transform of the input drug dose $u(t)$; k_1 , k_2 and k_3 are parameters that have been suitably determined in [2] for the muscle relaxants rocuronium and atracurium, and $\alpha > 0$ is a patientdependent parameter.

The statespace representation of the model is

$$\begin{cases} \dot{x}(t) = \alpha Ax(t) + \alpha Bu(t) \\ c_e(t) = [0 \ 0 \ 1] x(t) \end{cases} \quad (2)$$

where the matrix A and the vector B are defined as

$$A = \begin{bmatrix} -k_3 & 0 & 0 \\ k_2 & -k_2 & 0 \\ 0 & k_1 & -k_1 \end{bmatrix}, \quad B = \begin{bmatrix} k_3 \\ 0 \\ 0 \end{bmatrix}$$

The nonlinear static equation to describe the relation between the effect concentration and the actual drug effect is given by the following Hills equation

$$y(t) = \frac{100}{1 + \left(\frac{c_e(t)}{C_{50}}\right)^\gamma} \quad (3)$$

where C_{50} is the half of the maximum effect concentration and has fixed value according [6]; γ is the only other patient-dependent parameter.

2.2 Control Law for the NMB Level

The control law used in this paper is basically the one introduced in [3], which applied to control the NMB level in [4, 5]. The difference is that, here, the controller is independent from the parameter α , which constitutes a simplification with respect to the previous approaches. Both the original and our simplified law have the convergence of the total system mass $M(x) = \sum_{i=1}^3 x_i$ to a desired system mass M^* as control objective. So, our aim of tracking a desired NMB level is achieved by reaching and maintaining an appropriate mass of drug in the patients body (or system). More concretely, the simplified control law obtained is

$$\begin{cases} u(t) = \max(0, \tilde{u}(t)) \\ \tilde{u}(t) = - \left(\sum_{i=1}^3 b_i \right)^{-1} \left([1 \ 1 \ 1] Ax(t) + \lambda (M(x) - M^*) \right) \end{cases} \quad (4)$$

with $\lambda > 0$ being a design parameter and b_i are the entries of matrix B. Note the absence of the parameter α from (2). The parameter γ from (3) is implicitly present as it is used to compute M^* .

The proof that this control law achieves its mass tracking goal is similar to the one given in [3]. Here, just to give an idea of how it works, we consider the simple case when $\tilde{u}(t) \geq 0$. In this case, letting $\Delta M = M(x)M^*$:

$$\begin{aligned}
 \overbrace{\Delta M} &= \dot{M}(x) = [1 \ 1 \ 1] \dot{x}(t) \\
 &= \alpha [1 \ 1 \ 1] Ax + \alpha \left(\sum_{i=1}^3 b_i \right) \times \\
 &\quad \times \left(- \left(\sum_{i=1}^3 b_i \right)^{-1} \left([1 \ 1 \ 1] Ax(t) + \lambda (M(x) - M^*) \right) \right) \\
 &= -\alpha \lambda (M(x) - M^*) \\
 &= -\alpha \lambda \Delta M = -\lambda_\alpha \Delta M
 \end{aligned} \tag{5}$$

Note that, the derivative in (5) is the derivative with respect to t .

Since α and λ are positive, $\lambda_\alpha < 0$ and hence ΔM converges to zero, i.e., $M(x)$ converges to M^* .

Thus, the patient parameter α may indeed be left out of the control law for the rocuronium mass. Although α influences the speed of convergence, this can be compensated by the design parameter λ . As can be seen in (5) the controller action just depends on a suitable choice of the value for the desired mass M^* . To compute this value, the equilibrium point of the closed-loop system, when $M(x) = M^*$ was determined and the steady-state effect concentration c_e was shown to be equal to $\frac{M^*}{3}$. This enables to determine the value of the desired mass M^* by the inversion of the Hill equation (3) for a desired set-point value y^* for the NMB level. According to clinicians, during general anesthesia, this desired value should be equal to 10%. Indeed, we have

$$M^* = 3 \times \left(\frac{100}{y^*} - 1 \right)^{1/\gamma} C_{50} = 3 \times 9^{1/\gamma} C_{50} \tag{6}$$

Thus, once the patient-dependent parameter γ is known, the value of M^* is obtained by Eq. (6).

2.3 Parameter Estimation

Although, the controller action does not depend from the parameter of the linear model, the determination of the suitable mass M^* depends on the parameter γ . In

order to obtain the value of this parameter, a simple procedure for parameter estimation will be performed. Note that, γ appears in the Hill equation,

$$y(t) = \frac{100}{1 + \left(\frac{c_e(t)}{C_{50}}\right)^\gamma} \quad (7)$$

This parameter is identified when the controller action begins which corresponds to time instant of the initial recovery after an initial *bolus*. This time of recovery, t^* , is given by the algorithm OLARD [7]. So, at this time instant, an estimate $\hat{\gamma}$ of γ is obtained by the inversion of the Hill equation

$$\hat{\gamma} = \frac{\log\left(\frac{100}{y(t^*)} - 1\right)}{\log\left(\frac{c_e(t^*)}{C_{50}}\right)} \quad (8)$$

3 Simulation Results

This section presents the results obtained by the application of the control scheme proposed here to control the NMB level via the administration of the muscle relaxant *rocuronium*. Fifty real cases were collected using the Galeno platform developed in the framework of the Portuguese funding agency (FCT) project Galeno, that incorporates several identification and control procedures for automation in the administration of anesthetics. Furthermore, a Prediction Error Method was used to identify the patient-dependent parameters: $\theta_i = (\alpha_i, \gamma_i)$, $i = 1, \dots, 50$. Here, the values for the parameters corresponding to the patient number seven were used to represent the real patient and to obtain the real response: $\theta_7 = (0.0293, 1.4728)$. The values of k_1 , k_2 and k_3 are fixed and equal to 1, 4 and 10 respectively, and the values of C_{50} is 1 [8].

The value for the design parameter λ was taken as 0.2. Since for simplicity, we chose not to identify the parameter α , the control scheme is designed taking into account its mean value α : $\bar{\alpha} = 0.0307$. Moreover the identification of the parameter γ of the nonlinear model at the time instant $t^* = 40.7$ min is performed as mentioned in Eq. (8). The value of the estimated parameter is $\hat{\gamma} = 1.4728$. The proposed control scheme is applied from the time instant t^* on considering the obtained estimated for the parameter γ .

Figure 1 shows the patient response and the input signal obtained by applying the described strategy.

To analyze the performance of the identification procedure, the controlled NMB response was obtained considering the following scenarios:

1. $\bar{\alpha}$, $\bar{\gamma}$, *i.e.*, mean values for α and γ ($\bar{\gamma} = 1.8499$);
2. $\bar{\alpha}$, $\hat{\gamma}$, *i.e.*, mean value for α and the estimate obtained by the identification procedure for γ .

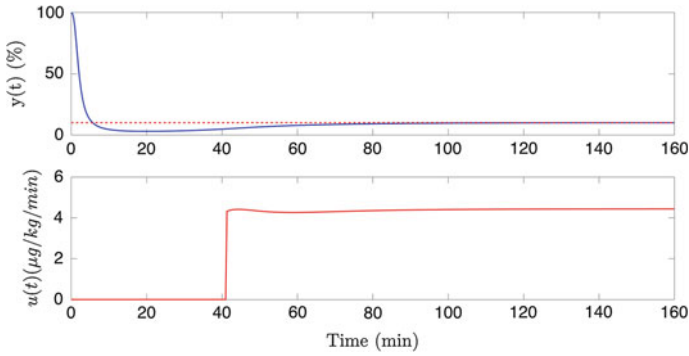


Fig. 1 NMB level evolution obtained with the application of the proposed control scheme applied at $t^* = 40.6$ min

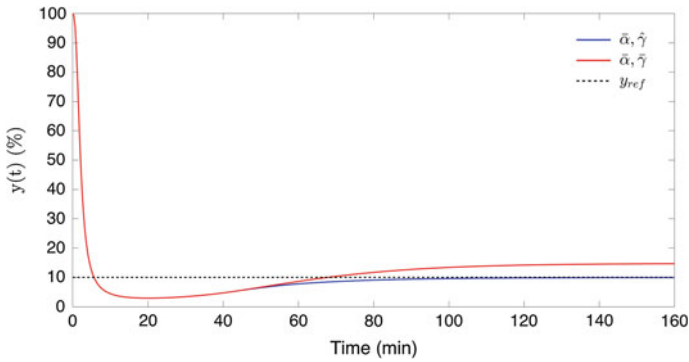


Fig. 2 NMB level evolution for scenarios (1) and (2) when the control law is applied at $t^* = 40.6$ min

The corresponding results can be observed in Fig. 2. As it is possible to see, with our identification procedure the NMB level tracks the desired NMB level of 10 %.

In order to analyze the performance of the control scheme under a more realistic scenario, a noise signal was added to the real response. The noise signal was obtained from a typical NMB real case. For this scenario, the value of $\hat{\gamma}$ is 1.3629. Figure 3 shows the NMB level evolution and the input signal when noise is considered.

4 Conclusions

In this paper a new simplified control scheme for the neuromuscular blockade that only requires the knowledge of the parameter of the nonlinear part of the model is proposed. The control law is designed to control the amount of the muscle relaxant that should be administered during a general anesthesia to track a desired NMB level

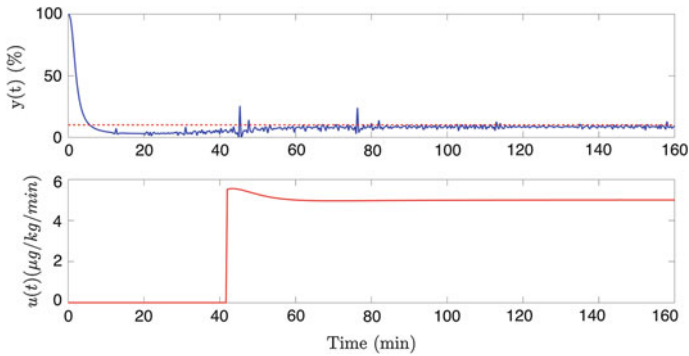


Fig. 3 NMB level evolution obtained with the application of the proposed control scheme at $t^* = 40.6$ min when noise is added to the real signal

of 10 %. In order to obtain the aforementioned parameter, an identification procedure based on the patients response was also proposed. The results were validated by simulations based on real collected data; although this is a preliminary study, the results are encouraging.

Acknowledgments This work was financially supported by: Project POCI-01-0145-FEDER-006933—SYSTEC—Research Center for Systems and Technologies—funded by FEDER funds through COMPETE2020—Programa Operacional Competitividade e Internacionalizao (POCI) and by national funds through FCT—Fundação para a Ciência e a Tecnologia; The author Juliana Almeida acknowledge the support from FCT Fundação para a Ciência e Tecnologia under the SFRH/BD/87128/2012.

References

1. Haddad, W.M.: Nonnegative and Compartmental Dynamical Systems. Princeton University Press (2010)
2. da Silva, M.M., Wigren, T., Mendonça, T.: Nonlinear identification of a minimal neuromuscular blockade model in anesthesia. *IEEE Trans. Control Syst. Technol.* **20**(1), 181–188 (2012)
3. Bastin, G., Provost, A.: Feedback stabilisation with positive control of dissipative compartmental systems. In: Proceedings of the 15th International Symposium on Mathematical Theory of Networks and Systems, pp. 1–9 (2002)
4. Almeida, J., da Silva, M.M., Mendonça, T., Rocha, P.: A compartmental model-based control strategy for neuromuscular blockade level. In: Proceedings of the 18th IFAC World Congress, pp. 599–604 (2011)
5. Almeida, J., Mendonça, T., Rocha, P.: An improved strategy for neuromuscular blockade control with parameter uncertainty. In: Proceedings of the 50th IEEE Conference on Decision and Control and European Control Conference, pp. 867–872 (2011)
6. Alonso, H., Mendonça, T., Rocha, P.: A hybrid method for parameter estimation and its application to biomedical systems. *Comput. Methods Programs Biomed.* **89**(2), 112–122 (2008)

7. da Silva, M.M., Sousa, C., Sebastião, R., Gama, J., Mendonça, T., Rocha, P., Esteves, S.: Total mass TCI driven by parametric estimation. In: Proceedings of the 17th Mediterranean Conference on Control and Automation, pp. 1149–1154 (2009)
8. da Silva, M.M., Lemos, J.M., Coito, A., Costa, B.A., Wigren, T., Menonça, T.: Local identifiability and sensitivity analysis of neuromuscular blockade and depth of hypnosis. *Comput. Methods Programs Biomed.* **113**(1), 23–36 (2014)

Disturbance Rejection Improvement for the Sliding Mode Smith Predictor Based on Bio-inspired Tuning

Josenalde Oliveira, José Boaventura-Cunha and Paulo Moura Oliveira

Abstract This paper addresses a strategy to improve disturbance rejection for the Sliding Mode Controller designed in a Smith Predictor scheme (SMC-SP), with its parameters tuned through the bio-inspired search algorithm—Particle Swarm Optimization (PSO). Conventional SMC-SP is commonly based on tuning equations derived from step response identification, when First Order Plus Dead Time models (FOPDT) are considered and therefore controller parameters are previously set. Online PSO tuning based on minimization of the Integral of Time Absolute Error (ITAE) can provide faster recovery from external disturbances without significant increase of energy consumption, and the Sliding Mode feature deals with possible model mismatch. Simulation results for time delayed systems corroborating these benefits are presented.

Keywords Smith predictor · Sliding modes · Disturbance rejection · Time delay systems · Particle swarm optimization

This work is financed by the ERDF—European Regional Development Fund through the Operational Programme for Competitiveness and Internationalisation—COMPETE 2020 Programme, and by National Funds through the FCT—Fundação para a Ciência e a Tecnologia (Portuguese Foundation for Science and Technology) within project POCI-01-0145-FEDER-006961.

J. Oliveira (✉) · J. Boaventura-Cunha · P.M. Oliveira
INESC TEC—INESC Technology and Science,
Campus da FEUP, 4200-465 Porto, Portugal
e-mail: josenalde@ej.ufpn.br

J. Oliveira
Agricultural School of Jundiaí—Federal University of Rio Grande Do Norte, UFRN,
Macaíba, RN 59280-000, Brazil

J. Boaventura-Cunha · P.M. Oliveira
University of Trás-os-Montes E Alto Douro, School of Sciences and Technology,
5000-801 Vila Real, Portugal
e-mail: jboavent@utad.pt

P.M. Oliveira
e-mail: oliveira@utad.pt

1 Introduction

Time delay is inherent in various process control problems and, therefore, the controllers must be designed to deal with it. The work by [1] proposed the well known Smith Predictor (SP) to compensate for time delay effects. Its basic idea relies on designing the controller considering the predicted outputs of a free delay model. For a First Order Plus Dead Time model (FOPDT) with the gain K , time constant τ and delay t_0

$$G(s) = \frac{K}{\tau s + 1} e^{-t_0 s}, \quad (1)$$

its control is yet difficult when the controllability ratio ($\frac{t_0}{\tau}$) exceeds two units, as stated in [2]. Original SP assumes model matching for appropriate tracking and disturbance rejection. It is well known that the actual system poles may drift from their nominal values, for instance, due to electromechanical aging or environmental conditions. As a promising alternative to overcome model-plant mismatches and external disturbances, [3, 4] designed a Sliding Mode Controller (SMC) on a SP structure (SMC-SP), getting better tracking and robustness features when compared to PI control. SMC [5] is a robust control technique, based upon a discontinuous control law (U_D) and the definition of a *sliding surface*, function of the system state variables. Recently, a work by [6] successfully applied the SMC-SP on a long time delay FOPDT model, for main steam pressure control in coal-fired power plant boiler. These previous works use some *offline* method to get an initial set of parameters for U_D , either based on open loop step responses [7] or on some numeric method, such as Nelder-Mead searching algorithm [4]. When load and/or output disturbances may arise *on the fly*, the hypothesis is that an online tuning scheme could improve or even anticipate disturbance rejection. This issue motivates research and it is within actual trends in Model Predictive Control [8]. Works on relay autotuning [9] and heuristic search algorithms, such as Particle Swarm Optimization (PSO) [10] are of increasing interest, being the latter successfully applied on many control structures, such as H_∞ [11], PID [12] and Generalized Predictive Control [13], just to name a few.

This paper presents a new design approach of SMC-SP [3], in which controller parameters are tuned by PSO, minimizing the Integral of Time Absolute Error (ITAE) index. Simulations on time delay systems under disturbances influence will show better tracking and disturbance rejection, without significant increase of energy consumption.

2 Problem Statement

2.1 Reviewing Sliding Mode Controller in a Smith Predictor Configuration—SMC-SP

This review closely follows [3] and gives the basis for this paper proposal. Consider the block diagram in Fig. 1: The actual plant $G(s)$ is given by (1) and the plant model may be splitted in two parts: a free delay part G_M^- and a noninvertible part G_M^+ . Therefore, one has

$$G_M(s) = G_M^- G_M^+ = \frac{K_M}{\tau_M s + 1} e^{-t_{0M}s}, \tag{2}$$

with $Y_M^- = G_M^- U$ and $Y_M = G_M U$. External signals D_L and D_O stand for load and output disturbances, respectively. From SP theory, the error signal $OFFSET = (Y + D_O) - Y_M$ is ideally null, when $D_O = 0$ and $Y = Y_M$, which means plant-model matching. In this case, system error $E = R - OFFSET - Y_M^-$ is not affected by delay, since outer loop has no influence. When $G \neq G_M$ (internal disturbances caused by plant-model mismatch) and/or at least an external disturbance enters the system, the more robust the controller the better the disturbance rejection, and thus SMC is an appropriate choice. If SMC parameters are previously set, its results are quite good [3]. Since disturbances are, in general, unforeseen, an even better behavior could be achieved with online tuning, which is the proposal of this work.

From Fig. 1 the derived closed loop transfer function is:

$$\frac{Y}{R} = \frac{CG}{1 + CG_M^- + C(G - G_M)} \tag{3}$$

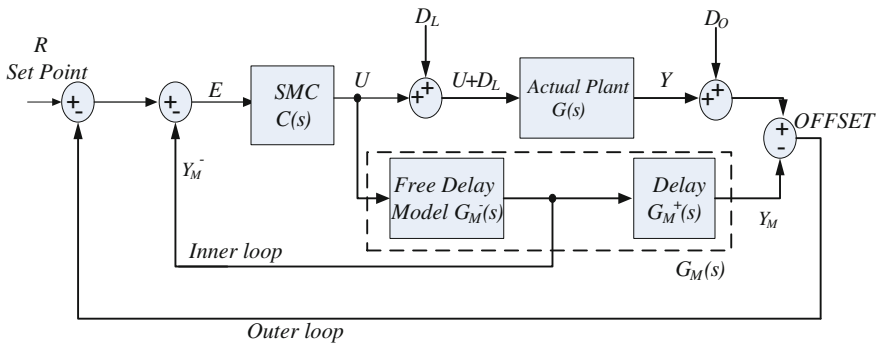


Fig. 1 Sliding mode controller on smith predictor configuration

From (3), one points out that when $G = G_M$ the characteristic equation does not depend on delay and, therefore, the controller can be designed taking this fact into account. However, true process is hardly ever perfectly known and therefore the controller must be robust. A deeper analysis may be found in [4].

2.2 Devising SMC

The well established robustness properties of SMC do guarantee low sensitivity to parameter uncertainties, disturbances and unmodeled dynamics, naturally within a tolerance range. The design consists of two steps: definition of a *sliding surface* $S(t)$, commonly a function of the system states and where the trajectories must reach in finite time. Once in $S(t)$ the system order is reduced and control aim is achieved. In this condition, named *sliding mode*, $\dot{S} = 0$ and a non switching control signal U_C , referred as *equivalent control* is designed. The second step consists of designing the control law U_D which drives the process variable to the sliding surface, during the *reaching mode* and it must obey a *reaching law*. Then, SMC control law is:

$$U = U_C + U_D. \quad (4)$$

Control Law for Sliding Mode— U_C Consider as the sliding surface S , the system error E in Fig. 1:

$$S(t) = E = R - OFFSET - Y_M^-. \quad (5)$$

For designing purposes and according to SP theory, (5) considers plant-model matching ($OFFSET = 0$) or a constant $OFFSET$, and thus only free delay model G_M^- is considered. Taking this fact into account and by applying the sliding condition $\dot{S} = 0$ in (5), one has

$$\frac{dS(t)}{dt} = \frac{dR(t)}{dt} - \frac{dY_M^-(t)}{dt} = 0. \quad (6)$$

From (2), and representing G_M^- into differential equation form:

$$G_M^- = \frac{Y_M^-}{U} = \frac{K_M}{\tau_M s + 1}, \quad (7)$$

$$\tau_M \frac{dY_M^-}{dt} + Y_M^- = K_M U, \quad (8)$$

$$\frac{dY_M^-}{dt} = \frac{-Y_M^- + K_M U}{\tau_M}. \quad (9)$$

With (9) in (6) and after some algebraic manipulation, the control signal is:

$$U(t) = \frac{\tau_M}{K_M} \left[\frac{dR(t)}{dt} + \frac{Y_M^-(t)}{\tau_M} \right]. \quad (10)$$

According to the work of [14] the derivative of reference can be discarded. Therefore, this component of control signal is indeed the equivalent control U_C , which turns into

$$U_C(t) = \frac{Y_M^-(t)}{K_M}. \quad (11)$$

Control Law for Reaching Mode— U_D This component is responsible for the corrective action, for driving system trajectories towards the sliding surface (5). When the trajectory is *sliding* and some disturbance occur, U_D acts to correct it. Therefore, it must be designed in such a way that the following reaching law (12) is satisfied,

$$S\dot{S} < 0. \quad (12)$$

Although a simple discontinuous signum function can be used, it is associated with high frequency output oscillations, named chattering effect. To overcome this, a more appropriate solution is the sigmoid-like function:

$$U_D(t) = K_D \frac{S(t)}{|S(t)| + \delta}, \quad (13)$$

where K_D is the gain responsible for how fast $S(t)$ is reached (and therefore it impacts disturbance rejection) and δ accounts for chattering reduction. It is noteworthy that the pair (K_D, δ) directly affects system performance and, moreover, there is some tradeoff between them. With optimization algorithms and time-domain performance methods, [4] proposed the following set of equations based on the system model in (2), for initial tuning:

$$K_D = \frac{0.72}{|K_M|} \left(\frac{\tau_M}{t_{0M}} \right)^{0.76}, \quad (14)$$

$$\delta = 0.68 + 0.12 |K_M| K_D \frac{t_{0M} + \tau_M}{t_{0M} \tau_M}. \quad (15)$$

In the proposal of this paper, these equations give center values for (K_D, δ) from which the online PSO algorithm defines a search space, to be detailed in next section.

3 SMC-SP Tuned by PSO

Particle Swarm Optimization is a stochastic population-based algorithm, as Genetic Algorithms, with simple understanding and implementation, due to its inspiration in the social behavior of swarms, as bird flocking or fish schooling [10]. The basic idea is: given an initial random population of particles, each particle must be viewed as a potential solution, whose *potentiality* is evaluated against an objective function to be minimized or maximized. Depending on its fitness value, at each iteration the particle is moved in the search space, according to position s and velocity v updates given by

$$v_k^i = \omega_k^i v_{k-1}^i + c_1 r_1 (p_{best}^i - s_{k-1}^i) + c_2 r_2 (g_{best}^i - s_{k-1}^i) \tag{16}$$

$$s_k^i = s_{k-1}^i + v_k^i, \tag{17}$$

where k is the epoch, i is a swarm particle, p_{best} is the best position visited by a particular particle, g_{best} is the best position visited by the entire swarm, c_1 and c_2 are constants which represent the cognitive and social parameters, r_1 and r_2 are uniform distribution random numbers in $[0, 1]$ interval, and ω is the inertia weight. Convergence studies have attracted many researchers and a recent review may be found in [15].

Consider the block diagram in Fig. 2. Now K_D and δ are tuned by a PSO block. An interesting and helpful issue is to limit particles within a feasible search space, that here is related to the use of equations (14) and (15) to define a range around the nominal values for the particles (K_D, δ). In simulations section, this range is set to $\pm 80\%$ and has enabled good results. The objective function to be minimized in this work is ITAE, which depends on the system error E , the chosen sliding surface (5). This is a common choice for controller tuning based on evolutionary/nature-inspired

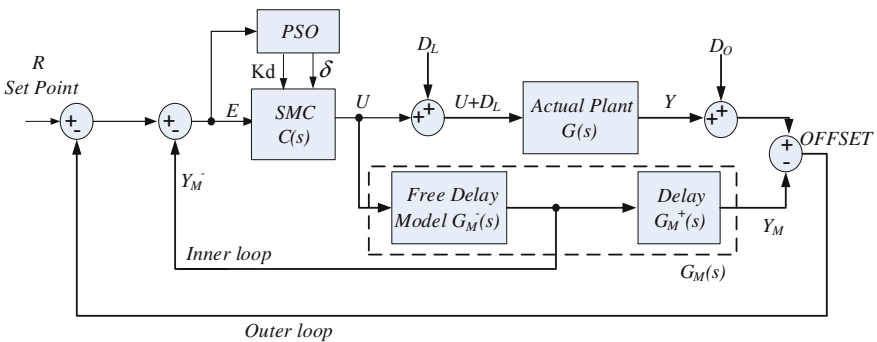


Fig. 2 Sliding mode controller tuned by particle swarm optimization in a Smith predictor structure

algorithms [16] and, in general, is preferable for quick settling time. Below, t_{sim} is the simulation time range.

$$ITAE = \int_{t=0}^{t=t_{sim}} t |S(t)| dt. \quad (18)$$

4 Simulations

Besides (18), the proposal of this paper is compared to SMC with fixed (K_D, δ) in terms of energy consumption, namely, Control Effort (CE) and Total Variation (TV), which gives an idea about control signal smoothness. The average indexes are thus calculated for a number of runs, $N_{runs} = 21$, like [13]:

$$CE = \int_{t=0}^{t=t_{sim}} |U(t)| dt, \quad (19)$$

$$TV = \int_{t=0}^{t=t_{sim}} |U(t) - U(t-1)| dt. \quad (20)$$

Two FOPDT plant models with $\left(\frac{t_0}{\tau}\right) \geq 2$ were selected, being G_{p1} also simulated in [3]:

$$G_{p1} = \frac{-0.78}{2s+1} e^{-5s} \quad (21a)$$

$$G_{p2} = \frac{1}{s+1} e^{-3s} \quad (21b)$$

The adopted PSO uses fixed inertia weight $\omega = 0.7298$, $c_1 = c_2 = 1.496$, and r_1, r_2 are random in the $[0, 1]$ interval. These values are known to provide swarm convergence. A swarm size of 30 particles and 30 epochs have shown to be sufficient for these plants. For each plant, four scenarios are considered, always considering the unit step as set point:

1. Plant-model matching, not disturbed: $G = G_M, D_L = D_O = 0$
2. Plant-model matching, disturbed: $G = G_M, D_L = D_O = 0.5$
3. Plant-model mismatch, disturbed: $G \neq G_M, D_L = D_O = 0.5$
4. Plant-model mismatch only on K and τ_M , disturbed: $G \neq G_M, D_L = D_O = 0.5$.

Simulation time is set to 150 s and each plant has an integration step of 10 % of its time constant. For the disturbed scenarios 2, 3 and 4, D_L acts at $t = 35$ s and D_O at $t = 60$ s. Plant-model mismatch is +20 % in each parameter of (21a) and (21b), except scenario 4. Once affecting the system, the disturbances are considered to not vanish by themselves, therefore depending on the controller. Equations (14) and (15)

Table 1 Parameters tuned by PSO

G_{p1}	K_D	δ
(1)	-0.8281	0.2055
(2)	-0.8281	0.1662
(3)	-0.8281	0.1707
(4)	-0.8281	0.1713
G_{p2}	K_D	δ
(1)	0.5623	0.3779
(2)	0.5623	0.3023
(3)	0.5623	0.3157
(4)	0.5623	0.3113

applied on (21a) and (21b), give the following fixed pairs (K_D, δ) for $G_{p1} : K_D = -0.46, \delta = 0.71$ and for $G_{p2} : K_D = 0.31, \delta = 0.73$.

4.1 Results and Discussion

This section shows representative figures for each plant and each scenario, comparing SMC fixed parameters for G_{p1} and G_{p2} given above, with the SMC tuned by PSO. Final parameters for all scenarios and plants is summarized in Table 1. Considering the data in Table 1, one sees the convergence for the upper bound of K_d and the tendency of δ approach its lower bound, in accordance to the objective of minimizing the system error. Figures 3, 4, 5, 6 and Table 2 refers to G_{p1} and Figures 3, 4, 5, 6 and Table 3 refers to G_{p2} . Regarding G_{p1} , ITAE is lower for all situations, although the presence of overshoot in Figs. 5 and 6 impacts TV index due to some oscillation (see Table 2). This initial overshoot effect on ITAE is then reduced during disturbance rejection. As expected, in disturbed cases, there is the online *choice* of other particle that better fits the need for disturbance rejection. In analyzing the figures and table for G_{p2} , one sees the equivalence in terms of control effort, with better disturbance rejection.

5 Conclusion and Further Work

In this study, it has been proposed the inclusion of a PSO search algorithm into the Sliding Mode Controller based on Smith Predictor structure. The hypothesis that an online tuning scheme could provide a better disturbance rejection, has been validated. Three performance indexes were compared to the conventional SMC-SP based on fixed parameters and have suggested fast tracking and recovery from distur-

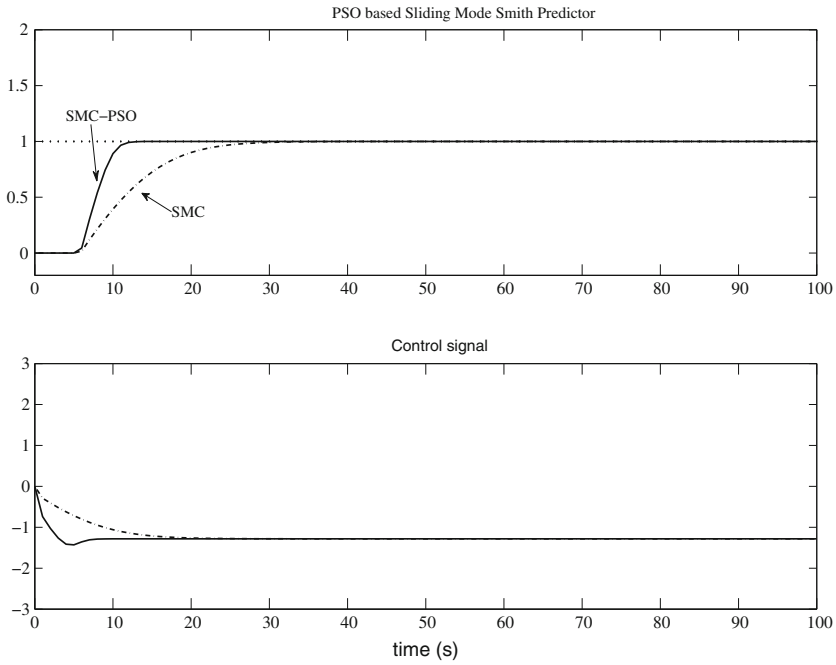


Fig. 3 G_{p1} —system output—scenario #1

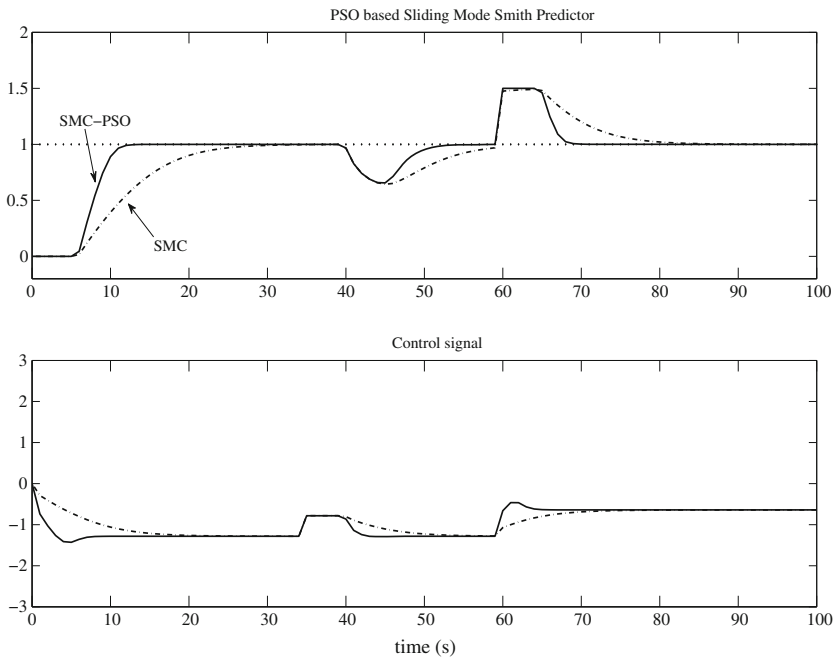


Fig. 4 G_{p1} —system output—scenario #2

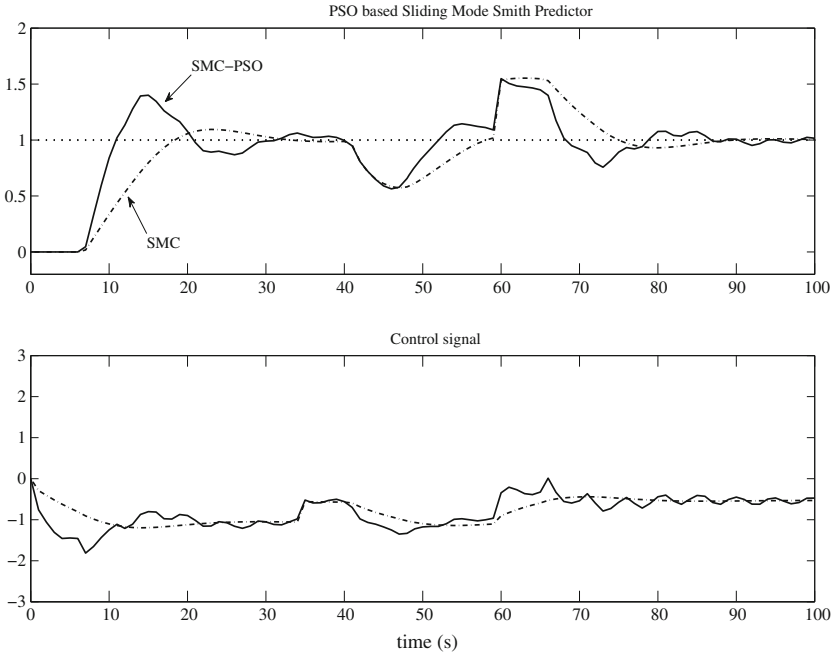


Fig. 5 G_{p1} —system output—scenario #3

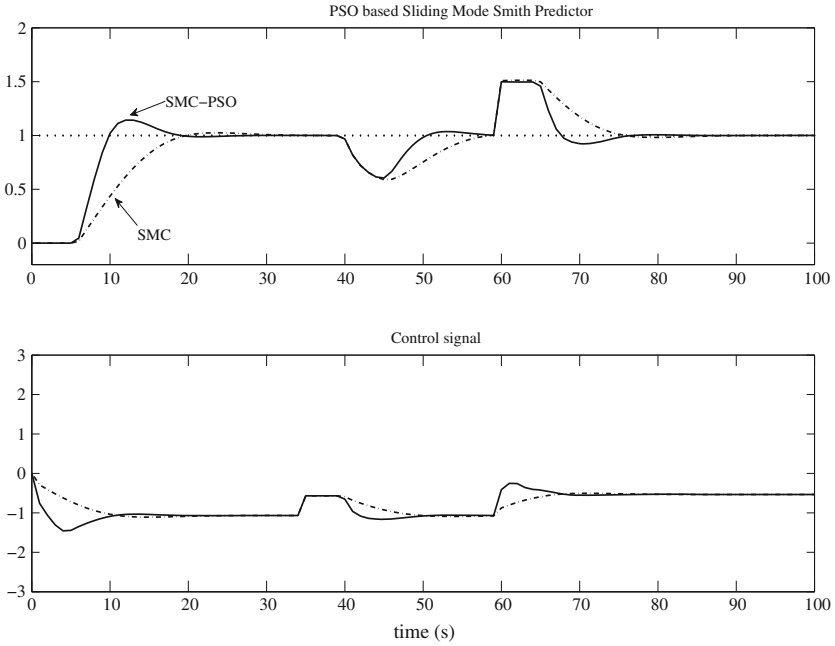


Fig. 6 G_{p1} —system output—scenario #4

Table 2 G_{p1} —performance indexes

		SMC-PSO	SMC	Figures
(1)	ITAE	5.6	43.2	Fig. 3
	CE	191.8	185.8	
	TV	1.5	1.2	
(2)	ITAE	69.5	305.6	Fig. 4
	CE	130.0	124.7	
	TV	3.5	2.9	
(3)	ITAE	170.3	376.7	Fig. 5
	CE	109.6	105.4	
	TV	12.7	3.2	
(4)	ITAE	74.7	297.5	Fig. 6
	CE	109.1	105.0	
	TV	4.2	2.7	

Table 3 G_{p2} —performance indexes

		SMC-PSO	SMC	Figures
(1)	ITAE	3.2	16.3	Fig. 7
	CE	149.3	146.7	
	TV	1.0	1.0	
(2)	ITAE	61.1	184.9	Fig. 8
	CE	105.9	105.6	
	TV	2.6	2.5	
(3)	ITAE	91.2	218.7	Fig. 9
	CE	88.9	88.8	
	TV	5.1	2.7	
(4)	ITAE	66.1	179.5	Fig. 10
	CE	88.6	88.6	
	TV	3.1	2.3	

bances, although some modifications on the proposal could improve control signal effort and smoothness in the scenario of plant-model mismatch, thus motivating further research. Some ideas for future works are the following:

- testing of other objective functions that better fit the mismatch scenario, including multi objective optimization
- testing of refined versions of PSO and other bio/nature-inspired algorithms.
- testing under noisy conditions

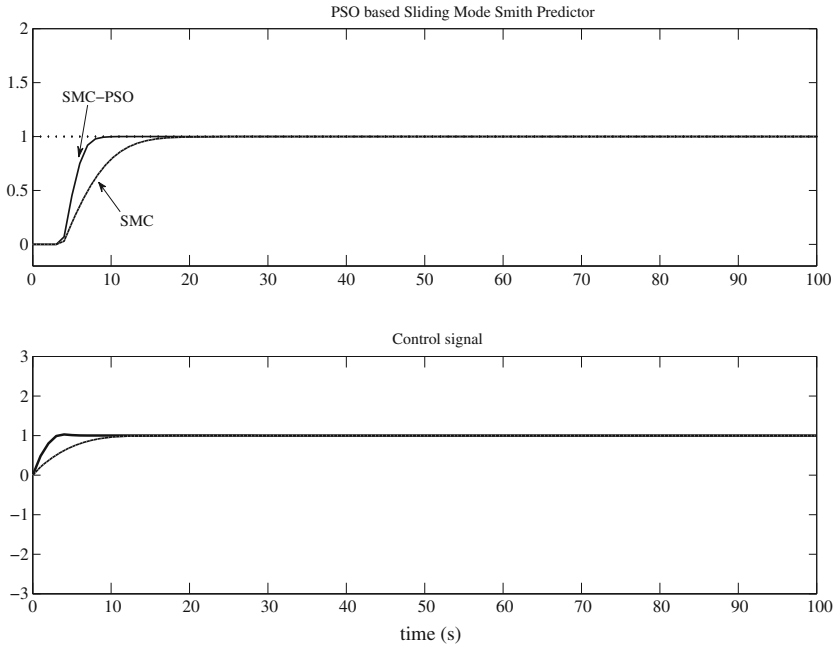


Fig. 7 G_{p2} —system output—scenario #1

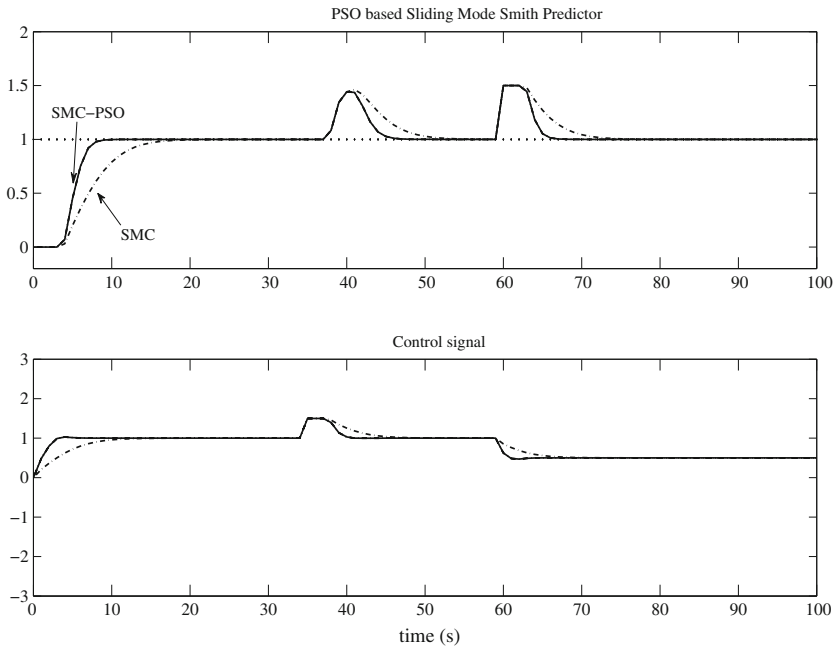


Fig. 8 G_{p2} —system output—scenario #2

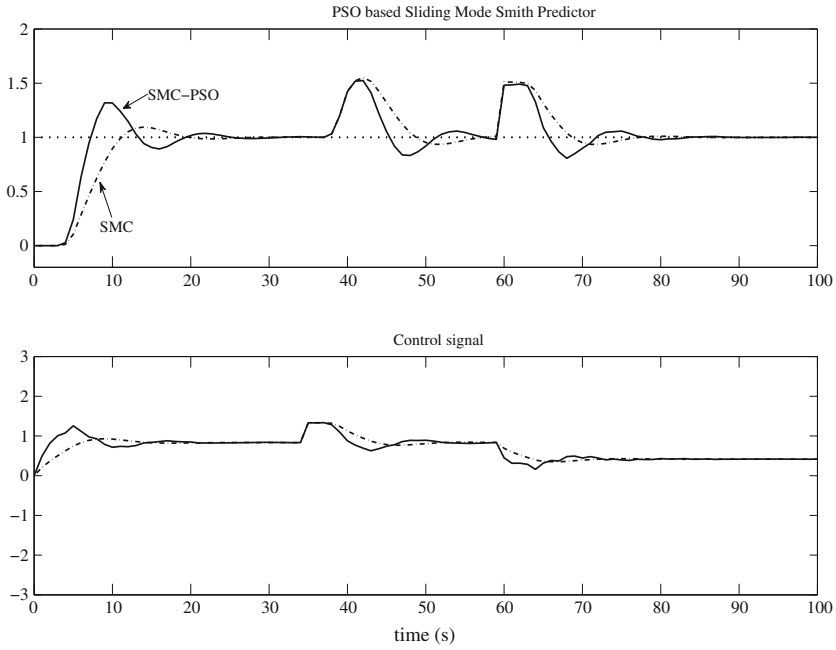


Fig. 9 G_{p2} —system output—scenario #3

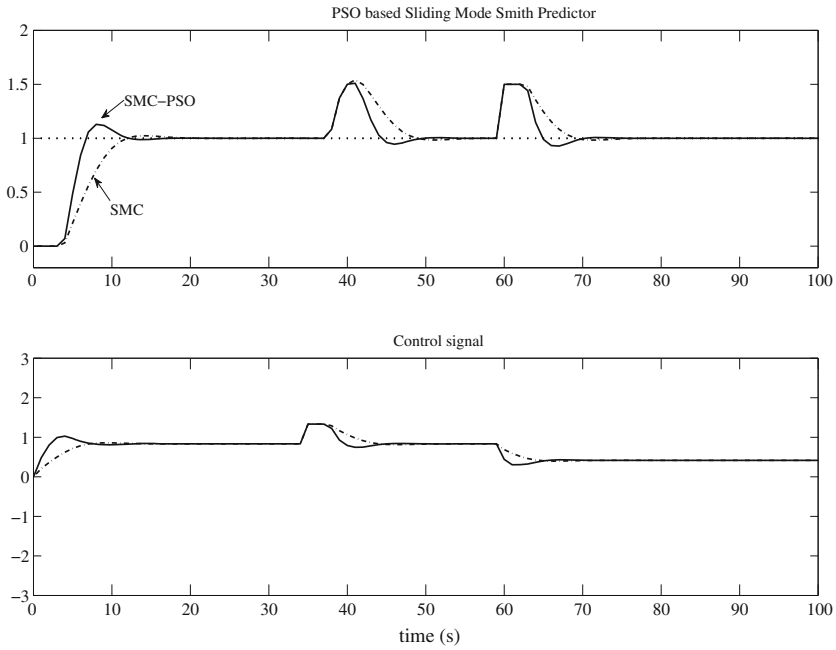


Fig. 10 G_{p2} —system output—scenario #4

References

1. Smith, O.J.: A controller to overcome dead time. *ISA J.* **6**, 28–33 (1959)
2. Smith, C.A., Corripio, A.B.: *Principles and Practice of Automatic Process Control*, 2nd edn. Wiley (1997)
3. Camacho, O.: Sliding Mode Control in Process Industry. In: *Instrument Engineer's Handbook*, vol. 2, 4th edn. Bela G. Liptak (2005)
4. Camacho, O., Smith, C., Moreno, W.: Development of an internal model sliding mode controller. *Ind. Eng. Chem. Res.* **42**(3), 568–573 (2003)
5. Utkin, V.I.: *Sliding Modes in Control and Optimization*. Springer, Berlin-Heidelberg (1992)
6. Yuanhao, S., Jingcheng, W., Yunfeng, Z.: Sliding mode predictive control of main steam pressure in coal-fired power plant boiler. *Chin. J. Chem. Eng.* **20**, 1107–1112 (2012)
7. Ingimundarson, A., Hagglund, T.: Robust tuning procedures of dead-time compensating controllers. *Control Eng. Pract.* **9**(11), 1195–1208 (2001)
8. Darby, M.L., Nikolaou, M.: MPC: current practice and challenges. *Control Eng. Pract.* **20**(4), 328–342 (2012)
9. Kaya, I.: IMC based automatic tuning method for PID controllers in a Smith predictor configuration. *Comput. Chem. Eng.* **28**, 281–290 (2004)
10. Kennedy, J., Eberhart, R.: Particle swarm optimization. In: *Proceedings of IEEE International Conference on Neural Networks*, vol. 4, pp. 1942–1948 (1995)
11. Jabri, K., Dumur, D., Godoy, E., Mouchette, A., Bèle, B.: Particle swarm optimization based tuning of a modified smith predictor for mould level control in continuous casting. *J. Process Control* **21**(2), 263–270 (2011)
12. Kanthaswamy, G., Jerome, J.: Control of dead-time systems using derivative free particle swarm optimization. *Int. J. Bio-inspired Comput.* **3**(2), 85–102 (2011)
13. Oliveira, J., Boaventura-Cunha, J., Oliveira, P.B.M., Freire, H.: A swarm intelligence-based tuning method for the sliding mode generalized predictive control. *ISA Trans.* **53**, 1501–1515 (2014)
14. Camacho, O., Rojas, R., García, W.: Variable structure control applied to chemical processes with inverse response. *ISA Trans.* **39**, 55–72 (1999)
15. Tian, D.P.: Review of convergence analysis of particle Swarm optimization. *Int. J. Grid Distrib. Comput.* **6**(6), 117–128 (2013)
16. Reynoso–Meza, G., Blasco, X., Sanchis, J., Martinez, M.: Controller tuning using evolutionary multi-objective optimization: current trends and applications. *Control Eng. Pract.* **28**(1), 58–73 (2014)

Quadruple Real Dominant Pole Tuning of a Filtered PID Controller

Mikuláš Huba and Pavol Bisták

Abstract This paper proposes an integrated tuning of a two degree of freedom (2DOF) PID controller extended by an n th order binomial low pass filter for first order plant with dead time. The task is motivated by enabling an flexible achievement of a required measurement noise attenuation. By comparing two modifications of a quadruple real dominant pole tuning derived for two elementary situations it proposes a simplified tuning modification that may be easily applied to a general situation.

Keywords PID control · Filtration · Noise attenuation

1 Introduction

Recently, design of filtered PID control attracted attention of several papers [1–4]. In [5], an alternative approach has been proposed based on application of the multiple real dominant pole method. Part of this approach related to the simplified two degree of freedom (2DOF) PI controller tuning has already been analyzed in [6]. This paper should underpin validity of the presented integrated PID controller tuning devoted to the first order time delayed (FOTD) plants extended by a n th order binomial filter to FPID control. The multiple real dominant pole method may be considered as one of the first known methods for analytical controller tuning [7]. This paper extends newer results of [8, 9], where it has been applied to a 2DOF PID tuning for the FOTD plants

$$S(s) = \frac{Y(s)}{U(s)} = \frac{K_s e^{-T_d s}}{s + a} \quad (1)$$

M. Huba (✉) · P. Bisták
Slovak University of Technology in Bratislava, Ilkovičova 3, 812 19 Bratislava, Slovakia
e-mail: mikulas.huba@stuba.sk

P. Bisták
e-mail: pavol.bistak@stuba.sk

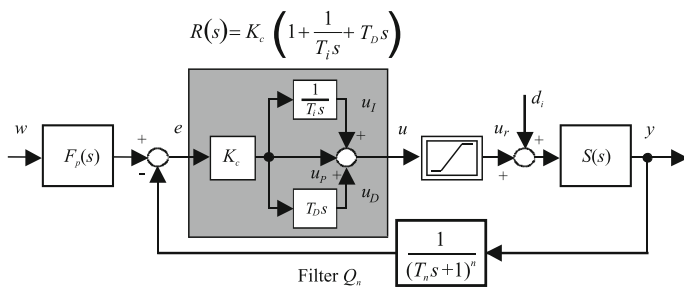


Fig. 1 One of two limit configurations of a filtered 2DOF PID control (FPID)

The 2DOF PID control has been considered as extension of a 1DOF $R(s)$ by a prefilter $F_p(s)$ with weighting coefficients b and c to speed up setpoint responses

$$R(s) = K_c \frac{1 + T_i s + T_i T_D s^2}{T_i s}; \quad F_p(s) = \frac{c T_i T_D s^2 + b T_i s + 1}{T_i T_D s^2 + T_i s + 1} \quad (2)$$

As in [5, 10] a binomial low-pass filter

$$Q_n(s) = 1/(T_n s + 1)^n; \quad n = 1, 2, \dots \quad (3)$$

may be introduced into the loop to attenuate measurement noise. Several papers (as e.g. [4]) considered its location in the feedback (Fig. 1). Since just the disturbance responses have been analyzed, its location in the loop was not important. However, for the setpoint responses its location at the controller input, output, or in the feedback path (Fig. 1) may play a significant role. Furthermore, location of at least first order filter in the feedforward path is required by the controller implementation. For $n > 1$, also combinations of all possibilities yielding the resulting transfer function $Q_n(s)$ may be interesting. In [5] a simplified method based on equivalence of time delays has been introduced appropriate for nearly optimal disturbance responses of FOTD plants. This paper extends this method also to the setpoint step responses design of the FPID control. It also aims at analyzing simplifications made and continuing in evaluation of an integrated tuning yielding by $R(s) + F_p(s) + Q_n(s)$ possibly fast transients with guaranteeing possibly low deviations from the ideal setpoint and disturbance response shapes at the plant input and output [11, 12]. It complements and extends similar analysis devoted to the PI control [6].

The rest of paper will be structured as follows. In Sect. 2, more detailed problem formulation will be given. Section 3 offers derivation of optimal $R(s) + F_p(s) + Q_n(s)$ tuning for $T_d = 0$ with $Q_n \neq 1$, or FOTD plants without Q_n . Section 4 compares the achieved results with those derived by the generalized tuning [5] based on equivalence of loop time delays. It also evaluates impact of a measurement noise. Results of the paper are summarized by Conclusions.

2 Problem Formulation

The aim of the integrated design is to work with possibly lowest values of the integral of absolute error (IAE) formed by the IAE_s values corresponding to the setpoint w steps

$$IAE_s = \int_0^{\infty} |e(t)| dt ; e = w - y ; d_i = 0 \quad (4)$$

and IAE_d corresponding to d_i steps with $w = 0$.

Thereby, the “integral” deviations from ideal shapes of the setpoint and disturbance step responses at the plant input and output [11, 12] should fulfill

$$\begin{aligned} TV_0(y_s) &\leq \epsilon_{ys} ; TV_1(y_d) \leq \epsilon_{yd} \\ TV_1(u_s) &\leq \epsilon_{us} ; TV_1(u_d) \leq \epsilon_{ud} \end{aligned} \quad (5)$$

with a vector $\epsilon_{ys}, \epsilon_{yd}, \epsilon_{us}, \epsilon_{ud}$ of chosen tolerable amplitude deviations. Again, the index s corresponding to the setpoint and d corresponding to the disturbance responses. The used performance measures represent modifications of the relative total variance (TV) [11–13]. With $y_{\infty} - y_0$ representing nett output change after a setpoint step with y_0 and y_{∞} denoting the initial and final values and $y_m \notin (y_0, y_{\infty})$ denoting an extreme value of an input disturbance step response,

$$TV_0(y) = \sum_i |y_{i+1} - y_i| - |y_{\infty} - y_0| ; TV_1(y) = \sum_i |y_{i+1} - y_i| - |2y_m - y_{\infty} - y_0|$$

represent deviations from monotonicity (MO) and from an ideal output pulse (1P) formed by two MO intervals separated by y_m . At the plant input $u(t)$, deviations from 1P step responses [11] will be evaluated by $TV_1(u)$ measures.

3 Optimal Tuning by QRDP Method

The setpoint-to-output transfer functions with $F_p(s)$, $R(s)$ and $Q_n(s)$ in the feedback, or in the feedforward path are

$$F_{wy1}(s) = \frac{F_p(s)R(s)S(s)}{1 + R(s)S(s)Q_n(s)} = \frac{K_c K_s (cT_i T_D s^2 + bT_i s + 1)(1 + T_n s)^n}{T_i s(s + a)e^{T_d s}(1 + T_n s)^n + K_c K_s (T_i T_D s^2 + T_i s + 1)} \quad (6)$$

$$F_{wy2}(s) = \frac{F_p(s)R(s)S(s)Q_n(s)}{1 + R(s)S(s)Q_n(s)} = \frac{K_c K_s (cT_i T_D s^2 + bT_i s + 1)}{T_i s(s + a)e^{T_d s}(1 + T_n s)^n + K_c K_s (T_i T_D s^2 + T_i s + 1)} \quad (7)$$

The aim of the controller tuning is to choose the loop parameters guaranteeing a quadruple real dominant pole (QRDP) of the characteristic quasi-polynomial

$$P(s) = T_i s(s+a)e^{T_d s}(1+T_n s)^n + K_c K_s (T_i T_D s^2 + T_i s + 1) \quad (8)$$

Such a pole s_o of $P(s)$ (8) has to fulfill conditions $P(s_o) = 0$, $\dot{P}(s_o) = 0$, $\ddot{P}(s_o) = 0$ and $\ddot{P}(s_o) = 0$. Since a general solution to this problem is not yet known (or too complex), we will deal in our analysis with particular solutions.

3.1 Optimal Tuning for $T_d > 0, T_n = 0$

An “optimal” design design yields parameters K_c, T_i, T_D , prefilter coefficients b, c and Q_n parameters n and T_n . They should give transients with minimal IAE_s , or IAE_d values satisfying constraints (5). Thereby, the admissible limits in (5) should be small positive numbers. For $T_n = 0$ the “optimal” parameters K_{co}, T_{Do} and T_{io} are given as

$$\begin{aligned} s_{od} &= -\frac{6+A_d-S_d}{2T_d}, \quad A_d = aT_d, \quad S_d = \sqrt{A_d^2 + 12} \\ K_{od} &= K_{co}K_sT_d = \frac{S(A+12) - (A^2 + 2A + 36)}{2} e^{(S-A-6)/2} \\ \tau_{iod} &= \frac{T_{io}}{T_d} = \frac{2(36 + 2A + A^2 - (A+12)S)}{A^3 + 12A^2 + 36A + 288 - (A^2 + 12A + 84)S} \\ \tau_{Dod} &= \frac{T_{Do}}{T_d} = \frac{2-S}{A^2 + 2A + 36 - (A+12)S} \end{aligned} \quad (9)$$

Optimal $F_p(s)$ may be determined to cancel zeros and two dominant poles s_o of the closed loop transfer functions (6) and (7) $b_o = -2/(T_i s_o), c_o = 1/(T_i T_D s_o^2)$

$$\begin{aligned} b_o &= -\frac{2}{\tau_{iod} T_d s_{od}} = 2 \frac{A^3 + 12A^2 + 36A + 288 - (A^2 + 12A + 84)S}{[A^2 + 2A + 36 - S(A+12)](A+6-S)} \\ c_o &= \frac{1}{\tau_{iod} \tau_{Dod} T_d^2 s_{od}^2} = \frac{A^3 + 12A^2 + 36A + 288 - (A^2 + 12A + 84)S}{(S-2)(A+6-S)} \end{aligned} \quad (10)$$

3.2 Optimal Tuning for $T_d = 0, T_n > 0$

Now, the method yields

$$\begin{aligned} s_{on} &= -\frac{(n+1)(6+A_n(n-1)) - S_n}{2(n+1)(n+2)T_n}, \quad A_n = aT_n \\ S_n &= \sqrt{(n^2-1)(A_n^2(n^2-1) - 12A_n + 12)} \end{aligned} \quad (11)$$

General solutions for the controller parameters are too complex. Therefore, they are displayed just for the two most important situations with $n = 2, 3$, when for $K_{on} = K_{co}K_sT_n$, $\tau_{ion} = T_{io}/T_n$ and $\tau_{Don} = T_{Do}/T_n$ one

$$\begin{aligned}
 n = 2; \quad K_{o2} &= \frac{A_n^3 + 6A_n^2 - 4A_n + 8}{16K_sT_n}; \\
 \tau_{io2} &= \frac{16(A_n^3 + 6A_n^2 - 4A_n + 8)}{A_n^4 + 8A_n^3 + 24A_n^2 + 32A_n + 16}; \quad \tau_{Do2} = \frac{2(3A_n^2 - 4A_n + 4)}{A_n^3 + 6A_n^2 - 4A_n + 8}; \\
 b &= \frac{A_n^4 + 8A_n^3 + 24A_n^2 + 32A_n + 16}{2(A_n^3 + 6A_n^2 - 4A_n + 8)(A_n + 2)}; \quad c = \frac{A_n^4 + 8A_n^3 + 24A_n^2 + 32A_n + 16}{2(3A_n^2 - 4A_n + 4)(A_n + 2)^2}
 \end{aligned} \tag{12}$$

$$\begin{aligned}
 n = 3; \quad K_{o3} &= \frac{\sum_{i=0}^4 \alpha_i A_n^i}{500} \quad \alpha_4 = -32; \quad \alpha_3 = 16S_n - 24; \quad \alpha_2 = 24S_n + 117; \\
 \tau_{io3} &= \frac{25T_n \sum_{i=0}^{i=4} \alpha_i A_n^i}{3 \sum_{i=0}^{i=5} \beta_i A_n^i}; \quad \text{where } \alpha_4 = -32; \quad \alpha_3 = -24 + 16S_n; \quad \alpha_2 = 24S_n + 117; \\
 \alpha_1 &= -48S_n + 94; \quad \alpha_0 = -27 + 72S_n; \quad \beta_5 = -32; \quad \beta_4 = 16S_n - 80; \quad \beta_3 = 52S_n - 5; \\
 \beta_2 &= 34S_n + 135; \quad \beta_1 = -72S_n + 765; \quad \beta_0 = 186S_n - 351; \\
 \tau_{Do3} &= \frac{\sum_{i=0}^{i=3} \alpha_i A_n^i}{\sum_{i=0}^{i=4} \beta_i A_n^i} \quad \text{where } \alpha_3 = 4; \quad \alpha_2 = -2S_n - 9; \quad \alpha_1 = 3S_n + 3; \quad \alpha_0 = -3S_n - 2 \\
 \beta_4 &= 32; \quad \beta_3 = 24S_n - 16; \quad \beta_2 = -24S_n - 117; \quad \beta_1 = 48S_n - 94; \quad \beta_0 = 27 - 72S_n \\
 b &= \frac{12 \sum_{i=0}^{i=5} \alpha_i A_n^i}{5(6 + 2A_n - S_n) \sum_{i=0}^{i=5} \beta_i A_n^i} \quad \text{where } \alpha_5 = 32; \quad \alpha_4 = 80 - 16S_n; \quad \alpha_3 = 5 - 52S_n; \\
 \alpha_2 &= -34S_n - 135; \quad \alpha_1 = 72S_n - 765; \quad \alpha_0 = 351 - 186S_n \quad \beta_4 = 32; \quad \beta_3 = 24 - 16S_n; \\
 \beta_2 &= -24 - 117S_n; \quad \beta_1 = 48S_n - 94; \quad \beta_0 = 27 - 72S_n \\
 c &= \frac{3 \sum_{i=0}^{i=5} \alpha_i A_n^i}{5(6 + 2A_n - S_n)^2 \sum_{i=0}^{i=3} \beta_i A_n^i} \quad \text{where } \alpha_5 = 32; \quad \alpha_4 = 80 - 16S_n; \quad \alpha_3 = 5 - 52S_n; \\
 \alpha_2 &= -34S_n - 135; \quad \alpha_1 = 72S_n - 765; \quad \alpha_0 = 351 - 186S_n \quad \beta_3 = 4; \quad \beta_2 = -9 - 2S_n; \\
 \beta_1 &= 3S_n + 3; \quad \beta_0 = -2 - 3S_n
 \end{aligned} \tag{13}$$

3.3 Stability Conditions

Stability requires the QRDP (9) and (11) to be negative, which leads to

$$\begin{aligned}
 s_{od} &= -\frac{6 + A_d - \sqrt{A^2 + 12}}{2T_d} < 0 \Rightarrow A_d > -2 \\
 s_{on} &= -\frac{(n+1)(6 + A_n(n-1)) - S_n}{2(n+1)(n+2)T_n} \Rightarrow A_n > \frac{-2}{n-1}
 \end{aligned} \tag{14}$$

Obviously, stability of the loop with Q_n depends on n .

3.4 Equivalence of the Time Delays

Up to now, just situations with a dead time, or with a filter have been considered. In the second case, the corresponding analytical formulas are rather complex and their derivation requires a computer algebra support. To avoid yet more complex situations in considering loops containing simultaneously both type of delays, in [5] a simplified method has been applied. It is based on equivalence of both delays under requirement of a fixed position of the QRDP in (9) and (11). From the requirement $s_{od} = s_{on}$ one gets

$$\begin{aligned} -\frac{6 + A_d - S_d}{2T_d} &= -\frac{(n+1)(6 + A_n(n-1)) - S_n}{2(n+1)(n+2)T_n} \\ A_d = aT_d, \quad S_d &= \sqrt{A_d^2 + 12} \\ A_n = aT_n, \quad S_n &= \sqrt{(n^2 - 1)(A_n^2(n^2 - 1) - 12A_n + 12)} \end{aligned} \quad (15)$$

Solving this equation for T_n yields for $n = 2$ and $n = 3$ roots

$$\begin{aligned} n = 2; \quad T_n &= \frac{2T_d}{12 + 2S_d - 3A_d} \\ n = 3; \quad S_{dd} &= \sqrt{33A_d^2 - 24S_dA_d + 288 + 72S_d - 144A_d} \\ T_{ne} &= -\frac{T_d}{2} \frac{-9A_d + 36 + 6S_d + S_{dd}}{7S_dA_d - 7A_d^2 - 120 - 30S_d + 42A_d} \end{aligned} \quad (16)$$

These may be interpreted in such a way that a dead time T_d has on the closed loop performance characterized by the QRDP s_{od} the same impact as an equivalent time constant T_n of the n -th order filter (3) yielding QRDP s_{on} . In controlling a loop with Q_n , Eq. (16) may be used to specify its parameters that have the same impact as a delay $T_d = T_e$. This new tuning parameter T_e has been introduced to distinguish the equivalent delay from a real plant dead time T_d . Subsequently, a new tuning procedure may be proposed based on additivity of several loop dead times in an optimal loop tuning.

It is also possible to solve Eq. (15) for $T_e = T_d$, when

$$\begin{aligned} n = 2; \quad T_e &= \frac{4T_n(6 + 9A_n + S_n)}{4 + 5A_n^2 + 12A_n} \\ n = 3; \quad S_{nn} &= \sqrt{234A_n + 309A_n^2 - 42S_nA_n + 126 - 36S_n} \\ T_e &= \frac{5T_n(18 + 21A_n - 3S_n - S_{nn})}{21 - 6S_n + 14A_n^2 - 7S_nA_n + 39A_n} \end{aligned} \quad (17)$$

It means that once choosing a filter Q_n , it is possible to find an equivalent dead time T_e that in tuning the loop according to (9) has to be added to the plant dead time T_d .

For a plant with parameters K_s, a and T_d and a closed loop tuning parameter $T_e > 0$ the filter impact leads to an enlarged loop dead time

$$\bar{T}_d = T_d + T_e \quad (18)$$

For a given plant (1) the controller may be chosen described in Sect. 3.1 which is tuned for \bar{T}_d . By substituting \bar{T}_d instead of T_d into (9), the controller tuning depends also on T_e . Furthermore, for an arbitrarily chosen n it offers the filter time constants T_n calculated according to (16).

The procedure may be summarized as follows:

1. Choose an appropriate value of the tuning parameter $T_e = \bar{T}_d - T_d > 0$ corresponding to a required degree of filtration;
2. Specify the controller parameters (9) corresponding to T_d replaced by \bar{T}_d in (18);
3. Choose a filter order n and by a delay equivalence $T_n = f(n, T_e)$ (16) specify the filter time constants T_n ;
4. By experimentally evaluating the loop properties for different n , choose an optimal filter $Q_n(s)$ guaranteeing the optimal loop performance.

Although the new method [5] showed interesting results, it is only intuitive and approximative and thus the question is, how it is possible to analyze its character more rigorously. Since for a general case with both $T_d > 0$ and $Q_n, n > 0$ an optimal tuning is not yet known, one possibility is to check its results for the situations treated in Sect. 3.2.

4 Comparing both Approaches in FO Plant Control

For a first order (FO) plant with $T_d = 0$ and Q_n specified by $n > 0$ and T_n fulfilling the stability conditions there exist an “optimal” TRDP controller tuning (11). At the same time, according to Sect. 3.4 it is possible to propose an equivalent controller based on equivalent dead time and to compare its results with the previous one. It means that for each n and T_n one has to derive from (15) an equivalent time constant T_e . Then, to calculate \bar{T}_d according to (18) with $T_d = 0$ and to propose a controller according to (9) and (10) with T_d substituted by \bar{T}_d . At the end, it is possible to compare the controller parameters and the resulting control performance.

In order to show imperfection of the tuning based on T_e , both tuning procedures are firstly compared for $T_n \in [0.049, 5]$ with $T_s = 0.001$ being the sampling period in an idealized loop without noise (measurement noise amplitude $\delta = 0$, Fig. 2). All performance measures have been evaluated for $T_{sim} = 50$. The responses tuned by T_e show $TV_0(y_s)$ values that are constant for a broad range of T_n and correspond to an output overshooting below 1%. It causes a slightly increased IAE_s values and

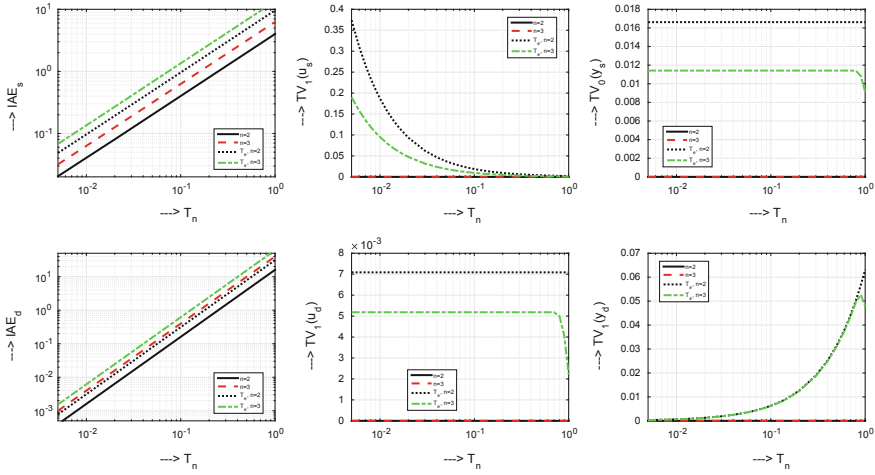


Fig. 2 FPID tunings based on n , T_n and T_e : $a = 0$, $T_s = 0.001$, $\delta = 0$, $T_{sim} = 50$

also increased shape related deviations at the plant input and output. Shape related deviations of solutions based on exact tuning by n and T_n caused just by imperfection of the numerical simulation are negligible. By increasing T_n the $TV_1(u_s)$ values characterizing an additional control effort due to the noise decrease.

For the disturbance steps, the situation is reversed. $TV_1(u_d)$ shows nearly constant values, whereas $TV_1(y_d)$ is increasing with T_n .

The shape related deviations of FPID tuned by T_e are decreasing with increasing n and the IAE values are with increasing n approaching those corresponding to the tuning based on n and T_n .

When repeating the same experiment for a noise amplitude $\delta = 0.01$ (noise generated with T_s by the Simulink block Uniform Random Number), one gets modified characteristics in Figs. 3 and 4.

Now, by increasing T_n all shape related deviations decrease (Fig. 3). Noise attenuation is effective just from some T_n . Below this value, IAE values increase (due to the noise impact). It is evident that the tuning by T_e leads to increased IAE values, but, for a given T_n , the shape related deviations may be lower than those corresponding to (faster) transients tuned by n and T_n . In each case, the imperfections due to the tuning by T_e may mostly be neglected with respect to the noise impact.

The loop performance under noise impact may also be characterized by the noise characteristics in Fig. 4. To get high speed responses (low IAE values) with a low additional control effort (low $TV_1(u)$ values), the characteristics should be as far as possible to the left (as high as possible). Obviously, use of a filter with $n = 3$ leads to significantly better results than for $n = 2$. However, for $n > 3$ the achieved performance is no more so intensive [5]. It is also to note that the simplified tuning by T_e leads to more significant performance decrease for the setpoint steps.

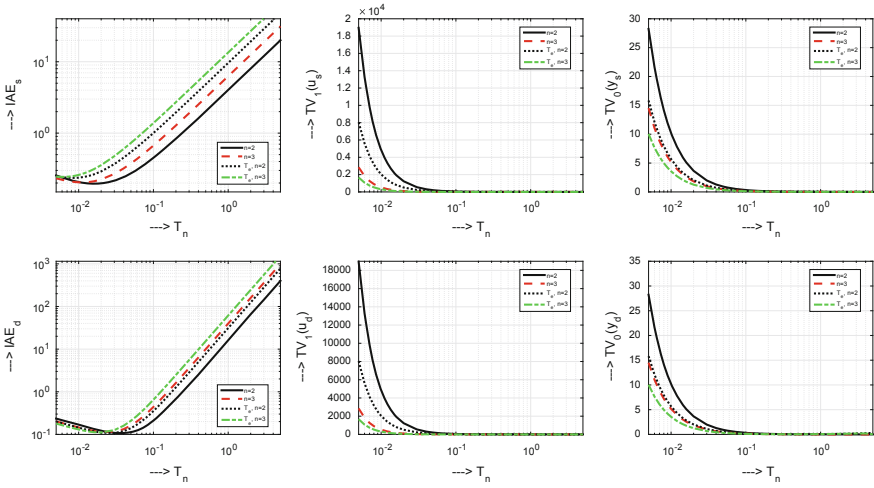


Fig. 3 FPID tunings based on n, T_n and T_e : $a = 0, T_s = 0.001, \delta = 0.01, T_{sim} = 200$

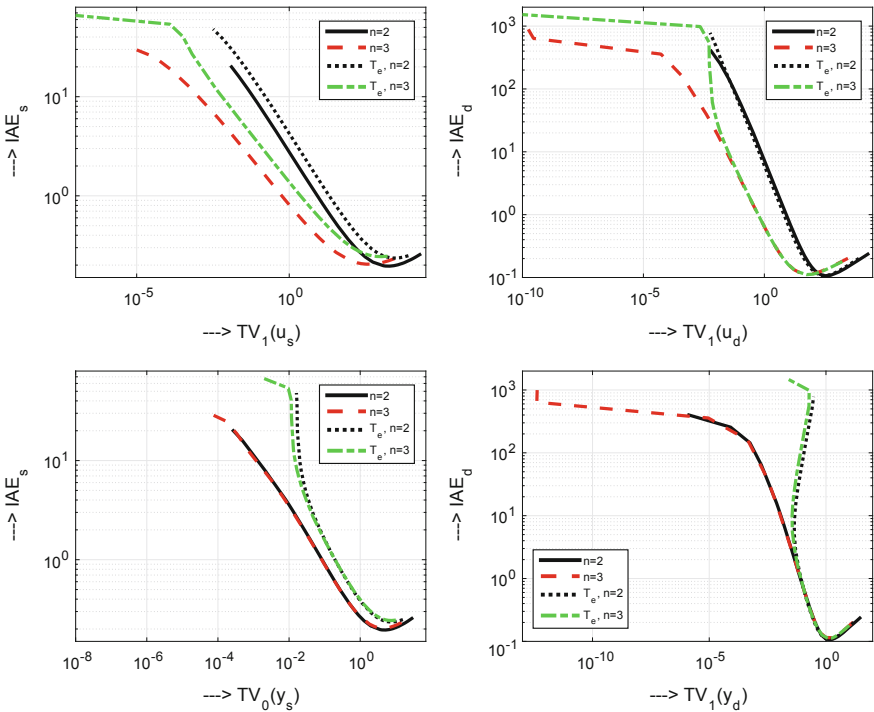


Fig. 4 IAE_s versus $TV_1(u_s)$ and $TV_0(y_s)$ and IAE_d versus $TV_1(u_d)$ and $TV_0(y_d)$ for analytical FPID tunings based on n and T_n and on T_e : $a = 0, \delta = 0.01; T_s = 0.001, T_{sim} = 200$

With respect to the possible noise impact these imperfections due to simplified tuning might be neglected. Obviously, with respect to the disturbance responses this simplified tuning is yet more attractive.

5 Conclusions and Future Works

The paper has extended the simplified integrated tuning of filtered PID control (FPID) for nearly optimal disturbance responses of FOTD systems from [5] also to the setpoint responses. At the same time, by deriving optimal control algorithms based on the quadruple real dominant pole method to the case of first order plants with n -th order binomial filter it established a basis for evaluating precision of the simplified tuning from [5].

Whereas the simplified tuning shows higher imperfections for the setpoint responses, it may still be improved by an appropriate feedforward. In the case of disturbance step responses the simplified method shows an increasing precision for an increasing filter order. With respect to a possible noise impact, in majority of practical applications the imperfections due to the simplified tuning might be negligible.

Intuitively one might also expect that the imperfections due to simplified tuning will decrease in dealing with n th order filters combined with plant dead time.

Acknowledgments This work has been partially supported by the grants APVV-0343-12 Computer aided robust nonlinear control design and VEGA 1/0937/14 Advanced methods for nonlinear modeling and control of mechatronic systems.

References

1. Isaksson, A., Graebe, S.: Derivative filter is an integral part of pid design. *Control Theory Appl. IEE Proc.* **149**(1), 41–45 (2002)
2. Hägglund, T.: Signal filtering in PID control. In: *IFAC Conference on Advances in PID Control PID'12*, vol. 2, Part 1 (2012)
3. Larsson, P., Hägglund, T.: Comparison between robust PID and predictive PI controllers with constrained control signal noise sensitivity. In: *IFAC Conference on Advances in PID Control PID'12*, vol. 2, Part 1, pp. 175–180 (2012)
4. Segovia, V.R., Hägglund, T., Aström, K.: Measurement noise filtering for PID controllers. *J. Process Control* **24**(4), 299–313 (2014)
5. Huba, M.: Filter Choice for an Effective Measurement Noise Attenuation in PI and PID Controllers, in *ICM2015*. Nagoya, Japan (2015)
6. Huba, M.: Triple real dominant pole tuning of a filtered PI controller. In: *28th International Conference on Cybernetics and Informatics*, Levoca, Slovakia (2016)
7. Oldenbourg, R., Sartorius, H.: *Dynamik selbsttätiger Regelungen*, 2nd edn, p. 1951. R. Oldenbourg-Verlag, München (1944)
8. Vítečková, M., Víteček, A.: Two-degree of freedom controller tuning for integral plus time delay plants, *ICIC Express Letters. Int. J. Res. Surv., Jpn.* **2**(3), 229–255 (2008)
9. Vítečková, M., Víteček, A.: 2DOF PI and PID controllers tuning. In: *9th IFAC Workshop on Time Delay Systems*, vol. 9, Praha, pp. 343–348 (2010)

10. Rivera, D.E., Morari, M., Skogestad, S.: Internal model control. 4. pid controller design. *Ind Eng. Chem. Res.* **25**(1), 252–265 (1986)
11. Huba, M.: Performance measures, performance limits and optimal PI control for the IPDT plant. *J. Process Control* **23**(4), 500–515 (2013)
12. Huba, M.: Comparing 2DOF PI and predictive disturbance observer based filtered PI control. *J. Process Control* **23**(10), 1379–1400 (2013)
13. Skogestad, S.: Simple analytic rules for model reduction and PID controller tuning. *J. Process Control* **13**, 291–309 (2003)

Smith Predictor Tuned Through Fuzzy Fractional PID Controller

Isabel S. Jesus and Ramiro S. Barbosa

Abstract In this paper we study the control of a stable oscillatory system with a time delay, based on the application of the fractional calculus concepts. In this perspective, several algorithms are investigated and compared, when integrated within a Smith predictor structure with a fuzzy fractional $PD^\beta+I$ controller in which the parameters are optimized by a genetic algorithm. Simulations are presented assessing the performance of the proposed fractional algorithms.

Keywords Fractional calculus · Fuzzy fractional PID control · Smith predictor · GA algorithm · Optimization

1 Introduction

In the last decades, the fractional order calculus (FC) had an growing interest in the scientific community, particularly in the application of modeling complex systems, and also in the process control. Some other works and applications are in the field of thermal systems, electrical transmission lines, electromagnetism, mechanical or robotic systems [1, 2].

In this paper we study several control strategies for systems with time delay, using fuzzy fractional control algorithms [3–5] inserted in a Smith predictor (SP) structure. The adoption of fractional controllers has been justified by its superior performance, particularly when used for the control of fractional dynamical systems. The fuzzy control methodology, which emerged on the foundations of Zadeh's fuzzy set theory [3, 4, 6], is used for solve control problems in complex and nonlinear systems. This algorithm is based in the human perception of the problem, and is applied in

I.S. Jesus (✉) · R.S. Barbosa

Department of Electrical Engineering, GECAD—Knowledge Engineering and Decision Support Research Center, Institute of Engineering/Polytechnic of Porto (ISEP/IPP), Bucharest, Romania
e-mail: isj@isep.ipp.pt

R.S. Barbosa
e-mail: rsb@isep.ipp.pt

many areas of science and engineering like industrial systems, economy or medicine. The SP algorithm was developed by O.J.M. Smith in 1957. This algorithm, have an internal model to predict the delay response of the process, which is very effective in improving their control [7, 8]. The SP can also be used for high order systems that exhibit apparent dead time.

In this way, the article is organized as follows. Section 2 gives the basics of fractional-order control systems. Section 3 presents the genetic optimization algorithm. Section 4 exposes the fuzzy fractional PID^β control. Section 5 gives the numerical results assessing the effectiveness of given scheme. Finally, Sect. 6 gives the conclusions.

2 Basics of Fractional Calculus

The definition of fractional-order derivatives and integrals has been the subject of different approaches [1, 2]. The Riemann-Liouville definition for the fractional order derivative is ($\alpha > 0$):

$${}_a D_t^\alpha f(t) = \frac{1}{\Gamma(n-\alpha)} \frac{d^n}{dt^n} \int_a^t \frac{f(\tau)}{(t-\tau)^{\alpha-n+1}} d\tau, \quad n-1 < \alpha < n \quad (1)$$

where n is integer and Γ is the Gamma function. The Grünwald-Letnikov definition is ($\alpha \in \mathfrak{R}$):

$${}_a D_t^\alpha f(t) = \lim_{h \rightarrow 0} \frac{1}{h^\alpha} \sum_{k=0}^{\lfloor \frac{t-a}{h} \rfloor} (-1)^k \binom{\alpha}{k} f(t-kh) \quad (2a)$$

$$\binom{\alpha}{k} = \frac{\Gamma(\alpha+1)}{\Gamma(k+1)\Gamma(\alpha-k+1)} \quad (2b)$$

where h is the time increment and $[x]$ means the integer part of x .

Considering vanishing initial conditions, the fractional *differintegration* is defined in the Laplace domain, $F(s) = L\{f(t)\}$, as:

$$L\{{}_a D_t^\alpha f(t)\} = s^\alpha F(s), \quad \alpha \in \mathfrak{R} \quad (3)$$

The usual approach for obtaining discrete equivalents of continuous operators of type s^α adopts the Euler, Tustin and Al-Alaoui generating functions [3]. Thus, by using the Euler operator $w(z^{-1}) = (1-z^{-1})/T_c$, and performing a power series expansion (PSE) of $[w(z^{-1})]^\alpha = [(1-z^{-1})/T_c]^\alpha$ gives the discretization formula corresponding to the Grünwald-Letnikov definition (2):

$$D^\alpha (z^{-1}) = \left(\frac{1 - z^{-1}}{T_c} \right)^\alpha = \sum_{k=0}^{\infty} \left(\frac{1}{T_c} \right)^\alpha (-1)^k \binom{\alpha}{k} z^{-k} \quad (4)$$

where T_c is the sampling period.

A rational-type approximation can be obtained through a Padé approximation to the Taylor series (4), yielding the discrete transfer function:

$$H(z^{-1}) = \frac{b_0 + b_1 z^{-1} + \dots + b_m z^{-m}}{1 + a_1 z^{-1} + \dots + a_n z^{-n}} \quad (5)$$

where $m \leq n$ and a_k and b_k are the coefficients to be determined by the Padé technique. The same procedure can be easily applied to other types of discretization schemes [3].

3 Genetic Optimization

GA is an evolutionary algorithm inspired in Darwin's ideas which use the concepts of evolutionary biology, such as crossover, mutation or natural selection, in order to produce solutions to a given problem [9, 10].

These algorithms start with a set of solutions, generated randomly, designated by chromosomes, which represent the population (P). The solutions from a population are used to form a new population, which is expected to be better than the older one. Individuals are then selected according to the fitness function to form a new offspring, in which the more appropriate they are the more chances they have to reproduce. This is repeated until some condition is satisfied, for example, an improvement in the solution is verified.

In this work we propose a fuzzy fractional PD^β+I, where the gains are tuned by a GA. The fitness function to be minimized corresponds to the integral time absolute error (ITAE) [6, 11]:

$$J(K_e, K_{ce}, K_{ie}, K_u) = \int_0^{\infty} t |r(t) - c(t)| dt \quad (6)$$

where $(K_e, K_{ce}, K_{ie}, K_u)$ are the fuzzy PD^β+I gains to be optimized.

4 Fuzzy Fractional PD^β+I Control

In the control systems of Figs. 1 and 2, we use a fuzzy logic control (FLC) for the PD^β part and the integral action is added to the output in order to give a fuzzy PD^β+I, as shown in Fig. 3 [3, 6, 11, 12]. This type of structure eliminates the steady state

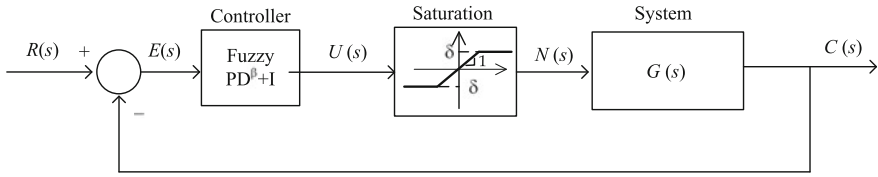


Fig. 1 Fuzzy logic control system

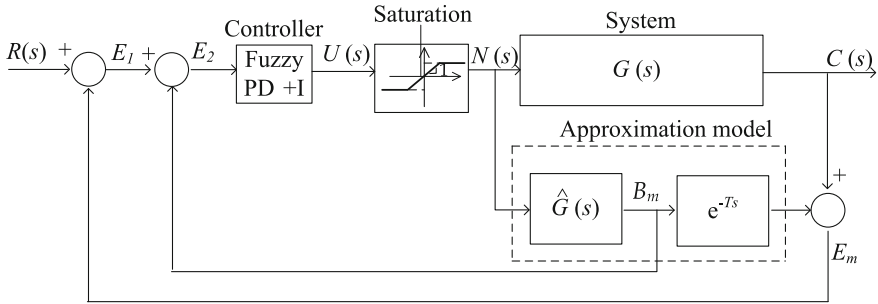


Fig. 2 Smith predictor with a fractional fuzzy PD^β+I

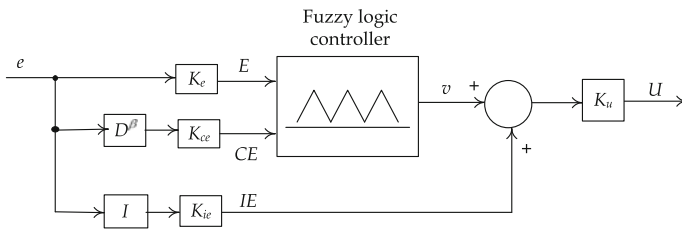


Fig. 3 Fuzzy PD^β+I

error due to the integrative action. The SP algorithm (Fig. 2), is a dead-time compensation technique, very effective in improving the control of processes having time delays [7].

The control output action U is usually a nonlinear function of E , CE and IE , given by:

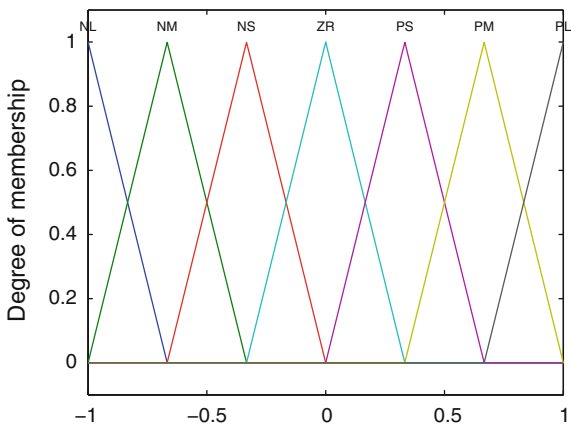
$$U(k) = [f(E, CE) + IE] K_u = [f(K_e e(k), K_{cc} D^\beta e(k)) + K_{ic} I e(k)] K_u \tag{7}$$

D^β is the discrete fractional derivative implemented as rational approximation (5) using scheme (4). In this work we consider only values of $\alpha = 1$, however we can apply an integral of fractional order, I^α , which leads to a fuzzy fractional PD^β+I^α [3].

Table 1 Fuzzy rules

E/CE	NL	NM	NS	ZR	PS	PM	PL
NL	NL	NL	NL	NL	NM	NS	ZR
NM	NL	NL	NL	NM	NS	ZR	PS
NS	NL	NL	NM	NS	ZR	PS	PM
ZR	NL	NM	NS	ZR	PS	PM	PL
PS	NM	NS	ZR	PS	PM	PL	PL
PM	NS	ZR	PS	PM	PL	PL	PL
PL	ZR	PS	PM	PL	PL	PL	PL

Fig. 4 Membership functions for E , CE and v

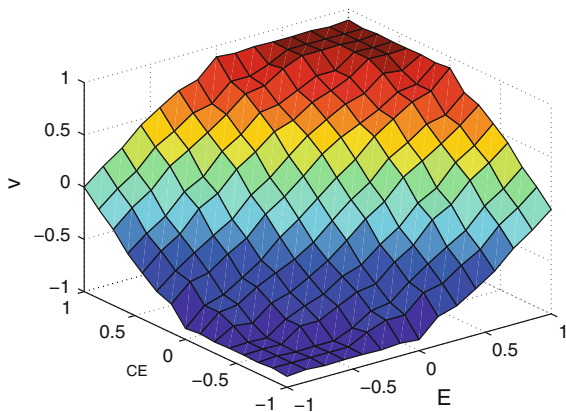


In this study we include a saturation nonlinearity in the closed-loop system of Figs. 1 and 2, inserted in series with the output of the FLC, defined as:

$$n(u) = \begin{cases} u, & |u| < \delta \\ \delta \operatorname{sign}(u), & |u| \geq \delta \end{cases} \quad (8)$$

where u and n are the input and the output of the saturation, respectively.

The basic structure for FLC is composed by a fuzzy rule base, a fuzzy inference, a fuzzification and a defuzzification process [13]. For the fuzzy $PD^\beta+I$ illustrated in Fig. 3, the rule-base is constructed as shown in Table 1, where v is the output of fuzzy controller. The fuzzy membership functions of the inputs (E , CE) and output (v) are labeled as {NL, NM, NS, ZR, PS, PM, PL}, being illustrated in Fig. 4. The control surface is presented in Fig. 5.

Fig. 5 Control surface

5 Numerical Results

In this section we analyze the control system of Figs. 1 and 2 with the fuzzy fractional $PD^\beta+I$ of Fig. 3, given by Eq. (7) with $0 \leq \beta \leq 1$.

In the closed-loop, the process corresponds to a stable oscillatory system [14] which reveals a time delay in the response, given by:

$$G(s) = \frac{2}{4s^2 + 2s + 1} e^{-4s} \quad (9)$$

In the case of SP, we consider two different approximation models inserted in the second branch of structure. In the first case, the approximation consists of an integer first order plus dead-time model $\hat{G}_{Int}(j\omega)$, resulting from the minimization of square error between the step responses of $G(j\omega)$ and $\hat{G}_{Int}(j\omega)$ (algorithm denoted by $SP_PID^\beta [\hat{G}_{Int}]$), given by:

$$\hat{G}_{Int}(s) = \frac{K_{p_{Int}}}{\tau_{Int} s + 1} e^{-sT_{Int}} \quad (10)$$

where $\{K_{p_{Int}}, \tau_{Int}, T_{Int}\} = \{2.024, 1.347, 5.375\}$, which leads to an error value of $J = 5.265$.

In the second case, the approximation is described by a fractional order plus dead-time model given by Eq. (11), with parameters estimated also in time domain, resulting from the same minimization process described previous.

$$\hat{G}_{Frac}(s) = \frac{K_{p_{Frac}}}{\tau_{Frac} s^\alpha + 1} e^{-sT_{Frac}} \quad (11)$$

where $\{K_{p_{Frac}}, \tau_{Frac}, \alpha, T_{Frac}\} = \{1.969, 2.922, 1.457, 4.9\}$, which leads to $J = 1.590$. As can be seen, the fractional order model gives a much better approximation than their integer model counterpart (10).

In this work, we compare the output response of SP, with $PD^\beta+I$ controlled system of Fig. 1, which leads in both cases to the lower error J .

In these experiments, a 4th order Padé fraction ($m = n = 4$) of type (5), is used to implement the fractional order derivative D^β , with a sampling period of $T_c = 0.01$ s. The $PD^\beta+I$ controller is tuned according ITAE (6) using a GA. The values used for the GA parameters are: population size $P = 50$, crossover probability $C = 0.8$, mutation probability $M = 0.05$ and number of generations $Ng = 100$, which are the values that lead to better simulation results. The experiments consist on executing the GA several times, for generating a combination of controller parameters, that guarantee the stochastic effects [9, 10]. In this study the GA is run 10 times and we get the best result, *i.e.* the simulation that leads to the smaller J . We set the intervals of the search space of K_e, K_{ce}, K_{ie} and $K_u \in [0, 50]$. The saturation is $\delta = 15$ and the system is simulated for 60 s.

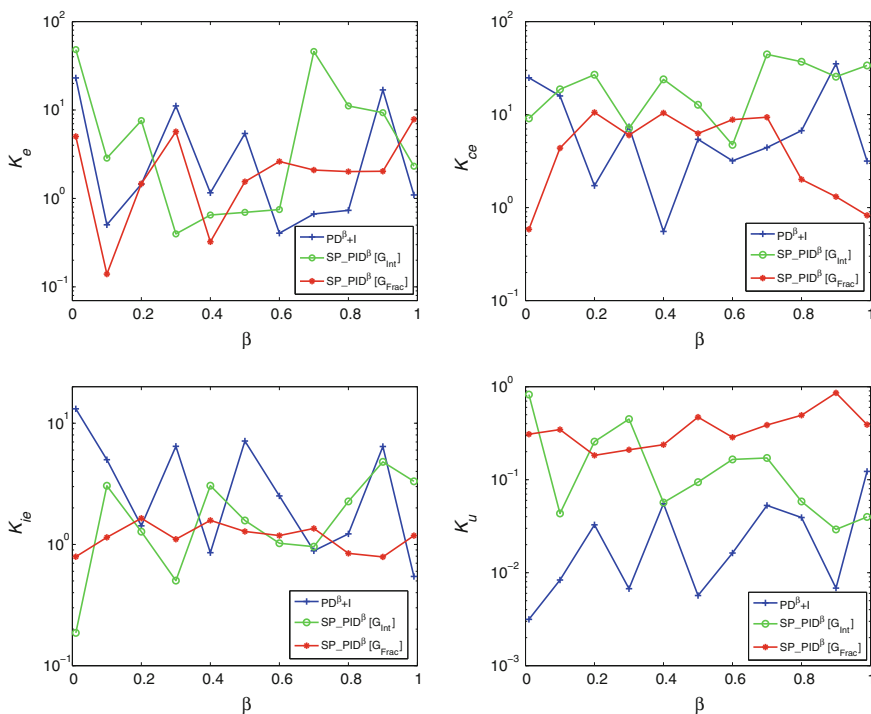


Fig. 6 Gains (K_e, K_{ce}, K_{ie} and K_u) versus β of the $PD^\beta+I, SP_PID^\beta [\hat{G}_{Int}]$ and $SP_PID^\beta [\hat{G}_{Frac}]$

Table 2 Values of the $PD^\beta+I$, $SP_PID^\beta [\hat{G}_{Int}]$ and $SP_PID^\beta [\hat{G}_{Frac}]$ for the best case

	K_e	K_{ce}	K_{ie}	K_u	β	J
$PD^\beta+I$	1.157	0.554	0.855	0.055	0.4	69.964
$SP_PID^\beta [\hat{G}_{Int}]$	0.748	4.721	1.023	0.165	0.6	48.290
$SP_PID^\beta [\hat{G}_{Frac}]$	2.031	1.309	0.789	0.858	0.9	31.180

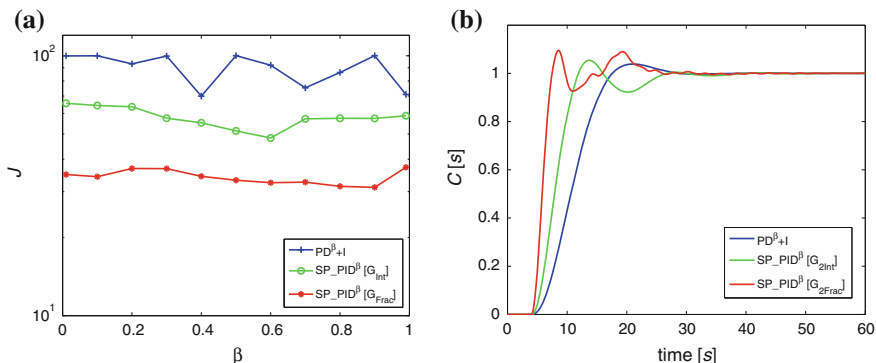
**Fig. 7** **a** Error versus β and **b** step responses for the $PD^\beta+I$, $SP_PID^\beta [\hat{G}_{Int}]$ and $SP_PID^\beta [\hat{G}_{Frac}]$, for the optimal values of β

Figure 6 illustrates the variation of the $PD^\beta+I$ gains (K_e , K_{ce} , K_{ie} and K_u) as β is varied. The controller parameters, corresponding to the minimization of those indices, for the best case (smaller error), are presented in Table 2.

Figure 7a depicts the variation of error J as function of β . In this case, it is clear that the control system with the SP algorithm improves the control system, and in particular with the fractional model. Figure 7b compares the step responses of the closed-loop systems of $SP_PID^\beta [\hat{G}_{Int}]$, $SP_PID^\beta [\hat{G}_{Frac}]$ and $PD^\beta+I$ without SP, for the best cases (smaller J). For $SP_PID^\beta [\hat{G}_{Int}]$ algorithm is adopted $\beta_{ITAE} = 0.6$, for $SP_PID^\beta [\hat{G}_{Frac}]$ $\beta_{ITAE} = 0.9$ and for $PD^\beta+I$ $\beta_{ITAE} = 0.4$.

The step responses reveals faster transient responses for both SP_PID^β algorithms, when compared with the controller without SP. Furthermore, the $SP_PID^\beta [\hat{G}_{Frac}]$ shows the faster transient response, namely the lower values of t_r and a faster steady state t_s . Figure 8 depicts the variation of the transient response parameters $\{t_s, t_r, t_p, ov(\%)\}$ for the closed-loop response with the $SP_PID^\beta [\hat{G}_{Int}]$, $SP_PID^\beta [\hat{G}_{Frac}]$ and the $PD^\beta+I$ without SP.

These results show that the SP with fuzzy fractional order $PD^\beta+I$ controller and fractional order model, give better performance than the integer one or $PD^\beta+I$ controller without SP. Moreover, we prove the effectiveness of this control structure when used in systems with time delay, which in general, are more difficult to be controlled with classical methodologies.

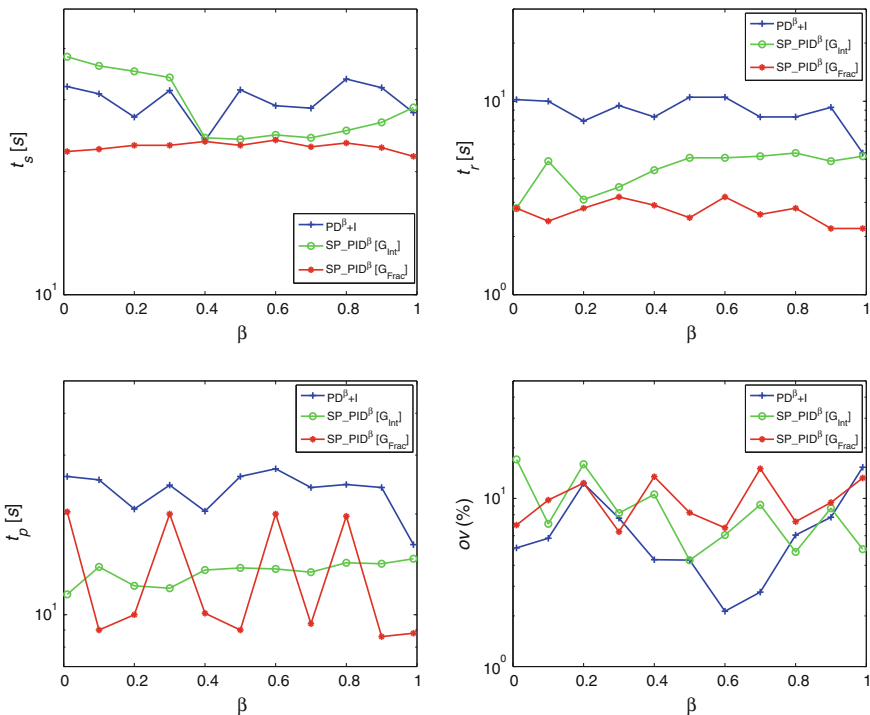


Fig. 8 Specifications of settling time t_s , rise time t_r , peak time t_p , overshoot $ov(\%)$ versus β for the step responses of the closed-loop system with a $PD^{\beta+I}$, $SP_PID^{\beta} [\hat{G}_{int}]$ and $SP_PID^{\beta} [\hat{G}_{frac}]$

6 Conclusions

This paper studied a typical plant with time delay, inserted in a SP structure. The parameters of the fuzzy PD+I controller were tuned using a GA. Two different approximation models (one integer and the other fractional) were used in order to understand their influence on system evaluation. The scheme proposed has shown improved performance over the classical integer order control schemes, proving its effectiveness in nonlinear control systems.

Acknowledgments This work is supported by FEDER Funds through the “Programa Operacional Factores de Competitividade—COMPETE” program and by National Funds through FCT “Fundação para a Ciência e a Tecnologia”.

References

1. Oldham, K.B., Spanier, J.: *The Fractional Calculus: Theory and Application of Differentiation and Integration to Arbitrary Order*. Academic Press, New York (1974)
2. Podlubny, I.: *Fractional Differential Equations*. Academic Press, San Diego (1999)
3. Barbosa, R.: On Linear Fuzzy Fractional PD and PD+I Controllers, The 4th IFAC Workshop Fractional Differentiation and its Applications - FDA'10. Badajoz, Spain (2010)
4. Carvajal, J., Chen, G., Ogmen, H.: Fuzzy PID controller: design, performance evaluation, and stability analysis. *J. Inform. Sci.* **123**, 249–270 (2000)
5. Mizumoto, M.: Realization of PID controls by fuzzy control methods. *J. Fuzzy Sets Syst.* **70**, 171–182 (1995)
6. Jesus, I.S., Ramiro, B.S.: Genetic optimization of fuzzy fractional PD+I controllers. *J. ISA Trans.* **57**, 220–230 (2015)
7. Smith, O.J.M.: Closed control of loops with dead time. *Chem. Eng. Process* **53**, 217–219 (1957)
8. Jesus, I.S., Machado, J.: Fractional control with a smith predictor. *J. Comput. Nonlinear Dyn.* **6**(3), 031014-1–031014-10 (2011) (ASME-AMER SOC MECHANICAL ENG)
9. Goldberg, E.: *Genetic Algorithms in Search Optimization and Machine Learning*. Addison-Wesley (1989)
10. Mitchell, M.: *An Introduction to Genetic Algorithms*. SMIT Press (1998)
11. Jesus, I.S., Barbosa, R.S.: Design of fuzzy fractional PD+I controllers tuned by a genetic algorithm. *J. Math. Probl. Eng. Hindawi*, **2014**(2014), Article ID 676121, 1–14 (2014)
12. Jantzen, J.: *Foundations of Fuzzy Controllers*. Wiley and Sans (2007)
13. Passino, K., Yurkovich, S.: *Fuzzy Control*. Addison-Wesley (1998)
14. Bobál, V., Matušů, R., Dostál, P.: Digital smith predictors—design and simulation study. In 25th EUROPEAN Conference on Modelling and Simulation, Krakow, Poland, June 7th–10th (2011)

The Model-Based Disturbance Rejection with MOMI Tuning Method for PID Controllers

Damir Vrančić, Paulo Moura Oliveira and Jan Cvejn

Abstract The paper presents a tuning method for PID controllers which substantially improves closed-loop disturbance rejection performance while keeping the tracking performance. The tuning method is based on the internal disturbance compensator which parameters are calculated according to the Magnitude Optimum criterion. The results of experiments show that the proposed model-based approach gives superior disturbance-rejection response and lower controller activity when compared to Disturbance Rejection Magnitude Optimum tuning method.

1 Introduction

Tuning of PID controllers has remained hot research topic for many decades. Besides Ziegler-Nichols, Cohen-Coon, Chien-Hrones-Reswick and similar classical tuning rules, there are many more contemporary rules existing [1–3, 7–11].

In general, the tuning methods, according to the type of experiment, can be divided between time-domain methods (e.g. step-response methods) and frequency-domain methods (e.g. relay-excitation methods) [1]. Another division between the existing tuning methods can be made according to the control goals to be achieved. Namely, the methods can be additionally divided between reference-tracking and disturbance-rejection methods.

D. Vrančić (✉)

Department of Systems and Control, J. Stefan Institute, SI-1000 Ljubljana, Slovenia
e-mail: damir.vrancic@ijs.si

P.M. Oliveira

Department of Engineering, School of Sciences and Technology, Universidade de Trás-os-Montes e Alto Douro, UTAD, 5001–801 Vila Real, Portugal
e-mail: oliveira@utad.pt

J. Cvejn

Faculty of Electrical Engineering and Informatics, University of Pardubice,
Studentska 95, 532 10 Pardubice, Czech Republic
e-mail: jan.cvejn@upce.cz

One of contemporary tuning methods, which has been developed for time-domain tuning, frequency-domain tuning, for reference tracking and for disturbance-rejection optimization, is Magnitude optimum (MO) method. Originally, the MO method has been developed for reference tracking based on process information in frequency domain [18]. However, in the last two decades, the method has been extended to experiments in time-domain by using Magnitude Optimum Multiple Integration (MOMI) tuning method [13, 15] and for optimisation of load disturbance-rejection by using Disturbance Rejection Magnitude Optimum (DRMO) method [12, 13]. Moreover, the method has been extended to cover optimisation of tracking and load disturbance rejection performance simultaneously by using 2-degree-of-freedom (2-DOF) controller [11–13]. The mentioned MOMI and DRMO tuning methods have been used in practice and have been proven to be computationally simple (when compared to the original MO method), while the closed-loop responses (reference tracking or disturbance-rejection) remained stable and relatively fast.

Although DRMO-based methods in 2-DOF controller configurations achieve very good disturbance-rejection and good tracking performance, it will be shown that there is still some place for improvements. This paper suggests change of the controller structure along with tuning procedure which even improves disturbance rejection performance of the DRMO method while the closed-loop stability is improved at the same time.

The paper is organised as follows: in Sect. 2, the MOMI and DRMO tuning methods are introduced. Proposed model-based disturbance rejection with the inner filter which improves load-disturbance performance is described in Sect. 3. Section 4 shows two examples, while the conclusions are given in Sect. 5.

2 MOMI and DRMO Tuning Methods

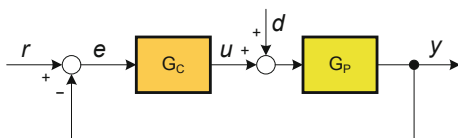
The tuning methods described in this section will be given for the following process (G_P) and controller (G_C) transfer functions:

$$G_P(s) = K_{PR} \frac{1 + b_1s + b_2s^2 + \dots + b_ms^m}{1 + a_1s + a_2s^2 + \dots + a_ns^n} e^{-sT_{delay}} \quad (1)$$

$$G_C(s) = \frac{K_I + K_Ps + K_Ds^2}{s(1 + sT_F)}, \quad (2)$$

where K_{PR} denotes the process steady-state gain, and a_1 to a_n and b_1 to b_m are the corresponding parameters ($m < n$) of the process transfer function, whereby n can be an arbitrary positive integer value and T_{delay} represents the process pure time delay. Note that the denominator in (1) contains only stable poles. The PID controller parameters are proportional gain K_P , integral gain K_I , derivative gain K_D , and filter time constant T_F . The process and controller in the closed-loop configuration are shown in Fig. 1.

Fig. 1 The closed-loop system using the PID controller



MOMI tuning method is based on the MO method [18]. The MO method optimises the closed-loop amplitude (magnitude) response so as to be close to one for as large bandwidth as possible. The closed-loop response, when using the MO tuning method, is usually fast and non-oscillatory. The MOMI tuning method keeps all advantages of the MO method while considerably simplifies calculation of the controller parameters and the type of process experiment (e.g. requiring only simple change of the process steady-state [12, 13] or few points in the Nyquist curve [14]).

Since the MOMI tuning method has been explained in the previous publications [13, 15], only the final tuning formulas will be given herein.

The MOMI tuning method results in the following controller parameters:

$$\begin{bmatrix} K_I \\ K_P \\ K_D \end{bmatrix} = \begin{bmatrix} -A_1^* & A_0^* & 0 \\ -A_3^* & A_2^* & -A_1^* \\ -A_5^* & A_4^* & -A_3^* \end{bmatrix}^{-1} \begin{bmatrix} -0.5 \\ 0 \\ 0 \end{bmatrix}, \tag{3}$$

where

$$\begin{aligned} A_0 &= K_{PR} \\ A_1 &= K_{PR}(a_1 - b_1 + T_{delay}) \\ A_2 &= K_{PR} \left[b_2 - a_2 - T_{delay}b_1 + \frac{T_{delay}^2}{2!} \right] + A_1a_1 \\ &\vdots \\ A_k &= K_{PR} \left((-1)^{k+1}(a_k - b_k) + \sum_{i=1}^k (-1)^{k+i} \frac{T_{delay}^i b_{k-i}}{i!} \right) \\ &\quad + \sum_{i=1}^{k-1} (-1)^{k+i-1} A_i a_{k-i} \end{aligned} \tag{4}$$

and

$$\begin{aligned} A_0^* &= A_0 \\ A_1^* &= A_1 + A_0 T_F \\ A_2^* &= A_2 + A_1 T_F + A_0 T_F^2 \\ &\vdots \end{aligned} \tag{5}$$

Note that the so-called characteristic areas or moments $A_0 \dots A_k$ can also be calculated directly from the process open-loop time-response (e.g. changing the process steady-state) by simple summation of time-domain signals [13, 15]. Also note that the process transfer function can be precisely described in frequency-domain by the infinite series of characteristic areas [13]:

$$G_P(s) = A_0 - A_1s + A_2s^2 - A_3s^3 + \dots \quad (6)$$

DRMO tuning method has been developed for improving the closed-loop disturbance-rejection performance. The original method [12] requires one-dimensional optimisation for the calculation of the controller parameters. However, in this paper a semi-optimal simplified method [16] will be applied, which does not require any iterative computations, but results in a similar controller parameters.

The DRMO tuning method results in the following controller parameters:

$$K_P = \frac{\beta - \sqrt{\beta^2 - \alpha\gamma}}{\alpha} \quad (7)$$

$$K_I = \frac{(1 + K_P A_0^*)^2}{2(K_D A_0^{*2} + A_1^*)}$$

where

$$\begin{aligned} \alpha &= A_1^{*3} + A_0^{*2} A_3^* - 2A_0^* A_1^* A_2^* \\ \beta &= A_1^* A_2^* - A_0^* A_3^* + 2K_D (A_0^* A_1^{*2} - A_0^{*2} A_2^*) \\ \gamma &= K_D^3 A_0^{*4} + 3K_D^2 A_0^{*2} A_1^* + K_D (2A_0^* A_2^* + A_1^{*2}) + A_3^* \end{aligned} \quad (8)$$

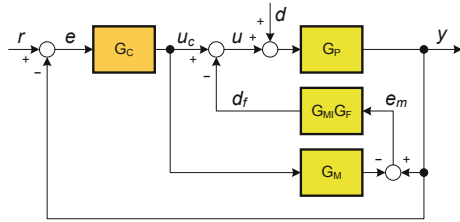
Note that the controller derivative gain K_D in expressions (7) and (8) are calculated by expression (3).

3 Model-Based Disturbance Rejection

The MOMI method optimises the tracking performance and process output disturbance rejection, while the DRMO method optimises the process input disturbance rejection. The disadvantage of the MOMI method is sub-optimal disturbance-rejection performance, while DRMO usually results in excessive overshoots on reference changes or output disturbances.

In order to substantially increase the process input disturbance-rejection performance, while keeping MOMI tracking performance, the model-based approach could be used, similar to ones given in [4–6]. One possible solution is shown in Fig. 2, where G_M stands for the process model, G_{MI} for the inverse of the process model and G_F for the disturbance filter transfer function.

Fig. 2 The model-based approach for improving disturbance-rejection



The model-based disturbance-rejection principle is straightforward and well-known from basic control theory. In order to compensate the process input disturbance d , the opposite estimated disturbance signal (d_f) can be fed back to the process input. If the process model is the same to the process ($G_M = G_P$), then the difference between the process and model outputs (e_m) equals to:

$$e_m = G_P d. \tag{9}$$

If the filter $G_F = 1$, and if

$$G_{MI} = G_M^{-1} \tag{10}$$

then

$$d_f = d. \tag{11}$$

Disturbances are therefore immediately compensated without alternating the tracking closed-loop performance.

However, in practice the process transfer functions usually have lower numerators orders than denominators ($m < n$ in (1)), the process models are not perfectly matching the actual processes, the actual process might have pure time delay and there is always some measurement noise present at the process output. Therefore, the estimated (filtered) disturbance signal d_f cannot entirely compensate the actual disturbance signal, but can still significantly increase disturbance-rejection performance.

There are two possible approaches for the calculation of models G_M , G_{MI} and G_F . The first one is based on a classic identification approach for determining G_M and G_{MI} , while the filter G_F parameters are calculated by means of optimisation.

The second approach, which is used herein, is the calculation of all models and filter parameters according to the previously identified characteristic areas. This approach significantly simplifies the calculations, it does not involve any optimisation and can be based on a simple time-domain experiment on the process.

In order to additionally simplify the proposed model-based disturbance rejection scheme, the following process model, inverse process model and filter have been chosen:

$$G_M = \frac{K_{PRM} e^{-sT_{delaym}}}{1 + a_{1m}s + a_{2m}s^2} \quad (12)$$

$$G_{MI} = \frac{1 + a_{1m}s + a_{2m}s^2}{K_{PRM}} \quad (13)$$

$$G_F = \frac{K_{FD}}{(1 + T_{FD}s)^3}, \quad (14)$$

where the process model parameters are calculated directly from the characteristic areas A_0 to A_3 in expression (4):

$$\begin{aligned} K_{PRM} &= A_0, & a_{1m} &= \frac{A_1}{A_0} - T_{delaym} \\ a_{2m} &= -\frac{A_2}{A_0} + \frac{a_{1m}A_1}{A_0} + \frac{T_{delaym}^2}{2} \end{aligned} \quad (15)$$

$$\frac{T_{delaym}^3}{6} - \frac{A_1}{2A_0} T_{delaym}^2 + \left(\frac{A_1^2}{A_0^2} - \frac{A_2}{A_0} \right) T_{delaym} + 2 \frac{A_1 A_2}{A_0^2} - \frac{A_3}{A_0} - \frac{A_1^3}{A_0^3} = 0. \quad (16)$$

Note that model time delay (T_{delaym}) is calculated from the roots of expression (16), where the chosen T_{delaym} is the minimum positive real root [17].

It is obvious that G_{MI} is the inverse of G_M without pure time-delay and that G_F should have higher denominator order than numerator order in G_{MI} in order to attenuate high-frequency process output and controller noise. Increasing filter parameter T_{FD} decreases disturbance compensator's noise and the speed of disturbance-rejection response, while K_{FD} optimises disturbance-rejection performance. Note that choosing $K_{FD} = 1$ does not result in optimal disturbance rejection performance. The parameter K_{FD} should be optimised according to the chosen T_{FD} , the process transfer function and controller parameters so as that the process response on input disturbance is optimal. Besides using optimisation, K_{FD} can be also analytically derived according to the MO criterion. Due to the limited space, only the final result will be given herein.

The optimal K_{FD} , according to the DRMO criterion, can be calculated by the following expression¹:

$$K_{FD} = \frac{-\beta - \sqrt{\beta^2 - 4\alpha\gamma}}{2\alpha}, \quad (17)$$

¹The filter T_F is assumed to be part of the process and the controller parameters are tuned according to such process. Due to negligible T_F , compared to the process time constants, the overall result for K_{FD} should not vary significantly and the change can be supposed to remain negligible.

where

$$\begin{aligned}
 \alpha &= A_0^{*2} K_I^2 (2a_{2m} + 3T_{FD}^2 - a_{1m}^2) + (1 + A_o^* K_P)^2 \\
 &\quad + K_I^2 (2A_o^* A_2^* - A_1^{*2}) - 2K_I (A_o^{*2} K_D + A_1^*) \\
 \beta &= -2A_0^{*2} K_I^2 (a_{2m} + 6T_{FD}^2 - 3T_{FD} a_{1m}) - 2(1 + A_o^* K_P)^2 \\
 &\quad - 2K_I^2 (A_o^* A_2^* - A_o^* A_1^* a_{1m} + 3T_{FD} A_o^* A_1^*) + 4K_I (A_o^{*2} K_D + A_1^*) \\
 \gamma &= (1 + A_o^* K_P)^2 - 2K_I (A_o^{*2} K_D + A_1^*).
 \end{aligned} \tag{18}$$

The overall tuning procedure therefore proceed as follows:

- For the given process (1), calculate characteristic areas from expression (4) or directly from the process steady-state change time-response [13, 15].
- Choose some appropriate controller filter time constant T_F according to required measuring noise suppression and re-calculate the characteristic areas from (5).
- Calculate MOMI controller parameters from (3).
- Calculate model pure delay T_{delaym} from (16) and the rest of parameters from (15).
- Choose appropriate T_{FD} filter value to decrease high-frequency noise at the output of the model-based disturbance compensator
- Calculate gain of the model-based compensator (K_{FD}) from expression (17).

4 Simulations

To illustrate the tuning procedure and show the advantages of the proposed disturbance-rejection method, we have made experiments on two different process models.

Case 1. The controller and inner model parameters will be calculated for the following process model:

$$G_{P1} = \frac{e^{-0.1s}}{(1+s)(1+0.2s)}. \tag{19}$$

By using the tuning procedure given in the previous section, the calculated characteristic areas, inner model and MOMI controller parameters, at chosen $T_F = 0.05$ s and $T_{FD} = 0.05$ s, are:

$$\begin{aligned}
 A_0 &= 1, A_1 = 1.3, A_2 = 1.365, A_3 = 1.378, A_4 = 1.381, A_5 = 1.381 \\
 A_0^* &= 1, A_1^* = 1.35, A_2^* = 1.433, A_3^* = 1.45, A_4^* = 1.453, A_5^* = 1.454 \\
 K_{PRm} &= 1, \quad a_{1m} = 1.2, \quad a_{2m} = 0.2, \quad T_{delaym} = 0.1 \\
 K_P &= 4.32, \quad K_I = 3.57, \quad K_D = 0.75 \\
 K_{FD} &= 0.743
 \end{aligned}
 \tag{20}$$

For comparison, the controller parameters when using DRMO method, are as follows (7):

$$K_P = 5.88, \quad K_I = 11.3, \quad K_D = 0.75
 \tag{21}$$

Figure 3 shows the process output and process input responses on reference change and step-like process input disturbance when using classical control loops (Fig. 1), tuned by MOMI and DRMO methods, and when using the proposed control scheme (see Fig. 2) with controller tuned by MOMI method. The MOMI method results in a relatively fast reference following and slow disturbance rejection. On contrary, DRMO method results in a relatively fast disturbance rejection, but the reference following exhibits large overshoot. It is obvious that the proposed model-based method offers even better disturbance rejection response than DRMO method and the same reference following performance as MOMI method, while the control output signal swings are lower than with DRMO method.

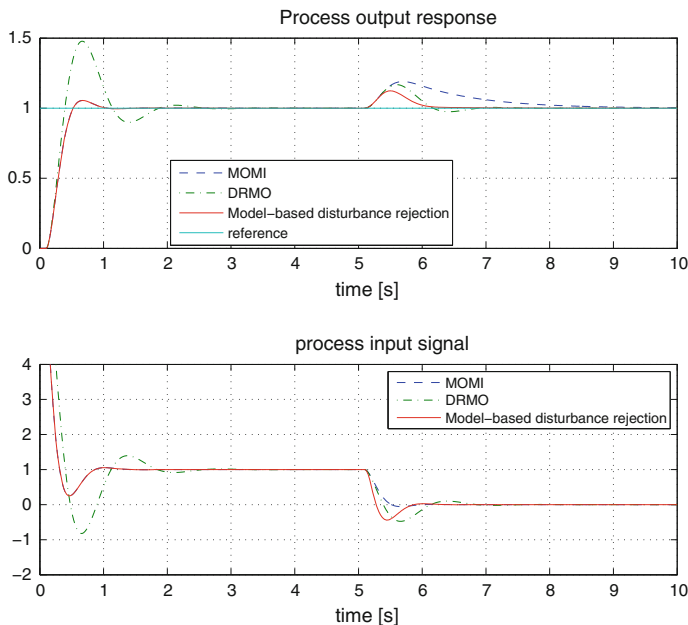


Fig. 3 The process G_{P1} output and input signals for three different methods

Case 2. The controller and inner model parameters are also calculated for the following process model:

$$G_{P2} = \frac{e^{-0.5s}}{(1+s)^3} \tag{22}$$

The calculated inner model and controller parameters, at chosen $T_F = 0.1$ s and $T_{FD} = 0.1$ s are:

$$\begin{aligned} A_0 &= 1, A_1 = 3.51, A_2 = 7.66, A_3 = 13.47, A_4 = 20.95, A_5 = 30.09 \\ A_0^* &= 1, A_1^* = 3.61, A_2^* = 8.02, A_3^* = 14.27, A_4^* = 22.38, A_5^* = 32.33 \\ K_{PRm} &= 1, \quad a_{1m} = 2.58, \quad a_{2m} = 1.84, \quad T_{delaym} = 0.93 \\ K_P &= 1.26, \quad K_I = 0.49, \quad K_D = 0.87 \\ K_{FD} &= 0.477 \end{aligned} \tag{23}$$

For comparison, the controller parameters when using DRMO method, are as follows (7):

$$K_P = 1.46, \quad K_I = 0.68, \quad K_D = 0.87 \tag{24}$$

Figure 4 show the process output and process input responses on reference change and step-like process input disturbance. It is again obvious that the proposed

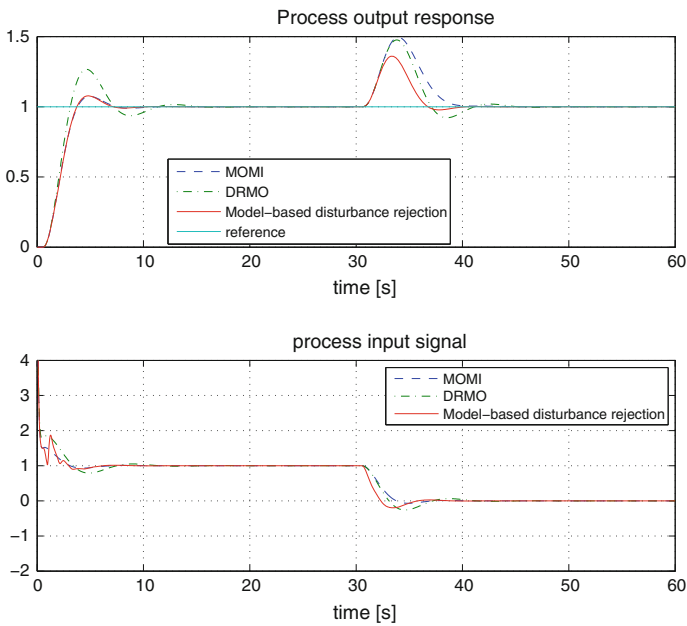


Fig. 4 The process G_{P2} output and input signals for three different methods

model-based method offers significantly better disturbance rejection response than DRMO method. The control output signal changes are comparable to DRMO method. It can be seen that the process input signal is not smooth due to model mismatch between the process and the model. On the other hand, the process output signal remains smooth and similar to the MOMI method.

5 Conclusions

The proposed model-based approach for improving disturbance rejection performance is based on a lower-order model obtained directly from the characteristic areas. The same areas are used for the calculation of the controller parameters. The proposed tuning and control method can be therefore applied either in frequency-domain (by using the process transfer function) or in time-domain (from the process steady-state change measurements).

The results of experiments on two different process models showed that the proposed method resulted in more efficient disturbance-rejection closed-loop responses than MOMI and DRMO method. Moreover, the control effort seems to remain relatively low.

The method produces some swings in control output signals if the process and the model differ. This swings can be seen during reference changes, but are much faster than the sum of process time constants so their effect hasn't been seen on the process output response.

Current research results, which are not presented in the paper due to the limited space, show that the proposed method is relatively immune to model mismatch and the process output noise.

In our further research, besides presenting robustness and noise sensitivity results, we are going to analyse the stability of the system and investigate optimal response on general disturbance signal.

Acknowledgments This work was supported in part by the Slovenian Research Agency through the programme P2-0001 and Grant L2-5476 and by EU's Seventh Framework Programme under grant agreement n°[621208].

References

1. Åström, K.J., Hägglund, T.: PID controllers: Theory, Design, and Tuning, 2nd edn. Instrument Society of America (1995)
2. Åström, K.J., Panagopoulos, H., Hägglund, T.: Design of PI controllers based on non-convex optimization. *Automatica* **34**(5), 585–601 (1998)
3. Freire, H., Moura, O.P., Solteiro, E.P., Bessa, M.: Many-Objective PSO PID Controller Tuning, *Controlo 2014*, pp. 183–192. Porto, Portugal (2014)

4. Garcia, C.E., Morari, M.: Internal model control. A unifying review and some new results. *Ind. Eng. Chem. Process Des. Dev.* **21**, 308–323 (1982)
5. Garcia, C.E., Morari, M.: Internal model control. 2. Design procedure for multivariable systems. *Ind. Eng. Chem. Process Des. Dev.* **24**, 472–484 (1985)
6. Garcia, C.E., Morari, M.: Internal model control. 3. Multivariable control law computation and tuning guidelines. *Ind. Eng. Chem. Process Des. Dev.* **24**, 484–494 (1985)
7. Gorez, R.: A survey of PID auto-tuning methods. *J. A* **38**(1), 3–10 (1997)
8. Huba, M.: Constrained pole assignment control. In: Menini, L., Zaccarian, L., Abdallah, Ch. T., (eds.) *Current Trends in Nonlinear Systems and Control*, pp. 163–183. Birkhäuser, Boston (2006)
9. Moura, O.P., Vrančić, D., Freire, H.: Dual Mode Feedforward-Feedback Control System, *Controlo 2014*, pp. 241–250. Porto, Portugal (2014)
10. O’Dwyer, A.: *Handbook of PI and PID Controller Tuning Rules*; 3rd edn. Imperial College Press (2009)
11. Taguchi, H., Araki, M.: Two-degree-of-freedom PID controllers—their functions and optimal tuning. In: *Proceedings of the IFAC Workshop on Digital Control (PID’00)*, pp. 95–100. Terrassa (2000)
12. Vrančić, D.: Magnitude optimum techniques for PID controllers. In: Rames R.C. (eds.) *Introduction to PID Controllers: Theory, Tuning and Application to Frontiers Areas*. pp. 75–102. InTech, cop., Rijeka (2011)
13. Vrančić D., Strmčnik S., Hanus R.: Magnitude optimum tuning using non-parametric data in the frequency domain. In: *PID’00: Preprints: IFAC Workshop on Digital Control: Past, Present and Future of PID Control*, pp. 438–443. Terrassa, Spain, 5–7 April 2000
14. Vrančić, D., Strmčnik, S., Juričić, Đ.: A magnitude optimum multiple integration method for filtered PID controller. *Automatica* **37**, 1473–1479 (2001)
15. Vrančić D., Kocijan J., Strmčnik S.: Simplified disturbance rejection tuning method for PID controllers. In: *ASCC the 5th Asian Control Conference, July 20–23, Melbourne, Australia. Conference Proceedings* (2004)
16. Vrančić D. Strmčnik S., Kocijan J. and Moura Oliveira P. B. de. (2010). Improving disturbance rejection of PID controllers by means of the magnitude optimum method. *ISA Trans.* **49**(1), 47–56. ISSN 0019-0578
17. Vrečko, D., Vrančić, D., Juričić, Đ., Strmčnik, S.: A new modified smith predictor: the concept, design and tuning. *ISA Trans.* **40**, 111–121 (2001). ISSN 0019-0578
18. Whiteley, A.L.: *Theory of servo systems, with particular reference to stabilization*. *J. IEE, Part II* **93**(34), 353–372 (1946)

Systemic Coordination Through Numeraires: Initial Simulation Results

Paulo Garrido and Pedro Osório

Abstract This paper presents initial results on the development of a paradigm for the coordination of large multi-agent systems abstracted from social coordination processes using money. We recall basic concepts and report on the development of a simulator for modeled systems. We present a “toy” example together with the determination and simulation of a steady-state for it. Next, we show results of perturbing the system parameters and the initial values of state variables in the steady-state. We conclude by reviewing the presented results, sketching a roadmap for development and considering the paradigm in a wider theoretical control perspective.

Keywords Systems coordination • Coordination through numeraires • Multi-agent simulation • String rewrite rules • Modeling through string rewrite rules

1 Introduction

In a recent paper [1], basic concepts for a coordination and control paradigm targeting large multi-agent systems were presented. The paradigm is abstracted from the process of human coordination that is mediated by money.

The abstraction follows the interpretation of money proposed by the so-called chartalist school of economics [2–4]: *modern* money is a creation of the states that have the power to issue and make accepted its own state currency, or, could we say, its own instance of money.

P. Garrido (✉)

Centro Algoritmi, Universidade do Minho, 4800 Guimarães, Portugal
e-mail: pgarrido@dei.uminho.pt

P. Osório

LIAAD, INESC TEC, 4200 Porto, Portugal
e-mail: pedroosorio.eeic@gmail.com

A state makes its own currency accepted by declaring it as the only means to pay taxes. The power of taxing means that governments can diminish the amount of currency that a legal person owns.

Taxing gives a government the power to spend its own currency as well, because people need to earn said currency to obtain things and pay taxes. Legal persons can only earn the currency to pay taxes by receiving it either directly from the governments or indirectly through other legal persons that are willing to transfer money to them, be it as a gift or in exchange for goods or services.

A government spends by increasing the amount of currency a legal person owns, either directly, as in the case of pensions, or in exchange for services or goods, as in the case of salaries or purchases.

This interpretation of modern money leads to abstracting the whole process as a coordination process led by a controller assigning values to variables that condition the behavior of the coordinated systems. I use the word ‘numeraire’ as a useful abstraction for money, as it denotes something that serves to assign numbers to things.

This work is somehow related to works of Tumer and Wolpert [5, 6]. But while they followed an approach of designing “agent-specific objective functions” that inherently lead agents to fulfill system-wide objectives, the “money abstraction” followed in this “numeraire approach” rests on a central controller setting the values of agents objective functions through “taxing rules”, which diminish the values, and “purchases”, which increase them.

In this paper, some advances beyond [1] are reported. In Sect. 2 some basic concepts are recalled in a larger explanatory perspective and a “toy” example of modeling is described. In Sect. 3, on-going development of a simulator is presented. In Sect. 4, we discuss determining a steady-state operation point for the “toy” example and present simulations of perturbing the steady-state. Section 5 reviews the presented results, sketches a roadmap for development and considers the paradigm in a wider perspective of developing control theory.

2 Basic Concepts of the Paradigm

2.1 *Numeraires as the Mediating Control Variables for Coordination*

The operation of money described as above can be mathematically formalized as a coordination process of a supersystem S constituted by a controller agent C and a finite number of coordinated agents $A(i)$, $i = 1, \dots, I$, each with a variable called a numeraire $N(i, k)$ possibly changing in discrete time, at instants k . The time interval $[t_{k-1}, t_k]$ is also indexed by k .

The controller C can change the numeric value, $N(i, k)$, of a coordinated agent i , either increasing it or decreasing it. In the first case, one will use the term

“controller’s payment”, in the second, one will use the term “tax collection”. A coordinated agent j can only increase the numeraire value of another agent i —in exchange for a “thing”—and for this it must decrease its own numeraire in the amount of the increase. We may say that j transfers a given amount of numeraire to i .

We symbolize a transfer of numeraire from an agent j to an agent i , recorded at instant k , as $n(i, j, k)$. While the variables denoted by N are stocks, transfers of numeraire between agents are flows. The value of a transfer $n(i, j, k)$ is always positive. The effect of a transfer is to decrease the numeraire of the “source” agent and to increase the numeraire of the “destination” agent in the same absolute value. Therefore, if along a period k only one transfer $n(i, j, k)$ occurs between agents i and j , the updating equations for their stocks of numeraire are:

$$\begin{cases} N(i, k) = N(i, k-1) + n(i, j, k) \\ N(j, k) = N(j, k-1) - n(i, j, k) \end{cases} \quad (1)$$

There is no actual meaning in saying that the controller C *owns* numeraire because, being an “issuer” or generator (source and sink) of numeraire, the controller will never “lack” numeraire units for whichever operation it intends. Virtually, the amount of numeraire C “owns” is infinite. Yet, for accounting and uniform notation, it may be useful to denote a payment made by the controller C to an agent $A(i)$ as a “transfer” $n(i, c, k)$; likewise tax collection can be denoted by a “transfer” $n(c, i, k)$, where c is a suitable index for the controller.

The equation describing the time evolution of $N_1(k)$, the sum of coordinated agents numeraires is:

$$N_1(k) = \sum_{\kappa=1}^k \sum_{i=1}^I (n(i, c, \kappa) - n(c, i, \kappa)) + N_1(0). \quad (2)$$

The variation $N_1(k) - N_1(0)$ equals the net sum of all payments and tax collections made by the controller along time up to instant k . It follows that for the sum total of coordinated agents’ numeraires *to increase* the sum of controller payments must be greater than the sum of tax collections.

At this stage of formalism development, we consider that the numeraire of agents can only be positive. If, for some reason, the stock of numeraire of an agent should become negative, then the agent is considered “dead” or disappears. This abstracts in some way the fact that if an organization in the economic world becomes insolvent, it will often disappear. This also rules out for the moment the consideration of credits and debts, allowing one to concentrate on more fundamental concepts.

A rich repertoire of behavior strategies both of controller and agents can be envisaged towards different aims. Although, before such behavior strategies can be studied, the question arises of how are we going to represent the coordination among agents that the controller tries to induce by payments and tax collections? Which model for the “coordinated and controlled system” should one choose?

2.2 Modeling Coordinated Agents

A main interest in the choice of a model for the coordinated systems is to get a general, abstract, but precise model of production processes. The formalism chosen in the previous paper [1] was to interpret models as structures of string rewrite rules. An agent can be interpreted as a set of string rewrite rules. Each rewrite rule specifies which components must come together or must be coordinated for the agent to generate a given output.

The content and atomic operation of a rewrite rule w can be represented by the expression:

$$w: c(b), m(c(b)) \rightarrow \eta b. \quad (3)$$

It means that if the agent has in its input store the input strings specified by c (b) in the amounts specified by $m(c(b))$ then an operation of the rule will *delete* the strings in the input store and will *create* η copies of string b at its output store.

Using the symbol “*” for *nil* we can also represent creation of strings from “nothing” (representing extraction of some natural resource), and destruction of strings to “nothing”:

$$w_{*}: * \rightarrow \eta b \quad (4)$$

$$w_{-*}: c(b), m(c(b)) \rightarrow * \quad (5)$$

For each rule, minimum, $ymin$, nominal, $ynom$, and maximum, $ymax$, outputs during each period k can be defined. Of course, the production of output requires that the corresponding components specified by (3) be present in the input store of the agent as inputs for the rule.

Rules can also be classified as of necessary and possible operation. A possible rule has $ymin = 0$. A necessary rule has $ymin > 0$. If an agent has a necessary rule and is unable to “fire” at the $ymin$ output, it will “die”.

Beyond modeling the operation of individual agents, one needs also to model the connection of agents in a structure. This means that some agents will supply products (represented by strings) to others. Supply is made in exchange for numeraire, therefore, the supplier agent will be selling its products while the supplied agent will buy them. Suppose that in period k agent j decides to buy $sx(i, k)$ copies of product ‘x’ from agent i at unit price $rx(i, k)$. The equations describing the transaction (independently of other transactions the agents may engage in) are as follows, where ux stands for the number of copies of ‘x’ at the input store of j :

$$\begin{cases} ux(j, k) = ux(j, k - 1) + sx(i, k) \\ N(i, k) = N(i, k - 1) + sx(i, k)rx(i, k) \\ N(j, k) = N(j, k - 1) - sx(i, k)rx(i, k) \end{cases} \quad (6)$$

Similar equations will apply in the case of the controller C being the buyer of a product. Let us give some interpretation to a product bought by the controller. It could represent some equipment or some kind of service or good fulfilling a global coordination system function. Therefore, the controller can be understood as an agent with rules to represent the “global coordinated system” use of equipment or consumption of goods. If some of these rules are necessary and the flows of corresponding inputs goes below minimum values, the whole coordinated system will disappear.

3 A Coordinated System ‘Toy’ Example

With this formalism, a “toy” example was set up considering five coordinated agents and a controller. Each agent has two necessary rules representing its necessities of consuming “energy” and “food”:

$$\begin{aligned} w_{n1}: 'e' &\rightarrow * \\ w_{n2}: 'f' &\rightarrow * \end{aligned} \tag{7}$$

This rules represent the fact that agents must use up resources to stay “alive”, even if they produce nothing. One assumes that the minimum and nominal flows for w_{n1} are 1 and 2 while for w_{n2} they are 2 and 4. This means that each agent needs to consume 2 units of ‘e’ and 4 units of ‘f’ to be “happy”, but can survive with 1 and 2 units, respectively.

Each agent also has a productive rule w_i , as follows:

$$\begin{aligned} w_1: * &\rightarrow 'a' \\ w_2: 3'e' &\rightarrow 'b' \\ w_3: \{2'a', 3'b', 4'e'\} &\rightarrow 'd' \\ w_4: * &\rightarrow 'e' \\ w_5: 2'e' &\rightarrow 'f' \end{aligned} \tag{8}$$

Only output ‘d’ is *bought* by the controller, which means that agents 1, 2, 4 must *sell* their outputs to other agents to earn numeraire. The nominal flow assumed for ‘d’ is 10. From this value and the nominal flows assumed for rules (7) one can calculate the nominal flows of ‘a’, ‘b’, ‘e’ and ‘f’ such that the system is at an operating steady-state point. In a steady-state no shortage or surplus of strings results. The result of the calculation is presented in the following table where *unom* means required input for the rule. Note that agents 4 and 5 must keep a fraction of their production for themselves and cannot sell it.

Unit prices— ra , rb , rc , rd , re , rf —of strings that agents must buy and sell were also determined as a function of re for the global nominal flow of products Y_{nom} , yielding:

$$Y_{nom} \rightarrow [ra \quad rb \quad rd \quad re \quad rf] = [0.625 \quad 3.417 \quad 16.75 \quad 1 \quad 2.625] \quad (9)$$

If prices are kept at the ratios implicit in (9) then only the producer of string ‘e’ receives more numeraire than it pays to other agents in the steady-state. All the others receive exactly the same amount of numeraire they pay.

For the steady-state to extend to the values of numeraires, a simple rule for tax collection was assumed: the controller would tax all the proceeds of sales in excess of the spending in purchases. The correctness of calculations was verified by simulating the operation of the system at the flows, prices and tax rule indicated.

4 Developing a Simulator

Development and exploration of ideas making up the paradigm requires a simulator for models written according to the formalism above. The novel Julia language [7] was chosen to write a simulator given its high-level and very good performance. A script written in Scilab [8] is being currently used for visualization of simulated time-series.

As of now, a simulation cycle for a period k includes the following operations:

- Firing all necessary rules in all agents. “Kill” all the agents that did not get to fire any of its necessary rules at the minimum flow. This can happen for the controller agent also—in this case the simulation stops because the controller not firing a necessary rule to the minimum flow means that the overall system went into a complete failure.
- Announcement by producer agents of the amounts they intend to supply in the period at the unit prices they will charge.
- Purchase process: agents decide which amounts of products to buy and purchase them. This includes the controller that has the power to set the price for the products it buys.
- Tax collection by the controller according to the given tax rule.

The simulation goes for the number K of specified periods. The configuration of the system to be simulated (agents, rules and flows), the initial conditions and parameters, including prices, are defined in a text file.

In designing the simulator, it became clear that a system as this one has three types of players. Coordinated agents, acting as sellers, decide how much to produce and at which price. Coordinated agents, acting as buyers, decide how much to purchase at the given prices. The controller decides the taxing rule and which products to buy.

As the subject of concern was to study steady-state behavior, the decisions of the three types of players were set in order to keep the system in the steady-state, as follows:

- Agents as producers always announce that they will produce at nominal flows with unit prices satisfying (9);
- Agents as buyers always buy exactly (only) the amounts of products they need for their necessary and producing rules to fire at nominal flow;
- The controller taxes any surplus numeraire that may result from an agent earning more in sales than it spends in purchases.

4.1 Simulation Results

With this frame, the ‘toy’ example system was simulated and the results indicated that the system was indeed in steady-state, see Fig. 1 a, b. All the coordinated agents were supposed to have three hundred units of numeraire for $k = 0$.

In the second experiment, we simulated a negative impulse perturbation in the parameter $ynom$ of an agent. We chose agent 1, producing string ‘a’, and diminished its output by 50 % on the first period. The results are depicted in Fig. 2a, b.

The results show that the taxing rule is very “rough” and does not match the “willingness” of agents to produce as much as possible at the nominal value. The loss of production of agent 1 results in agents 2 and 3 losing numeraire. Actually, for agents 2 and 3 not losing numeraire in the context, it would be necessary that they would reduce purchases and therefore production.

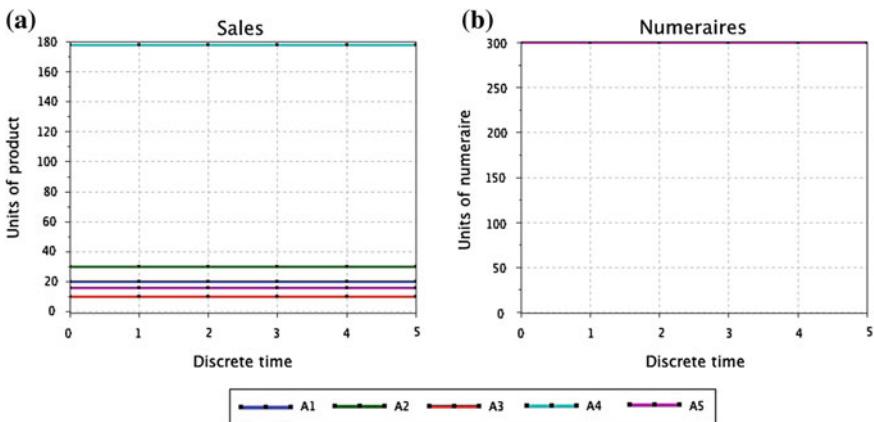


Fig. 1 Simulation of the ‘toy’ example system along 5 periods in discrete time for the steady-state conditions indicated. In **a** the evolution of the products sold by agents is represented. In **b** the evolution of agents’ numeraires is represented; the values of numeraire are equal for all. The system is indeed in a steady-state

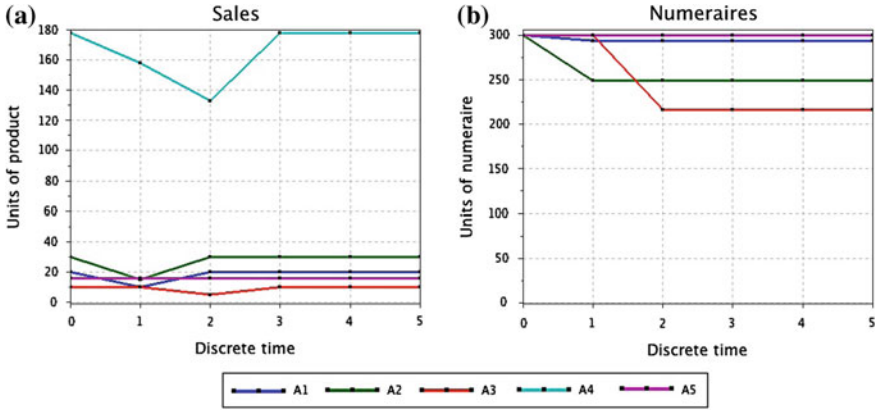


Fig. 2 Simulation of a 50 % reduction in output of agent 1 on period 1. In **a** one observes that, on period 1, agent 2 also sells only 50 % of the nominal value and there is a reduction in the amount sold by agent 4. This happens because agent 3 (buyer for 1, 2 and 4) refrains from buying unnecessary product from 2 and 4. In period 2, it is agent 2 (who has purchased product in excess from agent 4) that buys less from agent 4. In **b** one observes that agents 1, 2 and 3 lose numeraire as a result of selling less than the nominal values of products. Agent 4 (graph not visible) does not lose numeraire because it always receives more in sales than spends in purchases

Table 1 Determination of nominal input and output flows in example

Agent: product	Must output	Must sell	Must input			
			$unom$ 'a'	$unom$ 'b'	$unom$ 'e'	$unom$ 'f'
1:'a'	20	20			2	4
2:'b'	30	30			2 + 90	4
3:'d'	10	10	20	30	2 + 40	4
4:'e'	180	178			2	4
5:'f'	20	16			2 + 40	4

For a system as the one described, sales are not state variables. State variables are constituted by the values of numeraires and the amounts of each product that agents have in their input stores. The values in the input stores that induce this steady-state are listed in Table 1, at the rightmost four columns. In a third simulation, we tested for a negative impulse perturbation in the input stores of agent 2 and agent 3. We reduced in 50 % the amounts of strings 'e' for both agents and of strings 'a' and 'b' for agent 3. The results are represented in Fig. 3.

Under the assumed amplitude of the perturbations, we see that, although the controller strategy is not the best, the system is stable as it returns to the steady-state values. This does not occur for more intense perturbations that drive agents below their minimum flows, entailing their “death” and, possibly, the “death” of the system.

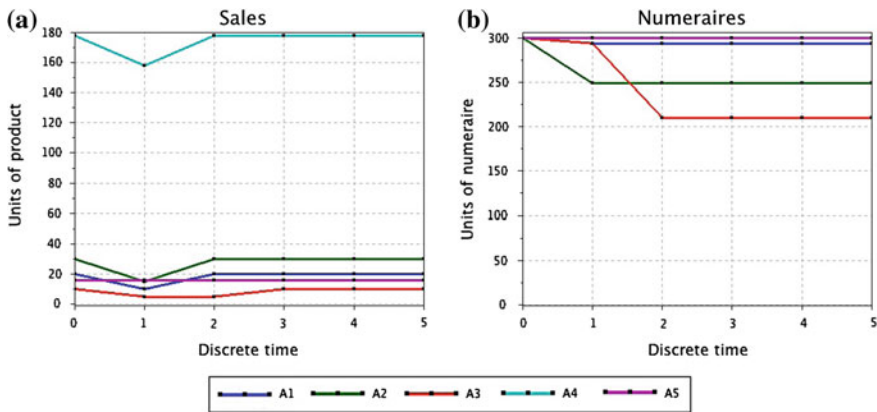


Fig. 3 Simulation of a 50 % reduction in the initial amounts of strings ‘e’ for agents 2 and 3 and of strings ‘a’ and ‘b’ for agent 3. Results are similar to those depicted in Fig. 2. In **a** one observes that, in period 1, agents 2 and 3 only sell half of their nominal output. As agent 3 can only buy half of the nominal output of agent 2, it also buys less from agents 1 and 4. In **b** one observes that agents 1, 2 and 3 lose numeraire as a result of selling less than the nominal values of products. Again, agent 4 (graph not visible) does not lose numeraire because it always receives more in sales than spends in purchases

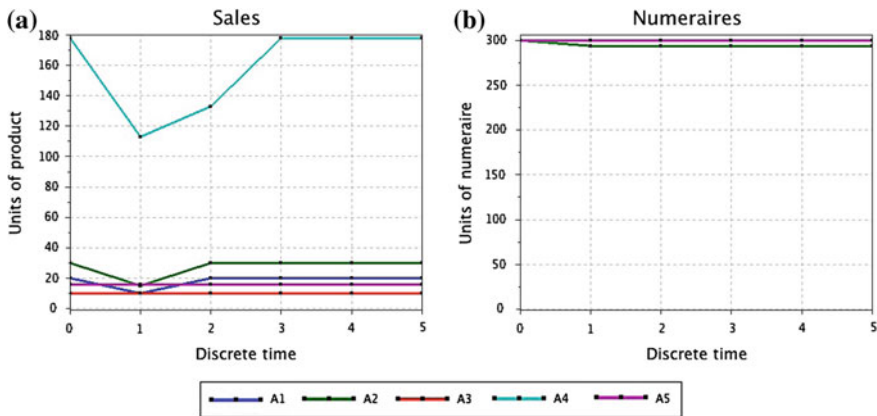


Fig. 4 Simulation of a 50 % increase in the amounts of strings ‘e’ for agents 2 and 3 and of strings ‘a’ and ‘b’ for agent 3. In **a** one observes that as agents 2 and 3 refrain from buying, so “to get rid of the excess”, sales of agents 1, 2 and 4 diminish. In **b** one observes an equal reduction in the numeraire stocks of agents 1 and 2

As a last test to present here, we repeated the last simulation, but under a positive impulse that increased the initial values of the input stores by 50 %. The results are depicted in Fig. 4. They show stability, but, curiously, the positive impulse leads to lowering sales and numeraires. This is because agents 2 and 3 drive their input stores to steady-state values and, in so doing, refrain from buying.

5 Conclusions and Perspectives

In this paper we have presented basic concepts, published in a previous paper, and recent work on a coordination paradigm for multi-agent systems abstracted from the use of money as a coordinating tool in the social realm. Money is abstracted as numeraire and this is understood as an individual agent criterion that can be manipulated by a central controller and used in transactions with other agents.

We are now developing a simulator for which we presented the main ideas. We also presented simulation results for a ‘toy’ example at steady-state and submitted to perturbations. The coordination among agents that we were able to show remains of a very elementary character. Agents need to buy products they need to “live”, say “energy” and “food”. To get the required numeraire they must produce at nominal output, selling at fixed prices, otherwise they lose numeraire and eventually will “die”. Yet, one must keep in mind that not all capabilities of this initial version have been explored, e.g., the simulator allows the controller to increase the sum of agents’ numeraire. Besides, as the simulator’s capabilities will enlarge, more interesting coordinating behaviors will become at reach for study.

We preview a development roadmap for the simulator whose first step will be to write algorithms for agents deciding to change production from zero up to maximum capacity, announce non-fixed prices, make storage of products and change consumption values.

Next, it comes to introduce credit operations on numeraire and a non-taxed “external sector”. Credit operations can go from agents going into negative values of numeraire to contracting loans.

To model systems with structural time-variant parameters, it will be necessary to implement producers that build and sell string rewrite rules (“equipment”) to other agents, and to accommodate for a variable number of agents in the system along time.

5.1 *A Wider Look and an Invitation*

The presented paradigm can be put to the service of human well-being if geared to the coordination of large-scale systems comprising robots and machines that will make useful things. But it can also be geared to the understanding and modeling of economic phenomena. This is not out of the reach of control as [9] attests.

Under the proposal of this paradigm it stands the aim of creating a theory for networked transaction systems. The choice of string rewrite rules to model agents’ production and consumption behaviors gives the potential capability of modeling systems as computing devices controlled by operations involving numeraires. It will not be an exaggeration to say that, in following the steps of Agent-Based Computational Economics [10], the proposed paradigm goes far to provide a representation of economic phenomena founded on system concepts that can become quite adherent to reality.

Yet, the intellectual problems ahead to be solved are many, big and demanding, as the reader can suspect. Proposals for cooperation in the project are very welcome.

Acknowledgments This work has been supported by COMPETE: POCI-01-0145-FEDER-007043 and FCT – Fundação para a Ciência e Tecnologia within the Project Scope: UID/CEC/00319/2013.

References

1. Garrido, P.: Coordination of Systems through Numeraires. *FME Trans.* **43**, 377–385 (2015). http://www.mas.bg.ac.rs/_media/istrazivanje/fme/vol43/4/14_garrido.pdf
2. Knapp, G.F.: *The State Theory of Money* (English translation). Macmillan, London (1924)
3. Lerner, A.P.: *The Economics of Control*. Macmillan, London (1946)
4. Mosler, W.: *Soft Currency Economics II*, Valance, (distr. by Amazon), 2013
5. Tumer, K., Knudson, M.: *Aligning Agent Objectives for Learning and Coordination in Multiagent Systems*. PerAda Magazine, IEEE Computer Society (2010)
6. Tumer, K., Wolpert, D.: *The Science of Collectives*. In: Tumer, K., Wolpert, D. (eds.) *Collectives and the Design of Complex Systems*, pp. 1–42. Springer, New York (2004)
7. Wikipedia: Julia (programming language) (2016). https://en.wikipedia.org/wiki/Julia_%28programming_language%29
8. Wikipedia: Scilab (2016). <https://en.wikipedia.org/wiki/Scilab>
9. IFAC: IFAC Technical Committee 9.1. Economic, Business, and Financial Systems (2016). <http://tc.ifac-control.org/9/1>
10. Tesfatsion, L. (maintainer): *Software for Agent-Based Computational Economics and CAS* (2016). <http://www2.econ.iastate.edu/tesfatsi/acecode.htm>

Wormhole Approach to Control in Distributed Computing Has Direct Relation to Physics

Nicolás F. Lori and Victor Alves

Abstract The topic of Wormholes in distributed computing is about creating two different realms with different characteristics, the synchronous Wormholes and the asynchronous payload with the goal of using the wormholes to control the synchronism of the payload processes. We describe the characteristics of Wormholes in distributed computing, and relate them to issues in Physics, specifically, wormholes in general relativity and entanglement in quantum mechanics. The entanglement in quantum mechanics is about the existence of fixed relations between different physical systems as if they were still the same system. The entanglement is made evident by the occurrence of decoherence, which transform the multiple outcome possibilities of quantum systems into a single outcome “classical physics”-like objective reality. It is here presented the similarity between the decoherence process in quantum physics and the consensus problem in distributed computing. The approach to quantum mechanics used is quantum Darwinism, a Darwinian approach to decoherence where the environment controls the outcome of a measurement. It is here proposed that wormhole systems can be used to implement environment-based control of distributed computing systems.

Keywords Wormholes · Distributed quantum computing control · Decoherence · Environment-based invariance

1 Introduction

In distributed computing the challenge of reconciling uncertainty with predictability is required by the simultaneous pressure of increasing the applications’ quality of service, and the degrading of the assurance given by the infrastructure. In the

N.F. Lori (✉) · V. Alves

Algoritmi Centre, University of Minho, Braga, Portugal
e-mail: Nicolas.Lori@algoritmi.uminho.pt; nlori@inecoorono.org

V. Alves

e-mail: Victor.Alves@algoritmi.uminho.pt

Wormhole paradigm of distributed computing [1] it is proposed the use of hybrid (vs. homogeneous) models as a key to overcoming some of the difficulties faced when asynchronous models (with associated uncertainty) occur simultaneously with timing specifications (which require predictability). In this work, we focus on the relation between the quantum mechanics (QM) [2] perspective on system's entanglement (meaning connection and/or interaction between systems), and the Wormholes approach to distributed computing. There are multiple approaches to QM, we choose quantum Darwinism (QD) [3–5].

Contemporary Physics is based on two approaches that have not yet been reconciled, quantum fields [2] and general relativity (GR) [6]. In stable conditions, meaning when the creation and destruction of fermions (e.g. electrons, protons, and neutrons) is small, the quantum fields can be represented by QM [2]. While GR is deterministic (implying that there are no fundamental uncertainties associated with physical variables), QM has intrinsic fundamental uncertainty which is dissipated by the interaction with the environment. It can be said that the uncertainty in QM is kept alive at long distances through the occurrence of entanglement along quantum tunnels, and some recent work has indicated that the existence of quantum tunneling might be based on the occurrence of extremely tiny Wormholes [7, 8]. This recent result implies that although physics' Wormholes (a.k.a. Einstein-Rosen bridges [9]) are a solution to the GR equations, they have strong structural similarities to a QM process called entanglement, a process by which the uncertainty associated to pairs of quantum systems can remain connected even if the systems are very far apart. Resolving the uncertainty about one of the quantum systems faster-than-light resolves the uncertainty on the quantum system, no matter how far apart the quantum systems are.

It is as if there was a Wormhole joining the pair of quantum systems. Thus, Wormholes in distributed computing can be associated to both the physics of GR's Wormholes and/or the entanglement of QM. In both QM and GR, the physical representation of a state is always about two realms, specifically, the system and the environment. The system is what we aim to represent, and the environment is everything else that influences the system (in extreme cases, it is the rest of the universe). The approach described here allows for a bridge between distributed computing and quantum physics, this bridge might open new perspectives on quantum computing. We first build the parallel between the wormhole approach to distributed computing and fundamental Physics, and then at the end of the Discussion we describe a possible distributed computing effect at a fundamental Physics level that has been experimentally detected.

2 Hybrid Distributed Systems

There are two aspects to the difficulty of reconciling uncertainty with predictability in distributed computing: i. Time, ii. Security. The asynchronous computing model is not capable of making timed requirements, which is a major drawback as today

there are very few useful applications where Time is absent from. Whereas, the crash fault model is not a realist form of constructing systems that are secure enough for being successful in the Security world market. Finally, the arbitrary (a.k. a. Byzantine fault model) is an over-pessimistic abstraction for safety-critical applications subject to independent accidental faults, because both of its lack of independence and its stochastic search of malicious faults. The intention of the Wormhole approach is to partially solve both the Time and Security issues [1].

The hybrid models in distributed computing have the positive relevant characteristics that they are expressive models with sound theoretical basis, and they are supported by hybrid architectures which allow for the development of new algorithms. They are expressive models because they mimic well real systems when those systems are partially synchronous in the time dimension, and because they generally have components that have different degrees of synchronism which homogeneous models cannot take advantage from, for such homogeneous models are confined to using the worst-case values (which ultimately implies asynchrony). They have sound theoretical basis, since by using a hybrid model the properties of the different loci of the system (the space dimension) are heterogeneous, and thus correctness assertions about each of the loci of the system can be made, which implies that it is possible to establish interfaces between loci without needing to make unrealistic homogeneous timing assumptions. [1]

In the Wormholes distributed systems model (see Fig. 1) [1] there is a payload system S_p , and a S_w wormhole sub-system. The payload system is where algorithms and applications are normally executed, and it is composed of N_p payload processes p_i that communicate by messages passing through payload channels. The payload system S_p follows a set of fault and synchrony assumptions H_p (which are normally weak such as asynchronous processing and communication, plus having the faulty behavior be Byzantine). The wormhole subsystem is composed of N_w wormhole processes w_i . The wormhole processes may or may not communicate amongst themselves, but if they communicate then they do so by having messages pass through Wormhole channels. The wormhole subsystem S_w follows a set of fault and synchrony assumptions H_w , which are normally stronger than the payload synchrony assumptions because, for example, in the wormhole subsystem the processing and communication are synchronous and have faulty behavior crashes. The only way for payload processes to communicate with Wormhole processes is through Wormhole gateways (WG) with well-defined interfaces.

Nevertheless, there are several things that the wormhole model does not specify: i. interface specificity; ii. relative number of payload vs. wormhole processes; iii. degree of knowledge payload processes have of the wormhole processes, and vice versa. Thus, for payload processes the properties offered by any wormhole are defined and expressed at a wormhole gateway. In fact, maybe not all payload processes access Wormholes in certain algorithms, or maybe in other algorithms more than one payload process can access the same wormhole.

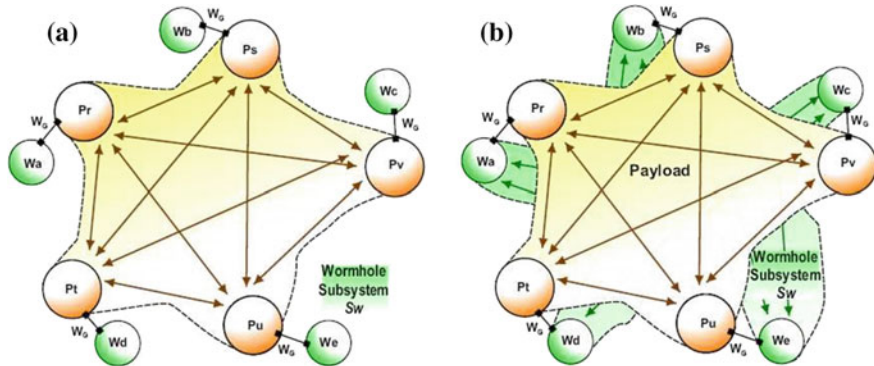


Fig. 1 The Wormhole model, with Wormholes in *green* and payloads in *yellow*: **a** Local Wormholes; **b** Distributed Wormholes. (from Verissimo [1])

It is common in science-fiction the use of space-time Wormholes for faster than-light travel and/or the use of quantum tunneling for teleportation (e.g. Star Trek). Thus, it is fair to ask if the use of Wormholes in distributed computing accomplishes what it sets out to achieve in the real world, or if it is a sort of computer-science equivalent to science-fiction. This question translates itself into two specific questions:

1. Is it feasible to construct Wormhole distributed systems?
2. Are systems with Wormholes useful?

To answer the first question, it should be noted that in the Wormhole model the architectural hybridization was proposed as a new paradigm. This implies that systems may have zones (a.k.a. realms) with different nonfunctional properties, such as synchronism, faulty behavior, and quality-of-service. This implies that the properties of each zone/realm are obtained by construction of the subsystem(s) therein, and that these subsystems have well-defined encapsulation and interface approaches through which these former properties become manifested. The Timely Computing Base (TCB) allows for the obtaining of timely actions in systems that can be asynchronous; which means that the TCB distributed wormhole gateway provides very helpful services such as: timely execution, duration measurement, and timing failure detection. Through the TCB, it is possible [1] to make an asynchronous system perform timely (synchronous) actions or detect the failure thereof. So, the answer to the first question is yes, it is feasible to construct Wormhole distributed systems.

To answer the second question, one must first focus on what are the most important implications of the use of hybrid distributed system models. Those implications are: quantification of the assumptions' substance rather than just

considering what the assumptions are, difference to partial synchrony models, a new approach to the FLP impossibility [10] result, and the existence of failure detectors (FDs). The substance of the assumptions becomes important because now it is the pair “assumption + coverage” that measures the weakness or strength of the model, and because the use of architectural hybridization can possibly improve the building of hybrid fault models. The Wormhole models are different from partial synchrony models in that the first are heterogeneous, whereas the second are homogeneous. Also, the Wormholes can circumvent the FLP impossibility result because a form of avoiding the FLP impossibility is by the use of synchronism [11]. The avoidance of the FLP impossibility in Wormholes model occurs by the use of FDs. The FDs in asynchronous systems are difficult, but the consensus in the payload systems agrees with FDs in the wormhole realm, which implies that functionality in a wormhole is not confined to FDs, thus opening towards other more generic approaches. The Wormhole model clarifies borderline situations where homogeneous asynchronous systems fail, and when asynchronous models must be complemented with timing assumptions to address timeliness specifications; thus there is no alternative to Wormholes for correct specification of such settings [1]. So, the answer to the second question is yes, it is useful to construct Wormhole distributed systems.

The Wormholes approach allows extending partial synchrony to the space dimension, meaning that, regardless of the asynchronism of the whole system, some parts of the system exhibit a well-defined (perpetual if desired) time-domain behavior. The parallel to QM is that before a measurement the quantum states behave as if they were the asynchronous components of the payload system, but as the quantum states interact (and thus become measured) they start behaving more as synchronous Wormholes. To better describe that parallel, we describe QD in the next section.

3 Quantum Darwinism

The following set of postulates is strongly based in the foundations of QD proposed by Zurek [3–5]. It is, however, our aim to formulate them more generally such that their range of application is wider and extends into a large range of issues (e.g. distributed computing). Essentially, we move away from the quantum mechanical interpretation of these postulates, but stay with their mathematical structure, which is given in terms of vector spaces. For instance, where one reads quantum system in the QD formalism, we write system, with the understanding that the characteristic property of such a system is to be individually accessible to measurements; likewise, the quantum state is replaced by a vector in a multidimensional vector space; and so on.

In Fig. 2 instead of the \rightarrow used in the vector states of the rest of the article, the $|>$ symbol will be used; and we use suits because that is a representation Zurek uses (e.g., Ref. [3]). In Fig. 2 is described how the principle of indifference, the basis of

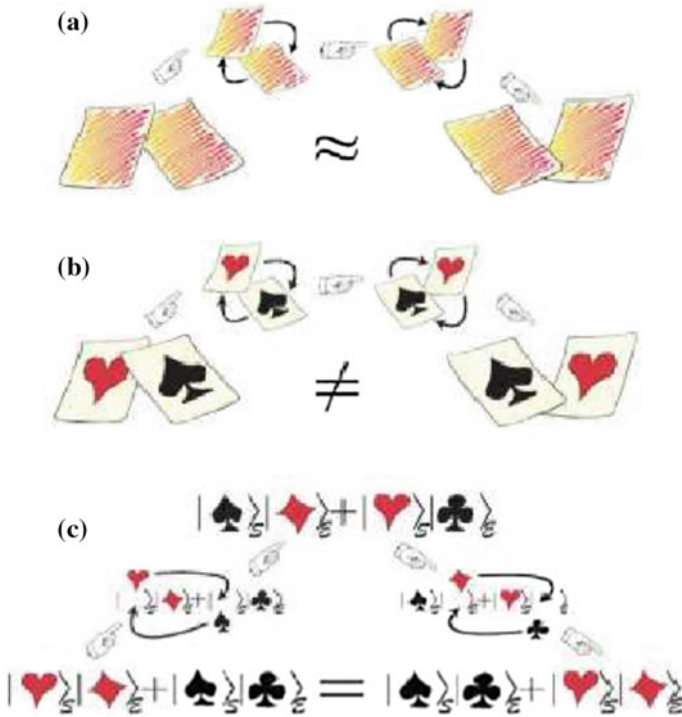


Fig. 2 **a** When the probability of a favorable swap is the same before and after the swap, then the states are equivalent (\approx). **b** In classical physics, because of its objective perspective, the states before and after the swap are equivalent (\approx) but not equal (\neq). **c** In QD, the swapping of ♠ and ♥ in the system *S* is possible to compensate by the swapping of ♦ and ♣ in the environment *E*, thus obtaining a state that is equal ($=$) to the original state. (from Zurek [3] [©2005 The American Physical Society])

statistics, has a different meaning in quantum versus classical physics. In Fig. 2a, the principle of indifference is described, and it states that a card player who knows one of the two cards is ♠ but does not see their faces, does not care—is indifferent—when cards get swapped. So, when the probability of a favorable swap is the same before and after the swap, then the states are equivalent (\approx). In Fig. 2b it is described how in classical physics, because of its objective perspective, the states before and after the swap are equivalent but not equal. In Fig. 2c it is described how in the QD perspective of quantum mechanics if the system *S* and the environment *E* interact (a.k.a. entangle), then the definition of the system *S* only exists in relation to the environment *E*, and so does not exist by itself, meaning that the states before and after the swap are equal. This means that the swapping of ♠ and ♥ in the system *S* is possible to compensate by the swapping of ♦ and ♣ in the environment *E*. [3]

The use of this new notation makes the QD postulates have the following aspect:

- o. The universe consists of systems individually accessible to observations.
- i. The state of a system is represented by a vector in a multidimensional vector space, and all converging series of vectors of the vector space converge to a vector of that same vector-space. To each vector is associated a dual vector. The inner product between a dual vector and a vector is a scalar.
- ii. The time-evolution of a vector is such that the inner product of a vector is preserved.
- iii. If the outside of a system (the environment) remains unchanged, then the observation of the system remains unchanged across time.

According to statement iii, there must be a set of states of the system that remains unaltered by the interaction with the environment, call it vector state set S_k . So, there must be an alteration of the environment leading to the environment being now represented by the vector state set E_k .

Let's consider that the possible states of the system S are ♠ and ♥, that the possible states of the environment E are ♦ and ♣. In that case, due to statements o and i, the state of the system can be represented by (α and β are scalars):

$$\vec{S} = \alpha \overrightarrow{\heartsuit} + \beta \overrightarrow{\spadesuit} \quad (1)$$

Consider that the environment E is capable of making one-to-one measurements of S , such that before interacting with S the environment E is represented by the vector state:

$$\overrightarrow{E_0} = \alpha \overrightarrow{\heartsuit_0} + \beta \overrightarrow{\clubsuit_0} \quad (2)$$

Consider that after S and E start interacting, the state vector of E is then:

$$\vec{E} = \alpha \overrightarrow{\heartsuit} + \beta \overrightarrow{\clubsuit} \quad (3)$$

Implying that before S and E start interacting, the state of “ $S + E$ ” is:

$$\overrightarrow{SE} = (\alpha \overrightarrow{\heartsuit} + \beta \overrightarrow{\spadesuit}) \otimes (\overrightarrow{\heartsuit_0} + \overrightarrow{\clubsuit_0}) \quad (4)$$

After S and E start interacting, for postulate iii to be valid it is necessary that the state of “ $S + E$ ” is:

$$\overrightarrow{SE} = (\alpha \overrightarrow{\heartsuit} \otimes \overrightarrow{\heartsuit} + \beta \overrightarrow{\spadesuit} \otimes \overrightarrow{\clubsuit}) \quad (5)$$

Due to statement ii, the evolution of the “ $S + E$ ” state must preserve the inner product, and thus also preserve the amplitude of the vector representing the state.

Thus, the joining of statements *o*, *i*, and *ii* implies that the evolution of the state of “*S* + *E*” during a measurement must be such that it is capable of going from a state of *S* and *E* being not-linked to a state of *S* and *E* being linked, without altering the amplitude of the vector representing the state. If the square amplitude of the “*S* + *E*” vector is the same before (Eq. 4) and after (Eq. 5) *S* and *E* start interacting, then:

$$\propto \beta (\overrightarrow{\heartsuit \bullet \spadesuit}) \left(\|\overrightarrow{\diamond_0} + \overrightarrow{\clubsuit_0}\|^2 - \overrightarrow{\diamond \bullet \clubsuit} \right) = 0 \quad (6)$$

Due to statement *iii*, the above equation should continue being valid long after *S* and *E* start interacting. Since this result must be valid for any value of α and β , there are only two possibilities:

$$\begin{cases} \|\overrightarrow{\diamond_0} + \overrightarrow{\clubsuit_0}\|^2 = \overrightarrow{\diamond \bullet \clubsuit} \\ \overrightarrow{\heartsuit \bullet \spadesuit} = 0 \end{cases} \quad (7)$$

The upper line of the previous equation implies that the system has no influence in the environment, whereas the lower line implies that the system states are orthogonal. The joint consequence of both lines is that: *the vector states of the system capable of leaving a print in the environment, no matter how small the print, will necessarily be orthogonal vector states.*

The Darwinian aspect of QD is that states of the system that fail to print themselves into the environment cease to exist, meaning they become extinct. This aspect of QD is called Quantum Existentialism (QE) because the states only survive by their capacity for printing information about themselves in the environment.

The preservation in the environment, after the measurement, of the information about the measurement in large enough quantities on the environment so as to be read by multiple observers creates the illusion of the state’s “objectivity”. The “reality” of the vector states of the system is given by their capacity to transmit information into the vector states of the environment. The successful transmission of information is the printing of the information about the system in the environment states, such that the environment states become themselves orthogonal. When that occurs, then the system and the environment become entangled.

An entangled combination of system and environment can be described by a vector state where each component of the vector state is the product of a system output state S_k with its corresponding environment output state E_k . The coefficient associated to that product of states is called the Schmidt coefficient, which is a complex number of amplitude one [12]. This implies that for an entangled “system + environment” state an action on the system causes an angle shift on the Schmidt coefficient phase θ_k , and that angle shift can be compensated by an action on the environment. This implies that in the presence of entanglement it is possible to describe a type of invariance where the system is altered by an action on the

system, but that alteration of the system can be totally compensated by an action on the environment without the occurrence of any further action on the system (see Fig. 2c). This type of invariance is called an environment-assisted invariance, which in short form is called *envariance* [3].

4 Discussion

The Wormholes model allows for different processes of the payload to communicate “immediately” through the synchronism of the wormholes, the wormholes thus play the same role as the entanglement in QD by assuring that there can be “immediate” connection between different components of the payload. This form of control of the payload by the wormholes is especially useful in representing distributed quantum computing control, since the wormholes in the Wormhole model can accurately represent the role of the environment in quantum entanglement.

To represent QD using the Wormholes model it should be noted that because the Wormholes are becoming synchronous within themselves, they then could be used to eliminate the time-evolution of the payload processes that are not in agreement with the Wormhole synchronization, so forcing the payload processes to become synchronous with the Wormholes or stop. So, it is possible to consider QD as a Wormhole control system occurring in quantum reality.

The parallels between distributed computing Wormholes and Physics as described in this work might be useful for quantum computing, for clarifying what are the computations associated to the occurrence of quantum gravity, and also might open new perspectives about the use of quantum decoherence as a describer of quantum computer performance within distributed quantum computing.

In the Laboratory for Attosecond Physics it was possible to generate for the first time, visible flashes of light in attosecond dimensions [13]. At this laboratory they dispatched light-flashes to the electrons in krypton atoms, and they were thus able to obtain that the electrons, which are stimulated by the flashes, needed roughly 100 attoseconds to respond to the incident light. Until now it was assumed that particles respond to incident light without delay.

These experimental results couple directly to the approach proposed here. The 100 attosecond of light traveling in vacuum correspond to a travel distance of about 300 Angstroms, which is too long to be the size of the electron or any fundamental particle. If it is considered that electrons have a finite computation capacity, as is proposed in the approach we developed in this work. Then electrons would need to take 100 attoseconds to process the corresponding Feynman diagrams, or the Physical equivalent of the mathematical object that the Feynman diagrams are, before the electron could compute the outputted light.

To check if this perspective makes mathematical sense, let’s check if the “lifetime of the excited state” described in Ref [13] is actually the computation time of the Planck volumes associated to the volume of the electron. If the lifetime is T and the particle is a sphere with volume V , then if each Planck cube (a cube with

sides equal to Planck length) is a processor that takes a Planck time to process the input information into output information, and A is the Planck area (a square with sides equal to Planck length) and c is the speed of light in vacuum, then the radius R of the electron would relate to T by the relation:

$$R = \sqrt[3]{\frac{3}{4\pi} c A T} \quad (8)$$

The Eq. (8) implies that the electron has a radius of about 25×10^{-28} m. It is usually assumed that “a search for a contact interaction at the LEP storage ring probes for electron structure at the 10 TeV energy scale in which case $R < 2 \times 10^{-20}$ m.” [14]. Which is in total compatibility with the result obtained in Eq. 8.

5 Conclusion

This work was able to establish a bridge between distributed computing Wormholes and the decoherence processes in QM, which was its objective. But, a bridge between QM decoherence and GR Wormholes has been recently proposed [7], and so it is possible that it exists. If it exists, this would create a direct link between distributed computing Wormholes and GR wormholes, which is an extra contribution of this work.

Acknowledgments Many thanks to Eduarda Gavino. The work has been supported by COMPETE: POCI-01-0145-FEDER-007043 and FCT (Fundação para a Ciência e Tecnologia) within the Project Scope: UID/CEC/00319/2013.

References

1. Veríssimo, P.E.: Travelling through wormholes: a new look at distributed systems models. ACM SIGACT News Distrib. Comput. Column 21 **37**(1), 66–81 (2006)
2. Sakurai, J.J.: Modern Quantum Mechanics. Addison-Wesley (1994)
3. Zurek, W.H.: Probabilities from entanglement, Born’s rule $p_k = |\psi_k|^2$ from envariance. Phys. Rev. A **71**, 052105 (2005)
4. Zurek, W.H. Relative states and the environment: Einselection, envariance, quantum darwinism, and existential interpretation. arXiv: 0707.2832v1. (2007)
5. Zurek, W.H.: Quantum Darwinism. Nat. Phys. **5**, 181–188 (2009)
6. Wald, R.: General Relativity. Chicago University Press (1984)
7. Sonner, J.: Holographic schwinger effect and the geometry of entanglement. Phys. Rev. Lett. **111**(21), 211603–211607 (2013)
8. Massachusetts Institute of Technology: You can’t get entangled without a wormhole: Physicist finds entanglement instantly gives rise to a wormhole. ScienceDaily. 5 December. (2013)
9. Einstein, A., Rosen, N.: The particle problem in the general theory of relativity. Phys. Rev. **48**, 73–77 (1935)

10. Fischer, M.J., Lynch, N.A., Paterson, M.S.: Impossibility of distributed consensus with one faulty process. *J. ACM* **32**(2), 374–382 (1985)
11. Chandra, T., Toueg, S.: Unreliable failure detectors for reliable distributed systems. *J. ACM* **43**(2), 225–267 (1996)
12. Ekert, A., Knight, P.L.: Entangled quantum systems and the schmidt decomposition. *Am. J. Phys.* **65**(5), 415–423 (1995)
13. Hassan, M. Th., Luu, T.T., Moulet, A., Raskazovskaya, O., Zhokhov, P., Garg, Karpowicz, N., Zheltikov, A.M., Pervak, V., Krausz, F., Goulielmakis, E.: Optical attosecond pulses and tracking the nonlinear response of bound electrons. *Nature* **530**, 66–70 (2016)
14. Bourilkov, D.: Hint for axial-vector contact interactions in the data on $e^+e^- \rightarrow e^+e^-(\gamma)$ at center-of-mass energies 192–208 GeV. *Phys. Rev. D* **64**, 071701R (2001)

A New Robust Control Scheme for LTV Systems Using Output Integral Discrete Synergetic Control Theory

Saeid Rastegar, Rui Araújo, Alireza Emami and Abdelhamid Iratni

Abstract This paper presents a new robust control strategy based on a synergetic control theory (SCT) approach for linear time varying (LTV) systems in the presence of unknown persistent disturbance. The proposed control scheme is featured by an integral type of SCT driving the system towards a macro-variable manifold based on output error. The proposed control methodology guarantees robust stability for LTV systems, affected by unmeasured bounded additive disturbances. Robust stability analysis proves that the error trajectory monotonically converges to the SCT macro-variable manifold. The effectiveness of the proposed method and the implications of the controller design on feasibility and closed-loop performance is demonstrated through an example of reactor temperature control of Continuous Stirred Tank Reactor (CSTR) plant.

1 Introduction

The design of robust control methodologies for linear time-variant (LTV) systems [1] when facing external unexpected disturbances is not a new issue [2, 3]. However, it is still considered as an significant research interest subject [4, 5]. In the presence of unmeasured disturbances, the analysis and ensurance closed-loop feasibility, stability, and robustness of control methodologies is a challenging issue and difficult to solve. Sliding mode control (SMC) is a well-known control approach [6, 7]. Sliding mode control has strong robustness for system parameter changes and external disturbances. However, due to chattering phenomena of sliding mode control [8, 9], the high frequency oscillation of control system brings challenge for the application

S. Rastegar (✉) · R. Araújo · A. Emami · A. Iratni
Department of Electrical and Computer Engineering (DEEC-UC),
Institute of Systems and Robotics (ISR-UC), University of Coimbra, Coimbra, Portugal
e-mail: srastegar@isr.uc.pt

A. Iratni
Faculty of Science and Technology, Electrical Engineering Department,
University of Bordj Bou Arreridj, El Anasser, Algeria
e-mail: iratni@gmail.com

of sliding mode. On the other hand, the choice of the sliding surface strictly requires system relative degree to be equal to 1, which limits the choice of sliding surface [10]. To overcome the chattering problem in SMC, synergetic control (SC) techniques may be an useful and also fast approach for a control design. To date, synergetic control (SC) theory has been utilized in power systems control [11–14]. The SC is an effective technique which can possess the properties of order reduction and decoupling in the design procedure [11]. But SCT has never been used for a robust control design. Therefore, the development of a robust control design based on SC theory, and the examination and evaluation of the corresponding robustness properties is an important and promising research subject. In this paper, achieving the control of LTV systems in the presence of disturbance, and a chatter-free operation will be a goal. The new SC control scheme is called robust discrete SCT control (RDSCTC) which carries robust properties. First an integral type SCT macro-variable is defined based on the output estimation error. To ensure asymptotic tracking error convergence to zero, an evolution constraint is given. Through combination of the evolution constraint and a macro-variable, the function dynamics of the error equation is constructed. Solving the dynamic stability equation results in a desired command signal to address the main control objectives. The effectiveness of the proposed method and the implications of the controller design on feasibility and closed-loop performance is demonstrated through an example of temperature control on a Continuous Stirred Tank Reactor (CSTR) plant.

The paper is organized as follows. Section 2 presents the problem formulation and preliminary results. Section 3 starts by briefly overviewing the synergetic control theory (SCT) approach, and then introduces the proposed robust online controller and presents its stability proof. In Sect. 4, results in the applications of the RDSCTC, its feasibility and closed-loop performance, are presented and analysed. Finally, Sect. 5 makes concluding remarks.

2 Problem Formulation and Preliminaries

Consider a class of discrete-time linear time varying (LTV) dynamical certain system with disturbance represented by the following equations:

$$\mathbf{x}(k+1) = \mathbf{A}(k)\mathbf{x}(k) + \mathbf{B}(k)\mathbf{u}(k) + \mathbf{w}(k), \quad (1a)$$

$$\mathbf{y}(k) = \mathbf{C}\mathbf{x}(k), \quad (1b)$$

where $\mathbf{x}(k) = [x_1(k), \dots, x_n(k)]^T \in \mathbb{R}^n$ is the plant state, and $\mathbf{u}(k) = [u_1(k), \dots, u_m(k)]^T \in \mathbb{R}^m$ is the control input. $\mathbf{w}(k) = [w_1(k), \dots, w_n(k)]^T \in \mathbb{R}^n$ is a bounded, and unmeasured disturbance, $\mathbf{y}(k) = [y_1(k), \dots, y_p(k)]^T \in \mathbb{R}^p$ is the output variable, and $\mathbf{C} = [c_{ij}] \in \mathbb{R}^{p \times n}$ is a non-negative matrix (i.e. $c_{ij} \geq 0$ for all $i = 1, \dots, p, j = 1, \dots, n$). $\mathbf{y}(k)$ is also considered the controlled variable, i.e. the variable to be controlled to a given desired setpoint $\mathbf{z}_d(k)$. The $\mathbf{A}(k)$ and $\mathbf{B}(k)$

matrices can be time-varying, but to simplify the notation, in the sequel they will be simply denoted by \mathbf{A} and \mathbf{B} , respectively. In addition, it is assumed that $\det(\mathbf{CB}) \neq 0$. It is assumed that a measurement of the plant state is available at each sample time k ; And system $\{\mathbf{A}, \mathbf{B}, \mathbf{C}\}$ is output controllable, i.e. it is possible to construct an input signal sequence to move the system output from any initial condition to any final condition in a finite time interval. Under fairly general conditions a state space model (1a)–(1b) can be transformed into an observability, observer, or observable canonical form/realization where $\mathbf{C}(k)$ is non-negative [15–17].

3 Synergetic Control Theory Approach

The foundations of the SC approach to the synthesis of nonlinear dynamic systems are based on three statements, or ideas. The SCT proposes creating attractors in systems at those areas of the state spaces that correspond to the control purposes. Depending on the dimensionality of the state space, attractors can be points, contours, tori or regions of fractal dimensionality. If the requirements that the controllers should provide to the system cannot be fulfilled, the attractors cannot be created, and the dynamical system may become unstable and not converge. The control purposes are formulated as a collection of aggregated macro-variables ψ_i that need to be zero. The aggregated macro-variables, ψ_i , $i = 1, \dots, r \leq m$, are functions of system variables \mathbf{x} , \mathbf{z}_d , and control signals \mathbf{u} : $\psi_i = \psi_i(\mathbf{x}, \mathbf{z}_d, \mathbf{u})$. Hence, to attain the control purposes, attractors are introduced where all the aggregated macro-variables are equal to zero. The SCT gives an equation which can be used for creating dynamical systems with attractors at $\psi_i = 0$ which is expressed as

$$T\dot{\boldsymbol{\psi}} + \boldsymbol{\phi}(\boldsymbol{\psi}) = 0, \quad (2)$$

where T determines the rate of convergence to the attractor, $\boldsymbol{\psi} = [\psi_1, \psi_2, \dots, \psi_r]^T$ is the vector of aggregated macro-variables, $\dot{\boldsymbol{\psi}}$ is the derivative of the aggregated macro-variable (vector) with respect to time, and $\boldsymbol{\phi}(\cdot)$ is some function that makes the solution of (2) approach the attractor. One of the possible expressions for $\boldsymbol{\phi}(\cdot)$ is $\boldsymbol{\phi}(\boldsymbol{\psi}) = \boldsymbol{\psi}$. In this case, Eq. (2) is rewritten as:

$$T\dot{\boldsymbol{\psi}} + \boldsymbol{\psi} = 0. \quad (3)$$

In this paper, it is assumed that the process to be controlled is a single-input single-output (SISO) plant, and $r = m = p = 1$.

3.1 Proposed Controller

In this section, the discrete time controller based on the synergetic control theory is designed in the presence of unmeasured bounded additive disturbances on state space discrete-time linear systems. First, let the tracking error be defined as $\mathbf{e}(k) = \mathbf{y}(k) - \mathbf{z}_d(k)$, where $\mathbf{z}_d(k)$ contains the setpoints, and define a proportional integral (PI) type macro-variable, as follows:

$$\mathbf{e}(k) = \mathbf{y}(k) - \mathbf{z}_d(k), \quad (4a)$$

$$\boldsymbol{\psi}(k) = \mathbf{K}_p \mathbf{e}(k) + \mathbf{K}_I \boldsymbol{\zeta}(k), \quad (4b)$$

$$\boldsymbol{\psi}(k+1) = \mathbf{K}_p \mathbf{e}(k+1) + \mathbf{K}_I \boldsymbol{\zeta}(k+1), \quad (4c)$$

where $\boldsymbol{\zeta}(k)$ is an integral of the error which is defined as $\boldsymbol{\zeta}(k) = \mathbf{e}(k) + \boldsymbol{\zeta}(k-1)$, and \mathbf{K}_p and \mathbf{K}_I are positive proportional and integral gains, respectively. Replacing (4b) and (4c) into discrete-time version of (3), discretized by the forward differences method, yields

$$T(\mathbf{K}_p + \mathbf{K}_I)\mathbf{e}(k+1) + T\mathbf{K}_I\boldsymbol{\zeta}(k) - (T - T_s)\boldsymbol{\psi}(k) = 0. \quad (5)$$

Equation (5) expresses dynamic error of the system, where T_s is the sampling time period. Using (1a), and (4a), the error dynamics (5) can be rewritten as:

$$T(\mathbf{K}_p + \mathbf{K}_I)[\mathbf{CAx}(k) + \mathbf{CBu}(k) + \mathbf{Cw}(k) - \mathbf{z}_d(k+1)] + T\mathbf{K}_I\boldsymbol{\zeta}(k) - (T - T_s)\boldsymbol{\psi}(k) = 0. \quad (6)$$

From (1b), (4a), and (6) and replacing the unknown bounded $\mathbf{w}(k)$ with its one-step delayed estimation [18], $\bar{\mathbf{w}}(k) = \mathbf{w}(k-1) \in \mathbb{R}^n$, yields

$$\begin{aligned} \mathbf{u}(k) = & - \left(T(\mathbf{K}_p + \mathbf{K}_I)\mathbf{CB} \right)^{-1} [-q\boldsymbol{\psi}(k) + T(\mathbf{K}_p + \mathbf{K}_I)\mathbf{CAx}(k) \\ & + T(\mathbf{K}_p + \mathbf{K}_I)\mathbf{Cw}(k-1) - T(\mathbf{K}_p + \mathbf{K}_I)\mathbf{z}_d(k+1) + T\mathbf{K}_I\boldsymbol{\zeta}(k)], \end{aligned} \quad (7)$$

where $q = T - T_s$. Recall that $\det(\mathbf{CB}) \neq 0$. In addition, from the assumptions of Theorem 1 on Sect. 3.2, it will be seen that $T > T_s/2 > 0$, and $-T_s < q < 0$.

3.2 Robust Closed-Loop Stability

To design the SCT control law, the SCT convergence law in Eq. (3) must guarantee the following desired attributes: (1) starting from any initial state, the error trajectory monotonically moves towards the SCT macro-variable manifold; (2) After the trajectory has reached a robust macro-variable manifold band (*RMMB*), then in each subsequent time step, the trajectory is confined to remain inside the *RMMB*, where

$$RMMB = \left\{ \mathbf{x} \in \mathbb{R}^n \mid |\boldsymbol{\psi}(\mathbf{x}, \mathbf{z}_d)| \leq M_\psi = \boldsymbol{\Omega}\mathbf{C}(\mathbf{w}_{max} - \mathbf{w}_{min}) \frac{T}{2T - T_s} \right\}, \quad (8)$$

where $\boldsymbol{\Omega} = \mathbf{K}_p + \mathbf{K}_I$, $\mathbf{w}_{min} \in \mathbb{R}^n$ and $\mathbf{w}_{max} \in \mathbb{R}^n$ are the row-wise minimum and row-wise maximum of $\mathbf{w}(k)$, respectively. Note that $M_\psi \geq 0$. The control law that enforces the SCT convergence law in Eq. (3) is given by (7) and is rewritten as follows:

$$\mathbf{u}(k) = - (T\boldsymbol{\Omega}\mathbf{C}\mathbf{B})^{-1} [-q\boldsymbol{\psi}(k) + T\boldsymbol{\Omega}\mathbf{C}\mathbf{A}\mathbf{x}(k) + T\boldsymbol{\Omega}\mathbf{C}\mathbf{w}(k-1) - T\boldsymbol{\Omega}\mathbf{z}_d(k+1) + T\mathbf{K}_I\boldsymbol{\zeta}(k)]. \quad (9)$$

Theorem 1 Consider the system (1) with control law (9). Suppose the reference/desired output variables are given by $\mathbf{z}_d(k)$, and the dynamic error is defined as $\mathbf{e}(k) = \mathbf{y}(k) - \mathbf{z}_d(k)$. Also assume that $T < T_s < 2T$, $\det(\mathbf{C}\mathbf{B}) \neq 0$, and $\mathbf{C} > \mathbf{0}$. Then, the closed-loop system (1) in the presence of unknown bounded disturbance $\mathbf{w}(k)$ is stable, and by using the control law (9) the error trajectory asymptotically converges to the RMMB. After the trajectory has reached the RMMB, then in each subsequent time step, the trajectory is confined to remain inside the RMMB.

Proof Using (4c), (1a), (9), start by noting that

$$\begin{aligned} \boldsymbol{\psi}(k+1) &= \boldsymbol{\Omega}\mathbf{e}(k+1) + \mathbf{K}_I\boldsymbol{\zeta}(k) \\ &= \boldsymbol{\Omega}[\mathbf{C}\mathbf{x}(k+1) - \mathbf{z}_d(k+1)] + \mathbf{K}_I\boldsymbol{\zeta}(k) \\ &= \boldsymbol{\Omega}[\mathbf{C}(\mathbf{A}\mathbf{x}(k) + \mathbf{B}\mathbf{u}(k) + \mathbf{w}(k)) - \mathbf{z}_d(k+1)] + \mathbf{K}_I\boldsymbol{\zeta}(k) \\ &= \mathbf{K}_I\boldsymbol{\zeta}(k) + \boldsymbol{\Omega}\mathbf{C}\mathbf{A}\mathbf{x}(k) + \boldsymbol{\Omega}\mathbf{C}\mathbf{B}(- (T\boldsymbol{\Omega}\mathbf{C}\mathbf{B})^{-1} [-q\boldsymbol{\psi}(k) + T\boldsymbol{\Omega}\mathbf{C}\mathbf{A}\mathbf{x}(k) \\ &\quad + T\boldsymbol{\Omega}\mathbf{C}\mathbf{w}(k-1) - T\boldsymbol{\Omega}\mathbf{z}_d(k+1) + T\mathbf{K}_I\boldsymbol{\zeta}(k)]) + \boldsymbol{\Omega}\mathbf{C}\mathbf{w}(k) - \boldsymbol{\Omega}\mathbf{z}_d(k+1) \\ &= \boldsymbol{\Omega}\mathbf{C}\mathbf{A}\mathbf{x}(k) + T^{-1}q\boldsymbol{\psi}(k) - \boldsymbol{\Omega}\mathbf{C}\mathbf{A}\mathbf{x}(k) - \boldsymbol{\Omega}\mathbf{C}\mathbf{w}(k-1) \\ &\quad + \boldsymbol{\Omega}\mathbf{z}_d(k+1) - \mathbf{K}_I\boldsymbol{\zeta}(k) + \boldsymbol{\Omega}\mathbf{C}\mathbf{w}(k) - \boldsymbol{\Omega}\mathbf{z}_d(k+1) + \mathbf{K}_I\boldsymbol{\zeta}(k) \\ &= \frac{T - T_s}{T}\boldsymbol{\psi}(k) + \boldsymbol{\Omega}\mathbf{C}(\mathbf{w}(k) - \mathbf{w}(k-1)). \end{aligned} \quad (10)$$

The proof will be made by showing that: (i) if $\boldsymbol{\psi}(k) \notin RMMB$, then by choosing the discrete-time Lyapunov function $V(k) = \boldsymbol{\psi}^2(k) := \boldsymbol{\psi}^T(k)\boldsymbol{\psi}(k)$, then $\Delta V = V(k+1) - V(k) < 0$, i.e. $\boldsymbol{\psi}^2(k+1) < \boldsymbol{\psi}^2(k)$; and (ii) if $\boldsymbol{\psi}(k) \in RMMB$, then $\boldsymbol{\psi}(k+1) \in RMMB$. Four cases are analyzed below. Note that several steps of the proof below are justified by the assumption that $\mathbf{C} > \mathbf{0}$.

Case 1: If $\mathbf{0} \leq \boldsymbol{\Omega}\mathbf{C}(\mathbf{w}_{max} - \mathbf{w}_{min}) \frac{T}{2T - T_s} < \boldsymbol{\psi}(k)$, then from (10)

$$\begin{aligned} \boldsymbol{\psi}(k+1) - \boldsymbol{\psi}(k) &= \left(\frac{T - T_s}{T} - 1 \right) \boldsymbol{\psi}(k) + \boldsymbol{\Omega}\mathbf{C}(\mathbf{w}(k) - \mathbf{w}(k-1)) \\ &\leq -\frac{T_s}{T}\boldsymbol{\psi}(k) + \boldsymbol{\Omega}\mathbf{C}(\mathbf{w}_{max} - \mathbf{w}_{min}) \\ &< -\frac{T_s}{T}\boldsymbol{\Omega}\mathbf{C}(\mathbf{w}_{max} - \mathbf{w}_{min}) \frac{T}{2T - T_s} + \boldsymbol{\Omega}\mathbf{C}(\mathbf{w}_{max} - \mathbf{w}_{min}) \end{aligned}$$

$$= 2 \frac{T - T_s}{2T - T_s} \Omega \mathbf{C}(\mathbf{w}_{max} - \mathbf{w}_{min}) < \mathbf{0}, \quad (11)$$

$$\begin{aligned} \boldsymbol{\psi}(k+1) + \boldsymbol{\psi}(k) &= \left(\frac{T - T_s}{T} + 1 \right) \boldsymbol{\psi}(k) + \Omega \mathbf{C}(\mathbf{w}(k) - \mathbf{w}(k-1)) \\ &> \left(\frac{2T - T_s}{T} \right) \Omega \mathbf{C}(\mathbf{w}_{max} - \mathbf{w}_{min}) \frac{T}{2T - T_s} \\ &\quad - \Omega \mathbf{C}(\mathbf{w}_{max} - \mathbf{w}_{min}) = \mathbf{0}, \end{aligned} \quad (12)$$

Therefore, from (11) and (12), $\boldsymbol{\psi}^2(k+1) < \boldsymbol{\psi}^2(k)$.

Case 2: If $\mathbf{0} < \boldsymbol{\psi}(k) \leq \Omega \mathbf{C}(\mathbf{w}_{max} - \mathbf{w}_{min}) \frac{T}{2T - T_s}$, then the condition which must be satisfied is $|\boldsymbol{\psi}(k+1)| \leq \Omega \mathbf{C}(\mathbf{w}_{max} - \mathbf{w}_{min}) \frac{T}{2T - T_s}$. Considering also (10), and the fact that $T - T_s < 0$, then

$$\begin{aligned} \frac{T - T_s}{2T - T_s} \Omega \mathbf{C}(\mathbf{w}_{max} - \mathbf{w}_{min}) + \Omega \mathbf{C}(\mathbf{w}(k) - \mathbf{w}(k-1)) &\leq \boldsymbol{\psi}(k+1) \\ &< \Omega \mathbf{C}(\mathbf{w}(k) - \mathbf{w}(k-1)). \end{aligned} \quad (13)$$

From (13), and considering that $|\mathbf{w}(k) - \mathbf{w}(k-1)| \leq \mathbf{w}_{max} - \mathbf{w}_{min}$, and $2T - T_s < T$, then (14) and (15) are obtained, which in turn imply (16):

$$\begin{aligned} \boldsymbol{\psi}(k+1) &< \Omega \mathbf{C}(\mathbf{w}(k) - \mathbf{w}(k-1)) \leq \Omega \mathbf{C}(\mathbf{w}_{max} - \mathbf{w}_{min}) \\ &< \Omega \mathbf{C}(\mathbf{w}_{max} - \mathbf{w}_{min}) \frac{T}{2T - T_s}, \end{aligned} \quad (14)$$

$$\begin{aligned} \boldsymbol{\psi}(k+1) &\geq \frac{T - T_s}{2T - T_s} \Omega \mathbf{C}(\mathbf{w}_{max} - \mathbf{w}_{min}) + \Omega \mathbf{C}(\mathbf{w}(k) - \mathbf{w}(k-1)) \\ &\geq \frac{T - T_s}{2T - T_s} \Omega \mathbf{C}(\mathbf{w}_{max} - \mathbf{w}_{min}) - \Omega \mathbf{C}(\mathbf{w}_{max} - \mathbf{w}_{min}) \\ &= -\frac{T}{2T - T_s} \Omega \mathbf{C}(\mathbf{w}_{max} - \mathbf{w}_{min}), \end{aligned} \quad (15)$$

$$|\boldsymbol{\psi}(k+1)| \leq \Omega \mathbf{C}(\mathbf{w}_{max} - \mathbf{w}_{min}) \frac{T}{2T - T_s}. \quad (16)$$

From (16), it is seen that after the trajectory has reached the upper positive side band of the *RMMB*, then in each subsequent time step, the trajectory is confined to remain inside the *RMMB*. Also note that in the case that $\boldsymbol{\psi}(k) = \mathbf{0}$, then (14), (15), and (16), still hold, except that the left most inequality in (14) becomes an equality. Therefore, the theorem also holds for $\boldsymbol{\psi}(k) = \mathbf{0}$.

Case 3: If $-\Omega \mathbf{C}(\mathbf{w}_{max} - \mathbf{w}_{min}) \frac{T}{2T - T_s} \leq \boldsymbol{\psi}(k) < \mathbf{0}$, then the condition that must be satisfied is (16). Considering also that $T < T_s < 2T$, then $\boldsymbol{\psi}(k) < \frac{T - T_s}{T} \boldsymbol{\psi}(k)$. Thus, from (10), then (17) and (18) hold, which imply (16).

$$\begin{aligned}
\boldsymbol{\psi}(k+1) &= \frac{T-T_s}{T}\boldsymbol{\psi}(k) + \boldsymbol{\Omega C}(\mathbf{w}(k) - \mathbf{w}(k-1)), \\
&> \boldsymbol{\Omega C}(\mathbf{w}(k) - \mathbf{w}(k-1)) \geq -\boldsymbol{\Omega C}(\mathbf{w}_{max} - \mathbf{w}_{min}), \\
&> -\frac{T}{2T-T_s}\boldsymbol{\Omega C}(\mathbf{w}_{max} - \mathbf{w}_{min}), \tag{17}
\end{aligned}$$

$$\begin{aligned}
\boldsymbol{\psi}(k+1) &= \frac{T-T_s}{T}\boldsymbol{\psi}(k) + \boldsymbol{\Omega C}(\mathbf{w}(k) - \mathbf{w}(k-1)), \\
&\leq -\frac{T-T_s}{T}\boldsymbol{\Omega C}(\mathbf{w}_{max} - \mathbf{w}_{min})\frac{T}{2T-T_s} + \boldsymbol{\Omega C}(\mathbf{w}(k) - \mathbf{w}(k-1)), \\
&\leq -\frac{T-T_s}{2T-T_s}\boldsymbol{\Omega C}(\mathbf{w}_{max} - \mathbf{w}_{min}) + \boldsymbol{\Omega C}(\mathbf{w}_{max} - \mathbf{w}_{min}) \\
&= \boldsymbol{\Omega C}(\mathbf{w}_{max} - \mathbf{w}_{min})\frac{T}{2T-T_s}. \tag{18}
\end{aligned}$$

Case 4: If $\boldsymbol{\psi}(k) < -\boldsymbol{\Omega C}(\mathbf{w}_{max} - \mathbf{w}_{min})\frac{T}{2T-T_s} \leq \mathbf{0}$, then from (10),

$$\begin{aligned}
\boldsymbol{\psi}(k+1) - \boldsymbol{\psi}(k) &= \frac{-T_s}{T}\boldsymbol{\psi}(k) + \boldsymbol{\Omega C}(\mathbf{w}(k) - \mathbf{w}(k-1)), \\
&> \frac{T_s}{2T-T_s}\boldsymbol{\Omega C}(\mathbf{w}_{max} - \mathbf{w}_{min}) + \boldsymbol{\Omega C}(\mathbf{w}(k) - \mathbf{w}(k-1)), \\
&\geq \frac{T_s}{2T-T_s}\boldsymbol{\Omega C}(\mathbf{w}_{max} - \mathbf{w}_{min}) - \boldsymbol{\Omega C}(\mathbf{w}_{max} - \mathbf{w}_{min}), \\
&= \frac{2(T_s - T)}{2T-T_s}\boldsymbol{\Omega C}(\mathbf{w}_{max} - \mathbf{w}_{min}) > \mathbf{0}, \tag{19}
\end{aligned}$$

$$\begin{aligned}
\boldsymbol{\psi}(k+1) + \boldsymbol{\psi}(k) &= \frac{2T-T_s}{T}\boldsymbol{\psi}(k) + \boldsymbol{\Omega C}(\mathbf{w}(k) - \mathbf{w}(k-1)), \\
&< -\frac{2T-T_s}{T} \times \frac{T}{2T-T_s}\boldsymbol{\Omega C}(\mathbf{w}_{max} - \mathbf{w}_{min}) \\
&\quad + \boldsymbol{\Omega C}(\mathbf{w}(k) - \mathbf{w}(k-1)), \\
&= -\boldsymbol{\Omega C}(\mathbf{w}_{max} - \mathbf{w}_{min}) + \boldsymbol{\Omega C}(\mathbf{w}(k) - \mathbf{w}(k-1)) < \mathbf{0}. \tag{20}
\end{aligned}$$

From (19) and (20) it is concluded that $\boldsymbol{\psi}^2(k+1) < \boldsymbol{\psi}^2(k)$. \square

4 Experiments and Results

This section presents results of the proposed controller in a Continuous Stirred Tank Reactor (CSTR), a process which is very common in chemical and petrochemical plants. In the process, a single irreversible exothermic reaction is assumed to occur in the reactor. The dynamic model of a CSTR for an exothermic irreversible

reaction was described in [19]. The objective is to control the reactor temperature $T_c(t)$ asymptotically by manipulating of the coolant flow rate $q_c(t)$ while the CSTR plant is exposed to external disturbances. The experiments will be focused on a linearized model of the CSTR at a steady operating point of $T_c = 394$ [K] and $C_A = 0.265$ [mol/l]. The model is discretized using a forward differences (Euler) method and the sampling time $T_s = 0.15$ [min], and is given in terms of perturbation variables as follows:

$$\mathbf{x}(k+1) = \begin{bmatrix} 0.7514 & -0.0014 \\ 0.9864 & 0.0627 \end{bmatrix} \mathbf{x}(k) + \begin{bmatrix} 0 \\ -0.912 \end{bmatrix} u(k) + \mathbf{w}(k), \quad (21a)$$

$$y(k) = \begin{bmatrix} 0 & 1 \end{bmatrix} \mathbf{x}(k). \quad (21b)$$

where $\mathbf{x}(k) = [x_1(k), x_2(k)]^T = [C_A(k), T_c(k)]^T$ is vector of the reactant concentration and the reactor temperature; $\mathbf{u}(k) = u(k) = q_c(k)$ represents the coolant flow rate; $\mathbf{w}(k) = [w_1(k), w_2(k)]^T$ represents a random disturbance uniformly distributed inside the rectangle defined by the following constraints on the admissible disturbance: $-[0.05, 0.25]^T \leq [w_1(k), w_2(k)]^T \leq [0.05, 0.25]^T$. For the RDSCT control scheme, $K_p = 1$, $K_I = 0.145$, $T = 0.084$ [min], and $T_s = 0.15$ [min] were chosen. Figure 1 presents the closed-loop simulation results obtained by the proposed RDSCTC, and a standard discrete-time sliding mode controller (SDSMC), starting from an initial state of $\mathbf{x}_A = [-0.12, 4.2]^T$, while the controlled variable setpoint $z_d(t)$ is changed during the simulation as follows:

$$z_d(t) = \begin{cases} 1, & 0 < t \leq 12 \text{ [h]}, \\ -1, & 12 \text{ [h]} < t \leq 24 \text{ [h]}, \\ 1, & 24 \text{ [h]} < t \leq 37.5 \text{ [h]}. \end{cases} \quad (22)$$

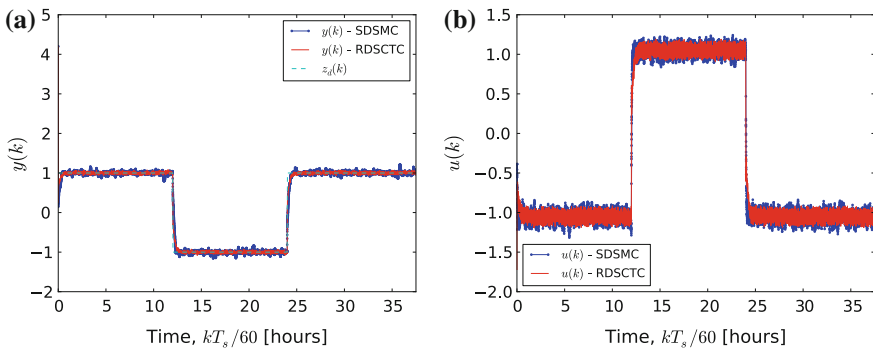


Fig. 1 **a** Closed loop simulation results of output $y(k)$ using the proposed RDSCTC, and SDSMC [20] on the CSTR plant; and **b** the respective applied command signals. The reference signal is given by (22)

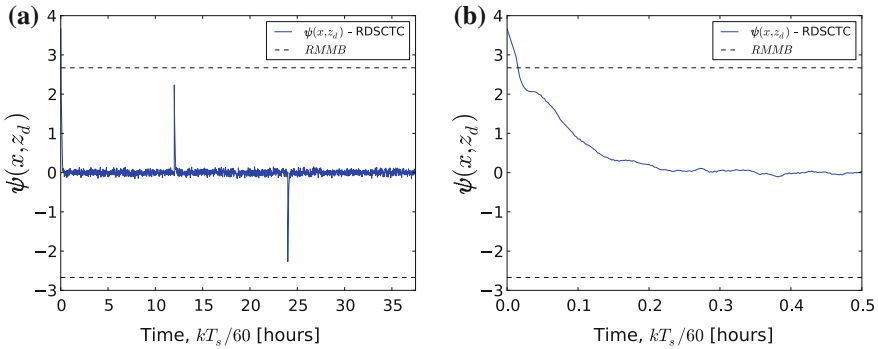


Fig. 2 **a** Illustration of the $\psi(k)$ functions with initial state of \mathbf{x}_A for the reference signal given by (22); and **b** Magnified plot of figure **a** for time period between 0 and 0.5 [h]

For the typical SDSMC [20], $\eta = 0.1$, $q = 0.95$, and $g = 0.8$ were chosen. The presented results are the best results corresponding to the best tuning of the controllers’ parameters in both the SDSMC and RDSCTC. As can be seen, comparing with SDSMC, the RDSCTC shows a better robust performance to reduce the disturbance effect. The result of the $\psi(k)$ function is depicted in Fig. 2. A value of $M_\psi = 2.6717$ was obtained from (8). As it can be seen in Fig. 2b, after the trajectory has entered the *RMMB*, then with every successive time step, the trajectory remains confined within the *RMMB*.

As another example, consider the reference as a constant signal $z_d(t) = 1$, the same bounded disturbance as was defined in the previous example, for all the $0 [h] < t \leq 37.5 [h]$. Also, in order to demonstrate results of the performance of the RDSCTC in a plant with changes, consider an internal process disturbance is applied as a simultaneous change on the feed concentration C_{A0} from 1 [mol/l] to 0.90 [mol/l], and a change of the inlet coolant temperature T_{c0} from 350 [K] to 345 [K], where both

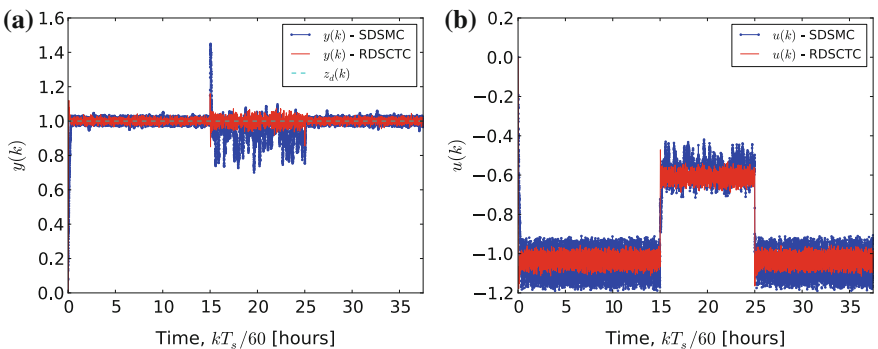


Fig. 3 **a** Closed loop simulation results of output $y(k)$ using the RDSCTC, and SDSMC on the CSTR plant with initial state of zero; and **b** the respective applied command signals

changes are in effect during $15 \text{ [h]} < t \leq 25 \text{ [h]}$. Figure 3 presents the closed-loop simulation results obtained by the proposed RDSCTC and result with SDSMC. The results show that the RDSCTC can react a fast robust response against this internal change in the plant model. Comparing with SDSMC a better setpoints tracking was obtained, when parameters changes occurred inside the CSTR plant.

5 Conclusion

An innovative robust control scheme based on the synergetic control theory (SCT) technique was presented in this paper. The proposed controller inherits robustness properties from the SC theory. The new controller constructed by the SCT technique, can be used to steer the state from any initial state to desired setpoints. The proposed discrete-time SCT control framework uses one-step delayed estimation for disturbance estimation. The closed-loop stability has been shown to be guaranteed. The robust performance of the proposed controller was demonstrated by simulations on a continuous stirred tank reactor. Future work could be to represent the *RMMB* more directly as a function of the error.

Acknowledgments Saied Rastegar was supported by Fundação para a Ciência e a Tecnologia (FCT) under grant SFRH/BD/89186/2012. The authors acknowledge the support of FCT project UID/EEA/00048/2013. A. Iratni was supported by the European Commission in the framework of the Erasmus Mundus—*Al Idrisi* II programme.

References

1. Shamma, J.S.: An overview of lpv systems. In: Mohammadpour, J., Scherer, C.W. (eds.) *Control of Linear Parameter Varying Systems with Applications*, pp. 3–26. Springer, New York, NY, USA (2012)
2. Bünte, T., Odenthal, D., Aksun-Güvenç, B., Güvenç, L.: Robust vehicle steering control design based on the disturbance observer. *Ann. Rev. Control* **26**(1), 139–149 (2002)
3. Ugrinovskii, V.A.: Robust controllability of linear stochastic uncertain systems. *Automatica* **41**(5), 807–813 (2005)
4. Léchappé, V., Moulay, E., Plestan, F., Glumineau, A., Chriette, A.: New predictive scheme for the control of lti systems with input delay and unknown disturbances. *Automatica* **52**, 179–184 (2015)
5. Fiter, C., Hetel, L., Perruquetti, W., Richard, J.P.: A robust stability framework for LTI systems with time-varying sampling. *Automatica* **54**, 56–64 (2015)
6. Ginoya, D., Shendge, P.D., Phadke, S.B.: Sliding mode control for mismatched uncertain systems using an extended disturbance observer. *IEEE Trans. Ind. Electron.* **61**(4), 1983–1992 (2014)
7. Khandekar, A.A., Patre, B.M.: Discrete sliding mode control for robust tracking of time-delay systems. *Syst. Sci. Control Eng. Open Access J.* **2**(1), 457–464 (2014)
8. Edwards, C., Spurgeon, S.: *Sliding Mode Control: Theory and Applications*. CRC Press (1998)
9. Fridman, L.M.: Chattering analysis in sliding mode systems with inertial sensors. *Int. J. Control* **76**(9–10), 906–912 (2003)

10. Romdhane, N.M.B., Damak, T.: Higher order sliding mode control of uncertain robot manipulators. In: Azar, A.T., Zhu, Q. (eds.) *Advances and Applications in Sliding Mode Control Systems*, pp. 327–352. Springer, Cham, Switzerland (2015)
11. Santi, E., Monti, A., Li, D., Proddatur, K., Dougal, R.A.: Synergetic control for DC-DC boost converter: implementation options. *IEEE Trans. Ind. Appl.* **39**(6), 1803–1813 (2003)
12. Santi, E., Monti, A., Li, D., Proddatur, K., Dougal, R.A.: Synergetic control for power electronics applications: a comparison with the sliding mode approach. *J. Circ. Syst. Comput.* **13**(04), 737–760, Aug 2004
13. Jiang, Z.: Design of a nonlinear power system stabilizer using synergetic control theory. *Electric Power Syst. Res.* **79**(6), 855–862 (2009)
14. Bai, Q., Niu, D., Bai, J.: Complex networks economy systems engineering in general synergetic structure. *Syst. Eng. Proc.* **4**, 252–258 (2012)
15. Sinha, N.K., Rózsa, P.: Some canonical forms for linear multivariable systems. *Int. J. Control* **23**(6), 865–883 (1976)
16. Antsaklis, P.J., Michel, A.N.: *A Linear Systems Primer*. Birkhäuser (2007)
17. Täth, R.: *Modeling and Identification of Linear Parameter-Varying Systems*. Springer, Berlin, Germany (2010)
18. Xu, Q., Li, Y.: Micro-/nanopositioning using model predictive output integral discrete sliding mode control. *IEEE Trans. Ind. Electron.* **59**(2), 1161–1170 (2012)
19. Morningred, J.D., Paden, B.E., Seborg, D.E., Mellichamp, D.A.: An adaptive nonlinear predictive controller. *Chem. Eng. Sci.* **47**(4), 755–762 (1992)
20. Eun, Y., Kim, J.H., Kim, K., Cho, D.I.: Discrete-time variable structure controller with a decoupled disturbance compensator and its application to a CNC servomechanism. *IEEE Trans. Control Syst. Technol.* **7**(4), 414–423, Jul 1999

Part II
Optimal and Predictive Control

Drug Administration Design for Cancer Gompertz Model Based on the Lyapunov Method

B. Andrade Costa and J. M. Lemos

Abstract This article addresses the design of therapeutic procedures for cancer using a control based on the Gompertz model, that describes the nonlinear dynamics of tumor growth. The aim is to reduce the tumor size according to a decreasing target reference. The approach presented on this work uses a control Lyapunov function and yields an adaptive PI strategy that results from the exact linearization. It is concluded that the closed-loop system is globally asymptotically stable and is robust with respect to the presence of model parameter uncertainty.

Keywords Cancer modeling · Gompertz model · Exact linearization · Adaptive control · Lyapunov stability analysis

1 Introduction

During the process of drug administration to control the progression of tumor cells it is necessary to adjust the drug amount in order to kill the tumor cells while, at the same time, avoiding the side-effects due to drug toxicity. The tumor dynamics and the effect of drug toxicity change from patient to patient suggesting the use of adaptive methods.

Several models have been proposed to represent different tumor dynamics [2, 4], the Gompertz model and the Logistic model being the ones that are most frequently used. Early studies [3] already show that the log growth rate embedded in the Gompertz model yields better fit to tumor growth data than other models such as the logistic model. These models do not take in account the drug pharmacokinetics (PK). The

This work was supported by Fundação para a Ciência e Tecnologia under the research project PTDC/EM-SIS/0642/2014 and the program UID/CEC/50021/2013.

B.A. Costa (✉) · J.M. Lemos
INESC-ID/IST, University of Lisbon, Rua Alves Redol, 9, 1000-029 Lisbon, Portugal
e-mail: bac@inesc-id.pt

J.M. Lemos
e-mail: jlml@inesc-id.pt

Gompertz and the Logistic models are nonlinear models where the state growth rate is a nonlinear function of the state and of the manipulated input. Although studies such as the ones referred in [5] provide a means to design a time profile of drug administration that optimizes in a systematic way the compromise between tumor cells killing and drug toxicity they do not consider feedback treatments that yield an asymptotically stable closed-loop. The use of a control Lyapunov function that is defined jointly for output regulation and parameter estimation allows to ensure global asymptotic stability. In this framework, in [1] a model reference adaptive controller is proposed. In [4] an adaptive controller for the chemotherapy process is presented.

The work described in this article also relies on an approach that uses Lyapunov stability theorems to obtain an adaptive nonlinear controllers, but has the following distinctive features. First a reference that represents the desired tumor size is introduced driving it close to zero. The rate at which this reference vanishes is an important knob that allows to manipulate the peak of drug delivery. Another major difference is the use of feedback linearization. In a first stage, the structure and the parameter values of the Gompertz model are assumed to be known. By exploring the structure of the model and by imposing a reference profile for the tumor growth, that decays exponentially, a nonlinear control law is designed using exact linearisation to cancel the effects of nonlinear terms. By analysing the structure of the exact linearization control law, a nonlinear adaptive PI controller with one adaptive element is proposed. It is assumed that bounds on the parameter values of the model are known. The global stability of the closed-loop dynamics is demonstrated and, as an important conclusion, the proposed adaptive PI controller is shown to be robust in the presence of parameter uncertainty. It is possible to explore the structure of the Gompertz model by applying the $\log()$ transformation to yield a new state representation that results in a linear model. From this point, a PI controller can be applied. However due to lack of space this approach is not presented.

2 Mathematical Modeling

From observed clinical data there is a general consensus that a tumor, in its initial stage has an exponential growth that slows and approaches a plateau value.

The tumor growth described by the Gompertz model is given by

$$\frac{dx(t)}{dt} = \alpha x(t) \log\left(\frac{m}{x(t)}\right) - \beta x(t) u(t), \quad (1)$$

where $x(t) \geq 0$ represents the total tumor volume, or the number of tumor cells ($1mm^3 \approx 10^5$ cells), $\alpha > 0$ is a parameter, m is a parameter that represents the plateau value, $u(t)$ quantifies the amount of therapeutic drug and $\beta > 0$ is a parameter that quantifies the intensity of drug.

Fig. 1 Illustration of the temporal behaviour of tumors that are described by the Gompertz model with the parameters shown on Table 1

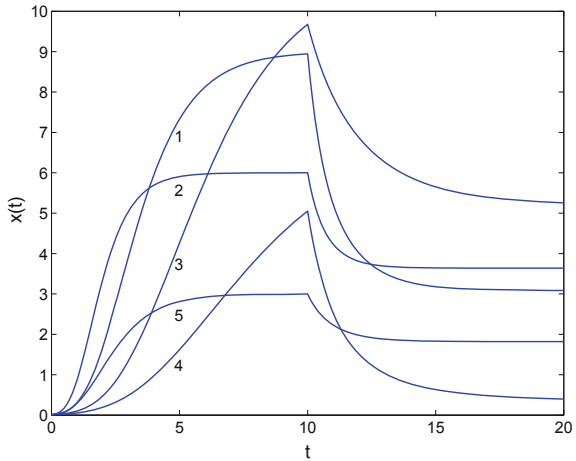


Table 1 Set of parameters for the Gompertz model to illustrate parameter uncertainty

Model	m	α	β
1	9	0.7	0.5
2	6	1.2	0.4
3	11	0.4	0.2
4	7	0.3	0.6
5	3	0.9	0.3

The models has two equilibrium points, one unstable ($x = 0$), and the other stable ($x = m$). The results obtained for the Gompertz model can be extended to the logistic model.

Figure 1 illustrates the temporal behaviour of the Gompertz model with different values for the parameters m , α and β presented in Table 1. Each time response is labeled with the model number presented in the first column of the Table 1. These parameter values are hypothetical and used to illustrate the effect of model parameters. During the first 10 time units, the therapeutic regimen is not applied ($u(t) = 0$) and the tumor increases. After time $t = 10$ the manipulated variable $u(t)$ is set to $u(t) = 1.5$. The response of the tumors to the drug is not identical and thus it can be concluded that personalized therapeutic must be used.

3 Design With Full Model Knowledge

The aim is to design a drug administration profile that decreases the tumor size but at the same time minimizes the undesired drug side-effects. To address this problem a reference profile for tumor size is designed that takes in account the objective to

decrease the tumor size and the undesired side-effects that are associated with the drug toxicity. The reference profile is represented by $r(t)$, and decays along time t to a small final value r^* that represents a tumor size that does not cause a life threat condition to the patient. In the present work the reference profile $r(t)$ is selected as the solution of

$$\frac{dr(t)}{dt} = -\theta r(t) + \theta r^*, \quad (2)$$

where $\theta > 0$ is an adjustable parameter.

The control design is formulated by defining the tracking error $e(t)$ as

$$e(t) = x(t) - r(t), \quad (3)$$

where $x(t)$ represents the tumor size. The error dynamics is

$$\frac{de(t)}{dt} = x(t)\alpha \log\left(\frac{m}{x(t)}\right) - \beta x(t)u(t) + \theta e_r(t) \quad (4)$$

where $e_r(t) = r(t) - r^*$. By selecting the $\frac{de(t)}{dt} = -\gamma e(t)$, where $\gamma > 0$ is an adjustable parameter, the error $e(t)$ decays exponentially to zero. To obtain this result, $u(t)$ is selected as

$$u(t) = \frac{\gamma}{\beta} \frac{e(t)}{x(t)} + \frac{\theta}{\beta} \frac{e_r(t)}{x(t)} + \frac{\alpha}{\beta} \log\left(\frac{m}{x(t)}\right). \quad (5)$$

This nonlinear control law implements the exact feedback linearization strategy, and as such, it cancels the nonlinear terms on the right side of equation (4). The application of this nonlinear control law implies a perfect knowledge of the parameter values of the model α , β , m .

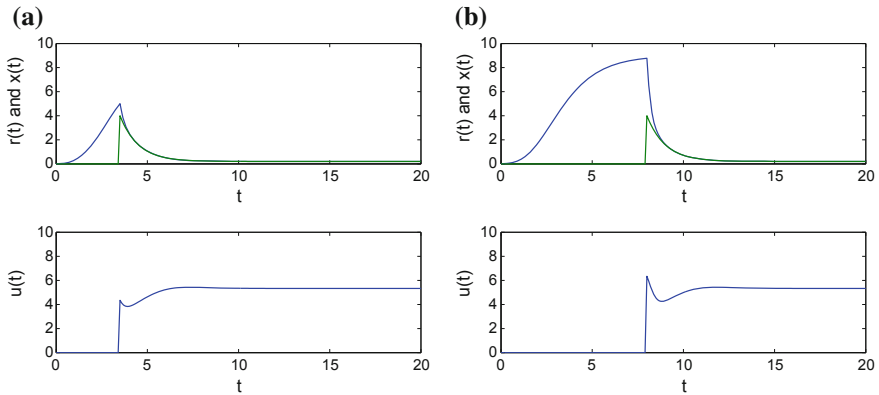


Fig. 2 Closed-loop control using the exact linearization controller and the Gompertz model 1 from Table 1. **a** Closed loop control $t \geq 3.5$. **b** Control is applied later, $t \geq 8$

Figure 2a, b illustrate the results obtained with the Gompertz model ($m = 9$, $\alpha = 0.7$, $b = 0.5$ and $x(0) = 0.01$) when the controller is applied at two different time instants corresponding to two different tumor level stages.

4 Adaptive PI Controller

Under the assumption that bounds on the model parameters are known, $\alpha_{min} \leq \alpha \leq \alpha_{max}$, $\beta_{min} \leq \beta \leq \beta_{max}$ and $m_{min} \leq m \leq m_{max}$ a modification of the above control law is proposed formed by

$$u(t) = K_p \frac{e(t)}{x(t)} + K_i s(t); \quad \text{with} \quad \frac{ds(t)}{dt} = w(t)e(t), \tag{6}$$

where $s(t)$ represents an integral action that is computed from $e(t)$ using the weighting function $w(t)$. The controller gains $K_p > 0$ and $K_i > 0$ substitute the constant gains $\frac{\gamma}{\beta}$ and $\frac{\alpha}{\beta}$ in Eq. (5). The nonlinear integral action $s(t)$ is adapted to compensate the term $\log(\frac{m}{x(t)})$, in particular during the steady state, when $x(t) \approx r(t) = r^*$, corresponding to the value $\log(\frac{m}{r^*})$. The function $w(t)$ is selected based on the application of the Lyapunov stability method, that yields $w(t) = x(t)$. To simplify the control law the term on $e_r(t)$ is not included.

The closed-loop dynamics with the proposed controller is described by

$$\begin{aligned} \frac{de(t)}{dt} &= -\beta K_p e(t) + \theta e_r(t) + x(t) [\alpha \log(\frac{m}{x(t)}) - \beta K_i s(t)] \\ \frac{ds(t)}{dt} &= x(t)e(t) \\ \frac{de_r(t)}{dt} &= -\theta e_r(t), \end{aligned}$$

where $e_r(t) = r(t) - r^*$, and it has the equilibrium point

$$e(t) = 0; \quad s(t) = s^* = \frac{\alpha}{\beta K_i} \log(\frac{m}{r^*}); \quad r(t) = r^* .$$

The error dynamics, defined in relation to the equilibrium point, is given by

$$\begin{aligned} \frac{de(t)}{dt} &= -\beta K_p e(t) + \theta e_r(t) + x(t) [-\beta K_i s(t) + \alpha, \log(\frac{r^*}{x(t)})], \\ \frac{de_s(t)}{dt} &= x(t)e(t), \\ \frac{de_r(t)}{dt} &= -\theta e_r(t), \end{aligned}$$

where $e_s(t) = s(t) - s^*$. Note that from the definition of $e(t)$, $x(t) = e(t) + r(t)$; $x(t) = e(t) + r(t) - r^* + r^*$; that yields $x(t) = e(t) + e_r(t) + r^*$.

4.1 Stability Analysis

The stability of the closed-loop is now analysed using the Lyapunov stability analysis, where the Lyapunov candidate function is selected as

$$V(t) = \frac{1}{2}e^2(t) + \frac{1}{2}\beta K_i e_s^2(t) + \frac{1}{2}\lambda e_r^2(t), \quad (7)$$

with $\lambda > 0$.

Computing the time derivative of $V(t)$ and substituting $\frac{de(t)}{dt}$, $\frac{de_s(t)}{dt}$ and $\frac{de_r(t)}{dt}$ yields

$$\begin{aligned} \frac{dV(t)}{dt} = & -\beta K_p e^2(t) - \alpha e(t)x(t) \log\left(\frac{x(t)}{r^*}\right) + \\ & + \theta e(t)e_r(t) - \lambda \theta e_r^2(t), \end{aligned} \quad (8)$$

that, after completing the square terms, can be rewritten as

$$\frac{dV(t)}{dt} = -p_1 e^2(t) - p_2(e(t), e_r(t)) - p_3(e(t), e_r(t)) \quad (9)$$

where

$$p_1 = \beta K_p - \frac{\theta}{2}, \quad (10)$$

$$p_2(e(t), e_r(t)) = \alpha e(t)x(t) \log\left(\frac{x(t)}{r^*}\right), \quad (11)$$

$$p_3(e(t), e_r(t)) = \frac{\theta}{2}[(e(t) - e_r^2(t))^2 + (\lambda - \frac{1}{2})e_r^2(t)]. \quad (12)$$

Proposition: The closed-loop dynamics is asymptotically stable for $x(t) > 0$, if the controller parameters fulfill the conditions $K_p > \frac{1}{\beta} \frac{\theta}{2}$, $K_i > 0$ and $\theta > 0$. The controller parameters do not depend on the model parameter m and α , and thus the controller is robust to model parameter uncertainty. It is remarked that for $x(t) \leq 0$ the dynamic model does not have a real solution because of the term $\log\left(\frac{m}{x(t)}\right)$, and thus $x(t) > 0$.

Proof: A sufficient condition that implies $\frac{V(t)}{dt} \leq 0$, is obtained with $p_1 > 0$ and $p_2(e(t), e_r(t)) + p_3(e(t), e_r(t)) > 0$. From the condition on p_1 results $K_p > \frac{1}{\beta} \frac{\theta}{2}$. The function $p_3(e(t), e_r(t))$ is non-negative and has the minimum at $e(t) = e_r(t)$. Inspecting $p_2(e(t), e_r(t))$, where $x(t) = e(t) + e_r(t) + r^*$ it is concluded that

$$p_2((e(t), e_r(t))) = \begin{cases} \geq 0 & e(t) \geq 0 \\ < 0 & -e_r(t) < e(t) < 0 \\ \geq 0 & -e_r(t) - r^* < e(t) < -e_r(t) \end{cases} \tag{13}$$

i.e., p_2 is negative in the interval $-e_r(t) < e(t) < 0$, where it has a minimum (that is represented by $-p_{2m} < 0$) and it is positive outside this interval. The minimum $-p_{2m}$ can be compensated with the function $p_3(e(t), e_r(t))$ such that $p_2(e(t), e_r(t)) + p_3(e(t), e_r(t)) > 0$.

In the interval $-e_r(t) < e(t) < 0$, the function $p_3(e(t), e_r(t))$ has the minimum at $e(t) = 0$, that is equal to $\frac{\theta}{2}(\lambda + \frac{\theta}{2})e_r^2(t)$.

In order to obtain $-p_{2m} + \frac{\theta}{2}(\lambda + \frac{\theta}{2})e_r^2(t) > 0$ at time t , it is necessary that

$$\lambda \geq \frac{2}{\theta} \frac{\Delta(e_r(t))}{e_r^2(t)} - \frac{1}{2}. \tag{14}$$

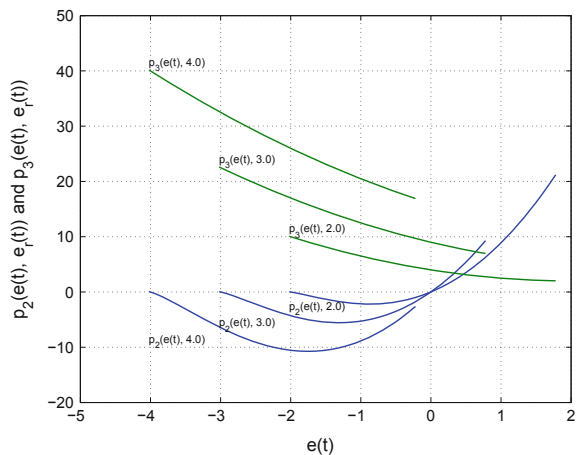
But, because $\frac{de_r(t)}{dt} = -\theta e_r(t)$, the above relation can be extended to $t = 0$, where $e_r(0) > 0$ is the maximum value. The parameter λ can now be selected according to

$$\lambda > \frac{2}{\theta} \frac{\Delta(e_r(0))}{e_r^2(0)} - \frac{1}{2}, \tag{15}$$

and it can be concluded that $p_2(e(t), e_r(t)) + p_3(e(t), e_r(t)) > 0$.

Figure 3 illustrates the behaviour of $p_2(e(t), e_r(t))$, and $p_3(e(t), e_r(t))$ in the interval $-e_r(t) < e(t) < 0$. As $e_r(t)$ tends to zero, the interval $-e_r(t) < e(t) < 0$ shrinks to zero and the minimum of $p_2(e(t), e_r(t))$ tends to zero.

Fig. 3 Illustration of functions $p_2(e(t), e_r(t))$ and $p_3(e(t), e_r(t))$ in the interval $-e_r(t) < e(t) < 0$ for three values of $e_r(t)$, 2, 3 and 4. The condition $p_2(e(t), e_r(t)) + p_3(e(t), e_r(t)) > 0$ is fulfilled by choosing the parameter $\lambda > 0$.



It is remarked that λ does not enter in the control law, being used just to demonstrate that $\frac{V(t)}{dt} < 0$ for $e(t) \neq 0$ and $e_r(t) \neq 0$.

In the particular case when $e(t) = 0$, $e_r(t) = 0$, and $e_s(t) \neq 0$, it follows that $\frac{V(t)}{dt} = 0$. But the state set defined by $e(t) = 0$, $e_r(t) = 0$ and $e_s(t) \neq 0$ does not correspond to equilibrium states of the closed-loop system. The time derivative of $[e(t) \ e_s(t) \ e_r(t)]'$ is not null for these states and the system will evolve to a state where $e(t) \neq 0$ that implies $\frac{V(t)}{dt} < 0$. In the limit, the system converges to the equilibrium point $[0 \ 0 \ 0]'$ (LaSalle's invariant principle [6]).

Thus, it is concluded that the closed-system is asymptotically stable for $x(t) > 0$ and the controller parameters do not depend on the model parameters m and α .

4.2 Model Parameter Uncertainty

Considering the bounds on β and using the previous results, the controller gains must be selected according to

$$0 < \beta_{\min} K_p - \frac{\theta}{2} \leq \beta K_p - \frac{\theta}{2} \leq \beta_{\max} K_p - \frac{\theta}{2}$$

that yields,

$$K_p > \frac{1}{\beta_{\min}} \frac{\theta}{2}; \text{ and } K_i > 0. \quad (16)$$

4.3 Local Approximation

From the results obtained, there is no guideline on how to select the value for the controller parameter K_i . To overcome this issue, the local behaviour of the closed-loop system is considered. In the case that $r(t) = r^*$ and $|e(t)| \ll r^*$ the closed-loop dynamics is simplified

$$\begin{aligned} \frac{de(t)}{dt} &= -\beta K_p e(t) + (e(t) + r^*)[-\beta K_i s(t) + \alpha \log\left(\frac{r^*}{e(t) + r^*}\right)] \\ \frac{de_s(t)}{dt} &= (e(t) + r^*)e(t) \end{aligned}$$

and can be approximated to

$$\begin{aligned} \frac{de(t)}{dt} &= -\beta K_p e(t) - r^* \beta K_i s(t) \\ \frac{de_s(t)}{dt} &= r^* e(t). \end{aligned}$$

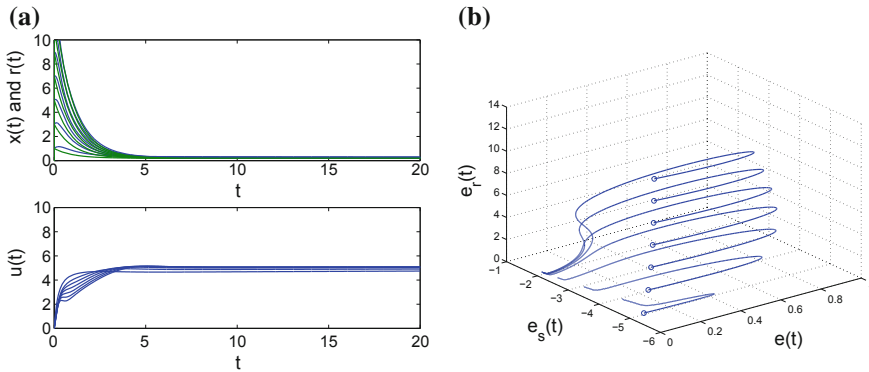


Fig. 4 Closed-loop control using the adaptive PI controller applied to model 1 with $K_p = 10$ and $K_i = 1$, for several initial tumor sizes, $\{1, 3, 5, 7, 9, 11, 13\}$ **a** Tracking the reference. **b** Phase plane of the $(e(t), e_s(t))$

The proposed controller becomes a standard PI controller $u(t) = (K_p/r^*)e(t) + (K_i r^*) \int e(\tau)d\tau$ and the closed-loop poles are computed from

$$p_{1,2} = -\frac{\beta K_p}{2} \left(1 \pm \sqrt{1 - \frac{4K_i(r^*)^2}{\beta K_p^2}} \right)$$

that can be used to select the value of K_i as a function of K_p .

4.4 Simulation Results

Figure 4a shows 7 simulations with the model (1) and with 7 initial tumor sizes $\{1, 3, 5, 7, 9, 11, 13\}$. The tumor size approaches the reference defined by the parameters $\theta = 1$ and the target value $r^* = 0.2$. The controller gains are $K_p = 10$ and $K_i = 1$. The initial value of the reference $r(0)$ is chosen to be near to $x(0)$. This avoids a sharp transition on $u(0)$. As $x(0)$ increases, the control signal tends to show a change on its behaviour, but in all the cases the tumor size follows the reference $r(t)$.

The behaviour of $e(t)$ and $e_s(t)$, for the adaptive controller corresponding to the results shown in the Fig. 4a, are presented in the form of the phase plane in the Fig. 4b. The starting points are marked with the symbol 'o', that are near $e(0) \approx 0$. As the reference changes there is an initial increase in the error $e(t)$ but $e_s(t)$ decreases. All trajectories converge to the equilibrium point $(0, 0)$. Note that the tracking error can be decreased by changing the controller gains.

For this tumor model, the stable equilibrium point is $x(t) = m = 9$ and the maximum value of $e(t)$ tends to decrease if the initial value of $x(0) > m$. Because in the

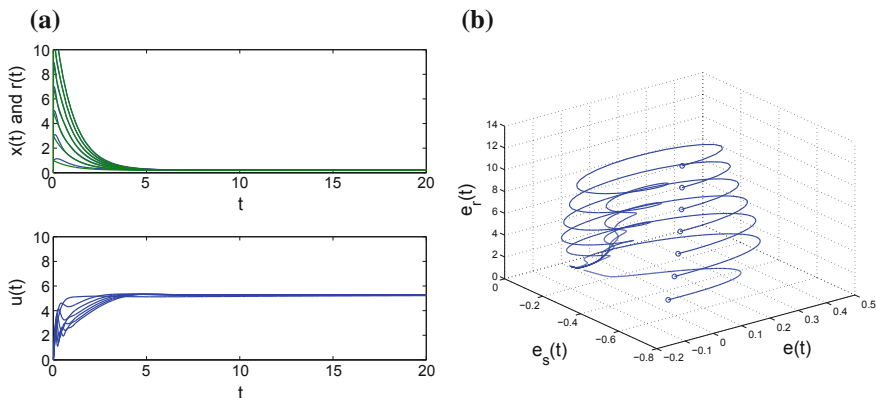


Fig. 5 Closed-loop control using the adaptive PI controller applied to model 1 with $K_p = 10$ and $K_i = 10$, for several initial tumor sizes, as in the Fig. 4a. **a** Tracking the reference. **b** Phase plane of the $(e(t), e_s(t))$

early working phase of the controller the reference decreases more rapidly than $x(t)$, then $e(t)$ is positive and increases.

The controller gain K_i is increased to $K_i = 10$ to obtain a faster decrease of the tracking error. The results are shown in Fig. 5a, b that illustrate the behaviour of the controller with $K_p = 10$ and $K_i = 10$ in the same conditions as the results shown in Fig. 4a, b. The control action of the controller can be adjusted/smoothed by changing the decay rate of the reference, that depends on the parameter θ . This is illustrate in the Fig. 6a where several references are specified using the parameter $\theta = \{0.2, 0.4, 0.6, 0.8, 1.0, 1.2, 1.4\}$ and the model starts with $x(0) = 7$ and is controlled with the adaptive controller ($K_p = 10, K_i = 10$). As the reference has a faster decay, the control action becomes stronger in order to decrease the tracking error $e(t)$.

Controller robustness in the presence of model parameter uncertainty is illustrated with the results shown in Fig. 6b. All models from Table 1 are controlled with the adaptive controller with $K_p = 10$ and $K_i = 10$. During the first 5 time units the models are in open loop and the controller is connect at $t = 5$, where the reference signal $r(5)$ is chosen to be equal to $x(5)$. In all the cases the tumor sizes evolve according with the reference used.

5 Conclusions

This article addresses the design of controllers for the Gompertz model that is used to describe the kinetic of tumors such in cancer diseases. The closed-loop stability is analysed using the Lyapunov stability method. It is concluded that the closed-

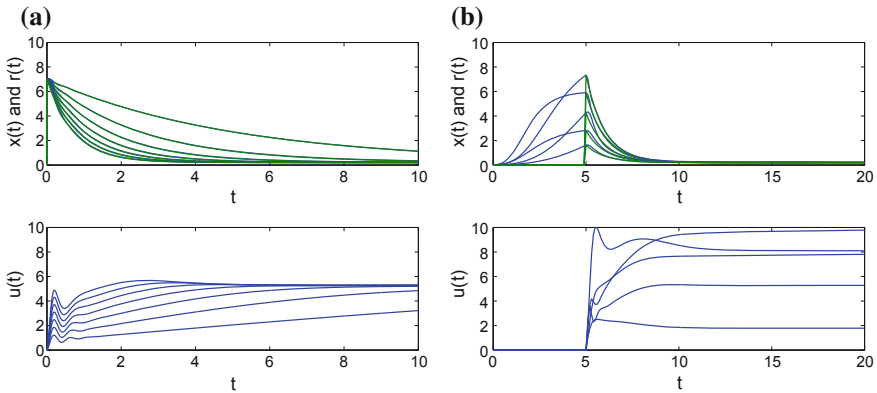


Fig. 6 Adaptive PI Controller with $K_p = 10$, $K_i = 10$. On the left, control behaviour as a function of reference parameter θ . As the reference has a faster decay (increasing the θ value) the control action becomes stronger to decrease the tracking error $e(t)$. On the right, closed-loop control of the Gompertz models of Table 1 with the adaptive PI controller applied after $t > 5$. All models are controlled and track the reference but need different steady state drug levels. **a** Control behaviour as a function of reference parameter θ . **b** Closed-loop control of the Gompertz models

loop system is global asymptotically stable and is robust to the presence of model parameter uncertainty.

References

1. Babaei, N., Salamci, M.U.: Personalized drug administration for cancer treatment using model reference adaptive control. *J. Theor. Biol.* **371**(0), 24–44 (2015). <http://www.sciencedirect.com/science/article/pii/S0022519315000557>
2. Benzekry, S., Lamont, C., Beheshti, A., Tracz, A., Ebos, J.M.L., Hlatky, L., Hahnfeldt, P.: Classical mathematical models for description and prediction of experimental tumor growth. *PLoS Comput. Biol.* **10**(8), e1003800 (08 2014)
3. Laird, A.K.: Dynamics of tumour growth. *Br. J. Cancer* **13**(3), 490–502 (1964)
4. Moradi, H., Sharifi, M., Vossoughi, G.: Adaptive robust control of cancer chemotherapy in the presence of parametric uncertainties: a comparison between three hypotheses. *Comput. Biol. Med.* **56**(0), 145–157 (2015). <http://www.sciencedirect.com/science/article/pii/S0010482514002996>
5. Shi, J., Alagoz, O., Erenay, F., Su, Q.: A survey of optimization models on cancer chemotherapy treatment planning. *Ann. Oper. Res.* **221**(1), 331–356 (2011). <http://dx.doi.org/10.1007/s10479-011-0869-4>
6. Slotine, J.J., Li, W.: *Applied Nonlinear Control*. Prentice-Hall, Englewood Cliffs, NJ (1991)

Sampled–Data Model Predictive Control Using Adaptive Time–Mesh Refinement Algorithms

Luís Tiago Paiva and Fernando A. C. C. Fontes

Abstract We address sampled–data nonlinear Model Predictive Control (MPC) schemes, in particular we address methods to efficiently and accurately solve the underlying continuous–time optimal control problems (OCP). In nonlinear OCPs, the number of discretization points is a major factor affecting the computational time. Also, the location of these points is a major factor affecting the accuracy of the solutions. We propose the use of an algorithm that iteratively finds the adequate time–mesh to satisfy some pre–defined error estimate on the obtained trajectories. The proposed adaptive time–mesh refinement algorithm provides local mesh resolution considering a time–dependent stopping criterion, enabling an higher accuracy in the initial parts of the receding horizon, which are more relevant to MPC. The results show the advantage of the proposed adaptive mesh strategy, which leads to results obtained approximately as fast as the ones given by a coarse equidistant–spaced mesh and as accurate as the ones given by a fine equidistant–spaced mesh.

Keywords Predictive control • Nonlinear systems • Optimal control • Real–time optimization • Continuous–time systems • Adaptive algorithms • Time–mesh refinement • Sampled–data systems

1 Introduction

This article discusses an adaptive time–mesh refinement algorithm to efficiently and accurately solve optimal control problems (OCP) and proposes its use in Model Predictive Control (MPC) schemes.

In the last decade, most of the MPC literature has been using discrete–time models (e.g. [12, 14, 27]). However, some of the earlier theoretical works on nonlinear MPC used continuous–time models (see [4, 9, 16, 17]). Recently, [13] proposed a multi–

L.T. Paiva (✉) · F.A.C.C. Fontes
Systec–ISR, Faculdade de Engenharia, Universidade do Porto, Porto, Portugal
e-mail: ltpaiva@fe.up.pt

F.A.C.C. Fontes
e-mail: faf@fe.up.pt

step MPC scheme, which despite still being a discrete-time scheme, has the optimization and feedback updates done at possibly different time instants. The authors show that such technique can lower the computational load while maintaining stability and quantifiable robust performance estimates. In [21], some of the authors that vastly contributed to spread the use of discrete-time MPC (c.f. [27]) show that a continuous-time method is significantly more efficient than standard discrete-time methods when solving constrained linear quadratic problems.

To implement MPC schemes, some form of discretization, or at least a finite parameterization, is eventually needed to solve the OCP. Nevertheless, there are several advantages in maintaining a continuous-time model until later stages. In addition to being able to obtain more accurate solution to OCPs faster, it might be essential in nonlinear systems that can rapidly change behavior in some short time intervals or even when there is a discontinuity at some critical instant (e.g. impulsive control [10, 23]). Also, path-following MPC strategies are more complex to implement in discrete-time than in sampled-data schemes (compare [24, 25] with [3, 28]).

We also argue that the time is ripe to start using continuous-time MPC, even in applications [8, 28]. Many theoretical questions of using sampled-data systems are well documented in the literature [5–7, 11, 15, 26] and there are now several ready available software packages to solve nonlinear OCP [18].

In OCP solvers using direct collocation methods, the control and the state are discretized in an appropriately chosen mesh of the time interval. Then, the continuous-time OCP is transcribed into a finite-dimensional nonlinear programming problem (NLP) which can be solved using widely available software packages [18]. Most frequently, in the discretization procedure, regular time meshes having equidistant spacing are used. However, in some cases, these meshes are not the most adequate to deal with nonlinear behaviours. One way to improve the accuracy of the results, while maintaining reasonable computational time and memory requirement, is to construct a mesh having different time steps. The best location for the smaller steps sizes is, in general, not known a priori, so the mesh is refined iteratively. In a mesh-refinement procedure the problem is solved, typically, in an initial coarse uniform mesh in order to capture the basic structure of the solution and of the error. Then, this initial mesh is repeatedly refined according to a chosen strategy until some stopping criterion is attained. Several mesh refinement methods employing direct collocation methods have been described in the recent years [1, 2, 22, 29].

In this paper, we adapt and apply to an MPC context an adaptive time-mesh refinement algorithm to solve nonlinear OCP [20]. The algorithm computes iteratively an adequate time-mesh that satisfies some pre-defined error estimates on the obtained trajectories. The refinement method used here (a) permits several levels of refinement, obtaining a multi-level time-mesh in a single iteration. (b) it also permits different refinement criteria – the relative error of the primal variables, the relative error of the dual variables or a combination of both; (c) it considers distinct criteria for refining the mesh and for stopping the refinement procedure – the refinement strategy can be driven by the information given by the dual variables and it can be stopped according to the information given by the primal variables. As described in [20], there are advantages in choosing the error of the adjoint multipliers as a refine-

ment criterion. To decrease the overall computational time, the solution computed in the previous iteration is used as a warm start in the next one, which proved to be of major importance to improve computational efficiency. This adaptive strategy leads to results with higher accuracy and yet with lower overall computational time, when compared to results obtained by meshes having equidistant spacing, as is the case when using discrete-time models from the beginning.

In MPC context, the prediction can be interpreted in the sense of planning. When we make plans for the future, we establish planning strategies with detail level depending on the prediction horizon. Combining this idea with the refinement strategy, we obtain an adaptive time-mesh refinement algorithm which generates meshes with higher concentration of node points in the beginning of the prediction horizon and less concentration of node points in the end of the same interval, enforcing the idea of having more nodes point where they are needed and keeping a low overall number of node points. This is an important issue, because we want to increase the accuracy of the solution without compromising CPU times.

2 The Adaptive Mesh Refinement Algorithm for Optimal Control Problems

Let us consider the optimal control problem:

$$\mathcal{P}(t_0, t_f) : \text{Minimise } \int_{t_0}^{t_f} L(t, \mathbf{x}(t), \mathbf{u}(t)) dt + G(\mathbf{x}(t_f)) \tag{1}$$

$$\text{subject to } \dot{\mathbf{x}}(t) = \mathbf{f}(t, \mathbf{x}(t), \mathbf{u}(t)) \quad \text{a.e. } t \in [t_0, t_f], \tag{2}$$

$$\mathbf{x}(t_0) = \mathbf{x}_0, \tag{3}$$

$$\mathbf{x}(t_f) \in \mathbb{X}_1 \subset \mathbb{R}^n, \tag{4}$$

$$\mathbf{x}(t) \in \mathbb{X} \subset \mathbb{R}^n \quad \text{a.e. } t \in [t_0, t_f], \tag{5}$$

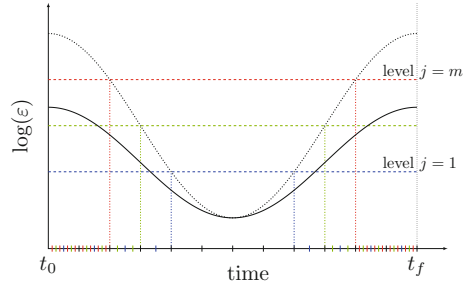
$$\mathbf{u}(t) \in \mathbb{U} \subset \mathbb{R}^m \quad \text{a.e. } t \in [t_0, t_f], \tag{6}$$

where $\mathbf{x} : [t_0, t_f] \rightarrow \mathbb{R}^n$ is the state, $\mathbf{u} : [t_0, t_f] \rightarrow \mathbb{R}^m$ is the control and $t \in [t_0, t_f]$ is time. The functions involved comprise the running cost $L : [t_0, t_f] \times \mathbb{R}^n \times \mathbb{R}^m \rightarrow \mathbb{R}$, the terminal cost $G : \mathbb{R}^n \rightarrow \mathbb{R}$ and the system dynamics $\mathbf{f} : [t_0, t_f] \times \mathbb{R}^n \times \mathbb{R}^m \rightarrow \mathbb{R}^n$.

As stated in [19, 20], the adaptive mesh refinement process starts by discretizing the time interval $[t_0, t_f]$ in a coarse mesh used to solve the NLP problem associated to the OCP in order to catch the main structure of the solution. According to some refinement criteria, the mesh is divided in $K \in \mathbb{N}$ mesh intervals

$$S_k = [\tau_{k-1}, \tau_k[, \quad k = 1, \dots, K,$$

Fig. 1 Illustration of the multi-level adaptive time-mesh refinement strategy



where (τ_0, \dots, τ_K) coincide with nodes. These mesh intervals S_k form a partition of the time interval while the mesh nodes have the property $\tau_0 < \tau_1 < \dots < \tau_K$.

The subintervals S_k that verify the refinement criteria are refined taking into account different levels of refinement in a single iteration, i.e., they are divided into smaller subintervals according to user-defined levels of refinement $\bar{\varepsilon} = [\varepsilon_1, \varepsilon_2, \dots, \varepsilon_m]$. The procedure is repeated until the stopping criterion is achieved. A subinterval $S_{k,j}$ is at the j^{th} level of refinement if

$$S_{k,j} = \{t \in S_k : \varepsilon(t) \in [\varepsilon_j, \varepsilon_{j+1}]\} \quad (7)$$

for $j = 1, \dots, m$. This procedure adds more node points to the subintervals in higher levels of refinement, corresponding to higher errors, and it adds less node points to those in lower refinement levels (Fig. 1). By defining several levels of refinement, we get a multi-level time-mesh in a single iteration.

3 The Model Predictive Control Framework

Consider a sampling step $\delta > 0$, the prediction horizon T and a sequence of sampling instants $\{t_i\}_{i \geq 0}$ with $t_{i+1} = t_i + \delta$. The sampled-data MPC algorithm follows the receding horizon strategy [9]:

1. Measure state of the plant \mathbf{x}_i ;
2. Determine $\bar{\mathbf{u}} : [t_i, t_i + T] \rightarrow \mathbb{R}^m$ solution to the OCP $\mathcal{P}(t_i, t_i + T)$ (1)-(6).
3. Apply the control $\mathbf{u}^*(t) := \bar{\mathbf{u}}(t)$ to the plant in the interval $t \in [t_i, t_i + \delta]$, disregarding the remaining control $\bar{\mathbf{u}}(t), t > t_i + \delta$;
4. Repeat this procedure for the next sampling time instant $t_i + \delta$.

We extend the adaptive time-mesh refinement algorithm described in [20] in order to allow different refinement levels according to some partition of the time domain. This extension is of relevance in the MPC context, since it is desirable to have a solution with higher accuracy in the initial part of the horizon.

Motivation. The time interval $t \in [t_0, t_f]$, the prediction horizon T , and the sampling step $\delta > 0$, satisfy $\delta \ll T \ll t_f - t_0$. When applying the MPC procedure to solve an OCP, at each time instant t_i we compute the solution in $[t_i, t_i + T]$ but we just implement the open-loop control until $t_i + \delta$. Therefore, taking into account the planning strategy discussed above, it would be an improvement if we have an adaptive time-mesh able to cope this feature, i.e., a time-mesh that is highly refined in the lower limit of the time interval $[t_i, t_i + T]$ and it is coarser in the upper limit of the same interval. Then, we would implement the control on the time interval $[t_i, t_i + \delta]$ computed with high accuracy in a refined mesh. For the remaining time interval we have an estimate of the solution.

Time-Mesh Refinement Algorithm. In this extension, we also consider a time-dependent stopping criterion for the mesh refinement algorithm with different levels $\bar{\epsilon}_x(t)$. Instead of having a fixed stopping criterion ϵ_x^{\max} , now we have a time-dependent $\bar{\epsilon}_x(t)$ stopping criterion which sets different levels of accuracy for the solution, along the time domain. For example, the time-dependent levels of refinement can be defined as

$$\bar{\epsilon}_x(t) = \begin{cases} \epsilon_x^{\max}, & t \in [t_i, t_i + \beta_1 T] \\ \alpha_1 \epsilon_x^{\max}, & t \in]t_i + \beta_1 T, t_i + \beta_2 T] \\ \dots & \\ \alpha_j \epsilon_x^{\max}, & t \in]t_i + \beta_j T, t_i + T] \end{cases}$$

where $1 < \alpha_1 < \dots < \alpha_j \leq \epsilon_x^{\max}$ and $0 < \beta_1 < \beta_2 < \dots < \beta_j < 1$ are user-defined scalars.

This procedure adds more node points to the subintervals that are in lower levels of the stopping criterion for the refinement procedure, corresponding to time instants close to the initial time as illustrated in Fig. 2.

Refinement and Stopping Criteria. In order to proceed with the mesh refinement strategy, we have to define some refinement criteria and a stopping criterion. We consider as refinement criteria: the estimate of the relative error of the adjoint

Fig. 2 Illustration of the extended (time-dependent) time-mesh refinement strategy

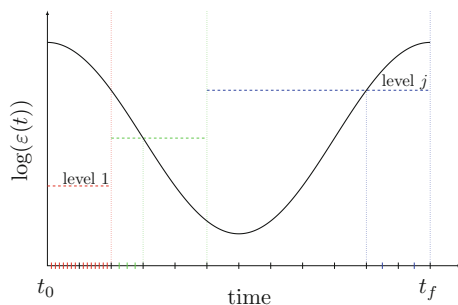
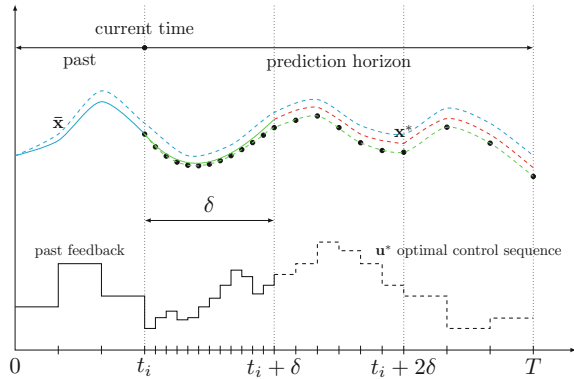


Fig. 3 Time-mesh refinement algorithm for MPC



multipliers (dual variables). For the stopping criterion, we consider a threshold for the relative error of the trajectory $\|\epsilon_{\bar{x}}\|_{\infty}$.

Warm Start. Since we are solving a sequence of open-loop OCPs, to decrease the CPU time, when going from the problem in $[t_i, t_i + T]$ to the one in $[t_i + \delta, t_i + T + \delta]$, the solution of the previous is used as a warm start for the problem. To create this warm start, the solution obtained in $[t_i, t_i + T]$ is projected in the new mesh in $[t_i + \delta, t_i + T + \delta]$ using the cubic Hermite interpolation.

Model Predictive Control coupled with the Extended Algorithm. We start the MPC procedure in the typical way but considering an adaptive mesh refinement strategy. We discretise the time interval $[t_0, t_f]$ and we solve our OCP in open-loop. Then, we implement the control in the first sampling interval. When starting the next MPC step, we apply the time-mesh refinement strategy in order to find the best mesh suited to solve the OCP in the second sampling interval (Fig. 3). In the MPC algorithm, step 2 is modified as follows:

2. (a) Select the intervals $S_{k,j}$ to be refined according to the time-dependent levels of refinement $\bar{\epsilon}_{\bar{x}}(t)$ and generate a new time grid;
- (b) Determine $\bar{\mathbf{u}} : [t_i, t_i + T] \rightarrow \mathbb{R}^m$ solution to the OCP $\mathcal{P}(t_i, t_i + T)$ (1)–(6), in the new time-grid;

4 Application: Parking Manoeuvres

In order to apply our MPC strategy, let us consider the car-like system problem with $t \in [0, 20]$, in seconds, $\mathbf{x}(t) = (x(t), y(t), \psi(t))$ and $\mathbf{u}(t) = (u(t), c(t))$. Aiming minimum energy, this problem (P_{CP}) can be stated as:

$$\text{Minimise } \int_0^{20} u^2(t) dt \tag{8}$$

$$\text{subject to } \begin{aligned} \dot{x}(t) &= u(t) \cos(\psi(t)) && \text{a.e. } t \in [0, 20] \\ \dot{y}(t) &= u(t) \sin(\psi(t)) && \text{a.e. } t \in [0, 20] \end{aligned} \tag{9}$$

$$\begin{aligned} \dot{\psi}(t) &= u(t) c(t) && \text{a.e. } t \in [0, 20] \\ \mathbf{x}(0) &= \mathbf{x}_0, && \tag{10} \end{aligned}$$

$$\mathbf{x}(20) \in \mathbb{X}_1, \tag{11}$$

$$\mathbf{x}(t) \in \mathbb{X}, \quad \forall t \in [t_0, t_f] \tag{12}$$

$$-1 \leq u(t) \leq 1 \quad \text{a.e. } t \in [0, 20] \tag{13}$$

$$-0.7 \leq c(t) \leq 0.7 \quad \text{a.e. } t \in [0, 20] \tag{14}$$

where $u(t)$ is the speed and $c(t)$ is the curvature. The end-point constraints are specified as

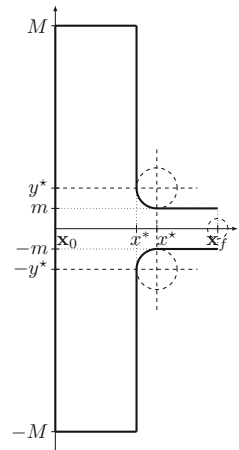
$$\mathbf{x}_0 = (x_0, y_0, \psi_0) = (1.5, 3.5, \pi/2) \tag{15}$$

$$\mathbb{X}_1 = \left\{ (x, y, \psi) : (x - x_f)^2 + (y - y_f)^2 + (\psi - \psi_f)^2 \leq r^2 \right\} \tag{16}$$

where $r^2 = 0.1$, and $\mathbf{x}_f = (x_f, y_f, \psi_f) = (4, 0, 0)$ is a user-defined target point. Moreover, we define a pathwise state constraint (see Fig. 4) set \mathbb{X} is the set of points (x, y, ψ) satisfying

$$\begin{cases} -M \leq y \leq M & \text{if } x \in [x_0, x^*] \\ -b(\mathbf{x}) \leq y \leq b(\mathbf{x}) & \text{if } x \in [x^*, x^*] \\ -m \leq y \leq m & \text{if } x \in [x^*, x_f] \end{cases} \tag{17}$$

Fig. 4 Pathwise state constraints (17) for (P_{CP})



where $x^* = 2, x^* = 3, y^* = -1.5, M = 4$ and

$$b(\mathbf{x}) = y^* - \sqrt{\rho^2 - (x - x^*)^2}, \quad \rho = |x^* - x^*|.$$

In order to test the MPC algorithm, we start by introducing some perturbations on the system dynamics test-plant:

$$\begin{cases} \dot{x}(t) = u(t) (1 + \delta_u) \cos(\psi(t)) \\ \dot{y}(t) = u(t) (1 + \delta_u) \sin(\psi(t)) \\ \dot{\psi}(t) = u(t) (1 + \delta_u) c(t) (1 + \delta_c) \end{cases} . \quad (18)$$

We consider $\delta = 2$ s which means that we will solve a sequence of 10 open-loop OCPs and we define $\delta_u = \delta_c = 0.1$. We also set $\epsilon_x^{\max} = 5 \times 10^{-5}$ and

$$\bar{\epsilon}_x(t) = \begin{cases} \epsilon_x^{\max}, & t \in [t_i, t_i + 0.1T] \\ 10 \times \epsilon_x^{\max}, & t \in]t_i + 0.1T, t_i + 0.3T] \\ 10^3 \times \epsilon_x^{\max}, & t \in]t_i + 0.3T, t_i + T] \end{cases}$$

This problem is solved considering three meshes:

- (a) π_{ML} : the multi-level time-mesh refinement strategy with MPC;
- (b) π_F : equidistant-spaced with the smallest time step of π_{ML} ;
- (c) π_C : equidistant-spaced with the largest time step of π_{ML} .

As it can be seen in Fig. 5a, considering the mesh π_{ML} , the car-like system successfully stops when the terminal condition (16) is satisfied without violating any constraint. The sequence of solutions given by each sampling step on MPC is shown in Fig. 5b. The predictions are plotted with a dashed line, while the implemented controls are plotted with a solid line. Each segment is drawn with a different color representing different MPC sampling times.

The numerical results concerning the three meshes are shown in Table 1, which shows information about the number of nodes, the smallest time step, the number of iterations needed to solve the NLP problem, the maximum absolute local errors of the trajectory, and the CPU times for solving the OCP problem and for computing the local error as well.

According to Table 1, the mesh π_{ML} has only 11.4 % of the nodes of π_F , nevertheless both meshes have maximum absolute local error of the same order of magnitude. Computing the solution using π_{ML} takes less than 20 % of the time needed to get a solution using π_F , resulting in significant savings in memory and computational cost.

The mesh π_C is the initial coarse mesh considering equidistant spacing. Without applying our refinement strategy, the MPC produces a solution with lower accuracy, $1.261E^{-3}$, when compared against the solution obtained via refinement procedure, $4.169E^{-5}$. Moreover, the CPU time spent to compute solution using π_{ML} is, as expected, 50 % higher than the one spent to obtain a solution using π_C , however

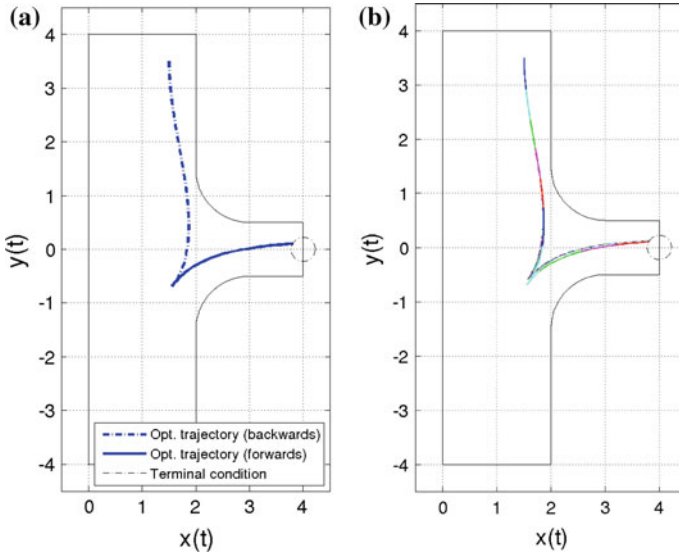


Fig. 5 Optimal trajectory for (P_{CP}) . **a** MPC trajectory, **b** Sequence of optimal trajectories

Table 1 Comparing MPC results for the problem (P_{CP})

π_j	N_j	Δt_j	I_j	$\ \epsilon_x^{(j)}\ _\infty$	CPU time solver	(s) ϵ_x
π_{ML}	365	$1/3200$	304 13 13 13 13 10 16 5 5 5	$4.169E^{-5}$	11.448	5.231
π_F	3201	$1/3200$	371 34 22 20 18 9 8 7 7 7	$3.730E^{-5}$	53.493	31.239
π_C	201	$1/200$	233 8 1 13 11 6 6 6 5 5 5	$1.261E^{-3}$	8.667	1.960

it is a good trade-off since the accuracy of the solution increases by two orders of magnitude. In all tests, the procedure gives the optimal solution which is computed spending a few seconds overall to solve 10 MPC steps.

The use of adaptive mesh refinement algorithm in real time optimization problems has additional benefits since it is possible to quickly obtain a solution even if the refinement procedure is interrupted at an early stage.

5 Conclusions

We develop an extended adaptive time-mesh refinement algorithm providing local mesh resolution refining only where it is required. In this extension, we consider a time-dependent stopping criterion for the mesh refinement algorithm with different levels $\bar{\epsilon}(t)$. In the end, the OCPs are solved within MPC with an adapted mesh with local mesh resolution which has less nodes in the overall procedure, yet having

maximum absolute local error of the same order of magnitude when compared against a refined mesh with equidistant-spacing.

Due to the fast response of the algorithm, it can be used to solve real-time optimization problems. The application demonstrates the advantage of the proposed adaptive mesh strategy, which leads to results obtained approximately as fast as the ones given by a coarse equidistant-spacing mesh and as accurate as the ones given by a fine equidistant-spacing mesh.

With this framework we can use continuous-time plant models directly. The discretization procedure can be automated and there is no need to select *a priori* the adequate time step.

Even if the optimization procedure is forced to stop in an early stage, as might be the case in real-time, we can still obtain a meaningful solution, although it might be a less accurate one.

Acknowledgments Research carried out while the 2nd author was a visiting scholar at Texas A&M University, College Station, USA. The support from Texas A&M and FEDER/COMPETE2020-POCI/FCT funds through grants POCI-01-0145-FEDER-006933 - SYSTEC and PTDC/EEL-AUT/2933/2014 is acknowledged.

References

1. Betts, J.T.: Practical methods for optimal control using nonlinear programming. SIAM (2001)
2. Betts, J.T., Huffman, W.P.: Mesh refinement in direct transcription methods for optimal control. *Optim. Control Appl. Methods* **19**(1), 1–21 (1998)
3. Caldeira, A., Fontes, F.: Model predictive control for path-following of nonholonomic systems. In: IFAC (ed.) Proceedings of the 10th Portuguese Conference in Automatic Control. pp. 374–379 (2010)
4. Chen, H., Allgöwer, F.: A quasi-infinite horizon nonlinear model predictive control scheme with guaranteed stability. *Automatica* **34**(10), 1205–1217 (1998)
5. Findeisen, R., Imsland, L., Allgöwer, F., Foss, B.: Towards a sampled-data theory for nonlinear model predictive control. In: Kang, W., Xiao, M., Borges, C. (eds.) *New Trends in Nonlinear Dynamics and Control, and their applications*. Lecture Notes in Control and Information Sciences, vol. 295, pp. 295–311. Springer Verlag, Berlin (2003)
6. Fontes, F.A.C.C., Magni, L.: Min-max model predictive control of nonlinear systems using discontinuous feedbacks. *IEEE Trans. Autom. Control* **48**, 1750–1755 (2003)
7. Fontes, F.A.C.C., Magni, L., Gyurkovics, E.: Sampled-data model predictive control for nonlinear time-varying systems: Stability and robustness. In: Allgöwer, F., Findeisen, R., Biegler, L. (eds.) *Assessment and Future Directions of Nonlinear Model Predictive Control*, Lecture Notes in Control and Information Systems, vol. 358, pp. 115–129. Springer Verlag (2007)
8. Fontes, F., Fontes, D., Caldeira, A.: Model Predictive Control of Vehicle Formations, Lecture Notes in Control and Information Sciences, vol. 381. Springer-Verlag (2009)
9. Fontes, F.A.C.C.: A general framework to design stabilizing nonlinear model predictive controllers. *Syst. Control Lett.* **42**(2), 127–143 (2001)
10. Fontes, F.A., Pereira, F.L.: Model predictive control of impulsive dynamical systems. In: Proceedings of the 4th IFAC conference on nonlinear model predictive control, NMPC'12. IFAC Proceedings Volumes (IFAC-PapersOnline), vol. 4, pp. 305–310. Noordwijkerhout; Netherlands (2012)

11. Grüne, L., Nescic, D., Pannek, J.: Model predictive control for nonlinear sampled-data systems. In: F. Allgöwer, L. Biegler, R.F.e. (eds.) *Assessment and Future Directions of Nonlinear Model Predictive Control (NMPC05)*, Lecture Notes in Control and Information Sciences, vol. 358, pp. 105–113. Springer Verlag, Heidelberg (2007)
12. Grüne, L., Pannek, J.: *Nonlinear model predictive control*. Springer (2011)
13. Grüne, L., Palma, V.G.: Robustness of performance and stability for multistep and updated multistep MPC schemes. *Discret. Contin. Dyn. Syst.* **35**(9), 4385–4414 (2015)
14. Lazar, M., Allgower, F., Van den Hof, P., Cott, B. (eds.): *4th IFAC Conference on Nonlinear Model Predictive Control, NMPC'12*. IFAC Proceedings Volumes (IFAC-PapersOnline), IFAC, Noordwijkerhout; Netherlands (2012)
15. Magni, L., Scattolini, R.: Model predictive control of continuous-time nonlinear systems with piecewise constant control. *IEEE Trans. Autom. Control* **49**, 900–906 (2004)
16. Mayne, D.Q., Michalska, H.: Receding horizon control of nonlinear systems. *IEEE Trans. Autom. Control* **35**, 814–824 (1990)
17. Michalska, H., Mayne, D.Q.: Robust receding horizon control of constrained nonlinear systems. *IEEE Trans. Autom. Control* **38**, 1623–1633 (1993)
18. Paiva, L.T.: *Optimal control in constrained and hybrid nonlinear system: Solvers and interfaces*. Faculdade de Engenharia, Universidade do Porto, Technical Report (2013)
19. Paiva, L.T.: *Numerical Methods in Optimal Control and Model Predictive Control*. Ph.D., Universidade do Porto, Porto, Portugal (Dec 2014)
20. Paiva, L.T., Fontes, F.A.: Adaptive time-mesh refinement in optimal control problems with state constraints. *Discret. Contin. Dyn. Syst.* **35**(9), 4553–4572 (2015)
21. Pannocchia, G., Rawlings, J., Mayne, D., Mancuso, G.: Whither discrete time model predictive control? *IEEE Trans. Autom. Control* **60**(1), 246–252 (2015)
22. Patterson, M.A., Hager, W.W., Rao, A.V.: A ph mesh refinement method for optimal control. *Optimal Control Applications and Methods* (Feb 2014)
23. Pereira, F.L., Fontes, F.A., Aguiar, A.P., de Sousa, J.B.: An optimization-based framework for impulsive control systems. In: *Developments in Model-Based Optimization and Control*, pp. 277–300. Springer (2015)
24. Prodan, I., Olaru, S., Fontes, F.A., Pereira, F.L., de Sousa, J.B., Maniu, C.S., Niculescu, S.I.: Predictive control for path-following. from trajectory generation to the parametrization of the discrete tracking sequences. In: *Developments in Model-Based Optimization and Control*, pp. 161–181. Springer (2015)
25. Prodan, I., Olaru, S., Fontes, F.A., Stoica, C., Niculescu, S.I.: A predictive control-based algorithm for path following of autonomous aerial vehicles. In: *2013 IEEE International Conference on Control Applications (CCA)*, pp. 1042–1047. IEEE (2013)
26. Raković, S.V., Kouramas, K.: Invariant approximations of the minimal robust positively invariant set via finite time Aumann integrals. In: *2007 46th IEEE Conference on Decision and Control*, pp. 194–199. IEEE (2007)
27. Rawlings, J.B., Mayne, D.Q.: *Model Predictive Control: Theory and Design*. Nob Hill Pub. (Aug 2009)
28. Rucco, A., Aguiar, A.P., Fontes, F.A., Pereira, F.L., de Sousa, J.B.: A model predictive control-based architecture for cooperative path-following of multiple unmanned aerial vehicles. In: *Developments in Model-Based Optimization and Control*, pp. 141–160. Springer (2015)
29. Zhao, Y., Tsiotras, P.: Density functions for mesh refinement in numerical optimal control. *J. Guid. Control Dyn.* **34**(1), 271–277 (2011)

Efficient Operations at Intermodal Terminals Using a Multi-agent System

Tomás Hipólito, João Lemos Nabais and Miguel Ayala Botto

Abstract Transport networks are large-scale complex systems whose objective is to deliver cargo at a specific time and at a specific location. Ports and intermodal container terminals behave as exchange hubs where containers are moved from a transport modality to a different one. Terminal operations management arise as a need to face the exponentially growth of the container traffic in the last few years. In this paper the Extended Formulation of the MPC is presented. This formulation accounts for the variation of the control action to reduce not only the amount of actions but to perform a wise and efficient use of handling resources. This formulation is based on the decomposition of the control action. The Extended Formulation is applied to a simulation case study based on a long-term scheduled scenario and compared with the Basic Formulation.

Keywords Model Predictive Control · Basic Formulation · Extended Formulation · Intermodal container terminal · Operations management

1 Introduction

The container emerged in 1950s as solution to transport goods over long distances. Container transportation networks are designed to deliver cargo at the agreed time and at the agreed location. Intermodal container terminals behave as exchange hubs where containers are handled, eventually stored or moved to other transport modality to reach the final destination at the agreed time. The need for operations management at intermodal container terminals arise from the need to offer effective and efficient processes which meet the network requirements, while minimizing operating costs

T. Hipólito · M.A. Botto
LAETA, IDMEC, Instituto Superior Técnico, Universidade de Lisboa,
Lisboa, Portugal

J.L. Nabais (✉)
LAETA, School of Business Administration, IDMEC, Polytechnical Institute
of Setúbal, Setúbal, Portugal
e-mail: joao.nabais@esce.ips.pt

[1]. The productivity of an intermodal terminal and thus of a network can be significantly improved by suitably modelling and optimizing the handling of terminal resources [2]. The operations management related to intermodal containers terminals can be analysed as a flow assignment problem, where the container flows are guaranteed by the allocation of the handling resources. The efficiency of a terminal is influenced by the ability to manage the transfer processes performed by the resources [2]. The operations management at container terminals has been widely studied by the operations research field [3–6]. These approaches focus on the optimization of individual terminal operations such as berth planning and container storage. However, they lack a general approach considering all terminal operations simultaneously. The control field has also done research in this area applying classic control techniques and assuming undistinguished containers [2, 7, 8]. The ability to distinguish containers is relevant to network operation because it creates the possibility to group them according their features. Containers can be distinguished according to some relevant criteria: weight, size, due time, final destination. More recently, a new control approach was developed considering Model Predictive Control (MPC) technique and distinguishable containers [9–11]. MPC is suitable for large dimensional problems with multiple variables and it has been used with success in petrochemical and electromechanical industry [12]. These approaches consider the control action as the decision variable intended to minimize. In MPC problems the cost function penalizes changes in the variation of the control action rather than the control action itself [12]. In terms of the terminal, variation of control action corresponds to the variation of the allocation of handling resources and the objective is to minimize it. In this paper, the container terminal is modelled from a push-pull container flow perspective. The model is used to develop a decomposition of the general flow assignment problem into subproblems which are handled by MPC control agents [9]. The main contribution of this paper is:

- formulation of the optimization problem considering the variation of control action $\Delta \mathbf{u}$ which focus on the variation of the utilization of handling resources.

In Sect. 2 the intermodal container terminal model is presented considering a generic framework that is able to capture different structural layouts. The control structure is presented in Sect. 3. For comparison purposes the optimization problem is formulated considering the control action \mathbf{u} , Basic Formulation (Sect. 3.1) and the variation of control action $\Delta \mathbf{u}$, Extended Formulation (Sect. 3.2). In Sect. 4 numerical results are presented, in which Extended Formulation is compared to Basic Formulation.

2 Background

The intermodal container terminal can be represented by a graph $\mathcal{G} = (\mathcal{V}, \mathcal{E})$, where the nodes \mathcal{V} stand for the storage areas and the links \mathcal{E} refer to the container flows between nodes (Fig. 1). The model describing the terminal dynamics is based on a flow perspective and it assumes two main concepts:

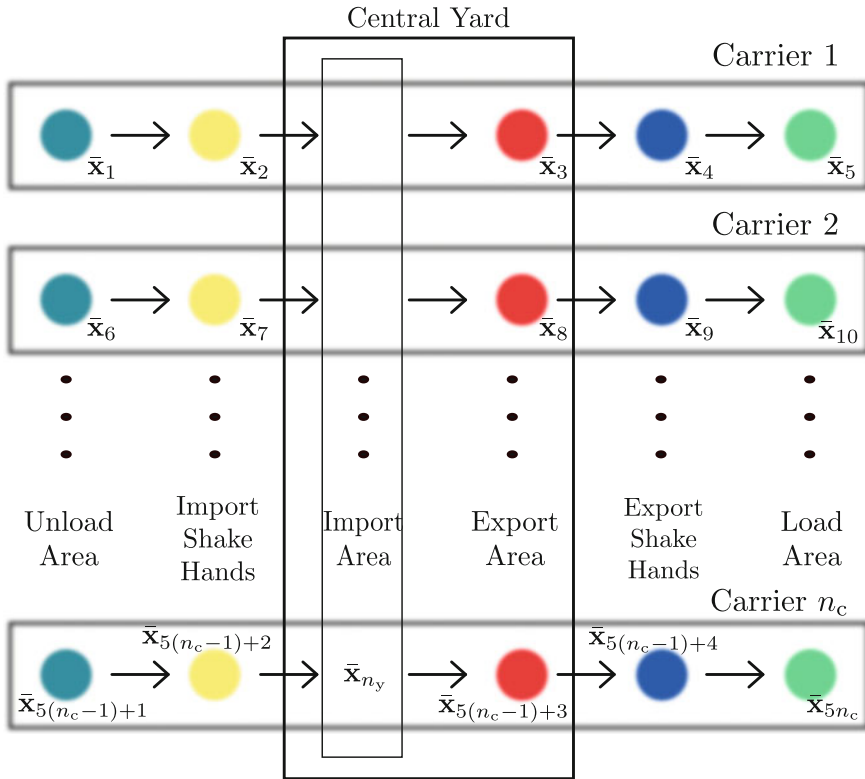


Fig. 1 Intermodal container terminal graph \mathcal{G} considering n_a exclusive areas per connection plus a common node for all connections

- storage areas—to model the storage capacity of terminal physical areas.
- container categorisation—to distinguish containers according its final destination and track them inside the terminal.

The model assumes that the terminal is split into five main areas (see Fig. 1):

- Unload Area—area related to the unloading of containers from the carriers to the terminal.
- Import Shake Hands—area connecting the Unload Area to the Central Yard where occurs a handling resource switch.
- Central Yard—core of the container terminal. It is divided into Import Area where the containers are stored and Export Area where the containers prepared to be exported.
- Export Shake Hands—area connecting the Central Yard and the Load Area where occurs a handling resource switch.
- Load Area—area related to the loading of containers from the terminal to the carriers.

For each connection arriving the terminal a container flow is established based on the movement of the containers promoted by handling resources from Unload Area to the Central Yard and from the Central Yard to the Load Area. The topology of the model depends on the following parameters: number of different container classes present in the terminal n_t which is related to the number of possible final destinations; number of connections provided by the terminal simultaneously n_c , which can be of different transport modalities; number of storage areas exclusive of a single connection n_a . The intermodal container terminal has n_c transport connections (see Fig. 1). The model considers each connection as a subsystem and a control agent is assigned to each subsystem. The subsystems have coupled dynamics because they share a common node, the Import Area of the Central Yard, and coupled constraints because connections share the handling resources available. Mathematically the model of terminal is formulated using a state-space approach. There are n_c state space vectors \mathbf{x}_i , where $i = 1 \dots n_c$. Each state space vector \mathbf{x}_i is composed of the corresponding $\bar{\mathbf{x}}_j$ state space vectors associated to the subsystem i specific nodes plus the state of the common node.

$$\mathbf{x}_i(k) = \begin{bmatrix} \bar{\mathbf{x}}_{n_{A_i}+1}(k) \\ \vdots \\ \bar{\mathbf{x}}_{n_{A_i}+n_{a_i}}(k) \\ \bar{\mathbf{x}}_{n_y}(k) \end{bmatrix}, \quad n_{A_i} = \sum_{j=1}^{i-1} n_a, \quad 1 \leq i \leq n_c \quad (1)$$

Each state space vector \mathbf{x}_i belongs to the state space set \mathcal{X}^i and its length is $(n_a + 1)n_t$. The state-space model for subsystem i is given by

$$\mathbf{x}_i(k+1) = \mathbf{A}_i \mathbf{x}_i(k) + \mathbf{B}_{u,i} \mathbf{u}_i(k) + \mathbf{B}_{d,i} \mathbf{d}_i(k) + \sum_{j=1, j \neq i}^{n_c} \mathbf{B}_{u,j} \mathbf{u}_j(k) \quad (2)$$

$$\mathbf{y}_i(k) = \mathbf{C}_i \mathbf{x}_i(k) \quad (3)$$

$$\mathbf{x}_i(k) \geq \mathbf{0} \quad (4)$$

$$\mathbf{u}_i(k) \geq \mathbf{0} \quad (5)$$

$$\mathbf{y}_i(k) \leq \mathbf{y}_{\max,i} \quad (6)$$

$$\mathbf{P}_{u,i} \mathbf{u}_i(k) \leq \mathbf{u}_{\max,i} \quad (7)$$

$$\mathbf{x}_i(k) \geq \mathbf{P}_{xu,i} \mathbf{u}_i(k) \quad (8)$$

$$\mathbf{x}_i(k) \in \mathcal{X}^i \quad (9)$$

$$\mathbf{u}_i(k) \in \mathcal{U}^i \quad (10)$$

where vector $\mathbf{u}_i(k)$ represents the control action for subsystem i and its length is $n_a n_t$, vector $\mathbf{d}_i(k)$ stands for the perturbation (arrival and departure of containers) in subsystem i and its length is $2n_t$, $\mathbf{y}_i(k)$ is the amount of containers present at the physical areas of subsystem i . Vectors $\mathbf{y}_{\max,i}$ and $\mathbf{u}_{\max,i}$ correspond to the maximum amount of containers possible at the terminal areas and to the maximum handling capacity

of subsystem i . Matrices \mathbf{A}_i , $\mathbf{B}_{u,i}$, $\mathbf{B}_{d,i}$, $\mathbf{B}_{u,ij}$ and \mathbf{C}_i are the state space matrices for subsystem i . $\mathbf{P}_{uu,i}$ is the projection matrix from the control action set \mathcal{U}^i into the maximum handling capacity set \mathcal{U}_{\max}^i , $\mathbf{P}_{xu,i}$ is the projection matrix from the control action set \mathcal{U}^i into the state space set \mathcal{X}^i .

3 Control

MPC is particularly suited to deal with terminal operations management since it is able to operate near the constraints limits, namely, the handling capacity and the storage capacity and perform the optimization of large dimensional problems as this one [12]. MPC has already been adopted successfully to control large and multi-variable processes in the industry [13, 14], structurally similar to the terminal operations management problem. The control goal is to perform an efficient flow assignment in order to increase the terminal performance according to a pre-defined parameter. The minimization of terminal operation costs is a desired goal which can be achieved by minimizing the amount of handling resources actions.

3.1 Basic MPC Formulation

The objective of the Basic Formulation is to minimize the control action $\mathbf{u}(k)$ while fulfilling the transport network requirements. At each time step, the controller finds the minimum amount of containers necessary to move in order to satisfy terminal constraints. The objective function for subsystem i is linear and consists on a weighted sum of the storage areas

$$J(k) = \sum_{j=0}^{N-1} \mathbf{q}_{p,i}^T \mathbf{x}_i(k+1+j) \quad (11)$$

where $\mathbf{q}_{p,i}$ correspond to the weights assigned to the storage areas. Combining (2) with (11), objective function is written in terms of the decision variable $\mathbf{u}_i(k)$

$$\begin{aligned} J(k) = & \sum_{j=0}^{N-1} \mathbf{q}_{p,i}^T [\mathbf{A}_i \mathbf{x}_i(k+j) + \mathbf{B}_{u,i} \mathbf{u}_i(k+j) \\ & + \mathbf{B}_{d,i} \mathbf{d}_i(k+j) + \sum_{j=1, j \neq i}^{n_c} \mathbf{B}_{u,ij} \mathbf{u}_j(k)] \end{aligned} \quad (12)$$

The Basic MPC formulation for control agent i which is responsible for subsystem i is presented as:

$$\min_{\tilde{\mathbf{u}}_i} \sum_{j=0}^{N_p-1} \mathbf{q}_{p,i}^T [\mathbf{A}_i \mathbf{x}_i(k+j) + \mathbf{B}_{u,i} \mathbf{u}_i(k+j) + \mathbf{B}_{d,i} \mathbf{d}_i(k+j) + \sum_{j=1, j \neq i}^{n_c} \mathbf{B}_{u,ij} \mathbf{u}_j(k)] \quad (13)$$

$$\text{s.t. } \mathbf{x}_i(k+1+j) = \mathbf{A}_i \mathbf{x}_i(k+j) + \mathbf{B}_{u,i} \mathbf{u}_i(k+j) + \mathbf{B}_{d,i} \mathbf{d}_i(k+j) + \sum_{j=1, j \neq i}^{n_c} \mathbf{B}_{u,ij} \mathbf{u}_j(k) \quad (14)$$

$$\mathbf{y}_i(k+j) = \mathbf{C}_i \mathbf{x}_i(k+j), j = 0, \dots, N_p - 1 \quad (15)$$

$$\mathbf{x}_i(k+j) \geq \mathbf{0} \quad (16)$$

$$\mathbf{u}_i(k+j) \geq \mathbf{0} \quad (17)$$

$$\mathbf{y}_i(k+j) \leq \mathbf{y}_{\max,i} \quad (18)$$

$$\mathbf{P}_{uu,i} \mathbf{u}_i(k+j) \leq \mathbf{u}_{\max,i} \quad (19)$$

$$\mathbf{x}_i(k) \geq \mathbf{P}_{xu,i} \mathbf{u}_i(k+j) \quad (20)$$

$$\mathbf{P}_{dx,i} \mathbf{x}_i(k+1+j) \leq \mathbf{w}_{d,i}(k+1+j) \quad (21)$$

where N_p is the prediction horizon, $\tilde{\mathbf{u}}_i$ is the control action sequence over the prediction horizon $[\mathbf{u}_i(k)^T \dots \mathbf{u}_i(k+N_p-1)^T]^T$, vector $\mathbf{w}_{d,i}(k)$ represents the forecast load request vector for subsystem i that is updated at each time step k and matrix $\mathbf{P}_{dx,i}$ is the projection matrix from the state space set \mathcal{X}^i into the load request set of subsystem i . The constraints are included in the optimization problem formulation to assure a meaningful terminal behaviour over the time. Equations (16) and (17) guarantee the non-negativity of the states, because it is not physically possible to have a negative storage in the nodes and the non-negativity of the control actions, which is a necessary condition to have a coherent model. Equation (18) imposes a storage capacity limit to each physical area of the terminal that needs to be respected because it is an inherent characteristic of the terminal. Equation (19) indicates that the control actions must respect the maximum handling capacity of the terminal resources. Equation (20) assures that is only possible to move containers from one node to another if there are effectively containers in those nodes. Equation (21) expresses the load request imposed by the clients. Control agents are solved sequentially according a pre-determined order. It is possible to choose any agent order at the beginning of the simulation but that order is constant. The MPC controller updates the state of the Import Area of the Central Yard and the resources available after solving a control agent.

3.2 Extended MPC Formulation

The objective of the Extended Formulation is to minimize the variation of the control action $\Delta \mathbf{u}(k)$ while fulfilling the transport network requirements. At each time

step, the controller allocates the resources keeping the flows constant between nodes. Using this approach and considering an ideal situation handling resources are being fully used or not used at all. This formulation is focused on the efficiency of the usage of handling resources which is desirable to reduce operation costs. Extended Formulation rewrites control action vector of subsystem i $\mathbf{u}_i(k)$ as:

$$\mathbf{u}_i(k) = \Delta \mathbf{u}_i(k) + \mathbf{u}_i(k-1) \quad (22)$$

The Extended MPC formulation for control agent i which is responsible for subsystem i is stated as:

$$\min_{\bar{\mathbf{u}}_i(k)} \sum_{j=0}^{N-1} \mathbf{q}_{p,i}^T \mathbf{x}_i(k+1+j) \quad (23)$$

$$\text{s.t. } \mathbf{x}_i(k+1+j) = \mathbf{A}_i \mathbf{x}_i(k+j) + \mathbf{B}_{u,i} [\Delta \mathbf{u}_i(k+j) + \mathbf{u}_i(k-1+j)] +$$

$$\mathbf{B}_{d,i} \mathbf{d}_i(k+j) + \sum_{j=1, j \neq i}^{n_c} \mathbf{B}_{u,ij} \mathbf{u}_j(k) \quad (24)$$

$$\mathbf{y}_i(k+j) = \mathbf{C}_i \mathbf{x}_i(k+j), \quad j = 0, \dots, N-1 \quad (25)$$

$$\mathbf{x}_i(k+j) \geq \mathbf{0} \quad (26)$$

$$[\Delta \mathbf{u}_i(k+j) + \mathbf{u}_i(k-1+j)] \geq \mathbf{0} \quad (27)$$

$$\mathbf{y}_i(k+j) \leq \mathbf{y}_{\max,i} \quad (28)$$

$$\mathbf{P}_{uu,i} [\Delta \mathbf{u}_i(k+j) + \mathbf{u}_i(k-1+j)] \leq \mathbf{u}_{\max,i} \quad (29)$$

$$\mathbf{x}_i(k) \geq \mathbf{P}_{xu,i} [\Delta \mathbf{u}_i(k+j) + \mathbf{u}_i(k-1+j)] \quad (30)$$

$$\mathbf{P}_{dx,i} \mathbf{x}_i(k+1+j) \leq \mathbf{w}_{d,i}(k+1+j) \quad (31)$$

To evaluate the performance of MPC controller under variable conditions and parameters Performance Metrics (PM) was designed. Performance Metrics is a metrics based on objective function. The expression, $\text{PM} = \mathbf{q}_p^T \mathbf{x}(k+1)$, takes into account just the control action of the current time step $\mathbf{u}(k)$ which corresponds to the actions that are being implemented in the terminal. This way bias effects of large control sequences are avoided.

4 Results

The presented MPC control structure will be used for controlling an hinterland terminal with the following layout (see Fig. 2):

- a quay area able to berth two barges simultaneously at maximum. Containers are unloaded/loaded from/to barges by Quay Cranes. QC maximum handling capacity is 90 TEU/hour. Berth A is able to use the maximum cranes capacity, while berth B is only able to use half of the maximum cranes capacity, 45 TEU/hour.

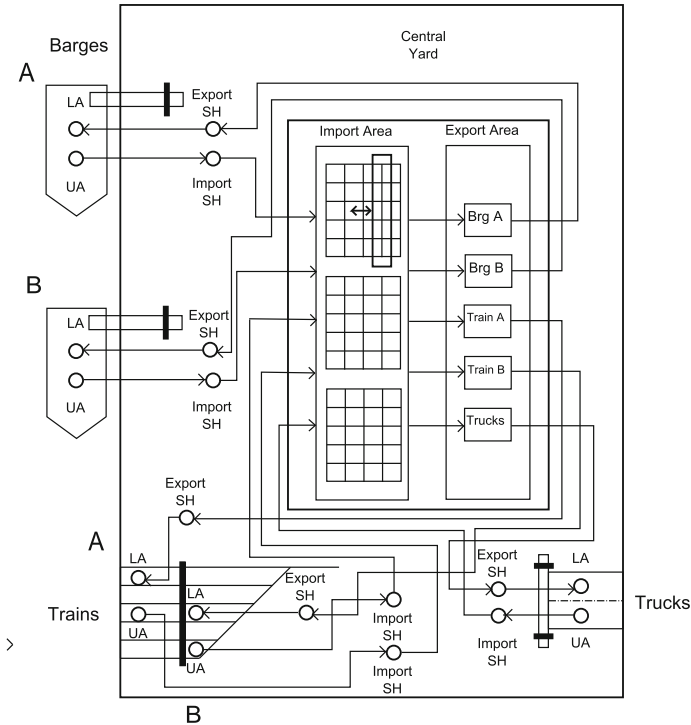


Fig. 2 Intermodal container terminal layout for simulation purposes

- a train area with two rail tracks available. Containers are unloaded/loaded from/to wagons by train gates. The maximum handling capacity of the train gates is 40 TEU/hour.
- a truck area, where there is a maximum handling capacity of 60 TEU/hour.

Focusing on storage capacity of the terminal areas, the Unload Area, the Load Area and the Central Yard are considered to be large enough to never compromise the terminal operations, so they have a storage capacity of 20000 TEU. The Import Shake Hands/Export Shake Hands are intermediate areas and are not designed to store cargo, so their storage capacities are limited to the respective unload/load maximum capacity for each carrier: 90 TEU for Barge A, 45 TEU for Barge B, 40 TEU for train A, 40 TEU for train B, 60 TEU for trucks.

A network of connections and weekly schedules is designed to manage the container flows of the hinterland terminal. This schedule is result of agreements between all the parts involved in the management and coordination of the transportation network so it is assumed to be fixed. Some assumptions are made per transport modality:

- Barges: it is assumed that three connections per day will be available in a 6-day week. An average handling of 280 TEU/demand and 120 TEU/demand for berth A and berth B, respectively, will be considered for numerical design.

- Trains: two rail tracks are available that serve exclusively one train. The schedule for trains is assumed fixed and four shipments per day for each rail track are available for a 6-day week. An average handling of 80 TEU/demand for both trains will be considered for numerical design.
- Trucks: truck gates are only open for a 16 h period on a 6-day week. Every hour trucks arrive and leave the train. An average handling of 60 TEU/demand for trucks will be considered for numerical design.

The container transfer towards the Central Yard is performed by Automatic Guided Vehicles (AGV) and the rehandling of containers at the Central Yard from Import Area to the Export Area is performed by Rail Mounted Gantry Cranes (RMGC). The terminal is integrated in a transport network composed by 4 terminals, so $n_t = 5$, including the empty containers. As stated above, the number of connections served by the terminal is $n_c = 5$. Each connection has 5 exclusive areas which are Unload Area, Import Shake Hands, Export Area, Export Shake Hands, Load Area, so $n_a = 5$. The scenario corresponds to one week of terminal operation, the prediction horizon considered is $N_p = 6$ and the sampling time assumed is $T_s = 1$ h.

MPC formulations are compared using two criteria: the performance metrics and the computation time. Figures 3 and 4 reveal that the behaviour of the two formulations is similar. The Performance Metrics values (see Table 1) confirm the similarity. This similarity is due to the strict structure of connections schedule. The schedule is based on time windows which are not long enough to see the effect of the variation of the control action. The Extended Formulation is justified because it consists on a tactical decision which is performed to achieve the strategic goal which can be the reduction of operational costs. In terms of computation time, Extended Formulation takes the double of the time of Basic Formulation. The decomposition of $\mathbf{u}(k)$ increases the complexity of Extended Formulation.

Fig. 3 Container storage at the import area considering the Basic Formulation and the Extended Formulation

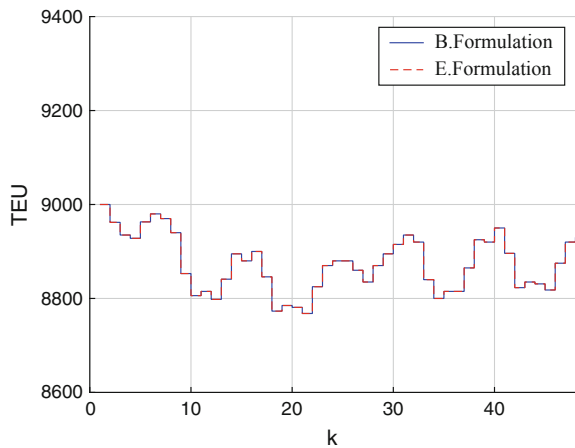


Fig. 4 Quay Crane allocation considering the Basic Formulation and Extended Formulation

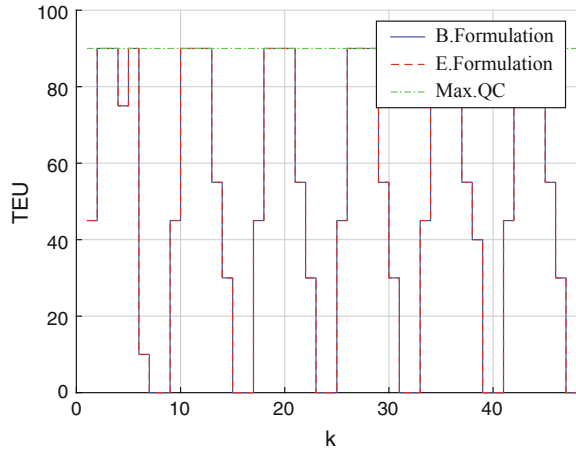


Table 1 Computation time and performance metrics

MPC formulation	Computation time			Performance metrics
	Max [s]	Mean [s]	Stdv [s]	
Basic	0.5304	0.3326	0.0689	-4317.2
Extended	0.8892	0.6111	0.821	-4318.4

5 Conclusions

In this paper, Extended Formulation of MPC is presented. Extended formulation consists in considering the control action variation as the decision variable of the optimization problem instead of the control action itself. The main advantage of the Extended Formulation consists on focusing on the monetization of handling resources movements instead of just minimize the amount of containers. This formulation introduces a tactical approach to operations management trying to meet management objectives namely cost reduction by reducing resources movements at the cost of not moving the minimum amount of containers at each time step. New terminal layouts, including more terminal areas and connections new schedules need to be tested using this formulation to validate it.

Acknowledgments This work was supported by Fundação para a Ciência e Tecnologia (FCT), through IDMEC, under LAETA, project UID/EMS/50022/2013 and by the FCT, through IDMEC, under LAETA Pest-OE/EME/LA0022.

References

1. Stahlbock, Robert, Voss, Stefan: Operations research at container terminals: a literature update. *OR Spectrum* **30**, 1–52 (2008)
2. Alessandri, A., Sacone, S., Siri, S.: Management of intermodal container terminals using feedback control. In: *Proceedings of The 7th International IEEE Conference on Intelligent Transportation Systems*, pp. 882–887 (2004)
3. Crainic, T.G., Kim, K.H.: Intermodal Transportation. *Technol. Teach.* **64**, 15–18 (2005)
4. Gambardella, L.M., Mastrolilli, M., Rizzoli, A.E., Zaffalon, M.: An optimization methodology for intermodal terminal management. *J. Intell. Manuf.* **12**, 5–6 (2001)
5. Kozan, E., Preston, Peter: Genetic algorithms to schedule container transfers at multimodal terminals. *Int. Trans. Oper. Res.* **6**, 311–329 (1999)
6. Legato, Pasquale, Mazza, Rina M.: Berth planning and resources optimisation at a container terminal via discrete event simulation. *Eur. J. Oper. Res.* **133**, 537–547 (2001)
7. Alessandri, Angelo, Cervellera, Cristiano, Cuneo, Marta, Gaggero, Mauro, Soncin, Giuseppe: Modeling and feedback control for resource allocation and performance analysis in container terminals. *IEEE Trans. Intell. Transp. Syst.* **9**, 601–614 (2008)
8. Alessandri, Angelo, Cervellera, Cristiano, Cuneo, Marta, Gaggero, Mauro, Soncin, Giuseppe: Management of logistics operations in intermodal terminals by using dynamic modelling and nonlinear programming. *Marit. Econ.* **11**, 58–76 (2009)
9. Nabais, J.L., Negenborn, R.R., Botto, M.A.: Hierarchical model predictive control for optimizing intermodal container terminal operations. *IEEE Conf. Intell. Transp. Syst. Proc.* 708–713 (2013)
10. Nabais, J.L., Negenborn, R.R., Botto, M.A.: A novel predictive control based framework for optimizing intermodal container terminal operations. In: *3rd International Conference on Computational Logistics*, pp. 53–71 (2012)
11. Negenborn, R.R.: Model predictive control for a sustainable transport modal split at intermodal container hubs (2013)
12. Maciejowski, J.M.: *Predictive Control with Constraints*. Prentice Hall (2002)
13. Stewart, Brett T., Venkat, Aswin N., Rawlings, James B., Wright, Stephen J., Pannocchia, Gabriele: Cooperative distributed model predictive control. *Syst. Control Lett.* **59**, 460–469 (2010)
14. Venkat, A.N., Hiskens, I.A., Rawlings, J.B., Wright, S.J.: Distributed MPC strategies with application to power system automatic generation control. *IEEE Trans. Control Syst. Technol.* **16**, 1192–1206 (2008)

Model Predictive Control Applied to a Supply Chain Management Problem

Tatiana M. Pinho, João Paulo Coelho, António Paulo Moreira
and José Boaventura-Cunha

Abstract Supply chains are ubiquitous in any commercial delivery systems. The exchange of goods and services, from different supply points to distinct destinations scattered along a given geographical area, requires the management of stocks and vehicles fleets in order to minimize costs while maintaining good quality services. Even if the operating conditions remain constant over a given time horizon, managing a supply chain is a very complex task. Its complexity increases exponentially with both the number of network nodes and the dynamical operational changes. Moreover, the management system must be adaptive in order to easily cope with several disturbances such as machinery and vehicles breakdowns or changes in demand. This work proposes the use of a model predictive control paradigm in order to tackle the above referred issues. The obtained simulation results suggest that this strategy promotes an easy tasks rescheduling in case of disturbances or anticipated changes in operating conditions.

Keywords Model predictive control · Supply chain modelling · Integer programming problems · Transportation scheduling

T.M. Pinho (✉) · J. Boaventura-Cunha
Universidade de Trás-os-Montes e Alto Douro, UTAD, Escola de Ciências e
Tecnologia, Quinta de Prados, 5000-801 Vila Real, Portugal
e-mail: tatianap@utad.pt

J. Boaventura-Cunha
e-mail: jboavent@utad.pt

J.P. Coelho
Instituto Politécnico de Bragança, Escola Superior de Tecnologia e Gestão,
Campus de Sta. Apolónia, 5300-253 Bragança, Portugal
e-mail: jpcoelho@ipb.pt

A.P. Moreira
Faculty of Engineering, University of Porto, Porto, Portugal
e-mail: amoreira@fe.up.pt

T.M. Pinho · J.P. Coelho · A.P. Moreira · J. Boaventura-Cunha
INESC TEC Technology and Science, Campus da FEUP, 4200-465 Porto, Portugal

1 Introduction

A supply chain can be defined as a network of different entities, namely producers, suppliers, distributors and retailers, whose final goal is to transform raw materials or ideas into finished products or services and deliver them to the final customer [1–3]. Thus, it can be noticed a direct flow of materials and an inverse flow of information within the supply chain [1]. Within the current economic reality, with increasing market competitiveness, companies aim to rapidly satisfy customers requirements, while maintaining operative costs at minimum. Besides that, the market has also nowadays evolved to a more dynamic environment, where time is a key factor together with the vast range of products' choice and more requirements in terms of quality and environment. For that reason, the focus on supply chain management has becoming stronger [4, 5].

Supply chain management techniques aim to respond to the customers requirements through efficient, responsive and profitable means. For that, organizations should be integrated and the material, information and financial flows coordinated [1, 6]. From a process point-of-view, the management of supply chains involves planning, sourcing, production and distribution logistics [7]. For this integration to be efficient, it is important to share information in an accurate and timely manner between the members of the supply chain [8]. However, this is not an easy task especially when the supply chain is multi-business oriented. If the management is not sufficiently efficient, the supply chain may become unstable [9]. Thus, the process of decision making should consider all the interactions and constraints between the stakeholders in order to create plans that lead to a profitable supply chain [10].

The supply chain dynamic, in addition to existing uncertainty, make the synchronization between the different levels a complex task, commonly leading to deviations from the original plan. However, supply chains should be flexible enough to take this recurrent variability and uncertainty into account [2, 11]. Furthermore, risk management is important in complex systems in which the current decisions will be influenced by future events [12]. Heuristics and mathematic programming techniques have been used in supply chain management as a mean to represent real systems in a simplified manner [13]. Although, considering the dynamic of the supply chain system, the existing static models are insufficient [1]. Control methodologies are advantageous to improve the supply chain responsiveness [11]. In particular, Model Predictive Control (MPC) has been used as an efficient management tool. The first implementation of MPC within inventory management occurred in Kapsiotis and Tzafestas [14, 15]. Since then, many others have proposed the implementation of MPC as supply chain management tool. In [10] it was proposed the application of MPC to a supply chain with multiproduct, multiechelon distribution networks with multiproduct batch plants. The main objective was to minimize the costs and customer satisfaction through the optimal definition of materials acquisition, production schedules, distributors' ordering policies and inventory levels, in a centralized approach. The obtained results were compared with the decentralized approach of [5], showing better performance. Based on tactical problems, such as high stochastic-

ity and nonlinearity in throughput times, yields and demand, encompassed in semiconductor manufacturing supply chains, [16], proposed the implementation of MPC to inventory control. Through a practical example it was proved the importance of tuning controller parameters in the MPC performance. The optimal control of the inventory level in a supply chain in order to have enough stock to satisfy demand without excessive costs is hampered due to demand uncertainty. To overcome this problem, [17] applied MPC to control inventory, encompassing demands' prediction. The application results shown good performance in systems with high dynamic and uncertainty with reductions in the bullwhip effect. The work of [14] used a centralized MPC approach in order to reduce the bullwhip effect present in supply chains. An example with four level, in which all nodes belonging to the same company, was tested. The inventories were controlled through a global controller, and the bullwhip effect was reduced in comparison to other decentralized MPC approaches. It was demonstrated that the impact of demand variability is reduced using the MPC-based ordering policies compared to conventional techniques. Besides these, other works have been reported. A more detailed review regarding control theory application and, in particular, MPC in supply chains management can be found in [18, 19].

In this paper a MPC approach is proposed to manage a biomass for energy production supply chain, in particular, the case of biomass transportation between supply and demand points. The objective will be to analyse the behaviour of a model predictive controller within a distribution and production chain regarding its disturbances rejection capability. In this case the disturbances are variations on the clients requests and on the total delivered material. Besides the current section, this paper is organized as follows: Sect. 2 describes the supply chain problem to be dealt with; Sect. 3 details the proposed MPC methodology, with a case study demonstration in Sect. 4; at last, Sect. 5 describes the main conclusions and future work perspectives.

2 Problem Statement

Supply chains are networks composed of several interconnected entities with direct flow of material and inverse flow of information. This mass/information flow paradigm is transversal to any business and can be applied to a broad range of examples. In particular, this work, a generic biomass supply network will be addressed. In any forest-based supply chain one can define, as main stakeholders, the forest owners, harvesting, forwarding, chipping and transportation companies, and power plants. Figure 1 represents the flows encompassed in this production model.

The dynamics of this supply chain can be summarized as follows. The trees standing in the forests are cut down (harvested) and the wood logs and branches transported (forwarded) into piles at the roadside. Afterwards, chipping machines, transform the logs into small wood chips directly to a truck. The trucks will then transport the wood chips to a power plant (client). At each week, the power plants require a certain amount of wood chips energy. Based on this demand, it is defined the amount

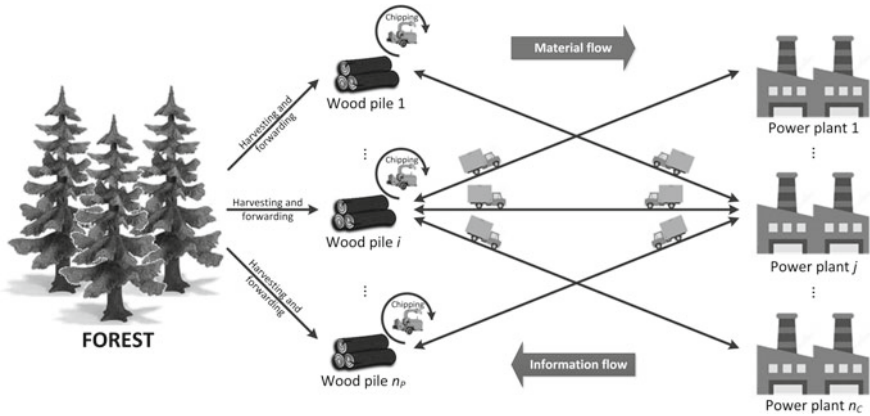


Fig. 1 Biomass supply chain description

of wood chips that need to be transported from the piles to the power plants to accommodate their needs.

The management of this supply chain involves two type of decisions: tactical and operational. The tactical decisions are focused in a time horizon of one week and addresses decisions of raw materials assignment to demand, fleet dimensioning and anticipates transportation decisions to be made at the operational level. The operational decisions encompass the vehicles routing and schedules for each working day, based on the tactical level outcomes.

In the biomass supply chain, a substantial part of the costs accrue from the wood chips transportation between supply and demand points [20]. As such, increasing interest has been denoted in the management and control of the transportation systems as a relevant issue to be improved [21, 22]. Considering these aspects, in the current work, decisions regarding the management and control of the transportation process, will be treated. In particular, attending the weekly energy demand from the clients, a MPC approach will be integrated to define and control the amount of energy that need to flow between piles and power plants, as well as the number of resources needed to fulfil the tasks, aiming to reduce the production costs.

3 Proposed MPC Methodology

The application of a model predictive control paradigm requires two main parts: an optimization algorithm and a system model. The former solves the controller law to find the control actions that will lead to an objective function optima whereas the latter will be used to evaluate the system future response to those control actions. The model is used to predict the system output based on the known history and a set of computed future control actions. The optimizer calculate this future actions

after looking for the objective function optima and by taking into consideration the current system state. At each time instant the problem optimization is performed and new decision variables are found.

Let's assume that the forest, in conjunction with the cutting and chipping working teams is the industrial plant which produces wood chips. Those wood chips can be viewed as stored into wood piles. Hence each wood pile will be analysed as being a warehouse where a finite amount of product is available and whose stock can be incremented by forwarding more wood logs into the pile. The distribution centre is composed by the set of vehicles that carries the wood chips from the piles location to the customers and the roads that link all the supply chain nodes. In order to apply MPC it is necessary to develop a discrete time model able to describe the system dynamics. Within the MPC context this model will be incorporated in the constraints set associated to the optimization problem. In the present case one seeks to minimize the costs in a weekly time scale. Following, the important aspects for the MPC controller will be defined, namely, the definition of the problem's constants, sets, variables, state variables, decision variables, balance equations, objective functions and constraints.

Constants

- HP Prediction horizon expressed in days;
 HC Control horizon expressed in days;
 np Number of wood piles ($np \in \mathbb{N}$);
 nc Number of power plants ($nc \in \mathbb{N}$);
 Qv Volume of wood chips, in m^3 , transported by a truck.

Sets

- $\mathcal{K} = \{1, \dots, HP\}$ Set of HP time periods;
 $\mathcal{P} = \{1, \dots, np\}$ Set of the np available wood piles for $np \in \mathbb{N}$;
 $\mathcal{C} = \{1, \dots, nc\}$ Set of the nc available clients for $nc \in \mathbb{N}$;
 $\mathcal{V}(k) = \{1, \dots, v(k)\}$ Set of the $v(k)$ vehicles (trucks) used during time period $k \in \mathcal{K}$ for $v(k) \in \mathbb{N}$.

Variables

- $V(k)$ Maximum number of available trucks at time period $k \in \mathcal{K}$;
 $H(k)$ Maximum number of available truck working hours in time period $k \in \mathcal{K}$;
 $s(k)$ Monetary cost, in monetary units (m.u.), of using a truck for a period of time $k \in \mathcal{K}$;
 $c_{ij}(k)$ Transportation cost, in m.u., of carrying a load from wood pile $i \in \mathcal{P}$ to the client $j \in \mathcal{C}$ during time period $k \in \mathcal{K}$;
 $\rho_i(k)$ Energy density per unit of wood chips volume, expressed in MWh/m^3 at pile $i \in \mathcal{P}$ during the time period $k \in \mathcal{K}$;
 $h_{ij}(k)$ Time required to perform a full load cycle from wood pile $i \in \mathcal{P}$ to client $j \in \mathcal{C}$ during time period $k \in \mathcal{K}$;
 d_j Amount of energy requested by client $j \in \mathcal{C}$ for the final period.

State Variables

$p_i(k)$ Currently available wood chips at pile $i \in \mathcal{P}$;

$\varepsilon_j(k)$ Currently available energy at client $j \in \mathcal{C}$.

Decision Variables

$\phi_{ij}(k)$ Number of trips between pile $i \in \mathcal{P}$ and client $j \in \mathcal{C}$ in time period $k \in \mathcal{K}$;

$v(k)$ Number of vehicles allocated for transport during time period $k \in \mathcal{K}$.

Balance Equations The overall energy delivered at power plant $j \in \mathcal{C}$ at the final of time period $k \in \mathcal{K}$ is equal to the sum of the available energy from the previous time period with the delivered energy taken from each of the possible wood piles $i \in \mathcal{P}$ to client j . This statement can be expressed mathematically using the following dynamic equation:

$$\varepsilon_j(k) = \varepsilon_j(k-1) + Qv \sum_{i \in \mathcal{P}} \phi_{ij}(k) \cdot \rho_i(k) \quad (1)$$

On the other hand, the currently available volume of wood chips at wood pile i is equal to the value existing in the previous time period minus the current wood volume shipped from this wood pile to the set of all clients.

$$p_i(k) = p_i(k-1) - Qv \sum_{j \in \mathcal{C}} \phi_{ij}(k) \quad (2)$$

Objective Function Several objective functions can be employed, generally to maximize profits and/or minimize costs. In this work we seek to minimize the costs involved in the transportation, analogous to the ones proposed in the works of [23, 24], along the full prediction horizon HP . This figure-of-merit, denoted hereafter by J , will be computed in the following way:

$$J = C_1 + C_2 \quad (3)$$

where C_1 denotes the cost of delivering the required amount of wood chips as is obtained by:

$$C_1 = \sum_{k \in \mathcal{K}} \sum_{i \in \mathcal{P}} \sum_{j \in \mathcal{C}} \phi_{ij}(k) \cdot c_{ij}(k) \quad (4)$$

and C_2 is the cost of using a fleet composed of an arbitrary number of vehicles. It is assumed that all the trucks have the same characteristics hence,

$$C_2 = \sum_{k \in \mathcal{K}} s(k) \cdot v(k) \quad (5)$$

Constraints In order to describe the operational behaviour of the addressed supply chain some constraints must be imposed to the optimization problem. First of all the positivity limits imposed to all the decision variables. In addition, the number of

vehicles used in a given time period k must be bounded by the maximum number of vehicles available to the day. That is,

$$v(k) \leq V(k) \quad (6)$$

moreover all the decision variables must be integer. Hence the optimization problem must be solved using integer programming problem approaches.

Let's assume that $\bar{h}(k) = \max\{h_{ij}(k)\}$ for all possible arcs connecting the piles $i \in \mathcal{P}$ to the clients $j \in \mathcal{C}$. In order to ensure that all the delivered energy must be made by a truck and that the number of trips are bounded by the number of available trucks, at that particular time instant, and by the available working hours per truck the following constraint is introduced:

$$\sum_{i \in \mathcal{P}} \sum_{j \in \mathcal{C}} \phi_{ij}(k) \leq v(k) \cdot \frac{H(k)}{\bar{h}(k)} \quad (7)$$

The next constraint is used to ensure that the delivered energy to the client $j \in \mathcal{C}$, at the end of the planning time horizon, must be within an interval of $d_j \pm \delta$. That is,

$$d_j - \delta \leq \varepsilon_j(HP) \leq d_j + \delta \quad (8)$$

The predicted value of $\varepsilon_j(k)$ at $k = HP$ can be computed by using the balance equation (1) leading to:

$$\varepsilon_j(HP) = \varepsilon_j(k) + Qv \sum_{i \in \mathcal{P}} \rho_i(k) \left[(HP - HC + 1) \cdot \phi_{ij}(HC) + \sum_{a=k+1}^{HC-1} \phi_{ij}(a) \right] \quad (9)$$

The last constraint is to ensure that, at the end of the planning horizon, the amount of wood chips at any pile $i \in \mathcal{P}$ is non-negative. That is,

$$p_i(HP) \geq 0 \quad (10)$$

One can get this predicted value iterating the balance equation (2), leading to:

$$p_i(HP) = p_i(k) - Qv \sum_{i \in \mathcal{P}} \left[(HP - HC + 1) \cdot \phi_{ij}(HC) + \sum_{a=k+1}^{HC-1} \phi_{ij}(a) \right] \quad (11)$$

Notice that, for both (9) and (11), it was supposed that $\phi_{ij}(a) = \phi_{ij}(HC)$ for $HC < a \leq HP$.

4 Case Study

The biomass supply chain considered as case study has nine piles, each one with different characteristics in terms of quantity and energy density, and three clients. Each client, starts with a certain level of energy, in this case study, $\epsilon_j(0) = 0 \forall j \in C$, and require different amounts of energy for a maximum period of five days. Table 1 represents some of the characteristics associated to the piles and clients. The considered time step is one day, and the prediction horizon and control horizon are initially equal to five steps ahead, corresponding to five working days, and consecutively decrease as the time progresses. The trucks' fleet is considered homogeneous, each one able to transport 25 m^3 and to work 9 h/day. In each day it is possible to use a maximum of four trucks. The monetary cost of using a truck, s , is 2 m.u. for any day. Table 2 shows the data correspondent to variables c_{ij} and h_{ij} . These variables' values are considered constant for the entire time period.

For each time period $k \in \mathcal{K}$ the controller must be able to compute the required number of trips, $\phi_{ij}(k)$, between pile $i \in \mathcal{P}$ and client $j \in C$, as well as the number of vehicles, $v(k)$, needed to perform the transportation. At the end of each time instant $k \in \mathcal{K}$, real input regarding the system states is feedback into the MPC controller and new decision variables are computed if needed. A disturbance in the delivery was introduced at the end of the second day. This was done in order to observe the controller behaviour on the tasks redistribution during the remaining days. In Table 3 it is possible to observe the controller performance for the total period of one week. As can be observed during simulation $k=1$, an initial distribution of tasks between piles and clients was proposed in order to comply with the orders to the final of the week. As defined in the MPC methodology, only the first decision variables are,

Table 1 Variables associated with piles (left): initial wood chips quantity, energy density; and clients (right): amount of energy requested for the period

i	1	2	3	4	5	6	7	8	9	j	1	2	3
$p_i(0)$ (m^3)	210	250	200	230	290	320	290	220	260	d_j (MWh)	1500	1000	2000
ρ_i (MWh/ m^3)	3.50	3.00	3.60	3.30	3.50	3.10	3.00	3.60	3.80				

Table 2 Transportation cost, c_{ij} , and required time, h_{ij} , for taking a load from pile $i \in \mathcal{P}$ to the client $j \in C$

i		1	2	3	4	5	6	7	8	9
$j = 1$	c_{ij} (m.u.)	4.00	3.14	3.99	2.50	5.49	10.45	2.28	5.61	9.75
	h_{ij} (h)	2.00	1.57	1.33	1.25	1.83	2.09	1.14	1.87	1.95
$j = 2$	c_{ij} (m.u.)	3.08	9.32	3.15	1.92	1.70	3.36	10.60	6.28	3.14
	h_{ij} (h)	1.54	2.33	1.05	1.92	0.85	1.12	2.65	3.14	1.57
$j = 3$	c_{ij} (m.u.)	2.34	3.30	6.15	8.85	1.98	3.18	4.20	5.08	4.46
	h_{ij} (h)	0.78	1.10	2.05	2.95	0.99	1.59	2.10	2.54	2.33

Table 3 Number of trips, $\phi_{ij}(k)$, between pile $i \in \mathcal{P}$ and client $j \in \mathcal{C}$ and number of vehicles, $v(k)$, needed in each time period

Simulation $k = 1$																																																	
Day 1 ($v = 4$)									Day 2 ($v = 3$)									Day 3 ($v = 4$)									Day 4 ($v = 4$)									Day 5 ($v = 4$)													
$j \setminus i$	1	2	3	4	5	6	7	8	9	$j \setminus i$	1	2	3	4	5	6	7	8	9	$j \setminus i$	1	2	3	4	5	6	7	8	9	$j \setminus i$	1	2	3	4	5	6	7	8	9	$j \setminus i$	1	2	3	4	5	6	7	8	9
1	0	0	0	0	0	0	2	0	0	1	0	0	0	2	0	0	6	0	0	1	0	0	3	0	0	0	0	0	0	1	0	0	1	0	0	0	3	0	0	1	0	1	0	0	0	0	0	0	0
2	0	0	0	0	0	0	0	0	0	2	0	0	0	0	0	0	0	0	0	2	0	0	0	6	0	0	0	0	1	2	0	0	0	1	1	0	0	0	1	2	0	0	0	0	0	0	0	0	2
3	0	0	0	0	8	1	0	0	0	3	0	0	0	0	0	0	0	0	0	3	0	0	0	0	1	0	0	0	0	3	0	0	0	0	1	1	0	0	1	3	8	0	0	0	0	0	1	0	0

Simulation $k = 2$																																							
Day 2 ($v = 4$)									Day 3 ($v = 4$)									Day 4 ($v = 4$)									Day 5 ($v = 3$)												
$j \setminus i$	1	2	3	4	5	6	7	8	9	$j \setminus i$	1	2	3	4	5	6	7	8	9	$j \setminus i$	1	2	3	4	5	6	7	8	9	$j \setminus i$	1	2	3	4	5	6	7	8	9
1	0	1	0	0	0	0	5	0	0	1	0	0	1	1	0	0	0	0	0	1	0	0	3	1	0	0	0	0	0	1	0	0	0	0	0	0	4	0	0
2	0	0	0	3	0	0	0	0	1	2	0	0	0	4	0	0	0	0	1	2	0	0	0	0	1	0	0	0	1	2	0	0	0	0	0	0	0	0	0
3	0	0	0	0	0	1	0	0	0	3	2	0	0	0	1	1	0	0	0	3	5	0	0	0	0	0	0	0	0	3	1	0	0	0	1	0	0	0	1

Simulation $k = 3$																													
Day 3 ($v = 4$)									Day 4 ($v = 4$)									Day 5 ($v = 3$)											
$j \setminus i$	1	2	3	4	5	6	7	8	9	$j \setminus i$	1	2	3	4	5	6	7	8	9	$j \setminus i$	1	2	3	4	5	6	7	8	9
1	0	1	0	0	0	0	1	0	0	1	0	0	0	1	0	0	2	0	0	1	0	0	4	1	0	0	2	0	0
2	0	0	0	1	0	0	0	0	0	2	0	0	0	3	1	0	0	0	2	2	0	0	0	0	0	0	0	0	0
3	7	0	0	0	1	0	0	0	0	3	0	0	0	0	1	0	0	0	1	3	1	0	0	0	0	0	0	0	0

Simulation $k = 4$																			
Day 4 ($v = 4$)									Day 5 ($v = 3$)										
$j \setminus i$	1	2	3	4	5	6	7	8	9	$j \setminus i$	1	2	3	4	5	6	7	8	9
1	0	0	2	2	0	0	4	0	0	1	0	0	2	0	0	0	0	0	0
2	0	0	0	3	0	0	0	0	0	2	0	0	0	0	1	0	0	0	2
3	0	0	0	0	0	0	0	0	0	3	1	0	0	0	1	0	0	0	1

Simulation $k = 5$									
Day 5 ($v = 3$)									
$j \setminus i$	1	2	3	4	5	6	7	8	9
1	0	0	2	0	0	0	0	0	0
2	0	0	0	0	1	0	0	0	2
3	1	0	0	0	1	0	0	0	1

in fact, implemented. At the end of the second day a disturbance, concerning the non-fulfillment of all the planned tasks, was introduced. Namely, with the defined by the controller, client 1 should stay with a total of 600 MWh at the end of day 2. However, 75 MWh were not delivered. The following simulations show that the MPC controller automatically redistributed the non-accomplished tasks for the remaining days, ensuring customers' requirements, with the lowest transportation costs.

5 Conclusions

Supply chains are complex systems that encompass several stakeholders and interdependent processes. This complexity is further evidenced when the supply chain nodes are geographically scattered. Thus, it is important to apply efficient management tools to manage stocks and vehicles fleets, aiming minimize costs while ensuring quality. Furthermore, it is necessary to create strategies able to overcome possible disturbances that may occur in the system. In this work, it was proposed a MPC methodology to manage the transportation needs of a biomass supply chain. In order to demonstrate the applicability of the proposed MPC methodology, an exemplificative case study was analysed. The obtained results demonstrated that the use of the MPC methodology promotes the easily and timely rescheduling of tasks to cope with disturbances that may occur in the system. In the future it is intended to improve the model formulation, in order to encompass the entire supply chain, including the harvesting, forwarding and chipping processes and, thus, globally manage the supply chain interactions.

Acknowledgments This work was supported by the FCT—Fundação para a Ciência e Tecnologia through the PhD Studentship SFRH/BD/98032/2013, program POPH—Programa Operacional Potencial Humano and FSE—Fundo Social Europeu.

References

1. Eshlaghy, A.T., Razavi, M.: Modeling and simulating supply chain management. *Appl. Math. Sci.* **5**(17), 817–828 (2011)
2. Janvier-James, A.M.: A new introduction to supply chains and supply chain management: definitions and theories perspective. *Int. Bus. Res.* **5**(1), 194–207 (2012)
3. Mestan, E., Trkay, M., Arkun, Y.: Optimization of operations in supply chain systems using hybrid systems approach and model predictive control. *Ind. Eng. Chem. Res.* **45**, 6493–9503 (2006)
4. Park, B.C., Jeong, S.: A modeling framework of supply chain simulation. *J. Supply Chain Oper. Manage.* **12**(2), 91–106 (2014)
5. Perea, E., Grossmann, I., Ydstie, E., Tahmassebi, T.: Dynamic modeling and classical control theory for supply chain management. *Comput. Chem. Eng.* **24**, 1143–1149 (2000)
6. Badole, C.M., Jain, R., Rathore, A.P.S., Nepal, B.: Research and opportunities in supply chain modeling: a review. *Int. J. Supply Chain Manage.* **1**(3), 63–86 (2012)
7. Brandenburg, M., Govindan, K., Sarkis, J., Seuring, S.: Quantitative models for sustainable supply chain management: developments and directions. *Eur. J. Oper. Res.* **233**(2), 299–312 (2014)
8. Min, H., Zhou, G.: Supply chain modeling: past, present and future. *Comput. Ind. Eng.* **43**, 231–249 (2002)
9. Mastragostino, R., Patel, S., Swartz, C.L.E.: Robust decision making for hybrid process supply chain systems via model predictive control. *Comput. Chem. Eng.* **62**, 37–55 (2014)
10. Perea-Lpez, E., Ydstie, B.E., Grossmann, I.E.: A model predictive control strategy for supply chain optimization. *Comput. Chem. Eng.* **27**, 1201–1218 (2003)
11. Puigjaner, L., Lanez, J.M.: Capturing dynamics in integrated supply chain management. *Comput. Chem. Eng.* **32**, 2582–2605 (2008)
12. e Hashem, S.M.J.M.A., Aryanezhad, M.B., Sadjadi, S.J.: An efficient algorithm to solve a multi-objective robust aggregate production planning in an uncertain environment. *Int. J. Adv. Manuf. Technol.* **58**(5–8), 765–782 (2012)
13. Li, X., Marlin, T.E.: Robust supply chain performance via model predictive control. *Comput. Chem. Eng.* **33**, 2134–2143 (2009)
14. Fu, D., Aghezzaf, E.H., Keyser, R.D.: A model predictive control framework for centralised management of a supply chain dynamical system. *Syst. Sci. Control Eng. Open Access J.* **2**(1), 250–260 (2014)
15. Kapsiotis, G., Tzafestas, S.: Decision making for inventory/production planning using model-based predictive control. *Parallel and Distributed Computing in Engineering Systems*, pp. 551–556 (1992)
16. Wang, W., Rivera, D.E., Kempf, K.G.: Model predictive control strategies for supply chain management in semiconductor manufacturing. *Int. J. Prod. Econ.* **107**, 56–77 (2007)
17. Hai, D., Hao, Z., Ping, L.Y.: Model predictive control for inventory management in supply chain planning. *Adv. Control Eng. Inf. Sci.* **15**, 1154–1159 (2011)
18. Pinho, T.M., Moreira, A.P., Veiga, G., Boaventura-Cunha, J.: Overview of mpc applications in supply chains: potential use and benefits in the management of forest-based supply chains. *For. Syst.* **24**(3), 1–15 (2015)
19. Sarimveis, H., Patrinos, P., Tarantilis, C.D., Kiranoudis, C.T.: Dynamic modeling and control of supply chain systems: a review. *Comput. Oper. Res.* **35**, 3530–3561 (2008)

20. Carlsson, D., Rnnqvist, M.: Backhauling in forest transportation: models, methods, and practical usage. *Can. J. For. Res.* **37**, 26122623 (2007)
21. Angus-Hankin, C., Stokes, B.: A.T.: The transportation of fuelwood from forest to facility. *Biomass Bioenergy* **9**(1–5), 191–203 (1995)
22. Mollera, B., Nielsenb, P.S.: Analysing transport costs of danish forest wood chip resources by means of continuous cost surfaces. *Biomass Bioenergy* **31**, 291–298 (2007)
23. Gunnarsson, H., Ronnqvist, M., Lundgren, J.T.: Supply chain modelling of forest fuel. *Eur. J. Oper. Res.* **158**, 103–123 (2004)
24. Frombo, F., Minciardi, R., Robba, M.B., Sacile, R.: A decision support system for planning biomass-based energy production. *Energy* **34**, 362–369 (2009)

Optimal Control for an Irrigation Problem with Several Fields and Common Reservoir

Sofia O. Lopes and Fernando A.C.C. Fontes

Abstract In a previous study, the authors developed the planning of the water used in the irrigation systems of a given farmland in order to ensure that the field cultivation is in a good state of preservation. In this paper, we introduce a model to minimize the water flowing into a reservoir that supplies different fields with different types of crops. This model is described as an optimal control problem where the water flow from a tap and the water used in the fields are the controls. The trajectories are described as the humidity in the soil and the amount of water in the reservoir.

1 Introduction

According to [1], the water demand in Portugal in the three sectors of activity—urban, industry and agriculture amounts to 7500×10^6 m³/year. The agriculture is responsible for 80 % of the water demand, most of it in the in the spring and summer periods, and it is estimated that 37.5 % is lost due to various inefficiencies. These facts affect strongly the agriculture production. It is, consequently, relevant to discuss the use of water in these conditions, and try to find the best technical solutions, economic and social, to improve the efficiency of water usage.

The irrigation planning systems here developed are based on the minimization of the volume of water used in irrigation (control), knowing that the variation of water in the soil (trajectory) is given by the hydrologic balance. The connections between an irrigation planning system and an optimal control problems are easily established, however this connection still has lot to be explored, see for example [2–4].

A model to optimize the water use in the irrigation of a farm field via optimal control (water flow) that takes into account the evapotranspiration, rainfall, losses by infiltration and runoff was developed in [5]. There, the solution was obtained

S.O. Lopes (✉) · F.A.C.C. Fontes
CMAT and Departamento de Matemática e Aplicações, Universidade do Minho,
Guimarães, Portugal
e-mail: sofialopes@math.uminho.pt

F.A.C.C. Fontes
Systec-ISR, Faculdade de Engenharia, Universidade do Porto, Porto, Portugal

for an “Yearly Planning” problem considering different weather scenarios with the help of the so called “precipitation factor” that is multiplied by the rainfall monthly average. In [6], the authors present the “Initial Planning Problem” for rainfall: this includes an extra term taking into account the rainfall in the previous time period (this rainfall model was statistically proven to be significant) where a comparison between this new model and the solution knowing the rainfall *a priori* was shown. A characterization of the solution using the necessary conditions of optimality was made in [7], and thereby the numerical results were validated. Most of these results and further details are collected in [8].

In this paper, we developed a model that allows to minimize the water used in a reservoir to supply different fields with different types of crops where the water of precipitation can be collected in a given area, having in mind that is crucial to ensure the good state of preservation of the cultivation field. The main contribution with respect to previous works is precisely the fact that the model includes several different fields that share a common reservoir.

This paper is organized as follows. Section 2 presents the problem formulation. Section 3 describes the numerical model and Sect. 4 reports numerical results in different scenarios. Concluding remarks are drawn in Sect. 5.

2 The Problem

In order to describe our problem, we start by defining the variables used. The controls are: v total water flow coming from the tap and u_j water flow introduced in field j via its irrigation system. The states are: x_j water in the soil of field j and y total of amount of water stored in reservoir.

We intend to minimize the total of water flow coming from the tap to a reservoir. The objective function is:

$$\min \int_0^T v(t)dt.$$

The variation of water in reservoir is given by:

$$\dot{y}(t) = v(t) - \sum_{j=1}^P A_j u_j(t) + Cg(t),$$

where A_j represents the area of each field j and $Cg(t)$ represents collected water in a certain area C coming from the precipitation g in the time t .

The variation of water in the soil is given by the hydrologic equation, that is, the variation of water in the soil is equal to what enters (water via irrigation systems and precipitation) minus the loss (evapotranspiration of each crop h_j and loss by deep percolation $\beta x_j(t)$, a percentage of water that is in the soil).

So,

$$\dot{x}_j(t) = u_j + g(t) - h_j(t) - \beta x_j(t), \quad \forall j = 1, \dots, P$$

We note that each field has only one crop.

In order to ensure that the crop is in good state of conservation, the water in the each field has to be sufficient to satisfy the hydric needs of each crop (x_{\min}), that is:

$$x_j(t) \geq x_{\min}.$$

The physical limitations of: the amount of water that comes from a tap, the amount of water that comes from the irrigation systems and the reservoir are given, respectively, by:

$$\begin{aligned} y(t) &\in [0, y_{\max}] \\ u_j(t) &\in [0, M_j] \\ v(t) &\in [0, \sum_j A_j M_j] \end{aligned}$$

where y_{\max} is the maximum quantity of water in the reservoir and M_j is the maximum water flow coming from the tap in each field.

We assume that at the initial time the humidity of the soil in each field and the water in the reservoir are given. Also, the water in the reservoir at the initial time and to the final time are imposed to be equal. So, we assume that:

$$\begin{aligned} x_j(0) &= x_{0j} \\ y(0) &= y(T) = y_0 \end{aligned}$$

In summary, the optimal control formulation for our problem is:

$$\min \int_0^T v(t) dt$$

subject to:

$$\dot{x}_j(t) = -\beta x_j(t) + u_j + g(t) - h_j(t) \quad \text{a.e. } t \in [0, T], \quad \forall j = 1, \dots, P$$

$$\dot{y}(t) = v(t) - \sum_{j=1}^P A_j u_j(t) + Cg(t) \quad \text{a.e. } t \in [0, T],$$

$$x_j(t) \geq x_{\min}, \quad \forall t \in [0, T], \quad \forall j = 1, \dots, P$$

$$y(t) \in [0, y_{\max}] \quad \forall t \in [0, T]$$

$$u_j(t) \in [0, M_j] \quad \text{a.e., } \forall j = 1, \dots, P$$

$$v(t) \in [0, \sum_j A_j M_j] \quad \text{a.e.}$$

$$x_j(0) = x_{0j}, \quad \forall j = 1, \dots, P$$

$$y(0) = y(T) = y_0$$

where the constant parameters involved are the following:

- P : number of fields;
- A_j : Area of field j ;
- C : Area of the collector of precipitation water;
- β : the percentage of loss in the soil;
- x_{\min_j} : hydric needs of the culture in each field (per m^2);
- y_{\max} : the maximum quantity of water in the reservoir;
- M_j : maximum water flow coming from the tap of time t in each field (per m^2);
- x_{0_j} : the humidity of the soil in each field (per m^2);
- y_0 : the quantity of water in the reservoir at initial time.

The decisions variables are the states (x_j, y) and the controls (u_j, v) functions for $j = 1, \dots, P$. These and other time-varying functions are described in the following way:

- $x_j(t)$: water in the soil of field j at time t (per m^2);
- $u_j(t)$: water flow introduced in field j via its irrigation systems at time t (per m^2);
- $y(t)$: total of amount of water stored in reservoir at time t (maximum capacity y_{\max});
- $v(t)$: total water flow coming from the tap at time t ;
- $g(t)$: the precipitation at time t (per m^2);
- $h_j(t)$: the evapotranspiration at time t of each field (culture) (per m^2);

The solution to this optimal control problem can be characterized by necessary conditions of optimality in the form of a maximum principle (see e.g. [8–13]). In this paper, however, we discuss the numerical results.

3 Numerical Model for the Irrigation Problem

In this section, we obtain the numerical solution to our problem transcribing it into a sequence of finite dimensional linear programming problems.

For that, we start by defining a finite number of time instants $i = 1, \dots, N + 1$

$$\begin{aligned}x_i &= x(t_i) \\u_i &= u(t_i)\end{aligned}$$

where $t_i = (i - 1)h$ and $h = T/N$.

We use the Euler-type discretization to the differential equations:

$$\dot{x} = f(t, x, u) \text{ is approximated to } x_i = x_{i-1} + hf(t_{i-1}, x_{i-1}, u_{i-1}).$$

To implement this optimization problem, we use *fmincon* function of MatLab with the algorithm “active set”, by default and the parameter “Tolfun” is considered $1E - 6$.

3.1 Rainfall Models

To estimate rainfall we use the monthly rainfall data from Instituto Português do Mar e da Atmosfera (<http://www.ipma.pt>), in the Lisbon area. We defined an average (using the 10 years data) rainfall for each month of the year, the *rain monthly average* is: $10^{-3} \times$

J	F	M	A	M	J	J	A	S	O	N	D
111.4	94.7	80.2	57.1	29.62	18.84	1.26	7.04	30.6	127	121.98	119.3 (m ³ /month)

Therefore $g(t_i) = \text{rain monthly average}(t_i)$.

3.2 Evapotranspiration Model

We used the Penman—Monteith methodology [14] to calculate evapotranspiration of our culture along the year. In order to do so, we use the formulation:

$$ET(t_i) = K_c ET_0(t_i),$$

where $K_c = 0.825$ is the culture coefficient for the evapotranspiration (in our case potatoes) and ET_0 is the tabulated reference value of evapotranspiration that we consulted in [15] for the Lisbon region. The evapotranspiration of our culture in Lisbon is given by the following table: $10^{-3} \times$

J	F	M	A	M	J	J	A	S	O	N	D
19.8	28.0	55.27	89.1	116.32	137.77	155.92	136.95	84.97	53.62	22.27	16.5 (m ³ /month)

So, $h(t_i) = Et(t_i)$.

4 Results

To simulate our problem, we assume that:

$$\begin{aligned}
 P &= 3 & T &= 12 & M_j &= 10 \text{ m}^3/\text{month for each field} \\
 y_{\max} &= 0.05 \times A_t & y_0 &= 0.01 \times A_t & \beta &= 15\%
 \end{aligned}$$

where A_t is the total area.

Our first simulation corresponds to a closed reservoir that supplies three fields with the same area in which each field has a different culture. In this example, we consider the three crops: wheat, sugar cane and olive, and the following parameters:

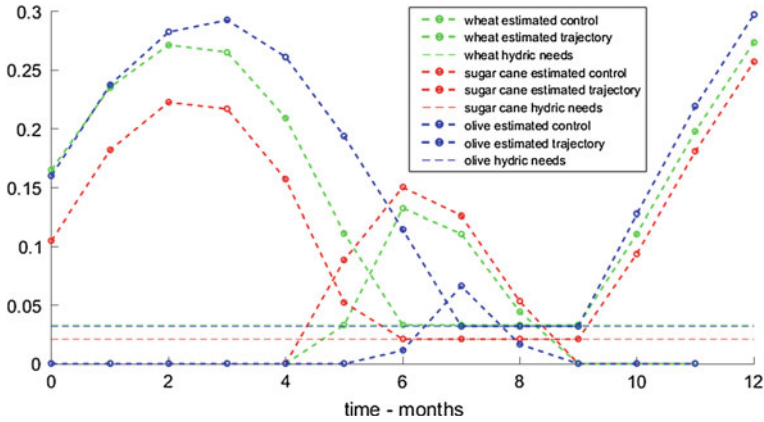


Fig. 1 Humidity in the soil

$$x_{\min} = [0.033 \ 0.021 \ 0.032] \quad K_c = [0.825 \ 0.95 \ 0.5] \quad \text{area} = [1 \ 1 \ 1]$$

$$x_0 = 5x_{\min} \quad C = 0$$

The humidity of the soil (estimated trajectory) and the amount of water used in each field (estimated control) is given in Fig. 1.

As expected, the crops need water between May and September, the months when the water consumption is higher are June, July, the crop that needs less water is olive, and the crop that needs more water is the sugar cane.

The estimated amount of water to irrigate the three field per m^2 is $0.8330 \text{ m}^3/\text{year}$, where in each field we spend the following amount of water per m^2 :

$$u_{wheat} := [0 \ 0 \ 0 \ 0 \ 0 \ 0.0331 \ 0.1323 \ 0.1109 \ 0.0445 \ 0 \ 0 \ 0];$$

$$u_{sugar \ cane} := [0 \ 0 \ 0 \ 0 \ 0 \ 0.0885 \ 0.1500 \ 0.1262 \ 0.0533 \ 0 \ 0 \ 0];$$

$$u_{olive} := [0 \ 0 \ 0 \ 0 \ 0 \ 0 \ 0.0113 \ 0.0662 \ 0.0167 \ 0 \ 0 \ 0].$$

In Fig. 2, we describe the variation of water in the reservoir and the amount of water that comes from a tap.

We note that the water in the reservoir at the initial time is equal to the water at the final time. The water that comes from the tap starts to be consumed earlier than the hydric needs of the crops, so the water storage in reservoir increases. June and July are the month when the irrigation takes the highest value, and also when the water in the reservoir decrease. For the water in the reservoir at the initial time to be equal to the one at the final time, the tap is closed later than the needs of the crop, in November.

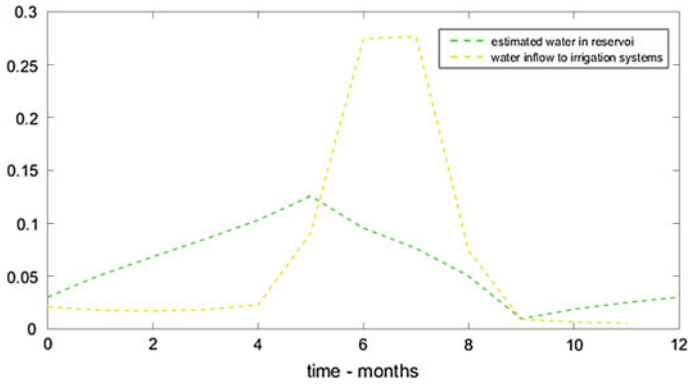


Fig. 2 Water needs

In the next simulation, we consider that the fields have different areas. We consider the same initial data of the previous problem and we assume that fields have 1000 m² of wheat, 750 m² of sugar cane and 1250 m² of olive. That is:

$$x_{\min} = [0.033 \ 0.021 \ 0.032] \quad K_c = [0.825 \ 0.95 \ 0.5] \quad A = [1000 \ 750 \ 1250]$$

$$x_0 = 5x_{\min} \quad C = 0$$

The results obtained are reported in Fig. 3:

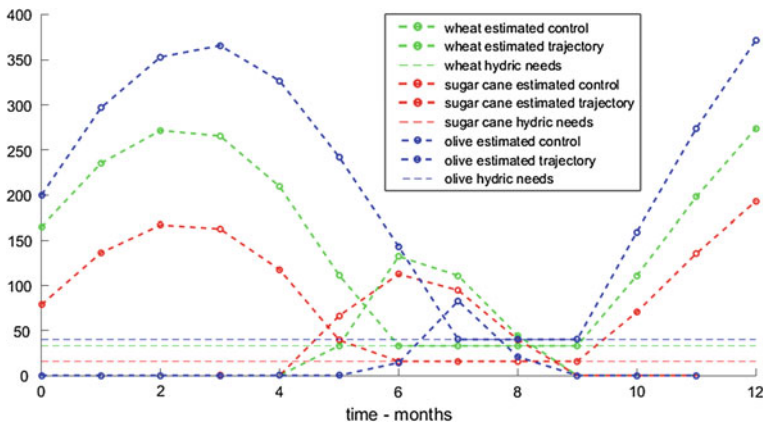


Fig. 3 Humidity in soil with fields having different areas

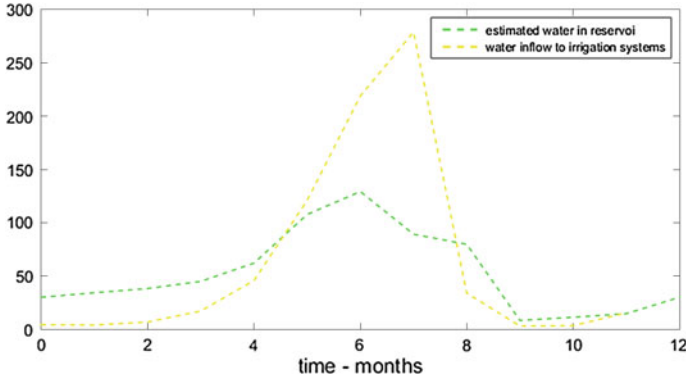


Fig. 4 Water needs where the fields have different areas

Comparing these results with the previous ones, we can see that in this case the needs of water for the wheat field are higher than the ones for sugar cane field.

The estimated amount of water to irrigate the three fields is 752.0795 m³/year, where in each field we spend the following amount of water:

$$\begin{aligned}
 u_{wheat} &:= [0 \ 0 \ 0 \ 0 \ 0 \ 33.06 \ 132.33 \ 110.8938 \ 44.45 \ 0 \ 0 \ 0]; \\
 u_{sugar\ cane} &:= [0 \ 0 \ 0 \ 0 \ 0 \ 566.37 \ 112.51 \ 94.66 \ 39.96 \ 0 \ 0 \ 0]; \\
 u_{olive} &:= [0 \ 0 \ 0 \ 0 \ 0 \ 14.19 \ 82.79 \ 20.86 \ 0 \ 0 \ 0].
 \end{aligned}$$

In Fig. 4, we describe the variation of water in the reservoir and the variations on the amount of water that comes from a tap.

We can see that variations of the water in the reservoir and the behaviour of the water that comes from the tap is similar to the previous simulation.

In the next simulation, as in previous ones, we consider the irrigating of three fields with different crops and different areas, however in this case we take advantage of the rainfall information. We assume that reservoir has an area of 30 m² to collect rain fall. That is,

$$\begin{aligned}
 x_{min} &= [0.033 \ 0.021 \ 0.032] & K_c &= [0.825 \ 0.95 \ 0.5] & A &= [1000 \ 750 \ 1250] \\
 x_0 &= 5x_{min} & C &= 30
 \end{aligned}$$

The variation of water in the reservoir and the variation of the amount of water that comes from a tap are described in Fig. 5.

In this case, the amount of water needed is 721.1735 m³/year, which results in a reduction of 4.1% in the water needs. We can see that in November the water that comes from the tap is less than the one in the previous simulation. However, the water saving is negligible. We may conclude that a larger collection area of the reservoir would be of advantage.

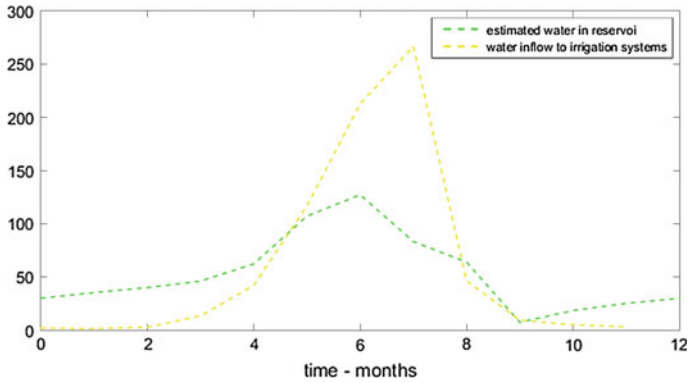


Fig. 5 Water needs with $C = 30$

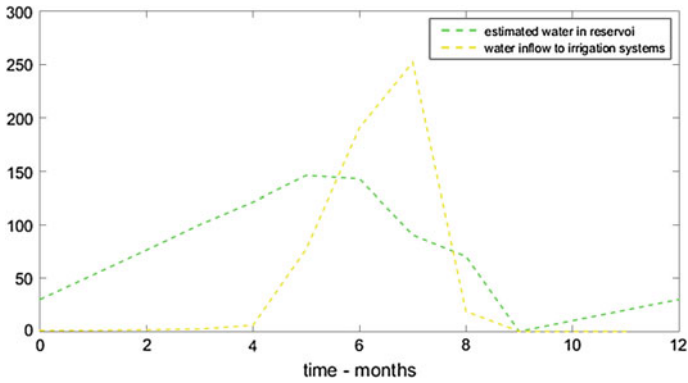


Fig. 6 Water needs with $C = 200$

In the last simulation, we assume that the top of reservoir has now 200 m^2 of area. The variation of water in the reservoir and the variation of the amount of water that comes from a tap is described in Fig. 6.

We can see that until April the water from the precipitation is saved in the reservoir and until this month the tap is not opened. The tap is closed earlier than the previous simulations; it is closed in September. In this case the amount of water needed is $550.2994 \text{ m}^3/\text{year}$, resulting in a reduction of 26, 83 % in the water needs.

5 Conclusion

We have developed an irrigation planning model to minimize the water used to supply different fields with different types of crops. The main contribution with respect to previous works is precisely the fact that the model includes several different fields

that share a common reservoir, which not only serves as storage, but also is from where the water inflow coming from either tap or rain fall is collected. The optimal control problem formulated is solved numerically for different scenarios of crop area and reservoir capacity.

Acknowledgments Research carried out while the 2nd author was a visiting scholar at Texas A&M University, College Station, USA. The support from Texas A&M and FEDER/COMPETE2020-POCI/FACT funds through grants POCI-01-0145-FEDER-006933 - SYSTEC, PTDC/EEI-AUT/2933/2014 and UID/MAT/00013/2013 are acknowledged.

References

1. Pedro, S., Luis, R., Alda, C.: *Usos da água na agricultura 2011*. Instituto Nacional de Estatística (2011)
2. Rigon, R., Bertoldi, G.: *GEOTOP A Hydrological Balance Model Technical Description and Programs Guide*. Università degli Studi di Trento, 2004
3. Cochrane, T.A., Krom, T.D., Brown, P.D.: Optimal on-farm irrigation scheduling with a seasonal water limit using simulated annealing. *Agric. Water Manage.* **97**, 892–900 (2010)
4. Gandolfi, C., Soncini-Sessa, R., Agostani, D., Galelli, S.: Building a metamodel of irrigation district distributed-parameter model. *Agric. Water Manage.* **97**, 187–200 (2010)
5. Lopes, S., Fontes, F., Pereira, R.M.S., Machado, G.J.: Irrigation planning in the context of climate change. In: *Mathematical Models for Engineering Science—MMES11*, pp. 239–244 (2011)
6. Lopes, S., Fontes, F., Pereira, R.M.S., Gonçalves, M., Machado, G.J.: Irrigation planning: an optimal control approach. In: *International Conference of Numerical Analysis and Applied Mathematics, AIP Conference Proceedings*, vol. 1558, pp. 622–626 (2013)
7. Lopes, S.O., Fontes, F.A.C.C., Pereira, R.M.S., de Pinho, M.D.R., Ribeiro, C.: Optimal control for an irrigation planning problem: characterization of solution and validation of the numerical results. *Lecture Notes in Electrical Engineering*, vol. 321, pp. 157–167 (2015)
8. Lopes, S.O., Fontes, F.A.C.C., Pereira, R.M.S., Pinho, M.D.R., Gonçalves, A.M.: Optimal control applied to an irrigation planning problem. *Math. Probl. Eng.* (2016)
9. de Pinho, M.R., Ferreira M.M., Fontes, F.A.C.C.: Unmaximized inclusion necessary conditions for nonconvex constrained optimal control problems. *ESAIM: Control Optimisation Calc. Var.* **11**(4), 614–632 (2005)
10. Fontes, F.A.C.C., Lopes, S.O.: Normal forms of necessary conditions for dynamic optimization problems with pathwise inequality constraints. *J. Math. Anal. Appl.* **399**(1), 27–37 (2013)
11. Lopes, S.O., Fontes, F.A.C.C., de Pinho, M.D.R.: On constraint qualifications for nondegenerate necessary conditions of optimality applied to optimal control problems. *Discrete Continuous Dyn. Syst.-A*, **29**(2) (2011)
12. Lopes, S.O., Fontes, F.A.C.C., de Pinho, M.D.R.: An integral-type constraint qualification to guarantee nondegeneracy of the maximum principle for optimal control problems with state constraints. *Syst. Control Lett.* **62**(8), 686–692 (2013)
13. Vinter, R.: *Optimal Control*. Birkhäuser, Boston (2000)
14. Walter, I.A., Allen, R.G., Elliott, R., Itenfisu, D., et al.: *The ASCE standardized reference evapotranspiration equation*. Representative Task Committee on Standardized Reference Evapotranspiration, 2002
15. Raposo, J.R.: *A REGA—dos primitivos regadios as modernas técnicas de rega*. Fundação Calouste Gulbenkian (1996)

Mechanical Multi-agent Maneuvering Using Noncooperative DMPC

José Igreja, Filipe A. Barata and Carla Viveiros

Abstract Distributed Model Predictive Control is used to coordinate agents in multi-agent systems by managing set-points and coupling constraints. The coordination of multi-agent systems concept regards all type of control algorithms dependent on information interchange between subsystems. The control algorithms are developed to solve a series of static optimization problems with nonlinear coupling constraints by means of a typical receding horizon policy applied in predictive control design. For distributed scenarios, the motion of each agent is determined by the distributed algorithm as function of the information shared with the other agents making the individual behavior implicitly dependent on a global outcome or cost. The control algorithm is used to maneuver dynamically decoupled mechanical agents in a two dimensional scenario with obstacles avoidance. The found solution is meaningful to realize how Predictive Control can be an alternative to other solutions obtained through Dynamic Games, where the agents play an important role, in a strategic space, as game players or Computational Intelligence technique, where the agents present a self-organized behavior. Hence, the developed algorithm is useful to maneuver unmanned vehicles in mazes, formations and also for collision avoidance.

Keywords Multi-agent systems · Dynamic game theory · Distributed model predictive control · Nonlinear optimization

J. Igreja (✉) · F.A. Barata · C. Viveiros
Instituto Superior de Engenharia de Lisboa, IPL,
Rua Conselheiro Emídio Navarro, 1, 1959-007 Lisboa, Portugal
e-mail: jigreja@deea.isel.ipl.pt

F.A. Barata
e-mail: fbarata@deea.isel.ipl.pt

C. Viveiros
e-mail: cviveiros@deea.isel.ipl.pt

J. Igreja
INESC-ID, Rua Alves Redol 9, 1000-029 Lisboa, Portugal

1 Introduction

Model Predictive Control (MPC) is a well understood control methodology and is known for its advantages in advanced control systems since it allows constraints inclusion. This controller presents significant advantages for engineering applications when compared to other methods [1, 2] and can be straightforwardly extended to decentralized control. For distributed scenarios, the motion of each agent is determined by the distributed algorithm as function of the information shared with the other agents making the individual behavior implicitly dependent on a global outcome or cost. In distributed predictive control systems [3] agents are allowed, in an open information interchange infrastructure, to communicate and ultimately collaborate with their neighbors, in order to achieve local performance indexes proper for a global objective [4, 5]. In this paper, agent coordination is understood as a weaker form of cooperation where each agent plays a preset role. The used algorithms for the agents are greedy or selfish and the role of each agent in the global objective is dictated by the coordination dependencies that are included in the algorithms. Cooperative or altruistic algorithms are not treated in this paper, see for instance [6]. Some examples of animal behavior coordination are cattle herds moving across savanna or feeding habits in packs. Animals are not altruistic, most of the time, but they can vaguely cooperate in order to survive. Other examples of weak cooperation, without altruism, can be found on human behavior in a working environment. In multi-agent systems (MAS), (Objective) Coordination has been defined as managing dependencies in inter-agent activities [7]. On distributed control, the coordination of MAS concept regards all type of control algorithms dependent on information interchange between subsystems [8].

The concept was validated by developing a distributed MPC algorithm specialized in maneuvering mechanical agents in multi-agent environment for two dimensional special scenarios with obstacles and collision avoidance. For distributed scenarios, the motion of each agent is determined by the distributed algorithm as function of the information shared with the other agents making the individual behavior implicitly dependent on a global outcome or cost. The control algorithm is used to maneuver dynamically decoupled mechanical agents in a two dimensional scenario with obstacles avoidance. The found solution is meaningful to realize how predictive control can be an alternative to other solutions obtained through dynamic games, where the agents play an important role, in a strategic space, as game players or computational intelligence technique, where the agents present a self-organized behavior [9]. Hence, the developed algorithm is useful to maneuver unmanned vehicles in mazes, formations and also for collision avoidance. Typical applications are AGVs coordination, cooperative vehicles safety systems and formations hovering control, among others. The approach is related to the one describe in [10] (in its *greedy* version) but in the present case, solutions are found by (weak) cooperation or coordinated noncooperative setups, creating implicit and more self-organized solutions with potentially faster computation. Recently developed dynamic programming methods for formation control and

obstacle avoidance can be found in [11, 12]. An example of different kind of coordination in distributed MPC applied to house comfort energy efficiency based on energy prices is given in [13].

The main contributions focus on coordinated behavior between agents using implicit rules or dependencies, on distributed MPC algorithms that can perform in complex mazes with several constraints and on the analysis of different scenarios using dynamic game theory and computational intelligence. Results show that Coordination can be an alternative to cooperative DMPC due to its lower computational burden and reveals itself as more self-organized solution to distributed control. The rest of the paper is organized as follows: Sect. 2 introduces Noncooperative Distributed MPC in general. Section 3 describes distributed MPC for dynamically decoupled subsystems with coordination and the main result is proved. In Sect. 4 the concept validation setup is described and the results are analyzed. Section 5 draws conclusions.

2 Noncooperative Distributed MPC

In the centralized MPC (for N_s subsystems) problem (1)–(3), the objective is to solve an optimization, thus obtaining, at each instant in discrete time k , the inputs $u_i(k)$. The linear global system model is given by:

$$\min_U J(U; x(k)) = \sum_{i=1}^{N_s} w_i J_i(U_i; x_i(k)). \quad (1)$$

Also the quadratic cost function $J(k)$ has symmetric weighting matrices R_i and Q_i ,

$$J_i(k) = \sum_{j=1}^N (x_i^T(k+j) Q_i x_i(k+j) + u_i^T(k+j-1) R_i u_i(k+j-1)), \quad (2)$$

$$\begin{aligned} \text{s. t. } x(k+j+1) &= Ax(k+j) + Bu(k+j), \\ u_i &\in \mathcal{U}_i, \end{aligned} \quad (3)$$

where $w_i > 0$, $\sum_i w_i = 1$, \mathcal{U}_i is an admissible control set, $Q_i \geq 0$, $R_i > 0$, the state at discrete time k , $x_i(k)$, is a known subsystem and the pair $(A_i, Q_i^{1/2})$ is measurable. The decision variables are the inputs along the prediction horizon:

$$U = [u^T(k) \ u^T(k+1) \ \dots \ u^T(k+N-1)]^T. \quad (4)$$

With centralized MPC the optimum reachable performance is obtained, Pareto Optimal, where the outcome of interconnections amongst subsystems are taken into

account accurately. In case of control objectives conflict, they will be solved optimally. The control law uses a receding horizon strategy by applying only the first column of the optimal solution found $u^*(k) = [I \ 0 \ \dots \ 0]U^*$.

In a distributed noncooperative version of MPC (5)–(7) the overall dynamical model is divided and the total cost function are both replaced by local ones. Each local cost measures the impact of local control action and uses the information broadcasting by the other agents to predict future states, see for instance [10, 14]. The optimization problem for each agent is given by:

$$\min_{U_i} J_i(U_i, x_i(k)) = \sum_{j=1}^N x_i^T(k+j) Q_i x_i(k+j) + \sum_{j=0}^{N-1} u_i^T(k+j) R_i u_i(k+j), \quad (5)$$

$$\begin{aligned} s.t. \quad & x_i(k+j+1) = A_{ii}x_i(k+j) + B_{ii}u_i(k+j) \\ & + \sum_{l \neq i} (A_{il}x_l^p(k+j) + B_{il}u_l^p(k+j)) \quad (j=0, \dots, N-1), \end{aligned} \quad (6)$$

$$u_i \in \mathcal{U}_i. \quad (7)$$

Remark that $x_l^p(k), \dots, x_l^p(k+N)$ and $u_l^p(k), \dots, u_l^p(k+N)$, with $l \neq i$, are respectively the *planned* state and control action information received by the agent from all the others. The information obtained from solving the optimization procedure for all the other $(N_s - 1)$ subsystems will be incorporated in Eqs. (5)–(7). This noncooperative or *greedy* version gives at best a stable Nash Equilibrium (NE) solution, since cost function (5) only penalizes the state and inputs of subsystem i .

3 DMPC for Decoupled Subsystems with Coordination

In this section the distributed MPC procedure, for dynamically decoupled subsystems with coordination, along with proposed algorithm and its connections with dynamic noncooperative game theory, are described. Consider the linear state model for each decoupled subsystem i ($A_{ii} \neq 0, B_{ii} \neq 0$):

$$\begin{bmatrix} x_i(k+1) \\ y_i(k) \end{bmatrix} = \begin{bmatrix} A_{ii} & B_{ii} \\ C_i & 0 \end{bmatrix} \begin{bmatrix} x_i(k) \\ u_i(k) \end{bmatrix} \quad (8)$$

where A_{ii} , B_{ii} and C_i have $(n_i \times n_i)$, $(n_i \times m_i)$ and $(p_i \times n_i)$ dimensions, and $x_i(k)$, $y_i(k)$ and $u_i(k)$ are respectively, the states, the outputs and inputs. The predicted outputs at time $(k+j)$ are given by:

$$\begin{aligned}\hat{y}_i(k+j) &= \sum_{l=0}^{j-1} C_i A_{ii}^{j-l-1} B_{ii} u_i(k+l) + \hat{y}_{i0}(k+j), \\ \hat{y}_{i0}(k+j) &= C_i A_{ii}^j x_i(k) = \Gamma_i x_i(k),\end{aligned}\quad (9)$$

where \hat{y}_0 is the predicted output when the input is zero. For $j = 1 \dots N$, (9) the next predictive equations, are produced:

$$\hat{Y}_i = G_i U_i + \Gamma_i x_i(k) = G_i U_i + \hat{Y}_{i0}, \quad (10)$$

with

$$\begin{aligned}\hat{Y}_i &= [y_i^T(k+1) \dots y_i^T(k+N)]^T, \\ U_i &= [u_i^T(k) \dots u_i^T(k+N-1)]^T.\end{aligned}\quad (11)$$

Remark that Γ_i and G_i are the observability and Haenkel matrices of subsystem i , see [15]. The cost function for the underlined stated problem is given by:

$$J_i(k) = \sum_{j=1}^N e_i^T(k+j) Q_i e_i(k+j) + \sum_{j=0}^{N-1} u_i^T(k+j) R_i u_i(k+j), \quad (12)$$

where $e_i(k) = r_i(k) - y_i(k)$ is the error, the set-point series is $r_i(k)$, $x_i(k)$ is known, the pair $(A_{ii}, Q_i^{1/2})$ is measurable, the pair (A_{ii}, B_{ii}) is stabilizable and $Q_i \geq 0$, $R_i > 0$. The constraints to which the minimization is subject are:

- (1) Linear equality model constraints form Eq. (10):

$$\begin{bmatrix} I & -G_i \end{bmatrix} \begin{bmatrix} \hat{Y}_i \\ U_i \end{bmatrix} - \hat{Y}_{i0} = 0. \quad (13)$$

- (2) Bounds in U_i :

$$\begin{bmatrix} -I \\ I \end{bmatrix} U_i \leq \begin{bmatrix} -\underline{U}_i \\ \bar{U}_i \end{bmatrix}, \quad (14)$$

where \underline{U}_i and \bar{U}_i are lower and upper bounds on U_i , and I is the identity matrix with proper dimension.

- (3) Bounds in \hat{Y}_i :

$$\begin{bmatrix} -I \\ I \end{bmatrix} \hat{Y}_i \leq \begin{bmatrix} -\underline{Y}_i \\ \bar{Y}_i \end{bmatrix}, \quad (15)$$

where \underline{Y}_i and \bar{Y}_i are lower and upper bounds on \hat{Y}_i ;

(4) Nonlinear constraints for coordination and states trajectories:

$$F_{1i}(\widehat{X}_i, \widehat{X}_{l \neq i}^p) \leq 0, \quad (16)$$

$$F_{2i}(\widehat{X}_i) \leq 0, \quad (17)$$

where $F_1(\widehat{X})$ and $F_2(\widehat{X})$ are vectors of functions used for coordination and for state space constraints respectively. Linear constraint (16) is related to collision avoidance and (17) with obstacle avoidance. The information received from the other agents, $\widehat{X}_{l \neq i}^p$, is a vector containing their planned trajectories or states during the prediction horizon, wherein this case it includes position and velocity in the horizon N . Coordination is also maintained with set-points that are in general functions of the planned trajectories by the other agents:

$$P_i(\widehat{X}_{l \neq i}^p) = [r_i^T(k+1) \dots r_i^T(k+N)]^T, \quad (18)$$

with

$$r_i(k+j) = r_{0i}(k+j) + \sum_{l \neq i}^{N_s} C_{il} x_l^p(k+l), \quad (19)$$

where $r_{0i}(k+j)$ is a given preset trajectory, C_{il} is a compatibility matrix and N_s the total number of agents. Note that the cost function could include a terminal cost (cost-to-go) term, in Q_i , for feedback stability guarantee or some equivalent ingredient. The terminal cost can be obtained via infinite horizon unconstrained optimal control that satisfies the control and state constraints such as obtained in [2], but it will not be further discussed here. Each agent (subsystem with individual control) solves a equivalent static optimization problem [16] with coupled constraints:

$$\min_{Z_i} J_i(Z_i, x_i(k)) = \|P_i - M_y Z_i\|_{Q_i}^2 + \|M_u Z_i\|_{\mathcal{R}_i}^2, \quad (20)$$

$$s. t. \quad [I \quad -G_i] Z_i - \widehat{Y}_{i0} = 0, \quad (21)$$

$$\begin{bmatrix} -I \\ I \end{bmatrix} Z_i \leq \begin{bmatrix} -\underline{Z}_i \\ \overline{Z}_i \end{bmatrix}, \quad (22)$$

$$F_{1i}(\widehat{X}_i, \widehat{X}_{l \neq i}^p) \leq 0, \quad (23)$$

$$F_{2i}(\widehat{X}_i) \leq 0, \quad (24)$$

with

$$Z_i = \begin{bmatrix} \widehat{Y}_i \\ U_i \end{bmatrix}, \quad (25)$$

$M_y Z_i = \widehat{Y}_i$, $M_u Z_i = U_i$, matrix Q_i and R_i are block diagonal with blocks Q_i and R_i respectively. Once the optimization (20)–(24) is solved and hence the optimal solution obtained, Z_i^* , the control action is implemented by updating $u_i(k)$ with:

$$u_i^*(k) = \begin{bmatrix} U_i^*(1) \\ \vdots \\ U_i^*(m_i) \end{bmatrix}. \quad (26)$$

Algorithm 1 describes how the former optimization problem can be implemented in a distributed manner and usable for MAS. Note that when the \mathbf{n} -tuple of $F_1(\widehat{X})$ is not empty (at least one pair of coupling constraints exists) the distributed optimization procedure is best understood as a noncooperative deterministic dynamic game (N_s -person dynamic game, $N_s > 1$, with prescribed fixed duration N stages), that admits a *open-loop* NE solution, accordingly with Theorem 4.3 in [17].

Algorithm (Multi-Agent Noncooperative with Coordination)

Begin with a feasible plan \widehat{X}_i^p broadcasted between all the agents, initializing references P_i and coupling constraints F_{1i} , for $\forall i$;

for $k=1:K$, for $\forall i$:

– Measure the state $x_i(k)$;

– Solve the optimization problem (20)–(24) for $\forall i$

agents obtaining Z_i^* ;

– Apply $u_i^*(k)$ (26);

– Broadcast the planned trajectories \widehat{X}_i^p updating

$P_{i \neq i}$ and $F_{1i \neq i}$;

End for

End.

4 Results

The distributed MPC algorithm was developed to control a system of mechanical agents in multi-agent environment for two dimensional special scenarios with obstacles and collision avoidance, where the state evolution is described by the Newton's laws of motion. The dynamical model is given by:

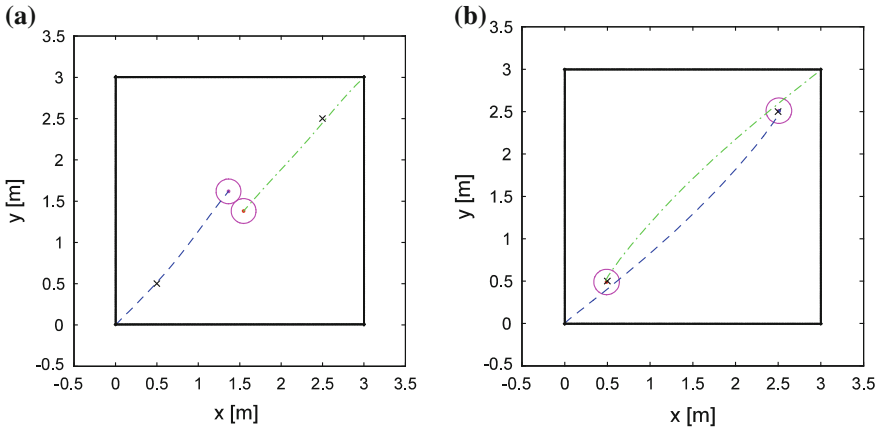


Fig. 1 Two agents, **a** frontal collision avoidance instant. Set-points x-marked ‘x’, **b** frontal collision avoidance optimal trajectories with no NE point

$$\dot{p} = \vec{v}, \quad (27)$$

$$\dot{\vec{v}} = \vec{F} + \beta \vec{v}, \quad (28)$$

where p , \vec{v} and \vec{F} are position, velocity and force respectively (with moving mass $m = 1$ kg) with friction coefficient ($\beta = 0$ kg/s). The 2-D scenario can include several obstacles that the agents must avoid. Each agent computes the optimization routine based on the optimization (20)–(24). In all the scenarios agents (point masses) have a security zone defined by the circle around the mass-dot that the other cannot cross. Results are shown in Figs. 1, 2, 3, 4, 5, 6, 7 and animations were created in MATLAB[®]. Simulations were done in a single machine using a sequential version of the proposed algorithm. The maximal computation time duration was of about 5 min for all the scenarios. Table 1 shows the typical ranges for agents cost functions.

Figures 1a–2a corresponds to a frontal collision avoidance scenario and Figs. 1b and 2a show two different types of equilibrium reached by changing only set-points.

In the next scenario two agents are travelling from a initial location to a common destination avoiding each other and obstacles (static objects) Figs. 2b–3b. Figures 4a–6a depict trajectories of different types of formations (*Follow the leader*, *Follow the pack leader* and *Indian file*) with two to five agents in the same scenario.

Changing from a pack leader to Indian file type of coordination, the NE appears only near to the destination point, and the leader reaches the set-point. Remark also that in all the cases the gap is always crossed, in a self-organized, queue formation independently of the type of coordination imposed to the particular scenario. Note that in Fig. 5a a Nash Equilibrium configuration starts far from the destination

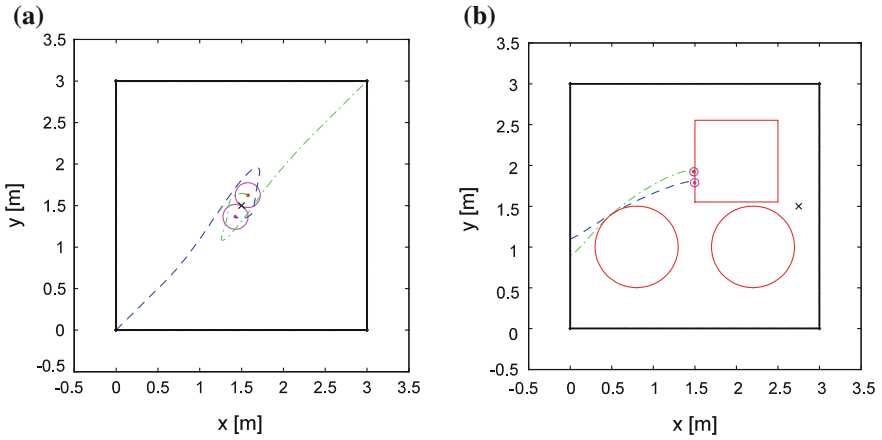


Fig. 2 Two agents, **a** frontal collision avoidance trajectories with NE point near the Pareto Optimal solution, **b** two fully noncooperative agents avoiding each other and the first obstacle, start to surround the wall

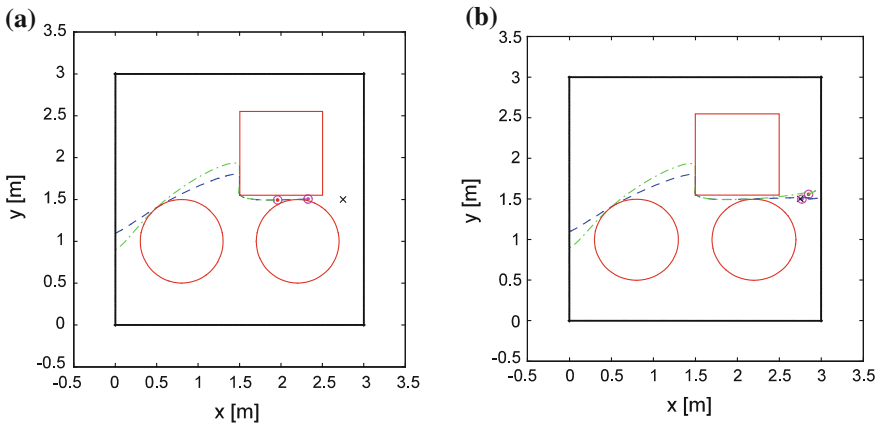


Fig. 3 Two agents, **a** two fully noncooperative agents surround the wall and go throughout the narrow gap, **b** two fully noncooperative agents arriving to the destination (set-point) converging to a nearby NE. Destination set-points x-marked 'x'

point. In this scenario two agents follow a third, the pack leader, that is trapped between the other two agents and the wall (boxing bound). Figures 6b–7b shows four agents manoeuvring in a maze. Each agent crosses the maze in a diagonal path from starting point and arriving to its destination, both marked with 'x', avoiding obstacles and collisions. No NE is originated.

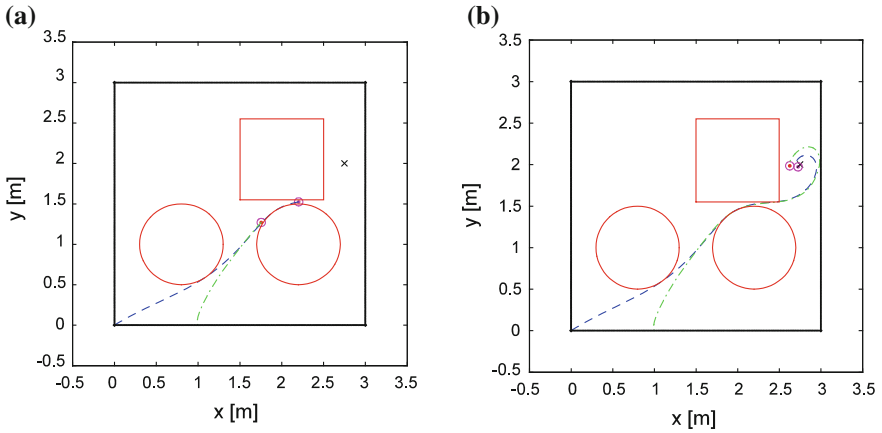


Fig. 4 Follow the leader: Two agents, **a** one agent follows the other avoiding obstacles passing throughout the narrow gap. Set-points x-marked 'x', **b** one agent follows the other stopping at set-point (destination) converging to a near NE. Set-points x-marked 'x'

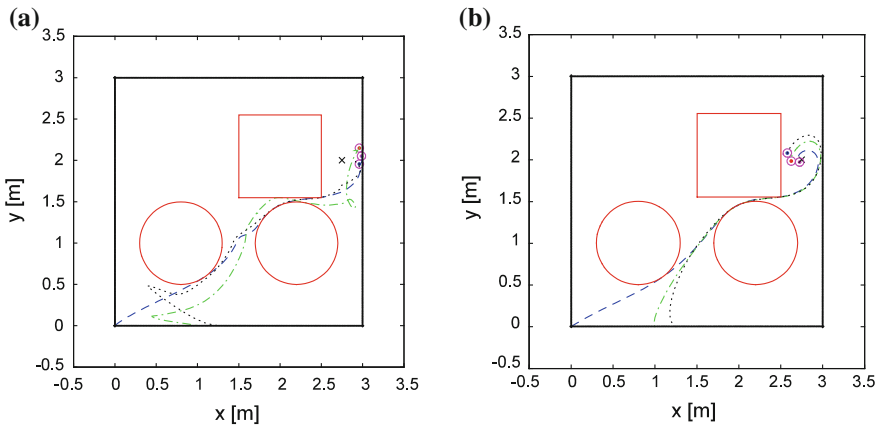


Fig. 5 Follow pack leader. Three agents, **a** a limit far NE is produced before arriving at set-point, **b** Indian file (convoy): Stopping at set-point (destination) converging to a nearby NE

5 Conclusions

The main contributions are in coordinated behavior between agents using implicit coordination for distributed MPC algorithms that can perform in the presence of numerous constraints. Coordination can be upheld as an alternative to cooperative distributed MPC due to its lower computational burden yielding more self-organized solutions to distributed control. Coordination management can prevent

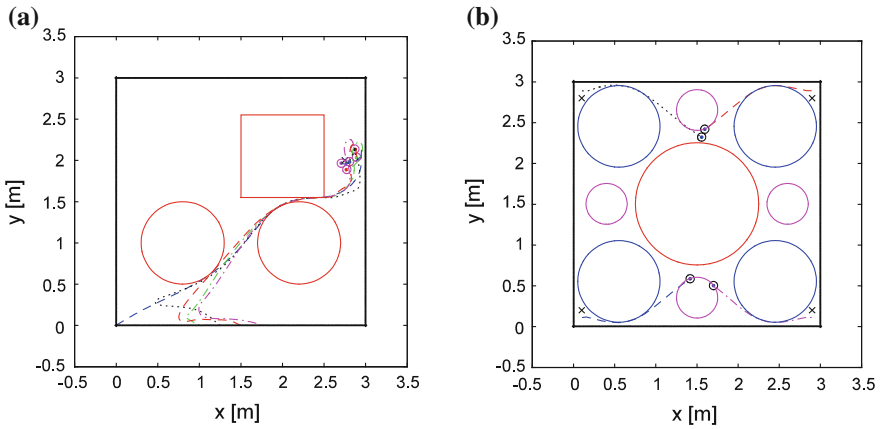


Fig. 6 Indian file (convoy): five agents (a), stopping at set-point (destination) converging to a nearby NE, b four agents performing in a maze avoiding collisions and obstacles

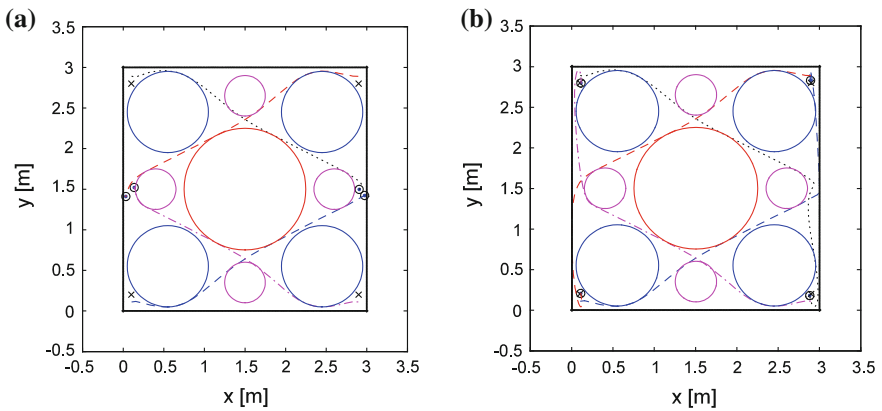


Fig. 7 Four agents (a), performing in a maze avoiding collisions and obstacles, (b) four agents performing in a maze arriving at destination (set-points)

Table 1 MPC parameters

Parameter	Symbol	Typical range
Horizon	N	10–20
Error weight	Q_i	$I - 10I$
Effort weight	R_i	0.005I – 0.5I

the arising of Nash Equilibrium point, far from Pareto Optimal solutions, as steady-states for the distributed control. These techniques emerging from distributed control can be an alternative to others from the computational intelligence area.

Acknowledgment Part of this work was supported by Fundação para a Ciência e a Tecnologia (Portugal) under the projects UID/CEC/50021/2013 and PTDC/EEI-PRO/0426/2014 (SPARSIS).

References

1. Grüne, L., Pannek, J.: *Nonlinear Model Predictive Control. Theory and Algorithms*. Springer (2011)
2. Rawlings, J.B., Mayne, D.Q.: *Model Predictive Control: Theory and Design*. Nob Hill Publishing (2009)
3. Negenborn, R.R., Lukszo, Z., Hellendoorn, H. (Eds.): *Intelligent Infrastructures, Control and Automation: Science and Engineering*, vol. 42, 1st edn. Springer (2010)
4. Camponogara, E., Jia, D., Krogh, B.H., Talukar, B.H.: Distributed model predictive control. *IEEE Control Syst Mag* (2002)
5. Zhang, Y., Li, S.: Networked model predictive control based on neighborhood optimization serially connected large-scale processes. *J. Process Control* **17**, 37–50 (2007)
6. Igreja, J.M., Lemos, J.M., Cadete, F.M., Rato, L., Rijo, M.: Control of a water delivery canal with cooperative distributed MPC. In: *American Control Conference, IEEE Xplore*, pp. 3346–3351 (2012)
7. Schumacher, M.: Objective coordination in multi-agent system engineering. *Lecture notes in computer science. Lecture Notes in Artificial Intelligence*, vol. 2039. Springer (2001)
8. Ren, W., Cao, Y.: *Distributed coordination of multi-agent networks: emergent problems, models and issues*. Communications and Control Engineering. Springer (2011)
9. Abbas, H., Bender, A., Gaidow, S., Whitbread, P.: Computational red teaming: past, present and future. *IEEE Comput. Intell. Mag.* (2011)
10. Trodden, P., Richards, A.: Cooperative distributed MPC of linear systems with coupled constraints. *Automatica* **40**, 479–487 (2013)
11. Silva, J.E., Sousa, J.B., Pereira, F.L.: Trajectory constraints for robust vehicle formation control. In: *Portuguese Conference on Automatic Control, Controlo' (2012)*
12. Fontes, F.A.C.C., Fontes, D.B.M.M, Caldeira, A.C.D: Obstacle avoidance in optimal switching of a formation geometry. In: *Conference on Automatic Control Controlo' (2012)*
13. Barata, F.A., Neves-Silva, R.: Distributed model predictive control for thermal house comfort with auction of available energy. In: *SG-TEP, IEEE International Conference on Smart Grid Technology, Economics and Policies (2012)*
14. Ventak, A.S., Hisken, I.A., Rawlings, J.B., Wright, S.J.: Distributed MPC strategies with application to power system automatic generation control. *IEEE Trans. Control Syst. Technol.* **16**(6) (2008)
15. Rugh, W.J.: *Linear System Theory*. Information and Systems Sciences Series. Prentice Hall, Upper Saddle River (2006)
16. Boyd, S.P., Vandenberghe, L.: *Convex Optimization*. Cambridge University Press (2004)

A Parametrized NMPC Strategy for Pressure Reducing Valves

Carlos Felipe Ilha Pereira, André Murilo, Anderson Quadros
and Walter de Britto Vidal Filho

Abstract Water loss due to leakage is a major concern for water distribution operations. Being mainly caused by pipe deterioration and high values of pressure, these have several negative features. Pressure Reducing Valves (PRV) are used in water supply networks to keep the pressure under acceptable values in order to reduce physical water losses. However, such process presents several nonlinearities and physical constraints leading to a highly complex model. In this paper, a parameterized Non-linear Model Predictive Control (NMPC) is proposed for the PRV combined with a water network. The NMPC consists in finding, at each sampling instant, an optimal solution over a prediction horizon taking into account the system nonlinearities and process constraints. Simulation results are proposed to show the efficiency of this control strategy and a performance comparison with standard PID control are also performed.

Keywords Parametrized NMPC · Pressure reducing valves · Water supply systems

1 Introduction

Physical water losses are represented by the volume of water captured that is lost before arriving to the final consumer. The leaks are the main events of physical losses and have several negative features: on environment, public health and business efficiency [1]. Pressure management and the leakage prevention provide a significant

C.F.I. Pereira (✉) · A. Murilo · A. Quadros · W. de Britto Vidal Filho
Faculdade de Tecnologia, Universidade de Brasília - UnB, Brasília, Brazil
e-mail: carlosfelipeilhapereira@gmail.com

A. Murilo
e-mail: andremurilo@unb.br

A. Quadros
e-mail: anderson@compesa.com.br

W. de Britto Vidal Filho
e-mail: wbritto1@gmail.com

positive impact on water distribution companies, improving the natural resource conservation and reducing the public water contamination risk.

One of the most important tools for reducing the incidence of leaks is the implementation of pressure control using Pressure Reducing Valves—(PRV) [4]. The oscillation on water demand leads to pressure peaks undesired fluctuations in the network leading to pipe damaging [3]. Therefore, the use of PRV can reduce the occurrence of water leakage from the system without loss of the hydraulic system performance [13]. The valve mechanism consists of an actuator that is activated when downstream pressure is too high. The control objective is to set the outlet pressure at the desired value.

Concerning PRV controllers, there are two main types discussed in the literature: direct action and indirect action. About direct action PRV controller, these require two on/off actuators working in a auxiliary circuit and change directly the control space pressure. On the other hand indirect action PRV controller, the control of the PRV downstream pressure is performed by the pilot valve set point [12].

In more recent work, PID controllers have been proposed for networks supplied through PRVs. The first one, proposed by [10], has direct action framework and that addresses undesirable transient pressure behaviors caused by demand fluctuation. A behavioral model was developed by these authors and the results showed that the reduction of the variance were quite significant in the worst case. Another contribution uses a PRV model based on indirect action, where a PID controller tuned by gain scheduling, Astrom-Hagglund and Genetic Algorithms (GA) was developed. The paper showed significant reductions of the pressure variance, and its the average deviation with respect to the set-point. Furthermore, authors also proposed the use of a linear proportional solenoid valve as actuator, enabling implementation of advanced controllers, such as adaptive, robust or nonlinear strategies [12].

The use of a nonlinear model for PRVs and the contemplation of its operational constraints enables higher performance gains. In this case, NMPC emerges as a suitable control strategy. Basically, this technique uses the process model to predict the future states of the system, minimizes a cost function to find a optimal sequence control and applies the first action of this sequence [2, 6]. In this paper, a NMPC approach using the simplified phenomenological model [10] is proposed, by means of the actuator proposed by [12]. A higher stability of the PRV downstream pressure allows a reduction of pressure peaks in the water supply network. However, due to the on-line optimization routines, a high processing power is generally required, specially where nonlinear systems are considered. In order to deal with this problem, a parametrization of the control sequence is proposed which enables a drastic reduction of the calculation time, without a noticeable reduction in the control performance [2].

This paper is organized as follows. First, in the Sect. 2, the nonlinear phenomenological model interacting with the water supply network is presented. Then, Sect. 3 presents the parametrized NMPC design and the optimization problem related for PRV case. Some simulation results are shown in Sect. 4 and the paper ends in Sect. 5 with conclusions and future works.

2 System Models

In this section, the models and process description are represented. Following the scheme presented in [12], the NMPC strategy is based on both the PRV’s and the network’s models. In the next sections, a PRV model is described followed by the construction of a distribution network model.

2.1 Simplified Phenomenological Model

A simplified PRV phenomenological model was developed by [9]. This PRV model is based on the dynamical phenomena of the PRV hydraulic circuit shown in the Fig. 1. Moreover, [12] proposed the introduction of a proportional valve that allows some improvements concerning the control design.

The PRV model is shown in Eqs. (1)–(7).

$$\dot{x}_m(t) = \frac{q_3(t)}{A_{cs}(x_m, t)} \tag{1}$$

$$\rho g(h_{in}(t) a_1 + h_{out}(t)(a_2 - a_1) - h_c(t)a_2) - m_m g + \frac{\rho q_m^2(t)}{a_1} = 0 \tag{2}$$

$$C_{vpp}(x_{pp}, t) = 0.2808 * x_{pp} \tag{3}$$

$$q_m(t) = C_{vm}(x_m, t) \sqrt{h_{in}(t) - h_{out}(t)} \tag{4}$$

$$q_1(t) = C_{vfo} \sqrt{h_{in}(t) - h_t(t)} \tag{5}$$

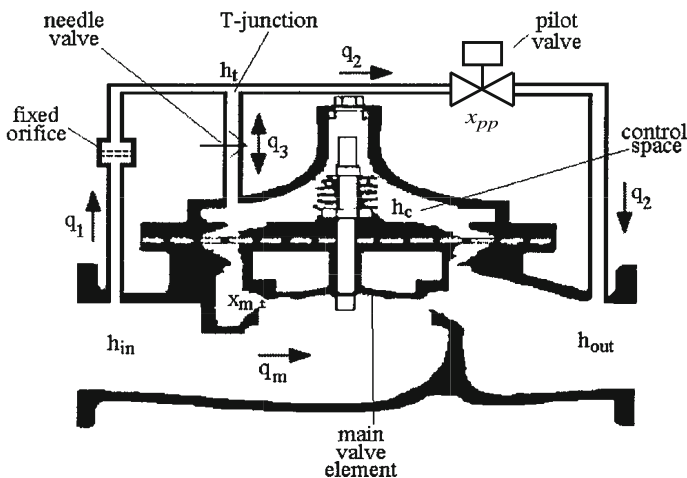


Fig. 1 Pressure Reducing Valve. Some dynamic variables related to the process are shown [9]

$$q_2(t) = C_{vpp}(x_{pp}, t) \sqrt{h_t(t) - h_{out}(t)} \quad (6)$$

$$q_3(t) = C_{vvn} \sqrt{|h_c(t) - h_t(t)|} \operatorname{sgn}(h_c(t) - h_t(t)) \quad (7)$$

$$q_2(t) = q_1(t) + q_3(t) \quad (8)$$

where $x_m(t)$: PRV opening; $x_{pp}(t)$: the linear valve opening; $\dot{x}_m(t)$: PRV opening rate; A_{cs} : the top surface area of the PRV diaphragm; a_1 : the area of the bottom of the main valve; a_2 : the area of the top of the main valve; m_m : the mass of the PRV; ρ : the density of water; g : acceleration of gravity; $h_{in}(t)$: the upstream PRV pressure; $h_{out}(t)$: the PRV downstream pressure; $h_t(t)$: the T-junction pressure; $h_c(t)$: the control center pressure; C_{vvn} : the needle valve capacity; $C_{vpp}(t)$: the proportional solenoid valve capacity; $C_{vm}(t)$: the PRV capacity; C_{vfo} : the fixed orifice capacity; $q_1(t)$: the fixed orifice flow; $q_2(t)$: the pilot flow; $q_3(t)$: the input or output flow in the control chamber; $q_m(t)$: the PRV flow.

In the simulations, the following parameters and variables were adopted: $a_1 = 0,0078 \text{ m}^2$, $a_2 = 0,0218 \text{ m}^2$, $m_m = 1 \text{ kg}$, $C_{vvn} = 2 * 10^{-6}$, $C_{vfo} = 3 * 10^{-5}$. The PRV capacity (C_{vm}) and the top surface area of the PRV diaphragm (A_{cs}) are given by the following equations.

$$C_{vm}(x_m, t) = 0,02107 - 0,02962e^{-51,1322x_m(t)} + 0,0109e^{-261x_m(t)} - 0,00325e^{-683,17x_m(t)} + 0,0009e^{-399,5x_m(t)} \quad (9)$$

$$A_{cs}(x_m, t) = \frac{1}{3700 * (0,02732 - x_m(t))} \quad (10)$$

2.2 Pipes and Gate Valves Models

The hydraulic network is submitted to small perturbations caused by the consumption variations, thus, a rigid column model (Eq. 11) is sufficient to accurately represent the dynamics of the simulation [9, 12].

$$\dot{q}(t) = \frac{gA}{L} (p_m(t) - p_j(t) - f_{DW} \frac{L}{D} \frac{v^2}{2g}) \quad (11)$$

where $\dot{q}(t)$: the derivative of the pipe section flow, A : the cross-section of the pipe, L : the pipe length, $p_m(t)$: the upstream pipe pressure, $p_j(t)$: the downstream pipe pressure, f_{DW} : the Darcy-Weisbach friction factor, D : the pipe diameter and v : the fluid velocity on the pipe.

The modelling of gate valves v_1 and v_2 will be represented as standard theory in Eq. (12).

$$q(t) = ca \sqrt{2g(p_m(t) - p_j(t))} \quad (12)$$

Here q : the flow through the valve, c : the discharge coefficient, a : the cross-sectional area of orifice. In the simulations the parameters have been set as: $g = 9.806 \text{ m/s}^2$ and $a = 0.007854 \text{ m}^2$.

2.3 Simulation Model

The simulation network is a coupling between the modeled components in the previous sections. As noted in the Fig. 2, some elements are arranged in series: a fixed pressure source, gate valves (v_1 and v_2), one PRV and four pipes. The actuation of the main valve (in PRV) is performed by the main hydraulic flow through the red control circuit composed of a fixed orifice, a needle valve, a control valve and pipes. While the valve v_1 has its characteristic coefficient constant, the v_2 coefficient was modified to represent the consumer behavior. To perform simulations, the water network and PRV were modeled separately. These models and its input and output variables are shown in Fig. 3. From the network, h_{out} , h_{in} and q_m are measured, which are feedback variables for the PRV model. The controlled variable is the h_{out} on PRV model.

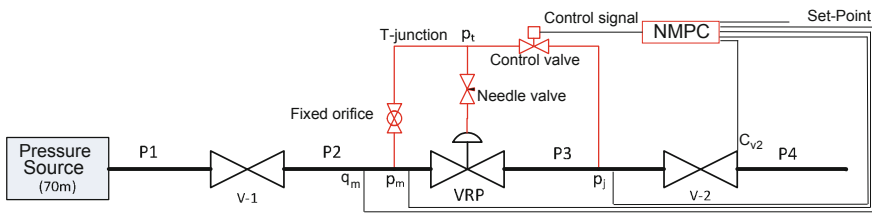


Fig. 2 Test Network layout. Adapted of [12]

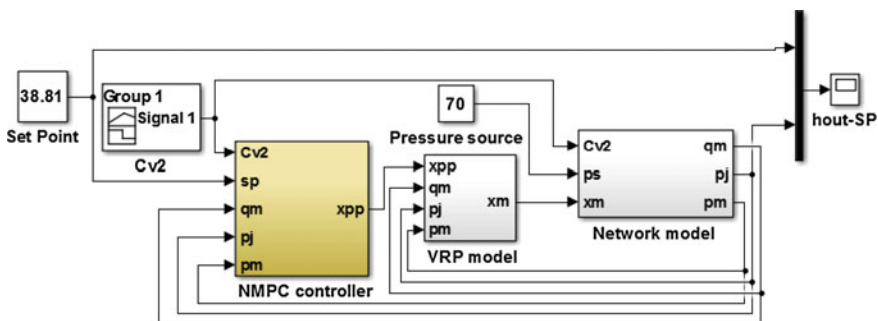


Fig. 3 Schematic view of simulation model

3 Controller Design

3.1 Definitions and Notations

Model Predictive Control (MPC) is an advanced/modern control strategy which uses explicitly the dynamic model to predict the future evolution of the process [6]. The basic idea of MPC consists in computing an optimal control sequence over a finite prediction horizon (N) at each decision instant, through the minimization of a cost function defined to express the control objective. However, only the first action of the optimal sequence is applied and the state of the system is then measured again at the next sampling instant. Moreover, with the MPC technique it is possible to respect the operational limits, with a systematic handling of constraints [2, 7].

Opposed to other conventional methods, that are generally based on off-line computed control law, the MPC formulation solves an on-line constrained optimal control problem for the current state at each sampling time [5]. The NMPC schemes are used in the same structure, but in this case by means of nonlinear representations. But while linear systems establish a convex cost function, nonlinear systems produce non-convex cost functions, which yields to more complex optimization problems [2]. Thus, the NMPC is highly dependent on computer resources to solve the on-line optimization problem which demands high computational cost. One way to address this issue is to define a control parametrization, a method that enables a reduction of the number of decision variables in the optimization problem without deteriorating of the control performance [2, 7].

The NMPC scheme holds some important advantages when compared with standard control laws [2]. First, the ability to handle control problems where off-line computation of a control law is difficult or impossible due to process characteristics. In fact, the possibility to deal systematically with process constraints, which is inherent to several real systems, is a powerful feature of NMPC. Another advantage is the adaptability of the controller (it is easy to change a NMPC for other control problems) and the possibility of handling multivariable and, of course, nonlinear models. All these features make NMPC an interesting solution to be applied in the PRV control problem.

The first step in the NMPC development is, the dynamical model that is defined here, for simplicity, as a general nonlinear system: $x(k+1) = f(x(k), u(k))$.

Where $k \in \mathbb{N}$ is the present instant, $x \in \mathbb{R}^n$ is the state vector n , $u \in \mathbb{R}^{n_u}$ is the control vector. Here it is assumed that the whole state $x(k)$ directly obtained by sensor measurement and all model parameters of $f(\cdot)$ are available. The PRV control input is the pilot valve opening (x_{pp}), in meters ($n_u = 1$). The output $y \in \mathbb{R}^{n_y}$ of the system is the PRV downstream pressure (h_{out}), where n_y is the output dimension vector ($n_y = 1$).

The next step consists in formalizing the control problem to be solved. The control task is therefore to adjust the pilot valve position to track the required PRV downstream pressure while the control input u must satisfy the following set of constraints, for $i \in 1, \dots, N$:

$$u^{min} \leq u(k+i-1) \leq u^{max} \quad (13)$$

$$\delta^{min} \leq u(k+i) - u(k+i-1) \leq \delta^{max} \quad (14)$$

where u^{min} is the minimal opening of the pilot valve, u^{max} is the maximal opening of pilot valve, δ^{min} is the minimum of the opening rate of pilot valve and δ^{max} is the maximum of the opening rate of pilot valve. In the next section, a parametrized NMPC scheme is presented.

3.2 Parametrized NMPC

In standard NMPC formulations the size of the decision variable is given by the product between the number of actuators and the prediction horizon ($n_u \cdot N$). With a parametrization, the control sequence can be defined by a low dimensional variable, allowing a reformulation in the optimization problem [8]. There are several ways to parametrize the NMPC control scheme. One possible solution comes from the exponential parametrization according to [7]. This parametrized control law involve the stationary control u^* and a exponential representation of the future control as follows:

$$u(i\tau + t) = Sat_{u_{min}}^{u_{max}}(u^* + \alpha_1 e^{-\lambda t} + \alpha_2 e^{-\lambda q \tau i}) \text{ for } t \in [(k-1)\tau, k\tau] \quad (15)$$

where τ is the sampling period, $i \in [0, \dots, N-1]$, $\lambda > 0$ and $q \in \mathbb{N}$ are tuning parameters, $\alpha_1, \alpha_2 \in \mathbb{R}^m$ are the coefficients to be determined and the saturation constraints are defined as follows:

$$Sat_{u_{min}}^{u_{max}}(u) = \begin{cases} u_{min} & \text{if } u_i \leq u_{min} \\ u_{max} & \text{if } u_i \geq u_{max} \\ u & \text{otherwise} \end{cases} \quad (16)$$

As a matter of fact, at instant k , the continuity of the control sequence must be guaranteed. Therefore, replacing $i = 0$ for the first step and $i = 1$ for the second one in (15), the following set of equations are obtained:

$$u(k-1) = u^* + \alpha_1 + \alpha_2 \quad (i = 0) \quad (17)$$

$$u(k) = u^* + \alpha_1 e^{-\lambda \tau} + \alpha_2 e^{-\lambda q \tau} \quad (i = 1) \quad (18)$$

$$u(k) - u(k-1) = \alpha_1 (e^{-\lambda \tau} - 1) + \alpha_2 (e^{-\lambda q \tau} - 1) = p_1 \cdot \Delta u \quad (19)$$

where $p_1 \in [-1, +1]$ is the first component of the new decision variable and limits the difference between two successive control inputs so they don't exceed the maximal allowable values Δu , in order to respect the constraints imposed by the equation (16). Moreover, the stationary control can also be considered a decision variable

by making $u^* = p_2$ with $p_2 \in [u_{min}, u_{max}]$. Arranging the terms, α_1 and α_2 can be obtained by solving a simple linear system depending on the parameters p_1 and p_2

$$\begin{bmatrix} \alpha_1(p) \\ \alpha_2(p) \end{bmatrix} = \begin{bmatrix} e^{-\lambda\tau} - 1 & e^{-\lambda q\tau} - 1 \\ 1 & 1 \end{bmatrix}^{-1} \begin{bmatrix} p_1 \Delta u \\ u(k-1) - p_2 \end{bmatrix} \quad (20)$$

Therefore, the new control sequence can be rewritten as follows:

$$u(i\tau + t, p) = Sat_{u_{min}}^{u_{max}}(p_2 + \alpha_1(p)e^{-\lambda_i\tau_i} + \alpha_2(p)e^{-\lambda_i q\tau_i}) \quad (21)$$

The above expression shows that the control profile depends on the parameter vector p , which are obtained by optimization. A set of optimized values p_{opt} leads to an optimized command profile u_{opt} over the prediction horizon N . As mentioned before, only the first control input of the sequence u_{opt} is actually applied to the process. After that, the system measurements are updated, a new prediction step is performed and another optimal control sequence is obtained.

3.3 Optimization Problem

In the parametrized NPMPC scheme, the optimization problem must return the optimum parameters p as mentioned previously. For that, it is necessary to define a cost function that take into account the control objective. In PRV case, this function must track the downstream pressure set-point y_{sp} , which means that the cost function must minimize the output tracking error $y_{sp} - y_{pred}$.

$$p_{opt} = arg \min_{p \in \mathbb{P}} [\rho_x \cdot \|X_f\| + \sum_{i=1}^N \|(y_{sp} - y_{pred})\|_{Q_y}^2] \quad (22)$$

where y_{pred} is the predicted output, X_f is the terminal cost on the state (for stability purposes), ρ_x is the weighting parameter of X_f and Q_y is a weighing term for the output y .

4 Simulation Results

In this section, some simulations are presented in order to show the efficiency of the proposed control scheme. The models were implemented in *Matlab/Simulink* (version R2012A) to represent the PRV and Network as well as the NMPC controller. A personal computer *Intel I5* processor and 8 GB of RAM memory was also used. A standard residential water consumption was used in the simulation with the v_2 coefficient profile with average of 0.029 and standard deviation of 0.0016. This profile

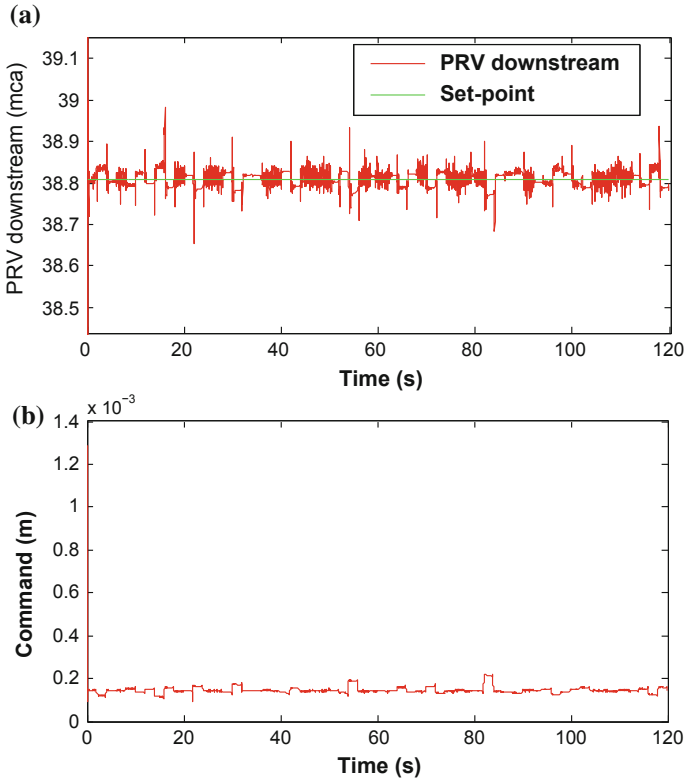


Fig. 4 The measured PRV output with the set-point of 38.81 (a) and the control profile using the NMPC (b). The pressure changes quickly at the first steps but it stabilizes before to 3 s. The constraints in the input are correctly respected

also indicates the minimum water flow of $5.34 L/s$ and the maximum water flow of $6.77 L/s$ in the simulated network. The parameters of the each pipe section in network are pipe number, length [m] and diameter [m] respectively: P1, 1.5, 0.05; P2, 4.0, 0.1; P3, 5.0, 0.1; P4, 6.6, 0.1. The set-point for the PRV downstream was set to 38.81.

Matlab’s optimization function *fmincon* is used along with the Sequential Quadratic Programming (SQP) algorithm. The set-up of the parametrized NMPC had $\lambda = 10$, $q = 2$, $N = 20$, $\rho_x = 0$ and $Q_y = [1]$. The simulations were performed over 120 s, and the results were analyzed by the following criteria: simulation time, measuring the computational effort spent by the controller; average, representing the average difference between the PRV downstream pressure and the set-point; variance, representing how far the downstream pressure is spread out in relation to the set point; maximum: representing the highest value of controlled signal; minimum: representing the smallest value of the controlled signal; ITAE criteria: representing the integral of the time multiplied by absolute output error. The simu-

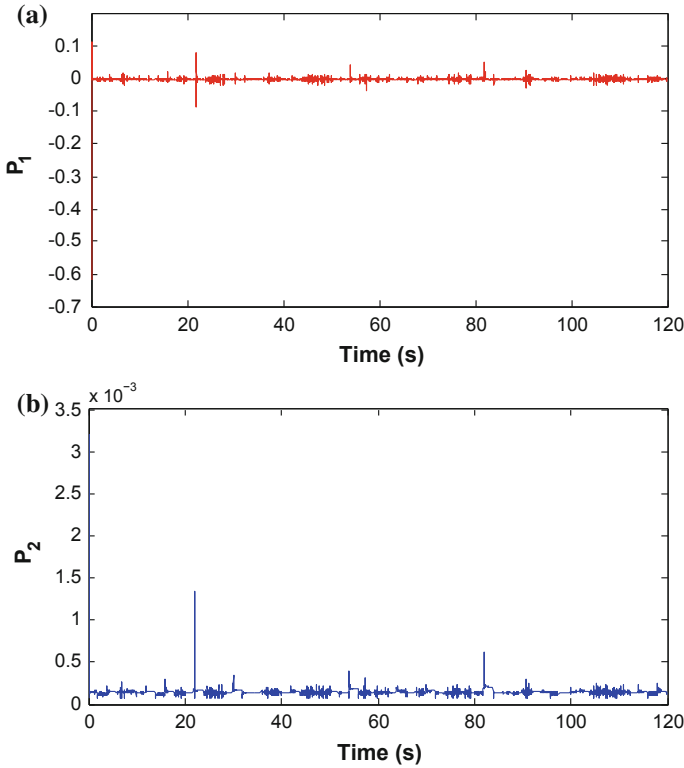


Fig. 5 Parameters p_1 (a) and p_2 (b). While p_1 ensures that the difference between two successive signals does not exceed the established fraction of δu , p_2 is limited by the constraints u_{min} and u_{max}

lation results for the PRV downstream pressure and the constrained control signal ($u^{min} = 6.4 \times 10^{-5}$, $u^{max} = 3.2 \times 10^{-3}$) are presented in Fig. 4. The evolution of parameters p_1 ($-1 \leq p_1 \leq 1$) and p_2 ($6.4 \times 10^{-5} \leq p_2 \leq 3.2 \times 10^{-3}$) are shown in Fig. 5.

The performance of the NMPC controller is compared with the best PID controller tuned by Genetic Algorithms (GA) presented in [11]. The results are identified in the Table 1. The NMPC scheme presents better performance indicators in most aspects, only losing in maximum and minimum due to the initial control steps. This loss may be associated to computational limitations in the optimization process. It is important to emphasize that the results presented in this section showed that the parametrized NMPC strategy is a quite promising technique for application in PRV control. The remaining issues consists of running the optimization routine in a real-time hardware and considering model mismatches between the real plant and the prediction model. The NMPC variance presented a 99 % reduction compared to the PRV with the pilot valve (mechanical control).

Table 1 Results of the NMPC controller compared to PID controller [11]

Controller	Sim. time	ITAE	Average	Variance	Max.	Min.
NMPC	444.46 s	$1.10 \cdot 10^4$ m.s	38.8097 m	0.002297 m^2	40.881 m	36.25 m
PID (GA)	680.49 s	$6.73 \cdot 10^4$ m.s	38.8026 m	0.0171 m^2	39.3490 m	37.8654 m

5 Conclusion and Future Works

In this paper, a parametrized NMPC strategy was proposed to address the PRV control in water supply networks. Simulation results showed that the NMPC is able to find an optimal solution with only two parameters that are obtained on-line. Moreover, the control scheme structurally respected the constraints on the control input and had an excellent performance in several indicators, which were compared with a standard PID control scheme tuned by the GA method. Future works include the validation of this control strategy in embedded systems and considering model uncertainties in the prediction model in order to reproduce a more realistic scenario for the NMPC.

References

1. ABES: Perdas em sistemas de abastecimento de água: diagnóstico, potencial de ganhos com sua redução e propostas de medidas para o efetivo combate. Associação Brasileira de Engenharia Sanitária e Ambiental (Sep 2013). www.abes-sp.org.br/arquivos/perdas_resumo.pdf
2. Alamir, M.: A Pragmatic Story of Model Predictive Control: Self-Contained Algorithms and Case-Studies, 1st edn. Saint-Martin-d'Hères, France (2013)
3. Force, I.W.L.T., Thornton, J.: Managing leakage by managing pressure: a practical approach. *Water* **21** (2003)
4. Gonçalves, E., Lima, C.V.: Controle de pressões e operação de válvulas redutoras de pressão. Ministério das cidades (2007)
5. Mayne, D.Q., Rawlings, J.B., Rao, C.V., Sokaert, P.O.M.: Constrained model predictive control: stability and optimality pp. 788–814 (2000)
6. Moutinho, M.N., Barreiras, J.A.L., Costa, C.T., Barra, W.: Técnica de controle preditivo baseado em modelo aplicada ao controle de tensão de um gerador síncrono—resultados experimentais (2012)
7. Murilo, A.: Contributions on Nonlinear Model Predictive Control for Fast Systems. Ph.D. thesis, Saint-Martin-d'Hères, França (2009)
8. Murilo, A., Alamir, M., Alberer, D.: A general nmpc framework for a diesel engine air path. *Int. J. Control* (2014)
9. Prescott, S.L., Ulanicki, B.: Dynamic modeling of pressure reducing valves **129**, 804–812 (2003)
10. Prescott, S.L., Ulanicki, B.: Improved control of pressure reducing valves in water distribution networks **134**, 56–65 (2008)
11. Quadros, A.S.: Sintonias automática e adaptativa de controladores pid para válvulas redutoras de pressão em sistemas de abastecimento de água. Master's thesis, Recife, Brazil (2013)
12. Quadros, A.S., Murilo, A.: Automatic and adaptive tuning of pid controllers for pressure reducing valves in water supply systems (2013)
13. Ramos, H., Covas, D., Araújo, L.: Válvulas redutoras de pressão e produção de energia (2004)

Part III
Fuzzy, Neural and Genetic Control

Fuzzy Kalman Filter Black Box Modeling Approach for Dynamic System with Partial Knowledge of States

Danúbia Soares Pires and Ginalber Luiz de Oliveira Serra

Abstract A strategy to Fuzzy Kalman Filter identification, is proposed. A mathematical formulation applied to fuzzy Takagi-Sugeno structure is presented: the algorithm FCM estimates the antecedent parameters; from the input and output data of dynamic system, the ERA/DC algorithm based on FCM clustering algorithm, is applied to obtain the state matrix, input influence matrix, output influence matrix, and direct transmission matrix (the matrices A, B, C, and D, respectively) to each rule of the consequent parameters. The Fuzzy Kalman Filter is applied to estimate states and output of a dynamic system with partial knowledge of states and the efficiency of the proposed methodology is shown in computational results, once that the Fuzzy Kalman Filter follows the dynamic behavior related to output and states of the dynamic system.

Keywords Dynamic system · Fuzzy Kalman Filter · Takagi-Sugeno fuzzy model

1 Introduction

Kalman Filter (KF) is a mathematical method widely extended in many areas of science, and is the popular method for estimating the states of dynamic system from an noisy or/and incomplete measurement. As a recursion algorithm, it more favorable in the real-time system application, because it has a small requirement on calculation and memory space. Applying KF, it is necessary to know the model based on space state, and in general, identification based on state space through input and output of a system is not trivial [1, 2]. Added to this, KF theory is only applicable for linear systems, while Extended Kalman Filter (EKF) is widely used in nonlinear filtering

D.S. Pires

Federal Institute of Education, Science and Technology, São Luís–ma, Brazil
e-mail: danubiapires@ifma.edu.br

G.L. de Oliveira Serra (✉)

Department of Electroelectronics, Laboratory of Computational Intelligence
Applied to Techonology, Seville, Spain
e-mail: ginalber@ifma.edu.br

applications. However, KF and EKF are not robust against modeling uncertainties and disturbances. This has motivated many studies on extending the Kalman filtering theory applied to uncertain and noisy systems [3–6]. Since 1980, fuzzy systems have been applied in identification and control of dynamic and/or nonlinear systems. Among several types of fuzzy systems, there is a very important class called Takagi-Sugeno (TS). Recently, it became a powerful tool applied to identification and control, because the structure based on rules allows approximation of functions, nonlinearities and uncertainties as well [7–9]. The methodology presented in this paper consists in a strategy to Fuzzy Kalman Filter identification. The mathematical formulation applied to fuzzy Takagi-Sugeno structure is presented: the algorithm FCM estimates the fuzzy sets; from the input and output data of a nonlinear dynamic system, the ERA/DC algorithm based on clustering, estimated by FCM algorithm, is applied to obtain the consequent models the state matrix, input influence matrix, output influence matrix, and direct transmission matrix (the matrices A, B, C, and D, respectively) to each rule of the Fuzzy Kalman Filter. Finally, the Fuzzy Kalman Filter is applied to estimate states and output of a dynamic system with partial knowledge of states and computational results about the Fuzzy Kalman Filter identification are presented.

2 Methodology for Fuzzy Kalman Filter Parametric Estimation

2.1 Clustering Algorithm for Antecedent Estimation

The TS fuzzy model antecedent parameters are estimated by Fuzzy C-Means (FCM) clustering algorithm, which is based on minimizing the functional given by [10]:

$$J(\mathbf{Z}; \mathbf{U}, \mathbf{V}) = \sum_{i=1}^c \sum_{k=1}^N (\mu_{ik})^w D_{ikL}^2 \quad (1)$$

where $\mathbf{U} = [\mu_{ik}] \in M_{fc}$ is a fuzzy partition matrix of data matrix $\mathbf{Z} = \{\mathbf{z}_1, \mathbf{z}_2, \dots, \mathbf{z}_N\}$, where μ_{ik} is a membership degree in the i -th cluster and at instant k , and

$$M_{fc} = \left\{ \mathbf{U} \in \mathfrak{R}^{c \times N} \mid \mu_{ik} \in [0, 1], \forall i, k; \right. \\ \left. \sum_{i=1}^c \mu_{ik} = 1, \forall k; 0 < \sum_{k=1}^N \mu_{ik} < N, \forall i \right\} \quad (2)$$

The vector of centers (cluster prototypes) is determined by $\mathbf{V} = [\mathbf{v}_1, \mathbf{v}_2, \dots, \mathbf{v}_c]$, $\mathbf{v}_i \in \mathfrak{R}^n$. A squared inner-product distance norm is determined by $D_{ikL}^2 =$

$\|\mathbf{z}_k - \mathbf{v}_i\|_L^2 = (\mathbf{z}_k - \mathbf{v}_i)^T \mathbf{L} (\mathbf{z}_k - \mathbf{v}_i)$ where $\|\cdot\|_L^2$ is the standard Euclidean norm with $\mathbf{L} = \mathbf{I}$, \mathbf{v}_i is associated with the coordinates of the clusters centers and \mathbf{z}_k represents the elements of each column of the data matrix \mathbf{Z} .

The FCM algorithm is realized using the following steps: given the data set \mathbf{Z} and the initial partition matrix $\mathbf{U}^{(0)} \in M_{fc}$, choose the number of clusters $1 < c < N$, the tolerance $\alpha > 0$ and the weighting exponent $w > 1$.

Repeat for $l = 1, 2, \dots$

Step 1: Compute the means (cluster prototypes):

$$\mathbf{v}_i^{(l)} = \frac{\sum_{k=1}^N \mu_{ik}^{(l-1)} \mathbf{z}_k}{\sum_{k=1}^N \left(\mu_{ik}^{(l-1)}\right)^w}, 1 \leq i \leq c \quad (3)$$

Step 2: Compute the distances:

$$D_{ikL}^2 = \left(\mathbf{z}_k - \mathbf{v}_i^{(l)}\right)^T \mathbf{L} \left(\mathbf{z}_k - \mathbf{v}_i^{(l)}\right), 1 \leq i \leq c, 1 \leq k \leq N \quad (4)$$

Step 3: Update the partition matrix:

If $\sqrt{D_{ikL}^2} > 0$ for $1 \leq i \leq c, 1 \leq k \leq N$,

$$\mu_{ik}^{(l)} = \frac{1}{\sum_{j=1}^c (D_{ikL}/D_{jkL})^{2/(w-1)}}, \quad (5)$$

otherwise

$$\mu_{ik}^{(l)} = 0 \quad \text{if } D_{ikL} > 0, \quad \text{and } \mu_{ik}^{(l)} \in [0, 1]$$

with $\sum_{i=1}^c \mu_{ik}^{(l)} = 1.$

Until $\|\mathbf{U}^{(l)} - \mathbf{U}^{(l-1)}\| < \alpha.$

Step 4: Compute the normalized membership degree from the i -th rule.

$$\gamma_i(\mathbf{X}_L) = \frac{1}{\sum_{j=1}^c \left(\frac{D_{L_i}^{\mathbf{X}_L}(\mathbf{X}_L, \mathbf{v}_i^{\mathbf{X}_L})}{D_{L_i}^{\mathbf{X}_L}(\mathbf{X}_L, \mathbf{v}_j^{\mathbf{X}_L})} \right)^{2/(w-1)}} \quad (6)$$

where:

$$D_{L_i^{X_L}} = \left(\mathbf{X}_{Lk} - \mathbf{v}_i^{X_L} \right) L \left(\mathbf{X}_{Lk} - \mathbf{v}_i^{X_L} \right)$$

and

$$\mathbf{X}_L = [y_1(k-1) \quad y_2(k-1) \quad \dots \quad y_m(k-1)]^T$$

where $y_{[1,2,\dots,m]}$ corresponds to output data.

2.2 The ERA/DC Algorithm Based on Clustering for Consequent Estimation

The ERA/DC (Eigensystem Realization Algorithm/Data Correlations) originally created by [11], presents the fuzzy structure given by the following steps:

Given l (number of points), p (appropriate number of observer Markov parameters from the given set of input-output data), $u_{r \times l}$ (input data, r is the number of inputs), and $y_{m \times l}$ (output data, m is the number of outputs).

Step 1: Compute the matrix of regressors, called \mathbf{V} .

$$\mathbf{V} = \begin{bmatrix} \mathbf{u}_0 & \mathbf{u}_1 & \dots & \mathbf{u}_p & \dots & \mathbf{u}_{l-1} \\ 0 & \mathbf{v}_0 & \dots & \mathbf{v}_{p-1} & \dots & \mathbf{v}_{l-2} \\ 0 & 0 & \dots & \mathbf{v}_{p-2} & \dots & \mathbf{v}_{l-3} \\ 0 & 0 & \ddots & \vdots & \dots & \vdots \\ 0 & 0 & \ddots & \mathbf{v}_0 & \dots & \mathbf{v}_{l-p-1} \end{bmatrix} \quad (7)$$

where $\mathbf{v}_k = [\mathbf{u}_k \quad \mathbf{y}_k]^T$ corresponds to input and output data at time k .

Step 2: Obtain from experimental data the Observer Markov Parameters $\tilde{\mathbf{Y}}$ based on fuzzy sets, as follow:

$$\tilde{\mathbf{y}} = \sum_{i=1}^l \tilde{\mathbf{Y}}^i \mathbf{V} \quad (8)$$

$$\tilde{\mathbf{Y}}^i = \mathbf{y} \Gamma^i \mathbf{V}^T [\mathbf{V} \Gamma^i \mathbf{V}^T]^{-1} \quad (9)$$

where $\mathbf{y} = [\mathbf{y}_0 \quad \mathbf{y}_1 \quad \dots \quad \mathbf{y}_p \quad \dots \quad \mathbf{y}_{l-1}]$ is the output matrix $m \times l$ of the dynamical system,

$$\Gamma^i = \begin{bmatrix} \gamma_0^i & 0 & \dots & 0 \\ 0 & \gamma_1^i & \dots & 0 \\ \vdots & \vdots & \ddots & \vdots \\ 0 & 0 & \dots & \gamma_{l-1}^i \end{bmatrix} \quad (10)$$

is the diagonal weighting matrix of membership values from the i -th rule.

$$\tilde{\mathbf{Y}}^i = \begin{bmatrix} \mathbf{D}^i(\gamma^i) \\ \mathbf{C}^i(\gamma^i) \bar{\mathbf{B}}^i(\gamma^i) \\ \mathbf{C}^i(\gamma^i) \bar{\mathbf{A}}^i(\gamma^i) \bar{\mathbf{B}}^i(\gamma^i) \\ \dots \\ \mathbf{C}^i(\gamma^i) \bar{\mathbf{A}}^{i(p-1)}(\gamma^i) \bar{\mathbf{B}}^i(\gamma^i) \end{bmatrix}^T \quad (11)$$

is the observer Markov Parameters of i -th rule, and

Step 3: Construct a block correlation matrix \mathbf{N}_τ^i with the elements $\mathbf{G}_{hh_{k+\tau}}^i$, which corresponds to product between \mathbf{H}_τ^i and $\mathbf{H}_{k+\tau}^i$.

$$\mathbf{G}_{hh_{k+\tau}}^i = \mathbf{H}_{k+\tau}^i \mathbf{H}_\tau^{iT}, \text{ with } \tau = 0 \quad (12)$$

$$\mathbf{G}_{hh_k}^i = \begin{bmatrix} \mathbf{Y}_{k+1}^i & \dots & \mathbf{Y}_{k+\beta}^i \\ \mathbf{Y}_{k+2}^i & \dots & \mathbf{Y}_{k+\beta+1}^i \\ \vdots & \ddots & \vdots \\ \mathbf{Y}_{k+\alpha}^i & \dots & \mathbf{Y}_{k+\alpha+\beta+1}^i \end{bmatrix} \begin{bmatrix} \mathbf{Y}_1^i & \dots & \mathbf{Y}_\beta^i \\ \mathbf{Y}_2^i & \dots & \mathbf{Y}_{\beta+1}^i \\ \vdots & \ddots & \vdots \\ \mathbf{Y}_\alpha^i & \dots & \mathbf{Y}_{\alpha+\beta+1}^i \end{bmatrix}^T \quad (13)$$

where \mathbf{Y}_k^i is a matrix $m \times r$, whose columns are the Markov parameters (sampled pulse response) correspond to m inputs. The size of \mathbf{H}_k^i and \mathbf{H}_0^i is $\alpha m \times \beta r$, since the size of $\mathbf{G}_{hh_k}^i$ is $\alpha m \times \alpha m$.

$$\mathbf{N}_k^i = \begin{bmatrix} \mathbf{G}_{hh_k}^i & \dots & \mathbf{G}_{hh_{k+\xi\tau}}^i \\ \mathbf{G}_{hh_{k+\tau}}^i & \dots & \mathbf{G}_{hh_{k+(\xi+1)\tau}}^i \\ \vdots & \ddots & \vdots \\ \mathbf{G}_{hh_{k+c\tau}}^i & \dots & \mathbf{G}_{hh_{k+(c+\xi)\tau}}^i \end{bmatrix} \quad (14)$$

$$= \begin{bmatrix} \mathbf{P}_\alpha^i \\ \mathbf{P}_\alpha^i \mathbf{A}^{i\tau} \\ \vdots \\ \mathbf{P}_\alpha^i \mathbf{A}^{i c\tau} \end{bmatrix} \mathbf{A}^{ik}(\gamma^i) \begin{bmatrix} \mathbf{Q}_c^i & \mathbf{A}^{i\tau} \mathbf{Q}_c^i & \dots & \mathbf{A}^{i\xi\tau} \mathbf{Q}_c^i \end{bmatrix} = \mathbf{P}_\epsilon^i \mathbf{A}^{ik}(\gamma^i) \mathbf{Q}_\xi^i \quad (15)$$

Step 4: Decompose \mathfrak{N}_0^i using singular value decomposition: $\mathfrak{N}_0^i = \mathbf{R}^i \boldsymbol{\Sigma}^i \mathbf{S}^{iT}$.

Step 5: Determine the order of the system by examining the singular values of Hankel matrix \mathfrak{N}_0^i .

Step 6: Construct a minimum order realization $[\mathbf{A}^i, \mathbf{Q}_c^i, \mathbf{P}_\alpha^i]$ using a shifted block Hankel matrix \mathfrak{N}_1^i .

$$\mathbf{G}_{hh_k}^i = \mathbf{H}_k^i \mathbf{H}_0^{iT} = \mathbf{P}_\alpha^i \mathbf{A}^{ik} (\gamma^i) \mathbf{Q}_\beta^i \mathbf{Q}_\beta^{iT} \mathbf{P}_\alpha^{iT} = \mathbf{P}_\alpha^i \mathbf{A}^{ik} (\gamma^i) \mathbf{Q}_c^i \quad (16)$$

Step 7: Calculate the controllability matrix \mathbf{Q}_β^i and determine a minimum order realization $[\mathbf{A}^i (\gamma^i), \mathbf{B}^i (\gamma^i), \mathbf{C}^i (\gamma^i)]$.

$$\mathbf{H}_0^i = \mathbf{P}_\alpha^i \mathbf{Q}_\beta^i \quad (17)$$

where:

$$\mathbf{P}_\alpha^i = \begin{bmatrix} \mathbf{C}^i (\gamma^i) \\ \mathbf{C}^i (\gamma^i) \mathbf{A}^i (\gamma^i) \\ \mathbf{C}^i (\gamma^i) \mathbf{A}^{i^2} (\gamma^i) \\ \vdots \\ \mathbf{C}^i (\gamma^i) \mathbf{A}^{i^{a-1}} (\gamma^i) \end{bmatrix} \quad (18)$$

$$\mathbf{Q}_\beta^i = \begin{bmatrix} \mathbf{B}^i (\gamma^i) & \mathbf{A}^i (\gamma^i) \mathbf{B}^i (\gamma^i) & \dots & \mathbf{A}^{i^{b-1}} (\gamma^i) \mathbf{B}^i (\gamma^i) \end{bmatrix} \quad (19)$$

so

$$\mathbf{Q}_\beta^i = \mathbf{P}_\alpha^{i+} \mathbf{H}_0^i \quad (20)$$

$$\mathbf{A}^i = (\boldsymbol{\Sigma}^i)^{-1/2} \mathbf{R}_n^{iT} \mathbf{H}_1^i \mathbf{S}_n^i (\boldsymbol{\Sigma}^i)^{-1/2} \quad (21)$$

$$\mathbf{D}^i = \bar{\mathbf{Y}}_{m \times 1}^i; \quad \mathbf{B}^i = \text{first } r \text{ columns of } \mathbf{Q}_\beta^i; \quad \mathbf{C}^i = \text{first } m \text{ rows of } \mathbf{P}_\alpha^i \quad (22)$$

3 Fuzzy Kalman Filter Algorithm

The TS fuzzy Kalman filter presents the $i^{|l|=1,2,\dots,l}$ -th rule, given by:

$R^{(i)}$: IF $\tilde{y}_{1_{k-1}}$ IS $F_{j|\tilde{y}_{1_{k-1}}}^i$ AND ... AND IF $\tilde{y}_{n_{k-1}}$ IS $F_{j|\tilde{y}_{n_{k-1}}}^i$ THEN

$$\begin{aligned} \mathbf{x}_k^i &= \mathbf{A}^i \mathbf{x}_{k-1}^i + \mathbf{K}_k^i (y_k^i - \mathbf{C}^i \mathbf{x}_k^i) \\ y_k^i &= \mathbf{C}^i \mathbf{x}_k^i + \mathbf{D}^i u_k \end{aligned} \quad (23)$$

where A^i , C^i , and D^i are matrices estimated by ERA/DC Algorithm based on clustering, as described in Sect. 2.2, in the i -th rule; and K^i corresponds to Kalman gain in the i -th rule. According to fuzzy clustering algorithm described in Sect. 2.1, and the ERA/DC algorithm based on clustering described in Sect. 2.2, the Kalman filter is given by:

$$\begin{aligned}\tilde{\mathbf{x}}_k &= \sum_{i=1}^l (A^i(\gamma_i)\mathbf{x}_{k-1}^i + \mathbf{K}_k^i(\gamma_i)(y_k^i - C^i(\gamma_i)\mathbf{x}_k^i)) \\ \tilde{y}_k &= \sum_{i=1}^l (C^i(\gamma_i)\mathbf{x}_k^i + D^i(\gamma_i)u_k)\end{aligned}\quad (24)$$

Initialize the $\hat{\mathbf{x}}_0^i, \mathbf{P}_0^i, k = 1, i = 1$;

while (need to estimate the system state and output) **do**

for $i = 1, 2, \dots, l$

Time Update:

$$\hat{\mathbf{x}}_k^{-i} = A^i(\gamma_i)\hat{\mathbf{x}}_{k-1}^i$$

$$\mathbf{P}_k^{-i} = A^i(\gamma_i)\mathbf{P}_{k-1}^i(\gamma_i)A^{iT}(\gamma_i) + \mathbf{Q}^i(\gamma_i)$$

Get the measurement y_k ;

Measurement Update:

$$\mathbf{K}_k^i = \mathbf{P}_k^{-i}(\gamma_i)C^{iT}(\gamma_i)(C^i(\gamma_i)\mathbf{P}_k^{-i}(\gamma_i)C^{iT}(\gamma_i) + \mathbf{R}^i(\gamma_i))^{-1}$$

$$\hat{\mathbf{x}}_k^i = \hat{\mathbf{x}}_k^{-i} + \mathbf{K}_k^i(\gamma_i)(y_k - C^i(\gamma_i)\hat{\mathbf{x}}_k^{-i})$$

$$\tilde{\hat{\mathbf{x}}}_k = \sum_{i=1}^l \gamma^i \hat{\mathbf{x}}_k^i$$

$$\mathbf{P}_k^i = (\mathbf{I} - \mathbf{K}_k^i(\gamma_i)C^i(\gamma_i))\mathbf{P}_k^{-i}(\gamma_i)$$

$$\hat{y}_k^i = C^i(\gamma_i)\hat{\mathbf{x}}_k^i + D^i(\gamma_i)u_k$$

$$\tilde{\hat{y}}_k = \sum_{i=1}^l \gamma^i \hat{y}_k^i$$

$i = i + 1$

end for

$k = k + 1$

end while

The \mathbf{I} is defined as an identity matrix $n \times n$; \mathbf{K}_k^i is the Kalman gain matrix to i -th rule of fuzzy model; \mathbf{P}_k^{-i} is the error covariance matrix *a priori* to i -th rule of fuzzy model; $\mathbf{P}_k^i = E[(x_k^i - \hat{x}_k^i)(x_k^i - \hat{x}_k^i)^T]$ is the error covariance matrix *a posteriori* to i -th rule of fuzzy model. The system noise covariance matrix and the measurement noise covariance matrix are defined by $\mathbf{Q}^i = \text{diag}(Q_{11}^i, Q_{22}^i, \dots, Q_{m_m}^i)$ and $\mathbf{R}^i = \text{diag}(R_{11}^i, R_{22}^i, \dots, R_{m_m}^i)$, respectively, with:

$$Q_{nm}^i = (\bar{x}_{n_k} - x_{n_k}^i)^2 \text{ and } R_{nm}^i = (\bar{y}_{n_k} - y_{n_k}^i)^2 \quad (25)$$

where \bar{x}_{n_k} and \bar{y}_{n_k} corresponds to mean value of x_{n_k} and y_{n_k} at time 1 to k , respectively; $x_{n_k}^i$ and $y_{n_k}^i$ corresponds to value of state and output n , at time k , in the i -th rule of fuzzy model, respectively.

4 Computational Results

4.1 Description of Nonlinear Dynamic System to Identify

Considering the time-variant nonlinear discrete-time system (truck-trailer model described in [12]) given by:

$$\begin{aligned} x_{1_{k+1}} &= \left(1 - \frac{v_k T}{L}\right) x_{1_k} + \frac{v_k T}{l} u_k \\ x_{2_{k+1}} &= \frac{v_k T}{L} x_{1_k} + x_{2_k} \\ x_{3_{k+1}} &= x_{3_k} + v_k T \sin(\theta_k) \\ y_k &= 7x_{1_k} - 2x_{2_k} + 0.03x_{3_k} \end{aligned} \quad (26)$$

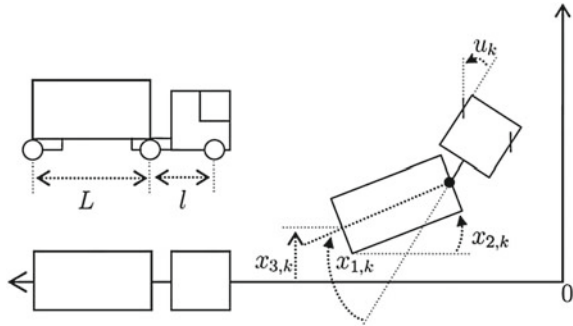
with $\theta_k = x_{2_k} + \frac{v_k T}{2L} x_{1_k}$; where x_{1_k} is the angle difference, in radians, between truck and trailer; x_{2_k} is the angle of trailer, in radians; x_{3_k} is the vertical position of rear of trailer, in meters; u_k is the steering angle, in radians; and, T is the sampling time, in seconds. Considering $T = 2.0$ s, $l = 2.8$ m, $L = 5.5$ m and the speed of truck-trailer, called v_k , with random values between -0.4 m/s and -1 m/s. The diagram about the truck-trailer model is described in Fig. 1.

The input applied in the time-variant nonlinear dynamic system correspond to $N(0, 2)$. In order to estimate the fuzzy sets, the FCM (Fuzzy C-Means) algorithm was implemented for 2 clusters, tolerance $\alpha = 0.001$ and weighting exponent $w = 1.2$. From the input and output data of the nonlinear dynamic system, taking into account the weights of fuzzy sets, the identified Fuzzy Kalman Filter, as defined in Eq. (23), with the following matrices in the rules 1 and 2, is given by:

Matrices in the rule 1:

$$A^1 = \begin{bmatrix} 1.004 & 1.426 \times 10^{-4} & 1.584 \times 10^{-8} \\ 0.062 & 0.005 & -4.317 \times 10^{-6} \\ -4.274 \times 10^{-6} & -3.247 \times 10^{-5} & 1.053 \end{bmatrix} \quad \begin{aligned} C^1 &= [-0.225 \quad 6.445 \times 10^{-5} \quad 0] \\ D^1 &= -0.007 \end{aligned}$$

Fig. 1 Truck-trailer model, originally described in [12]



Matrices in the rule 2:

$$A^2 = \begin{bmatrix} 1.007 & 1.074 \times 10^{-4} & -4.182 \times 10^{-9} \\ -0.048 & 0.177 & -2.493 \times 10^{-5} \\ -2.798 \times 10^{-7} & -6.375 \times 10^{-5} & 0.396 \end{bmatrix} \quad C^2 = [-0.148 \quad 2.901 \times 10^{-5} \quad 0]$$

$$D^2 = -0.003$$

and

$$F_1(y_k, a, b) |_{(a=-0.133; b=-0.0481)} = \begin{cases} 1, & y_k \leq a \\ 1 - 2 \left(\frac{y_k - a}{b - a} \right)^2, & a \leq y_k \leq \frac{a + b}{2} \\ 2 \left(\frac{y_k - a}{b - a} \right)^2, & \frac{a + b}{2} \leq y_k \leq b \\ 0, & y_k \geq b \end{cases}$$

with $F_2 = 1 - F_1$.

The system model output obtained through proposed methodology compared to the time-variant nonlinear dynamic system output, the instantaneous membership values, and the values of speed v_k , are shown in Fig. 2, respectively. In this experiment, no knowledge of state x_3 , was considered. The states x_1 , x_2 , and x_3 of time-variant nonlinear dynamic system are compared to states estimated by Fuzzy Kalman Filter, are shown in Fig. 3, respectively. It is observed that the states estimated by Fuzzy Kalman Filter follow the behavior of the states of time-variant nonlinear dynamic system. The metrics RMSE (Root Mean Square Error) and VAF (Variance Accounted For) were used to evaluate the performance of the Fuzzy Kalman Filter. The Fuzzy Kalman Filter presents RMSE and VAF values of 0.0306 and 96.8919,

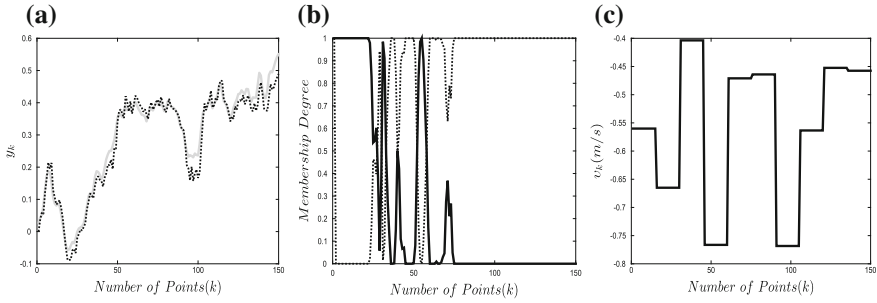


Fig. 2 **a** The system model output obtained through proposed methodology (in gray line) compared to the time-variant nonlinear dynamic system output (dotted line, in black); **b** the instantaneous membership values F^1 (in black) and F^2 (dotted line, in black); **c** the instantaneous values of v_k

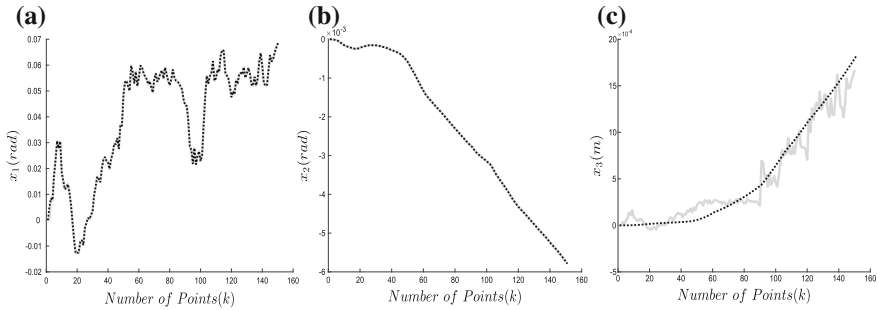


Fig. 3 State estimation by Fuzzy Kalman Filter (in gray line) and state of time-variant nonlinear dynamic system (dotted line, in black): **a** state x_1 , **b** state x_2 , **c** unknown state x_3

respectively for output estimation; values of 3.6680×10^{-4} and 99.9629 , respectively for estimation of state x_1 ; values of 0 and 100 , respectively for estimation of state x_2 ; values of 1.1105×10^{-4} and 94.7150 , respectively for estimation of state x_3 .

5 Conclusion

The strategy to Fuzzy Kalman Filter identification, proposed in this paper, was efficient about tracking the dynamic behavior related to output and states of a time-variant nonlinear dynamic system, with partial knowledge of state.

Acknowledgments This work was encouraged by FAPEMA and by Ph.D. Program in Electrical Engineering of Federal University of Maranhão (PPGEE/UFMA).

References

1. Wu, C.Y., Tsai, J.S.H., Guo, S.M., Shieh, L.S., Canelon, J.I., Ebrahimzadeh, F., Wang, L.: A novel on-line observer Kalman filter identification method and its application to input-constrained active fault-tolerance tracker design for unknown stochastic systems. *J. Franklin Inst.* **352**, 1119–1151 (2015)
2. Juang, J.N.: *Applied System Identification*. Prentice Hall, United States (1994)
3. Kordik, V.: *Kalman Filter*. InTech (2010)
4. Huo, Y., Cai, Z., Gong, W., Liu, Q.: A new adaptive kalman filter by combining evolutionary algorithm and fuzzy inference system. In: *China: IEEE Congress on Evolutionary Computation (CEC)*, pp. 2893–2899 (2014)
5. Lima, D.P., Kato, E.R.R., Tsunaki, R.H.: A new comparison of Kalman filtering methods for chaotic series. In: *California: IEEE International Conference on Systems, Man and Cybernetics (SMC)*, pp. 3531–3536 (2014)
6. Inoue, R.S., Terra, M.H., Cerri, J.P.: Extended robust Kalman filter for attitude estimation. *IET Control Theory Appl.* **10**, 162–172 (2016)
7. Serra, G.L.O.: *Frontiers in Advanced Control Systems*. InTech, Croatia (2012)
8. Zadeh, L.A.: Fuzzy sets. *Inf. Control* **8**, 338–353 (1965)
9. Grigorie, T.L.: *Fuzzy Controllers, Theory and Applications*. InTech, Croatia (2011)
10. Babuska, R., Schutter, B.D., Lendek, Z., Guerra, T.M.: *Stability Analysis and Nonlinear Observer Design Using Takagi-Sugeno Fuzzy Models*. Springer Publishing Company, Incorporated (2010)
11. Juang, J.N., Pappa, R.S.: An eigensystem realization algorithm for modal parameter identification and model reduction. *J. Guidance Control Dyn.* **8**(5), 620–627 (1985)
12. Zhang, J., Shi, P., Qiu, J., Nguang, S.K.: A novel observer-based output feedback controller design for discrete-time fuzzy systems. *IEEE Trans. Fuzzy Syst.* **23**(1), 223–229 (2015)

Neural Network Control Strategies Applied to a DC Motor with a Nonlinear Load

Luís M.M. Ferreira and Ramiro S. Barbosa

Abstract This paper investigates the use of neural networks in the design of control systems. For that, it was considered two different neural control structures, namely the stabilizing and the adaptive reference model control systems. The analysis tries to understand to which extent the introduction of neural networks improves a process control. The control systems are simulated and analyzed for several reference inputs with and without added noise in the sensor. The simulation results show the improved performance of the control systems with neural networks.

Keywords Neural network · Control · Backpropagation · Proportional-integral-derivative controller · Stabilizing controller · Reference adaptive controller

1 Introduction

Neural networks (NNs) are a method of information processing inspired in the way that the nervous biological system, more specifically the brain, processes information and acquire knowledge through experience. The NN is capable of processing information, recognize errors, learn from those errors and adapt itself [1–3]. One of the biggest problems faced by systems designers in different areas is to find the means to control and tune the system under consideration given the uncertainty about the underlying process nature. The adaptive control processes, or adaptive processes which learn through time, have been designed to aim this problem for

L.M.M. Ferreira · R.S. Barbosa (✉)
Department of Electrical Engineering,
GECAD—Knowledge Engineering and Decision Support Research Center,
Institute of Engineering/Polytechnic of Porto (ISEP/IPP), Porto, Portugal
e-mail: rsb@isep.ipp.pt

L.M.M. Ferreira
e-mail: 1080500@isep.ipp.pt

certain types of system models, where only the model parameters are unknown [4]. One area that is receiving special attention is the use of these networks for nonlinear dynamic systems control and tuning.

In this work we use two different control strategies based in NNs, namely the stabilizing controller and the reference adaptive controller, to control a DC motor with a nonlinear load. The DC motor is a common actuator used in many practical applications. The proposed methodology should be capable of mimic the nonlinear process and control it in an effective way. The performance of the proposed NN control structures is analyzed and compared with the classical PID controller tuning schemes.

2 System Description

2.1 DC Motor Model

The schematic of the Direct Current (DC) motor is presented in Fig. 1(left). We will use input/output patterns generated by simulation of this model for training the NN.

The DC motor dynamics is given by the following equation [5, 6]:

$$L_a J \frac{d^2 \omega(t)}{dt^2} + (R_a J + L_a B) \frac{d\omega(t)}{dt} + (R_a B + K_b K_T) \omega(t) + L_a \frac{dT_L(t)}{dt} + R_a [T_L(t) + T_F] + K_T v_a(t) = 0 \quad (1)$$

where $\omega(t)$ is the angular velocity, R_a the armature resistance, L_a the armature inductance, B the viscous-friction coefficient with attached mechanical load, J the moment of inertia with attached mechanical load, K_T the torque constant, K_b the back emf constant, T_F the frictional torque, and $v_a(t)$ the applied armature voltage.

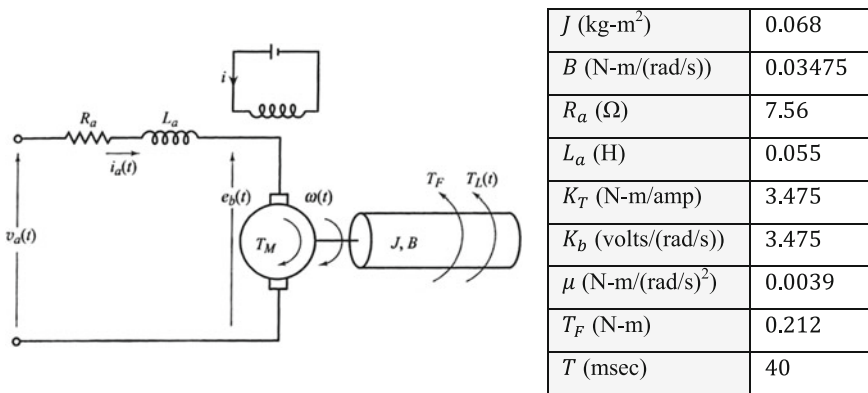


Fig. 1 Schematic of the DC motor model (left) and DC motor parameter values (right) [5]

Table 1 DC motor constant values K_i ($i = 1, 2, \dots, 6$)

$K_1 = \frac{2L_a J + T(R_a J + L_a B) - T^2(R_a B + K_b K_T)}{L_a J + T(R_a J + L_a B)}$	0.34366
$K_2 = -\frac{L_a J}{L_a J + T(R_a J + L_a B)}$	-0.1534069
$K_3 = -\frac{T(\mu L_a + \mu R_a T)}{L_a J + T(R_a J + L_a B)}$	-2.28692810^{-3}
$K_4 = \frac{T\mu L_a}{L_a J + T(R_a J + L_a B)}$	3.519335810^{-4}
$K_5 = \frac{K_T T^2}{L_a J + T(R_a J + L_a B)}$	0.2280595
$K_6 = -\frac{T_f R_a T^2}{L_a J + T(R_a J + L_a B)}$	-0.105184

The disturbance load torque $T_L(t)$ corresponds to a propeller driven or fan type load, which takes the following form:

$$T_L(t) = \mu[\omega(t)]^2 [\text{sgn}\omega(t)] \quad (2)$$

where μ is a constant. Figure 1(right) present the parameter values associated with the DC motor [5].

The discrete-time model is derived by replacing all continuous differentials with finite differences [5, 7], yielding:

$$\begin{aligned} \omega(k+1) = & K_1\omega(k) + K_2\omega(k-1) + K_3[\text{sgn}(\omega(k))]\omega^2(k) \\ & + K_4[\text{sgn}(\omega(k))]\omega^2(k-1) + K_5v_a(k) + K_6 \end{aligned} \quad (3)$$

where the K_i ($i = 1, 2, \dots, 6$) expressions and corresponding values are presented in Table 1, in which T is the sampling period.

2.2 Identification of Inverse Dynamics

Equation (3) can be manipulated to obtain the inverse dynamic model of the DC motor system as:

$$\begin{aligned} v_a(k) = & f[\omega(k+1), \omega(k), \omega(k-1)] \\ = & \frac{1}{K_5} [\omega(k+1) - K_1\omega(k) - K_2\omega(k-1) - K_3\{\text{sgn}(\omega(k))\}\omega^2(k) - K_4\{\text{sgn}(\omega(k))\}\omega^2(k-1) - K_6] \end{aligned} \quad (4)$$

A NN is trained to emulate the assumed unknown nonlinear function (4). Randomly generated input patterns of $[\omega(k+1), \omega(k), \omega(k-1)]$ and the corresponding target $v_a(k)$, are used for *off-line* training. In conforming to the mechanical and electrical hardware limitations of the motor, the following constrained operating space is defined: $-30 < \omega(k) < 30$ rad/s, $|\omega(k-1) - \omega(k)| < 1.0$ rad/s and $|v_a(k)| < 100$ V.

2.3 PID Controller

The PID controller will be used for comparison purposes. It is given by the following transfer function:

$$G_c(s) = \frac{U(s)}{E(s)} = K_p + \frac{K_i}{s} + K_d s \tag{5}$$

where the proportional gain (K_p), the integral gain (K_i) and derivative gain (K_d) are the parameters to be tuned. $E(s)$ is the input error and $U(s)$ the output of the PID controller.

In the stabilizing controller, the PID controller is tuned using the Ziegler-Nichols (Z-N) and the Coon-Cohen (C-C) heuristic rules [5, 6], and the Zhuang-Atherton (Z-A) optimal tuning method [7].

3 Neural Control Strategies

3.1 Stabilizing Controller

Figure 2 depicts the stabilizing control structure. The feedforward control is used for improving the reference tracking, while feedback is used for stabilizing the system and for suppressing disturbances. Initially the stabilizing controller has complete control over the process. However, over time the inverse model will learn through the adaptive algorithm and feedback control signal, and eventually take over the process control. The NN is trained to emulate the process output-input mapping and generate the feedforward control signal. The normalization blocks are used to convert the input and output network values into a compatible range to the network itself and to the process. A saturation block is used to convert the control signal into the operational range of the process. Usually an adaptive algorithm is used but in this scheme this block was removed because the network is already trained. The feedback control is performed by a PID controller.

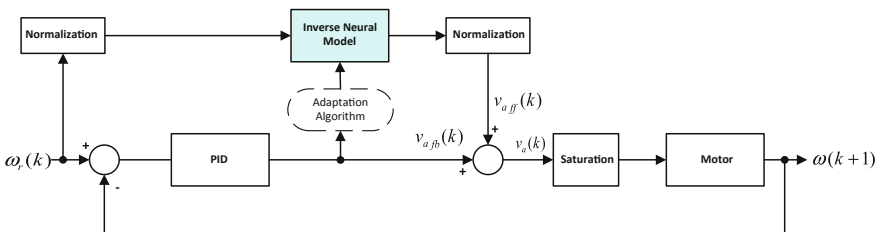


Fig. 2 Stabilizing controller

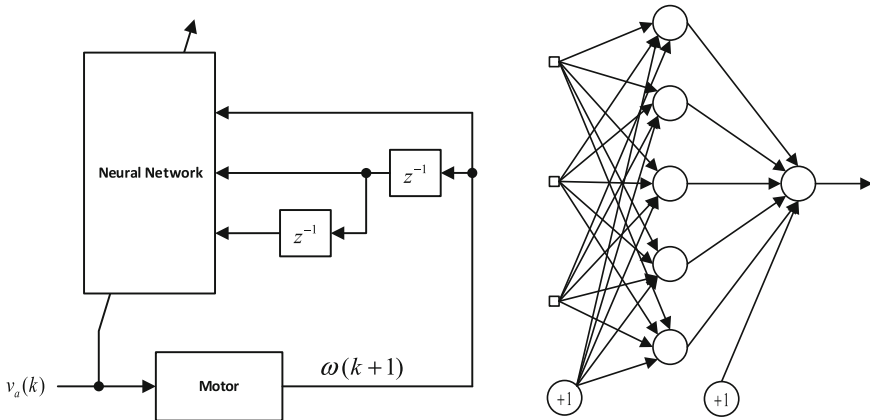


Fig. 3 Scheme used for training (*left*) and NN structure (*right*) for the stabilizing controller

Neural network training. Figure 3 depicts the scheme used for training the NN and its structure. The inputs of the NN (Fig. 3, right) are the speed values of $[\omega(k + 1), \omega(k), \omega(k - 1)]$ and the desired target is $v_a(k)$, since the neural model should represent the inverse dynamics of the system, as expressed by Eq. (4). The inputs and output are normalized to interval $[0, 1]$. The NN has an input layer, a hidden layer and an output layer. Several tests were performed to determine the number of neurons in the hidden layer. The NN with five neurons showed the best performance. The hidden layer uses a hyperbolic tangent activation function and the output layer the linear activation function. The weights are initialized with random values in the interval $[-0.5, 0.5]$ [8]. The NN is trained by applying the Levenberg-Marquardt (LM) algorithm with a learning rate of $lr = 0.1$. It was used the LM algorithm due to its fast convergence and robustness during the training process [1, 3].

3.2 Reference Adaptive Controller

Figure 4 illustrates the reference adaptive controller. It consists of two neural networks: a controller network and a model network. The controller network performs the PID tuning and is adaptively trained to force the output to track a reference (i.e., it is trained *online*). The model network is an input-output mapping of the process trained a priori, and is used to predict the effect of controller changes on output, which allows the updating of controller parameters. It is also included a saturation block for control signal limitation. The system starts by analyzing the process behavior in the previous sample and calculates the error. It is necessary to apply the training algorithm to change the network weights so it can compute the PID gains and then generate the correct control signal. The motor input (control

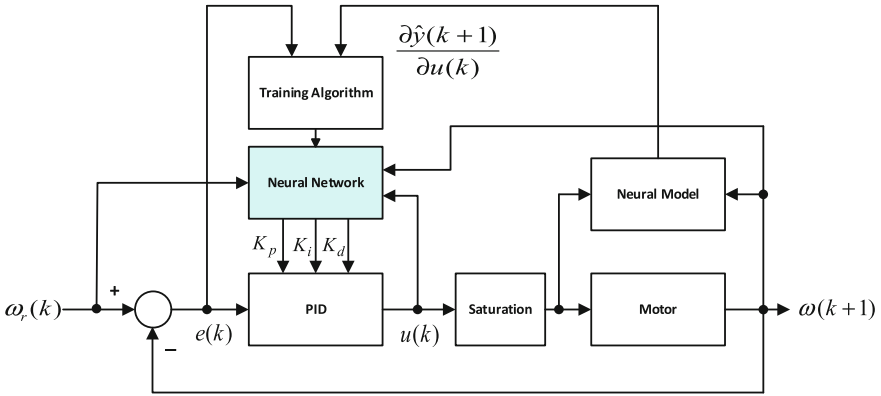


Fig. 4 Reference adaptive controller

signal) will determine the process response which is going to be used to calculate the system error for the next sample. At the same time, the neural model of the process computes the Jacobian to be used as input in the training algorithm.

Neural model training. First, we must define the neural model of motor system. Figure 5 depicts the scheme used for training and the adopted NN structure. As opposed to previous stabilizing controller, it is desired to map the input-output behavior (i.e., process identification), and so there are some differences in terms of training and configuration between the two control strategies. Here, the desired output is the angular speed of the motor. The number of inputs is determined taking into account their influence in the output, resulting changes in terms of the structure of the network as well in the training scheme. The inputs and output are normalized to the interval $[0, 1]$. The NN has an input layer, a hidden layer and an output layer.

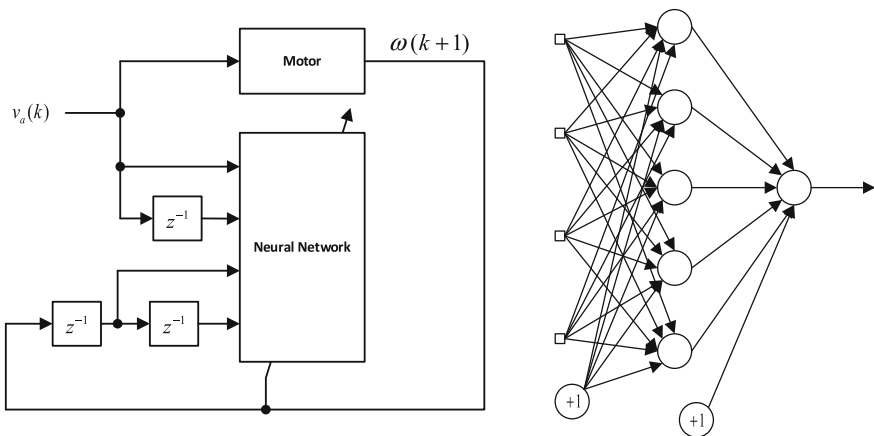


Fig. 5 Scheme used for training (left) and NN structure (right) for the adaptive controller

The hidden layer uses a hyperbolic tangent activation function and the output layer a linear activation function. The weights are initialized with random values in the interval $[-0.5, 0.5]$ [8]. The NN is trained by applying the LM algorithm with a learning rate of $lr = 0.1$. It was used the LM algorithm due to its fast convergence and robustness during the training process [1, 3].

PID controller. In the reference adaptive controller, the PID controller is implemented digitally. So, by using the Euler backward rule ($s \cong (z - 1)/Tz$) in transfer function of Eq. (5), and a sampling period of $T = 1$ s, the discrete PID controller is given by the following difference equation:

$$u(k + 1) = u(k) + K_p(e(k + 1) - e(k)) + K_i e(k + 1) + K_d(e(k + 1) - 2e(k) + e(k - 1)) \tag{6}$$

Neural network for PID tuning. The NN for PID tuning involves two blocks as shown in Fig. 4. The neural network calculates the PID gains while the training algorithm includes all the necessary equations for updating the weights. The structure of the NN consists of an input layer, a hidden layer with six neurons and an output layer with three neurons. The hidden layer uses a hyperbolic tangent activation function and the output layer uses an activation function of the form $g(x) = [1 + \tanh(x)]/2$, which gives output values in the interval $[0, 1]$. The network parameters were selected to give the best performance while considering the values for the corresponding output. Scaling factors were applied to output values of network in order to increase the range of values admissible by the PID gains. This network solves the nonlinear function:

$$[K_p(k), K_i(k), K_d(k)] = f[u(k - 1), u(k - 2), \omega(k), \omega(k - 1), \omega_r(k), \omega_r(k - 1)] \tag{7}$$

However, the output values must be correctly determined, and for that it is necessary to train the network. In this scheme, the network training is executed *online*. It is used the backpropagation training algorithm as this procedure is implemented in an effective way through MATLAB code [5]. This algorithm will change the network weights in each iteration so that the calculated PID gains can minimize the difference between the reference and motor speeds, using the following cost function:

$$E = \frac{1}{2} [r(k + 1) - y(k + 1)]^2 = \frac{1}{2} e^2(k + 1) \tag{8}$$

Before initiating the training it is also necessary to define adequately the initial network weights, since these are essential for the whole learning process, particularly in which regards the convergence of the algorithm to the optimal value. The network weights are initialized with random values in the interval $[-0.5, 0.5]$ and the inputs and the output values of (K_p, K_i, K_d) are initialized to 0.5. These initial values were determined taking into account the best convergence of the network [8].

Neural model. The neuronal network model corresponds to a function that contains the calculations of the neural model of the process. The neuronal network processes the inputs and calculates the predicted value for the output of the process. For this case this calculation becomes redundant, because the network is already trained, i.e. the weights of the connections of the network structure (Fig. 5, right) are already optimized, making it capable of emulating the process. Thus, if the neuronal model is well implemented, the error between the model and the process is close to 0. This network can be expressed as $[\hat{y}(k+1), J(k+1)] = f[\omega(k), \omega(k-1), u(k), u(k-1)]$, where \hat{y} is the predicted response of process, and J is the Jacobian. The main purpose of this block is the calculation of the Jacobian $J = \partial y(k+1) / \partial u(k)$, which a priori is unknown. However, it is possible to calculate this value by using the predicted value of output, i.e. the output of the neural model, as

$$\partial y(k+1) / \partial u(k) \approx \partial \hat{y}(k+1) / \partial u(k).$$

4 Simulation Results

4.1 Stabilizing Controller

The simulations involve a comparison of responses regarding a simple feedback system that uses a single PID controller and the stabilizing controller. The main difference between the two systems is the addition of a trained NN in the feed-forward path of the stabilizing controller (see Fig. 2). The two systems are simulated with and without added white noise in the sensor, and applying the three tuning methods of Z-N, C-C and Z-A, for a sinusoidal and square wave type inputs. All simulations are performed in the Simulink environment.

Figures 6 and 7 show correspondingly the responses of stabilizing controller for the sinusoidal and square wave type inputs when applying the three tuning methods (Z-N, C-C and Z-A). For comparison purposes, the response of the feedback control PID system is also plotted. For the sinusoidal input, the responses follow the reference almost perfectly, except the PID tuned with Z-N method that deviates substantially from the desired. In general, the stabilizing controller shows a better performance than the PID controller. We get the same conclusions when analyzing the responses of the systems to the square wave type input. If noise is added to the system, we verify that the responses of both systems (PID and stabilizing controller) are very similar to those obtained without added noise. However, as noted, the noise is not completely eliminated by the controllers.

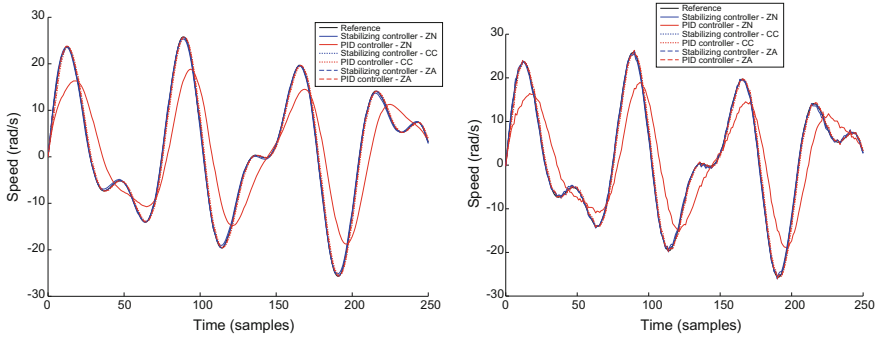


Fig. 6 Responses of the stabilizing controller for a sinusoidal input without noise (*left*) and with added noise in the sensor (*right*)

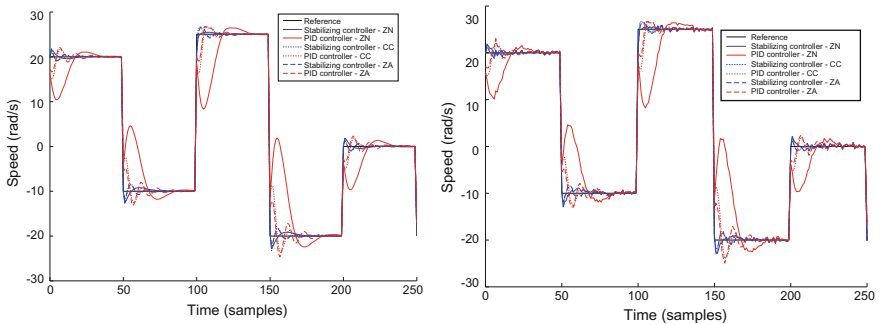


Fig. 7 Responses of the stabilizing controller for a square wave input without noise (*left*) and with added noise in the sensor (*right*)

4.2 Reference Adaptive Controller

Unlike the stabilizing controller, the reference adaptive controller has a neural network trained *online*. Thus, the learning process, which includes a wide number of variables, may influence the output responses and the system performance. One of the most important variables is the initial weight values. To guarantee that the weights allow the system to reach a minimum error, one must gather a set of simulations and choose the set that lead the system to a better performance. The initial random weights should take small values. Also, their variations should be small, ensuring that the weights increase in each iteration and helping the network to converge more quickly. After consideration of these assumptions, it was defined that the initial weights have random values in the interval $[-0.5, 0.5]$. Other parameters like the learning rate, *momentum*, number neurons in hidden layer, and range of outputs or gains, may also influence the performance of system. Several tests were performed to find the most suitable values for these parameters. For that,

it was performed 50 simulations and the set of values with best Mean Square Error (MSE) index was chosen. The obtained parameters were: learning rate $lr = 0.3$, momentum $\mu = 0.8$ and five neurons in hidden layer. The PID gain intervals were established as $K_p \in [0, 3]$, $K_i \in [0, 5]$, and $K_d \in [0, 1]$.

For this controller the simulation schemes were implemented in MATLAB code. Figure 8(right) shows the response of the reference adaptive controller for a sinusoidal type input with white Gaussian noise added to the sensor, while Fig. 8(left) presents the response of system without noise. Figure 9 illustrates the responses of the system for a square wave type input. For the system without the noise, and in the case of a sinusoidal input, the controller gives a very good response following the input precisely. For the square wave, although the tuning of network is performed *online*, the performance is very acceptable. When added noise, the controller have difficulty in dealing with it and the responses show some oscillations that the system is not capable to eliminate. This is verified for both the sinusoidal and square wave type inputs. In general, the reference adaptive controller gives an acceptable response.

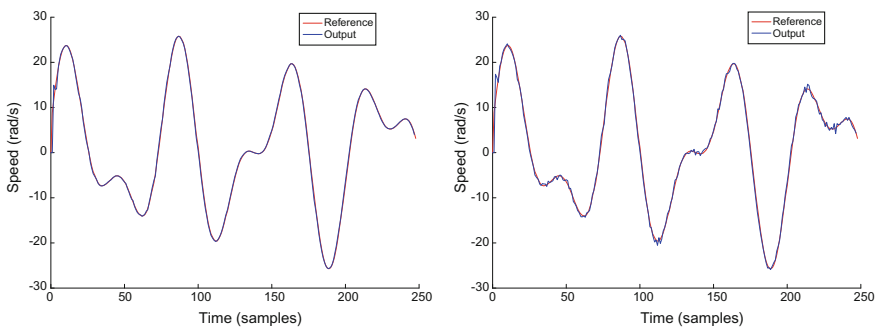


Fig. 8 Responses of the reference adaptive controller for a sinusoidal input without noise (*left*) and with added noise in the sensor (*right*)

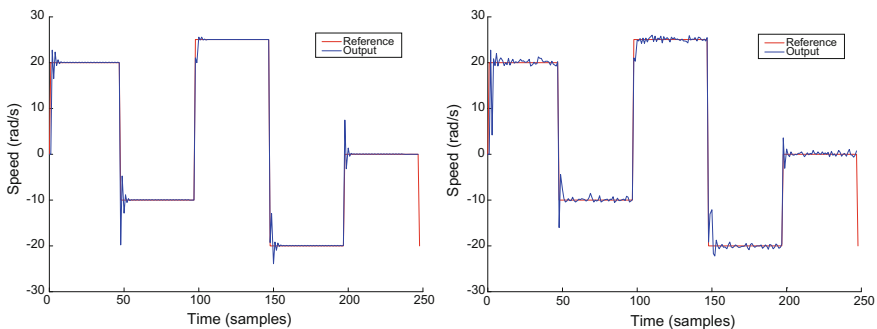


Fig. 9 Responses of the reference adaptive controller for a square wave input without noise (*left*) and with added noise in the sensor (*right*)

5 Conclusions

This paper compared two controller strategies that use NNs for the control of a DC motor with a nonlinear load. The results proved the effectiveness of NNs in control applications. The stabilizing controller has an obvious superiority over other studied control systems. However, it is important to state that the reference adaptive controller is not fully optimized. Additionally, we could also use different training algorithms.

Acknowledgments This work is supported by FEDER Funds through the “Programa Operacional Factores de Competitividade - COMPETE” program and by National Funds through FCT “Fundação para a Ciência e a Tecnologia”.

References

1. Haykin, S.: *Neural Networks and Learning Machines*, 3rd edn. Pearson (2009)
2. Hagan, M.T., Demuth, H.B.: Neural networks for control. In: *American Control Conference*, pp. 1642–1656. IEEE, San Diego (1999)
3. Rojas, R.: *Neural Networks: A Systematic Introduction*. Springer, Berlin (1996)
4. Spall, J.C.: A neural network controller for systems with unmodeled dynamics with applications to wastewater treatment. *IEEE Trans Syst Man Cybernet Part B: Cybernet* **27**(3), 369–375 (1997)
5. Gopal, M.: *Digital Control and State Variable Methods: Conventional and Intelligent Control Systems*, 3rd edn. McGraw-Hill, Singapore (2010)
6. Åström, K.J., Hägglund, T.: *PID Controllers: Theory, Design, and Tuning*. Instrument Society of America, North Carolina (1995)
7. Zhuang, M., Atherton, D.P.: Automatic tuning of optimum PID controllers. *IEEE Proc D* **140** (3), 216–224 (1993)
8. Nguyen, D., Widrow, B.: Improving the learning speed of 2-layer neural networks by choosing initial values of the adaptive weights. In: *Proceedings of the International Joint Conference on Neural Networks (IJCNN)*, pp. 21–26. Edward Brothers, San Diego (1990)

Grey Wolf, Gravitational Search and Particle Swarm Optimizers: A Comparison for PID Controller Design

Paulo Moura Oliveira and Damir Vrančić

Abstract Nature and biologically inspired metaheuristics can be powerful tools to design PID controllers. The grey wolf optimization is one of these promising and interesting metaheuristics, recently introduced. In this study the grey wolf optimization algorithm is proposed to design PID controllers, and the results obtained compared with the ones obtained with gravitational search and particle swarm optimization algorithms. Simulation results obtained with these three bio-inspired metaheuristics applied to a set of benchmark linear plants are presented, considering the design objective of set-point tracking. The results are also compared with two non-iterative PID tuning techniques.

1 Introduction

Metaheuristics which are based on natural and biological concepts have been proposed in the last decades. Some of the most well-known nature and bio-inspired (NABI) metaheuristics are: Simulated Annealing (SA) [1], Evolutionary Programming (EP) [2], Evolutionary Strategy (EG) [3], Genetic Algorithm (GA) [4], Population-Based Incremental Learning (PBIL) [5], Ant-Colony Optimization (ACO) [6], Genetic Programming (GP) [7], Differential Evolution (DE) [8] and Particle Swarm Optimization (PSO) [9]. All the former metaheuristics have been extensively applied to successfully solve search and optimization problems in a wide range of scientific areas, and are considered well established techniques. These

P.M. Oliveira (✉)

INESC TEC—INESC Technology and Science Department of Engineering,
School of Sciences and Technology, Universidade de Trás-os-Montes e Alto Douro,
UTAD, 5001-801 Vila Real, Portugal
e-mail: oliveira@utad.pt

D. Vrančić

Department of Systems and Control, Jožef Stefan Institute, Jamova cesta 39,
Ljubljana, Slovenia
e-mail: damir.vrancic@ijs.si

techniques can be classified using different criteria which may be sub-divided according to the inspiration motivation: physically and/or chemically inspired (e.g. SA); evolutionary algorithms (e.g. EP, EG, GA, GP, DE); swarm intelligence algorithms (e.g. ACO, PSO). However, many other classification criteria can be used, such as: single-solution or population based, single-criteria or multi-criteria, single-population or multi-population, co-evolutionary, etc. Moreover, many of the former algorithms have also been proposed in hybridized versions. Apart from the afore-mentioned set of well-established algorithms, recently other NABI meta-heuristics have been reported as viable alternatives to solve search and optimization problems. This is the case of the following selection: Cuckoo Search Algorithm (CS) [10], Firefly Algorithm (FA) [11], Glowworm Swarm Optimization (GSO) [12], Gravitational Search Algorithm (GSA) [13] and more recently the Grey Wolf Optimization (GWO) [14]. Most of these methods, when originally proposed were tested in a wide range of benchmark functions: unimodal, multi-modal, composite, etc., and the results compared with the most well-known meta-heuristics. Thus, when a new NABI metaheuristic is reported, it raises the million dollar question: is this technique also better for a given engineering problem? The specific problem in this study is proportional integrative and derivative (PID) controller design, and the research question addressed is: how does the GWO algorithm performs versus GSA and PSO algorithms to design PID controllers?

The use of PID controllers in industrial automation applications is dominant compared to other increasingly popular (and more powerful) techniques, such as predictive control, particularly in the process control area. Reasons for the success and resilience of PID control are primarily based on the following: simplicity of use and good performance over a wide range of system dynamics. One of the issues involved in the design of PID controller is the most appropriate selection of weighting factors associated with the proportional, integrative and derivative components. These weights are commonly known as gains, and their adjustment is referred to as the tuning problem. Since the pioneering work proposed by Ziegler and Nichols [15] regarding the open loop reaction curve and closed-loop oscillation methods, a myriad of techniques have been proposed and this problem continues to receive significant research efforts. Despite the high number of existing techniques, there is not a single technique which can be used for all types of systems. For instance: open-loop step based methods cannot be applied to open-loop unstable systems; tuning rules derived specifically for first order plus time delay models, can fail to tune higher order systems; plenty of tuning rules were refined for a specific control design criterion, performing badly regarding other design criteria. The authors of this work believe that NABI techniques can provide a generalized answer to this problem. With the increase of computational power, programmable logic controllers will need just a few seconds to derive near optimal PID settings for a specific system. Indeed, NABI techniques have been applied successfully in designing PID based process control considering both single-objective [16–18] and multi-objective [e.g. 19, 20] algorithms.

The GWO algorithm recently proposed by [14] has been applied to solve several problems [21–23] providing good performance indications. As it will be reviewed in sequel, the GWO biological algorithm inspiration is mainly based on the wolf pack structure and internal hierarchical organization. This organization uses four hierarchical levels, with alpha representing the highest rank (pack leaders), followed by beta, omega and delta elements. Deltas represent the pack lowest rank. In this paper the GWO algorithm is proposed to design PID Controllers and its performance compared with two other NABI algorithms: GSA and PSO, as well as with two non-iterative tuning techniques [25, 26]. The remaining of the paper is organized as follows. Section 2 reviews the GWO algorithm and specific GSA and PSO algorithms issues. Section 3 states the PID design control problem. In Sect. 4, key implementation aspects regarding the methodology used to conduct the simulation experiments are presented. Section 5 presents results and respective discussion. Finally, Sect. 6 presents some concluding remarks and outlines further research work.

2 Grey Wolf Optimization Fundamental Issues

The GWO algorithm [14] is based on the wolf pack social hierarchy, using four levels:

1. Alphas (α), leaders are dominant wolfs, which are followed by the rest of the pack and are the prime decision-makers;
2. Betas (β), are second in command helping alphas in the decision process and establishes a bridge between alphas and the lower levels;
3. Deltas (δ), are third in the social hierarchy, while submitted to alphas and betas, they submit the lowest rank which is called omega. According to [14], delta represent wolfs such as: scouts, sentinels, elders, hunters and caretakers.
4. Omegas (ω), are the lowest ranked wolfs in the pack, and have to submit to the other three levels.

GWO determines the three best population solutions in terms of fitness, classifying the best as α wolf, the second best as β wolf and the third best as δ wolf. All the other population members are considered to be ω wolfs. The encircling of a prey by the three higher ranked wolfs is mimic by the following equation [15]:

$$\vec{D} = \left| \vec{C} \cdot \vec{X}_p(t) - \vec{X}(t) \right|, \quad \text{with} \quad \vec{C} = 2 \cdot \vec{r}_2 \quad (1)$$

where: t , represents the current iteration, D a difference vector, X_p the prey position vector, X a grey wolf position and C a coefficient vector which is evaluated using a

uniformly random vector, r_2 , generated in the interval $[0, 1]$. The difference vector is used to determine the new position for a wolf regarding the prey position using:

$$\vec{X}(t + 1) = \vec{X}_p(t) - A \cdot \vec{D}, \quad \text{with } A = 2a(t)r_1 - a(t) \quad (2)$$

where: r_1 , represents a uniformly random generated number in the interval $[0, 1]$ and a is linearly decreased vector from $a_{max} = 2$ to $a_{min} = 0$ through the evolutionary process. If the absolute value of A is smaller than 1, this corresponds to an exploitation behavior and mimics the wolf attacking the prey. Otherwise, if the absolute value of A is larger than 1, this corresponds to an exploration behavior and mimics the wolf diverging from the prey. The values of A are in the interval of $[-2, 2]$. Equations (1) and (2) are applied to the three hierarchical leaders as follows:

$$\vec{D}_\alpha = \left| \vec{C}_1 \cdot \vec{X}_\alpha(t) - \vec{X}(t) \right|, \quad \vec{D}_\beta = \left| \vec{C}_2 \cdot \vec{X}_\beta(t) - \vec{X}(t) \right|, \quad \vec{D}_\delta = \left| \vec{C}_3 \cdot \vec{X}_\delta(t) - \vec{X}(t) \right| \quad (3)$$

$$\vec{X}_1 = \vec{X}_\alpha - A_1 \cdot \vec{D}_\alpha, \quad \vec{X}_2 = \vec{X}_\beta - A_2 \cdot \vec{D}_\beta, \quad \vec{X}_3 = \vec{X}_\delta - A_3 \cdot \vec{D}_\delta \quad (4)$$

As it can be observed from (3)–(4), the position of the prey represents the best fitness obtained for the α , (X_α), β , (X_β) and δ , (X_δ) wolves. All wolves positions are updated using the following average formula:

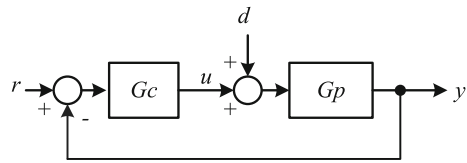
$$\vec{X}(t + 1) = \frac{\vec{X}_1 + \vec{X}_2 + \vec{X}_3}{3} \quad (5)$$

The GWO algorithm is presented in Fig. 1a. For exposition sake, the standard GSA and PSO algorithms used are also presented in Fig. 1b and c, respectively. Specific details and more information regarding GSA can be found in [13, 18] and about the canonical PSO in any topic publication.

(a)	(b)	(c)
$t = 0$ initialize population $X(t)$ initialize a while(!(termination criterion)) evaluate $X(t)$ update $X_\alpha, X_\beta, X_\delta$ update $X(t)$ positions evaluate $X(t)$ update a, A and C $t = t + 1$ end	$t = 0$ initialize swarm $X(t)$ while(!(termination criterion)) evaluate $X(t)$ update $G, best, worst$ evaluate particles M and a update particles velocity, v update particles position, x $t = t + 1$ end	$t = 0$ initialize swarm $X(t)$ initialize ω while(!(termination criterion)) evaluate $X(t)$ update local and global best(s) update particles velocity, v update particles position, x update ω $t = t + 1$ end
<i>Grey wolf</i>	<i>Gravitational search</i>	<i>Particle swarm</i>

Fig. 1 Grey wolf, gravitational search and particle swarm optimization algorithms

Fig. 2 Classical single-input single-output feedback control loop



3 PID Controller Design: Problem Statement

The problem statement can be presented based on a classical control system block diagram representation presented in Fig. 2:

where: r represents the reference input (set-point), y the controlled output, d a load disturbance, u the controller output, G_c the controller and G_p the system or process to control. Two of the major control design objectives are set-point tracking (SPT) and load disturbance rejection (LDR). The objective of SPT can be stated in simple terms as finding the best controller gains which make the system output to track as close as possible the reference input signal variations. While designing a PID controller to achieve LDR is also a relevant design issue it is not addressed in this study. The PID controllers are designed by minimizing the well-known integral of time weighted absolute error (ITAE). The controller transfer function considered in this study is represented by:

$$G_{cPID}(s) = \left(K_p + \frac{K_i}{s} + sK_d \right) \left(\frac{1}{1 + sT_f} \right) \tag{6}$$

where: K_p , K_i and K_d represents, respectively, the proportional, integrative and derivative gains and T_f , the filter time constant.

4 Algorithms Implementation Issues

In order to make a fair comparison between the GWO, GSA and PSO, the criteria should be clearly specified so that the results presented here can be replicated. Some crucial aspects, many times neglected in some reports, are the following:

- Population initialization methodology: often randomly generated solutions for the PID controller gains result in unstable control systems. To overcome this problem, the method used in this study randomly generates trial solutions, examine the solutions in terms of stability fulfillments; It only allows their integration in the initial population, if the resulting control system is stable. In this paper, for each run the same initial population is used for all three algorithms (GWO, GSA and PSO). However a different initial population is used for each of the 10 runs.

- Methodology used to repair new solutions generated out of the adopted search space limits: randomly re-initialize these solutions in the predefined search boundaries.
- Presentation of specific heuristic parameters inherent to each NABI meta-heuristic: for the GWO algorithm (pseudo-code presented in Fig. 1a) is the following: a —linearly decreased from 2 to 0 along the number of iterations used. For the GSA (pseudo-code presented in Fig. 1b), the originally proposed [13] expression (7a) to update G was found, by prior experimentation, not to work in this design leading to premature convergence. Thus, the alternative linearly decaying expression represented in (7b) is used to update G along the evolutionary process:

$$G(t) = G_0 \exp\frac{-at}{t_{\max}}, \quad a) \quad G(t) = G_0 \left(1 - \frac{t}{t_{\max}}\right), \quad b) \quad (7)$$

Given the small number of iterations considered the value of $G_0 = 0.9$ is used here. For the PSO (pseudo-code presented in Fig. 1c): ω —linearly decreased from 0.9 to 0.2 along the number of iterations used and $c_1 = c_2 = 2$.

5 Simulation Results and Discussion

Three plant models considered relevant [24] to test PID controllers are considered in this study representing a double lag pole with time delay, G_{p1} , a non-minimum phase system, G_{p2} , and a fourth order system with multiple equal poles G_{p3} , expressed by:

$$G_{p1}(s) = \frac{1}{(1+s)^2} e^{-s}, \quad G_{p2}(s) = \frac{1-0.5s}{(s+1)^3}, \quad G_{p3}(s) = \frac{1}{(s+1)^4} \quad (8)$$

The PID controller parameters are obtained by minimizing the ITAE when a unit step is applied to the reference input. The controller gains are allowed to change in the following interval [0.1, 5] for K_p , K_i and K_d . The population sizes are $m = 15$ and each algorithm is evolved using 150 iteration per run. Each algorithm was run 10 times. All simulations were carried out in Matlab/Simulink environment with a fixed solver step interval of 0.1 s. For all three cases the filter time constant was set to $T_f = 0.1$ s. However, the actual T_f used in (6) depends on the system noise, the process time constants and the controller sampling time. In practice it should be the highest value which does not degrade the control performance noticeably. The results obtained for each plant system are presented in Table 1, where the bold values represent the best values achieved. For each NABI method tested (GWO,

Table 1 Results obtained for PID gains and ITAE

System	Method	Best PID gains			Best ITAE	Avg. ITAE	Std. ITAE
		K_p	K_i	K_d			
Gp_1	GWO	1.168	0.538	0.774	2.39	2.39	0.001
	GSA	1.163	0.536	0.770	2.39	2.39	0.000
	PSO	1.160	0.534	0.767	2.39	2.39	0.001
	MOMI	1.106	0.518	0.611	2.81	–	–
	VR	1.109	0.529	0.588	3.08	–	–
Gp_2	GWO	1.432	0.549	1.236	2.52	2.52	0.001
	GSA	1.428	0.547	1.232	2.52	2.52	0.000
	PSO	1.428	0.547	1.232	2.52	2.52	0.003
	MOMI	1.199	0.472	0.810	3.36	–	–
	VR	1.227	0.480	0.723	4.21	–	–
Gp_3	GWO	1.584	0.522	1.777	3.55	3.55	0.001
	GSA	1.571	0.515	1.752	3.55	3.55	0.000
	PSO	1.571	0.515	1.752	3.55	3.55	0.180
	MOMI	1.295	0.438	1.041	5.09	–	–
	VR	1.305	0.429	0.866	6.55	–	–

GSA and PSO) the PID gains corresponding to the best results in terms of ITAE are presented.

Table 1 presents also the average between the final achieved ITAE for the 10 runs, as well as the corresponding standard deviation for all the best results. The obtained values show that all three tested NABI metaheuristics converged to the same controller gains and thus the same ITAE value was achieved for each system. These results also confirm that the 150 iterations are enough for achieving fast convergence in all methods, as the average value is the same as the best value achieved. Also the standard deviation values are small, apart from the PSO results for Gp_3 which are higher than the ones for GSA and GWO. While the results presented in Table 1 show that in this study, for PID controller design all three methods result in the same gains, with similar performance, in terms of the convergence rate the three methods are quite different. The differences can be perceived by analyzing the results presented in Figs. 3, 4 and 5, where (a) denotes plots presenting the average evolution between the best values in the 10 runs and (b) denotes plots presenting the average evolution between the mean population values in the 10 runs. In terms of the best value evolution the behavior is quite similar for the three methods. However, in terms of the average behavior it indicates that the faster convergence algorithm is the GSA followed by GWO and PSO. The results obtained for the best PID controller settings in the three methods are presented in Fig. 6 for systems Gp_1 , Gp_2 and Fig. 7a for Gp_3 .

For comparison purposes, the optimization methods have been compared with non-iterative tuning methods: Vinoth Ray tuning method based on the ITAE criterion (VR) [26] and the Magnitude Optimum Multiple Integration (MOMI) [25].

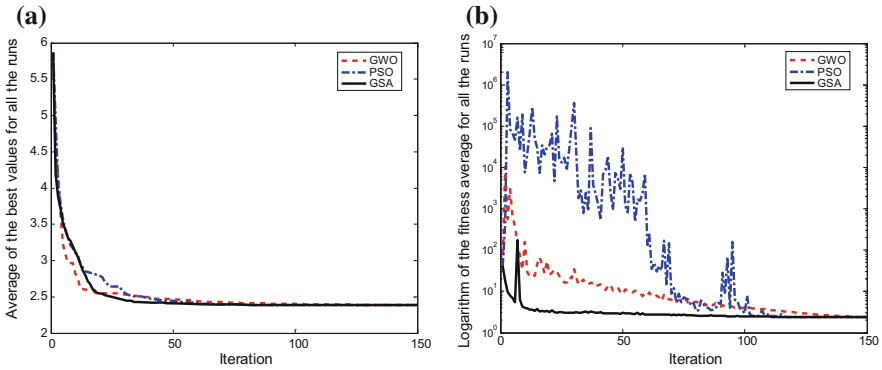


Fig. 3 Results obtained for system Gp_1 with GWO, PSO and GSA. **a** Average of the best value in 10 runs. **b** Average of the mean value in the 10 runs

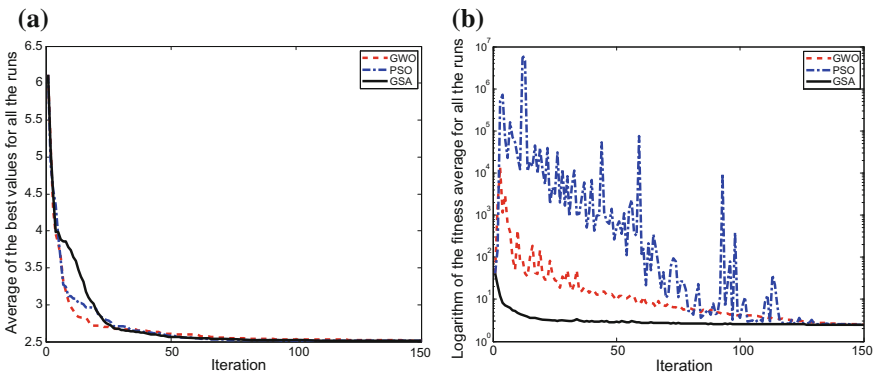


Fig. 4 Results obtained for system Gp_2 with GWO, PSO and GSA. **a** Average of the best value in the 10 runs. **b** Average of the mean value in the 10 runs

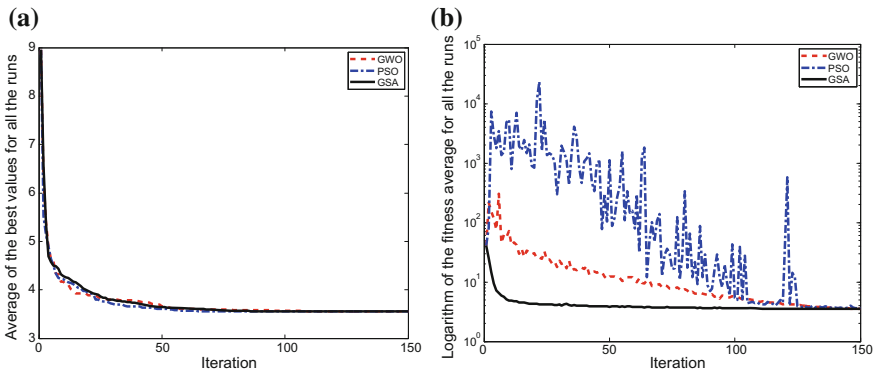


Fig. 5 Results obtained for system Gp_3 , with GWO, PSO and GSA. **a** Average of the best value in the 10 runs. **b** Average of the mean value in the 10 runs

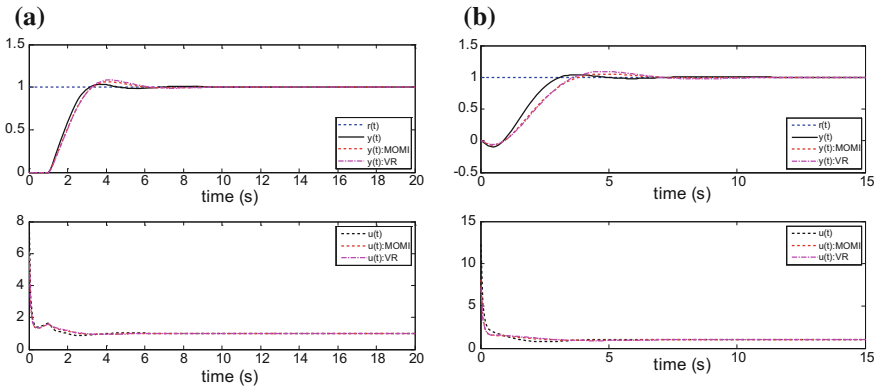


Fig. 6 Set-point tracking responses. GWO gains versus MOMI and VR methods. **a** For system Gp_1 . **b** For system Gp_2

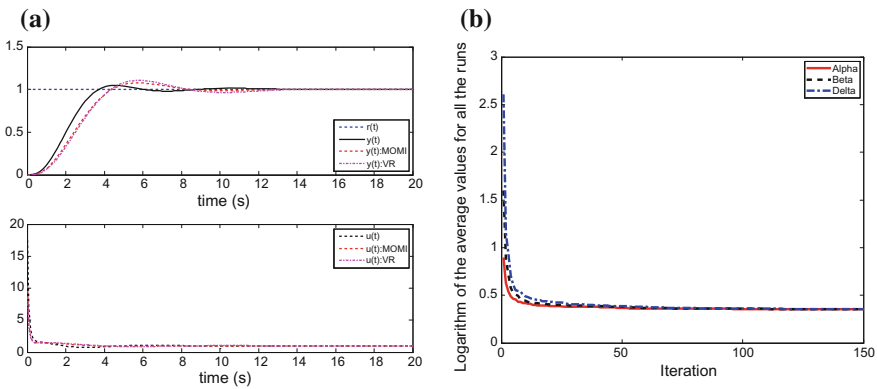


Fig. 7 Results for system Gp_3 . **a** Set-point tracking responses. **b** GWO: average values for alpha, beta and delta

The results obtained with these two methods are also presented in Table 1 and the respective responses are shown in Figs. 6 and 7a. As it can be observed from these figures and Table 1, the results obtained with the bio-inspired metaheuristics are better in terms of the ITAE achieved. In Fig. 7b the results obtained for the average in the 10 GWO runs for system Gp_3 is presented, in terms of the Alpha, Beta and Delta fitness values. As it can be observed from this figure confirms the achieved social hierarchical evolution mimic in the GWO algorithm, in terms of the performance of the different elements.

6 Conclusion

The GWO algorithm was proposed in this paper to design PID controllers for the design objective of set-point tracking. This bio-inspired metaheuristic is applied to a set of benchmark linear model plants, and the results obtained compared with the one achieved with particle swarm optimization and gravitational search algorithm. For the simulation test conditions considered, namely a small population size and a low number of iterations, the results achieved by the three meta-heuristics are very similar in terms of the final values of the performance index deployed: the ITAE. Thus GWO, performs as well as PSO and GSA algorithms. However, in terms of convergence the three tested algorithm presented different behaviors. The GSA showed to be the fastest to converge, followed by the grey wolf optimization and finally the PSO. The results obtained with the three bio-inspired meta-heuristics were compared with two tuning methods, showing better performance as the results can be considered to be tailor made to each of the considered systems dynamics tested. Further research efforts must be endeavored to fully explore the grey wolf optimization algorithm considering other PID controller design criteria.

References

1. Kirkpatrick, S., Gellet, C.D., Vecchi, M.P.: Optimization by simulated annealing. *Science* **220**, 671–680 (1983)
2. Fogel, L.J., Owens, A.J., Walsh, M.J.: *Artificial Intelligence through Simulated Evolution*. Wiley, New York (1966)
3. Rechenberg, I., Eigen, M.: *Evolutionsstrategie: Optimierung Technischer Systeme nach Prinzipien der Biologischen Evolution*. Frommann-Holzboog Stuttgart (1973)
4. Holland, J.H.: *Adaptation in Natural and Artificial Systems*. The University of Michigan Press, Ann Arbor (1975)
5. Baluja, S.: Population-based incremental learning: a method for integrating genetic search based function optimization and competitive learning. Technical Report CMU-CS-94-163. Carnegie Mellon University (1994)
6. Dorigo, M., Birattari, M., Stutzle, T.: Ant colony optimization theory: a survey. *Theoret. Comput. Sci.* **344**, 243–278 (2005)
7. Koza, J.R.: Genetic programming: a paradigm for breeding populations of computers programs to solve problems. Technical report STAN-CS-90-1314. Stanford University (1990)
8. Storn, R., Price, K.V.: Differential evolution—a simple and efficient adaptive scheme for global optimization over continuous spaces. Technical Report TR-95-012, ICSI (1995)
9. Kennedy, J., Eberhart, R.C.: Particle swarm optimization. In: *Proceedings of the IEEE International Conference on Neural Networks IV, Piscataway*, pp. 1942–1948 (1995)
10. Yang, X.-S., Deb, S.: Cuckoo search via Lévy flights. In: *Proceedings of World Congress on Nature & Biologically Inspired Computing (NaBIC 2009)*, pp. 210–214. IEEE Publications, India (2009)
11. Yang, X.-S.: Firefly algorithm, Lévy flights and global optimization. In: Bramer, M. et al. (eds.) *Research and Development in Intelligent Systems XXVI*. Springer, London (2010). doi:[10.1007/978-1-84882-983-1-15](https://doi.org/10.1007/978-1-84882-983-1-15)

12. Krishnanand, K.N., Ghose, D.: Glowworm swarm based optimization algorithm for multimodal functions with collective robotics applications. *Multiagent Grid Syst Int J* 209–222 (2006) (IOS Press)
13. Rashedi, E., Nezamabadi-Pour, H., Saryazdi, S.: GSA: a gravitational search algorithm. *Inf. Sci.* **179**, 2232–2248 (2009)
14. Seyedali, M., Mohammad, S.M., Lewis, A.: Grey Wolf optimizer. *Adv. Eng. Softw.* 46–61 (2014)
15. Ziegler, J.G., Nichols, N.B.: Optimum settings for automatic controllers. *Trans. ASME* 759–768 (1942)
16. Jones, A.H., Moura Oliveira, P.B.: Genetic auto-tuning of PID controllers. Genetic algorithms in engineering systems: innovations and applications, GALEZIA. In: Fifth IEEE Conference on Genetic Algorithms in Engineering Systems: Innovations and Applications, No. 414, pp. 141–145 (1995)
17. Moura Oliveira, P.B.: Modern heuristics review for PID control systems optimization: a teaching experiment. In: IEEE-International Conference on Control and Automation (ICCA 2005), pp. 828–833 (2005)
18. Moura Oliveira, P.B., Solteiro Pires, E.J., Novais, P.: Design of Posicast PID control systems using a gravitational search algorithm. *Neurocomputing*. Available online 9 May 2015. doi:[10.1016/j.neucom.2014.12.101](https://doi.org/10.1016/j.neucom.2014.12.101). Elsevier
19. Zhao, S.-Z., Iruthayarajan, M.W., Baskar, S., Suganthan, P.N.: Multi-objective robust PID controller tuning using two lbests multi-objective particle swarm optimization. *Inf. Sci. (Elsevier)* **181**(16), 3323–3335 (2011)
20. Freire, H.F., Moura Oliveira, P.B., Solteiro Pires, E.J., Bessa, M.: Many-objective PSO PID controller tuning. In: *CONTROLO'2014—Proceedings of the 11th Portuguese Conference on Automatic Control Lecture Notes in Electrical Engineering*, vol. 321, pp. 183–192. Springer (2014)
21. Sharma, Y., Saikia, L.C.: Automatic generation control of a multi-area ST—thermal power system using Grey Wolf optimizer algorithm based classical controllers. *Electr. Power Energy Syst.* **73**, 853–862 (2015)
22. Madadi, A., Motlagh, M.M.: Optimal control of DC motor using Grey Wolf optimizer algorithm. *Tech. J. Eng. Appl. Sci.* (2014). ISSN 2051-0853
23. Korayem, L., Khorsid, M., Kassem, S.S.: Using Grey Wolf algorithm to solve the capacitated vehicle routing problem. In: *IOP Conference Series: Mathematical Science and Engineering* 83 (2015)
24. Åström, K.J., Hägglund, T.: Benchmark systems for PID control. In: *IFAC Workshop on Digital Control: Past, Present and Future*, Spain, pp. 181–183 (2000)
25. Vrančić, D., Strmčnik, S., Juričić, Đ.: A magnitude optimum multiple integration method for filtered PID controller. *Automatica* **37**, 1473–1479 (2001)
26. Vinoth-Ray, A.: Stepwise method for tuning PI controllers using ITAE criteria (2012). <http://www.embedded.com/design/prototyping-and-development/4391181/A-stepwise-method-for-tuning-PI-controllers-using-ITAE-criteria>. Accessed 13 Jan 2016

Part IV
Modeling and Identification

Construction of Confidence Sets for Markov Chain Model

Dmitry Zavalishchin and Galina Timofeeva

Abstract The problem of forecasting the state probabilities vector for a stationary Markov chain with discrete time in case of transition probabilities are not exactly known and measured during the system operation is investigated. An auxiliary dynamic system with uncertainty and observation showing the dynamics of the state probabilities vector is constructed. Two approaches to the determination of the guaranteed with a given probability estimates are proposed. The first approach uses confidence sets for rows of the matrix of transition probabilities and the ellipsoidal calculus. The second approach is based on simulation and finding a sample quantile of an objective function, which determines the form of a confidence set for the system state.

Keywords Markov chain · Incomplete information · Confidence estimate

1 Introduction

Markov chain models are widely used to explain the dynamics of state changes for different systems. They are often used as mathematical models for random physical and chemical processes. Markov chains are used in finance and economics to model a variety of different phenomena, including asset prices, market crashes and credit portfolio dynamics [6, 11].

D. Zavalishchin (✉)

Department of Optimal Control, Institute of Mathematics and Mechanics,
Ural Branch of the Russian Academy of Sciences, S. Kovalevskaya str., 16,
620990 Ekaterinburg, Russia
e-mail: dzaval@mail.ru

D. Zavalishchin · G. Timofeeva

Ural State University of Railway Transport, Kolmogorov str., 64,
620034 Ekaterinburg, Russia

D. Zavalishchin · G. Timofeeva

Ural Federal University, Mira str., 19, 62002 Ekaterinburg, Russia

It is assumed that a change of the system state is described by a Markov chain with discrete time and constant transition probabilities. If the transition probability matrix of the Markov chain is known then dynamics of the system states probabilities is completely described by a system of difference equations. As a rule the transition probabilities are unknown and estimated during the system evolution.

The problem of estimating for a Markov chain is considered. At each step there is a large number of objects moving from one state to another. Statistical estimates of transition probabilities can be calculated on the basis of information about the number of transitions. The problem of constructing confidence interval estimating one of the coordinates of the state vector of a Markov chain was investigated in [5, 10]. The purpose of this paper is to construct confidence sets for vector state probabilities of the system on a few steps forward, taking into account the incoming statistical data on the number of transitions. Various approaches to the estimation of the matrix of transition probabilities are compared.

2 Dynamics of System States Probabilities

We consider a system with k states, the probability that the system is in i th state at moment t denote by $x_i(t)$, $i = 1, \dots, k$, i.e.

$$x_i(t) = \mathcal{P}\{\xi(t) = e_i\}, \quad i = 1, \dots, k.$$

Here $\{e_1, \dots, e_k\}$ is the unit basis in \mathbb{R}^k , $\mathcal{P}(A)$ is a probability of a random event A .

Let us denote by $x(t)$ a vector of states probabilities $x(t) = \{x_1(t), \dots, x_k(t)\}^\top$, and define a simplex $Z_+^k \subset \mathbb{R}^k$

$$Z_+^k = \{z = \{z_1, \dots, z_k\} \in \mathbb{R}^k : 0 \leq z_i \leq 1, \sum_{i=1}^k z_i = 1\}, \quad (1)$$

then $x(t) \in Z_+^k$.

Denote by p_{ij} a probability of going from state i to state j in one step

$$\mathcal{P}\{\xi(t+1) = e_j | \xi(t) = e_i\} = p_{ij}.$$

We impose a simple Markov structure on the transition probabilities and restrict our attention to the first-order stationary Markov processes.

Thus, it is supposed that these probabilities are constant $p_{ij}(t) \equiv p_{ij}$, $i = 1, \dots, k$, $j = 1, \dots, k$. Criteria for testing the adequacy of the stationary Markov chain model on statistical data on the number of transitions are formulated in the classical work [1].

The dynamics of state probabilities of the system is described by difference equations

$$x_j(t + 1) = \sum_{i=1}^k p_{ij}x_i(t), \quad t = 0, 1, \dots, T. \tag{2}$$

Let's denote by P a $k \times k$ -matrix of the transition probabilities $P = \{p_{ij}\}$ and rewrite Eq. (2) in the vector form:

$$x(t + 1) = P^T x(t), \quad t = 0, 1, \dots, T. \tag{3}$$

When the transition probability matrix P is known incompletely there is a problem to estimate $x(T)$. It is assumed that we have information about the number of transitions from i th state to j th on t step, $t = t_0, \dots, t_1$. Different approaches to the estimation of vector $x(t_1 + T)$ are investigated.

3 Estimation of Transition Probabilities

To estimate the probability p_{ij} one can use the statistics of transitions from one state to another. Let us denote by $n_i(t)$ the number of objects, which are in state S_i at the moment t . Then $n_{ij}(t)$ denotes the number of objects that pass from the state S_i to the state S_j during the period $(t - 1; t]$.

The probability of transition $p_{ij}(t)$ from a given state S_i is approximated by the proportion

$$w_{ij}(t) = \frac{n_{ij}(t)}{n_i(t - 1)}. \tag{4}$$

Anderson and Goodman [1] calculated statistical moments of random values $\xi_{ij}(t) = n_{ij} - p_{ij}n_i(t - 1)$ and proved the asymptotically Gaussian distribution of them. If on the t th step $n_i(t - 1) \triangleq n_i, i = 1, \dots, k$ are known, then

$$E(w_{ij}) = p_{ij}, \tag{5}$$

where $E(\xi)$ is a mean value of a random value ξ .

Denote by $w^{(i)}$ a vector $w^{(i)} = \{w_{i1}, \dots, w_{ik}\}$. If $i \neq c$ then $w^{(i)}$ and $w^{(c)}$ are non-correlated vectors and

$$Cov(w_{ij}, w_{cl}) = 0, \quad i \neq c, \quad j = 1, \dots, k, \quad l = 1, \dots, k, \tag{6}$$

where $Cov(\xi, \zeta)$ is a covariance between ξ and ζ . The covariance matrix of the vector $w^{(i)}$ is the following

$$E(w^{(i)}(w^{(i)})^T) = K^{(i)}, \quad K_{jj}^{(i)} = \frac{p_{ij}(1 - p_{ij})}{n_i}, \quad K_{jl}^{(i)} = -\frac{p_{ij}p_{il}}{n_i}, \quad j \neq l. \tag{7}$$

4 Construction of Confidence Sets

4.1 Multistage System with Uncertainty

To forecast the probability distribution of the states of a Markov chain, let us consider a multistage system with an observation, which approximates the dynamics of the Markov chain with incompletely known transition probabilities:

$$x(t + 1) = P^T x(t), \quad t = t_0, \dots, \quad x(t_0) = x_0, \tag{8}$$

where the matrix P is not given at moment t_0 , and the state $x(t)$ of the system on the interval $[t_0; t_1]$ is available for measurement.

Rows $p^{(i)} = \{p_{ij}, j = 1, \dots, k\}$ of the matrix P are unknown vectors, which are estimated from observations $y^{(i)}(t)$. The rows satisfy the constraint

$$p^{(i)} \in Z_+^k, \tag{9}$$

here Z_+^k is the simplex defined by (1).

Information about rows $p^{(i)}, i = 1, \dots, k$ is given by observations

$$y^{(i)}(t) = p^{(i)} + \eta^{(i)}(t), \quad i = 1, \dots, k, \quad t = t_0, \dots, t_1, \tag{10}$$

where $\eta^{(i)}(t)$ are independent Gaussian random vectors with given statistical moments

$$E(\eta^{(i)}(t)) = 0, \quad E(\eta^{(i)}(t)(\eta^{(i)}(t))^T) = G^{(i)}(y(t - 1)).$$

It is required to make a forecast for state $x(t_1 + T)$ of the system (8) on the basis of observations (10) in the interval $[t_0, t_1]$.

From properties of linear multistage systems [2] the statement is followed.

Property 1 *If all rows of the matrix P satisfy condition (9) and at the initial time $x(t_0) \in Z_+^k$, then for the state of the system (8) holds*

$$x(t) \in Z_+^k, \quad t = t_0 + 1, \dots$$

According to a modern approach forecasting stochastic systems is not limited to the calculation of the expected average value. It involves finding quantiles for an objective function [7, 9] or guaranteed with a certain probability α estimate in the form of a confidence set. Thus, we investigate the problem of constructing the confidence set $X_\alpha(t_1 + T)$ for the system states such as

$$\mathcal{P}\{x(t_1 + T) \in X_\alpha(t_1 + T)\} = \alpha.$$

The problem of the confidence set constructing for the state of the system (8) and (9) is a complex problem due to the facts that:

- there are uncertain parameters included in the system multiplicatively;
- there are correlations between the elements of each row of the matrix P , but the vector of the system states multiplies to columns of the matrix, as matrix P is transposed in (8). This leads to the need to estimate all elements of the matrix simultaneously;
- there are additional restrictions (9).

In the papers [10, 11] two approaches to constructing a confidence interval for one of the components of the vector $x(t_1 + T)$ for state of the system (8) and (10) are proposed. The first approach is based on constructing confidence sets for the rows of the matrix P in the form of ellipsoids or parallelotopes and obtaining estimates using the theory of multi-valued tubes [8], the second approach is based on simulation modeling. Here we considered two ways to forecast a state of the system (8) taking into account the uncertainty of the matrix P . There are a confidence estimation method and a simulation method.

4.2 Confidence Estimates for Matrix Rows

The method based on the confidence estimation of the matrix rows consists of two stages: construction of a confidence set Z_α for the transition probabilities matrix based on observation $y^{(i)}$ and the analysis of all possible trajectories of the system (8) taking into account that probabilities p_{ij} are constant but uncertain.

Let us estimate the elements of matrix P . Denote the confidence region for $\{p_{ij} = z_s, i = 1, \dots, k, j = 1, \dots, k, j \neq i\}$ on moment t_1 by $Z_\alpha \subset \mathbb{R}^K, s = 1, \dots, K, K = k(k - 1)$.

Thus, p_{ij} are the transition probabilities then $Z_\alpha \subset Z_+^0 \subset \mathbb{R}^K$, where Z_+^0 is the set of all possible values of transition probabilities $\{p_{ij}, j \neq i\}$. Estimation for p_{ii} follows from the equalities

$$p_{i1} + \dots + p_{ik} = 1, \quad i = 1, \dots, k. \tag{11}$$

In the considered model the distribution of p_{ij} approximates to truncated Gaussian distribution with mean values equal to w_{ij} [1]. A covariance $K \times K$ matrix G is estimated on the basis of relations (6) and (7) with substitution p_{ij} by w_{ij} . Therefore we may use the confidence set Z_α defined by joint restrictions [11]:

$$Z_\alpha = \{z \in Z_+ : (z - \bar{z})^\top G(z - \bar{z}) \leq b_K^{(\alpha)}\}, \tag{12}$$

where $b_K^{(\alpha)}$ is the α -quantile of χ^2 distribution with K degrees of freedom, $\bar{z}_s = w_{ij}, s = 1, \dots, K$.

The next step is to solve the state estimation problem of a multistage deterministic system with uncertain matrix P :

$$\begin{aligned} x(t + 1) &= P^\top x(t), \quad t = t_1, \dots, t_1 + T, \\ x(t_1) &= x^*, \quad P \in Z_\alpha, \end{aligned} \tag{13}$$

and to find an information set

$$X(t_1 + T, Z_\alpha) = \{x \in R_+^k : x = (P^\top)^T x^*, \quad P \in Z_\alpha\}. \tag{14}$$

We constructed the information sets for the system (13) using the ellipsoidal estimation approach [8]. Algorithms of estimation system state in case of uncertainty in the matrix coefficients are obtained in [3, 4]. However, in these papers restrictions to matrix elements are specified in the form $|p_{ij} - p_{ij}^{(0)}| < \Delta_{ij}$ with given $p_{ij}^{(0)}$ and Δ_{ij} . The calculations show that the application of these algorithms for the evaluation of the phase state of the system (13) gives too wide assessment, as it does not take into account features of the system, in particular the condition (11). Therefore, the parameterization of the set Z_α of possible values of the elements of the matrix P was used to estimate the system state. This approach is applicable only to systems of small dimension $n \leq 4$.

Example 1 Let us consider the estimation problem for a Markov chain with 3 states (Fig. 1). An investigation of this example allows to define the most important features of the model.

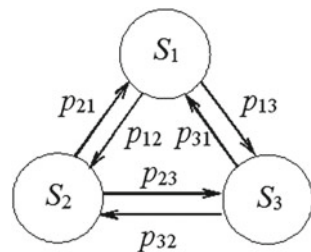
For this Markov chain the matrix of transition probabilities has a form

$$P = \begin{pmatrix} 1 - p_{12} & p_{12} & p_{13} \\ p_{21} & 1 - p_{21} - p_{23} & p_{23} \\ p_{31} & p_{32} & 1 - p_{32} \end{pmatrix},$$

and six transition probabilities p_{ij} should be estimated.

It is sufficient to evaluate the first two coordinates, since the coordinates of the system state vector are related by the equality $x_1(t) + x_2(t) + x_3(t) \equiv 1$. Let us denote $x(t) = \{x_1(t), x_2(t)\}$ and write the dynamic equation for the vector. We obtain the system

Fig. 1 Graph of the Markov chain with three states



$$\begin{cases} x_1(t+1) = (1 - p_{11} - p_{13})x_1(t) + p_{21}x_2(t) + p_{31}(1 - x_1(t) - x_2(t)) \\ x_2(t+1) = p_{12}x_1(t) + (1 - p_{21} - p_{23})x_2(t) + p_{32}(1 - x_1(t) - x_2(t)) \end{cases} \quad (15)$$

From the observation $y^{(i)}(t)$, $t = t_0, \dots, t_1$ mean values $\bar{p}_{ij} = w_{ij}$ are estimated. Let $p^{(1)} = \{p_{12}, p_{13}\}, p^{(2)} = \{p_{21}, p_{23}\}, p^{(3)} = \{p_{31}, p_{32}\}$. Covariance matrices G_i for estimates of vectors $p^{(i)}$ are calculated by using relations (6) and (7), where estimates \bar{p}_{ij} substituted instead of values p_{ij} .

As in the article [11] the confidence set for the elements of the matrix P is chosen as the product of ellipsoids:

$$Z_\alpha = Z_\beta^{(1)} \times Z_\beta^{(2)} \times Z_\beta^{(3)},$$

where $1 - \beta = \sqrt[3]{1 - \alpha}$. Here $Z_\beta^{(i)}$ is confidence set for $p^{(i)}$ in the form

$$Z_\beta^{(i)} = \{z \in \mathbb{R}^2 : (z - \bar{p}^{(i)})^\top G_i (z - \bar{p}^{(i)}) \leq b_2^{(\beta)}\}, \quad i = 1, 2, 3,$$

$b_2^{(\beta)}$ is the β -quantile of χ^2 distribution with two degrees of freedom.

Denote by $\mathbb{R}_+^2 = \{x \in \mathbb{R}^2 : 0 \leq x_i \leq 1, x_1 + x_2 \leq 1\}$ the set of possible probabilities $p^{(i)}$. If the condition

$$Z_\beta^{(i)} \subset \mathbb{R}_+^2, \quad \text{for all } i = 1, 2, 3, \quad (16)$$

is not satisfied, we change radiuses of ellipses so that the relations (16) would hold and $1 - \alpha = (1 - \beta_1)(1 - \beta_2)(1 - \beta_3)$.

Further calculations for the considered scheme with 3 states are based on the parameterization of the set Z_α and runs of the system (15) for every permissible value of the parameters. Thus, we get the upper confidence estimate $\hat{X}_\alpha(t_1 + T)$ of the system state $x(t_1 + T)$, i.e. $\mathcal{P}\{x(t_1 + T) \in \hat{X}_\alpha(t_1 + T)\} \geq \alpha$.

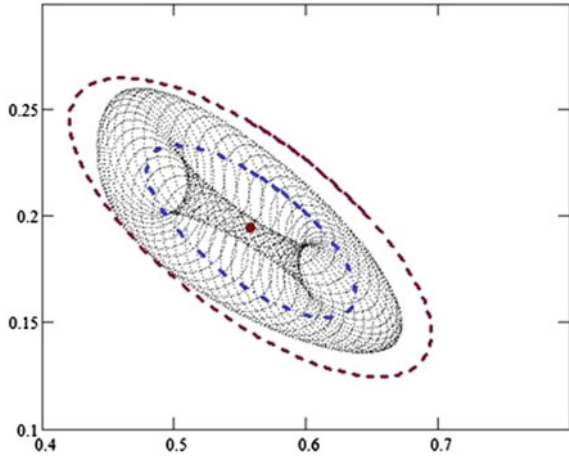
The calculation results are presented in Fig. 2. The external ellipse is described around a constructed set $\hat{X}_\alpha(t_1 + T)$.

The amount of computation rapidly increases with increasing the dimension of matrix P . This method is very time-consuming because the number of estimated elements of the matrix is large. Simulation of random perturbations allows to get more precise confidence estimate for the vector $x(t_1 + T)$. The internal ellipse on Fig. 2 is obtained by the simulation method.

4.3 Simulation Method

It is known that there is an infinite multitude of different confidence sets of the same level of the probability for a random vector. The first step is to choose the form confidence sets, i.e. to choose a type of a convex function $\varphi(x) : R^k \mapsto R^1$, which level sets will be considered as confidence sets

Fig. 2 Estimation using confidence estimates for matrix rows



$$X_\alpha = \{x \in R^k : \varphi(x) \leq c_\alpha\}.$$

Depending on a purpose of forecasting the function $\varphi(x)$ may be a linear function (i.e. in the problem of estimating the proportion of bad loans [11]) or the distance to a fixed point. On the other hand, the selection of the confidence set form may be based on a graphical analysis scatter points obtained by the simulation.

It is universal enough to use quadratic functions with ellipsoidal level sets. In order the form of an ellipsoid should correspond to variability of data, the average value of \bar{x} and covariance matrix \bar{G} for the generated data are taken as the center and the form matrix of the ellipsoid, respectively:

$$\varphi(x) = (x - \bar{x})^T \bar{G}^{-1} (x - \bar{x}). \tag{17}$$

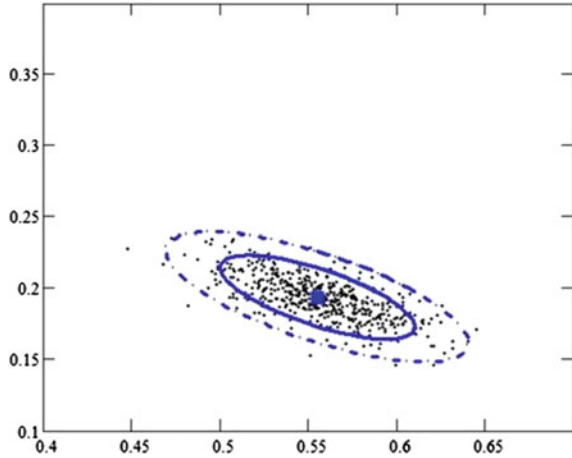
We calculate quantile q_α of a sample distribution $\eta^{(j)}$ and get the confidence set

$$X_\alpha = \{x \in R^k : (x - \bar{x})^T \bar{G}^{-1} (x - \bar{x}) \leq q_\alpha\}. \tag{18}$$

The algorithm of simulation is the following:

1. Determine statistical moments for rows $p^{(i)}$ of the matrix P from observations (10) $y_i(t)$ on the interval $t = t_0, \dots, t_1$;
2. Generate the large number times M the random vectors of unknown elements of the matrix P as the truncated Gaussian vector with given statistical moments;
3. Simulate M times the dynamics of system (8) on the interval $[t_1; t_1 + T]$;
4. Divide the resulting sample values of $\{x^{(j)}(t_1 + T), j = 1, \dots, M\}$ on two samples of length M_1 and M_2 respectively, $M_1 + M_2 = M$. For the first sample estimate statistical moments

Fig. 3 Confidence sets constructed by simulation method



$$\bar{x} = \frac{1}{M_1} \sum_{j=1}^{M_1} x^{(j)}(t_1 + T),$$

$$\bar{G} = \frac{1}{M_1} \sum_{j=1}^{M_1} (x^{(j)}(t_1 + T) - \bar{x})(x^{(j)}(t_1 + T) - \bar{x})^T; \tag{19}$$

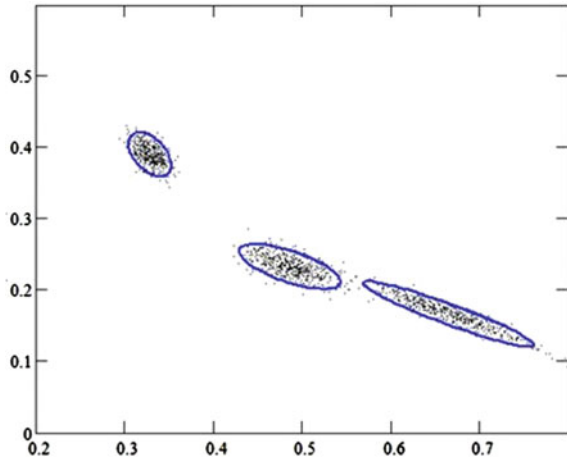
5. Compose function (17) and calculate its values $v^{(j)} = \varphi(x^{(j)})$ for generated vectors $\{x^{(j)}, j = M_1 + 1, \dots, M\}$;
6. Find the sample quantile q_α for $\{v^{(j)}, j = M_1, \dots, M\}$;
7. Get the confidence set in form (18).

The points shown on Fig. 3 are system states $\{x^{(j)}\}$ obtained by simulation, the ellipses are confidence sets X_α with levels $\alpha = 0.9$ and $\alpha = 0.99$ for $\{x_1(t_1 + T), x_2(t_1 + T)\}$, calculated as level sets (18). The number of runs M was chosen with the order of 10^4 because of the slow convergence (of the order of \sqrt{M}) of quantile estimates to its value. We used the estimates of variance of sample quantile obtained in [12].

The results obtained by simulation methods are more precise than the confidence sets obtained by using the confidence estimates for matrix rows (Fig. 2). The simulation method shows that estimates obtained by means of the ellipsoidal confidence estimation for matrix rows are much overestimated and the use of parallelotopes gives more rough results. As it's known [7], the ellipsoidal form of confidence sets is not optimal in case of multiplicative random perturbations. It should be noted that if the random perturbations are included in the system additively, both confidence estimates are almost identical.

Figure 4 shows the dynamics of 95 % confidence regions for the state of the system (15) when the number of steps equal $t_1 + 6, t_1 + 12, t_1 + 20$. The results are given for the other than in Figs. 2 and 3 sample data $\{y^{(i)}, i = 0, \dots, t_1\}$.

Fig. 4 Dynamics of confidence estimates



5 Conclusion

The discrete Markov chain model is studied. It is proposed that transition probabilities are unknown and estimated during the process. Methods to estimate system state probabilities in future are constructed. Two approaches to the determination of the guaranteed with a given probability estimates of the state vector are proposed. The first approach uses a confidence set for rows of the matrix of transition probabilities and the ellipsoidal calculus. The second approach is based on the simulation and finding the sample quantile of the objective quadratic function. It should be noted that in both methods confidence sets are obtained in the form of ellipsoids but the simulation method gives more accurate estimates.

References

1. Anderson, T.W., Goodman, L.A.: Statistical inference about Markov chains. *Anal. Math. Stat.* **28**, 89–110 (1957)
2. Bellman, R.: *Introduction to Matrix Analysis*, 2nd edn. Society for Industrial and Applied Mathematics (1987)
3. Chernousko, F.L., Ovseevich, A.I.: Properties of the optimal ellipsoids approximating the reachable sets of uncertain systems. *J. Optim. Theory Appl.* **120**(2), 223–246 (2004)
4. Filippova, T.F., Matviychuk, O.G.: Estimates of reachable sets of control systems with bilinear quadratic nonlinearities. *Ural Math. J.* **1**(1), 45–54 (2015)
5. Hanson, S., Schuermann, T.: Confidence intervals for probabilities of default. *J. Bank. Finan.* **30**(8), 2281–2301 (2006). Elsevier
6. Jafry, Y., Schuermann, T.: Measurement, estimation and comparison of credit migration matrices. *J. Bank. Finan.* **28** (2004)
7. Kibzun, A.I., Kan, Yu. S.: *Stochastic Programming Problem with Probability and Quantile Functions*. Wiley, Chichester (1996)

8. Kurzhanski, A.B., Vályi, I.: Ellipsoidal Calculus for Estimation and Control. Birkhäuser, Boston (1997)
9. Precopa, A.: Stochastic Programming. Kluwer Acad. Publ., Dordrecht (1995)
10. Timofeeva, G.A., Timofeev, N.A.: Predicting the components of credit portfolio based on a Markov chain model. *Autom. Remote Control* **73**(4), 637–651 (2012)
11. Timofeev, N., Timofeeva, G.: Estimation of loan portfolio risk on the basis of Markov chain model. In: Hömberg, D., Tröltzsch, F. (eds.) *IFIP Advances in Information and Communication Technology*. Volume 391: System Modeling and Optimization. IFIP TC7 Conference: CSMO 2011, pp. 207–216. Springer (2013)
12. Vishnyakov, B.V., Kibzun, A.I.: Application of the bootstrap method for estimation of the quantile function. *Autom. Remote Control* **68**(11), 1931–1944 (2007)

Monitoring and Simulation of Gas Pipelines Through Quadripole Models

S.T. Baltazar, T.-P. Azevedo Perdicóulis and P. Lopes dos Santos

Abstract In this paper we propose to model a high pressure gas network using a quadripole approach. Although being simple, the proposed model seems to be adequate to network analysis and control, and is directly extendible to more complex networks, i.e., networks with junctions and loops. The model is proven to be liable on a case study constructed from data supplied by REN Gasodutos, where we investigate the effect of a leakage on the mass flow and pressure along the pipeline with the final objective to define a model based methodology for leakage detection and location.

Keywords Inverse approach · Leakage detection · Gas networks · Quadripole models · Modelling · Large scale systems

1 Introduction

Natural gas, as a highly used commodity, is transported and distributed all over the world mainly through networks of pipelines that require permanent monitoring and control [1]. Due to the problem inherent characteristics, namely its large scale, non linearities and transient behaviour, its models are always very complex. However, the derivation of simpler models is crucial [7] to various management problems, as is the case of an effective leakage detection, which is a decisive factor in gas network operation, specially with the ageing of the infrastructures; this is likewise

S.T. Baltazar (✉)

Universidade de Trás-os-Montes e Alto Douro (UTAD), Vila Real, Portugal
e-mail: sarabaltazar@gmail.com

T.-P.A. Perdicóulis

UTAD and ISR-Coimbra, Vila Real, Portugal
e-mail: tazevedo@utad.pt

P.L. dos Santos

Faculdade de Engenharia da Universidade do Porto, Porto, Portugal
e-mail: pjsantos@fe.up.pt

true for leakage location and estimation of its size. It is also very relevant to detect and locate a leakage in real time [2], as well as in case of small leakages.

Nowadays, one can find various fault detection methods, however many of these methods present a high frequency of false alarms caused by controller desensitization and thereupon are ignored or not given the proper consideration [5]. The most popular ones are the internal or software methods, since these are the most economical, less intrusive and simpler to implement [6]. These class of methods continuously monitor values of pressure and mass flow mostly only at the extremes of the pipeline using algorithms based on some mathematical method and, although its use may be considered adequate when combined with other methods, more research in this area is required, specially to overcome the shortage of mass flow measurements in the intermediate points of the line [11] and the measurements inaccuracy.

The main purpose of this article is to develop a simple model to monitor the pipeline in order to investigate the effect of a leakage on the mass flow and pressure along the pipeline using the quadripole theory. As a result, we obtain mass flow soft sensors along the pipeline. Increasing the “measuring points” allows to generate more accurate and sensitive leakage detectors/locators and therefore conveys a higher responsiveness of the network operational staff in case of leakage.

The article is organised as follows: In Sect. 2, using transfer function (TF) models derived from a nonlinear first order PDE, a representation of the pipeline intermediate values of mass flow/pressure are obtained. These models are adapted to the leakage situation in Sect. 3. In Sect. 4, a case study is build using a mix of operational and simulated data in order to illustrate the use of soft sensors in the leakage detection. The approach described here is very modular and able to be directly adapted to complex networks and leakage location. Conclusions and directions for future work are outlined in the last section.

2 Junction Equations

The gas dynamics in the pipeline is represented by non linear partial differential equations (PDE), whose particular form is defined according to different assumptions and operational conditions [9, 10]. Due to its complexity simplified versions of these models are used in the practice, inclusive linearised ones. The PDE is linearised by considering the secant of the curve, parallel to the tangent at the middle point (for more details see [4]), thus:

$$\begin{cases} \frac{\partial q(\ell, t)}{\partial t} = -\mathcal{A} \frac{\partial p(\ell, t)}{\partial \ell} - 2\alpha q(\ell, t) \\ \frac{\partial p(\ell, t)}{\partial t} = -\frac{c^2}{\mathcal{A}} \frac{\partial q(\ell, t)}{\partial \ell}, \end{cases} \quad (1)$$

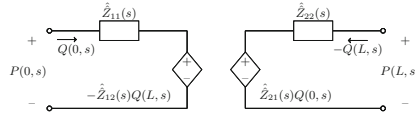


Fig. 1 Gas mass flow quadripole

where q is node mass flow, ℓ is space, t is time, \mathcal{A} is the cross-sectional area, p is edge pressure-drop, f is the friction factor, c is the isothermal speed of sound, D is the pipe diameter and $\alpha := \frac{fc^2}{4D\mathcal{A}\bar{p}} \bar{q}$, with \bar{q} and \bar{p} operational levels.

Although the angle inclination of the pipeline is not negligible [4], here we consider a horizontal pipeline, according to the data of the case study.

Using a quadripole analogy, different models can be withdrawn (see [3]). In the present work, second approximations of these TF models are used (see [8] for details).

Defining $P(0, s)$ and $P(L, s)$ as intake and out take pressures, and $Q(0, s)$ and $Q(L, s)$ as intake and out take mass flow, the impedance model is described in Fig. 1, with $T_d = \frac{L}{c}$, $\hat{Z}_{11}(s) = \hat{Z}_{22}(s) = \frac{c}{\mathcal{A}\alpha T_d} \left(\frac{s + \alpha}{s} \right)$, and $\hat{Z}_{12}(s) = \hat{Z}_{21}(s) = \frac{c}{\mathcal{A}\alpha T_d} \left(\frac{s + \alpha}{s} \right) e^{-T_d s}$.

$$\begin{cases} P(0, s) = \hat{Z}_{11}(s)Q(0, s) - \hat{Z}_{12}(s)Q(L, s) \\ P(L, s) = \hat{Z}_{21}(s)Q(0, s) - \hat{Z}_{22}(s)Q(L, s). \end{cases} \quad (2)$$

Likewise, the admittance model is described in Fig. 2, with $\hat{Y}_{11}(s) = \hat{Y}_{22}(s) = \frac{\mathcal{A}}{c\alpha T_d} \left(\frac{s + \alpha}{s + 2\alpha} \right)$ and $\hat{Y}_{12}(s) = \hat{Y}_{21}(s) = -\frac{\mathcal{A}}{c\alpha T_d} \left(\frac{s + \alpha}{s + 2\alpha} \right) e^{-T_d s}$.

$$\begin{cases} Q(0, s) = \hat{Y}_{11}(s)P(0, s) + \hat{Y}_{12}(s)P(L, s) \\ Q(L, s) = -\hat{Y}_{21}(s)P(0, s) - \hat{Y}_{22}(s)P(L, s). \end{cases} \quad (3)$$

To represent intermediate values of mass flow/pressure, we have the pipeline of Fig. 3, omitting s for simplicity sake, and the respective quadripole in Fig. 4.

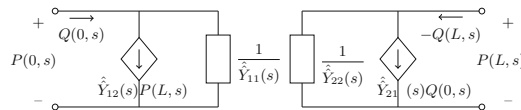


Fig. 2 Gas pressure quadripole

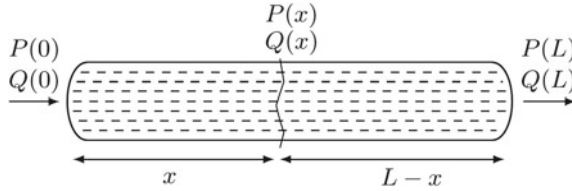


Fig. 3 Junction of two pipelines

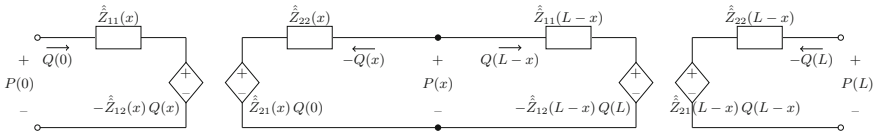


Fig. 4 Circuit equivalent to a junction of two pipelines quadripole

Applying the impedance model, both pipelines of Fig. 3 are written, respectively, as:

$$\begin{cases} P(0) = \hat{Z}_{11}(x)Q(0) - \hat{Z}_{12}(x)Q(x) \\ P(x) = \hat{Z}_{21}(x)Q(0) - \hat{Z}_{22}(x)Q(x), \end{cases} \quad \text{and} \quad (4)$$

$$\begin{cases} P(x) = \hat{Z}_{11}(L-x)Q(x) - \hat{Z}_{12}(L-x)Q(L) \\ P(L) = \hat{Z}_{21}(L-x)Q(x) - \hat{Z}_{22}(L-x)Q(L). \end{cases} \quad (5)$$

Using the last equation of (4) together with the first of (5), we obtain a representation for the flow at any intermediate point of the pipeline:

$$Q(x) = \frac{L-x}{L}e^{-\frac{x}{c}s}Q(0) + \frac{x}{L}e^{-\frac{L-x}{c}s}Q(L). \quad (6)$$

In equal manner, the admittance model is used to obtain a representation for the intermediate values of pressure [3].

$$P(x) = \frac{L-x}{L}e^{-\frac{x}{c}s}P(0) + \frac{x}{L}e^{-\frac{L-x}{c}s}P(L). \quad (7)$$

3 Leakage Detection

A leakage point is modelled using the quadripole approach described in Sect. 2. Thus, considering the pipeline of Fig. 3 with a leak at x point and the corresponding leakage Q_{Leak} , it can be represented by the circuit of Fig. 5, where the subscript $-L$ stands for left and $-R$ for right.

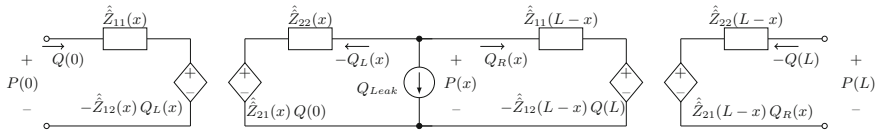


Fig. 5 Circuit equivalent to a pipeline with a leak at point x

We impose the positive direction of flow from left to right. Hence:

$$\begin{cases} P(0) = \hat{Z}_{11}(x)Q(0) - \hat{Z}_{12}(x)Q_L(x) \\ P_L(x) = \hat{Z}_{21}(x)Q(0) - \hat{Z}_{22}(x)Q_L(x), \end{cases} \quad \text{and} \quad (8)$$

$$\begin{cases} P_R(x) = \hat{Z}_{11}(L-x)Q_R(x) - \hat{Z}_{12}(L-x)Q(L) \\ P(L) = \hat{Z}_{21}(L-x)Q_R(x) - \hat{Z}_{22}(L-x)Q(L). \end{cases} \quad (9)$$

The occurrence of a leakage translates into a mass flow loss at the leakage point, $Q_{Leak}(x)$, which propagates left, $Q_{Lk}(x)$, and right, $Q_{Rk}(x)$, and produces impacts on the mass flow/pressure along the pipeline. Terms relating to a leakage have the subscript Lk , while subscript nLk is use for non leakage terms. Hence:

$$P(\ell) = P_{nLk}(\ell) + P_{Lk}(\ell); \quad Q(\ell) = Q_{nLk}(\ell) + Q_{Lk}(\ell). \quad (10)$$

$P_{nLk}(\ell) = P(\ell)|_{Q_{Leak}=0}$, $P_{Lk}(\ell) = P(\ell)|_{Q(0)=Q(L)=0}$, $\ell = [0, L]$. Substituting (10) in (8) and (9), and using the superposition principle together with the Kirchhoff Current Law (KCL), we have the left and right leakage propagation:

$$Q_{Lk}(x) = \frac{x}{L}Q_{Leak}(x); \quad Q_{Rk}(x) = -\frac{L-x}{L}Q_{Leak}(x). \quad (11)$$

Using expression (11) and after a few simple calculations we have a representation for the propagation of the leakage effect on the left and the right side of the leak point in terms of the leakage size.

$$P_{Lk}(0) = -\hat{Z}_{11}(L)e^{-\frac{x}{c}s}Q_{Leak}(x); \quad P_{Lk}(L) = -\hat{Z}_{11}(L)e^{-\frac{L-x}{c}s}Q_{Leak}(x). \quad (12)$$

Moreover, it is also possible to obtain expressions for the influence of the leakage on the pressure along the pipeline, however these representations depend on the leakage location and observation point, as we will see in the next section.

4 Case Study

The case study was constructed from REN Gasodutos data (with $N = 720$ data, corresponding to a 24 h day work) using (2), (3), (6) and (7). We were able to obtain the values $P(L_i)$ and $Q(L_i)$, at every point L_i , $i = 0, 4$, every 30 km We may also repre-

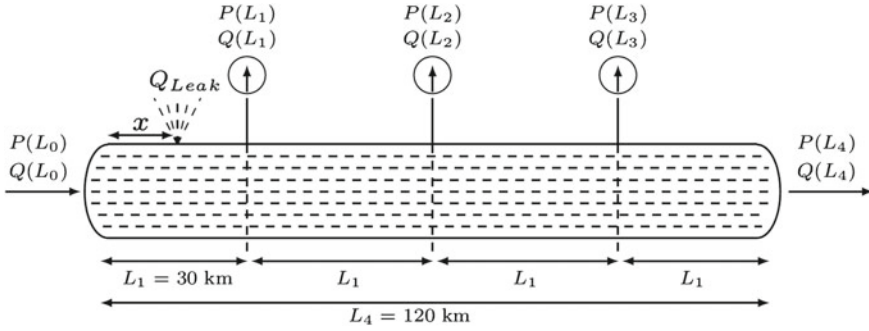


Fig. 6 Pipeline 120 km with a leak at point $x = 5$ km

sent the effect of the leakage on the pressures at the endpoints of the pipeline. This is rather interesting due to the shortage of mass flow measurements along the gas distribution/transportation pipeline, then these mass flows values can be viewed as soft sensors. Consider that a leakage occurs at 5 km from the inlet point, between sensors L_0 and L_1 , as depicted in Fig. 6, and from the instant $N = 300$.

We model the situation described in Fig. 6 in order to obtain representations for pressure, $P_{Lk}(L_i)$, and mass flow, $Q_{Lk}(L_i)$, at every point $L_i, i = \overline{0, 4}$, in a leakage situation, with fix $Q(L_0)$. Hence assuming $\Delta L = L_{i+1} - L_i$, we have:

$$\begin{cases} P(L_0) = \hat{Z}_{11}(x)Q(L_0) - \hat{Z}_{12}(x)Q_L(x) \\ P_L(x) = \hat{Z}_{21}(x)Q(L_0) - \hat{Z}_{22}(x)Q_L(x), \end{cases} \quad (13)$$

$$\begin{cases} P_R(x) = \hat{Z}_{11}(L_1 - x)Q_R(x) - \hat{Z}_{12}(L_1 - x)Q(L_1) \\ P(L_1) = \hat{Z}_{21}(L_1 - x)Q_R(x) - \hat{Z}_{22}(L_1 - x)Q(L_1), \end{cases} \quad (14)$$

$$\begin{cases} P(L_i) = \hat{Z}_{i,i}(\Delta L)Q(L_i) - \hat{Z}_{i,i+1}(\Delta L)Q(L_{i+1}) \\ P(L_{i+1}) = \hat{Z}_{i+1,i}(\Delta L)Q(L_i) - \hat{Z}_{i+1,i+1}(\Delta L)Q(L_{i+1}), \text{ with } i = \overline{1, 3}. \end{cases} \quad (15)$$

After a few simpler calculations, we obtain:

$$Q_{Lk}(L_i) = -\frac{L_4 - L_i}{L_4} e^{-\frac{L_i - x}{c}s} Q_{Leak}(x), \text{ with } i = \overline{1, 3}, \quad (16)$$

$$P_{Lk}(L_1) = -Z_{11}(L_4) e^{-\frac{L_1 - x}{c}s} Q_{Leak}(x). \quad (17)$$

$$P_{Lk}(L_2) = Z_{11}(L_2) Q_{Lk}(L_2). \quad (18)$$

$$P_{Lk}(L_3) = -Z_{11}(L_1) Q_{Lk}(L_3). \quad (19)$$

The purpose now is to detect a leakage in this pipeline without knowing of its existence. In a real situation we can access all the information described in Fig. 7 and mass flow can be calculated at any intermediate point, as described in the previous sections.

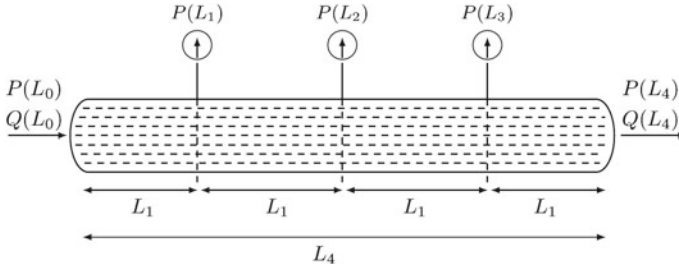


Fig. 7 Pipeline 120 km long with intermediate pressure sensors every 30 km

We start by calculating mass flow values using $Q(L_0)$ and the values of pressure in the leak case, $P_{Lk}(L_i)$, $i = \overline{0, 4}$, using models described in Sect. 2, that from now on we refer to as calculated mass flows, $Q_c(L_i)$, $i = \overline{1, 4}$.

The simulations are obtained using nominal mass flow, $\bar{q} = 60 \text{ Kg/s}$, nominal pressure, $\bar{p} = 81 \text{ bar} = 81 \times 10^5 \text{ Pa}$, and the parameter values $\alpha = 0.05$, $\mathcal{A} = 0.5 \text{ m}^2$ and $c = 300 \text{ m/s}$.

In Fig. 8 it is shown the comparison of three distinct mass flow levels at the observation points: (i) in a non leak situation—standard values $Q(L_i)$, $i = \overline{0, 4}$, (in blue); (ii) with 10 % leakage of a nominal mass flow $Q_{Lk}(L_i)$, $i = \overline{1, 4}$ (in bold red); and (iii) of the calculated mass flow $Q_c(L_i)$, $i = \overline{1, 4}$, (in dashed green).

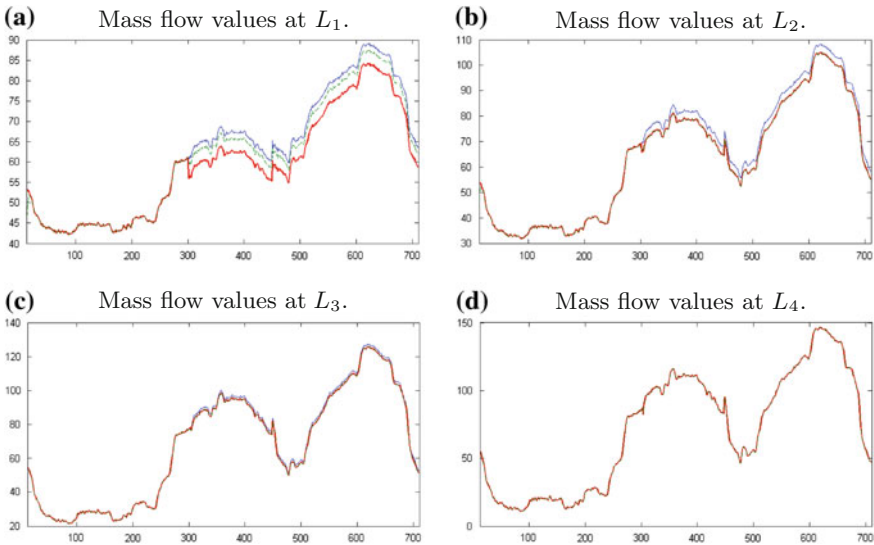


Fig. 8 Standard (blue), in leak case (bold red) and calculated (dashed green) mass flow values at stations L_i , with $i = \overline{1, 4}$

Analysing Fig. 8, the leakage is perceived by the mass flow values at every station being more noticed at the observation points closer to the leakage point, both mass flows resulting directly from the leakage impact (in bold red) and mass flow calculated (in dashed green), using the pressures resulting directly from the leakage impact.

Next, we determine pressure from the calculated mass flows $Q_c(L_i)$, with a fixed $Q(L_0)$, and using the models of Sect. 2, that we refer to as calculated pressures, $P_c(L_i)$, $i = 0, 4$.

In Fig. 9 it is shown the comparison of three distinct pressures levels at the observation points: (i) in a non leak situation—standard values $P(L_i)$ (in blue); (ii) with a 10% leakage $P_{Lk}(L_i)$ (in bold red); and (iii) of the calculated mass flow $P_c(L_i)$, $i = 0, 4$, (in dashed green).

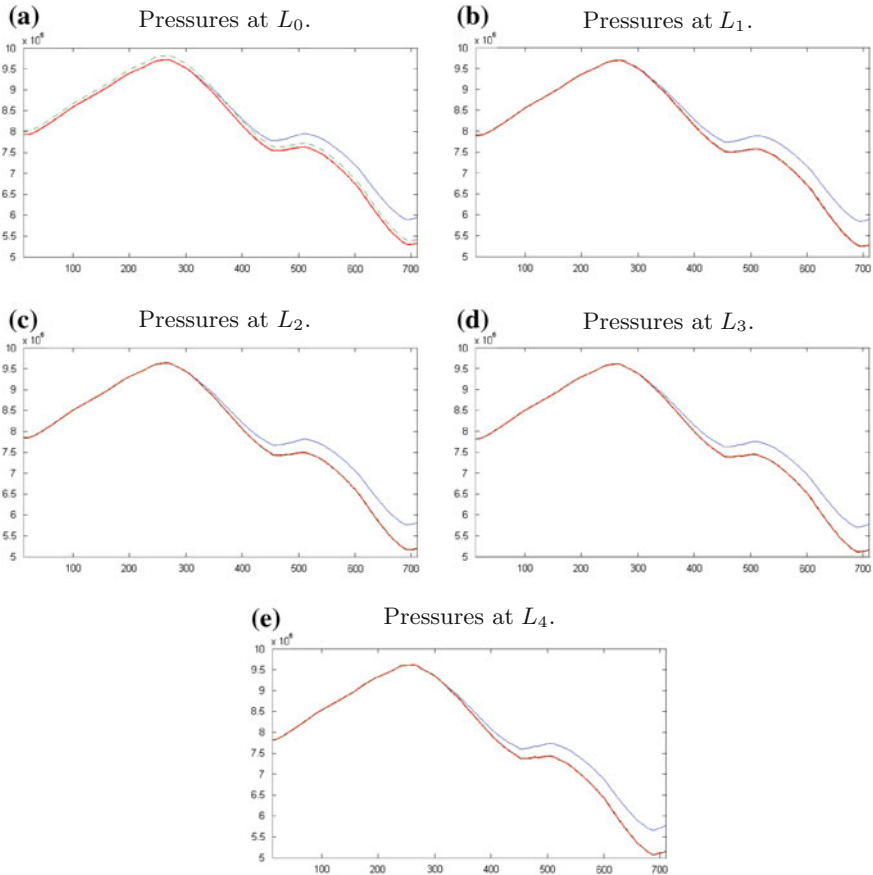


Fig. 9 Standard (in blue), in leak case (bold red) and calculated (in dashed green) pressure values at stations L_i , with $i = \overline{0, 4}$

Although a leakage is noted, in Fig. 9 we can see there is not sensitivity enough to locate it from the point of view of pressure drop in each sensor, since the instant at which happens appears to be constant along the pipeline. However, there is a delay in the pressures profiles in the leakage case. Along the pipeline, the standard pressures in the non leakage case (in blue) are decreasing.

5 Conclusion and Future Work

Starting from a first order hyperbolic PDE, we developed TF simpler models that easily can be used in the management and operation of gas network, as for instance in leakage detection. Although mass flow sensors are more sensitive to leakage than pressure sensors, its shortage along the pipeline is a difficulty that we overcome by using soft sensors. The leakage is perceived with a delay that increases as we walk away from the leakage point, in both directions. This model can be extended to the study of leakage location and leakage size estimation. In future work, after studying the effects of a leakage at different locus, we plan to apply a Linear Parameter Varying leakage detector/locator guided by information supplied by the models described here.

Acknowledgments The authors are very grateful to the reviewers for their insightful comments that greatly contributed to improve the work. The second author would like to thank FCT (Project ref. UID/EEA/00048/2013) for their support to this research and its dissemination.

References

1. Adnan, N.F., et al.: Leak detection in MDPE gas pipeline using dual-tree complex wavelet transform. *Aust. J. Basic Appl. Sci.* **8**(15), 356–360 (2014)
2. Bagajewicz, M., Valtinson, G.: Leak detection in gas pipelines using accurate hydraulic models. *Ind. Eng. Chem. Res.* **53**(44), 16964–16972 (2014)
3. Baltazar, S.T., Azevedo Perdicóulis, T.-P., Lopes dos Santos, P.: Quadripole models for simulation and leak detection on gas pipelines. In: *Proceedings of 47th PSIG Annual Meeting*, Vancouver, Canada (2016)
4. Baltazar, S.T., Lopes dos Santos, P., Azevedo Perdicóulis, T.-P.: Quadripole models for gas networks. In: *Proceedings of XVI Congreso Latino Americano de Control Automático (CLCA)*, Cancn, Mexico (2014)
5. Blasi, M. Di, et al.: Overview of Enbridge's rupture recognition program. In: *Proceedings of 46th PSIG Annual Meeting*, New Orleans (LA), USA (2015)
6. Geiger, G.: State-of-the-art in leak detection and localisation. In: *Proceedings of Pipeline Technology 2006 Conference*, Hannover, Germany (2006)
7. Lopes dos Santos, P., et al.: A lumped transfer function model for high pressure gas pipelines. In: *Proceedings of 49th IEEE Conference on Decision and Control (CDC)*, Atlanta, GA, USA (2010)
8. Lopes dos Santos, P., et al.: Modelling a leakage in high pressure gas network using a quadripole approach. In: *Proceedings of 10th Simone Congress*, Lisbon, Portugal (2010)
9. Osiadacz, A.J.: *Simulation and Analysis of Gas Networks*. E. and F.N. Spon, London (1987)

10. Reddy, H.P., Narasimhan, S., Bhallamudi, S.M.: Simulation and state estimation of transient flow in gas pipeline networks using a transfer function model. *Ind. Eng. Chem. Res.* **45**, 3853–3863 (2006)
11. REN-Gasodutos: Personal Communication (2014)

Data Based Modeling of a Large Scale Water Delivery System

Marta Fernandes, Paulo Oliveira, Susana Vieira, Luís Mendonça,
João Lemos Nabais and Miguel Ayala Botto

Abstract Water is a vital resource and the growing populations and economies around the globe are pushing its demand worldwide. Therefore, the water conveyance operation should be well managed and improved. This paper proposes the development of reliable models able to predict water levels of a real 24.4 km water delivery channel in real time. This is a difficult task because this is a time-delayed dynamical system distributed over a long distance with nonlinear characteristics and external perturbations. Artificial neural networks are used, which are a well-known modeling technique that has been applied to complex and nonlinear systems. Real data is used for the design and validation of the models. The model obtained has the ability to predict water levels along the channel with minimum error, which can result in significant reduction of wasted water when implementing an automatic controller.

Keywords Data based modeling · Water delivery systems · Artificial neural networks · Nonlinear autoregressive exogenous model

1 Introduction

Water is the most important resource for human life therefore it has to be efficiently managed. An increase of 55 % in global water demand is expected by 2050, mainly influenced by the projected growing demands from manufacturing, thermal electricity generation and domestic use [1].

M. Fernandes (✉) · P. Oliveira · S. Vieira · L. Mendonça · J.L. Nabais · M.A. Botto
IDMEC, LAETA, Instituto Superior Técnico, Universidade de Lisboa,
Lisbon, Portugal
e-mail: marta.fernandes@tecnico.ulisboa.pt

L. Mendonça
Department of Marine Engineering, Escola Superior Náutica Infante
D. Henrique, Oeiras, Portugal

J.L. Nabais
School of Business Administration, Polytechnical Institute of Setúbal,
Setúbal, Portugal

The development of models and the design of controllers for irrigation channel systems has been a difficult task since these systems are distributed over long distances and present a dynamic behavior characterized by time delays, strong nonlinearities, unknown perturbations and numerous interactions among sub-systems [2].

Control of irrigation channels has been driving the attention of engineers since immemorial times and several papers have been published in this field [3–12]. One of the most accepted and used models for simulation of the physical dynamics of a real main irrigation channel pool is the system described by the Saint-Venant equations [13]. However, the difficulty in determining the parameters of these equations remains as one of the main drawbacks of this physically oriented modeling approach. As a consequence, new alternative modeling approaches, namely both parametric and nonparametric data-driving models, have been proposed, in which the model parameters are optimized to match real data [14].

The water delivery system which the authors intend to model is the Milfontes Canal, a large scale open water channel supplying water to the village of Vila Nova de Milfontes as well as to local farmers. The facilities are equipped with a basic monitoring system that provides information on the water depth and gate aperture levels along the channel. The absence of an automatic control system together with the necessity of ensuring the clients' water requests results in large amounts of wasted water at the end of the channel.

As far as the authors are aware of, Artificial Neural Networks (ANN) have never been applied to real irrigation channels in normal operation. In this paper, ANN are employed to create a nonlinear dynamic model of the Milfontes Canal using real operation data from 2013. This model has the ability to predict future water levels along the infrastructure, from the perspective of signal prediction in real time. Well-known performance measures are used to assess the models performance. The model developed may ensure a significant reduction of wasted water when implementing an automatic controller.

The paper is organized as follows. In Sect. 2, the system modeling is addressed. The results obtained are shown and discussed in Sect. 3 and conclusions are drawn in Sect. 4.

2 Artificial Neural Networks

ANN are self-organizing systems, having the ability to learn from examples, that is, to be trained with provided data. This feature makes them extremely useful to model complex or unfamiliar systems, since it does not require system in-depth knowledge from the designer. Usually, ANN modeling follows three steps: structure identification, parameter estimation and model validation.

The system to be identified can be represented as a Multiple-Input Multiple-Output (MIMO) Nonlinear Auto Regressive with exogenous inputs (NARX) model:

$$\mathbf{y} = f(\mathbf{x}), \quad (1)$$

where \mathbf{x} is a state vector obtained from input-output data and \mathbf{y} the system output. In this case, the state vector \mathbf{x} at each time step k can be obtained from the inputs and outputs of the system, joining them in a vector:

$$\mathbf{x}(k) = [y_1(k), \dots, y_1(k - p_1 + 1), \dots, y_p(k), \dots, y_p(k - p_p + 1), \dots, u_1(k), \dots, u_1(k - m_1 + 1), \dots, u_m(k), \dots, u_m(k - m_m + 1)]^T. \quad (2)$$

The parameters m_1, \dots, m_m are the orders of the inputs u_1, \dots, u_m , and the parameters p_1, \dots, p_p are the orders of the outputs y_1, \dots, y_p , respectively. Note that the dimension of the state vector is given by $D = \sum_{j=1}^m m_j + \sum_{j=1}^p p_j$ [15]. For a dynamic system using this state vector, the model is represented by:

$$\hat{\mathbf{y}}(k + 1) = f(\mathbf{x}(k)) \quad (3)$$

The state variables \mathbf{x} are called the regressor and the predicted outputs $\hat{\mathbf{y}}$ the regressand.

In the present case, the system model will take the form of a neural network and the tuning mechanism is known as training the network. This training consists on adjusting the network parameters the connection weights and the node biases according to an error backpropagation algorithm.

In this type of problems, data is usually divided for model training and testing. Training a neural network model is based on a learning algorithm. For this work, the Levenberg-Marquardt backpropagation algorithm is employed. The performance measures used were the mean square error (MSE) for both model training and testing. Mean absolute error (MAE) and mean absolute relative error (MARE) were used as well to assess the performance of model testing.

3 Results and Discussion

3.1 System Configuration

A schematic representation of the system inputs and outputs used in the system identification procedure is presented in Fig. 1. The group of major offtakes (u_2 to u_7) plus the flow rate entering the channel inlet (u_1) are the inputs of the system, in a total of 7. The outputs consist on two types of sensors, in a total of 10: upstream (y_1, y_4, y_7 and y_{10}) and downstream (y_3, y_6 and y_9) water depth sensors and gate aperture sensors (y_2, y_5 and y_8), which measure the correspondent gate openings percentage.

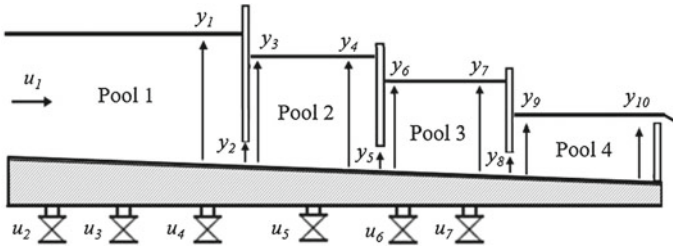


Fig. 1 Schematic representation of the channel inputs and outputs

3.2 Database

In order to carry out this work, the Associação de Beneficiários do Mira (ABM), a non-profit organization in charge of this hydro agricultural infrastructure, provided the database files. These files contained the sensor measurements plus a client order book containing the water requests during 2013, which were considered as the effective outflows of the channel.

A procedure was applied in order to import the data from the database files into well-formatted datasets. All data points considered as outliers were removed. An outlier data point consisted on all negative values and all values that stood out by differing more than 15 units from their precedent. For the datasets, upon missing data, all the identified missing segments were recovered when possible using the zero order hold (ZOH).

Lack of either sensor or flow rates information reduced the list of potential datasets to the ones depicted in Table 1. The information regarding the number of data points before and after outliers removal and missing data processing is presented for each dataset. The percentage of missing data here presented represents the number of missing data points considering the total number of data points of each dataset.

It was verified that the sampling times of the sensors signals were not constant, usually falling in the 65–100 s range. Furthermore, the signals were not synchronized, therefore requiring further data processing. After signal processing, it was found that the time step, k , should be 90 s in order to take advantage of the available data provided by ABM.

Table 1 Final datasets obtained after identification of missing data and outliers and reconstruction with ZOH

Dataset ID	Data points before	Missing data (%)	Number of outliers	Data points after
49	6200	5.5	0	6199
50	6203	0.0	168	6203
51	6202	0.0	1	6202
53	6187	1.3	6	6187

3.3 System Delay

The system delay associated with the channel arises from the fact that the water levels do not immediately change when the water flow rates inwards and/or outwards of the channel are adjusted. Hence, the computation of the system delay has to take into account the location of the offtakes to estimate the delay caused by the time the water takes to arrive to the place where these offtakes are located.

According to tests performed on a site visit, the water speed on the channel was about 2.7 m/s. Considering the total length of the channel, the delay from the channel's intake flow to the water level measured on the other end of the channel was approximately 100 time steps, which translates to about 2 and a half hours.

The followed approach consisted on using an input-output delay as parameter of the system where the delay due to water flow rates was the same as the one in the water levels.

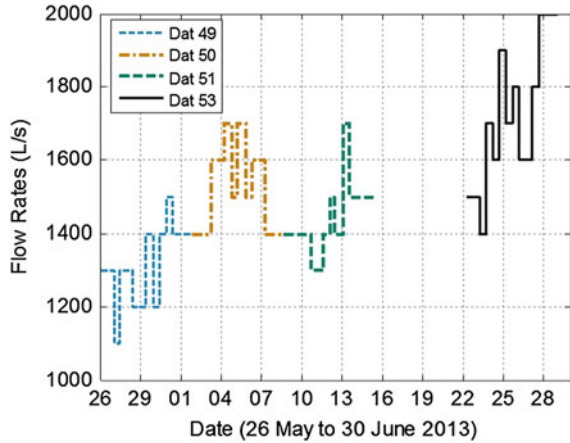
Given that the system delay may be set by many data points that situation would inevitably lead to an impracticable network model. In order to overcome this problem, a subset of the past data up to the system delay (100 time steps) was fed into the model. In terms of time steps, that corresponded to the set of delays $\tau = [1, 11, 21, 31, 41, 51, 61, 71, 81, 91, 101]$, with a time step of $5 \times k$, which translates to 7.5 min.

3.4 Model Parameterization, Training and Validation

Regarding the model parameterization, the number of hidden layers and neurons in each layer were varied. In order to reduce variability and to find the best model, ten rounds of the same model were performed with different random initializations of network input weights. This was performed for each possible system delay, from 1 step to 100 time steps in time. The final system delay found corresponded to the model with best performance overall.

In this paper, the software Matlab® 2014a default stopping conditions were used, except for the training epochs, which were set to 200. The model training dataset was divided using the function *divideblock* from Matlab, where 70% of data was used for train, 15% for validation and 15% for test. A linear autoregressive model with exogenous inputs (ARX) was estimated with the same regressor as the NARX networks for comparison, using the default conditions of ARX function from Matlab. The same subsets for train and test were used and the system delay was varied as performed for the NARX models.

Fig. 2 Channel inlet flow rates corresponding to input u_1 for the datasets used for model training (Dat 49, 51 and 53) and testing (Dat 50)



3.5 Modeling Results

The model training dataset was obtained by joining datasets 49, 51 and 53. Each one of these datasets represent, respectively, a low, medium and high range of the variability that can be found in the system. The criterion for defining this variability was based on the flow rates values of the channel main inlet, u_1 , as it can be confirmed in Fig. 2. Dataset 50 was selected for test, given that it represents a medium range, considered suited for testing the model. In Fig. 2, the lack of data between datasets 51 and 53 corresponds to a dataset which was not used for system modeling due to significant percentage of missing data.

The average performances of the best NARX and ARX models as well as of the NARX models obtained over the 10 rounds, are presented in Table 2. The NARX model has a better performance than the ARX. Therefore, only the performance results of the best NARX model are presented for each output in Table 3. This best model configuration was a single hidden layer with 10 neurons. More or less neurons in the hidden layer resulted in worst results, which happened as well when adding more layers.

The system delay found was 11 time steps which corresponds to approximately 16 min. This system delay is a result of a balance between the delays caused by the

Table 2 Models average performance results, for a 16 min delay, where the best model results are presented in more detail in Table 3

MIMO models	MSE (cm ²)	MAE (cm)	MARE (cm)
10 rounds (NARX)	0.12 ± 0.01	0.16 ± 0.01	0.01 ± 0.01
Best NARX	0.11 ± 0.09	0.14 ± 0.08	0.01 ± 0.01
Best ARX	25.42 ± 41.31	3.13 ± 2.73	0.05 ± 0.07

Table 3 Best NARX model performance results for each output and correspondent pool

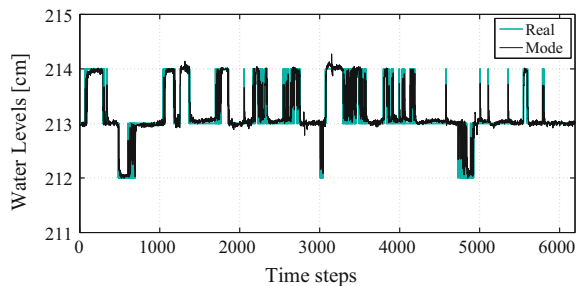
Sensor types		MSE (cm ²)	MAE (cm)	MARE (cm)	Pool
Water levels	y_1	0.05	0.10	0.01	1
	y_3	0.20	0.31	0.01	2
	y_4	0.05	0.09	0.01	2
	y_6	0.07	0.15	0.01	3
	y_7	0.31	0.18	0.01	3
	y_9	0.18	0.22	0.01	4
	y_{10}	0.05	0.13	0.01	4
		MSE (% ²)	MAE (%)	MARE (%)	
Gate openings	y_2	0.01	0.03	0.01	–
	y_5	0.16	0.10	0.01	–
	y_8	0.05	0.12	0.01	–

channel intake flow rates and offtakes. The delay of each input or output depends on its location, therefore the delay caused by a flow rate located at the beginning of the channel is not the same as one at the middle or at the end.

Compared to the other outputs correspondent to the water levels, the output correspondent to downstream pool 3, y_7 , presents the higher MSE. The output of water level measured upstream pool 4, y_9 also presents a high error.

It is worth noting that both the water level outputs y_7 and y_9 are located, respectively, immediately before and after the gate that separates both pools 3 and 4, thus the cause to obtain these errors may be due to noise, a failure in the sensors measurement. The water level sensor represented by y_3 also presents a high MSE and MAE values, which may be due to the same cause. Regarding the remaining outputs, the model has the ability to predict one step ahead the water levels and the gate apertures with a minimum error. The best prediction model is presented in Figs. 3, 4, 5 and 6, for each pool of the channel.

Fig. 3 Pool 1 downstream model response



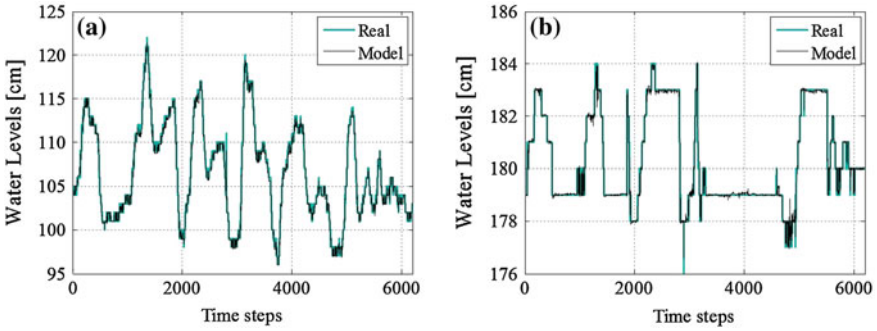


Fig. 4 Pool 2 model response: a upstream, b downstream

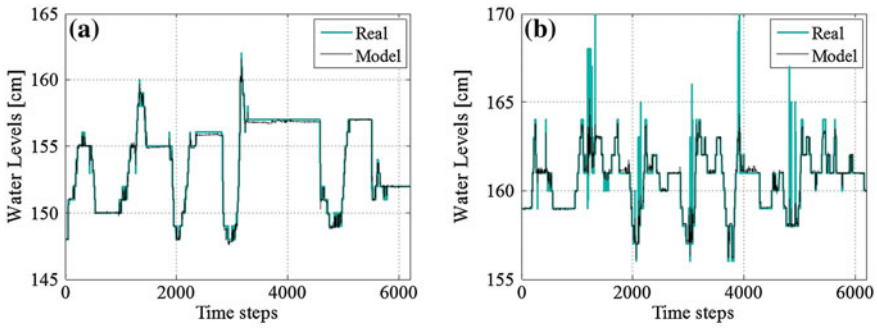


Fig. 5 Pool 3 model response: a upstream, b downstream

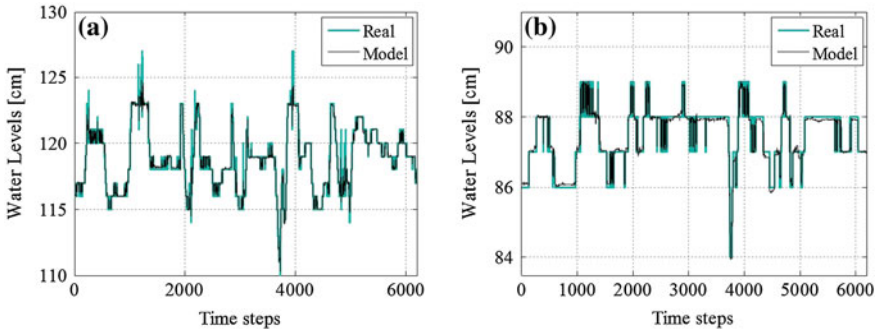
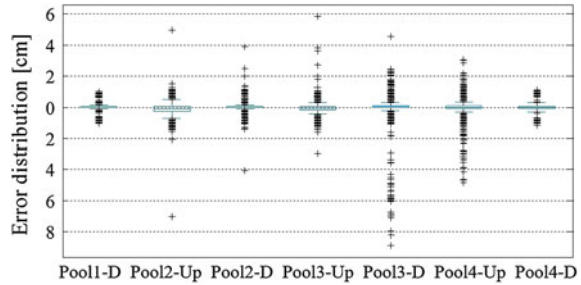


Fig. 6 Pool 4 model response: a upstream, b downstream

When analysing the prediction model results, it can be observed that the main system dynamics are being predicted correctly. Indeed, the great majority of the relative error values are within the 5 cm band, which may be better visualized in Fig. 7.

As previously referred, the model presents higher prediction error when predicting water levels in pool 3. An approximate maximum error of almost 9 cm can be

Fig. 7 Model prediction errors distribution for each pool: upstream (Up) and downstream (D)



visualized when analyzing Fig. 7, which is caused by an isolated spike in the output prediction. The occurrence of such phenomenon may indicate the used network is unable to model a minor system mode. For instance, it may be the case that the used network is not able to model the reflected water waves effect. Other complex flow phenomena may explain this behavior. Not to mention that noise is surely present in the real value measurements.

4 Conclusions

In this work, artificial neural networks were employed to model a real large scale water channel, using real operation data. This model has the ability to predict future water levels along the infrastructure in real time and in the future it may be used in a planning perspective, for control design or as an assistance tool for a FDI system.

The best one step ahead prediction NARX model parameterization presented consists on a single-layered network with 10 neurons and a delay of approximately 16 min. The performance achieved by this model parameterization was equivalent to a MSE mean of $0.11 \pm 0.09 \text{ cm}^2$, which is considered reasonable given that the average real values range between 85 and 250 cm. The absence of other models of the same channel precludes a well-supported validation of the proposed model. Nevertheless, an independent test dataset, not used to train the models, was used with the purpose of validating them.

The application of neural network models to water delivery systems proved to be a good opportunity to show the benefits and features of using these type of black-box models. As a result, in the future the water waste at the end of the channel can be significantly reduced when applying an automatic controller, assisted by the model obtained in this paper.

Acknowledgments This work is supported by the Fundação para a Ciência e a Tecnologia (FCT), through IDMEC, under LAETA Pest-OE/EME/LA0022, and supported by the project PTDC/EMS-CRO/2042/2012. Susana Vieira acknowledges the support by the Program Investigador FCT (IF/00833/2014) from FCT, cofunded by the European Social Fund (ESF) through the Operational Program Human Potential (POPH).

References

1. Water, U.: The United Nations World Water Development Report 2014: Water and Energy. UNESCO, Paris (2014)
2. Malaterre, P., Baume, J.: Modeling and regulation of irrigation canals: existing applications and ongoing researches. In: IEEE International Conference on Systems Man and Cybernetics, vol. 4, pp. 3850–3855. Institute of Electrical Engineers Inc. (IEEE) (1998)
3. Zimbelman, D.D., Bedworth, D.D.: Computer control for irrigation-canal system. *J. Irrig. Drainage Eng.* **109**(1), 43–59 (1983)
4. Mareels, I., Weyer, E., Ooi, S.K., Cantoni, M., Li, Y., Nair, G.: Systems engineering for irrigation systems: successes and challenges. *Annu. Rev. Control* **29**(2), 191–204 (2005)
5. Weyer, E.: System identification of an open water channel. *Control Eng. Pract.* **9**(12), 1289–1299 (2001)
6. Weyer, E.: Control of irrigation channels. *IEEE Trans. Control Syst. Technol.* **16**(4), 664–675 (2008)
7. Eurén, K., Weyer, E.: System identification of open water channels with undershot and overshoot gates. *Control Eng. Pract.* **15**(7), 813–824 (2007)
8. Karunanithi, N., Grenney, W.J., Whitley, D., Bovee, K.: Neural networks for river flow prediction. *J. Comput. Civ. Eng.* **8**(2), 201–220 (1994)
9. Vieira, S., Sousa, J., Durao, F.: Fuzzy modelling strategies applied to a column flotation process. *Miner. Eng.* **18**(7), 725–729 (2005)
10. Lourenço, J., Botto, M., et al.: Modular modeling for large scale canal networks. In: 10th Portuguese Conference on Automatic Control, Funchal, Portugal, pp. 347–352 (2012)
11. Nabais, J., Duarte, J., Botto, M., Rijo, M.: Flexible framework for modeling water conveyance networks (2011). In: 1st International Conference on Simulation and Modeling Methodologies, Technologies and Applications (SIMULTECH 2011), pp. 142–147, Noordwijkerhout, The Netherlands (2011)
12. Nabais, J.M.L.C., Botto, M.A.: Linear model for canal pools. In: 8th International Conference on Informatics in Control, Automation and Robotics, ICINCO 2011, vol. 1, pp. 303–313, Noordwijkerhout, The Netherlands (2011)
13. Rivas-Perez, R., Feliu-Battle, V., Castillo-Garcia, F., Linarez-Saez, A.: System identification for control of a main irrigation canal pool. In: Proceedings of the 17th International Federation of Automatic Control (IFAC) World Congress, Seoul, South Korea, vol. 17 Part 1 (2008)
14. Zhuang, X., Xia, X.: Models and control methodologies in open water flow dynamics: a survey. In: AFRICON 2007, pp. 1–7. IEEE (2007)
15. Sousa, J.M., Kaymak, U.: Fuzzy decision making in modeling and control, vol. 27. World Scientific (2002)

PDE Model for Leakage Detection in High Pressure Gas Networks

T.-P. Azevedo Perdicóúlis, R. Almeida, P. Lopes dos Santos
and G. Jank

Abstract In this paper we design a model based method to locate a leakage and estimate its size in a gas network, using a linearised version of an hyperbolic PDE. To do this, the problem is reduced to two identical ODEs, allowing in this way for a representation of the pressure as well as the mass flow in terms of its system of fundamental solutions. Then using the available measurements at the grid boundary points, the correspondent coefficients can be determined. Assuming pressure continuity, we check for consistency of the coefficients in order to find faulty pipelines. Thence, the location of the leakage can be found either graphically or using a numerical method for a specific pipe. Next, its size can also be estimated.

Keywords Leakage detection · Leakage location · Gas networks · PDE linearisation

1 Introduction

Gas transport and distribution networks comprise a large number of interconnected pipeline that operate at different pressures and are able to transport gas along immense distances from its supply points to high industrial customers, networks of smaller dimension and reservoirs. This costly transportation system is build according to

T.-P. Azevedo Perdicóúlis (✉)
UTAD and ISR Coimbra, Coimbra, Portugal
e-mail: tazevedo@utad.pt

R. Almeida
UTAD and Mathematics Centre CMAT, Pole CMAT-UTAD, Braga, Portugal
e-mail: ralmeida@utad.pt

P. Lopes dos Santos
Faculdade de Engenharia da Universidade do Porto, Porto, Portugal
e-mail: pjsantos@fe.up.pt

G. Jank
Aachen University, Aachen, Germany
e-mail: jank@math2.rwth-aachen.de

very strict regulations and recommendations whose purpose is to secure a long-lasting gas grid. However, damage may occur due to corrosion or erosion, natural disasters, material defects or other unknown factors. Therefore, in the operation, control and optimisation of gas networks, paramount is an effective failure detection system. Besides the detection of a leakage, these systems should also be able to locate the leakage, estimate its size and be resilient to false alarms, since a high rate of false alarms reduces the reliability of fault detection system [4, 6, 11]. Different leakage detection systems exist, among which we highlight the model based ones, since these are implemented more easily, less costly and non-intrusive. These latter methods use different principles, as for instance the pressure wave, mass flow balance or are based on a mathematical model and measurements acquired usually by a Scada system [1–3, 7].

In this work we present a new method for leakage detection location where the grid integrity is first verified. Once a faulty pipeleg is found, the leakage is located and then its size estimated using a numerical method. To do this, in Sect. 2 we start with a nonlinear PDE that after separating its time and space variables, is linearised around some operational levels in order to obtain an ODE whose general solution can be represented in terms of its fundamental system. The proposed analytic solution to this model allows to represent pressure and mass flow on the right and left size of the unknown leak. Thence, the intersection of the pressure profiles pinpoints the leakage location in Sect. 3. In Sect. 4 we setup a tool to obtain a leakage detector in a grid. The leakage detection method is illustrated on Sect. 5. In Sect. 6 we withdraw some conclusions and outline some directions for future work.

2 Mathematical Model

Consider the following hyperbolic PDE to represent the gas dynamics in the pipe legs [8, 9]:

$$\begin{cases} \frac{\partial q(x, t)}{\partial t} = -S \frac{\partial p(x, t)}{\partial x} + \frac{\lambda c^2}{2dS} \frac{q^2(x, t)}{p(x, t)} \\ \frac{\partial p(x, t)}{\partial t} = -\frac{c^2}{S} \frac{\partial q(x, t)}{\partial x} \end{cases}, \tag{1}$$

where x is space, t is time, p is edge pressure-drop, q is mass flow, S is the cross-sectional area, d is the pipe diameter, c is the isothermal speed of sound, and λ is the friction factor. Together with this model, one also needs to consider adequate initial or boundary conditions.

In order to solve this system of equations we consider the following separation of time and space variables:

$$\begin{cases} q(x, t) = q_0(x)e^{\alpha t} \\ p(x, t) = p_0(x)e^{\alpha t} \end{cases}, \alpha \in \mathbb{R}, \tag{2}$$

where the parameter α gives the time dependence of pressure and mass flow although in a special form $e^{\alpha t}$. Hence, from (1) we obtain the following set of ordinary differential equations for $q_0(x), p_0(x)$:

$$\begin{cases} \alpha q_0(x) = -S p_0'(x) + \frac{\lambda c^2}{2dS} \frac{q_0^2(x)}{p_0(x)} \\ \alpha p_0(x) = -\frac{c^2}{S} q_0'(x) \end{cases} \quad (3)$$

To obtain simpler results we linearise system (3). To do this, we consider $p_0(x), q_0(x)$ as variations around some operational levels of pressure and mass flow, (\bar{p}, \bar{q}) , that is, $p_0(x) = \bar{p} + \Delta p_0(x)$ and $q_0(x) = \bar{q} + \Delta q_0(x)$, with Δp_0 and Δq_0 as the deviations from the pressure-drop and mass flow, respectively. Assuming $\frac{\Delta p_0(x)}{\bar{p}} \ll 1$, as well as $\frac{\Delta q_0(x)}{\bar{q}} \ll 1$, and neglecting terms of higher order and some simple calculations, we can approximate the nonlinear term as:

$$\frac{q_0^2(x)}{p_0(x)} = \frac{(\bar{q} + \Delta q_0(x))^2}{\bar{p} + \Delta p_0(x)} \cong \frac{\bar{q}^2}{\bar{p}} + 2\frac{\bar{q}}{\bar{p}} \Delta q_0(x) - \frac{\bar{q}^2}{\bar{p}^2} \Delta p_0(x). \quad (4)$$

Substituting (4) into (3), yields:

$$\begin{cases} \alpha (\bar{q} + \Delta q_0(x)) = -S \Delta p_0'(x) + \frac{\lambda c^2}{2dS} \left(\frac{\bar{q}^2}{\bar{p}} + 2\frac{\bar{q}}{\bar{p}} \Delta q_0(x) - \frac{\bar{q}^2}{\bar{p}^2} \Delta p_0(x) \right) \\ \alpha (\bar{p} + \Delta p_0(x)) = -\frac{c^2}{S} \Delta q_0'(x) \end{cases} \quad (5)$$

Hence:

$$\begin{cases} \Delta p_0'(x) = \left(\frac{\lambda c^2}{dS^2} \frac{\bar{q}}{\bar{p}} - \frac{\alpha}{S} \right) \Delta q_0(x) - \frac{\lambda c^2}{2dS^2} \frac{\bar{q}^2}{\bar{p}^2} \Delta p_0(x) + \frac{\lambda c^2}{2dS^2} \frac{\bar{q}^2}{\bar{p}} - \frac{\alpha}{S} \bar{q} \\ \Delta q_0'(x) = -\frac{\alpha S}{c^2} \Delta p_0(x) - \frac{\alpha S}{c^2} \bar{p} \end{cases} \quad (6)$$

From this system of differential equations we can eliminate either $\Delta p_0(x)$ or $\Delta q_0(x)$ and then obtain a second order ODE in either one of these variables. Let us start with the mass flow. Hence, differentiating the second equation of (6), i.e., $\Delta p_0'(x) = -\frac{c^2}{\alpha S} \Delta q_0''(x)$, and substituting it together with the second equation of (6) into the first equation of (6), one obtains a second order inhomogeneous ODE, in terms of $\Delta q_0(x)$:

$$\Delta q_0''(x) + \frac{\lambda c^2}{2dS^2} \frac{\bar{q}^2}{\bar{p}^2} \Delta q_0'(x) + \left(\frac{\lambda \alpha}{dS} \frac{\bar{q}}{\bar{p}} - \frac{\alpha^2}{c^2} \right) \Delta q_0(x) = - \left(\frac{\lambda \alpha}{dS} \frac{\bar{q}}{\bar{p}} - \frac{\alpha^2}{c^2} \right) \bar{q} \quad (7)$$

In order to obtain an ODE in terms of $\Delta p_0(x)$, we take the first equation of (6):

$$\left(\frac{\lambda c^2 \bar{q}}{dS^2 \bar{p}} - \frac{\alpha}{S} \right) \Delta q_0(x) = \Delta p'_0(x) + \frac{\lambda c^2 \bar{q}^2}{2dS^2 \bar{p}} \Delta p_0(x) - \frac{\lambda c^2 \bar{q}^2}{2dS^2 \bar{p}} + \frac{\alpha}{S} \bar{q} \quad (8)$$

which differentiating yields:

$$\left(\frac{\lambda c^2 \bar{q}}{dS^2 \bar{p}} - \frac{\alpha}{S} \right) \Delta q'_0(x) = \Delta p''_0(x) + \frac{\lambda c^2 \bar{q}^2}{2dS \bar{p}} \Delta p'_0(x) . \quad (9)$$

Inserting the second equation of (6) into (9) and after a few simple calculations, we have an inhomogeneous ODE in terms of $\Delta p_0(x)$:

$$\Delta p''_0(x) + \frac{\lambda c^2 \bar{q}^2}{2dS^2 \bar{p}^2} \Delta p'_0(x) + \left(\frac{\lambda \alpha \bar{q}}{dS \bar{p}} - \frac{\alpha^2}{c^2} \right) \Delta p_0(x) = - \left(\frac{\lambda \alpha \bar{q}}{dS \bar{p}} - \frac{\alpha^2}{c^2} \right) \bar{p} . \quad (10)$$

In both cases, we obtain an ODE of the form:

$$z''(x) + \frac{\lambda c^2 \bar{q}^2}{2dS^2 \bar{p}^2} z'(x) + \left(\frac{\lambda \alpha \bar{q}}{dS \bar{p}} - \frac{\alpha^2}{c^2} \right) z(x) = - \left(\frac{\lambda \alpha \bar{q}}{dS \bar{p}} - \frac{\alpha^2}{c^2} \right) \bar{z} . \quad (11)$$

Assume $z_1(x, \alpha), z_2(x, \alpha)$ as a fundamental system of solutions of the homogeneous equation in (11). Since $-\bar{z}$ is a solution of the inhomogeneous equation (11), thus we can write the general solution of that equation:

$$z(x) = D_{1,\alpha} z_1(x, \alpha) + D_{2,\alpha} z_2(x, \alpha) - \bar{z}, \quad (12)$$

where $D_{1,\alpha}, D_{2,\alpha} \in \mathbb{R}$ and can be determined by given initial or boundary data which comes from measurements or estimations. Considering a pipeline of length ℓ , then $x \in [0, \ell]$, the ODE for the pressure (10) and using (12) we have:

$$p_0(x) = \bar{p} + \Delta p_0(x) = D_{1,\alpha} z_1(x, \alpha) + D_{2,\alpha} z_2(x, \alpha). \quad (13)$$

Considering x as the pipe-ends, one can easily determine coefficients $D_{1,\alpha}, D_{2,\alpha}$ using the mean value of pressure and mass flow at these points. Once obtained $p_0(x)$ in (13) and differentiating it, we substitute it in the first equation of (6) and mass flow can then be determined:

$$q_0(x) = \left(\frac{\lambda c^2 \bar{q}}{dS^2 \bar{p}} - \frac{\alpha}{S} \right)^{-1} \left(p'_0(x) + \frac{\lambda c^2 \bar{q}^2}{2dS^2 \bar{p}^2} p_0(x) \right). \quad (14)$$

3 Leakage Detection in a Single Pipe

To model the leakage, we consider a pipeline with a leak at distance ξ from the inlet where the mass flow has a jump $q_{leak}(\xi) = \delta q_0^-(\xi) = q_0^-(\xi) - q_0^+(\xi)$, $\delta \in (0, 1)$ and $\delta q_0^-(\xi)$ is the percentage of leakage flow (Fig. 1).

Thence, we have to consider two pipeleg sections, the left section denoted with the superscript “L” and the right one denoted with the superscript “R”. Considering Eq. (13) for the left and right pipes, respectively, we obtain:

$$p_0^L(x) = D_{1,\alpha}^L z_1(x, \alpha) + D_{2,\alpha}^L z_2(x, \alpha) \tag{15}$$

$$p_0^R(x) = D_{1,\alpha}^R z_1(x, \alpha) + D_{2,\alpha}^R z_2(x, \alpha). \tag{16}$$

Also, considering Eq. (14) for both pipes, after substituting (15)–(16):

$$q_0^L(x) = \left(\frac{\lambda c^2 \bar{q}}{dS^2 \bar{p}} - \frac{\alpha}{S} \right)^{-1} \left(D_{1,\alpha}^L z_1'(x, \alpha) + D_{2,\alpha}^L z_2'(x, \alpha) + \frac{\lambda c^2 \bar{q}^2}{2dS^2 \bar{p}^2} \left(D_{1,\alpha}^L z_1(x, \alpha) + D_{2,\alpha}^L z_2(x, \alpha) \right) \right) \tag{17}$$

$$q_0^R(x) = \left(\frac{\lambda c^2 \bar{q}}{dS^2 \bar{p}} - \frac{\alpha}{S} \right)^{-1} \left(D_{1,\alpha}^R z_1'(x, \alpha) + D_{2,\alpha}^R z_2'(x, \alpha) + \frac{\lambda c^2 \bar{q}^2}{2dS^2 \bar{p}^2} \left(D_{1,\alpha}^R z_1(x, \alpha) + D_{2,\alpha}^R z_2(x, \alpha) \right) \right). \tag{18}$$

In order to determine the parameters, $D_{1,\alpha}^L, D_{2,\alpha}^L, D_{1,\alpha}^R, D_{2,\alpha}^R$, one needs some boundary conditions, which can be obtained from the measurements. Assume that the values of pressure and mass flow at both ends of the pipeline are given:

$$p_0^L(0) = p_0(0), q_0^L(0) = q_0(0), p_0^R(\ell) = p_0(\ell), q_0^R(\ell) = q_0(\ell). \tag{19}$$

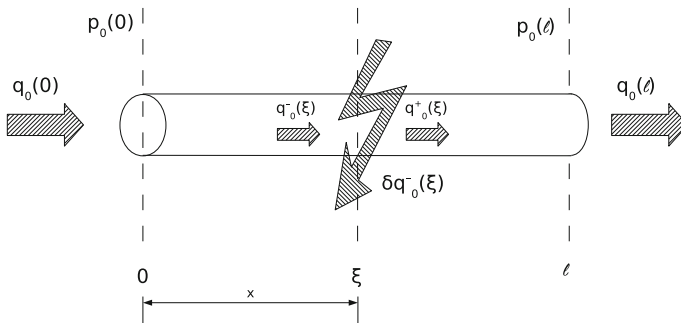


Fig. 1 Pipe leg model with a leak at $\xi \in (0, \ell)$

We can write Eqs. (15)–(18) in matrix form:

$$ZD = B, \tag{20}$$

with $D = (D_{1,\alpha}^L, D_{2,\alpha}^L, D_{1,\alpha}^R, D_{2,\alpha}^R)^T$, $B = (p_0(0), p_0(\ell), K_2q_0(0), K_2q_0(\ell))^T$ and Z as

$$\begin{pmatrix} z_1(0, \alpha) & z_2(0, \alpha) & 0 & 0 \\ 0 & 0 & z_1(\ell, \alpha) & z_2(\ell, \alpha) \\ z_1'(0, \alpha) + K_1z_1(0, \alpha) & z_2'(0, \alpha) + K_1z_2(0, \alpha) & 0 & 0 \\ 0 & 0 & z_1'(\ell, \alpha) + K_1z_1(\ell, \alpha) & z_2'(\ell, \alpha) + K_1z_2(\ell, \alpha) \end{pmatrix}$$

with $K_1 = \frac{\lambda c^2 \bar{q}^2}{2dS \bar{p}^2}$ and $K_2 = \frac{\lambda c^2 \bar{q}}{dS \bar{p}} - \frac{\alpha}{S}$. Whenever $\det Z \neq 0$ we have a unique solution. Then, using Eqs. (15)–(16), we obtain the nonlinear equation to locate the leakage:

$$D_{1,\alpha}^L z_1(\xi, \alpha) + D_{2,\alpha}^L z_2(\xi, \alpha) = D_{1,\alpha}^R z_1(\xi, \alpha) + D_{2,\alpha}^R z_2(\xi, \alpha) . \tag{21}$$

To obtain $\xi(\alpha)$, this equation can be solved either graphically, as we will show in Sect. 5, or by applying a numerical method in order to obtain more precise results. Then, we may estimate the leakage size:

$$\begin{aligned} q_{\text{leak}}(\xi) &= q_0^-(\xi) - q_0^+(\xi) = \lim_{x \rightarrow \xi^-} q_0^L(x) - \lim_{x \rightarrow \xi^+} q_0^R(x) \\ &= \left(\frac{\lambda c^2 \bar{q}}{dS^2 \bar{p}} - \frac{\alpha}{S} \right)^{-1} \left[\lim_{x \rightarrow \xi} \left(\frac{dp_0^L(x)}{dx} + \frac{\lambda c^2 \bar{q}^2}{2dS^2 \bar{p}^2} p_0^L(x) \right) \right. \\ &\quad \left. - \lim_{x \rightarrow \xi} \left(\frac{dp_0^R(x)}{dx} + \frac{\lambda c^2 \bar{q}^2}{2dS^2 \bar{p}^2} p_0^R(x) \right) \right] \Big|_{x=\xi} \\ &= \left(\frac{\lambda c^2 \bar{q}}{dS^2 \bar{p}} - \frac{\alpha}{S} \right)^{-1} \left(\frac{dp_0^L(x)}{dx} - \frac{dp_0^R(x)}{dx} \right) \Big|_{x=\xi} . \end{aligned} \tag{22}$$

This method locates the leakage by intersecting pressure profiles obtained using boundary data at the pipe inlet/outlet, whether other methods use the pressure gradients and also the propagation of the negative pressure wave [6, 11].

4 Leakage Detection in the Grid

In this section we develop relations to obtain a leakage detection tool in a gas net with a predefined topology [5, 10]. To do this, let $\Gamma(V, E, \varphi)$ be a directed, finite and connected graph, describing the topology of the network. V is the set of nodes, E is the set of edges and φ , the nodal pressure, is defined as:

$$\begin{aligned} \varphi : E &\longrightarrow V \times V \\ e &\rightsquigarrow \varphi(e) = (\varphi_1(e), \varphi_2(e)) \ . \end{aligned}$$

Moreover, let \mathcal{R} be the ring of real valued functions defined over the set of real numbers be defined on $\mathbb{R}_{\geq 0}$. Whence we can define the mass flow along the edges by $q : E \longrightarrow \mathcal{R}$:

$$e_i \mapsto q(e_i) = \begin{cases} q_i(x) , & x \in [0, |e_i|] \\ 0 , & x > |e_i| , 1 = 1, \dots, m = |E| \end{cases} \ ,$$

where $|E|$ is the cardinality of E . In the same way, we define pressure along the edges by $p : E \longrightarrow \mathcal{R}$:

$$e_i \mapsto p(e_i) = \begin{cases} p_i(x) , & x \in [0, |e_i|] \\ 0 , & x > |e_i| , 1 = 1, \dots, m = |E| \end{cases} \ .$$

For mass flow q , it makes sense to define the *boundary operator* $\partial : V \longrightarrow \mathbb{R}$

$$v \mapsto (\partial q)(v) := \sum_{e_i \in E, s.th. \varphi_1(e_i)=v} q_i(0) - \sum_{e_i \in E, s.th. \varphi_2(e_i)=v} q_i(|e_i|) ,$$

which calculates outflow minus inflow at node v . Hence, in a closed system is valid Kirchhoff First Law (KFL):

$$(\partial q)(v) = 0 \text{ for all } v \in V. \tag{23}$$

Moreover, we can define mappings Q^+, Q^- and ∇Q by $Q^+(e_i) = q_i(0)$, $Q^-(e_i) = q_i(|e_i|)$ and then $\nabla Q : E \longrightarrow \mathbb{R}$ with $\nabla Q = Q^+ - Q^-$. Hence, we may write the matrix form of the KFL as:

$$A \nabla Q = 0, \tag{24}$$

where $A \in \mathbb{R}^{n \times m}$ is the nodal-edge incidence matrix of Γ defined by:

$$A = (a_{ij}) , \quad a_{ij} = \begin{cases} 1 , & \varphi_1(e_j) = v_i \\ -1 , & \varphi_2(e_j) = v_i \\ 0 , & \text{otherwise} \end{cases} ,$$

where n is the number of nodes and m the number of edges. Clearly, if the system is not a closed one, outflows and inflows need to be considered on the right side of equation (24) and it becomes $A \nabla Q = S$ instead.

Similarly, we define the nodal pressures and pressure drop in the edge by P^+, P^- , $\nabla P : E \longrightarrow \mathbb{R}$ by $P^+(e_i) = p_i(0)$, $P^-(e_i) = p_i(|e_i|)$ and the pressure drop in the pipe

edges is $\nabla P = P^+ - P^-$, respectively. With this notation, we can formulate the Kirchhoff Second Law (KSL) for a closed system in the matrix form:

$$B^T \nabla P = 0, \tag{25}$$

where matrix $B \in \mathbb{Z}^{m \times (m-n+1)}$ is the edge-loop incidence matrix and is defined by the fundamental loops of Γ as follows:

$$B = (b_{ij}), \quad b_{ij} = \begin{cases} 1, & \text{if the } j \text{ th fundamental loop contains } e_i \\ -1, & \text{if the } j \text{ th fundamental loop contains } -e_i, \\ 0, & \text{otherwise} \end{cases}$$

with $(m - n + 1)$ as the number of fundamental loops assuming a single reference node. Since $\text{Im}(B) = \text{Ker}(A)$ we infer that $AB = 0$. Moreover, if there exists a function $\Phi : V \rightarrow \mathbb{R}$, Eq. (25) is equivalent to $\nabla P = A^T \Phi$. This ‘‘nodal pressure’’ Φ can be considered as a pressure potential and is uniquely defined up to an arbitrary constant. Defining the following bilinear forms on Γ :

$$\langle \cdot, \cdot \rangle_V : \mathbb{R}^V \times \mathbb{R}^V \rightarrow \mathbb{R}, \quad (f_1, f_2) \mapsto \sum_{v \in V} f_1(v) f_2(v) \tag{26}$$

$$\langle \cdot, \cdot \rangle_E : \mathbb{R}^E \times \mathbb{R}^E \rightarrow \mathbb{R}, \quad (g_1, g_2) \mapsto \sum_{v \in V} g_1(e) g_2(e), \tag{27}$$

thence we obtain in a closed system the following identity which is known as Tellegen Law:

$$\langle \nabla Q, \nabla P \rangle_E = \langle \nabla Q, A^T \Phi \rangle_E = \langle A \nabla Q, \Phi \rangle_V = 0. \tag{28}$$

Now, we apply Eq. (20) to every edge of Γ :

$$Z(e_i) D(e_i) = B(e_i), \quad i = 1, \dots, m, \tag{29}$$

where the sought coefficients are $D(e_i) = (D_{1,\alpha}^L(e_i), D_{2,\alpha}^L(e_i), D_{1,\alpha}^R(e_i), D_{2,\alpha}^R(e_i))^T$, and the parameters are

$$\begin{aligned} B(e_i) &= (P^+(e_i), P^-(e_i), K_2 Q^+(e_i), K_2 Q^-(e_i))^T \\ &= (p_i(0), p_i(|e_i|), K_2 q_i(0), K_2 q_i(|e_i|))^T, \end{aligned}$$

for simplicity of notation, we drop α in what follows and then write $Z(e_i)$ as

$$\begin{pmatrix} z_1(0) & z_2(0) & 0 & 0 \\ 0 & 0 & z_1(|e_i|) & z_2(|e_i|) \\ z'_1(0) + K_1 z_1(0) & z'_2(0) + K_1 z_2(0) & 0 & 0 \\ 0 & 0 & z'_1(|e_i|) + K_1 z_1(|e_i|) & z'_2(|e_i|) + K_1 z_2(|e_i|) \end{pmatrix}.$$

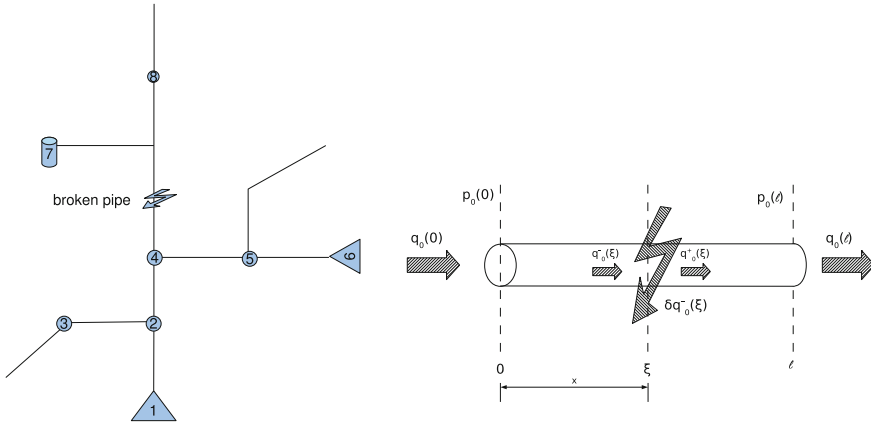


Fig. 2 Example of a gas grid

Likewise as for a single pipeline, the coefficients are uniquely determined whenever $\det Z(e_i) \neq 0, i = 1, \dots, m$. From our previous considerations, we then infer that whenever there is no leakage in pipe leg e_i then $D_1^L(e_i) = D_1^R(e_i)$ and $D_2^L(e_i) = D_2^R(e_i)$. Whenever one of these conditions is violated for an index i_0 then we infer that in a pipe leg e_{i_0} a leakage must occur and its position and size can then be calculated from Eqs. (21) and (22), respectively (Fig. 2).

5 Illustrative Example

To illustrate this method we consider a small example. To do this, consider as parameters $\bar{q} = 130 \text{ Kg/s}, \bar{p} = 6.0000 \times 10^5 \text{ kPa}, c = 300 \text{ m/s}, \lambda = 0.0030, d = 2 \text{ m}$ and $\ell = 10000 \text{ m}$. Considering these values in (11), the respective characteristic equation is:

$$\omega^2 + 3.2106 \times 10^{-7} \omega + 1.0345 \times 10^{-7} \alpha - 1.1111 \times 10^{-5} \alpha^2 = 0. \tag{30}$$

Taking α^- as 2.4911×10^{-7} and α^+ as 0.0093 , we can infer that for $\alpha \in]\alpha^-, \alpha^+[$, (30) has complex roots say $\omega = a \pm ib$, then the fundamental system of (11) is given by:

$$\tilde{z}_1(x, \alpha) = e^{ax} \cos(bx) \text{ and } \tilde{z}_2(x, \alpha) = e^{ax} \sin(bx). \tag{31}$$

For the case where $\alpha \in \mathbb{R} \setminus [\alpha^-, \alpha^+]$, (30) has two distinct real roots, ω_1, ω_2 . In this case, the fundamental system of (11) can be defined for every value of α as

$$\tilde{z}_1(x, \alpha) = e^{\omega_1 x} \text{ and } \tilde{z}_2(x, \alpha) = e^{\omega_2 x}. \tag{32}$$

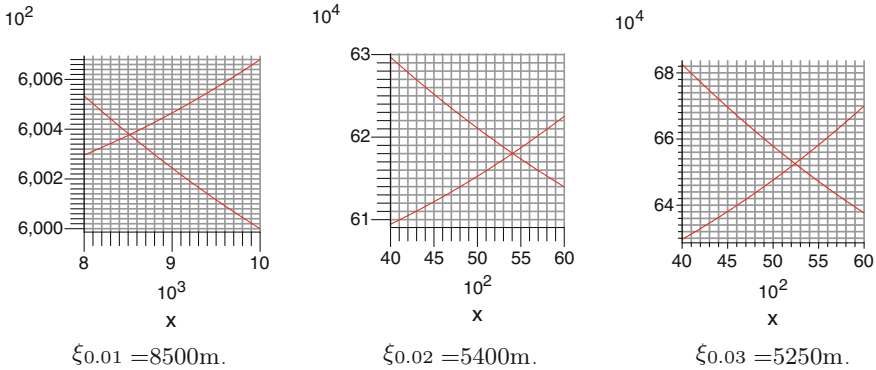


Fig. 3 Leakage location, ξ_α , considering different values of α

Taking, for example, different values of α we obtain:

$\alpha = 0.01$, the roots are $\omega_1 = -0.8914 \times 10^{-5}$ and $\omega_2 = 0.8593 \times 10^{-5}$.

$\alpha = 0.02$, the roots are $\omega_1 = -0.4890 \times 10^{-4}$ and $\omega_2 = 0.4858 \times 10^{-5}$.

$\alpha = 0.03$, the roots are $\omega_1 = -0.8321 \times 10^{-4}$ and $\omega_2 = 0.8288 \times 10^{-5}$.

The normalised fundamental system, as previously used, can be obtained from (32) by an appropriate linear combination. We also assume the knowledge of the measured data at the boundaries, i.e.

$$\begin{aligned}
 p(0) &= 6.0060 \times 10^5, \text{ and } q(0) = 133 \\
 p(\ell) &= 6.0000 \times 10^5, \text{ and } q(\ell) = 128.
 \end{aligned}$$

Then calculating the left and right solutions, we obtain the graphics of Fig. 3 for pressure (given in kPa) for different space dependencies represented by α .

6 Conclusions and Further Work

The gas dynamics in the pipeline is represented by a first order hyperbolic PDE. Using the separation of time and space variables, we obtain a simpler representation of the solution that will be used as a model for leakage location and leakage size estimation in a pipeline. Furthermore, using the graph theory framework the method is generalised to a gas grid. The main idea presented in the paper is illustrated in a simple academic example. In the future, we would like to obtain a representation of the solution of the nonlinear hyperbolic PDE in order to compare faulty models with the full ones. Furthermore, we expect to apply the method to a real pipeline and then to a simple gas grid.

Acknowledgments The first author is financed by FCT (Project ref. UID/EEA/00048/2013). The second author is financed by Portuguese Funds through FCT, within the Project UID/MAT/00013/2013.

References

1. Bagajewicz, M., Valtinson, G.: Leak detection in gas pipelines using accurate hydraulic models. *Ind. Eng. Chem. Res.* **53**(44), 16964–16972 (2014)
2. Baltazar, S.T., Azevedo Perdicóulis, T.-P., Lopes dos Santos, P.: Quadripole models for simulation and leak detection on gas pipelines. Presented at the 47th PSIG Annual Meeting, Vancouver, Canada, 11–13 de Maio 2016
3. Baptista, H., Wagner, G., Bernhard, W.: Hydraulic model based gas leak detection and location. Presented at the 7th Global Congress on Information and Communication Technology in Energy, Busan, Korea (2005)
4. Bilman, L., Isermann, R.: Leak detection methods for pipelines. *Automatica* **23**(3), 381–385 (1987)
5. Dymkou, S., Jank, G., Azevedo Perdicóulis, T.-P.: Graph and 2-D systems approach in gas transport network modelling. *Int. J. Tomogr. Stat. Special Issue Control Appl. Optim. Appl. Optim. Control Rob. Control Stabil. Appl. Ind.* **6**, 21–27 (2007)
6. Geiger, G.: State-of-the-art in leak detection and localisation. In: Pipeline Technology 2006 Conference, Hannover, Germany, 25 Apr 2006
7. Lopes dos Santos, P., Azevedo Perdicóulis, T.-P., Ramos, J.A., Jank, G., Martins de Carvalho, J.L.: Leakage detection and location in gas pipelines through an LPV identification approach. Baleanu, D., Tenreiro Machado, J.A. (eds.) *Commun. Nonlinear Sci. Numer. Simul.* **16**(12), 4657–4665 (2011)
8. Niepłocha, J.: Discrete-time quadratic optimal control of gas network systems. *Found. Control Eng.* **13**(4), 175–186 (1988)
9. Osiadacz, A.J.: *Simulation and Analysis of Gas Networks*. E. & F.N. Spon, London (1987)
10. Zerz, E.: *Topics in Multidimensional Linear Systems Theory*. Lecture Notes in Control and Information Sciences, vol. 256. Springer, London (2000)
11. Turkowski, M., Bratek, A., Słowikowski, M.: Methods and systems of leak detection in long range pipelines. *J. Autom. Mob. Rob. Intell. Syst.* **1**(3), 39–46 (2007)

Part V
Sensing and Estimation

Sensorless Nonlinear Control of Fed-Batch *Escherichia coli* Cultivation Bioprocess Using the State-Dependent Approach

Abdelhamid Iratni, Rui Araújo, Saeid Rastegar
and Mohammed Mostefai

Abstract The cultivation of *Escherichia coli* bacteria is widely used by geneticists and biopharmaceuticals to produce medicines and vaccines. In such industries, Bioprocesses are known by their harsh environment and very expensive physical sensors. This paper deals with nonlinear estimation and control of fed-batch *Escherichia coli* bioprocess. Enhancing the process performance and maximizing its efficiency by optimizing the control of *Escherichia coli* cultures depends on the availability of appropriate online sensors for the main culture components. In this study, an innovative method for nonlinear estimation and control of bioprocesses is designed and assessed. The new algorithm for control and estimation of *Escherichia coli* bioprocess states, based on the State-Dependent Riccati Equation technique, is validated by numerical simulation. The results obtained clearly demonstrate the effectiveness of the proposed technique for Biosystems in measuring, monitoring, and control of their natural nonlinear dynamics.

Keywords Nonlinear estimation · Nonlinear control · *E. coli* bioprocess · State-Dependent Riccati Equation · Extended Kalman filter

A. Iratni (✉)

Faculty of Science and Technology, Electrical Engineering Department,
University of Bordj Bou Arreridj, El Anasser, Algeria
e-mail: iratni@gmail.com

A. Iratni · R. Araújo · S. Rastegar

Department of Electrical and Computer Engineering, Institute for Systems
and Robotics, University of Coimbra, Coimbra, Portugal
e-mail: rui@isr.uc.pt

M. Mostefai

Automatic Control Laboratory of Setif, Electrical Engineering Department,
Faculty of Technology, University of Setif1, Sétif, Algeria
e-mail: mostefai@univ-setif.dz

1 Introduction

Nowadays many proteins are produced by genetically altered microorganisms. Since the biochemical and genetic properties of the *Escherichia coli* bacteria are known better, they are the most generic host microorganisms used for the production of recombinant proteins. The *E. coli* bacteria represents the universal cell factory for the fermentative production of biopharmaceuticals. Several valuable products are today commercially produced using fermentation techniques and there is an enormous economic incentive to optimize such processes [1].

Control of bioprocesses is a delicate task due to the process complexity, non-linearity, and non-stationary behavior, as well as the scarcity of online measurements of the primary process variables such as component concentrations. Some of these measurements are essential to guarantee the successful operation and automatic control at their optimal state. In fact, in many practical applications, only some of the state variables involved are available for online measurement.

The development and design of software sensors have led to numerous practical applications, several works related to state observers for bioprocesses can be found in the literature [2–4]. However, only a few examples refer to their implementation in complex bioprocesses, described by nonlinear dynamic models containing several balance equations and with complex kinetics.

Several works related to the control of the *E. coli* bioprocess exist. Indeed, in the interest ensuring aerobic conditions in the bioprocess for the bacterial life, a regulation of the oxygen concentration, for example using a correction by gain scheduling by adjusting the feed rate substrate is proposed in [5] and using an adaptive predictive control by acting on the stirring rate was proposed in [6]. This control strategy has also been used to achieve the same objective in [7] but this time by simultaneously controlling the partial pressure of oxygen and carbon dioxide and acting respectively on the stirring rate and the airflow rate. A controller resulting from the Generic Model Control methodology was developed in [8], in order to regulate the specific growth rate in biomass by acting on the substrate feed rate. To attain the same goal, the control strategy developed in [9] is applied by Rocha [10]. It is a linearizing adaptive control, regulate the concentration of acetate by considering the dilution rate as a control variable.

Since the 1990s, State-Dependent Riccati Equation (SDRE) strategies have emerged as general design methods that provide a systematic and effective means of designing nonlinear controllers and filters. These methods overcome many of the difficulties and shortcomings of other methodologies and deliver computationally simple algorithms that have been highly effective in a variety of practical and meaningful applications in very diverse fields of study [11].

This paper introduces for the first time an application of the SDRE approach for nonlinear estimation and control of a recombinant *E. coli* process. A software sensor can be used for states estimation/measurement to overcome the high costs of physical sensors and their positioning difficulties. Most methods proposed in the literature for *E. coli* control, use linearization approaches around the operating point. The control architecture proposed in this paper integrates a state estimator and a feedback con-

trol law, both based on the SDRE approach, for the nonlinear control of the acetate concentration and substrate. The control architecture does not use sensors to measure the controlled variables (sensorless control), they are estimated. The original system model is written in a particular configuration, called the State-Dependent coefficient form (SDCF), without affecting the nonlinear nature of the plant model. This approach has proven its excellence in several nonlinear applications. Such superiority will be proven in this work, where its performance will be demonstrated in the adequate control of the *E. coli* processes, enabling the maximization of the production of biomass.

The paper is organized as follows. In Sect. 2, the basic structure of the *E. coli* model is presented. Section 3 presents the estimators and introduces the SDRE methodology versus EKF. A review of the SDRE nonlinear control, in addition, to its implementation for the *E. coli* process, are presented in Sect. 4. Section 5 concludes the paper.

2 *E. coli* Bioprocess Modeling

The growth of the *E. coli* bacteria follows the bottleneck theory. Indeed, *E. coli* has a limited respiratory capacity. Acetate is produced when glucose exceeds the respiratory capacity, which corresponds to the oxido-fermentative regime. Acetate is consumed when glucose is less than the respiratory capacity; which is the oxidative regime. When the quantity of glucose exactly fills the respiratory capacity, the system operates in optimal conditions. This case corresponds to the edge between the two regimes when acetate is not produced nor consumed. It will be seen in further developments that the aim of the control is to force the *E. coli* culture to remain at the edge between these regimes [10, 12].

Based on the previous scheme, mass balances yield the dynamic model [9]:

$$\frac{d}{dt} \begin{bmatrix} X \\ S \\ A \\ O \\ C \end{bmatrix} = \underbrace{\begin{bmatrix} 1 & 1 & 1 \\ -k_1 & -k_2 & 0 \\ 0 & k_3 & -k_4 \\ 0 & -k_6 & -k_7 \\ k_8 & k_9 & k_{10} \end{bmatrix}}_K \underbrace{\begin{bmatrix} r_1 \\ r_2 \\ r_3 \end{bmatrix}}_\varphi - \frac{F_{in}}{W} \underbrace{\begin{bmatrix} X \\ S \\ A \\ O \\ C \end{bmatrix}}_\xi + \underbrace{\begin{bmatrix} 0 \\ S_{in}D \\ 0 \\ O_{tr} \\ 0 \end{bmatrix}}_F - \underbrace{\begin{bmatrix} 0 \\ 0 \\ 0 \\ 0 \\ C_{tr} \end{bmatrix}}_Q, \quad (1)$$

$$\frac{dW}{dt} = \frac{F_{in}}{W} W,$$

where S , O , X , C and A represent glucose (substrate), oxygen, biomass, carbon dioxide and acetate respectively. k_i are the stoichiometric coefficients. r_j are the growth rates. W is the culture medium weight [Kg], F_{in} is the influent flow rate [kg/h], S_{in} is the influent glucose concentration [g/kg], O_{tr} is the oxygen transfer rate from gas to liquid phase, C_{tr} the carbon dioxide transfer rate from liquid to gas phase. Considering the bottleneck assumption, the kinetic terms associated with the glucose con-

Table 1 Expressions of r_x and r_A

Growth rates	Oxido-fermentative regime	Oxidative regime	
		Sub-regime 1	Sub-regime 2
r_X	$\frac{q_S - q_{S,crit}}{k_2} + \frac{q_{S,crit}}{k_1}$	$\frac{q_S + q_{AC}}{k_1 + k_4}$	$\frac{q_S}{k_1} + \frac{k_{OS}}{k_4} \frac{q_{S,crit} - q_S}{k_{OA}}$
r_A	$k_3 \frac{q_S - q_{S,crit}}{k_2}$	$-q_{AC}$	$k_{OS} \frac{q_S - q_{S,crit}}{k_{OA}}$

sumption q_S , the critical glucose specific uptake rate $q_{S,crit}$ and the specific acetate uptake rate q_{AC} are expressed by:

$$q_S = q_{Smax} \frac{S}{K_S + S}, \quad (2)$$

$$q_{S,crit} = \frac{q_{Omax}}{k_{OS}} \frac{K_{i,O}}{K_{i,O} + A}, \quad (3)$$

$$q_{AC} = q_{ACmax} \frac{A}{K_A + A} \frac{K_{i,A}}{K_{i,A} + A}, \quad (4)$$

where q_{Smax} , q_{Omax} and q_{ACmax} are the maximum specific growth rates, K_S and K_A are the saturation constants of substrate (glucose) and acetate respectively, k_{OS} is the oxygen yield related to glucose, and $K_{i,O}$ and $K_{i,A}$ are the inhibition constants related to oxygen uptake and acetate uptake, respectively.

Finally, since oxygen is always regulated to induce no influence on the growth of bacteria, the dynamic model (1) can be formulated in a compact form:

$$\begin{aligned} \frac{dX}{dt} &= r_X X - \frac{F_{in}}{W} X, & \frac{dS}{dt} &= -q_S X - \frac{F_{in}}{W} (S - S_{in}), \\ \frac{dA}{dt} &= r_A X - \frac{F_{in}}{W} A, & \frac{dW}{dt} &= F_{in}, \end{aligned} \quad (5)$$

denoted in further developments as $\dot{x}(t) = f(x(t), F_{in}(t))$, with $x = [x_1, x_2, x_3, x_4]^T = [X, S, A, W]^T$. r_x and r_A in (5) depend on the operating regime and are given in Table 1. Further details on the model formulation can be found in [10, 12]. The final model (5) will serve to the theoretical development in Sects. 3 and 4 for the design of the estimator and control law.

3 Estimator Design

In this section, the design of a State-Dependent Riccati Estimator (SDRE) for the estimation of biomass, glucose and acetate concentrations in the fed-batch fermentation of *E. coli* is discussed. The proposed estimator is also compared with a classical observer (Extended Kalman Estimator (EKE)).

3.1 Extended Kalman Estimator

The Extended Kalman Estimator uses local linearization to extend the scope of the Kalman estimator to systems described by nonlinear differential equations [13]. The evolution of the system in time is expressed by:

$$\begin{aligned}\dot{x}(t) &= f(x(t), u(t), t) + G(t)w(t), \\ y(t) &= h(x(t), t) + v(t),\end{aligned}\tag{6}$$

where $x(t) \in \mathbb{R}^n$, $u(t) \in \mathbb{R}^m$, and $y(t) \in \mathbb{R}^r$ are state, input and measurement vectors, respectively. f and h are assumed to be continuously differentiable. $w(t)$ and $v(t)$ are the uncorrelated n -dimensional and r -dimensional zero-mean white noise vectors, with $Q(t)$ and $R(t)$ covariances, respectively. The EKE algorithm proceeds as follows [13, 14]:

$$\hat{x}(t_0) = \hat{x}_0, P_0 = E \{ \tilde{x}(t_0) \tilde{x}^T(t_0) \} \quad (\text{initialization}),\tag{7}$$

$$K(t) = P(t)H^T(\hat{x}, t)R^{-1}(t) \quad (\text{gain}),\tag{8}$$

$$\begin{aligned}\dot{P}(t) &= F(\hat{x}, t)P(t) + P(t)F^T(\hat{x}, t) \quad (\text{covariance}), \\ &\quad - P(t)H^T(\hat{x}, t)R^{-1}(t)H^T(\hat{x}, t)P(t) + G(t)Q(t)G^T(t),\end{aligned}\tag{9}$$

$$F(\hat{x}, t) = \left. \frac{\partial f}{\partial x} \right|_{\hat{x}(t)}; \quad H(\hat{x}, t) = \left. \frac{\partial h}{\partial x} \right|_{\hat{x}(t)},\tag{10}$$

$$\dot{\hat{x}}(t) = f(\hat{x}, u, t) + K(t)[y(t) - h(\hat{x}, t)] \quad (\text{estimate}).\tag{11}$$

EKE is a sequential estimator and hence suitable for online applications, but the accuracy of the estimates depends on the accuracy of equations (10).

3.2 State-Dependent Riccati Estimator

The State-Dependent Riccati Estimator (SDRE) method has been used successfully in nonlinear estimation and control [14, 15]. While the linear models used in EKE are based on a first-order Taylor series approximation, there is no approximation involved in the nonlinear models used in SDRE.

Consider the same system dynamics given by (6), and assume that can be formulated into the state-dependent coefficient form as follows [16]:

$$\begin{aligned}\dot{x}(t) &= A(x)x(t) + B(x)u(t) + G(x)w(t), \\ y(t) &= C(x) + v(x).\end{aligned}\tag{12}$$

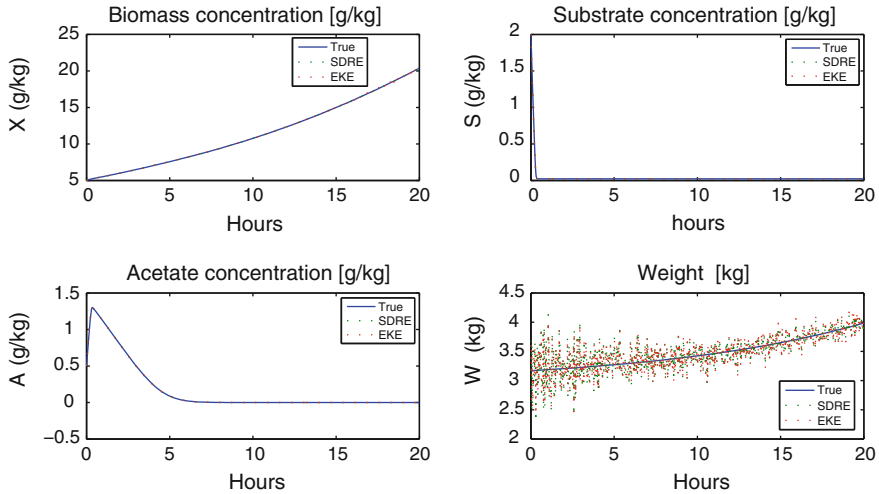


Fig. 1 Comparison of EKE and SDRE estimators in the *E. coli* nonlinear process

The SDRE is then formulated as follows:

$$\hat{x}(t_0) = \hat{x}_0, P_0 = E \{ \tilde{x}(t_0) \tilde{x}^T(t_0) \} \quad (\text{initialization}), \quad (13)$$

$$K(t) = P(t) C^T(\hat{x}) R^{-1} \quad (\text{gain}), \quad (14)$$

$$\dot{P}(t) = P(t) A^T(\hat{x}) + A(\hat{x}) P(t) - P(t) C^T(\hat{x}) R^{-1} C(\hat{x}) P(t) + G^T Q G \quad (\text{covariance}), \quad (15)$$

$$\dot{\hat{x}}(t) = A(\hat{x}) \hat{x}(t) + K(t) [y(t) - C(\hat{x}) \hat{x}(t)] \quad (\text{estimate}). \quad (16)$$

The above equations show that the structure of the SDRE is similar to EKE but the main difference is the way the model is built, for SDRE, the state-dependent linear model is exact assuming the state estimates are accurate while for EKE, the linear model suffers from linearization error.

3.3 Simulation Results

In this section, a numerical simulation will be used to demonstrate the performance of the SDRE in comparison with EKE. The measurements are assumed to be the weight ($y = W$). The initial conditions for SDRE and EKE are $[X_0 \ S_0 \ A_0 \ W_0] = [5 \ \text{g/Kg}; 0.03 \ \text{g/Kg}; 0.55 \ \text{g/Kg}; 3.17 \ \text{Kg}]$. For parameters values and process initial values please refer to [10]. The process noise is assumed to be $w \sim \mathcal{N}(0, 0.001)$ and the sensor noise is $v \sim \mathcal{N}(0, 2.5)$. Simulation results are shown in Fig. 1.

Table 2 RMSE of the different estimators

State	SDRE	EKE
X	0.004749	0.06261
S	3.7445×10^{-6}	3.7458×10^{-6}
A	3.538×10^{-7}	3.9426×10^{-7}
W	0.11924	0.13598

For comparison and performance analysis, the Root Mean Squared Errors (RMSEs) is presented in Table 2, where the estimation results are summarized. The data clearly demonstrates that the performances of the SDRE are superior to the EKE. The second performance index tested is the computation load. All computations are performed in MATLAB R2011b on a 2.53 GHz Pentium computer with 3.00 GB RAM. The processor times required by SDRE and EKE are 0.34 [s], and 0.39 [s], respectively.

The evolution of the different states shown in Fig. 1 are very close. However, we can notice the superiority of the SDRE filter. Even more for the E.Coli process where the sensors are very expensive and costly. The reliability and computational time cost to estimate the acetate attained by the proposed methodology make it useful for integration with nonlinear control of the cultivation process.

4 State-Dependent Riccati Equation Control

The State-Dependent Riccati Control (SDRC) technique refers to the use of State-Dependent Riccati Equation to construct nonlinear feedback control law for nonlinear systems. The main idea is to represent the nonlinear system [17]

$$\dot{x}(t) = f(x) + B(x)u(t), \quad x(0) = x_0, \tag{17}$$

in the form

$$\dot{x}(t) = A(x)x(t) + B(x)u(t), \tag{18}$$

and to use the feedback

$$u(x) = -\bar{R}^{-1}(x)B^T(x)P(x)x, \tag{19}$$

where $P(x)$ is obtained from the SDRE

$$\dot{P}(t) = P(t)A(\hat{x}) + A^T(\hat{x})P(t) - P(t)B(\hat{x})\bar{R}^{-1}B^T(\hat{x})P(t) + \bar{Q}, \tag{20}$$

and $\bar{Q}(\cdot)$ and $\bar{R}(\cdot)$ are design parameters which are weighting matrices for x and u in a cost functional, such that $\bar{Q}(\cdot)$ is positive-semidefinite ($\bar{Q}(x) \geq 0$) and $\bar{R}(\cdot)$ is positive-definite ($\bar{R}(x) > 0$). The closed loop dynamics have a linear-like structure given by $\dot{x} = ACL(x)x$ where $ACL(x)$ is the closed loop system matrix.

4.1 State-Dependent Coefficient Form (SDCF)

Matrices $A(x)$, $B(x)$ and $C(x)$ in (18) are not unique. Efficient selection of these matrices is known as the “parameterization problem” [18] and may affect the performance of the ensuing observer or control system. For the *E. coli* process, from Eq. (5), and for the different regimes presented in Table 1, the state-dependent matrices of the SDCF nonlinear model (18) are given as follows:

1. Operating mode: oxidative regime:

(a) Sub-regime 1:

$$A(x) = \begin{bmatrix} q_{Smax} \frac{x_2}{(k_s+x_2)k_1} & 0 & q_{acmax} \frac{x_1}{k_a+x_3} \frac{k_{io}}{k_{io}+x_3} \frac{1}{k_4} & 0 \\ -q_{Smax} \frac{x_2}{k_s+x_2} & 0 & 0 & 0 \\ 0 & 0 & q_{acmax} \frac{x_1}{k_a+x_3} \frac{k_{io}}{k_{io}+x_3} & 0 \\ 0 & 0 & 0 & 0 \end{bmatrix}.$$

(b) Sub-regime 2:

$$A(x) = \begin{bmatrix} r_x & 0 & 0 & 0 \\ -q_s & 0 & 0 & 0 \\ \frac{-k_{os}}{k_{oa}} \frac{q_{omax}}{q_{os}} \frac{k_{io}}{k_{io}+x_3} & \frac{k_{os}}{k_{oa}} q_{Smax} \frac{x_1}{k_s+x_2} & 0 & 0 \\ 0 & 0 & 0 & 0 \end{bmatrix}.$$

2. Oxido-fermentative regime:

$$A(x) = \begin{bmatrix} \frac{q_{omax}}{k_{os}} \frac{k_{io}}{k_1} \frac{1}{k_{io}+x_3} & q_{Smax} \frac{x_1}{k_s+x_2} - \frac{q_{omax}}{k_{os}k_2} \frac{k_{io}}{k_{io}+x_3} & 0 & 0 \\ -q_s & 0 & 0 & 0 \\ \frac{-k_3}{k_2} \frac{q_{omax}}{k_{os}} \frac{k_{io}}{k_{io}+x_3} & \frac{k_3}{k_2} q_{Smax} \frac{x_1}{k_s+x_2} & 0 & 0 \\ 0 & 0 & 0 & 0 \end{bmatrix}.$$

$$B(x) = \begin{bmatrix} \frac{-x_1}{x_4} & \frac{S_{in}-x_2}{x_4} & \frac{-x_3}{x_4} & 1 \end{bmatrix}^T.$$

4.2 Simulation Results

The strategy proposed for the *E. coli* process control (SDRC) is now implemented to the acetate concentration $A(t)$ regulation in the *E. coli* bioreactor. Parameters values considered for simulations are reported in [10]. The chosen set point is $A_{set} = 0.5$ [g/Kg]. The initial condition is $[X_0 \ S_0 \ A_0 \ W_0] = [5$ [g/Kg]; 0.03 [g/Kg];

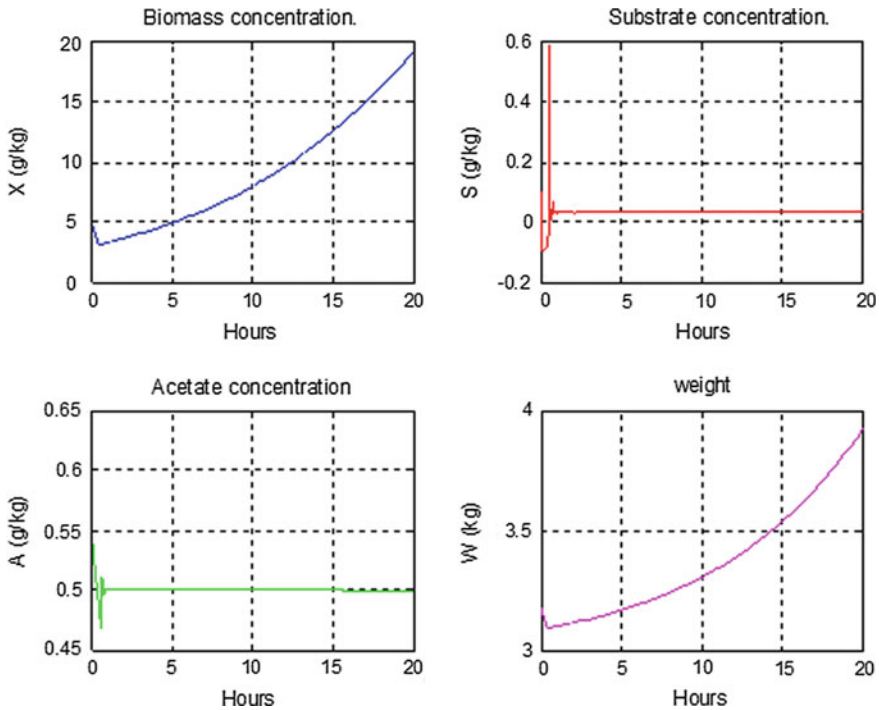


Fig. 2 Evolutions of the state variables of the model (5) using the SDRE control

0.55 [g/Kg]; 3.17 [Kg]]. The weighting matrices $\bar{Q}(x)$ and $\bar{R}(x)$ are state-dependent. For simplicity, we use constant matrices for $\bar{Q}(x)$ and $\bar{R}(x)$ in the simulations. The weighting matrices are selected as $\bar{Q}(x) = \text{diag}(0.1, 0.1, 0.1, 0.1)$ and $\bar{R}(x) = 0.06$.

Figure 2 shows the evolution of the state and control variables over 20 [h]. Figure 3 shows that the concentrations of acetate and substrate respectively attain the desired values $A = 0.5$ [g/Kg] and $S = 0.0319$ [g/Kg] after 42 [min]. The acetate regulation works well, which was the objective of the control strategy.

The presented results confirm the performance and effectiveness of the SDRE control strategy applied to the *E. coli* bioprocess. In this case, good controller performance allows the cultivation process to be carried out for almost 20 [h]. Based on the control system with SDRE, the biomass concentration at the end of the process is 19 [g/Kg]. Thus, after a short time, the SDRE controller sets the process output variables and maintains them at the desired set points ($A = 0.5$ [g/Kg] and $S = 0.0319$ [g/Kg]) to the end of the fed-batch cultivation process. Finally, it is important to note that the results were obtained without any simplifying assumptions on the nonlinear dynamic aspect of the process. Despite the complexity of operating the cultivation of the bacteria, the choice of a SDCF factorization for different operating regimes has greatly facilitated the design of regulator using the information

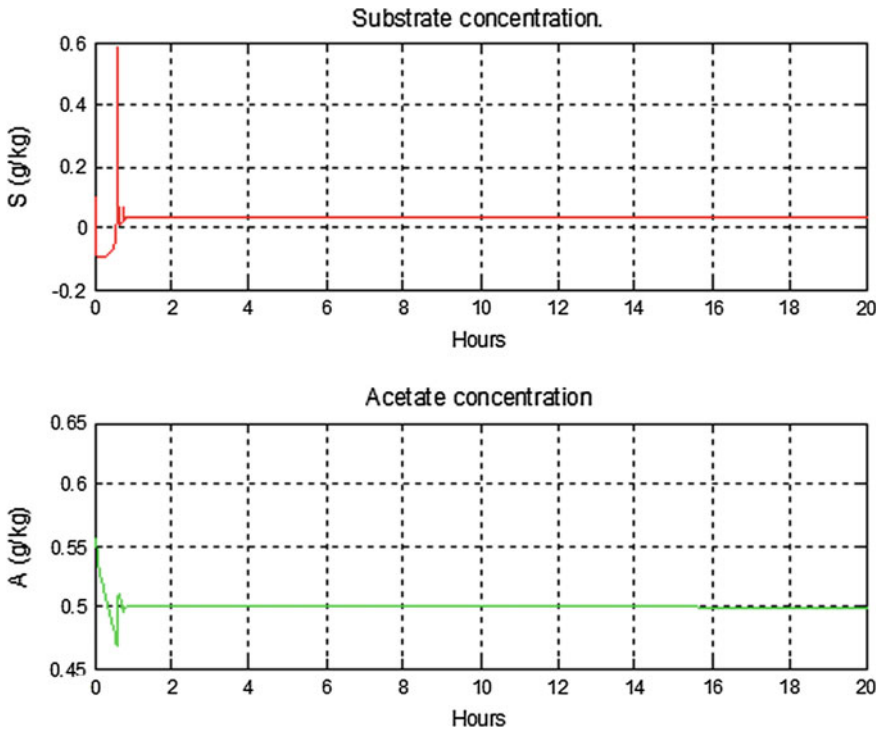


Fig. 3 Substrate and acetate concentration evolution with SDRE control

delivered by the designed SDRE estimator. The proposed control technique ensures favorable conditions for the growing of the bacteria while producing the maximum amount of biomass without changing the nonlinear nature of the model used in the controller.

5 Conclusion

This paper presented a new control structure to improve the performance of the fed-batch culture of the *E. coli* nonlinear bioprocess. It was shown that the presented SDRE State-Dependent estimator can be successfully used to estimate the states of the process and that this estimator has a much better performance when compared to the Kalman filter. The main control objective is to maximize the growth of the bacteria. It has been shown that the presented nonlinear control structure composed of the SDRE estimator in combination with the presented optimal SDRE nonlinear control technique can be used to achieve this objective. Simulation results have shown the performance and effectiveness of the approach proposed for estimation and control

of the *E. coli* bioprocess. Future research is dedicated to the experimental assessment of the robustness of the estimation and control scheme. The main perspective is to bring all these algorithms to the real life.

Acknowledgments A. Iratni was supported by the European Commission in the framework of the Erasmus Mundus - *Al Idrisi* II programme. S. Rastegar was supported by Fundação para a Ciência e a Tecnologia (FCT) under grant SFRH/BD/89186/2012. The authors acknowledge the support of FCT project UID/EEA/00048/2013.

References

1. Hafidi, G., Tebbani, S., Dumur, D., Wouwer, A.V.: Nonlinear model predictive control applied to *E. coli* cultures. In: Proceedings of 17th World Congress the International Federation of Automatic Control. IFAC-WC 2008, pp. 14570–14575, 6–11 Jul 2008
2. Ko, C.L., Wang, F.S.: On-line estimation of biomass and intracellular protein for recombinant *Escherichia coli* cultivated in batch and fed-batch modes. *J. Chin. Inst. Chem. Eng.* **38**(3–4), May–July 2007
3. Veloso, A.C.A., Rocha, I., Ferreira, E.C.: Monitoring of fed-batch *E. coli* fermentations with software sensors. *Bioprocess Biosyst. Eng.* **32**(3), 381–388 (2009)
4. Dewasme, L., Goffaux, G., Hantson, A.L., Wouwer, A.V.: Nonlinear model predictive control applied to *E. coli* cultures. In: Proceedings 18th World Congress the International Federation of Automatic Control. IFAC-WC 2011, pp. 6218–6223, 28 Aug–2 Sept 2011
5. Åkesson, M.: Probing Control of glucose feeding in *Escherichia coli* cultivations. Ph.D. thesis, Department of Automatic Control, Lund Institute of Technology, Lund, Sweden (1999)
6. Diaz, C., Dieu, P., Feuillerat, C., Lelong, P., Salome, M.: Adaptive predictive control of dissolved oxygen concentration in a laboratory-scale bioreactor. *J. Biotechnol.* **43**(1), 21–32 (1995)
7. Diaz, C., Dieu, P., Feuillerat, C., Lelong, P., Salomé, M.: Simultaneous adaptive predictive control of the partial pressures of dissolved oxygen (pO_2) and dissolved carbon dioxide (pCO_2) in a laboratory-scale bioreactor. *J. Biotechnol.* **52**(2), 135–150 (1996)
8. Jenzsch, M., Simutis, R., Luebbert, A.: Generic model control of the specific growth rate in recombinant *Escherichia coli* cultivations. *J. Biotechnol.* **122**(4), 483–493 (2006)
9. Bastin, G., Dochain, D.: *On-line Estimation and Adaptive Control of Bioreactors*. Elsevier, Amsterdam, Holland (1990)
10. Rocha, I.C.A.P.: Model-based strategies for computer-aided operation of a recombinant *E. Coli* fermentation. Ph.D. thesis, Department of Biological Engineering, School of Engineering, University of Minho, Braga, Portugal (2003)
11. Çimen, T.: Systematic and effective design of nonlinear feedback controllers via the state-dependent riccati equation (SDRE) method. *Ann. Rev. Control* **34**(1), Apr 2010
12. Hafidi, G.: Application de la Commande Prédictive Non-linéaire à la Commande de Culture de Bactéries *Escherichia Coli*. Ph.D. thesis, Faculté des Sciences d’Orsay, Supélec, Université Paris-Sud 11, Paris, France (2008). (in French)
13. Maybeck, P.S.: *Stochastic Models, Estimation, and Control*, vols. 1–3. Academic Press, New York, NY, USA (1982)
14. Iratni, A., Katebi, R., Mostefai, M.: On-line robust nonlinear state estimators for nonlinear bioprocess systems. *Commun. Nonlinear Sci. Numer. Simul.* **14**(4), 1739–1752 (2012)
15. Mracek, C.P., Clontier, J.R., D’Souza, C.A.: A new technique for nonlinear estimation. In: Proceedings 1996 IEEE International Conference on Control Applications. ICCA 96, pp. 338–343 (1996)

16. Iratni, A., Katebi, R., Vilanova, R., Mostefai, M.: On estimation of unknown state variables in wastewater systems. In: Proceedings of the 14th IEEE International Conference on Emerging Technologies and Factory Automation. ETFA 2009, pp. 1–6, 22–26 Sept 2009
17. Banks, H.T., Lewis, B.M., Tran, H.T.: Nonlinear feedback controllers and compensators: a state-dependent Riccati equation approach. *Comput. Optim. Appl.* **37**(2), 177–218 (2007)
18. Cloutier, J.R., D'Souza, C.N., Mracek, C.P.: Nonlinear regulation and nonlinear H_∞ control via the state-dependent riccati equation technique; part 1: theory; part 2: examples. In: Proceedings of International Conference on Nonlinear Problems in Aviation and Aerospace. ICNPAA 96, pp. 1–20, 9–11 May 1996

Velocity and Brightness Control in Prototype for Blood Type Determination

Ana Ferraz, Vítor Carvalho and José Machado

Abstract This paper presents algorithms and methodologies used for controlling operating parameters of a prototype developed for the determination of human blood types. Being the illumination and mixing between blood and reagents keys for a secure identification of the test results (blood types), it becomes necessary to include, in the prototype, brightness and velocity control to increase the efficiency and safety of results.

Keywords Blood type determination · Brightness control · Velocity control

1 Introduction

Pre-transfusion tests are essential before performing a blood transfusion to determine the compatibility between the transfusion receiver and the unit of blood from a donor. To perform these tests there are: manual procedures, in which the technical analyst performs all the steps, or nearly all, involved in the testing procedure, for example, the test plate and the test tube; systems that automatically perform tests, not requiring the intervention of the technical analyst in most procedures. There are several commercial systems that have emerged in order to carry out the

A. Ferraz (✉) · V. Carvalho
R&D ALGORITMI Center, School of Engineering, University of Minho,
4800-058 Guimarães, Portugal
e-mail: aps_ferraz@hotmail.com

V. Carvalho
e-mail: vcarvalho@ipca.pt

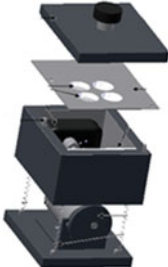

A. Ferraz · J. Machado
MEtRICs Research Center, School of Engineering, University of Minho,
4800-058 Guimarães, Portugal
e-mail: jmachado@dem.uminho.pt

V. Carvalho
IPCA-EST, Polytechnic Institute of Cávado and Ave, 4750-810 Barcelos, Portugal

pre-transfusion testing, among others: Immucor Galileo® [1, 2], Ortho ProVue® [3], PK7300 [4], Galileo Echo® [5], Neo® [3, 6], and the Techno TwinStation [7]. However, these systems are large and can not be easily transported out of the laboratory, they are slow in achieving results, even more adding the time spent traveling to the laboratory for the tests and, moreover, they are expensive, as they can reach values of hundreds of thousand euros [2, 7].

The fact that commercial systems are large and slow in getting the test results, make them less suitable for emergency situations, where due to the lack of time to conduct the pre-transfusion testing it is administered the O negative blood type, considered the universal donor. However, taking into consideration that this type of blood becomes scarce due to the extensive use and the fact that the ideal scenario should consider the administration of a corresponding type of blood, the need to provide a system which is able of in urgent situations perform the essential pre-transfusion tests arises. In this way, efforts have been taken for the development of a system that is quick to obtain results, that is portable so that it can be used directly with the patient (by eliminating the move to the laboratory for testing and the additional time that it involves) and that is reliable and of low cost, being so proper for emergency situations. Previous studies of the research team, have considered different prototypes [8–12]. Table 1 shows the characteristics of some of the developed prototypes.

Table 1 Other prototypes developed to perform the emergency tests

Prototype	Constitution	Features
 <p>(image edited from [8, 9])</p>	<p>This prototype is constituted by a DC motor which rotates a cam for moving the box; a web camera to capture the image of the test; a mirror that reflects the samples plates test acquired by the camera; a sample plates test to make mixtures of blood and reagents; and a top cover</p> <p>This prototype uses image processing techniques [12]</p>	<p>It uses two LEDs (Light Emitting Diodes) for illumination, and an Arduino Duemilanove platform for lighting control; moreover, it uses a DC (Direct Current) motor, an encoder and an Arduino Duemilanove platform for velocity control</p> <p>This is a mechatronic prototype and had as specifications the fast operation of blood type testing, portability and automation [12]</p>
 <p>(image edited from [11, 12])</p>	<p>This solution consists of a base containing the rotation system, being this constituted by two bars which allows the rotation of the sample plates test. It also has a web camera to capture the image of the test and a cap to seal and avoid outside interferences. The analysis and interpretation of the results also considers the use of image processing techniques [10–12]</p>	<p>Without brightness control, neither velocity control</p> <p>It may be particularly useful in situations where electrical power is not available</p> <p>The user is required and interferes with the test procedure, being its intervention essential for the mixture to be promoted</p>

This paper presents a new prototype developed by the research team, highlighting the speed and the brightness control procedures. The paper is divided into five chapters: Chap. 2 addresses the velocity and brightness control used in the prototype to acquire images with quality to enable the detection of reactions; the Chap. 3 presents the developed prototype that incorporates all the electronic components required for its operation; and, the 4th chapter presents the conclusions and the work to be developed in future.

2 Velocity and Brightness Control

It is extremely important to ensure that tests for determining blood types ABO and Rh are performed properly and with stable conditions of operation. Following this, it was necessary to introduce brightness and velocity control in the developed prototype. Through the introduction of the brightness control there can be set conditions of adequate illumination to proper display and capture the image inside the prototype (good visualization of reactions within the test container). In turn, the introduction of the velocity control and motor rotational direction, allows to make the mixing of blood with reagents effective for the occurrence of reactions that can be detected by image processing techniques.

It is used the Arduino Duemilanove platform for performing brightness control of the LEDs and the motor rotational velocity control; while, the Arduino Ethernet Shield is used for communication with the computer application that is developed in the interface device (laptop or mobile) [13, 14]. For brightness control were used six white LEDs [15] and an LDR (Light Dependent Resistor) [16] sensor, Fig. 1. For the DC motor velocity control [17–19] it was used an encoder, [20], Fig. 1, and a driver circuit (H-bridge) that allows motor operation and reversing the direction of rotation [17, 21].

2.1 *Brightness Control*

As previously referred, the prototype has six white LEDs [8] to provide lighting levels necessary and appropriate for testing. By carrying out various tests, it was possible to define the recommended minimum brightness level for the reliable visualization of agglutination reactions in tests. It was chosen to place six LEDs (one for each container—Fig. 5) since it is guaranteed more uniform lighting conditions for the samples blood/reagents, avoiding shadows and glare concentrated. For protection of the LEDs, resistors were placed in series to limit the current. A potentiometer was used to adjust the sensitivity of the LDR sensor.

The brightness control is necessary to ensure that the conditions of brightness are constant for all tests (preventing e.g. LEDs scenarios damaged) as well as to ensure that the brightness inside the prototype is always within the range of values desired.

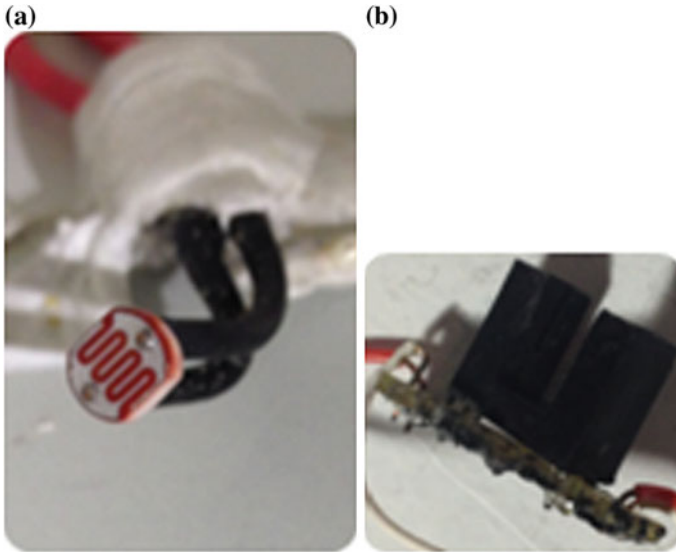


Fig. 1 Sensors used in the prototype 2; a LDR; b encoder

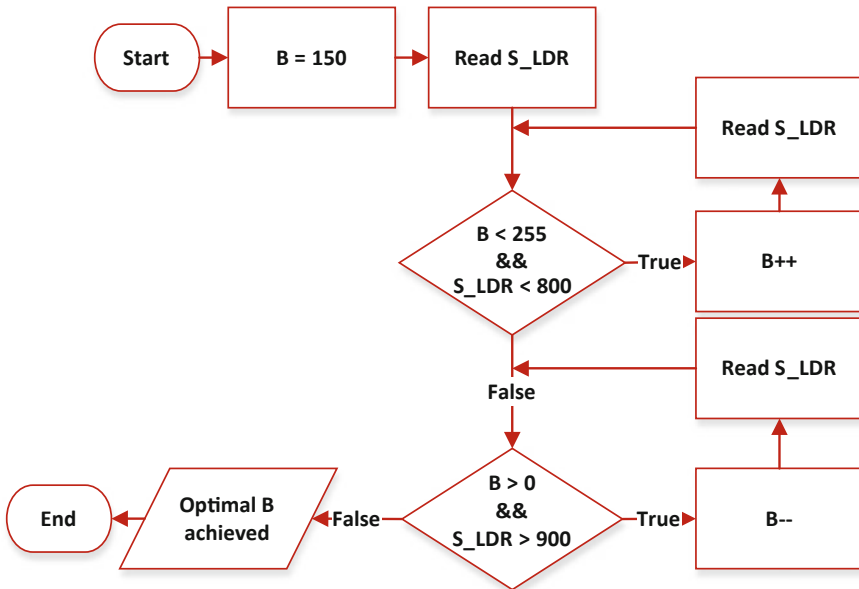


Fig. 2 Flowchart of brightness control algorithm. *B* Brightness variable, *S_LDR* sensor LDR variable

The on-off algorithm used for performing the brightness control is represented by the flowchart of Fig. 2. In the flowchart of Fig. 2 there are used variables B and S_LDR. Variable B corresponds to the brightness and it is the variable that controls the brightness of LEDs, where 0 corresponds to completely turn off of the LEDs and the value 255 corresponds to the LEDs at maximum brightness possible to achieve, with the electronic circuit used. The S_LDR variable corresponds to the digital value that the LDR sensor measures according to the brightness inside the prototype. The value of 800 for the S_LDR variable was defined as the minimum value from which the brightness inside the equipment has the appropriate conditions for a good image acquisition. The value 900 corresponds to the maximum value set for the variable S_LDR to ensure that there is no glare caused by the LEDs.

The range of brightness values of the LEDs set to ensure proper conditions of luminosity to capture the image and performing the tests shall be between 12.00 and 16.50 lux.

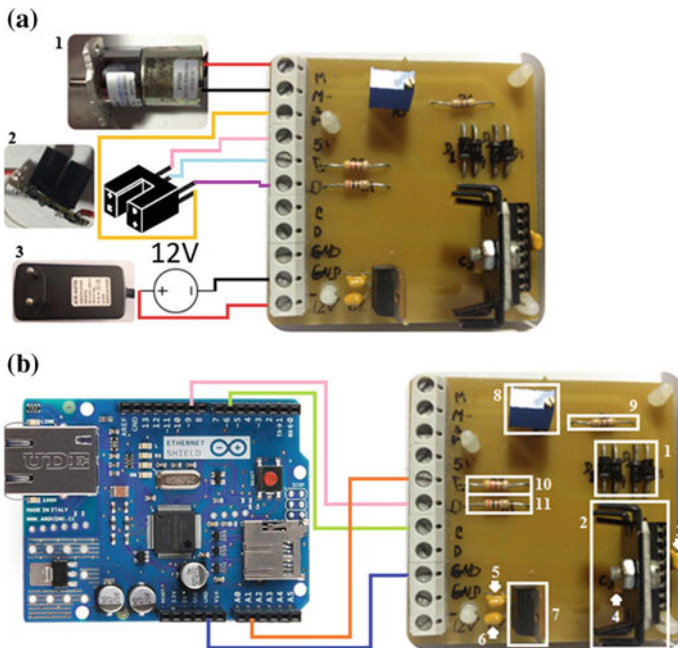


Fig. 3 Driver used in the prototype. **a** Driver with connections to the components involved in the control of the engine and the connection to the power driver. 1 DC motor used, 2 infrared optical sensor [22], 3 AC-DC adapter. **b** Driver Links to Arduino Ethernet Shield. 1 bridge diodes, 2 integrated L298 [8], 3 condenser 1, 4 condenser 2, 5 condenser 3, 6 condenser 4, 7 integrated LM7805 [350], 8 potentiometer, 9 resistance 4, 10 resistance 2, 11 resistance

2.2 Velocity Control

To operate the DC motor, implement the velocity control, as well as setting the direction of rotation, it was necessary to use a driver circuit that is based on the H-bridge L298 [19]. In Fig. 3 it is presented the PCB of the built driver [21, 22].

By introducing the velocity control it was possible to specify which conditions best suit to perform the tests. The flowchart of the on-off algorithm used to perform the DC motor velocity control is shown in Fig. 4. The v_m variable corresponds to the engine velocity and starts at 55 corresponding to a slow speed. The $Time_M$ variable is the time the motor takes to complete a full rotation. As time is the inverse of the velocity, i.e., the longer it takes the motor to make one complete revolution, the lower is the motor rotation velocity, it becomes possible to perform the control through the measurement of the variable. So being time ($Time_M$) nonzero it is verified if time ($Time_M$) is between 110 and 87 μs . If the condition is true, it is within the limits of the desired velocity and control is achieved. If the condition is false, it is verified if the time ($Time_M$) is less than 87 μs (i.e. greater than the desired velocity) and if the condition is true, it is decreased the motor velocity (v_m). If the condition is false, it is verified if time ($Time_M$) is greater than 110 μs

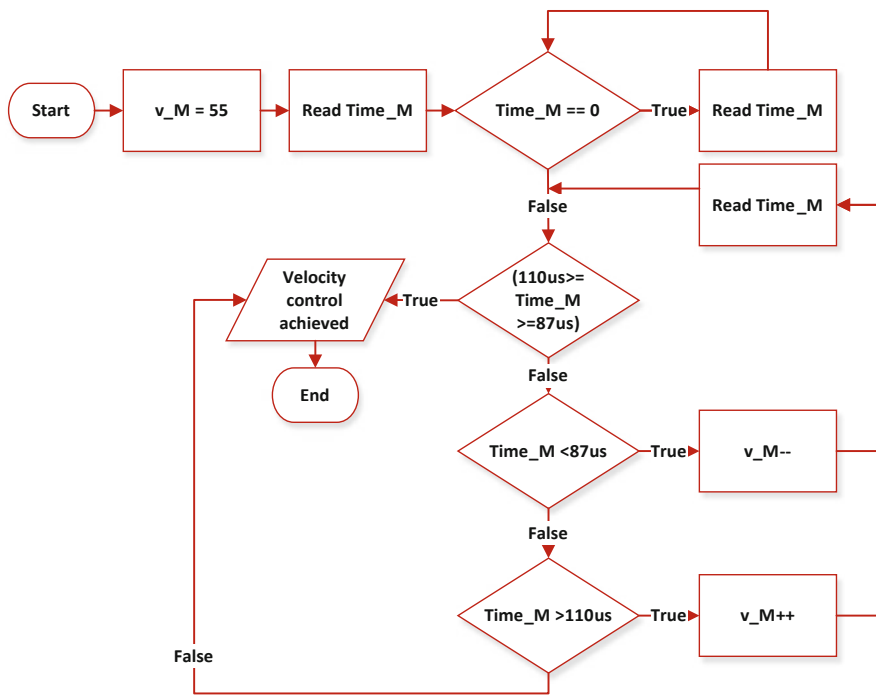


Fig. 4 Flowchart of velocity control algorithm. v_M motor velocity, $Time_M$ time the motor needs to complete one rotation

(speed below the desired) and if the condition is verified, it is increased the motor velocity (v_m). The cycle is repeated until it reaches the initial condition, i.e. the time (Time_M) is between 110 and 87 μ s. The amount of time 110 μ s is associated to 65 rpm and the time of 87 μ s is associated to 180 rpm, which are the desired range of rotational velocity for effective promotion of blood mixed with reagents. It is highlighted that the control is performed with similarity for both rotation directions, forward direction and reverse direction.

3 Developed Prototype and Software

This section describes the software application interface with the prototype, as well as the full description of the integrated components in the prototype [23].

The developed software application was developed in C# and html languages with Visual Studio 2014 software from Microsoft [24]. It presents a user friendly interface in order to facilitate its use and ensure a fast and efficient interaction with the health professionals. There are used buttons for the main functions and the data necessary to insert during a test its reduced. To store the relevant information involved in testing, especially its results, the analyzed images, the type of test and stakeholders (patient and healthcare professional), it was developed a database using SQL Server from Microsoft [25, 26].

The prototype, presented in Fig. 5 [27], was modeled using the Autodesk Inventor 2013 software [28, 29].

The prototype presented in Fig. 5 was modeled based on previously developed prototypes [30]. It is constituted by an upper part (components E, F, G, H, I, J, K, L) and a lower part (components A, B, N). Between the upper and the lower part there is a rotation axis (C) and a separation plane (D), allowing the substitution of the plate test used in each blood test. The outer cylindrical body (E) along with the part (F) constitutes the chassis of the prototype. The prototype has a part (I), which supports the motor (J) and the plate test (K), which has six containers, where the mixture of blood and reagents is performed. The base (F) contains an Arduino Duemilanove [15] (G), an Arduino Ethernet Shield [16] (G), a battery (H), an encoder (Q) for motor velocity control (J) and an LDR sensor (R), for brightness control of the LEDs (N). The upper part of the prototype (B), contains an HD camera (M) to capture images of the performed tests and around the camera contains white LEDs (N) for illumination of the samples presented in the plate test. The prototype has a top cover (A) to allow easy access to the camera (M) and the LEDs (N). Furthermore, the body (E) and the base (F) allows easy access to the inside of the prototype base where the required hardware is placed. The dimensions of the prototype are 160 mm of height and 100 mm of diameter [30].

Through the software application that operates with the prototype, it is possible to obtain the image of the test performed and process it to obtain the test result. As an example it is presented in Fig. 6 an image obtained when carrying out the tests.

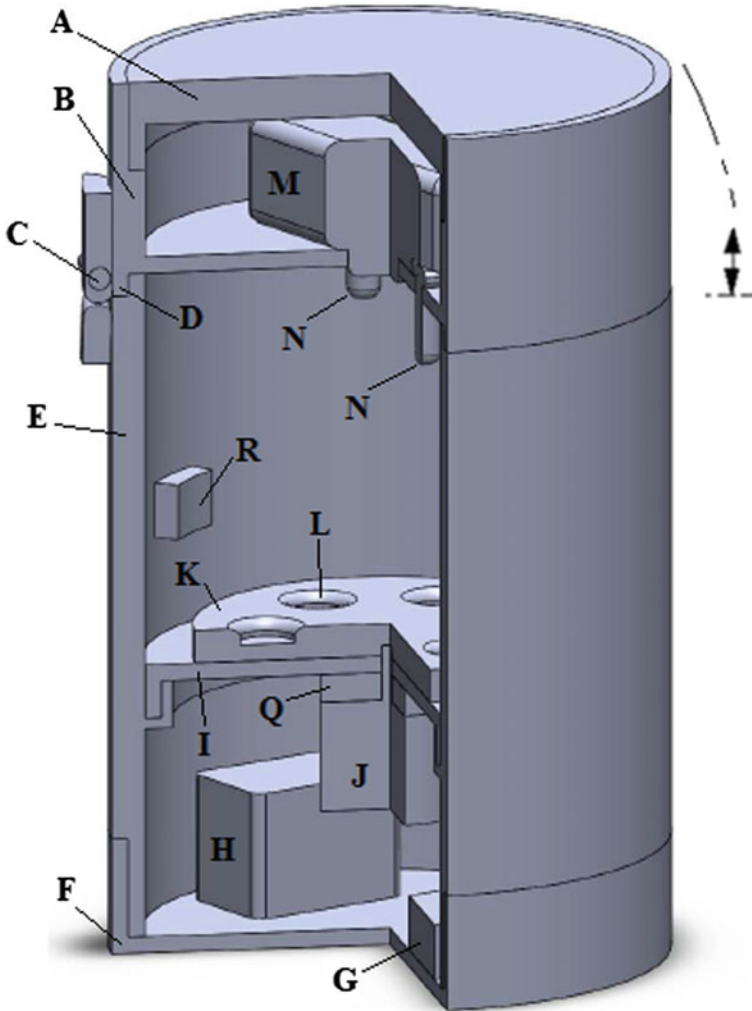
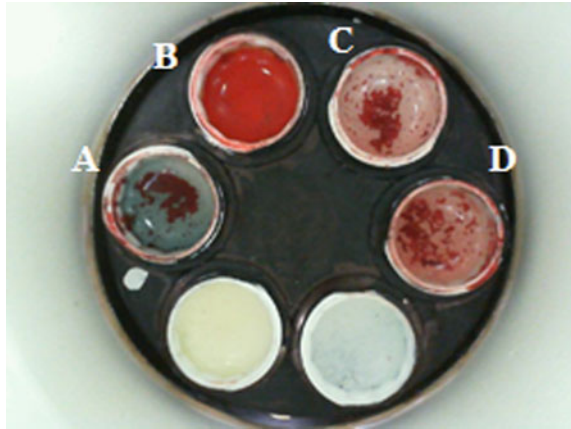


Fig. 5 Functional scheme of the final prototype modeled in 3D. [A Top cover; B upper support; C rotation axis of the upper part; D separation plan between top and the bottom parts; E cylindrical body; F basis where it is fitted the outer cylindrical body; G both Arduino boards and electronic components; H Battery; I plate test holder; J DC motor, Q encoder; K plate test; L container for mixing of blood and reagents; M HD (High Definition) Camera; N LED for illumination, R LDR sensor] [27]

Fig. 6 Original image obtained with the prototype after brightness and speed control



In Fig. 6 it is possible to verify that the plate test has six test containers; in this case the test is performed using only 4 containers (ABO test). The developed software is responsible for determining the test result using image processing techniques and deterministic algorithms.

4 Conclusions and Future Work

This work presents a new prototype for determining human blood types, highlighting the velocity and the brightness control procedures.

With the work developed it was possible to verify the correct operation of the prototype, able to perform pre-transfusion testing ABO and Rh, quickly and effectively. The results of this development, bring improvements in the plate test, making it more suitable for carrying out the tests and to incorporate all the components required to achieve the brightness and velocity control.

By introducing the brightness control it was possible to achieve the lighting conditions suitable for proper capture of the image inside the prototype, ensuring reduction of glare and good visualization of reactions. Moreover, the introduction of the velocity control and motor rotation direction, allows to make the mixture of the blood with the reagents, efficient and suitable for the reactions occurrence and further detection by the developed software using image processing techniques.

The obtained solution thus satisfies the performance requirements in terms of lighting and mixture still being a quick, portable and low cost solution compared to the solutions available on the market.

Future work includes the physical implementation of the final prototype modeled as well as the emergencies context testing where it will be used.

References

1. ABS2000 Immucor Inc. <http://www.fda.gov/downloads/BiologicsBloodVaccines/BloodBloodProducts/ApprovedProducts/SubstantiallyEquivalent510kDeviceInformation/UCM079230.pdf>
2. Wittmann, F.G., Schram, W.J., Spannagl, M.: Automation and data processing with the Immucor Galileo® system in a university blood bank. *Transfus. Med. Hemother.* **34**, 347–352 (2007)
3. Dolmashkin, A.A., Doubrovski, V.A.: Blood group typing based on digital imaging of sedimentation of erythrocytes and their agglutinates. *Biomed. Eng.* **46**(2), 65–70 (2012) (New York)
4. PK7300 LabWrench. <http://www.labwrench.com/?equipment.view/equipmentNo/8094/SCIEX/PK7300/>
5. Wittmann, G., Frank, J., Schramm, W., Spannagl, M.: Automation and data processing with the Immucor Galileo® system in a university blood bank. *Transfus. Med Hemother.* **34**, 347–352 (2007)
6. NEO® Brochure Immucor Inc. http://www.immucor.com/en-in/Products/Documents/Immucor_NEO-Brochure_US_web.pdf
7. Techno TwinStation #009895KT Bio-Rad Laboratories Inc. <http://www.bio-rad.com/en-mx/sku/009895kt-techno-twinstation>
8. Moreira, V.: Desenvolvimento de um Sistema Automático para Determinação do Tipo Sanguíneo. Universidade do Minho (2012)
9. Moreira, V., Ferraz, A., Carvalho, V., Soares, F., Machado, J.: Design of a mechatronic system for human blood typing in emergency situations. In: IEEE International Conference on Emerging Technologies and Factory Automation. ETFA (2012)
10. Bezerra, K., Ferraz, A., Carvalho, V., Machado, J., Matos, D., Soares, F.: Advanced design of a mechatronic system for human blood typing (2012)
11. Bezerra, K., Machado, J., Matos, D., Carvalho, V., Soares, F., Ferraz, A.: Boletim da Propriedade Industrial No 2015/01/21—SISTEMA DE MISTURA DE LÍQUIDOS. INPI (2015). http://www.marcaspatentes.pt/files/collections/pt_PT/49/55/533/534/2015-01-21.pdf
12. Bezerra, K., Machado, J., Matos, D., Carvalho, V., Soares, F., Ferraz, A.: Sistema de Mistura de Líquidos 107064 (2013)
13. Ferraz, A.: Automatic system for determination of blood types using image processing techniques. In: 2013 IEEE 3rd Port, Bioengineering Meeting, pp. 1–6 (2013)
14. LifeCam HD-5000. <http://www.microsoft.com/hardware/es-es/d/lifecam-hd-5000>
15. Arduino Duemilanove. <http://arduino.cc/en/Main/arduinoBoardDuemilanove>
16. Arduino Ethernet Shield. <http://arduino.cc/en/Main/ArduinoEthernetShield>
17. ZGA37RG/ZGB37RG ZHENGKE. <http://www.zhengkemotor.com/product/product48.html>
18. Datasheet LED 5 mm branco alto brilho. Lucky Light Electronics (2006). <http://www.soldafria.com.br/datasheet/LL-504-WC2E-W2-3UC.pdf>
19. Datasheet LDR. RS Components (1997). http://www.biltek.tubitak.gov.tr/gelisim/elektronik/dosyalar/40/LDR_NSL19_M51.pdf
20. Datasheet ZGB37RG. ZHENGKE. <http://wzh001.gotoip55.com/upload/file/ZGA37RG&ZGB37RG.pdf>
21. DUAL FULL-BRIDGE DRIVER: L298. STMicroelectronics (2000). <http://www.st.com/web/en/resource/technical/document/datasheet/CD00000240.pdf>
22. MC78XX/LM78XX/MC78XXA 3-Terminal 1A Positive Voltage Regulator. Fairchild Semiconductor Corporation (2001)
23. Ferraz, A.: Sistema para Determinação do Tipo Sanguíneo de Humanos Utilizando Técnicas de Processamento de Imagem. University of Minho - Guimarães (To approval) (2015)
24. Visual Studio (2014). <http://www.visualstudio.com/>
25. Damas, L.: SQL. 12a ed. FCA – Editora de Informática (2005)
26. SQLite. <https://www.sqlite.org/>

27. Ferraz, A., Brito, J.H., Carvalho, V., Machado, J.: Blood type classification using computer vision and machine learning. *Neural Comput. Appl.* pp. 1–12 (2016)
28. Inventor Professional. <http://www.autodesk.com/education/free-software/inventor-professional>
29. Costa, A.: Autodesk Inventor 2013—Curso Completo. FCA
30. Ferraz, A., Carvalho, V., Soares, F.: A prototype for blood typing based on image processing. In: *SensorDevices 2013: The Fourth International Conference on Sensor Device Technologies and Applications* (2013)
31. Datasheet TCST1000/TCST2000. VISHAY (1999). <http://www.spelelektronikka.fi/kuvat/tcst1000.pdf>

Development of Soft Sensors Based on Analytical and Spectral Data on a Real Small Size Wastewater Treatment Plant

C. Leitão, L. Fernandes, R. Ribeiro, M.C. Almeida, C.I.C. Pinheiro and H.M. Pinheiro

Abstract Advances in measurement and automation have recently enabled the deployment of monitoring systems with high frequency data acquisition in Wastewater Treatment Plants (WWTP). In this context, this work aims to design soft sensors to predict hard-to-measure wastewater quality variables required for mechanistic modeling of biological treatment in a real municipal WWTP. Input data collected at the WWTP using a flowmeter, online spectrophotometric and electrochemical probes, sampling campaigns and off-line analyses, are here used for the development of soft sensors through multivariate methods, i.e., Principal Component Analysis (PCA) and Partial Least Squares (PLS) regression. Exploratory data analysis is performed to detect outliers, patterns and correlations. Soft sensor PLS models are optimized using leave-one-out cross validation and the root mean squared error (RMSE) for the prediction of an independent dataset is computed. Normalized RMSE values for organic nitrogen prediction result in 19.5 % and 18.1 % for sensors using analytical and spectral data, respectively. The possibility of using a single wavelength spectrophotometric probe is here evaluated aiming to reduce the online monitoring investment costs.

Keywords Wastewater treatment · Municipal WWTP · Online monitoring · Prediction · Partial least squares · Soft sensors

C. Leitão · L. Fernandes · H.M. Pinheiro
iBB—Institute for Bioengineering and Biosciences, Instituto Superior Técnico,
Universidade de Lisboa, Av. Rovisco Pais, Lisbon 1049-001, Portugal

R. Ribeiro · M.C. Almeida
Departamento de Hidráulica e Ambiente, Laboratório Nacional de Engenharia Civil,
Avenida do Brasil 101, Lisbon 1700-066, Portugal

C.I.C. Pinheiro (✉)
Centro de Química Estrutural (CQE), Instituto Superior Técnico, Universidade de Lisboa,
Av. Rovisco Pais, Lisbon 1049-001, Portugal
e-mail: carla.pinheiro@tecnico.ulisboa.pt

1 Introduction

In recent years an increase has been observed in the number of decentralized wastewater treatment units in operation, in relation to that of centralized units [1]. A decentralized system collects, treats and reuses or disposes of wastewater at or near its generation point, the latter being mostly urban. Small decentralized WWTP in particular are designed for rural communities and peri-urban areas, providing reduced investment and maintenance costs and more flexible management [2].

Monitoring in WWTP usually aims to control wastewater quality prior to discharge and to measure a few parameters to support operation decisions. However, more advanced monitoring is at present possible through sensors providing real-time information which can be used to upgrade process control. Control objectives depend on WWTP characteristics. Whereas in large units control is directed to nitrogen and phosphorus removal, in small-scale systems the goal is to increase organic matter removal efficiency [2]. The activated sludge (AS) process is the most commonly used biological treatment method. In this, a microbial biomass suspension carries out the removal of pollutants through organic matter oxidation, and nitrogen conversion through nitrification and denitrification [3]. The Activated Sludge Model no. 1 (ASM1) is considered a reference in the mechanistic modeling of these AS systems. This model describes the organic matter and nitrogen removal processes using stoichiometric and kinetic expressions characterizing biochemical transformations involving soluble and particulate pollutants [4]. In order to apply ASM1, input data on carbonaceous and nitrogenous load fractions are required. Progress in measurement and data processing technologies has enabled online monitoring of an array of variables with data acquisition at a high frequency at WWTPs. These variables can be used for the prediction of hard-to-measure variables like pollutant concentrations using soft sensors. Soft sensors are computer models that use the information contained in secondary variables as input and provide information about primary, hard-to-measure variables as output, similarly to hardware sensors. The use of data-derived soft sensors for online variable prediction and process and sensor fault monitoring in wastewater treatment plants has been recently reviewed [5]. The authors identify parameters such as pH, temperature, flow rate, dissolved oxygen, conductivity and oxidation-reduction potential as the secondary input variables typically used, and organic carbon, solids, nitrogen and phosphorus fractions as the most addressed primary variables. The authors also review the array of multivariate data processing methods which have been applied in this context.

The use of ultraviolet-visible (UV/Vis) spectroscopy is rapidly increasing in online monitoring. The information contained in spectra provides a fingerprint of the monitored bioprocess with good potential for supervision/diagnosis and parameter estimation [6]. Soft sensors have been developed using spectral

information (i.e., absorbance values at different wavelengths) as secondary variables for wastewater quality parameter prediction. Partial Least Squares (PLS) models built from spectra were shown to be effective in the prediction of chemical oxygen demand (COD), total organic carbon (TOC), total suspended solids (TSS) and nitrate levels in wastewater [6–8].

The aim of the present work is to assess the use of online measurements, namely flow rate, ammonia concentration, UV-vis spectra and COD (derived from spectra using a soft sensor software included in the commercial instrument), as possible secondary variable inputs for the development of soft sensors for the prediction of organic nitrogen or total nitrogen levels in raw wastewater. The latter are hard-to-measure variables required for the ASM1 model, which have been scarcely addressed as primary variables in data-driven soft sensor studies [5]. The present case-study is the AS system in a real decentralized WWTP located near Bucelas (Portugal).

2 WWTP Characteristics and Data Collection

The Bucelas WWTP is a small-size unit (serving a population of 5,000) comprising 3 treatment levels. Preliminary treatment includes sieving and grit removal. Secondary treatment is performed in 2 activated sludge oxidation ditches operated in extended aeration mode combined with 2 gravity clarifiers. The clarified effluent is polished by sand filtration and UV disinfection. The biomass sludge wasted from the system goes through gravity thickening and mechanical dewatering.

Data used in the soft sensor development was collected through online measurements and sampling campaigns. The inlet flowrate was measured in a Parshall flume. Further online monitoring at the wastewater inlet consisted of a submersible UV/vis spectrometer (spectro::lyser) and an electrochemical sensor (ammo:lyser), both from s::can Messtechnik GmbH, Austria. The former provides absorbance measurements in the 200–750 nm wavelength range and surrogate values for COD and TSS, based on factory-calibrated models. It is equipped with an optical window auto cleaning system using pressurised air. UV/vis spectra were acquired between 220 and 737.5 nm (at 2.5 nm increment) with an optical path of 5 mm. The acquisition frequency was hourly for inlet flowrate, and every 10 min for water quality readings. A five-point Hamming Window filter was applied to surrogate and flowrate data to minimize noise and drift phenomena. Laboratory analyses followed standard methods [9] or used kits provided by Hach-Lange, Germany. The sampling campaigns took place during the period July 2014 to June 2015. The collected point-samples were refrigerated and analysed with no prior filtration. Table 1 summarizes the relevant information on analytical data samples collected during the campaigns.

Table 1 Information on analytical data samples collected during sampling campaigns at the Bucelas WWTP; Campaign ID prefixes P, C and V stand for preliminary, calibration and validation campaigns, respectively. *TSS* Total Suspended Solids, *COD_t* Total Chemical Oxygen Demand, *NH₄-N* Ammonia Nitrogen, *N_{total}* Total Kjeldahl Nitrogen

Campaign ID	Duration (h)	Sample frequency (h)	TSS samples (no.)	COD _t samples (no.)	NH ₄ -N samples (no.)	N _{total} samples (no.)
P1	24	2	12	12	6	6
P2	48	4	12	12	6	6
C1	48	2	0 ^a	24	12	12
C2	48	2	24	24	12	12
C3	48	2	24	24	12	12
V1	96	4	24	24	12	12
V2	96	4	18	18	9	9

^aTSS data from C1 is unavailable due to a failure of the sample cooling system

3 Soft Sensors Development

The soft sensors were developed using flow rate, analytical and spectral data. The analytical data based sensors were designed in the perspective of using them with online measured data for the same secondary variables. However, only analytical campaign data were used for PLS model calibrations, since they represent more reliable measurements. Among spectral data based sensors, PLS models for COD estimation were also developed to test the online probe factory calibration. The first step in the design of both soft sensors types involved the use of Principal Component Analysis (PCA) models on the secondary variables in order to identify outliers and evaluate correlations between these variables. In spectra pre-treatment, excluded outliers either coincided with analytical data outliers or exhibited a very different spectrum format when compared with average spectral dataset. After outlier exclusion, data from the P and C campaigns were split into training (70 %) and test (30 %) datasets for PLS model calibration and subsequent external validation. Input variable and model structure optimization was performed using leave-one-out cross validation applied to the training set. The number of latent variables (LV) to retain in PLS models was established by evaluation of the root mean square error of cross validation, RMSECV. In order to test each model's prediction ability, the test set and the V1 campaign dataset were predicted using the calibrated PLS model. The prediction performance was expressed in terms of the root mean square error of prediction, RMSEP. Both error values are determined from Eq. 1. Finally, the model robustness was evaluated by comparing the prediction errors of the test set and V1 campaign dataset using the Mann-Whitney-Wilcoxon test.

$$RMSE = \sqrt{\frac{1}{n} \sum_{j=1}^n (y_j - \hat{y}_j)^2} \tag{1}$$

An essential requirement for a PLS model based on spectral data is wavelength selection since part of the information in the full spectrum is redundant. Wavelength selection using the interval PLS algorithm (iPLS) was carried out, testing 20 wavelengths per interval, 10 wavelengths per interval, and 1 wavelength and 1 single interval. The latter was designated as “low cost” and corresponds to a probe providing measurements at a single wavelength. The PLS Toolbox 5.0 (Eigenvector Research, USA) in MATLAB (MathWorks, USA) was used for all modelling.

3.1 Soft Sensors Based on Analytical Data

Analytical data pre-treatment excluded 3 outliers, all from campaign C2. The PLS models were developed using analytical and flow rate (F_{in}) information collected in sampling campaigns. Figure 1 shows the PCA biplot of all input variables considered in PLS model development. The load variables were calculated from the products $COD \times F_{in}$ and $N_{total} \times F_{in}$. Tables 2 and 3 summarize the results obtained for the calibration and validation steps of the PLS models. In all models, the calibration and test sets include data from campaigns P1 to C3, except the models including TSS values (data from campaign C1 was not used).

The initial goal was to predict the concentration of N_{org} based on NH_4-N measurements. However, the biplot in Fig. 1 reveals that these variables are almost uncorrelated. The scores of the data points on each of the two PCs are represented in Fig. 1, as well as the loadings vectors for each of the original variables. Small

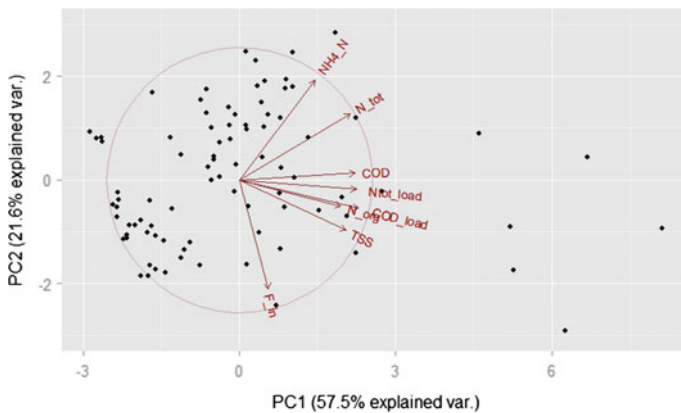


Fig. 1 Biplot of the first 2 principal components (PCs) of the PCA including the indicated parameter values measured on 5 of the campaigns at the case-study WWTP (728 data points)

Table 2 Input variables, number of LV, % of explained variance of input variables and RMSECV for the tested PLS models; RMSECV was normalized (NRMSECV) with the dataset value range (difference between maximum and minimum values); the ranges were 5–23.8 mg/L, 20–42.75 mg/L and 297–786 mg/s for N_{org} , N_{total} and N_{total} load, respectively

Output variable	Input variables	LV	% variance explained	RMSECV (mg/L)	NRMSECV (%)	
N_{org}	COD	1	100	3.71	16.3	
	COD load	1	100	3.72	16.3	
N_{org}	COD, $\text{NH}_4\text{-N}$, TSS, F_{in} , COD load	1	55.23	3.62	15.9	
		2	63.94	3.90	17.1	
		3	89.18	3.82	16.8	
		4	99.83	3.75	16.4	
		5	100	3.96	17.4	
N_{total}	COD, $\text{NH}_4\text{-N}$	1	69.62	3.92	10.6	
		2	100	3.80	10.3	
	COD	1	100	7.00	18.9	
	$\text{NH}_4\text{-N}$	1	100	4.26	11.5	
	COD, $\text{NH}_4\text{-N}$, TSS, F_{in} , COD load	1	48.36	5.48	14.8	
		2	82.99	4.46	12.1	
		3	93.72	3.88	10.5	
		4	99.84	3.75	10.1	
		5	100	3.94	10.6	
	N_{total} load	COD, COD load	1	97.73	131	13.3
			2	100	127	12.9
		COD	1	100	136	13.8
		COD, $\text{NH}_4\text{-N}$, TSS, F_{in} , COD load	1	54.44	118	12.0
			2	67.41	81.5	8.29
			3	94.03	77.3	7.86
4			99.84	74.7	7.60	
5			100	79.6	8.10	

Table 3 Test set and V1 campaign dataset prediction performance of the developed PLS models. The RMSEP was normalized (NRMSEP) using the dataset value range; the V1 campaign set ranges were 4.3–15.6 mg/L, 20–46.2 mg/L and 199–630 mg/s for N_{org} , N_{total} and N_{total} load, respectively

Output variable	Input variables	LV	RMSEP (mg/L)		NRMSEP (%)		Wilcoxon test value
			Test	V1	Test	V1	
N_{org}	COD	1	3.78	3.31	20.1	29.3	0.0826
	COD load	1	3.70	3.01	19.5	26.6	0.0559
N_{total}	COD, $\text{NH}_4\text{-N}$	1	3.68	3.36	16.2	12.8	0.0943
	COD	1	5.39	7.13	23.7	27.2	0.0269
N_{total} load	COD	1	123	115	24.2	26.7	0.1566

angles between the vectors indicate a direct correlation between the involved parameters, orthogonal vectors indicate zero correlation and opposite vectors indicate inverse correlation. In fact, the variables most correlated with N_{org} are TSS and COD. Since reproducibility problems were detected in the TSS online measurements, this variable was not further considered as an input, so the first PLS model to be tested for N_{org} was based on only COD. Predictions resulted in moderate RMSEP values and the Wilcoxon test indicated that the error distributions in the test and V1 campaign datasets were comparable (p -value > 0.05 , 95 % confidence). However, the model failed to accurately predict the time variations of N_{org} measured in the V1 campaign. This can be explained by the biochemical processes possibly occurring in the sewage pipeline feeding the WWTP. The urban wastewater load is mainly composed of COD and N_{org} . N_{org} is converted to $\text{NH}_4\text{-N}$ via ammonification. The higher the residence time of wastewater in the sewer system, the greater the ammonification extent tends to be. Since this extent is not known, an option is to predict N_{total} ($=N_{\text{org}} + \text{NH}_4\text{-N}$) instead of N_{org} . Also, the load variables contain information on the residence time in the pipeline, through the value of F_{in} . The lower F_{in} is the higher the residence time and consequently the extension of ammonification. This relationship could explain the anti-correlation observed between $\text{NH}_4\text{-N}$ and F_{in} in the PCA biplot (Fig. 1). The load variables were also represented in this biplot and their directions and correlations were evaluated to direct the testing of PLS models with improved prediction ability for N_{total} and N_{total} load. The results showed that predictions of the latter load variable were not substantially improved when compared with the N_{total} models. The best performing model predicts N_{total} using COD and $\text{NH}_4\text{-N}$ data as inputs. However, online data on $\text{NH}_4\text{-N}$ are required to obtain the N_{org} values from the predicted N_{total} , and online nutrient probes are still prone to fouling and interferences [5]. Alternatively, another model for direct prediction of N_{org} was tested, considering COD load as single input. This model is more promising than the first using COD as input, since COD load and organic nitrogen concentration are more correlated (Fig. 1). Overall, Table 3 shows that the best two of the developed PLS models predicted N_{total} using COD and $\text{NH}_4\text{-N}$ data as input variables and N_{org} using the COD load as input variable. The predictions obtained using these two models and both analytical and online data from campaign V1 are shown in Fig. 2. In contrast to the N_{total} model, the model for N_{org} estimation is not able to predict peak values, but main data trends are captured and the problem of ammonia nitrogen data availability is avoided. Thus, the latter was chosen as the best compromise for a soft sensor using analytical data, predicting N_{org} concentration using the COD load as input variable.

3.2 *Soft Sensors Based on Spectral Data*

The spectral data collected during campaign periods were analyzed by PCA to identify outliers. In all, 21 outliers were identified and excluded from the dataset.

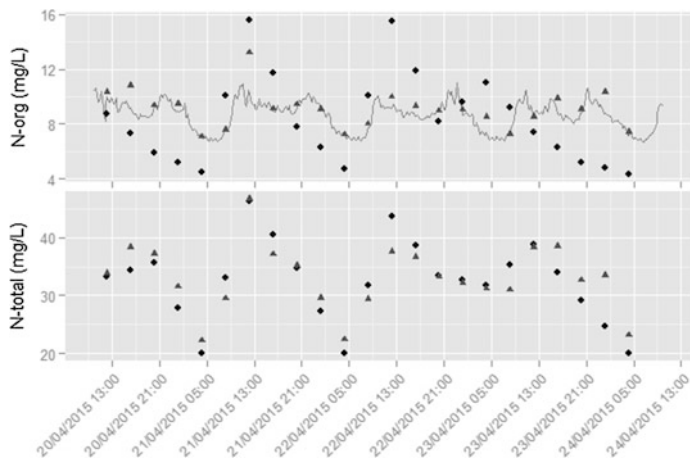


Fig. 2 Predictions of N_{org} and N_{total} concentrations for campaign V1 with the PLS models developed with data from the other campaigns: *dots* are the measured values, *triangles* the values predicted from analytical data and the *grey line* represents the prediction from online COD data; due to the different acquisition frequency for online COD and inlet flow rate data, the latter were considered as hourly steps

From the retained dataset, only the spectra with corresponding analytical values in campaign periods (i.e., simultaneous spectra acquisition and sampling) were considered for soft sensor design. These were mean centered prior to PLS model development. The PLS models using the whole spectral range were optimized using leave-one-out cross-validation and an external validation step was performed through the prediction of an independent dataset. With the aim of reducing the investment cost in online spectral monitoring instrumentation, wavelength selection using iPLS was carried out. A performance comparison between the built PLS models is important to decide if online probes providing smaller wavelength ranges, representing a lower investment cost, may alternatively be used without compromising output variable prediction capability. The main features of all the wavelength-optimized PLS models tested are presented in Table 4, together with those of the models which used the whole spectral range. COD predictions were not significantly affected and the low cost version (single wavelength) actually gave the best predictions for both COD and N_{org} . For N_{org} estimation, the predictive ability for the test dataset was markedly deteriorated for iPLS models using intervals of 20 and 10 wavelengths and for the PLS model using whole spectra, when compared to the low cost model.

In an attempt to obtain PLS models with improved prediction ability, the inclusion in the models of input variables other than spectral data was considered. For N_{org} estimation, the addition of $\text{NH}_4\text{-N}$ concentration and F_{in} data was tested, given the results and reasoning presented in Sect. 3.1. For COD only F_{in} data was added. The obtained PLS models revealed that the addition of external factors does not significantly affect prediction ability when compared with the spectra-only

Table 4 PLS models for COD and N_{org} prediction using the entire spectral range and using iPLS-selected wavelength (λ) intervals; the COD models were constructed using 90 datapoints; the value ranges for the training and test sets are 48–738 and 66–747 mgO_2/L , respectively; the N_{org} models include 44 datapoints and the value ranges for the training and test sets are 4.3–27.1 and 6–18.2 mg/L , respectively

Output variable	Model ID	LV	λ intervals (nm)	NRMSECV (%)	NRMSEP (%)
COD	Whole spectrum	5	220–737.5	9.9	20.7
	iPLS20	5	220–417.5 670–717.5	10.0	20.1
	iPLS10	5	220–242.5 395–417.5 445.0–467.5 595–617.5	10.4	23.9
	Low cost	1	362.5	10.2	14.5
N_{org}	Whole spectrum	5	220–737.5	21.1	38.7
	iPLS20	5	420–517.5	19.3	47.0
	iPLS10	5	520–542.5	22.8	23.5
	Low cost	1	542.5	22.5	19.8

Table 5 NMSE values for the calibration and test sets and for the V1 campaign dataset and Wilcoxon test results comparing the latter two, for the selected soft sensors for N_{org}

Sensor type	NRMSECV (%)	NRMSEP (test set, %)	NRMSEP (V1 set, %)	Wilcoxon test value
Analytical data	16.30	19.50	26.60	0.0559
Spectral data	22.37	18.10	25.50	2.50×10^{-5}

models. As an exception, a slight improvement in N_{org} prediction was obtained by including $\text{NH}_4\text{-N}$ analytical data as input together with the spectral data, indicating the importance of having reliable online monitoring on this variable. Finally, the predictive ability of the best models for COD and N_{org} estimation was assessed once more through the prediction of campaign V1 values and the Mann-Whitney-Wilcoxon test was used to compare the results to those obtained with the test dataset. The statistical test evidenced non-identical distributions for the N_{org} prediction errors of the test and campaign V1 datasets ($p\text{-value} = 2.5 \times 10^{-5}$, see Table 5), indicating that the sensor is not robust enough and needs updating.

3.3 Soft Sensors Comparison

The performance of the soft sensors developed using analytical and spectral data as input variables was compared, so as decide which is the best for N_{org} estimation. The results are summarized in Table 5 for the best sensors in each group.

The sensor based on analytical data, although showing a worse predictive performance, is more robust, according to the Mann-Whitney-Wilcoxon test result. However, since the result for the analytical data based sensor is very close to the Wilcoxon test limit of acceptability, it is advisable to review and update both sensors in the future and establish a new comparison.

The results for COD in Table 4 were also compared with the COD prediction ability of the factory calibration of the spectrophotometric online probe used in this study. For RMSEP calculation, only the probe COD data with coincident sampling timestamps in campaigns P1-V1 campaign periods was considered. The value obtained was 231.17 mg/L, corresponding to a NRMSEP of 13.45 %. This value is lower than that obtained for the test set with the best of the models in Table 4, but only slightly. The expected lower cost of a single wavelength probe could justify this small loss in COD predictive ability.

4 Conclusion

The results show that PLS techniques are a suitable basis for soft sensors for the prediction of hard-to-measure variables required as inputs for mechanistic models of biological treatment in the WWTP context. The designed sensors, in general, show acceptable prediction errors. Soft sensors based on spectral data provide more accurate N_{org} estimations when compared with soft sensors based on analytical data. However, the first show lower robustness in the prediction of two different independent datasets, evidencing the need for model update. Another relevant conclusion is that models for N_{org} prediction show better results when $\text{NH}_4\text{-N}$ is included as input variable, suggesting the importance of having reliable online monitoring providing data on this variable. The main advantage of an online monitoring system in municipal WWTP is the possibility of using mechanistic modelling to anticipate the consequences of changes in the inlet wastewater quality, allowing the adoption of more efficient control strategies. However, the high investment cost in real-time monitoring equipment is probably the most fundamental barrier. In view of cost reduction, the possibility of using cheaper probes was tested by selecting the wavelength range used in the spectra based soft sensors. The single wavelength sensors thus identified as low cost revealed a better predictive ability for both COD and organic nitrogen, when compared with sensors using data from a wider range of wavelengths, sustaining the possibility of having less expensive online monitoring systems operating in municipal WWTP.

Acknowledgments The authors gratefully acknowledge the contractor of the case study WWTP, Águas de Lisboa e Vale do Tejo (AdLVT), for technical support and information. This work was financed by Programa Operacional Regional de Lisboa 2020 (Project N. 007317) and by Fundação para a Ciência e Tecnologia (Portugal) through project PTDC/AAG-TEC/4124/2012, and through the funding received by the iBB - Institute for Bioengineering and Biosciences (UID/BIO/04565/2013) and by the CQE - Centro de Química Estrutural.

References

1. Libralato, G., Ghirardini, A.V., Avezzu, F.: To centralise or to decentralise: an overview of the most recent trends in wastewater treatment management. *J. Environ. Manag.* **94**(1), 61–68 (2012)
2. Massoud, M.A., Tarhini, A., Nasr, J.A.: Decentralized approaches to wastewater treatment and management: applicability in developing countries. *J. Environ. Manag.* **90**(1), 652–659 (2009)
3. Gernaey, K.V., van Loosdrecht, M., Henze, M., Lind, M., Jorgensen, S.B.: Activated sludge wastewater treatment plant modelling and simulation: state of the art. *Environ. Model Softw.* **19**(9), 763–783 (2004)
4. Henze, M.: *Activated Sludge Models ASM1, ASM2, ASM2d and ASM3*, vol. 9. IWA Publishing, London (2000)
5. Haimi, H., Mulas, M., Corona, F., Vahala, R.: Data-derived soft-sensors for biological wastewater treatment plants: an overview. *Environ. Model Softw.* **47**, 88–107 (2013)
6. Lourenço, N.D., Lopes, J.A., Almeida, C.F., Sarraguça, M.C., Pinheiro, H.M.: Bioreactor monitoring with spectroscopy and chemometrics: a review. *Anal. Bioanal. Chem.* **404**(4), 1211–1237 (2012)
7. Lourenço, N.D., Paixão, F., Pinheiro, H.M., Sousa, A.: Use of spectra in the visible and near-mid-ultraviolet range with principal component analysis and partial least squares processing for monitoring of suspended solids in municipal wastewater treatment plants. *Appl. Spectrosc.* **64**(9), 1061–1067 (2010)
8. Lourenço, N.D., Menezes, J.C., Pinheiro, H.M., Diniz, D.: Development of PLS calibration models from UV-Vis spectra for toc estimation at the outlet of a fuel park wastewater treatment plant. *Environ. Technol.* **29**(8), 891–898 (2008)
9. Eaton, A.D., Clesceri, L.S., Greenberg, A.E. (eds.): *Standard methods for the examination of water and wastewater*, 19th edn. American Public Health Association, Washington, DC (1995)

Solar Pyramidal Sensor

Paulo Salgado, Beatriz Pereira, Lara Félix and Paulo Afonso

Abstract The use of solar radiation, as a renewable energy source, is a concern and a technological challenge of management and economic profitability. In this context it is paramount the knowledge about the position and movement of the Sun as well as the characteristics of sun radiation. Any new solution is required to bring a higher yield, better forecasting methods and better energy management, with lower technology costs and higher management effectiveness. This paper presents a simple and low-cost approach to determine the elevation and azimuth of the Sun, and the direct and diffuse radiation. This task is performed by a pyramid made of LDR sensor-coated surfaces connected to a microcontroller and a built-in mathematical model to compute the data. This device reads the radiation values of the sensors and sends them to a computer for further analysis, processing and presentation of useful information about the incoming sun radiation.

1 Introduction

Accurate information about the global solar radiation hitting the earth surface is important for many natural and technological systems. Although weather stations can provide reliable records of solar radiation, they usually only record the radiation on the horizontal surface. Solar radiation on undulating terrain requires more

P. Salgado · B. Pereira · L. Félix
Dpt. Engenharias – ECT, Universidade de Trás-Os-Montes e Alto Douro, Vila Real de Santo António, Portugal
e-mail: psal@utad.pt

B. Pereira
e-mail: biapereira3@hotmail.com

L. Félix
e-mail: lara_felix_@hotmail.com

P. Afonso (✉)
ESTGA/Instituto de Telecomunicações, Universidade de Aveiro, Aveiro, Portugal
e-mail: pafnaa@ua.pt

complex calculation due to the high variability of the tilted guidance relative to the Sun [1]. Often this measurement process is incomplete, failing to provide the light direction and radiation components, important information in many real-world applications [2].

Solar radiation data is crucial in various solar-powered applications, such as photovoltaic systems, thermal solar systems and active and passive solar design. They are also needed for the motorization of thermal solar systems and luminosity performance analysis in vertical glass buildings [3] or in agricultural greenhouses [4], but also in open field and in ecological systems modelling [5]. In many such situations monitoring the solar radiation enables the implementation of control strategies so as to make an intelligent use of the energy of the Sun. At the same time this data is useful to engineers in the design of various solar energy conversion devices and for the accurate modelling of solar gains impact through glass, which is especially important when simulating the thermal behaviour of such buildings [6].

The knowledge of the Sun position is essential for numerous areas of science and applications. One of them is monitoring the production and controlling the opening of photovoltaic panels solar blinds in smart homes. For instance, increasing energy production will require a panel with automatic guidance, thus following the solar radiation direction in order to always keep the panel perpendicular to the incident radiation. Also, the new method of monitoring photovoltaic panel system installations can increase the energy production. The performance of these monitoring systems is mostly increased in the early morning and late afternoon, increasing the total amount of power produced by about 20–25 % for a single axis tracker, and about 30–45 % for a dual axis tracker, depending on latitude [7].

For a geographic position on the Earth and for a specific date and hour of the day, there are a set of mathematical equations that provide an exact position of the Sun [8]. With this information in hand, it is theoretically possible to align the photovoltaic panel with the Sun's rays, thus increasing the energy production. However, often weather conditions and erroneous panel's reference orientation compromise the results. For instance, incorrect clock setting and bad orientation of the sensor reference relatively to the geographic North are frequent, particularly in mobile platforms such as robots, caravans, or boats.

The goal of this work is to present a low-cost sensor for the determination of the solar beaming radiation direction and the values of direct and diffuse radiation components, giving an answer to the needs of a wide range of real applications of solar technology. The system is based on a set of 6 LDRs (Light-Dependent Resistors) attached to an equal number of surfaces. These surfaces are oriented so as to cover the entire Sun annual motion on local earth surface horizon. The adopted shape was that of a regular polyhedron [9].

The sensors are electrically connected to the Arduino UNO. The inboard microcontroller reads the sensor signals, processes them to remove noise and erroneous readings, and sends them directly to a computer with MATLAB programming. MATLAB will then take these values and—after more sophisticated processing and data analysis—present an estimation for the elevation and azimuth of the Sun, and the measured direct and diffuse radiation.

This article is organized as follows. The next section characterizes the solar radiation component to be measured by the sensor. The geometric structure of the sensor and its electric configuration is presented in Sect. 3. Here we deduce the fundamental equations that relate the measured values with the intensity of the radiation vector and the diffuse radiation components. Section 4 describes the proposed sensor, namely its functionalities and characteristics. Computational results of the testing and model validation and sensor structure are also shown. The sensor’s performance is analysed and validated by real tests. Finally, we present the necessary conclusions about the proposed sensor’s performance and discuss its real practical merit.

2 Models for Predicting Solar Radiation on Tilted Surfaces

2.1 Radiation Components

The amount of solar radiation that actually arrives at a particular point is called Global or Total Solar Radiation, and it mainly depends on cloudiness, the time of the year, latitude and surface geometry. The global radiation for horizontal surfaces is the sum of direct radiation and diffuse solar radiation that results from light dispersion as it goes through the atmosphere. On foggy days the direct radiation can be a small fraction of overall radiation. A third radiation component, that reflected by mountainous regions or other objects, may also be important.

The Global Solar Radiation incident on inclined surfaces (G_φ) includes the direct (B_φ), diffuse (D_φ), and reflected components (R_φ), linking up as follows:

$$G_\varphi = B_\varphi + D_\varphi + R_\varphi \tag{1}$$

where $\varphi = [\alpha, \beta]$ represents the orientation of the surface.

While the direct radiation is converted into incident radiation on the inclined surface by the simple geometrical relation between two surfaces, the same cannot be said in the case of diffuse radiation. This is because diffuse radiation reaches the surface from all points of the sky except the Sun [2], as depicted in Fig. 1.

Fig. 1 Solar radiation components

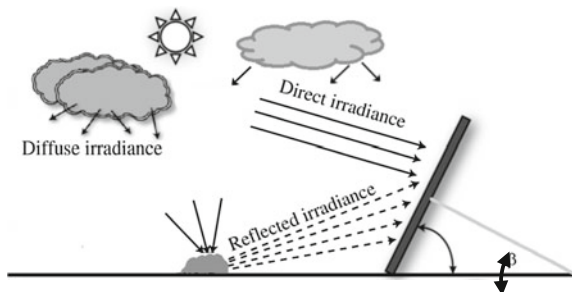
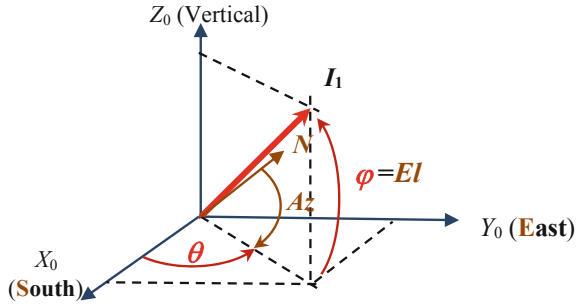


Fig. 2 Representation of the El and Az angles. I_1 is the incident radiation vector



The quantitative evaluation of the incident solar radiation in inclined surfaces is important, for example, for engineers designing the control of photovoltaic panels to find the ideal inclination and azimuth angles. However, note that the Global Radiation received by a surface is largely dependent on atmospheric and topographic conditions.

Direct radiation is characterized by being parallel light rays with a given direction and amplitude. This suggests it may be adequately represented by a vector (I_1), as shown in Fig. 2. The Elevation Angle (El) is the angle of the Sun above the horizon, as seen from the observation point, while the Azimuth (Az) is the angle measured, in the clockwise direction, from the North (N) to the horizontal projection of the line connecting the Sun to the observation point (ISO19115).

From Fig. 2, the direction of vector I_1 can be defined by a pair of angles, azimuth (Az) and elevation (El). These vector components may be given by matrix multiplication of R_z and R_y rotation associated, respectively, with Az e El angles, according to the following matrix equation:

$$\vec{T}_1 = \begin{bmatrix} I_x \\ I_y \\ I_z \end{bmatrix} = \begin{bmatrix} -\cos Az & -\sin Az & 0 \\ \sin Az & -\cos Az & 0 \\ 0 & 0 & 1 \end{bmatrix} \begin{bmatrix} \cos El & 0 & -\sin El \\ 0 & 1 & 0 \\ \sin El & 0 & \cos El \end{bmatrix} \begin{bmatrix} 1 \\ 0 \\ 0 \end{bmatrix} = R_z(Az) \cdot R_y(El) \cdot \hat{e}_x \tag{2}$$

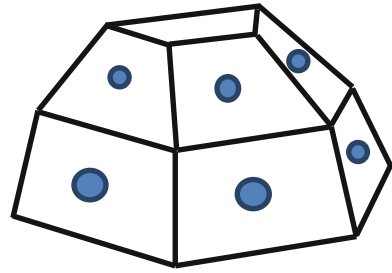
where \hat{e}_x is the unitary vector pointing to the geographic south of the land site. R_z e R_y are elementary rotation matrixes around the z and y axes, respectively.

3 The Sensor Architecture

3.1 Geometrical Shape

The proposed radiation sensor has the shape of a polyhedron, as illustrated in Fig. 3.

Fig. 3 Geometrical shape of the sensor “pyramid”, with six LDRs



For simplicity and evocative reasons, we refer to it—with a certain degree of literary licence—as a “pyramid”. The blue circles are the LDR radiation sensors measuring the radiation intensity on their individual surfaces.

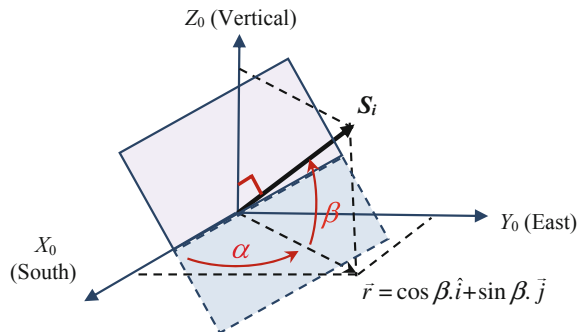
Polyhedron surfaces are represented by vectors perpendicular to the surface plane with a magnitude equal to their areas, which are here considered as unitary. Let $\vec{S}_i = (S_{i,x}, S_{i,y}, S_{i,z})$ be the vector of i th surface associated to the i th LDR sensor (see Fig. 4). This surface has an orientation such that it is misaligned with the South direction by an angle α and it is inclined relative to the horizontal (ground) plane by an angle β .

Taking into account the chosen reference X_0, Y_0, Z_0 , with X_0 aligned with the South direction, the unitary surface vector is given by:

$$\vec{S} = \begin{bmatrix} S_x \\ S_y \\ S_z \end{bmatrix} = \begin{bmatrix} \cos \alpha & -\sin \alpha & 0 \\ \sin \alpha & \cos \alpha & 0 \\ 0 & 0 & 1 \end{bmatrix} \begin{bmatrix} \cos \beta & 0 & -\sin \beta \\ 0 & 1 & 0 \\ \sin \beta & 0 & \cos \beta \end{bmatrix} \begin{bmatrix} 1 \\ 0 \\ 0 \end{bmatrix} = R_z(\alpha) \cdot R_y(\beta) \cdot \hat{e}_x \tag{3}$$

i.e., the vector coordinates are $S_x = \cos \alpha \cdot \cos \beta$, $S_y = \sin \alpha \cdot \cos \beta$ and $S_z = \sin \beta$. In Fig. 4 the surface S and its vector is depicted. The radiation on the surface is the sum of the direct projection of light radiation on the surface [2, 10].

Fig. 4 Surface’s vector (\vec{S}) corresponding to a side of the pyramid



3.2 Radiation Estimation

For a surface vector $\vec{S} = (S_x, S_y, S_z)$ beaming with incoming light intensity I_1 , the received surface energy power is equal to:

$$R_i = \vec{S}_i \cdot \vec{I}_1 = \vec{S}_i^T \vec{I}_1. \tag{4}$$

In other words, R_i is equal to the scalar product between vectors \vec{S}_i and \vec{I}_1 , or the value of the product between the transposed of the vector \vec{S}_i^T (where T is the matrix transpose operator) and vector \vec{I}_1 , in the space of coordinates. The direct radiation is a fraction of the global radiation, $\vec{I}_1 = \delta \vec{I}$, which is a vector with dimensions 3×1 . Added to this power is the value of the diffuse radiation, $I_0 = (1 - \delta)I$, which comes from all direction and reaches with same value all LDR sensors. The measured radiation of i th sensor is given by:

$$R_i = \delta(\cos \alpha_i \cdot \cos \beta_i \cdot I_x + \sin \alpha_i \cdot \cos \beta_i \cdot I_y + \sin \beta_i \cdot I_z) + I_0 \tag{5}$$

with the surface plane of the sensor defined by angles α_i and β_i . Taking into account all sensors values and surfaces, we have the equation:

$$\vec{R} = \bar{R} + \vec{N} \tag{6}$$

where $\vec{R} = [R_1 \ \dots \ R_i \ \dots \ R_n]^T$ is the vector of the measured radiation sensors, \vec{N} is the vector of sensor's error that includes the uncertainly model and the electronic noise of signals, and $\bar{R} = \Omega \cdot \vec{I}_1 + I_0$, with $\Omega = [S_1 \ \dots \ S_i \ \dots \ S_n]^T$ being the $n \times 3$ matrix of vectors of the polyhedron surfaces.

$$\vec{R} = [\Omega \ 1] \cdot \begin{bmatrix} \delta \vec{I} \\ I_0 \end{bmatrix} + noise \quad \text{or} \quad \vec{R} = \Omega \cdot \vec{J} + noise \tag{7}$$

where $\Omega = [\Omega \ 1]$ (the last column being of unit values) and $\vec{J} = [\delta \vec{I} \ I_0]^T$ is a 4×1 matrix of estimations of the direct radiation (the first 3 components) and the diffuse radiation (the last component of the vector).

Our goal is, with the values of 6 sensors (vector coordinates R), to determine the \vec{J} vector (vector of light intensity). This problem can be solved by:

$$\begin{bmatrix} \delta \vec{I} \\ I_0 \end{bmatrix} \approx [\Omega \ 1]^{-1} \cdot \vec{R} \quad \text{or} \quad \vec{J} \approx \Omega^{-1} \cdot \vec{R} \tag{8}$$

if matrix Ω^{-1} exists. However, Ω is not a square matrix ($n \times 4$), unless we have $n = 4$, and so Ω^{-1} does not exist. Only with the pseudo-inverse is it possible to find

a solution that results on the minimization of the sum of squared approximation errors, i.e.:

$$\vec{J} \approx (\Omega^T \Omega)^{-1} \cdot \Omega \cdot ^T \vec{R} \tag{9}$$

Finally, by this estimation of radiation it is possible to estimate the radiation components $\vec{J} = [\delta \vec{I} \ I_0]^T$ and to calculate the Elevation (El) and Azimuth (Az) angles:

$$El = tg^{-1} \left(\frac{I_z}{\sqrt{I_x^2 + I_y^2}} \right) \quad \text{and} \quad Az = \pi - tg^{-1} \left(\frac{I_y}{I_x} \right) \tag{10}$$

This method is used for computing the radiation components, J , and the elevation and azimuth angles of Sun position. Its results are displayed directly in a window of the MATLAB platform.

3.3 Electronic System

The electronic part of the sensor has three components: LDRs; the microcontroller (with Multiplexer; ADC) and a communication USB module. Figure 5 illustrates a scheme of the sensor where the LDRs are connected to an analogue channel of the Arduino board. This reads the radiation values. After some processing, they are sent to the main computer.

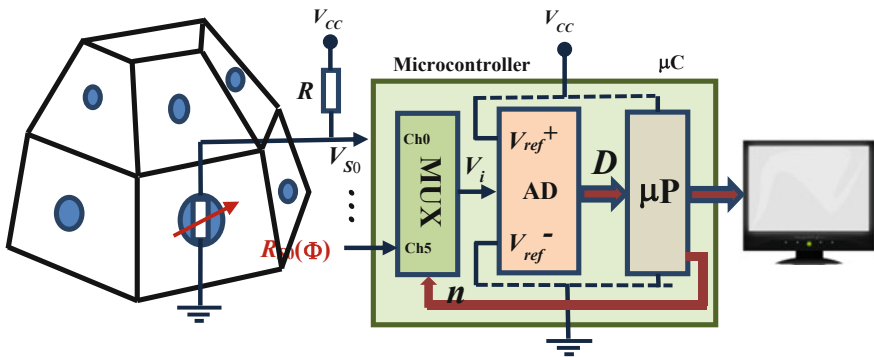


Fig. 5 Schematic illustration of the operation of the sensor

LDR is a light-dependent resistor with characteristic function is given by:

$$R_S = R_0 \Phi^{-\gamma} \quad (11)$$

where Φ is the radiation light, and with model parameters $R_0 = 127,410 \Omega$ and $\gamma = 0.8582$, for the LDRs used. The 10-bit ADC of the ATME1328P microcontroller acquires the voltage V_S of sensor, which depends on value of the LDR resistor, R_S :

$$V_S = \frac{R}{R_S + R} V_{cc} \quad (12)$$

Finally, from the value of ADC conversion, D , the radiation light value is computed by the following equation:

$$\Phi = \left(\frac{R}{R_0} \frac{1023}{D} - 1 \right)^{-\frac{1}{\gamma}} + n \quad (13)$$

where n is the sum of all uncertainty or random errors, such as the quantification error of the ADC and inaccurate values of the resistors and of voltage references.

4 Experimental Results

The Arduino reads the six values of the LDR sensors and sends them to MATLAB via the USB port. After the computation of sensor data, MATLAB displays the information about Elevation angle, Azimuth angle, Direct Radiation, and Diffuse Radiation in a graphical window, as shown in Fig. 6. Also, the Sun position is accordingly adjusted into a 3D graphical model.

During a few days in January 2016 a series of tests were carried out. These showed that, during the early hours of the day, the values given by the sensor were frequently inconstant and often also presented wrong values. The same problem occurred in days of great cloudiness index. On other days or periods of the day the angle errors were within a margin of less than 15° . These results were compared with values given by a NASA program [8]. For all tests, the global radiation of the sensor was in accordance with the values given by the TLS250 sensor of TI Company [11].

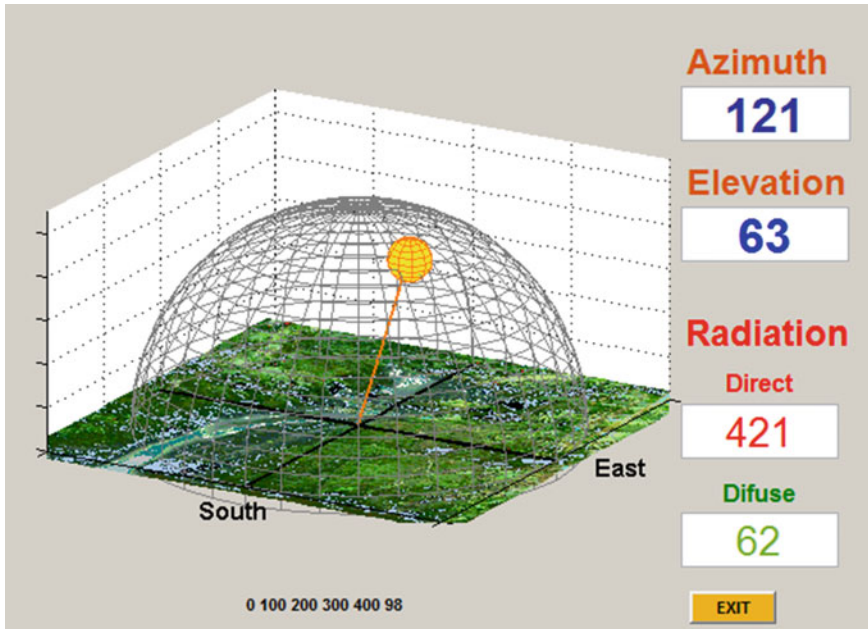


Fig. 6 Diagram illustrating the position of the Sun (according to the cardinal points), depending on the values of Azimuth, Elevation, Direct Radiation, and Diffuse Radiation. The Earth is represented by a half sphere and the Sun, by the *yellow sphere*

5 Conclusions

In this paper we presented a low-cost and feasible sensor for measuring Sun radiation. It is made of six LDR electronic components set on polyhedron faces and an 8-bit microcontroller connected to a PC with MATLAB. This sensor design allows radiation measurements from various directions. By computing these values it was possible to estimate with good approximation the Sun elevation and azimuth angles, as well measure the direct and diffuse components of Sun radiation.

Some tests have been made by comparing the values of *El* and *Az* angles. Their results showed a reasonable agreement between the displayed sensor information and the values given by the mathematical equations for calculating the position of the Sun.

However, the tests should continue, subjecting the sensor to a longer period of work and under more diverse weather conditions. In the near future, the sensor performance in the management and control of photovoltaic panels should also be tested.

References

1. Tian, Y.Q., Davies-Colley, R.J., Gong, P., Thorrold, B.W.: Estimating solar radiation on slopes of arbitrary aspect. *Agr. Forest Meteorol.* **109**, 67–74 (2001)
2. Demain, C., Journée, M., Bertrand, C.: Evaluation of different models to estimate the global solar radiation on inclined surfaces. *Renew. Energy* **50**, 710–721 (2013)
3. Young, C.-H., Chen, Y.-L., Chen, P.-C.: Heat insulation solar glass and application on energy efficiency buildings. *Energy Build.* **78**, 66–78 (2014)
4. Hassanien, R., Hassanien, E., Li, M., Dong Lin, W.: Advanced applications of solar energy in agricultural greenhouses. *Renew. Sustain. Energy Rev.* **54**, 989–1001 (2016)
5. Herrmann-Pillath, C.: Energy, growth, and evolution: towards a naturalistic ontology of economics. *Ecol. Econ.* **119**, 432–442 (2015)
6. Rizvi, A.A., Addoweesh, K., El-Leathy, A., Al-Ansary, H.: Sun position algorithm for sun tracking applications. In: *IECON 2014—40th Annual Conference of the IEEE Industrial Electronics Society*, Dallas, Texas (2014)
7. Gulin, M., Vašak, M., Baotić, M.: Estimation of the global solar irradiance on tilted surfaces. In: *EDPE 2013—International Conference on Electrical Drives and Power Electronics*, Dubrovnik, Croatia (2013)
8. NOAA Solar Calculator, <http://www.esrl.noaa.gov/gmd/grad/solcalc/>
9. Faceira, J.: Sistema de monitorização, diagnóstico e controlo de painéis fotovoltaicos. Master Thesis, Universidade de Trás-os-Montes e Alto Douro, Portugal (2007)
10. Wang, J.: An orientation method and analysis of optical radiation sources based on polyhedron and parallel incident light. *Sci. China Technol. Sci.* **56**, 475–483 (2013)
11. Texas Instruments Company, www.ti.com

Actuator Fault Detection and Isolation Based on Multiple-Model Adaptive Estimation (MMAE)

Diogo Monteiro, Paulo Rosa, Paulo Oliveira and Carlos Silvestre

Abstract This paper proposes the application of Multiple-Model Adaptive Estimation (MMAE) to the detection and isolation of a broad category of actuator faults. An in-depth study on this methodology is provided, including the study of the asymptotic properties of the model probability signals for a non-discrete uncertainty domain. The design of the bank of filters is tackled by a performance-based design algorithm originally developed for the bi-dimensional additive fault model considered. Simulations are performed using a generic linearized model, enabling the validation of the methodology, and confirming the potentialities of the method for both fault diagnosis and estimation under model uncertainty.

Keywords Multiple-Model Adaptive Estimation · Model-based fault detection and isolation · Infinite model adaptive estimation performance

1 Introduction

Safety and reliability of control systems is a long-standing concern and is becoming increasingly important as automated systems start to take a central role in our lives. The occurrence of abnormal events on processes may lead to malfunctions and disasters in ultimate fault conditions, as witnessed in the past. As an example see reports in [1, 2] which explore two severe aircraft accidents that had as primary cause unexpected failures in the control systems. However, it is arguable that if proper diagnosis measures, for an early fault detection, were undertaken, these events would possibly have been avoided by a simple advisory warning or, at an advanced level, a controller reconfiguration. Both from an economic perspective and even more importantly to

D. Monteiro (✉) · P. Oliveira
IST/ISR, Lisbon, Portugal
e-mail: diogo.c.monteiro@tecnico.ulisboa.pt

P. Rosa
Deimos Engenharia, Lisbon, Portugal

C. Silvestre
ECE-FST/UM, Macao, China, on Leave from IST, Lisbon, Portugal

© Springer International Publishing Switzerland 2017
P. Garrido et al. (eds.), *CONTROLO 2016*, Lecture Notes
in Electrical Engineering 402, DOI 10.1007/978-3-319-43671-5_30

prevent threats to humans in safety critical applications, the topic of fault detection and isolation (FDI) has become a research priority across many fields of study. In the last decades, several strategies have been developed on fault diagnosis, as documented in the survey papers [3–5] and books [6, 7], and references therein. Part of that research focuses on observer-based methods, and, more specifically, on multiple-model approaches. Multiple-model strategies may be interpreted as an extension of the observer-based methods, in the sense that all the information about the system process and admissible fault characteristics is used to build a set of dedicated filters, each of which designed for a particular fault scenario. A rising interest on this method is recognized, mainly due to its flexible structure, that allows an intuitive modeling of faults, and the increasing support in modern computers for larger processing loads. Some examples of successful applications of multiple-model FDI methods may be found in [8–10].

In this paper, it is proposed the application of a Multiple-Model Adaptive Estimation (MMAE) system applied to actuator fault detection and isolation. As a contribution to the state-of-the-art practices, a 2D (bi-dimensional) actuator fault model, which define an extended uncertainty domain, is considered. In this way, it is expected that a broader category of faults may be diagnosed and accommodated online. Moreover, the design considered applies a performance-based algorithm which intuitively enables the settling of the bank of filters.

The remainder of the paper is organized as follows: in Sect. 2, the actuator fault model is developed, resembling the most recognized types of actuator faults; in Sect. 3, the MMAE architecture is studied with emphasis on its asymptotic properties; in Sect. 4, an innovative bank design procedure is described for a 2D uncertain domain framework; in Sect. 5, simulations results are discussed for a generic linearized model borrowed from [11]; conclusions are presented in Sect. 6.

About the notation used: regular lower case letters denote scalars, bold lower case letters stand for vectors, and matrices are represented by regular upper case letters.

2 Actuators Fault Model

Four classes of actuator faults [12] are considered in this paper: floating around trim, locked-in-place, hard-over, and loss of effectiveness. One may note that the considered actuator types of faults may be seen as a modification of the system input signals. Hence, a possible additive fault model for each actuator signal may be accomplished by the combination of two scalar parameters: (i) an effectiveness parameter $\lambda \in [0, 1]$ and (ii) an offset parameter $u_0 \in [u_{\min}, u_{\max}]$ such that the system input vector \mathbf{u} is given by

$$\mathbf{u}(t) = \Lambda \mathbf{u}_c(t) + \mathbf{u}_0 \quad (1)$$

with $\Lambda = \text{diag}([\lambda_1, \lambda_2, \dots, \lambda_m])$ and $\mathbf{u}_0 = [u_{01}, u_{02}, \dots, u_{0m}]^T$, where m is the number of actuators and \mathbf{u}_c the control input vector, generated by the nominal controller.

3 Multiple-Model Adaptive Estimation (MMAE)

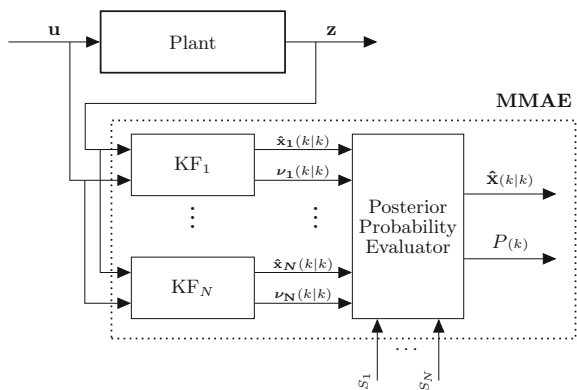
The Multiple-Model Adaptive Estimation (MMAE) technique is a model-based estimation approach specially suitable for linear systems subject to parameter uncertainty. If some information is known about the uncertain parameter, such as its domain of uncertainty, then a multiple-estimator bank structure may be designed covering an adequate range of possible models. A specific probability analysis tool may then be applied to analyze the local state-estimation and associated innovations, for a stochastic setting, generated by each estimator in order to obtain the optimal combined estimation. The architecture of the aforementioned technique is shown in Fig. 1.

Recall that in a scenario without parameter uncertainty, the Kalman filter (KF) is the optimal state-estimation filter, as shown in [13], under mild assumptions on the disturbances and measurement noise. It is also known that under those conditions and some linear-Gaussian assumptions the KF provides the true conditional mean and covariance of the state vector given the past control inputs and observations. Therefore, based on the previously given assumptions about the uncertain parameters set, each estimator of the bank may be designed as a KF tuned for a certain admissible parameter vector.

Besides the bank of KFs, the MMAE has in its structure a Posterior Probability Evaluator (PPE) which owns the responsibility of assessing the estimation performance of each filter at every time-step. This performance information is provided as the conditional probability of each estimator model to match the true system, given the past sequence of measurements and inputs. The global state-estimate provided by the MMAE is then the posterior probabilities weighted sum of each local estimate [14].

Note that system faults may be interpreted as uncertainties in the model. Thus, the MMAE turns out to be an interesting tool under the scope of fault detection and isolation. Accordingly, consider a discrete-time, Linear Time-Invariant (LTI),

Fig. 1 Multiple-Model Adaptive Estimation (MMAE) architecture



Multi-Input/Multi-Output (MIMO) system subject to actuator uncertainties in line with the actuator fault model described in Sect. 2.

$$\mathbf{x}(k+1) = A\mathbf{x}(k) + B \left(A^\kappa \mathbf{u}(k) + \mathbf{u}_0^\kappa \right) + G\mathbf{w}(k) \quad (2a)$$

$$\mathbf{z}(k) = C\mathbf{x}(k) + \mathbf{v}(k) \quad (2b)$$

where $\mathbf{x}(k) \in \mathbb{R}^n$ denotes the system state, $\mathbf{u}(k) \in \mathbb{R}^m$ its control input, $\mathbf{z}(k) \in \mathbb{R}^q$ the measured output, $\mathbf{w}(k) \in \mathbb{R}^n$ the disturbance input, and $\mathbf{v}(k) \in \mathbb{R}^q$ the measurement noise. The noise vectors, which are assumed white noise Gaussian sequences, satisfy the relations $\mathbf{E}\{\mathbf{w}(k)\} = 0$, $\mathbf{E}\{\mathbf{w}(k)\mathbf{w}(t)^T\} = Q\delta_{kt}$, $\mathbf{E}\{\mathbf{v}(k)\} = 0$, and $\mathbf{E}\{\mathbf{v}(k)\mathbf{v}(t)^T\} = R\delta_{kt}$. A , B , and C are the state, input, and output matrices of appropriate dimensions, respectively. Matrix A^κ and vector \mathbf{u}_0^κ are unknown and define the uncertain parameters of system in Eq. (2) that belong or are “close” to a finite discrete parameter set, $\kappa := \{\kappa_1, \kappa_2, \dots, \kappa_n\}$ indexed by $i \in \{1, 2, \dots, N\}$ which characterize the tuning points of the bank of KFs. The MMAE approach suggests that the global estimate is given by

$$\hat{\mathbf{x}}(k|k) = \sum_{i=1}^N P_i(k) \hat{\mathbf{x}}_i(k|k) \quad (3)$$

where $P_i(k)$ stands for the conditional posterior probability of $\kappa_i = \kappa$, i.e. that i^{th} estimator’s model matches the true system dynamics. It can be shown that, if $\kappa \in \kappa$, Eq. (3) represents the true conditional expectation and conditional covariance of the state estimate [15].

3.1 Posterior Probability Evaluator (PPE)

The central element of the MMAE is the previously mentioned Posterior Probability Evaluator (PPE), which is responsible for computing the posterior conditional probability of each model, at every instant, to match the real one. As shown in [14], the recursive law that relates the *posterior* $P_i(k+1)$ with the *prior* $P_i(k)$ is given by

$$P_i(k+1) = \left(\frac{\zeta_i(k+1) e^{-\frac{1}{2}\omega_i(k+1)}}{\sum_{j=1}^N \zeta_j(k+1) e^{-\frac{1}{2}\omega_j(k+1)} P_j(k)} \right) \cdot P_i(k) \quad (4)$$

with $\zeta_i(k+1) \equiv \frac{1}{(2\pi)^{\frac{m}{2}} \sqrt{\det S_i(k+1)}}$ and $\omega_i(k+1) \equiv \mathbf{v}_i(k+1)^T S_i(k+1)^{-1} \mathbf{v}_i(k+1)$ for a given initial *prior* $P_i(0)$, where $S_i(k)$ denote the design covariance of the filter innovations $\mathbf{v}_i(k)$, i.e. the value of $\mathbf{E}\{\mathbf{v}_i(k)\mathbf{v}_i(k)^T\}$, should the real model satisfy $\kappa = \kappa_i$.

3.2 Convergence Properties

This section details the asymptotic properties of the MMAE. Due to the actuator fault model considered, it is straightforward to conclude that the admissible models define an infinite set and, thus, impossible to be fully included in the estimators' bank. As a consequence, it becomes particularly interesting to study the convergence behaviour of Eq. (4) in the case that the faulty model of the system does not belong to the set of models in the bank of estimators. In [16, p. 274], it is shown that the MMAE will converge to the closest matching model in a probabilistic sense, defined by

$$\beta_j^i = \ln(\det S_j) + \text{Tr}(S_j^{-1} \Gamma_j^i) \quad (5)$$

where Γ_j^i denotes the actual limiting mean-squared innovations of filter j if model κ_i holds as the true one. This equation is also commonly referred to as the Baram Proximity Measure (BPM) [17–19] and plays an important role within the MMAE bank design discussed in Sect. 4. In other words, one may say that if the uncertain parameter κ_i is the representation of the true model, then the MMAE governed by Eq. (4) will converge to the c^{th} filter whose BPM satisfies $\beta_c^i = \min_j \beta_j^i \quad \forall j \in \{1, 2, \dots, N\}$. Moreover, it is stressed that, in this scenario, Eq. (3) provides no longer the true conditional expectation and conditional covariance of the state estimate, but still the most truthful expectation owing the convergence result discussed in this section.

4 Multiple-Model Bank Design

As stated earlier, the actuator fault model considered leads to an infinite uncertain parameters set. From this set, one shall pick N admissible values which will be the tuning parameters of the N KFs. In what follows, two main questions arise in this design process

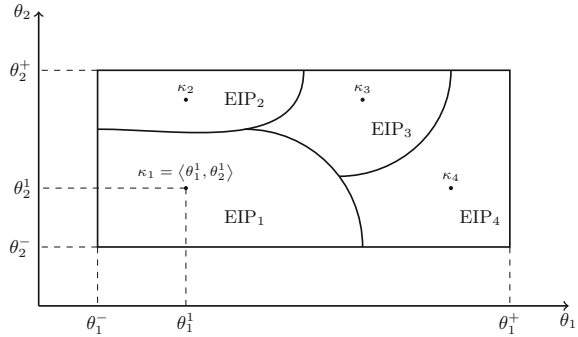
1. What should be the size of the representative parameter set given by N ?
2. How can one establish the representative parameter set κ ?

Before facing the design problem to answer these two questions, let be introduced the important concept of EIP and discuss two relevant details about the estimators' bank properties.

4.1 Equivalently Identified Plants (EIP)

The fault domain assumed is infinite, meaning that most of the admissible models will not be represented in the model set. However, from the convergence results presented in Sect. 3.2, one knows that the closest matching model (in a probabilistic

Fig. 2 Equivalently Identified Plants (EIP)



sense defined by the BPM metric) will have its probability, say P_i , converging to 1 while the others, $P_j \quad \forall j \neq i$, will converge to 0. This property encloses the definition of regions in the uncertain parameter domain that are characterized by the model which is converged given all the admissible parameters and the representative set κ . Each of these regions is called the set of Equivalently Identified Plants (EIP) [20]. An exemplification of this representation is given in Fig. 2, considering a bi-dimensional limited parameter uncertainty, which is equivalent to the design problem at hand.

4.2 Equivalent Kalman Filter Dynamics

Given the system model in Eq. (2), it is clear that the uncertain parameters only affect the control input elements, meaning that the KF dynamics are equivalent for every tuning parameter in the model set. Recall that the KF minimizes the estimation error covariance considering the stochastic inputs, given by $w(k)$ and $v(k)$. Since the system dynamics matrix A and matrix G are not affected, the transfer function from the noise inputs to the estimation error is not modified for any admissible uncertain parameters in set κ . Moreover, given that the system is time-invariant from the filters perspective and under a few additional assumptions [21], in steady-state the Kalman gain is constant and the filter dynamics is also time-invariant. Similarly, the steady-state estimation error and innovation covariance matrices are again constant. As a consequence of this analysis, the optimal performance of every EIP_i is equivalent, occurring when $\kappa = \kappa_i \quad \forall i \in \{1, 2, \dots, N\}$.

4.3 Independent Bank Design per Actuator

We finally stress that our design procedure considers each actuator individually, i.e. for every model the uncertain domain is characterized by only two scalar uncertain parameters λ_j and u_{0j} with $j \in \{1, 2, \dots, m\}$ indexing the actuator under analysis.

The reason for this strategy lies in the convenience of performing the bank design in a \mathbb{R}^2 domain, rather than a larger dimension domain. Observe that this is one of the highest contributions of the present paper, as the state-of-the-art studies explored on this matter only consider the single dimension problem. The final approach is to build the bank of KFs by the union of the sub-banks designed for each actuator fault model.

4.4 Design Procedure

Having discussed the relevant preliminary aspects in the prequel, we shall now focus on the design procedure. The first step towards this design is to reason that the ideal way to deal with the questions stated in the beginning of the section would be to find a performance measure that could permit the definition of the discretized representative parameter set κ in a systematic procedure. In [20], the author suggests a performance-based model set design strategy for the MMAE, in a one dimension parameter vector framework. The presented strategy introduces the concept Infinite Model Adaptive Estimation Performance (IMAE) index which provides the best performance in terms of BPM considering an ideal bank design with $N \rightarrow \infty$. The IMAE may be obtained by computing S_i in Eq. (5)

$$\beta_i^i \equiv \beta_i = \ln(\det S_i) + \frac{q}{2} \tag{6}$$

where q stands for the dimension of the measurement vector $\mathbf{z}^{(k)}$, as identified in Eq. (2). In fact, this corresponds to the scenario of having the true parameter vector $\kappa = \kappa_i$, being κ_i part of the representative parameter set κ . The designer input to this approach is provided as a percentage of Eq. (6), $x\%$ IMAE, which defines the worst admissible performance. Consequently, every covered parameters, given by κ_i , in a EIP region, say EIP_j , must satisfy $\beta_i \leq \beta_j^i \leq x\% \beta_i$. As an example see Fig. 3, which considers a one dimension parameter vector known to be inside a domain region limited by κ^- and κ^+ . The algorithm starts in one of the domain limits, and progressively computes the BPM values until it reaches the opposite limit with a minimum number models that satisfy the performance interval imposed by the $x\%$ IMAE curve. As a consequence of the design strategy introduced, we are able to easily answer both questions presented in the beginning. Moreover, this performance-based design provides an intuitive manner of interpreting the design process.

Recall that in a bi-dimensional uncertain parameter domain, which characterizes the fault model in Eq. (1), the BPM curves will become surfaces. Although the baseline idea is preserved, this fact leads to an adaptation of the performance-based algorithm exploited. The first aspect to notice is that the intersection between two surfaces is a curve and no longer a point as depicted in Fig. 3. A second challenge imposed is that it is no longer straightforward how to define a progression direction between each defined model. Therefore, a few additions and small modifications are

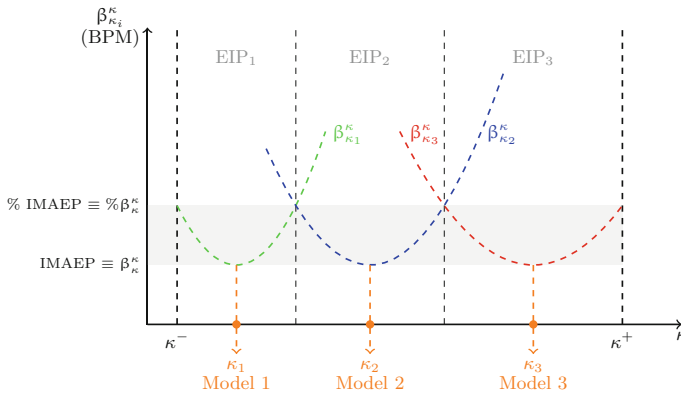


Fig. 3 Representative parameter set definition via IMAEP approach for a one-dimension uncertainty parameter domain

required. It is immediate that the nominal model must be included since faults are, generally, assumed to be infrequent. Hence, this is defined as the initial point for the model set “search” problem. It what follows, a fair progression direction to be assumed is the straight line connecting the nominal parameter vector point κ_0 and one of the most extreme¹ fault models to be admitted, $\kappa_e^+ = \langle 0, 1 \rangle$ or $\kappa_e^- = \langle 0, -1 \rangle$. The defined strategy is illustrated in Fig. 4. Obviously this design procedure admits an infinity of variations considering the 180° window from the nominal point, hence no guarantees are given in terms of minimization of the model set size for a given performance criterion. It should be mentioned that no similar bi-dimensional uncertainty MMAE bank design problem was found in the investigated literature. It is, therefore, an interesting topic for future research due to its relevance. Note that the approximated uncertainty domain considered, and revealed in Fig. 4 by parameter λ_e , is due to the stability conditions imposed in the computation of the BPM, see [12] for details. Finally, it is stressed that the symmetry nature on the λ axis, for the computation of the mean-squared innovations of the filters, causes to be indifferent the choice between the two alternative progression directions presented in Fig. 4.

4.5 Design Results

The results obtained from the estimators’ bank design are now presented. Due to the independence of design of each actuator, we only considered in this process the δ_B actuator of the system treated [11], which is deemed sufficient to validate the developed technique. Two distinct performance criteria were chosen: 80 % IMAEP and

¹The word extreme is used here in the sense that those points provide the largest norm difference to the nominal model in the uncertain parameter vector domain, i.e. $\|\kappa_e - \kappa_0\|_2 > \|\kappa - \kappa_0\|_2 \forall \kappa \neq \kappa_e$.

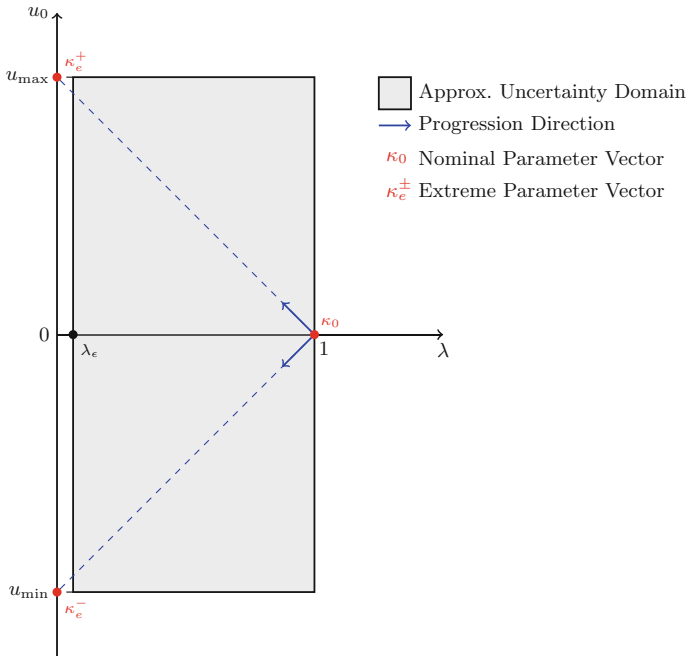


Fig. 4 Model-set design strategy illustration

Table 1 Model set obtained for a 50 % IMAEP minimum performance criterion

	κ_0	$\kappa_{1/2}$	$\kappa_{3/4}$	$\kappa_{5/6}$	$\kappa_{7/8}$
λ	1	0.53	0.28	0.15	0.10
u_0	0	± 0.47	± 0.72	± 0.85	± 0.90

50 % IMAEP. As expected, the former criterion revealed the need for a larger amount of filters, 15 in total, whereas when defining 50 % IMAEP as minimum performance 9 filters were obtained. Table 1 provides the exact location of each parameter vector for 50 % IMAEP design, that is to be applied in the forthcoming section.

5 Experiments on Simulation Environment

This section aims to present the results of the simulations tests performed on the MMAE approach. On this battery of simulations the estimators' bank designed with a 50 % IMAEP criterion was applied and run for about 300 s along with the incidence of 4 distinct abrupt faults, randomly chosen, at different instants. These faults are clearly characterised in Table 2 and associated locations on the EIP regions are

Table 2 Faults description

	Fault 1 (F#1)	Fault 2 (F#2)	Fault 3 (F#3)	Fault 4 (F#4)
λ	0.60	0.50	0.80	0.15
u_0	0.47	-0.90	0	0.7
EIP	1	4	0	5
Occurrence time	30–60 s	90–120 s	150–180 s	210–240 s

shown in Fig. 5 in blue. In the time between the faults incidence, which lasts 30 s for each, the nominal model is applied.

For this simulation setup, two main assessment goals were settled: (i) evaluate the identifiability of the models by verifying the conditional posterior probability convergence to different models along with the faults incidence and removal and (ii) compare the converged models with the expected results arisen from the estimators' bank design.

Figure 6 displays the conditional posterior probability of each of the nine models included in the bank of KFs. Analyzing the initial moments, one may see that the system clearly identifies the nominal model as the true one, until the first fault (F#1) occurrence at time 30 s. Although the convergence to the 1st KF is achieved rapidly,

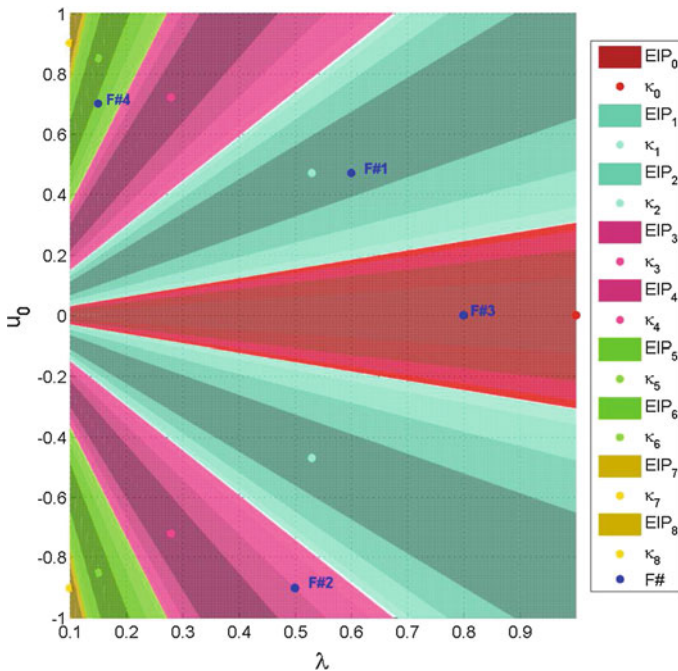


Fig. 5 Faults on the EIP regions graph

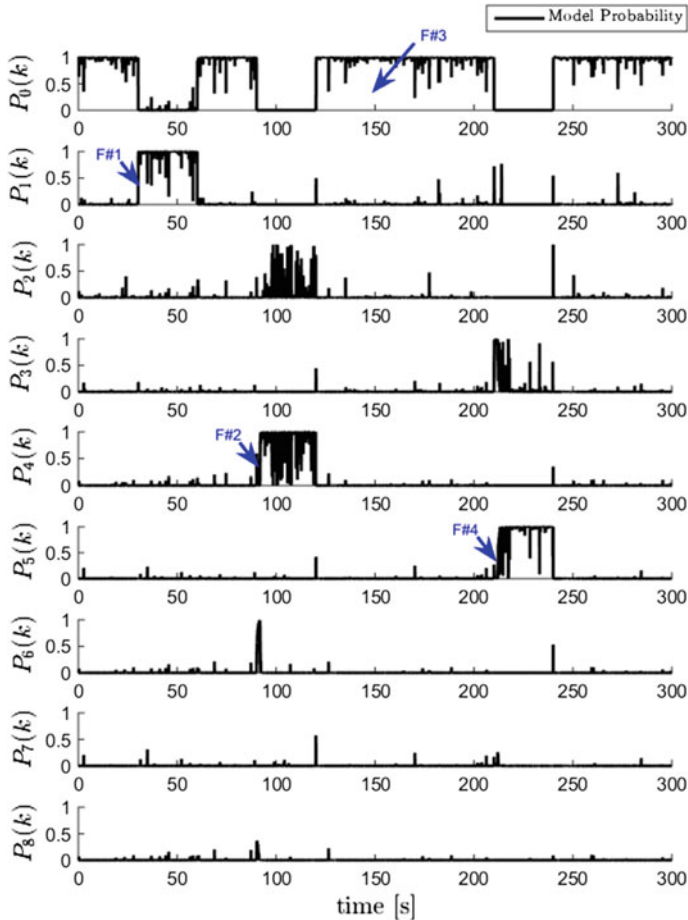


Fig. 6 Conditional posterior probability of each model

some oscillations during the fault incidence period are noticed. Fault 2 (F#2) occurs at time 90 s and a probability convergence is also verified for model 4. In this case, the oscillatory behaviour is even more evident due to a frequent probability exchange with model 2. Note that the closest non-overlapping EIP region to fault 2 parameter vector is, indeed, EIP_2 . Fault 3 (F#3) is specially interesting because its parameter vector is located in the same EIP region as the nominal model. Therefore, from time 120 s to 210 s, $P_0(k)$ is kept closer to 1, despite the fault incidence at time 150 s. Finally, fault 4 (F#4) causes an initial convergence to model 3, which is the closest non-overlapping EIP region. Still, a few seconds later (≈ 5 s) the identification of model 4 is attained matching the expectations of the bank design.

6 Conclusions

This paper considered the problem of actuator FDI by applying a strategy of multiple-model adaptive estimation, in which each model is tuned to a certain admissible fault. A full performance-based design strategy is developed for a 2D uncertainty domain defined by an additive actuator fault model. The performed experiments showed that the MMAE approach allows to clearly identify different models under distinct fault occurrences. Despite this fact, an oscillatory behaviour of the conditional probabilities was verified. As a consequence, the analysis of these probabilities requires proper care, with emphasis on the initial instants of a fault incidence.

It should be also noted that the MMAE approach, as designed in this paper, only allows for the domain region identification of the incident fault parameters. It is, therefore, suggested for future research the development of a system capable of clearly identifying the λ and u_0 , in a robust framework with proven convergence results, inline with what is presented in this paper. A possible approach to this problem, but not ideal, is to consider a larger model set for the MMAE design, with the drawback of a higher computational load.

Finally, it is stressed that the developed research resulted in a powerful system design for state estimation under parameter uncertainty. Note that a good state estimation is crucial for the performance of the control systems, which is aimed to be adapted on the long run under a fault occurrence scenario.

References

1. Cornelius, J.D., Orr, J.S., Barshi, I., Statler, I.C.: A Comprehensive Analysis of the X-15 Flight 3–65 Accident. Technical Report, October, National Aeronautics and Space Administration (NASA), Langley Research Center (2014)
2. NTSB. Loss of Control and Impact with Pacific Ocean Alaska Airlines Flight 261. Technical report, National Transportation Safety Board (NTSB) (2000)
3. Visinsky, M., Cavallaro, J., Walker, I.: Robotic fault detection and fault tolerance: a survey. *Reliab. Eng. Syst. Safety* **46**(2), 139–158 (1994)
4. Isermann, R.: *Fault-Diagnosis Systems*. Springer, Berlin Heidelberg (2006)
5. Hwang, I., Kim, S., Kim, Y., Seah, C.E.: A survey of fault detection, isolation, and reconfiguration methods. *IEEE Trans. Control Syst. Technol.* **18**(3), 636–653 (2010)
6. Chen, J.: Robust residual generation for model-based fault diagnosis of dynamic systems. Ph.D. thesis, University of York, UK (1995)
7. Chen, J., Patton, R.J.: Robust model-based fault diagnosis for dynamic systems. In: *Kluwer International Series on Asian Studies in Computer and Information Science*. Kluwer Academic Publishers (1999)
8. Maybeck, P.S.: Multiple model adaptive algorithms for detecting and compensating sensor and actuator/surface failures in aircraft flight control systems. *Int. J. Robust Nonlinear Control* **1051–1070**, 1999 (1070)
9. Hallouzi, R.: Multiple-model based diagnosis for adaptive fault-tolerant control. Ph.D. thesis, Technical University of Delft (2008)
10. Jacques, G., Ducard, J.: Fault-tolerant flight control and guidance systems for a small unmanned aerial vehicle. Ph.D. thesis, ETH Zurich (2007)

11. Hess, R.: Analytical assessment of performance, handling qualities, and added dynamics in rotorcraft flight control. *IEEE Trans. Syst. Man Cybern. Part A Syst. Hum.* **39**(1), 262–271 (2009)
12. Monteiro, D.: Fault detection and isolation for linear dynamical systems. Master's thesis, Instituto Superior Técnico, Lisboa, Portugal (2015). <https://goo.gl/7CPP8g>
13. Kalman, R.E.: A new approach to linear filtering and prediction problems. *J. Basic Eng.* **82**(1), 35 (1960)
14. Athans, M., Chang, C.-B.: Adaptive Estimation and Parameter Identification Using Multiple Model Estimation Algorithm. Massachusetts Institute of Technology Lincoln Lab, Technical report (1976)
15. Athans, M.: Lecture notes: Multiple-Model Adaptive Estimation (MMAE) (2001)
16. Anderson, B.D.O., Moore, J.B.: Optimal Filtering. Prentice-Hall (1979)
17. Baram, Y.: Information, consistent estimation and dynamic system identification. Ph.D. thesis, Massachusetts Institute of Technology (1976)
18. Baram, Y., Sandell, N.R.: An information theoretic approach to dynamical systems modeling and identification. In: Decision and Control including the 16th Symposium on Adaptive Processes and A Special Symposium on Fuzzy Set Theory and Applications, 1977 IEEE Conference on, pp. 1113–1118 (1977)
19. Fekri, S., Athans, M., Pascoal, A.: Issues, progress and new results in robust adaptive control. *Int. J. Adapt. Control Signal Process.* **20**(10), 519–579 (2006)
20. Hassani, V., Aguiar, A.P., Athans, M., Pascoal, A.M.: Multiple model adaptive estimation and model identification using a minimum energy criterion. In: American Control Conference (ACC), pp. 518–523 (2009)
21. Ribeiro, M.I.: Kalman and Extended Kalman Filters: Concept. Derivation and Properties. Technical report, Institute for Systems and Robotics Lisboa Portugal (2004)

Part VI

Robotics

Wheels for Staircases

Fátima Silva Leite, Jorge Batista, Krzysztof Krakowski, André Carvalho,
Tiago Cruz, Eduardo Domingues, André Lizardo and Gonçalo Saraiva

Abstract Our objective is to design innovative robot wheels capable of rolling on staircases, without sliding and without bouncing. This is the first step to reach the ultimate goal of building wheelchairs capable to overcome the obstacles imposed by staircases on people with limited mobility. We show that, given a staircase with equal steps, there is an infinite number of wheels that roll over it, with the constraints of no-sliding and no-bouncing. Some of these wheels appear to be very interesting for real applications. We also present an algorithm for the construction of a wheel, which depends only on the measures of the tread (the part of the staircase that is stepped on) and the riser (the vertical portion between each tread) of the step.

Keywords Robot wheels · Stairs climbing wheels · Rolling · Bouncing · Sliding · Bernoulli spirals

F.S. Leite (✉) · J. Batista · K. Krakowski
Institute of Systems and Robotics, University of Coimbra,
3030-290 Coimbra, Portugal
e-mail: fleite@mat.uc.pt

F.S. Leite · T. Cruz · G. Saraiva
Department of Mathematics, University of Coimbra,
3001-501 Coimbra, Portugal

J. Batista · E. Domingues
Department of Electrical Engineering and Computers, University of Coimbra,
3030-290 Coimbra, Portugal

K. Krakowski
Wydział Matematyczno-Przyrodniczy, Uniwersytet Kardynała Stefana
Wyszyńskiego, ul. Dewajtis 5, 01-815 Warsaw, Poland

A. Lizardo
Department of Informatics Engineering, University of Coimbra,
3030-290 Coimbra, Portugal

A. Carvalho
Department of Electrical Engineering and Computers, University of Lisbon,
1049-001 Lisboa, Portugal

1 Introduction

Mobile robot technology is playing a key role in order to provide increased freedom in terms of mobility for the elderly or disabled. Wheelchairs are one of the most commonly used assistive devices for mobility of people within their homes and communities, but stairs are also a symbol of inaccessibility.

Over the years, a multitude of mechanisms have been developed to improve robots mobility in environments having stairs. For instance, wheel-based robots are simple in design and control but not appropriate to surmount risers higher than their wheel radius. In contrast, tracked-type robots can climb over higher risers, but require complex control strategies, move slowly, and are not particularly oriented to indoor environments. The Kenaf robot [1] and the TAQT robot [2] are examples of tracked-type robots. Legged robots, such as Honda's ASIMO [3, 4], AIST's HRP [5], and Waseda University legged robot [6] are examples of mechanisms well suited for climbing stairs, but require a complex control involving multiple degrees of freedom. Exploring the advantages of the previous, several hybrid configurations have been proposed. Using six motorised wheels, the rover Shrimp [7] can easily move in rough terrain, also showing good climbing and steering capabilities. Combining wheels and legs, the Charibe robot [8] takes advantages of its wheels to move over flat terrain and of its legs to overcome rough terrain such as steps and stairs. Using compliant rotary legs, the RHex robot [9] can efficiently move up and down stairs, being also appropriate to other types of rough terrains. Other more complicated mechanisms have been proposed, such as articulated snake-like robots [10] that can climb stairs through shape adaptation. In spite of the quality of these devices, if the focus is to carry human beings smoothly and without bouncing up and down stairs, other issues must be taken into account.

A large list of stair mobility assistance mechanisms can be found in the literature, spanning a broad set of solutions. The Galileo wheelchair [11] is a hybrid solution that combines wheels and tracks in a single vehicle with good stair-climbing ability. The PW-4×4Q [12] is another stair-climbing wheelchair which is able to handle difficult terrains, climb up and down stairs and overcome steep slopes. Combining wheels and tracks, the Topchair-S [13] is capable of autonomously cope with straight stairs and other obstacles. The iBOT wheelchair [14] is one of the few purely wheel-based solutions that gives wheelchair drivers some automated support to overcome stairs. This is done by rotating its two sets of powered wheels about each other, much like rack and pinion with the two wheels as the "teeth" of the gear.

The aforementioned wheelchairs are certainly interesting, but most of them have complex design, are not particularly oriented to indoor environments and, most importantly, don't guarantee a smooth motion and the constraints of no-bouncing.

Our objective is to contribute to the ultimate goal of building wheelchairs with the ability to overcome the obstacles imposed by staircases. The first step to reach such an important goal is the design of wheels capable of rolling on stairs, without sliding and without bouncing. The latter condition provides comfort to the driver. We will show that given a staircase there is an infinite number of exotic wheels that

perform that task nicely. Most of them have no practical use due to its size when compared with the size of the steps, but some provide interesting solutions to real stair climbing wheelchairs. In order to accomplish our goal we first formulate the problem mathematically, identifying staircases and wheels with their vertical cross sections, so that they are represented by plane curves, and then find the equations of rolling with the constraints of no-sliding and no-bouncing. Our inspiration came from the interesting work of Hall and Wagon [15] where one can find the design of a wheel for a staircase with tread and riser having the same measure. As far as we know, the more general and difficult situation when the riser and tread are unequal has not appeared in the literature before. As it will become clear throughout the text, the wheels will be composed of pieces of Bernoulli spirals, which are equiangular plane curves studied by Jacob Bernoulli (1654–1705). Recently, we became aware of the work of Modak and Bhoomkar [16], where an innovative graphical design of wheels for staircase climbing wheelchairs is proposed. This paper includes drawings of wheels that resemble some of those that we will generate later on. Although quite ingenious, there is no mathematics that supports their results. This is in contrast to our detailed mathematical analysis. The organisation of the paper is as follows. In Sect. 2, we formulate mathematically the problem of pairing a wheel with a flat road represented by a straight line, and then move to the problem of finding a wheel for a staircase (a road composed of straight line segments meeting at right angles). In Sect. 3 we include all the necessary ingredients and results that lead to the design of wheels for staircases. Section 4 contains the main result and an algorithm to construct the wheels given the tread and riser of the step. The paper ends with final remarks and conclusions.

2 Pairing Roads and Wheels

We start with the more general case of pairing roads and wheels, studied by Hall and Wagon in [15]. Roads and wheels are represented by curves in the xy -plane, the roads being graphs of functions given by their parametric equations and wheels given in polar coordinates. The rolling motion of the wheel over the road is a rigid motion subject to some constraints. The pair road/wheel must have a point of contact during the whole motion, sliding is forbidden and no-bouncing is required.

2.1 *The Mathematics of the Rolling Motion*

Let I_1 and I_2 be real time intervals. A road is a curve given by parametric equations $x = x(t)$, $y = y(t)$, $t \in I_1$, while a wheel is a curve given in polar equations $r = r(\theta)$, $\theta \in I_2$. Without loss of generality we may assume that at the beginning of the motion ($t = 0$) the wheel is centered at the origin and the point of contact between the road and the wheel has coordinates $(0, -y_0)$, with $y_0 > 0$, so that

$x(0) = 0, y(0) = -y_0, \theta(0) = -\frac{\pi}{2}$. We also assume that the road is always located below the x-axis and that during the motion the center of the wheel stays on that axis.

No-sliding means that at each instant of time the distance travelled on the road equals the amount unravelled on the wheel. That is, $\forall t \in I_1$,

$$\int_0^t \sqrt{\left(\frac{dx}{dt}\right)^2 + \left(\frac{dy}{dt}\right)^2} dt = \int_{-\frac{\pi}{2}}^{\theta(t)} \sqrt{(r(\theta))^2 + \left(\frac{dr}{d\theta}\right)^2} d\theta. \tag{1}$$

No-bouncing means that, at every point of contact, the radius of the wheel coincides with the depth of the road. That is, $\forall t \in I_1$,

$$r(\theta(t)) = -y(t). \tag{2}$$

Hall and Wagon have shown in [15] that given the parametric equations of a road it is enough to use the constraints to obtain the equation of the corresponding wheel. More precisely, the no-sliding constraint breaks down to the following initial value problem:

$$\frac{d\theta}{dt} = -\frac{1}{y(t)} \frac{dx}{dt}, \quad \theta(0) = -\frac{\pi}{2}. \tag{3}$$

After obtaining $\theta(t)$, one must invert this function to get $t(\theta)$, and then use the no-bouncing constraint to get $r(\theta) = -y(t(\theta))$.

If the road is given by a cartesian equation $y = f(x)$, the parametrisation $x(t) = t, y(t) = f(t)$, reduces (3) to

$$\frac{d\theta}{dt} = -\frac{1}{y(t)}, \quad \theta(0) = -\frac{\pi}{2}. \tag{4}$$

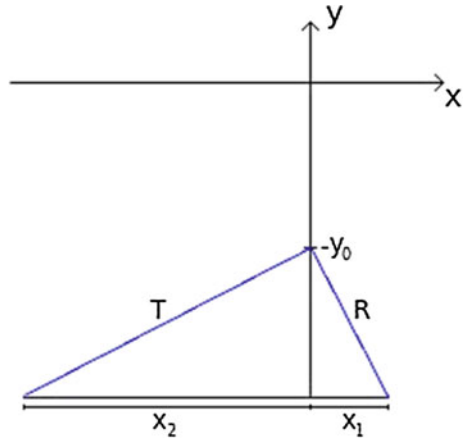
3 Building a Wheel for the Staircase

Before solving this problem, we look to the simpler problem of finding the wheel for a straight line road with nonzero slope. According to the end of the previous section, it is straightforward to prove the following result.

Proposition 1 *If $y(x) = -y_0 - mx$ is the equation of a road, then $r(\theta) = y_0 e^{(\theta+\pi/2)m}$ is the polar equation of the corresponding wheel.*

Remark 1 The wheel given by the previous equation is a Bernoulli spiral, which is not a closed curve. Bernoulli spirals possess the *equiangular* property, which means that at every point the angle that the radial line makes with the tangent line is an invariant for each spiral. As will be shown later, the wheel for the staircase is a

Fig. 1 One step of the staircase



closed curve, composed of several Bernoulli spirals, which resembles the petals of a flower.

We now proceed with the problem of finding a wheel for the staircase. To simplify notations and computations, we lay down the staircase so that the hand rail, or the pitch, is parallel to the x-axis. By doing this, we are reduced to the situation described in the last section. Let T and R denote the tread (the horizontal section of each step) and the riser (the vertical section of each step), respectively. Without loss of generality we assume that the staircase is the graph of a periodic function, given in cartesian coordinates by

$$y(x) = \begin{cases} y_1(x) = -y_0 - mx, & x \in [0, x_1] \\ y_2(x) = -y_0 + \frac{1}{m}x, & x \in [-x_2, 0] \end{cases}, \tag{5}$$

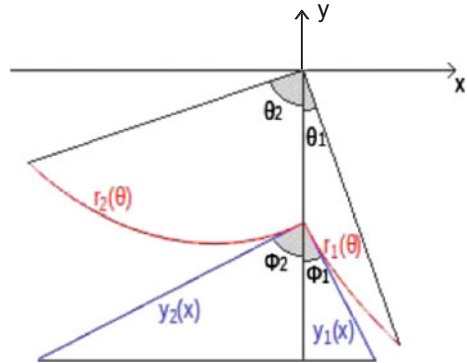
where x_1, x_2 and m are positive real numbers, depending on T and R and, as before, $y_0 > 0$. In particular, $m = T/R$. Note that the straight line segments given by y_1 and y_2 are perpendicular. Figure 1 below shows the first step of the staircase, where the previous positive quantities have been marked.

3.1 Building the Portion of the Wheel for the First Step

Using Proposition 1, one can conclude that part of the wheel rolling on the first step, given by (5), has polar equation

$$r(\theta) = \begin{cases} r_1(\theta) = y_0 e^{m(\theta + \frac{\pi}{2})}, & \theta \in [-\frac{\pi}{2}, -\frac{\pi}{2} + \theta_1] \\ r_2(\theta) = y_0 e^{-\frac{1}{m}(\theta + \frac{\pi}{2})}, & \theta \in [-\frac{\pi}{2} - \theta_2, -\frac{\pi}{2}] \end{cases}, \tag{6}$$

Fig. 2 First step and corresponding wheel



where θ_1 and θ_2 must satisfy the no-sliding constraints. In our case, those constraints simplify to

$$R = \int_{-\frac{\pi}{2}}^{-\frac{\pi}{2}+\theta_1} r_1(\theta)\sqrt{m^2 + 1} d\theta, \quad T = \int_{-\frac{\pi}{2}-\theta_2}^{-\frac{\pi}{2}} r_2(\theta)\sqrt{\frac{1}{m^2} + 1} d\theta.$$

Solving for θ_1 and θ_2 , and taking into account that $T = mR$, one obtains

$$\theta_1 = \frac{1}{m} \ln \left(\frac{T}{y_0 \sqrt{m^2 + 1}} + 1 \right), \quad \theta_2 = m \ln \left(\frac{T}{y_0 \sqrt{m^2 + 1}} + 1 \right). \quad (7)$$

Figure 2 shows the first step of the staircase (in blue) and the two pieces of Bernoulli spirals (in red) that roll without sliding over the tread and the riser of the step. In the particular case when $T = R$ ($m = 1$), we have $\theta_1 = \theta_2$ and the design of wheels is more straightforward.

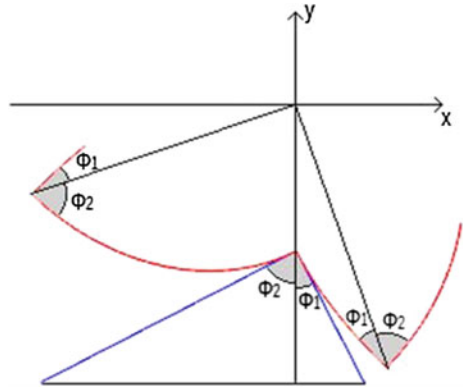
3.2 Constructing the Wheel Piece by Piece

In order to design a closed wheel for the staircase, one must prove the following properties.

1. When the first two pieces of the wheel are rotated around the origin with angle $\theta_1 + \theta_2$, the radial distances $r_2(-\pi/2 - \theta_2)$ and $r_1(-\pi/2 + \theta_1)$ match.
2. Whenever the spirals that form the wheel intersect, they must form a right angle, so that, when the wheel rolls over the staircase, there is a perfect match at every point of contact, including at the cusp points.

Proposition 2 *If r_1 and r_2 are the functions defined in (6) and θ_1 and θ_2 are given by (7), then*

Fig. 3 Spirals intersecting at 90°



$$r_1\left(-\frac{\pi}{2} + \theta_1\right) = r_2\left(-\frac{\pi}{2} - \theta_2\right) = \frac{T}{\sqrt{1 + m^2}} + y_0. \tag{8}$$

The proof requires only a few simple calculations. To show that the angle of any two intersecting spirals is a right angle, one must use the equiangular property of Bernoulli spirals, mentioned in Remark 1. Using this, we conclude that the angles in Fig. 3 marked with ϕ_1 (similarly for those marked with ϕ_2) are equal.

3.3 Making Sure that the Wheel Closes

Now we show that it is always possible to choose y_0 so that the wheel closes. Moreover, the wheel can be chosen with as many petals as we wish. A *petal* of the wheel is defined as the portion of the wheel between two consecutive points of minimal radius.

Proposition 3 *Assuming that the wheel for the staircase defined in (5) is a closed curve with N petals ($N \in \mathbb{N}$), then*

$$y_0 = \frac{T}{\sqrt{m^2 + 1} \left(e^{\frac{2\pi m}{(m^2+1)N}} - 1 \right)}. \tag{9}$$

Proof The assumption that the wheel closes with N petals, is equivalent to the condition $\theta_1 + \theta_2 = 2\pi/N$. Using the formulas for θ_1 and θ_2 given by (7), we may write

$$\theta_1 + \theta_2 = \frac{2\pi}{N} \Leftrightarrow \frac{m^2+1}{m} \ln \left(\frac{T}{y_0 \sqrt{m^2+1}} + 1 \right) = \frac{2\pi}{N}. \text{ Solving for } y_0, \text{ one gets}$$

$$y_0 = \frac{T}{\sqrt{m^2 + 1} \left(e^{\frac{2\pi m}{(m^2+1)N}} - 1 \right)}. \tag{10}$$

Remark 2 According to the previous results, given a staircase (i.e., given T and R , and consequently $m = T/R$), it is always possible to choose y_0 , so that the wheel that rolls over the staircase without sliding and without bouncing has N petals, for any $N \in \mathbb{N}$. Also note that y_0 increases with N . And since $r(-\pi/2) = y_0$, y_0 is equal to the internal radius of the wheel. So, we can conclude that the number of petals determines the size of the wheel.

4 The Main Result

As a consequence of the comments and results included in the previous section, we are now ready to state the main contribution of our paper.

Theorem 1 *Given a staircase with equal steps, there is an infinite number of (closed) wheels that can roll over that staircase without sliding and without bouncing. The size of each wheel is proportional to the number of petals, so that the smallest wheel has one petal only.*

Remark 3 It is clear, from all the previous remarks, that y_0 is independent of the size of the staircase and only influences the size of the wheel and the number of its petals. Next algorithm summarises how to design a wheel for a given staircase.

Algorithm to design a closed wheel with N petals:

Step 1. Compute $m = T/R$, T and R being the tread and riser of the staircase.

Step 2. Compute y_0 according to the formula (9), i.e.,

$$y_0 = \frac{T}{\sqrt{m^2 + 1} \left(e^{\frac{2\pi m}{(m^2+1)N}} - 1 \right)}.$$

Step 3. Compute the angles θ_1 and θ_2 according to the formula (7), i.e.,

$$\theta_1 = \frac{1}{m} \ln \left(\frac{T}{y_0 \sqrt{m^2+1}} + 1 \right), \quad \theta_2 = m \ln \left(\frac{T}{y_0 \sqrt{m^2+1}} + 1 \right).$$

Step 4. Design the part of the wheel that rolls over the first step, according to its polar equation given by the formula (6), i.e.,

$$r(\theta) = \begin{cases} r_1(\theta) = y_0 e^{m(\theta+\frac{\pi}{2})}, & \theta \in [-\frac{\pi}{2}, -\frac{\pi}{2} + \theta_1] \\ r_2(\theta) = y_0 e^{-\frac{1}{m}(\theta+\frac{\pi}{2})}, & \theta \in [-\frac{\pi}{2} - \theta_2, -\frac{\pi}{2}] \end{cases}.$$

If $N = 1$ the wheel is complete. Otherwise, go to next step for completion.

Step 5. Complete the wheel, by performing $N - 1$ successive rotations, around the origin, of the curve obtained in the previous step, with angles of rotation equal to $2(k - 1)\pi/N$, for $k = 2, 3, \dots N$.

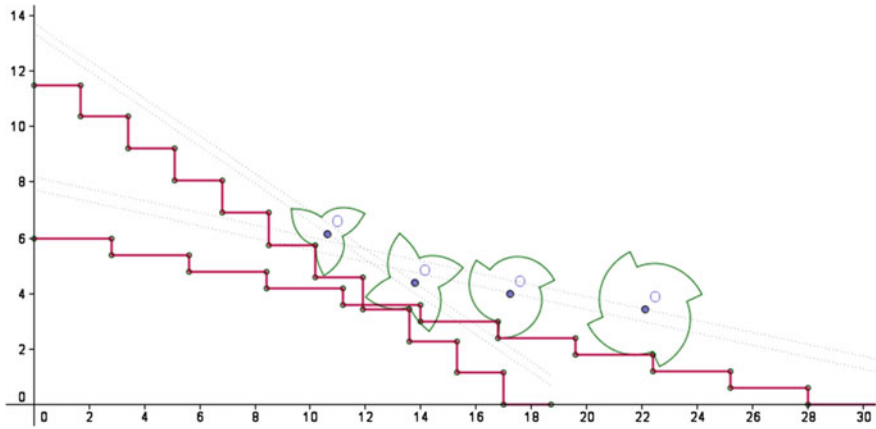


Fig. 4 Different wheels ($N = 3; 4$) rolling on different staircases ($m = 1.47; 4.66$)

Remark 4 When building a staircase, there should be ergonomic concerns. One of them is the tradeoff between the tread and the riser. One formula that is commonly used, known as Blondel’s formula, establishes that $2R + T = S$, where S is the average step length that may vary from country to country but is usually in the interval 62–64 cm. But we remark that the design of a wheel for a staircase is always possible, no matter whether the step size satisfies Blondel’s formula or not (see Fig. 4). In that sense, our results are universal.

Figure 5 below shows several possible wheels rolling on the same staircase.

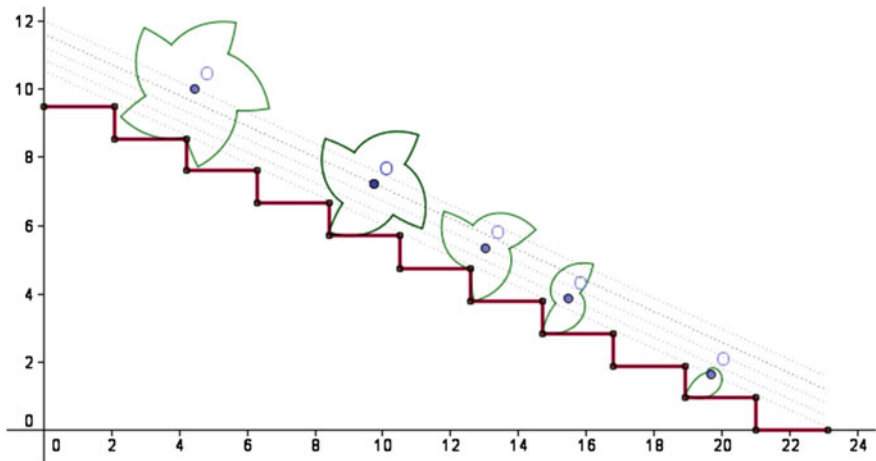


Fig. 5 Several wheels rolling on a staircase

5 Conclusion

We have shown that, given a staircase with equal steps and right angles, it is possible to construct an infinite number of exotic wheels that roll over that staircase without sliding and without bouncing. The boundary of these wheels are always pieces of Bernoulli spirals, joined together so that the constraints are not violated. We have also shown that the size of each wheel increases with the number of petals. Finally, we have presented an algorithm to construct a wheel with N petals for a staircase with given tread and riser. All this extends to less conventional staircases. This study was the first step to accomplish the ultimate goal of designing mobility systems able to overcome stairs and steps with additional levels of comfort and usability. By combining exotic wheels with circular wheels, or by incorporating mechanisms able to deform a standard wheel into a stair climbing wheel, much simpler mobility systems can be designed and constructed, avoiding complex mechanical structures and complex control systems, and providing at the same time good maneuverability with minimum drive and control skills from the user.

References

1. Yoshida, T., Koyanagi, E., Tadokoro, E., Yoshida, K., Nagatani, K., Ohno, K., Tsubouchi, T., Maeyama, S., Noda, I., Takizawa, O., Hada, Y.: A high mobility 6-crawler mobile robot *Kenaf*. In: Proceedings of 4th International Workshop on Synthetic Simulation and Robotics to Mitigate Earthquake Disaster (SRMED2007), Atlanta, USA, p. 38, July, 2007
2. Hirose, S., Senu, T., Aoki, S.: The TAQT carrier: a practical terrain-adaptive quadru-track carrier robot. In: Proceedings of IEEE/RSJ International conference on Intelligent Robots and Systems, Tokyo, Japan, pp. 2068–2073, July 1992
3. Hirai, K., Hirose, M., Haikawa, Y., Takenaka, T.: The development of honda humanoid robot. In: Proceedings of IEEE International Conference on Robotics and Automation (ICRA98), Leuven, Belgium, pp. 1321–1326, May 1998
4. ASIMO—the world’s most advanced humanoid robot. <http://asimo.honda.com/>
5. Harada, K., Kajita, S., Kaneko, K., Hirukawa, H.: Dynamics and balance of a humanoid robot during manipulation tasks. *IEEE Trans. Robot.* **22**(3), 568–575 (2006)
6. Sugahara, Y., Carbone, G., Hashimoto, K., Ceccarelli, M., Lim, H., Takanishi, A.: Experimental stiffness measurement of WL-16R11 biped walking vehicle during walking operation. *J. Robot. Mechatron.* **19**(3), 272–280 (2007)
7. Siegwart, R., Lamon, P., Estier, T., Lauria, M., Piguat, R.: Innovative design for wheeled locomotion in rough terrain. *Robot. Auton. Syst.* **40**(2–3), 152–162 (2002)
8. Nakajima, S., Nakano, E., Takahashi, T.: Motion control technique for practical use of a leg-wheel robot on unknown outdoor rough terrains. *Proc. IEEE/RSJ Int. Conf. Intell. Robots Syst.* **1**, 1353–1358 (2004). Oct
9. Altendorfer, R., Moore, E.Z., Komsuoglu, H., Buehler, M., Brown, H., McMordie, D., Saranli, U., Full, R., Koditschek, D.E.: A biologically inspired hexapod runner. *Auton. Robots* **11**, 207–213 (2001)
10. Yim, M.H., Homans, S.B., Roufas, K.D.: Climbing with snake-like robots. In: IFAC Workshop on Mobile Robot Technology, Korea, pp. 21–22, May 2001
11. The Galileo wheelchair. <https://www.galileomobility.com>
12. PW-4x4Q wheelchair. <http://www.wheelchair88.com/product/pw-4x4q/>

13. TopChair-S a powered wheelchair. <https://www.topchair.fr>
14. iBOT mobility system. <https://www.msu.edu/luckie/segway/iBOT/iBOT.html>
15. Hall, L., Wagon, S.: Roads and wheels. *Math. Mag.* **65**(5), 283–301 (1992)
16. Modak, G.S., Bhoomkar, M.M.: Innovative design of staircase climbing wheelchair. *Int. J. Eng. Res. Technol. (IJERT)* **2**(2), 1–6 (2013)
17. Asai, Y., Chiba, Y., Sakaguchi, K., Sudo, T., Bushida, N., Otsuka, H., Saito, Y., Kikuchi, K.: Wheel-based stair-climbing robot with hopping mechanism—demonstration of continuous stair climbing using vibration. *J. Robot. Mechatron.* **20**(2), 221–227 (2008)
18. Hirose, S., Yoneda, Y.: Toward development of practical quadruped walking vehicles. *J. Robot. Mechatron.* **6**, 498–504 (1993)
19. Kikuchi, K., Sakaguchi, K., Sudo, T., Bushida, N., Chiba, Y., Asai, Y.: A study on wheel-based stair-climbing robot with hopping mechanism. *Mech. Syst. Signal Process. (MSSP)* **22**(6), 1316–1326 (2008)
20. Lawn, M.J.: Study of stair-climbing assistive mechanisms for the disabled. Ph.D. thesis, Nagasaki University, Japan, Dec 2002
21. Matsumoto, O., Kajita, S., Saigo, M., Tani, K.: Biped-type leg-wheeled robot. *Adv. Robot.* **13**(3), 235–236 (1999). Oct
22. Nakajima, S.: Development of a personal mobility vehicle for rough terrain. In: Proceedings of 14th CLAWAR, pp. 650–657 (2011)
23. Nakajima, S.: Mobile platform with leg-wheel mechanism for practical use. In: Gacovski, Z. (ed.) *Mobile Robots—Current Trends* (2011). doi:10.5772/25517. <http://www.intechopen.com/books/mobile-robots-current-trends/mobile-platform-with-leg-wheel-mechanism-for-practical-use>
24. Nakajima, S., Fujikawa, T.: Proposal for personal mobility vehicle supported by mobility support system. In: 2012 IEEE International Electric Vehicle Conference (IEVC), pp. 1–6 (2012)
25. Wellman, P., Krovi, W., Kuma, V., Harwin, W.: Design of a wheelchair with legs for people with motor disabilities. *IEEE Trans. Rehabil. Eng.* **3**, 343–353 (1995)
26. Scalamobile, Ulrich Alber GmbH + Co. KG, Sigmaringer Str. 100, D-72458, Albstadt, Germany

***Imitate Me!*—Preliminary Tests on an Upper Members Gestures Recognition System**

Vinícius Silva, Pedro Leite, Filomena Soares, João Sena Esteves and Sandra Costa

Abstract This work describes the design, implementation, and preliminary tests of a system that uses a humanoid robot to mimic non-standard upper members gestures of a human body. The final goal is to use the robot as a mediator in motor imitation activities with children with special needs, either cognitive or motor impairments. A *Kinect* sensor and the humanoid robot ZECA (a *Zeno R-50* robot from *Hanson RoboKind*) are used to identify and mimic upper members gestures. The system allows direct control of the humanoid robot by the user. The proposed system was tested in laboratory environment with adults with typical development. Furthermore, the system was tested with three children between 4 and 12 years old with motor and cognitive difficulties in a clinical-like environment. The main goal of these preliminary tests was to detect the constraints of the system.

Keywords Human-Robot interaction · *Kinect* · Upper members gestures recognition · *Zeno*

V. Silva · P. Leite · S. Costa
Industrial Electronics Department, University of Minho, Guimarães, Portugal
e-mail: a65312@alunos.uminho.pt

P. Leite
e-mail: a66161@alunos.uminho.pt

S. Costa
e-mail: scosta@dei.uminho.pt

F. Soares · J.S. Esteves (✉)
Industrial Electronics Department, R&D Centre Algoritmi School of Engineering,
University of Minho, Guimarães, Portugal
e-mail: sena@dei.uminho.pt

F. Soares
e-mail: fsoares@dei.uminho.pt

1 Introduction

The development of research projects that use humanoid robots to copy/imitate movements and actions performed by humans has been receiving particular attention in the scientific community, implementing new tools and techniques in robot learning, and also enabling more natural robotic movements and actions. In particular, in the literature there are several studies on imitation of the human movements by humanoid robots, developing optimized algorithms that allow reproducing natural actions, avoiding the typical unnatural robotized movements [1–7].

The work developed by Manasrah [3] consisted in developing a three-dimensional imitation process of a human being using *Kinect* and NAO robot developed by Aldebaran Robotics [8]. The role of *Kinect* in this work was to obtain the positions of the joints of a human operator's body. The angles and user's center of mass were calculated to allow the robot to mimic the position of the operator. One of the positions required the user to balance on one foot and the robot was able to mimic the position, recalculating its center of mass. The author also investigated how individuals who had suffered a stroke lean when subjected to balance training assisted by the robot. The *Kinect* was used to help optimizing patient outcomes by providing graphical information regarding the patient's mass distribution.

In [4], it was analyzed the potential of using the robot *Robota* that was adapted from a typical commercial doll. This robot has five servomotors that provide a degree of freedom for each of the limbs (arms and legs) and also for the head (more specifically, the neck). Moreover, it has the ability to individually blink and move each eye. Its application to the imitation process is highly reduced, since it can only mimic, in a limited way, rotation movements of the head and of each arm and leg (one degree of freedom in each member). In addition, for complete body imitation, the robot must be placed in a support, since it was not possible to implement locomotion processes and equilibrium algorithms.

Yihong and Qijun [5] developed a task-prior algorithm to solve the physical kinematic constraints of the full-body humanoid robot NAO on real-time imitation. A redundant kinematic system was built in order to track the trajectory of the wrist position as a primary task. The method was tested in a simulation environment as well as on the NAO robot, allowing it to imitate humans' movements with the *Kinect* sensor.

The humanoid robot NAO was also used in [6] to replicate the upper body movements of humans by using motion capture data acquired with *Bio-motion* + sensors, developed by the *Hamlyn Centre*. The authors proposed an upper limb motion imitation module that calculates the joint angle trajectories, based on motion capture data, and sends the results to the robot. The experimental results show the effectiveness of the proposed system regarding the postural similarity between the captured human movements and the corresponding robot motions.

Another project was developed by the *Korean Institute of Science and Technology* (KIST), which used the robot *Mahru*, developed in collaboration with *Samsung Electronics* [7]. The robot was able to mimic the movements of a human operator

through two different approaches. The first approach consists of placing classic markers in the human body and track the user's movements using a traditional capture system and motion capture processing. The other method involved the use of an inertial motion-capture suit. The person with the suit performed various movements that were recorded and subsequently executed by the robot in real time [9].

The referred works are relevant in motion recognition. Nevertheless, they have some constraints when working with children with special needs. Usually, these children reject wearing suits or markers; it is desirable to use non-invasive technology to detect the movements. Also, a real time system is required in order to replicate non-standard movements, allowing a natural interaction with the children.

Following this trend, the work presented in this paper uses a *Zeno R-50* robot from *Hanson RoboKind* (<http://www.robokindrobots.com/>) as a mediator in motor imitation activities with children with special needs. To achieve that goal, an experimental setup was designed and implemented using a *Kinect*-Computer-Robot configuration. The system is able to identify the movements of the upper limbs of a human operator and the robot reproduces them correctly in real time. It is worth noting that the gestures are freely performed by the user/child without any predefined choreography. The overall system was first tested in a laboratory environment with adults with typical development in order to check the integration and operation of the system. Subsequently, tests were conducted in a clinical-like setting using a triadic test setup, i.e. child-therapist-robot. It was intended to detect the system constraints in an intervention session.

The paper is organized in four sections. Section 2 details the developed system; Sect. 3 shows the preliminary results obtained in laboratorial environment and clinical-like environment; the conclusions and future perspectives of the work are addressed in Sect. 4.

2 Proposed System

In this section it is described the proposed system that allows the *Zeno R-50* humanoid robot *ZECA* (*Zeno Engaging Children with Autism*) to mimic the upper members gestures of a human body. *ZECA* was supported by *Robotica-Autismo* research project com) and it is an appropriate robot to promote the interactions with children with impairments.

2.1 Experimental Setup

The system implemented in this work (Fig. 1) consists of a *Kinect* sensor, a computer and the robot *ZECA*.

Kinect is a motion sensing input device developed by Microsoft. It can provide a depth map by projecting a fixed pattern of infrared spots onto the object; then, the



Fig. 1 Experimental set-up: *Kinect*, computer and ZECA

receiver captures a shifted grid of these spots and the processor calculates the offset of each of the spots. This depth map can be used to find a skeleton representation of the user [10, 11]. The *Kinect*, along with the required Windows software, *Kinect* SDK, was used to obtain the coordinates of the major joints of the user. From these coordinates described in the Cartesian space of the *Kinect*, the user pose can be approximated in the joint space of the robot. The pose is only an approximation because the kinematics of the robot arm are not a replica of the human arm.

ZECA (Fig. 1) is a humanoid child-like robot with 34 degrees of freedom: 4 in each arm, 6 in each leg, 11 in the head, and 1 in the waist [12].

2.2 System Description

Figure 2 shows the block diagram of the developed system. The data obtained from the *Kinect* sensor (upper members movement) is filtered. Then, the joint angles are calculated and normalized, and the data package is then generated and sent to the robot for actuation of the joints.

The computer runs an application developed in C# that implements the algorithms for detecting the user movements and establishing the communication with ZECA. The robot runs an application in Java to actuate the servos in order to replicate the user upper members movements.

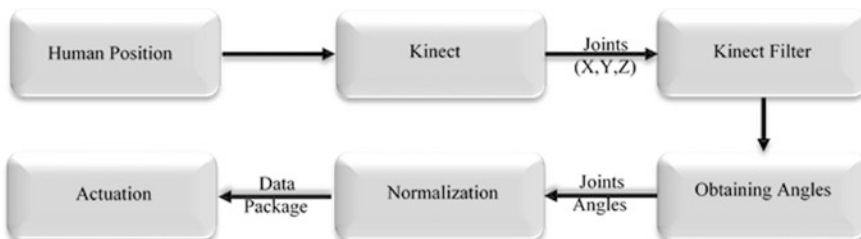


Fig. 2 Block diagram of the developed system

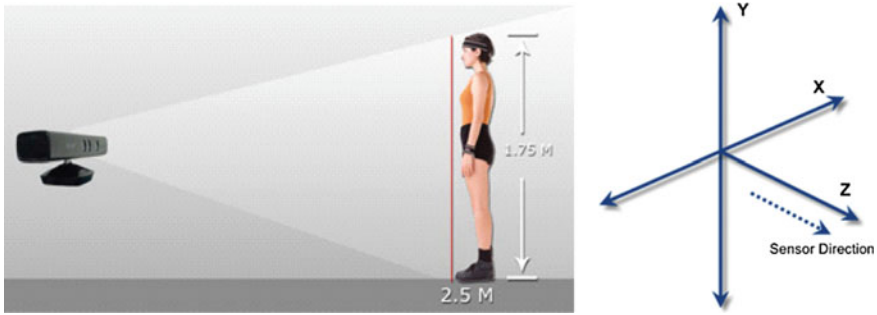


Fig. 3 Human position and *Kinect*: On the *left*—recommended user position. On the *right*—the *Kinect* axis system [13]

2.2.1 Human Position and *Kinect*

Kinect is able to build a virtual human skeleton from the data of the depth map. This skeleton with the joints detected is used to calculate the joints angles. The user must be in front of the *Kinect* as shown in Fig. 3. The *Kinect* must be placed 1.2 m above the floor and the user has to be distanced from 2 m. The environment must be well illuminated.

2.2.2 *Kinect* Filter

The skeletal tracking joint information can be adjusted (smoothed) across different frames to minimize jittering and stabilize the joint positions over time.

The *Kinect* for Windows SDK provides a mechanism to smooth the joint positions in a frame. *Kinect* will adjust the position of the joints calculated in that frame according to the desired smoothing behavior [14].

The filter can be controlled via five smoothing parameters: *Smoothing*, *Correction*, *Prediction*, *JitterRadius* and *MaxDeviationRadius*. More information about this filter is available in [14]. The values used in this project for the filter parameters, Table 1, were obtained by trial and error.

Table 1 Filter parameters value

<i>Smoothing</i>	0.3
<i>Correction</i>	0.0
<i>Prediction</i>	0.0
<i>JitterRadius</i>	1.0
<i>MaxDeviationRadius</i>	0.5

2.2.3 Obtaining Angles and Normalization

The *Kinect* sensor provides the coordinates (x, y, z) of each joint of the human body. Figure 4 shows ZECA shoulder pitch θ (yellow), shoulder roll β (green), elbow yaw α and elbow roll γ (blue and red). The methodology is replicated for both arms.

The angle δ between two vectors, \vec{u} and \vec{v} , is obtained through Eq. 1, where \vec{u} is the vector norm. Figure 5 shows a visual representation of how to calculate the pitch and roll angles, θ and β , for the shoulder.

$$\delta = \cos^{-1} \left(\frac{\vec{u} \cdot \vec{v}}{\|\vec{u}\| \|\vec{v}\|} \right) \tag{1}$$

Figure 6 shows a representation of how to calculate the yaw and roll angles, α and γ for the elbow. The yaw angle α (Fig. 6, on the right) is found by calculating the angle between two vectors, \vec{V}_{se} and \vec{V}_{ew} , applying Eq. 1. The roll angle γ

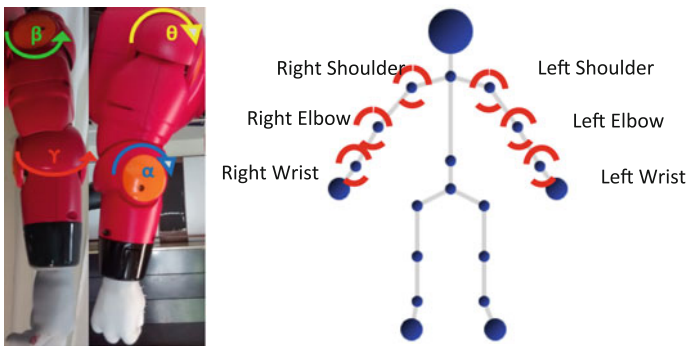


Fig. 4 On the left—angles of each joint of the robot arms. On the right—the selected joints

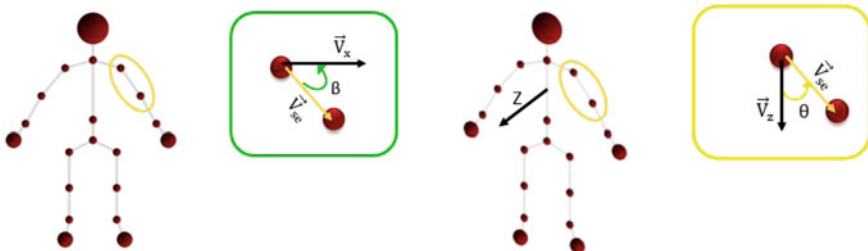


Fig. 5 On the left—roll angle β . Using Eq. 1 it is possible to find the angle between the vectors \vec{V}_{se} and \vec{V}_x . On the right—using the same method it is possible to obtain the pitch angle θ of the shoulder

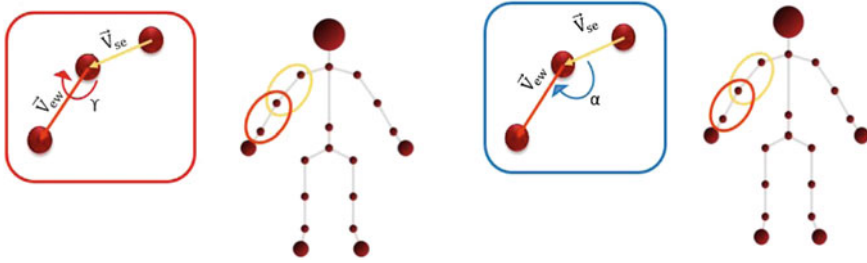


Fig. 6 On the left—elbow roll angle γ . On the right—elbow yaw angle α

(Fig. 6—on the left) is found by calculating two vectors, nc and ni , [15]. The variable nc is a vector normal to the plane formed by the shoulder, elbow, and hand. It has the same direction of the cross product of \vec{V}_{se} and \vec{V}_{ew} . Then, the vector ni is calculated (Eq. 3) multiplying vector \vec{V}_z , $[0, 0, 1]$ by the rotation matrix $R_{\theta\beta}$. $R_{\theta\beta}$ results from the multiplication of two matrices: R_θ , a rotation matrix of the pitch shoulder angle θ in X, and R_β , a rotation matrix of the roll shoulder angle β in Z. Finally, the angle between nc and ni is determined by applying Eq. 1 in order to obtain the elbow roll angle γ . For more details see [16].

$$nc = \vec{V}_{se} \times \vec{V}_{ew} \tag{2}$$

$$ni = R_\theta^* [0 \ 0 \ 1]^T \tag{3}$$

Due to the robot mobility limitations, it is necessary to delimit the movements of the upper limbs. For example, the human shoulder joint has three degrees of freedom (pitch, yaw and roll), but the same joint of the robot has only two degrees of freedom (pitch and roll), [17]. This limits the correct replication of some human movements.

2.2.4 Communication and Protocol

The *Kinect* subsystem is connected to the robot ZECA through a local network, communicating via TCP/IP socket. A client application that runs on PC, transmits the data to the robot allowing it to actuate. The angles package consists of the eight angles corresponding to the four joints of each arm (Fig. 7).

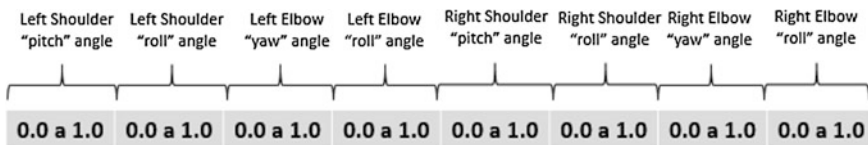


Fig. 7 Package with the joints angles that can be played through the robot

2.2.5 Interface

In order to follow the recognition of the movements and the angles of each joint, a user interface called *Kinect Joints Mapping Interface* was created. This interface has three windows: the *Main* window, the *Graph_K* window and the *Debug* window. In the *Main* window (left side of Fig. 8) it is possible to visualize the user and the position of each joint detected by the *Kinect* (blue circles). In this window it is possible to control the whole system through voice commands: *Connect* (for establishing the connection with the robot), *Pause* (to have a pause in the communication), *Start* (to initiate the communication) and *Close* (to finish the communication).

The *Graph_K* window (right side of Fig. 8) displays in real time a graph with the values (0 to 1) of the amplitude of the degrees of freedom of each joint calculated for the robot.

The *Debug* window shows the value of the angle (in degrees) of each joint, calculated for the robot, for each degree of freedom. It is also possible to send text messages to the robot (for example: "Hello everyone") so that the robot repeats them orally.

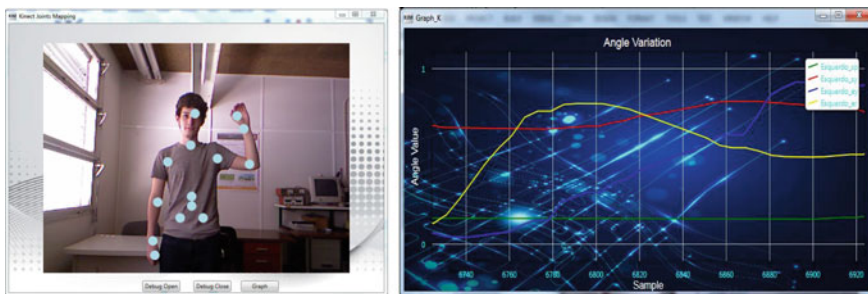


Fig. 8 On the left side: *Main* window. The user and the joints positions (blue circles); On the right side: *Graph_K* windows displaying the graph in real time

3 Results

The overall system was first tested in a laboratory environment to verify its correct functioning. The imitation performance of the robot can be seen in a video available at <https://www.youtube.com/watch?v=-hNwkY7QARY>.

The system was then tested in a clinical-like environment in order to tune the conditions of the experimental scheme. Other objective of these tests was to understand the appropriateness of the system in a real situation with children with special needs. The main question was: can a humanoid robot be used as an eligible mediator in upper members imitation activities with children with motor and cognitive difficulties? The result analysis was qualitative (opposed to a quantitative and structured assessment). Further tests are mandatory in order to conclude the suitability of the proposed system to be used as a complement to the traditional clinical interventions. The validation of the system for clinical interventions must be performed with a larger sample, with a quantified imitation success rate and a quantified children evolution in terms of predefined behaviour indicators. Following this trend, a motor coordination activity and gestures imitation with the robot ZECA was designed. The system allows non-standard gestures of the upper members performed in a random choreography. The system was tested with three children aged between four and twelve. The results obtained with two of them are presented in the following. Child A has hyperactivity and deficit of attention; Child B has specific disorder of language and deficits in the global and fine motor coordination. The experiments were performed individually in activities involving the therapist, the robot and the child in two configurations. The robot had the role of mediator in the process of imitation of the movements of the upper limbs. Two experimental configurations (Fig. 9) were tested.

In the first configuration (Fig. 9, on the left) the therapist was positioned within the *Kinect* field of vision and performed random upper members movements. ZECA imitated the therapist's movements. The child stood in front of the robot mimicking its movements. The system was tuned to work with slow movements. Quick and sudden movements are not recognized by the system. As a conclusion for the first test, it is highlighted that the slow movements of the robot are an asset for the learning of the

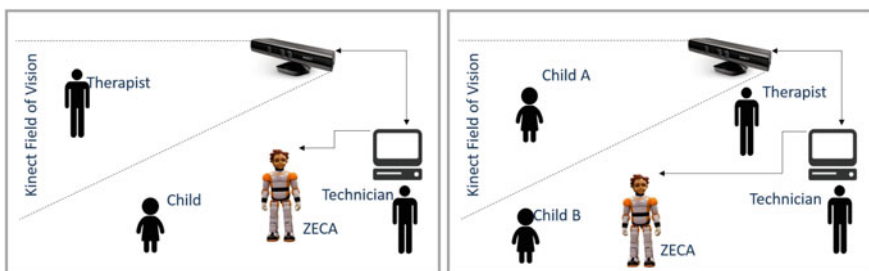


Fig. 9 Experimental configurations. On the *left*—first configuration: Therapist-Kinect-ZECA-Child. On the *right*—second configuration: Therapist-Child A-Kinect-ZECA-Child B

movements and for the coordination activities. Furthermore, the possibility of performing individual or simultaneous movements is an important functionality as it allows to detect coordinated/uncoordinated movement impairments.

The objective of the second experiment (Fig. 9, on the right) was to ascertain if the system is able to operate in a different configuration, i.e., in a cooperative task (two children and the robot). Child A was within the *Kinect* field of view and facing the therapist, receiving guidance on how to perform the movements and execute them. The robot mimicked the movements of Child A. Child B was facing the robot, tracking and reproducing the robot movements. With this test it was noted that Child A was focused on the task (in spite of having hyperactivity and deficit of attention and being without medication) due to her responsibility to control the robot movements. Child B successfully followed the movements of the robot. It is worth transcribing the therapist's opinion regarding this test:

The coordination of activity and imitation of gestures performed with the Robot ZECA was fantastic on a personal basis and as a health professional. The possibility of improving and amplifying the movements of the robot ZECA indicate that this can be a challenging and a motivating tool for working with children with attention deficit and hyperactivity; motor disorders and other pathologies.

4 Final Remarks

Several works in the literature are focused on mimicking the human movements by humanoid robots. In particular, the work presented in this paper considers the use of ZECA (a *Zeno R-50* robot from *Hanson RoboKind*) to foster imitation motor activities with children with special needs. The proposed system includes a *Kinect* sensor, a computer and the ZECA robot. The robot manages to mimic non-standard movements randomly performed by the user/child. The overall system was first tested in laboratorial environment with adults. The system was able to identify the movements of the upper limbs of a human operator and the robot reproduces them correctly. The tests conducted in a clinical-like setting used a triadic setup, i.e. child-therapist-robot. The robot had the role of mediator in the process of imitation of movements of the upper limbs: the therapist performed the intended movement, the robot moved accordingly and the child imitated the movements of the robot. ZECA showed to be an adequate tool to be used as a social mediator in upper limbs movement imitation with impaired children. Due to the lack of arm DoF, the robot cannot accurately replicate some human movements in a natural way. This is an inherent limitation regarding mimicking human upper members movements.

Future work considers including the lower members movements of ZECA, enabling it to be a challenging and motivating tool for working with children with deficit of attention and hyperactivity, motor disorders and other diseases. Then, the system will be ready to be tested in clinical environment under a predefined qualitative and quantitative validation methodology.

Acknowledgments This work has been supported by COMPETE: POCI-01-0145-FEDER-007043 and FCT—Fundação para a Ciência e Tecnologia within the Project Scope: UID/CEC/00319/2013.

References

1. Liu, H.Y., Wang, W.J., Wang, R.J., Tung, C.W., Wang, P.J., Chang, I.P.: Image recognition and force measurement application in the humanoid robot imitation. *IEEE Trans. Instrum. Meas.* **61**(1), 149–161 (2012)
2. Nguyen, V.V., Lee, J.-H.: Full-body imitation of human motions with *Kinect* and heterogeneous kinematic structure of humanoid robot. In: *IEEE/SICE International Symposium on System Integration (SII)*. Fukuoka, pp. 93–98, 16–18 Dec 2012
3. Manasrah, A.A.: Human motion tracking for assisting balance. Master Thesis, University of South Florida, Florida (2012)
4. Billard, B.R., Nadel, J., Dautenhahn, K.: Building Robota, a mini-humanoid robot for the rehabilitation of children with autism. *RESNA Assist. Technol. J.* 1–5 (2006)
5. Yihong, C., Qijun, C.: Real-time imitation human upper-body movement with joint and self-collision constraints. In: *2013 6th IEEE Conference on Robotics, Automation and Mechatronics (RAM)*, Manila, 12–15 Nov 2013
6. Teachasrisaksakul, K., Zhang, Z., Yang, G.-Z.: Demo abstract: upper limb motion imitation module for humanoid robot using biomotion + sensors. In: *IEEE International Conference on Body Sensor Networks (BSN)*, Cambridge, MA, USA, 6–9 May 2013
7. Guizzo, E.: Humanoid robot Mahru mimics a person’s movements in real time (2010). *IEEE Spectrum*, <http://spectrum.ieee.org/automaton/robotics/humanoids/042710-humanoid-robot-mahru-real-time-teleoperation>. Accessed on July 2015
8. Aldebaran Robotics NAO. (2015). From Active Robots: <http://www.active-robots.com/aldebaran-robotics-nao-evol-humanoid-robot>. Accessed on July 2015
9. Mahru Humanoid Robot Real-Time Teleoperation. From Youtube: <https://www.youtube.com/watch?v=TJmQqC1Nhtu>. Accessed on July 2015
10. *Kinect* the technology (2015). <http://www.i-programmer.info/babbages-bag/2003-Kinect-the-technology-.html>. Accessed on July 2015
11. *Kinect* for Windows Sensor Components and Specifications (2015). <https://msdn.microsoft.com/en-us/library/jj131033.aspx>. Accessed on July 2015
12. Arngren (2015). <http://www.arngren.net/ZENO-2.R50Data.jpg>. Accessed on July 2015
13. Coordinate Spaces (2015). <https://msdn.microsoft.com/en-us/library/hh973078.aspx>. Accessed on July 2015
14. Joint Filtering (2015). <https://msdn.microsoft.com/en-us/library/jj131024.aspx>. Accessed on July 2015
15. Torres, N.A., Clark, N., Ranatunga, I., Popa, D.: Implementation of interactive arm playback behaviors of social robot zeno for autism spectrum disorder therapy. In: *PETRA2012—Proceedings of the 5th International Conference on PErvasive Technologies Related to Assistive Environments*, Crete, Greece (2012)
16. Weisstein, E.W.: Rotation Matrix (2015). <http://mathworld.wolfram.com/RotationMatrix.html>. Accessed on 05 Jul 2015
17. R50 Documentation (2015). <http://www.robkindrobots.com/support-documentation/r50/>. Accessed on July 2015

Happiness and Sadness Recognition System—Preliminary Results with an *Intel RealSense 3D* Sensor

Vinícius Silva, Filomena Soares, João Sena Esteves, Joana Figueiredo, Cristina Santos and Ana Paula Pereira

Abstract Systems and devices that can recognize human affects have been in development for a considerable time. Facial features are usually extracted by using video data or a *Microsoft Kinect* sensor. The present paper proposes an emotion recognition system that uses the recent *Intel RealSense 3D* sensor, whose reliability and validity in the field of emotion recognition has not yet been studied. This preliminary work focus on happiness and sadness. The system extracts the user's facial Action Units and head motion data. Then, it uses a Support Vector Machine to automatically classify the emotion expressed by the user. The results point out the adequacy of *Intel RealSense* for facial features extraction in emotion recognition systems as well as the importance of determining head motion when recognizing sadness.

V. Silva · J. Figueiredo
Industrial Electronics Department, School of Engineering,
University of Minho, Guimarães, Portugal
e-mail: a65312@alunos.uminho.pt

J. Figueiredo
e-mail: id6003@alunos.uminho.pt

F. Soares · J.S. Esteves (✉)
Industrial Electronics Department, R&D Centre Algoritmi,
School of Engineering, University of Minho, Guimarães, Portugal
e-mail: sena@dei.uminho.pt

F. Soares
e-mail: fsoares@dei.uminho.pt

C. Santos
Industrial Electronics Department, R&D Centre MEMS,
School of Engineering, University of Minho, Guimarães, Portugal
e-mail: cristina@dei.uminho.pt

A.P. Pereira
Education Research Center, Institute of Education, University of Minho,
Braga, Portugal
e-mail: appereira@ie.uminho.pt

Keywords Happiness and sadness recognition system • *Intel RealSense* • Support vector machine

1 Introduction

Faces contain a large portion of the human emotionally expressive behaviour. Sometimes they reveal what the words hide. Moreover, facial expressions are used to display emotional states and to manage interactions. Systems and devices that can recognize, interpret, process and simulate human affects have been in development for a considerable time. With many possible applications, such as marketing systems [1], online learning systems [2], and even robotic systems [3], the research on automatic perception of human emotions has opened a new era for Human-Computer Interaction research. Following this trend, there has been an extensive research focusing on automatic facial emotion recognition.

Michel and Kaliouby [4] presented an approach to emotion recognition in live video. Initially, the system extracted 22 facial features from the live video stream of a camera. Then, the displacements for each feature between a neutral and a representative frame of an emotion were calculated. These data, as well as the correspondent labels, were used as an input to the training stage of a Support Vector Machine (SVM) classifier. Posteriorly, the trained SVM model was used to classify an emotion between the six pre-defined emotions: happiness, sadness, angry, surprise, fear, and disgust. Finally, the system was evaluated in a first stage by a professional user, familiar with the approach and aware of how the basic emotions are typically expressed, with an accuracy for all emotions of 87.5 %. Then, the system was evaluated in a more challenging scenario, where inexperienced users were asked to naturally express the emotions. The accuracy achieved in this last evaluation was 60.7 % for all emotions.

Yousef et al. [5], proposed a system that attempts to recognize the six basic emotions using a *Microsoft Kinect* sensor. The database used for training contained 4D data of 14 different persons performing the 6 basic emotions. SVM and k-Nearest Neighbour (k-NN) were used to classify the emotions with an accuracy of 38.8 % and 34.0 %, respectively, for individuals who did not participate in the training of the classifiers. However, the accuracy levels rose to 78.6 % (SVM) and 81.8 % (k-NN), when considering only the individuals that participated in the training.

The work developed by Alabbasi [6] consisted in a system that uses a *Microsoft Kinect* for *Windows* sensor V2 and the face tracking SDK to recognize eight emotions. The implementation of the emotion recognition application was developed with *Visual Studio* 2013 (C++) and *Matlab* 2014. The *Kinect* sensor and the face tracking SDK were used to obtain the facial Action Units (AUs). Firstly, on the application interface, the face features values were saved into a *.mat* file. Then, using *Matlab* it was implemented an Artificial Neural Network (ANN) that classified the emotions based on the facial features. The training set contained the facial

AUs from 12 persons for each of the eight emotions. The overall accuracy for all emotions was 92 %.

In the works related in the literature, facial features are usually extracted by using video data or a *Microsoft Kinect* sensor. No studies have yet been conducted to evaluate both the reliability and the validity of the recent *Intel RealSense 3D* sensor in the field of emotion recognition. Therefore, the present paper proposes an emotion recognition system that uses an *Intel RealSense 3D* sensor. This sensor was chosen mainly because of its small size, which is an advantage when designing embedded systems. Also, it has several libraries to work with facial expressions. This preliminary work focus on happiness and sadness, which are opposite emotions. The system extracts the user's facial AUs and head motion data. Then, it uses SVM to automatically classify the emotion expressed by the user.

This paper is organized in four sections. Section 2 describes the proposed system; Sect. 3 shows the preliminary results obtained; and the conclusions and future work are addressed in Sect. 4.

2 Proposed System

In this section it is described the proposed system that allows emotion recognition. It presents the experimental rig used as well as the methodology to extract the facial features.

2.1 Experimental Setup

The system implemented in this work (Fig. 1) consists of an *Intel RealSense 3D* sensor and a computer.

Intel RealSense is a recent platform for implementing gesture-based Human Computer Interaction (HCI) techniques [7]. It contains a conventional RGB (Red, Green, and Blue) camera, an infrared laser projector, an infrared camera, and a microphone array. The infrared laser projects a grid onto the scene and the infrared

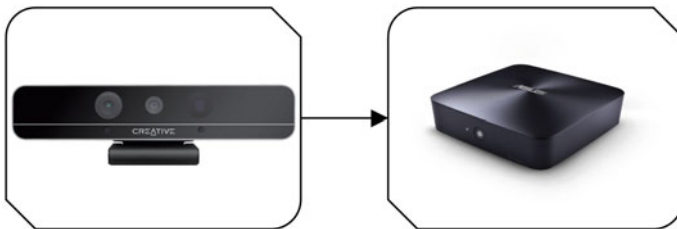


Fig. 1 The proposed system. *On the left Intel RealSense 3D sensor. On the right a computer*

camera records it, computing the depth information. The microphone array allows localizing sound sources in space and performing background noise cancellation. *Intel* announced two models with distinct specifications [8]. The present work uses the *Intel RealSense* model F200, which is a front facing camera dedicated to analyse the human face and hand. The camera, along with the required *Windows* software, *Intel RealSense* SDK, was used to obtain the face data from the user.

2.2 Facial Features Extraction

Generally, an emotion is expressed by a person when reacting to a certain event. Emotions are normally characterized as negative (sadness, anger or fear), positive (happiness or surprise) or neutral. Developed by Paul Ekman and Wallace Friesen in 1978, the earliest method for characterizing the physical expression of emotions is the Facial Action Coding System (FACS) [9]. This system associates the action of the muscles to the changes in facial appearance. The measurements of the FACS are called Action Units (AUs) which are actions performed by a muscle or a group of muscles. There are a total of 46 AUs, from which 12 are for the upper face and 18 are for the lower face. The AUs 1 through 7 refer to brows, forehead or eyelids [9, 10]. Each emotion is then characterized by a combination of the action of specific muscles.

The two emotions considered in this work, happiness and sadness, are characterized by the following facial features:

- Happiness—muscle around the eyes are tightened, wrinkles appears around the eyes, cheeks are raised and lip corners are raised diagonally [10];
- Sadness—inner corner of the eyebrows are raised, eyelids are loose and lip corners are pulled down [10].

The *Intel RealSense* 3D sensor along with *Intel RealSense* SDK can provide up to 78 facial landmarks, and a total of 16 facial expressions [12]. The user must be in front of the *Intel RealSense* as shown in Fig. 2. The effective range for face tracking is 35–120 cm. However, as *Intel RealSense* is still under development, some facial expressions are detected with low accuracy and some expressions are not yet available. To solve this problem, in this work, certain facial expressions were obtained through facial landmarks. Table 1 lists the facial expressions from *Intel RealSense* that were used in this work, as well as, the facial expressions obtained through facial landmarks.

In order to obtain the facial expressions from landmarks, 8 facial landmarks were selected. Figure 3 shows the selected and labelled facial landmarks for geometric features extraction. Table 2 lists the significance of the selected 8 facial landmarks.

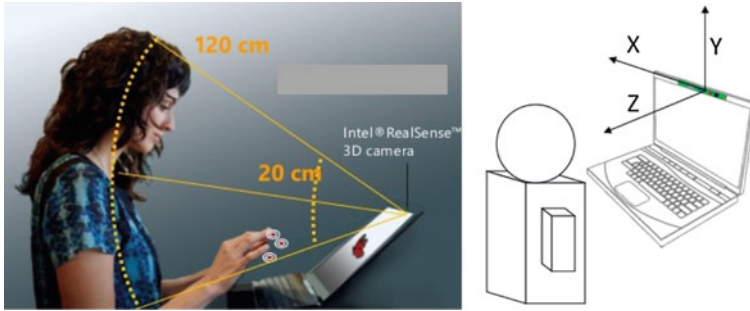
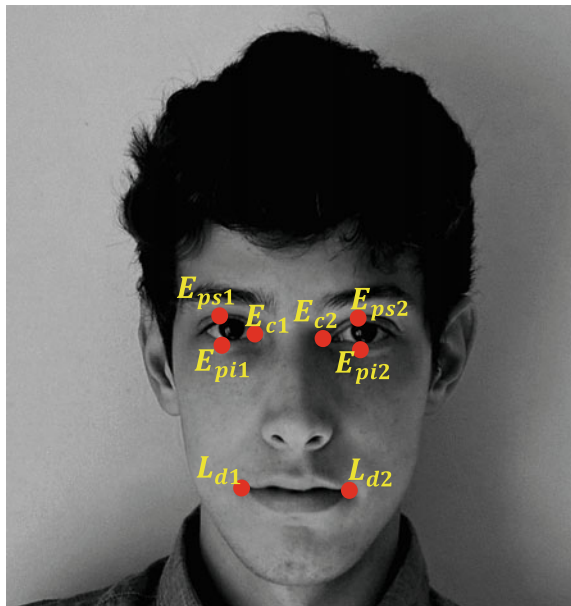


Fig. 2 On the left the recommended user position. On the right the Intel RealSense coordinates system [12]

Table 1 Selected facial features

Facial expressions	Intel RealSense	Facial landmarks
Eyelids		✓
Lip stretcher	✓	
Lip depressor		✓

Fig. 3 Selected and labelled facial landmarks



The geometric features were determined by calculating linear distances between couples of landmarks. The following Eqs. (1–4) show how the distances were obtained, whereas x and y indicate, respectively, the horizontal and the vertical components of a point in the image space.

Table 2 Facial landmarks significance

Facial landmark	Significance
E_{c1}	Eye corner
E_{c2}	Eye corner
L_{d1}	Lip depressor
L_{d2}	Lip depressor
E_{ps1}	Eye palpebrale superius
E_{ps2}	Eye palpebrale superius
E_{pi1}	Eye palpebrale inferius
E_{pi2}	Eye palpebrale inferius

$$Lip\ depressor_{right} = \sqrt{(E_{c1x} - L_{d1x})^2 + (E_{c1y} - L_{d1y})^2} \quad (1)$$

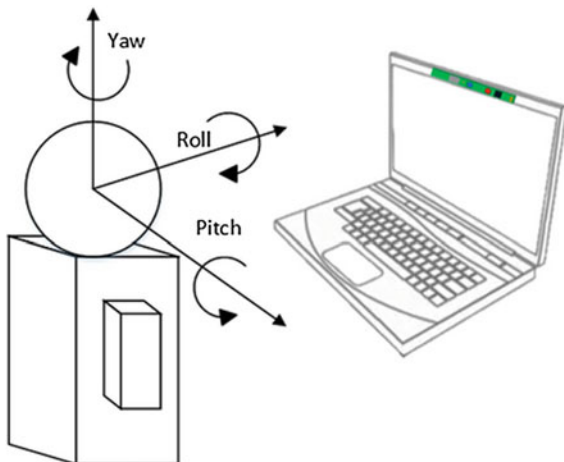
$$Lip\ depressor_{left} = \sqrt{(E_{c2x} - L_{d2x})^2 + (E_{c2y} - L_{d2y})^2} \quad (2)$$

$$Eye_{right} = E_{ps1y} - E_{pi1y} \quad (3)$$

$$Eye_{left} = E_{ps2y} - E_{pi2y} \quad (4)$$

The *Intel RealSense* SDK can return the user head angles, Euler angles [14]. The Euler angles indicate where the face pose is in terms of rotation along the three axes, as illustrated in Fig. 4. This allows obtaining the user's head motion, which is important in the emotion communication process.

Fig. 4 Face pose angles (pitch, roll, and yaw) according to the *Intel RealSense* coordinate system [14]



3 Experimental Results

This section presents the results obtained with the proposed system in the recognition of the two emotions: happiness and sadness. The process includes the database construction, the support vector machine model definition and the assessment of the two emotions recognition system.

3.1 Database Construction

The database was constructed using the eight head features (face and neck) mentioned in Sect. 2, acquired from the *Intel RealSense* 3D sensor, and corresponding to happiness and sadness emotions.

The tests for the database construction considered 32 typically developing children from the 1st cycle with 6–9 years old. The tests were performed in school environment in a closed room.

The child sat in front of the camera, looked at the *Intel RealSense* and performed the emotion, happiness and sadness, requested by the researcher. The researcher showed a photograph corresponding to each emotion in order to serve as a clue. It is worth mention that sadness was performed in two different ways, with and without head bowed, categorized both as being sad.

The acquired data, facial AUs and geometric features were saved in a *.mat* file.

In order to obtain the best performance, the geometric features were scaled to the range (0, 100), applying Eq. 5.

$$N = \frac{W - \min_v}{\max_v - \min_v} (B - A) + A \quad (5)$$

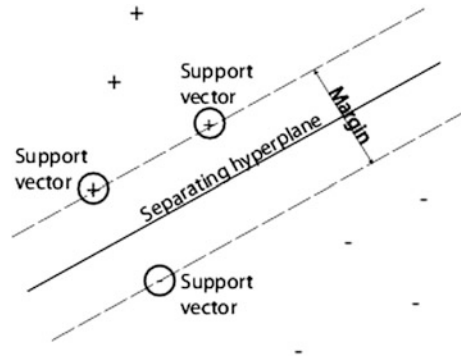
where:

- N Normalized Facial Feature value
- W Facial Feature value to normalize
- \min_v Minimum value from the normalized set
- \max_v Maximum value from the normalized set
- $[A, B]$ Range for value (W) after normalization

3.2 Training a Support Vector Machine (SVM)

Initially introduced by Vapnik [15], SVM is a supervised learning method capable of analysing data for classification and regression analysis. Usually implemented in binary classification, the classification is performed in the feature space through the construction of a linear separating hyperplane [15]. Therefore, the goal of the SVM

Fig. 5 SVM classification: to find the Optimal Separating Hyperplane that separates all data points of the two classes. Margin is the maximal width that has no interior data points [15]



is to find an Optimal Separating Hyperplane (OSH) that divides all the data points from one class of the other class. This is achieved by finding the largest margin between two classes, which is the OSH (Fig. 5). In order to obtain the maximum width of the margin, an optimization problem is computed. This problem is controlled by a parameter C , a trade-off between the maximum width of margin and minimum classification error [15]. The data points closest to the separating hyperplane are the support vectors (SVs). However, some binary classification problems do not have a simple hyperplane as a useful separating criterion. Thus, SVM employs kernel methods allowing nonlinear classification. The commonly used kernels of the SVM are: linear, polynomial, radial basis function (RBF), and sigmoid [16].

The present work uses the SVM to classify the user's emotions. Accordingly to [17], SVM show high classification accuracy even when a small amount of training data is available, making them particularly suitable to a dynamic, interactive approach to face expression recognition. The trained classifier provides a model that can be used to predict the emotion corresponding to a set of features. To quantify the classification accuracy of the SVM, it was used the k-Fold Cross Validation method (k-Fold CV). The k-Fold CV method divides the total data set in k subsets (in this case $k = 10$), and one subset is used for training and the remaining subsets ($k - 1$) are used for testing, calculating the accuracy of the model [18]. CV contributes for the generalization of the classifier and also it avoids overfitting. Two classes were defined: happiness and sadness.

3.3 Results Evaluation

The SVM model was implemented using the function *fitsvm* from *Matlab*, with the SVM kernel set to RBF, and the cost and gamma values were found interactively. Though, there is no analytical study about the optimal choice of the kernel function, the RBF kernel was chosen because it is widely used as a kernel function in emotion classification [5]. In order to verify if the head motion data influences in

the accuracy of the system, in a first stage the SVM model was trained without the head motion data (pitch, roll and yaw). Then, the model was trained with all the features (face features and head motion). The results of the full analysis, accuracy and confusion matrices, conducted using SVM classifier, are shown in Figs. 6 and 7. In Fig. 6 are presented the results with only facial features, where was obtained an accuracy of 89.06 % after cross-validation. Figure 7 shows the results with facial features and head motion, in which, after cross validation, point out an accuracy value of 95.31 %. The labels 1 and 2, on the vertical and horizontal axis, stand for happiness and sadness, respectively.

As shown in Figs. 6 and 7 the dataset containing the head motion data generated an accuracy of 95.31 % after cross-validation against 89.06 % from the data set without the head motion features, which point out the importance of determining head motion when recognizing sadness. Also, it can be concluded that the use of different types of features improves the classifier performance, as mentioned in the literature. The features have relevant information to characterize the two emotions.

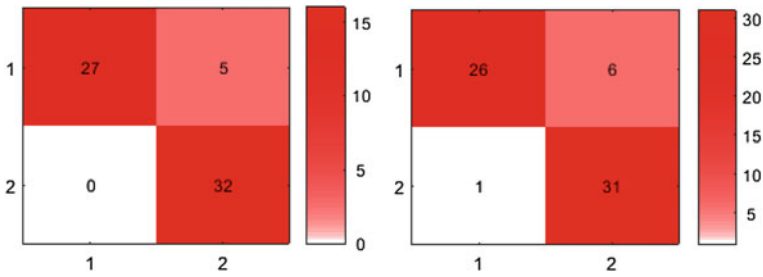


Fig. 6 Experimental results with only facial features. *On the left* the confusion matrix after training the SVM, with an accuracy of 92.19 %. *On the right* the confusion matrix after cross-validation, with an accuracy of 89.06 %

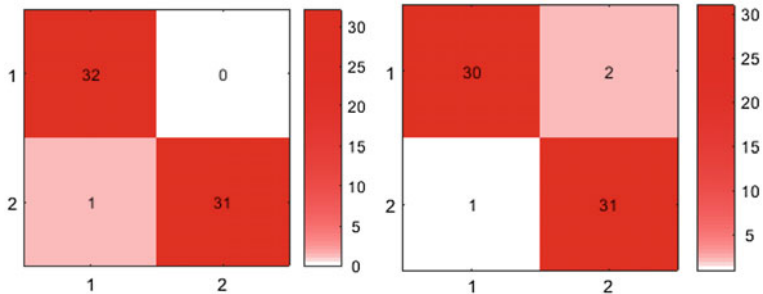


Fig. 7 Experimental results with facial features and head motion. *On the left* the confusion matrix after training the SVM, with an accuracy of 98.44 %. *On the right* the confusion matrix after cross-validation, with an accuracy of 95.31 %

4 Conclusions and Future Work

Several works in the literature are focused on recognizing the human emotions by using video images or a *Kinect* sensor to acquire the human face data. Regarding emotions classification methods, SVM, neural networks and Markov models, among others, are used.

The present work considers the use of the recent *Intel RealSense* 3D sensor for facial features extraction in an emotion recognition system applied to the recognition of happiness and sadness. The sensor dimensions are 150 mm × 30 mm × 58 mm. The built-in camera measures only 3.8 mm thin, 100 mm long and 8 mm high, which is an advantage when designing embedded systems. The goal was to verify if the *Intel RealSense* is a valid option for developing emotion recognition systems. The two opposite emotions, happiness and sadness, were considered in this preliminary analysis. SVM was used to classify the user's emotions and the classification accuracy was determined by k-Fold Cross Validation. 32 children from 6 to 9 years old participated in the system training for happiness and sadness. Sadness was registered with and without head movement. An accuracy of 95.31 % after cross-validation with head movement against 89.06 % from the data set without the head motion features was obtained.

The results point out the adequacy of *Intel RealSense* for facial features extraction in emotion recognition systems as well as the importance of determining head motion when recognizing sadness.

Future work considers recognizing, with the proposed system, the other four basic emotions: surprise, fear, angry, and neutral. The final goal of the project is to work with children with autism spectrum disorders, promoting social activities of recognizing and mimicking emotions.

Acknowledgments The authors would like to express their acknowledgments to all students for their voluntary co-operation. This work has been supported by COMPETE: POCI-01-0145-FEDER-007043 and FCT—Fundação para a Ciência e Tecnologia within the Project Scope: UID/CEC/00319/2013.

References

1. Jham, V., Puri, S.: Cases on consumer-centric marketing management. IGI Global (2014)
2. D'Mello, S., Calvo, R.: Beyond the basic emotions: what should affective computing compute? *Abstr. Hum. Factors Comput.* 2287–2294 (2013)
3. Rani, P., Sarkar, N.: Operator engagement detection for robot behavior adaptation. *Int. J. Adv. Robot. Syst.* **4**, 1–12 (2007)
4. Michel, P., El Kaliouby, R.: Real time facial expression recognition in video using support vector machines. In: *Proceedings of 5th International Conference on Multimodal Interfaces—ICMI'03*, p. 258 (2003)
5. Youssef, E., Aly, S.F., Ibrahim, A.S., Abbott, L.: Auto-optimized multimodal expression recognition framework using 3D kinect data for ASD therapeutic aid. *Int. J. Model. Optim.* **3** (2), 112–115 (2013)

6. Alabbasi, H.A., Moldoveanu, P., Moldoveanu, A.: Real time facial emotion recognition using kinect V2 sensor. *IOSR J. Comput. Eng. Ver. II* **17**(3), 2278–2661 (2015)
7. Intel® RealSense™ Technology. <http://www.Intel.com/content/www/us/en/architecture-and-technology/RealSense-overview.html>. Accessed 15 Jan 2016
8. RealSense—Get Started with RealSense Technology|Intel® Developer Zone. <https://software.Intel.com/en-us/RealSense/devkit>. Accessed 15 Jan 2016
9. Ekman, P., Rosenberg, E.: *What the face reveals* (2005)
10. FACS (Facial Action Coding System). <http://www.cs.cmu.edu/~face/facs.htm>. Accessed 25 Jan 2016
11. Sacavém, A., Wezowski, K., Wezowski, P., Linguagem, A.: *Corporal Revela o que as Palavras Escondem*. Top Books (2014) (in Portuguese)
12. Face Landmark Data. https://software.Intel.com/sites/landingpage/RealSense/camera-sdk/v1.1/documentation/html/index.html?doc_face_face_landmark_data.html. Accessed 16 Jan 2016
13. camera2.png (imagem PNG, 384 x 213 pixels). <https://software.Intel.com/sites/default/files/managed/99/95/camera2.png>. Accessed 04 Feb 2016
14. Face Pose Data [F200, SR300]. https://software.Intel.com/sites/landingpage/RealSense/camera-sdk/v1.1/documentation/html/index.html?doc_face_face_pose_data.html. Accessed 16 Jan 2016
15. Burges, C.C.: A tutorial on support vector machines for pattern recognition. *Data Min. Knowl. Discov.* **2**(2), 121–167 (1998)
16. Support Vector Machines (SVM)—MATLAB & Simulink. <http://www.mathworks.com/help/stats/support-vector-machines-svm.html>. Accessed 20 Jan 2016
17. Michel, P., El Kaliouby, R.: *Facial expression recognition using support vector machines* (2000)
18. Cross-Validation—MATLAB. <http://www.mathworks.com/discovery/cross-validation.html>. Accessed 20 Jan 2016

A Simple Control Approach for Stereotactic Neurosurgery Using a Robotic Manipulator

Carlos Faria, Carolina Vale, Manuel Rito, Wolfram Erlhagen
and Estela Bicho

Abstract In this paper, it is described a simple, expandable and easily integrable robotic system to be a direct replacement to the stereotactic frame in minimally invasive neurosurgeries. Robotic systems have several advantages over the traditional frame used in stereotactic neurosurgeries such as, improved precision, steadiness and flexibility. However, the robotic systems cleared to perform this procedure are closed and costly. A robotic manipulator was selected, based on repeatability, compactness and controller accessibility. The control application developed includes a registration module to calibrate the robot to the surgical reference frame and several algorithms that allow a precise and consistent, drilling and electrode guidance. Safety was the most important factor when designing the control application, and several mechanisms were implemented that replicate the market cleared robotic systems.

Keywords Stereotactic neurosurgery · Surgical instrumentation · Robotics

C. Faria (✉) · E. Bicho
Industrial Electronics Department, University of Minho, Guimarães, Portugal
e-mail: cfaria@dei.uminho.pt

E. Bicho
e-mail: bicho@dei.uminho.pt

C. Vale
Physics Department, Sciences Faculty, University of Lisbon, Lisbon, Portugal

M. Rito
Neurosurgery Service, Coimbra University Hospital Centre, Coimbra, Portugal

W. Erlhagen
Mathematics Department, University of Minho, Guimarães, Portugal

1 Introduction

Stereotactic neurosurgery is a minimally invasive surgical technique based on a well-defined three dimensional and coordinate space to map and pinpoint the anatomical structures to be operated [1]. The invasiveness of traditional open neurosurgery poses a significant threat to the patient due to the inevitably affecting surrounding structures. Reducing the procedure invasiveness and still accurately reaching even deep targets in the brain poses a significant advantage. Contrary to open surgery where neurosurgeons have a direct visual feedback of the operating field, in stereotactic neurosurgery the exposed surgical area is narrower [2]. Thus, the execution of the surgery relies on the precise location and reaching of the anatomical targets through the access points.

Typical examples of stereotactic neurosurgery include diagnostic procedures such as: biopsy, endoscopy, stereo-electroencephalography; and therapeutic treatments, which include but are not limited to: ablation, stimulation, lesion or radiosurgery. A device is required to precisely guide the probes according to pre-operative defined trajectories [3]. The most commonly used device for this purpose is the “stereotactic frame”, first reported in 1947 by Spiegel et al. [4]. Stereotactic frames, however, are considered unwieldy and inflexible, imposing limitations to the instrumentation handled and requiring extra setup steps for each surgical trajectory [5, 6].

A new approach based on robotic technology has been adopted to substitute the stereotactic frame. Robotic systems are inexhaustible, extremely precise and reliable. They excel at handling spatial information, provide more flexibility to reach even eccentric surgical trajectories and potentiate a friendlier interface [7–9]. Moreover, their sturdy structure allows it to assist the neurosurgeon during the drilling process, by controlling drill orientation and depth.

Robotic neurosurgery is a vibrant and active research field, with only a handful of robotic systems validated and market-ready. However, all of these systems share high acquisition and maintenance costs and have their control scheme closed [6, 10, 11]. The development of a robotic system for neurosurgery follows one of two approaches, either the robot is originally designed for the task, or it is adapted from an industrial robot. Nonetheless, this development process seldom follows a straight path from concept to development. And it is here precisely that the presented system fits its role, not only as a proof and testing tool, but it also as a solution for research problems like (electrode implantation in mice).

In this paper it is proposed a simple robotic system for precise instrumentation guidance that includes the features of the listed commercially available products such as, dexterity, precision, steadiness as well as several safety mechanisms. The presented apparatus is intended to be a direct replacement of the stereotactic frame, hence the surgical workflow is kept unchanged for the most part.

2 Surgical Technique Description

The objective of this robotic system is to provide a direct and viable replacement for the stereotactic frame whilst keeping the surgical procedure unchanged. To better explain how the robot fits in the neurosurgical room, it is described the surgical technique of a traditional stereotactic neurosurgery (in this case a deep brain stimulation surgery to treat Parkinson's disease symptoms).

Initially the patient undergoes a non-stereotactic MRI (Magnetic Resonance Imaging) exam, which is later matched to a stereotactic CT (Computed Tomography) scan, Fig. 1. The electrodes trajectories towards the clinical target are decided by the neurosurgeons in the planning software to reach the target and avoid vessels, sulci or ventricles. When the trajectories are confirmed, the planning software calculates the stereotactic coordinates to be set on the ZD frame (INOMED, Emmendingen, Germany).

Inside the operating room, these coordinates are first tested in a phantom device, Fig. 2. After confirmation, the frame is unmounted from the phantom and placed in the reference ring. The neurosurgeon makes a scalp incision and drills a burr hole directly above the spot which approximates the electrodes entry point, Fig. 3. The drilling process is manually executed with no assistance or frame guidance.

The frame must once again be configured to the correct orientation coordinates. A device is attached to lower the electrodes to the initial stimulation position, Fig. 4. The microelectrodes are lowered in millimetre steps and the stimulation parameters adjusted to find the optimal configuration which allow for the best possible symptomatic improvement. A permanent macroelectrode replaces the microelectrodes once the best parameters are found. The implantation of the Implanted Pulse Generator is performed afterwards.

Fig. 1 Stereotactic reference ring with attached fiducial plates

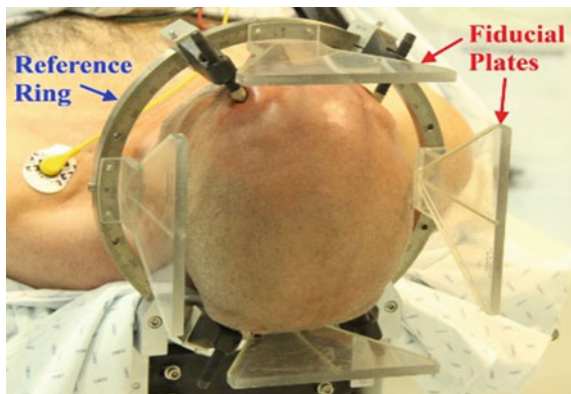


Fig. 2 Confirmation of planned trajectories using a phantom device

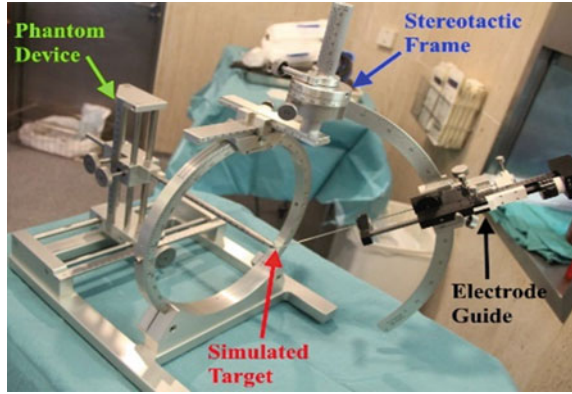


Fig. 3 Drilling of the burr hole



Fig. 4 Electrodes placement



3 Materials and Methods

After acquiring some insight about stereotactic neurosurgery and testing with three different robotic systems in a simulation environment [12, 13], it was time to port the developed control code to a real robot platform.

3.1 Robotic System

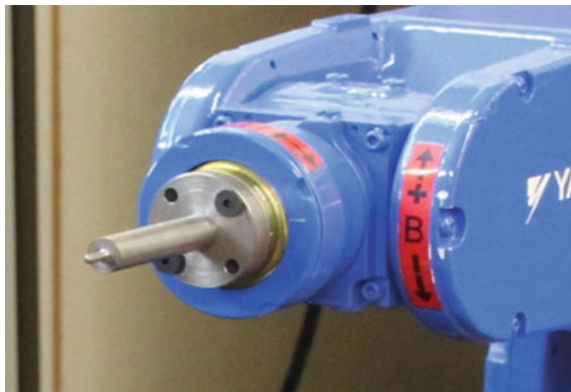
The tests were performed with a lightweight Yaskawa Motoman MH5 robotic arm and the NXC100 controller. The robotic arm has a 706 mm horizontal reach, 5 kg payload and achieves a repeatability of ± 0.02 mm. The controller features a built-in Ethernet and an easy connection protocol through standard TCP/IP to access the controller methods in an on-line programming mode.

To register the robot to the surgical space and to incorporate the same guiding tools as the stereotactic frame, it was designed a pivot point end-effector (Fig. 5) for the registration procedure, and an end-effector for porting the electrode drive (Fig. 6). One of the pieces of the electrode drive was used as the drill fitting.

3.2 Registration

In stereotactic surgery, it is paramount to keep a rigid relation between the guiding instrumentation and the patient. The reference ring of the ZD Frame keeps the patient's head immobile by fixing it to the operating table and provides the common reference for the surgery. An end-effector pivot tool was designed to touch the divot markings on the reference ring, Fig. 7. Hence, it is known the position of the four divots ($i = 1, 2, 3, 4$) on the reference ring (${}^R P$) and the position of the divots on the

Fig. 5 Pivot point end-effector



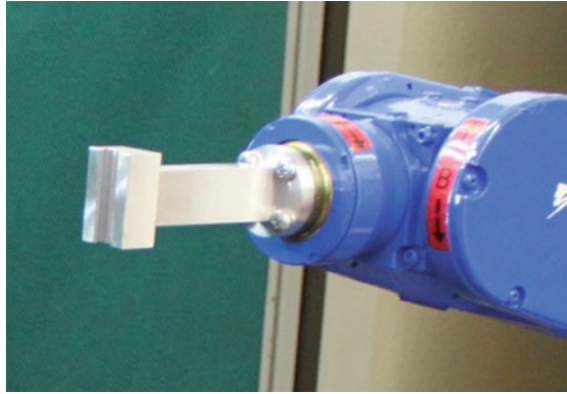


Fig. 6 Tool-holder end-effector

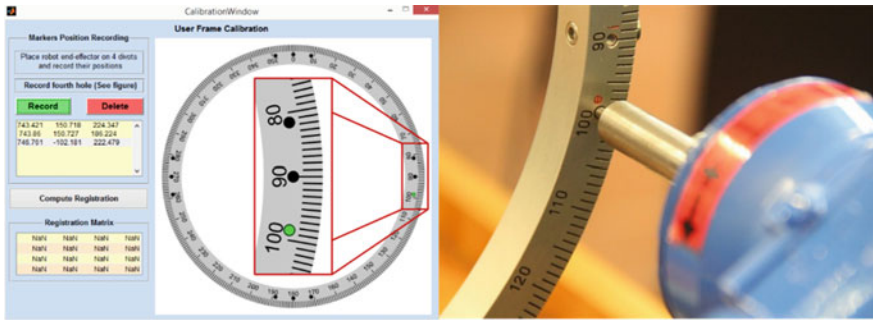


Fig. 7 Pivot end-effector touching the reference ring divots

robot base reference frame (B_iP)—calculated through direct kinematics. To find the rigid transformation that relates the robot to the surgery space, a least squares fitting algorithm was applied.

$${}^B_iP = {}^B R_i^R P + P_0 \tag{1}$$

This closed-form solution allows the calculation of the translation (P_0) and rotation (${}^B R_i^R$) components that specify the rigid transformation that maps the reference ring coordinates into the robot base frame. Since the measurements are not exact in a real scenario, the algorithm minimizes the residual sum of squared errors, i.e.,

$$e_i = {}^B R_i^R P + P_0 - {}^B_iP \tag{2}$$

$$\min_{R, P_0} \sum_{i=1}^4 \|e_i\|^2 \quad (3)$$

For more details refer to [14].

3.3 Coordinate Convention

To guarantee a transition from the stereotactic frame to the robotic system, it was necessary to convert ZD frame coordinates¹ to Cartesian space coordinates. The ZD stereotactic frame requires the user to input five scalar coordinates: {A, B, C} directly relate to the y-, x- and z-axis position coordinates in the reference ring; and {D, E} where D represents a rotation around the y-axis (ψ) and E a consecutive rotation around the x-axis (θ).

$${}^S P = [B \ A \ C]^T \quad (4)$$

$$\psi = D - 90^\circ \quad \text{and} \quad \theta = E - 90^\circ \quad (5)$$

The ZD frame only specifies the y- and x-axis rotations, while the z-axis rotation (ϕ) is in fact an extra degree of freedom. The z-axis rotation coordinate was calculated to maximize the dexterity of the robot to reach each trajectory. The trajectory vector (\vec{t}) is calculated as:

$$\vec{t} = \text{rot}_y(\psi) \cdot \text{rot}_x(\theta) \cdot [0 \ 0 \ -1]^T \quad (6)$$

By projecting the trajectory vector on the *xy-plane* of the reference ring (t_{xy} with only x- and y-components, $t_{xy,x}, t_{xy,y}$), the z-axis rotation can be calculated:

$$\phi = \begin{cases} 90^\circ, & t_{xy} = \vec{0} \\ -\text{atan}_2(-t_{xy,x}, -t_{xy,y}), & t_{xy} \neq \vec{0} \end{cases} \quad (7)$$

With the position and orientation completely defined the robot can position its tool to match the electrode's insertion trajectories.

¹These coordinates are directly computed by the surgery planning software after selecting the electrodes' trajectories. The ZD frame is considered to have been mounted in its 0° position.

3.4 *Robotic Motions*

To keep the system simple yet functional, it was used the motion commands of the NXC100 controller. The commands listed below are common among industrial controllers.

For this particular application three types of motions were used.

1. *Joint motion*, typical point-to-point motion where the position of each joint is interpolated to move from the initial to the target position individually, but synchronously; the end-effector trajectory in Cartesian space is not relevant.
2. *Linear motion*, each joint executes a coordinated motion, such that the end-effector describes a line in Cartesian space to reach the specified Joint or Cartesian position;
3. *Incremental motion*, similar to *Linear motion*, however it is specified the increment of the end-effector position in Cartesian coordinates (only), instead of the absolute target;

Additional parameters for the motion commands include: joint and Cartesian velocity limits, the tool dimensions, and the reference frame whenever Cartesian coordinates are involved.

The motion planning was divided into the *approach* and the *tool handling* phase. The *approach* phase involves the movements between the robot home or safe position and the stereotactic trajectory—manipulator is at least 250 mm away from the patient’s head. The *tool handling* movement phase starts when the manipulator end-effector is already aligned with the stereotactic trajectory and it just translates along this trajectory.

To enforce safety, the manipulator joint speed is maxed at 15 % during its *approach* phase, and 3–5 % during the *tool handling* phase. As neither high-forces nor velocities are required in stereotactic neurosurgeries, functioning at a lower speeds causes less stress to the joints, makes the robot motions more predictable and provides the operator more control over the robot actions [15].

3.5 *High-Level Control Scheme*

The presented control scheme features a control application developed in MATLAB (a requirement of the neurosurgeons’ team), a middleware communication layer using YARP and a wrapper to interface with the robotic controller methods written in C#.

Control Application

The control application includes: (i) the coordinate conversion module to translate the ZD frame coordinates to Cartesian space, (ii) the registration module to calculate the transformation between the robot and the reference ring, (iii) the motion planning module that defines the robot movements during each step, according to

the NXC100 controller functions, (iv) the communication module and (v) a user interface module. The graphical user interface (GUI) includes simple surgery related commands and cycles through different windows guiding the neurosurgeon at each step.

Middleware Layer

The robotic system communication layer was implemented using the YARP (Yet Another Robotic Platform) framework. This allows seamless integration and control over different devices, using different programming languages, with a simple abstract messaging system. The communication is processed between network sockets following the TCP/IP protocol to exchange messages that obey to a specific predefined format.

4 Procedure Execution

After connecting to the robot controller and inserting the pre-operative plan the user interface guides the surgeon through the operation, changing its interface dynamically as the procedure unfolds.²

Approaching the Selected Trajectory

After selecting trajectory, the *Approach* task is ready to be executed. It is calculated the end-effector coordinates to position the robot's tool holder z-axis collinear to the stereotactic trajectory, distanced 350 mm from the target. Then, the robot executes a sequential *Joint motion* from its home/safe position to this new calculated reference. Immediately after, another command is sent to move the robot in a *Linear Motion* along its tool reference z-axis until reaching a distance of 250 mm from the target.

The neurosurgeon can now attach the surgical tool to the tool holder, and adjust the robot's orientation to a more favourable posture. This change in the robot's orientation involves rotating the robot's end-effector around its tool's z-axis in steps of 10°, using an *Incremental motion* and without changing any other position or rotation variables.

Assisted-Drilling

When executing the *Drill* task, the manipulator advances its end-effector in an *Incremental motion* collinear to the electrode's trajectory towards the target. The distance between the tool and the target was set in accordance to the drill length. After reaching the target position, the joint brakes are engaged and the neurosurgeon may perform the drill step. The tool holder controls the drill orientation as well as its depth, to avoid damaging structures beyond the skull's inner wall (Fig. 8).

²The procedure demonstration can be visualised at: <http://marl.dei.uminho.pt/public/videos/RoboticNeurosurgeryDemonstration.html>.



Fig. 8 Performing assisted drilling, with orientation- and depth-control

Returning to a Safe Position

At this point, the *Retreat* task is the only step available. By selecting it, the robot moves its end-effector in a *Linear motion* along the electrode's trajectory outwards/away from the patient's head, until a distance of 250 mm from the target. The current tool is substituted by the electrode's microdrive.

Assisted Electrode's Guidance

Once more, the robot advances its end-effector collinear to the electrode's trajectory towards the target in an *Incremental motion* (again, for demonstration, the distance was set in accordance to the microdrive with the defined electrode depth), and assisted electrode's guidance is executed. The surgery phantom device is used to simulate the target coordinates instead of the dummy model in order to demonstrate the electrode, positioned along the selected trajectory, reaching the selected target (Fig. 9).



Fig. 9 Holding electrode guide to position electrode at the surgical target

Finishing the Procedure—Returning to Home Position

At the end, the robotic manipulator retracts in a composed motion mirroring the initial approach movement. Initially the robot moves its end-effector outwards and along the trajectory in a *Linear motion* until reaching 350 mm from the patient's head. Then, and after removing the electrode's microdrive, the robot moves to home position in a *Joint motion*.

By following a sequence of centripetal motions when approaching or moving away from the patient, it makes the robot action more predictable and avoids movements between trajectories that could potentially collide with the patient.

For safety reasons and when initiating a new procedure—before approaching a selected trajectory—the robotic controller checks the robot and connection state, and if the arm is at its home position. If the robotic system gathers all the ideal conditions to operate, the user is informed and asked to give consent move the robotic arm. Whenever the robot moves, the servo power is activated, and the user is informed that it is moving. When the robot is not moving, its joint brakes are activated.

At any moment the user can stop/prevent the robot movement, either using a hardware or software trigger—Emergency and Hold buttons—found at the programming pendant, robot controller or in the graphical user interface. If the desired position/orientation is not reached, in case robot movements are stopped during the process or, for example, if the robot reaches a joint limit, an alarm is triggered reporting the position and orientation errors.

When executing a stereotactic procedure using the developed control application, task buttons are enable/disable according to the next step of the procedure, guiding the user through the execution of the procedure. During the robot motion all task buttons are disable. A green/red colour is used to notify the user for the success of performing the required task.

5 Conclusions

Robotic intervention in neurosurgery is a growing trend with the entry on the market of new systems and constant breakthroughs in terms of provided technology. Robotic agents offer multiple advantages when compared to more traditional hardware like stereotactic frames, namely, in terms of improved precision, consistency and flexibility. However, market available robotic systems are pricy and closed.

Here it was presented a simple solution that has the potential to work as a direct replacement to the stereotactic frame, bringing all the advantages of a robotic system while scaling down system complexity. It provides an easily integrable, expandable and low-cost system for stereotactic neurosurgery.

Even though the system is not permitted to perform neurosurgery as-is, it can be used as a proof-of-concept instrument, or in a research environment to catalyse the development of new systems for stereotactic neurosurgery.

Future work includes adding sensor redundancy, i.e., it is common for surgical robots to have a fiducial marker at its end-effector that is continuously tracked by an optical tracking system. At any given moment, the end-effector's position read on this tracking system and from the robot's end-effector position should overlap. This system is also being implemented in manipulators with more degrees of freedom to evaluate how the elbow redundancy enhances the system's flexibility while adjusting to the available workspace.

References

1. Gildenberg, P.: The history of stereotactic and functional neurosurgery. In: Gildenberg, P., Tasker, R., Franklin, P. (eds.) *Textbook of Stereotactic and Functional Neurosurgery*, 1st edn, pp. 5–19. McGraw-Hill Companies (1998)
2. Rhodes, M., Glenn, W., Azzawi, Y., Slater, R.: Stereotactic neurosurgery using 3-D image data from computed tomography. *J. Med. Syst.* **6**(1), 105–119 (1982)
3. Gabriel, E., Nashold, B.: Historical development of stereotactic frames. In: Gildenberg, P., Tasker, R., Franklin, P. (eds.) *Textbook of Stereotactic and Functional Neurosurgery*, 1st edn, pp. 29–49. McGraw-Hill Companies (1998)
4. Spiegel, E., Wycis, H., Marks, M., Lee, A.: Stereotaxic apparatus for operations on the human brain. *Science* (80) **106**(2754), 349–350 (1947)
5. Dorward, N., Paleologos, T., Alberti, O., Thomas, D.: The advantages of frameless stereotactic biopsy over frame-based biopsy. *Br. J. Neurosurg.* **16**(2), 110–118 (2002)
6. Faria, C., Erlhagen, W., Rito, M., De Momi, E., Ferrigno, G., Bicho, E.: Review of robotic technology for stereotactic neurosurgery. *IEEE Rev. Biomed. Eng.* (2015)
7. Mattei, T., Rodriguez, A., Sambhara, D., Mendel, E.: Current state-of-the-art and future perspectives of robotic technology in neurosurgery. *Neurosurg. Rev.* (2014)
8. Beasley, R.: Medical robots: current systems and research directions. *J. Robot.* **2012**, 1–14 (2012)
9. Nathoo, N., Cavaşođlu, M.C., Vogelbaum, M.A., Barnett, G.H.: In touch with robotics: neurosurgery for the future. *Neurosurgery* **56**(3), 421–33; Discussion 421–33, Mar 2005
10. Gomes, P.: Surgical robotics: reviewing the past, analysing the present, imagining the future. *Robot. Comput. Integr. Manuf.* **27**(2), 261–266 (2011)
11. Doulgeris, J., Gonzalez-Blohm, S., Filis, A., Shea, T., Aghayev, K., Vrionis, F.: Robotics in neurosurgery: evolution, current challenges, and compromises. *Cancer Control J. Moffitt Cancer Cent.* **22**(3), 352–359 (2015)
12. Faria, C., Bicho, E., Rito, M., Louro, L., Monteiro, S., Erlhagen, W.: Robotic assisted deep brain stimulation neurosurgery: first steps on system development. In: *IASTED International Conference on Biomedical Engineering*, no. BioMed, pp. 331–338 (2013)
13. Faria, C., Vale, C., Machado, T., Erlhagen, W., Rito, M., Monteiro, S., Bicho, E.: Experiential learning of robotics fundamentals based on a case study of robot-assisted stereotactic neurosurgery. *IEEE Trans. Educ.* 1–1 (2015)
14. Horn, B.: Closed-form solution of absolute orientation using unit quaternions. *J. Opt. Soc. Am.* **4**(April), 629–642 (1987)
15. Fei, B., Ng, W.S., Chauhan, S., Kwok, C.K.: The safety issues of medical robotics. *Reliab. Eng. Syst. Saf.* **73**(2), 183–192 (2001)

Motion Control of Mobile Autonomous Robots Using Non-linear Dynamical Systems Approach

Fernando Ribeiro, Gil Lopes, Tiago Maia, Hélder Ribeiro, Pedro Osório, Ricardo Roriz and Nuno Ferreira

Abstract This paper presents a solution to the problem of motion control of an autonomous robot, moving in a dynamical and unstable environment. It is based on non-linear dynamical systems, modelling the state variables that define the motion of a robot under an omnidirectional platform, like its direction of navigation and velocity. The approach used, is based on a set of non-linear differential equations that model the evolution of state variables along time, based on the concept of attractors and repellers. In the official RoboCup Middle Size League field, a target is used to attract the robot to a certain position (could be the ball or a desired position to receive the ball), while a repeller could move the robot away from its original path (given by obstacles in the surrounding environment). The research was firstly carried out in a computational simulation environment and later on with robots in a real environment.

Keywords Dynamical environments • Non-linear dynamical systems • Middle size league • MSL • RoboCup • Mobile autonomous robots • Motion control

F. Ribeiro (✉) · G. Lopes · T. Maia · H. Ribeiro · P. Osório · R. Roriz · N. Ferreira
Laboratório de Automação e Robótica, University of Minho, Braga, Portugal
e-mail: fernando@dei.uminho.pt

G. Lopes
e-mail: gil@dei.uminho.pt

T. Maia
e-mail: a57126@alunos.uminho.pt

H. Ribeiro
e-mail: a58795@alunos.uminho.pt

P. Osório
e-mail: a68541@alunos.uminho.pt

R. Roriz
e-mail: a68536@alunos.uminho.pt

N. Ferreira
e-mail: a68624@alunos.uminho.pt

1 Introduction

This paper intends to describe a solution for the motion control system of RoboCup's Middle Size League Team, MINHO TEAM, from University of Minho. The proposed method uses world state information gathered by the various on-board sensing systems, to build a meaningful world model, representing the current state of the world the robot is inserted in. Using that information, the robot plans its motion path using non-linear differential equations to model the state variables that define the robot's behavior. Targets act like "attractors" of the system and obstacles act like "repellers", providing a heading, rotational and linear velocities that the robot has to follow. This is performed in order to avoid collisions and meet his target, in an ideal manner. The application of non-linear dynamical systems theories has become more and more important, given the continuous evolution of computational technology. The capability of building powerful control systems that can now be mobile, small, autonomous, and usually act in dynamical environments, creates different and new problems, in comparison to controlled environments. The MSL RoboCup league has been throughout the years, the most evolving and competitive league in RoboCup. As the robots move faster, the existence of highly dynamical environments is inevitable, creating new challenges to the teams. Robots have to cope with the fast-changing dynamical environments and coordinate the motion of every agent on the field. This stimulates great developments in control applications, computer vision, artificial intelligence, cooperative behaviors, always regarding autonomous robots.

Section 2 addresses a general overview over the RoboCup's Middle Size League, while in Sect. 3 a closer look to the robots motion system is taken, the world modelling approaches and how this relates to the basic intrinsic of the proposed approach. Section 4 describes the mathematical equations, also highlighting the importance and meaning of every variable. Results are presented in Sect. 5, followed by a discussion. Section 6 presents some conclusions and future work to be performed.

2 RoboCup's Middle Size League

One of the most important leagues in the international RoboCup initiative is the Middle Size League [1], commonly referred to as MSL. It was created in 1997, where MINHO TEAM [2] was a part of it since 1999. Throughout the years, many rule changes have been carried out to increase expectations for the league, coping with the continuous advances in computing technology. This changes forced the teams to evolve, developing new systems and approaches, to both old and new problems, coming up with diverse solutions. The ultimate goal of the RoboCup initiative is to have a team of fully autonomous humanoid robots that will play, and hopefully win, against the winners of the human soccer World Cup, by the year of 2050.

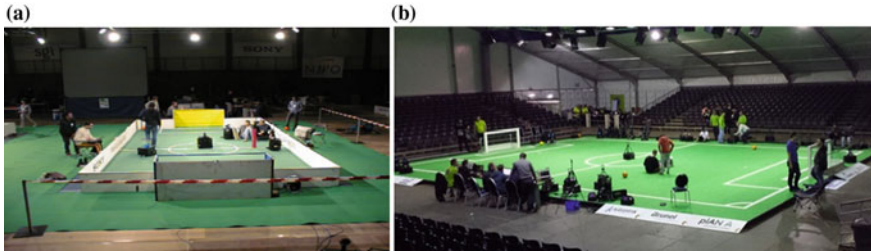


Fig. 1 MSL soccer field: **a** previous version with walls and colored markings in the corners and goals; **b** actual field with no walls, white goals and no color markings

The field of the MSL competition tries to replicate, in a reduced scale, the field of an ordinary human soccer game. In a more basic setup, it uses a green carpet, white line markings and reduced size goals. As the technology of cameras and computers evolve, the processing power and image quality is also visibly better, making very difficult tasks to be performed easier and faster nowadays. The MSL field also increased in size and no longer has the original color markings both on the goals and corners. It is at the moment quite similar to a conventional soccer field but at a scale (Fig. 1).

This evolution is highly related to the public and scientific community demand to see more spectacular games, provided by the MSL Teams and their robots. The rules have little restrictions regarding the development of hardware and software, allowing the teams to be more creative, coming up with new solutions that are shared after the competitions. Next, a typical MSL robot motion system is presented, mainly addressing its omnidirectional nature and the world state modelling mechanisms, which are crucial to the proposed method development.

3 Robotic Platform and World Modelling

The motion system from every team is almost the same, having little mechanical twists from team to team, having three or four-wheeled systems, but always relying on the omnidirectional [3] capabilities. Having an omnidirectional mobile robotic system is a major improvement from two driving wheel systems, allowing movement in every direction without performing maneuvers. It also allows independent rotational and linear velocities to be achieved. The fact that an omnidirectional platform provides this kind of movements, it allows for faster and direct paths to be made, increasing the dynamical nature of the environment. Robots can actually reach very high motion speeds of up to 4 m/s. The wheels are positioned at the base platform displaced at an angle of 120° from each other as shown in Fig. 2. Special wheels (also known as Swedish wheels) are used, that allow sideway or lateral movement of the wheels. Depending on the speed of each wheel, all sort of platform movements and directions can be attained (linear, rotational, etc.).

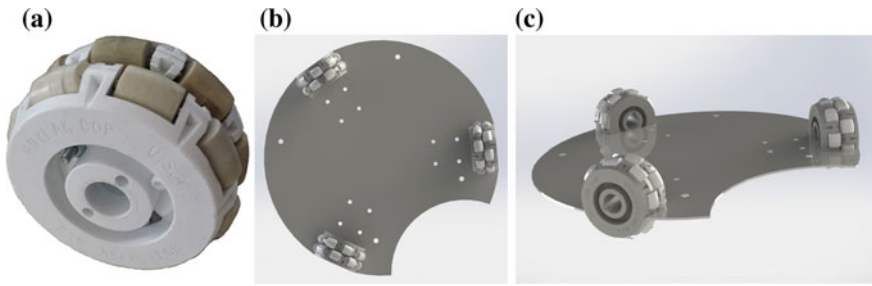


Fig. 2 Omnidirectional motion: **a** Swedish wheel; **b** Base platform with three wheels displaced 120° from each other (*top view*); **c** Base platform on the floor

To gather information of the surrounding environment and build an accurate and efficient world model, the robot uses a Gigabit RGB camera, pointing upwards to a catadioptric mirror [4], thus capturing a “top view” image of 360° around the robot center point (Fig. 3). Using the white field markings captured by the camera, the robot is able to perform self-localization, knowing its global position in the soccer field. It is aided by an Inertial Measurement Unit (IMU), to provide the robot’s true heading. Furthermore, using the vision system, the robot is allowed to know the ball’s position, which is usually a target (an attractor) and the position of obstacles (the repellers), both of human, robotic or static (infrastructure) nature.

The capability of self-localization and world modelling [5, 6] is crucial to the proposed method, as the differential equations use this information to model the state variables, defining the desired and optimal motion. As a basic preposition for further developments and explanations of the application, the resultant motion is a combination of the contribution of obstacles, which exerts a repulsive force in the “force field”, and the target, which contributes with an attractive force. One can think this through regarding magnetic fields, as the robot being a “north-pole”, the target (or targets) being a “south-pole” (which north-poles are attracted to) and the obstacles also as “north-poles”, that repel other “north-poles”.

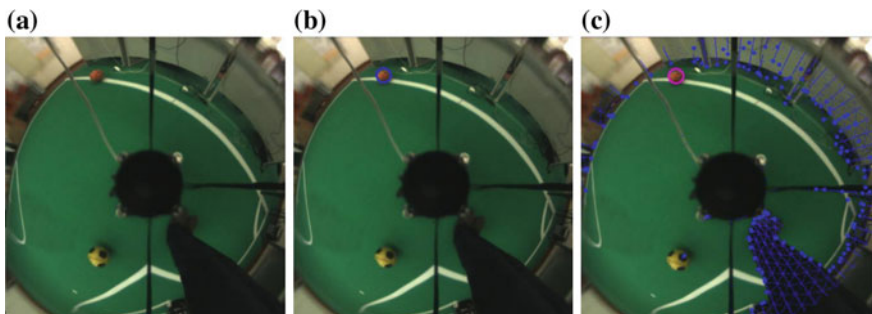


Fig. 3 Robot’s vision using a catadioptric mirror: **a** raw image; **b** detection of the orange ball (attractor); **c** the *blue dots* are self-detections of obstacle points (repeller)

Obstacles can be addressed in two different ways: (a) by the use of radial scan lines (vision system) as “virtual distance sensors”, computing the global obstacle contribution using individual contributions from this “virtual sensors”; (b) estimation of the world position of the obstacles, using all the obstacle points gathered, to create the repellers, instead of summing individual contributions. Every pixel in the image is directly mapped to a world distance. In other words, for every pixel in the image, there is a relative value in meters regarding the robot position. With this, after knowing the robot’s global positioning, the world and relative positions (in meters) of targets and obstacles can be estimated. Next section addresses the mathematical and theoretical approach taken.

4 Theoretical Approach and Considerations

Before presenting the theoretical approach and the mathematical equations using non-linear dynamical systems [7–9], one should be reminded that a global positioning of the robot in the field is calculated. Therefore, the robot’s relative position to a target (the ball which is a moving target) and obstacles are accurately obtained, whether by local or shared information. When analyzing a non-linear dynamical system, a linearization process is necessary, at least around the point of operation, to enquire the behavior of the system. It is not enough to fully analyse and model the behavior of more complex non-linear dynamical systems. This linearization process raises two basic limitations:

- (a) As the linearization consists in an approximation in the neighborhood of a point of operation, it only allows to predict the behavior of the system locally, around that point, not allowing predictions far from the operation point, making a global prediction along time difficult.
- (b) The dynamics of non-linear systems are much richer and complex than a linear system, existing various phenomena that are direct consequences of the nature of the system, helping to describe and predict the behavior of the system along time. The phenomena are, for example, the existence of bifurcations, that can model behaviors, the existence of various equilibrium points, where the system can converge (be attracted) or diverge (be repelled) from, defining heavily the global behavior of the system, and even chaos.

Regarding the practical application, it is crucial to be able to control and predict the behavior of the robot in every possible situation, even when the environment changes dramatically, being this the base premise to use this approach, instead of others. The existence of equilibrium points is the key, as one can place attracting and repelling equilibrium points (Fig. 4), wherever it is wanted to (global positions in the field or directions/headings), ending up with the desired behavior.

Furthermore, it should be stated that the slope of an equilibrium point represents the “force” that a particular attractor or repeller exerts on the system. After explaining the basic concepts that involve the proposed method, clearly the

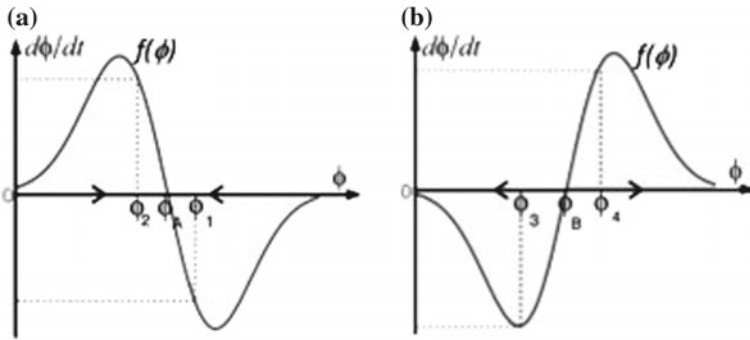


Fig. 4 Phase plots of dimensional dynamical system: **a** An attractor in the direction ϕ_A ; **b** A repeller in direction ϕ_B (Source [7], p.11)

concepts of equilibrium points, attractors, repellers and “force magnitudes”, it should be now stated the theory applied to the practical situation. Every robot should be capable to move smoothly towards its target while avoiding collisions, with one or more obstacles, being robots from the other team or teammates (Fig. 5).

The robot’s navigation direction Φ_{robot} , in relation to an external coordinated system is a behavioral variable, representing the direction that the robot should follow along time. Likewise, Ψ_{target} represents the direction of the target from the robot’s point of view and $\Psi_{obstacle}$ the direction of an obstacle. This non-linear dynamical systems approach taken here can be divided in two separate subsystems: (a) The control of the direction of navigation; (b) The control of the robot’s velocity.

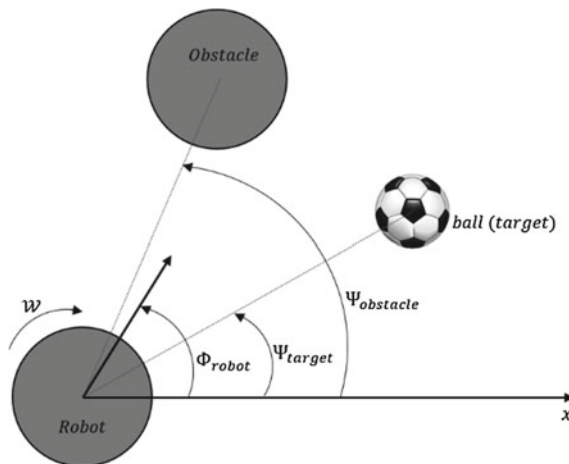


Fig. 5 Common situation where a robot aims to a target while being disturbed by an obstacle. Different variables/identities can be identified that will take place as world information in the differential equations

4.1 Direction of Navigation

During every time step in the robot's movement, the behavioral variable Φ_{robot} is updated using differential Eq. (1).

$$\frac{d\Phi_{robot}}{dt} = f(\Phi_{robot}) = f_{target}(\Phi_{robot}) + f_{obstacle}(\Phi_{robot}) \quad (1)$$

The vector field of Eq. (1) is built under additive forces, both negative and positive signed, where the evolution of the direction of navigation is a function of forces exerted by the target, f_{target} , which is an attractive force, and a sum of forces exerted by all the existing obstacles, $f_{obstacle}$, having a repelling nature. When controlling the motion of a robot during a soccer game, the objective is to drive the robot to a certain location, whether to go after the ball or reach a certain position in the field (tactical positioning, both attacking and defensive). The desired location has the direction Ψ_{target} , causing the system to "drive" to that equilibrium point (that direction), being the force it exerts expressed by (2).

$$f_{target}(\Phi_{robot}) = -\lambda_{target} \sin(\Phi_{robot} - \Psi_{target}) \quad (2)$$

The fixed/equilibrium points of Eq. (2) are Ψ_{target} and $\Psi_{target} + \pi$, with a magnitude of $-\lambda_{target}$, meaning that the first fixed point will have negative slope, being an attractor, and the other fixed point, right in the opposite direction, that has positive slope, is a repeller, so, f_{target} will only drive the system towards the target if $\lambda_{target} > 0$. The bigger the λ_{target} the faster the robot will go towards the direction of the target. But an upper limit has to be considered, otherwise the repulsive force of the obstacles will be minimal, comparing to the attractive force of the target, and the robot will not avoid obstacles, crashing into them if they step in the path between the robot and the target.

Through the radial scan lines used in the vision system presented in Sect. 3, a set of 72 distances, spaced by 5° each, make up the real time virtual distance sensors set (Fig. 6).

The radial scan lines provide the distance to the nearest obstacle, computing then the contribution of each virtual sensor using Eq. (3).

$$f_{obstacle,i}(\Phi_{robot}) = \lambda_i (\Phi_{robot} - \Psi_i) \exp \left[-\frac{(\Phi_{robot} - \Psi_i)^2}{2\sigma_i^2} \right] \quad (3)$$

The force exerted by each sensor i is a repulsive force in the Ψ_i direction, where $\Phi_{robot} - \Psi_i$ is a known and constant value, σ_i is the field of view of the sensor, not relating to the external referential whatsoever. The farther the obstacle is, the weaker is its repulsive force, much like a magnet, being a strong repulsive force when the obstacle is detected near the robot. λ_i is the magnitude of the repulsion force, and is given by (4), where β_1 is the maximum force magnitude of the

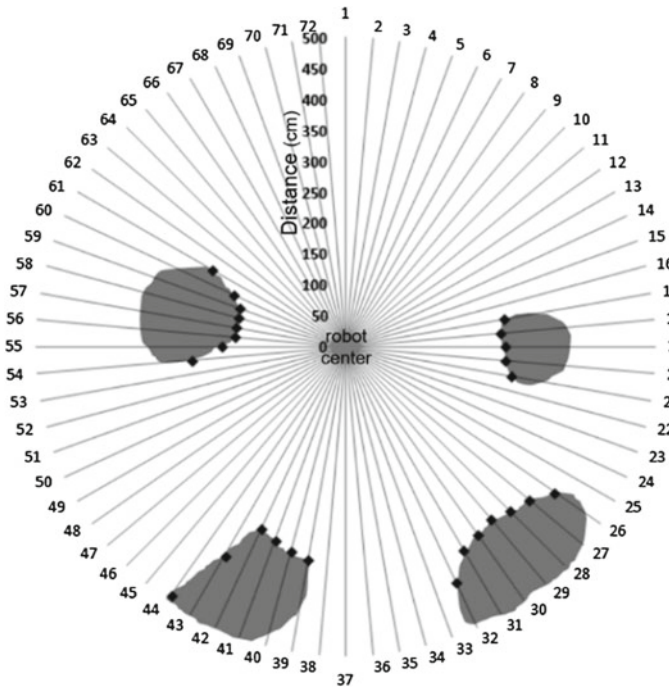


Fig. 6 Radial scan lines and the resulting set of virtual sensors and world obstacles, relative to the robot center

repulsion force, while β_2 is the decay rate of the function, finally, having d_i as the distance measured by the virtual sensor, from the robot to the obstacle:

$$\lambda_i = \beta_1 \exp \left[- \frac{d_i}{\beta_2} \right] \tag{4}$$

To obtain the final obstacle contribution, a summation of the individual repulsive forces has to be done, coming up with the total dynamics for the direction of navigation (5).

$$\frac{d\Phi_{robot}}{dt} = \sum_{i=1}^{72} f_{obstacle,i}(\Phi_{robot}) + f_{target}(\Phi_{robot}) \tag{5}$$

The resultant dynamics is then a combination of the obstacle contributions and the target, resulting in a final attractor that changes in time accordingly to the surrounding environment (Fig. 7).

This makes sense because, when the robot is driving towards its goal under the attractive force, should an obstacle come into play, the robot must avoid the obstacle while keeping his track towards the target. When it avoids the target, the repulsive

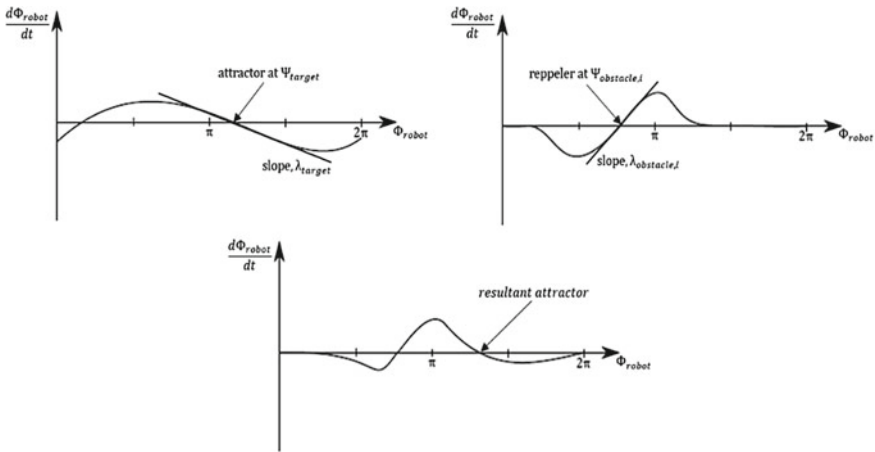


Fig. 7 Resultant attractor towards the target, combining the forces of attraction from the target and the forces of repulsion from an obstacle (Source adapted from [7], p.11)

force ceases to exist or it can continue if another moving obstacle shows up, like a defender, always providing the optimal direction of navigation.

4.2 Robot's Velocity

When controlling the velocity that the robot is moving, it is highly desirable that a maximum velocity is present to ensure platform stability. It is also desirable to have the robot moving at faster velocities when it is far from the target, and slower when it is near, to avoid hitting the ball when trying to catch it or to stop in the desired position. The hyperbolic tangent function does exactly that, being the velocity modelled by Eqs. (6) and (7):

$$v_{desired}(t) = -v_{max} \tanh(d_{target}) \tag{6}$$

$$\frac{dv}{dt} = \lambda_{velocity}(v - v_{desired}) \tag{7}$$

The desired velocity is computed from the hyperbolic tangent function, given the distance to the target, performing then a calculation of its acceleration. Through Forward Euler numeric integration, the velocity is computed, achieving a smooth trajectory in dynamic environments, always accounting interferences and preventing collisions.

5 Practical Application and Results

Regarding the highly dynamical environment of a MSL game, using the proposed method has numerous advantages, having also some disadvantages, bringing the necessity to use other supplementary algorithms to build a complete control solution. When it comes to decision making and path planning, this method offers the bifurcations as an inherited property of the non-linear dynamical systems, which models the behavioral variables. The team makes use of other complementary algorithms like the A* algorithm, to help improving the path planning of each robot, using then other complements of path planning in the artificial intelligence layer.

To validate all the prepositions and theoretical results, some tests were carried out using the robots from MINHO TEAM, who comply with all MSL rules, having also the other robots and humans as stationary obstacles, and the ball as a target. A 2D visualization tool was built to aid on the visualization task, in order to debug and help taking some conclusions on the system's performance (Fig. 8). The dark line represents the trajectory of the robot, the black robot is the robot moving with the ball, and the numbered robots the stationary obstacles.

In the first test (Fig. 8a) the obstacle 1 has little or no influence to the resulting motion, as it is not blocking the direct path between the robot and the target. Since no obstacle is in the way, the robot follows a straight path towards the target. The robot eventually gets himself near and between obstacles 2 and 3. It then verifies that the gap between them is not enough for it to pass in-between. A repeller is created with the direction in-between the two obstacles, starting to turn around. The system is now under the influence of the obstacles and the target, where the repulsion forces are bigger than the attraction force, due to the proximity of the robot to the obstacles.

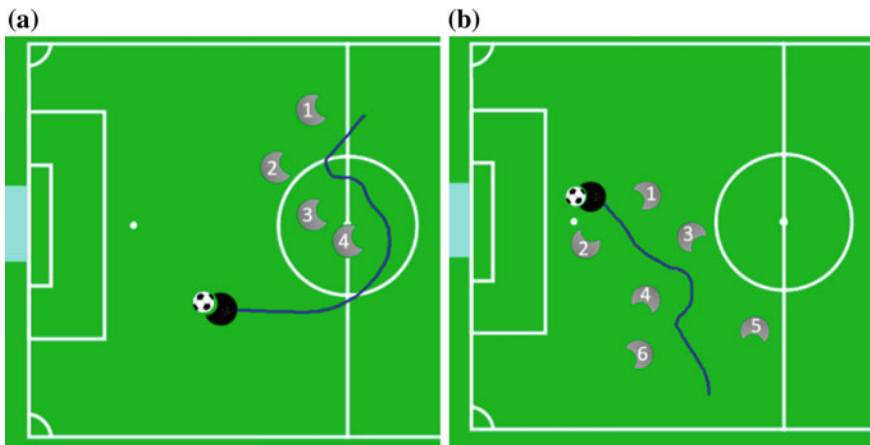


Fig. 8 Two separate conducted tests with the robot moving towards the ball: **a** The path chosen was around the obstacles; **b** The path chosen was through spaces between obstacles

The target attracts the system towards it (to the right-center), while the repellers push the robot in the opposite direction, forcing it to follow an almost straight line along the position of the obstacles. Once the robot passes by obstacle 4, the target once again becomes the stronger force in the system’s force field, turning straight towards the target, reaching the ball’s position without colliding with any of the obstacles. The same happens in the second test (Fig. 8b), where the system is running through an unknown environment, trying to move towards its target, being pushed to other routes given the existence of obstacles, but reaching successfully its target, as it is always trying to meet it in a straight line Fig. 9.

The direction of the target is near π but, due to the action of the obstacles and the resultant attractor, the system is attracted to another position while influenced by obstacles, making the robot’s direction of navigation to be somewhere near $7 \cdot \pi/4$. As the robot avoids the obstacles, their influence goes to zero, making the non-linear dynamical system that models the direction of navigation to have an attractor flowing to the target’s attractor.

The proposed method has the advantage of allowing a continuous influence in the robot’s motion plan, merging the higher level of intelligence with the lower lever control, with an intelligent layer that this method represents. In a higher level, one can plan the path for the robot to reach tactical positioning to receive a pass or drive the ball into a goal scoring position, with artificial intelligence algorithms. But those algorithms alone, cannot forecast the fast movement of obstacles, being expensive, both in performance and processing time, to use them alone. Instead, the presented approach takes on in a local basis, dealing with changes in the closer surrounding environment. It allows the system to accomplish the path defined by the higher level, while taking care of every environment change. It yields a complete smart autonomous system that provides a smooth, fast and trustworthy robot behavior.

During the tests, the robot achieved 80 % of its maximum velocity, an encouraging 2.1 m/s, with a processing time under 5 ms, never getting closer than

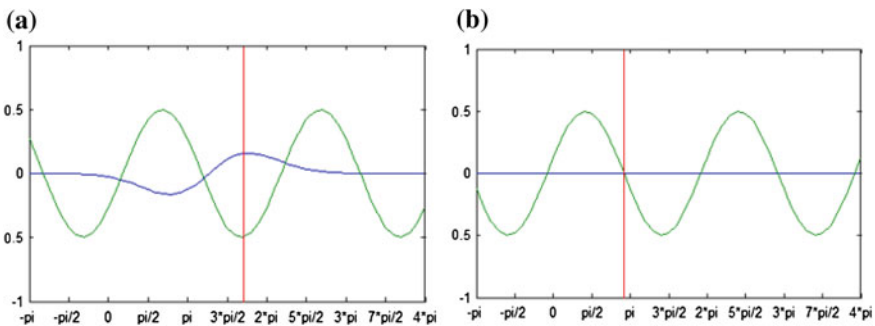


Fig. 9 Influence of the targets and obstacles on the system: **a** the system is under influence of the target and obstacles; **b** the system is only under influence of the target

50 cm from the obstacles (predetermined distance). The robot's task becomes more difficult when driving to a certain position while having the ball in its possession, performing rotations (towards the goal) in directions that are not the direction of navigation, making use of the omnidirectional capabilities of the platform. The motion planning is always above the path planning because, should a robot driving the ball towards a goal kick lose the ball, it cannot just keep moving. It has to change his course, retrieve the ball, changing its target, and re-target the goal scoring position, overriding the path planning directives.

6 Conclusion

This paper has made a theoretical and practical analysis to the motion control method, based on behavioral variables modelled by non-linear dynamical systems, applied to the robots and requirements of RoboCup's Middle Size League. The presented method is not sufficient alone. It does not provide a higher level (global) intelligent path planning. It only allows a very efficient and smooth motion (local) planning, when the necessity of avoiding dynamic obstacles or pursuing a moving target comes into place. It will be perfectly integrated with the higher level path planning algorithms, producing an intelligent, efficient and accurate motion and path planning system. Using the attractor-repeller mechanism, it is allowed to strategically place both attractors and repellers in the system. This produces a high impact in the robot's behavior, modelling its motion path at all time steps, accurately, faster and yielding smooth motion even at velocities up to 2 m/s. The results obtained met the expectations once the robot successfully reached its targets, driving the ball to kicking positions, while avoiding obstacles.

As for further work, various high level path planning algorithms shall be tested and implemented, compared with each other, trying to achieve the best cooperation possible between the higher, middle and lower layers of the motion control system. This will promote the creation of a hybrid system, which is more efficient and robust than any of the layers alone, creating a control system that is good enough to control a team of robots able to play a RoboCup's Middle Size League game.

Acknowledgment This work was developed at the Automation and Robotics Laboratory by MINHO R&D TEAM, University of Minho, under the supervision of Professor A. Fernando Ribeiro and A. Gil Lopes. The knowledge exchanging between the RoboCup's MSL teams and community contributed greatly for the development of this work.

This work has been supported by COMPETE: POCI-01-0145-FEDER-007043 and FCT—Fundação para a Ciência e Tecnologia within the Project Scope: UID/CEC/00319/2013.

References

1. Soetens, R., van de Molengraft e, R., Cunha, B.: RoboCup MSL—History, Accomplishments, Current Status and Challenges Ahead. In: em RoboCup Symposium Invited Paper on League Progress, João Pessoa, Brazil (2014)
2. Ribeiro, A.F., Lopes, G., Silva, P., Maia, T., Roriz, R., Gomes e N. Ferreira, A.: Minho Team'2016: Team description paper. Automation and Robotics Laboratory, University of Minho, Portugal (2016)
3. Doroftei, I., Grosu e V. Spinu, V.: Design and control of an omni-directional mobile robot. In: Novel Algorithms and Techniques in Telecommunications, Automation and Industrial Electronics, pp. 105–110. Springer, Netherlands (2008)
4. Perline, R., Köse, E., Zaslavski, A.: Achieving wide field of view using double-mirror catadioptric sensors. In: Multiscale Optimization Methods and Applications, June 2006, pp. 327–335 (2006)
5. Lauer, M., Lange, S., Riedmiller, M.: Calculating the perfect match: an efficient and accurate approach for robot self-localization. In: RoboCup 2005: Robot Soccer World Cup IX. Lecture Notes in Computer Science, vol. 4020, pp. 142–153. Springer, Berlin, Heidelberg (2006)
6. Silva, J., Lau, N., Neves, A.J., Rodrigues, J., Azevedo, L.: World modeling on an MSL robotic soccer team. In: Mechatronics: Special Issue on Advances in intelligent robot design for the Robocup Middle Size League, vol. 21, no. 2, pp. 411–422, March 2011
7. Bicho, E.: Dynamic approach to behavior based robotics: desing, specification, analysis, simulation and implementation. PhD thesis, University of Minho, Portugal (1999)
8. Scheinerman, E.R.: Invitation to Dynamical Systems. Prentice Hall College, New Jersey (2000)
9. Monteiro, S., Bicho, E.: A dynamical systems approach to behavior-based formation control. In: Proceedings. ICRA '02. IEEE International Conference on Robotics and Automation, pp. 2606–2611, Washington, DC (2002)

Autonomous UAV Outdoor Flight Controlled by an Embedded System Using Odroid and ROS

João Pedro Carvalho, Marco Aurélio Jucá, Alexandre Menezes, Leonardo Rocha Olivi, André Luis Marques Marcato and Alexandre Bessa dos Santos

Abstract Unmanned Aerial Vehicles (UAVs) have become a prominent research field due to their vast applicability and reduced size. An appealing aspect of the UAVs is the ability to accomplish autonomous flights in several contexts and purposes, and a variety of applications have been developed, from military to civilian fields. The system proposed in this work is a novel and simplified interaction between the user and the UAV for autonomous flight, where the necessary computation is performed in an embedded computer, decreasing response time and eliminating the necessity of long-distance communication links with base stations. Results are presented with both hardware in the loop simulations and a real UAV using Pixhawk, and Odroid and ROS as companion computer and software platform for code development.

Keywords Outdoor autonomous flight · Onboard processing · Control · Pixhawk · Odroid · ROS · UAV

1 Introduction

Recently, studies regarding Unmanned Aerial Vehicles (UAVs) field of research have gained prominence and prestige since these aircrafts became gradually more highlighted in modern community with a great number of applications. The large variability of types, forms and shapes of these vehicles their applications are vast, from environmental monitoring to aerial image making for digital terrain modeling [1], civil surveillance [2], military [3], delivery in commercial field [4], amongst others.

The proposal of aircrafts with the ability of executing a complete autonomous mission by pursuing a number of desired waypoints determined by a user has grown.

J.P. Carvalho · M.A. Jucá · A. Menezes · L.R. Olivi (✉) · A.L.M. Marcato · A.B. dos Santos
Department of Electrical Energy and Circuits, School of Engineering,
Federal University of Juiz de Fora, Juiz de Fora City, Minas Gerais State, Brazil
e-mail: leonardo.olivi@ufjf.edu.br

A.L.M. Marcato
e-mail: andre.marcato@ufjf.edu.br

The Robot Operating System (ROS) [5] provides a fast developing environment for testing and delivering the algorithms responsible for control and path planning for the aerial robots towards these waypoints. Among the many packages available at ROS community, MAVROS interfaces the MAVlink communication protocol to the ROS architecture. Therefore, MAVROS package allows MAVlink functionalities in association with the tools provided by ROS.

This work presents the design and the integration of a framework with the robot's hardware for executing an autonomous outdoor flight mission with a companion computer (Odroid). Therefore, the companion computer can process real time hard data, dispensing long-distance communication link to a base station, saving battery and, mainly, enlarging the robot's reach. Also, it enables the execution of certain maneuvers with the aircraft that are unavailable in the most used ground stations throughout the world, Mission Planner [6] and QGroundControl [7]. The paper structure is as follows: Sect. 2 has the related works in the area. Section 3 describes the whole system, such as the UAV, the control method, etc. Section 4 shows the results of the experiments. Finally, Sect. 5 concludes the paper.

2 Related Works

Several works have been researching autonomous flight of UAVs. Mathematical models of a quadrotor used along its sensors to design controllers and probabilistic filters, such as Kalman, to obtain more precise measurements of position, ensuring more reliability to the autonomous missions are shown in [1, 8, 9]. However, authors describe control processing in a base station and, therefore, the autonomous flight is bounded to a long-distance communication link.

In [10], authors relate an open hardware platform named Pixhawk [11] developed for use in Micro Air Vehicles (MAVs). This flight controller have become well accepted because it offers it offers good intercommunication between hardware and software for aerial vehicle robotics, facilitating the development of studies in various applications such as the creation of digital models of buildings and houses, for example, with smaller aircraft operating nearby obstacles and people. Human-machine interfaces are also addressed, such as QGroundControl and Arduino Pilot Meta (APM) Planner.

Meier et al. [12] also addresses the PX4 firmware in their work. When associated with Pixhawk hardware, PX4 is configured as a multithreaded embedded system developed for robotics applications with robust architecture and easy integration with Linux, working as a middleware between hardware and users applications, since its processing is multitask and it resembles a UNIX system.

The ROS architecture have become a consolidated robotic tool for all community. Considering its compatibility with Pixhawk through MAVROS, a large number of applications for UAVs have been recently proposed, for wide variety of applications. They involve inspection and military surveillance [3], autonomous landing [13] and

cooperation between robotic bases and aerial vehicles, for several mission accomplishments and enhancing aircraft's autonomy [14].

These applications are not focused on onboard processing neither on simplified interactions with applications developed by users. This work shows a lightweight platform with high computational power for development of autonomous navigation of UAVs with real time hard data processing, such as computer vision, without relying on ground station communication link.

3 System Description

The application proposed in this work uses a commercial quadrotor IRIS+ [?] to accomplish a fully autonomous mission without relying on ground bases. Thus, a companion computer (Odroid) is embedded in the aircraft to calculate its control commands during the mission. The hardware setup is shown in Fig. 1.

The user predefines a general mission with desired waypoints. Then, a flash drive containing a text file with the waypoints is inserted in Odroid. When the drone is powered on, the Odroid's algorithms execute autonomously the commands for the Pixhawk's controller, since the aircraft's arming, setting the system to offboard mode and allowing the autonomous control.

3.1 Hardware Integration

In order to fulfill the needed functionalities, peripherals, processor with real-time operating system, compatibility with ROS, Linux and PX4 firmware, a quadrotor

Fig. 1 Quadrotor with embedded Odroid computer

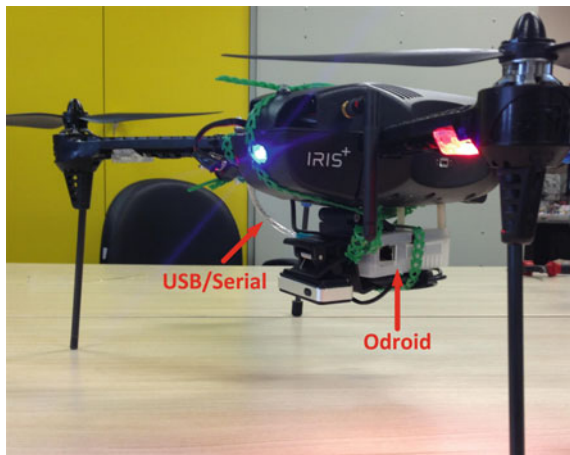
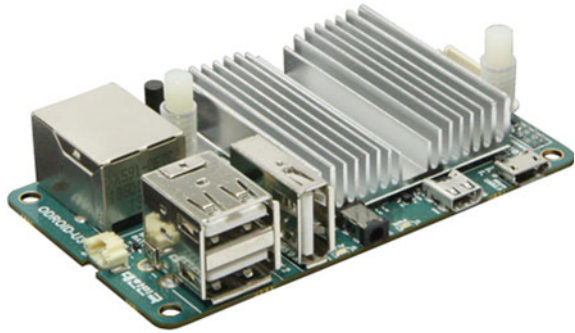


Fig. 2 The Odroid U3 OBC



with the Pixhawk Flight Control Unit (FCU) was obtained, as shown in Fig. 1. Pixhawk is the UAV’s low-level controller with low-energy consuming computer. For high-end computer, the Odroid U3 (Fig. 2) was chosen because its inherent processing power, which is compatible with the online flight processing necessities of the Nuttx OS embedded in the Pixhawk, and also, is lightweight, what is essential for a UAV application.

The power module shown in Fig. 3 must be set in series with the battery. It presents a 5 V voltage regulator that was used to supply Odroid’s functionalities. For the purpose of this application, a push button was set in series with the circuit to allow for its interruption. It was fixed onto one of the aircraft arms, allowing easy access for starting the On-Board Computer.

In order to establish the connection between Pixhawk and Odroid, a cable with USB/Serial connections and an FTDI (Future Technology Devices International) converter was used to ensure thee compatibility between the two devices. The baud rate was seen as 921,600 bits per second to ensure high-speed data transmission, which is required by the application.

Fig. 3 Power module



3.2 Framework Development

The proposed integration was implemented in C++ making use of the functionalities provided by ROS framework through the package MAVROS. The code is composed of 3 nodes of execution, namely *controller*, *toPublish* and *verify*. A diagram of this connection is shown in Fig. 4 showing the structure of control. The PX4 firmware was embedded in the Pixhawk and the Odroid U3 received the LUbuntu operating system with ROS Indigo bare bones.

The node *controller* is the main control code of the application. Initially, *controller* checks the entry of mission data inside the memory card device as shown in Fig. 5, and reads the points, which are found in a *txt* extension file. As we defined as protocol for this application, each of the several waypoints to be followed by the UAV must be written in a row consisting of a 4-element vector, referenced from an inertial frame that is coincident with the starting position of the UAV, where it is switched on by the user.

The third element is the relative height for the aircraft, also based on the initial frame. The fourth value is a boolean number which commands to the UAV a +360° yaw rotation (counterclockwise direction) when the UAV reaches the current way-

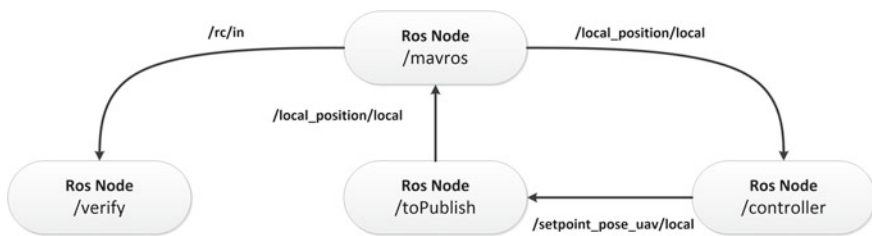


Fig. 4 Main control system structure

Fig. 5 Hardware connection



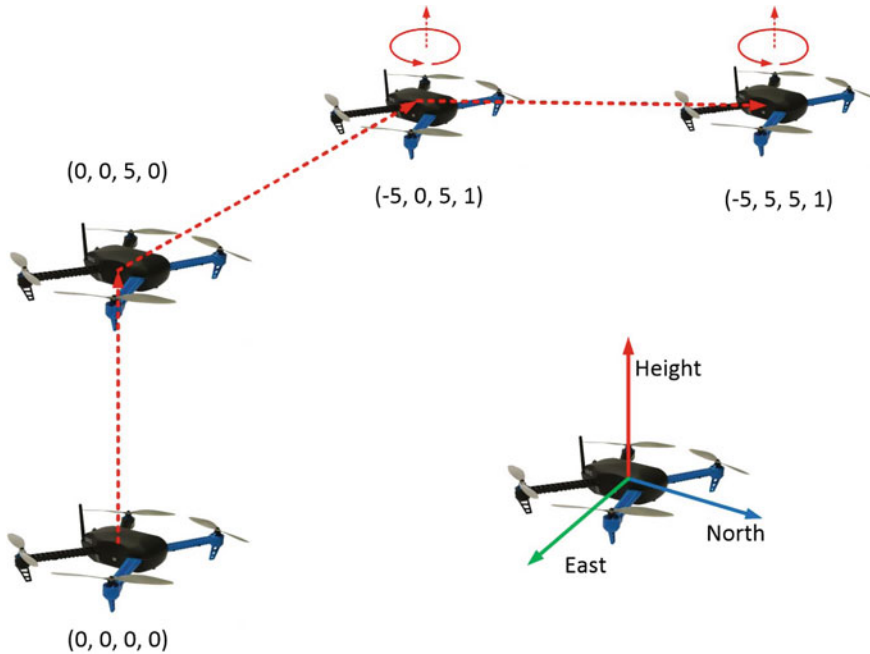


Fig. 6 Example mission

point. Figure 6 exemplifies the UAV actuation according to the mission, as described above.

After obtaining the mission from the *txt* file, the framework code calculates if the total distance to be traveled exceeds the total battery autonomy available. Through experimental tests it was noted that, using a fully charged 3-cell 5100 mAh battery, the aircraft can travel an approximate distance of 480 m, with horizontal and vertical velocities of 1 m/s and 2 m/s, respectively, before it reaches its minimum acceptable level of 10.5 V, where the robot is forced to land in a secure area, which can be obtained by computer vision algorithms, such as the *ar_track_alvar* package, built in ROS. In addition, the average battery consumption was 0.0044 V per meter traveled in this application.

If the total distance is equal or minor than the maximum allowed, the mission is validated and the control code starts two services from the MAVROS package in sequence: firstly, the topic */cmd/arming* to power on the UAV motors with minimum angular velocity rotation and, secondly, the topic */cmd/guided_enabled* to enable the offboard flight mode, where the manual radio controller is dismissed. Then, the missions are structured in the ROS message model */geometry_msgs/PoseStamped*, a ROS message that comprises a header, 3-dimensional values of position and a quaternion for orientation, which fully describes the robot's pose. If the total distance is higher than the maximum allowed for the robot, the mission is not validated and the

UAV will blink its main LED with red color, indicating to the user that the mission must be remodeled.

With a validated mission, the communication messages are published to the topic */SetpointPose_UAV* towards the node *toPublish*. The *controller* topic receives a feedback from the topic */local_position/local*, and compares the current 3D position of the UAV with the waypoints from the mission.

If the positioning error between the robot's position and the current waypoint is in an acceptable region, according to a predefined acceptance threshold, the current waypoint will be considered accomplished and the control will proceed to the next waypoint in list. This is also calculated for the robot's orientation, which is transformed from quaternion to Euler angles for threshold validation.

The flowchart in Fig. 7 summarizes all the steps described above. The node *toPublish* is responsible for maintaining a minimum of 2 Hz of communication flow between Odroid and Pixhawk. This communication rate is necessary to maintain the aircraft in offboard flight mode (Fig. 8).

The function of the node *toPublish* (Fig. 4) is to receive the current values of actuation from *controller* to the UAV through the topic */SetpointPose_UAV*, and to keep unremitting the publishing flow between the Odroid and the Pixhawk through the MAVROS' topic */setpoint_position/local*. For the applications in this work, the publishing frequency were set as 10 Hz, in order to ensure the offboard flight mode through all the experiments.

The function *verify* is designed to ensure the safety of the design tests. It monitors the radio channels through MAVROS topic */rc/in*, principally the pulse width of radio channel 7's PWM pulse. Once this channel is actuated, the pulse width is altered and the UAV's flight mode service takes control of the aircraft. With this application, it is possible to toggle the control of the flight mode from offboard to manual, or vice-versa, by switching a configured button on the manual control. Although not necessary for the autonomous mission, this procedure allows the user to assume the control of the aircraft through potential unexpected situations during the tests.

4 Results

This section describes the experiments designed to evaluate the performance of the framework's platform. To evaluate this work, simulated and practical tests were conducted to check the performance of the autonomous mission and the behavior of the algorithms in two distinct missions. All tests were repeated 20 times to build a more reliable base for analysis of the results.

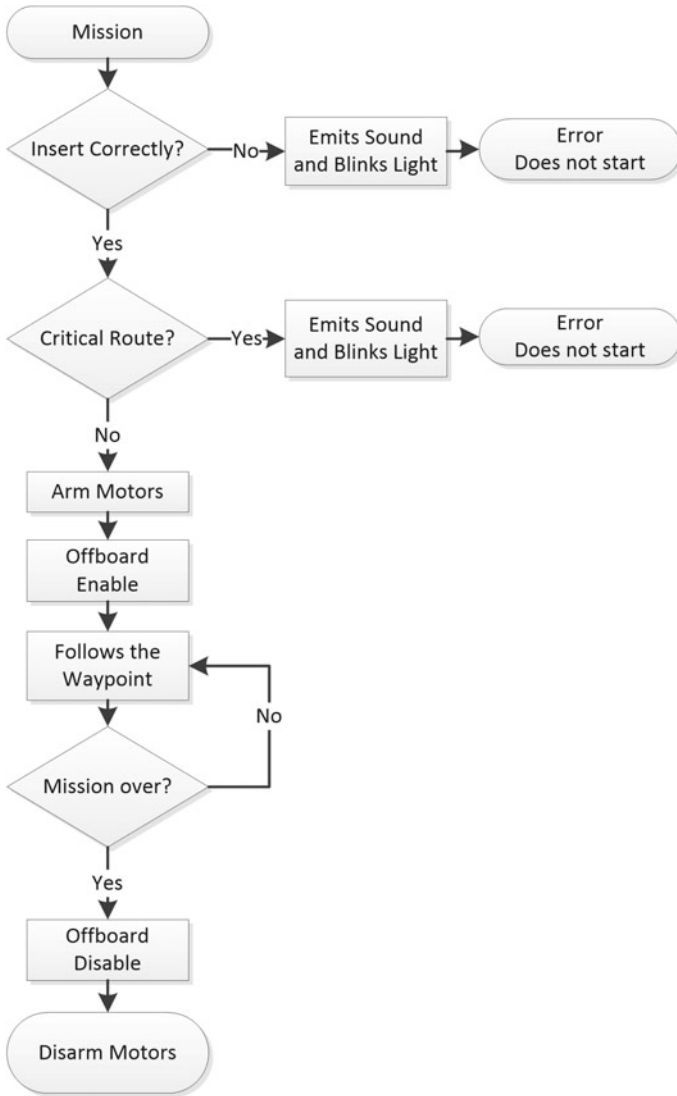


Fig. 7 Flowchart describing the operations performed by the developed framework

4.1 Simulation with Hardware in the Loop

Simulations were run in order to check for potential inconsistencies in the control codes and also in the information exchange between the Pixhawk and the Odroid. In order to evaluate the real hardware control, the integration between Pixhawk and Odroid, the process is done by using Hardware In the Loop (HIL), where the robot is

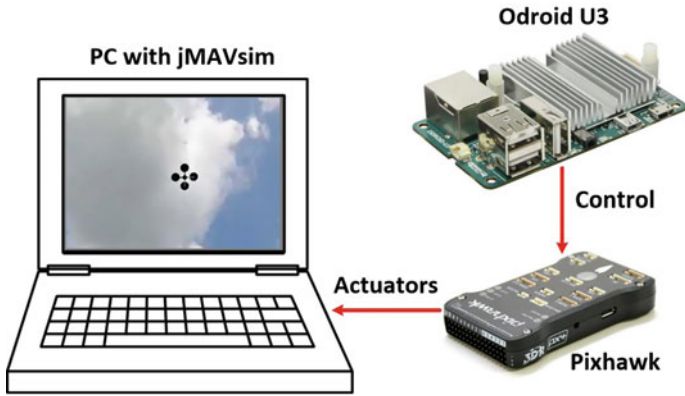
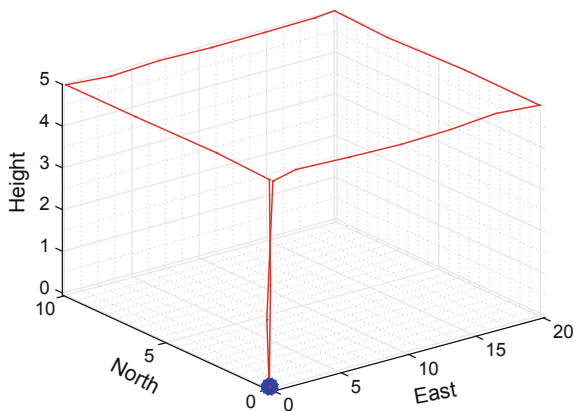


Fig. 8 Hardware in the loop schematics

substituted by a mathematical model provided by a simulator, however all simulation controls are provided by the real hardware.

For this section, two missions were designed. In the first mission, the UAV traveled a rectangular route and, in the second, a triangular route. The positions estimated by the HIL control during the mission were recorded and are shown in Figs. 9 and 10, which denotes the missions 1 and 2, respectively. According to these Figures, the Pixhawk corresponded satisfactorily to the Odroid’s commands as expected for the simulation since the proposed mission is the displacement of the aircraft. Tables 1 and 2 show the quantitative results.

Fig. 9 HIL: mission 1



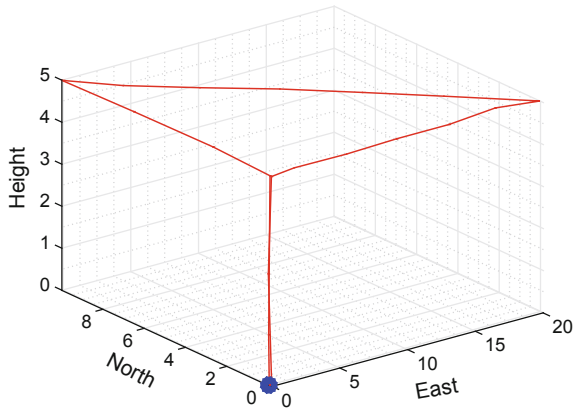


Fig. 10 HIL: mission 2

Table 1 Results for HIL’s mission 1

Mission 1					
Desired waypoint			Achieved waypoint		
East	North	Height	East	North	Height
0	0	5	-0,0790	0,0297	5,3898
0	10	5	-0,2265	10,0969	4,9697
20	10	5	19,7688	10,0717	4,9837
20	0	5	19,8906	0,3977	4,9872
0	0	5	0,3435	0,0776	4,9863
0	0	0	-0,0274	0,0654	-0,2627

Table 2 Results for HIL’s mission 2

Mission 2					
Desired waypoint			Achieved waypoint		
East	North	Height	East	North	Height
0	0	5	0,0186	-0,508	4,6644
0	10	5	-0,1228	10,0939	4,9890
20	0	5	19,2631	0,4787	4,9987
0	0	5	-0,0296	-0,0463	4,9921
0	0	0	-0,0771	-0,0029	-0,3284

4.2 Outdoor Flight with Real UAV

With the algorithms approved by HIL, the second step consisted in repeating the flight tests proposed in simulation with the real aircraft, shown in Fig. 1, in a real

Fig. 11 Outdoor flight

outdoor environment. Figure 11 shows the quadrotor performing one of its outdoor's missions with influence of environment stochastic effects (Figs. 12 and 13).

During the mission, all data were recorded for further analysis. The position logs were generated and the result paths executed by the real UAV and the control algorithm are shown in Figs. 14 and 15 for missions 1 (rectangular) and 2 (triangular), respectively. The quantitative results are shown in Tables 3 and 4, summarizing the data regarding missions 1 and 2.

The Tables 3 and 4 show the desired waypoints and respective average values extracted from 20 repetitions for each experiment. The displacements between the desired positions and the actual positions achieved by the UAV are inserted by the GPS and none of them registered a value higher than 1 m and, therefore, may be considered acceptable given the proposed application.

Fig. 12 Flash drive



Fig. 13 UAV power on

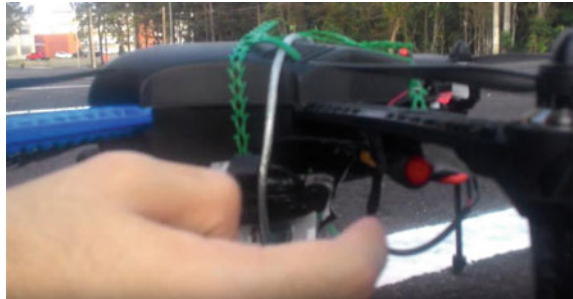
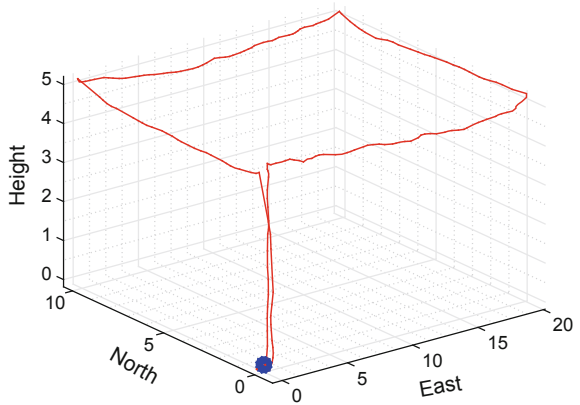


Fig. 14 Real: mission 1
(*rectangular*)



As it can be seen in Figs. 14 and 15, the real flight, despite GPS signal fluctuation, has shown good-shaped paths when compared to the HIL results, as HIL results are not affected by random errors. Therefore, is possible to conclude that the strategy achieved it's main autonomous navigation goal under real environments conditions.

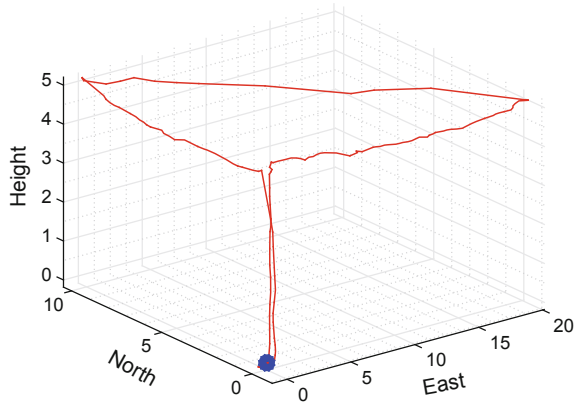


Fig. 15 Real: mission 2 (*triangular*)

Table 3 Data: mission 1 in real flight

Mission 1					
Desired waypoint			Achieved waypoint		
East	North	Height	East	North	Height
0	0	5	-0,0935	-0,3974	4,0055
0	10	5	-0,2763	9,0418	4,9681
20	10	5	19,2133	9,2601	5,0837
20	0	5	20,1115	0,9534	5,0668
0	0	5	0,6317	-0,3686	5,0197
0	0	0	0,0840	0,6406	-0,2301

Table 4 Data: mission 2 in real flight

Mission 2					
Desired waypoint			Achieved waypoint		
East	North	Height	Earth	North	Height
0	0	5	0,3531	0,0548	4,1389
0	10	5	-0,0995	9,0825	4,9325
20	0	5	19,0482	0,2358	5,0426
0	0	5	0,2521	-0,0554	5,0665
0	0	0	0,3114	-0,0256	-0,1127

5 Conclusions

This work presented a novel platform for aircrafts autonomous missions without relying on ground based stations. After performing the tests described in the previous section, the results show that the proposed objectives were accomplished, since the UAV performed the designed missions as expected, both in simulation with HIL and in real conditions under nondeterministic noise. A commercial drone with adapted companion computer with powerful capabilities for autonomous high level control was used in this work.

The aircraft responded satisfactorily even under random disturbances such as wind and GPS signal fluctuation, being able to accomplish its mission with acceptable errors. That situation is evident when observing the average value indicated by the sensors at the end of the landing, as shown at table results. In addition, the minor imprecisions shown in Tables 3 and 4, although small, were expected for a real robot since filtering algorithms were not implemented.

For hardware integration between both computers, Pixhawk and Odroid, it was noted that there were not incompatibility nor failures during the exchange of information between these devices. The ROS platform provided a communication interface and robotic packages to build missions at will. Furthermore, the embedded computer released the UAV from maintaining a radio communication link with ground stations, increasing its range of action. With this approach, the UAV is bounded only by its batteries capacities of supplying power.

Acknowledgments The authors would like to thank Duke Energy Electricity Company, FAPEMIG, CNPq and FADEPE/UFJF.

References

1. Santana, L.V., Brandão, A.S., Sarcinelli-Filho, M.: Outdoor waypoint navigation with the AR.Drone quadrotor. In: International Conference on Unmanned Aircraft Systems (ICUAS), pp. 303–311 (2015)
2. Nagarjuna, K., Suresh, G.R.: Design of effective landing mechanism for fully autonomous Unmanned Aerial Vehicle. In: International Conference on Signal Processing, Communication and Networking (ICSCN), pp. 1–6 (2015)
3. Ma'sum, M.A., Arrofi, M.K., Jati, G., Arifin, F., Kurniawan, M.N., Mursanto, P., Jatmiko, W.: Simulation of intelligent Unmanned Aerial Vehicle (UAV) For military surveillance. In: International Conference on Advanced Computer Science and Information Systems (ICACSIS), pp. 161–166 (2013)
4. Amazon.com: Amazon Prime Air, 05-30-2016 (2016). <http://www.amazon.com/b?node=8037720011>
5. The Open Source Robotics Foundation: Robot Operating System (ROS), 05-30-2016 (2016). <http://www.ros.org/>
6. Arduino Ardupilot: Mission Planer, 05-30-2016 (2016). <http://planner.ardupilot.com/>
7. QGroundControl: QGroundControl, 05-30-2016 (2016). <http://qgroundcontrol.org/>
8. Curi, S., Mas, I., Sanchez Pena, R.: Autonomous Flight of a Commercial Quadrotor. IEEE Latin Am. Trans. vol. 12, Num. 5, pp. 853–858 (2014)

9. Engel, J., Sturm, J., Cremers, D.: Camera-based navigation of a low-cost quadcopter. In: International Conference on Intelligent Robots and Systems (IROS), pp. 2815–2821 (2012)
10. Arduino: Arduino Pilot Meta, 05-30-2016 (2016). <http://ardupilot.com/>
11. Meier, L., Tanskanen, P., Fraundorfer, F., Pollefeys, M.: The PIXHAWK open-source computer vision framework for MAVs. In: The International Archives of the Photogrammetry, Remote Sensing and Spatial Information Sciences, vol. 38, Num. 1, C22 (2011)
12. Meier, L., Honegger, D., Pollefeys, M.: PX4: A node-based multithreaded open source robotics framework for deeply embedded platforms. In: IEEE International Conference on Robotics and Automation, pp. 6235–6240 (2015)
13. Olivares-Mendez, M.A., Kannan, S., Voos, H.: Vision based fuzzy control autonomous landing with UAVs: From V-REP to real experiments. Mediterranean Conference on Control and Automation, pp. 14–21 (2015)
14. Cocchioni, F., Pierfelice, V., Benini, A., Mancini, A., Frontoni, E., Zingaretti, P., Ippoliti, G., Longhi, S.: Unmanned ground and aerial vehicles in extended range indoor and outdoor missions. International Conference on Unmanned Aircraft Systems, pp. 374–382 (2014)
15. 3DRobotics: IRIS+ quadrotor, 05-30-2016 (2016). <http://store.3drobotics.com/products/iris>

Tracking of Physiotherapy Exercises Using Image Processing Techniques

Tiago Martins, Vítor Carvalho and Filomena Soares

Abstract It is increasing the number of people with reduced mobility as a result of neurological disease. This impairment requires adequate physical therapy plans to improve the quality of life. Serious games are able to give an important contribution in the field of physiotherapy, as they create a pleasant environment to lead patients to overcome the lack of motivation they may feel with the repetitive and boring exercises of traditional physical therapy. We have developed a serious game for physical therapy of patients with neurological diseases, based on image processing techniques, allowing monitoring some exercises.

Keywords Reduced mobility · Physiotherapy · Serious games · Motivation · Image processing

1 Introduction

The patients with motor impairments resulting from neurological diseases require physical therapy plans that respond to their limitations and give them a better quality of life. But with repetitive and boring exercises of traditional physical therapy they may feel discouraged and end up abandoning the treatment before it

T. Martins (✉) · V. Carvalho · F. Soares
R&D Algoritmi, School of Engineering, University of Minho,
Guimarães, Portugal
e-mail: tiago.rodrigues@algoritmi.uminho.pt

V. Carvalho
e-mail: vcarvalho@ipca.pt

F. Soares
e-mail: fsoares@dei.uminho.pt

V. Carvalho
School of Technology, IPCA, Barcelos, Portugal

has ended [1, 2]. Therefore, it is required to seek pleasant environments where they feel motivated to carry out the exercises with enthusiasm, even forgetting they are doing a therapy [3, 4]. Several studies have shown that serious games, when placed at the service of physical therapy, are able to create such environments. These games often use forms of feedback that challenge patients to obtain better results, thus leading them to get involved more actively in their rehabilitation [4].

The authors feel that there is a gap in relation to games which are intended exclusively for a broad spectrum of physical therapy exercises designed to improve the mobility of patients with neurological diseases. Following this trend, a serious game based on image processing techniques was developed. The objective of this paper is to present how to monitor three physical therapy exercises, for people with neurological diseases, using a serious game based on image processing techniques.

This paper is organized as follows: Sect. 2, presents some of the Neurological Diseases, Sect. 3, introduces the Physical Therapy, Sect. 4, details the Image Processing techniques, Sect. 5, presents the Motion Tracking of Physical Therapy Exercises, and Sect. 6 concludes with the Final Remarks.

2 Neurological Diseases

A neurological disease is a disease that affects the Nervous System. This system is divided into two structural parts: Central Nervous System comprising the brain and spinal cord, engaged by the bones of the skull and spinal column, respectively; and Peripheral Nervous System, that includes the nerves and the ganglia without any protection bone [5]. Its basic unit is the neuron whose functions are to receive and impart information in the form of electrical impulses. Neurons do not have cellular continuity, being separated by a space called the synapse [6].

Genetic, congenital or acquired damages occurring in neurons triggers cell dysfunctions, with loss of the transmission of electrical signals, culminating in neuronal death and therefore in a neurological disease [7]. Examples of such diseases are multiple sclerosis, stroke, Friedreich's ataxia and Parkinson's disease. Although different in their origins, as the causes of neuronal damage vary, they all have something in common: the transmission of electrical signals for movement ceases, the muscles gradually lose activity and atrophy, compromising the mobility of the affected patients [8].

Neurons are cells that do not divide so that when they suffer injury, they cannot be recovered. However, the Nervous System has the ability to modify its structural and functional organization, since it is subject to repeated stimuli. So, when there is loss of neurons, new alternative neural circuits that can replace the damaged structures are sought [9].

To stimulate neuroplasticity, in cases of physical disabilities, physical therapy is extremely important.

3 Physical Therapy

According to the World Confederation for Physical Therapy (WCPT), physical therapy is a health care specialty that provides services targeted “to develop, maintain and restore maximum movement and functional ability throughout the lifespan”, encompassing physical, psychological, emotional, and social wellbeing. To this end, therapists have a wide range of exercises [10].

Together with physiatrists and physical therapists from the Physical therapy Clinic of Santa Casa da Misericórdia de Arouca, our research team examined the physical therapy exercises targeted to neurological patients to choose the ones that could be included in the serious game. The chosen exercises were as follows (Fig. 1) [11, 12]:

- Glenohumeral joint abduction (Fig. 1);
- Radiohumeral joint flexion (Fig. 2);
- Pulleys (Fig. 3).

The glenohumeral joint abduction consists of the movement that pulls the arm from the body midline being performed in the frontal plane around a horizontal axis directed dorsoventrally [11]. The radiohumeral joint flexion, also performed in the frontal plane can be defined as the movement of the arm towards the shoulder [11]. The pulleys may be considered as a combined movement of glenohumeral joint

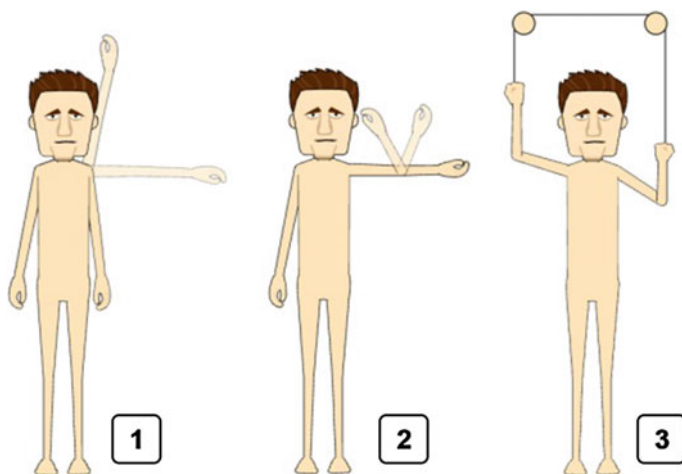


Fig. 1 The chosen exercises: 1—Glenohumeral joint abduction; 2—Radiohumeral joint flexion; 3—Pulleys [11, 12]

Skeleton Data

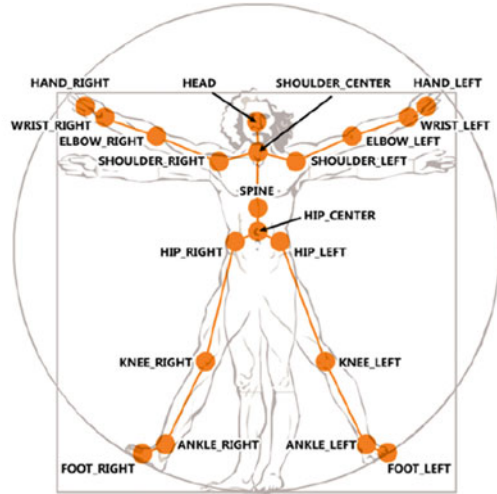
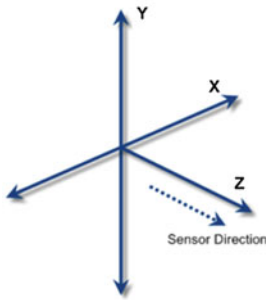


Fig. 2 Map of human body joints

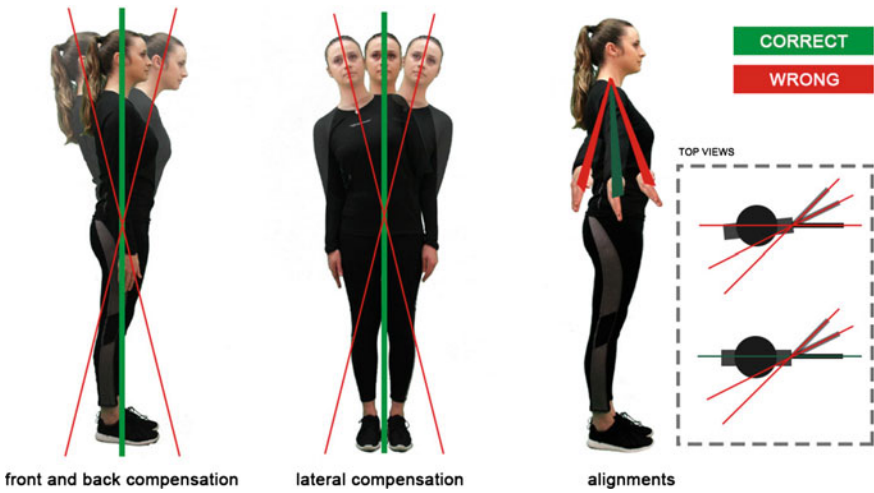


Fig. 3 Correct and wrong alignments and compensation

abduction and radiohumeral joint flexion and therefore, as the previous exercises, is performed in the frontal plane [12].

The selection criteria of these exercises considered their highest frequency of use, they are common to several neurological diseases, and, above all, the possibility of being monitored by image processing techniques.

4 Image Processing

The advent of modern digital technology has made possible the manipulation of multidimensional signals through various systems, among which is included the image processing [13].

The images are signals that constitute the physical support of certain information. To simplify the extraction of this information it is essential to subject it to repeated transformation, which is the goal of the image processing. Even before processing itself, which occurs in three stages, it is necessary to capture a real image, in the form of an analog signal, using a camera or a sensor which sends the obtained information to an analog-digital converter [14]. The original image is converted into pixels containing all the information that is necessary to play it on the screen, being ready to be understood by the computer language [15]. Obtained the digital image, then takes place the first step, called preprocessing, which consists of a set of steps to minimize as much as possible, the distortion of the image. The following step is the enhancement of images, which is a technique that intends to improve the visual quality using mathematical functions, in order to facilitate the next step. Finally, the analysis of images including segmentation and classification of images is related to the attribute extraction [16].

5 Motion Tracking of Physical Therapy Exercises

To make the motion tracking of the therapeutic exercises performed by the patients it was used only one *Microsoft Kinect* sensor, using mainly the Infrared (IR) sensor. The initial goal was to recognize the joints of the human body and for that we resorted to some functions already available in the SDK *Microsoft Kinect*. Since it is not the goal of this work, we will not deepen the technique used by the skeleton function available in that SDK and that is the main function for recognition of the joints of the human skeleton and which are shown in Fig. 2. This function allows us to extract the coordinates of each joint of the patient's body, which will later be used for the validation process of physical therapy exercises.

Throughout our research and after monitoring various physical therapy sessions accompanied by physiotherapists, the research team realizes that there are four main features to detect, through image processing techniques, if a particular physical therapy exercise is being properly executed, concerning alignment, compensation, performance and speed.

The first (alignment) requires that the joints are aligned with each other in the exercise execution plan. Compensation refers mainly to the body inclination, lateral (right or left), forward or backward. The execution of each exercise requires a specific technique. The speed and the acceleration during the execution of the exercises are also important features to consider (Fig. 3).

Considering the purpose of this paper, we propose to describe the technique used to detect correct or incorrect implementation of each of the three exercises mentioned above (glenohumeral joint abduction, radiohumeral joint flexion and pulleys).

Regarding the glenohumeral joint abduction, as stated earlier, it is executed in the frontal plane. Theoretically, the exercise should be performed at arm's length, that is, with an amplitude equal to 180° for the angle arm-forearm. The angle formed by the upper limb and the body's midline should range between 0° and 180° . The joints must be aligned in the frontal plane and so that there is no body compensation; the corresponding joints on both sides of the body should be aligned horizontally and vertically. Its performance must maintain a constant speed, that corresponds to zero acceleration.

However, these notes are only theoretical. In fact, the anatomy of the human body does not allow achieving the theoretical values and so they must be adjusted to practical values. It is almost impossible to find a fully lined body and without compensation.

In order to perform the motion tracking of the glenohumeral joint abduction we started by using the skeleton function SDK *Microsoft Kinect*. After we got the x , y , z of each joint, some routines were developed, namely: check of the angle between the arm and the forearm, the angle between the arm and the body's midline, the alignment of the joints in relation to x , y and z , and the speed and acceleration of execution of the exercise (Fig. 4).

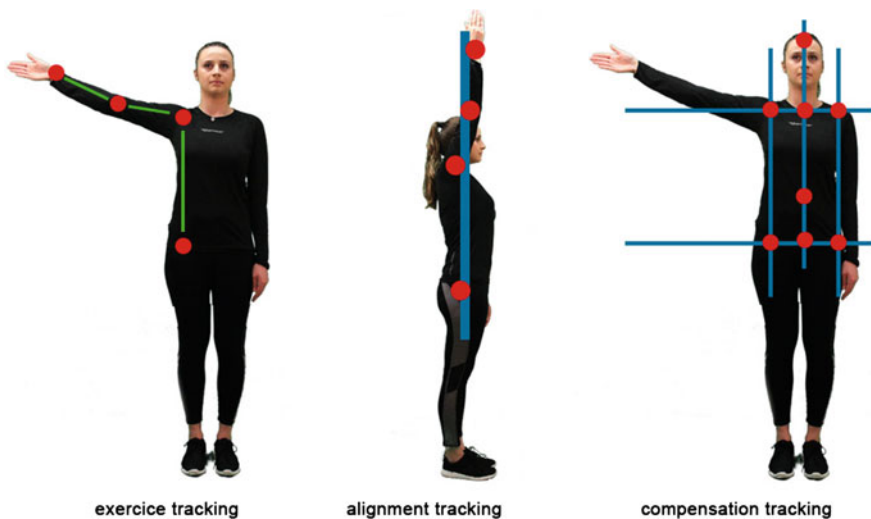


Fig. 4 Execution, alignment and compensation of the glenohumeral joint abduction

With the coordinates of the joints, Wrist (W), Elbow (E) and Shoulder (S), are determined the following vectors, \vec{v}_1 and \vec{v}_2 , Eqs. (1) and (2):

$$\vec{v}_1 = \overrightarrow{EW} = W - E \quad (1)$$

$$\vec{v}_2 = \overrightarrow{ES} = S - E \quad (2)$$

The amplitude θ of the angle of the two vectors is given by the Eq. (3):

$$\theta = \cos^{-1} \frac{\overrightarrow{EW} \cdot \overrightarrow{ES}}{\|\overrightarrow{EW}\| \times \|\overrightarrow{ES}\|} \quad (3)$$

The same process is used to determine the angle arm-body's midline, using now the coordinates of the joints Elbow, Shoulder and Hip.

To verify if the patient is performing the exercise with the joints aligned we make the bilateral screening of the coordinates relative to z of Hip (H), Shoulder (S), Elbow (E) and Wrist (R) and should have minimal differences; if it is impossible they are all alike:

$$z_H \cong z_S \cong z_E \cong z_R \quad (4)$$

The same procedure is used to detect the compensation forwards or backwards in the joints head, center shoulder, spine and hip center.

Regarding the lateral compensation, we make the bilateral screening of coordinates of the different joints relative to y . The coordinates of the corresponding joints on both sides of the body must show minimal differences; if it is impossible they are equal due to the human body anatomy.

Being θ the angle arm-body's midline, the average angular speed of the exercise execution in rad/s is calculated using the formula of the angular velocity, Eq. (5):

$$\omega = \frac{\Delta\theta}{\Delta t} \quad (5)$$

By using Eq. (6) the average angular acceleration of the performance of the exercise γ is obtained.

$$\gamma = \frac{\Delta\omega}{\Delta t} \quad (6)$$

The second chosen exercise, the radiohumeral joint flexion, is also performed in the frontal plane. Theoretically, the angle arm-body's midline should remain 90° during the entire run. The angle formed by the arm and forearm should range

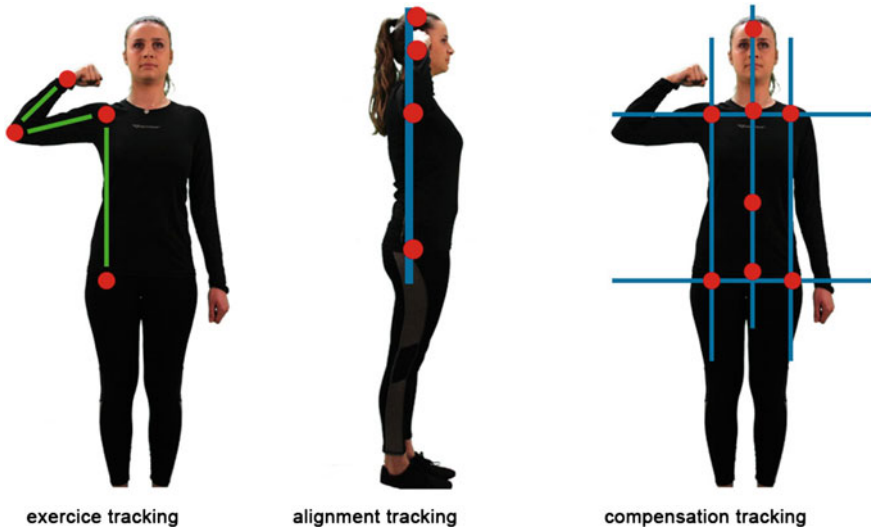


Fig. 5 Execution, alignment and compensation of the radiohumeral joint flexion

between 180° and approximately 30° (hand on shoulder). The body must remain aligned as in the previous exercise.

For the determination of the angles, the checking of the alignments and compensations, the calculation of velocity and acceleration, the procedures are the same as those used for the previous exercise (Fig. 5).

For the last exercise, pulleys, the patient uses a system based on a string that passes through two fixed pulleys in a structure that forces him/her to do a combination of glenohumeral joint abduction and radiohumeral joint flexion. The techniques used to monitor this exercise are similar to the previous ones with regard to the determination of the angles, the verification of alignments and compensations and also to the calculation of the speed and acceleration (Fig. 6). The angles arm-body's midline on both sides have to be supplementary, that is, the sum of them is equal to 180° . Once more we have to take into account the anatomy of the body that does not allow the expected theoretical values.

It is worth notice, in the three proposed exercises, specified for upper limbs, we do not validate the compensation and alignment for the lower limbs since many patients who suffer from neurological diseases have balance problems and therefore they have to be seated while they are performing the exercises.

After several tests performed with the developed algorithms it was found that the accuracy level is between 90 and 95 %, depending on patient height and the color and type of clothing that he uses, however he can not wear loose clothing and the worst color is black.

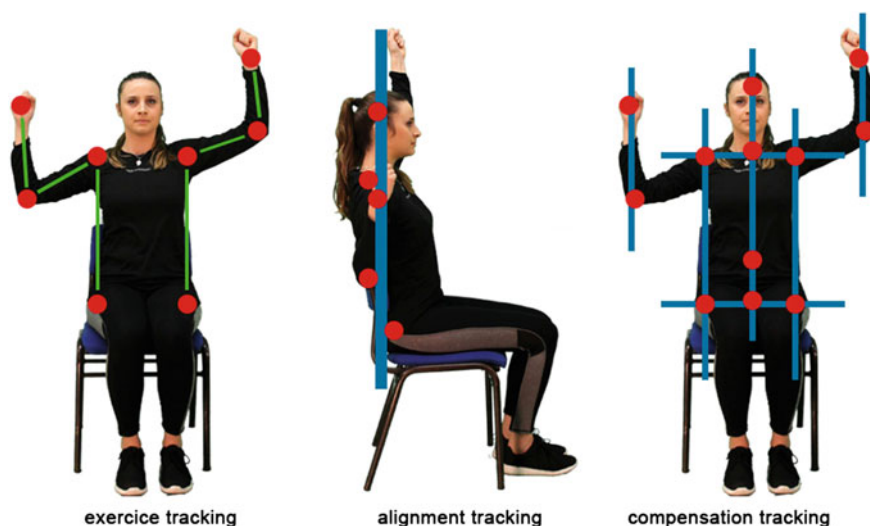


Fig. 6 Execution, alignment and compensation of the pulleys

6 Final Remarks

As final remarks we can state that image processing is a powerful tool for monitoring movements, in this case directed to the detection and monitoring of physical therapy exercises. Although, it was not the purpose of this paper the integration of the monitoring algorithms of physiotherapy exercises in the serious game that was developed specifically to be used as a complement to traditional physical therapy for people with neurological disorders, it has been successfully achieved. The first tests in a clinical environment have shown very positive results. The game where the algorithms were applied for the tracking of physical therapy exercises using image processing techniques was applied to ten patients in a case study, in a clinical, for fifteen individual sessions, over three months. Although the results are not yet fully analyzed, in a technical level the overall results were very satisfactory, since the system answered in a favorable way to the proposed objective.

As future work we intend to integrate the monitoring of new exercises and to adapt them again to electronic games for motivation of neurological patients when they perform their physical therapy plans and test it in a clinical environment.

Acknowledgments This work has been supported by COMPETE: POCI-01-0145-FEDER-007043 and FCT—Fundação para a Ciência e Tecnologia within the Project Scope: UID/CEC/00319/2013.

References

1. Ryan, M., Smith, S., Chung, B., Cossell, S., Jackman, N., Kong, J., Mak, O., Ong, V.: Rehabilitation games – designing computer games for balance rehabilitation in the elderly. ACM, Australia (2009)
2. Carvalho, V., Leão, C., Soares, F., Cunha, M.: Games development for pedagogical and educational purposes. In: Cunha, M.M.C., Carvalho, V.H., Tavares, P. (eds.) Business Technological and social dimension of computer games, pp. 1–9. IGI-Global, Hershey PA (2011)
3. Martins, T., Carvalho, V., Soares, F.: Application for physiotherapy and tracking of patients with neurological diseases—preliminary studies. In: IEEE 2nd International Conference on Serious Games and Applications for Health, 2013, pp. 1–8
4. Martins, T., Carvalho, V., Soares, F.: Monitoring of patients with neurological diseases: development of a motion tracking application using image processing techniques. *Int. J. Biomed. Clinical Eng.* **2**(2), 37–55 (2013)
5. Spence, A.P.: *Anatomia Humana Básica*, 2ª ed. São Paulo, Brasil: Manole, (1991). (in Portuguese)
6. Santos, K.G.L.: *Bases Anatômofisiológicas do Corpo Humano I*. Rio de Janeiro, Brasil: Universidade Castelo Branco, (2010). (in Portuguese)
7. Reed, U.C. (n.d.): *Neurologia: Noções básicas sobre a especialidade*. [Online]. Disponível em: <http://www2.fm.usp.br/pdf/neurologia.pdf>. (in Portuguese)
8. Afonso, Í., Suzart, F., Carneiro, M., Matos, M., Oliveira, P., Barros, R.: *Doenças Neurológicas*. Salvador, Brasil: Faculdade de São Salvador (2011). (in Portuguese)
9. Ribeiro Sobrinho, J.B.: Neuroplasticidade e a recuperação da função após lesões cerebrais, *Acta Fisiátrica*, **2**(3), 27–30 (1995). (in Portuguese)
10. WCPT, Policy statement: Description of physical therapy (June, 2014). Disponível em: <http://www.wcpt.org/policy/ps-descriptionPT>
11. Maciel, A.; *Modelagem de articulações para humanos virtuais baseada em anatomia*, Dissertação de Mestrado, Universidade Federal do Rio Grande do Sul, Porto Alegre, Brasil, (2001). (in Portuguese)
12. Martins, T., Araújo, M., Carvalho, V., Soares, F., Torrão, L.: PhysioVinci—A first approach on a physical rehabilitation game. *The Fifth International Conference on Serious Games Development & Applications*, pp. 1–9. Berlin, Germany (Oct. 2014)
13. Young, I.T., Gerbrands, J.J., van Vliet, L.J.: *Fundamentals of Image Processing*. Delft University of Technology, Delft, Netherlands (1998)
14. Queiroz, J.E.R., Gomes, H.M.: Introdução ao processamento digital de imagens. *Revista de Informática Teórica e Aplicada (RITA)*, **VIII**(1), 1–31 (2001). (in Portuguese)
15. Scuri, A.E.: *Fundamentos da Imagem Digital*. Tecgraf/PUC, Rio de Janeiro (2002)
16. Santos, A.R., Peluzio, T.M.O., Saito, N.S.: *SPRING 5.1.2: Passo a Passo: Aplicações Práticas*. Alegre, ES, Brasil: CAUFES (2010). (in Portuguese)

Inside Pipe Inspection: A Review Considering the Locomotion Systems

Everson Brum Siqueira, Rodrigo Zelir Azzolin, Silvia Silva da Costa Botelho
and Vinicius Menezes de Oliveira

Abstract It is possible to observe that the fast technological development in the fields of instrumentation, control and embedded systems are increasing the employment of robotic systems for the execution of a large variety of tasks, for example, oil exploration or load transportation. In this way, there are many situations where it is very reasonable to use automatized systems, with special attention to the inspection of pipelines in the oil industry. There is a large quantity of systems developed and in the literature it is possible to find several reviews about inspection robots considering specific applications. However, none of those reviews presents the methodology to acquire defect's position. The main objective of this paper is to review the technical literature, describing the differences between robots employed to internal pipe inspection considering some features as application, adaptability, locomotion, sensors inspection and odometers.

Keywords Pipeline · Inspection robot · Odometer · Locomotion systems

1 Introduction

It is possible to observe that the fast technological development in the fields of instrumentation, control and embedded systems are increasing the employment of robotic systems for the execution of a large variety of tasks, for example, oil exploration or load transportation.

E.B. Siqueira · R.Z. Azzolin · S.S. da Costa Botelho · V.M. de Oliveira (✉)
Center for Computational Sciences – C3,
Federal University of Rio Grande – FURG, Rio Grande, Brazil
e-mail: vinicius@furg.br

E.B. Siqueira
e-mail: everson.brumm@furg.br

R.Z. Azzolin
e-mail: rodrigoazzolin@furg.br

S.S. da Costa Botelho
e-mail: silviacb@furg.br

In industry, pipelines have been used to the transportation of liquids and gases for decades [16]. There are several problems that impact the lifetime of the structures, such as aging, corrosion, cracks and mechanical damages, depending on the hazardousness of the product that is being conveyed. Considering the maintenance of the pipelines to guarantee the quality of this structure, it is necessary to prevent such problems using a very effective inspection approach. Considering that some of the structures are inaccessible by human operators due to, for example, size constraints, extreme temperature, immersion in liquids or unsafe conditions, it is common to use robots to perform the inspection tasks. There are many different materials and diameter pipes, consequently, there are several robots with different locomotion systems, capable to inspect inside or outside pipe, with different constraints.

Considering the inspection of pipes, it is very important to determine with accuracy the location of possible points of interest, points that probably will need to be fixed or, at least, observed more carefully. The accuracy of the location is closely related with the locomotion system considered for the robot and the odometry itself. Depending on the conditions of the structure to be inspected, locomotion systems, different sensors are necessary to be installed. The main objective of this paper is to review the technical literature, describing the differences between robots employed to internal pipe inspection considering some features as application, adaptability, locomotion, sensors inspection and odometers.

In the literature one can find several works about robotic inspection as [17] which presents a survey about inspection techniques and technologies towards condition assessment of water distribution and transmission lines. [21] present a survey associated with specific to water and oil/gas pipes inspection until 2010. [33] proposes a review comparing different types of robots for pipe inspection. A detailed survey about robotic inspection considering the last two decades [10], which describes advantages and disadvantages, depending on design requirements and purpose of inspection. [34] presents a review related to the application of robotic solutions considering in-pipe inspection robots and tank inspection robots at onshore oil and gas facilities.

The in-pipe inspection robotic systems can be classified into many types according to the locomotion system considered like pig, wheeled, tracks, legged, inchworm, snake and screw type [21]. It is important to observe that the task to be executed and the conditions of the facilities are very important to determine which locomotion systems is more suitable to accomplish the task.

The pig type is passively driven by the fluid pressure inside of pipelines [23, 25, 38, 41, 42]. Drawback of the employment ultrasonic tool sensor is the use of liquid couplant [19, 38] to inspect. Also, it can not operates in vertical pipes and does not have steerability.

The wheel type is an active locomotion that keeps in contact on the pipe. It can easily adapt diameters pipes using springs or DC motors to press wheels to the pipe wall as [4, 6, 11, 16, 18, 20, 26, 29, 30, 32, 36, 37, 40].

The tracks type offers advantages over wheeled robot in soft ground. Track locomotion is used primarily for flotation and traction. On the other hand, the robot is generally larger and more complex than others, which means increased energy expenditure. This methodology to move inside the pipe can be seen in [12, 13, 15, 31].

The legged type possessing articulated legs can produce motions. One advantage is the robot is more capable to overcome obstacles inside the pipes than other locomotion types. Nonetheless, the control approach for such locomotion system is more complex and it is not energetically efficient, as presented in [8, 14, 24].

The snake type system is usually employed for pipelines with very small diameters. This type of locomotion is composed of many linking which implies a development of a control more complex, however, it provides adaptability on irregular environment. Some robots snake type are presented in [2, 5, 27, 28, 35, 39, 43].

The inch-worm type is divided basically in clamber and extensor actuator. The clamber is used to adhere the device securely onto the locomotion environment, while the extensor produces a positive displacement, the difference in length of the extensor in its elongated and retracted phases as [1, 3]. Other type called screw type allows to advance in spiral fashion as [7, 9, 22].

This work is organized as follows: Sect. 2 presents robots which employs passive locomotion, known as pig robots, while in Sect. 3 presents the well known wheeled robotic inspection. It is explained in Sect. 4 the tracks robots. Sections 5 and 6 present snake robot and screw locomotion robot, respectively. The final discussion is presented in Sect. 7.

2 In-Pipe Inspection Robot—PIG Locomotion System

In [25, 38, 41] we can notice the use of an autonomous on-line intelligent inspection pig using ultrasonic tool to detect defects and acquired data and stored for off-line analysis. Basically, the difference between this robots are: number of ultrasonic sensors, pipe diameter and length inspected by once. In [38] a robot with 128 ultrasonic transducers that inspect 150–350 mm pipe diameter and the operational range of over 20 km. The system introduced by [42] has 32 ultrasonic transducers and utilizes the extra low frequency to communicate with the central computer. This method does not use wire but reduces the effective communication range in 11 m and it is illustrated in Fig. 1a. On the other hand, [25] does not specify the number of transducers, but considers the inspection task into two distinct problems: wall thickness and crack detection. The pipeline diameter to identify wall thickness is 508–1422 mm and 508–1066 mm for crack detection in Fig. 1b. Then, all robots presented in this paragraph, utilizes wheels encoder to acquire the defect's position in-pipe.

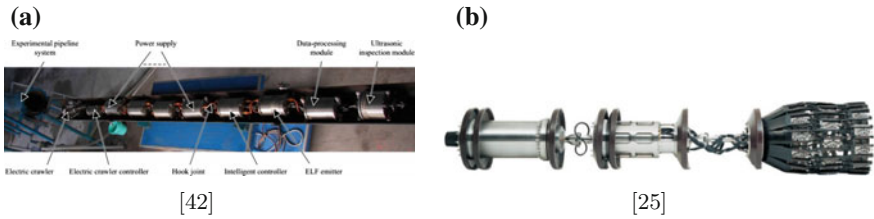


Fig. 1 Some examples of PIG robots

3 Wheeled Locomotion Systems

In [4, 26] are proposed semi autonomous robot to inspect the urban gas pipes. While MRINSPECT IV ([26]) is a miniature differential-drive as be seen Fig. 2b, the [4] is a modular articulated structure as illustrated Fig. 2a. To acquire the position inside the pipeline is utilised visual or landmark information in [26], although, [4] can construct a 3D graphical model representing the configuration of pipelines called Virtual Map. Other difference is that MRINSPECT-IV is developed to inspect 85–109 mm diameter pipes and [4] is proposed to inspect 160–240 mm diameter pipes.

In [20] it is present a semi-autonomous concept of mechanism to inspect the vertical and branch pipes. It is a modular robot composed of rotation part, center part and holding part. It can applied to inspect between 150 and 500 mm diameter pipe. Self position and self posture was proposed using a CCD camera, laser equipment and fiber grating to recognise the shape of pipe and a distance to branch. The system can be seen in Fig. 3.

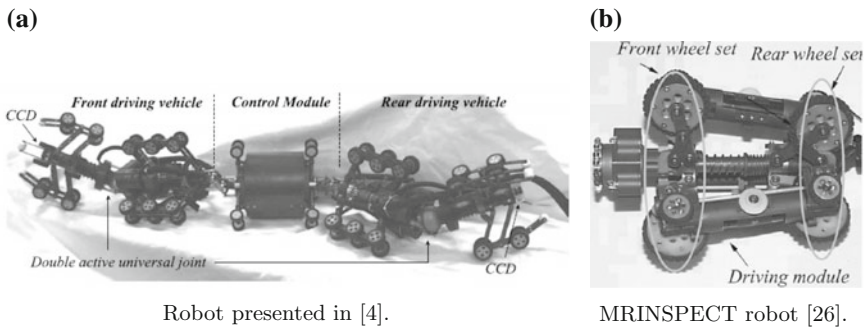
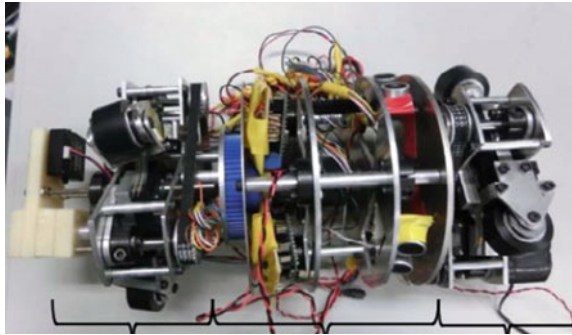


Fig. 2 Wheeled robots applied to gas pipe inspection

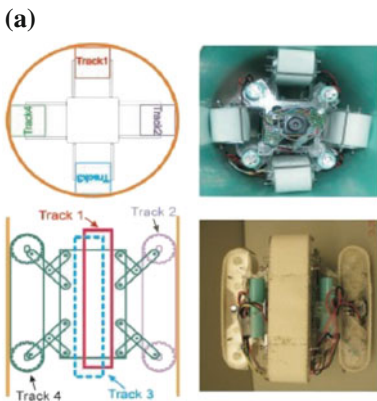
Fig. 3 Robot introduced by [20]



4 Track-Type Robots

A design with 4 wall-press caterpillars called FAMPER is presented in [13]. It is a fully autonomous mobile robot that can be used to inspect 150 mm diameter sewer pipes. FAMPER can be seen in Fig. 4a. Another robot inspection, employs a crawler-type pipeline inspection robot [15] which is designed to inspect 80–100 mm diameter pipelines, as depicted in Fig. 4b. It is a semi-autonomous robot which can be controlled using joystick.

A magnet caterpillar combined with a triangular shape robot to inspect ferromagnetic pipes called TRIPILLAR [31]. This robot can be seen in Fig. 5. It is a miniature magnetic utilised for inspect power plants, such as coal-fired boilers. The processor presented in Mega Arduino calculates the displacement and rotation of the robot by using the sensor signals and transfer the measured values to the PC (ground base).



FAMPER robot [13].



Locomotion system from [15].

Fig. 4 Example of track robots

Fig. 5 3D view of a TRIPILLAR robot

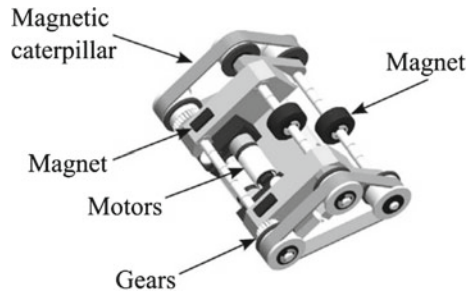


Fig. 6 The Explorer robot presented in [29]



5 Snake-Like Locomotion Systems

A snake robot called Explorer is applied for inspection of approximately 152 and 203 mm natural gas distribution system pipelines [29]. The CMOS camera in front of robotic takes the image. The robot remotely send the image to the operator console. Also, the robot has passive wheels and an embedded magnets with hall-effect encoding to determine the position via dead-reckoning. The prototype is depicted in Fig. 6.

6 Inch-Worm Locomotion System

A micro robot inspection in 17 mm diameter pipes found in nuclear generator [1]. The robot is electro-pneumatically driven illustrated in Fig. 7. The compressor, servo valves, electro valves for rear legs and hall effect sensor are parts of a micro robot. Inside the actuator, there is a Hall sensor glued on cylinder back and the magnet glued on the rod. To extract the position, a second order model is considered that consists in internal and atmospheric pressure, mass in translation, actual and initial rod position, also, viscous friction and bellows section.

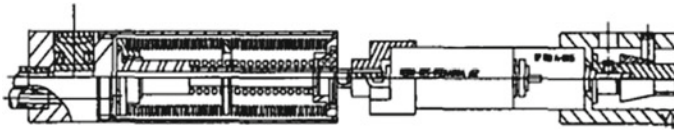


Fig. 7 Micro robot introduced by [1]

7 Discussions

The Brazilian petroleum refinery company (IPIRANGA) is composed by several tips of ducts. Nowadays, the inspection is realised using a ccd camera. Then, we are develop a platform/robot to acquire the location of possible points of interest points that probably will need to be fixed or, at least, observed more carefully using cam-

Table 1 Reference and their mainly characteristics

Loc	Ref	Appli	Adapta	Insp-System	Odometry
PIG	[23, 25, 38, 41]	Oil	–	Sonic sensor	Encoder
Wheel	[4]	Gas	160–240 mm	Camera	VL
	[11]	Sewer	300–600 mm	Camera	Encoder
	[13]	ND	–	Camera	SSensor
	[16]	ND	175–205 mm	Camera	ND
	[18]	ND	ND	Camera	VL
	[20]	ND	150–500 mm	Camera	Cam, laser, VL
	[26]	Oil/Gas	85–109 mm	Camera	VL
	[30]	G-Power	ND	Camera	3D- Ac, Encoder
	[32]	Sewer	300–600 mm	Camera	VL, Cam, Encoder
Track	[13]	Sewer	= 150 mm	CCD camera	Sonar
	[15]	ND	80–100 mm	Camera	Encoder
	[31]	-P	ND	Camera	Ac, Gyro, Encoder
Snake	[2]	ND	>100 mm	–	P-Bellows
	[6]	ND	ND	Camera	Encoder
	[27]	Sewer	100–150 mm	ND	Encoder
	[29]	ND	–	Camera	Encoder
InchWorm	[1]	ND	–	ND	Hall sensor
	[3]	Reac-Nucl	38–64 mm	U-S	ND
	[5]	Refinery	76–150 mm	Camera	ND
	[7]	Gas/Water	27 mm	ND	Encoder
	[22]	ND	= 10 mm	Camera	ND
	[28]	ND	= 100 mm	ND	ND
	[35]	Gas/Water	80–200 mm	Camera	ND
	[39]	ND	–	Camera	ND

eras and sensors. The aim of this article is to consolidate a review in the technical literature considering the use of robotic systems for the in-pipe inspection task. The importance of such classification is due to the accuracy of the robot's position inside the pipe. Moreover, the odometry to be design for each type of robot is closely related with the locomotion system. In Table 1 can be seen the mainly works found in literature, where comparison would be realised. Many works does not describe (ND) applicability (AP), Adaptation (Adapta), Inspection System (Insp-System), however, design or odometry seems so interesting.

In the sequel we intend to present another classification of inspection robots considering the application, another important feature for the odometry of such systems. The overall work pretends to formalize a widespread classification for in-pipe inspection robots.

References

1. Anthierens, C., Ciftci, A., Betemps, M.: Design of an electro pneumatic micro robot for in-pipe inspection. In: Proceedings of the IEEE International Symposium on Industrial Electronics, 1999. ISIE'99, vol. 2, pp. 968–972. IEEE (1999)
2. Borenstein, J., Borrell, A.: The omnitread ot-4 serpentine robot. In: IEEE International Conference on Robotics and Automation, 2008. ICRA 2008, pp. 1766–1767. IEEE (2008)
3. Choi, C.H., Jung, S.H., Kim, S.H.: Feeder pipe inspection robot using an inch-worm mechanism with pneumatic actuators. In: IEEE International Conference on Robotics and Biomimetics, 2004. ROBIO 2004, pp. 889–894. IEEE (2004)
4. Choi, H., Ryew, S.: Robotic system with active steering capability for internal inspection of urban gas pipelines. *Mechatronics* **12**(5), 713–736 (2002)
5. Debenest, P., Guarnieri, M., Hirose, S.: Pipetron series-robots for pipe inspection. In: 2014 3rd International Conference on Applied Robotics for the Power Industry (CARPI), pp. 1–6. IEEE (2014)
6. Fjerdingen, S., Liljebäck, P., Transeth, A., et al.: A snake-like robot for internal inspection of complex pipe structures (piko). In: IEEE/RSJ International Conference on Intelligent Robots and Systems, 2009. IROS 2009, pp. 5665–5671. IEEE (2009)
7. Hayashi, I., Iwatsuki, N., Iwashina, S.: The running characteristics of a screw-principle micro-robot in a small bent pipe. In: Proceedings of the Sixth International Symposium on Micro Machine and Human Science, 1995. MHS'95, pp. 225–228. IEEE (1995)
8. Hirose, S., Ohno, H., Mitsui, T., Suyama, K.: Design of in-pipe inspection vehicles for $\varphi 25$, $\varphi 50$, $\varphi 150$ pipes. In: Proceedings. 1999 IEEE International Conference on Robotics and Automation, 1999, vol. 3, pp. 2309–2314. IEEE (1999)
9. Horodincea, M., Doroftei, I., Mignon, E., Preumont, A.: A simple architecture for in-pipe inspection robots. In: Proceedings International Colloquium Mobile, Autonomous Systems, pp. 61–64. Citeseer (2002)
10. Ismail, I.N., Anuar, A., Sahari, K.S.M., Baharuddin, M.Z., Fairuz, M., Saad, J., et al.: Development of in-pipe inspection robot: a review. In: 2012 IEEE Conference on Sustainable Utilization and Development in Engineering and Technology (STUDENT), pp. 310–315. IEEE (2012)
11. Kepplin, V., Scholl, K.U., Berns, K.: A mechatronic concept for a sewer inspection robot. In: Proceedings. 1999 IEEE/ASME International Conference on Advanced Intelligent Mechatronics, 1999, pp. 724–729. IEEE (1999)
12. Kim, D.W., Park, C.H., Kim, H.K., Kim, S.B.: Force adjustment of an active pipe inspection robot. In: ICCAS-SICE, 2009, pp. 3792–3797. IEEE (2009)

13. Kim, J.H., Sharma, G., Iyengar, S.S.: Famer: A fully autonomous mobile robot for pipeline exploration. In: 2010 IEEE International Conference on Industrial Technology (ICIT), pp. 517–523. IEEE (2010)
14. Kostin, G.V., Chernousko, F.L., Bolotnik, N.N., Pfeiffer, F.: Regular motions of a tube-crawling robot: simulation and optimization. In: Proceedings of the First Workshop on Robot Motion and Control, 1999. RoMoCo'99, pp. 45–50. IEEE (1999)
15. Kwon, Y.S., Yi, B.J.: Design and motion planning of a two-module collaborative indoor pipeline inspection robot. IEEE Trans. Robot. **28**(3), 681–696 (2012)
16. Li, P., Ma, S., Li, B., Wang, Y.: Design of a mobile mechanism possessing driving ability and detecting function for in-pipe inspection. In: IEEE International Conference on Robotics and Automation, 2008. ICRA 2008, pp. 3992–3997. IEEE (2008)
17. Liu, Z., Kleiner, Y.: State of the art review of inspection technologies for condition assessment of water pipes. Measurement **46**(1), 1–15 (2013)
18. Lu, C.P., Huang, H.P., Yan, J.L., Cheng, T.H.: Development of a pipe inspection robot. In: Industrial Electronics Society, 2007. IECON 2007. 33rd Annual Conference of the IEEE, pp. 626–631. IEEE (2007)
19. Mandal, K., Dufour, D., Atherton, D.: Use of magnetic barkhausen noise and magnetic flux leakage signals for analysis of defects in pipeline steel. IEEE Trans. Magn. **35**(3), 2007–2017 (1999)
20. Masuta, H., Watanabe, H., Sato, K., Lim, H.o.: Recognition of branch pipe for pipe inspection robot using fiber grating vision sensor. In: 2013 10th International Conference on Ubiquitous Robots and Ambient Intelligence (URAI), pp. 633–638. IEEE (2013)
21. Mirats Tur: J.M., Garthwaite, W.: Robotic devices for water main in-pipe inspection: a survey. J. Field Robot. **27**(4), 491–508 (2010)
22. Nishikawa, H., Sasaya, T., Shibata, T., Kaneko, T., Mitumoto, N., Kawakita, S., Kawahara, N.: In-pipe wireless micro locomotive system. In: Proceedings of 1999 International Symposium on Micromechatronics and Human Science, 1999. MHS'99, pp. 141–147. IEEE (1999)
23. Okamoto, J., Adamowski, J.C., Tsuzuki, M.S., Buiochi, F., Camerini, C.S.: Autonomous system for oil pipelines inspection. Mechatronics **9**(7), 731–743 (1999)
24. Pfeiffer, F., Rossmann, T., Löffler, K.: Control of a tube crawling machine. In: Proceedings 2000 2nd International Conference on Control of Oscillations and Chaos, 2000, vol. 3, pp. 586–591. IEEE (2000)
25. Reber, K., Beller, M., Willems, H., Barbian, O.: A new generation of ultrasonic in-line inspection tools for detecting, sizing and locating metal loss and cracks in transmission pipelines. In: Ultrasonics Symposium, 2002. Proceedings 2002 IEEE. vol. 1, pp. 665–671. IEEE (2002)
26. Roh, S.G., Choi, H.R.: Differential-drive in-pipe robot for moving inside urban gas pipelines. IEEE Trans. Robot. **21**(1), 1–17 (2005)
27. Rollinson, D., Choset, H.: Pipe network locomotion with a snake robot. J. Field Robot. (2014)
28. Ruggiu, M., et al.: In-pipe inch-worm pneumatic flexible robot. In: Proceedings 2001 IEEE/ASME International Conference on Advanced Intelligent Mechatronics, 2001, vol. 2, pp. 1226–1231. IEEE (2001)
29. Schempf, H., Mutschler, E., Goltsberg, V., Skoptsov, G., Gavaert, A., Vradis, G.: Explorer: Untethered real-time gas main assessment robot system. In: Proceedings of International Workshop on Advances in Service Robotics, ASER, vol. 3 (2003)
30. Schoeneich, P., Rochat, F., Nguyen, O.T.D., Caprari, G., Moser, R., Bleuler, H., Mondada, F.: Tubulo-a train-like miniature inspection climbing robot for ferromagnetic tubes. In: Proceedings of the 1st International Conference on Applied Robotics for the Power Industry. pp. 1–5. No. EPFL-CONF-149354, IEEE Press (2010)
31. Schoeneich, P., Rochat, F., Nguyen, O.T.D., Moser, R., Mondada, F.: Tripillar: a miniature magnetic caterpillar climbing robot with plane transition ability. Robotica **29**(07), 1075–1081 (2011)
32. Scholl, K.U., Kepplin, V., Berns, K., Dillmann, R.: Controlling a multi-joint robot for autonomous sewer inspection. In: Proceedings. ICRA'00. IEEE International Conference on Robotics and Automation, 2000, vol. 2, pp. 1701–1706. IEEE (2000)

33. Shao, L., Wang, Y., Guo, B., Chen, X.: A review over state of the art of in-pipe robot. In: 2015 IEEE International Conference on Mechatronics and Automation (ICMA), pp. 2180–2185. IEEE (2015)
34. Shukla, A., Karki, H.: A review of robotics in onshore oil-gas industry. In: 2013 IEEE International Conference on Mechatronics and Automation (ICMA), pp. 1153–1160. IEEE (2013)
35. Suzumori, K., Wakimoto, S., Takata, M.: A miniature inspection robot negotiating pipes of widely varying diameter. In: 2003. Proceedings ICRA'03. IEEE International Conference on Robotics and Automation, vol. 2, pp. 2735–2740. IEEE (2003)
36. Tâche, F., Fischer, W., Caprari, G., Siegart, R., Moser, R., Mondada, F.: Magnebike: a magnetic wheeled robot with high mobility for inspecting complex-shaped structures. *J. Field Robot.* **26**(5), 453–476 (2009)
37. Tâche, F., Pomerleau, F., Fischer, W., Caprari, G., Mondada, F., Moser, R., Siegart, R.: Magnebike: compact magnetic wheeled robot for power plant inspection. In: 2010 1st International Conference on Applied Robotics for the Power Industry (CARPI), pp. 1–2. IEEE (2010)
38. Tianlu, C., Peiwen, Q., Tao, J., Zhigang, Z.: Designing and signal processing of intelligent inspection pig applying ultrasonic a-scan. In: Ultrasonics Symposium, 2005 IEEE. vol. 3, pp. 1484–1487. IEEE (2005)
39. Tsuruta, K., Sasaya, T., Shibata, T., Kawahara, N.: Control circuit in an in-pipe wireless micro inspection robot. In: Proceedings of 2000 International Symposium on Micromechatronics and Human Science, 2000. MHS 2000, pp. 59–64. IEEE (2000)
40. Walter, C., Saenz, J., Elkmann, N., Althoff, H., Kutzner, S., Stuerze, T.: Design considerations of robotic system for cleaning and inspection of large-diameter sewers. *J. Field Robot.* **29**(1), 186–214 (2012)
41. Wang, Z., Cao, Q., Luan, N., Zhang, L.: Development of new pipeline maintenance system for repairing early-built offshore oil pipelines. In: IEEE International Conference on Industrial Technology, 2008. ICIT 2008, pp. 1–6. IEEE (2008)
42. Wang, Z., Cao, Q., Luan, N., Zhang, L.: Development of an autonomous in-pipe robot for offshore pipeline maintenance. *Ind. Robot Int. J.* **37**(2), 177–184 (2010)
43. Yoon, K.H., Park, Y.W.: Pipe inspection robot actuated by using compressed air. In: 2010 IEEE/ASME International Conference on Advanced Intelligent Mechatronics (AIM), pp. 1345–1349. IEEE (2010)

Part VII
Mechatronics

SmartBath: A New Bathing Concept for Disabled People

Karolina Bezerra, José Machado, Filomena Soares, Vítor Carvalho and Demétrio Matos

Abstract Nowadays, the development of equipment for the elderly care is of great importance due to the increased number of elderlies. The requirements and failures of the existing elderly-care devices were studied in order to identify the most important needs of the bathing activity and then a new concept is proposed ‘SmartBath’. The SmartBath is a new assistive technology to improve autonomy, quality, safety, comfort and hygiene of bathing for elderly or bedridden. The bathing is a daily activity that requires physical effort, dedication and time to perform from the caregiver. This new concept integrates an automatic control of the bathing temperature, water flow-rate and light intensity. This concept can be operated directly or remotely into the system using mobile devices.

Keywords Well-being · Assistive technology · Elderlies · Assistive bath · Medical devices

K. Bezerra · J. Machado · D. Matos
R&D Metrics, School of Engineering, University of Minho, Guimarães, Portugal
e-mail: karolceli@dem.uminho.pt

J. Machado
e-mail: jmachado@dem.uminho.pt

D. Matos
e-mail: dmatos@ipca.pt

F. Soares (✉) · V. Carvalho
R&D Algoritmi, School of Engineering, University of Minho, Guimarães, Portugal
e-mail: fsoares@dei.uminho.pt

V. Carvalho
e-mail: vcarvalho@ipca.pt

V. Carvalho · D. Matos
Polytechnic Institute of Cávado and Ave, Barcelos, Portugal

1 Introduction

Based on the statistics [1], there is an increase in the number of aging population, which draws more attention to the development of medical devices for elderlies or disabled persons.

In this context, the healthcare should include services to promote better conditions for elderly groups and should comprise a complex system that integrates both process and the product [2, 3].

The entire development process was focused on the security and comfort for the bedridden or the disabled through medical devices that allow more independence. There is a wide range of equipment existing in the market, but they are usually used with the help of caregivers to perform daily care. Assistive technology is an alternative to solve and prevent problems such as the risk of falling, pressure sores areas, lack of mobility and cleaning [3, 4].

Particularly in the bath area, it is important to consider that not only elderly people have difficulties in bathing, and it is believed that about 5 % of the population needs help performing this task [4].

There are devices designed to help in different areas of care including bath, such as wheelchairs, support belts, smart environments, transfer chairs, among others [4, 6].

For a society to have good living conditions it requires some technologies that are comfortable and safe for the user [5, 6].

The highlight of this problem, the bath area, is conducted to the home in care given. Therefore, the device should be designed to integrate the care provided by caregivers (family or professionals) which however, will be given to only one person to perform the activities and required efforts with the bedridden [7–10].

This work is a product development process that seeks to transmit a new concept for care in the home and in the bath area. Therefore, conceptualize an intelligent bath to assist elderly people and/or their physical limitations in trying to improve the quality of life for both the user and the caregiver. It requires that the needs and limitations, due to lack of autonomy of users, are taken into account. This concept allows it to be handled by just one person, it is lightweight, portable, and easy to use, it promotes independence and good hygiene conditions.

The SmartBath development process described in this article is divided into five sections that explain its way of working, besides the introduction there is the related work; new approach of medical device; proposed control system and the final remarks of the work.

2 Related Work

Devices for assisting bath of older people and people with physical limitations are already commercialized. Among the existing devices some examples are presented below.

The Essence™ Apollo, Fig. 1 [11], aims to provide the care in assistive life, allowing easy and safe bathing experience for bedridden and caregivers. It has a lateral face structure which engages in various environments to allow an easy installation. The seat material is of glass fiber and it has a water drain system and removable side panels for convenient access of the flow components. The product has a safety system that closes the access door to the interior of the system. The product performs automatic cleaning and disinfection. This system promotes safety, comfort and hygiene of the user. The system disadvantage lies in the difficulty to transfer the bedridden into the system.

Another system that allows assisted baths is the Parker Bath® [12]. This is a safe solution; its structure has side access to the users. The shape gives caregivers contact with the patient to perform cleaning. The system includes a soap dispenser for cleaning and disinfection of the structure of the system. The structure should be fixed in the care facility. However, if the care facility does not have enough space, the installation is not possible.

The bath structure Bolero®, shown in Fig. 2, is a mobile device that collects the bedridden person from bed and transports them to the bath. It has a lift to adjust the required height, a lifting capacity of 136 kg and wheels with brakes. This product is efficient because it transmits comfort, security, mobility and hygiene. However, it has no support to be used without the elevator.

Considering the three presented equipment, the Essence Applo® has a functional drawback as it is not easy to transfer the bedridden into the system. The Parker Bath® has the aim to promote the bath care, but it does not allow to be used without the elevator. The Bolero® proved to be the most complete system but caregivers are not comfortable to provide care for a longer time using this equipment.

Table 1 presents the functional features of the commercial equipment presented.

By the performed analysis, it is possible to verify that the presented devices partially achieve the design requirements. From this, it is proposed a new approach of a medical device to afford better conditions of shower in bedridden people. The

Fig. 1 Apollo Essence™ equipment for bathing [11]



Fig. 2 Bolero[®] bathing mobile device [13]



Table 1 Functional features from the analyses of equipment

Equipment	Requirements
Essense Applo [®]	Fixed structure Installation needs bathroom changes Transportation needs more than one caregivers
The Parker Bath [®]	Mobile device Lift and easy to use Not comfortable for a long time Does not support use without elevator
The Bolero [®]	Mobile device Heavy structure Not easy to clean the back and waist area Not comfortable for a long time

aims to overcome the limitations of the referred systems, which could significantly improve the action of bath of elderly and/or bedridden people.

3 New Approach of Medical Device

Following the needs of the requirements to take care of bedridden people a new approach has been developed considering the concepts of Ambient Assisted Living (AAL). Basically it is designed to provide to a better quality of life in daily situations which will demand a lot of effort from to caregivers. The mechatronic system was projected to control all its integrated parts. The SmartBath (SB) provides to

older people a secure shower. This part has an integrated SmartBath Controller (SBC) to monitor and control system with the specifications of bath operation [14, 15] The two parts of the integrated system are connected through the contact of the base of the SB to the SCB, by a central plate fixed to the structure of the SCB [15] (Fig. 3). The system supervises, among other functions, the water flow rate, the water temperature and the light intensity.

The SmartBath (SB) is a design concept with a light and flexible surface which promotes an easy transportation. This approach was idealized with a washable material, specifically polyester. The system weight is around 30 kg. The SB integrates some technologies, such as motion detector to certify the correct adjustment of the person inside of the equipment [14].

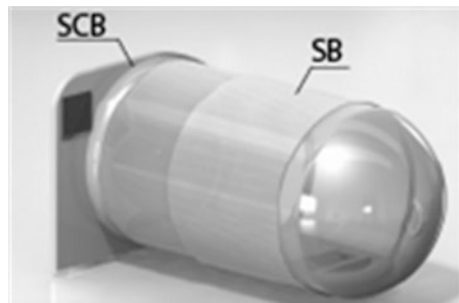
Figure 4 presents the usage sequence of the SB. In the first step, transportation is executed by the caregiver, basically, the equipment must be picked and placed at the desired location. The second step, is to position the device on the horizontal plane. In the third step, the caregiver pulls the carry handle, thus extending all parts of the structure. In the fourth step, with the structure opened, the caregiver needs to organize the SB to start using it. By the fifth step, the door is opened to adapt the elder inside of the equipment. The sixth step, to finish this process, requires checking the position of the elder inside the equipment and, with the caregiver on the outside of the SB, the bath process starts.

The equipment has some functional parts. The structure is mobile, on the top it has a specific part, a grip specific for the product to be carried by hand. There is a side door to enter and exit the equipment. A retractable structure is considered to allow the door manual close and opening (Fig. 4-Open Door (5)) [15]. The system shows when it is prepared to begin. The structure is fixed by attaching rubbers between the frames and applying pressure. When the weight decreases, the pressure also reduces and the system can be removed for transportation. The showers have tuning capability with an extension of up to 1.50 m. The user is capable of moving his/her arms being able to control the bath (Fig. 5).

Table 2 presents the specific project parameters.

Moreover, the project should take into account the human factor requirements allowing the user to remain seated and that his limbs can move in order to perform a clean task. It intends to improve the performance of the equipment and to minimize

Fig. 3 SmartBath concept compose of two parts [15]



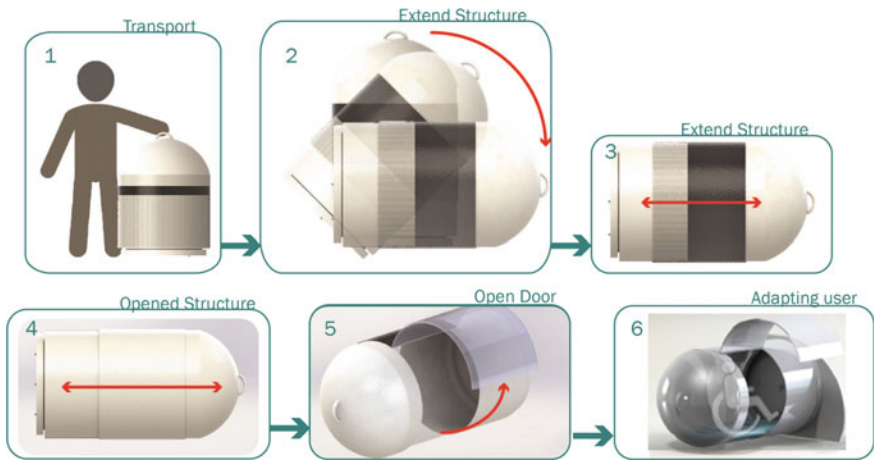


Fig. 4 The functioning steps of SB by caregiver

Fig. 5 Closed structure [14]

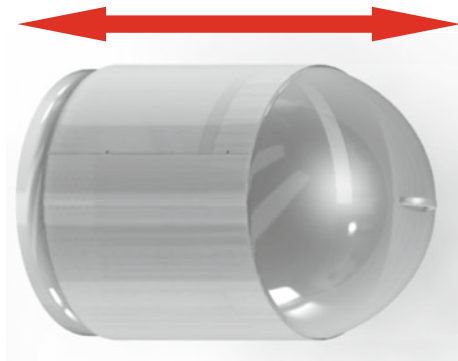
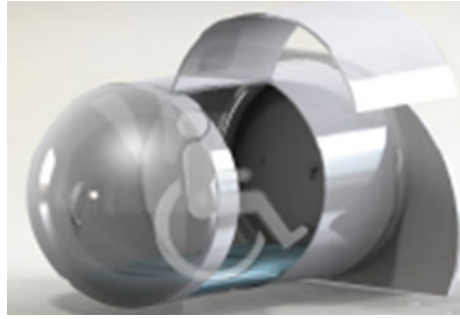


Table 2 Project Requirements

Requirements	Parameters
Average weight	120 kg—Maximum weight allowed to borne by structure [16]
Water temperature	From 0 to 40 °C [17]
General dimensions	1500 mm length, 770 mm width and 770 mm high
Volume of the reservoirs of water	Considered to be sufficient for 25 L of tank volume [18]

the risks related to the movement of bedridden between different environments. The user remains in his wheelchair to take a bath inside the SmartBath. Figure 6 represents a simulation of usage. Caregivers use the side door to put the elder inside

Fig. 6 Simulation of the usage



and then exit the SB. Only one person can enter the equipment as the person needs to stay seated to be able to bath.

Parallel to this bath system design it is being developed a water supply system. This is a modular system responsible for supplying the water for the bath and drain the used water. This will facilitate and make possible the versatility of the bath system.

4 Proposed Control System

The SmartBath (SB) can be installed inside any bathroom without compromising the aesthetics and performance. The design considers the usage in any environment with drainage for the evacuation of water. The temperature and flow rate are individually controlled unlike any other shower system, allowing a personal configuration.

For safety reasons, the device is designed with the possibility of mechanical use, not being restricted by possible electronic failure.

The interface used in the structure of the SmartBath controller (SCB) is used for control and monitoring of the bath operation (Fig. 7).

The main user of this equipment is the caregiver (a member of the family or a health technician). The primary control function is the ON/OFF button, followed by the desired water temperature (0–40 °C), light intensity (0–100 lx) and shower flow (water on/rinse off). The water flow can be controlled, as well as the rinsing function when the user is managing the bath. In general, the bath activity takes between 15 and 20 min, it has an alarm that indicates to the caregiver when entering the last 5 min.

For safety reasons, the system has a motion sensor implemented to ensure the correct position when the use is within the shower environment, as well as it is prepared to stop the operation at any time, if necessary.

In Fig. 6, the side door enables a better view for the caregiver during the bath, since the material used is transparent. The door can be handled both electronic or manually. The control part of the SCB is connected to the SmartBath and is removable and easy to transport. The designed control panel can be seen in Fig. 8.

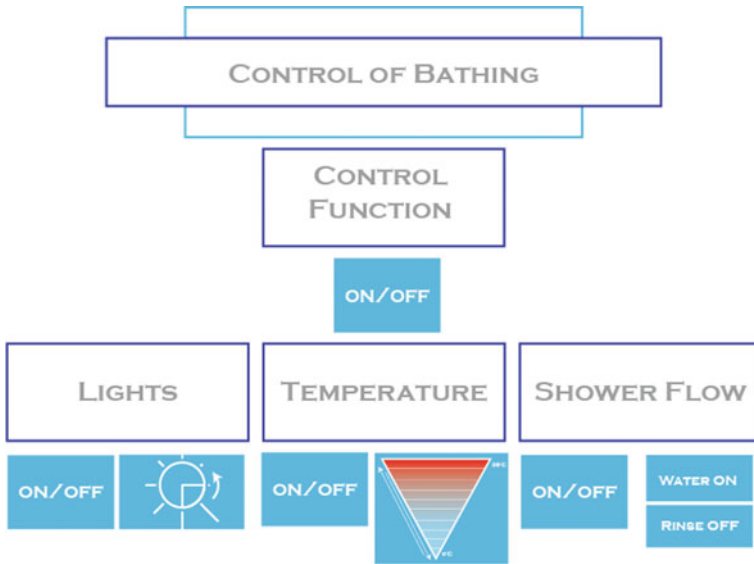


Fig. 7 System control panel

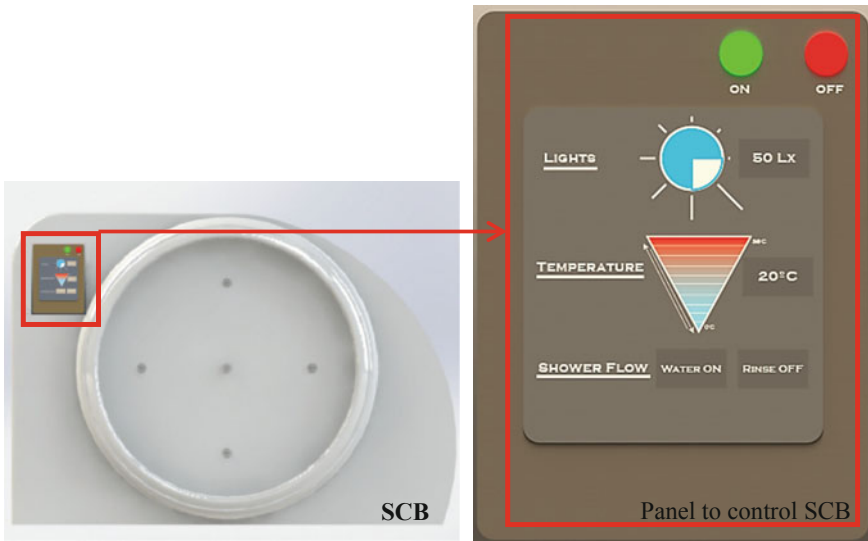


Fig. 8 The SmartBath (SCB) control panel

Once the system starts operating the functionalities can be activated by the caregiver and, following a sequence of options, which must be followed in the sequence described first, to connect the control functions for all the following

options to be enabled. This option was implemented to ensure that the device will not be activated without the user's permission, thus avoiding future errors in operation.

Therefore, after activating the control functions, the lights should be turned ON and set in a range between 0 and 100 lx, then turn ON the temperature option and set the desired temperature between 0 and 40 °C and finally enable the water flow ON and select the options of water or rinse.

The water supply system holds about 25 L [14, 15, 18] to support home environments. The shower is built-in the structure itself, at the top, its water supply is electronically controlled but in case of error automatically turns to manual override. The water control collects all the water already used and eliminates domestic sewer routes. The functions of the SB and SCB in this device provides the caregiver greater confidence that the bath is finally a pleasure, not an obligation, and through its use can have a higher quality of life.

5 Final Remarks

In this paper it was presented the design of a device to give bath to bedridden elderly people that can be operated by a single person (caregiver). The system integrates functions such as, the automatic control of bath temperature, water flow-rate and light intensity. It is capable of being operated directly by the SmartBath controller (SBC) and it is designed to optimize the care in the daily life of the bedridden elderly people. Moreover, it includes safety procedures allowing reducing possible errors, as well as physical efforts to caregivers.

It will be possible consider as future work a severe redesign. This project still has some shortcomings to be a final concept and an idealization of what would be best for the use of the caregivers in the bath task.

Acknowledgments This work has been supported by COMPETE: POCI-01-0145-FEDER-007043 and FCT – Fundação para a Ciência e Tecnologia within the Project Scope: UID/CEC/00319/2013.

References

1. Gallagher, A., Murphy, E., Fennell, A.: Ageing, Vision Impairment and Digital Inclusion in Ireland, pp. 1–7 (2014)
2. Després, C.L., Ramadier, T.: When mobility makes sense: a qualitative and longitudinal study of the daily mobility of the elderly. *J. Environ. Psychol.* **31**(1), 52–61 (2011)
3. Started, G.: *Selecting the Right Bathing Systems for Your Facility*, vol. 1, no. 1 (2005)
4. Brummel-Smith, K., Dangiolo, M.: *Assistive Technologies in the Home: Clinic Geriatric Medical*, vol. 25(1), pp. 61–77. Elsevier, Amsterdam (2014)
5. José, F., Cláudio, L.: Paulo Hartung Anselmo Tozi secretário de estado da saúde gerente de regulação assistencial, pp. 1–180 (2008)

6. Pinto, C.: Validação do Índice de Barthel numa amostra de idosos não institucionalizados. **25**, 59–66 (2007)
7. Mohamed, Z., Capi, G.: Development of a new mobile humanoid robot for assisting elderly people. *Procedia Eng.* **41**(Iris), 345–351 (2012)
8. MIT House_n Research Group. http://architecture.mit.edu/house_n/documents/2006
9. Friedewald, M., Punie, Y., Alahuhta, P., Heinonen, S.: Perspectives of ambient intelligence in the home environment. *Telemat. Inf.* **22**(3), 221–238 (2005)
10. Park, H.K., Hong, H.S., Kwon, H.J., Chung, M.J.: A nursing robot system for the elderly and the disabled. *Int. J. Human-Friendly Welf. Robot. Syst.* **2**(4), 11–16 (2001)
11. Apollo Essence™. <http://apollobath.com/bathing-systems/essence-7000> (2015)
12. Parker Bath®. <http://www.arjohuntleigh.pt> (2015)
13. Bolero®. <http://www.arjohuntleigh.pt> (2015)
14. Bezerra, K., Machado, J., Carvalho, V., Soares, F., Silva, B., Matos, D., Leão, C.P.: System for assistance on bath of bedridden elderly people. In: ASME International Mechanical Engineering Congress and Exposition, Proceedings (2014)
15. Bezerra, K., Machado, J.M., Silva, B., Carvalho, V., Soares, F., Matos, D.: Mechatronic system for assistance on bath of bedridden elderly people. In: IEEE 4th Portuguese Meeting on Bioengineering, pp. 1–4 (2015)
16. Lima, R.F.: Adaptação ergonómica e antropométrica: Universidade do Minho (2012)
17. Ordem Arquitectos. Decreto-Lei n.º 163/2006 de 8 de Agosto. *Diário da República* (2006)
18. Smas-sintra Tecnirede. http://www.smas-sintra.pt/index.php?option=com_content&task=view&id=76 (2015)

A New Approach for Dynamic Analysis of Overhead Crane Systems Under Moving Loads

Şahin Yildirim and Emir Esim

Abstract Nowadays, dynamic effects of overhead cranes are usually neglected because of their operation at low speed but they can be designed considering the static effects. However, the production rate increases with the development of technology and the increase in the number of proper places for product handling and cargo ships loading in the harbour. So the need for working cranes is growing. Therefore, in this study we have analysed both single bridge and double bridges crane systems and the load dynamic effects occurring on the bridge during the movement of carriages. The analysis was based on the Finite Element Method (FEM). The conclusion of the study was that double bridge cranes have had less dynamic effects under the same loads as single bridge cranes so they proved to be working faster.

Keywords Overhead crane • Multi-machine crane systems • Finite Element Method (FEM) • Dynamic load

1 Introduction

Engineering systems are exposed to dynamic effects because of the change in the location of the loads in the system over time. In such a structure, there is a dynamic response according to changing conditions that depends both on the loads acting on the system, and on the changes in the amplitude of loads. One of the moving load systems is a crane system on top of which there are moving carriages. Currently, there is a rich corpus of theoretical and experimental work on moving-load problems and a lot of related works and studies that can be outlined below.

K.H. Low presented a vibration analysis by using eigenfunctions for the various beams carrying multiple masses. Polynomial approximation mode analysis was

Ş. Yildirim (✉) · E. Esim

Faculty of Engineering, Mechatronic Engineering Department, Erciyes University, Kayseri, Turkey

e-mail: sahiny@erciyes.edu.tr

given in comparison with analytical and experimental results in order to compare and validate the results for the proposed models [1].

Another study was outlined by K.H. Low—a comparative study of the eigenfrequency analysis for an Euler-Bernoulli beam carrying a concentrated mass to an arbitrary location [2].

Cha briefly summarized researches on the approximate and exact analyses and classified the analyzing approaches commonly used on the free vibration of a linear elastic structure carrying lumped mass, spring and damping at different points (such as Lagrange approach, Dynamic Green function approach, Laplace transform, and analytical and numerical solution methods) [3–5].

In a study conducted by Gürgöze, there were added several spring and mass systems along Euler-Bernoulli beam equations and it was developed an alternative formulation for the frequency of the beam [6]. Then, in another study by Gürgöze and Erol, was conducted a vibration analysis of the beam in which the system made of a spring and of a damper was investigated [7].

A simple supported uniformly Euler-Bernoulli beam carrying a crane which consisted of a carriage and a payload was modelled by D.C.D. Oguamanamand, J.S. Hansen, and G.R. Heppler. The crane carriage was modelled as a particle as the payload was assumed to be suspended from the carriage on a massless rigid rod and restricted to motion in the plane defined by the beam axis and the gravity vector. The two coupled integro-differential equations of motion were derived using Hamilton's principle and the operational calculus was used to determine the vibration of the beam. Beam-natural frequencies of the vibrations for a crane system were detected, and the precise frequency was derived from the equations for these cases. Were presented numerical examples which covered the range of carriage speeds, carriage masses, pendulum lengths, and payload masses. The maximum deflection of the beam occurred at the end of the beam at high speeds because of inertia effects and in the middle of the beam at low speed because of the fact that the system was reduced to a quasi-static situation [8, 9].

In this study, was investigated a crane systems bridge element with both a single beam and two beams. Also, we considered a different number of carriages moving on top of the beams on the dynamic and the subsequent effects that occur under the moving load were analyzed by using FEM.

2 Dynamics of Bridge Crane System

Three dimensional bridge cranes are systems in which the load is lifted, moved, and dropped to the desired location by means of carriages. They are used in all factories and ports in different industries that handle heavy loads. The main requirement related to the crane is that the operations are performed to the desired destination as quickly as possible. Overhead cranes, built to support high constructions, consist of a bridge placed between the two crane paths. The movement to be performed by an overhead crane can be defined as follows:

- Vertical movement along the OY axis: lifting and lowering movement;
- Horizontal movement along the OZ axis: translational motion of the bridge;
- Horizontal movement along the OX axis: the translational motion of the carriage on the bridge.

The front of a crane system while lifting and lowering and in the moving state of the carriage is shown in Fig. 1. Each state of the crane is specified in the system with a different available dynamic response. In this study, the carriage is moving on the crane system and all of the carried loads are applied. The total force in this case is shown in Fig. 2.

A dynamic analysis is also performed for the case in which these forces move at a constant velocity on the system. Here, the bridge is considered both as a single beam and as double beam, and the beam is divided into 20 equal parts. The 20 separate loads are assumed to be moving to another area every one second and the time for moving a load is identified as shown in Fig. 3.

The general motion equation with multiple degrees of freedom of the systems is given by [10]:

$$[m]\{\ddot{q}\} + [c]\{\dot{q}\} + [k]\{q\} = \{P(t)\} \tag{1}$$

where; $[m]$ is the matrix of mass of the classified structure, $[c]$ is the damping matrix, $[k]$ is the rigidity matrix, $\{\ddot{q}\}$ is the vector of acceleration of all structures, $\{\dot{q}\}$ is the vector of velocity of all structures, $\{q\}$ is the vector of displacement of all structures, and $\{P(t)\}$ is the vector or all external forces to the system.

Moving load analysis was performed on the basis of this simulation as external load time-dependent finite elements are applied to the model. As can be seen in Fig. 3, the maximum load specified when applying to the first region and other regions is considered to be zero. According to the time, other field force definition is

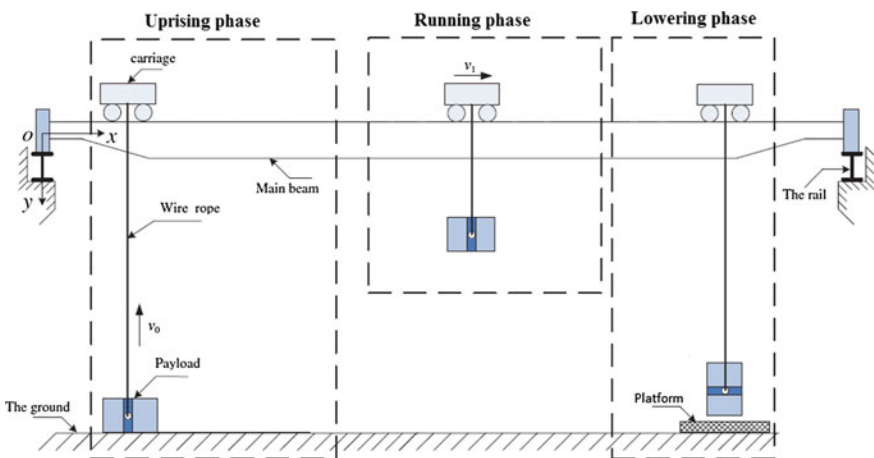


Fig. 1 Bridge crane system and load carrying stages

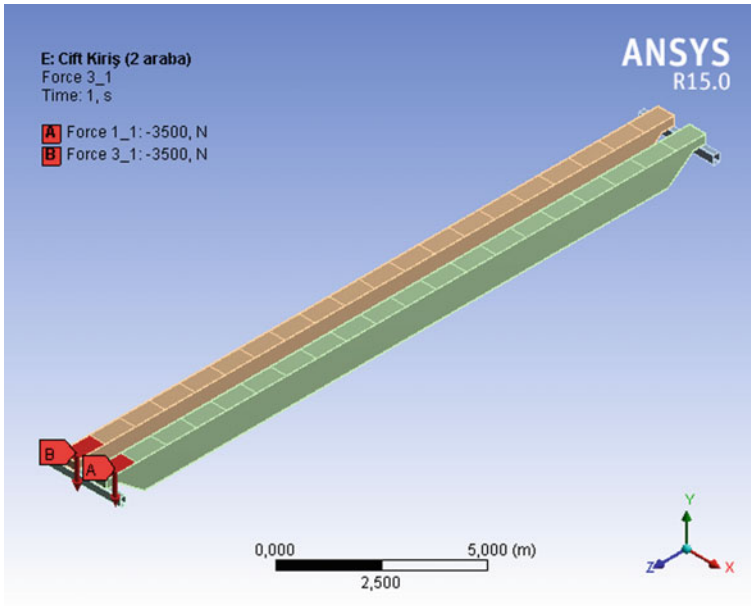


Fig. 2 Analysis of loads moving on a beam

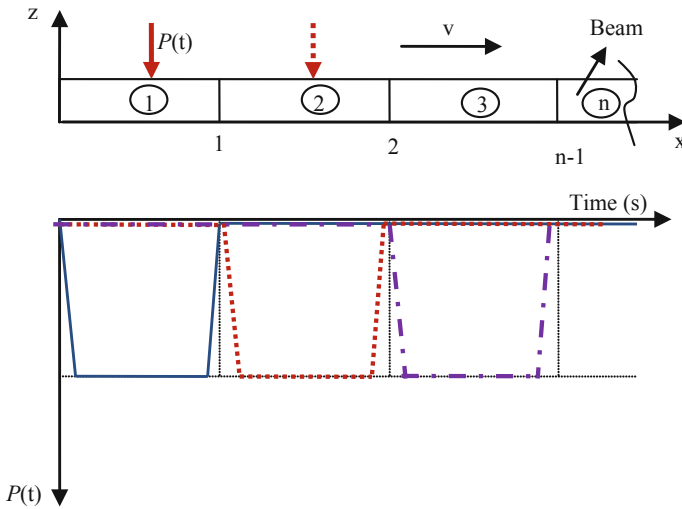


Fig. 3 Moving load modelling

considered zero. Clough and Penzien have expressed the specified outer force vector in the form defined according to [11]:

$$\{P(t)\} = \{0 \ 0 \ 0 \ \dots \ f_1^{(s)} f_2^{(s)} f_3^{(s)} f_4^{(s)} \ \dots \ 0 \ 0 \ 0\} \tag{2}$$

where $f_i^{(s)}(t)$, ($i = 1, 2, 3, 4$) is defined as equivalent node forces:

$$\{f^{(s)}(t)\} = P\{N\} \tag{3}$$

where P is the value of the vertical force applied from the top of the beam and $\{N\}$ is a function of shape and is expressed as follows:

$$\{N\} = [N_1 N_2 N_3 N_4]^T \tag{4}$$

Shape functions can be described in the following equations as in [11, 12]:

$$N_1 = 1 - 3\xi^2 + 2\xi^3 \tag{5}$$

$$N_2 = l(\xi - 2\xi^2 + \xi^3) \tag{6}$$

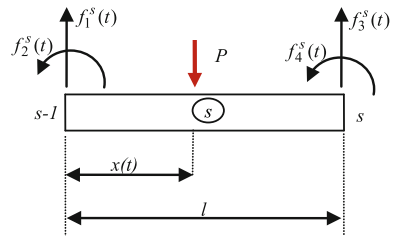
$$N_3 = 3\xi^2 - 2\xi^3 \tag{7}$$

$$N_4 = l(-\xi^2 + \xi^3) \tag{8}$$

$$\xi = \frac{x}{l} \tag{9}$$

where l is the length of the element (s), implemented on the vertical direction along the element x . P is the distance from the point where the force was applied, as shown in Fig. 4.

Fig. 4 Equivalent nodal forces of the element s subjected to a moving load



3 Simulation Results and Discussions

In this study, the length of the bridge is $L = 20$ m both on one beam and on two beams. 600 mm width 1000 mm height and 8 mm thickness rectangular box profiles are taken as sections of the beam (-s). The selected parameters for the bridge material are the following. The material is steel St37; the density of material is $\rho = 7850 \text{ kg/m}^3$, the Poisson ratio used is $\nu = 0.3$, and the modulus of elasticity is $E = 210 \text{ GPa}$.

As shown in Fig. 1, a one beam and a two beam bridge solid models were created after a transient structural analysis, the (Finite Element Software) ANSYS Workbench 15.0 was used. The results obtained were presented at the mid-point of the bridge span compared to the results of the mid-point of the bridge due to displacement of the main design parameters in crane design.

The design taken into account uses cranes on top of which there is one or several cars for investigating the dynamic effects occurred. Therefore we performed an analysis with one carriage and two carriages using FEM, considering a carriage moving on a girder bridge with the total moving load of 12,000 N applied and assuming a payload of 10,000 N and a carriage weight of 2000 N. When transporting two carriages with the same load on a beam two separate moving loads in the system a 7000 N load was applied. Displacement, velocity and acceleration results at the mid-point of the beam are given in Figs. 5, 6, and 7. As shown in Fig. 5 when using a two-carriage beam the displacement at midpoint is greater than when using a single carriage beam.

In Figs. 6 and 7 are depicted the speed and acceleration changes examined for both the cases of one and of two carriages and the dynamic response of a crane system with a carriage system is very much the same as in the case of two carriages and both speed and acceleration increase are depicted below. This slight increase in

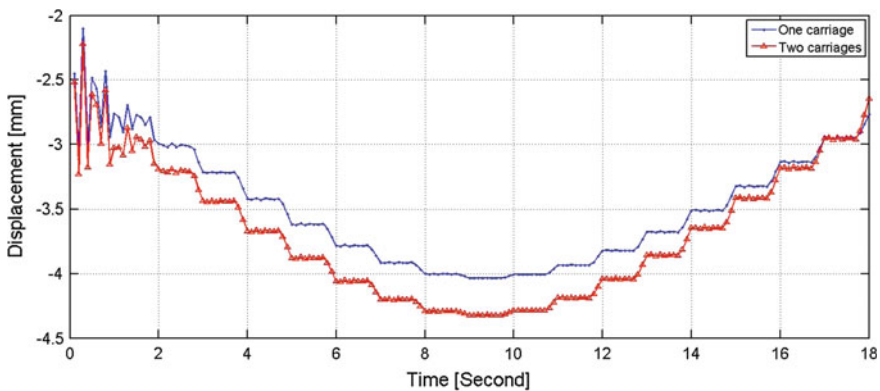


Fig. 5 Displacement variation at the mid-point of a single beam, with one carriage and two carriages

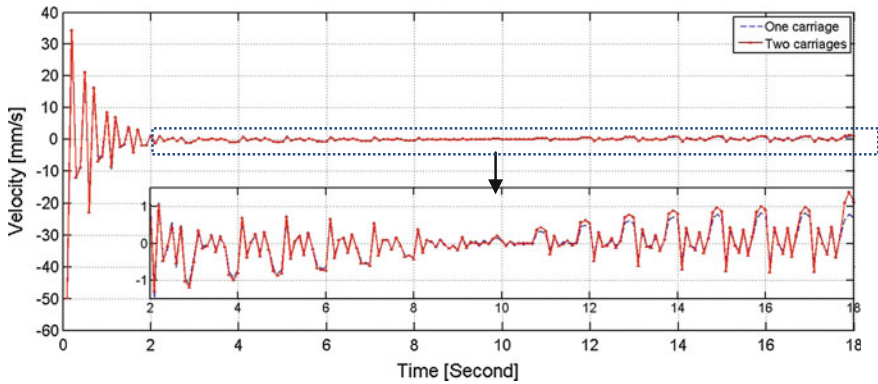


Fig. 6 Velocity variation at the mid-point of a single beam, with one carriage and two carriages

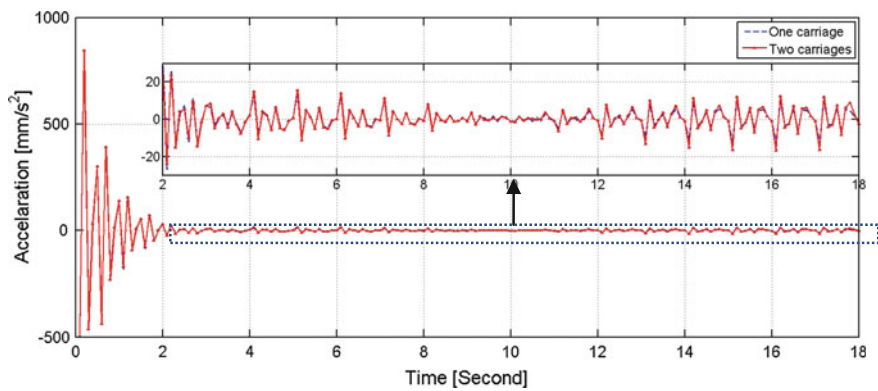


Fig. 7 Acceleration variation at the mid-point of a single beam, with one carriage and two carriages

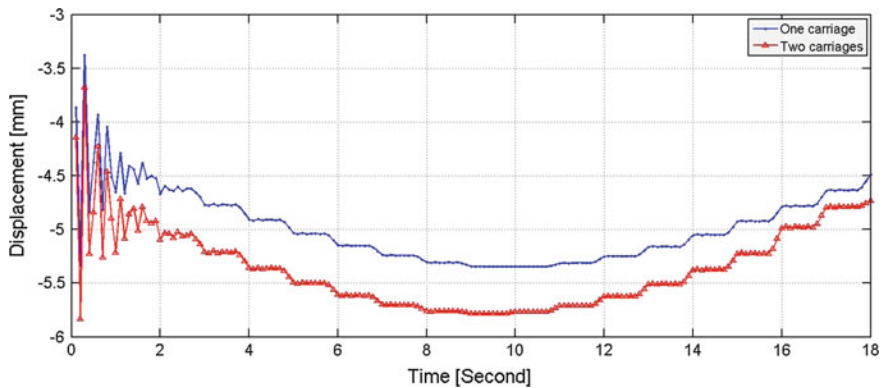


Fig. 8 Displacement variation at the mid-point of a double beam, with one carriage and two carriages on the first beam

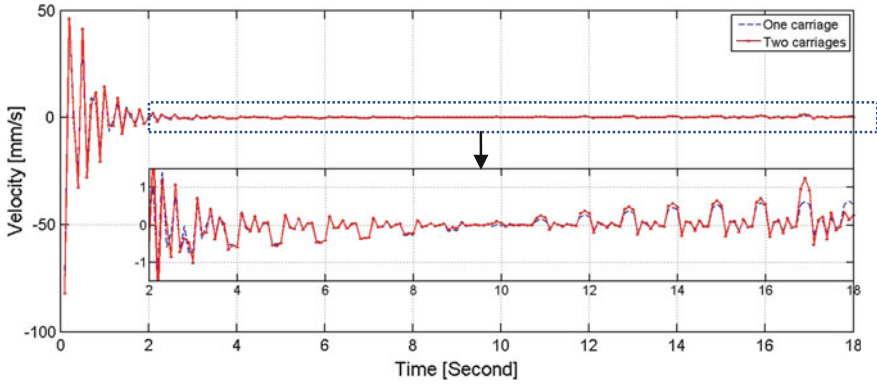


Fig. 9 Velocity variation at the mid-point of a double beam, with one and two carriages on the first beam

values in the second scenario can be considered as dynamic effects that are brought into the system by the weight of the second carriage.

In the event of a single carriage on a double beam, a 6000 N force was applied to both one and two beams as the payload and the weight of the carriage was split in two. The load moving model defined in the single beam scenario was also defined for a double beam. The double beam payload and weight of the two cars were divided into 4 moving loads and 4 separate forces of 3500 N were identified. According to the circumstances mentioned above, the first displacement, velocity and acceleration changes occurring on the double beam are given in Figs. 8, 9, and 10. Also, when the second beam substitution occurred, the changes in velocity and acceleration were given in Figs. 11, 12, and 13.

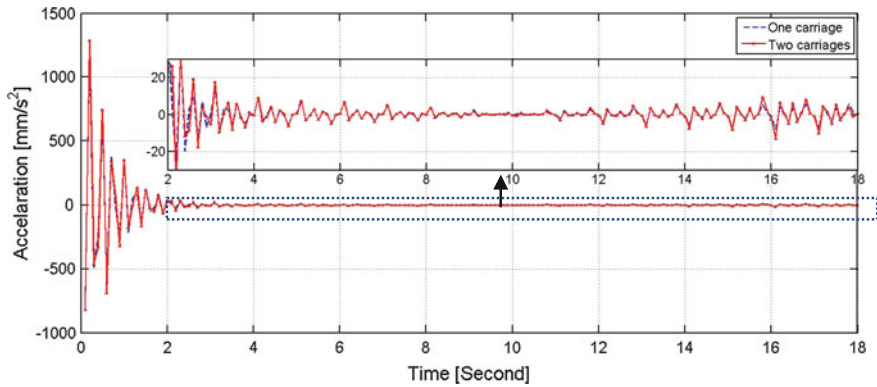


Fig. 10 Acceleration variation at the mid-point of a double beam, with one and two carriages on the first beam

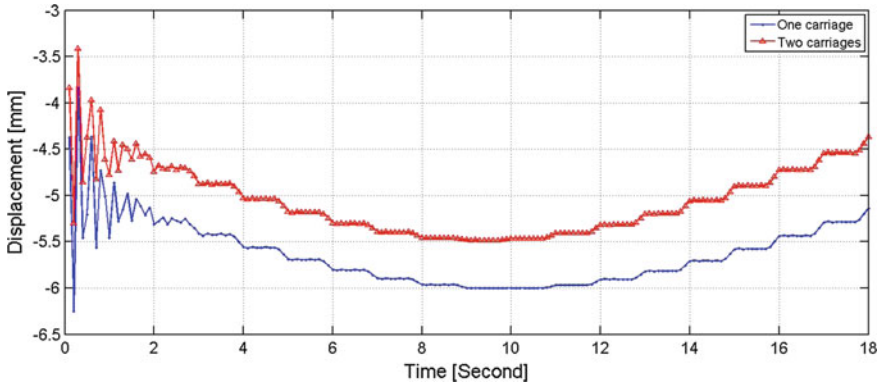


Fig. 11 Displacement variation at the mid-point of a double beam, with one and two cars on the second beam

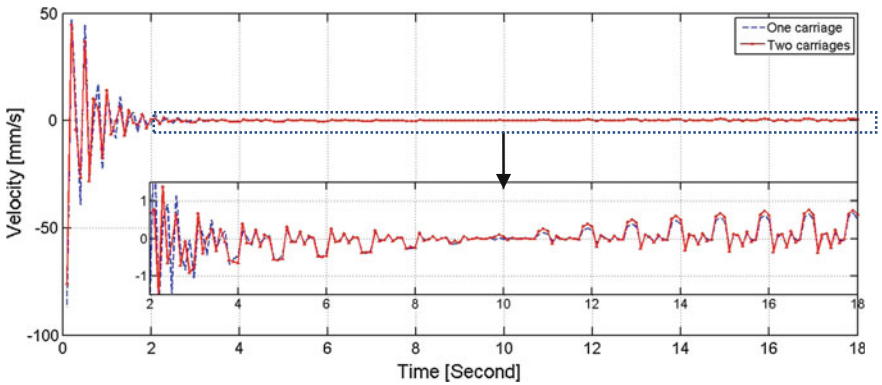


Fig. 12 Velocity variation at the mid-point of a double beam, with one and two cars on the second beam

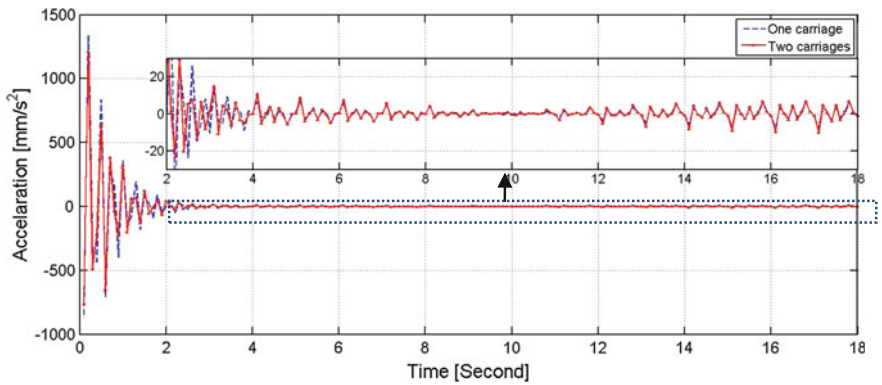


Fig. 13 Acceleration variation at the mid-point of a double beam, with one and two cars on the second beam

In case of a double beam with two carriages the larger displacement is shown in Fig. 8. As can be seen from, Figs. 9 and 10, in the case of using two carriages, the velocity and acceleration produces the same effects. Figure 9 describes the two carriage case velocity change on the second beam, and the effect on the beam is less visible. Also, Fig. 11 shows the changes in acceleration.

Figure 11 shows the changes in displacement caused by the second beam and Fig. 12 shows speed variation caused by the second. The change in acceleration induced by the second beam is shown in Fig. 13.

4 Conclusions

Cranes systems are designed to move the carriages on double beam bridges. However, the design of the bridge was analyzed taking into account dynamic effects and based on a FEM. As can be seen from the results, both single carriage and two carriages move in these systems. Furthermore, the total force for moving the second carriage has increased in each of the two beam system, thus the increases in dynamic effects. At the same time, using a double beam system reduces the dynamic effects that strongly impact on the results. As a result, based on a double beam bridge system, although the system domain consists of both beams, the symmetric displacement, velocity and acceleration values can help to determine the different behaviour of the system.

As can be outlined from the results, the carriage has high vibrations caused by the effects of inertia in the system during the first move. They decreased after a while under the operating conditions and, at the same time, when the moving load approaches the point of the measurement, there is a decrease in velocity and acceleration amplitude and after passing this point, both values increase again.

Acknowledgments Authors would like to express their deepest appreciation to Erciyes University, which provided us the opportunity to support the **FCD-2015-5162** project for designing and experimental applications and testing of crane systems.

References

1. Low, K.H.: An analytical-experimental comparative study of vibration analysis for loaded beams with variable boundary conditions. *Comput. Struct.* **65**(1), 97–107 (1997)
2. Low, K.H.: A comparative study of the eigenvalue solutions for mass-loaded beams under classical boundary conditions. *Int. J. Mech. Sci.* **43**, 237–244 (2001)
3. Cha, P.D., Wong, W.C.: A novel approach to determine the frequency equation of combined dynamical systems. *J. Sound Vib.* **219**, 689–706 (1999)
4. Cha, P.D.: Eigenvalues of a linear elastic carrying lumped masses, springs and viscous dampers. *J. Sound Vib.* **257**, 798–808 (2002)
5. Cha, P.D.: A general approach to formulating the frequency equation for a beam carrying miscellaneous attachments. *J. Sound Vib.* **286**, 921–939 (2005)

6. Gürgöze, M.: On the alternative formulations of the frequency equation of a Bernoulli-Euler beam to which several spring mass systems are attached in-span. *J. Sound Vib.* **217**, 585–595 (1998)
7. Gürgöze, M., Erol, H.: On the Eigen characteristics of longitudinally vibrating rods carrying a tip mass and viscously damped spring-mass in-span. *J. Sound Vib.* **255**(3), 489–500 (2002)
8. Oguamanan, D.C.D., Hansen, J.S., Heppler, G.R.: Dynamic response of an overhead crane system. *J. Sound Vib.* **213**(5), 889–906 (1998)
9. Oguamanan, D.C.D., Hansen, J.S., Heppler, G.R.: Dynamics of a three-dimensional overhead crane system. *J. Sound Vib.* **242**(3), 411–426 (2001)
10. Gasic, V., Zrnic, N., Obrodavic, A., Bosnjak, S.: Consideration of moving oscillator problem in dynamic responses of bridge cranes. *FME Trans* **39**, 17–24 (2011)
11. Clough, R., Penzien, V.: *Dynamics of Structures*. McGraw-Hill, New York (1993)
12. Meirowitch, M.: *Element of Vibration Analysis*. McGraw-Hill, New York (1986)

CMOS Transducer with Linear Response Using Negative Capacity that Can Be Used in Mechatronic Systems for Force Measurement in Human Walking Analysis and in the Future in MEMS and NEMS Applications

Anghel Constantin and Gheorghe I. Gheorghe

Abstract The paper describes a methodology to linearize the signals obtained from capacitive force sensors. The approach is based on the theoretical analysis of a negative capacitance circuit adjusted to compensate to the parasitic capacitances that are formed in parallel with the sensor. I describe an original method of linearization using a negative capacitance calculated based on the Laplace Analysis of the one auxiliary circuit added to the main oscillator. This auxiliary circuit, called “Neutrodyne” is a neutralization circuit and provides a negative capacitance that compensates the parasitic one. The result is a rectangular signal with linear frequency dependent on the force or pressure applied. This linearization method can be used in a variety of other applications: mechatronic systems, gait analysis, microelectromechanical systems (MEMS) and nanoelectromechanical systems (NEMS). In our project, the transducer is used for measuring the calibrated Ground Reaction Force during gait in order to calculate the total caloric consumption of the body for horizontal components of forces application points.

Keywords Negative capacitance • Ground reaction force • Capacitive force transducer

A. Constantin (✉) · G.I. Gheorghe
Doctoral School of Valahia University, Targoviste, Romania
e-mail: anghel.constantin@incdmtm.ro

G.I. Gheorghe
e-mail: incdmtm@incdmtm.ro

G.I. Gheorghe
National Institute of Research and Development in Mechatronics and Measurement
Technique, Bucharest, Romania

1 Introduction and Rationale

Within a larger project that aims to analyze human walking by measuring ground reaction forces, we investigated solutions for building force sensors with linear response and good signal to noise ratio [1]. One of my previous papers [2] presents an approach based on the use of thermal resistive touch sensors, together with a solution for linearization of the transfer characteristics. Tactile sensors produce an analog output that must be transmitted differentially to the A/D conversion block in order to minimize perturbation factors. This approach has the drawback of requiring a relatively large number of components (analog amplifiers, etc.). We have therefore designed a simpler solution that provides directly a digital output signal, with very few noise distortions. The research for an optimal solution has led to the idea that we can use an oscillator made of a Schmitt Trigger “Not AND” (NAND) logical gate, with the circuit capacitor serving as the sensing element of the transducer. Of course that simplicity has its cost, so we also had to solve the issue of linearity. In the following, we present an original method to obtain linearity using a negative capacitance calculated via a Laplace transform.

1.1 *Structure of the Paper and Objectives*

The purpose of the paper is to present a theoretical calculation method and practically implementation for a circuit that ensures the negative capacitance function by integrating it directly to a wide area of sensors that use sensitive capacitive elements such as force to frequency transducers.

We will also present the schematic of the circuit for the particular case in which force transducers are used in the gait analysis by measuring ground reaction force.

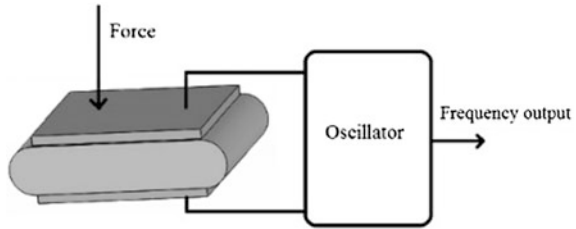
1.2 *Study Area and Previous Work*

The research area is in the domain of electronic circuit theory with applications in the sensors development for human walking analysis.

Results are based on a vast experience in the field of simulation of electronic circuits with SPICE model and different software as Altium-Designer.

The result of this research is the development of common circuit suitable for different applications. The presented circuit was designed using a CMOS integrated circuits and can be integrated into design of various capacitive transducers.

Fig. 1 The block diagram of capacitive sensing transducer



1.3 Materials and Method for CMOS Capacitive Transducer

The transducer we used employs an original system which consists of an elastic isolator material, used to create artificial muscles, placed between two conductive armatures. Obviously, the capacitance that appears is variable and will depend upon the distance between the armatures which in turn is relative to the applied force. The result is a capacitor to frequency converter. The output of these circuits is a digital parameter (frequency), not voltage, which is advantageous because it doesn't require an analog to digital converter for measuring with a microcontroller based system [3].

This paper does not present the realization of the capacitance sensor or the mechanical building, but only the linearization methodology of the transfer characteristic. The variable capacitor determines the oscillation function of a damped circuit.

The principle of general capacitive sensing topology is illustrated in Fig. 1.

In order to reduce the effect of parasitic capacitance influence on the main oscillator and improve the linearity I designed the second circuit with negative capacitance by using the Laplace transform of the complex impedance.

2 Oscillator Design Details

In order to keep things simple, we used an oscillator schematic with a CMOS NAND gate—type HCT4093 (Schmitt Trigger)—circuit which is depicted below (Fig. 2.)

Without external RC elements, the Schmitt Trigger gate can be assimilated with an amplifier with supra-unitary positive reaction $Fr > 1$ (Fr is feedback ratio). We know that the positive reaction implies a switching with a high speed variation of the output voltage. We also know the output frequency depends only from the resistance (R) and capacitor (C) values with initial voltage U_0 .

The HCT4093 circuit is a NAND gate, so the RC components create a delayed negative reaction. Thus the final circuitry will not have a stable state, but will become unstable [3].

Waveforms in points A and B are shown in Fig. 3.

Fig. 2 The basic topology of Schmitt Trigger oscillator

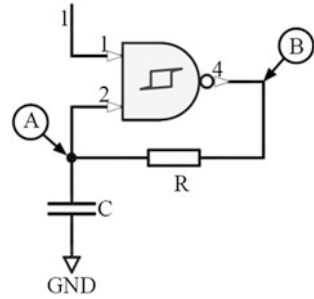
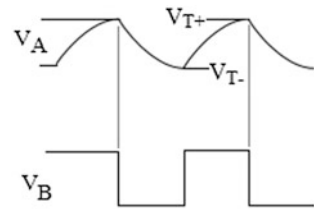


Fig. 3 The waveform of the input V_A and output V_B



In order to find out the oscillation period T we must solve the following differential equation—see the expressions (1), (2), (3):

$$\frac{1}{C} \int_0^{\frac{T}{2}} i_c dt + R \cdot i_c = U_0 \tag{1}$$

$$RC \cdot \frac{di_c}{dt} + i_c = U_0 \cdot C \text{ or } \frac{di_c}{dt} + \frac{1}{RC} \cdot i_c = \frac{U_0}{R} \tag{2}$$

Which leads to:

$$i_c = \frac{U_0}{R} \cdot e^{-\frac{t}{RC}} \text{ or } u_c = U_0 \left(1 - e^{-\frac{t}{RC}} \right) \tag{3}$$

When

$$\begin{cases} u_c = V_{T+} \rightarrow U_0 = V_{OL} \\ u_c = V_{T-} \rightarrow U_0 = V_{OH} \end{cases} \tag{4}$$

By solving the equation system above we obtain the expression of Period T as:

$$T = t_1 + t_2 \tag{5}$$

$$t_1 = RC \cdot \ln \left(\frac{V_{DD} - V_{T-}}{V_{DD} - V_{T+}} \right) \tag{6}$$

$$t_2 = RC \cdot \ln\left(\frac{V_{T+}}{V_{T-}}\right) \tag{7}$$

We can notice that

$$T = K_1 \cdot RC \text{ and } C = \frac{\epsilon_0 \cdot S}{d} \rightarrow T = K_1 \cdot RC \tag{8}$$

The notations used in expressions (4), (5), (6), (7) and (8) are as follows: the V_{DD} is the drain power supply voltage and the V_{T-} and V_{T+} is the threshold voltage. The K_1 depends on power supply V_{DD} because this defines the V_{T-} and V_{T+} according with CMOS class manufacture tolerance, which must be stable regardless of temperature variations at least when using a Zener diode.

If we apply the general plate capacitive formula, we obtain relations (9), (10) and (11).

$$f = \frac{d}{K_1 \cdot R \cdot \epsilon_0 \cdot S} \text{ and } d = d_0 - x \tag{9}$$

where x is the capacitor layer relative displacement, d and d_0 is distance between armatures of capacitor.

$$x = K_2 \cdot F \tag{10}$$

$$f = \frac{d_0}{K_1 \cdot R \cdot \epsilon_0 \cdot S} - \frac{K_2}{K_1 \cdot R \cdot \epsilon_0 \cdot S} \cdot F = f_0 - K \cdot F \tag{11}$$

From (11) we then obtain the relation (12).

$$f_0 = \frac{d_0}{K_1 \cdot R \cdot \epsilon_0 \cdot S} \text{ and } K = \frac{K_2}{K_1 \cdot R \cdot \epsilon_0 \cdot S} \tag{12}$$

Theoretically the variation should be linear; but in a real system the parasitic capacitances that occur are not negligible. The CMOS NAND gate datasheet says the input capacitance is 5 pF, but the useful capacitance for disk type armatures with a 20 mm diameter and distance $d_0 = 1$ mm is initial $C_0 \approx 4.7$ pF, which is very close to the parasitic one. Also, we must add the capacitance of the mechanical system, which leads us to reconsider the relation (11) as described in relations (13) and (14):

$$f = \frac{1}{T} = \frac{1}{K_1 \cdot R \cdot \left(\frac{\epsilon_0 \cdot S}{d_0 - x} + C_p\right)} = \frac{1}{K_1 \cdot R \cdot \left(\frac{\epsilon_0 \cdot S + C_p(d_0 - x)}{d_0 - x}\right)} \tag{13}$$

Or

$$f = \frac{d_0}{K_1 \cdot R \cdot (\epsilon_0 \cdot S + C_p \cdot (d_0 - x))} - \frac{K_2}{K_1 \cdot R \cdot (\epsilon_0 \cdot S + C_p \cdot (d_0 - x))} \cdot F \quad (14)$$

We can notice that both (initial frequency) f_0 and K depend on x , but in a very non-linear way.

Using $R = 2 \text{ M}\Omega$ for measurements we noticed that the experimental curve has a parabolic shape that's hard to compensate.

The solution is electronic compensation of parasitic capacitance using a “neurodyne” circuit (achieving a negative capacitance).

3 The Negative Capacitance Circuit

The non-linearity of the response is the result of the parasitic capacitance which appears in parallel with the measuring transducer, respectively of the CMOS-NAND gate input capacitance.

We studied several frequency response linearization methods [3] and in the end decided to use the analysis based on frequency-domain approach for continuous time signals using LAPLACE transform.

The solution is given by the equivalent impedance at the input of the circuit below—Fig. 4. Where K is assimilated with one ipothetic amplifier factor to be determinated.

$$i = i_1 + i_2 \quad (15)$$

$$sC_e u = sC_1 u + sC_2(ku - u) \quad (16)$$

where

$$C_1 = C_2 \quad (17)$$

$$C_e = C_1(1 - k) \quad (18)$$

Relations (15) and (16) result from the Kirkoff and Laplace theorem; and with the assumption from relation (17) we obtain (18) where the notations is showed in the Fig. 4.

The amplifier must provide a zero phase shift on the entire frequency domain of the transducer and a high impedance input to collect the voltage in input point of V_A (shown the diagram in Fig. 2). These requirements can be achieved using a phase-equalized broadband amplifier with direct coupling, such as the type shown in Fig. 5.

Q_1 was chosen to be of type BFW11 that has (threshold voltage) $U_{th} = -6 \text{ V}$ and $I_{DSS} = 10 \text{ mA}$.

Fig. 4 The negative capacitance circuit using LAPLACE transform

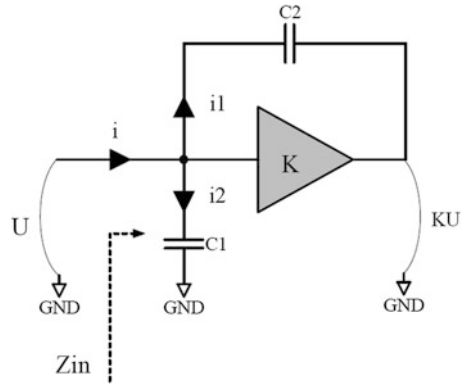
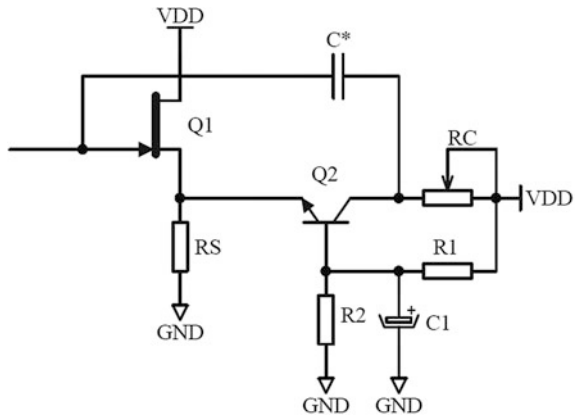


Fig. 5 The detailed schematic designed



Q_2 was chosen to be of type 2N918 that has (cut of frequency) $f_T = 900$ MHz to ensure a constant null amplifier and phase-shift band.

Q_1 works as a repeater on the high impedance generator and Q_2 serves as a base common amplifier. For $V_{DD} = 6$ V (see Fig. 5) we can determine the current drain i_{T1} with the following formula (19):

$$i_D = I_{Dss} \left(1 - \frac{U_{GS}}{U_{th}} \right)^2 \tag{19}$$

For $U_S = 3.5$ V it results that $U_{GS} = -3.5$ V thus $i_D = 3.5$ mA and we select $R_S = 1$ k Ω .

The R_1, R_2 are computed so that the current value will be around 1 mA and $U_{R2} = 3$ V (to polarize in Active Normal bias mode on Q_2).

Thus relation (20) can be written:

$$R_1 + R_2 = \frac{V_{DD}}{10^{-4}} \Omega \quad (20)$$

We choose $R_1 = 47 \text{ k}\Omega$ and $R_2 = 12 \text{ k}\Omega$.

C_1 is chosen in order to become a short-circuit in alternative mode and thus it results that $C_1 = 10 \text{ }\mu\text{F}$ ceramic with low ESR (equivalent series resistor):

$$A_{Q1} = \frac{g_{m1} \cdot R_s}{1 + g_{m1} \cdot R_s} \quad (21)$$

where in formula (21) A_{Q1} is amplification factor of Q_1 and g_{m1} is corresponding transconductance.

$$g_{m1} = \frac{\partial i_D}{\partial U_{GS}} = 2 \cdot I_{Dss} \cdot \left(1 - \frac{U_{GS}}{U_{th}} \right) = 2.5 \text{ mA/V} \quad (22)$$

From relations (21), (22) and (23) results the following amplification: $A_{T1} = 0.7$.

$$A_{Q2} \cong g_{m2} \cdot R_c \quad (23)$$

The global amplification (A) must be $A = A_{Q1} \cdot A_{Q2} > 1$, resulting in $A_{Q2} > 1$ and $A_{Q1} = 1.4$

We select R_c so that $R_c \times I_c \cong 1.5 \text{ V} \rightarrow R_c \cong 3 \text{ k}\Omega$. We choose a potentiometer of $2.2 \text{ k}\Omega$ for a fine tuning of the amplification (which is considered to be half a course). Then from relations (21), (22) and (23) the amplification factor of the Q_2 is $A_{Q2} \cong 120$.

$$g_{m2} \cong 40 \cdot I_c \quad (24)$$

If in relation (24) consider the temperature $T = 25 \text{ }^\circ\text{C}$ and $I_c = 2 \text{ mA}$ then $g_{m2} = 80 \text{ mA/V}$. We choose the collector resistance R_c such that $R_c I_c = 1.5 \text{ V}$. Thus result $R_c = 3 \text{ k}\Omega$ but we replace it with a potentiometer that will allow a fine tuning of amplification. If the Q_1 output impedance is $|Z_{OQ1}| < R_s = 1 \text{ k}\Omega$ then the Q_2 output impedance is determined with relation (25).

$$|Z_{inQ2}| \cong \frac{R_{be}}{\beta} = \frac{\beta}{\beta} = \frac{1}{g_m} = \frac{1}{80} \Omega \quad (25)$$

A current node division with a coupling factor occurs is determined with relation (26)

$$k = \frac{|Z_{inT2}|}{|Z_{inT2}| + |Z_{oT1}|} \quad (26)$$

Typically, the coefficient k result is determined with relation (27)

$$|Z_{oT1}| = R_s \cdot \frac{r_{ds}}{2R_s + r_{ds}} \cong 10 \Omega \rightarrow k = \frac{1}{15} \tag{27}$$

So, the global amplification will be relation (28):

$$A = A_{T1} \cdot A_{T2} \cdot k \cong 3 \tag{28}$$

The parasitic capacitance that must be compensated is of 6 pF, so we select C* such that C*(1 - k) = -6 pF. This results in C* = 3 pF. We choose C* = 2.2 pF to be under the critical values and k is set using a potentiometer.

4 Results

The experimental results reported here are obtained using the authors' research is one original solution of schematic diagram and is given in Fig. 6.

Taking into account the aforementioned, the relation (13) can be written as follows—relation (29):

$$f = \frac{1}{k_1 \cdot R \left[\frac{\epsilon_0 \cdot S}{d_0 - dx} + (C_p + C_e) \right]} = \frac{1}{k_1 \cdot R \left[\frac{\epsilon_0 \cdot S + (C_p + C_e) \cdot (d_0 - dx)}{d_0 - dx} \right]} \tag{29}$$

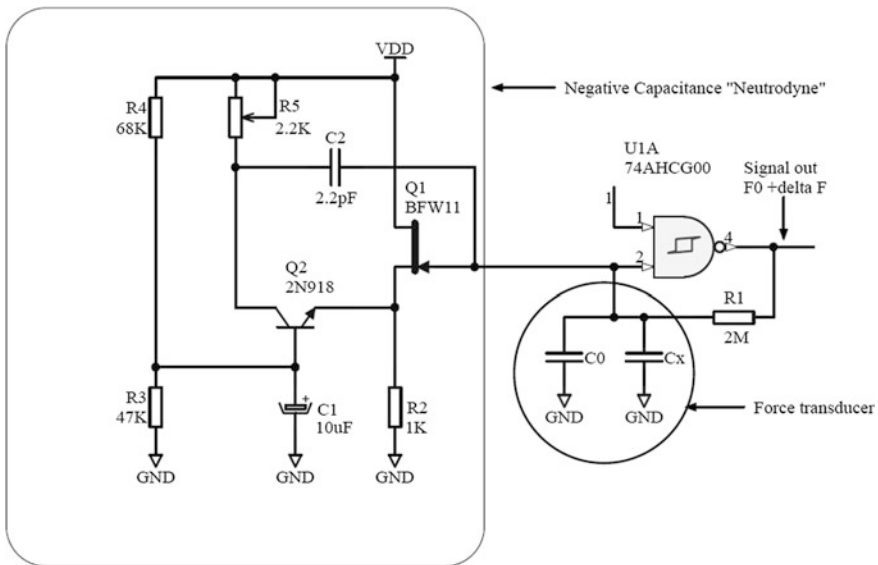


Fig. 6 The schematic used in experimental research

Which can be written as relation (30)

$$f = \frac{d_0}{k_1 \cdot R [\varepsilon_0 \cdot S + (C_p + C_e) \cdot (d_0 - dx)]} - \frac{k_2}{k_1 \cdot R \left[\frac{\varepsilon_0 S}{d_0 - dx} + (C_p + C_e) \cdot (d_0 - dx) \right]} \cdot F \tag{30}$$

where F is the applied force expressed in [N] and the experimental adjustment of C_e is made so that the global coefficient (K) is showed in relation (31):

$$K = \frac{k_2}{k_1 \cdot R \left[\frac{\varepsilon_0 S}{d_0 - dx} + (C_p + C_e) \cdot (d_0 - dx) \right]} \tag{31}$$

Measurements effectuated in the Metrology Laboratory of the Mechatronics Institute from Bucharest shows that the output frequency response becomes linear with force applied, as showed in Fig. 7.

In fact, if we write relation (32):

$$f_0 = \frac{d_0}{k_1 \cdot R [\varepsilon_0 S + (C_p + C_e) \cdot (d_0 - dx)]} \tag{32}$$

The above relation becomes—relation (33):

$$f = f_0 - K \cdot F \tag{33}$$

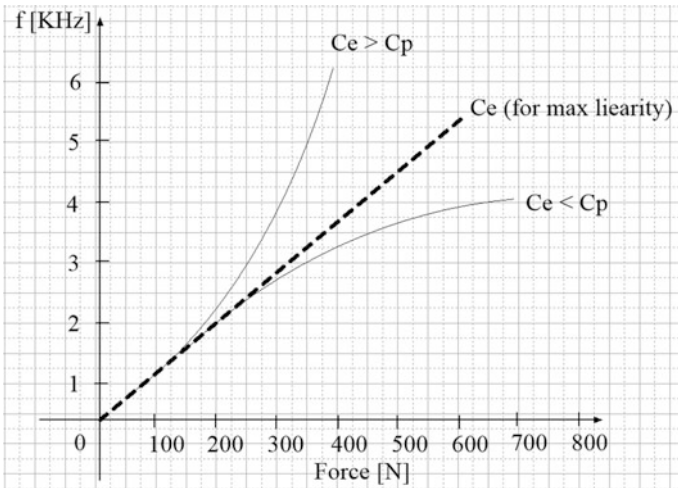


Fig. 7 The equivalent capacitance (C_e) and the linearity influence of K

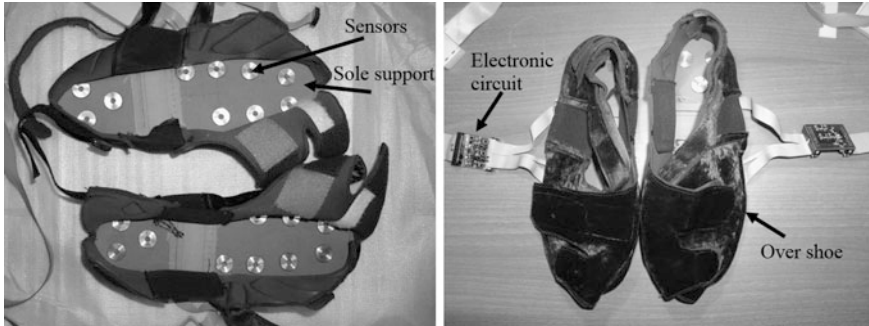


Fig. 8 The original over shoe system for ground reaction force measuring during walking

The above relation was validated experimentally and linearization of response was confirmed as the rule (30). For the used transducer, after the linearization with the method described above. The experimental results are based on the practical implementation of the scheme in Fig. 6 which yielded the following values of the constants (which correspond with theoretical calculations): $f_0 = 278$ kHz and $K = 695$ Hz/N.

The circuit presented works well in an application for measuring ground reaction forces during human walking. Figure 8 shows the soles sensors system used in the experiments, which is applied over shoes. The system has 10 sensors per sole but achieving sensors is presented by the author in another article [4].

5 Conclusions

We described a circuit for ensuring a negative capacitance. We presented an original design and implementation of a solution applied to mechatronic systems and gait analysis, which is also relevant for future MEMS and NEMS use cases., The idea of parasitic capacitance can be applied on a large class of electronic circuits that use amplifiers, oscillators and interfacing for capacitive circuits made by hybrid technology or by integrating into MEMS & NEMS technology [4, 5]. The circuits proposed in this work are characterized by low power consumption, high linearity response and low cost, which are important criteria for portable systems.

The authors are currently working on methods to improve stability and reproducibility in the long run, and on the miniaturization of mechatronic systems and in future even for MEMS and NEMS.

References

1. Gheorghe, G.I., Constantin, A., Dumitru, S.: *Microingineria Mems & Nems Inteligente*, Editura CEFIN, București, Romania, 2013, p. 38. ISBN: 978-606-8261-18-8
2. Pasca, S., Strungaru, R., Constantin, A., Capris, G.: New data acquisition and processing methods for resistive sensors in pedometric measurement systems. *Nonlinear Opt. Quantum Opt. Concepts Modern Opt.* **39**(2), 117–136 (2009). NLOQO 39.2-3
3. Strungaru, R., Pasca, S., Popescu, S.: *Electronica si Informatica Medicala Indrumar de Laborator pentru uzul studentilor – Bucuresti*, UPB 1992, p. 35
4. Anghel, V.C., Gheorghe, I.: Research on tactile sensors interface—review of theoretical and practical approach. *Appl. Mech. Mater.* **772** (2015). Submitted: 2015-02-02 © (2015). Trans Tech Publications, Switzerland Revised: 2015-02-11, pp. 299–304
5. Gardner, J.W., Varadan, V.K.: *Microsensors MEMS and smart devices*, England 2002, British Library Cataloguing in Publication Data, pp. 105–106. ISBN: 0-471-86109-X
6. Gheorghe, G.I., Istriteanu, S.: Technological and cross-border mixture value chain of science and engineering of multi-integrative mechatronics-integrionics-adaptronics with use in the construction of intelligent systems/micro-nano-systems. *Int. J. Res. Eng. Technol.—IJRET* (2013). ISSN (Print): 2321–7308

Behavior of the Elastomers Used in Prehension Systems for Small Cylindrical Objects

Vlad Cârlescu, Mihai Adrian Rusu, Gheorghe Prisăcaru, Emanuel Miron, José Machado and Dumitru Olaru

Abstract To use the elastomers as a interfacial surface in the prehension systems, the authors experimentally determined the elastic deformation and sliding friction of a plane elastomer sample in contact with small steel roller for normal loads up to maximum 9 N and linear speed of 0.1 mm/s. The experiments were realized on a Tribometer CETR UMT 2, by using two procedures: firstly was determined the Young's modulus of the elastomer by indentation with a steel roller with normal loads between 1 and 9 N and secondly was determined the friction forces in sliding of the steel roller on elastomer sample with normal loads between 1 and 5 N. On contact surfaces was experimentally determined the total friction force including both elastic deformation force and sliding force. Also, an analytical model for friction force has been developed.

Keywords Friction · Elastomers · Sliding motion · Adherence · Friction coefficient

V. Cârlescu · M.A. Rusu · G. Prisăcaru · E. Miron · D. Olaru (✉)
Department of Mechanical Engineering, Mechatronics and Robotics,
The „Gheorghe Asachi” Technical University of Iasi, Iasi, Romania
e-mail: dolaru@mail.tuiasi.ro

V. Cârlescu
e-mail: carlescu.vlad@yahoo.com

M.A. Rusu
e-mail: mihaiadrianrusu@yahoo.com

G. Prisăcaru
e-mail: prisacaru_ghe2004@yahoo.com

E. Miron
e-mail: miron@dem.uminho.pt

J. Machado
Department of Mechanical Engineering, University of Minho, Braga, Portugal
e-mail: jmachado@dem.uminho.pt

1 Introduction

In a lot of micro actuators and micro prehension devices the various elastomers are usually used as surface layers. In the micro prehension systems manipulating small objects with small prehension loads, the elastomers layers with high adherence it is necessary to be used. The finger prehension is based both on the adhesive forces with the objects and on the tactile skin sensors to evaluate the slip tendency of the object. The tendency to develop prehension systems based on the human hand manipulation generated new and complex devices [1]. To simulate the prehension of the small cylindrical objects with two fingers, Barnea et al. [2, 3] investigated the friction in sliding motion between the small cylindrical surfaces and both human fingers and fingers realized by elastomers for normal loads between 1 and 5 N. Depending on the materials of cylindrical objects and the normal load Barnea et al. [2, 3] evidenced that the friction force is dominated both by adhesion and sliding. Original “butterfly” diagrams have been obtained as a result of the successive elastic deformations, adhesion, sliding and relaxations of the finger skin and elastomer in the contact with the cylindrical objects during the experimental tests. The experiments realized by Kwiatkowska et al. [4] evidenced the skin deformation behaviour in relation to the friction and experimentally determined the Young’s modulus of the human skin by using the ball-skin sliding contact. Modifi and Prakash [5] experimentally determined the friction coefficient between a steel cylinder in rotational motion and plate elastomer specimens having Young’s modulus of about 10 MPa. The values of friction coefficient obtained for very low speed (0.2 mm/s) varied between 0.25 and 0.5, depending of the elastomer type. In the last period Rusu et al. [6, 7] experimentally determined the friction behaviour of some polyurethane using the sliding contact between a steel roller and polyurethane plane sample. Also, by indentation of the polyurethane with a steel roller obtained the Young’s modulus of some types of polyurethane realized by “Petru Poni” Macromolecular Research Institute from Iasi, Romania.

To use elastomers as surface layers in the prehension devices, the authors investigated experimentally the elastic deformation, friction and adherence of the plane elastomer specimen in contact with a steel small roller. The indentation experiences were realized for the normal loads between 1 and 9 N and the friction experiments were realized with normal loads between 1 and 5 N and sliding speed of 0.1 mm/s. An analytical method to validate the experimental values of the friction forces has been developed. The objective of the paper is to present the methodology and the most important results.

2 Experimental Procedure and Equipments

The experiments were realized by using the Tribometer CETR UMT 2 from the Laboratory of Tribology as is presented in Fig. 1. The cylindrical steel roller are fixed on the top of the pin and the pin is mounted in the sensor of the Tribometer able to indicate the normal force F_z and friction force F_x . On the linear table of the Tribometer was mounted the elastomer sample and the roller is put in contact with the sample as is presented in Fig. 1. The sample realize linear displacement on a distance of 8 mm in one direction and in opposite direction. The friction force between cylindrical object and elastomer for various normal loads are registered in the computer of the Tribometer. The tests were realized by using steel roller having diameter of 7 mm and surface roughness $R_a = 0.06 \mu\text{m}$.

Two types of tests were realized: (i) indentation tests to determine the Young's modulus for compression of the elastomer and (ii) friction tests to determine both elastic deformation and sliding friction of the elastomer in contact with the roller. The sliding tests were realized for linear speed of 0.1 mm/s and normal force F_z varied between 1 and 5 N. All the experiments were realized in dry conditions. The tests were realized with elastomer sample obtained from Polydimethylsiloxane- α,ω -diol (PDMS) as matrix with 20 % oxide hematite (Fe_2O_3) having the chemical structure presented in [8]. The dimensions of the sample were: 30 mm length, 10 mm wide and 2 mm thickness.

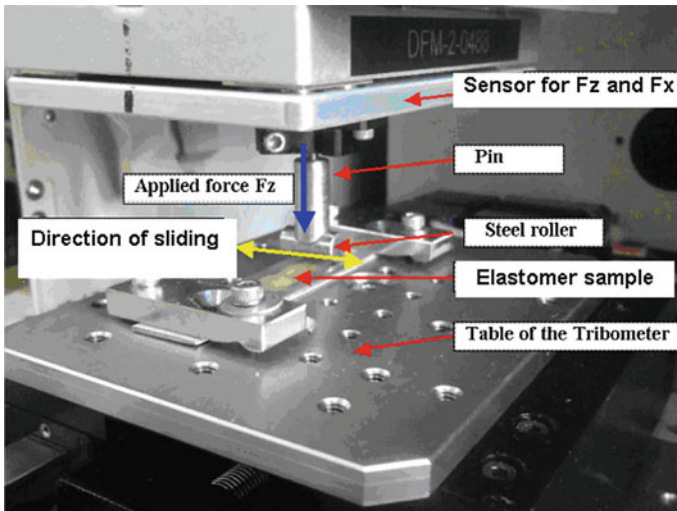


Fig. 1 The Tribometer CETR UMT 2 with the cylindrical object attached on the pin

3 Determination of the Young's Modulus for Elastomer

In the contact problems of the elastomers the Young's modulus have different values like in traction problems. To determine the variation of the Young's modulus as function of applied force the authors proposed the experimental methodology validated for some types of polyurethane by Rusu et al. [7]. The methodology consists in following steps: In the first step was realized the indentation of the elastomer sample with the steel roller and obtained the dependence curve between elastic deformation of the elastomer δ and the applied force F_z .

In the second step, the experimental values for elastic deformation δ were approximated in the vicinity of the various applied forces F_z (1, 2, 3 to 9 N) with theoretical Hertzian's deformation given by the equation for elastic deformation δ in a contact between a roller and a plan surface [9]:

$$\delta = 0.39 \cdot \left[\frac{4 \cdot (1 - \nu_1^2)}{E_1} + \frac{4 \cdot (1 - \nu_2^2)}{E_2} \right]^{0.90} \cdot \frac{F_z^{0.90}}{L^{0.80}} \quad (1)$$

In Eq. (1) E_1 and E_2 are Young's modulus for steel cylinder and elastomer sample, respectively, expressed in Pa, ν_1 and ν_2 are the Poisson's coefficients for steel and elastomer, respectively, F_z is normal applied force expressed in N and L is the wide of the elastomer, expressed in m. By imposing in the Eq. (1) the value of the elastic deformation δ obtained from the experiment for a given applied force F_z and imposing for the Poisson's coefficient of the elastomer a value of 0.5 [3], we obtained the Young's modulus E_2 of the elastomer in the vicinity of the given force F_z . For steel cylinder $E_1 = 210$ GPa and $\nu_1 = 0.3$.

The indentation experiments were realized with Tribometer CETR UMT-2 as is presented in Fig. 2. The applied force F_z varied between zero and 9 N. In Fig. 2 is presented the deformation curve of the PDMS elastomer.

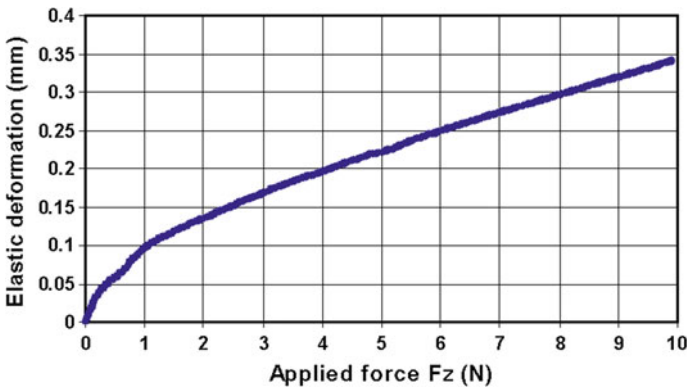


Fig. 2 The experimental indentation diagram for the elastomer

The numerical values for F_z and elastic deformation of the elastomer δ obtained from the Tribometer soft were used to determine the Young's modulus of the elastomer in the vicinity of applied forces $F_z = 1, 2, 3, 4, 5, 6, 7, 8$ and 9 N. In Fig. 3 is presented the curve fitted of the values of δ in the vicinity of the force $F_z = 3$ N. Similar curve-fitting processes were realized in the vicinity of all above-mentioned applied forces F_z .

For the applied forces F_z between 1 and 9 N the Young's modulus of the elastomer have values between 2 and 4.5 MPa, as it can be see in Fig. 4.

Following empirical equation between Young's modulus of the elastomer E_2 and applied force F_z has been obtained (red curve in Fig. 4):

$$E_2(F_z) = 1.97 \cdot F_z^{0.37} \text{ MPa} \tag{2}$$

where F_z is expressed in Newtons.

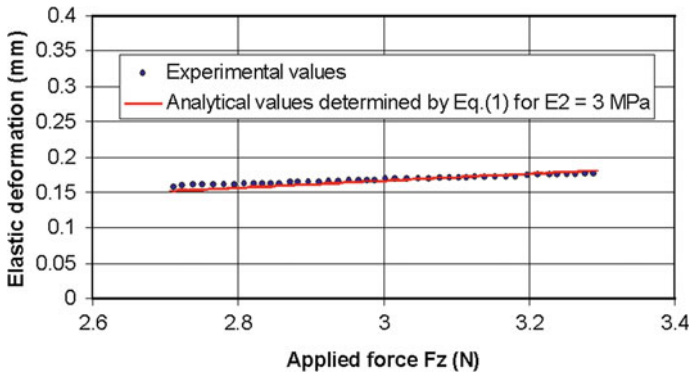


Fig. 3 The curve-fitting of the experimental values with Eq. (1) in the vicinity of the applied force $F_z = 3$ N

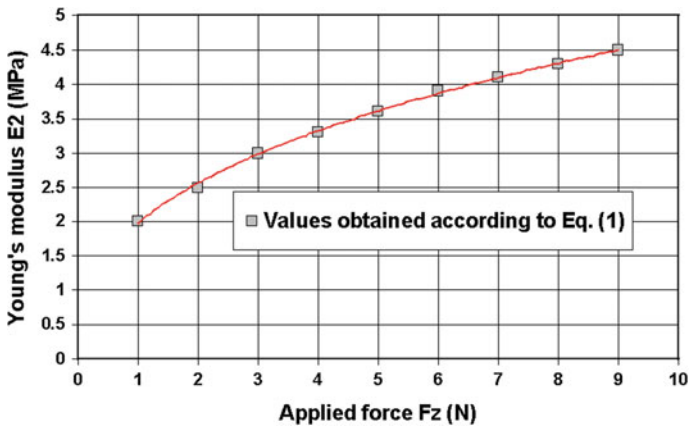


Fig. 4 The variation of the Young's modulus of the elastomer with applied force F_z

4 Experimental Results on Friction Behavior of Elastomer

4.1 Friction Coefficients

The experimental results are presented as variations of the friction coefficient COF in function of the displacement of the sample on the distance Y for a number of strokes, depending of the linear speed. In Fig. 5 are presented typical variations of the friction coefficient as function of linear distance Y for linear speed of 0.1 mm/s and for applied force $F_z = 1$ and 5 N. Following phases have been identified in the friction process. The point O represents the start of the displacement in positive direction.

From the point O to the point A it can be observed the adhesion between roller and elastomer with a continuum increasing of the friction coefficient COF caused by the elastic deformation of the elastomer. From the point A to the end of the stroke (point B) the roller sliding on the elastomer with a quasi-constant friction coefficient, having various values as function of applied load F_z . At the end of stroke, in the point B the direction of the displacement is changed and the elastomer is under a relaxation process from point B to point C. A new elastic deformation of

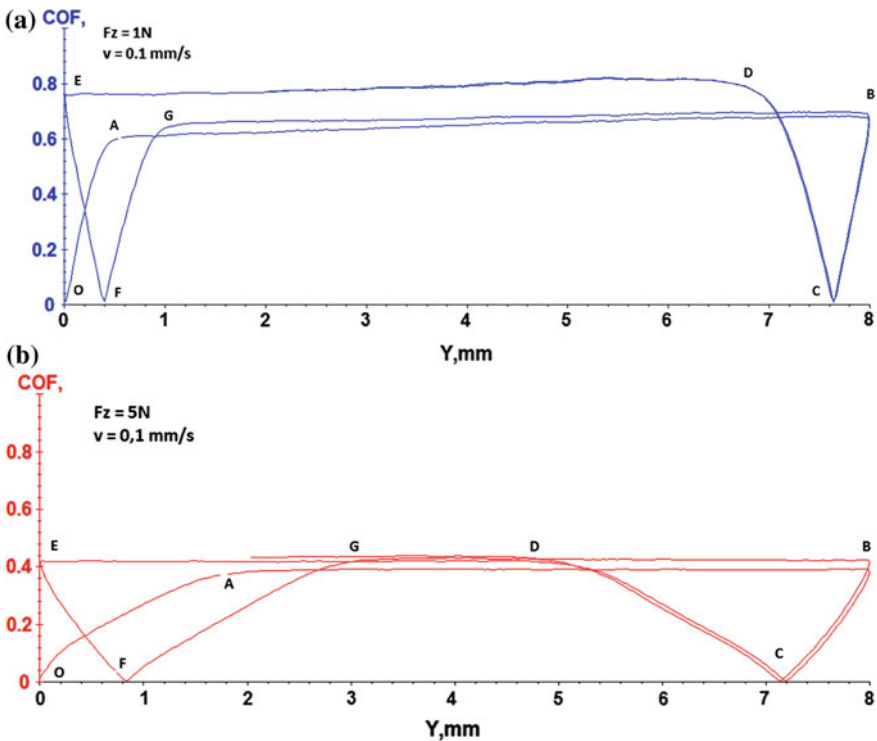


Fig. 5 Variations of the friction coefficient with applied normal force F_z

the elastomer starts in the point C during to the point D. Follows a sliding process from point D to the end of the negative stroke in point E. From the point E the direction of the displacement is changed, the elastomer realize a relaxation process to the point F and the alternative processes including elastic deformation, sliding and elastic relaxation have been repeated. By increasing of the applied normal force F_z two processes can be observed: (i) a decreasing of the friction coefficient; (ii) the decreasing of the sliding zones and increasing of the elastic deformation zones.

Based on the experimental values of the friction coefficient, an empirical equation between friction coefficient COF and applied normal load F_z has been obtained:

$$COF(F_z) = 0.7 \cdot F_z^{-0.36} \tag{3}$$

The valability of the Eq. (3) corresponds to the tests conditions: sliding speed of 0.1 mm/s and applied normal load F_z between 1 and 5 N.

4.2 Friction Forces and Dissipated Energy

The variations of the friction force F_x developed between roller and elastomer sample in the displacement on the stroke Y , in positive and negative directions are presented in the Fig. 6 and Fig. 7 for applied normal force $F_z = 1$ N and $F_z = 5$ N, respectively.

The friction force F_x both in positive and in negative direction have three successive zones: (i) an increasing zone from zero to a constant value caused by elastic deformation of the elastomer; (ii) a zone with constant value corresponds to the sliding process between roller and elastomer; (iii) an elastic relaxation zone with decreasing of the friction force from the constant value to zero.

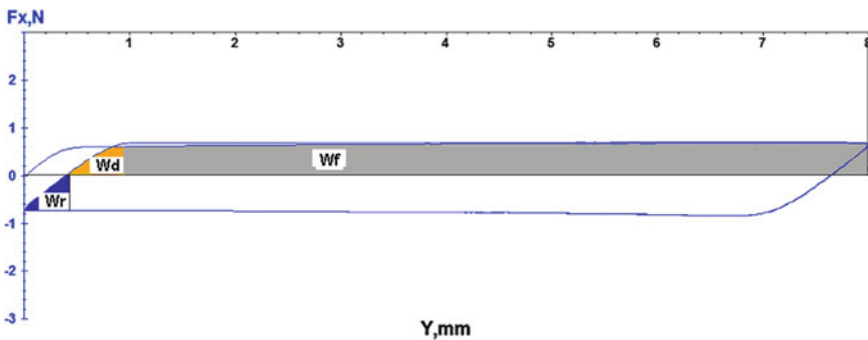


Fig. 6 Variations of the tangential forces F_x along of the stroke Y in positive and negative direction for $F_z = 1$ N and for linear speed of 0.1 mm/s

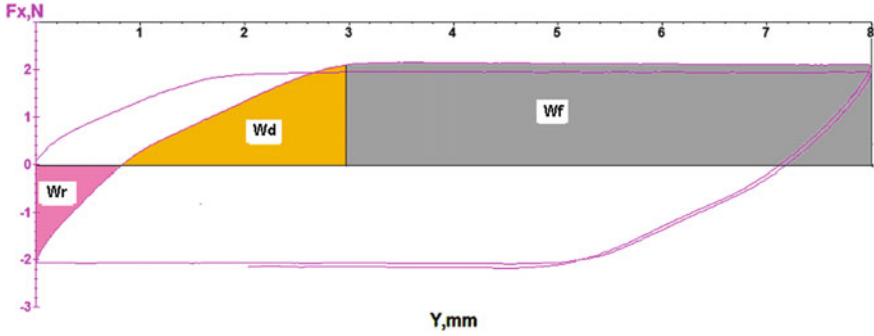


Fig. 7 Variations of the tangential forces F_x along of the stroke Y in positive and negative direction for $F_z = 5 \text{ N}$ and for linear speed of 0.1 mm/s

The energy dissipated in each of the three zones W can be estimated from the F_x - Y diagrams according to the following general equation:

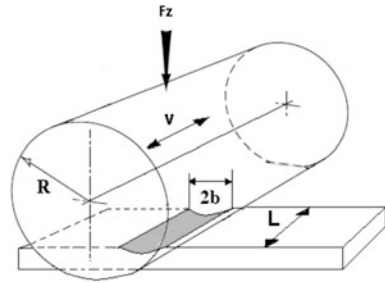
$$W = \int_{y_1}^{y_2} F_x \cdot dy \tag{4}$$

where y_1 and y_2 are the limits of the zones. In Figs. 6 and 7 the dissipated energy for every zone is presented as area of surface between OY axis and F_x - Y diagram. So, W_d is the energy dissipated by elastic deformation, W_f is the energy dissipated by friction process and W_r is the elastic relaxation energy. The energy dissipated by friction is depending of the friction coefficient and the length of the stroke. In our experiments this energy is dominant. In prehension process of the small cylindrical objects to avoid the sliding of the cylinder, it is important to evaluate the difference between elastic deformation energy and relaxation energy. So, for tested elastomer, when the applied normal force $F_z = 1 \text{ N}$ (Fig. 6), is not important difference between elastic deformation energy and elastic relaxation energy ($W_d \approx W_r$). It can be neglected the energy lost by internal friction in the elastomer. When the applied normal force increases to $F_z = 5 \text{ N}$ (Fig. 7), important difference between elastic deformation energy W_d and elastic relaxation energy W_r can be observed. A simplified estimation evidenced that $W_d \approx 2 \cdot W_r$, so about 50 % from the elastic deformation is lost by internal friction in the elastomer.

5 Analytical Model for Friction Force

The contact between a steel roller and the elastomer sample is presented in Fig. 8. By considering the viability of the Hertz equation, the half width $b(F_z)$ of the contact between roller and elastomer as function of F_z , can be expressed by equation [9]:

Fig. 8 The surface contact between the roller and elastomer sample



$$b(Fz) = 2 \cdot \sqrt{\frac{Fz \cdot R}{\pi \cdot L} \cdot \left[\frac{1 - \nu_1^2}{E_1} + \frac{1 - \nu_2^2}{E_2(Fz)} \right]} \tag{5}$$

where R is radius of the roller and $E_2(Fz)$ is given by Eq. (3).

The real contact area between the cylinder and the elastomer sample are presented in Fig. 8 as a slide from a circular surface having a length L and a circular segment lc as wide. The circular segment $lc(Fz)$ depending of the applied force Fz can be determined by equation:

$$lc(Fz) = 2 \cdot R \cdot \arcsin(b(Fz)/R) \tag{6}$$

On the contact surface the Hertzian pressure as function of applied normal force Fz and coordinate position x is given by following equation:

$$p(Fz, x) = p_{\max}(Fz) \cdot \left[1 - \left(\frac{2 \cdot x}{lc(Fz)} \right)^2 \right]^{0.5} \tag{7}$$

where x is the coordinate of a point in the interval between $-lc/2$ and $+lc/2$ and $p_{\max}(Fz)$ is the maximum contact pressure in the center of the contact surface having following relation [9]:

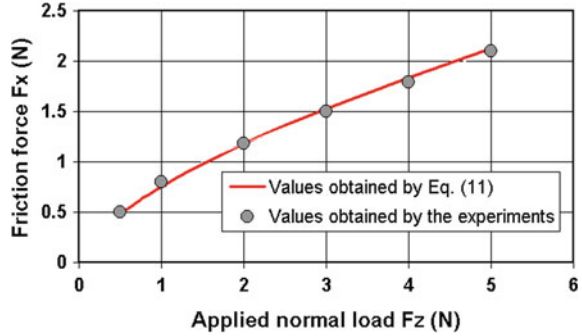
$$p_{\max}(Fz) = \frac{2 \cdot Fz}{\pi \cdot b(Fz) \cdot L} \tag{8}$$

For every point on the contact area, in the sliding process, a tangential shear stress $\tau(x)$ is developed in the direction of the motion and can be estimated by equation:

$$\tau(x) = \mu \cdot p(x) \tag{9}$$

where μ is the local friction coefficient. Because the friction coefficient is depending of the applied normal load Fz according to Eq. (3) and the pressure has a parabolic

Fig. 9 Analytical and experimental variation of the friction force F_x as function of the applied normal force F_z



variation given by Eq. (7) we propose for the local friction coefficient following equation:

$$\mu(F_z, x) = 0.7 \cdot F_z^{-0.36} \cdot \left\{ \left[1 - \left(\frac{2 \cdot x}{lc(F_z)} \right)^2 \right]^{0.5} \right\}^{-0.36} \quad (10)$$

The total friction force F_x as function of applied normal load F_z is obtained by integration of the shear stresses on all contact surfaces. According to the above-mentioned equations, the total friction force has following analytical equation:

$$F_x(F_z) = \int_{-lc(F_z)/2}^{lc(F_z)/2} p_{\max}(F_z) \cdot L \cdot \mu(F_z, x) \cdot \left[1 - \left(\frac{2x}{lc} \right)^2 \right]^{0.5} dx \quad (11)$$

Equation (11) has been solved and the variation of the friction force F_x with applied normal force F_z is presented in Fig. 9. Also, in Fig. 9 are presented the average values of the friction forces F_x obtained by the experimental tests.

6 Conclusions

To use the elastomer PDMS as plane surface layers for prehension devices of the small cylindrical objects following experiments and results were realized and obtained by the authors:

Indentation of the elastomer plane sample with a steel cylinder and approximate the Young’s modulus by using the Hertzian deformation model in the vicinity of each applied normal forces.

For indentation forces between 1 and 9 N the Young’s modulus in compression for PDMS elastomer varies between 2 and 4.5 MPa.

An empirical equation for variation of the elastomer Young's modulus and applied normal force has been obtained.

The friction behaviour of the PDMS elastomer in contact with a steel roller has been experimentally determined for a linear speed of 0.1 mm/s and applied normal forces between 1 and 5 N.

The three zones has been observed in the oscillating sliding process of the roller over the elastomer: an adhesion zone with elastic deformation of the elastomer in positive direction, a sliding zone with a constant friction coefficient and an elastic relaxation zone when the movement change the direction.

An empirical equation for the variation of the friction coefficient with applied normal force has been developed and values of friction coefficient between 0.7 and 0.4 have been obtained when the applied force increases from 1 to 5 N.

Based on the friction forces diagrams the energy dissipated in elastic deformation and relaxation of the elastomer and in sliding process have been determined.

Was evidenced that by increasing of the applied normal force increases the lost energy by internal friction in the elastomer. So, if for normal force of 1 N is not differences between elastic deformation and elastic relaxation energy, for normal force of 5 N about 50 % of deformation energy is lost in elastomer internal friction.

Based on the empirical equations for Young's modulus of elastomer and friction coefficient, a theoretical equation for friction force in contact between roller and elastomer has been developed and good correlation with the experiments has been obtained.

References

1. Odhner, L.U., et al.: A compliant, underactuated hand for robust manipulation. *Int. Robot. Res.* **33**(5), 736–752 (2014)
2. Barnea, A., Oprisan, C., Oлару, D.: Prehension of the small cylindrical objects by the human fingers. Friction and adherence processes. In: *Applied Mechanics and Materials—Advanced Concepts in Mechanical Engineering I*, vol. 658, pp. 721–727 (2014)
3. Barnea, A., Rusu, M.A., Oprisan, C., Carlescu, V., Prisacaru, Gh., Oлару, D.: Friction between cylindrical objects and prehension elastomer fingers. *Rom. Rev. Precis. Mech. Opt. Mechatron.* **48**, 219–223 (2015)
4. Kwiatkowska, M., Franklin, S., Hendriks, C., Kwiatkowski, K.: Friction and deformation behaviour of human skin. *Wear* **267**, 1264–1273 (2009)
5. Mofidi, M., Prakash, B.: Frictional behaviour of some sealing elastomers in lubricated sliding conditions. In: *Proceedings of NORDTRIB Conference* (2012)
6. Rusu, M.A., Ionita, D., Cârlescu, V., Prisacaru, Gh., Oлару, D.: Characterization of some types of polymers by friction behaviour. *Rom. Rev. Precis. Mech. Opt. Mechatron.* **48**, 110–116 (2015)
7. Rusu, M. A., Ioniță, D., Benchea, M., Cârlescu, V., Oлару, D.: Analytical model for friction force between a steel roller and a plane polymer sample in sliding motion. In: *Proceedings of 6th International Conference COMEC, Braşov* (2015)
8. Marcu, M., Simionescu, M., Cazacu, M., Lazarescu, S., Ibanescu, C.: Obtaining poly (dimethylsiloxane) α,ω -diols using the heterogeneous catalysis. The optimization of the reaction conditions. *Iran. J. Polym. Sci.* **3**, 95–104 (1994)
9. Stachowiak, G.W., Batchelor, A.W.: *Engineering Tribology*. Butterworth Heinemann (2013)

Part VIII
Manufacturing Systems and Scheduling

Collaborative Portal for Supporting Manufacturing Resources Selection in a Global Market

Vaibhav Shah, Maria Leonilde Rocha Varela and Goran D. Putnik

Abstract In the last decades the manufacturing industry has shifted from largely single location centralized manufacturing towards networked manufacturing spread over multiple sites. Companies have either established new production sites in multiple locations or established strategic partnerships to respond to market changes more rapidly as well as for more efficient and effective sharing of resources, through the so-called integrated manufacturing systems environments. In this context, proper collaboration among different locations and/or partners becomes more critical. Thus, development of appropriate integrated tools, to enable clients or network partners to accurately select appropriate manufacturing resource from the widened global market context, becomes emergent. Therefore, this work is aimed at providing a contribution to maximize overall benefit of businesses, in the context of a networked scenario, and subject to a set of configurations and restrictions on part of the manufacturing resources providers and searchers. Thus, the authors propose a collaborative portal to enable to perform a better manufacturing resources selection, based on technologies integration for supporting accurate orders processing.

Keywords Collaborative portal · Ubiquitous manufacturing system · Global market · Resources selection

V. Shah · M.L.R. Varela (✉) · G.D. Putnik
ALGORITMI Research Centre, University of Minho, Guimarães, Portugal
e-mail: leonilde@dps.uminho.pt

V. Shah
e-mail: vaibhav.shah@dps.uminho.pt

G.D. Putnik
e-mail: putnikgd@dps.uminho.pt

M.L.R. Varela · G.D. Putnik
Department of Production and Systems, University of Minho, Guimarães, Portugal

1 Introduction

Collaborative work environments have rapidly emerged recently, from various contributions to ensure more efficient decision-making in manufacturing systems management, to fulfil functional and other requirements of globally spread companies. The present work proposes a web-based Portal for supporting collaborative manufacturing resources selection within a global market scenario in the context of a Ubiquitous Manufacturing System (UMS). Hence, an interactive portal, with a peer-to-peer (P2P) network based architecture, using web services and other Internet based technology offering support for resources selection for orders processing is proposed. The collaboration functionality is supported by several tools provided for handling such conditions. The purpose of the presented work is to describe the proposed collaborative portal to enable full potential of the network-based manufacturing systems in order to facilitate information sharing as well as collaboration among globally distributed users [1].

The web portal underlying this work includes a set of functionalities throughout several peers in the network, which holds manufacturing resources for processing different kind of orders. The integrated tools enable to more easily identify manufacturing resources that are available for processing orders, to be delivered according to a set of specified requirements. These requirements include due dates satisfaction, along with other more specific ones, namely related to processing and quality functional requirements, as well as conditions imposed on logistics, costs and payments processing, while considering other restrictions imposed by producers, related to their manufacturing resources, namely regarding resources availability and corresponding time restrictions and consequent due dates negotiation.

The rest of this paper is organized as follows. In Sect. 2 a brief contextualization about a ubiquitous manufacturing system is provided. Section 3 refers to collaborative manufacturing resources selection within the UMS context. In Sect. 4, a portal for technologies integration is given, as well as the underlying data model for manufacturing resources selection and web-based communication data exchange. Moreover, the web-based interface for supporting the resources selection problem solving is also illustrated, through a use-case. Finally, in Sect. 5, some more discussion and concluding remarks are given.

2 Ubiquitous Manufacturing System

Ubiquitous Manufacturing System (UMS), at a higher level, can be seen as a platform to connect people, knowledge, processes, decision-making and data (information). In this context, it is our conviction that through a UMS, innovation plays a fundamental role for Virtual Enterprise (VE) integration. The UMS environment's characteristic is that it is possible to enable a system of distributed,

manufacturing sub-systems or cells, integrating the corresponding technologies for management support, which work in a collaborative interconnected way, under the supervision of a market-of-resources (MR) manager, who controls the entire UMS, which includes connections among clients, that may or may not belong to the Meta-Organization (MO) environment. Here, brokering services play an important role too, to accomplish an integrated real-time collaborative management, in the true sense, of the whole networked/distributed manufacturing environment [2]. Here a decision-supported manufacturing resources selection process is an important functionality.

Figure 1 shows an outline of UMS network environment. Here, it's important to enable co-innovation rather than focusing on individual innovation. This kind of innovation can be enabled by technology integration, which can also be seen as a

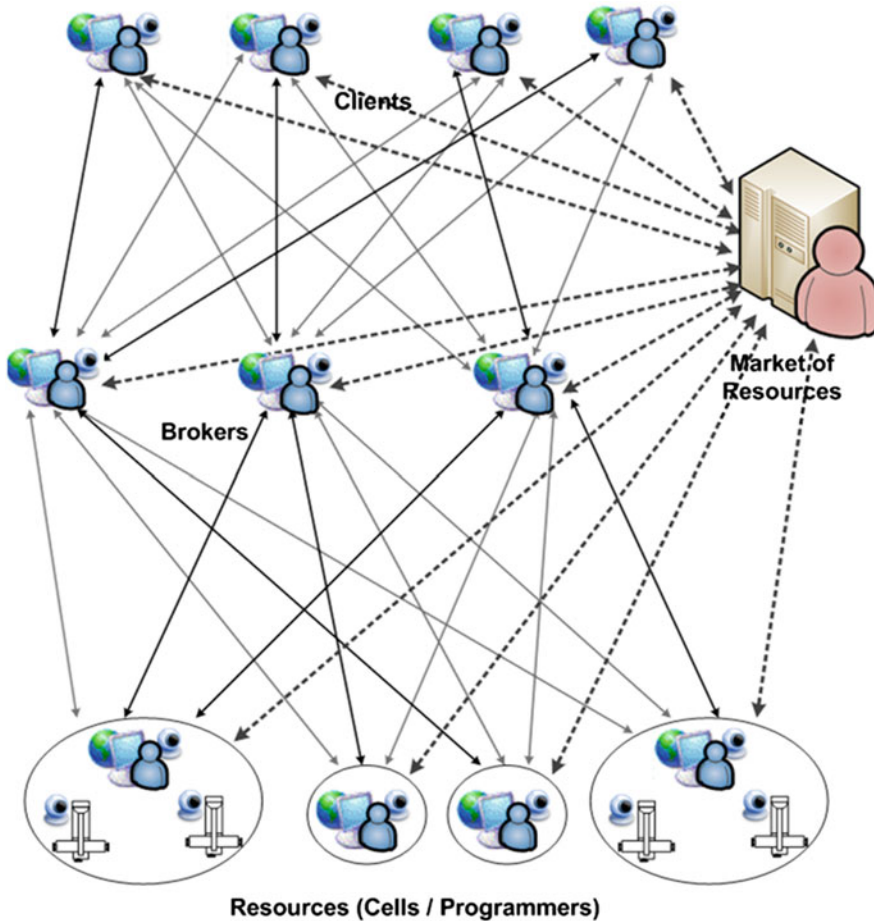


Fig. 1 Meta-organizational environment of a ubiquitous manufacturing system [3, 4]

commodity. Hence giving a real shape to an abstract concept of UMS and with the presented work it is intended to contribute in this direction, by enabling technologies integration to support selection of resources for collaborative manufacturing in a global MR [2].

3 Collaborative Resources Selection in a UMS

Manufacturing resources selection (MRS) issues are strategic in nowadays innovative enterprises that are expected to provide products under an unpredictably changing market. Considering a distributed manufacturing environment, enterprises have to form alliances with suppliers, other business partners and customers, and then, one enterprise often takes care of only a part of the entire production process [5] Because of this, problems related to MRS should be considered decentralized decision processes [2] In other words, to support the decentralized MRS, an information infrastructure is necessary, namely for coordination, collaboration as well as communication among different partners or enterprises [6] Manufacturing resources selection is a widely investigated topic along the past two-three decades and currently, in the context of VE and Global Markets it plays a critical role as it enables to fulfil the requirements of this type of network based manufacturing environments [7, 8].

A critical success factor to consider while implementing Collaborative Manufacturing Resources Selection (CMRS) is the system's possibility to deal with different constraints, regarding each of the manufacturing processes, since different characteristics of a manufacturing system result through a set of imposed constraints, throughout the concerned manufacturing processes. Though it's not entirely possible to classify and consider all different constraints, some major categories can be defined and integrated through a rather simple schema, and some important ones of these are briefly described below (as given in [2]).

Precedence Constraint: These constraints are well-known in MRS and scheduling problems. In forward scheduling, a job can be started only after all of its predecessor jobs are completed. On the other hand, in backward scheduling, a job must be completed before all of its successor jobs are started. All jobs have events such as start and completion. Additionally, there are other independent events such as products shipping, arrival of materials or parts, change or beginning of production shifts and so on. Any of these events can have a precedence constraint also. Moreover, precedence constraints have several variations according to manufacturing processes characteristics, e.g., within some scenarios a precedence constraint with min. or max. interval time may occur. Another case may be, for instance, that two jobs could be overlapped for a particular timeframe, due to continuous manufacturing processes. This can also be included in a certain category of types of precedence constraints.

Switching Constraint: If two jobs are executed over the same resource, then they have an exclusive relation, i.e. one job should be started after another is

finished. Hence, the two cannot be executed at the same time. The proposed model includes this constraint—which may have many variations too. Generally, practical MRS and scheduling problems deal with switching constraints in a context, in which constraints are predefined according some engineering reasons. For instance, one job can be started after some time-period, after the end of another one, or a case where one job should be begun just after another is finished. Another practical case of use of this constraint happens due to changing interval setup-time, depending on the combination characteristics of two jobs.

Stock Constraint: Stock level of an item/component can change during the scheduling time period. Every type of items, such as finished products, work-in-progress inventory, components and raw materials may have some stock. Hence, stock constraints can be defined where the stock-level should be more than a min. level value and less than a max. level value. Normally, safety stock levels are defined just as max. stock levels, which may be related to space constraints of buffers and/or to the manufacturing politics used, such as just-in-time (JIT).

Loading Constraint: These constraints deal with the items' levels. These kinds of constraints concern about a usage level of charged resources, during the planning horizon. Thus, the level of jobs related resource usage allocated to that resource at that time should be within a predefined range between a min. and a max level. A maximum level is defined as availability of the resource performance in this type of constraint. The allowable range of the constraint may vary from 0 to 1, if the target resource is occupied, and the level of usage may take either 0 or 1. The maximum and the minimum levels of each loading constraint are static sometimes, but variable usually, during the planning period, for example, due to a changing number of workers on part-time regime.

State Constraint: They restrict the execution of jobs or events in a general form. This type of constraints is represented using pre-conditions and post-conditions, for execution of particular events or jobs. Post-conditions perform as actions of events or jobs. These conditions are defined through primitives attributes and some mathematical expressions. These primitives attributes are altered during the planning timeline, by the execution of the events or jobs arising from allocation of resource and schedule plan.

Figure 2 shows an illustrative interface for supporting businesses or clients to select appropriate resources for processing orders according to some imposed constraints, from a list of resources available through a P2P network of globally distributed resources.

The order related information, as illustrated in Fig. 2, has to be automatically generated, according to the information provided by each business, in real-time and with dynamically updated information regarding each production plan obtained through each business methods and approaches for Collaborative Manufacturing Scheduling Resources Selection and Scheduling (CMRSS). Therefore, the framework put forward in this paper, for supporting CMRSS problems resolution aims at providing an easy integration of legacy systems existing on each business, belonging to the P2P network, offering the possibility of different technology and

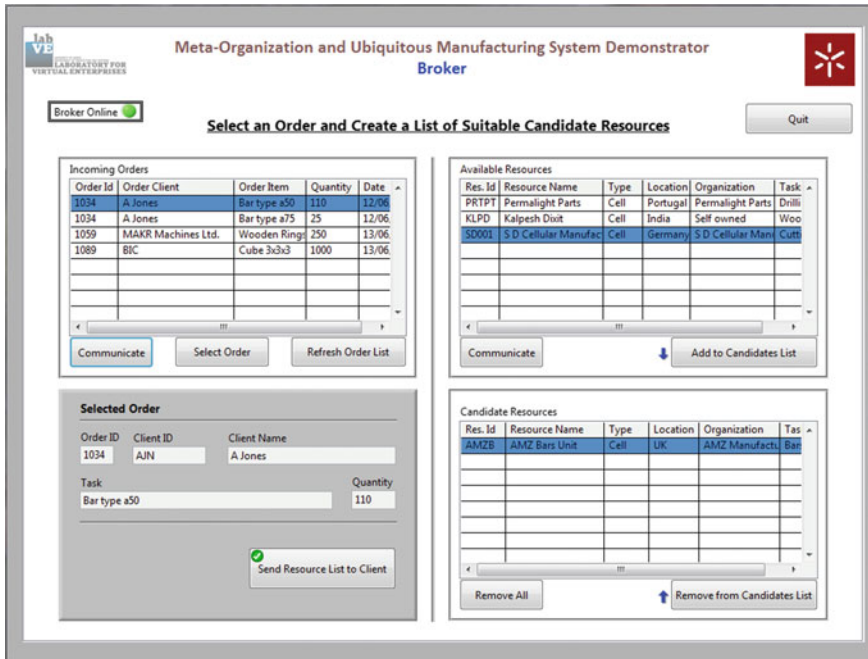


Fig. 2 Interface illustration for supporting resources selection

back-end systems integration, in order to facilitate the corresponding decision-making processes.

Moreover, the collaborative approach proposed includes a brokering service for enabling further refinement and adjustments to the ordering plans, based on human interactions, which are enhanced through diverse kinds of media-based communications put available through the underlying portal that is described next.

4 Portal for Technologies Integration

Collaborative manufacturing resources selection and scheduling (CMRSS), in terms of optimal plans, means finding the best solution absolutely, for a problem. But practical CMRSS problems, as encountered in real world, normally do not reach such an optimal solution, since most of these deal with a lot of constraints, as described above, which only enables to arrive at some feasible solutions. Furthermore, usually it is hard to see an explicit relationship between a desired solution and its appropriate solving action. Hence, different optimization procedures can also be used, to try to find a better solution.

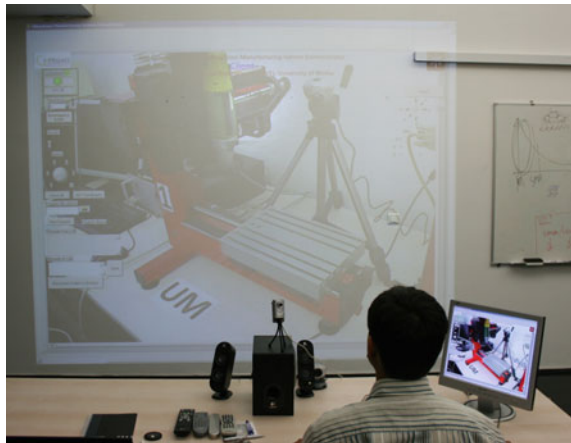
In the presented paper the authors propose an integrated decentralized CMRSS approach, through combining a different kind of technology, including back-office applications, for instance based on, Visual Basic programs and excel or simulation-based ones, which are usually locally used businesses.

Moreover, the underlying problem data representation schema permits users to add their own domain specific constraints. These constraints are later on used through dispatching rules, namely when a resource of a (manufacturing) system is ready to start, and that there are more than one jobs ready to begin on a given resource. The dispatching rules are part of the proposed CMRSS approach. They are used as a step on the global CMRSS approach. Therefore, there are two main approaches. One that is based on an automatically generated solution, usually performed as a first step of the whole CMRSS process, based on some kind of back-office application or some other approach, based on heuristics or meta-heuristics, such as genetic algorithms (GA), simulated annealing or “Tabu search” or even other simulation procedures based approaches. And another approach, usually at a second step of the CMRSS process is an approach, based on direct communication, through a brokering service. The latter doesn’t directly focus on optimization, but it’s very practical and important for real-world problems solving, e.g. for final adjustments of ordering plans in the context of the UMS. Therefore, the proposed system approach enables various types of procedures and technologies integration for supporting CMRSS.

4.1 Interfaces to Interact with Businesses

Figure 3 shows an interface for supporting the communication-based step of the CMRSS approach, typically used for the final refining and adjustments of the ordering plans through communication based on a complete media support between

Fig. 3 Interactive portal



businesses and some broker available on the P2P network of users. The visual image of plans and schedules, which are managed in various locations, is important especially in a decentralized manufacturing system. If each manufacturing site has its own schedulers developed by various IT vendors, their production plans cannot be visualized by a common viewer normally, without particular adapting programs. This actually creates a huge effort on implementation of systems, and both, the cost as well as the risk of the system's useful functionality, will be increased.

Using interfaces developed in a general way, enables end-users to get personalized plan viewers. This provides visualizing flexibility, for instance, distributed schedules, anywhere over the Internet. Therefore, this work is based on a general model for ordering and production plans and underlying important data for supporting decision-making and corresponding data representation and processing. In order to present the model better, an illustration of the proposed portal is provided through Figs. 4 and 5. In Fig. 4 it is possible to see an interface for supporting human interaction, between some client and a business provider, and both can share and visualize important information for enabling a better understanding about ordering data, like orders detailed scheduling and product prices and due dates establishment. In Fig. 5 it is possible to see an interface about the execution of the Hungarian algorithm, for doing the assignment of each of a set of parts to be processed on a set of machines and corresponding graphics including planned starting and finishing times of orders on the corresponding processing machines.

To contribute to a specification standard for CMRSS problems, the data is given through XML, based on a data structure which can be easily visualized through the Internet. In Fig. 5 a chart about a scheduling plan obtained is given. It gives an effective visualization tool. Furthermore, by using XML based problem specifications, another type of charts, namely the Gantt charts, can easily be presented and visualized on the web through the proposed portal.

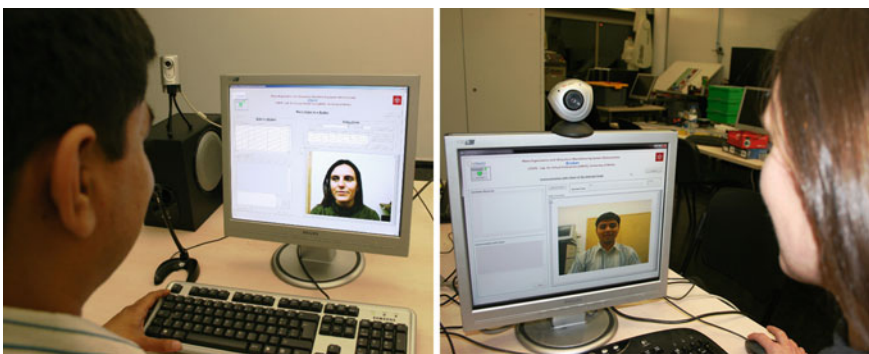


Fig. 4 Interface illustration—resources selection supported by a broker

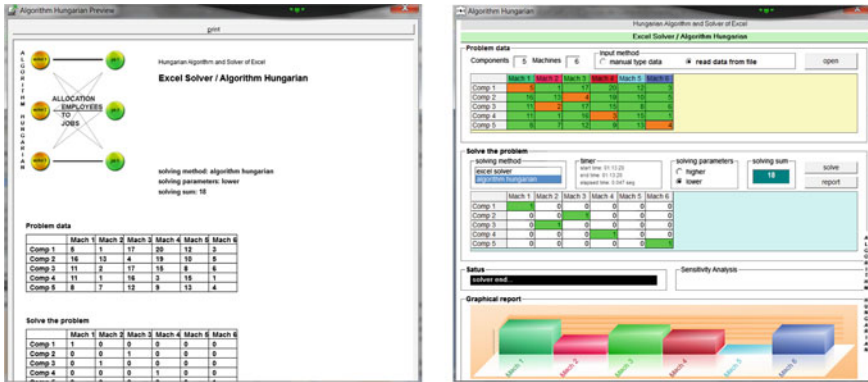


Fig. 5 Interface illustration—report with statistical data about orders processing

4.2 Distributed Knowledge Base and Control

The proposed innovative approach includes a two step framework for fully enabling CMRSS. First, each business integrating a P2P network may use its own technology, as described above, to provide its ordering and production plans for being able to provide useful and accurate information, on a real-time basis, to other businesses on the network or to outside clients, based on its own legacy systems, which can be easily integrated through appropriate interfaces. Second, communication through a brokering service enables to establish final adjustments to ordering plans between businesses or between each business and outside clients. These brokering services are fully media-oriented and based on a distributed knowledge base for enabling to more easily share and dynamically update important information regarding CMRSS problems solving.

Moreover, the proposed approach and underlying portal also enables functional support for remotely controlling manufacturing devices, as illustrated through Figs. 6 and 7.

The proposed portal is based on a standardized format to exchange data among different businesses. In manufacturing enterprises, there are various ICT applications including distinct planning and scheduling software. In order to make a pliant communication between different applications, XML based data-modeling is used. A significant aspect of this approach is generation and visualisation of data by computers in proper and unique ways. Therefore, it's important to notice that the schema of data representation is general in order to fulfil the different kind of manufacturing enterprises requirements.

Regarding the management of networked manufacturing processes, CMRSS problems play a significant role. Hence, frameworks for supporting collaboration and communication between businesses enable to enrich business models, in the context of integrated businesses in the context of a UMS and global market.

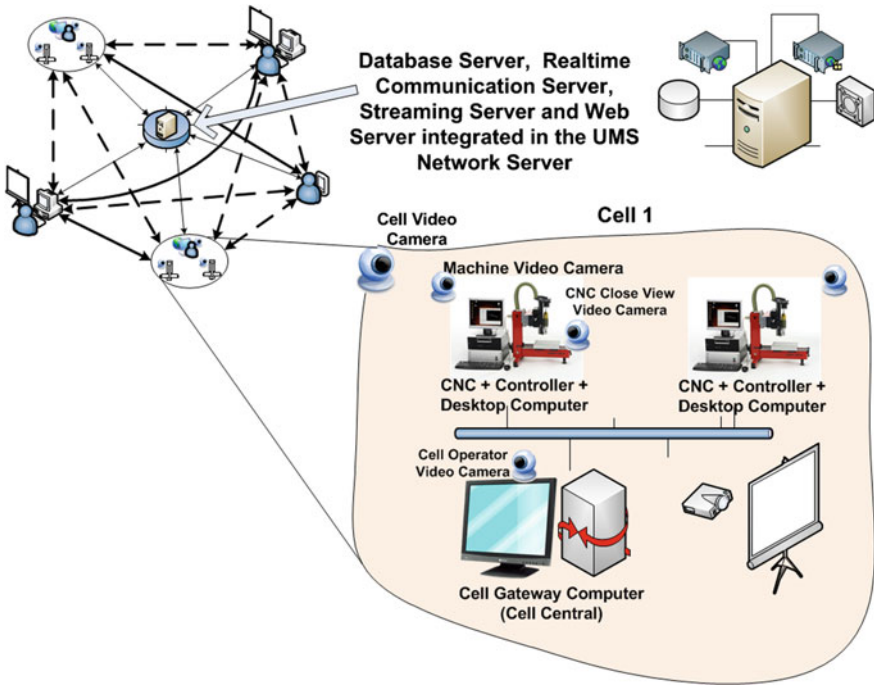


Fig. 6 Distributed knowledge base representation within the P2P network



Fig. 7 Illustration of a remotely controlled machine cell

5 Conclusion

This paper presented a portal for collaborative manufacturing resources selection and scheduling (CMRSS), which enables to easily and interactively communicate and establish orders among businesses and clients, based on an innovative approach and media-based communication. The innovative approach includes a two step framework for fully enabling CMRSS. Moreover, the proposed portal also enables functional support for remotely controlling manufacturing devices.

The effectiveness of the proposed integrated approaches was briefly described through some illustrations. A significant aspect of this approach is generation and visualisation of data by computers in proper and unique ways. It is necessary that the schema for data representation is general for different kinds of manufacturing enterprises requirements. Furthermore, collaboration also provides infrastructure for web-based application integration for all manufacturing enterprises, inside a Virtual Enterprise and Global Markets in a UMS environment.

Acknowledgments The authors wish to acknowledge the support of the Foundation for Science and Technology—FCT, under the scope of the financed Project with reference: PEst2015-2020, as well as the FCT Doctoral grant referenced SFRH/BD/62313/2009.

References

1. Varela, L.R., Putnik, G.D. Ribeiro, R.A.: A web-based platform for collaborative manufacturing scheduling in a virtual enterprise. In: Information and Communication Technologies for the Advance Enterprise, vol. 2, pp. 87–108, Portugal (2012)
2. Vieira, G., Varela, M.L., Putnik, G.D.: Technologies integration for distributed manufacturing scheduling in a virtual enterprise. In: Communications in Computer and Information Science: Virtual and Networked Organizations, Emergent Technologies and Tools, ViNOrg11, Portugal, Revised Selected Papers, vol. 248, pp. 337–347. Springer, Heidelberg (2012)
3. Putnik, G.D.: BM_virtual enterprise architecture reference model. Technical report RT-CESP-GIS-2000-<GP-01>. Universidade do Minho, Portugal (2000)
4. Putnik, G.D.: BM_virtual enterprise architecture reference model. In: Gunasekaran, A. (ed.) Agile Manufacturing: 21st Century Manufacturing Strategy, pp. 73–93. Elsevier, UK (2001)
5. Weiming, S., Lihui, W., Qi, H.: Agent-based distributed manufacturing process planning and scheduling: a state-of-the-art survey. *IEEE Trans. Syst. Man Cybern. Part C Appl. Rev.* **36**(4) (2006)
6. Herbsleb, J.D., Grinter, R.E.: Splitting the organization and integrating the code: Conway's law revisited. In: 21st International Conference on Software Engineering (ICSE'99), ICSE, p. 85 (1999)
7. Wu, S.H., Fuh, J.Y.H., Nee, A.Y.C.: Concurrent process planning and scheduling in distributed virtual manufacturing. *IIE Trans.* **34**(1), 77–89 (2002)
8. Hong, D., Li, C., Chentao, W., Qianni, D.: A grid-based scheduling system of manufacturing resources for a virtual enterprise. *Int. J. Adv. Manufact. Technol.* **28**(1–2), 137–141 (2006)

A Simulation Platform Prototype for Evaluating Alternative Scenarios of Members Integration in Virtual Organizations

António Arrais-Castro, Gaspar Vieira, Maria Leonilde Rocha Varela, Goran D. Putnik and José Machado

Abstract Companies are facing growing challenges motivated by globalization. A globalized market means that the number of companies with which they will need to compete to maintain or enlarge their market share is increased. Additionally, it also brings greater opportunities to conquer new markets and increase existing market shares, since the geographical, political and economical boundaries are gradually being removed. This paper proposes and illustrates the use of a platform prototype for enabling the evaluation and selection of attractive members for being included as members in a virtual organization. An extended simulation study is described and results obtained presented which show advantage of a used dynamic evaluation and selection model, based on a varying set of criteria.

Keywords Simulation platform • Dynamic evaluation model • Virtual organization • Suppliers and partners selection

A. Arrais-Castro · G. Vieira · M.L.R. Varela (✉) · G.D. Putnik
Department of Production and Systems, School of Engineering,
University of Minho, Braga, Portugal
e-mail: leonilde@dps.uminho.pt

A. Arrais-Castro
e-mail: arraiscastro@gmail.com

G. Vieira
e-mail: gaspar_vieira@hotmail.com

G.D. Putnik
e-mail: putnikgd@dps.uminho.pt

J. Machado
Department of Mechanical Engineering, School of Engineering,
University of Minho, Braga, Portugal
e-mail: jmachado@dem.uminho.pt

1 Introduction

In this paper a multi-agent approach is presented to provide operational support for virtual organizations and collaborative networks, along with a proposed platform prototype that can be applied to multiple business areas, supporting the rapid integration of new businesses and the community of the member with which they operate. The proposed platform is particularly focused on the process of identification, evaluation and selection of suppliers and businesses and integrates services based on the cloud to increase its flexibility and scalability. In order to provide a contribution in this context, besides the existence of some existing work in this area [1–5], our proposal is based on previous contributions, which include [6–11].

Regarding the problem of selection and evaluation of suppliers, as a problem of multi-criteria decision (MCDM), the main contribution of this work was the development of an approach that, jointly, (1) supports, in a complete manner, the process of decision based on multiple criteria in the identification, selection and evaluation of suppliers, (2) using a dynamic model capable of integrating a variable number of criteria (spatial variation) and their associated values over time (temporal variation, including past, present and future data), (3) supporting the inaccuracy and lack of confidence, using fuzzy logic for evaluation criteria, allowing (4) applying different weights to different time stages or evaluation criteria, adapted from previous work in [6–11].

This paper aims at analyzing the ability of the proposed platform to identify, evaluate and select a best suited partner and/or supplier, for acting as collaborating member in a VO (Virtual Organization) context, according to its previous performance and present ranking, by using the dynamic approach underlying to this work [6–11]. Therefore, we present the results of a simulation carried out on the implementation of the proposed approach regarding an illustrative example used. First is described the process through which the simulation was performed. Then, the alternative application scenarios are described and finally the obtained results are analyzed and its practical implications explained.

2 Definition of the Proposed Platform

The work performed led to the definition of a proposed platform to support the life cycle of collaborative networks (CN) and virtual organizations (VO), based on a community of software agents [11–18] that cooperate to support the operation of the network. The platform is designed to promote high levels of scalability through its modular approach based on autonomous and encapsulated components, supported by a flexible and moldable infrastructure, based on a distributed approach, which integrates local systems to companies, virtualized systems and cloud-based services. Besides supporting the creation, operation and dissolution of virtual enterprises in the context of collaborative network, the platform is designed to

support the rapid identification and selection of partners and suppliers that will consolidate the approach to a business opportunity identified and captured.

The work also resulted in the definition of a dynamic approach capable of supporting decision-making processes that take into account not only the proposals received from a number of suppliers or business partners, but also incorporate information relating to historical performance and its future projection. This dynamic nature of the approach allows reducing the risk inherent in the decision-making process, particularly when various possible solutions must be evaluated in a balanced way in the context of a comprehensive set of evaluation criteria. To enable evaluation of different sets of criteria for past, present and future data, the approach allows to evaluate, in a more balanced way, different providers. By incorporating the treatment of uncertainty, it better supports its use even in scenarios where the completeness and quality of data is not guaranteed.

The research results have an enlarged spectrum of use as it was designed and based on a dynamic multi-criteria decision model (DMCDM) [6–11] for evaluating alternative proposals that are not restricted to a given business model or particular sector. On the other hand, it can be highly beneficial regarding competitiveness of companies where we want to apply it, by allowing the instantiation of collaborative networks that enable the creation of synergies and sustain symbiotic relationships in order to expand the potential market, promote a more agile response to market changes, and faster response to changing competition.

The platform proposal supports the creation, operation and dissolution of collaborative networks. One of its main pillars is its ability to decide which are the best partners to establish the network, which are the most suitable companies to integrate VEs (Virtual Enterprises) created on its context and which are the best companies to implement the provision of services or components required to meet the requests about received orders, as illustrated next through Fig. 1.

The businesses evaluation and selection process start with the submission of a request for qualification (RFQ) from a order agent (OA) to the order processing agents (OPAs), according to the agreed protocol, stating which values it wants to receive (for example, price, delivery time and lead time). Additionally, the OA may highlight the evaluation criteria it will use, if appropriate. After receiving an RFQ, each of the OPAs starts a budgeting process. They calculate the price and may also interact with production agents (PA), associated with their Company, in order to obtain the delivery and lead times it can propose, according to the current production schedule.

Additionally, the production agents may report the production capacity during the period, if that parameter is part of the negotiation protocol. Finally, the OPA will issue the proposal to the OA, according to the defined protocol (Fig. 1).

The Order Agent which submitted the initial RFQ will evaluate all proposals/quotes it received, comparing the criteria it established for evaluation. It may include criteria associated with the proposal (price, delivery time, lead time) and criteria associated with the business performance (On Time Delivery Performance, Defect Free delivery, Delivery delay mitigation, Defect Mitigation). The

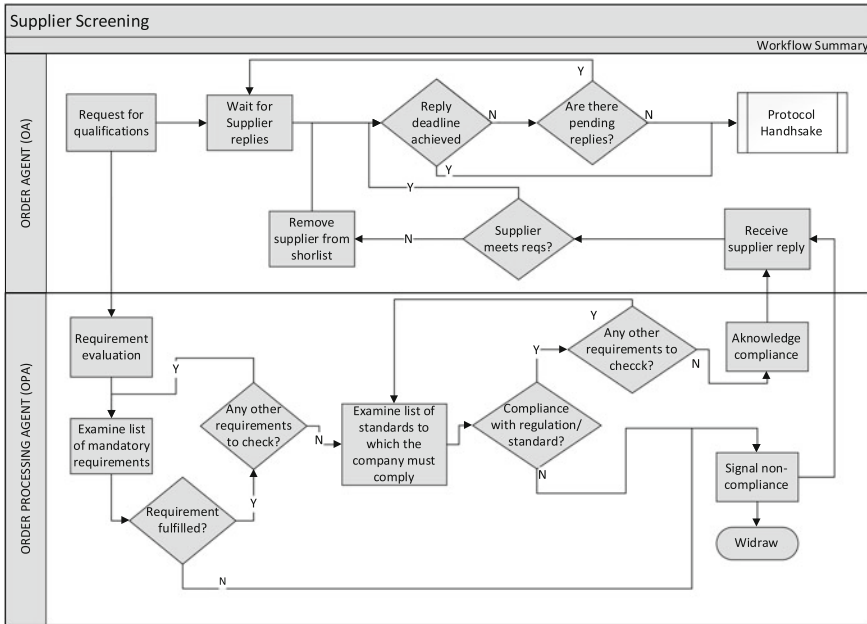


Fig. 1 Business screening workflow

evaluation will be performed using historical information, information contained in the received quotes and also forecasting data.

To evaluate the potential associated to our proposed platform we decided to analyze to which extend the underlying dynamic approach really supports the process of evaluation and selection of the best proposals on a given context of application.

Confirmed to obtain good results for some scenarios tested, progress was made towards the creation of an interactive prototype that supports the generation of multiple requests for proposals through successive iterations, submitted to an arbitrary set of businesses. To allow for simulations based on realistic scenarios, the prototype was extended to allow partners (suppliers and/or businesses) consulted to be associated with a matrix of rankings about their profile, in order to introduce a random component, based on known performance of these suppliers/businesses and standards associated to their evolution. This extension of the prototype was used to generate multiple simulations with different configuration parameters for analysis of results and assessment of the dynamic model performance.

To facilitate the execution of multiple analyzes and it's viewing by multiple stakeholders, the prototype was developed using web technologies (PHP, Javascript, CSS, HTML) and on a database MySQL, and focused on the application of the underlying dynamic approach.

The prototype supports the viewing of the main application steps of the dynamic selection and evaluation approach, which in this work was applied to a given

scenario of application. Additionally, it allows the execution of various types of simulations, implemented as described next.

To evaluate the performance of the dynamic evaluation approach, it was decided to carry out simulations of its application using the dynamic generation of proposed applications and the evaluation of the answers received. The evaluation was based on three different approaches: (1) a dynamic evaluation, covering the use of historical matrices, present data (resulting from proposals received) and forecasts; (2) assessment regarding historical and present information; (3) evaluation exclusively based on the proposals received.

To analyze the results obtained by applying our underlying dynamic model we proceeded to its application on an illustrative scenario about the selection of a business, among a set of 6 available for the production of a particular product and knowing some additional features, which will be described in more detail below, to allow clearly illustrate the potential of the deployed prototype.

The simulation process begins with its preparation. The first set of simulation of the preparation process of the tasks consists on defining the parameters that will condition its implementation. This set includes the number of iterations to be performed, the number of queries to simulate by iteration, the group of suppliers to be consulted, the number of evaluation criteria to be used and the approaches on which they are used. Additionally, matrices are configured for historical data view and associated future data prediction, along with histograms that are used to simulate the behavior of businesses. Table 1 shows the chosen parameters.

Next, it is needed to define the criteria to be used for historical, present and future evaluations. To make the clearest illustration in terms of prototyping, it was selected a representative set of criteria used, related to different kind of cost, as expressed in Table 2, and this data was jointly used with the information provided through the criteria used for historical and future evaluation of businesses delivery times in order to better support decision making regarding the these underlying criteria.

For the implementation of the dynamic model, the various evaluation criteria were mapped on their type (“higher is better” or “lower is better”), uncertainty, confidence level. In addition, the α values were defined and β for each criterion and $\lambda = 1$ [6–11].

The values used as a reference are shown in Table 3.

Table 1 Simulation parameters definition

Parameter	Meaning	Value
n	Number of iterations	10, 100, 200
m	Number of approaches used	3
w	Number of suppliers consulted	6
h	Number of historical evaluation criteria	4
q	Number of present evaluation criteria	2
f	Number of future evaluation criteria	2
p	Number of proposal requests made on each iteration	10, 20, 50

Table 2 Criteria definition

Moment	Criterion	Description
Past	Cost practiced in the past (CPP)	costs charged by the supplier to supply the product in the last 12 months
Past	Total time for delivery (TTD)	Total time elapsed between the award and the delivery of products from the award date in the past, for orders of the same product
Past	Delivery performance (DPE)	Previous performance of the supplier in terms of timely delivery of orders (0–100 %)
Past	Quality performance (DP)	Previous performance of the supplier in terms of delivery of orders without defects (0–100 %)
Present	Cost per unit (CPU)	Cost proposed by the supplier for the execution of one unit (€)
Present	Total time for delivery, for present (TTD)	Total time elapsed between the award and the delivery of products from the award of the contract
Future	Estimated unit cost (EUC)	Estimated cost per unit of the same product in the future, according to the evolution of the in supplier's prices
Future	Total time for delivery, for future (FTTD)	Total delivery time estimated per product unit

Table 3 Criteria parameters associated with the selected criteria

Moment	Criteria	Type	Uncertainty (%)	Confidence (%)	α	β	λ
Past	CPP	Lower is better	0	100	1	0.67	1
Past	TTD	Lower is better	0	90	0.8	0.67	1
Past	DPE	Higher is better	2	80	0.8	0.67	1
Past	DP	Higher is better	2	80	0.8	0.67	1
Present	CPU	Lower is better	0	100	1	1	1
Present	TTD	Lower is better	0	100	0.8	0.67	1
Future	EUC	Lower is better	5	80	0.6	0.67	1
Future	FTTD	Lower is better	5	60	0.6	0.67	1

To evaluate the criteria were used three approaches related to dynamic evaluation model underlying to this work, which were the following: 1. Historical, present and future evaluations (HPF); 2. Historical and present evaluations (HP), and 3. Only present evaluation (P). Therefore, these three approaches require the use of one up to three evaluation matrices, which express the total cost underlying each candidate supplier or business ranking through an underlying data fusion approach used within our dynamic decision model [6–11].

In practice it is considered the same reference time for all repetitions of query request, performing successive simulations of the application of the evaluation approaches at this reference time, and next the results are compared.

Each of the consulted businesses submits a proposal for providing a unit of product, randomly generating values proposed for the unit cost and for the total

time of delivery (corresponding to the sum of the production time and the order preparation time).

To support the randomness in terms of generation of proposals, each business has been classified according to four main areas: (1) delivery optimization potential, emphasizing the efforts the business has done, namely to reduce the delivery time; (2) potential changes in prices, reflecting the trend observed by the business to increase, decrease or maintain the prices offered; (3) risk of late delivery, reflecting businesses' performance in terms of delivery and the potential of further delays; (4) the risk of defects, reflecting the likelihood of defects in future deliveries.

The classification of the businesses on the areas mentioned allowed introducing random behavior in terms of proposals submitted by them. To generate a new value for each area were used random number between zero and ninety-nine, generated by computer. The random numbers were used as the input key to a histogram that maps each of the areas aforementioned for each business.

The presentation of data is done in order to permit adequate visualization of each type of data analysis and matching results, allowing different views, with more or less detailed information.

Figure 2 illustrates the prototype's interface regarding the simulation results obtained after 20 iterations, each of which covering the evaluation of 20 proposals about each of the 6 analyzed businesses. For each iteration were added costs generated by each of the approaches according to the data provided by them, taking into account the profile associated with each business concerning the occurrence of faults or delays. In the generated results table presented, we can see the green and underlined values, which correspond to the lower costs (corresponding to the best solution), and in red the highest costs. For example, from a quick look at the data in this figure, it is clear that the dynamic evaluation approach (HPF) enabled to provide the best results in all of the iterations for the scenario under study, by comparison with the other simpler alternative approaches (HP and P).

The prototype allows alternative views of results, along the detailed simulation process. Namely, allowing following the evaluation process of winning proposals for each of the alternative approaches considered, and consultation of the respective total costs.

The prototype also provides an additional mode of simulation, to facilitate the generation of a large number of records and their subsequent analysis. Supporting the definition of the number of iterations (n) and consultations (m), and the same are associated with the 6 businesses considered in this example.

In this case, the prototype generates $x * m * 6$ random proposals and evaluates them using each of the three approaches considered for this purpose in this study. Once the evaluation, the prototype selects the most advantageous solution, considering the profile of each business (regarding their tendency to deliver orders late or defective), and the resulting costs. At the end we can see a graph comparing the performance of the three approaches used.

The Fig. 3 illustrates the execution of the simulation process for 100 iterations, each of which includes 20 proposal requests (resulting in a total of 2,000 consultations, which generated 12,000 proposals, and these have been evaluated in the

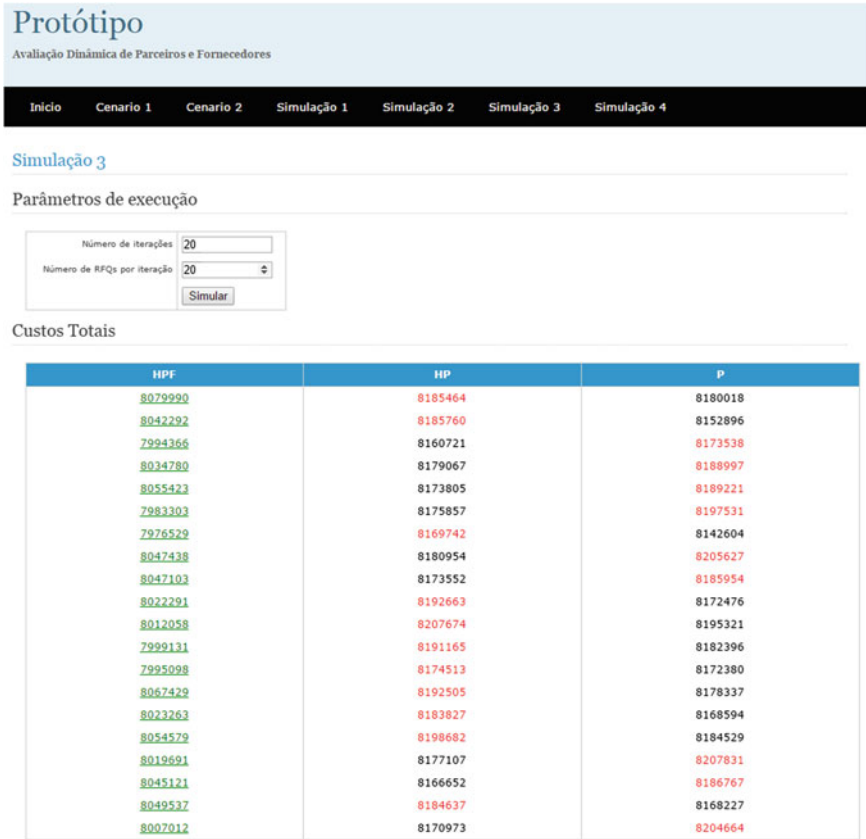


Fig. 2 Simulation results visualization

context of each of the three approaches under consideration, resulting in a total of 36000 ratings). According to defined profiles, the dynamic (HPF) approach was the only one that did enable to generate the best solution in 1071 consultations. Moreover, in 1808 cases it reached the best solution in conjunction with one or both alternative approaches.

The diverse records execution results were recorded in databases, enabling to further make queries and export data and results for further analysis, namely through external tools such as SPSS and Microsoft Excel.

Comparing the cost of each of the solutions generated by each of the three approaches considered we can realize that the dynamic approach was the one that did produce the economically most advantageous solution, as we can see through Fig. 4, which expresses the cost of each solution and the cost of the best one.

In practice, since the dynamic approach is responsible for the largest number of best proposals in economic terms, its value is always closest to the best solution value.

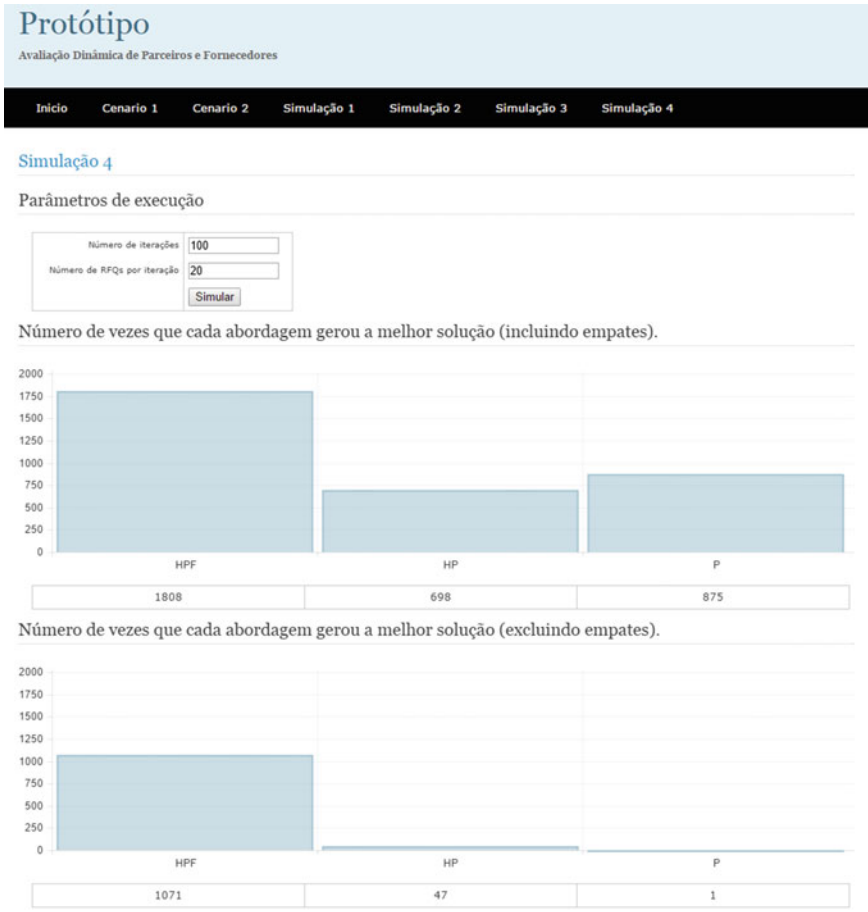
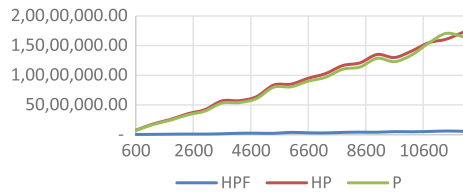


Fig. 3 Visualization of the results of the evaluation process for 2000 consultations and 12,000 proposals analyzed

Fig. 4 Evolution of the difference in cost between the three approaches and the best solution obtained on each iteration



3 Conclusion

In a collaborative network, relations between integrating members generate information that is highly valuable to support a useful decision-making process, minimizing the costs associated to its operation and thus contributing to the maximization of potentially associated income opportunities. In order to provide a contribution in this context, besides interesting existing work in this area, such as [1–5], our proposal is based on previous work, such as [6–11]. Moreover, we did not come across any proposal that jointly considers the application of a dynamic multi-criteria decision approach, integrating a data fusion model for improving collaboration and better supporting businesses integration within a virtual enterprise context, not being restricted to a given business model or particular industrial sector. Therefore, in intended to contribute for properly supporting the operation of collaborative networked organizations, and enhancing their continuous reconfiguration process, based on market evolution, Company's members or business partners performance, network size and associated requirements, along with a varying set of parameters for evaluating and selecting appropriate business partners in a dynamic and flexible way. In this study it became clear, through the simulations results obtained, that there are big differences in terms of costs regarding the application of different approaches for alternative businesses' of partners' evaluation and subsequent selection. In all the simulations performed, our proposed dynamic evaluation model, which includes not just present and past data, but also future predictions, produced the best results in the majority of the evaluations carried out. There are several factors that affect the greater or lesser efficiency of each evaluation approach. For the analysis carried out in this work we used a representative set of businesses, through an industrial example. The quality and scope of existing historical data affects the results produced. Moreover, the approaches can be used in environments with more or less amount of uncertainty, and enable the use of distinct sets of parameters (e.g. confidence, accuracy, weights), which enable filtering of uncertainty and producing a final rating according to the importance of the various evaluation criteria used by each Company.

Acknowledgments This work has been supported by COMPETE: POCI-01-0145-FEDER-007043 and FCT—Fundação para a Ciência e Tecnologia within the Project Scope: UID/CEC/00319/2013.

References

1. Camarinha-Matos, L., Afsarmanesh, H.: Virtual enterprise modeling and support infrastructures: applying multi-agent system approaches. In: Carbonell, J., Siekmann, J. (eds.) *Multiagents Systems and Applications*, pp. 335–364, Sanibel Island, FL (2001)

2. Ghiassi, M., Spera, C.: Defining the internet-based supply chain system for mass customized markets. *Comput. Ind. Eng.* **45**, 17–41 (2003)
3. Malucelli, A., Rocha, A., Oliveira, E.: B2B Transactions enhanced with ontology-based services. In: ICETE 1, pp. 10–17. INSTICC Press (2004)
4. Eymann, T., Müller, G., Strasser, M.: Self-organized scheduling in hospitals by connecting agents and mobile devices. In: Kim, S., et al. (eds.) *Multiagent Engineering—Theory and Applications in Enterprises*, International Handbooks on Information Systems, pp. 319–337. Springer, Heidelberg (2006)
5. Smirnov, A., Sheremetov, L., Chilov, N., Sanchez-Sanchez, C.: Agent-based technological framework for dynamic configuration of a cooperative supply chain. *Multiagent Based Supply Chain Manage.* **28**(2006), 217–246 (2006)
6. Ribeiro, R.A., Falcão, A., Mora, A., Fonseca, J.M.: FIF: a fuzzy information fusion algorithm based on multi-criteria decision-making. *Knowl. Based Syst.* (2013)
7. Jassbi, J.J., Ribeiro, R.A., Varela, L.: Dynamic MCDM with future knowledge for supplier selection. *J. Decis. Syst.* **23**(3), 232–248 (2014). ISSN 1246-0125
8. Campanella, G., Ribeiro, R.A.: A framework for dynamic multiple criteria decision making. *Decis. Support Syst.* **52**(1), 52–60 (2011)
9. Campanella, G., Ribeiro, R.A., Varela, L.R.: A Model for B2B supplier selection. In: *Advances in Intelligent and Soft Computing*, vol. 107, pp. 221–228. Springer, Warsaw (2011)
10. Campanella, G., Pereira, A., Ribeiro, R.A., Varela, L.R.: Collaborative dynamic decision making: a case study from B2B supplier selection. In: Hernández, J.E., et al. (eds.) *Decision Support Systems*, LNBIP, vol. 121, pp. 88–102. Springer, Heidelberg (2012)
11. Ribeiro, R.A.: Fuzzy multiple attribute decision-making: a review and new preference elicitation techniques. *Fuzzy Sets Syst.* **78**, 155–181 (1996)
12. Rabelo, R., Camarinha-Matos, L.M., Vallejos, R.: Agent-based brokerage for virtual enterprise creation in the moulds industry. In: *E-Business and Virtual Enterprises*, volume 184 of IFIP Conference Proceedings, pp. 281–290, Kluwer (2000)
13. Thorat, P., Sarje, A.: MobiLim: an agent based license management for cloud computing. *IC3*, Volume 168 of *Communications in Computer and Information Science*, pp. 335–346. Springer (2011)
14. Tveit, A.: A survey of agent-oriented software engineering. *NTNU CSGSC* **4**, 367 (2001)
15. Wang, M., Wang, H., Vogel, D., Kumar, K., Chiu, D.K.W.: Agent-based negotiation and decision making for dynamic supply chain formation. *Eng. Appl. Artif. Intell.* **22**, 1046–1055 (2009). doi:[10.1016/j.engappai.2008.09.001](https://doi.org/10.1016/j.engappai.2008.09.001)
16. Wooldridge, M.: *Intelligent Agents*. In: Weiss, G. (ed.) *Multi-agent Systems—A Modern Approach to Distributed Artificial Intelligence*. The MIT Press, Cambridge, MA (1999)
17. Wooldridge, M., Ciancarini, P.: Agent-oriented software engineering: the state of the art. *Agent-Oriented Softw. Eng.* **1957**, 55–82 (2001). doi:[10.1007/3-540-44564-1_1](https://doi.org/10.1007/3-540-44564-1_1)
18. Xue, X., Li, X., Shen, Q., Wang, Y.: An agent-based framework for supply chain coordination in construction. *Autom. Constr.* **14**, 413–430 (2005). doi:[10.1016/j.autcon.2004.08.010](https://doi.org/10.1016/j.autcon.2004.08.010)

Formal Analysis of an Urban Road Traffic Model

Camelia Avram, Eduardo Valente, Adina Aștilean, José Machado and Dan Radu

Abstract The paper proposes a method based on timed automata to validate different road traffic control scenarios. In order to estimate the current traffic state, a strategy in which a special attention was given to information collected from the streets converging to main crossroads was elaborated. Then, the up to dated information was used by a complex road traffic model to improve the traffic flow. The validation and verification of the road traffic model was realized using UPPAAL model-checker. A representative area of Cluj Napoca city center was modeled and simulated in order to determine the right parameters for traffic control. The proposed model, validated in UPPAAL, can be extended to any road structure for analysis purposes.

Keywords Modelling and simulation · Urban traffic · Road traffic control · Formal validation

C. Avram (✉) · A. Aștilean · D. Radu
Automation Department, Technical University of Cluj Napoca, Cluj-Napoca, Romania
e-mail: camelia.avram@aut.utcluj.ro

A. Aștilean
e-mail: adina.astilean@aut.utcluj.ro

D. Radu
e-mail: dan.radu@aut.utcluj.ro

E. Valente · J. Machado
Department of Mechanical Engineering, University of Minho, Braga, Portugal
e-mail: jmachado@dem.uminho.pt

1 Introduction

A new road traffic modeling framework based on the theory of timed automata, UPPAAL model-checker and the corresponding associated language is presented in this paper. Focusing especially on the necessity of validation and verification of micro simulation traffic models, this approach was chosen taking into account that UPPAAL is a tool designed to verify systems that can be modeled as networks of timed automata extended with integer variables, structured data types, user defined functions, and channel synchronization [1].

During the last decades, a considerable number of road traffic simulators were proposed, a particular importance being according to micro-simulation models. In this context, many microscopic simulation tools were developed.

In different studies, the functionalities and capabilities of micro simulation tools were compared together with a detailed analysis of their mechanisms of vehicle generation, car-following and lane changing models, traffic control options, network modeling capabilities, statistical output, user interface, run-time performance and other advanced features of road traffic simulators [2–4].

Advantages and disadvantages of different specific tools were highlighted, the gaps and the necessities of new applications were emphasized and new development orientations were proposed. The need for a detailed examination of the existing microscopic models to determine which components and parameters have an effect on some specified indicators was also marked out.

Recent researches show that the potential of traffic simulators can be increased, corresponding effort being oriented to pedestrian, safety traffic, [5–7], new algorithms [8], calibration, verification and validation [9].

The Federal Highway Administration of the U.S. Department of Transportation has originated the Next Generation SIMulation community (NGSIM) in order to—improve the quality and performance of simulation tools, promote the use of simulation for research and applications, and achieve wider acceptance of validated simulation results [10].

The complexity and high computational cost of microsimulation models fully motivate the usage of artificial intelligence methods to solve difficult, specific problems [11].

It is obviously that modeling techniques lead to different modeling performances, e.g. fuzzy logic could be suitable for data interpretation and analysis, genetic algorithms and neural networks offering a good alternative for decision support. Many results demonstrate the feasibility of using genetic algorithms to calibrate different microsimulation models [12, 13], but also for solve origin-destination estimation problem [14, 15].

In this context, the choosing of a model suited for specific applications remains a challenge. On the other part, all models need improved calibration, verification and validation, the fulfillment of imposed requirements implying the usage of more performer simulation and analysis tools.

Accordingly to the above considerations, the proposed modeling and analysis framework offers a new perspective and a favorable development in this direction.

2 Road Traffic Modeling

The main goal of this work is to validate a mathematical formalism and to extend the UPPAAL model from [16].

In this purpose, a detailed timed automata based model of urban road traffic was previously developed, this section presenting only its main features. For a more systematic approach a modular structure was considered. The resulted model is easily extendable and can be reused and detailed in order to implement complex scenario.

Because UPPAAL simulation and verification environment was utilized for analysis, the obtained model was implemented on the editor of this software tool.

The resulted model can be easily extended and reused and could be particularized to implement the desired scenario.

Several parameters (traffic actors) were taken into consideration:

- automobiles: speed (characterized by minimal, maximal and average values, breaking, accelerating, stopping), length (average), path to follow (this parameter can be setup or not, in the case of an automobile with no configured path to follow, it's randomly traveling on the map);
- traffic lanes: length (having as attributes: number of cells (dynamically calculated based on velocity, automobile length and safety distance), next lanes (one or more lanes);
- streets: composed of one ore more traffic lanes;
- crossroads: as connection points of three ore more streets;
- traffic lights: control the traffic (considering fix or adaptive values for read, green, yellow);
- traffic quality: characterized as congested, fluid, sporadic (each traffic type imply parameters to monitor like noise and air quality);
- pedestrian lanes with special places to cross the street.

The implemented solution to obtain the required versatility consist of introducing matrices which provide a compact environment for discretization and modeling the physical environment. The maximum speed was setup for each segment, the minimum value being dictated by traffic.

The Timed Automata allows to monitor each time each followed parameter. "Traffic actors" can communicate among them using: messages, global or local variables and synchronization channels. The road segments which are on the border of the simulated area are considered input/output points, according to the traffic directions. In order to tune the traffic parameters in the used microscopic model real measurements were performed. A configuration file was utilized to setup the traffic parameters. An important advantage of this approach is that only a change of a configuration file is needed.

The model was conceived in order to develop an adaptive controller as decision support system, when extreme conditions of urban road traffic (bottleneck traffic) appear. Its suggesting different options and configurations of roads to achieve a fluid traffic in the context of the existing exigencies of modern (bustle) life.

It must be mention that a dynamic decision support system for drivers, implemented in this context, has a lot of direct and indirect benefits for users such as: reduction of stress, shortest time to arrive to final destinations, low traffic pollution; reduction of energy consumption.

3 Testing and Simulation

A representative area of Cluj Napoca city center was modeled and simulated in order to determine the right parameters for traffic control (duration of semaphores traffic lights), Fig. 1 and to obtain the green light wave. The simulations were performed using a Windows 7 64B computer with 8 processors and 16 GB memory. As future work we intend to extend the simulation for the entire Cluj Napoca downtown using an Ubuntu server with 16 processors and 32 GB memory. Some limitations depends on the fact that the windows version of the software is not using all the available processors.

On the considered map CRS-x, represents the five simulated crossroads and MP-y correspond to four measuring points. The traffic parameter taken into account was the number of vehicles, the noise level (measured in dB) being an indicator of the congestion level.

The measurements were performed in two distinct real scenarios according to Tables 1 and 2.



Fig. 1 The Cluj Napoca map considered for simulation

Table 1 Measured values of noise for a congested traffic

No	MP	Noise	Vech. No./min
1	P1	83	30
2	P2	77	30
3	P3	80	30
4	P4	78	30

Table 2 Measured values of noise for a regular traffic

No	MP	Noise	Vech. No./min
1	P1	83	20
2	P2	72.3	17
3	P3	67.4	16
4	P4	70.4	19

4 Formal Validation of the Model

The initial values taken into consideration were:

- Number of vehicles = 100;
- Number of cross roads = 5;
- Number of streets = 20; (each traffic lane is considered a street in this model)
- Number of street cell per each street—is dynamic calculated based on average automobile length, safety distance and speed;
- noise: measurements from Tables 1 and 2.

Several validations predicates were used to verify the average, minimal and maximal time needed for an automobile to pass each street and if these values fall between some specified limits.

- An example of speed limit verification is given below:
 - $E[] \text{ forall } (i : idA) \text{ automobile}(i).time_per_street(j) > 0.5 * indexSC[j][p]$
 - $E<> \text{ forall } (i : idA) \text{ automobile}(i).time_per_street(j) > 0.5 * indexSC[j][p]$
 - $E[] \text{ forall } (i : idA) \text{ automobile}(i).time_per_street(j) < 27 * indexSC[j][p]$
 - $E<> \text{ forall } (i : idA) \text{ automobile}(i).time_per_street(j) < 27 * indexSC[j][p]$
- Possible stuck of automobiles on the streets is also verified as follows:
 - $E<> \text{ forall } (i : idA) \text{ automobile}(i).response = -1$
 - A[] not deadlock—Verify if deadlock can occur on the model.

Table 3 The verification of the time needed to pass each traffic lane

Description	Property to validate Greater than a minimum value	Result
Test the value of the time for each automobile on street 0	$E[] \text{ forall } (i : \text{idA}) \text{ automobile}(i). \text{ time_per_street}(0) > 0.5 * \text{indexSC}[0][0] \ E \langle \rangle \text{ forall } (i : \text{idA}) \text{ automobile}(i). \text{ time_per_street}(0) > 0.5 * \text{indexSC}[0][0]$	Yes
Test the value of the time for each automobile on street 1	$E[] \text{ forall } (i : \text{idA}) \text{ automobile}(i). \text{ time_per_street}(1) > 0.5 * \text{indexSC}[1][0] \ E \langle \rangle \text{ forall } (i : \text{idA}) \text{ automobile}(i). \text{ time_per_street}(1) > 0.5 * \text{indexSC}[1][0]$	Yes
Test the value of the time for each automobile on street 2	$E[] \text{ forall } (i : \text{idA}) \text{ automobile}(i). \text{ time_per_street}(2) > 0.5 * \text{indexSC}[2][0] \ E \langle \rangle \text{ forall } (i : \text{idA}) \text{ automobile}(i). \text{ time_per_street}(2) > 0.5 * \text{indexSC}[2][0]$	Yes
...		

Tables 3 and 4 present the properties validation.

The queries have the role to verify the possibility to reach many real states and to exclude ambiguities.

Some results obtained after validations are represented in Figs. 2, 3, 4, 5, 6, 7, 8 and 9.

In further developments aiming to determine the best route for various situations, including a green light pass, the presented results will be used to control the road traffic.

The results obtained from UPPAAL regarding the traffic flow, the instantaneous number of passed vehicles and the verifications results are used later to control the traffic by determining the best route to follow in various situations and to determine the green light wave.

For interrogation purposes a java program was implemented to generate queries to be validated. A part of these queries are presented in Tables 3 and 4. From command line, the .xml file (which contains the models of the vehicles, segments and instantiations) are “called” in order to be verified and validated. The behavioral properties are checked after the model is validated.

For a large simulated map an interrogation tool could be proposed in order to send interrogations to UPPAAL, to interpret the results file and to put the information in a form that can be used during the control process.

5 Conclusions

Timed automata as formalism, and UPPAAL as validation tool allowed to verify and adapt the road traffic parameters to various traffic situations. The proposed developed model, validated in UPPAAL, can be extended to any road structure for analysis

Table 4 UPPAAL properties validation for speed limit

Description	Property to validate Speed in legal limit	Result
Test the value of the time for each automobile on street 0	$E[] \text{ forall } (i : \text{idA}) \text{ automobile}(i), \text{ time_per_street}(0) > 0.5 * \text{ indexSC}[0][0] \ \&\& \ \text{forall } (i : \text{idA}) \text{ automobile}(i). \text{ time_per_street}(0) < 27 * \text{ indexSC}[0][0] \ E \leftrightarrow \text{forall } (i : \text{idA}) \text{ automobile}(i), \text{ time_per_street}(0) > 0.5 * \text{ indexSC}[0][0] \ \&\& \ \text{forall } (i : \text{idA}) \text{ automobile}(i), \text{ time_per_street}(0) < 27 * \text{ indexSC}[0][0]$	Yes
Test the value of the time for each automobile on street 1	$E[] \text{ forall } (i : \text{idA}) \text{ automobile}(i), \text{ time_per_street}(1) > 0.5 * \text{ indexSC}[1][0] \ \&\& \ \text{forall } (i : \text{idA}) \text{ automobile}(i). \text{ time_per_street}(1) < 27 * \text{ indexSC}[1][0] \ E \leftrightarrow \text{forall } (i : \text{idA}) \text{ automobile}(i), \text{ time_per_street}(1) > 0.5 * \text{ indexSC}[1][0] \ \&\& \ \text{forall } (i : \text{idA}) \text{ automobile}(i), \text{ time_per_street}(1) < 27 * \text{ indexSC}[1][0]$	Yes
Test the value of the time for each automobile on street 2	$E[] \text{ forall } (i : \text{idA}) \text{ automobile}(i), \text{ time_per_street}(2) > 0.5 * \text{ indexSC}[2][0] \ \&\& \ \text{forall } (i : \text{idA}) \text{ automobile}(i). \text{ time_per_street}(2) < 27 * \text{ indexSC}[2][0] \ E \leftrightarrow \text{forall } (i : \text{idA}) \text{ automobile}(i), \text{ time_per_street}(2) > 0.5 * \text{ indexSC}[2][0] \ \&\& \ \text{forall } (i : \text{idA}) \text{ automobile}(i), \text{ time_per_street}(2) < 27 * \text{ indexSC}[2][0]$	Yes
Test the value of the time for each automobile on street 3	$E[] \text{ forall } (i : \text{idA}) \text{ automobile}(i), \text{ time_per_street}(3) > 0.5 * \text{ indexSC}[3][0] \ \&\& \ \text{forall } (i : \text{idA}) \text{ automobile}(i). \text{ time_per_street}(3) < 27 * \text{ indexSC}[3][0] \ E \leftrightarrow \text{forall } (i : \text{idA}) \text{ automobile}(i), \text{ time_per_street}(3) > 0.5 * \text{ indexSC}[3][0] \ \&\& \ \text{forall } (i : \text{idA}) \text{ automobile}(i), \text{ time_per_street}(3) < 27 * \text{ indexSC}[3][0]$	Yes
...		

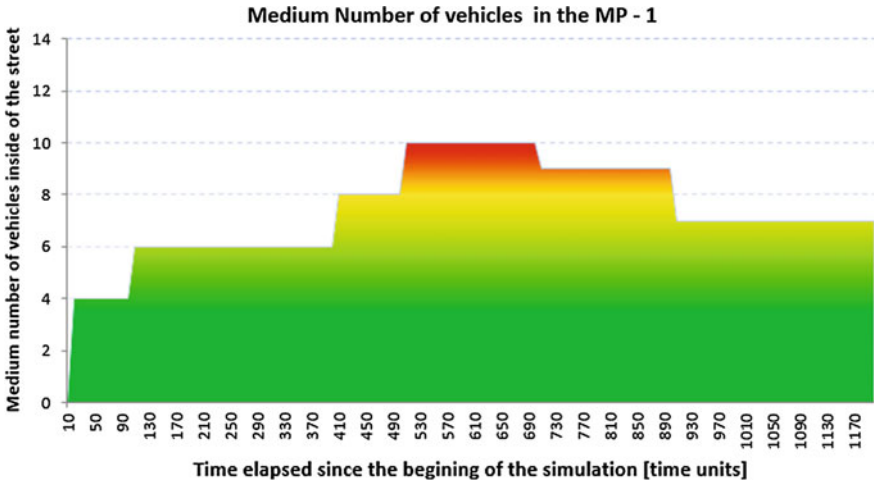


Fig. 2 Medium number of vehicles in MP1, congested traffic

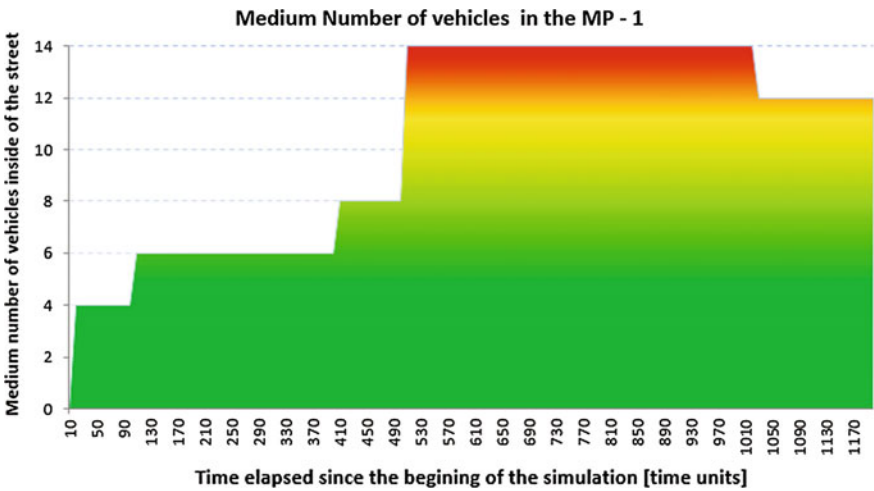


Fig. 3 Medium number of vehicles in MP1, regular traffic

purposes. Because the proposed UPPAAL models are modular and the initialization of the road traffic parameters are read from a configuration file, it is easier to change the simulation scenario without redrawing operations. In a future project the obtained measured and determined values will be used in adaptive costs routing algorithms to control and estimate the traffic flow and to advise road traffic participants using on-line mobile and web application.

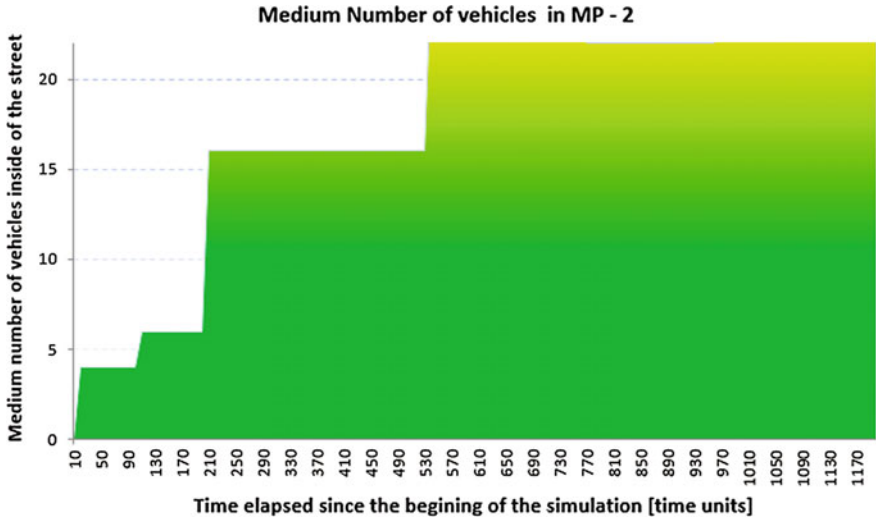


Fig. 4 Medium number of vehicles in MP2, congested traffic

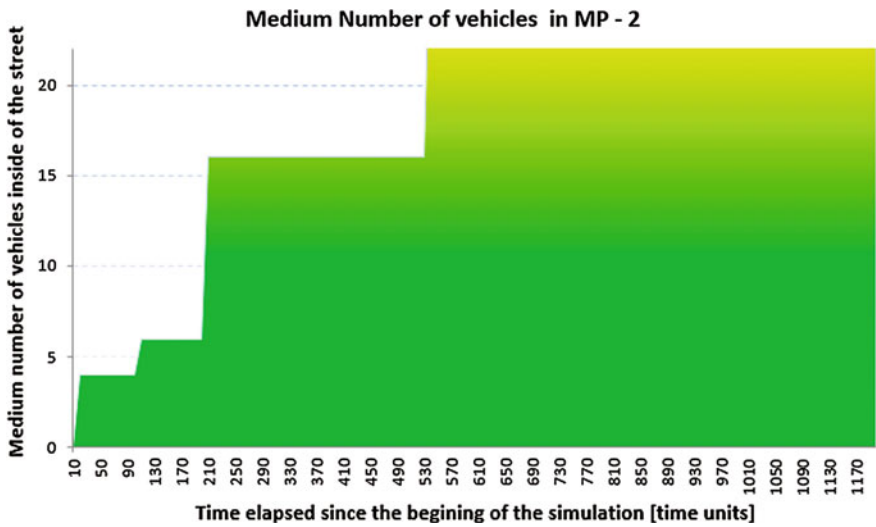


Fig. 5 Medium number of vehicles in MP2, regular traffic

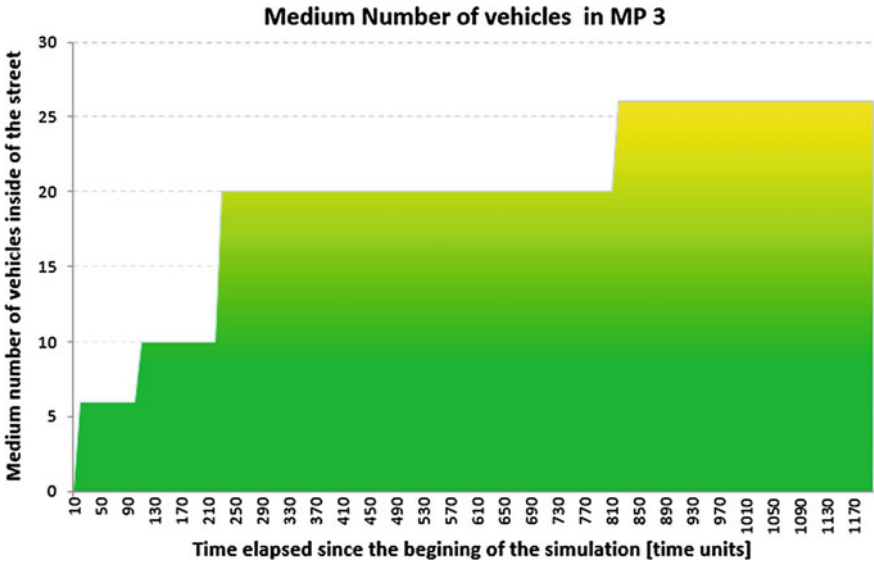


Fig. 6 Medium number of vehicles in MP3, congested traffic

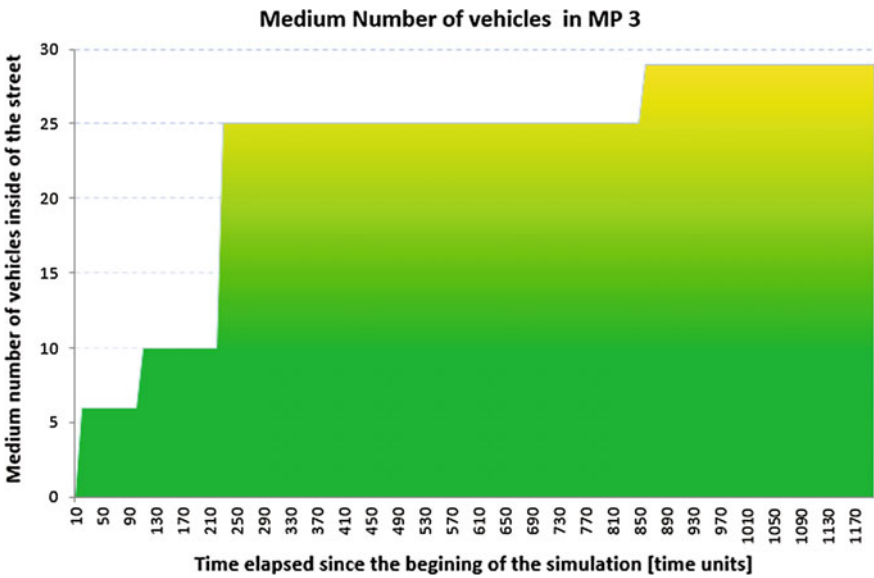


Fig. 7 Medium number of vehicles in MP3, regular traffic

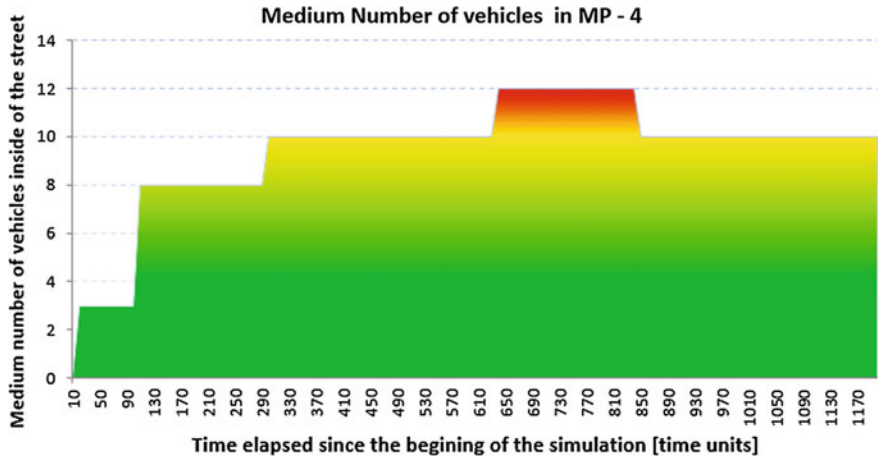


Fig. 8 Medium number of vehicles in MP4, congested traffic

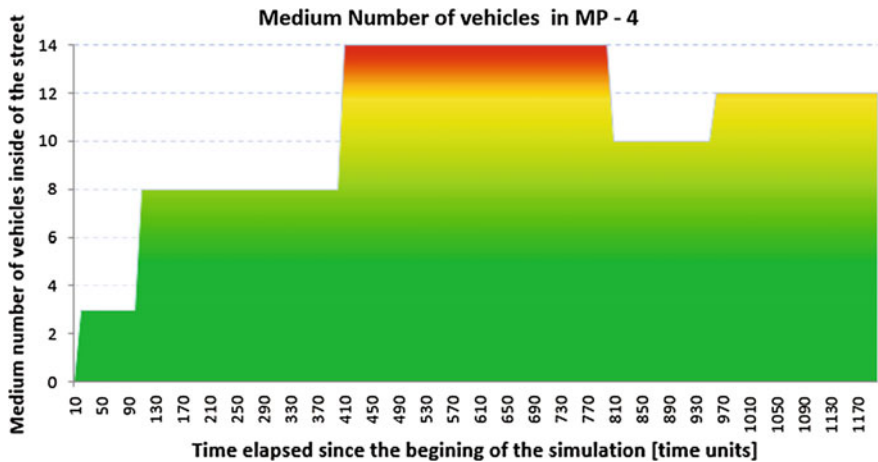


Fig. 9 Medium number of vehicles in MP4, regular traffic

References

1. Behrmann, G., David, A., Guldstrand Larsen, K.: A Tutorial on Uppaal. SFM 2004:200–236 (2004)
2. Olstam, J., Tapini, A.: Comparison of Car-Following Models. VTI Publication M960A.2004, Swedish National Road and Transport Research Institute, Linköping, Sweden (2004)
3. Panwai, S., Dia, H.: Comparative evaluation of microscopic car-following behavior. IEEE Trans. Intell. Transp. Syst. **6**(3) (2005)
4. Sbayti, H., Roden, D.: Best Practices in the Use of Micro Simulation Models American Association of State Highway and Transportation Officials (AASHTO), Prepared as part of NCHRP Project-36, Task 90. National Cooperative Highway Research Program, Transportation Research Board, March (2010)

5. Ishaque, M.M., Noland, R.B.: Behavioural issues in pedestrian speed choice and street crossing behaviour: a review. *Transp. Rev.* **28**(1), 61–85 (2008)
6. Waizman, G., Shoval, S., Benenson I.: Micro-simulation model for assessing the risk of car-pedestrian road accidents. *J. Intell. Transp. Syst.: Technol. Plann. Oper.* (2013)
7. Astarita, V., Guido, G., Vitale, A., Giofré, V.: A new microsimulation model for the evaluation of traffic safety performances. *Eur. Transp. Trasporti Europei* (Issue 51), Paper No 1. ISSN: 1825-3997 (2012)
8. Zhang, H.C., Liang, X., Xu, K.: VISSIM network simulation under actuated signal control. *J. Comput. Inf. Syst.* **10**(4), 1573–1580 (2014)
9. Dowling, R., Skabardonis, A., Halkias, J., McHale, G., Zammit, G.: Guidelines for calibration of microsimulation models: framework and application. In: *Proceedings of the 83rd Annual Meeting of the Transportation Research Board, Washington, D.C.* (2004)
10. Thiemann, C., Treiber, M., Kesting, A.: Estimating acceleration and lane-changing dynamics based on NGSIM trajectory data. *Transp. Res. Rec.: J. Transp. Res. Board* **2088**, 90–101 (2008)
11. Huang, S., Sadek, A.W.: Artificial intelligence and microscopic traffic simulation- models applications to parameter calibration and origin–destination estimation. *Artificial intelligence applications to critical transportation issues. Transp. Res. Circ. E-C168* (2012). ISSN: 097-8515
12. Cunha, A.L., Bessa, J.E., Setti, J.R.: Genetic algorithm for the calibration of vehicle performance models of microscopic traffic simulators. *Prog. Artif. Intell.* **5816**, 3–14 (2009)
13. Huang, S., Sadek, A.W., Casas, I., Guo, L.: Calibrating travel demand in large-scale micro-simulation models with genetic algorithms: A TRANSIMS model case study. Presented at 89th Annual Meeting of the Transportation Research Board, Washington, D.C. (2010)
14. Huang, S., Sadek, A.W., Casas, I., Guo, L.: Calibrating travel demand in large-scale micro-simulation models with genetic algorithms: aTRANSIMS model case study. Presented at 89th Annual Meeting of the Transportation Research Board, Washington, D.C. (2010)
15. Kattan, L., Abdulhai, B.: Noniterative approach to dynamic traffic origin–destination estimation using parallel evolutionary algorithms. *Transp. Res. Rec.: J. Transp. Res. Board* 1964, 201–210. Transportation Research Board of the National Academies, Washington, D.C. (2006)
16. Avram, C., Machado, J., Astilean, A.: Modeling and formal analysis of urban road traffic. In: *11th International Conference of Numerical Analysis and Applied Mathematics (ICNAAM) in 11th International Conference on Numerical Analysis and Applied Mathematics 2013, pts 1 and 2 (ICNAAM 2013), vol. 1558* (2013)

Part IX
Vibration Control

Brain Emotional Learning Based Control of a SDOF Structural System with a MR Damper

Manuel Braz César, José Gonçalves, João Coelho
and Rui Carneiro de Barros

Abstract This paper describes the application of a Brain Emotional Learning (BEL) controller to improve the response of a SDOF structural system under an earthquake excitation using a magnetorheological (MR) damper. The main goal is to study the performance of a BEL based semi-active control system to generate the control signal for a MR damper. The proposed approach consists of a two controllers: a primary controller based on a BEL algorithm that determines the desired damping force from the system response and a secondary controller that modifies the input current to the MR damper to generate a reference damping force. A parametric model of the damper is used to predict the damping force based on the piston motion and also the current input. A Simulink model of the structural system is developed to analyze the effectiveness of the semi-active controller. Finally, the numerical results are presented and discussed.

Keywords Semi-active control · Brain Emotional Learning · MR damper

M.B. César (✉) · J. Gonçalves · J. Coelho
Polytechnic Institute of Bragança, Bragança, Portugal
e-mail: brazcesar@ipb.pt

J. Gonçalves
e-mail: goncalves@ipb.pt

J. Coelho
e-mail: jpcoelho@ipb.pt

M.B. César · R.C. de Barros
CONSTRUCT R&D Unit, Faculty of Engineering of the University of Porto,
Porto, Portugal
e-mail: rcb@fe.up.pt

J. Gonçalves · J. Coelho
INESC-TEC, Porto, Portugal

R.C. de Barros
Faculty of Engineering of the University of Porto, Porto, Portugal

1 Introduction

Over the last two decades many R&D projects have been devoted to develop vibration control systems for civil structures. Passive and active control systems are two well-known methodologies to mitigate wind and/or seismic-induced vibrations in slender and tall structures. In the last years, semi-active and hybrid control systems have been studied and proposed as a feasible alternative to traditional control approaches. Also, advanced controllers or soft computing techniques have been studied to take full advantage of these control systems.

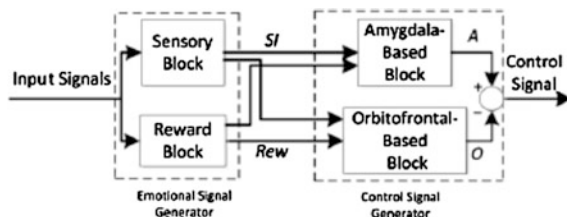
In this regard, this study presents the application of a bio-inspired semi-active control system based on the brain limbic system of the human brain. A single-story, one-bay frame (SDOF system) with a MR damper located between the base and the top floor will be used to investigate the effectiveness of the proposed controller. In this case, the sensor and the actuator are placed in the same position and the control system has a collocated configuration. Initially, the uncontrolled response of the SDOF system the NS component of the El Centro earthquake loading was obtained, which is used as the reference response for the remaining numerical simulations. Then, passive and semi-active control modes are used to assess the efficiency of the proposed control strategy in reducing the response of the structural system. The modified Bouc-Wen model of a commercial MR damper (RD-1005-3 model) was used to represent the actuator in a passive configuration.

2 Brain Emotional Learning Controller

The Brain Emotional Learning (BEL) controller is a bio-inspired control algorithm based on the emotional learning mechanism of the brain limbic system, which has been employed to develop feedback controllers for complex control problems [1–4]. Basically, the BEL controller contains four main components: the amygdala (Am), the orbitofrontal cortex (OC), the sensory cortex (SC) and the thalamus (Th). The main control blocks of the BEL controller are illustrated in Fig. 1.

The amygdala and the orbitofrontal cortex are used to process the emotional signal (SE) while the sensory cortex and the thalamus receive and processes sensory inputs (SI). Sensory inputs (SI) are processed in the thalamus initiating the process of response to stimuli and passing those signals to the amygdala and the sensory

Fig. 1 Basic structure of Brain Emotional Learning controller [4]



cortex. Then, the sensory cortex operates by distributing the incoming signals properly between the amygdala and the orbitofrontal cortex. In this controller, the learning procedure is mainly processed in the orbitofrontal cortex and is based on the difference between an expected punishment or reward and the received punishment or reward (Rew). The perceived punishment/reward (ES) is processed in the brain using learning mechanisms while the received punishment/reward represents an external input. If these signals are not identical, the orbitofrontal cortex inhibits and restrains the emotional response for further learning. Otherwise, the controller generates an output response [1, 2]. An important feature of this controller is its ability to gradually learn to deal with new situations and also the low computational requirements compared with other advanced controllers, which make the BEL controller particularly suitable to design real-time control and decision systems. Thus, the BEL controller presents significant advantages that can be exploited to design advanced control systems, particularly structural control systems for civil engineering applications. In what follows, a semi-active control system was developed based on this bio-inspired controller. A Simulink model of the proposed BEL controller is depicted in Fig. 2.

The principle of operation of the BEL controller can be summarized as follows: Sensory inputs (SI) enter through the thalamus, which has the task of initiating the process of a response to stimuli, and then pass those signals to the amygdala and the sensory cortex. The sensory cortex operates by distributing the incoming signals appropriately between the amygdala and the orbitofrontal cortex. The learning procedure is mainly processed in the orbitofrontal cortex and is based on the difference between an expected punishment/reward and the actual received punishment/reward (Rew). The perceived reward/punishment is developed in the brain using learning mechanisms while the received reward/punishment is an

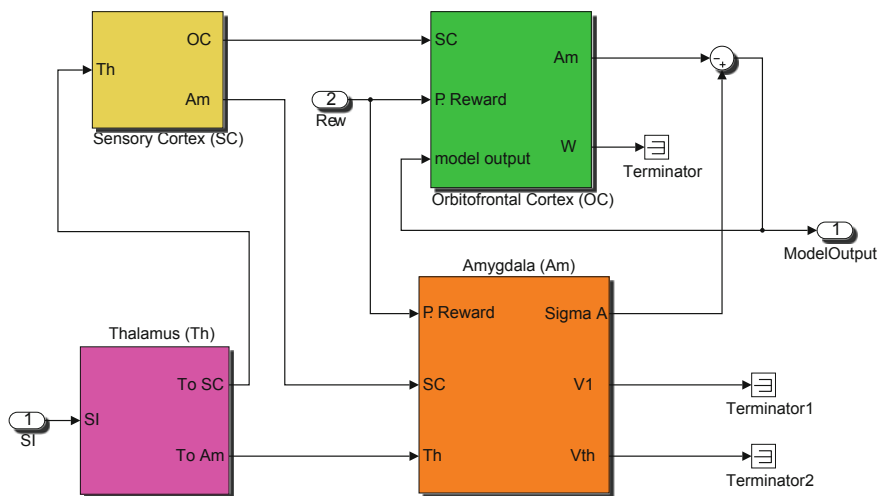


Fig. 2 Simulink model of the BEL controller

external input. If these signals are not identical, the orbitofrontal cortex inhibits and restrains the emotional response for further learning otherwise the controller produces a response output [1, 2].

The design procedure of a BEL based controller requires the definition of some model parameters to obtain the required control action. First, the sensory input signal should be adjusted before being forwarded to the sensory cortex. This modification is obtained using

$$A_i = G_{A,i} \cdot SI_i \quad (1)$$

$$OC_i = G_{OC,i} \cdot SI_i \quad (2)$$

where, $G_{A,i}$ and $G_{OC,i}$ represent gains of the amygdala and the orbitofrontal cortex, respectively. Then, the amygdala and the orbitofrontal cortex learning processes occur through their internal weights update rule given by

$$\frac{dG_{Am,i}}{dt} = \alpha \cdot SI_i \cdot \max(0, ES - \sum A_{m,i}) \quad (3)$$

$$\frac{dG_{OC,i}}{dt} = \beta \cdot SI_i (MO - ES) \quad (4)$$

where α is the learning rate of Amygdala, β is the learning rate of orbitofrontal cortex, ES and MO are the emotional signal and the model output, respectively. The main drawback in designing this type of controller is mainly related with the appropriate definition of the emotional and the sensory signals so that they are able to approximately represent the state and the objective of the system and allowing the control system to achieve the best performance. Although there are several optimization procedures available for tuning these parameters, a common approach is to use a trial-and-error procedure.

3 Numerical Simulations

Consider the mass-spring-damper system excited by an earthquake loading as shown in Fig. 3. The SDOF system represents a scaled structure with the following properties: mass, $m = 1000$ kg; stiffness, $k = 404,200$ N/m and damping coefficient, $\zeta = 0.02$.

In this case, the motion of the mass is defined by the absolute displacement $x_1(t)$ and consequently the relative displacement between the mass and the ground is given by $x(t) = x_1(t) - x_g(t)$, where $x_g(t)$ represent the absolute displacement of the ground. Thus, using a state space formulation, the equation of motion can be written as

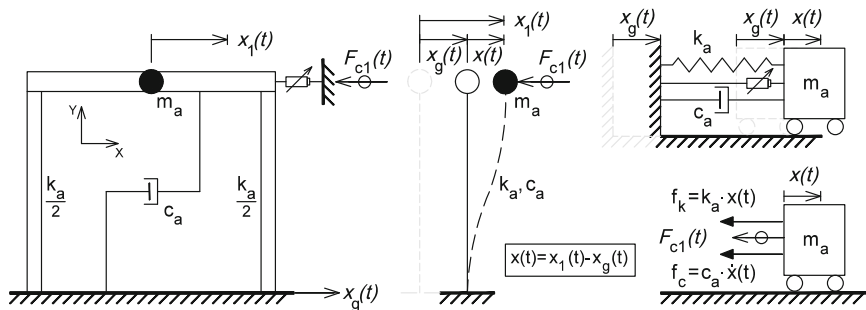


Fig. 3 SDOF system with a MR damper under earthquake excitation

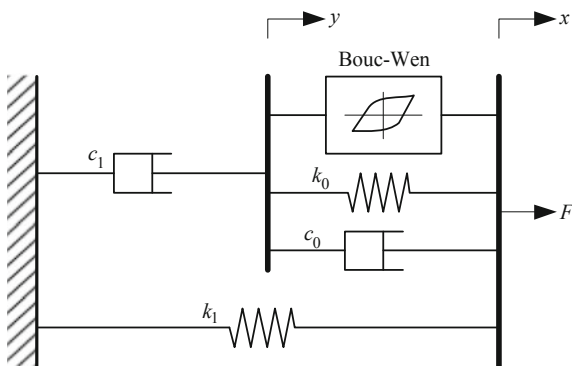
$$z(t) = \begin{Bmatrix} \dot{x}(t) \\ \ddot{x}(t) \end{Bmatrix} = \begin{bmatrix} 0 & 1 \\ -k/m & -c/m \end{bmatrix} \begin{Bmatrix} x(t) \\ \dot{x}(t) \end{Bmatrix} + \begin{Bmatrix} 0 \\ -1/m \end{Bmatrix} f_c(t) + \begin{Bmatrix} 0 \\ -1 \end{Bmatrix} \ddot{x}_g(t) \quad (5)$$

and response can be calculated using the state space output vector

$$y(t) = \begin{Bmatrix} x(t) \\ \dot{x}(t) \\ \ddot{x}(t) \end{Bmatrix} = \begin{bmatrix} 1 & 0 \\ 0 & 1 \\ -k/m & -c/m \end{bmatrix} \begin{Bmatrix} x(t) \\ \dot{x}(t) \end{Bmatrix} + \begin{Bmatrix} 0 \\ 0 \\ -1/m \end{Bmatrix} f_c(t) + \begin{Bmatrix} 0 \\ 0 \\ -1 \end{Bmatrix} \ddot{x}_g(t) \quad (6)$$

As can be seen, the system is being controlled by a generic actuator whose effect is defined by the control force $f_c(t)$ included into the equation of motion. In this case, the actuator is a MR damper that can be operated as a passive or semi-active device. In this type of smart damping devices, the viscosity of the MR fluid within the damper can be controlled depending on a prescribed input voltage or current. There are several numerical models to represent the hysteretic behavior of MR dampers. A common approach is to use the modified Bouc-Wen model represented in Fig. 4 [5].

Fig. 4 Schematic representation of the modified Bouc-Wen model



The numerical formulation of this parametric and the corresponding model parameters are described by the following equations

$$F(t) = c_1 \dot{y} + k_1(x - x_0) \quad (7)$$

$$\dot{y} = \frac{1}{c_0 + c_1} [\alpha z + c_0 \dot{x} + k_0(x - y)] \quad (8)$$

$$\dot{z}(t) = -\beta |\dot{x}(t)| |z(t)|^{n-1} - \gamma \dot{x}(t) |z(t)|^n + A \dot{x}(t) \quad (9)$$

The model parameters are defined based on experimental tests and some parameters are current (or voltage) independent, i.e., their values are not significantly affected by the magnetic field applied to the MR fluid. A commercial MR damper (RD-1005-3 by Lord Corp., USA) was experientially tested to obtain the model parameters [6]. In this case, the current/voltage independent parameters are $A = 10.013$, $\beta = 3.044 \text{ mm}^{-1}$, $\gamma = 0.103 \text{ mm}^{-1}$, $k_0 = 1.121 \text{ N/mm}$, $f_0 = 40 \text{ N}$ and $n = 2$. The remaining parameters are current dependent and can be defined by the following polynomial expressions

$$\alpha(I) = -826.67I^3 + 905.14I^2 + 412.52I + 38.24 \quad (10)$$

$$c_0(I) = -11.73I^3 + 10.51I^2 + 11.02I + 0.59 \quad (11)$$

$$c_1(I) = -54.40I^3 + 57.03I^2 + 64.57I + 4.73 \quad (12)$$

A first-order time lag involved in the current driver/electromagnet during a step command signal is also included in the numerical model of the device, which in this case is defined by a first order filter ($\eta = 130 \text{ s}^{-1}$).

The SDOF system will be now subjected to the 1940 N-S component of the El-Centro earthquake time history (peak acceleration of 3.42 m/s^2). Since the current SDOF system represents a scaled structure, the earthquake signal needs to be decreased to represent the magnitude of displacements that would be observed in experiments tests. In this particular case, the time was scaled to 50 % of the full-scale earthquake time history as shown in Fig. 5.

It is important to notice that MR dampers are semi-active devices in the sense that they are passive actuators with adjustable properties. Also, they cannot be directly controlled to generate a specific damper force because the damper response is dependent on the local motion of the structure where the device is located. A practical approach to control the MR damper is to adjust the voltage applied to the current driver to increase or decrease the damper force [7]. A Simulink model of the proposed semi-active BEL controller was developed as shown in Fig. 6.

The BEL block represents the primary controller that computes the required control action and the clipping block is a secondary control unit that adjusts the desired damping force to the MR damper control signal (operating current). The Simulink model of the BEL controller is shown in Fig. 7.

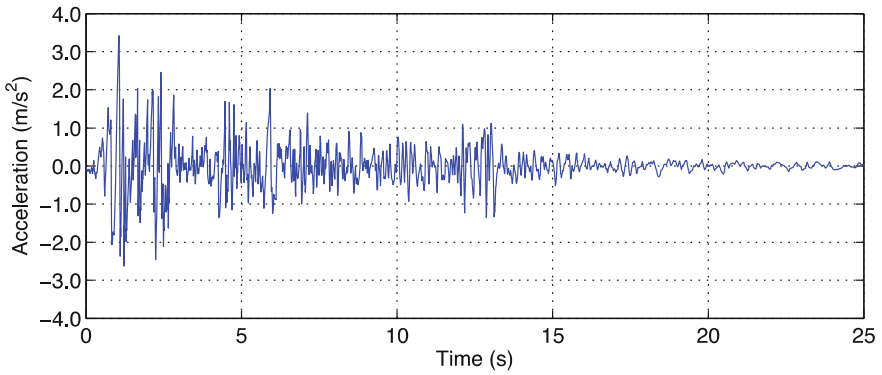


Fig. 5 Time-scaled N-S component of El-Centro earthquake ground motion

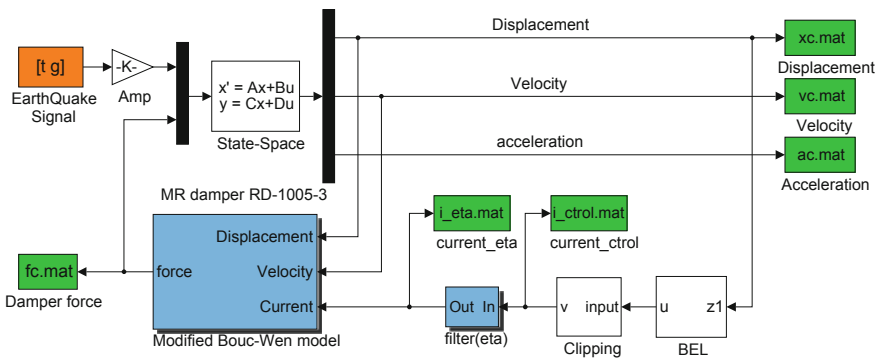


Fig. 6 Simulink model of the BEL control system

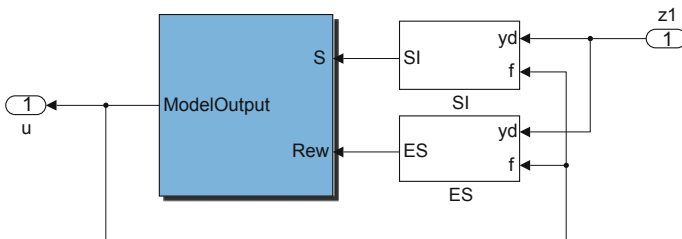


Fig. 7 Simulink model of the BEL controller for the SDOF system

In this case the sensory input (SI) and the emotional signal (ES) can be related with the system response y_d and the BEL model output u , which are determined by

$$SI = w_1 y_d + w_2 u \quad (13)$$

$$ES = w_3 y_d + w_4 \int u dt \quad (14)$$

where w_i are weight factors that define the relative importance given to the drift response ($z_1 = y_d$) and the output of the BEL controller ($f = u$). The sensory and emotional outputs are forwarded as the stimuli and the reward/punishment for the BEL controller, respectively. Finally, the BEL control block uses this information to construct a response (model output) that represents the control action. The learning rates (α and β) represent model parameters that must be adjusted in accordance with the input variables to achieve the required control action. The main drawback of the BEL controller is related essentially with the appropriate definition of emotional and sensory signals that are able to represent with sufficient precision the system state and the control objective in order to maximize the performance of the control system. In this study, the learning rates for the amygdala and orbito-frontal cortex are defined as $\alpha = 1$ and $\beta = 1$, respectively. The sensory and the emotional outputs are determined by applying weight factors $w_1 = 2$, $w_2 = 1$, $w_3 = 2$ and $w_4 = 1$, which provide the best results for the SDOF system under control and were found after a trial-and-error procedure.

4 Results

The MR damper will be used in both passive and semi-active configurations, i.e., with a constant operating current during the numerical analysis and in a controllable mode in which the semi-active BEL controller is used to determine the control action.

Two passive configurations are used: Passive OFF, a passive control mode in which the MR damper is operating with zero input current (i.e., $I = 0.00$ A) and Passive ON, a passive configuration in which the MR damper has a constant current $I = 0.50$ A (selected as the maximum operating level).

The time responses obtained with the BEL control algorithm along with the uncontrolled responses are displayed in Fig. 8. In general terms, the results demonstrate that the BEL controller is effective in commanding the MR damper allowing a significant reduction of the structural response.

The damper force and the corresponding control signal times histories obtained with the BEL controller are presented in Fig. 9. As can be observed in the Simulink model of the control system, a clipping unit is responsible to change the controller output to a bi-state control output (minimum and maximum operating current) compatible with the semi-active control operation of the MR damper. This principle

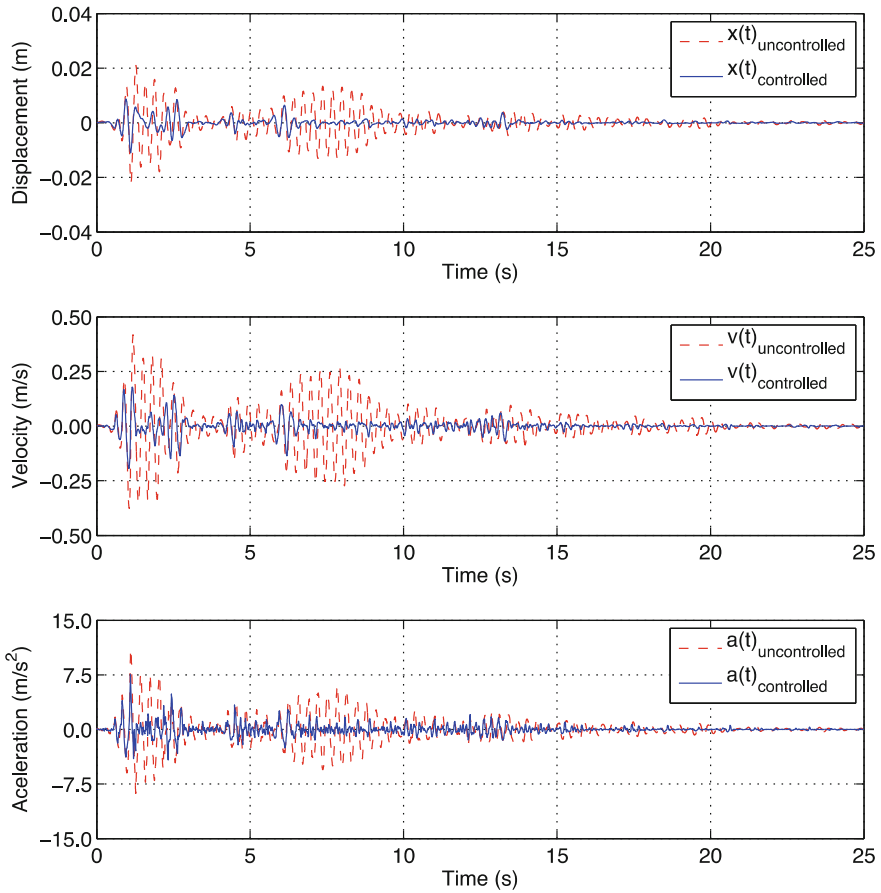


Fig. 8 Structural response obtained with the semi-active BEL controller

is analogous to that used in other clipped based controllers and therefore the present control strategy can be classified as a clipped-BEL controller.

The evaluation criteria are based on a comparison of the peak responses of the controlled system to those of the uncontrolled system, passive OFF and ON cases. The results of achieved with this analysis are summarized in Table 1.

Regarding the passive control mode, it can be seen that the passive OFF configuration has almost no effect in the system response, especially in reducing the peak acceleration (around 3 %). The passive ON mode has a major effect in the system response that results in peak responses being significantly reduced (around 60 % in peak displacement/velocity and 40 % in peak acceleration). The clipped-BEL controller presents a significant improvement over the passive OFF case but is not as effective as the passive ON case. This is related with the weighting parameters used in this study.

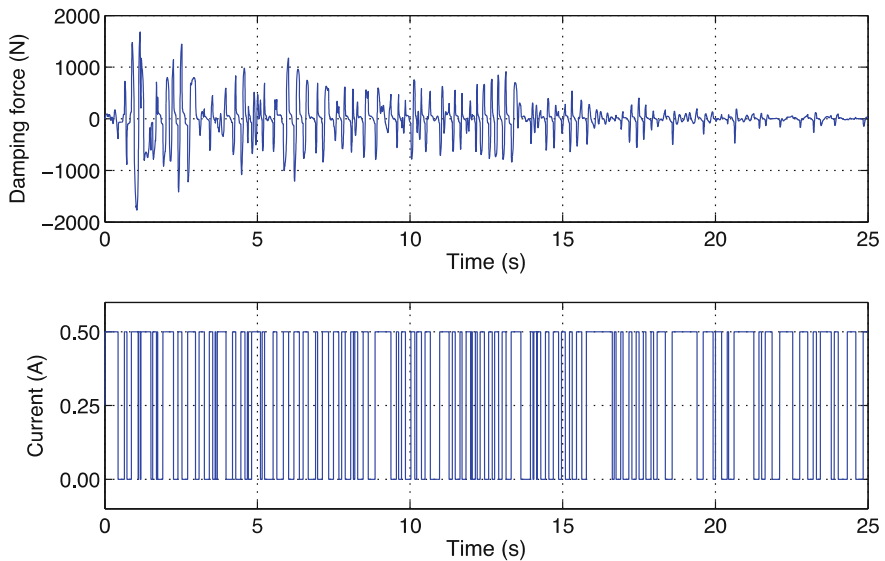


Fig. 9 Damper force and corresponding operating current (BEL controller)

Table 1 Peak responses under the time-scaled El-Centro earthquake

Control strategy		x (m)	\dot{x} (m/s)	\ddot{x} (m/s ²)	f (N)
Uncontrolled		0.0221 (1.00)	0.4184 (1.00)	10.761 (1.00)	–
Passive OFF	Modified Bouc-Wen	0.0203 (0.09)	0.3859 (0.08)	10.475 (0.03)	261.5
Passive ON	Modified Bouc-Wen	0.0093 (0.59)	0.1573 (0.62)	6.8376 (0.36)	1542.9
Clipped-BEL		0.0110 (0.50)	0.1934 (0.54)	7.5481 (0.30)	1768.1

Note values under parenthesis represent the percentage of response reduction

As already stated, the main drawback regarding the implementation of the BEL based control system is related with the optimization of the controller parameters. The selection of appropriate weight factors is decisive to obtain the best performance of the BEL controller. This can be done by using an optimization technique (e.g., genetic algorithms) instead of the trial-and-error procedure used in this case. Nevertheless, it was verified that the proposed BEL controller can be implemented in structural control systems with MR dampers, although further research is required to improve the performance of the proposed controller in order to take advantage of the properties of this type of controllable devices. It is also important to mention that this is a SDOF structure with a collocated control system (variable damping system) and therefore the outcome of the variable damping system is not as effective or visible as for multi-DOFs structural systems.

5 Conclusions

A Brain Emotional Learning based semi-active control system was implemented to reduce the response of a SDOF structure. It was verified that the BEL controller was able to reduce the system response compared with the uncontrolled case and the passive OFF control mode. However, the performance of the proposed controller was not as good as using the MR damper in a passive ON mode. This poor performance is mainly related with a weak weighting parameter optimization procedure. Despite that, this study has proven the potential of the BEL algorithm to develop semi-active control system for structural applications. The main advantage of the proposed BEL controller is that only the drift response of the structure is required to determine the control action, i.e., in this SDOF structural system only the floor displacement need to be measured. This can be a significant advantage for multi-DOFs systems.

References

1. Lucas, C., Shahmirzadi, D., Sheikholeslami, N.: Introducing BELBIC: brain emotional learning based intelligent. *Int. J. Intell. Autom. Soft Comput.* **10**, 11–21 (2004)
2. Shahmirzadi, D.: Computational Modeling of the Brain Limbic System and its Application in Control Engineering. Texas A & M University, Thesis (2005)
3. Javan Roshtkhari, M., Arami, A., Lucas, C.: Emotional control of inverted pendulum system. In: *A Soft Switching from Imitative to Emotional Learning*, pp. 651–656 (2009)
4. Garmsiri, N., Sepehri, N.: Emotional learning based position control of pneumatic actuators. *Intell. Autom. Soft Comput.* **20**(3) (2014)
5. Spencer Jr., B.F., Dyke, S.J., Sain, M.K., Carlson, J.D.: Phenomenological model of a magnetorheological damper. *J. Eng. Mech.* **123**, 230–238 (1997)
6. Braz César, M., Barros, R.: Experimental behaviour and numerical analysis of MR dampers. In: *15WCEE—15th World Conference on Earthquake Engineering*, Lisbon, Portugal, 2012
7. Jansen, L.M., Dyke, S.J.: Semiactive control strategies for MR dampers: a comparative study. *J. Eng. Mech. ASCE* **126**(8), 795 (2000)

Pendulum TMD's in Building Vibration Control

Rui Carneiro de Barros and Catarina M.A. Sousa

Abstract The theory behind small amplitude movement of a pendulum is stated, followed by construction of a simple example with two degrees of freedom including the unidirectional movement of the structure and the pendulum angle in relation to vertical. This simple model and the finite elements software *SAP2000* are also applied to a multiple degree of freedom one bay-frame building. The application of the pendulum TMD to control the building vibrations is validated by numerical modelling. An additional case with a more complex model was also studied, comprising a reaction tower of a transmission tower testing station which dynamic behavior under wind action is benefited from placement of a pendulum TMD. The numerical modelling of the studied indicate that the application of pendulum TMD's is worthwhile in civil engineering structures.

Keywords TMD's • Pendulum • Vibration control

1 Introduction

The interest to control the dynamic responses of civil engineering structures is found in various aspects, from the rehabilitation of existing buildings enabling them to withstand new levels of demand in service limit states under wind action, to the guarantee not to collapse of fundamental structures operating in a city under the occurrence of major earthquakes, to even material savings in the construction of new structures guaranteeing the resistance and the stability of such systems by devices not included in the original structure [1].

R.C. de Barros (✉)

FEUP-Faculty of Engineering, University of Porto, Department of Civil Engineering,
Structural Division, Porto, Portugal
e-mail: rcb@fe.up.pt

C.M.A. Sousa

Constructure Ltd, 15 Bell Yard Mews, London SE1 3TY, England, UK
e-mail: catarina.mas@gmail.com

This control can be embodied in various ways including acting on the characteristics of the structure, changing its natural frequency and rigidity, although this change is often difficult to achieve due to architectural and material constraints. Another current and feasible way to achieve structural vibration control, is the introduction of devices forming external control systems under two main types of systems: passive control systems and active control systems; other variations of these are the semi-active systems and the hybrid systems.

Passive control systems and techniques use devices that do not require external energy source to operate them. Current examples of these passive systems are the base isolation devices, tuned mass dampers (TMD) and tuned liquid dampers (TLD).

The base isolation devices are directed only to control of dynamic response in the event of an earthquake, and the operating principle of these devices is based upon a frequency shift. In fact the fundamental frequency of structure vibration is increased through the introduction of blocks of large vertical stiffness and reduced horizontal stiffness, at the connections of the structure to the foundation.

In the case of TMDs typically is used a secondary mass (which may be a concrete block or even a water tank) attached to the main frame by means of springs and small additional buffers or dampers, giving the overall system the required dissipative capacity for the structure to have a satisfactory response when subjected to dynamic actions.

The TLDs are a particular case of the TMDs in which the liquid is used to conceal all the features necessary for the secondary structure, such as mass and damping capacity through viscous damping action.

The active damping systems seeks to impose forces or displacements in strategic points of the structure according to measurements made in real time or according to a history of measurements. This control system requires a system of sensors, signal processing, control strategy and a system that can trigger responses in real time, that is requires a major source of external power. The semi-active control systems combine the main advantages of active and passive systems but require less amount of outside energy, and can even run on batteries resources, which makes them very effective in the event of general power distribution faults and cut-offs. Hybrid systems consist in most cases on the simultaneous operation of passive and active systems.

So this work focuses primarily on the operation of TMDs, and in particular in the case of pendulum TMDs, wherein the TMD is materialized in a body (usually spherical) attached to the end of a wire, forming a flywheel pendulum fixed to the structure. The main feature of the pendulum is its oscillation frequency that depends entirely on the length of wire (when the wire is of negligible weight and without rotational stiffness), which often requires excessively large lengths of wire. If it is impossible to implement the required length leading to an optimal tuning, it is possible to achieve positive results for some cases, although the pendulum is not working at its possible full efficiency.

2 Theoretical Background and Pendulum Equations

2.1 Background on TMDs for SDOF Systems

Den Hartog [2] was among the first mechanical engineering researchers that addressed the control of vibrations of a primary major structure by using a secondary structure (TMD), whose existence would affect and reduce the dynamic amplification factor of the primary structure. When the primary system has no damping, the optimal parameters of the secondary TMD structure are such that the optimal frequency ratio α_{opt} between the natural frequency of the secondary structure (TMD) and the natural frequency of the primary structure is given by

$$\alpha_{opt} = \frac{1}{1 + \mu} \quad (1)$$

where μ is the mass ratio between the mass of the secondary structure (TMD) and the primary structure to be controlled.

Accordingly, a good estimate of the optimal critical damping factor ζ_{opt} required for the secondary structure (TMD) also based upon the philosophy of minimizing the dynamic amplification factor of the primary structure, is given by

$$\zeta_{opt} = \sqrt{\frac{3\mu}{8(1+\mu)^3}} \quad (2)$$

The structures in reality always have some damping, however small it may be. In the case of buildings, bridges and large structures, it is desirable that they should have a considerable damping, since the dynamic loads that they are subjected to usually vary significantly in the range of excitation frequencies, and there could be cases of quite disturbing resonances.

For the cases where the primary systems have some damping, and providing that the critical damping factor of the primary structure is below 1 %, solutions for the optimal secondary structure (TMD) parameters are still possible based upon the philosophy of minimizing the dynamic amplification factor of the primary structure.

In the general case when the critical damping factor of the primary structure is above 1 %, either empirical formulations should be used with minor approximation errors, or alternatively use the following non-linear graphs or abacus (Figs. 1 and 2) of the numerical solutions that were obtained with expression of the dynamic amplification factor of the primary structure [3].

The later non-linear abacus constitute the most adequate and practical method for determining the optimal parameters of the secondary structure (TMD) from the selected mass ratio μ and the given critical damping factor of the primary structure ζ_1 .

It should be beard in mind that the tuning sensitivity of the frequency ratio values is much higher than the one for the critical damping factor values; this

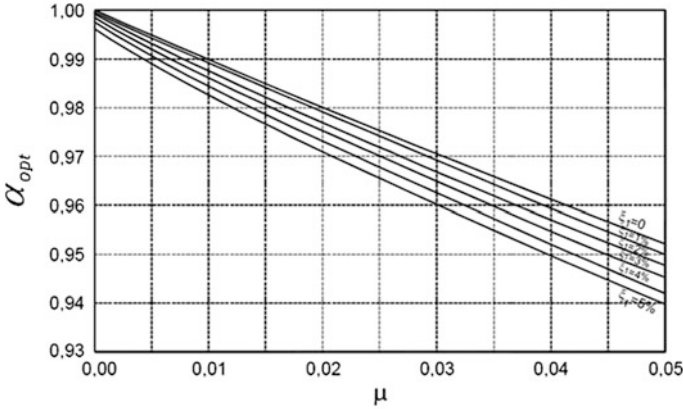


Fig. 1 Non-linear curves for obtaining the optimal frequency ratio. Source Barros et al. [3]

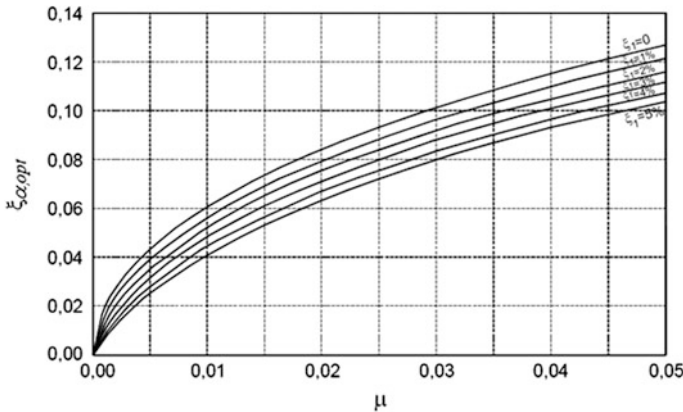


Fig. 2 Curves for obtaining the optimal critical damping factor. Source Barros et al. [3]

implies that a greater care is needed in determining the value of the stiffness of the secondary system.

2.2 Background on TMDs for MDOF Systems, with One Degree Equivalencies

The tuning of a TMD according to the process described above is only valid for single degree of freedom systems (SDOF); but as it is known, most civil engineering structures have multiple degrees of freedom (MDOF). Through a modal analysis it is possible to obtain various systems of one degree of freedom and

therefore it is possible to tune a TMD to each of these systems SDOF; on doing so, it would be necessary to determine the values of mass, stiffness and damping corresponding to each mode.

But to evaluate these modal quantities for each vibration mode, it is needed to determine the configuration of the vibration mode which is possible only arbitrating a component of the vibration mode to which correspond infinite configurations with same proportionalities between components. This myriad of possible solutions leads also to infinite number of possible values for the modal mass, modal stiffness and modal damping. Therefore it should be adopted as a criterion for standardization of these modal settings, by normalizing the modes by setting a unit value in the component for the degree of freedom corresponding to the implementation of the TMD [1, 3].

Taking the example of a multi-story building wherein the first mode is dominant in the wind response to lateral actions, studies by Kwok and Samali [4] showed that the vibration modes controlled by TMDs experience significant decreases in their response contributions and that the vibration of higher order modes are not affected.

Using the same example of a multi-story building now under the influence of seismic action, studies by Wirsching and Campbell [5] (to minimize the response to the first mode through the design of the optimal parameters of TMDs for a building of one, five and ten stories) showed that: (i) the optimal value of the stiffness of the TMD becomes less and less sensitive to changes in the structural damping and in the mass ratio, as the number of stories increases; (ii) the optimum value of the critical damping factor for the TMD, is not sensitive to the value of structural damping of the primary structure, even in case of buildings with just one floor [4].

2.3 Background on Pendulum Equations

Pendulum TMD are quite specific in relation to the classic common TMD, since they are not connected by springs to the primary main system; therefore the pendulum stiffness cannot be determined in a classical way, as this depends on the length of wire or bars that bind the secondary mass (the pendulum TMD) to the main primary structure.

Three distinct pendulum configurations cases were considered by the second author [1] and their corresponding mathematical equations of motion were obtained using the Euler-Lagrange formulation of classical mechanics. Such three pendulum cases were respectively: (i) simple pendulum (Fig. 3i); (ii) coupled pendulum harmonically forced (Fig. 3ii); (iii) coupled pendulum with a base motion excitation (Fig. 3iii).

When an isolated pendulum (Fig. 3i), with a possible rotation spring (of stiffness k_m) at the suspension point, is subjected to an exterior horizontal force $F_a(t)$, the known equation of motion of such simple pendulum is given by:

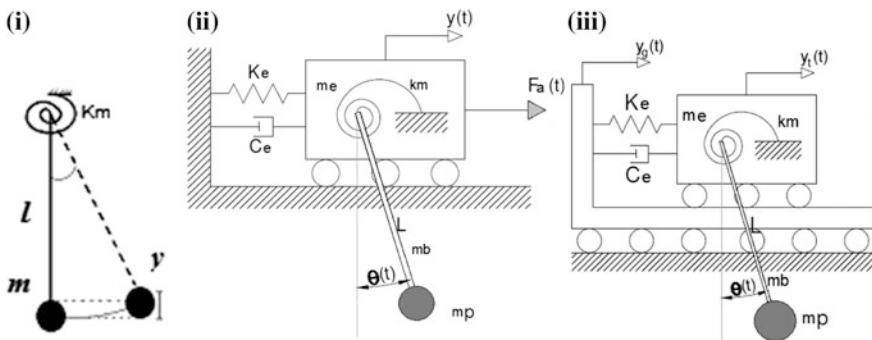


Fig. 3 Pendulum models considered: **i** simple pendulum; **ii** coupled pendulum acted by force; **iii** coupled pendulum with base motion of the support

$$m l^2 \ddot{\theta} + (k_m + m g l)\theta = F_a(t) l \tag{3}$$

The natural frequency is expressed by one of the following expressions: the former, for a pendulum with a rotation spring at the suspension point; the later, for a simple pendulum (when such spring does not exist).

$$\omega = \sqrt{\frac{k_m + m g l}{m l^2}} \quad \text{or} \quad \omega = \sqrt{\frac{g}{l}} \tag{4}$$

Figure 3ii represents a SDOF system with a coupled pendulum, constituting a MDOF system with 2 degrees of freedom. The pendulum is a rigid bar with uniformly distributed mass of total value m_b , also with a concentrated mass m_p at its bottom tip materialized as a sphere of radius R_p . This coupled system is subjected to a horizontal harmonic force $F_a(t)$, acting on the primary system whose displacement is $y(t)$.

The equations of motion of this coupled pendulum with harmonic force are given in Eqs. (5) and (6). Notice that the coupled pendulum with base-motion excitation has distinct equations of motion [1], but Eq. (7) is general in calculating the natural frequency of the coupled pendulum secondary structure.

$$(m_e + m_b + m_p)\ddot{y} + \left(m_p(R_p + l_b) + \frac{1}{2}m_b l_b\right)\ddot{\theta} + C_e\dot{y} + K_e y = F_a(t) \tag{5}$$

$$\begin{aligned} &\left(\frac{1}{3}m_b l_b^2 + \frac{2}{5}m_p R_p^2 + m_p(R_p + l_b)^2\right)\ddot{\theta} + \left(m_p(R_p + l_b) + \frac{1}{2}m_b l_b\right)\ddot{y} \\ &+ k_m \theta + \left(m_p(R_p + l_b) + \frac{1}{2}m_b l_b\right)g\theta = 0 \end{aligned} \tag{6}$$

$$\omega = \sqrt{\frac{k_m + (m_p(R_p + l_b) + \frac{1}{2}m_b l_b)g}{\frac{1}{3}m_b l_b^2 + \frac{2}{3}m_p R_p^2 + m_p(R_p + l_b)^2}} \quad (7)$$

The natural frequency of the pendulum is invariant with respect to changes of the type of actions that excite or force to vibrate the primary structural system [1].

3 Application of a Pendulum TMD to Calibration Frames

3.1 Pendulum TMD on SDOF and MDOF Shear Frames

In order to demonstrate the applicability of this type of pendulum TMD to some didactic hypothetical frame for numerical calibration tests, a SDOF shear frame 2 m high and 2 m wide span was considered made of concrete (mass density 2500 kg/m³); the floor beam is a 12 cm × 26 cm rectangular section, and the two equal square columns (built-in at the base and at the floor level) are 3 cm wide. The columns total stiffness is 4050 N, and the total mass for sway dynamic analysis (considering only half of the column's masses concentrated or lumped at the floor) is 160.5 kg. With these data, the natural frequency of the primary shear frame is 0.7995 Hz. This same natural frequency was obtained when modelling the frame by the finite element analysis software SAP 2000 (Fig. 4). This figure also shows the SDOF shear frame acted at the floor level, by a horizontal harmonic force, almost resonance with the primary frame and expressed by $F(t) = 10 \sin(2\pi(0.8)t)$. For numerical purposes, a damping factor of 0.01 (or 1 % of critical) was used for this test demonstration frame.

Designing a simple pendulum TMD with mass ratio $\mu = 0.01$ for optimal tuning of this test frame led to the use of a wire length of 1.091 m as well as a rotation spring stiffness of 30 Nm/rad at the hanging point. Other non-optimal configurations can also be used, with different efficiencies, whose results are graphically shown in Fig. 5 [1].

A second example considers the use of one or two pendulum TMD to control the lateral vibrations of a 10 floor MDOF shear building, acted upon by harmonic forces in every floor almost resonant with the fundamental frequency of the building, with decreasing amplitudes from 3.5 kN in top floor to 0.35 kN in first floor. The MDOF building data is detailed by Sousa [1], also with the 12 natural frequencies and modes shapes.

A schematic view of the 10 floor MDOF shear-frame as well as of the building inter-story characteristics are given in Fig. 6. Also Fig. 7 details part of the output of SAP 2000 software, concerning the values of the 12 first natural frequencies (Hz).

The maximum top floor displacement and acceleration responses, for the set of harmonic forces considered, will be reduced by using a pendulum TMD at top floor.

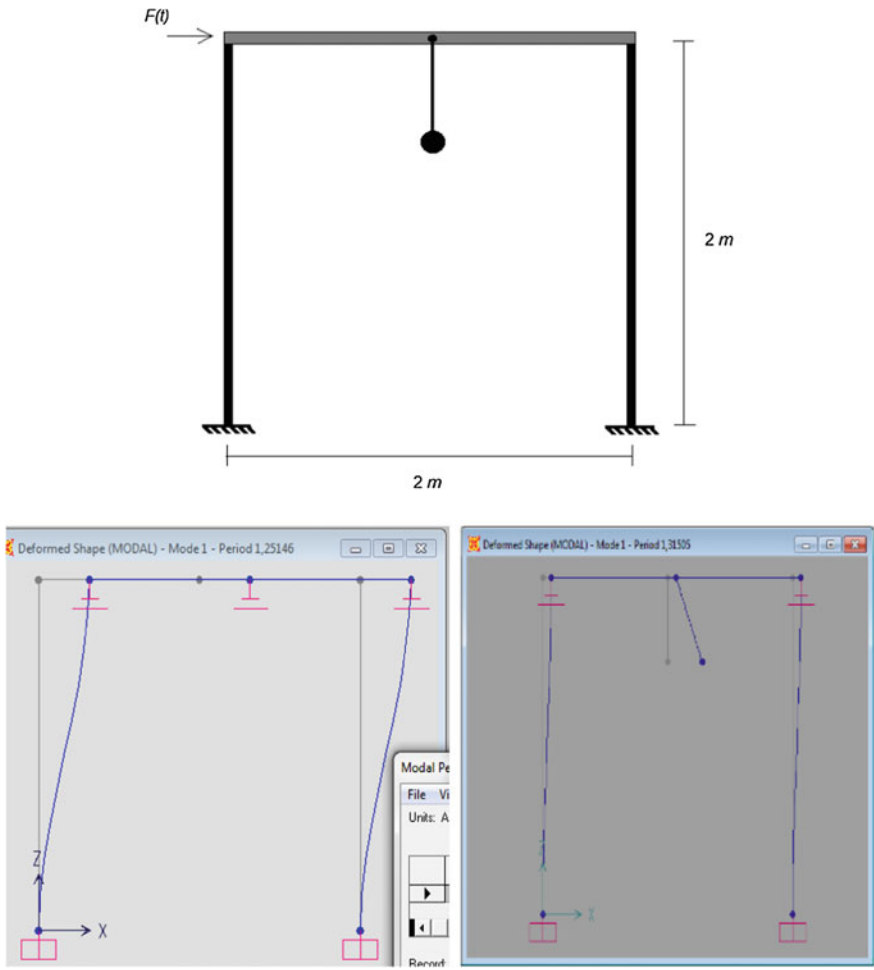


Fig. 4 SDOF shear frame with pendulum TMD and its modeling using SAP2000

With the building data the first modal mass is $M_1 = 589083$ kg; using a mass ratio of 1 %, it was possible to find the frequency of the secondary system from Eq. (1) and to select the pendulum properties by Eq. (4): with a rotational spring of 50 Nm/rad, the optimal pendulum length was found to be 1.069 m [1].

Figure 8 shows the reduced and modulated building top floor displacement response when the building is controlled solely by such pendulum TMD suspended from top floor: a displacement reduction of 52.8 % was observed from 0.1277 to 0.0603 m; an acceleration reduction of 49 % was also observed from 1.209 to 0.611 m/s^2 .

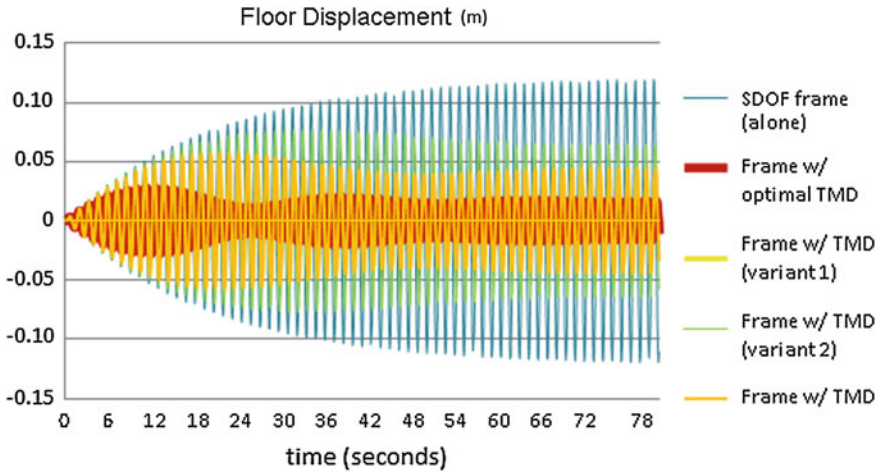


Fig. 5 Floor displacements for optimal pendulum TMD and some variants of optimal case

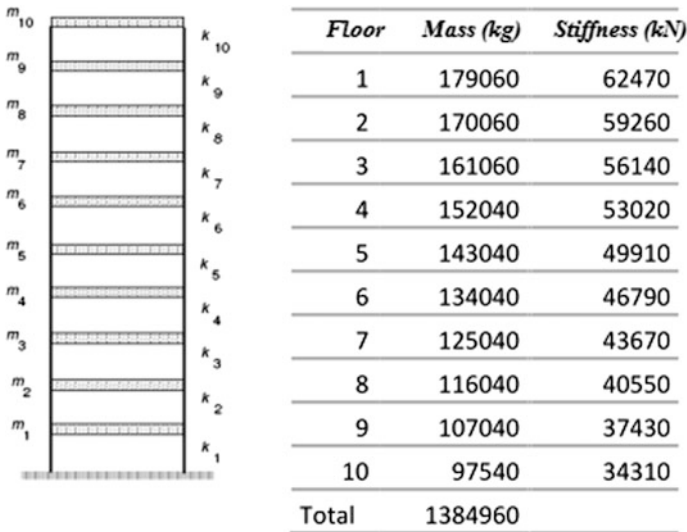


Fig. 6 Detail view and mechanical properties of the 10-floor MDOF shear building

3.2 Pendulum TMD on a MDOF Real Tower of a Transmission Tower Test Site

These ideas and methodology were also successfully applied [1] simulating the control of wind vibrations of the secondary reaction tower of a transmission tower testing site [6]. Although reaction walls are very stiff, the tuning by a very short

Modal Periods And Frequencies

File View Format-Filter-Sort Select Options

Units: As Noted Modal Periods And Frequencies

	OutputCase Text	StepType Text	StepNum Unitless	Period Sec	Frequency Cyc/sec	CircFreq rad/sec	Eigenvalue rad2/sec2
▶	MODAL	Mode	1	2.04848	0.48817	3.0672	9.408
	MODAL	Mode	2	0.773037	1.2936	8.1279	66.063
	MODAL	Mode	3	0.477123	2.0959	13.169	173.42
	MODAL	Mode	4	0.349566	2.8607	17.974	323.07
	MODAL	Mode	5	0.280263	3.5681	22.419	502.61
	MODAL	Mode	6	0.238448	4.1938	26.35	694.34
	MODAL	Mode	7	0.21196	4.7179	29.643	878.73
	MODAL	Mode	8	0.194729	5.1353	32.266	1041.1
	MODAL	Mode	9	0.183545	5.4483	34.232	1171.9
	MODAL	Mode	10	0.177063	5.6477	35.486	1259.2
	MODAL	Mode	11	0.008303	120.44	756.75	572670
	MODAL	Mode	12	0.008302	120.45	756.78	572720

Record: 1 of 12

Add Tables... Done

Fig. 7 SAP 2000 results for the 12 first natural periods (s) and frequencies (Hz)

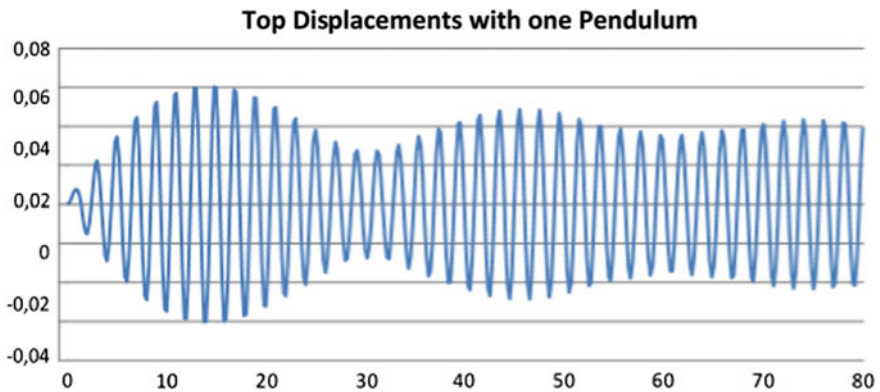


Fig. 8 Time-history of top displacements (m) for MDOF building with optimum pendulum

(0.1613 m) but heavy (191.86 ton) pendulum reduced tower displacement significantly from 4.8 to 0.2 mm, compatible with tower motionless and precision needs.

4 Conclusions

Some review on the design of optimal TMD was presented in the context of SDOF and MDOF structures, which included the non-linear abacus for selection of the design parameters of the secondary structure. Also some fundamental properties of pendulum cases are synthesized, to be used as general expressions for selecting the fundamental properties of secondary pendulum TMD systems. The concepts were numerically applied with efficiency to practical structural cases, showing the validity and interest.

References

1. Sousa, C.M.A.: Controlo de respostas dinâmicas em estruturas através de TMD's pendulares. MSc Thesis in Structural Engineering, FEUP, Porto, Portugal (2013)
2. Den Hartog, J.P.: Mechanical Vibrations, 4th edn. McGraw-Hill, New York (1956)
3. Barros, J.E., Moutinho, C., Barros, R.C.: The use of TMD's with heavy mass to mitigate the seismic response of structures. ECCOMAS Thematic Conference COMPDYN 2011, MS 8: Control of Vibrations in Civil Engineering by Passive Active and Semi-Active Devices (org.: R. C. Barros), Corfu, Greece (2011)
4. Kwok, K., Samali, B.: Performance of tuned mass dampers under wind loads. *Eng. Struct.* **17** (9), 655–667 (1995)
5. Wirsching, P.H., Campbell, G.W.: Minimal structural response under random excitation using vibration absorber. *Earthquake Eng. Struct. Dynam.* **2**(4), 303–312 (1974)
6. Barros, R.C.: VHSS Poles – Desenvolvimento de um Banco de Ensaios para Validação de Apoios Tubulares em Aço de Alta Resistência para Linhas de Transmissão. FEUP, Porto, Portugal (2015)

Fuzzy Based Control of a Vehicle Suspension System Using a MR Damper

Kellie F. Oliveira, Manuel Braz César and José Gonçalves

Abstract Vehicle suspension systems are usually based on passive actuators and control modes in which the damping and stiffness parameters are predefined and kept constant for all road profiles and vehicle response. A different approach is to use active systems to monitor and control the suspension motion in order to improve the vehicle handling and comfort. However, these systems have a complex design requiring a relatively high power source to operate. Semi-active systems are also capable to modify the properties of the vehicle suspension but with low power requirements making them a promising technology for demanding vibration control systems. This paper presents the findings of a numerical simulation involving a simplified model of a vehicle suspension system equipped with a MR actuator. The system is designed to improve the behavior (comfort and handling) of the vehicle compared with a traditional passive suspension system. A simple fuzzy logic controller is used to decide the control action in accordance with the measured system response.

Keywords MR damper · Semi-active control · Fuzzy based control

K.F. Oliveira · M.B. César · J. Gonçalves
Polytechnic Institute of Bragança, Bragança, Portugal
e-mail: a25496@alunos.ipb.pt

J. Gonçalves
e-mail: goncalves@ipb.pt

M.B. César (✉)
CONSTRUCT R&D Unit, Faculty of Engineering of the University of Porto,
Porto, Portugal
e-mail: brazcesar@ipb.pt

J. Gonçalves
INESC-TEC, Porto, Portugal

1 Introduction

Attenuation or control of vibrations in mechanical systems is a common requirement in several engineering applications such as automotive suspension systems. In this case, the main goal is to minimize the impact of the road roughness in the vehicle body to promote a safe vehicle handling and provide a smooth driving when riding over bumps and holes in the road or pavement.

Passive, active and semi-active control systems are the three main approaches to decrease the effects caused by unwanted vibrations. These systems are designed to reduce and dissipate quickly large oscillations. Passive systems are simple and inexpensive compared with active and semi-active control approaches. These systems operate directly based on the system motion without any energy requirement. The main drawback of passive control systems is that they are not able to change or adapt its behavior to different road conditions, actuating in a narrow frequency bandwidth. The disadvantages of passive systems can be resolved using active control systems, which are able to deal with modifications in the system properties and road disturbances. However, these systems require sensors, actuators, controllers and an external power source (usually with high power requirements), which make them more complex and expensive than passive systems. Semi-active control systems are seen as a promising technology for automotive suspension systems. This vibration control approach uses simple controllable or adjustable semi-active devices with low power requirements, which represent a clear advantage over both active and passive control systems. Another important issue is the selection of an appropriate controller for a specific vibration control application. There have been proposed and developed a wide range of controllers for vehicle suspension systems. Among them, fuzzy logic based controllers seems to be a good approach to design advanced control systems due to its robustness to deal with the inherent uncertainty of automotive suspension systems [1–5].

Thus, this paper presents a numerical analysis of a fuzzy based semi-active control for a vehicle suspension system. The proposed control system uses a magneto-rheological (MR) damper in combination with a fuzzy controller to increase the ride comfort and road handling of a conventional vehicle. The results obtained with the MR damper operating in a passive mode are compared with those of a semi-active control mode to assess the effectiveness of the proposed suspension control system.

2 Vehicle Suspension System

The vehicle suspension system is designed using a 1/4 model (i.e., one of the four wheels) as shown in Fig. 1. This allows a simplification of the vibration analysis to a simple two degrees-of-freedom (DOFs) spring-damper-mass system.

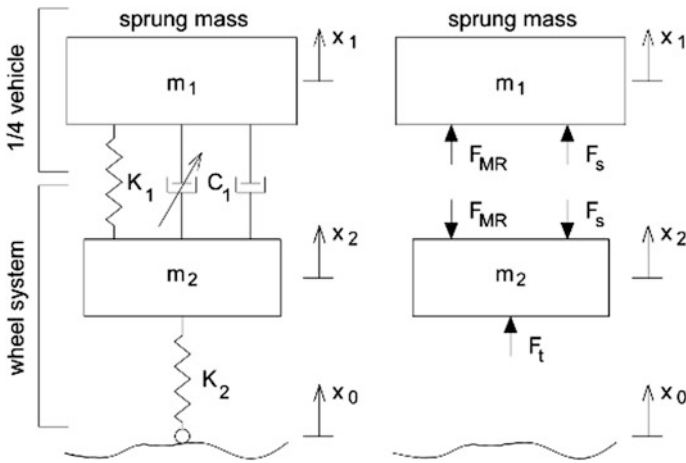


Fig. 1 Model of a 1/4 vehicle suspension system

According with the representation of the suspension system depicted in Fig. 1, the equations of motion can be written as

$$m_1 \ddot{x}_1 = F_s + F_{MR} \tag{1}$$

$$m_2 \ddot{x}_2 = F_t - F_s - F_{MR} \tag{2}$$

in which F_s and F_t represent the suspension and tire forces, respectively. These forces can be defined by

$$F_s = k_1(x_2 - x_1) + c_1(\dot{x}_2 - \dot{x}_1) \tag{3}$$

$$F_t = k_2(x_0 - x_2) \tag{4}$$

where m_1 e m_2 are the mass of the 1/4 vehicle and wheel, respectively, x_1 represents the motion of the vehicle body and x_2 is the wheel displacement, k_1 is the suspension stiffness and k_2 the spring constant of the tire and finally c_1 represent the damping coefficient of the suspension system. In this case, x_0 is the road disturbance. Thus, the equations of motion can be rewritten as

$$\ddot{x}_1 = \frac{1}{m_1} [+ k_1(x_2 - x_1) + c_1(\dot{x}_2 - \dot{x}_1)] + F_{MR} \tag{5}$$

$$\ddot{x}_2 = \frac{1}{m_2} [k_2(x_0 - x_2) - k_1(x_2 - x_1) - c_1(\dot{x}_2 - \dot{x}_1)] - F_{MR} \tag{6}$$

which can be described using a state space representation

$$\dot{X} = AX + Bx_0 + B_1 F_{MR} \quad (7)$$

where X is the state vector, x_0 is the input vector,

$$A = \begin{bmatrix} 0 & 0 & 1 & 0 \\ 0 & 0 & 0 & 1 \\ -\frac{(k_1+k_2)}{m_2} & \frac{k_1}{m_2} & -\frac{c_1}{m_2} & \frac{c_1}{m_2} \\ \frac{k_1}{m_1} & -\frac{k_1}{m_1} & \frac{c_1}{m_1} & -\frac{c_1}{m_1} \end{bmatrix} \quad (8)$$

is the state or system matrix, B and B_1 are the disturbance and control input vectors, respectively given by

$$B = \left\{ 0, 0, \frac{k_2}{m_2}, 0 \right\}^T ; \quad B_1 = \left\{ 0, 0, \frac{1}{m_1}, -\frac{1}{m_2} \right\}^T \quad (9)$$

3 MR Damper

The suspension system can be designed using a MR damper instead of a typical shock absorber. These semi-active devices use MR fluid whose behavior can be controlled by a magnetic field in order to change the damping characteristics of the damper. This allows a passive or semi-active operation of the suspension controlled by keeping constant or varying the power of the electromagnet within the damper, respectively. Besides, they have as small power requirement, reliability and inexpensiveness to manufacture. These unique features makes them particularly appropriate to design advanced automotive suspensions that can adapt the damping force according with the vehicle body motion (monitored through sensors in the vehicle) and road condition. The principle of operation of a MR damper is shown in Fig. 2 [6].

These semi-active actuators present a highly non-linear hysteretic behavior that can be numerically modeled by well-known parametric models such as the modified Bouc-Wen model by Spencer et al. [7] illustrated in Fig. 3.

According with this formulation, the predicted damper force is obtained by

$$F(t) = c_1 \dot{y} + k_1(x - x_0) \quad (10)$$

in which

$$\dot{y} = \frac{1}{c_0 + c_1} [az + c_0 \dot{x} + k_0(x - y)] \quad (11)$$

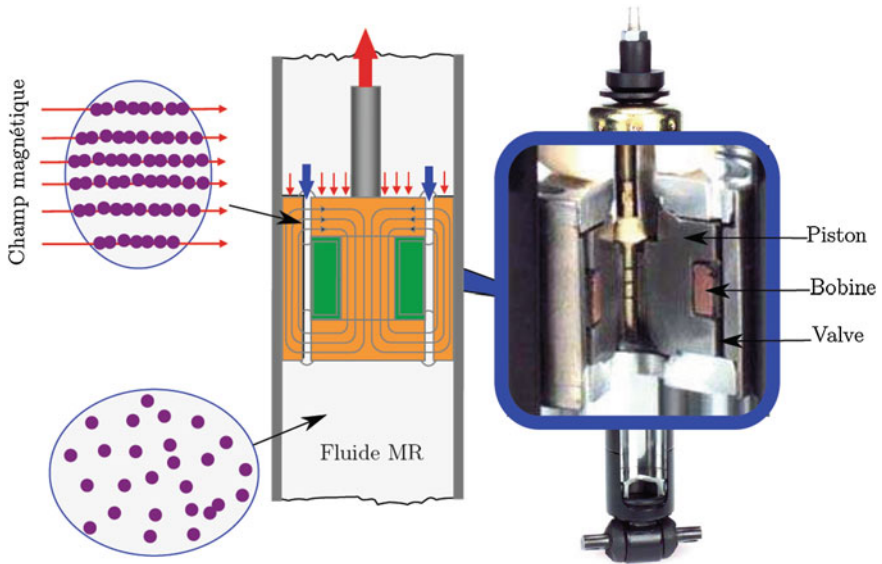
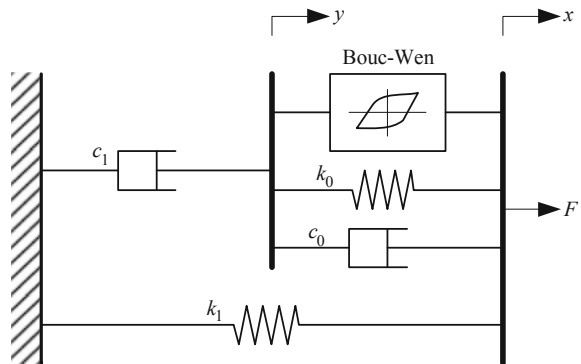


Fig. 2 Principle of operation of a MR damper [6]

Fig. 3 Numerical model of the MR damper—modified Bouc-Wen model [8]



is dependent on the evolutionary variable

$$\dot{z}(t) = -\beta|\dot{x}(t)|z(t)|z(t)|^{n-1} - \gamma\dot{x}(t)|z(t)|^n + A\dot{x}(t) \tag{12}$$

Generally, α , c_0 and c_1 are current dependent and can be described by

$$\alpha(i) = \alpha_a + \alpha_b i \tag{13}$$

$$c_0(i) = c_{0a} + c_{0b} i \tag{14}$$

$$c_1(i) = c_{1a} + c_{1b}i \tag{15}$$

The dynamics involved in the MR fluid reaching equilibrium state is represented through first order filter given by

$$\dot{u} = -\eta(u - i) \tag{16}$$

in which the applied current u is described with a time delay relative to the desired current i and η is the filter constant.

4 Fuzzy Logic Controller

Frequently, MR dampers are controlled us in classical control algorithms in combination with a clipping unit that generates a bang-bang control operation. In recent years, advanced semi-active control systems have been proposed based of soft computing and intelligent algorithms. In this regard, several fuzzy logic based controllers have been studied to operate MR dampers. These control systems incorporates the human-like reasoning through the use of fuzzy sets and linguistic variables related by a set of IF-THEN fuzzy rules. In what follows, a simple fuzzy based controller is presented for the semi-active suspension system using a MR damper (Figs. 4 and 5).

Triangular shaped membership functions (MFs) are used to represent the input variables, which are the relative displacement and velocity across the MR damper

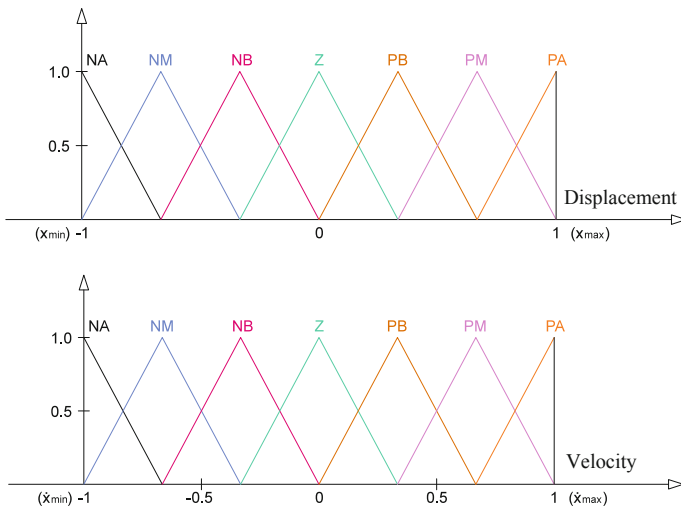


Fig. 4 Membership functions (MFs) for displacement and velocity variables

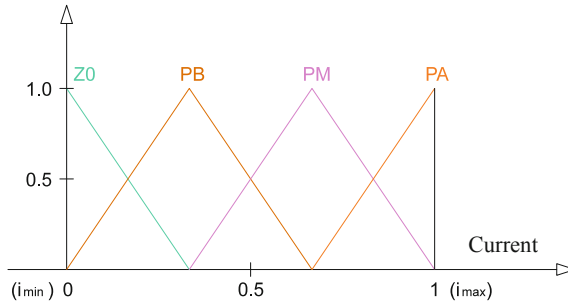


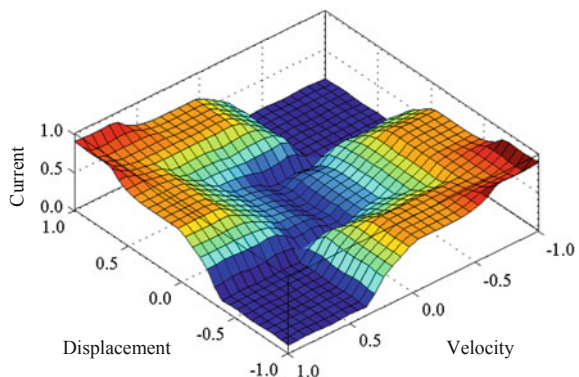
Fig. 5 Membership functions (MFs) for fuzzy output variable (operating current)

Table 1 Fuzzy inference rule

Velocity		NA	NM	NB	Z	PB	PM	PA
Displacement	NA	PA	PA	PM	PM	Z	Z	Z
	NM	PA	PM	PM	PM	Z	Z	Z
	NB	PM	PM	PB	Z	Z	Z	Z
	Z	PM	PM	PB	Z	PB	PM	PM
	PB	Z	Z	Z	Z	PB	PM	PM
	PM	Z	Z	Z	PM	PM	PM	PA
	PA	Z	Z	Z	PM	PM	PA	PA

(Fig. 4). The controller uses seven linguistic variables for each input: NA—negative high, NM—negative medium, NB, negative low, Z—zero, PB—positive low, PM—positive medium, PA—positive high. Triangular MFs are also used to represent the applied current (Fig. 5): ZO—zero, PB—positive low, PM—positive medium and PA—positive high. The basic concept of the inference rule is that, if the displacement and velocity across the damper are very large, then the output current is also large. The fuzzy inference rule is represented in Table 1 and the corresponding fuzzy surface is shown in Fig. 6.

Fig. 6 Fuzzy surface of the proposed semi-active controller



5 Numerical Simulation

A numerical analysis was carried out to evaluate the performance of the proposed semi-active fuzzy controller with respect to a passive suspension system. The $\frac{1}{4}$ suspension system parameters are as follows: $m_1 = 350$ kg; $m_2 = 40$ kg; $k_1 = 50,000$ N/m; $k_2 = 190,000$ N/m and $c_1 = 500$ N s/m (passive shock absorber). The road disturbance is modeled as impulse signals as shown in Fig. 7. In this case, two positive impulses with 5.0 mm of amplitude alternated with a negative impulse with 2.5 mm are used.

In this study, the RD-1005-3 MR damper is used to control the vibration of the suspension system. The semi-active actuator is located between the two masses. The parameters of the modified Bouc-Wen model are given in Table 2 [9].

A first-order time lag involved in the current driver/electromagnet during a step command signal is modeled by a first order filter with $\eta = 130$ s⁻¹.

The numerical simulation of the passive and semi-active suspension system was carried out in Matlab/Simulink. The results obtained with the two control approaches are shown in Fig. 8 (displacements of each mass and relative displacement between the two masses) and Fig. 9 (acceleration of each mass).

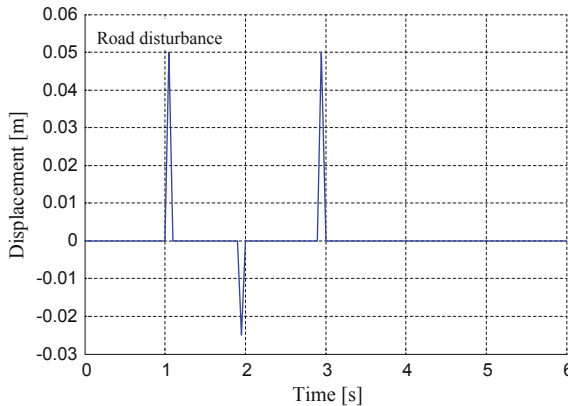


Fig. 7 Road disturbance (impulsive signals)

Table 2 Modified Bouc-Wen model parameters (RD-1005-3 MR damper)

Current independent parameters	A [-]	β [mm ⁻¹]	γ [mm ⁻¹]	k_0 [N/mm]	f_0 [N]	n
	10.013	3.044	0.103	1.121	40	2
Current dependent parameters	$\alpha(I) = -826.67I^3 + 905.14I^2 + 412.52I + 38.24$ [N]					
	$c_0(I) = -11.73I^3 + 10.51I^2 + 11.02I + 0.59$ [N s/mm]					
	$c_1(I) = -54.40I^3 + 57.03I^2 + 64.57I + 4.73$ [N s/mm]					

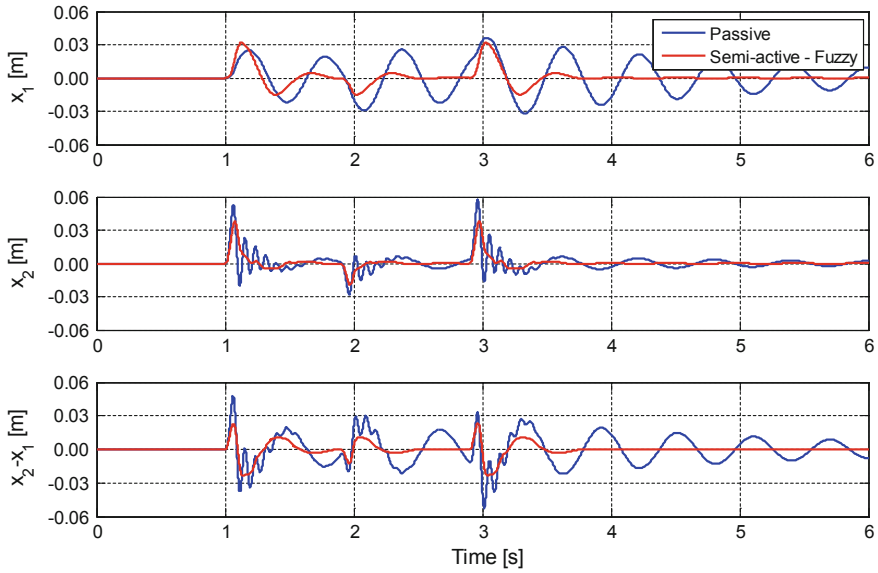


Fig. 8 Displacements (passive and semi-active fuzzy control systems)

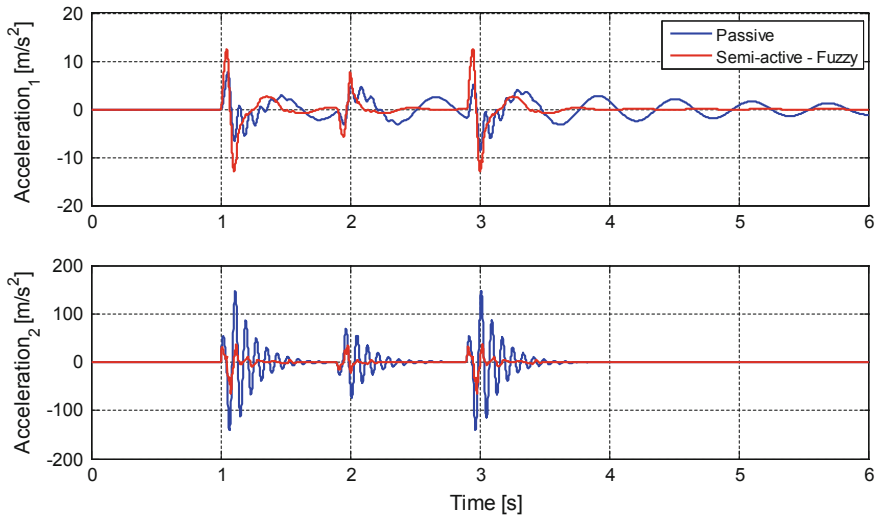


Fig. 9 Accelerations (passive and semi-active fuzzy control systems)

As can be seen by analyzing the system response, the semi-active fuzzy controller presents a significant improvement over the passive system in reducing the vibration level of both vehicle body and wheel. The peak displacement response achieved with the semi-active fuzzy control system is lower than that obtained with

Table 3 RMS values—
Passive and fuzzy controlled
systems

Control system	RMS x_1	RMS \ddot{x}_1
Passive	0.0148	1.9369
SA—Fuzzy	0.0073	2.1138

the passive system. Although the peak values of the body vertical acceleration is increased, the semi-active approach is more effective than the passive mode in eliminating the oscillation of the individual components.

The effectiveness of the proposed semi-active suspension system can be assessed measuring the root mean square (RMS) value of the body vertical motion (m_1) in both passive and semi-active control modes. The results are summarized in Table 3.

Essentially, the results show that the proposed semi-active control system presents a higher performance in reducing the vehicle body vertical displacements than that obtained with the passive control system. However and as expected, the semi-active fuzzy controller is less effective in reducing the peak vertical acceleration than the passive approach. This issue is mainly related with the fuzzy MFs and the fuzzy inference rules selected to design the semi-active fuzzy controller. The MFs present the same triangular shape and overlapping, and the fuzzy rules were defined using a simple human reasoning. The present fuzzy controller could be further improved (i.e., MFs and fuzzy rules) using an optimization procedure such as a genetic algorithm or a neuro-fuzzy approach. Thus, further research on this topic is still required to enhance the effectiveness of the semi-active controller in order to achieve the desired performance in both displacement and acceleration responses.

6 Conclusions

In general and despite the low performance in reducing the peak accelerations, the proposed fuzzy based semi-active control mode is more effective in reducing the oscillation of the vehicle body than the passive system, which represent an improvement of the vehicle ride comfort and handling stability. Besides, this controller is able to determine a continuous operation of the MR damper instead of traditional bang-bang type approaches. It is also important to notice that the proposed fuzzy controller rely only on the displacement and velocity across the damper, which means that the sensors can be integrated in the actuator without the need of additional measurements.

Acknowledgments This work is financed by the “Project TEC4Growth - Pervasive Intelligence, Enhancers and Proofs of Concept with Industrial Impact/NORTE-01-0145-FEDER-000020”, which is financed by the North Portugal Regional Operational Programme (NORTE 2020), under the PORTUGAL 2020 Partnership Agreement, and through the European Regional Development Fund (ERDF).

References

1. Cherry, A.S., Jones, R.P.: Fuzzy logic control of an automotive suspension system. *IEE* **142**(2), 149–160 (1995)
2. Sapinski, B.: Fuzzy Control for MR dampers in a Driver's Seat Suspension. *J. Theor. Appl. Mech.* **43–1**, 179–201 (2005)
3. Jialing, Y., Weiyi, C., Ning, C.: A review on the development status of automotive semi-active suspension systems. *Autom. Eng.* **3**, 276–280 (2006)
4. Cheng, L., Qiang, Z.: Fuzzy control of vehicle semi-active suspension with MR damper. In: 2010 WASE International Conference on Information Engineering (ICIE), vol. 3, pp. 426–429 (2010)
5. Devdutt, M.L., Aggarwal: Fuzzy logic control of a semi-active quarter car system. *Int. J. Mech. Ind. Sci. Eng.* **8**(1) (2014)
6. Sleiman, H.: Systèmes de Suspension Semi-active à Base de Fluide Magnétorhéologique pour L'automobile. École Nationale Supérieure d'Arts et Métiers, Paris (2010)
7. Spencer Jr., B.F., Dyke, S.J., Sain, M.K., Carlson, J.D.: Phenomenological model of a magnetorheological damper. *J. Eng. Mech.* **123**, 230–238 (1997)
8. Wang, D.H.: Magnetorheological fluid dampers: a review of parametric modelling. *Smart Mater. Struct.* (2011)
9. Braz César, M., Barros, R.: Experimental behaviour and numerical analysis of MR dampers. In: 15WCEE—15th World Conference on Earthquake Engineering, Lisbon, Portugal (2012)

Milling Parameters Optimization for Surface Quality

Tânia Dias, Nuno Paulo, Luís Queijo, Hernâni Reis Lopes,
Manuel Braz César and João Eduardo Ribeiro

Abstract The Taguchi method is a powerful tool to experiment design optimization and is used in this work to optimize the cutting parameters, which reduce the chatter effect on surface quality. The present study includes feed per tooth, cutting speed, radial and axial depth of cut as control factors. An orthogonal array of L16 was used with the ANOVA analyses in order to identify the significant factors associated to the surface roughness and chatter vibration in three different directions. The optimal cutting combination for the surface finishing was determined through the analysis of surface roughness. This are correlated with the vibrations levels recorded during the experimental tests. The study was carry-out by machining a hardened steel block with tungsten carbide coated tools. The results led to the minimum of arithmetic mean surface roughness of 1.05 μm which corresponded to a minimum of the mean vibration level.

Keywords Milling · Chatter vibrations · Surface roughness · Taguchi method

1 Introduction

The global economy brings growth of manufacturing corporation's competitiveness. For this reason, the machining industrial companies search for higher productivity, production systems flexibility, cost reduction and better surface and dimensional quality. However, these goals only can be reached if the manufacturing parameters are well defined and controlled, and also are dependable of the machine condition and selecting the adequate material and geometry tool. The understanding

T. Dias (✉) · N. Paulo · L. Queijo · M.B. César · J.E. Ribeiro
Polytechnic Institute of Bragança, ESTIG/IPB, C. Sta. Apolónia,
5301-857 Bragança, Portugal
e-mail: jribeiro@ipb.pt

H.R. Lopes
Polytechnic Institute of Porto, DEM/ISEP, R. Dr. António Bernardino de Almeida,
4200-072 Porto, Portugal

of metal cutting fundamentals has become essential in last decades to reach the best machining results. However, this is not an easy task due to the complexity of the chip formation mechanism. Modern tendencies of machining are focused online monitoring and control of the machining process, thought the use of sensors and computers. Numerous types of sensors and signal processing techniques have been developed for the direct or indirect diagnosis of aspects, such as the workpiece condition like integrity, surface roughness, dimensional accuracy, the detection of tool wear and breakage, the identification of chatter and analysis of machine component conditions. In spite of all these developments, chatter vibration has been a constraint to improve the productivity and the quality when using metal removal processes [1].

The chatter can occur in most of metal removal processes, namely in turning [2, 3], milling [4, 5], drilling [6, 7], grinding [8, 9], boring [10, 11] and broaching [12, 13]. Chatter is classified in two different categories: primary and secondary. The primary, chatter is produced by the cutting process like, i.e. the friction between the tool and the workpiece [14], thermo-mechanical effects on the chip development [15] or by mode coupling [16, 17]. In secondary category, chatter can be caused by waviness regeneration of the workpiece surface. The effect of regeneration is the most significant cause of chatter and, for because of that, some authors associated the term chatter to phenomena regenerative chatter.

The influence of the chatter in the machining is usually negative effect, causing poor surface quality, machine tool damage, excessive noise, unacceptable inaccuracies, reduced material removal rate etc. Many research works are focus in the characterization of chatter influence as negative effects like in producing low surface quality [18, 19], excessive tool wear [20] or reduced material removal rate [21, 22]. They measured the vibration during the machining in order to estimate the produced surface roughness, tool life and Material Removal Rate.

In the propose work, the authors implemented a design of experiments using the Taguchi method [23] to determine the optimal parameters in order to obtain the lowest surface roughness. This are correlated with vibration levels measured during the experimental tests.

2 Design of Experiments and Experimentation

A specially designed orthogonal array of Taguchi, presented in Table 1, is used to study the effects of the milling parameters through a small number of experiments, allowing a reduction in the time required for all experimental work. The design of experiments is shown with four columns, corresponding of two levels of cutting speed, feed rate, radial depth cut and axial depth cut.

The experimental tests were performed through a machining operation of face milling around a cylindrical workpiece under dry conditions, which were conducted according to design of experiments defined by the orthogonal array L16. The initial dimensions of workpiece were 200 mm of diameter and 200 mm of height.

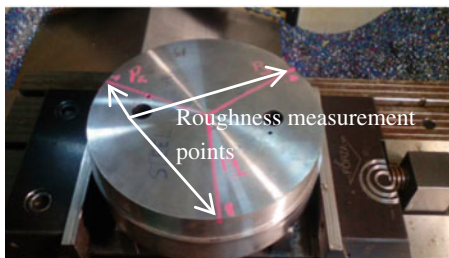
Table 1 Design of experiment (orthogonal array)

Test No.	A cutting speed (m/min)	B feed rate (mm/tooth)	C radial depth cut (mm)	D axial depth cut (mm)
1	200	0.1	1	0.1
2	200	0.1	1	0.35
3	200	0.1	2	0.1
4	200	0.1	2	0.35
5	200	0.3	1	0.1
6	200	0.3	1	0.35
7	200	0.3	2	0.1
8	200	0.3	2	0.35
9	300	0.1	1	0.1
10	300	0.1	1	0.35
11	300	0.1	2	0.1
12	300	0.1	2	0.35
13	300	0.3	1	0.1
14	300	0.3	1	0.35
15	300	0.3	2	0.1
16	300	0.3	2	0.35

The material of the cylinder was obtained from mould steel GMTC 1.2738 with a hardness of 45 Rockwell C.

The tests were carried out on a vertical machining center, Deckel Maho DMC 63 V, using WC coated tools. The tool inserts were WNHU 04T310, manufactured by Palbit®. The milling operations was performed using circular path and around the cylinder perimeter, until reaching the 50 mm of depth (Fig. 1).

(a)



(b)

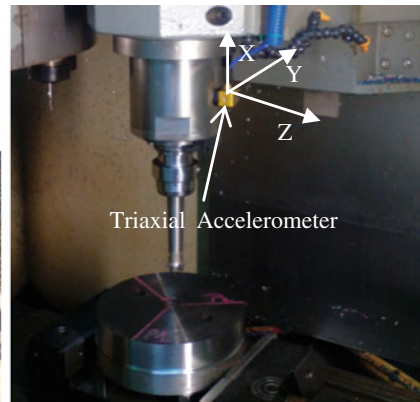


Fig. 1 Workpiece on the milling machine table: **a** details of roughness measurement points. **a** and **b** 3D accelerometer

For the present study, was used the R_a parameter. The Mitutoyo SJ-301 Portable Surface Roughness Tester was used for the measurement of surface roughness along of cylinder axial direction and in three equidistance orientations separate by 120° angle (P1, P2, P3), see Fig. 1a. For each orientation were taken five measurements, being the lowest and the highest result neglected. Final average R_a value is taken by considering the average value of the whole measurements on the three directions.

For the acquisition of chatter vibration produced during the milling tests, a triaxial accelerometer (PCB Piezotronics, model 356B18) was placed on the center of the spindle milling (Fig. 1b). The signal was processed using a vibration signal acquisition USB NI-4431 and post-processed. The RMS and the absolute maximum vibration values were extracted from the measurement and later used for control.

3 Results

In Table 3 is represented the results obtained for the experimental tests. The arithmetic mean roughness presented is the mean of the measurements on the three positions, see Fig. 1a. The RMS vibration levels were computed by considering the entire signal recorded during each test, being their values for the three sensor directions, which corresponds to X, Y and Z directions in Fig. 1b, presented in Table 3.

Analyzing the Table 3 is possible verify that the combination of parameters which cause the low value of mean surface roughness, \bar{R}_a equal to $1.05 \mu\text{m}$, are the cutting feed of 300 m/min, feed rate of 0.1 mm/tooth, radial depth cut of 2 mm and axial depth cut of 0.35 mm (test number 12). However, another parameters combination (teste number 1) gives a mean surface roughness value very low, $1.06 \mu\text{m}$, and for that case, the cutting feed was 200 m/min, the feed rate is 0.1 mm/tooth, the radial depth cut is 1 mm and axial depth cut of 0.1 mm.

The vibration analysis is based in RMS values obtained from measurements made with the triaxial accelerometer. From Table 3 is possible to observe that the combination of milling parameters which caused the lowest values of vibration for the three directions is the correspondent to test number 12, cutting feed of 300 m/min, feed rate of 0.1 mm/tooth, radial depth cut of 2 mm and axial depth cut of 0.35 mm. In this case, vibration levels for the X, Y and Z directions were 1.944 m/s^2 , 1.949 m/s^2 and 5.818 m/s^2 , respectively, having Euclidean norm of 3.237 m/s^2 . As mentioned above, the lowest value of R_a occurred also for the same test number 12. (Table 2).

Another observation about the vibration level is the difference between the average values of each direction, the average value for X direction is 4.316 m/s^2 , Y direction is 4.386 m/s^2 and for Z direction is 9.999 m/s^2 . In other words, the average values for the X and Y are very close while for the Z has an average value

Table 2 Experimental results of surface roughness and vibration level of workpiece

Test No.	A (m/min)	B (mm/tooth)	C (mm)	D (mm)	\bar{R}_a (μm)	RMS_X (m/s^2)	RMS_Y (m/s^2)	RMS_Z (m/s^2)	$\bar{\text{RMS}}$ (m/s^2)
1	200	0.1	1	0.1	1.06	3.692	3.698	8.810	5.400
2	200	0.1	1	0.35	1.61	4.774	5.043	9.238	6.352
3	200	0.1	2	0.1	3.84	4.187	3.902	9.012	5.700
4	200	0.1	2	0.35	4.07	4.077	4.301	8.834	5.737
5	200	0.3	1	0.1	1.30	4.104	4.154	10.279	6.179
6	200	0.3	1	0.35	2.36	5.211	5.419	12.226	7.619
7	200	0.3	2	0.1	3.67	4.860	4.815	7.417	5.682
8	200	0.3	2	0.35	2.63	8.776	10.146	9.089	9.337
9	300	0.1	1	0.1	1.26	9.169	10.432	17.133	12.245
10	300	0.1	1	0.35	3.72	3.078	2.777	8.591	4.815
11	300	0.1	2	0.1	2.54	2.737	2.301	5.841	3.626
12	300	0.1	2	0.35	1.05	1.944	1.949	5.817	3.237
13	300	0.3	1	0.1	1.10	3.111	2.686	8.136	4.644
14	300	0.3	1	0.35	1.32	3.212	2.849	9.018	5.026
15	300	0.3	2	0.1	3.04	3.504	3.090	8.640	5.078
16	300	0.3	2	0.35	2.01	3.189	2.620	7.685	4.498

that is more than twice of the others. However, the RMS in the Z direction is not important for the chatter vibration and for that reason will not appear in the following analysis.

4 Data Analysis and Discussion

The Taguchi analysis procedure can be described in three steps. In the first, is implemented the evaluation signal-to-noise ratio (S/N) and allows to define the level of variation for each parameter. This is followed by a comparison of each evaluate characteristic (R_a and RMS) among all the tests. The third is based on analysis of variance, which is used to define the influence of each parameter [23].

The S/N defined by Taguchi is a measure of robustness used to identify control factors, which decrease the variability in a process by minimizing the effects of uncontrollable factors or noise factors. In the Taguchi designed experiment, is possible to influence the noise factors and forcing the occurrence of variability. From the results, it is identified the optimal control factor that make the process robust or resilient to variation from the noise factors. Higher values of the S/N recognize control factor settings that minimize the effects of the noise factors. Taguchi considered three categories of the performance characteristic in the analysis of the S/N [23], namely: nominal is the best, larger is the better and smaller is the better. The follow equations define mathematically the used category in this work.

Table 3 Tests results and S/N ratio for the arithmetic mean roughness

Test No.	R _a S/N _s (dB)	RMS vibration	
		S/N _s (dB)	
		X	Y
1	-0.517	-11.37	-11.38
2	-4.301	-13.64	-14.12
3	-11.699	-12.44	-11.83
4	-12.215	-12.21	-12.70
5	-2.356	-12.29	-12.43
6	-7.483	-14.45	-14.81
7	-11.335	-13.78	-13.69
8	-8.501	-18.87	-20.13
9	-2.008	-19.26	-20.37
10	-11.455	-9.77	-8.89
11	-8.192	-8.75	-7.24
12	-0.436	-5.86	-5.83
13	-0.860	-9.86	-8.59
14	-2.460	-10.14	-9.10
15	-9.655	-10.89	-9.80
16	-6.145	-10.08	-8.38

Smaller is the better (minimize)

$$S/N_s = -10 \times \log \left(\frac{1}{n} \sum_{i=1}^n y_i^2 \right) \tag{1}$$

where y_i is the observed data and n is the number of observations.

For present work the S/N category used for the surface roughness and for chatter vibration was the “smaller is the better” because the goal is to minimize the roughness on workpiece surface and the tool vibration.

By analyzing the Table 3, is possible verify that the highest value of S/N_s ratio for R_a occur for the test number 12 and is -0.436 dB, this meaning that value corresponds to the smaller variance of the output characteristic around the desired value.

In the Table 3 are also presented the of S/N_s ratio values for RMS vibration determined in the three measurement directions. In this case the highest value of S/N_s ratio for RMS vibration occur also for the test number 12 with an average value for the three directions of -9.03 dB and better value is in the Y direction (-5.83 dB).

4.1 Analysis of the Signal-to-Noise Ratio

The signal term in the Taguchi method represents the wanted value (mean) for the output attribute and the noise represents unwanted square deviation value for the output attribute. Thus, S/N ratio is the ratio of the mean to the square deviation. The S/N ratio is used by Taguchi to measure the quality attribute or characteristic from the wanted value. The smaller S/N, the better category is applied with the objective of minimizing the surface roughness and chatter vibration. The results of S/N for the sixteen combinations (L16) are presented in Table 3. Their analyses allow to split the effect of each cutting parameter for the different levels. The mean S/N ratio for each cutting parameter at levels 1 and 2 can be computed by averaging the S/N ratios for correspondent experiments. The mean of S/N ratio for each level of cutting parameters are presented in Tables 4 and 5, common defined as the mean S/N ratio response table for Ra and RMS vibration. The total mean of S/N ratio for Ra is -6.232 dB, being the vibration for the X direction -12.103 dB and Y direction -11.830 dB.

In the Tables 4 and 5 are shown the S/N ratio response graph for roughness and vibration, respectively. One gets a high S/N ratio for smaller variance of surface roughness and vibration level around the desired value. Nevertheless, the relative importance among the milling parameters for the surface roughness still required to be identified so optimal combinations of the milling parameter levels can be determine more accurately using an ANOVA analysis.

The optimal cutting parameters are the levels with the highest value of the mean S/N ratio for each parameter. In Table 4 is presented the mean S/N ratio values for Ra and is possible to conclude that the combination of optimal parameters is A2B2C1D1. Another observation that can be done is the variation of mean S/N ratio for each parameter, thus, C parameter (radial depth cut) suffer the highest variation (4.604 dB), which denote a very important influence in the surface quality. In contrast, the variation of level for B parameter (feed rate), cause the lowest difference in the mean S/N ratio (0.265 dB).

From Table 5 one sees that the optimal combination of parameters are the same for vibration in X and Y directions (RMS_X and RMS_Y), A2B1C2D2.

Table 4 Response table mean S/N ratio for Ra factor and significant interaction

Symbol	Cutting parameters	Mean S/N ratio (dB)		
		Level 1	Level 2	Max-min
A	Cutting speed (m/min)	-7.301	-5.163	2.138
B	Feed rate (mm/tooth)	-6.364	-6.099	0.265
C	Radial depth cut (mm)	-3.930	-8.534	4.604
D	Axial depth cut (mm)	-5.828	-6.636	0.808

Table 5 Response table mean S/N ratio for RMS vibration factor and significant interaction

Symbol	Cutting parameters	Direction	Mean S/N ratio (dB)		
			Level 1	Level 2	Max-min
A	Cutting speed (m/min)	X	-13.629	-10.576	3.053
		Y	-13.885	-9.775	4.110
B	Feed rate (mm/tooth)	X	-11.661	-12.544	0.883
		Y	-11.546	-12.114	0.568
C	Radial depth cut (mm)	X	-12.596	-11.610	0.986
		Y	-12.460	-11.200	1.260
D	Axial depth cut (mm)	X	-12.329	-11.876	0.453
		Y	-11.915	-11.745	0.170

The S/N ratio of the RMS vibration can be analyzed by looking at Table 5. The cutting speed (parameter A) is the most influent parameter in the vibration levels for the three directions. Indeed, the maximum mean S/N ratio variation occurs for Y direction (RMS_Y) and has the value of 4.110 dB.

4.2 Analysis of Variance

The goal of the variance analysis is to determine which design parameters affect meaningfully the surface roughness and chatter vibration. The results of variance of each cutting parameter and their interactions are shown in Tables 6, 7, 8 and 9.

The F-Ratio test is a statistic tool to verify which design parameters affect significantly in the quality characteristic. This is defined as the ratio of the mean squared deviations to the mean squared error. Generally, when show a value greater

Table 6 ANOVA results for surface roughness

Source	Degrees of freedom	Sum of squares	Mean squares	F-ratio	Contribution (%)
A	1	18.287	18.287	1.27	6.4
B	1	0.281	0.281	0.02	0.1
C	1	84.772	84.772	5.9	29.6
D	1	2.612	2.612	0.18	0.9
A × B	1	1.002	1.002	0.07	0.4
A × C	1	28.505	28.505	1.99	10.0
A × D	1	2.822	2.822	0.2	1.0
B × C	1	4.124	4.124	0.29	1.4
B × D	1	2.029	2.029	0.14	0.7
C × D	1	69.938	69.938	4.87	24.4
Residual	5	71.800	14.360		25.1
Total	15	286.171	18.287		100.0

Table 7 ANOVA results for vibration in X-direction (RMS_X) and Y-direction (RMS_Y)

Source	Degrees freedom	Sum of squares	Mean squares	F-ratio	Contribution (%)
	X-Y	X-Y	X-Y	X-Y	X-Y
A	1	37.297–67.560	37.297–67.560	9.02–10.33	20.9–25.9
B	1	3.121–1.292	3.121–1.292	0.76–0.20	1.7–0.5
C	1	3.890–6.355	3.889–6.355	0.94–0.97	2.2–2.4
D	1	0.820–0.116	0.820–0.116	0.20–0.02	0.5–0.0
A × B	1	9.620–19.156	9.620–19.156	2.33–2.93	5.4–7.4
A × C	1	22.562–28.406	22.562–28.406	5.46–4.34	12.6–10.9
A × D	1	30.784–42.999	30.784–42.999	7.45–6.57	17.2 – 16.5
B × C	1	29.330–36.723	29.330–36.723	7.10–5.62	16.4–14.1
B × D	1	18.203–18.397	18.203–18.397	4.40–2.81	10.2–7.1
C × D	1	2.205–6.670	2.205–6.670	0.53–1.02	1.2–2.6
Residual	5	20.664–32.699	4.133–6.540		11.6–12.6
Total	15	178.496–260.372			100.0–100.0

than four, it means the variation of the design or cutting parameter has an important effect in the quality characteristic.

In this study was determined the contribution of each machining parameter and their interaction. The analysis of the F-Ratio values reveals that more significant factors are the radial depth cut and the interaction between radial depth cut and axial depth cut for minimize the surface roughness. They have contributions about 30 % and 24 %, respectively, as can be seen in Table 6. The optimal cutting parameters for the surface roughness are the cutting speed of level 2, the feed rate of level 2, the radial depth of cut of level 1 and the axial depth of cut of level 1.

From Table 7 is possible to verify that the most important contributions for minimize the tool vibration in X direction. The cutting speed, the interaction between the cutting speed and the axial depth of cut, and the interaction between the feed rate and the radial depth of cut are the more significant factors with a contribution of almost 21 %, 17 %, 16 %, respectively.

The Table 7 shows the contribution of each milling parameter and their interaction for RMS vibration value in Y direction. Is observed that the cutting speed, the interaction between the cutting speed and the axial depth of cut, and the interaction between the feed rate and the radial depth of cut have contribution of 26 %, 17 %, 14 %, respectively. For the X and Y directions, the optimal cutting parameters to minimize the chatter vibration are the cutting speed of level 2, the feed rate of level 1, the radial depth of cut of level 2 and the axial depth of cut of level 2.

5 Conclusions

The application of the parameter design of the Taguchi method in the optimization of milling operations is presented. The following conclusions can be drawn based on the experimental results of this study:

Taguchi show to be very robust method and allows to improve the surface roughness and minimized the chatter vibration phenomenon.

For a specific range of parameters, the experimental results from the Taguchi method and ANOVA analysis, was possible to identify the test 12, with a cutting speed of 300 m/min, the feed rate of 0.1 mm/t, the radial depth of cut of 2 mm and the axial depth of cut of 0.35 mm, as the best cutting parameters, leading to average surface roughness of 1.05 μm and average RMS vibration of 3.237 m/s^2 .

From the ANOVA analysis, we could identify the most influent parameters for surface average roughness and root mean square. For the R_a the most influent parameter is the radial depth cut with a contribution of 30 %. In relation to the vibration, this will dependent on the direction. Therefore, in X and Y direction the radial depth cut is the most significant factor, having a contribution of 21 % and 26 %, respectively.

This study proved the importance of the interactions between some cutting parameters. The interactions significance is clearly visible in the ANOVA and for both analysis: surface roughness and chatter vibration.

It is verified a relevant relation between the surface roughness and the chatter vibration. It was observed that the parameters combination that leads to the lower roughness is the same for the lower value of RMS vibration values.

References

1. Quintana, G., Ciurana, J.: Chatter in machining processes: a review. *Int. J. Mach. Tools Manuf.* **51**(5), 363–376 (2011)
2. Sadek, M.M.: Stability of centre lathes in orthogonal cutting. *Int. J. Prod. Res.* **12**(5), 547–560 (1974)
3. Devillez, A., Dudzinski, D.: Tool vibration detection with eddy current sensors in machining process and computation of stability lobes using fuzzy classifiers. *Mech. Syst. Signal Process.* **21**(1), 441–456 (2007)
4. Ahmadi, K., Ismail, F.: Machining chatter in flank milling. *Int. J. Mach. Tools Manuf.* **50**(1), 75–85 (2010)
5. Dombovari, Z., Altintas, Y., Stepan, G.: The effect of serration on mechanics and stability of milling cutters. *Int. J. Mach. Tools Manuf.* **50**(6), 511–520 (2010)
6. Roukema, J.C., Altintas, Y.: Time domain simulation of torsional-axial vibrations in drilling. *Int. J. Mach. Tools Manuf.* **46**(15), 2073–2085 (2006)
7. Mehrabadi, I.M., Nouri, M., Madoliat, R.: Investigating chatter vibration in deep drilling, including process damping and the gyroscopic effect. *Int. J. Mach. Tools Manuf.* **49**(12–13), 939–946 (2009)
8. Hassui, A., Diniz, A.E.: Correlating surface roughness and vibration on plunge cylindrical grinding of steel. *Int. J. Mach. Tools Manuf.* **43**, 855–862 (2003)

9. Gradisek, J., Baus, A., Govekar, E., Klocke, F., Grabec, I.: Automatic chatter detection in grinding. *Int. J. Mach. Tools Manuf.* **43**(14), 1397–1403 (2003)
10. Atabey, F., Lazoglu, I., Altintas, Y.: Mechanics of boring processes—part I. *Int. J. Mach. Tools Manuf.* **43**(5), 463–476 (2003)
11. Moetakef-Imani, B., Yussefian, N.Z.: Dynamic simulation of boring process. *Int. J. Mach. Tools Manuf.* **49**(14), 1096–1103 (2009)
12. Axinte, D.A., Gindy, N., Fox, K., Unanue, I.: Process monitoring to assist the workpiece surface quality in machining. *Int. J. Mach. Tools Manuf.* **44**(10), 1091–1108 (2004)
13. Axinte, D.A.: An experimental analysis of damped coupled vibrations in broaching. *Int. J. Mach. Tools Manuf.* **47**(14), 2182–2188 (2007)
14. Wiercigroch, M., Krivtsov, A.M.: Frictional chatter in orthogonal metal cutting. *Philos. Trans.: Math. Phys. Eng. Sci. (Series A)* **359**(1781), 713–738 (2001)
15. Wiercigroch, M., Budak, E.: Sources of nonlinearities, chatter generation and suppression in metal cutting. *Philos. Trans. Royal Soc. Lond.* **359**, 663–693 (2001)
16. Tobias, S.A.: *Machine Tools Vibrations*. Wiley, New York (1965)
17. Tlustý, J., Poláček, M.: The stability of machine tools against self-excited vibrations in machining. *Int. Res. Product. Eng.* 465–474 (1963)
18. Jang, D.Y., Choi, Y., Kim, H., Hsiao, A.: Study of the correlation between surface roughness and cutting vibrations to develop an on-line roughness measuring technique in hard turning. *Int. J. Mach. Tools Manuf.* **36**(4), 453–464 (1996)
19. Chen, J., Fang, Q., Lib, P.: Effect of grinding wheel spindle vibration on surface roughness and subsurface damage in brittle material grinding. *Int. J. Mach. Tools Manuf.* **91**, 12–23 (2015)
20. Rao, K.V., Murthy, B.S.N., Rao, N.M.: Prediction of cutting tool wear, surface roughness and vibration of work piece in boring of AISI 316 steel with artificial neural network. *Measurement* **51**, 63–70 (2014)
21. Budak, E., Tekeli, A.: Maximizing chatter free material removal rate in milling through optimal selection of axial and radial depth of cut Pairs. *CIRP Ann. Manuf. Technol.* **54**(1), 353–356 (2005)
22. Tang, W.X., Song, Q.H., Yu, S.Q., Sun, S.S., Li, B.B., Du, B., Ai, X.: Prediction of chatter stability in high-speed finishing end milling considering multi-mode dynamics. *J. Mater. Process. Technol.* **209**(5), 2585–2591 (2009)
23. Ross, P.J.: *Taguchi Techniques for Quality Engineering*, 2nd edn. McGraw-Hill, New York (1996)

Part X
Applications in Agricultural Systems

Automation and Control in Greenhouses: State-of-the-Art and Future Trends

Josenalde Oliveira, José Boaventura-Cunha and Paulo Moura Oliveira

Abstract This paper presents the state-of-the-art in terms of automation and control for protected cultivation in greenhouses. Aspects such as modeling, instrumentation, energy optimization and applied robotics are considered, aiming at not only to identify latest research topics, but also to foster continuous improvement in key cutting-edge problems.

Keywords Greenhouse · Controlled Environment Agriculture · Energy optimization · Crop protection

1 Introduction

Nowadays, aspects such as climate changes and an increasingly rising population highlight the need for sustainable solutions, mainly in terms of energy, water and food throughout the cycle: raw materials (sources)–production–consumption. Regarding food, a relevant question is: how to increase production yearround, with the same available area and balanced costs? Growers and multidisciplinary researches have devoted their attention to the so-called Controlled Environment Agriculture (CEA) [1], basically a way of not only to grow regardless of the season, but also to

J. Oliveira (✉) · J. Boaventura-Cunha · P.M. Oliveira
INESC TEC - INESC Technology and Science,
Campus da FEUP, 4200-465 Porto, Portugal
e-mail: josenalde@ej.ufrn.br

J. Boaventura-Cunha
e-mail: jboavent@utad.pt

P.M. Oliveira
e-mail: oliveira@utad.pt

J. Oliveira
Agricultural School of Jundiá - Federal University of Rio Grande do Norte, UFRN,
Macaíba, RN 59280-000, Brazil

J. Boaventura-Cunha · P.M. Oliveira
School of Sciences and Technology, University of Trás-os-Montes and Alto Douro,
5000-801 Vila Real, Portugal

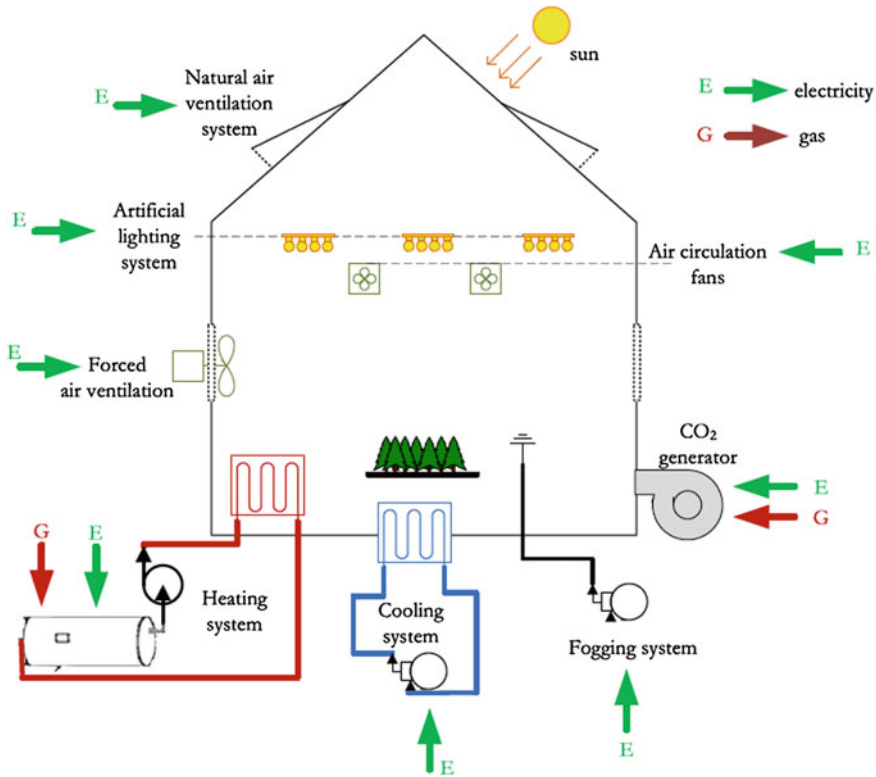


Fig. 1 Greenhouse energy system [2]

protect cash crops (vegetables, fruits, flowers etc.) against severe weather conditions. This is accomplished by the creation of an artificial climate inside a greenhouse, with suitable control of temperature, humidity, CO₂ concentration, pH, nutrients by means of precise cooling, heating, ventilation, lighting and fogging, among other actuators. An overview of the energy system involved and their sources (E—Electricity, G—Gas) may be seen in Fig. 1 [2], where a full energy consumption optimization for greenhouses is proposed based on several internal variables, actual electricity prices and weather forecasting. Co-generation of energy from biomass is also an excellent option for growers, as currently biomass is a cheaper energy source for heating.

Although not new [3], the topics *greenhouses* and closed production systems are quite associated to cutting-edge subjects within *precision agriculture/farming* such as energy optimization and robotics, with related conferences [4], journals [5] and magazines [6]. If one looks at a glance the topics of interest of recent and forthcoming related conferences,¹ technologies for all chain of protected cultivation are included (modelling, sensing+control, robot-based harvesting and weed/pest control).

¹for example, IFAC Agricontrol, EFITA WCCA-CIGR.

Another interesting issue and motivation is the continuous EU public investments in projects such as FutureFarm²: Integration of Farm Management Information Systems to Support Real-time Management Decisions and Compliance of Standards (2008–2011), CROPS³: Clever Robots for Crops—Intelligent Sensing and Manipulation for Sustainable Production and Harvesting of High Value Crops (2010–2014) and the ongoing project SWEEPER⁴: Sweet Pepper Harvesting Robot (2015–2018). There is a call entitled Robotics Advances for Precision Farming⁵ to be open in October 2016, within the program Horizon 2020, welcoming proposals addressing improvements on flexibility, efficiency and robustness of autonomous robots for applications such as selective harvesting, targeted weed reduction, environment friendly fertilization/irrigation, livestock management and traceability.

This work presents some impressions based on published material from 2010 to february 2016, regarding specifically researches related to greenhouses. The main objective is to identify hot topics for present and future research.

2 State of the Art

Research on CEA and greenhouses has significant impact on scientific community. Considering the period January 2010–February 2016, the *IEEE Xplore* digital library gives 1,861 results, among conference publications, journals, magazines, books and early access papers. The same search on ScienceDirect gives 76,879 results, from topics such as types of cover materials (plastic, glass etc.), design, sensors and equipments, clean energy sources (photovoltaic, eolic), optimization, modeling, identification and control. More specifically, a journal such as *Computers and Electronics in Agriculture*⁶ had 153 related papers published in the same period. The latest specific books were published in 2010 [7] (reviewing 30 years of research) and 2012 [8].

Other point of view is to quantify how much effort countries are applying in greenhouses research, reflected, for instance, in their participation with papers in conferences. As an example, the proceedings of Greensys 2015,⁷ held in Évora-Portugal, with the following participation organized by country and by number of papers: Japan (23), The Netherlands (20), China (17), Mexico (14), Germany (13), USA (12), Israel (11), Brazil (8), Portugal (7) and other minor participations. The greenhouse market in Portugal has higher impact in lettuce for salads, followed by

²<http://www.futurefarm.eu>.

³<http://www.crops-robots.eu>.

⁴<http://www.sweeper-robot.eu>.

⁵<https://ec.europa.eu/research/participants/portal/desktop/en/opportunities/h2020/topics/6063-sfs-05-2017.html>.

⁶Elsevier®, available at: <http://www.journals.elsevier.com/computers-and-electronics-in-agriculture/>.

⁷<http://greensys2015.uevora.pt/>.

carrots, flowers, mushrooms and blueberries as trends [9]. However, although there is an interest in increasing greenhouse areas, a precise evaluation is difficult due to lack of recent data.⁸

In the following, some recent research topics and results are presented.

2.1 Greenhouse—Modeling

Greenhouses are known as a complex system (MIMO, nonlinear), since many physical coupled variables and heat and mass exchanges are involved. Besides the internal complexity, external factors such as wind speed, outside temperature and humidity, solar light and others act as input disturbances and must be taken into account to optimize the greenhouse environment. Soil, growing needs, cover material, area, sensors, actuators and the crop itself, have their specifications, constraints and demands, thus contributing for this complexity.

An appropriate control is based on a reliable model and, therefore, some works are very detailed in the sense of incorporating as many variables and dynamics as possible [2], taking into account all necessary energy balance laws. Others consider the existence of coupling [10] but use some strategy as the fractional calculus, to reduce the number of parameters to be identified. When some aspects may be neglected, linearization [11] and temperature-humidity decoupling is an option and has achieved good results [12]. For black-box identification, [13] used the nature inspired algorithm Particle Swarm Optimization and other recent algorithms may be compared, such as Gravitational Search Algorithm [14], Grey Wolf Optimizer [15] and Ant Lion Optimizer [16], therefore an open field for researching. When the greenhouse is taken as a hybrid system where continuous signals (environmental factors) and logical switching states (ventilation windows, wet-fans, shade nets etc.) interact, the Mixed Logical Dynamical (MLD) approach has been investigated [17] and it suggests a better modeling technique. A suitable modeling and prediction scheme can be the basis for the development of virtual greenhouses [18], where the user can simulate various scenarios, for different crops and weather conditions. An user case in Mexico for internal temperature control based on fuzzy modeling may be found in [19].

2.2 Greenhouse—Sensors, Control and Energy Optimization

Sensors play a decisive role for a complete solution for automated operation of the greenhouse, since its the basis for both, modeling and control. Therefore, they must offer accuracy, reliability and flexibility. The greenhouse complexity is also reflected

⁸Last report on horticulture, flowers and other crops date from 2007. <http://www.gpp.pt/pbl/diagnosticos/SubFileiras/Horticultura.pdf>.

in the various types of variables to be measured [20]. Besides the conventional temperature and humidity (soil, air) sensors, wind speed, solar radiation, lighting, gases concentration (carbon dioxide, oxygen, nitrogen etc.), pH, soil electric conductivity, and others sensors, may be necessary depending on the crop or the specific application. It is noteworthy the present interest for disseminating Wireless Sensor Networks (WSN) [21], as an efficient alternative to conventional *cabled* sensors. Solutions for integrated greenhouses [22] and that incorporate some clean energy source for the sensors [23] are available and undergoing research, targeted into the new paradigm called Internet of Things (IoT).

In terms of control strategy, Model Predictive Control (MPC) still is a suitable and feasible solution, mainly when it is incorporated into a hierarchical control structure, as the low level controller, or as the high level controller, providing the optimal set points (targets). The high level controller usually is connected to an optimization block, which may incorporate weather forecasts [24], electricity costs [2], user defined profiles and other inputs, generally in order to minimize the energy consumption. Although most effort is on temperature-humidity control, lighting conditions control is also relevant [25], since it affects directly photosynthesis and other crop aspects. Likewise in modeling, optimization algorithms are of continuous interest for tuning the controller parameters [26].

The feasibility of production in greenhouses [27] depends on the costs, and energy consumption is a key issue. Therefore, clean and freely available sources as solar energy, are currently the main topic of interest [28, 29]. Other solutions use some thermal storage device [30] and appropriate cover materials to accumulate energy and save electricity.

2.3 Greenhouse—Robotics

The research on applied robotics are concentrated in helping labour tasks inside the greenhouses, such as weed and pest control [31], either individual or with a robot fleet, watering and tilling [6], and harvesting [32]. A work by [33], for example, presents a robotic detection system for combined detection of two major threats of greenhouse bell peppers: powdery mildew and tomato spotted wilt virus. The robots may be autonomous [34] or semi-autonomous [5] to reduce costs and complexity. In [5] a proof-of-concept prototype was built as an user case for harvesting and spraying tasks in greenhouses located in Haifa, Israel. Robotics is strictly related to machine vision and digital image processing, and therefore has motivated continuous development, for instance for fruits [35] and flowers [36] classification and picking. Ongoing projects such as SWEEPER [37] and new funding opportunities as the EU call **Robotics Advances for Precision Farming** [38] point out mainly for robot-based tasks in agriculture as a promising trend and an opportunity to toptier research.

Table 1 summarizes some relevant works and their main contributions:

Table 1 Works related to greenhouse automation and control—main contributions

Work	Contributions
[2]	Modeling based on energy balance laws, with updated electricity costs and weather forecast as inputs for the optimization block
[17]	Greenhouse is taken as a hybrid system, modeled by the Mixed Logical Dynamical (MLD) approach
[23]	Developed a wireless sensor network for distributed greenhouses under the IoT paradigm
[25]	Focus on optimized lighting control
[28]	Analysis of solar trough plants as an efficient energy source
[33]	Presents a robotic detection system for combined detection of threats on greenhouse bell peppers

3 Future Trends: Water and Nutrient Management

There is an increasing governmental demand for a better efficiency on the water use as well on the reduction of soil and water pollution. In this context, the protected agriculture plays an important role with the treatment and recycling of the drainage water. Most state-of-the-art systems for automatic control of nutrients/water are based on pH and ElectroConductivity (EC) sensors, providing precise nutrification and dosing control of the nutritive solution. The idea is: the more you recycle, the more you gain (the environment and the grower). Usually, the water is prepared for reuse by mixing it with clean water. Netajet series, from the Israeli Netafim, use a pH-EC fuzzy logic control and the Dutch HortiMax uses the same measurements in its customizable controller. For irrigation/drainage control, crop transpiration and saturation level of the substrate give relevant data. When this irrigation water needs to be flushed, after an appropriate and efficient disinfection method (UV, heat, H_2O_2 , biologic filter, chloride) it must contain a minimum quantity of salts and minerals, obeying the present waste legislation mainly regarding nitrates. Specific water quality sensors may be applied to this goal. This topic has motivated the development of electrochemical sensors, namely Ion Selective Electrode (ISE), Ion Selective Field Effect Transistor (ISFET) and CHEMFET (Chemical Field Effect Transistor) with deep investigation in past decade [40, 41], including the project Hydrion-line, with an overview of its components in Fig. 2.

These works concluded with the motivation for research on stability and robustness improvements of the measurement system and a better life expectation of the sensors. Recent works such as [42] and [44] still explore this matter, suggesting renewed and updated interest and development. [42] built a NFT hydroponic closed system (prototype) for lettuce and measured, besides pH, EC and dissolved oxygen, the concentrations of NO_3^- (nitrate), NO_4^+ (ammonium), Ca^{+2} (calcium) and K^+ (potassium). Generally speaking, plants need macronutrients (Ca, K, nitrates, P, Mg, Na, Cl) and micronutrients, such as Fe, Mn, B, Cu, Zn, Mo, but it is difficult and expensive to measure all of them. In case of measurement, it is necessary to study

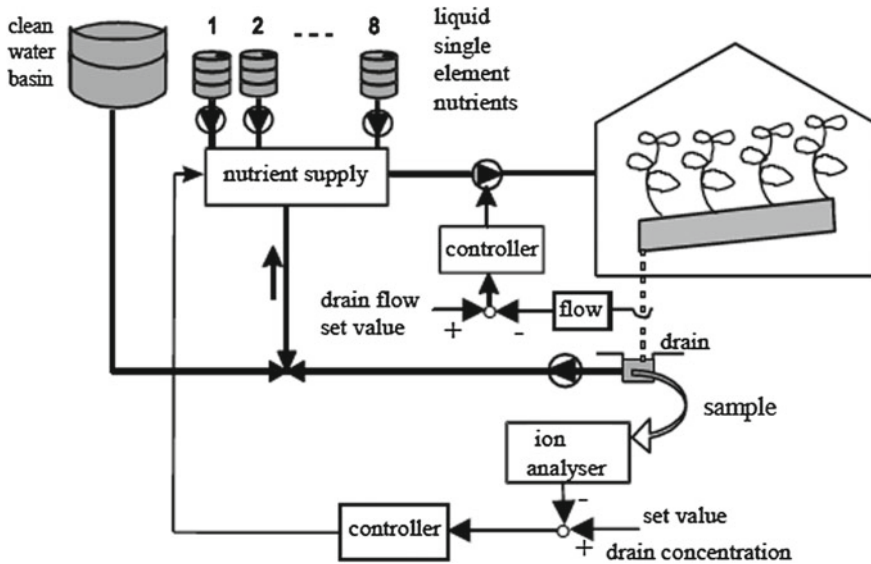


Fig. 2 Hydrion-line project—control system [41]

which ones are more relevant and decisive for feedback control and to use models which correlate the uptake of measurable ions or other measurable variables [43]. Some multi-ion probes are commercially available, for example from NTSensors (seven ions) and from Specmeters (individual sensors). Their cost and communication interfaces must be taken into account for decision making. Publication [44] also highlights unstable sensor performance as a critical issue to consider, but also encourages further development of ISEs and other technologies, such as optical sensors.

4 Final Notes

This paper presented recent developments related to modeling, sensing and control in greenhouses, showing some topics of interest which have been investigated and, therefore, may point towards relevant improvement opportunities. This state-of-the-art revision points out for the following promising themes:

- Optimization under uncertainty of both stages of modeling and control, incorporating economic costs and weather forecasts;
- Treatment of the greenhouse as a hybrid system, incorporating modeling approaches such as Mixed Logic Dynamical;
- Study of robust nonlinear MPC and fuzzy approaches into a hierarchical structure for full greenhouse control;

- IoT based wireless sensor network;
- Development of virtual greenhouses and decision support systems;
- Applied robotics for: weed and pest control, harvesting;
- New sensing devices for water and nutrient management.

These subjects must take into account the need for sustainability with clean energy sources, such as solar energy, and the new scenario of soilless production [39], with the aim of achieving high quality crops with low environment impact.

Acknowledgments This work is financed by the ERDF – European Regional Development Fund through the Operational Programme for Competitiveness and Internationalisation – COMPETE 2020 Programme, and by National Funds through the FCT – Fundação para a Ciência e a Tecnologia (Portuguese Foundation for Science and Technology) within project POCI-01-0145-FEDER-006961.

References

1. Madden, N.: Future of farming, Part 1: Controlling the environment. <http://www.technewsworld.com/story/78646.html> (2013). Accessed 25 Jan 2016
2. Bozchalui, M.C., Cañizares, C.A., Battacharya, K.: Optimal energy management of greenhouses in smart grids. *IEEE Trans. Smart Grid* **6**(2), 827–835 (2015)
3. Hashimoto, Y. (ed.): *The Computerized Greenhouse: Automatic Control Application in Plant Production*. Academic Press (1993)
4. Hemming, S.: Innovations in greenhouse systems—energy conservation by system design, sensors and decision support systems (invited speaker). In: *Greensys 2015: International Symposium on New Technologies and Management for Greenhouses*, Évora, Portugal. <http://www.greensys2015.uevora.pt/> (2015)
5. Gat, G., Gan-Mor, S., Degani, A.: Stable and robust vehicle steering control using an overhead guide in greenhouse tasks. *Comput. Electron. Agric.* **121**, 234–244 (2016)
6. Wright, J.: Agbotic builds greenhouse to test precision watering and tilling robot. *Greenhouse Grower Mag.* <http://www.greenhousegrower.com/industry-news/agbotic-builds-greenhouse-to-test-precision-watering-and-tilling-robot/> (2015). Accessed 25 Jan 2016
7. van Straten, G., van Willigenburg, G., van Henten, E., van Ooteghem, R.: *Optimal Control of Greenhouse Cultivation*. CRC Press (2010)
8. Castilla, N.: *Greenhouse Technology and Management*, 2nd edn. Cabi (2012)
9. Casimiro, N.: Produção em estufa. *Agricultura do futuro*. <http://investidor.pt/producao-em-estufa-agricultura-do-futuro/#ixzz3xtb6jdJ5>. http://www.observatorioagricola.pt/item.asp?idasp?id_item=133 (2012). Accessed 25 Jan 2016
10. Mhenni, Z., Abbes, M., Mami, A.: Fractional order model of a greenhouse. In: *6th International Renewable Energy Congress*, pp. 1–5 (2015)
11. Xiu-hua, W., Lei, Z.: Simulation on temperature and humidity nonlinear controller for greenhouses. In: *4th International Conference on Intelligent Computation Technology and Automation*, pp. 500–503 (2011)
12. Gao, Y., Song, X., Liu, C., He, S.: Feedback feed-forward linearization and decoupling for greenhouse environment control. In: *International Conference on Mechatronics and Control*, pp. 179–183 (2014)
13. Pérez-González, A., Begovich, O., Ruiz-Léon, J.: Modeling of a greenhouse prototype using PSO algorithm based on a LabViewTM application. In: *11th International Conference on Electrical Engineering, Computing Science and Automatic Control*, pp. 1–6 (2014)

14. Rashedi, E., Nezamadi-Pour, H., Saryazdi, S.: GSA: a gravitational search algorithm. *Inf. Sci.* **179**, 2232–2248 (2009)
15. Mirjalili, S., Mirjalili, S.M., Lewis, A.: Grey wolf optimizer. *Adv. Eng. Softw.* **69**, 46–61 (2014)
16. Mirjalili, S.: The ant lion optimizer. *Adv. Eng. Softw.* **83**, 80–98 (2015)
17. Guoqi, M., Linlin, Q., Xinghua, L., Gang, W.: Modeling and predictive control of greenhouse temperature-humidity system based on MLD and time-series. In: 34th Chinese Control Conference, pp. 2234–2239 (2015)
18. <http://www.agrotech.dk/uk/virtual-greenhouse>. Accessed 27 Jan 2016
19. Márquez-Vera, M.A., Ramos-Fernández, J.C., Cerecero-Natale, L.F., Lafont, F., Balmat, J.-F., Esparza-Villanueva, J.I.: Temperature control in a MISO greenhouse by inverting its fuzzy model. *Comput. Electron. Agric.* **124**, 168–174 (2016)
20. Qhan, V.M., Gupta, G.S., Mukhopadhyay, S.: Review of sensors for greenhouse climate monitoring. In: 2011 IEEE Sensors Applications Symposium, pp. 112–118 (2011)
21. Al-ubidy, K.M., Ali, M.M., Derbas, A.M., Al-mutairi, A.W.: Real-time monitoring and intelligent control for greenhouses based on wireless sensor network. In: 11th Multi-conference on Systems, Signals and Devices, pp. 1–7 (2014)
22. Kuroda, M., Ibayashi, H., Mineno, H.: Affordable 400 MHz Long-haul sensor network for greenhouse horticulture. In: IEEE International Conference on Information Networking, pp. 19–24 (2015)
23. Gomes, T., Brito, J., Abreu, H., Gomes, H., Cabral, J.: GreenMon: an efficient wireless sensor network monitoring solution for greenhouses. In: IEEE International Conference on Industrial Technology, pp. 2192–2197 (2015)
24. Chen, J., Yang, J., Zhao, J., Xu, F., Shen, Z., Zhang, L.: Energy demand forecasting of the greenhouses using nonlinear models based on model optimized prediction method. *Neurocomputing* **174**, 1087–1100 (2016)
25. Mahdavian, M., Wattanapongsakorn, N.: Optimizing PID controller tuning for greenhouse lighting control system by varying number of objectives. In: 11th International Conference on Electrical Engineering/Electronics, Computer, Telecommunications and Information Technology, pp. 1–6 (2014)
26. Zou, Q., Ji, J., Zhang, S., Shi, M., Luo, Y.: Model predictive control based on particle swarm optimization of greenhouse climate for saving energy consumption. In: World Automation Congress, pp. 123–128 (2010)
27. Oliveira, J.B., Boaventura-Cunha, J., Oliveira, P.B.M.: A feasibility study of sliding mode predictive control for greenhouses. *Optim. Control Appl. Methods* (2015). doi:10.1002/oca.2189
28. Camacho, E.F., Gallego, A.J.: Model predictive control in solar trough plants: a review. *IFAC-PapersOnline* **48–23**, 278–285 (2015)
29. Hassanian, R.H.E., Li, M., Lin, W.D.: Advanced applications of solar energy in agricultural greenhouses. *Renew. Sustain. Energy Rev.* **54**, 989–1001 (2016)
30. Vadiée, A., Martin, V.: Energy management in horticultural applications through closed greenhouse concept, state of the art. *Renew. Sustain. Energy Rev.* **16**, 5087–5100 (2012)
31. Komasilovs, V., Stalidzans, E., Osadcuks, V., Mednis, M.: Specification development of robotic system for pesticide spraying in greenhouse. In: 14th IEEE International Symposium on Computational Intelligence and Informatics, pp. 453–457 (2013)
32. Bac, C.W., van Henten, E.J., Hemming, J., Edan, Y.: Harvesting robots for high-value crops: state-of-the-art review and challenges ahead. *J. Field Robot.* **31**(6), 888–911 (2014)
33. Shor, N., Bechar, A., Ignat, T., Dombrovsky, A., Elad, Y., Berman, S.: Robotic disease detection in greenhouses: combined detection of powdery mildew and tomato spotted wilt virus. *IEEE Robot. Autom. Lett.* **1**(1), 354–360 (2016)
34. Gao, G., Li, M.: Study on navigating path recognition for the greenhouse mobile robot based on K-means algorithm. In: IEEE 11th International Conference on Networking, Sensing and Control, pp. 451–456 (2014)
35. Kapach, K., Barnea, E., Mairon, R., Edan, Y., Ben-Shahar, O.: Computer vision for fruit harvesting robots: state of the art and challenges ahead. *Int. J. Comput. Vis. Robot.* **3**(1, 2), 4–34 (2012)

36. Tarry, C., Wspanialy, P., Veres, M., Moussa, M.: An integrated bud detection and localization system for application in greenhouse automation. In: 2014 Canadian Conference on Computer and Robot Vision, pp. 344–348 (2014)
37. <http://www.sweeper-robot.eu>. Accessed 26 Jan 2016
38. <https://ec.europa.eu/research/participants/portal/desktop/en/opportunities/h2020/topics/6063-sfs-05-2017.html>. Accessed 26 Jan 2016
39. https://www.netafim.com/Greenhouse_Technology/growing_methods. Accessed 27 Jan 2016
40. Gieling, T.H., van Straten, G., Janssen, H.J.J., Wouters, H.: ISE and Chemfet sensors in greenhouse cultivation. *Sensors Actuators B* **105**, 74–80 (2005)
41. Gieling, T.H., Corver, F.J.M., Janssen, H.J.J.: Hydrión-line, towards a closed system for water and nutrients: feedback control of water and nutrients in the drain. *Acta Horticulture* **691**, 259–266 (2005)
42. Manqueros-Aviles, V.E.: Mediciones Nutritivas En Un Sistema Hidropnico NFT Mediante El Uso De Sensores De Iones Selectivos Y LabVIEW. In: 1er Congreso Internacional de Ciencias de la Ingeniería, pp. 1–8 (2015)
43. Neto, A.J.S., Zolnier, S., Lopes, D.S.: Development and evaluation of an automated system for fertigation control in soilless tomato production. *Comput. Electron. Agric.* **103**, 17–25 (2014)
44. He, D., Du, W., Hu, J.: Water quality dynamics monitoring technology and application based on ion selective electrodes. In: Macas, J.P. (ed.) *Recent Developments in Mobile Communications: A Multidisciplinary Approach*. InTech (2011)

A New Plant Growth System Rig Based on Thermodynamic Solar Energy: A Study for Energy Efficiency Assessment

João Paulo Coelho, José Gonçalves, Manuel Braz César and José Dias

Abstract At the present there is a high pressure toward the improvement of all production processes. Those improvements can target distinct factors along the production chain. In particular, and due to recent tight energy efficiency policies, those that involve energy efficiency. As can be expected, agricultural processes are not immune to this tendency. Even more when dealing with indoor productions. In this context, this work presents an innovative system that aims to improve the energy efficiency of a trees growing platform. This improvement in energy consumption is accomplished by replacing an electric heating system by one based on thermodynamic panels. The assessment of the heating fluid caudal and its temperature was experimentally obtained by means of a custom made scaled prototype whose actuators status are commanded by a Fuzzy-based controller. The obtained results suggest that the change in the heating paradigm will lead to overall savings that can easily reach 60 % on the energy bill.

Keywords Energy efficiency · Renewable energy · Fuzzy controller · Agriculture

J.P. Coelho (✉) · J. Gonçalves · M. Braz César · J. Dias
Instituto Politécnico de Bragança, Escola Superior de Tecnologia e Gestão,
Campus de Sta., 5300-253 Apolónia, Bragança, Portugal
e-mail: jpcoelho@ipb.pt

J. Gonçalves
e-mail: goncalves@ipb.pt

M. Braz César
e-mail: brazcesar@ipb.pt

J.P. Coelho · J. Gonçalves
INESC TEC Technology and Science, Campus da FEUP, 4200-465 Porto, Portugal

M. Braz César
Faculty of Engineering of the University of Porto,
CONSTRUCT R&D Center, Porto, Portugal

1 Introduction

Nowadays, in order to increase the companies competitiveness, all the production processes are subject to rigorous audits. The output of such studies leads to changes in several key variables that will, ultimately, give rise to a performance increase. Those changes can happen at multiple levels, ranging from plant layout, tasks scheduling, rework or scrap minimization and, of course, energy efficiency.

Energy efficiency is a pressing problem that is addressed at several levels. Particularly in the countries that are part of European Union (EU), there are currently several political mechanisms undergoing pushing for energy consumption reduction and, simultaneously, to promote renewable-based energy production systems [1].

Since economic growth is tightly connected to an increase in energy consumption, the way to cope to the EU energy policies while simultaneously maintaining the upward trend on the economic behaviour, will be to replace the current processes feeding energy solutions by more efficient ones. In particular energy production methods that will not scale up with the required economic development as the ones existing nowadays.

Even if unnoticed, agricultural processes are not immune to this tendency. As a matter of fact, agricultural production systems require lot of energy and natural resources such as water. Within a global market paradigm, the costs reduction, while maintaining the products quality, is a constant grower concern. Hence keeping market competitiveness can then be a challenge tackled at both operational and technological fronts.

Regarding the latter, it is often possible to transpose solutions used in different contexts to alternative applications bringing increased value to a new process. For example the water heating systems, based on thermodynamic pumps used in domestic applications, can be also used in agricultural processes as is the case of greenhouses productions.

This paper deals with a new devised strategy to improve the energy efficiency of a tree nursing station. It is intended to replace the current resistor based heating system by an alternative solution using circulation of hot water in a closed pipe circuit. The heating and recirculation of the water will be performed by a thermodynamic solar system composed by a heat pump and solar thermal collectors.

However, prior to the effective implementation of this solution, it is required to test if this alternative heating system can, in fact, be used to replace the old one. In order to do this a scaled version of a growing platform was built where the thermodynamic heating system was replaced by a butane gas water heater system. Both the water pump and the gas heating system must be controlled taking into consideration the imposed temperature set-point while maintaining system integrity. The actuator states will be function of exogenous information, provided by an array of sensors, and a control law imposed by a Fuzzy controller. The choice of this control strategy was mainly due to the fact that, under this paradigm, an expert based controller is easily translated to a Fuzzy behaviour system [6] leading to a reduced controller development time.

The remain of this paper will be divided into four additional sections. After a more thorough presentation of the addressed problem at Sect. 2, the Fuzzy controller design strategy will be described along Sect. 3. Here the obtained results, regarding both set-point tracking and actuator wearing, will be presented. The economic viability of the purposed method will be described during Sect. 4. Final concluding remarks, as well as future work directions, will be presented in Sect. 5.

2 Problem Description

One of the main objectives of this work is to evaluate the economic profit that could be obtained from replacing the current heating system of a plant growth system by a renewable energy-based system.

This trees growing system consists on platforms placed inside greenhouses where the air temperature is roughly controlled. In particular, the inside air temperature ranges, in average, from 10 to 30 °C. The current growing platforms installation spans five distinct agricultural buildings as can be seen from Fig. 1a. All the platforms have the standard width of 1.6 m. The greenhouse identified by the letter **A** has 3 growing platforms each one with 10 m long and the one denoted by **B** has two platforms also with 10 m long. The building distinguished by **C** does not have any growing platform installed. Building **D** has two of them, each one with 5 m long, and building **E** has only one 5 m long platform.

At the present the installed growing platforms are used to nurse olive trees and chestnuts, among others, until they are sufficiently resistant to be planted outdoors [3]. The system structure is composed by a metallic tray, covered with perlite, and with an electric resistance coil running along the covered area. The power consump-

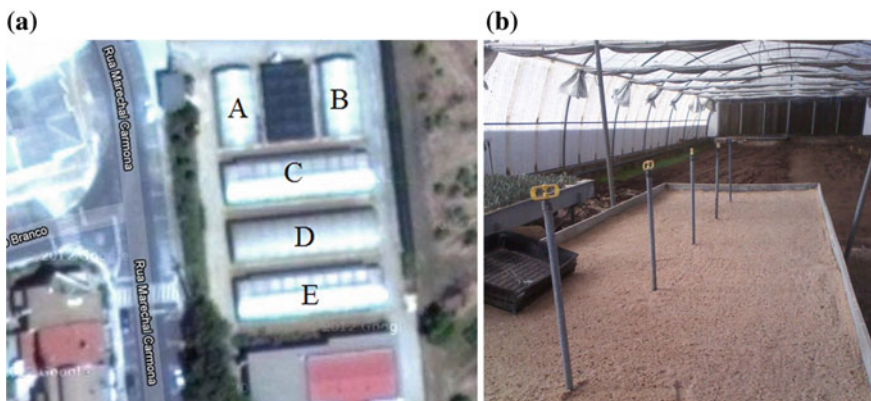


Fig. 1 Greenhouses based platform growing system. **a** Aerial view of the production greenhouses (41° 47' N, 6° 45' W). **b** Growing platform inside the greenhouse. The center pipes are for irrigation purposes

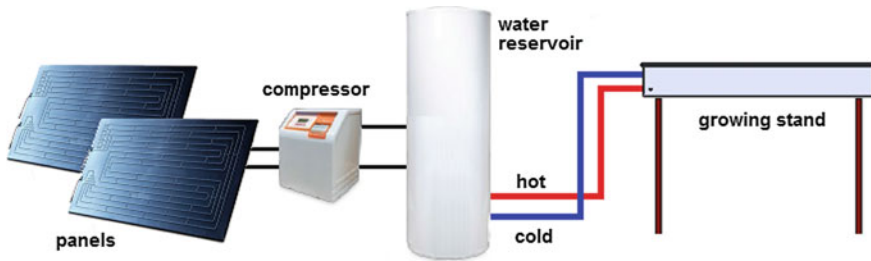


Fig. 2 Block diagram of the growing platform heating system

tion of this heating system goes around 1 kW per meter of platform length. Figure 1b depicts one of the above referred platform system.

The current installation is equivalent to 65 m of production platform which is equivalent to an installed capacity of around 65 kW. During the winter time, when the indoor temperatures are lower, the average energy spent in the growing platforms is around 100 kWh per day. Assuming an average cost of 0.25 € per kWh this will lead to a total of 25 € per day. This number is excessive and import high production costs. In order to reduce it, an alternative heating system was devised by replacing the inefficient resistance based heating element by a water heating system driven by a solar thermodynamic panels system [5, 9]. The devised heating process is straightforward as can be exemplified in the diagram of Fig. 2.

Since both the water temperature and flow requirements for the new devised heating system, under nominal and extreme conditions, are unknown, a scaled prototype was built. First of all the test rig was implemented using galvanized steel: the same material used in the already existent greenhouse stands. Only its dimensions was scaled down to a platform of 1.25 m × 0.65 m. The height of 18 cm was deliberately let equal to the original in order to easily integrate the solution devised for the prototype into the real system.

The heated water piping system was embedded in a special modeled styrofoam as shown in Fig. 3a. Then this assembly was placed inside the metal frame and filled with around 5 cm of dry sand and 10 cm of perlite.

In the developed test rig, the thermodynamic heating system was replaced by a butane gas heating. This operating change was mainly due to controllability and logistics. Nevertheless, the information that one seeks to find could also be easily obtained by this new approach. Figure 3b shows an image of this alternative structure.

Additionally an array of sensors was scattered along the system in several key points. Six waterproof temperature sensors (DS18B20) were distributed along the perlite surface. This set of sensors allows to analyze how well and uniform the heat spreads along the working area. In addition other temperature sensors are available: one to measure the heater outlet water temperature, the water temperature at a reservoir and the environment air temperature. The water flow is also measured through a flow sensor.

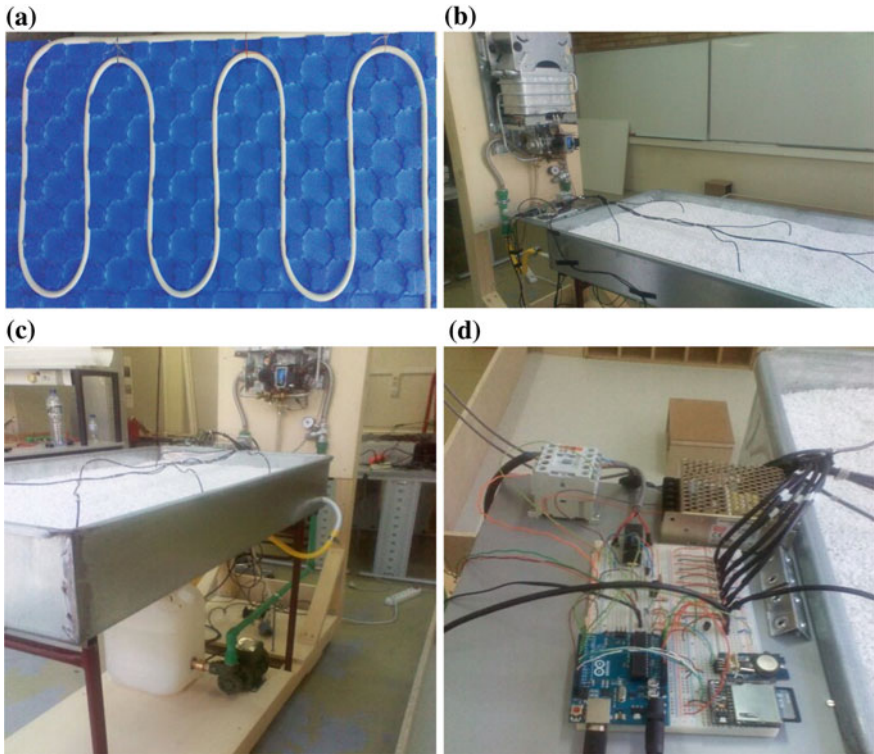


Fig. 3 Experimental rig components. **a** The growing platform internal piping system. **b** Distribution of the temperature sensors along the perlite. **c** Detail on the water system. *Below* the table it is possible to observe both the water pump and the reservoir. **d** Control and data acquisition hardware built around an Arduino Uno board

The water is made circulating by means of a 1/2 HP water pump system as can be observed in Fig. 3c. The water pump is connected to the gas heater system by means of 1 in. pipes. On the other hand, the heater outlet pipe feeds the growing table. The circuit is closed by means of a return pipe from the table to the reservoir.

The control and data acquisition system was built around an Arduino Uno R3.0 [2]. Most temperature sensors connect to the micro-controller board by means of One-Wire communication protocol. Others require the use of an analog to digital (A/D) input. The time is kept tracked using a real-time clock (RTC) and data is locally saved in a secure digital (SD) memory card. The former is connected to the Arduino Uno platform using an inter-integrated circuit communication protocol (I²C) and the latter by serial peripheral interface (SPI). This hardware setup can be observed in Fig. 3d.

The trees nursing process requires that the surface temperature be maintained around 23 °C. In this process the main external disturbances are the indoor air temperature fluctuations and the load imposed by periodic irrigations. However, in this work, the latter is not considered.

In order to cope with the required surface temperature set-point two manipulated variables are available. The heater and the water pump states. Both have an important role in temperature regulation that will be further explained in the next section along with the control law devised to regulate this system.

3 The Fuzzy Controller

Besides set-point tracking, the addressed system also requires water temperature supervision in order to prevent the system collapse. Moreover, due to the actuators nature, a bang-bang approach to control was performed. Moreover, and in order to easily design a MIMO controller by emulating its behavior through an expert system paradigm, a Fuzzy-based controller was devised [2].

The controller design was carried out using the MATLAB[®] Fuzzy Logic Toolbox taking into consideration empirical knowledge. The controller structure, within the Fuzzy Toolbox context, can be observed in Fig. 5a. This is a multi-input, multi-output controller system whose inputs are the average perlite surface temperature and the water temperature inside the reservoir. The output variables are the heater and water pump states.

The fuzzy inference mechanism selected was a Mamdani type [7, 8]. Moreover the conjunction and disjunction operation rules were the minimum and maximum respectively. The defuzzification process is carried out by means of a centroid operation over the feature space.

Concerning the surface temperature variable, the input space was partitioned into five Gaussian type Fuzzy sets. Each one was labelled as 'cold', 'cool', 'good', 'warm' and 'hot'. This fragmentation can be depicted from Fig. 4a.

Regarding the reservoir water temperature, the input space was divided into three sets labelled 'cold', 'good' and 'hot'. The sets distribution along the input space range can be observed in Fig. 4b. On the other hand, the output space for the water pump was split into three triangle type membership functions as can be concluded from Fig. 4c. The same operation was carried out for the heater variable. However, in this case, a five membership functions set was used to describe the output space. Nevertheless the same triangular shape membership functions were used as in the previous case as can be seen from Fig. 4d.

The Fuzzy controller rules were produced automatically by the MATLAB[®] software. In particular a total of 15 rules were generated. This rule based controller structure can be easily analyzed by means of a graphical output available from the toolbox. A screenshot of this rule viewer graphical tool is presented in Fig. 5b.

In the next section the above designed Fuzzy controller behaviour will be presented. Its performance will be analysed regarding both set-point tracking and actuators stress. Even if the former figure of merit can be slightly relaxed the latter is of extreme importance in order to reduce wearing of both the water pump and the gas heating system by preventing high frequency switching states.

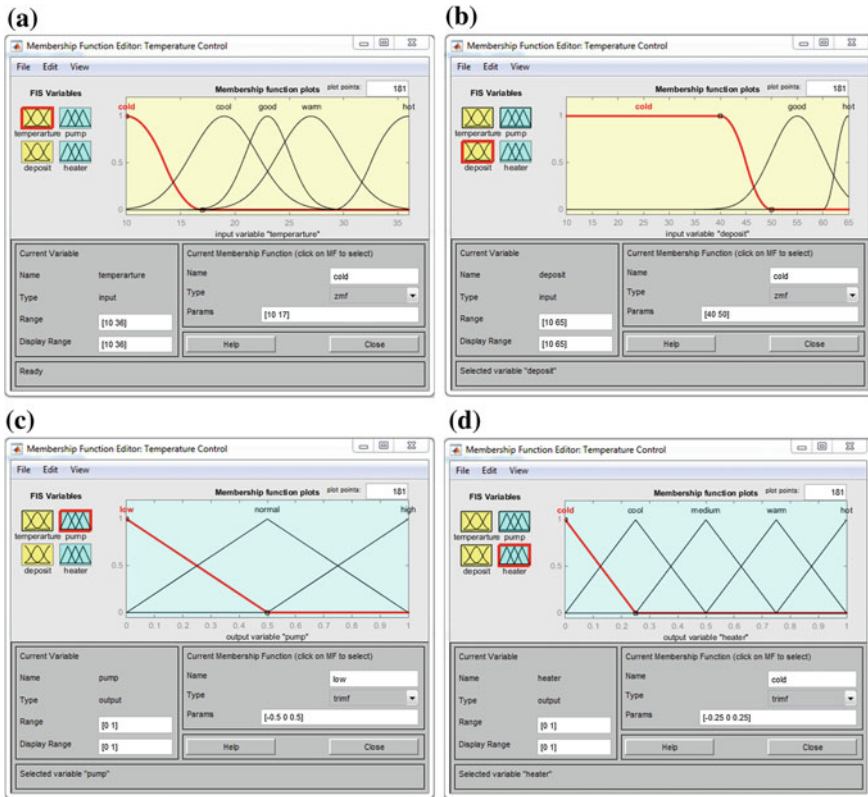


Fig. 4 Input and output fuzzy partition space. **a** Surface temperature fuzzification. This input variable was differentiated into five partially overlapped sets. **b** Reservoir water temperature fuzzification. Three sets were used over the range from 10 °C to 65 °C. **c** Output space partition for the water pump using *three triangle* shaped membership function. **d** Output space partition for the gas heating system using *five triangular* shaped membership functions

Several tests were performed, always giving priority to the worst case scenario, with ambient temperatures close to 10 °C. In all the performed tests the desired set-point temperature is considered constant and equal to 23 °C. Below are presented the results of two tests. The first, whose results are illustrated in Fig. 6a, has a temperature starting point of around 16 °C.

A second experiment, with lower water temperature starting point, was also performed. In this second case the initial system temperature is approximately 14 °C and the average temperature environment stays around 11 °C. The obtained results are presented in Fig. 6b.

From both experiments it is possible to conclude that, in both cases, the controller was able to reach, and maintain, the set-point temperature. Moreover one can see that the closed loop system exhibits an over-damped response type. In addition it is possible to observe the heater state change during the operation. Notice that the

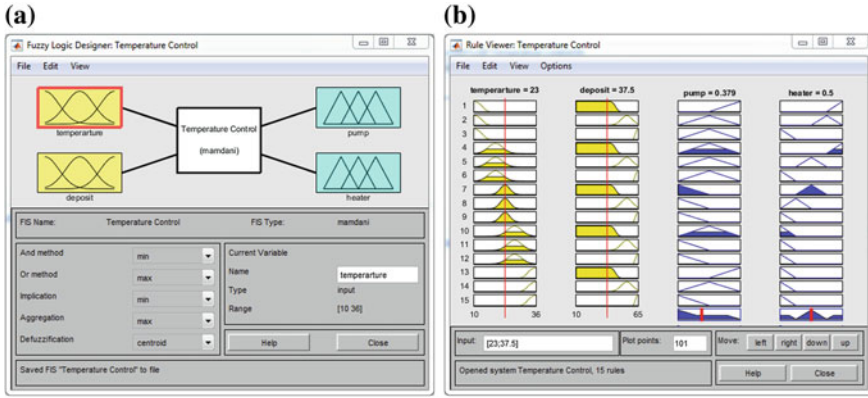


Fig. 5 Controller structure and internal operative rules. **a** Overall Fuzzy controller structure and parametrization. **b** The rule viewer assuming an surface temperature of 23 °C and a reservoir water temperature of 37.5 °C

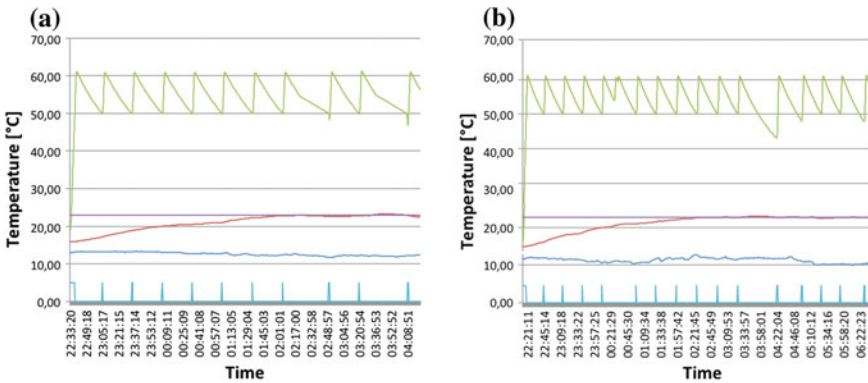


Fig. 6 Measured results. From *top to bottom* one can observe the following curves: deposit water temperature, temperature set-point, average surface temperature, ambient temperature and heater control signal. **a** Results obtained during the first test. **b** Results obtained after test two

water pump state did not change during the experiments and was always on. From the obtained data it is possible to conclude that the rate of change of the heater state has a period of around 30 min. Hence the designed controller did not lead to an aggressive closed loop response from the actuators point-of-view.

4 Cost Analysis and Economic Viability

From the performed test we have concluded that the circulating water temperature must be around 55 °C. The water mass needed, per meter of platform, is around 5 L. For 65 m long platform sets it will be needed to maintain, at least, 325 L of

water at the target temperature (for the worst case scenario). Those conditions can be easily kept by a typical thermodynamic solar system. For example the Eco450 is commercialized by the ENERGIE® company is capable of heating 450 L of water and only requires a peak power lower than 1 kW to produce around 3 kW of thermal power. This system combines a heat pump and two solar thermal collectors. The refrigerant fluid enters the solar panel and gains heat. After this stage the heat is transferred to a heat exchanger, through the help of a small compressor, which heats the water. Since the cooling fluid has a boiling temperature point of approximately -30°C , the system works even with the complete absence of sunlight [4].

The price of this system is around 4000 € and will reduce, at least, the electrical energy consumption by a factor of 3. This will lead to a mensal saving of around 250 €. Hence the value of the equipment can be amortized in a time period less than one and a half years. Assuming an equipment average operating time of 20 years, more than 18 years of energy savings can be supposed. Neglecting the evolution of the money value along time, and that the system will only operates in half of the year, more than 20,000 € can be saved along the assumed operating time.

5 Conclusion

This paper presents the economical viability of a new devised growing trees platform system based on thermodynamic panels. This alternative strategy, was proven to be economically viable, and may replace the older system whose heating system is based on electric elements. In order to infer about the applicability of this technique a scaled test rig was built. This test rig was used to evaluate if it was possible to attain the set-point temperature in the worst operating conditions and, if so, what would be the water temperature required and its mass flow. In the test rig the water was heated, not using the thermodynamic heating system, but a gas boiler whose state could be easily controlled and minimizing logistic problems. In addition, a half horse power water pump was installed, in order to make the water circulating. The pump operation was controlled by a simple on-off strategy. In order to maintain the system state variables in the required range a multi-input, multi-output Fuzzy controller was designed. The controller input is the temperature information collected by an array of sensors and its output signals are the commands for both the water pump and the gas heater. The choice of this controller paradigm was mainly due to its simplicity and proximity to empirical control based on expert knowledge. The designed controller was able to maintain the average surface temperature at the set-point level without generating any high frequency control signals. This is very important in order to reduce the wearing inherent to rapid on-off actuator state changes.

From the current results one can conclude that the replacement of the existent heating system by another based on thermodynamic solar system not only is viable but will also lead to an energy savings of more than 60 %.

However, further tests must still be performed using different operating conditions such as increased air temperature, adding moisture to the perlite substrate since, in

real operating conditions, the irrigation system periodically sprinkle the small trees. It is necessary to analyse how this change in thermal conductivity will be noticed in the overall system performance.

Acknowledgments This work is financed by the Project TEC4Growth - Pervasive Intelligence, Enhancers and Proofs of Concept with Industrial Impact/NORTE-01-0145-FEDER-000020”, which is financed by the North Portugal Regional Operational Programme (NORTE 2020), under the PORTUGAL 2020 Partnership Agreement, and through the European Regional Development Fund (ERDF).

References

1. Armstrong, F., Blundell, K.: *Energy—Beyond Oil*. Oxford University Press (2007)
2. Dhamakale, D., Patil, S.: Fuzzy logic approach with microcontroller for climate controlling in green house. *Int. J. Emerg. Technol.* **2**, 17–19 (2011)
3. Dumroese, R.K., Service, P.N.R.F., Luna, T., Landis, T.D. (eds.): *Nursery manual for native plants*. Nursery Management (Book 1), Forest Service (2009)
4. *Energie: Energia solar termodinamica*. Technical report, ENERGIE (2015)
5. Huiling, Z., Xiangzhao, F.: An experimental research on the application of ground source heat pump and floor-heating system in the greenhouse. In: *Power and Energy Engineering Conference*, pp. 1–4 (2012)
6. Kia, P.J., Far, A.T., Omid, M., Alimardani, R., Naderloo, L.: Intelligent control based fuzzy logic for automation of greenhouse irrigation system and evaluation in relation to conventional systems. *World Appl. Sci. J.* **6**(1), 16–23 (2009)
7. Mamdani, E., Assilian, S.: An experiment in linguistic synthesis with a fuzzy controller. *Int. J. Man-Mach. Stud.* **7**, 1–13 (1975)
8. Sakti, I.: Methodology of fuzzy logic with Mamdani fuzzy models applied to the microcontroller. *Inf. Technol. Comput. Electr. Eng.* 93–98 (2014)
9. Yang, Z., Pedersen, G., Larsen, L., Thybo, H.: Modeling and control of indoor climate using a heat pump based floor heating system. In: *IECON 2007—33rd Annual Conference of the IEEE Industrial Electronics Society*, pp. 2985–2990 (2007)

Model Predictive Control of a Conveyor-Based Drying Process Applied to Cork Stoppers

Pedro Tavares, Tatiana M. Pinho, José Boaventura-Cunha
and António Paulo Moreira

Abstract Control applications are a key aspect of current industrial environments. Regarding cork industries, there is a particular process that needs to be addressed: the cork stoppers drying. Currently the methodology used in this process delays the overall production cycle and lacks in the drying efficiency itself. This paper presents the development of a cork stopper drying system based on the control of a conveyor based machine using Model Predictive Control (MPC). Throughout the project it was also developed a drying kinetics model for the cork stoppers and an extension of such model to a discrete space state model. By applying the proposed methodology it is assured the cork stoppers' drying in a faster and more efficient way.

Keywords Model predictive control · Industrial drying · Modelling · Cork stoppers · Conveyor-based system

1 Introduction

Drying operations have become one of the industrial key steps in several products development. Therefore, the scientific and research community has shown interest in develop drying solutions to improve the efficiency in several processes. The ambition of obtaining streamlining industrial drying operations has led to the developed of specialized solutions in several industrial areas [9]. In particular, the cork-based industry has strict requirements concerning moisture levels and the drying process efficiency. Generally, cork-based products are realized in a complex production chain [10]. Despite cork can be used to produce several products, in order to maximize raw

P. Tavares (✉) · T.M. Pinho · J. Boaventura-Cunha · A.P. Moreira
INESC TEC - INESC Technology and Science, Porto, Portugal
e-mail: pedro.ms.tavares@gmail.com

P. Tavares · A.P. Moreira
FEUP - Faculty of Engineering of University of Porto, Porto, Portugal

T.M. Pinho · J. Boaventura-Cunha
UTAD - University of Trás-os-Montes and Alto Douro, Vila Real, Portugal

material use, the first transformation objective is to develop natural cork products. Among these, cork stoppers represent the biggest portion of cork industry [6].

Considering these premises and the ever-growing need to maximize the efficiency in drying operations, there is an evident interest in developing drying methods and machines for cork stoppers. These products need to present moisture contents levels below a pre-defined fixed value. Although there have been studies regarding the kinetics and dynamics of the drying operation in multiple areas (including cork stoppers [2, 8]), lately the goal is to maximize the efficiency of the drying operation regarding the time and energy consumption.

In this paper, it will be presented a generic control approach, that, due to its flexibility, has potential to be applied to any drying scenario using conveyor-belts. It will also be proposed the modelling of the cork stopper drying process and a new model predictive controller designed for this application. The main goal of this approach is its integration in the cork stoppers production line, allowing the optimization of the plant layout reducing delays in the production, with the guarantee of the requirements in the moisture content level in less time.

The current paper is structured in five main sections. Section 2 aims to provide an overview of the evolution in drying process optimization approaches. Section 3 (System Architecture) describes the developed approach to solve the proposed problem. Within this section are also described the developed modelling and control architectures. Section 4 (Experimental Validation) synthesizes the results obtained by the developed system in both simulated and real environments. Section 5 (Discussion and Future Perspectives) reviews the contribution of this project to the scientific world and points some issues for improvements.

2 Related Work

The control architecture development in industrial environment is associated with the scientific and technological development. Currently, drying solutions can be classified as static or dynamic. The first one considers that the product of interest is fixed above a flat bed dryer. The conventional flat bed dryer has the problem of producing nonhomogeneous drying results. Thus, the second approach considers that the product is moved throughout the process trying to create homogeneous results. There are several examples of this type of approach that allows the maximization of the drying efficiency [3, 12].

Focusing on the dynamic drying processes, one of the major contributions is the use of conveyor-belts design to increase the process quality. In 2008, Zanoelo et al. proposed to reproduce the drying kinetics in a continuous shallow packed bed dryer of mate leaves at transient conditions by adjusting the conveyor-belt velocity to compensate disturbances in the operating conditions [13]. Years later, in 2015, Alamia et al. proposed an integrated dryer and conveyor belt for woody biofuels with steam as the heat transfer medium [1]. This approach can be valuable as it achieves higher energy and exergy efficiencies. Furthermore, there are recent studies that consider

drying methods, such as micro waves, with enough energy to remove completely the moisture from a product [7]. However this technique can degrade some properties of the material and can not be applied to all drying processes. Currently the removal of moisture from the cork stoppers is assured by placing these within drying chambers. In this context, drying chambers replacement for a new drying method proves to be beneficial as the time and energy consumption related to the drying of cork stoppers in drying chambers creates a delay in the production as well as excessive energy expenditure.

Although all strategies presented have been implemented and validated in the industrial world they have limitations when applied to cork stoppers drying and thus considerations must be taken for each given application.

3 System Architecture

The proposed system is a flexible model predictive controller capable of assuring the drying of cork stoppers in multiple conditions with a conveyor-belt based solution. As such in this section it will be presented the main tiers of flexible control application: modelling and discretization (Sects. 3.1 and 3.2) and control and actuation methodology based on the developed model (Sect. 3.3).

3.1 System Modelling

Throughout the drying process it were considered four types of state variables, namely the temperature and humidity of both cork stoppers and the surrounding environment air. Previous works state that the evolution of these variables is expressed as a set of equations (see parameters list in Table 1) [4].

The drying process is essentially defined as an exchange of water between the product intended to dry and the surrounding atmosphere. As such, it can be represented by a mass variation between the product M_p and the air M_a , see Eq. 1.

$$\frac{\partial M_p}{\partial t} = \delta_m \quad \& \quad \frac{\partial M_a}{\partial t} = -\delta_m \tag{1}$$

There is a grounded relation between mass and humidity values. The mass variation is directly connected to the humidity variation in the cork stopper (α) by a multiplier factor.

$$\frac{\partial M_p}{\partial t} = K * \frac{\partial \alpha}{\partial t} \tag{2}$$

Table 1 Parameters involved in the drying process

Parameter	Parameter specification	Unit
δ_m	Drying rate	$\frac{\text{kg}}{\text{s} \cdot \text{m}^3}$
ρ_a	Air density	$\frac{\text{kg}}{\text{m}^3}$
λ_0	Latent heat of vaporization at the atmospheric pressure	$\frac{\text{J}}{\text{kg}}$
R_v	Individual air constant	$\frac{\text{J}}{\text{kg} \cdot \text{K}}$
β	Dry air specific mass ratio	–
T_{dp}	Dew point temperature	K
T_0	Triple point temperature	K
P_{atm}	Atmospheric pressure	Pa
$P_{s,0}$	Partial pressure at the reference temperature	–
ζ	Falling rate multiplier of the drying rate	–
h	Heat transfer coefficient	$\frac{\text{W}}{\text{m}^2 \cdot \text{K}}$
ϵ	Evaporation area over product volume ratio	$\frac{1}{\text{m}}$

The proposed solution runs in a conveyor-based platform. As such there is the need to add a term in the direction of movement (x , for the cork stoppers and z , for the air). Due to the architecture used in the machine construction there will be three air temperature and humidity measurements and, thus, eight global variables.

Concerning the drying systems modelling, there are works defending the need to establish a threshold for the product minimum humidity value [5]. In this particular case, the cork stoppers minimum humidity value is 5 %. However, at the drying step it is required only a mean humidity of 7.5 %. Furthermore, attending to the developed hardware solution that is going to be used, there are some assumptions and simplifications to consider:

- The cork stoppers are evenly distributed on the conveyor-belt.
- The height at each section is the height of a single cork stopper.
- The volume shrinkage of the cork stopper is negligible.
- All mass lost in the cork stopper is only due to the humidity evaporation.
- The heat losses from the machine interior to its exterior are negligible.
- It is assumed constant pressure throughout the different conveyor-belt zones.
- Densities, specific heat capacities and evaporation/volume ratio are constant.
- The velocity of the hot air that promotes the drying process is constant.

The model described by the initial equations is clearly non-linear since it is mostly defined using partial differential equations. As such a way to simplify this model is by using a finite difference approximation. In this way it is possible to separate the model in small blocks that allow implementing an approximation to the partial differential equations.

Considering one infinitesimal section travelling throughout the conveyor at each iteration we can take into consideration only the variation of humidity with time $\frac{\partial \alpha}{\partial t}$ (bypassing the term dependent of the distance travelled, $v_x * \frac{\partial \alpha}{\partial x}$).

Another modelling aspect is related to the temperatures variation. In this particular project the objective is to maintain the heating temperature constant. As such the air temperature variation ($\frac{\partial T_a}{\partial t}$) is zero. As a result of fixing the heating temperature constant, the cork stoppers' temperature will only depend on the thermal conductivity of cork (C_c) (or the cork to air thermal resistance R_{ac}) and on the temperature difference between the air and the cork stopper. Based on these considerations it is possible to obtain a single difference equation to express the previous presented state variables evolution, cork stopper humidity α and temperature T_p and air humidity γ .

$$\frac{\partial \alpha}{\partial t} = (\alpha - \alpha_e) * K * \delta_m \quad \& \quad \frac{\partial T_p}{\partial t} = C_c * \frac{T_a - T_p}{R_{ac}} \quad (3)$$

$$\frac{\partial \gamma}{\partial t} = -\frac{1}{K} * \frac{\partial \alpha}{\partial t} * \frac{1}{\rho_a * v_z} \quad (4)$$

Finally, in order to apply this model, is mandatory to define the drying rate, δ_m . This value can be calculated using the following equations [4]:

$$T_{dp} = \left(\left(\frac{1}{T_0} \right) - \left(\left(\frac{R_y}{\lambda_0} \right) * \log \left(\frac{P_{atm} * \gamma}{\rho_{s,0} * (\beta + \zeta)} \right) \right) \right)^{-1}$$

$$\zeta = \frac{0.9}{\alpha_{crit} - 0.02} * \alpha + \frac{0.9}{\alpha_{crit} - 0.02} * \alpha_{crit} \quad V \quad \zeta = 1 \quad (5)$$

$$\delta_m = \frac{h * \epsilon}{\lambda_0} * (T_{dp} - T_a) * \zeta$$

3.2 State Representation Model

Once modelled the process, it is necessary to adapt its formulation in order to become faster in computational processing. As such it was chosen a non linear space-state representation model defined as:

$$x_{t_{k+1}} = f(x_{t_k}, u_{t_k}, \alpha_e) \quad (6)$$

$$y_{t_k} = C * x_{t_k} + D * u_{t_k}$$

In state models representation, x_{t_k} , u_{t_k} and y_{t_k} are respectively the state, the control variables and the output in a given instant t_k .

$$x_{t_k} = [\alpha_{t_k}; T_{pt_k}; \gamma_{zt_k}; T_{azt_k}]' \quad \& \quad y_{t_k} = \alpha_{t_k} \quad (7)$$

Fig. 1 Real machine and zones 1 in red, 2 in yellow, 3 in blue



α_k and T_{pt_k} represent, respectively, the cork stopper humidity and temperature in the time instant t_k while γ_{z_k} and T_{az_k} correspond to the air humidity and temperature values in the zone 1, 2 or 3 (see Fig. 1) where the infinitesimal section of cork stoppers is in that instant. Besides these zones, there is also a stabilizing zone that is not monitored (green zone in Fig. 1).

Another important structure that we need to consider is the system input at each instant t_k, u_k . Namely, we have the control variables (v_x and the activation of the boost heater (present in zones 2 and 3)). As such we can define:

$$u_k = \left[\frac{1}{v_x}; boost_{on} \right]^T \tag{8}$$

During the process there are also measured variables (air temperatures and humidities in several zones). These variables are important as they allow the controller to estimate the cork humidity and to send a feedback and correct prediction errors. Finally there is an important consideration to have in order to recreate the drying model that is the minimum threshold for the humidity value, α_e (5%). The controller can be described by the block diagram presented in Fig. 2.

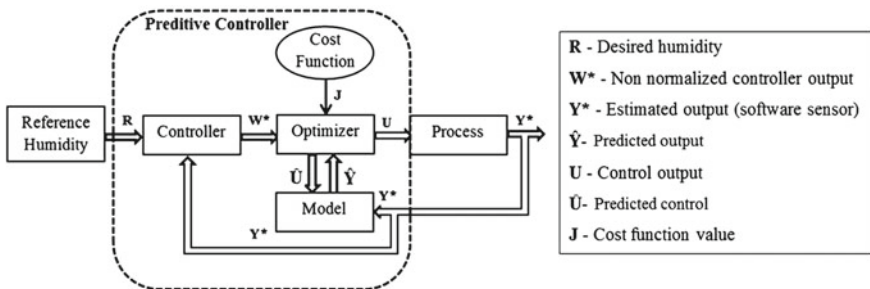


Fig. 2 MPC controller diagram

Furthermore the “Model” block in Fig. 2 is responsible for representing the equations of the drying system. That is, it is the block responsible for the space state implementation. The state representation function and matrices C and D were defined considering a space discretization so that in each section of space there is a corresponding set of parameters values (see Eq. 9). Moreover, based on the space discretization, there is the possibility of considering a variable temporal step dependent of both space and control velocity ($\delta_t = \frac{\delta_x}{v_x}$), where δ_t is the difference of time instants ($t_{k+1} - t_k$). Finally it was used the finite difference method for the discretization.

$$\begin{aligned}
 \alpha_{t_{k+1}} &= (1 + \delta_t * K * \delta_m) * \alpha_{t_k} - \alpha_e * \delta_t * K * \delta_m \\
 T_{pt_{k+1}} &= 1 - \frac{\delta_t}{R_{ac}} * T_{pt_k} + \frac{z * \delta_t}{R_{ac}} * T_{azt_k} \\
 \gamma_{t_{k+1}} &= \gamma_{t_k} - \frac{-z * \delta_t * \alpha_{t_k}}{K * \rho_a} \\
 T_{azt_{k+1}} &= c_z * (MaxTemp - T_{azt_k}) * boost_{on} + T_{azt_k} \\
 C &= [1 \ 0 \ 0 \ 0]; \quad D = [0 \ 0]
 \end{aligned}
 \tag{9}$$

One final consideration is related to c_z value. Due to a physical separation of zones implemented in the machine, this value is considered as zero for zone 1 and one for zones 2 and 3 (zones affected by the boost heater).

3.3 Model Predictive Control

The model predictive control is an advanced control method implemented in several industrial applications. The main advantage of this control is the ability to anticipate future states, use future reference evolution and future disturbances for taking appropriate control actions. In the cork stoppers drying process presented in this work, the model predictive control goal is to define the conveyor speed and the necessity of the boost heater, in order to completely dry the cork stoppers inserted in the machine. This is achieved using an optimization procedure that allows minimizing the overall cork stoppers drying time. The sequence of operations of this process is the reading of the initial humidity of the cork stoppers that will be compared to a standard reference (in this case 7.5 %). While the estimated cork stoppers humidity does not reach that goal, the error that come from the comparison between cork stopper predicted and measured humidity will enter the optimization module and new control actions (conveyor velocity and booster) that minimize the cost function will be computed. This cost function can be defined as the weighted sum of three components: the error between estimated humidity at a set of conditions and the established goal humidity, variation of required speed and the activation of the boost (see Eq. 10).

$$\text{Goal} : \min_{v_{xk}, \text{boost}_{on}} J_k = \min(w_1 * H_k + w_2 * (v_{xk} - v_{x(k-1)}) + w_3 * \text{boost}_{on}) \quad (10)$$

J_k is the value of the cost function at each iteration, w_1 , w_2 and w_3 are the weights for each section of the cost function. The second term is the variation of required belt speed responsible for smoothing the control signal and avoiding oscillations. boost_{on} describes the current activation state of the boost heater and is the term that considers the energy costs. Finally, H_k is the difference between the predicted and the goal humidity of the cork stoppers.

The choice of prediction and control horizons are key aspect when applying model predictive control. Typically, in these controllers, future outputs \hat{y} at each sampling instant t_k , are estimated over a prediction horizon HP . For this particular case the HP value is defined as the number of steps remaining until the process' end. In order to keep the system as near as possible to the set point, the cost function is minimized to compute the set of future control actions, u_k , over a control horizon M [11]. In this case, a control horizon of 1 step ahead is considered. Only the first control action is actually implemented because at the next sampling instant the process is repeated with updated information (air temperature and humidities that allow to estimate the cork stopper humidity). In this way, it is possible to achieve the desired goal in the minimum time possible or minimizing a balance between time and energy costs.

4 Experimental Validation

The validation of both the model and the developed model predictive controller was done using two approaches. The first one was the simulation of those in MATLAB using the developed model as reference (Sect. 4.1). The second one was the testing of the controller in a real environment (a drying prototype developed throughout the project, Sect. 4.2).

4.1 Simulated Environment

Throughout the simulations, several strategies were evaluated considering different prediction and control horizons. Moreover there were simulated random disturbances in the system evolution in order to evaluate its response. The best results (for a full prediction horizon and a control horizon of one) are described graphically in Fig. 3.

It was verified that using a full prediction horizon (this is considering every step remaining until the end of the process), the desired results can be achieved successfully with less computational effort. Then it were performed simulations with several control horizons in order to determine the most appropriated. When we increase the control horizon, the complexity is also increased and the time spent in the prediction

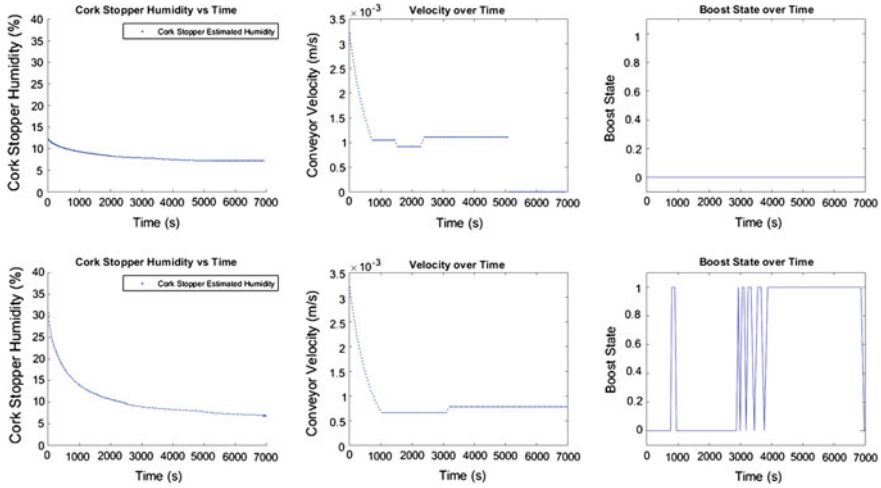


Fig. 3 Simulated cork stoppers humidity and control signals for the best case (at the *top*) and the worst case (at the *bottom*)

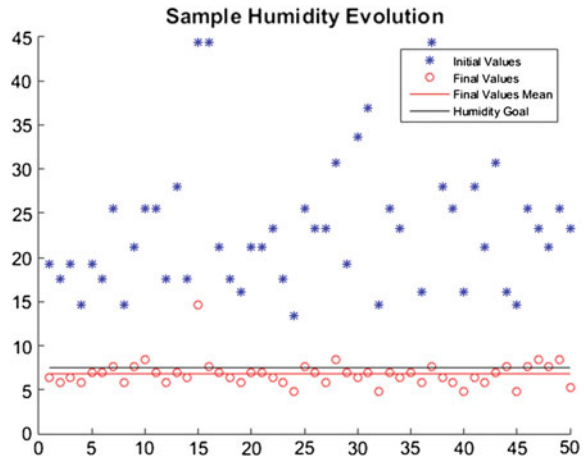
reaches a point in which the control is no longer viable for real-time implementation. After some simulations, we conclude that a prediction control horizon of one iteration is preferable for this application in terms of efficiency and complexity, which means that the goal is reached faster and the processing time is lower. This proves to be beneficial since the proposed model is intended to be implemented in a PLC.

4.2 Drying Machine Test

Multiple tests were also conducted using a real machine in order to validate all the modelling and control methods described. We can evaluate the consistency of the developed control strategy by measuring the mass of a set of cork stoppers or using the measurements obtain by the AQUABOY sensor throughout the overall drying process. The complete protocol used was:

1. Choose a set of cork stoppers (in this case fifty) and measure their humidities using the AQUABOY sensor and a precise scale.
2. Pre-heating the real machine until it reaches the stabilization point of 60 °C.
3. Insert the cork stoppers average humidity and quantity in the LCD console in order to update the drying parameters needed to start the process.
4. Place the cork stoppers in the real machine and begin the drying process, activating the movement of the conveyors.
5. At the end, pick the cork stoppers and measure their humidity values.

Fig. 4 Set of cork stoppers before and after the drying process



The cork stoppers' humidity can be approximated by a Gaussian distribution. Data from a recent test will be used to exemplify the initial and final humidity of a set of cork stoppers. Initially the mean of this set was 23.5 % with a standard deviation of 7.7 %. At the end the mean was 6.8 % with a standard deviation of 1.5 %. These results are pictured below in Fig. 4. These results represent a recent test using a total of 1500 cork stoppers and monitoring randomly 50 pre-selected cork stoppers.

5 Discussion and Future Work

Throughout this project, it was proposed a model and a controller for the cork stoppers drying process that can be applied to the industrial environment and valuable to the engineering and research community.

One of the most frequent problems associated with drying systems is the non-linearity of the models that describe the process. This paper presented a structured approach to this issue focusing a particular process, the cork stoppers' drying. There were defined equations for the continuous process and then they were discretized into a space state model so that such equations can be computed in a faster (although precise) way. Another feature of our proposed methodology is the model predictive control layer of our solution. One of the key objectives of the proposed solution was the ability to adapt to several requirements in terms of environment conditions and initial humidity demands. It was proved that the current solution is able to dry the cork stoppers until they reach the pre-determined humidity values (below 7.5 %). Finally, the presented solution feedback was tested in a simulated environment. Currently we are developing a software sensor that can be applied in the real environment. Although this solution shows good results, the proposed approach can be improved. The model developed did not took into consideration a deviation as big as detected with the test

in the real prototype. Moreover, it was found that the cork stopper model can not be defined as a simple composition of cork and water. There are some volatiles that influence the mass of the cork stopper that need to be considered. In the future a refinement of the model would be advantageous.

In conclusion, the work presented formalizes a cork stoppers drying approach. This solution can be valuable in several fields of control based on its flexibility as it produces interesting results for any required initial parameters as long as they remain within the pre-determined range of initial values.

Acknowledgments This research has received funding from the European Union Seventh Framework Programme (FP7/2007-2013) under grant agreement n.[604286]. The authors wish to acknowledge the contributions of the members of the FOCUS consortium.

References

1. Alamia, A., Strm, H., Thunman, H.: Design of an integrated dryer and conveyor belt for woody biofuels. *Biomass Bioenergy* **77**, 92–109 (2015)
2. Belghit, A., Bennis, A.: Experimental analysis of the drying kinetics of cork. *Energy Convers. Manage.* **50**(3), 618–625 (2009)
3. Chan, Y., Dyah, T., Kamaruddin, A.: Solar dryer with pneumatic conveyor. *Energy Procedia* **65**, 378–385 (2015)
4. van Deft, T.J.: Modeling and model predictive control of a conveyor-belt dryer. Ph.D. thesis, Norwegian University of Science and Technology (2010)
5. Dimitriadis, A., Akritidis, C.: A model to simulate chopped alfalfa drying in a fixed deep bed. *Drying Technol.* **22**(3), 479–490 (2004)
6. Fortes, M., Rosa, M., Pereira, H.: A cortiça. Instituto Superior Técnico (2004)
7. Hassini, L., Peczalski, R., Gelet, J.L.: Drying of granular medium by hot air and microwaves. Modeling and prediction of internal gas pressure and binder distribution. *Powder Technol.* **286**, 636–644 (2015)
8. Magalhães, A., Pinho, C.: Spouted bed drying of cork stoppers. *Chem. Eng. Process.: Process Intensif.* **47**(12), 2395–2401 (2008)
9. Mujumdar, A.: *Handbook of Industrial Drying*, vol. 1, 2nd edn. Revised and Expanded. Taylor & Francis (1995)
10. Pereira, H.: *Cork: Biology, Production and Uses*. Elsevier (2007)
11. Seborg, D., Mellichamp, D., Edgar, T., Doyle, F.: *Process Dynamics and Control*. Wiley (2010)
12. Wang, X., Qin, B., Xu, H., Zhu, W.: Rotary drying process modeling and online compensation. *Control Eng. Pract.* **41**, 38–46 (2015)
13. Zanoelo, E., Abitante, A., Meleiro, L.: Dynamic modeling and feedback control for conveyors-belt dryers of mate leaves. *J. Food Eng.* **84**(3), 458–468 (2008)

Robust Control of Agroindustrial Drying Process of Grains Based on Sliding Modes and Gravitational Search Algorithm

Josenalde Oliveira, José Boaventura-Cunha and Paulo Moura Oliveira

Abstract This paper proposes the recently introduced Gravitational Search Algorithm (GSA) to tune a Sliding Mode Controller (SMC) applied on the temperature control of a grains drying system. The problem of maintaining the temperature precisely adjusted inside a silo is relevant to avoid thermal damage and spoilage losses, and thus guarantee the right conditions for storage. The objectives of set-point tracking and disturbance rejection are incorporated into the minimization of the integral of the time-weighted absolute error. Simulation results are presented and compared with PID and with SMC tuned by Particle Swarm Optimization (PSO) and by earlier proposed tuning equations.

Keywords Sliding modes · Optimization · Robustness · Process control · Gravitational search algorithm

1 Introduction

Drying is a decisive process present in a wide variety of agroindustrial areas such as food [1] and forestry [2]. Specifically in food sector, post-harvest techniques such as grains drying process play an important role in modern agricultural industry, since grains represent a worldwide source of food. Harvest, handling, storage and

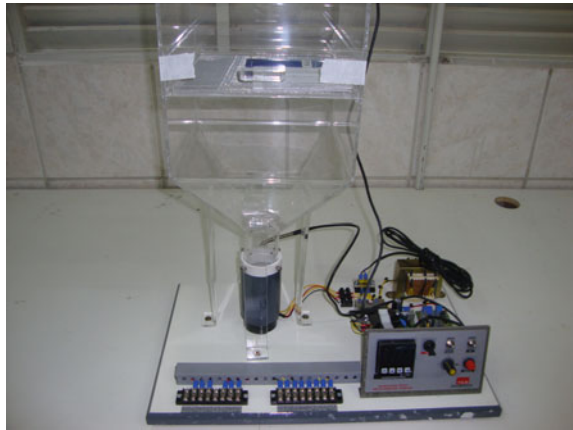
J. Oliveira (✉) · J. Boaventura-Cunha · P.M. Oliveira
INESC TEC—INESC Technology and Science, Campus da FEUP, 4200-465 Porto, Portugal
e-mail: josenalde@ej.ufrr.br

J. Oliveira
Agricultural School of Jundiá—Federal University of Rio Grande do Norte, UFRN,
Macaíba, RN 59280-000, Brazil

J. Boaventura-Cunha · P.M. Oliveira
School of Sciences and Technology, University of Trás-os-Montes and Alto Douro,
5000-801 Vila Real, Portugal
e-mail: jboavent@utad.pt

P.M. Oliveira
e-mail: oliveira@utad.pt

Fig. 1 Laboratory-scale educational kit—grains drying process



appropriate drying must be carried out properly in order to guarantee the quality and to maximize the utilization of production.

Researchers have given attention to proper modeling [3], since usually these systems present large time delays, nonlinearities, multi disturbance and strong coupling. However, besides a highly-accurate modelling, robust control techniques must be investigated, since grains are biological entities extremely sensible to heat and temperature effects, which may cause severe damage to the expected final characteristics. Therefore, it is recommended the choice of control techniques that offer the guarantee of insensibility to possible abrupt temperature variations generated from external disturbances and/or physical parameters variations as well, reflected on the mathematical model of the system. Reduced order models, such as First Order Plus Dead Time (FOPDT), although can incorporate the dominant process behavior, also demand robust schemes to compensate some unmodeled dynamics. The most common agroindustrial control systems are based on the Proportional-Integrative-Derivative (PID) controller and very often new proposals are compared with PID, as may be seen in [4–6]. This work is based on the FOPDT model obtained in [6] for temperature control, with a laboratory-scale fixed-bed drying system presented in Fig. 1, simulating a real silo as in Fig. 2.

When time delay is present, the Smith Predictor (SP) [8] is a good strategy to compensate it. Its basic idea relies on designing the controller considering the predicted outputs of a free delay highly-accurate model. Original SP assumes model matching for appropriate tracking and disturbance rejection. As a promising alternative to overcome model-plant mismatches and external disturbances, [9] proposed a Sliding Mode Controller (SMC) based on a SP structure (SMC–SP), getting better tracking and robustness features when compared to PI control. SMC [10] is a robust control technique, based upon a discontinuous control law (U_D) and the definition of a *sliding surface*, function of the system state variables. Recently, a work by [11] successfully applied this SMC–SP on a long time delay FOPDT model, for main steam pressure control in coal-fired power plant boiler. These previous works use some

Fig. 2 Grains storage silo [7]



method to get an initial set of parameters for U_D , either based on open-loop step responses or on some numeric method, such as Nelder-Mead searching algorithm [9]. As it will be detailed further, these parameters require considerable trade-off.

This work proposes the search for optimized design parameters using the recently proposed Gravitational Search Algorithm (GSA) [12], which has been shown efficiency for evaluating global optimum in various scenarios, such as PID design [13], smart grid power systems [14] and hydrothermal dispatch [15], just to name a few. Besides, it is in continuous improvement [16] and has shown reliability [17] when compared to other nature-inspired heuristics, such as Particle Swarm Optimization (PSO) [18]. This paper is structured as follows: Sect. 2 states the problem and reviews the controller design. Section 3 presents the motivation for using GSA and its main equations, incorporated to the controller. Section 4 presents simulations results on the drying process model and compare them with PID and SMC-SP tuned by PSO and by the equations proposed by [9], considering disturbed scenarios. Section 5 concludes the work and proposes next steps for continuous research.

2 Problem Statement

Consider the block diagram in Fig. 3:

For a First Order Plus Dead Time model (FOPDT) with the gain K , time constant τ and delay t_0

$$G(s) = \frac{K}{\tau s + 1} e^{-t_0 s}. \tag{1}$$

The actual plant $G(s)$ is given by (1) and the plant model may be splitted in two parts: a free delay part G_M^- and a noninvertible part G_M^+ associated with the delay. Therefore, one has

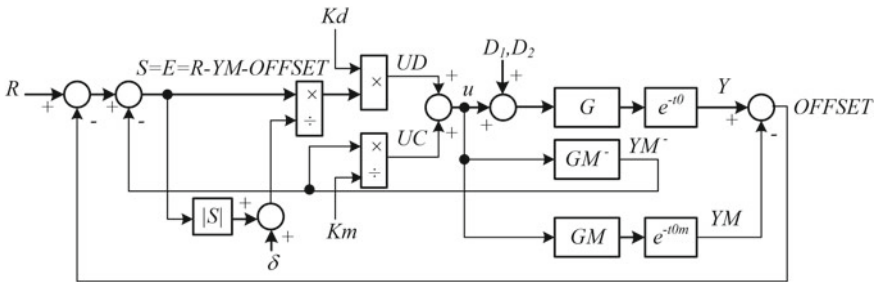


Fig. 3 Sliding mode controller on smith predictor configuration

$$G_M(s) = G_M^- G_M^+ = \frac{K_M}{\tau_M s + 1} e^{-t_{0M} s}, \tag{2}$$

with $Y_M^- = G_M^- U$ and $Y_M = G_M U^1$. External signals d_1 and d_2 represent load disturbances. From SP theory, the error signal $OFFSET = Y - Y_M$ is ideally null when $Y = Y_M$, which means plant-model matching. In this case, system error $E = R - OFFSET - Y_M^-$ is not affected by delay, since outer loop has no influence. When $G \neq G_M$ (caused by plant-model mismatch) and/or at least an external disturbance enters the system, the more robust the controller the better the disturbance rejection, and thus SMC is an appropriate choice.

2.1 Devising SMC

The design consists of two steps: first, the definition of a *sliding surface* $S(t)$, commonly a function of the system states and where the trajectories must reach in finite time. Once in $S(t)$ the system order is reduced and control aim is achieved. In this condition, named *sliding mode*, $\dot{S} = 0$ and a non switching control signal U_C , referred as *equivalent control* is designed. The second step consists of designing the control law U_D which drives the process variable to the sliding surface, during the *reaching mode* and it must obey a *reaching law*. Then, SMC control law in Fig. 3 is:

$$U = U_C + U_D. \tag{3}$$

Control Law for Sliding Mode— U_C Consider as sliding surface S the system error E in Fig. 3:

$$S(t) = E = R - OFFSET - Y_M^-. \tag{4}$$

¹s is the Laplace variable or $\frac{d}{dt}$ operator, depending on the context. From this point on it will be omitted to simplify notation.

For designing purposes and according to SP theory, (4) considers plant-model matching ($OFFSET = 0$) or a constant OFFSET, and thus only free delay model G_M^- is considered. Taking this fact into account and by applying the sliding condition $\dot{S} = 0$ in (4), one has

$$\frac{dS(t)}{dt} = \frac{dR(t)}{dt} - \frac{dY_M^-(t)}{dt} = 0. \tag{5}$$

From (2), and representing G_M^- into differential equation form:

$$G_M^- = \frac{Y_M^-}{U} = \frac{K_M}{\tau_M s + 1}, \quad \frac{dY_M^-}{dt} = \frac{-Y_M^- + K_M U}{\tau_M}. \tag{6}$$

Replacing (6) in (5) and after some algebraic manipulation,

$$U(t) = \frac{\tau_M}{K_M} \left[\frac{dR(t)}{dt} + \frac{Y_M^-(t)}{\tau_M} \right]. \tag{7}$$

According to the work of [9] the derivative of the reference signal can be discarded. Therefore, this component of control signal is indeed the equivalent control signal U_C , which turns into

$$U_C(t) = \frac{Y_M^-(t)}{K_M}. \tag{8}$$

Control Law for Reaching Mode— U_D This component is responsible for the corrective action, for driving system trajectories towards $S(t)$ (4). When the trajectory is *sliding* and some disturbance occur, U_D acts to correct it. Therefore, it must be designed in such a way that the reaching law (9) is satisfied,

$$S\dot{S} < 0. \tag{9}$$

To cope with output chattering, instead of a signum function, [9] proposed:

$$U_D(t) = K_D \frac{S(t)}{|S(t)| + \delta}, \tag{10}$$

where K_D is the gain responsible for how fast $S(t)$ is reached (and therefore it impacts disturbance rejection) and δ accounts for chattering reduction. It is noteworthy that the pair (K_D, δ) directly affects system performance and, moreover, there is some tradeoff between them. With optimization algorithms and time-domain performance methods, [9] proposed the following set of equations based on system model (2), for initial tuning:

$$K_D = \frac{0.72}{|K_M|} \left(\frac{\tau_M}{t_{0M}} \right)^{0.76}, \quad (11)$$

$$\delta = 0.68 + 0.12 |K_M| K_D \frac{t_{0M} + \tau_M}{t_{0M} \tau_M}. \quad (12)$$

In the proposal of this paper, these equations give center values for (K_D, δ) from which the GSA algorithm defines a search space, to be detailed in next section.

3 Gravitational Search Algorithm

GSA is a heuristic optimization algorithm based on the Newtonian's law of gravity and motion [12], and therefore incorporates physical concepts of how masses interact with each other. Since GSA is a population-based approach, each *mass* is considered a potential solution and it is named an *agent*. Higher mass agents are thus considered as better solutions for a particular cost function.

Consider a population of N agents, moving in a n -dimensional search space, with vectors x and v representing, respectively, the agent position and velocity. The interaction force between agents i and j , for dimension d and iteration t is given by

$$F_{ij}^d(t) = G(t) \frac{M_i(t)M_j(t)}{R_{ij}} \left(x_j^d(t) - x_i^d(t) \right), \quad (13)$$

with the gravitational constant modified as in [13], since it presented better convergence. With G_0 as the initial gravitational constant and n_{it} the total number of iterations, one has

$$G(t) = G_0 \left(1 - \frac{t}{n_{it}} \right). \quad (14)$$

The total force that acts in each agent i , for a particular dimension d , is:

$$F_i^d(t) = \sum_{j \in k_{best}, j \neq i}^N \phi_{1j} F_{ij}^d(t), \quad (15)$$

where ϕ_{1j} represents an uniform randomly number generated in the interval $[0, 1]$ and k_{best} is the set of best agents, with size set to $k_0 = N$ at the beginning of the search procedure and decreased linearly over time. To calculate the acceleration a of each agent i based on the Newton's second law, and respective velocity and position, the following set of equations are evaluated:

$$m_i(t) = \frac{fit_i(t) - worst(t)}{best(t) - worst(t)}, \quad M_i(t) = \frac{m_i(t)}{\sum_{j=1}^N m_j(t)}, \quad (16)$$

$$a_i^d(t) = \frac{F_i^d(t)}{M_i(t)}, \quad (17)$$

$$v_i^d(t + 1) = \phi_{2i} v_i^d(t) + a_i^d(t), \quad x_i^d(t + 1) = x_i^d(t) + v_i^d(t + 1), \quad (18)$$

with the following definitions: ϕ_{2i} is defined as ϕ_{1j} in (15), *fit* is the current fitness value for agent *i* in iteration *t*, *best*, *worst* represent the population best and worst fitness values in iteration *t*, respectively.

3.1 Materials and Methods

The proposal of this paper is the application of GSA to tune parameters K_D and δ of (10) and compare the results when they are set by equations (11) and (12), and by Particle Swarm Optimization [18]. Moreover, for a fair comparison, a PID controller is also tuned by GSA and all results are compared in terms of Integral of Time-weighted Absolute Error ITAE, Control Effort (CE) and Total Variation (TV), both for control signal and process variable. The average indexes are thus calculated for a number of runs, $N_{runs} = 21$, and are evaluated as:

$$ITAE = \sum_{j=0}^T j |S(j)|, \quad CE = \sum_{j=0}^T |(U(j))|, \quad (19)$$

$$TV_U = \sum_{j=1}^T |U(j) - U(j - 1)|, \quad TV_Y = \sum_{j=1}^T |Y(j) - Y(j - 1)|. \quad (20)$$

From [6], the model for the drying process plant is:

$$G(s) = \frac{10}{80s + 1} e^{-3s}. \quad (21)$$

The educational system in Fig. 1 is composed by an acrylic silo, a heater and a fan which blows the air through the silo, where exists a screened drawer, like a strainer, in which the grains are deposited, characterizing a fixed-bed drying. The temperature adjustment is made by an industrial PID controller, being the temperature under the screened drawer obtained from a Pt100 sensor. The air flow control is manually made by a potentiometer that acts on the PWM signal generator. For modeling purposes in [6], the air flow actuating signal was fixed approximately in 46.7 % of the total power. The PID output signal is applied on a Solid State Relay (SSR), which, by its turn, acts on the electrical resistance. The graphical method of open-loop step

response with an amplitude of 40 % was chosen to get the mathematical model that better describes the practical system, being appropriately validated. This is the model used in the simulations.

Both delays t_0 in (1) and t_{0M} in (2) are approximated by a fourth order Padé's rational function. Two step load disturbances affects the plant: $d_1 = 2^\circ\text{C}$ for $t \geq 100$ s and $d_2 = 2^\circ\text{C}$ for $t \geq 410$ s. In some cases to be mentioned, a parameter variation of +30 % is considered in (21) for $t \geq 0$. Both GSA and PSO run during 200 iterations ($n_{it} = 200$), with a population of 100 agents ($N = 100$). Specific parameter for GSA is the final percentage of agents that attract others agents, and is set to 2 %, while $G_0 = 0.1$. For PSO, $c_1 = c_2 = 2$ and inertia weight ω is linearly decaying from 0.9 to 0.4. The PID is implemented in parallel form, with a low-pass filter in derivative component with time constant 0.1 and anti-reset windup scheme, tuned by GSA with the same configuration and objective function used for SMC, within the range $0.1 \leq P, I, D \leq 5$, providing the parameters $P = 3.68$, $I = 2.16$ and $D = 2.49$. Temperature set point is assumed to be 35°C for $0 \leq t < 164$ s, 30°C for $164 \leq t < 320$ s and again 35°C for $t \geq 320$ s. Simulation time is 560 s with a step size of 1 s. From (11), (12) and (21), $K_D = 0.87$ and $\delta = 1.04$, and as initial search space for GSA and PSO, the range is set to $\pm 80\%$ of these values, but set unconstrained for search phase, since it was observed a tendency of the agents to move towards these limits and stay there thereafter.

4 Results and Discussion

Given the several possible combinations for (K_D, δ) in (10), an optimization strategy such as GSA can provide better results for a given cost function. However, considering grains drying, energy consumption is mandatory and must be compared with the common use of PID. In Figs. 4 and 5, *eq* stands for the output by using (11) and (12). Figure 4 gives an overview of all controllers outputs when the system is subject to external disturbances, including PSO, just to highlight the better disturbance rejection properties with optimization (PSO or GSA). However, for this scenario, PSO found higher parameters ($K_D = 330.98$, $\delta = 40.81$), which tend to increase control signal effort. This behavior is equivalent to the PID, but the latter also presents an overshoot. Unlikely PSO, GSA do not search far away from the initial region and with a gravitational constant $G_0 = 0.1$ found ($K_D = 3.43$, $\delta = 0.94$), which was selected to keep the control effort equivalent to the results found with the SMC equations, even when parameter variations are considered (Fig. 5). The results in Table 1 suggests the best performance for GSA in terms of control effort while the disturbance rejection is well balanced among the controllers.

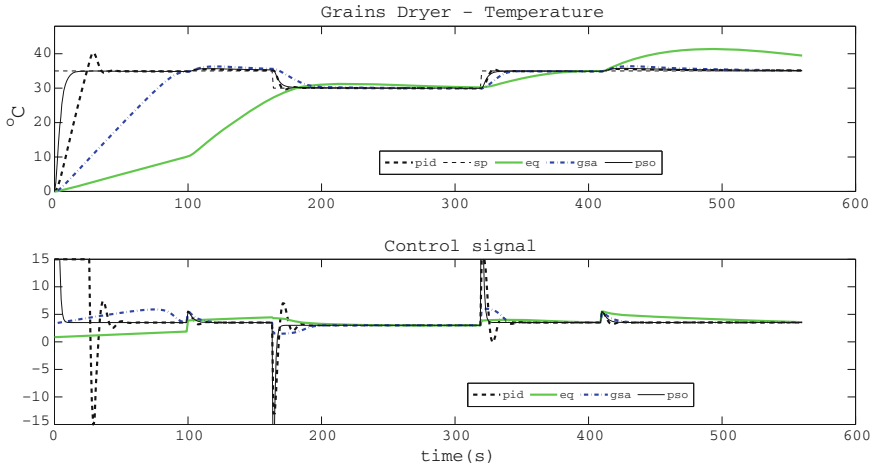


Fig. 4 The *top plot* presents the set-point tracking response and load rejection with a two units step perturbation applied at $t = 100$ s and $t = 410$ s. The *bottom plot* presents the corresponding control signal. In the figure legend **eq** is associated with (11) and (12)

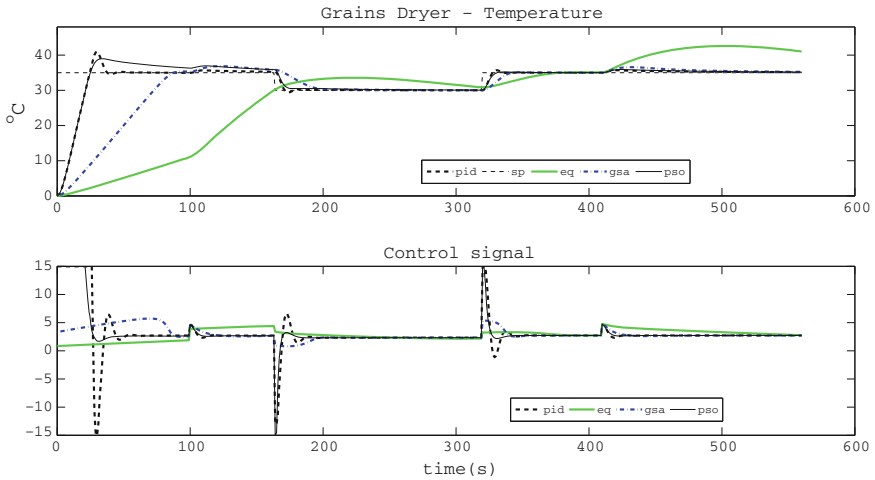


Fig. 5 The *top plot* presents the set-point tracking response and load rejection with a two units step perturbation applied at $t = 100$ s and $t = 410$ s, and a general parameter variation of +30% in the nominal plant $G(s)$. The *bottom plot* presents the corresponding control signal. In the figure legend **eq** is associated with (11) and (12)

Table 1 Controllers parameters and performance—disturbed case

	K_D	δ	ITAE	CE	TV_U	TV_Y
PID	–	–	1.3×10^4	2.3×10^3	62.8	144.9
SMC–PSO	330.98	40.81	2.4×10^4	2.2×10^3	53.6	81.3
SMC–GSA	3.43	0.94	1.0×10^5	2.0×10^3	50.3	22.3
SMC–Equation	0.87	1.04	6.9×10^5	1.9×10^3	45.3	10.5

5 Conclusion and Further Work

This study has proposed the GSA optimization for the Sliding Mode Controller based on Smith Predictor structure. The results showed similar performance to PID in terms of robustness to parameter variations and load disturbances, but with a lower and smooth control effort, and therefore has achieved the objectives of this paper. When compared to PSO, it presented lower optimal values which is interesting from the perspective of control signal feasibility. Four performance indexes were also compared to the conventional SMC based on tuning equations and have suggested fast tracking and recovery from disturbances, since these equations take into account only the plant model. Among the ideas for future works, one has the practical experiment, the comparison with other robust controllers and other recently proposed heuristics.

Acknowledgments This work is financed by the ERDF—European Regional Development Fund through the Operational Programme for Competitiveness and Internationalisation—COMPETE 2020 Programme, and by National Funds through the FCT—Fundação para a Ciência e a Tecnologia (Portuguese Foundation for Science and Technology) within project POCI-01-0145-FEDER-006961.

References

1. Ma, H., Zhang, W., Yang, S.X.: Systems modeling and intelligent control of meat drying process. In: 10th IEEE System of Systems Engineering Conference, pp. 238–243 (2015)
2. Pinho, T.M., Boaventura-Cunha, J., Azevedo, A., Moreira, A.P.: Reduction of drying process time of natural cork stoppers process in lean improvement efforts. In: 9th International Conference on Industrial Engineering and Industrial Management, pp. 1–9 (2015)
3. Lutfy, O.F.: Modelling of a conveyor-belt grain dryer utilizing a sigmoid network. In: 10th Asian Control Conference, pp. 1–5 (2015)
4. Aini, D., Xiaoguang, Z., Chi, Z., Xiangdong, L., Huiling, Z.: Design and simulation of dual fuzzy self-adjusting immune PID controller for grain drying system. In: 2015 International Conference on Advanced Mechatronic Systems, pp. 503–507 (2015)
5. Petersen, L.N., Poulsen, N.K., Niemann, H.H., Utzen, C., Jørgensen, J.B.: Economic optimization of spray dryer operation using nonlinear model predictive control. In: 53rd IEEE Conference on Decision and Control, pp. 6794–6800 (2014)
6. Oliveira, J.: Smooth adaptive robust temperature control of a seed drying system. In: Proceedings of 4th IFAC Conference on Modelling and Control in Agriculture, Horticulture and Post Harvest Industry, pp. 6–11 (2013)

7. https://commons.wikimedia.org/wiki/File:Grain_Silos_at_Manor_Farm_-_geograph.org.uk_-_1706973.jpg. Accessed 18 Jan 2016
8. Smith, O.J.: A controller to overcome dead time. *ISA J.* **6**, 28–33 (1959)
9. Camacho, O.: Sliding Mode Control in Process Industry, in *Instrument Engineer's Handbook*, vol. 2, 4th edn. Bela G. Liptak (2005)
10. Utkin, V.I.: *Sliding modes in control and optimization*. Springer, Berlin-Heidelberg (1992)
11. Yuanhao, S., Jingcheng, W., Yunfeng, Z.: Sliding mode predictive control of main steam pressure in coal-fired power plant boiler. *Chin. J. Chem. Eng.* **20**, 1107–1112 (2012)
12. Rashedi, E., Nezamadi-Pour, H., Saryazdi, S.: GSA: a gravitational search algorithm. *Inf. Sci.* **179**, 2232–2248 (2009)
13. Oliveira, P.B.M., Pires, E.J.S., Novais, P.: Design of posicast PID control systems using a gravitational search algorithm. *Neurocomputing*, **167**(1), 18–23 (2015)
14. Bhattacharyya, B., Kumar, S.: Loadability enhancement with FACTS devices using gravitational search algorithm. *Int. J. Electr. Power Energy Syst.* **78**, 470–479 (2016)
15. Yuan, X., Ji, B., Chen, Z., Chen, Z.: A novel approach for economic dispatch of hydrothermal system via gravitational search algorithm. *Appl. Math. Comput.* **247**, 535–546 (2014)
16. Jiang, S., Wang, Y., Li, Z.: Convergence analysis and performance of an improved gravitational search algorithm. *Appl. Soft Comput.* **24**, 363–384 (2014)
17. Rosali, S.M., Rahman, M.F., Husain, A.R.: Performance comparison of particle swarm optimization and gravitational search algorithm to the design of controller for nonlinear system. *J. Appl. Math.* **2014**, 1–9 (2014)
18. Clerc, M., Kennedy, J.: The particle swarm—explosion, stability and convergence in a multi-dimensional complex space. *IEEE Trans. Evol. Comput.* **6**(1), 58–73 (2002)

Part XI
Power Systems Applications

Model Predictive Current Control of a Slow Battery Charger for Electric Mobility Applications

Delfim Pedrosa, Ricardo Gomes, Vitor Monteiro, José A. Afonso and João L. Afonso

Abstract This paper presents a model predictive current control applied to a slow electric vehicle (EV) battery charger. Taking into account the similarities between the power converters inside the EV, it is possible to combine the battery charger and the motor driver in a single integrated converter, thus reducing the weight and volume of the proposed solution, and also contributing to reduce the final price of the EV. Due to the bidirectional power flow capability of the integrated power converter, when working as a slow EV battery charger it can operate in grid-to-vehicle (G2V) mode and in vehicle-to-grid (V2G) mode, contributing to make EVs an important assets in the future smart grids. The integrated power converter working as battery charger operates with sinusoidal current and unitary power factor, contributing to improve the power quality of the electrical grid. This paper provides simulation and experimental results that validate the model predictive control algorithm applied to the proposed integrated power converter working as slow EV battery charger.

Keywords Electric vehicles • Slow battery charger • Model predictive current control • G2V—Grid-to-Vehicle • V2G—Vehicle-to-Grid

D. Pedrosa (✉) · R. Gomes · V. Monteiro · J.L. Afonso
Centro ALGORITMI, University of Minho, 4804-533 Guimarães, Portugal
e-mail: delfim.pedrosa@algoritmi.uminho.pt; delfim.pedrosa@dei.uminho.pt

R. Gomes
e-mail: ricardo.gomes@algoritmi.uminho.pt

V. Monteiro
e-mail: vitor.monteiro@algoritmi.uminho.pt

J.L. Afonso
e-mail: joao.l.afonso@algoritmi.uminho.pt

J.A. Afonso
CMEMS-UMinho R&D Center, University of Minho, 4804-533 Guimarães, Portugal
e-mail: jose.afonso@dei.uminho.pt

1 Introduction

Nowadays, electric vehicles (EVs) are emerging as the most sustainable alternative to support the expected number of vehicles in circulation around the world, as well as to reduce the impact of the transportation sector on the environment. Typically, an EV has a motor drive system and an on-board battery charger that allows charging its battery pack almost anywhere, as long as there is an electrical outlet available [1]. Taking into account the similarities between the EV motor drive and the EV battery charger, it is possible the unification in a single converter, allowing to optimize the size and weight of the power components inside the EV [2]. Moreover, the bidirectional power flow capability of the converter offers some extra features for the EV operation into the power grid. Besides the grid-to-vehicle (G2V) operation mode, where the EV batteries are charged from the power grid, the EV battery charger can also be used to return part of the energy stored in the batteries back to the power grid. This operation mode is identified in the literature as vehicle-to-grid (V2G). Both G2V and V2G operation modes contribute to the development and expansion of technologies to integrate the EV into the smart grids [3, 4]. In order to mitigate power quality problems, the EV battery charger should operate with unitary power factor and sinusoidal currents, i.e., with low total harmonic distortion [2, 5].

Figure 1 presents the topology of the integrated power converter that is used as EV motor driver or as slow EV battery charger. As it can be seen, this topology can be used to perform the EV motor driver or the slow EV battery charging, since these operations do not happen simultaneously. From Fig. 1, it is possible to observe that the EV battery charging process is performed from the power grid using only two legs of the three-phase voltage source converter. It is important to note that the presented topology is compatible with any type of EV motor, nevertheless, an extra

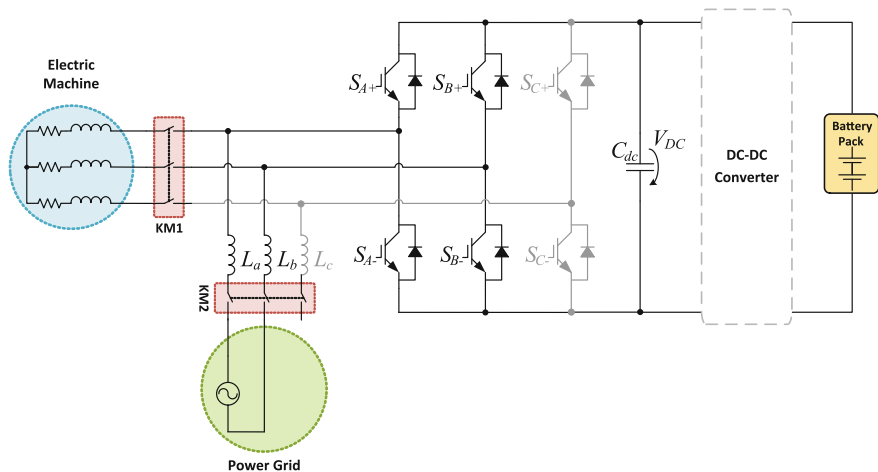


Fig. 1 Topology of the integrated power converter used both as EV motor driver and as slow EV battery charger

relay is necessary to disconnect the EV motor during the EV battery charging process. This converter can also be used as fast EV battery charger, however, this paper only focus in the slow EV battery charging process.

2 Predictive Current Control

Figure 2 describes the control algorithm to perform the slow EV battery charging process. Analyzing the voltages between the power grid and the AC-DC converter, it can be established that:

$$v_s(t) = v_R(t) + v_L(t) + v_{in}(t) = R_s i_s(t) + L_s \frac{di_s(t)}{dt} + v_{in}(t) \tag{1}$$

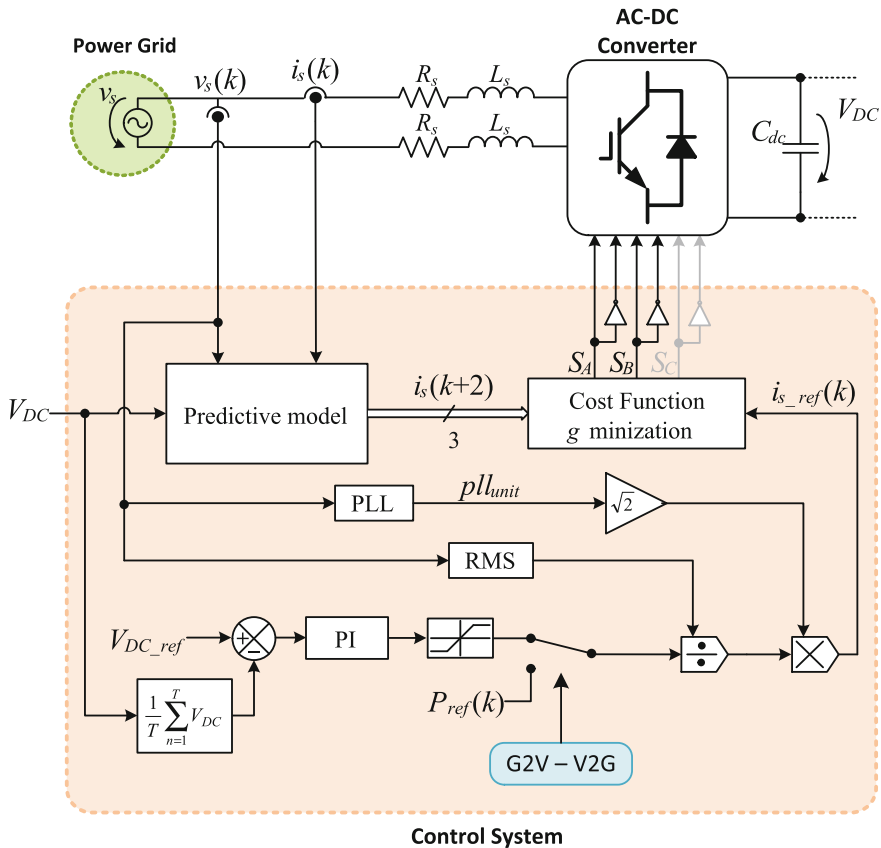


Fig. 2 Block diagram of the model predictive current control for the slow EV battery charger

where, $v_s(t)$ is the power grid voltage, $v_R(t)$ is the voltage across the internal resistance of the inductor, $v_L(t)$ is the voltage across the inductor, $v_{in}(t)$ is the input voltage in converter, $R_s(t)$ is the internal resistance of the inductor, and $i_s(t)$ is the grid current. From Eq. (1), the derivative can be described by:

$$\frac{di_s(t)}{dt} = \frac{1}{L_s} [v_s(t) - R_s i_s(t) - v_{in}(t)] \quad (2)$$

Applying the forward Euler approximation to the derivative of the grid current results in:

$$\frac{di_s(t)}{dt} \cong \frac{i_s(k+1) - i_s(k)}{T_s} \quad (3)$$

where, the predicted input current is established by:

$$i_s(k+1) = \left(1 - \frac{R_s T_s}{L_s}\right) i_s(k) + \frac{T_s}{L_s} [v_s(k) - v_m(k)] \quad (4)$$

Using a high sampling frequency, the voltage in the instant $(k+1)$ can be approximated by the voltage in the instant (k) , according to:

$$v_s(k+1) \approx v_s(k) \quad (5)$$

Taking into account that it is not possible to measure the control variables, predict the future values and apply the control during the same sampling period, the measured variables in the instant (k) will result in changes in the instant $(k+2)$, causing a two-step-ahead prediction [6, 7]. The output of the prediction can only be applied at the next sample $(k+1)$. Thus, it is necessary to predict the current value at the sample $(k+2)$, which is obtained by time shifting Eq. (4) one step forward, resulting in (6).

$$i_s(k+2) = \left(1 - \frac{R_s T_s}{L_s}\right) i_s(k+1) + \frac{T_s}{L_s} [v_s(k+1) - v_{in}(k+1)] \quad (6)$$

First, it is calculated $i_s(k+1)$ using Eq. (4), since the voltage and current measured were obtained as consequence of the switching state desired in the previous sampling time. In the next steps the predicted current is obtained with (6). Taking into account that the EV battery charger is connected to a single-phase system, it is used a cost function widely used in [8, 9], which is described by:

$$g = |i_{s_ref}(k+2) - i_s(k+2)| \quad (7)$$

From [4], where it is proposed a bidirectional single-phase battery charger for an EV, the reference current during the G2 V operation mode is generated according to

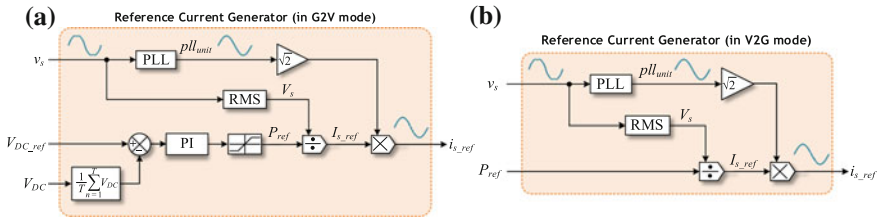


Fig. 3 Block diagram to obtain the grid current reference during: **a** G2 V operation mode; **b** V2G operation mode

Fig. 4 Phase-locked loop algorithm used to synchronize the slow EV battery charger with the power grid voltage

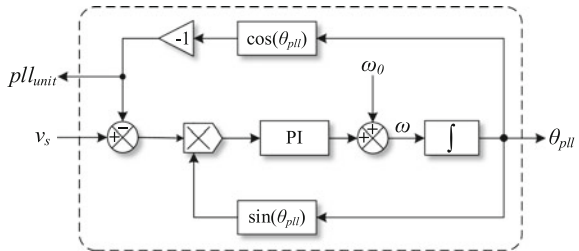


Fig. 3a. In order to avoid the harmonic content of the power grid voltage it is used a phase-locked loop (PLL) algorithm, which is synchronized with the fundamental component of the power grid voltage. The RMS value of the grid current reference (I_{S_ref}) is obtained from a PI controller, which is used to maintain the DC-bus voltage regulated, divided by the RMS value of the power grid voltage. The RMS value of the grid current reference (I_{S_ref}) is then multiplied by the output signal of the PLL in order to obtain the instantaneous value of the grid current reference in phase with the power grid voltage. On the other hand, during the V2G operation mode the grid current reference is in phase opposition with the power grid voltage. This is obtained using the same PI controller, but multiplying by minus one the output signal of the PLL. The block diagram that allows obtain the grid current reference during the V2G operation mode is shown in Fig. 3b.

As aforementioned, in order to obtain the grid current reference it is necessary to use a PLL algorithm. In this paper it was chosen to use the PLL algorithm shown in Fig. 4. This PLL algorithm results from the adaptation of the enhanced PLL (ePLL) presented in [10, 11].

3 Simulations Results

This item presents the main simulation results obtained to validate the control algorithm of the slow EV battery charger. The simulation model was implemented as close as possible of the real implementation. With the realization of the

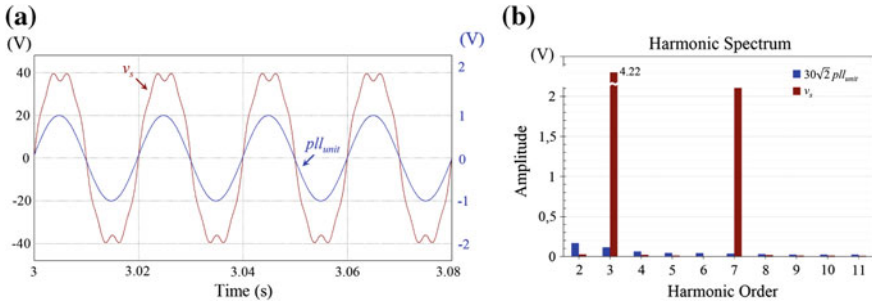


Fig. 5 Simulations of the PLL algorithm: **a** Power grid voltage (v_s) and output signal of the PLL (pll_{unit}); **b** Detail of the harmonic spectrum of the power grid voltage (v_s) and output signal of the PLL (pll_{unit})

simulations, it was possible to reduce time and financial resources during the implementation of the laboratorial prototype. The simulation results were obtained with the simulation software PSIM, v9.0. The simulations of the slow EV battery charger were performed for both G2 V and V2G operations modes.

3.1 Phase-Locked Loop Algorithm

The performance of the PLL algorithm has high influence on the obtained results. Thus, the first simulations were done with the purpose of evaluating the performance of the PLL algorithm and tuning its parameters. In order to approximate the simulation model to the real implementation, it was considered a power grid voltage (v_s) with harmonic content (third order harmonic with 15 % of the amplitude of the fundamental component and seventh order harmonic with 10 % of the amplitude of the fundamental component).

Figure 5a shows the output signal of the PLL algorithm (pll_{unit}) in comparison with the power grid voltage (v_s). In this case, the measured THD of the power grid voltage (v_s) was 10.99 %, while the measured THD of the PLL (pll_{unit}) was 0.42 %, demonstrating the good performance of the PLL algorithm.

Figure 5b presents the harmonic spectrum of the power grid voltage (v_s) in comparison with the PLL (pll_{unit}). The obtained results show that the PLL algorithm was capable to synchronize with the fundamental component of the power grid voltage, even considering a power grid voltage with a THD of 10.99 %.

It is important to note that the obtained results with the PLL algorithm can be improved by readjusting the gains of the PI controller.

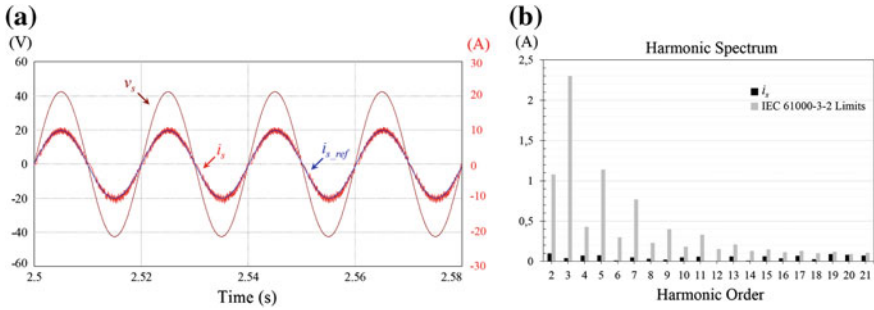


Fig. 6 Simulation results during the G2 V operation mode: **a** Power grid voltage (v_s), grid current (i_s), and grid current reference (i_{s_ref}); **b** Detail of the harmonic spectrum of the grid current (i_s) in comparison with the limits established by the standard IEC 61000-3-2

3.2 Grid-to-Vehicle Operation Mode

This item presents the simulation results during the G2V operation mode. For such purpose it was established a reference voltage for the DC-bus (V_{DC_ref}) of 110 V.

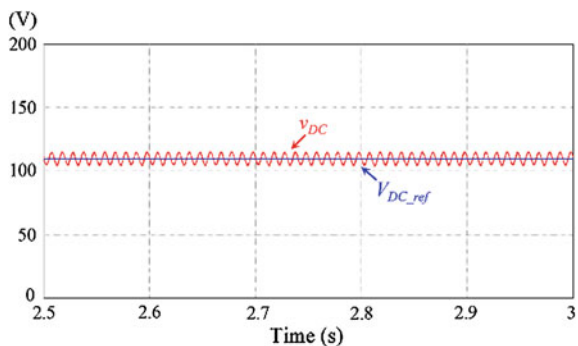
The obtained waveforms of the power grid voltage (v_s) and grid current (i_s) are presented in Fig. 6a. The measured RMS value of the grid current (i_s) was 7.14 A, the measured THD was 9.57 %, and the measured total power factor was 0.99. The detailed harmonic spectrum of the grid current (i_s), in comparison with the limits established by the standard IEC 61000-3-2, is presented in Fig. 6b.

Figure 7 shows the DC-bus voltage. As it can be seen, the DC-bus voltage is centered in its reference (110 V) with a voltage ripple of 9.80 %.

3.3 Vehicle-to-Grid Operation Mode

This item presents the simulation results during the V2G operation mode. For this operation mode it was established an operation power of 0.2 kW. The obtained

Fig. 7 Simulation results of the DC-bus voltage (v_{DC}) and its reference (V_{DC_ref}) during G2 V operation mode



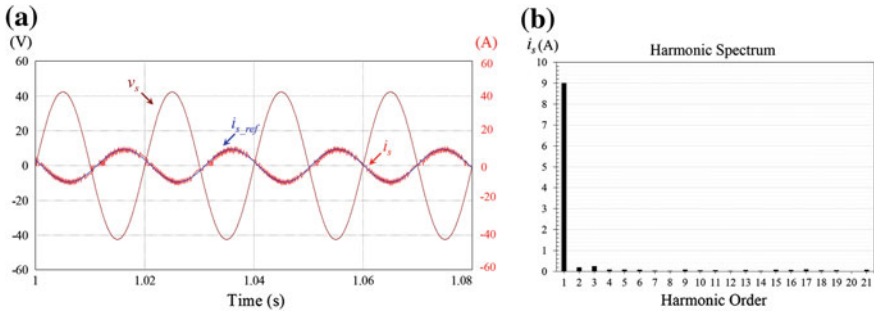


Fig. 8 Simulation results during the V2G operation mode: **a** Power grid voltage (v_s), grid current (i_s) and grid current reference (i_{s_ref}); **b** Harmonic spectrum of the grid current (i_s)

waveforms of the power grid voltage (v_s) and grid current (i_s) are shown in Fig. 8a. The grid current (i_s) has a RMS value of 6.58 A and a THD value of 17.46 %. The harmonic spectrum of the grid current is shown in Fig. 8b.

4 System Implementation

Figure 9 shows the developed laboratorial prototype, which is divided in two fundamental parts: power converter and digital control. The power converter is a three-phase voltage source converter that is used as EV motor driver or as slow EV battery charger. Taking into account the operation as slow EV battery charger are only used two IGBTs legs, the inductors filters and the DC-bus capacitors.

The digital control system is composed by a digital signal controller (DSC), the current and voltage sensors, the signal conditioning circuits (one to adequate the signals from the sensors to the DSC and other to adapt the signals from the DSC to IGBTs drivers), and the IGBTs gate drivers. The power converter is isolated from the digital control system through the hall-effect sensors and the IGBTs gate drivers.

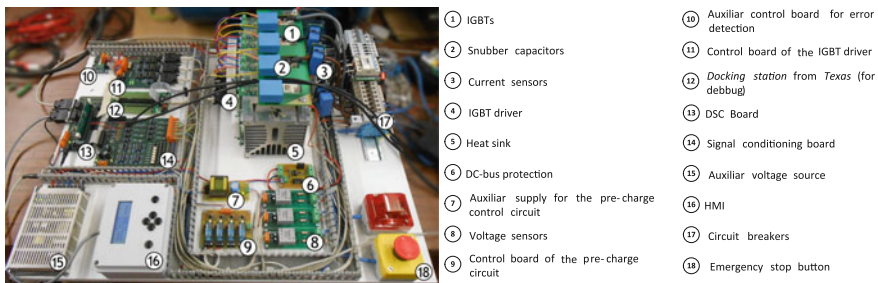
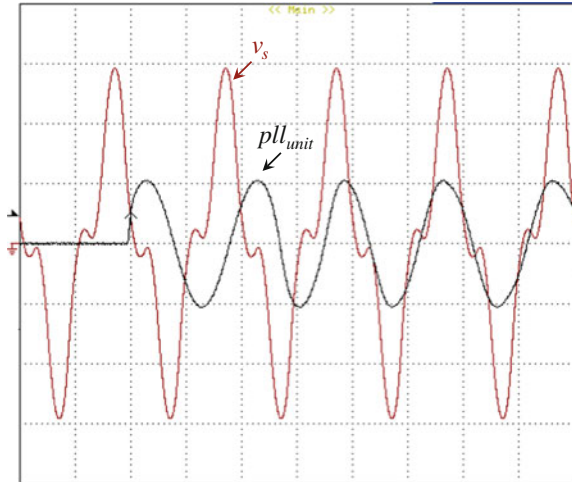


Fig. 9 Photograph and description of the developed laboratory prototype

Fig. 10 Experimental results of the power grid voltage (v_s : 20 V/div) and the output signal of the PLL algorithm (pll_{unit} : 1 V/div) (Time: 10 ms/div)



5 Experimental Results

This section presents the main experimental results obtained with the slow EV battery charger connected to the power grid with a nominal voltage of about 30 V RMS and a frequency of 50 Hz. As aforementioned in the simulations section, the performance of the PLL system has high influence on the obtained results in both G2V and V2G operation modes.

The first step of the control system consists in evaluating the performance of the PLL algorithm. Figure 10 shows the obtained results of the power grid voltage (v_s) and the output signal of the PLL algorithm (pll_{unit}). As it can be seen, the PLL algorithm is capable of locking with the power grid voltage (v_s).

After validating the PLL algorithm, the next step consists in regulating the DC-bus voltage (V_{DC_ref}) to 110 V. Figure 11a presents the obtained waveforms of the power grid voltage (v_s), the output signal of the PLL (pll_{unit}), the grid current (i_s) and its reference (i_{s_ref}), as well as the DC-bus voltage (V_{DC}). The harmonic spectrum and the RMS value of the grid current (i_s) are shown in Fig. 11b.

6 Conclusions

This paper presents a slow electric vehicle (EV) battery charger that uses a model predictive current control algorithm. This slow EV battery charger is part of an integrated power converter that can also be used as EV motor drive. This integrated converter contributes to optimize the weight and volume of the required power electronics when compared with the traditional solutions, where it is necessary to use a power converter to the EV motor driver and another to the slow EV battery charger.

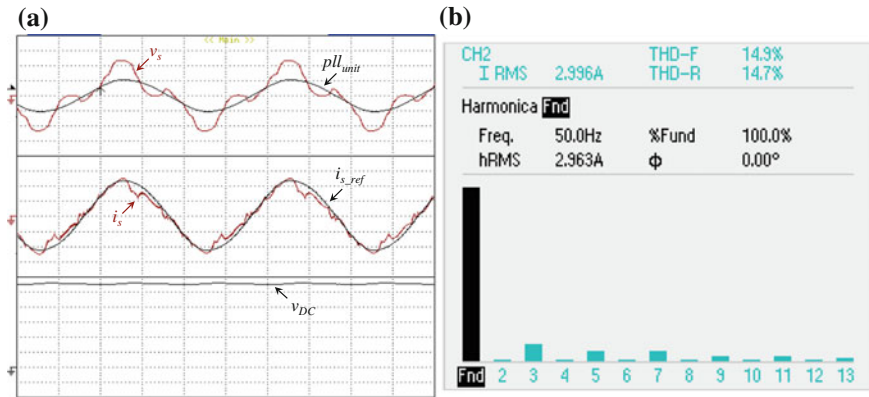


Fig. 11 Experimental results during the G2 V operation mode: **a** Power grid voltage (v_s ; 20 V/div), PLL output signal (pll_{unit} ; 1 V/div), grid current (i_s ; 2 A/div), grid current reference (i_{s_ref} ; 2 A/div), DC-bus voltage (v_{DC} ; 20 V/div) (Time: 5 ms/div); **b** Harmonic spectrum of the grid current (i_s)

Along the paper are presented the main simulation results about the synchronization of the phase-locked loop (PLL) with the power grid voltage, as well as the power grid voltage and the grid current during the grid-to-vehicle (G2 V) and vehicle-to-grid (V2G) operation modes. The experimental results show the proper operation of the slow EV battery charger, which presents sinusoidal grid current with unitary power factor, contributing to mitigate power quality problems. The obtained results allow the validation of the model predictive current control applied to the slow EV battery charger, which is part of an integrated power converter used both as EV motor driver and as slow EV battery charger.

Acknowledgments This work has been supported by COMPETE: POCI-01-0145-FEDER-007043 and FCT – Fundação para a Ciência e Tecnologia within the Project Scope: UID/CEC/00319/2013. Mr. Delfim Pedrosa was supported by the doctoral scholarship SFRH/BD/86628/2012 granted by the FCT agency.

References

1. Haghbin, S., Lundmark, S., Carlson, O., Alakula, M.: A Combined motor/drive/battery charger based on a split-windings PMSM. In: IEEE Vehicle Power and Propulsion Conference (VPPC), pp. 1–6. IEEE Press, Chicago (2011)
2. Haghbin, S., Khan, K., Lundmark, S., Alakula, M., Carlson, O., Leks, M., Wallmark, O.: Integrated chargers for EV's and PHEV's: examples and new solutions. In: XIX International Conference on Electrical Machines (ICEM), pp. 1–6. IEEE Press, Rome (2010)
3. Yilmaz, M., Krein, P.T.: Review of battery charger topologies, charging power levels, and infrastructure for plug-in electric and hybrid vehicles. IEEE Trans. Power Electron. **28**(5), 2151–2169 (2013)

4. Pinto, J.G., Monteiro, V., Goncalves, H., Exposto, B., Pedrosa, D., Couto, C., Afonso, J.L.: Bidirectional battery charger with grid-to-vehicle, vehicle-to-grid and vehicle-to-home technologies. In: 39th Annual Conference of the IEEE industrial Electronics Society (IECON 2013), pp. 5934–5939. IEEE Press, Vienna (2013)
5. Monteiro, V., Pedrosa, D., Exposto, B., Ferreira, J.C., Afonso, J.L.: Smart charging system of the electric vehicle CEPIUM. In: Annual Seminar on Automation, Industrial Electronics and Instrumentation (SAAEI'12), pp. 500–505 (2012)
6. Cortes, P., Rodriguez, J., Antoniewicz, P., Kazmierkowski, M.: Direct power control of an afe using predictive control. *IEEE Trans. Power Electron.* **23**(5), 2516–2523 (2008)
7. Kouro, S., Cortes, P., Vargas, R., Ammann, U., Rodriguez, J.: Model predictive control—a simple and powerful method to control power converters. *IEEE Trans. Power Electron.* **56**(6), 1826–1838 (2009)
8. Parvez, M., Mekhilef, S., Tan, N.M.L., Akagi, H.: Model predictive control of a bidirectional AC-DC converter for V2G and G2V applications in electric vehicle battery charger. In: IEEE Transportation Electrification Conference and Expo (ITEC), pp. 1–6. IEEE Press, Dearborn (2014)
9. Xingwu, Y., Hongchao, J., Wei, G.: Model predictive control of single phase grid-connected inverter. In: IEEE PES Asia-Pacific Power and Energy Engineering Conference (APPEEC), pp. 1–4. IEEE Press, Hong Kong (2014)
10. Karimi-Ghartemani, M., Iravani, M.R.: A new phase-locked loop (PLL) system. In: Proceedings of the 44th IEEE 2001 Midwest Symposium on Circuits and Systems, vol. 1, pp. 421–424. IEEE Press, Dayton (2001)
11. Karimi-Ghartemani, M., Iravani, M.R.: A nonlinear adaptive filter for online signal analysis in power systems: Applications. *IEEE Trans. Power Delivery* **17**(2), 617–622 (2002)

Comprehensive Analysis and Comparison of Digital Current Control Techniques for Active Rectifiers

Vítor Monteiro, João C. Ferreira, Delfim Pedrosa, M.J. Sepúlveda, J.C. Aparício Fernandes and João L. Afonso

Abstract This paper presents a comprehensive analysis and comparison of digital current control techniques for active rectifiers. These rectifiers are connected to the power grid and are controlled aiming to obtain sinusoidal grid currents and unitary power factor. In this context this paper presents the principle of operation of a full-bridge full-controlled active rectifier, which is controlled by different digital current control techniques, namely, proportional-integral (PI) in stationary frame, PI in synchronous frame, PI sinewave (PIS), feedforward, sliding mode, and predictive. These digital current control techniques are explained in detail and is established a comparison in terms of their current errors in steady-state, as well as in terms of their digital implementation using the digital signal processor (DSP) TMS320F28335 from Texas Instruments.

Keywords Digital current control · Active rectifier · PI stationary frame · PI synchronous frame · PI sinewave · Feedforward · Sliding mode · Predictive

V. Monteiro (✉) · D. Pedrosa · M.J. Sepúlveda · J.C. Aparício Fernandes · J.L. Afonso
Centro Algoritmi, University of Minho, Guimarães, Portugal
e-mail: vitor.monteiro@algoritmi.uminho.pt; vmonteiro@dei.uminho.pt

D. Pedrosa
e-mail: delfim.pedrosa@algoritmi.uminho.pt

M.J. Sepúlveda
e-mail: sepulveda.freitas@algoritmi.uminho.pt

J.C. Aparício Fernandes
e-mail: aparicio.fernandes@algoritmi.uminho.pt

J.L. Afonso
e-mail: joao.l.afonso@algoritmi.uminho.pt

J.C. Ferreira
ISCTE, Instituto Universitário de Lisboa, Lisbon, Portugal
e-mail: jcaf2001@gmail.com

1 Introduction

The use of power electronics converters has been increasing for a wide range of applications, e.g., for electric mobility [1], renewable energy systems [2], power grid conditioners [3], and power factor correctors [4]. Taking into account that these converters are connected to the power grid through ac-dc converters, the grid current is the variable that must be controlled in order to adjust the active and reactive power, optimize the performance of the converter, and mitigate power quality problems [5]. For such purpose, it is necessary to use a current control technique. As consequence, new control schemes have been proposed for the aforementioned power applications. Along the last decades, several analog and digital current control techniques have been proposed with different levels of complexity [6]. Although analog techniques have fastest transient response and no delay caused by the analog-to-digital conversion, digital techniques have been explored more intensively mainly due to the advances in digital signal processors (DSP) [7].

The classical analog current techniques applied to active rectifiers are: hysteresis and proportional-integral (PI) in stationary frame. On the other hand, the most common digital current techniques are: digital PI in stationary frame, digital PI in synchronous frame, and feedforward [8–10]. More recently, sliding mode and predictive have gained more importance for power electronics converters (e.g., active rectifiers) [11–13]. For instance, when compared with analog techniques, the main advantage of digital techniques is the possibility of including the nonlinearities of the coupling inductance, e.g., the nonlinear variation between the inductance and the current. Both analog and digital current control techniques can be used to obtain a resultant grid current with fixed or variable switching frequency. However, it is important to note that fixed switching frequency has more advantages, e.g., in the design of the passive filters [14].

In this context, this paper presents a comprehensive analysis and comparison of digital current control techniques with fixed switching frequency for a full-bridge full-controlled active rectifier, namely: PI in stationary frame, PI in synchronous frame, PI sinewave (PIS), feedforward, sliding mode, and predictive. The main goal of these techniques is to determine the voltage that the converter must produce in order to obtain zero steady-state error between the grid current and its reference after a predetermined sampling period [15].

2 Active Rectifier: Principle of Operation

This section introduces the principle of operation of the full-bridge full-controlled active rectifier that was used to compare the digital current control techniques. Figure 1 shows the active rectifier connected to the power grid through an inductance.

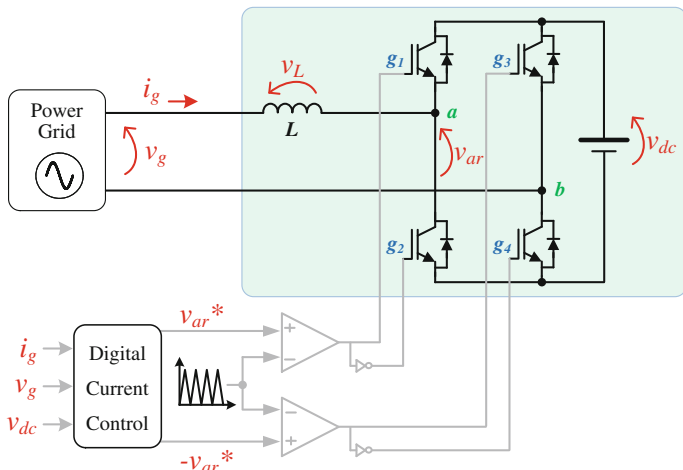


Fig. 1 Interface between the power grid and the full-bridge full-controlled active rectifier

As it can be observed in Fig. 1, in order to obtain fixed switching frequency, it is used a unipolar center-aligned pulse-width modulation (PWM) strategy, i.e., each leg of the active rectifier is controlled individually. Using this strategy, the voltage produced by the active rectifier (v_{ar}) can assume three distinct values. When the IGBT g_1 is on (the IGBT g_2 is off) and the IGBT g_3 is on (the IGBT g_4 is off) the voltage v_{ar} is 0. When the IGBT g_1 is on (the IGBT g_2 is off) and the IGBT g_3 is off (the IGBT g_4 is on) the voltage v_{ar} is v_{dc} . When the IGBT g_1 is off (the IGBT g_2 is on) and the IGBT g_3 is off (the IGBT g_4 is on) the voltage v_{ar} is 0. When the IGBT g_1 is off (the IGBT g_2 is on) and the IGBT g_3 is on (the IGBT g_4 is off) the voltage v_{ar} is $-v_{dc}$. Taking into account the dynamic behavior of the IGBTs (i.e., transition between on and off and vice-versa) it is used a dead-time of $2 \mu s$ between the IGBTs of the same leg. The characteristics of the active rectifier presented in Fig. 1 are shown in Table 1.

Table 1 Characteristics of the active rectifier

Parameter	Value	Unit
Power grid voltage (v_g)	230	V
Power grid frequency (f)	50	Hz
Sampling frequency (f_s)	40	kHz
Switching frequency (f_{sw})	20	kHz
Dc-link voltage (v_{dc})	400	V
Peak grid current reference (i_g^*)	20	A
Inductance (L)	5	mH

3 Digital Current Control Algorithms

This item presents in detail the principle of operation of each digital current control technique, highlighting the complexity of the digital implementation.

3.1 Proportional-Integral (PI) in Stationary Frame

This current control technique consists in obtaining the voltage reference (v_{ar}^*) from a PI applied to the grid current error [16]. One of the main advantages of this current control technique is the compensation of the nonlinearities of the systems, e.g., the required dead-time between IGBTs of the same leg. However, it is not possible to obtain zero steady-state error when the reference is sinusoidal. The relation between the grid current error and the grid current is established according to:

$$i_g(t) = \frac{g_{PI(t)}g_{ar(t)}}{g_{PI(t)}g_{ar(t)} + 1} i_g^*(t), \quad (1)$$

where, $g_{PI(t)}$ represents the gain of the PI controller and $g_{ar(t)}$ the gain of the converter. Taking into account that $g_{ar(t)}$ assumes a constant value, the zero error is obtained adjusting the PI controller. There are some possibilities to the digital implementation of this PI, however, the most common in power electronics consists in:

$$m_P[k] = k_p(i_g^*[k] - i_g[k]), \quad (2)$$

$$m_I[k] = k_i f_s (i_g^*[k] - i_g[k]) + m_I[k-1], \quad (3)$$

where, the voltage reference for the active rectifier is obtained according to:

$$v_{ar}^*[k] = m_P[k] + m_I[k]. \quad (4)$$

3.2 Proportional-Integral in Synchronous Frame

This current control technique also consists in obtaining the voltage reference (v_{ar}^*) from a PI applied to the grid current error, however, this PI is applied in the $dq0$ referential [8]. Taking into account that the variables are in the $dq0$ referential, it is possible to obtain zero steady-state error. It is important to note that this current control technique is applied to three-phase systems, however, it can be adjusted to single-phase systems emulating two grid currents (i_{gb} and i_{gc}) from the measured

grid current (i_g). The grid current in the $dq0$ referential is obtained using the Park transformation according to:

$$\begin{bmatrix} i_d \\ i_q \\ i_0 \end{bmatrix} = \frac{2}{3} \begin{bmatrix} \cos(\theta) & \cos(\theta - \frac{2}{3}\pi) & \cos(\theta + \frac{2}{3}\pi) \\ -\sin(\theta) & -\sin(\theta - \frac{2}{3}\pi) & -\sin(\theta + \frac{2}{3}\pi) \\ 1/2 & 1/2 & 1/2 \end{bmatrix} \begin{bmatrix} i_g \\ i_{gb} \\ i_{gc} \end{bmatrix}. \tag{5}$$

With these currents and the grid currents references also in the $dq0$ referential, it is used a PI according to the aforementioned implementation (cf. Eq. (4)). With the voltage reference that the active rectifier must produce in the $dq0$ referential ($v_{ar_d}^*$), it is used the Park invert transformation according to:

$$\begin{bmatrix} v_{ar}^* \\ v_{arb}^* \\ v_{arc}^* \end{bmatrix} = \frac{2}{3} \begin{bmatrix} \cos(\theta) & -\sin(\theta) & 1 \\ \cos(\theta - \frac{2}{3}\pi) & -\sin(\theta - \frac{2}{3}\pi) & 1 \\ \cos(\theta + \frac{2}{3}\pi) & -\sin(\theta + \frac{2}{3}\pi) & 1 \end{bmatrix} \begin{bmatrix} v_{ar_d} \\ v_{arb_q} \\ v_{arc_0} \end{bmatrix}, \tag{6}$$

in order to obtain the voltage reference that is used in the PWM. The digital implementation of this current control technique is very similar to the implementation presented for the PI in stationary frame, however, in this case the variables are in a synchronous frame.

3.3 Proportional-Integral Sinewave (PIS)

This current control technique is similar to the PI in stationary frame, however, it is added a sinusoidal signal to the output result of the PI controller [10]. The sinusoidal signal is described by:

$$g_S(s) = \frac{k_S}{s^2 + \omega_0^2}, \tag{7}$$

where, ω_0 corresponds to the frequency of the grid current frequency. Therefore, the controller is described by:

$$g(s) = k_p + k_i \frac{1}{s} + \frac{k_S}{s^2 + \omega_0^2}. \tag{8}$$

The digital implementation of this current control technique is similar to the previous one, and is obtained according to:

$$\begin{aligned} v_{ar}^*[k] = & k_p (i_g^*[k] - i_g[k]) + k_i f_s (i_g^*[k] - i_g[k]) \\ & + m_I [k - 1] + \sin(\omega_0[k]). \end{aligned} \tag{9}$$

3.4 Feedforward

This current control technique consists in adding a duty-cycle reference to the voltage reference that the active rectifier must produce aiming to reduce the influence of the PI [9]. For the aforementioned active rectifier (boost-type voltage source converter), the duty-cycle reference is defined by:

$$\delta = 1 - \frac{v_g}{v_{dc}}, \quad (10)$$

where, v_g is the power grid voltage and v_{dc} is the dc-link voltage. This duty-cycle is added to a PI, resulting in a digital implementation according to:

$$\begin{aligned} v_{ar}^*[k] = & k_p(i_g^*[k] - i_g[k]) + k_{ifs}(i_g^*[k] - i_g[k]) \\ & + m_I[k-1] + \left(1 - \frac{v_g[k]}{v_{dc}[k]}\right). \end{aligned} \quad (11)$$

3.5 Sliding Mode

This current control technique consists in controlling the voltage produced by the active rectifier through a control law resulting from the circuit analysis [11]. The control law can be expressed by:

$$u = \begin{cases} 1, & S > 0 \\ 0, & S < 0 \end{cases}, \quad (12)$$

where, S is the value of the control trajectory, which is defined by:

$$S = \alpha_1 x_1 + \alpha_2 x_2, \quad (13)$$

where, α_1 and α_2 are the sliding coefficients and x_1 and x_2 are defined by:

$$\begin{bmatrix} x_1 \\ x_2 \end{bmatrix} = \begin{bmatrix} i_g^* - \frac{1}{L} \int (v_g - uv_L) dt \\ \int x_1 dt \end{bmatrix}. \quad (14)$$

In order to guarantee the sliding mode operation, it is required that:

$$\lim_{S \rightarrow 0} S\dot{S} < 0, \quad (15)$$

where, \dot{S} is the derivative of S . Therefore, it should be analyzed two cases: where, when $S \rightarrow 0^+$ and when $S \rightarrow 0^-$. For the first case, according to (14), it results in:

$$\alpha_1 \left(\frac{di_g^*}{dt} - \frac{1}{L} v_g \right) + \alpha_2 (i_g^* - i_g) < \alpha_1 \frac{1}{L} v_{dc}. \quad (16)$$

For the second case, according to (14), it results in:

$$\alpha_1 \left(\frac{di_g^*}{dt} - \frac{1}{L} v_g \right) + \alpha_2 (i_g^* - i_g) > 0. \quad (17)$$

Combining both cases, it is obtained the control law established by:

$$0 < L \frac{di_g^*}{dt} - v_g + L \frac{\alpha_2}{\alpha_1} (i_g^* - i_g) < v_{dc}, \quad (18)$$

where, the sliding coefficients are obtained doing $S = 0$, i.e., according to:

$$\frac{dx_1}{dt} + \frac{\alpha_2}{\alpha_1} x_1 = 0, \quad (19)$$

resulting in a sliding coefficients defined by:

$$\alpha_2 = \alpha_1 f_s. \quad (20)$$

The digital implementation of this current control is obtained according to:

$$v_{ar}^*[k] = L f_s (i_g^*[k] - i_g^*[k-1]) + L f_s (i_g^* - i_g) - v_g[k]. \quad (21)$$

3.6 Predictive

This current control technique consists in determining the voltage that the active rectifier must produce in order to obtain zero steady-state error between the grid current and its reference after a pre-determined number of sampling periods. Analyzing Fig. 1, it can be established:

$$v_g(t) = v_L(t) + v_{ar}(t), \quad (22)$$

where, v_g , v_L and v_{ar} are, respectively, the instantaneous values of the power grid voltage, the voltage across the inductance, and the voltage produced by the active rectifier. Substituting the voltage across the inductance and rearranging in order to the voltage that the active rectifier must produce, Eq. (22) can be rewritten by:

$$v_{ar}(t) = v_g(t) - L \frac{di_g(t)}{dt} \quad (23)$$

Taking into account that the grid current error is defined by:

$$i_{g_error}(t) = i_g^*(t) - i_g(t), \quad (24)$$

according to [17], Eq. (23) can be rewritten by:

$$v_{ar} = v_g - L \frac{di_g^*}{dt} + L \frac{di_{g_error}}{dt}. \quad (25)$$

Using the backward Euler method, the digital implementation of (25) results in:

$$v_{ar}^*[k] = v_g[k] - \frac{L}{T_s} (2i_g^*[k] - i_g^*[k-1] - i_g[k]). \quad (26)$$

4 Analysis and Comparison

Taking into account that the active rectifier under study operates with sinusoidal grid current in phase with the power grid voltage, Fig. 2a shows the power grid voltage (v_g) and the grid current (i_g) during 40 ms. It is important to note that the obtained results for the grid current (i_g) are very similar using all the aforementioned current control techniques, i.e., using these scales of current and time, it is not possible to identify differences between the current control techniques. Using a sinusoidal current reference (cf. Table 1) the measured total harmonic distortion (THD) using all the current control techniques was about 0.8 % and the measured total power factor (TPF) was 0.99. Figure 2b shows in a time interval of 40 ms the digital current errors of all the current control techniques: i_{gA} (PI stationary frame), i_{gB} (PI synchronous frame), i_{gC} (PI sinewave), i_{gD} (feedforward), i_{gE} (sliding mode), and i_{gF} (predictive). As it can be seen, the higher error is obtained with the PI in stationary frame and the lower error is obtained with the predictive control. Figure 2c shows a detail of 0.4 ms extracted from Fig. 2b of the digital current errors of all the current control techniques.

Figure 3 shows a comparison of the current control techniques in terms of the relation between the measured grid current and the error in steady state. As it can be seen, the best result is for the PI in synchronous frame and the worst case is for the PI in stationary frame. The aforementioned current control techniques were also compared in terms of the time required to perform the digital implementation. In power electronics applications this time is very important, since during the sampling period $[k, k + 1]$ are performed other tasks besides the current control

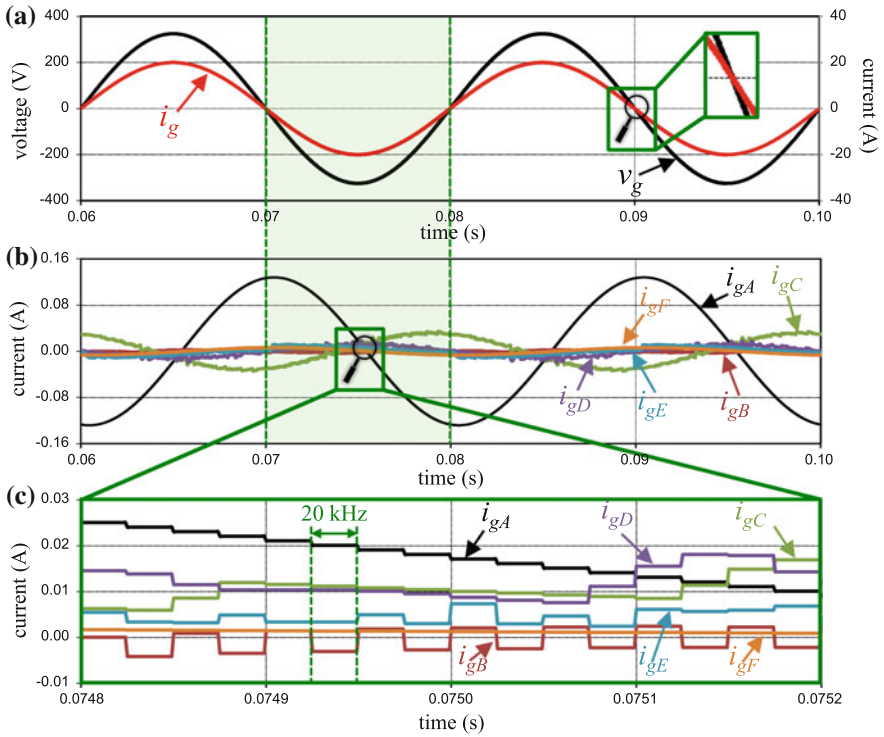


Fig. 2 Simulation results: **a** power grid voltage (v_g) and grid current (i_g); **b** digital errors of all the current control techniques; **c** detail of the digital current errors of all the current control techniques (i_{gA} —PI stationary frame, i_{gB} —PI synchronous frame, i_{gC} —PI sinewave, i_{gD} —feedforward, i_{gE} —sliding mode, i_{gF} —predictive)

technique, e.g., analog-to-digital conversion, phase-locked loop synchronization with the power grid voltage, and application of the power theory to establish the grid current reference (i_g^*). For such purpose, all the current control techniques were programmed in the digital signal processor (DSP) TMS320F28335 from Texas Instruments. This DSP was programmed for a cycle-time of 150 MHz and a sampling frequency of 40 kHz. Table 2 shows the time period required to execute each current control technique. These time periods were measured using one of the features available in the Code Composer Studio from Texas Instruments (the software used to program the DSP). As expected, the PI in synchronous frame is the current control technique that requires more time due to the Park transformations. On the other hand, the predictive is the current control technique that requires less

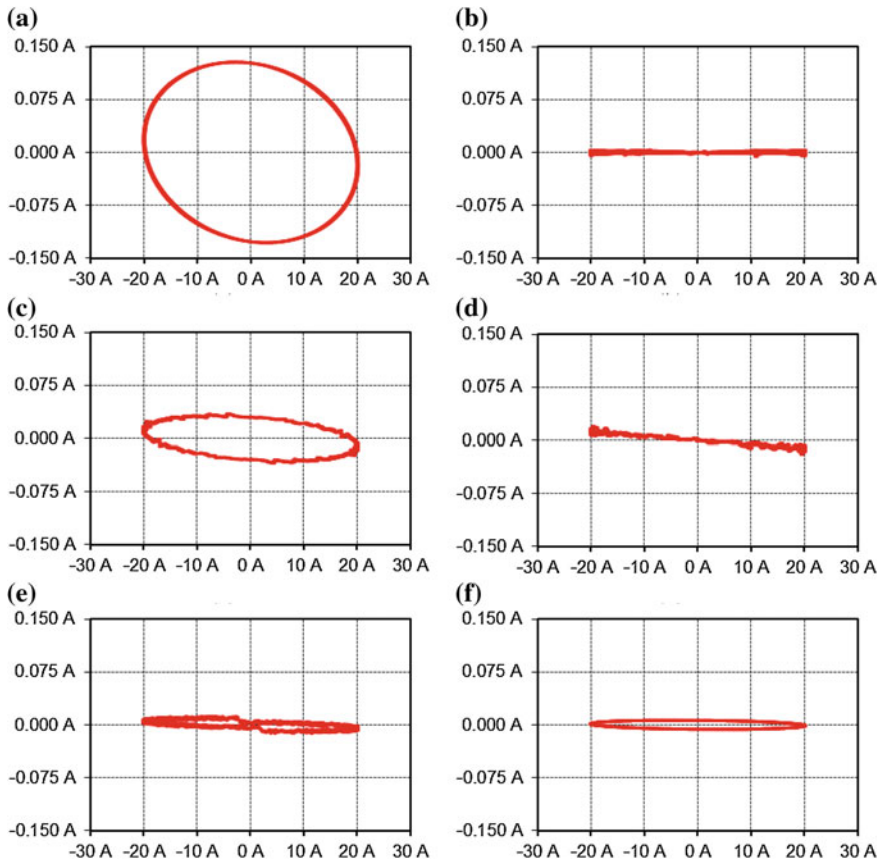


Fig. 3 Comparison of the current control techniques in terms of the relation between the measured grid current and the error in steady state: **a** PI in stationary frame; **b** PI in synchronous frame; **c** PI sinewave (PIS); **d** feedforward; **e** sliding mode; **f** predictive

Table 2 Time period required to execute each current control technique in the DSP TMS320F28335

Current control	Value	Unit
PI stationary frame	333	ns
PI synchronous frame	8940	ns
PI sinewave	800	ns
Feedforward	1927	ns
Sliding mode	320	ns
Predictive	247	ns

time due to the simple control law equation. Using the aforementioned conditions for the DSP, according to Table 2, the predictive current control is almost 97.2 % faster than the PI in synchronous frame.

5 Conclusions

This paper presents a comprehensive analysis and comparison of digital current control techniques that can be applied to control the grid current of active rectifiers. In this paper it is used a full-bridge full-controlled active rectifier to compare the different digital current control techniques, namely, proportional-integral (PI) in stationary frame, (PI) in synchronous frame, PI sinewave (PIS), feedforward, sliding mode, and predictive. These digital current control techniques are presented and explained in detail along the paper, where is also established a comparison in terms of the current error in steady-state and the time period required to execute each current control using the digital signal processor (DSP) TMS320F28335 from Texas Instruments. Using a sinusoidal current reference, the measured total harmonic distortion (THD) for all the current control techniques was about 0.8 %, and the total power factor was 0.99. When the comparison is performed in terms of the relation between the measured grid current and the error in steady state, the best result is for the PI in synchronous frame and the worst case is for the PI in stationary frame. However, the PI in synchronous frame is the current control technique that requires more time to be executed in the DSP. On the other hand, the predictive is the current control technique that requires less time. The predictive current control is almost 97.2 % faster than the PI in synchronous frame. For the active rectifier under study in this paper, using a PI in synchronous frame it is possible obtain zero error, however, the digital implementation is more complex and requires more computational resources.

Acknowledgments This work has been supported by COMPETE: POCI-01-0145-FEDER-007043 and FCT – Fundação para a Ciência e Tecnologia within the Project Scope: UID/CEC/00319/2013. The PhD student Vítor Monteiro was supported by the doctoral scholarship SFRH/BD/80155/2011 granted by the FCT agency.

References

1. Monteiro, V., Pinto, J.G., Afonso, J.L.: Operation modes for the electric vehicle in smart grids and smart homes: present and proposed modes. *IEEE Trans. Veh. Technol.* **65**(3), 1007–1020 (2016)
2. Kempton, W., Tomic, J.: Vehicle-to-grid power implementation: from stabilizing the grid to supporting large-scale renewable energy. *ELSEVIER J. Power Sour.* **144**(1), 280–294 (2015)
3. Afonso, J.L., Couto, C., Martins, J.: Active filters with control based on the p-q theory. *IEEE Ind. Electr. Soc. Newsl.* **47**(3), 5–10 (2000)
4. Huber, L., Jang, Y., Jovanovic, M.: Performance evaluation of bridgeless PFC boost rectifier. *IEEE Trans. Power Electron.* **23**(3), 1381–1390 (2008)
5. Monteiro, V., Gonçalves, H., Afonso, J.A.: Impact of electric vehicles on power quality in a smart grid context. In *IEEE EPQU International Conference on Electrical Power Quality and Utilisation*, pp. 1–6 (2011)
6. Buso, S., Malesani, L., Mattavelli, P.: Comparison of current control techniques for active filter applications. *IEEE Trans. Industr. Electron.* **45**(5), 722–729 (1998)

7. Buso, S., Mattavelli, P.: Digital control in power electronics. In Morgan and Claypool Publishers (2006)
8. Miranda, U.A., Aredes, M., Rolim, L.G.B.: A DQ synchronous reference frame control for single-phase converters. In: IEEE PESC Power Electronics Specialists Conference, pp. 1377–1381. IEEE Press, Recife (2005)
9. Chen, M., Sun, J.: Feedforward current control of boost single-phase PFC converters. *IEEE Trans. Power Electron.* **21**(2), 338–345 (2006)
10. Fukuda, S., Imamura, R.: Application of a sinusoidal internal model to current control of three-phase utility-interface converters. *IEEE Trans. Industr. Electron.* **52**(2), 420–426 (2005)
11. Tan, S.C., Lai, Y.M., Tse, C.K., Wu, C.K.: A pulsewidth modulation based integral sliding mode current controller for boost converters. In: IEEE PESC Power Electronics Specialists Conference, pp. 1–7. IEEE Press, Jeju (2006)
12. Rodríguez, J., Pontt, J., Silva, C.A., Correa, P., Lezana, P., Cortés, P., Ammann, U.: Predictive current control of a voltage source inverter. *IEEE Trans. Industr. Electron.* **54**(1), 495–503 (2007)
13. Monteiro, V., Ferreira, J.C., Melendez, A.A.N., Afonso, J.A.: Model predictive control applied to an improved five-level bidirectional converter. *IEEE Trans. Ind. Electr.* (2016)
14. Muhlethaler, J., Schweizer, M., Blattmann, R., Kolar, J.W., Ecklebe, A.: Optimal design of LCL harmonic filters for three-phase PFC rectifier. *IEEE Trans. Power Electron.* **28**(7), 3114–3125 (2013)
15. Bode, G.H., Loh, P.C., Newman, M.J., Holmes, D.G.: An improved robust predictive current regulation algorithm. *IEEE Trans. Ind. Appl.* **41**(6), 1720–1733 (2005)
16. Brod, D.M., Novotny, D.W.: Current control of VSI-PWM inverters. *IEEE Trans. Ind. Appl.* **IA-21**(3), 562–570 (1985)
17. Orts-Grau, S., Gimeno-Sales, F.J., Abellan-Garcia, A., Segui-Chilet, S., Alfonso-Gil, J.C.: Improved shunt active power compensator for IEEE standard 1459 compliance. *IEEE Trans. Power Deliv.* **25**(4), 2692–2701 (2010)

Digital Control of a Novel Single-Phase Three-Port Bidirectional Converter to Interface Renewables and Electric Vehicles with the Power Grid

Vítor Monteiro, José A. Afonso, Delfim Pedrosa, Júlio S. Martins
and João L. Afonso

Abstract This paper presents the digital control of a novel single-phase three-port bidirectional (STB) converter used to interface renewables from solar photovoltaic (PV) panels and electric vehicles (EVs) with the power grid. Using an appropriated power theory, the STB converter can be used to exchange energy between the PVs, the EVs and the power grid in four distinct modes: (1) The EV receives energy from the power grid (G2V—grid-to-vehicle operation mode) or delivers energy to the power grid (V2G—vehicle-to-grid operation mode); (2) All the energy produced by the PV panels is delivery to the power grid; (3) All the energy produced by the PV panels is delivery to the EV; (4) The EV can receive energy simultaneously from the PV panels and from the power grid (G2V). The currents of the power grid, PV panels and EV are controlled through independent predictive current control strategies, which ensure good power quality levels. This paper presents the architecture of the proposed STB converter and the detailed explanation of the digital implementation of the control algorithms, namely, the power theory and the predictive current control strategies. The control algorithms were validated through computational simulations and experimental results.

Keywords Digital control · Predictive current control · Three-port converter · Renewables · Electric vehicle · Power grid

V. Monteiro (✉) · D. Pedrosa · J.S. Martins · J.L. Afonso
Centro Algoritmi, University of Minho, Guimarães, Portugal
e-mail: vitor.monteiro@algoritmi.uminho.pt; vmonteiro@dei.uminho.pt

D. Pedrosa
e-mail: delfim.pedrosa@algoritmi.uminho.pt

J.S. Martins
e-mail: julio.martins@algoritmi.uminho.pt

J.L. Afonso
e-mail: joao.l.afonso@algoritmi.uminho.pt

J.A. Afonso
CMEMS-UMinho R&D Center,
University of Minho, Guimarães, Portugal
e-mail: jose.afonso@dei.uminho.pt

1 Introduction

Nowadays, the electric vehicle (EV) is considered the main alternative to reduce the energy consumption associated to the transport sector [1, 2]. Consequently, with the EV introduction in power grids, new opportunities emerge for the EV users and for the power grids towards smart grids [3–6]. Some of these opportunities are related with the grid-to-vehicle (G2V) and the vehicle-to-grid (V2G) operation modes. In this context, a flexible infrastructure for dynamic power control of EV battery chargers is presented in [7]. Taking into account the advances in microgeneration, also emerge new opportunities to integrate the EV with renewables. For instance, a study about the utility of the EV to help to stabilize the power grid voltage with a large-scale renewable energy introduction is presented in [8], an energy management strategy to integrate EVs and renewables is presented in [9], and an optimal dispatch of EVs with renewables (wind power) is presented in [10]. Moreover, the integration of EVs with renewables will allow mitigating the greenhouse gas emissions [11, 12]. Although there are collaborative control strategies to integrate EVs and renewables in power grids, these systems are physically independents.

This paper proposes a novel single-phase three-port bidirectional (STB) converter to interface renewables from solar photovoltaic (PV) panels and the EVs in power grids. Figure 1 presents the proposed STB converter. As it can be seen, it is composed by an ac-dc stage to interface the power grid, a dc-dc stage to interface the EV, and other dc-dc stage to interface the PV panels. Comparing with the traditional solutions, the main advantage of the proposed solution is the possibility to charge the EV batteries from the PV panels without the ac-dc stage. The three stages are connected to the same dc-link, which is controlled by the ac-dc stage, and the current of each stage is controlled through individual predictive current controllers.

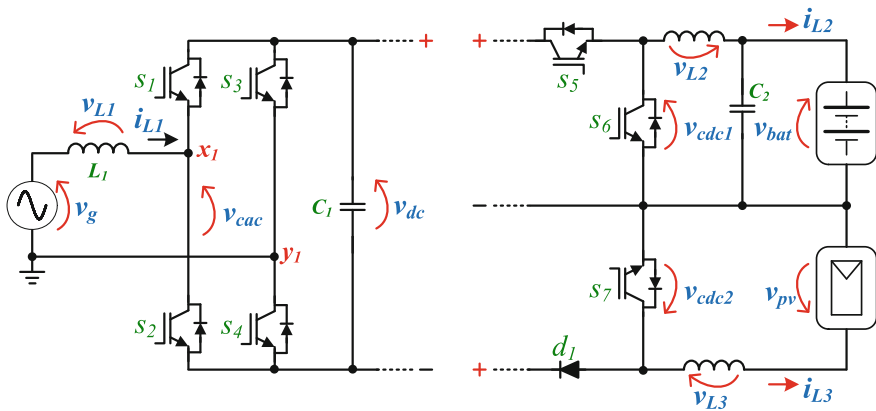


Fig. 1 Proposed single-phase three-port bidirectional (STB) converter

2 Proposed Single-Phase Three-Port Bidirectional Converter

This section presents the proposed STB converter. As shown in Fig. 1, the ac–dc stage is a full-bridge voltage–source converter, which is used to control the dc–link voltage and to control the amplitude and phase of the power grid current. When the STB receives energy from the power grid, the grid current is in phase with the power grid voltage. When the STB converter delivers energy to the power grid, the grid current is in phase opposition with the power grid voltage. The voltage produced by the converter (v_{cac}), i.e., the voltage between the points x_1 and y_1 identified in Fig. 1, can assume three distinct values. When the power grid voltage is positive, the voltage v_{cac} can be $+v_{dc}$ or 0. When the IGBTs s_1 and s_4 are on and the IGBTs s_2 and s_3 are off, the voltage v_{cac} is $+v_{dc}$. When the IGBTs s_1 and s_3 are on and the IGBTs s_2 and s_4 are off, the voltage v_{cac} is 0. On the other hand, when the power grid voltage is negative, the voltage v_{cac} can be $-v_{dc}$ or 0. When the IGBTs s_2 and s_3 are on and the IGBTs s_1 and s_4 are off, the voltage v_{cac} is $-v_{dc}$. When the IGBTs s_2 and s_4 are on and the IGBTs s_1 and s_3 are off, the voltage v_{cac} is 0.

As shown in Fig. 1, both dc–dc stages are composed by half-bridge voltage–source converters. The dc–dc stage used to interface the EV can operate in bidirectional mode. During the EV batteries charging process (G2V) it operates as a buck-type converter, i.e., the IGBT s_6 is always off. When the IGBT s_5 is on, the voltage produced by this converter, v_{cdc1} (i.e., the voltage between the points x_2 and y_2 identified in Fig. 1), is v_{dc} , and when the IGBT s_5 is off the voltage v_{cdc1} is 0. During the EV batteries discharging process (V2G) it operates as a boost-type converter, i.e., the IGBT s_5 is always off. When the IGBT s_6 is on, the voltage produced by this converter (v_{cdc1}) is 0 and when the IGBT s_6 is off the voltage v_{cdc1} is v_{dc} . On the other hand, the dc–dc stage used to interface the PV panels operates in unidirectional mode. When the IGBT s_7 is on, the voltage produced by this converter, v_{cdc2} (i.e., the voltage between the points x_3 and y_3 identified in Fig. 1), is 0, and when the IGBT s_7 is off the voltage v_{cdc2} is v_{dc} .

3 Digital Control Algorithm Analysis

This section presents the detailed analysis of the digital control algorithm for both ac–dc and dc–dc stages, which is implemented in the digital signal processor (DSP) TMS320F28335 from Texas Instruments. Figure 2 shows the digital control algorithm of the STB converter and Fig. 3 shows the time required to perform the main tasks of the digital control algorithm.

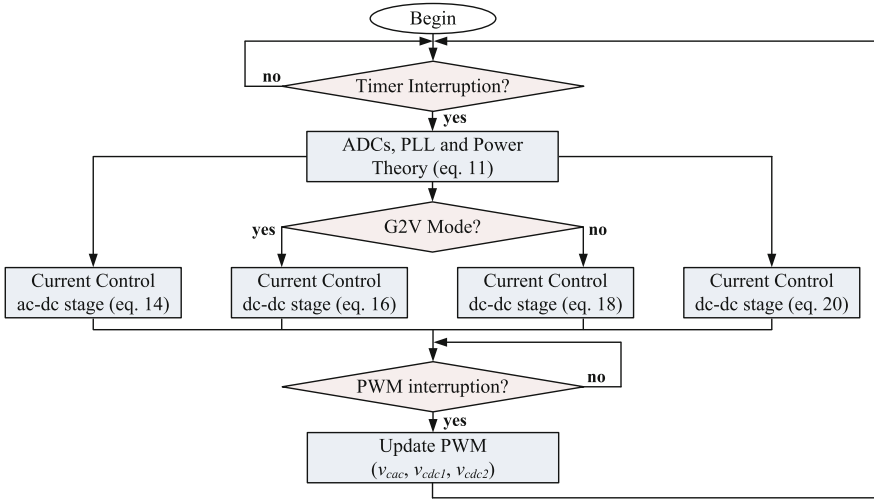


Fig. 2 Control algorithm of the proposed single-phase three-port bidirectional (STB) converter

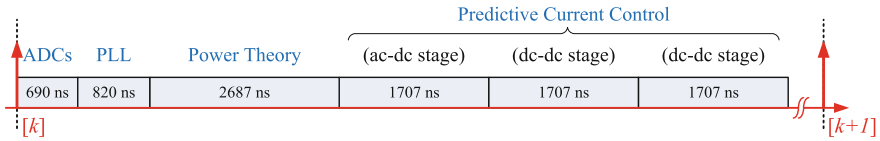


Fig. 3 Time required to perform the main tasks of the digital control algorithm

3.1 Power Theory

The power theory consists in determining the operation power of the STB converter. From the point of view of the power grid, this operation power is defined by:

$$P_G = V_G I_G, \tag{1}$$

where V_G is the rms value of the power grid voltage and I_G is the rms value of the grid current. Taking into account that the STB converter should operate with unitary power factor, the grid current should be in phase with the power grid voltage, therefore, it can be established that:

$$i_g = G_G v_g, \tag{2}$$

where G_G defines the STB converter as an conductance from the point of view of the power grid. Rearranging (1) it can be established that:

$$P_G = G_G V_G^2. \quad (3)$$

Merging (2) and (3), the operation power can be defined by:

$$P_G = \frac{i_g}{v_g} V_G^2. \quad (4)$$

On the other hand, from the point of view of the dc-link, the operation power is defined by the power to maintain the dc-link voltage regulated (P_{DC}), by the power of the EV batteries (P_{BAT}), and by the power of the PV panels (P_{PV}), according to:

$$P_G - P_{DC} - P_{EV} - P_{PV} = 0. \quad (5)$$

Merging (4) and (5), the final control law that defines the operation power of the STB converter is established by:

$$\frac{i_g}{v_g} V_G^2 - P_{DC} - v_{bat} i_{bat} - v_{pv} i_{pv} = 0, \quad (6)$$

where P_{DC} is obtained from a PI controller, whose digital implementation is obtained from:

$$m_P[k] = k_p (v_{dc}^*[k] - \overline{v_{dc}}[k]), \quad (7)$$

$$m_I[k] = k_i f_s (v_{dc}^*[k] - \overline{v_{dc}}[k]) + m_I[k-1], \quad (8)$$

$$P_{DC}[k] = m_P[k] + m_I[k]. \quad (9)$$

$\overline{v_{dc}}$ represents the average value of the dc-link voltage during one cycle of the power grid voltage (50 Hz). It is used $\overline{v_{dc}}$ instead of v_{dc} in order to avoid introducing the dc-link voltage oscillation into the control. The discrete implementation is obtained according to:

$$\overline{v_{dc}}[n] = \frac{1}{M} \sum_{n=1}^T v_{dc}[n]. \quad (10)$$

Using a sampling frequency of 20 kHz, M corresponds to 400 samples. The digital implementation of the final control law is defined by:

$$\frac{i_g[k]}{v_g[k]} V_G^2[k] - m_P[k] + m_I[k] - v_{bat}[k] i_{bat}[k] - v_{pv}[k] i_{pv}[k] = 0. \quad (11)$$

Nowadays, due to the nonlinear loads and the line impedance, the power grid voltage can have harmonic content. Therefore, instead of use the power grid voltage, it is used a phase-locked loop (PLL) algorithm, where the output signal is proportional only to the fundamental component (50 Hz) of the power grid voltage.

3.2 Predictive Current Control

The grid current (i_g), the EV battery charging current (i_{bat}), and the PV panels current are controlled independently by predictive current controllers. The current reference for the ac–dc stage is defined by Eq. (11), the current reference for the EV batteries charging is defined by the battery management system (BMS), and the current reference for the PV panels is obtained from a maximum power point tracking (MPPT) algorithm. It is important to note that the BMS and the MPPT are not explained in detail, since they are out of the scope of this paper.

For the ac–dc stage, from Fig. 1, analyzing the voltages between the power grid and the STB converter, it can be established that:

$$v_g - v_{L1} - v_{cac1} = 0, \quad (12)$$

where v_g , v_{L1} and v_{cac} are, respectively, the instantaneous values of the power grid voltage, the inductance voltage, and the voltage between the points x_1 and y_1 . Substituting the inductance voltage, it can be established that:

$$v_g - L_1 \frac{di_{L1}}{dt} - v_{cac1} = 0, \quad (13)$$

where the current in the inductance (i_{L1}) is the power grid current (i_g). Using the forward Euler method, Eq. (13) can be rewritten in terms of discrete samples as:

$$v_g[k] - \frac{L_1}{T_s} (i_g[k+1] - i_g[k]) - v_{cac1}[k] = 0, \quad (14)$$

where the grid current in the instant $[k+1]$ should be equal to the current reference in the instant $[k]$. The current reference is obtained from (11). During each period $[k, k+1]$ the voltage v_{cac} is updated and compared with a unipolar pulse–width modulator (PWM) output in order to obtain the IGBTs gate pulse patterns, i.e., to define the state of the ac–dc stage. Considering that it is used a unipolar PWM, it is also used a voltage ($-v_{cac}$) symmetrical in relation to the horizontal middle of the PWM carrier.

For the dc–dc stage used to interface the VE, the current is analyzed for the G2 V and V2G operation modes. During the G2 V operation mode, from Fig. 1, analyzing the voltages between the STB converter and the dc–dc stage, it can be established that:

$$v_{bat} + v_{L2} - v_{cdc1} = 0, \quad (15)$$

where v_{bat} , v_{L2} and v_{cdc1} are, respectively, the instantaneous values of the EV batteries voltage, the inductance voltage, and the voltage between the points x_2 and y_2 . Knowing that the current in the inductance (i_{L2}) is the EV batteries current (i_{bat}),

substituting the inductance voltage and using the forward Euler method, the discrete implementation of (15) results in:

$$v_{bat}[k] + \frac{L_2}{T_s}(i_{bat}[k+1] - i_{bat}[k]) - v_{cdc1}[k] = 0. \quad (16)$$

where the EV batteries current in the instant $[k + 1]$ should be equal to the current reference in the instant $[k]$. On the other hand, during the V2G operation mode, from Fig. 1, analyzing the voltages between the STB converter and the EV batteries, it can be established that:

$$v_{bat} - v_{L2} - v_{cdc1} = 0, \quad (17)$$

where the digital implementation results in:

$$v_{bat}[k] - \frac{L_2}{T_s}(i_{bat}[k+1] - i_{bat}[k]) - v_{cdc1}[k] = 0. \quad (18)$$

Taking into account that the current will follow in the opposite direction, in the digital implementation the current $i_{bat}[k]$ represented in (18) should be $-i_{bat}[k]$. For both situations (G2 V and V2G), the voltage v_{cdc1} is actualized and compared, during each period $[k, k + 1]$, with a PWM, in order to obtain the IGBTs gate pulse patterns of the dc–dc stage used to interface the EV batteries.

For the dc–dc stage used to interface the PV panels, from Fig. 1, analyzing the voltages between the STB converter and the PV panels, it can be established that:

$$v_{pv} - v_{L3} - v_{cdc2} = 0, \quad (19)$$

where the digital implementation results in:

$$v_{pv}[k] - \frac{L_3}{T_s}(i_{pv}[k+1] - i_{pv}[k]) - v_{cdc2}[k] = 0. \quad (20)$$

Also, for this stage, the voltage v_{cdc2} is updated and compared, during each period $[k, k + 1]$, with a PWM, in order to obtain the IGBT gate pulse patterns of the dc–dc stage used to interface the PV panels.

4 Simulations and Experimental Results

This section presents the main simulations and experimental results obtained to validate the power theory and the predictive current control strategies of the proposed STB converter. Figure 4 shows some simulations results of the STB converter. Figure 4a shows the grid current (i_g), as well as the digital grid current (i_{gd}) and the digital current reference (i_{gd}^*). As it can be seen, due to the unipolar PWM

the resulting frequency of the grid current is 40 kHz and the current $i_{gd}[k, k + 1]$ is equal to the current reference $i_{gd}^*[k-1, k]$. Figure 4b shows the EV batteries current (i_{bat}), as well as the digital EV batteries current (i_{batd}) and its reference (i_{batd}^*). It is possible to observe that the switching frequency is 20 kHz and the current $i_{batd}[k-1, k]$ is practically equal to the current reference $i_{batd}^*[k-1, k]$. Figure 4(c) shows the PV panels current (i_{pv}), as well as the digital PV panels current (i_{pvd}) and its reference (i_{pvd}^*). Also in this figure, it is possible to observe that the switching frequency is 20 kHz and the current $i_{pvd}[k-1, k]$ is practically equal to the current reference $i_{pvd}^*[k-1, k]$. Figure 4d shows the PWM carrier and the digital voltages produced by the ac–dc stage ($v_{cac1d}[k-1, k]$ and $v_{cac2d}[k-1, k]$) and by both dc–dc stages ($v_{cdc1d}[k-1, k]$ and $v_{cdc2d}[k-1, k]$). As expected, the voltages $v_{cac1d}[k-1, k]$,

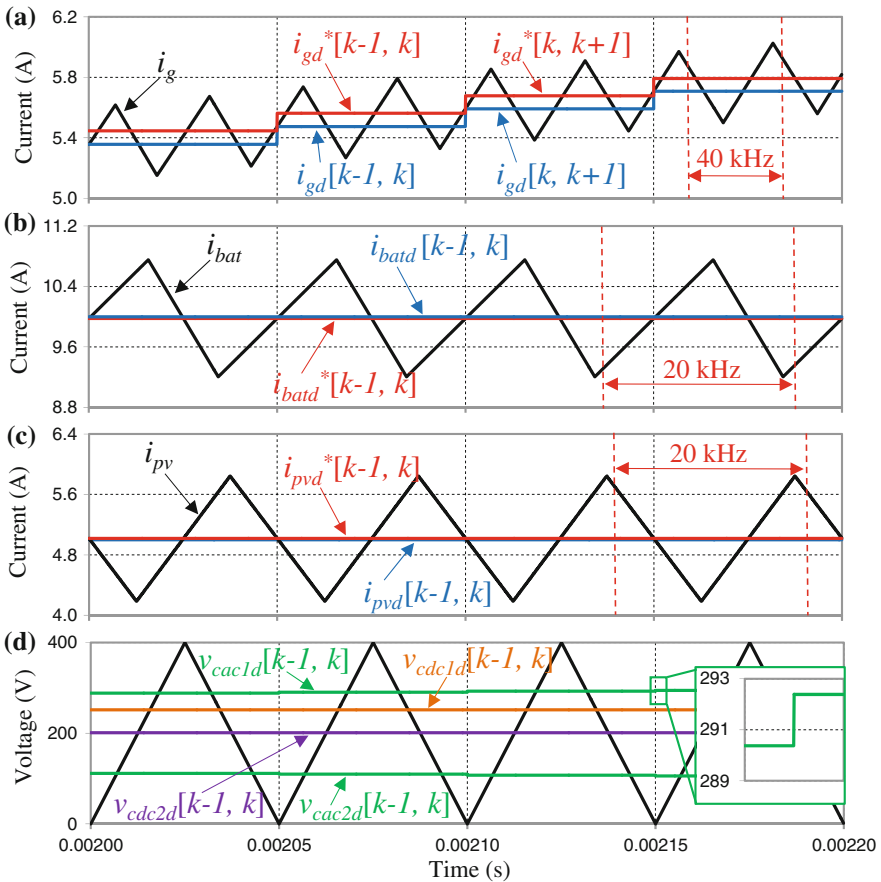


Fig. 4 Simulation results of the STB converter: **a** Grid current (i_g), digital grid current (i_{gd}), and its reference (i_{gd}^*); **b** EV batteries current (i_{bat}), digital EV batteries current (i_{batd}) and its reference (i_{batd}^*); **c** PV panels current (i_{pv}), digital PV panels current (i_{pvd}) and its reference (i_{pvd}^*); **d** PWM carrier and digital voltages produced by the ac–dc stage ($v_{cac1d}[k-1, k]$ and $v_{cac2d}[k-1, k]$) and by both dc–dc stages ($v_{cdc1d}[k-1, k]$ and $v_{cdc2d}[k-1, k]$)

$k]$ and $v_{cac2d}[k-1, k]$ are symmetrical in relation to the horizontal middle of the PWM carrier. Figure 5a shows the power grid voltage (v_g), the grid current (i_g), and the voltage produced by the converter (v_{cac}) when the STB converter receives energy from the power grid. This experimental result was obtained with the dc-link voltage controlled for 370 V and for an operating power of 2.5 kW. Figure 5b shows the same variables, but when the STB converter delivers energy to the power grid. This experimental result was obtained with the dc-link voltage controlled for 410 V and for an operating power of 2 kW. As it can be observed, in both cases, the grid current is sinusoidal and the voltage produced by the STB converter can assume three distinct values: $-v_{dc}$, 0 or $+v_{dc}$. Figure 6a shows the grid current (i_g) in detail in order to illustrate the current ripple (0.5 A) and the switching frequency

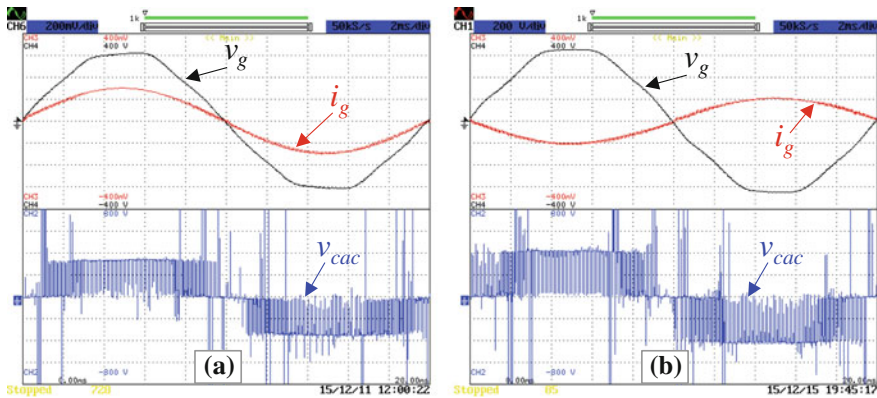


Fig. 5 Experimental results of the power grid voltage (v_g), grid current (i_g), and voltage produced by the converter (v_{cac}): **a** When the STB receives energy from the power grid; **b** When the STB delivers energy to the power grid

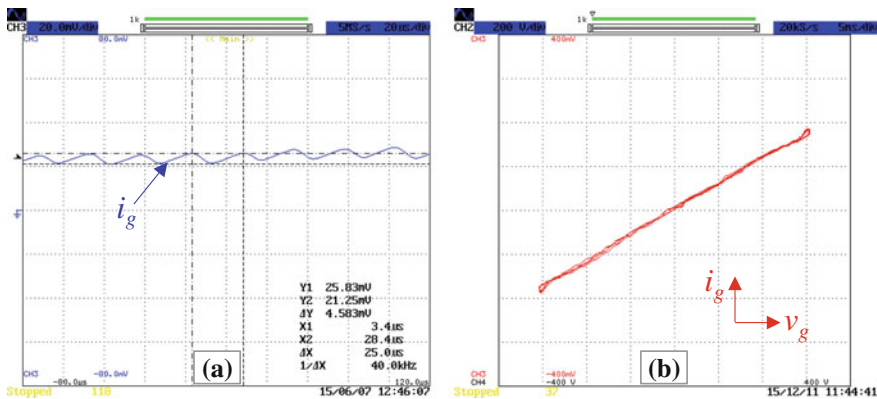


Fig. 6 Experimental results: **a** Detail of the grid current (i_g); **b** Relation between the grid current and the power grid voltage (X-Y mode)

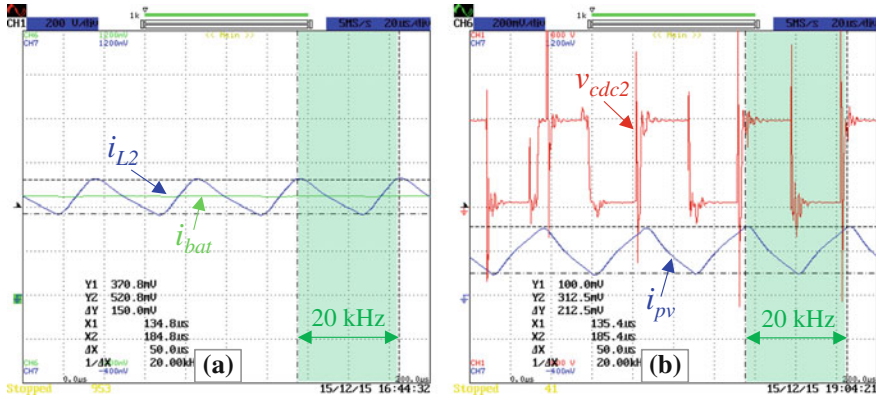


Fig. 7 Experimental results: **a** EV batteries current (i_{bat}) and current in the inductance L_2 (i_{L2}); **b** PV panels current (i_{pv}) and voltage produced by the converter (v_{cdc2})

(20 kHz). Figure 6b shows the grid current in function of the power grid voltage. The relation is almost purely linear due to the power theory and the predictive current control.

Figure 7 shows the experimental results when the power produced by the PV panels is used to charge the EV batteries, i.e., the ac–dc stage is used only to regulate the dc–link voltage. Figure 7a shows the EV batteries current (i_{bat}) and the current in the inductance L_2 (i_{L2}). During this operation mode the IGBT s_6 is always off. When the IGBT s_5 is on the voltage produced by the converter is v_{dc} and the inductance stores energy. When the IGBT s_5 is off the voltage produced by the converter is 0 and the inductance delivers energy. Figure 7b shows the PV panels current (i_{pv}) and the voltage produced the converter (v_{cdc2}). When the IGBT s_7 is on, the voltage produced by the converter is 0 and the inductance stores energy. When the IGBT s_7 is off, the voltage produced by the converter is v_{dc} and the inductance delivers energy.

5 Conclusions

This paper presents the digital control of a novel single–phase three–port bidirectional (STB) converter. This converter is used to interface renewables from photovoltaic (PV) panels and electric vehicles (EV) with the power grid taking into account power quality issues. The principle of operation of the proposed STB converter is explained in detail. Also, the digital control algorithms are explained in detail, including the power theory and the predictive current control strategies to control the grid current, the EV batteries charging current, and the PV panels current. The proposed STB converter, as well as the digital control algorithm, were validated through simulations and experimental results. For the ac–dc stage, the

experimental results show that the grid current is sinusoidal during the G2 V and V2G operation modes, and that the voltage produced by the STB converter can assume three distinct values: $+v_{dc}$, 0 , $-v_{dc}$. Therefore, it was possible to confirm the proper operation of the predictive current control and the dc-link voltage control strategy. For both dc-dc stages, the experimental results show the proper operation of the predictive current control for controlling the PV panels current (operation as boost type converter) and the EV batteries current (operation as buck type converter).

Acknowledgments This work is supported by FCT with the reference project UID/EEA/04436/2013, by FEDER funds through the COMPETE 2020—Programa Operacional Competitividade e Internacionalização (POCI) with the reference project POCI-01-0145-FEDER-006941. The PhD student Vítor Monteiro was supported by the doctoral scholarship SFRH/BD/80155/2011 granted by the FCT agency.

References

1. Dyke, K.J., Schofield, N., Barnes, M.: The impact of transport electrification on electrical networks. *IEEE Trans. Ind. Electron.* **57**(12), 3917–3926 (2010)
2. Rajashekara, K.: present status and future trends in electric vehicle propulsion technologies. *IEEE J. Emerg. Sel. Top. Power Electron.* **1**(1), 3–10 (2013)
3. Monteiro, V., Pinto, J.G., Afonso, J.L.: Operation modes for the electric vehicle in smart grids and smart homes: present and proposed modes. *IEEE Trans. Veh. Technol.* **65**(3), 1007–1020 (2016)
4. Gungor, V.C., Sahin, D., Kocak, T., Ergut, S., Buccella, C., Cecati, C., Hancke, G.P.: Smart grid and smart homes—key players and pilot projects. *IEEE Ind. Electron. Mag.* **6**, 18–34 (2012)
5. Ferreira, J.C., Monteiro, V., Afonso, J.L.: Vehicle-to-everything application (v2anything app) for electric vehicles. *IEEE Trans. Ind. Inf.* **10**(3), 1927–1937 (2014)
6. Monteiro, V., Exposto, B., Ferreira, J.C., Afonso, J.L.: Improved vehicle-to-home (iV2H) operation mode: experimental analysis of the electric vehicle as off-line UPS. *IEEE Trans. Smart Grid* (2016)
7. Monteiro, V., Carmo, J.P., Pinto, J.G., Afonso, J.L.: A flexible infrastructure for dynamic power control of electric vehicle battery chargers. *IEEE Trans. Veh. Technol.* (2015)
8. Kempton, W., Tomic, J.: Vehicle-to-grid power implementation: from stabilizing the grid to supporting large-scale renewable energy. *ELSEVIER J. Power Sources* **144**, 280–294 (2015)
9. Gao, S., Chau, K.T., Liu, C., Wu, D., Chan, C.C.: Integrated energy management of plug-in electric vehicles in power grid with renewables. *IEEE Trans. Veh. Technol.* **63**(7), 3019–3027 (2014)
10. Zhao, J.H., Wen, F., Dong, Z.Y., Xue, Y., Wong, K.P.: Optimal dispatch of electric vehicles and wind power using enhanced particle swarm optimization. *IEEE Trans. Ind. Inf.* **8**(4), 889–899 (2012)
11. Environmental Assessment of Plug-In Hybrid Electric Vehicles. Electric Power Research Institute and Natural Resources Defense Council, vol. 1: Nationwide Greenhouse Gas Emissions (2007)
12. Saber, A.Y., Venayagamoorthy, G.K.: Plug-in vehicles and renewable energy sources for cost and emission reductions. *IEEE Trans. Ind. Electron.* **58**(4), 1229–1238 (2011)

Model Predictive Control of an On-Board Fast Battery Charger for Electric Mobility Applications

Delfim Pedrosa, Ricardo Gomes, Vitor Monteiro,
J.C. Aparício Fernandes, João Monteiro and João L. Afonso

Abstract Under the necessities of reducing emissions and air pollution, and also for increasing fuel economy, automotive companies have been developing electric and plug-in hybrid electric vehicles. Since these vehicles are parked when the batteries are being charged, it is possible to use the traction power converter as on-board charger, also allowing to reduce weight, volume and costs of components in the vehicle. In this context, this paper presents a model predictive control algorithm for an on-board fast battery charging that uses the traction power converter of an electric vehicle. Simulation results and system implementation are depicted, and finally, are presented some experimental results obtained with the proposed control system.

Keywords Electric vehicles · Fast battery charger · Model predictive control · G2 V—Grid-to-Vehicle · V2G—Vehicle-to-Grid

D. Pedrosa (✉) · R. Gomes · V. Monteiro · J.C. Aparício Fernandes · J. Monteiro · J.L. Afonso

Centro ALGORITMI, University of Minho, 4804-533 Guimarães, Portugal
e-mail: delfim.pedrosa@algoritmi.uminho.pt; delfim.pedrosa@dei.uminho.pt

R. Gomes
e-mail: ricardo.gomes@algoritmi.uminho.pt

V. Monteiro
e-mail: vitor.monteiro@algoritmi.uminho.pt

J.C. Aparício Fernandes
e-mail: aparicio.fernandes@algoritmi.uminho.pt

J. Monteiro
e-mail: joao.monteiro@algoritmi.uminho.pt

J.L. Afonso
e-mail: joao.l.afonso@algoritmi.uminho.pt

1 Introduction

Batteries are the most common source of energy for electric vehicles (EVs) [1]. Therefore, many charging systems have been developed in order to provide energy to the batteries of EVs, usually from the electrical power grid. EVs have typically two types of battery chargers: on-board and off-board (or standalone) charging systems [2].

On-board charging systems are installed inside the vehicle, and thus the cost, weight and space minimization are the main requirements considered [3]. Hence, this system is commonly implemented using low-power converters [3]. Commercially available on-board battery chargers have typical power density and weight of approximately 0.6 kW/kg and 6.2 kg, respectively [4]. Hence, the battery charging process has a typical duration of a few hours [5]. Unlike the off-board type, the on-board charging can be done, practically, in any location, as long as there is an electrical network outlet available [2, 6], for level 1 (slow) charging. Thus, this type of charging contributes to increase the acceptance of EVs and to reduce the cost of the infrastructure network for public charging [7].

A bidirectional power flow capability is also a relevant feature for a battery charger of an EV, since it provides some additional features. In addition to the normal battery charging process, known as grid-to-vehicle (G2V) operation mode, it also supports energy injection back to the electrical grid, known as vehicle-to-grid (V2G) operation mode, contributing to the development of the smart grids [6, 8]. Besides the G2V and V2G operation modes, a bidirectional battery charger can also be used to supply home loads during power outages, or to supply loads in places without connection to the power grid, known as vehicle-to-home (V2H) operation mode [8].

A battery charger can operate isolated (with galvanic isolation) or non-isolated from the electrical grid. Isolated chargers are preferred for safety reasons, but due to its impact on the vehicles' cost and weight they are usually avoided. Thus, most of the reported integrated chargers are non-isolated [2, 3].

EVs have different power electronics converters, where the battery charger converter and the motor drive converter are the main converters. Due to the similarities between both, it is possible to join them together in a single power converter. It is important to note that this is only possible knowing that the motor drive and the battery charging operations are not performed simultaneously. This type of solution is identified in the literature as an integrated motor drive and battery charger, or simply as an integrated charger [9].

An integrated charger aims to reduce the size, number of components and the weight of the power converters in the EV. Ideally, the goal is to have an on-board battery charger without requiring any extra hardware in addition to the components of the motor drive system.

Figure 1 presents a topology that concretizes both of these modes, motor drive and battery charger, in the same power converter. One interesting feature is associated with the compatibility with any electrical machines, with or without access to

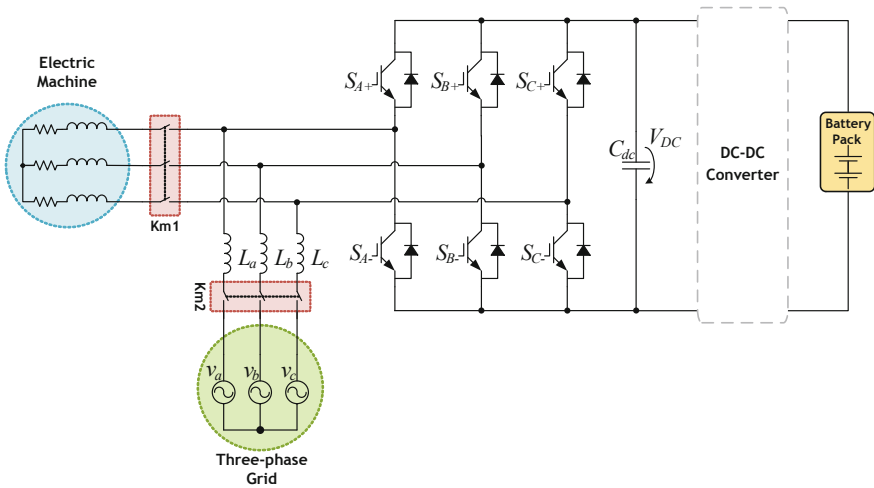


Fig. 1 Integrated power converter for EV motor drive or EV battery charger

the neutral point. However, this solution requires a relay for disconnecting the electric machine during the battery charging process.

This topology allows the slow EV battery charging, but also is compatible with the fast EV battery charging through an AC three-phase power grid system. One of the main concerns regarding the battery charging operation is its influence on the power quality of the electrical grid. Therefore, the battery charging operation should be performed with unitary power factor and with consumption of almost sinusoidal currents, i.e., with low harmonic content [9, 10].

The focus of this paper is the operation of an on-board fast battery charger that uses the traction power converter of an EV.

2 Predictive Control

Classic linear controllers with modulation techniques and nonlinear controllers based on hysteresis comparators are the most widely used in control algorithms. However, the developments achieved over the last years on digital electronics, including digital signal controllers (DSCs), offer more computational power, potentiating the development of new and more effective and complex control techniques, such as the model predictive control (MPC) [11].

In [12] is propose a type of finite control set model predictive control (FCS-MPC), mentioned as direct power control based on model predictive control (DPC-MPC), for controlling a boost AC-DC converter. The dynamical model of the three-phase boost AC-DC converter is shown in Eq. (1) and the derivative is described in Eq. (2), where, $v_s(t)$ is the power grid voltage, $v_R(t)$ is the voltage

across the internal resistance of the inductor, $v_L(t)$ is the voltage across the inductor, $v_{in}(t)$ is the input voltage in converter, $R_s(t)$ is the internal resistance of the inductor, and $i_s(t)$ is the grid current.

$$v_s(t) = v_R(t) + v_L(t) + v_{in}(t) = R_s i_s(t) + L_s \frac{di_s(t)}{dt} + v_{in}(t) \quad (1)$$

$$\frac{di_s(t)}{dt} = \frac{1}{L_s} [v_s(t) - R_s i_s(t) - v_{in}(t)] \quad (2)$$

Using the forward Euler approximation, the derivative of the current is approximated to Eq. (3), and thus the input predicted current (i_s) is discretized for a sample period T_s , resulting in Eq. (4), where L_s is the inductance of the extra inductor.

$$\frac{di_s(t)}{dt} \cong \frac{i_s(k+1) - i_s(k)}{T_s} \quad (3)$$

$$i_s(k+1) = \left(1 - \frac{R_s T_s}{L_s}\right) i_s(k) + \frac{T_s}{L_s} [v_s(k) - v_{in}(k)] \quad (4)$$

To accommodate all the three-phase components of the system, the input currents and voltages are defined as space vectors, according to Eqs. (5) and (6) respectively, where $\alpha = e^{j(2\pi/\beta)}$.

$$i_s = \frac{2}{3} (i_a + \alpha i_b + \alpha^2 i_c) \quad (5)$$

$$v_s = \frac{2}{3} (v_a + \alpha v_b + \alpha^2 v_c) \quad (6)$$

The voltage v_{in} is dependent on the switching state of the power electronics converter and the voltage of the DC-bus. In this case, [12] propose to define v_{in} as a space vector according to Eq. (7), and the value of S is defined according to Eq. (8), where S_a , S_b and S_c are the switching states of each leg of the converter.

$$v_{in} = S V_{DC} \quad (7)$$

$$S = \frac{2}{3} (S_a + \alpha S_b + \alpha^2 S_c) \quad (8)$$

Considering the space vector definitions used for the voltage and current values, the predicted values for the instantaneous real power (p) and imaginary power (q) are defined according to Eqs. (9) and (10), respectively.

$$p(k + 1) = v_{s\alpha} i_{s\alpha} + v_{s\beta} i_{s\beta} = \Re\{v_s(k + 1) \bar{i}_s(k + 1)\} \tag{9}$$

$$q(k + 1) = v_{s\beta} i_{s\alpha} - v_{s\alpha} i_{s\beta} = \Im\{v_s(k + 1) \bar{i}_s(k + 1)\} \tag{10}$$

Using a high sampling frequency, it can be used the approximation defined by:

$$v_s(k + 1) \approx v_s(k) \tag{11}$$

The MPC is based in the control of the instantaneous powers p and q and thus, in [12] is proposed a cost function g defined according to:

$$g = |q_{ref}(k) - q(k + 1)| + |p_{ref}(k) - p(k + 1)| \tag{12}$$

In real-time applications it is not possible to measure variables, predict their future values and apply the respective control action at the same instant. Thus, it is not correct to determine the predicted values considering that it is possible to apply the desired switching state at the same instant. Hence, to avoiding errors with the predictions, a delay in the predictive model has to be considered, resulting in a two-step-ahead prediction [12, 13].

Since the selected voltage can only be applied at the next step ($k + 1$), it is necessary to predict the current obtained as consequence of the select switching state, i.e., the current at ($k + 2$). This current is obtained by shifting Eq. (4) one step forward, resulting in:

$$i_s(k + 2) = \left(1 - \frac{R_s T_s}{L_s}\right) i_s(k + 1) + \frac{T_s}{L_s} [v_s(k + 1) - v_{in}(k + 1)] \tag{13}$$

Thus, first time of $i_s(k + 1)$ is calculated using Eq. (4), considering the current and voltage measured and the value of v_{in} obtained as consequence of the switching state selected in the previous sampling. Then, the obtained predicted current uses the Eq. (13).

In this paper, it is used the cost function:

$$g = |q_{ref}(k) - q(k + 2)| + |p_{ref}(k) - p(k + 2)| + \lambda C \tag{14}$$

The cost function includes a third component, with the purpose of overcoming the high frequency components around the commutation frequency. Before computing the cost function result, the control system checks if the switching state under analysis is equal to the last selected switching state. If it is equal, the value of C in Eq. (15) is set to 1, otherwise the value of C is set to 0. The parameter λ defines the weight of this component in the cost function.

Figure 2 describes the MPC algorithm to perform the fast EV battery charger.

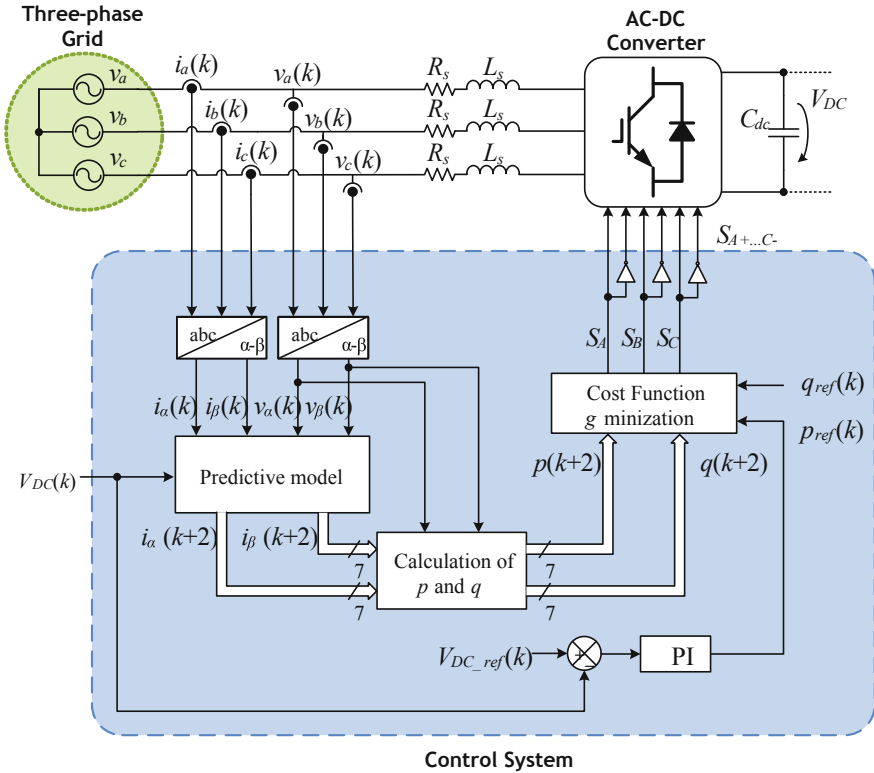


Fig. 2 Block diagram of the presented MPC algorithm

3 Simulation Results

This section presents the main simulation results obtained to validate the model predictive control applied to a fast EV battery charger during the G2 V operation mode. The simulations stage is a process of great importance, since it allows the anticipation of some problems that might occur in a real implementation. Hence, it contributes to the optimization of the time required for the development, as well as to reduce the financial resources required. The simulation results were obtained with the simulation software PSIM v9.0.

3.1 Grid-to-Vehicle Operation Without Reactive Power Compensation

This section presents the simulation results considering an instantaneous real power reference (p_{ref}) of 15 kW and an instantaneous imaginary power reference (q_{ref}) of

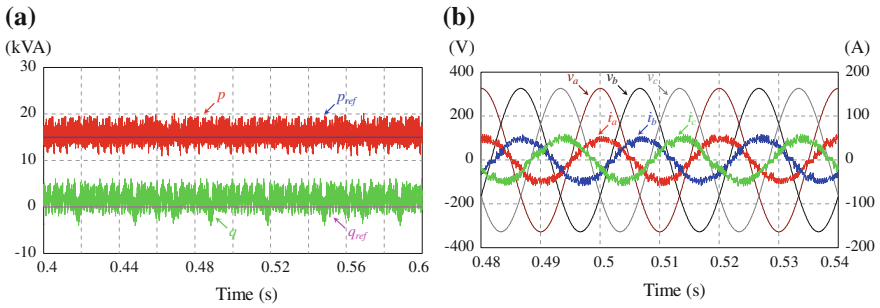


Fig. 3 Simulation results of the fast EV battery charging process in steady-state: **a** Instantaneous p - q powers (p and q) and respective references (p_{ref} and q_{ref}); **b** Power grid voltages (v_a , v_b and v_c) and grid currents (i_a , i_b and i_c)

Table 1 Measured RMS values, THD values and power factor of the grid currents during the fast EV battery charging process

	RMS (A)	THD (%)	Power factor
i_a	34.97	15.42	0.98
i_b	34.85	15.09	0.98
i_c	34.92	16.20	0.98

0 kVAr. Figure 3a shows the obtained results of the instantaneous real power (p) and the instantaneous imaginary power (q), and the respective references (p_{ref}) and (q_{ref}). On the other hand, the obtained waveforms of the power grid voltages (v_a , v_b and v_c) and the grid currents (i_a , i_b and i_c) are shown in Fig. 3b. The measured RMS values, THD values and Power Factor of the grid currents are presented in Table 1.

3.2 Grid-to-Vehicle Operation with Reactive Power Compensation

This section presents the main simulation results performed with a reference of the instantaneous imaginary power (q_{ref}) different from 0, i.e., the fast EV battery charger operates as a reactive power compensator.

The reference of the instantaneous real power (p_{ref}) is set to 15 kW. To evaluate the dynamic response of the charging system as a reactive power compensator, the reference of the instantaneous imaginary power (q_{ref}) is defined to be -10 kVAr from the instant $t = 0$ s and 10 kVAr after the instant $t = 0.5$ s.

The obtained results of the instantaneous real power (p) and the instantaneous imaginary power (q), and their respective references (p_{ref} and q_{ref}), are presented in Fig. 4a, while the obtained waveforms of the power grid voltage in phase a (v_a) and

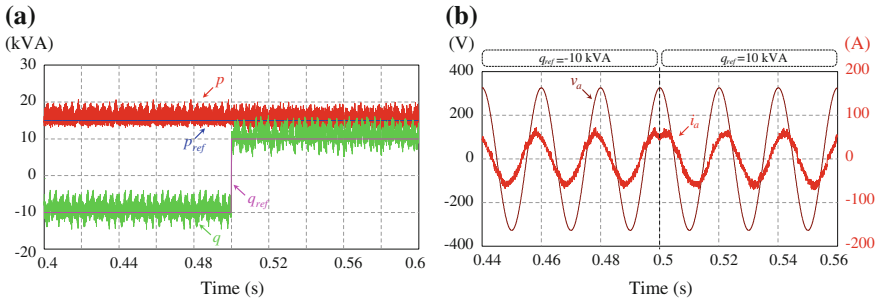


Fig. 4 Simulation results of the fast EV battery charging process in transient-state: **a** Instantaneous p - q powers (p and q) and respective references (p_{ref} and q_{ref}); **b** Power grid voltage in phase a (v_a) and grid current also in phase a (i_a)

the grid current also in phase a (i_a), are presented in Fig. 4b. As expected, the instantaneous imaginary power follows its reference without sudden variations, demonstrating the fast dynamic response of the model predictive control.

4 System Implementation

The developed laboratorial prototype can be divided in two main parts, the power converter and the digital control. The power converter is composed by a three-phase AC-DC power inverter and by a DC-DC. This converter is composed by four IGBTs legs, and it is used as EV motor drive or as fast EV battery charger. On the other hand, the digital control is composed by several circuits,

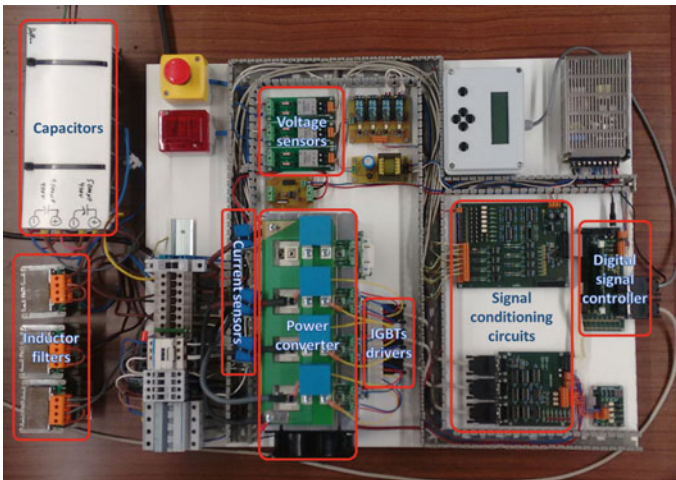


Fig. 5 Photograph of the developed laboratorial prototype

predominantly by the DSC (TMS320F28335), the signal conditioning circuit (where is used an analog-to-digital converter to convert the signal from the sensors to the DSC), and the IGBTs gate drivers. The digital control is isolated from the power converters through hall-effect sensors and IGBTs gate drivers. The power converter and the digital control of the developed laboratorial prototype are presented in Fig. 5.

5 Experimental Results

This section presents the main experimental results obtained with the developed laboratorial prototype. The experimental results were obtained with the developed laboratorial prototype connected to the power grid with a nominal voltage of about 75 V and a frequency of 50 Hz.

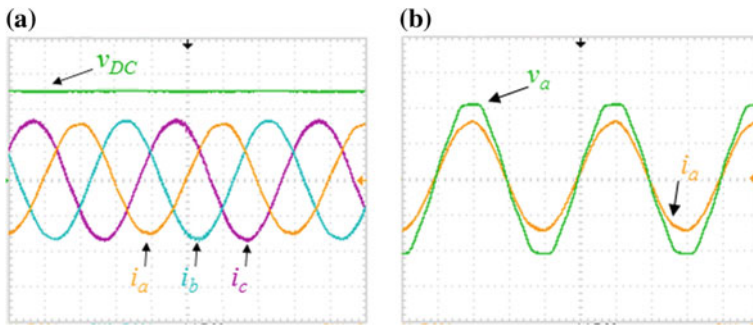
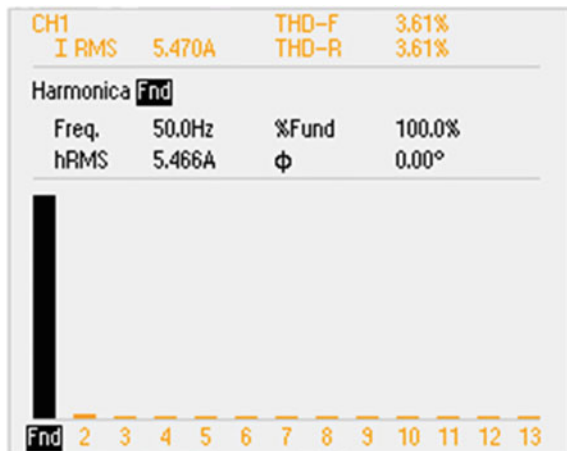


Fig. 6 Experimental results of the fast EV battery charging process in steady-state: **a** Grid currents (i_a , i_b and i_c : 5 A/div), and DC-bus voltage (v_{DC} : 50 V/div); **b** Power grid voltage (v_a : 50 V/div) and grid current (i_a : 5 A/div)

Fig. 7 Harmonic spectrum of the grid current for the phase a (i_a)



The first experimental results were obtained for an instantaneous real power (p_{ref}) of 1200 W and an instantaneous imaginary power (q_{ref}) of 0 VAr. Figure 6a shows the obtained results of the grid currents (i_a , i_b and i_c), as well as the voltage in DC-bus (v_{DC}). On the other hand, Fig. 6b shows the experimental results of the power grid voltage (v_a) and the grid current (i_a). The harmonic spectrum and the RMS value of the grid current for the phase a (i_a) are presented in Fig. 7.

6 Conclusions

This paper presents an on-board fast battery charger for electric vehicle (EV) based on a model predictive control (MPC) algorithm.

The obtained simulation results allow validating the proposed control algorithms for the fast EV battery charger. The MPC permits to control the instantaneous real power (p) and the imaginary power (q) exchanged between the electrical grid and the EV battery charger, based on using a dynamical model of the system in order to predict its future behavior.

It was presented the operation of the EV battery charger with sinusoidal current and high power factor. These characteristics represent an important contribute, increasing the capabilities of the EVs and their potential role in order to improve the power quality of the electrical power grid.

The proposed integrated EV motor drive and EV battery charger applied to EVs contribute to optimize the space, weight and cost of the power electronics components inside the vehicle. The adopted topology allows fast EV battery charger operation, but needs extra inductor filters.

Acknowledgments This work has been supported by COMPETE: POCI-01-0145-FEDER-007043 and FCT—Fundação para a Ciência e Tecnologia within the Project Scope: UID/CEC/00319/2013. Mr. Delfim Pedrosa was supported by the doctoral scholarship SFRH/BD/86628/2012 granted by the FCT agency.

References

1. Monteiro, V., Ferreira, J.C., Pinto, G., Pedrosa, D., Afonso, J.L.: iV2G charging platform. In: 13th International IEEE Conference on Intelligent Transportation Systems (ITSC), pp. 409–414. IEEE Press, Funchal (2010)
2. Haghbin, S., Khan, K., Zhao, S., Alakula, M., Lundmark, S., Carlson, O.: An integrated 20 kw motor drive and isolated battery charger for plug-in vehicles. *IEEE Trans. Power Electron.* **28** (8), 4013–4029 (2013)
3. Haghbin, S., Lundmark, S., Carlson, O., Alakula, M.: A combined motor/drive/battery charger based on a split-windings PMSM. In: IEEE Vehicle Power and Propulsion Conference (VPPC), pp. 1–6. IEEE Press, Chicago (2011)

4. Dusmez, S., Khaligh, A.: A charge-nonlinear-carrier-controlled reduced-part single-stage integrated power electronics interface for automotive applications. *IEEE Trans. Veh. Technol.* **63**(3), 1091–1103 (2014)
5. Yilmaz, M., Krein, P.T.: Review of charging power levels and infrastructure for plug-in electric and hybrid vehicles. In: *IEEE International Electric Vehicle Conference (IEVC)*, pp. 1–8. IEEE Press, Greenville (2012)
6. Yilmaz, M., Krein, P.T.: Review of battery charger topologies, charging power levels, and infrastructure for plug-in electric and hybrid vehicles. *IEEE Trans. Power Electron.* **28**(5), 2151–2169 (2013)
7. Sakr, N., Sadarnac, D., Gascher, A.: A review of on-board integrated chargers for electric vehicles. In *16th European Conference on Power Electronics and Applications*, pp. 1–10. IEEE Press, Lappeenranta (2014)
8. Pinto, J.G., Monteiro, V., Goncalves, H., Exposto, B., Pedrosa, D., Couto, C., Afonso, J.L.: Bidirectional battery charger with grid-to-vehicle, vehicle-to-grid and vehicle-to-home technologies. In *39th Annual Conference of the IEEE industrial Electronics Society (IECON 2013)*, pp. 5934–5939. IEEE Press, Vienna (2013)
9. Haghbin, S., Khan, K., Lundmark, S., Alakula, M., Carlson, O., Leks, M., Wallmark, O.: Integrated chargers for EV's and PHEV's: examples and new solutions. In: *XIX International Conference on Electrical Machines (ICEM)*, pp. 1–6. IEEE Press, Rome (2010)
10. Monteiro, V., Pedrosa, D., Exposto, B., Ferreira, J.C., Afonso, J.L.: Smart charging system of the electric vehicle CEPIUM. In: *Annual Seminar on Automation, Industrial Electronics and Instrumentation (SAAEI'12)*, pp. 500–505 (2012)
11. Rodriguez, J., Kazmierkowski, M.P., Espinoza, J.R., Zanchetta, P., Abu-Rub, H., Young, H. A., Rojas, C.A.: State of the art of finite control set model predictive control in power electronics. *IEEE Trans. Ind. Inf.* **9**(2), 1003–1016 (2012)
12. Cortes, P., Rodriguez, J., Antoniewicz, P., Kazmierkowski, M.: Direct power control of an AFE Using predictive control. *IEEE Trans. Power Electron.* **23**(5), 2516–2523 (2008)
13. Kouro, S., Cortes, P., Vargas, R., Ammann, U., Rodriguez, J.: Model predictive control—a simple and powerful method to control power converters. *IEEE Trans. Power Electron.* **56**(6), 1826–1838 (2009)
14. Lim, J.S., Lee, Y.H.: Model predictive control of current and voltage for Li-ion battery charger using 3-phase AC/DC converter. In: *Proceedings of SICE Annual Conference 2010*, pp. 215–218. IEEE Press, Taipei (2010)

Family Houses Energy Consumption Forecast Tools for Smart Grid Management

F. Rodrigues, C. Cardeira, J.M.F. Calado and R. Melício

Abstract This paper presents a short term (ST) load forecast (FC) using Artificial Neural Networks (ANNs) or Generalized Reduced Gradient (GRG). Despite the apparent natural unforeseeable behavior of humans, electricity consumption (EC) of a family home can be forecast with some accuracy, similarly to what the electric utilities can do to an agglomerate of family houses. In an existing electric grid, it is important to understand and forecast family house daily or hourly EC with a reliable model for EC and load profile (PF). Demand side management (DSM) programs required this information to adequate the PF of energy load diagram to Electric Generation (EG). In the ST, for load FC model, ANNs were used, taking data from a EC records database. The results show that ANNs or GRG provide a reliable model for FC family house EC and load PF. The use of smart devices such as Cyber-Physical Systems (CPS) for monitoring, gathering and computing a database, improves the FC quality for the next hours, which is a strong tool for Demand Response (DR) and DSM.

Keywords Energy forecasting · Energy management · Smart grids · Artificial neural networks · Gradient methods

F. Rodrigues · C. Cardeira · J.M.F. Calado · R. Melício (✉)
IDMEC, Instituto Superior Técnico, Universidade de Lisboa, Lisbon, Portugal
e-mail: ruimelicio@gmail.com

F. Rodrigues
MIT Portugal, Porto Salvo, Portugal

J.M.F. Calado
Departamento de Engenharia Mecânica, Instituto Superior de Engenharia de Lisboa,
Lisbon, Portugal

R. Melício
Departamento de Física, Escola de Ciências e Tecnologia, Universidade de Évora,
Évora, Portugal

1 Introduction

The major objective of DSM is to encourage customer to participate in schemes to reduce peak demand and shifting the load. One such mechanism is DR, in which the system allows end users to alter their load shape to reduce the overall peak of the system [1]. An important tactic to DR and energy management to promote a more efficient energy end user is DSM [2]. DSM is based on a set of tools for shaping the load diagram, through peak clipping, valley filling, and shift of some loads, among others [3]. These strategies are required to conveniently shape the load EC diagram. In a Smart Grid (SGr) context, a consumer active role is essential for grid management in order to efficiently assure EG and usage.

Using the knowledge about the PF curve of power EC of each family house, a model for optimizing the electrical energy can be generated [4]. Tools for providing an accurate ST Load FC (STLFC) will enhance the quality of the DSM.

The aim of this paper is to show the use of an ANN and GRG to develop a simple and reliable method for STLFC of family houses' daily and hourly EC for residential and small buildings.

ANNs are well known by their ability of self learning and provide accurate predictions for many applications. Models achieved using ANN are inspired on the human neurons behavior. Simple 'neuron' computations are performed locally and the connections among are adapted for defining the model. In [5] ANNs are used for predicting room temperatures. For this work, it was used a set of EC data from different family houses to train the ANN. The database used in this work comes from a study performed on 93 family houses, in Portugal [6].

The paper organization is as follows: Sect. 2 presents the state of the art. Section 3 presents the methodologies used in the paper: ANN and GRG. Section 4 presents case studies and results. Finally, conclusions are drawn in Sect. 5.

2 State of the Art

A large number of scientific works have been carried out about techniques for STLFC. Some techniques are very successful for power systems, while they underperform on other occasions due to the specific features of the local EC load: Models are difficult, are not linear and are subject to specific conditions like weather or social unexpected impacts.

Some scientific surveys were dedicated to ANNs for STLFC [7, 9–14]. Other techniques were used such as time series and regression models [15, 16]. In [17] a general overview of FC techniques is presented. ANNs have received a large share of attention and interest.

There is a direct connection of this work to SGRs and CPS. Renewable technologies highly present large production variation in function of the local weather. Their highly unpredictable nature increases the difficulty regarding their incorporation into the electric power distribution. This issue needs to be fully solved in SGR systems scope [7, 8].

Sustainability is a major challenge for SGR [9]. Currently power systems are largely distributed and demand precise control. The need of an adequate response to severe faults is even more important, due to the generalization of the electrical markets. Power system currently based on SCADA systems are expected to evolved into SCADA systems, integrated in SGR systems. SCADA systems are usually pointed out as an reference example of CPS [10], intended to achieve a blackout-free EG and distribution system, for building SGRs, or for optimization of EC [9].

CPS can be described as smart systems including software and hardware, namely components for sensing, monitoring, gathering, actuating, computing, communication and controlling physical infrastructures, completely integrated and directly interacting to sense the alterations in the state of the surrounding environment [11].

The integration of renewable energy resources and electro-mobility into an electric grid, raises many concerns regarding operation, balance and reliability. Thus, the use of smart devices such as CPS, to assist monitoring, control and operating renewable energy systems in a SGR context [12, 18] are fundamental pieces in the success of these systems. Also, in an existing electric grid, it is important to understand and FC family house daily or hourly EC with a reliable model for EC and load PF. The effectiveness of the DSM and DR programs highly depend on the quality of energy FC. DSM and DR programs require to adequate the PF of energy load diagram to EG. In STLFC model ANN have been used with an EC records database. However, using smart devices such as CPS monitoring, gathering and computing in real time a database with weekdays and weekend, the use of two groups of days, allow developing STLFC models with better results than a model that used a single week [13].

3 Methodologies

3.1 ANN

The network architecture that was built for FC is a feed-forward type of ANN. The backpropagation learning algorithm was used to train the ANN. Backpropagation learning algorithms are based on steepest descent methods. Looking to the output neurons results error, connections are updated to make the ANN closer to the model. As learning phase goes on the error is minimized.

The Levenberg-Marquardt Algorithm (LMA) consists in finding the update given by:

$$\Delta c = - [J^T(c)J(c) + \mu I]^{-1} J^T(c) e(c) \tag{1}$$

where:

$J(c)$ is the Jacobian;

μ is a adjustable factor; and

$e(c)$ is the error

A small μ is turns the LMA into a classic Gauss-Newton algorithm. Higher μ values turn the LMA into a steepest descent algorithm. The LMA, parametrized by μ may take advantage on the Gauss-Newton algorithm faster convergence or on the Steepest descent convergence guarantee [19].

Furthermore, the output of any neuron is shown in Fig. 1.

The neuron output value is given by:

$$y_k = f(u_k) = f\left(\sum_{j=1}^m W_{kj}x_j + b_k\right). \tag{2}$$

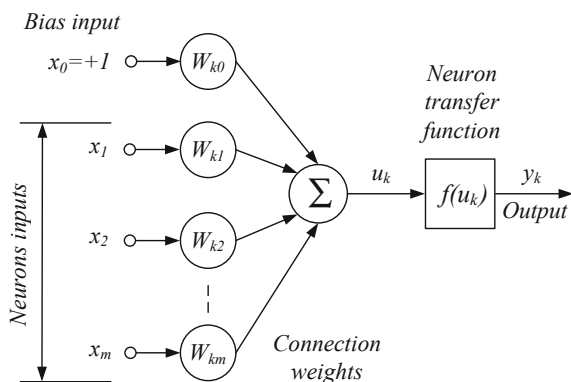
or considering bias as input value $x_0 = 1$ and weight $W_{k0} = b_k$:

$$y_k = f(u_k) = f\left(\sum_{j=0}^m W_{kj}x_j\right) \tag{3}$$

The number of inputs determines the number of input neurons. Accordingly, the number of variables to estimate determines the number of output neurons. The number of hidden neurons depends on the model.

Transfer functions of the neurons have to be differentiable and with a positive (or null) derivate [13]: Sigmoid functions are relatively common. Moreover, these functions scale the inputs to a continuous value between 0 a 1.

Fig. 1 Neuron model



The ANN architecture was built with three-layer feedforward configuration. The network was optimized as mentioned in [4].

Figure 2 shows the network used for predicting the hourly EC for an usual day. ANN inputs are the hourly EC of each family house.

For each family house around 500 h of logged EC were available. 66 % of this data was used for training, 2/3 of those data were used for ANN training and validation. 33 % of those data were used to evaluate the FC quality.

Binary inputs were used to code the previous hours [20] for the hourly load FC [21].

The 11 input neurons are distributed as follows. Five correspond to the last five previous hours EC. The 6th input neuron corresponds to the EC during the last 24th hour. Five neurons are used to binary encode the hours. The hidden layer is composed by twenty neurons. The output is the next hour EC prediction.

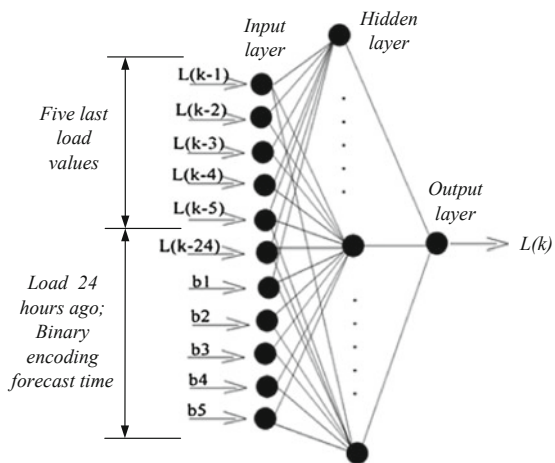
3.2 GRG

GRG is another popular technique. The original method, the Reduced Gradient Method has seen several different customizations due several researchers [22, 23]. The GRG formulation is given by the maximization of the following function:

$$\min f(c_k): g(c_k) = 0, L \leq c \leq U \tag{4}$$

where $f(c_k)$ is the objective function, subject to $g(c_k)$ function, where c_k values are constrained to the $[L, U]$ interval.

Fig. 2 Simplified ANN architecture used to FC hourly load



4 Case Studies

Two case studies were performed to validate the models based on information from monitoring carried out in [4]. The algorithms were implemented in tool Matlab environment.

4.1 Case 1

Using Fig. 2 model, the ANN 2 weeks of hourly EC were used for learning and the third week was used for testing the model. Results are shown in Fig. 3a, b.

Table 1 summarizes the results obtained for the linear correlation R and linear regression R^2 , mean absolute percent error (MAPE) and the standard deviation of error (SDE).

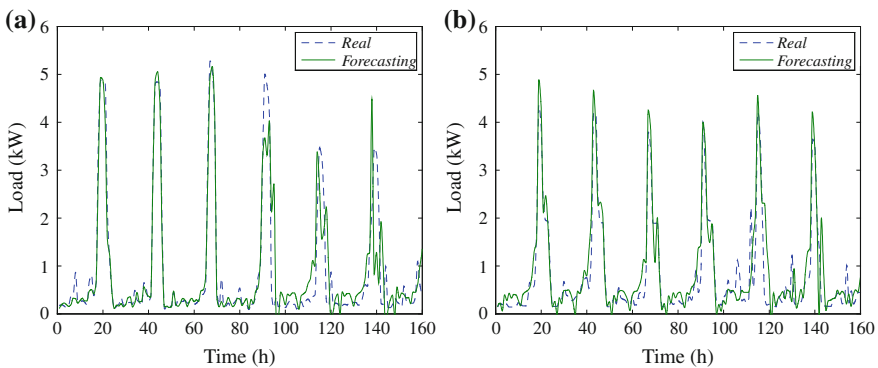


Fig. 3 FC hourly load of two random family houses

Table 1 ANN FC results

	Family house n° 64				Family house n° 65			
	R (%)	R^2 (%)	MAPE (%)	SDE	R (%)	R^2 (%)	MAPE (%)	SDE
Day 1	99	98	16	0.2	98	97	22	0.2
Day 2	99	99	10	0.1	98	95	19	0.2
Day 3	99	99	13	0.1	98	93	24	0.2
Day 4	87	75	37	0.7	96	92	23	0.2
Day 5	72	52	61	0.5	90	68	44	0.5
Day 6	43	18	87	0.8	86	71	45	0.4
Day 7	93	87	30	0.4	93	89	37	0.2

As the family house EC load may be zero or change orders of magnitude along the day, the average load was used in MAPE to avoid the problem caused by zero loads. In linear correlation (R) and regression (R^2) show how accurately the estimates compare to the real data.

Figure 3 and Table 1 show that method proposed shows a decent FC performance.

4.2 Case 2

To optimize the solution and identify the type of function (linear or nonlinear) it was used the GRG method used by Solver. The results showed the functions of daily EC are nonlinear and the optimization tool can be used to FC annual EC average.

Using GRG, the research has shown the ability to converge the FC function to the function of real EC with an error $MSE \cong 0$.

The comparison of an average annual daily EC with accumulative EC electric appliance FC is shown in Fig. 4a.

The modeling tested results of Portuguese family house average annual daily EC is shown in Fig. 4a. The horizontal axis identifies the family house number. The vertical axis shows the average annual daily EC in kWh per day. The straight blue line (from the top, first one) represents the total real average annual daily EC. The green line (second) represents accumulated average annual EC from appliances FC. Other colors represent the monitored electric appliance FC consumptions.

The comparison of hourly EC average using electric appliance FC is shown in Fig. 4b. Figure 4b shows the modeling tested results of family house hourly EC average. The blue line represents the hourly EC average and the green line represents the EC weights and the contribution of each appliance in a family house.

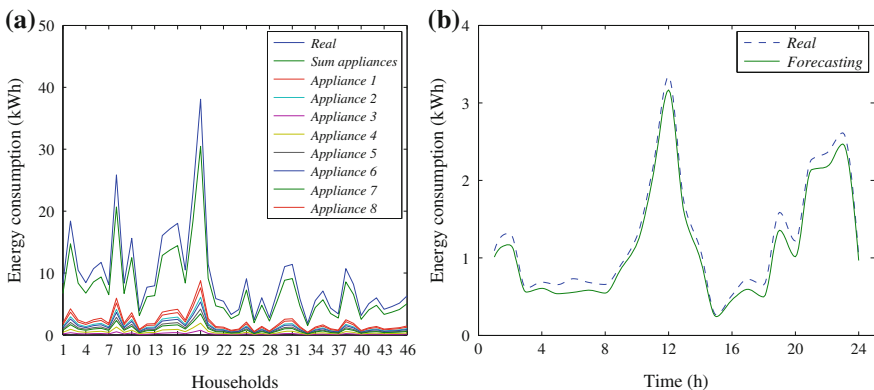


Fig. 4 Average annual EC FC: a appliance samples; b random house

The results show also the real load PF is always above the FC. One reason for this fact is that FC did not include all electric appliances (e.g.: microwave, coffee machine, vacuum machine). The used database included total energy family house EC and EC of some specific electric appliance (washer, fridge, TV). The partial measures do not add-up total EC, because some other ECs were not measured and introduced in database. Therefore, is not surprising the estimated energy load PF is bellow than total EC.

However, Fig. 4 shows the FC follows the shape of the real load PF with a relative low offset. One explanation is that some ECs might exist besides the monitored electric appliances.

5 Conclusion

This paper present ANN and GRG methods for estimation of hourly EC. The FC models provided estimates of hourly EC and load PF with significant accuracy. The results show that ANNs performed well forecasting the load for the next days and GRG also exhibit good performance for the annual average EC.

FC hourly and daily EC are useful for DSM to fit the energy production to the expected consumption. Moreover, the knowledge about future consumption, it becomes possible to do shedding (anticipate or postpone) of the EC.

Future researches will be in towards the integration of these techniques into smart devices such as CPS, to assist monitoring, control and operation of SGRs.

Acknowledgments The authors thank for the Portuguese Funds support, through the FCT, project LAETA2015/2020, ref.UID/EMS/50022/2013.

References

1. Sofana, R.S., Ramesh, V.: A demand response modeling for residential consumers in smart grid environment using game theory based energy scheduling algorithm. *Ain Shams Eng. J.* (2016)
2. Rodrigues, F., Cardeira, C., Calado, J.M.F., Melcio, R.: Energy household forecast with ANN for demand response and demand side management. *Renew. Energy Power Qual. J.-ICREPQ* **14**, 1–4 (2016)
3. Macedo, M.N.Q., Galo, J.J.M., de Almeida, L.A.L., de Lima, A.C.: Demand side management using artificial neural networks in a smart grid environment. *Renew. Sustain. Energy Rev.* **41**, 128–133 (2015)
4. Rodrigues, F., Cardeira, C., Calado, J.M.F.: The daily and hourly energy consumption and load forecasting using artificial neural network method: a case study using a set of 93 households in Portugal. *Energy Procedia* **62**, 220–229 (2014)
5. Yang, I.H., Kim, K.W.: Prediction of the time of room air temperature descending for heating systems in buildings. *Build. Environ.* **39**(1), 19–29 (2004)
6. Sidler, O.: Demand side management. End-use metering campaign in 400 households of the European Community. SAVE Programme, Project EURECO. Commission of the European Communities: France (2002)

7. Blaabjerg, F., Ionel, M.: Renewable energy devices and systems—state-of-the-art technology, research and development, challenges and future trends. *Electr. Power Compon. Syst.* **43**(12), 1319–1328 (2015)
8. Viegas, J.L., Vieira, S.M., Melicio, R., Mendes, V.M.F., Sousa, J.M.C.: Classification of new electricity customers based on surveys and smart metering data. *Energy* **107**, 804–817 (2016)
9. Ramos, C., Vale, Z., Faria, L.: Cyber-physical intelligence in the context of power systems. *Future Gener. Inf. Technol.* **7105**, 19–29 (2011)
10. Faria, L., Silva, A., Ramos, C., Vale, Z., Marques, A.: Intelligent behavior in a cyber-ambient training system for control center operators. *Proc. ISAP* 1–6 (2011)
11. Ying, S.: Foundations for innovation in cyber-physical systems. Workshop Report, Energetics Incorporated, Columbia, Maryland, US (2013)
12. Seixas, M., Melicio, R., Mendes, V.M.F.: Simulation of rectifier voltage malfunction on OWECS, four-level converter, HVDC light link: smart grid context tool. *Energy Convers. Manag.* **97**, 140–153 (2015)
13. Hippert, H., Pedreira, C., Souza, R.: Neural networks for short-term load forecasting: a review and evaluation. *IEEE Trans. Power Syst.* **16**(1), 44–55 (2001)
14. Carpinteiro, O., Reis, A., Silva, A.: A hierarchical neural model in short-term load forecasting. *Appl. Soft Comput.* **4**(4), 405–412 (2004)
15. Gross, G., Galiana, F.: Short-term load forecasting. *Proc. IEEE* **75**(12), 1558–1573 (1987)
16. Taylor, J.: Short-term load forecasting with exponentially weighted methods. *IEEE Trans. Power Syst.* **27**(1), 458–464 (2012)
17. Feinberg, E., Genethliou, D.: Load forecasting. *Applied mathematics for restructured electric power systems*. Springer US:269–285 (2005)
18. Viegas, J.L., Vieira, S.M., Melicio, R., Mendes, V.M.F., Sousa, J.M.C.: GA-ANN short-term electricity load forecasting. In: Camarinha-Matos, L.M., Falcão, A.J., Vafaei, N., Najdi, S. (eds.) 7th IFIP AICT, Technological Innovation for Cyber-Physical Systems, vol. 470, pp. 485–493. Springer (2016)
19. Saini, L., Soni, M.: Artificial neural network based peak load forecasting using Levenberg-Marquardt and quasi-Newton methods. *IEE Proc.-Gener. Transm. Distrib.* **149**(5), 578–584 (2002)
20. Holderbaum, W., Canart, R., Borne, P.: Artificial neural networks application to boolean input systems control. *Stud. Inf. Control* **8**, 107–120 (1999)
21. Zebulum, R.S., Vellasco, M., Guedes, K., Pacheco, M.A.: Short-term load forecasting using neural nets. In: *Natural to Artificial Neural Computation*, pp. 1001–1008 (1995)
22. Luenberger, D.G., Ye, Y.: *Linear and nonlinear programming*. Springer, Stanford, USA (2008)
23. Lasdon, L.S., Waren, A.D., Jain, A., Ratner, M.: Design and testing of a generalized reduced gradient code for nonlinear programming. *ACM Trans. Math. Softw.* **4**(1), 34–50 (1978)

Renewable Energy System for an Isolated Sustainable Social Centre

J.G. Pinto, Fábio Fernandes, Bruno Exposto, Vitor Monteiro
and João L. Afonso

Abstract This paper describes the development of the power converters and control algorithms to implement an isolated microgrid based in renewable energy sources used to feed a Sustainable Social Centre in a remote place. The microgrid is designed to work with photovoltaic panels, micro-wind and micro-hydro turbines, or even with diesel generators. The control system of the power converters is totally digital and implemented by means of a TMS320f28335 Digital Signal Controller (DSC) from Texas Instruments. One of the most important requirements imposed for the microgrid power system is the capability of providing a sinusoidal supply voltage with low harmonic distortion even in the presence of non-linear electrical loads. The hardware topologies and the digital control systems of the power converters are evaluated through experimental results obtained with a developed laboratory prototype. This work is focused in the DC-AC converter of the renewable energy system for the isolated Sustainable Centre.

Keywords Renewable energy · Microgrid · Power electronics converters · Digital control

J.G. Pinto (✉) · F. Fernandes · B. Exposto · V. Monteiro · J.L. Afonso
Centro Algoritmi, University of Minho, Guimarães, Portugal
e-mail: gabriel.pinto@algoritmi.uminho.pt

F. Fernandes
e-mail: fabio.fernandes@algoritmi.uminho.pt

B. Exposto
e-mail: bruno.exposto@algoritmi.uminho.pt

V. Monteiro
e-mail: vitor.monteiro@algoritmi.uminho.pt

J.L. Afonso
e-mail: joao.l.afonso@algoritmi.uminho.pt

1 Introduction

The present energy challenges that the world faces are forcing the shift to a new energy paradigm and the search of new energy sources. The problems associated with greenhouse gas emissions resulting from the use of fossil fuels, and the nuclear power safety issues, as well as the increased energy demand, are the main drivers to expand the use of renewable energy sources. If during several years the renewable energy sources were not intensively explored to the production of electrical energy (except hydroelectric energy), today's energy challenges are forcing the diversification of renewable energy sources. Wind and solar photovoltaics are the most promising renewable energy sources, considering that the costs of the wind and photovoltaic systems are lowering consistently each year [1]. Also the energy access problems, particularly in small, isolated and standalone communities, where the access to renewable energy sources may be the only solution to meet their energy needs, is contributing to the expansion of the use of renewable energy sources [2]. In fact a large share of the world's population still has no access to electrical energy, depending only on traditional energy sources, such as wood, kerosene and candles to provide heat and lighting [3]. Considering that, remote and small communities with low economical index are not attractive to energy investments [2], one way to take electricity to these people homes is the development of stand-alone grids. Besides, the cost of creating a stand-alone grid can be lower than connecting the remote location to the electrical power grid [4]. Stand-alone micro-grids are isolated from any external network, which means that every load requirement must be sustained by the local available energy sources. The main advantages of this approach are the inexistence of costs associated with the long distance of the connection with the main grid, the local production enabling, the reduction of losses by placing the generation near the demand, and the social improvement resulting from the energy supply to isolated communities [5, 6].

This paper describes the development of the power electronics converters to create an islanded microgrid based in renewable energy sources. The main objective is to develop a flexible solution to provide energy to the electrical loads of a Sustainable Social Centre, or medical assistance point, or even a school in remote villages of economically emerging regions. The system integrates several distributed power generating units to produce electrical energy, creating an islanded single-phase microgrid with conventional and stable characteristics: 230 V, 50 Hz. This includes the production of electrical energy from renewable sources and from a motor-generator set (biodiesel), an energy storage system, and an electrical system with linear and non-linear loads. This paper presents the power converter topology and the control architecture of the proposed solution. Then are presented experimental results, and is done an analysis of the performance of the developed prototype. Finally are drawn several conclusions.

2 Architecture of the Power Converters

The energy provided by renewable sources is very dependent on the climate conditions, and as such, the production is intermittent and is difficult to reliably predict the production capability even for a near future. Considering this, a power system based in this kind of energy sources needs to be supported by energy storage elements. For an islanded power system with a nominal power lower than 10 kW, in terms of storage elements, electrochemical batteries can be a compromising solution in terms of usability, storage capacity, initial and operating costs [7].

In order to ensure the energy conversion, necessary in the various stages of the system, power electronics converters are the best solution. In Fig. 1. is presented a block diagram of the proposed renewable energy system for the isolated Sustainable Centre.

The system was designed to work with 48 V in the DC-link and with a load voltage of 230 V/50 Hz. There are several publications in literature about DC-DC converters and Maximum Power Point Tracker (MPPT) algorithms for solar photovoltaic systems [8] and micro-wind turbine systems [9]. In this case was implemented a Perturbation and Observation algorithm for the wind turbine system, and an Incremental Conductance algorithm for the photovoltaic panels. These algorithms ensure that the microgrid receives all the energy generated by the renewable energy sources.

This paper is more focused in the DC-AC converter of the renewable energy system for the isolated Sustainable Centre. It is important to explain that the DC-AC converter can be implemented by a single-stage [10] or by a multistage converter topology [11–13]. In order to accommodate the large difference between the voltage level in the DC-link and the voltage level required to produce the output sinewave voltage without compromising the converter efficiency, the adoption of a converter topology with isolating transformer is a good solution.

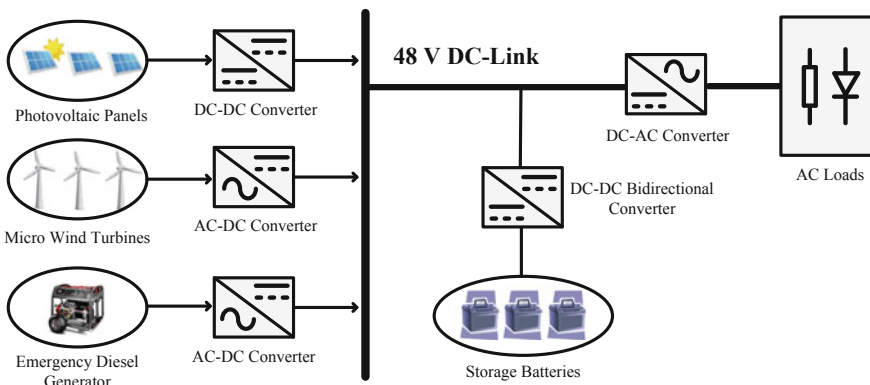


Fig. 1 Block diagram of the renewable energy system for the isolated sustainable centre

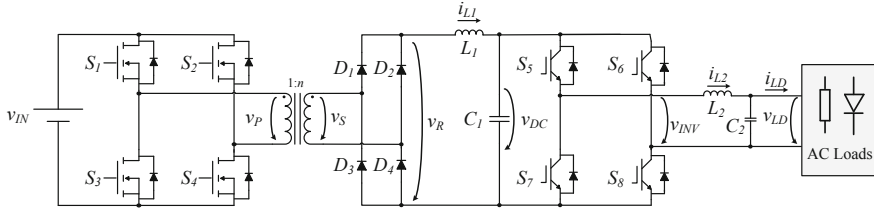


Fig. 2 Multistage DC-AC converter with isolating transformer

The topology selected for the DC-AC converter is based in a multistage converter composed by a full-bridge isolated DC-DC converter followed by a full-bridge DC-AC converter. The topology of the multistage DC-AC converter with isolating transformer is presented in Fig. 2.

2.1 Full-Bridge Isolated DC-DC Converter

The full-bridge isolated DC-DC converter is composed by an active full-bridge in the primary side of the isolation transformer ($S_1 - S_4$), a full-bridge diode rectifier in the secondary side of the isolating transformer ($D_1 - D_4$) and a LC output filter (L_1 and C_1). The objective of this converter is to produce a constant voltage around 400 V from the 48 V DC-link. To accomplish with these requirements was selected a transformer with a ratio of 1:13.

Considering that the active full-bridge in the primary side of the isolating transformer is connected to the DC-link, and that the maximum voltage in these power switches is 48 V, power MOSFETs are the more proficient technology for this part of the converter [14]. The active full-bridge is used to produce a high frequency (40 kHz) square wave to be applied to the primary winding of the isolating transformer. The voltage in the secondary winding of the transformer (v_S), will present the same shape as the primary one (v_P), but with amplitude thirteen times higher as consequence of the relation in the winding turns number. The voltage of secondary winding of the transformer is rectified by the diode full-bridge, resulting in a positive square wave (v_R) with a fixed frequency (double the switching frequency of the active bridge). The LC filter is used to remove the high-frequency component, resulting in a constant output voltage. The constant output voltage presents amplitude equal to the mean value of the square wave at the input of the LC filter (v_R), and so, it is possible to control the value of the output voltage by adjusting the duty-cycle of the square wave. Table 1 presents the circuit parameters of the full-bridge isolated DC-DC converter.

Table 1 Circuit parameters of the full-bridge isolated DC-DC converter

Parameter	Description	Value
$S_1 - S_4$	Power MOSFETs	IXFQ50N50P3
$D_1 - D_4$	Ultrafast recovery diode	STTH3012
L_1	Iron powder core inductor	3 mH
$C1$	Electrolytic capacitor	3.4 mF
$N_1:N_2$	Ferrite core transformer	1:13
f_s	Sampling frequency	40 kHz
f_{sw}	Switching frequency	40 kHz

Table 2 Circuit parameters of the full-bridge DC-AC converter

Parameter	Description	Value
$S_5 - S_8$	Power IGBTs	FGA25N120
L_1	Ferrite core inductor	50 μ H
$C2$	Film capacitor	20 μ F
f_s	Sampling frequency	40 kHz
f_{sw}	Switching frequency	40 kHz

2.2 Full-Bridge DC-AC Converter

The full-bridge DC-AC converter is composed by an active full-bridge ($S_5 - S_8$) and a LC output filter (L_2 and C_2). The objective of this converter is to produce a 50 Hz sinewave voltage with amplitude of 325 V from the 400 V DC voltage provided by the previous converter. As the active full-bridge is connected to the 400 V DC-Link, this part of the converter is composed by IGBTs technology [14].

In order to produce a sinewave from a DC voltage it is used a bipolar Sinusoidal PWM (SPWM) technique with a switching frequency of 40 kHz. By controlling the duty-cycle applied to the IGBTs it is possible to adjust the mean value of the voltage produced by the converter. The LC output filter extracts the high frequency components of the voltage produced by the converter to obtain a sinusoidal voltage at the output (v_{LD}). The circuit parameters of the full-bridge DC-AC converter are presented in Table 2.

3 Control Algorithms Architecture

Modern power electronics controllers are implemented totally digital by means of microcontrollers units (MCUs), digital signal processors (DSP) or field programmable gate arrays (FPGAs). The main advantages of digital controllers over analog controllers are the flexibility, and the robustness against aging in the components and influence of environmental degradation.

The control system of the DC-AC converter was implemented in the digital platform Texas Instruments TMS320F28335. It was also implemented a signal conditioning circuit that receives the measured signals from Hall-effect current and voltage sensors, and adjust these signals to the range of values of the DSP ADCs. The implemented switching technique was a Pulse-Width Modulation (PWM). The determination of the conduction time for each semiconductor of the power converter is done by the controller circuit.

3.1 Control of the Full-Bridge Isolated DC-DC Converter

The objective of the full-bridge isolated DC-DC converter is to produce a constant DC voltage of 400 V from the 48 V DC-link. The controller of this converter needs to maintain the output voltage at the reference value independently of number of electrical loads connected in the Sustainable Social Centre. It is important to explain that more electrical loads connected consume more energy, and so the full-bridge isolated DC-DC converter needs to transfer more energy from the DC-link to the output, maintaining the voltage in the reference value. Other important aspect is the fact that electrical loads are connected and disconnected randomly and the control algorithm needs to respond adequately to these perturbations. Although these previous constraints, the DC-AC converter has a large capacitor in the DC side that works as a short term energy storage device, facilitating the converter controller design. In fact, it is allowed that the output voltage slightly oscillates around the 400 V value without compromising the entire system performance.

To accomplish with these requirements, the full-bridge isolated DC-DC converter uses a Proportional Integral (PI) controller to eliminate the error between the output voltage (v_{DC}) and the reference (v_{DC}^*). The output of the PI controller is used to adjust the duty-cycle of the power MOSFETs by means of bipolar PWM switching technique. The block diagram of the full-bridge DC-DC controller is presented in Fig. 3.

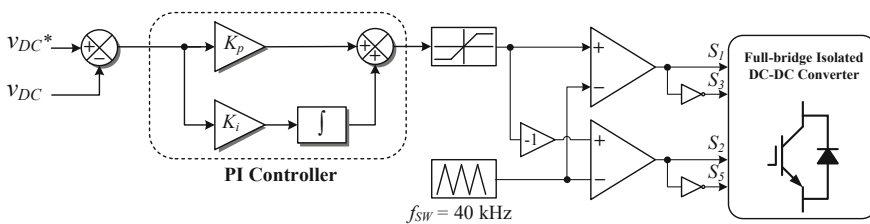


Fig. 3 Block diagram of the full-bridge isolated DC-DC controller

3.2 Control of the Full-Bridge DC-AC Converter

The objective of the full-bridge DC-AC converter is to produce a 50 Hz sinewave voltage with amplitude of 325 V from the 400 V DC voltage provided by the previous converter. To ensure that all electrical loads operate properly, it is necessary to ensure a good quality waveform in any operating condition.

To produce a sinusoidal voltage is relatively simple in the presence of linear loads that consume sinusoidal currents. However, in the presence of non-linear loads, that consume distorted currents, the quality of the produced waveform can be easily degraded if the controller is not fast enough to compensate the voltage deformations. This problem is more pronounced in the presence of loads with high di/dt or during transients caused by connection or disconnection of loads.

Most of the modern electrical loads that can be connected in the Sustainable Social Centre, like computers, TV sets, radio-sets, led-lamps, cell-phone chargers, and other communication equipment, are known to present a very non-linear voltage current characteristic. This type of equipment drains currents with very high Total Harmonic Distortions (THD), thus requiring a voltage controller with good performance for the DC-AC converter. To accomplish with this task in this work, it is used a predictive deadbeat controller based in [15].

In accordance with Fig. 2 the space state equations of the full-bridge DC-AC converter with LC output filter can be expressed as in (1).

$$\begin{bmatrix} \frac{di_{L2}}{dt} \\ \frac{dv_{LD}}{dt} \end{bmatrix} = \begin{bmatrix} 0 & \frac{-1}{L_2} \\ \frac{1}{C_2} & 0 \end{bmatrix} \begin{bmatrix} i_{L2} \\ v_{LD} \end{bmatrix} + \begin{bmatrix} \frac{1}{L_2} \\ 0 \end{bmatrix} v_{INV} + \begin{bmatrix} 0 \\ \frac{-1}{C_2} \end{bmatrix} i_{LD} \quad (1)$$

Equation (1) shows that the load current (i_{LD}) acts as a disturbance in the output voltage (v_{LD}) and the output voltage as disturbance in the inductance current (i_{L2}) [15]. Considering a given sampling period T_S , the state equations can be re-written as:

$$x[n+1] = \phi(T_S)x[n] + \Gamma(T_S)v_{LD}[n] + \Delta(T_S)[n], \quad (2)$$

where:

$$\phi(T_S) = \begin{bmatrix} \cos(\omega T_S) & \frac{-1}{\omega L_2} \sin(\omega T_S) \\ \frac{1}{\omega C_2} \sin(\omega T_S) & \cos(\omega T_S) \end{bmatrix} = \begin{bmatrix} \phi_{11} & \phi_{12} \\ \phi_{21} & \phi_{22} \end{bmatrix}, \quad (3)$$

$$\Gamma(T_S) = \begin{bmatrix} \frac{1}{\omega L_2} \sin(\omega T_S) \\ 2 \sin^2(\frac{\omega T_S}{2}) \end{bmatrix} = \begin{bmatrix} \gamma_1 \\ \gamma_2 \end{bmatrix}, \quad (4)$$

$$\Delta(T_S) = \begin{bmatrix} 2 \sin^2(\frac{\omega T_S}{2}) \\ \frac{-1}{\omega C_2} \sin(\omega T_S) \end{bmatrix} = \begin{bmatrix} \delta_1 \\ \delta_2 \end{bmatrix}. \quad (5)$$

The resonance frequency of the LC filter is:

$$\omega = \frac{1}{\sqrt{L_2 C_2}}. \quad (6)$$

It must be referred that:

$$x[n] = \begin{bmatrix} i_{L2}[n] \\ v_{LD}[n] \end{bmatrix}. \quad (7)$$

As said before, the load voltage (v_{LD}) acts as a disturbance in the inductor current (i_{L2}) and the load current (i_{LD}) acts as a disturbance in the output voltage (v_{LD}) so, to improve the load voltage controller performance, it is possible to add the values of the disturbances to the voltage controller and current controller. This improves the controller response and its robustness. These values are calculated as shown in (8) and (9).

$$v_{dist}[n] = -\frac{\gamma_2}{\phi_{21}} v_{INV}[n] - \frac{\delta_2}{\phi_{21}} i_{LD}[n] \quad (8)$$

$$i_{dist}[n] = -\frac{\phi_{12}}{\gamma_1} v_{LD}[n] - \frac{\delta_1}{\gamma_1} i_{LD}[n] \quad (9)$$

To increase the performance of the controller it is also possible to add two feed-forward components (10) and (11) to the control loop, that incorporate $v_{LD}^*[n]$, $v_{LD}^*[n+1]$, $v_{LD}^*[n+2]$ and the estimated values of $\hat{\phi}(T_S)$ and $\hat{\gamma}(T_S)$. It must be referred that v_{LD}^* consists in a sinusoidal waveform previously stored in a look up table with 800 positions, so the $n+1$ and $n+2$ samples can be easily accessed. The values of $\hat{\phi}(T_S)$ and $\hat{\gamma}(T_S)$ can also be estimated considering the values of ωT_S for the $n+1$ sample:

$$FF_1[n] = \frac{v_{LD}^*[n+1] - \hat{\phi}_{22} v_{LD}^*[n]}{\hat{\phi}_{21}}, \quad (10)$$

$$FF_2[n] = \frac{v_{LD}^*[n+2] - 2\hat{\phi}_{11} v_{LD}^*[n+1] + \hat{\phi}_{11} v_{LD}^*[n]}{\hat{\phi}_{21} \hat{\gamma}_1}. \quad (11)$$

Finally, the current and voltage errors are multiplied by two gains, G_i and G_v , respectively, which can be calculated as:

$$G_i = \frac{2\phi_{11}}{\gamma_1} = \frac{2\omega L \cos(\omega T_S)}{\sin(\omega T_S)}, \quad (12)$$

$$G_v = \frac{\phi_{11}}{2\phi_{21}} = \frac{\omega C \cos(\omega T_S)}{2 \sin(\omega T_S)}. \quad (13)$$

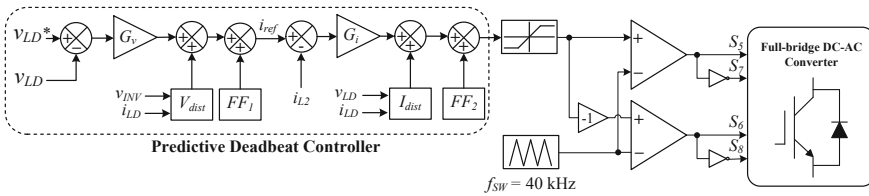


Fig. 4 Block diagram of the predictive deadbeat controller

To obtain the power converter switching signals, the output value of the controller is passed through a limiter, and after that, the output value is compared with a triangular carrier with a frequency of 40 kHz. In Fig. 4 it can be seen the block diagram of the control architecture for the full-bridge DC-AC converter.

4 Experimental Validation

To assess the behavior of the predictive deadbeat controller was developed a laboratory prototype (Fig. 5) of the converter shown in Fig. 2. This converter, controlled by predictive deadbeat controller, was tested using a non-linear load constituted by a single-phase full-bridge rectifier with a RC load placed in the DC side.

In Fig. 6. it is possible to see the experimental results obtained with the aforementioned load. This figure shows that although that the load presents a highly distorted current (i_{LD}), with a THD of 107 % (Fig. 6c), the voltage produced by the

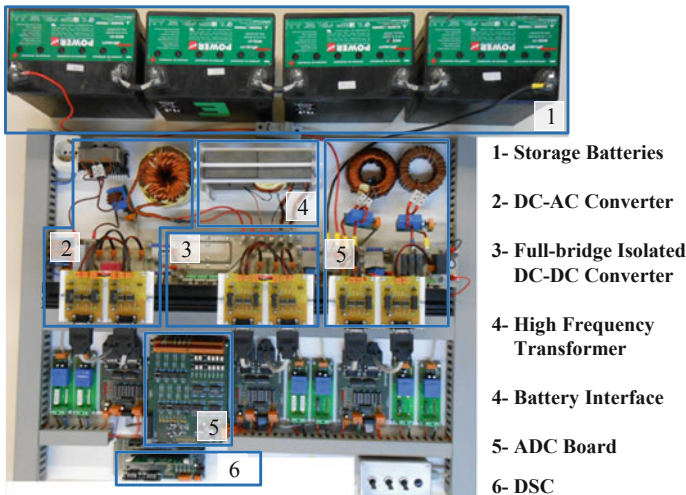


Fig. 5 Developed laboratory prototype of the multistage DC-AC converter

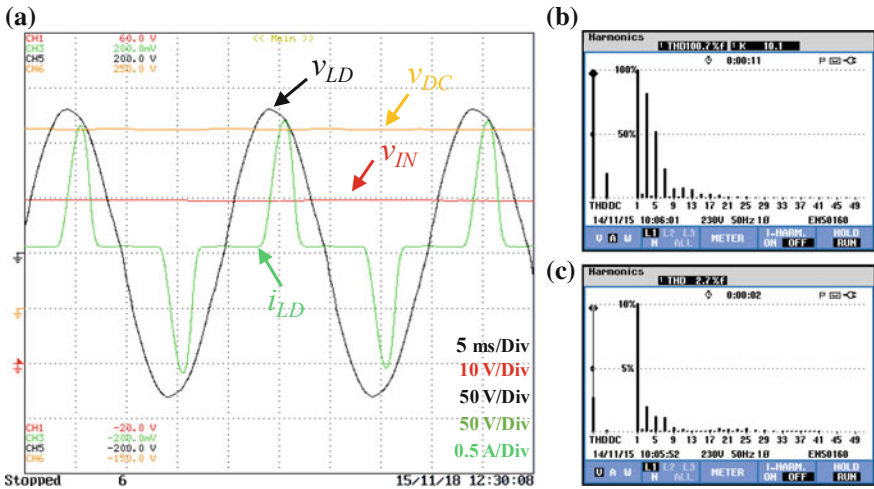


Fig. 6 Experimental results of the DC-AC converter operating in steady state with a non-linear load: **a** input voltage (v_{IN}), DC voltage (v_{DC}), output voltage (v_{LD}) and load current (i_{LD}); **b** Harmonics and THD of output voltage; **c** Harmonics and THD of load current

DC-AC converter (v_{LD}) is nearly sinusoidal. This is confirmed by the harmonic spectrum shown in Fig. 6b that shows a THD of 2.7 %. This value is perfectly acceptable for most loads, and is in accordance with standard EN 50160. Also, it is important to highlight that the voltage waveform does not present any sign of resonance motivated by the passive filter.

5 Conclusions

In this paper was presented the development of power electronics converters to create an islanded microgrid, based in renewable energy sources, to feed the electrical loads of an isolated Sustainable Social Centre. This system integrates several power converters, in order to convert the energy from the renewable energy sources like photovoltaic panels, micro-wind and micro-hydro turbines, to be stored in a battery pack, which translates in added flexibility. The conversion between the DC-link bus and the loads is performed using a multistage DC-AC converter which is controlled by a PI and a predictive deadbeat controller. The topology and the control algorithms of the presented DC-AC converter were validated through experimental tests. These tests show that the implemented control shows a good performance even in the presence of non-linear loads, which consume a current with high level of distortion. This type of current usually causes distortion in the output voltage that is difficult to be compensated by the control algorithms. With the developed system was achieved a voltage with a THD value lower than 3 % even with a load current with a value of THD greater than 100 %.

Acknowledgments This work has been supported by COMPETE: POCI-01-0145-FEDER-007043 and FCT—Fundação para a Ciência e Tecnologia within the Project Scope: UID/CEC/00319/2013. Bruno Exposto is supported by the doctoral scholarship SFRH/BD/87999/2012 granted by FCT.

References

1. Yang, X., Song, Y., Wang, G., Wang, W.: A comprehensive review on the development of sustainable energy strategy and implementation in China. *Sustain. Energ. IEEE Trans.* **1**, 57–65 (2010)
2. Ma, T., Yang, H., Lu, L.: Study on stand-alone power supply options for an isolated community. *Int. J. Electr. Power Energ. Syst.* **65**, 1–11 (2015)
3. Ghosh Banerjee, S., Bhatia, M., Portale, E., Soni, R., Angelou, N.: Energy access challenge: strategies from the world bank group [In My View]. In: *Power and Energy Magazine*, IEEE, vol. 12, pp. 96–94 (2014)
4. Parhizi, S., Lotfi, H., Khodaei, A., Bahramirad, S.: State of the art in research on microgrids: a review. *Access, IEEE.* **3**, 890–925 (2015)
5. Rocabert, J., Luna, A., Blaabjerg, F., Rodríguez, P.: Control of power converters in AC microgrids. *Power Electron. IEEE Trans.* **27**, 4734–4749 (2012)
6. Ton, D.T., Smith, M.A.: The US department of energy’s microgrid initiative. *Electr. J.* **25**, 84–94 (2012)
7. Duryea, S., Islam, S., Lawrance, W.: A battery management system for stand alone photovoltaic energy systems. In: *Industry Applications Conference, 1999. Thirty-Fourth IAS Annual Meeting. Conference Record of the 1999 IEEE*, pp. 2649–2654 (1999)
8. Subudhi, B., Pradhan, R.: A comparative study on maximum power point tracking techniques for photovoltaic power systems. *Sustain. Energ. IEEE Trans.* **4**, 89–98 (2013)
9. Liu, C., Chau, K., Zhang, X.: An efficient wind-photovoltaic hybrid generation system using doubly excited permanent-magnet brushless machine. *Ind. Electron. IEEE Trans.* **57**, 831–839 (2010)
10. Attanasio, R., Cacciato, M., Gennaro, F., Scarcella, G.: Review on single-phase PV inverters for grid-connected applications. In: *4th IASME/WSEAS International Conference on Energy, Environment, Ecosystems and Sustainable Development (EEESD’08)*, Algarve, Portugal (2008)
11. Teodorescu, R., Rodriguez, P., Liserre, M.: Power electronics for PV power systems integration. In: *2010 IEEE International Symposium on Industrial Electronics (ISIE)*, pp. 4532–4614 (2010)
12. Blaabjerg, F., Teodorescu, R., Chen, Z., Liserre, M.: Power converters and control of renewable energy systems. *ICPE (ISPE) 2–20* (2004)
13. Kouro, S., Leon, J.I., Vinnikov, D., Franquelo, L.G.: Grid-connected photovoltaic systems: an overview of recent research and emerging PV converter technology. *Ind. Electron. Mag IEEE.* **9**, 47–61 (2015)
14. Blake, C., Bull, C.: IGBT or MOSFET: choose wisely. *International Rectifier*. (2001)
15. Mihalache, L.: DSP control method of single-phase inverters for UPS applications. In: *Applied Power Electronics Conference and Exposition, APEC 2002 Seventeenth Annual IEEE*, pp. 590–596 (2002)

Evaluation of the Introduction of Electric Vehicles in the Power Grid—A Study for the Island of Maio in Cape Verde

Vitor Monteiro, M.J. Sepúlveda, J.C. Aparício Fernandes, J.G. Pinto and João L. Afonso

Abstract This paper presents an evaluation of the introduction of electric vehicles (EVs) in an electrical power grid. The main contribution is the control analysis of the power quality considering simultaneous battery charging processes. The methodology used can be applied to any known power grid; however, it was considered the case of the island of Maio, in Cape Verde, in continuation of previous works concerning that power grid. Two commercial different types of battery chargers were considered: a traditional model with highly distorted current consumption (that causes distortion in the power grid voltage), and another with almost sinusoidal current consumption. Considering simultaneous battery charging processes, it can be concluded that the power grid structure (composed by three medium voltage branches) with the current power demands of the consumers of the island of Maio have a potential integration for 300 EVs if battery chargers with almost sinusoidal current consumption are used, i.e., 152 for the first medium voltage branch, 35 for the second branch, and 113 for the third branch. Moreover, the results show that the first medium voltage branch of the distribution system, which has the capability to support the integration of 152 EVs if the battery chargers have sinusoidal current consumption (presenting a maximum value of THD_v % in the power grid voltage of 1.8 %), only can support 27 EVs if are used traditional battery chargers, with highly distorted current consumption (considering a maximum THD_v % of 5 %).

V. Monteiro (✉) · M.J. Sepúlveda · J.C. Aparício Fernandes · J.G. Pinto · J.L. Afonso
Centro Algoritmi, University of Minho, Guimarães, Portugal
e-mail: vitor.monteiro@algoritmi.uminho.pt; vmonteiro@dei.uminho.pt

M.J. Sepúlveda
e-mail: sepulveda.freitas@algoritmi.uminho.pt

J.C. Aparício Fernandes
e-mail: aparicio.fernandes@algoritmi.uminho.pt

J.G. Pinto
e-mail: gabriel.pinto@algoritmi.uminho.pt

J.L. Afonso
e-mail: joao.l.afonso@algoritmi.uminho.pt

Keywords Cape verde • Electric vehicle • Harmonic distortion • Power quality

1 Introduction

The vehicles with internal combustion engines (ICE) in use in the transportation systems are responsible for a large amount of CO₂ emissions, and this is a major concern. Also it is estimated that 55 % of the total oil consumption in the world in 2030 will be in the transportation sector [1]. It is envisaged the use of electric motors in order to diminish not only the output of greenhouse gases such as the CO₂ but also to minimize both the fuel and the lubricant oil consumptions that ICE imposes. Although the avoidance of CO₂ exhaust is not fully avoided in the general picture, because electric power needs to be generated and in most cases ICE systems are employed, it can be a much lower emission situation by burning fossil fuels at a more efficient power plant (and at a larger distance from the intense human occupation cities where transportation is needed). Also a more efficient power usage in the traction is possible using electric instead of ICE. The actual practical motoring solutions are the electric vehicles (EV) and plug-in hybrid electric vehicles (PHEV). Hydrogen based systems and others have not been shown, at least not yet, viable economic proposals. Some of these alternatives are already available in the market such as Nissan Leaf (EV) or Toyota Prius (PHEV). These vehicles allow performing the battery charging from a standard outlet (public or private). In this case the energy flows from the power grid to the batteries. This method is denominated grid-to-vehicle (G2V). However, from the moment that the vehicle is plugged into the power grid, theoretically, the energy may flow in bidirectional way (vehicle-to-grid, V2G). The V2G operation may be a key technology in the future smart grids [2, 3]. Focusing the smart grids, in [4] is analyzed the upcoming power grid considering the introduction of EVs and PHEVs. In this scenario, in [5] the advances of a concrete project to integrate EVs into smart grids are presented. In this project is also analyzed the possible integration of renewable energies as a contribution to the EV battery charging process. In this context, EVs can play an important role to smoothing the natural intermittency of the renewable energies through the operation as energy storage system. Besides these contributions, the EVs can also be used to ensure the power grid stability in terms of voltage and frequency. Nevertheless, depending of the topology of the battery charger, the introduction of EVs can bring problems to the power grid, contributing to the degradation of the power quality [6]. In [7, 8] are presented studies that analyze the impact of the introduction of EVs at residential level. From these studies it may be concluded that the simultaneously battery charging process can cause power quality problems. Thereby, the actual power grids are facing new challenges, mainly taking into account the different energy storage systems [9], and their integration [10–13]. Considering the pros and cons of the EVs integration, in this paper is evaluated the impact of the EV battery charging process in the power

grid of the island of Maio in Cape Verde. This island is part of the leeward group of islands of Cape Verde archipelago and it has about 9000 inhabitants and an area of 269 km² (length of 31 km and width of 25 km). Although this study has been conducted to the island of Maio, the method used may also be employed in other known power grid. In this paper it is mainly analyzed the influence in the power grid voltage along the distribution grid. Two different types of EV battery chargers were considered: a traditional battery charger with high level of total harmonic distortion; and a battery charger with sinusoidal current consumption.

2 Power Grid of the Island of Maio in Cape Verde

In order to characterize and obtain reliable data related with the power grid in the island of Maio in Cape Verde, it was conducted an inquiry in the residential and industrial sectors. Thus, this section is divided in two parts: the power grid structure and the EV current consumption profile. The description of both parts is made in accordance with the data provided by ELECTRA SARL, which is a company that has as aim the production, transport and distribution of electricity across the territory of Cape Verde [14].

The distribution power grid in Cape Verde is divided in medium and low voltage. In medium voltage (MV) the nominal voltage is 20 kV, and in low voltage (LV) the nominal voltage is 220 V (phase–neutral). According to the inquiry, 19 % of the industrial sector is connected to the power grid in LV and 81 % in MV [15]. Another important fact that results from this inquiry in the industrial sector is that 30 % compensates reactive power, 61 % does not compensate, and 9 % does not have knowledge about it [15]. In 2010 starts the construction of a substation in the Santiago island in order to distribute energy in high voltage (HV) 60 kV, and aiming to integrate some isolated grids. From the inquiry, both to the residential and industrial sectors, it was concluded that 18 % classifies as good the energy distribution system, 30 % classifies as bad, and 52 % classifies as acceptable [15]. Related with the energy production, in Table 1 are presented the values of the energy production (MWh) according to the different types of generation, from 2006 to 2010. In Cape Verde the energy production is essential based on synchronous generators. This table shows that the diesel production has increased, meaning that the greenhouse effect gases also have increased. However, taking into account the geographic and climatic location of Cape Verde, it has a large potential to the renewable energy introduction, mainly photovoltaic and wind. In this context, from 2010 starts the photovoltaic production [15]. Besides the aforementioned inquiry, the power grid voltage was monitored in the residential (private) and industrial sector (SITA—Sociedade Industrial de Tintas, SA), aiming to register their variations along 5 and 14 days, respectively. For such purpose it was used the equipment VLog Q from LEM, which allows to determine power quality parameters according to the NP EN 50160 standard. This equipment was programmed to register the parameters at each 5 min. The minimum registered value was 173.6 V, and the

Table 1 Energy production (MWh) in the archipelago off Cape Verde, from 2006 to 2010, according to the different types of energy generation

	2006	2007	2008	2009	2010
Type of generation	Energy production (MWh)				
Diesel	241 709	260 465	279 645	290 273	314 315
Solar photovoltaic	0	0	0	0	2105
Wind	7441	6869	5510	4661	1992
Steam	1772	1185	640	0	0

maximum 224.5 V. During this period three power outages were registered, which occurred in the same day, with 7 h 2 min and 14 s (first outage), 14 s (second outage), and 2 min and 6 s (third outage). The minimum registered value (in an industry along 14 days) was 178.3 V, and the maximum 249.5 V. In this case four power outages were registered, two during 20 s and two during 5 s. Besides the registration of the voltage RMS values variation, it was also registered the THD_v % of the power grid voltage. In the residence the THD_v % registered was 3.5 % and in the industry was 1.6 %.

2.1 Description of the Power Grid Structure

In this item is described the power grid structure. Figure 1 represents the single-line diagram of the medium voltage (MV) power grid. It is important to refer that just one of the transformers is used. The other transformer is installed, however, it is

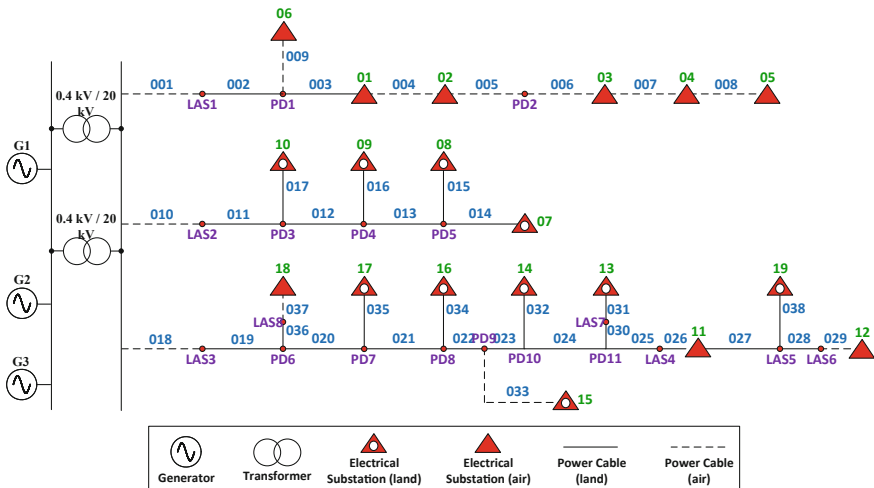


Fig. 1 Medium voltage single-line power grid diagram of the island of Maio in Cape Verde

Table 2 Nominal power and voltages (MV side) in each distribution transformer

Distribution transformer	Location	Power (kW)	Voltage (kV)	Distribution transformer	Location	Power (kW)	Voltage (kV)
DT01	Shell	80.3	19.97	DT11	Pedro Vaz	19.4	19.88
DT02	Cemiterio	16.6	19.96	DT12	Alcatraz/Pilão Cão	9.4	19.88
DT03	Estella Maris	8.2	19.96	DT13	Cascabulho	7.2	19.89
DT04	Farol	105.2	19.95	DT14	Morrinho	10.5	19.90
DT05	Fontona	55.4	19.95	DT15	Centro Zootecnico	8.3	19.90
DT06	Centro Formação	5.5	19.97	DT16	Calheta	36.0	19.91
DT07*	Ribeira Don João	–	–	DT17	Morro	8.9	19.95
DT08	Figueira Seca	5.5	19.98	DT18	Bela Vista	16.6	19.95
DT09	Figueira Horta	9.4	19.98	DT19*	Praia Gonçalo	–	19.88
DT10	Barreiro	10.5	19.99	*Out of operation			

only used as a substitute. Another important parameter that was included in this description is the line impedance. This parameter is extremely important to analyze the voltage distortion along the power grid (from the generation until the more distant distribution transformer). Due to the line impedance and the consumed current profile, the power grid voltage is more affected in the longest power lines, where this power quality problem can cause problems of malfunctioning in the connected loads. Table 2 shows the nominal power and voltages (MV side) in each distribution transformer and Table 3 shows the characteristics of each line of the island of Maio.

2.2 Description of the Different Battery Chargers

This section describes in detail the battery chargers that were considered in this paper. Taking into account that the main goal of this paper is analyze the potential impacts of the battery chargers on the power quality, two different types of battery chargers were considered. The first is a traditional unidirectional battery charger with highly distorted current consumption [16]. Figure 2a shows the grid current and Fig. 2b the spectral analysis and the THD_i %. The second is also a unidirectional battery charger, however with unitary power factor and sinusoidal current consumption. It was used the Renault Fluence EV as an example [17]. Figure 3a shows the grid current and Fig. 3b shows spectral analysis and the THD_i %.

Table 3 Characteristics of each line of the island of Maio

Line	Type	Conductor	Length (m)	Resistance (Ω)	Inductance (mH)	Capacitance (μ F)
001	Underground	Copper	100	0.0727	0.0399	0.0150
002	Aerial	ACSR	1000	0.9593	1.2319	
003	Underground	Copper	200	0.1454	0.0799	0.0300
004	Underground	Copper	551	0.2132	0.2093	0.0827
005	Underground	Aluminum	290	0.2384	0.1274	0.0522
006	Underground	Copper	250	0.1818	0.0999	0.0375
007	Underground	Copper	884	0.6427	0.3534	0.1326
008	Underground	Copper	550	0.3999	0.2199	0.0825
009	Underground	Copper	80	0.0582	0.0319	0.0139
010	Underground	Copper	100	0.0727	0.0399	0.0160
011	Aerial	ACSR	3580	3.4343	4.4101	
012	Aerial	ACSR	2850	2.7340	3.5108	
013	Aerial	ACSR	680	0.6523	0.8377	
014	Aerial	ACSR	2650	2.5421	3.2644	
015	Aerial	ACSR	120	0.1151	0.1478	
016	Aerial	ACSR	350	0.3358	0.4312	
017	Aerial	ACSR	250	0.2398	0.3079	
018	Underground	Copper	40	0.0291	0.0159	0.0060
019	Aerial	ACSR	4530	4.3456	5.5803	
020	Aerial	ACSR	500	0.4797	0.6159	
021	Aerial	ACSR	5640	5.4105	6.9477	
022	Aerial	ACSR	1900	1.8227	2.3405	
023	Aerial	ACSR	1560	1.4965	1.9217	
024	Aerial	ACSR	3480	2.1158	4.1318	
025	Aerial	ACSR	7499	4.5594	8.9035	
026	Underground	Copper	30	0.0116	0.0114	0.0048
027	Underground	Copper	35	0.0135	0.0133	0.0056
028	Aerial	ACSR	4500	4.3169	5.5434	
029	Underground	Copper	15	0.0058	0.0057	0.0024
030	Aerial	ACSR	332	0.2019	0.3942	
031	Underground	Aluminum	30	0.0039	0.0063	0.0054
032	Aerial	ACSR	300	0.2878	0.3696	
033	Underground	Aluminum	860	0.7069	0.3778	0.1548
034	Aerial	ACSR	350	0.3358	0.4312	
035	Aerial	ACSR	250	0.2398	0.3079	
036	Aerial	ACSR	1200	1.1512	1.4782	
037	Underground	Copper	20	0.0105	0.0139	0.0035
038	Aerial	ACSR	2024	1.2306	2.4031	

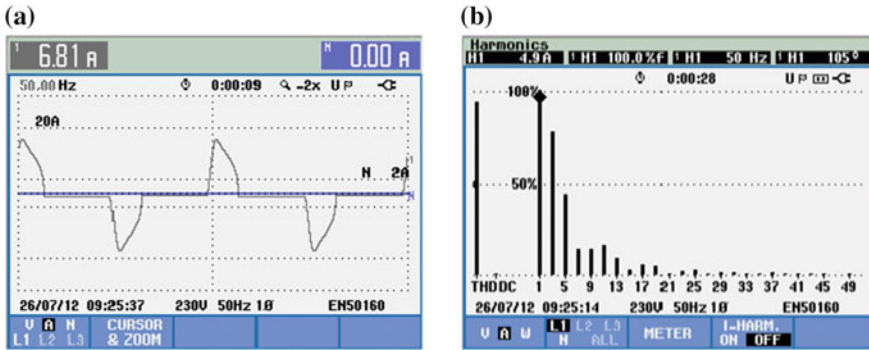


Fig. 2 Traditional unidirectional battery charger: a Power grid current; b Spectral analysis and THDi %

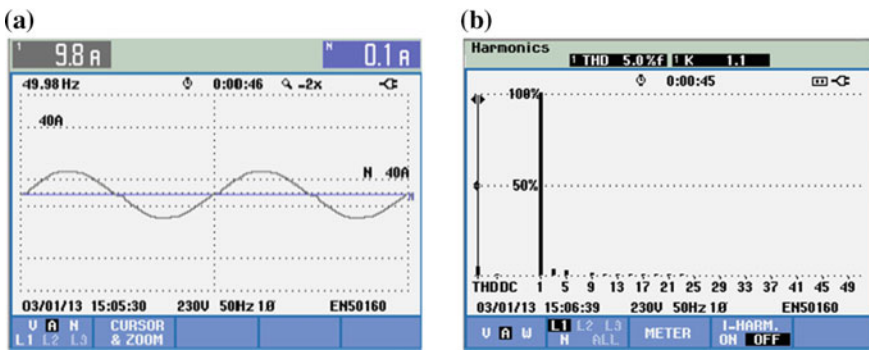


Fig. 3 Unidirectional battery charger with sinusoidal current consumption: a Power grid current; b Spectral analysis and THDi %

3 Simulation of the Power Grid Operation

In order to analyze the potential impacts of the EVs battery chargers in the power grid, mainly their impact in terms of power quality, several simulations using the simulation tool PSIM 9.1 were performed. The power grid structure (Sect. 2.1), and the introduction of different battery chargers (Sect. 2.2) were included in the simulation model. In the simulation model, the electrical appliances are composed by linear (resistances and inductances) and nonlinear loads (diode bridge rectifiers with output capacitive filter and resistive load). The EV battery charger are composed by two topologies: diode bridge rectifiers with output capacitive filter and resistive load (without sinusoidal current consumption); full-bridge full-controlled active rectifier (with sinusoidal current consumption). This item is divided in two parts: power grid without EVs; and power grid with EVs connected in coordinated and uncoordinated way. In the controlled way, the battery charging process occurs in accordance with

the power grid capabilities and also considering the EV driver benefits, like the schedules where the energy is cheaper. On the other hand, in the uncontrolled way, which is the most common charge procedure, each EV can be connected to the power grid neglecting the power grid capabilities. These processes are further presented in detail.

3.1 Power Grid Without EVs

Taking into account the aforementioned loads in this item are presented the power grid voltage and the consumed current considering the power grid without EVs. Figure 4a shows the obtained results of the power grid voltage (217.82 V) and the line current (122.90 A) in the distribution transformer DT01, which is the beginning of the line. In this case the lagging power factor is 0.88 and the voltage THD_v % and current THD_i % are 1.83 % and 12.14 %, respectively. On the other side, Fig. 4b shows the power grid voltage (218.15 V) and the line current (84.79 A) in the distribution transformer DT05, which is the end of the line. In this case the lagging power factor is 0.88 and the voltage THD_v % and current THD_i % is 1.78 % and 12.14 %, respectively. Considering that the distance between the Distribution Transformer DT01 and DT05 is about 3.8 km and the low power (i.e., it was simulated the power grid only with the loads) the THD_v % in both distribution transformers is almost equal. This situation occurs in all the power grid.

3.2 Power Grid with EVs

Considering the EVs integration in the power grid, the battery charging process can be performed in two different ways: coordinated or uncoordinated. The coordinated battery charging process is performed in accordance with the power grid capabilities in real time, and also taking into account the driver convenience. Thus, it must

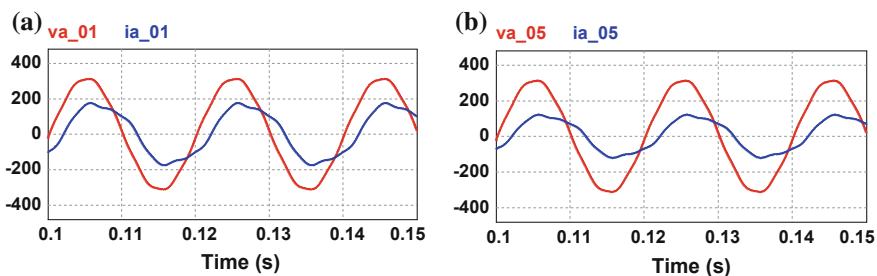


Fig. 4 Power grid voltage and consumed current considering the power grid without EVs in: **a** Distribution Transformer DT01; **b** Distribution Transformer DT05

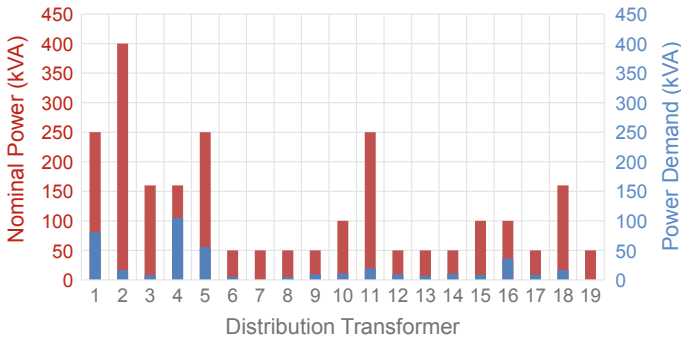


Fig. 5 Nominal power (kVA) and power demand (kVA) for each distribution transformer

be considered the period of the day, the energy price to sell or buy and the remaining energy stored in the batteries (state-of-charge). On the other hand, with the uncoordinated way, the battery charging process is performed immediately or after a fixed time delay. This is the most common charge procedure, however, it can strength a large peak of power demand from the power grid. Considering the maximum power of each distribution transformer and the power demand for the connected loads, it was analyzed the maximum number of EVs that can be introduced simultaneous in each one. Figure 5 shows the nominal power (kVA) and the power demand (kVA) for each distribution transformer. From Fig. 5 it can be concluded that only the distribution transformer DT04 is used more than half of the nominal power. On the other side, the distribution transformer DT02 is the least used in terms of nominal power. Taking into account the aforementioned battery chargers and that the maximum consumed current is 10 A (rms value), in Fig. 6 is shown the hypothetical maximum number of EVs that can be introduced in each distribution transformer. Globally, it can be introduced nearly 300 vehicles. The EVs were introduced in each distribution transformer through the three branches according to the hypothetical number of EVs. The introduction of the number of

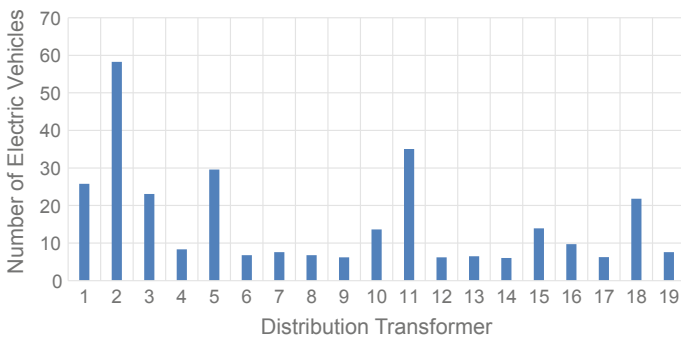


Fig. 6 Hypothetical number of EVs that can be introduced in each distribution transformer

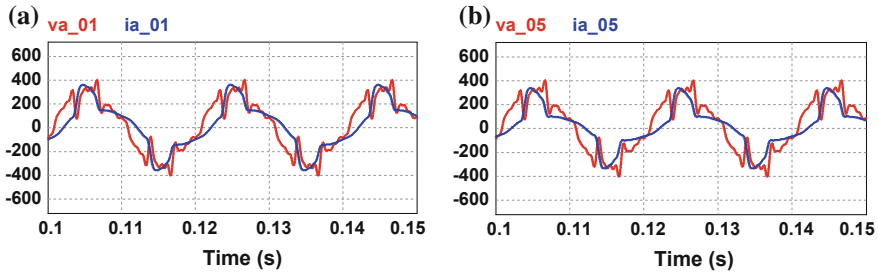


Fig. 7 Power grid voltage and current waveforms for the first branch considering the integration of 152 EVs without sinusoidal current consumption: **a** In the distribution transformer DT01; **b** In the distribution transformer DT05

EVs represented in Fig. 7 is the worst case. This situation was simulated in order to analyze the potential impacts of the two different battery chargers on the power quality. Figure 7 also shows the power grid voltage and the current waveforms but considering the integration of EVs without sinusoidal current consumption: (a) in the distribution transformer DT01; and (b) in the distribution transformer DT05. On the other hand, Fig. 8 shows the power grid voltage and the current waveforms considering the integration of EVs with sinusoidal current consumption: (a) in the distribution transformer DT01; and (b) in the distribution transformer DT05. The value of THD_v % obtained with the introduction of EVs with highly distorted current consumption (THD_v % ≈ 27 %) is much greater than the THD_v % with the introduction of EVs with sinusoidal current consumption (THD_v % ≈ 2 %). However, the value of THD_v % in the first case is very high and can cause malfunctioning in other equipment connected to the power grid. Thus, in order to obtain a maximum value of THD_v % = 5 % the maximum number of EVs with highly distorted current consumption that can be connected simultaneously, from the distribution transformer DT01 to the DT06, are 27. This value represents 18 % of the hypothetical number of EV (152) that can be introduced in the referred

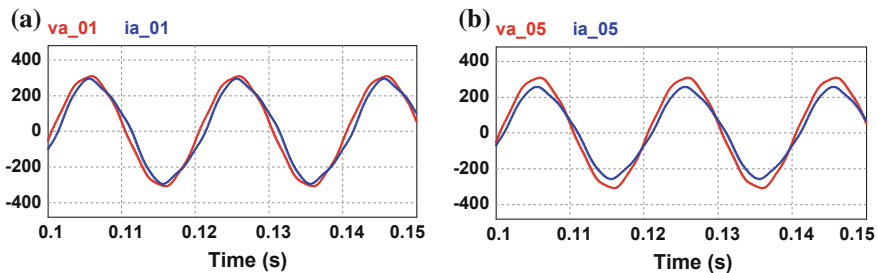


Fig. 8 Power grid voltage and current waveforms for the first branch considering the integration of 152 EVs with sinusoidal current consumption: **a** In the distribution transformer DT01; **b** In the distribution transformer DT05

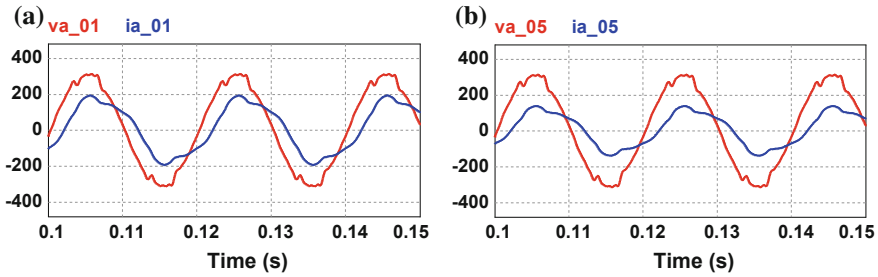


Fig. 9 Power grid voltage and current waveforms for the first branch considering the integration of 27 EVs without sinusoidal current consumption: **a** In the distribution transformer DT01; **b** In the distribution transformer DT05

distribution transformers. Clearly, these EVs can be distributed through these distribution transformers in several ways. Figure 9 shows the power grid voltage and the current waveforms: (a) in the distribution transformer DT01; and (b) in the distribution transformer DT05.

4 Conclusion

In this paper were presented studies to evaluate the impact of the introduction of electric vehicles (EVs) in the power grid of the island of Maio, in Cape Verde. It was assessed the impact derived from the utilization of two different types of battery chargers, with highly distorted current consumption and with almost sinusoidal current consumption. Considering the current power demand and the power grid structure composed by three medium voltage branches, a hypothetical number of 300 EVs (152 for the first branch, 35 for the second branch and 113 for the third branch) were able to perform the battery charging processes at the same time, if properly distributed in the power grid, and using battery chargers with almost sinusoidal current consumption. Considering only the first medium voltage branch, charging 152 EVs at the same time using battery chargers with sinusoidal current consumption results in a maximum value of THD_v % of only 1.8 %, while charging the same number of EVs at the same time using battery chargers with highly distorted current consumption results in a maximum value of THD_v % of 27.5 %, which is a totally unacceptable situation. Also for the first medium voltage branch, using battery chargers with highly distorted current consumption, and limiting the maximum value of THD_v -5 %, would result in the charging at the same time of a maximum of only 27 EVs (less than 1/5 of the number of EVs that could be charged using battery chargers with sinusoidal current consumption).

Acknowledgments This work has been supported by COMPETE: POCI-01-0145-FEDER-007043 and FCT—Fundação para a Ciência e Tecnologia within the Project Scope: UID/CEC/00319/2013. The PhD student Vítor Monteiro was supported by the doctoral scholarship SFRH/BD/80155/2011 granted by the FCT agency.

References

1. International Energy Outlook 2009: Energy Information Administration Office of Integrated Analysis and Forecasting U.S. Department of Energy. Washington DC (2009)
2. Monteiro, V., Pinto, J.G., Afonso, J.L.: operation modes for the electric vehicle in smart grids and smart homes: present and proposed modes. *IEEE Trans. Veh. Technol.* **65**(3), 1007–1020 (2016)
3. Han, S., Han, S., Sezaki, K.: Development of an optimal vehicle-to-grid aggregator for frequency regulation. *IEEE Trans. Smart Grid* **1**, 65–72 (2010)
4. Ipakchi, A., Albuyeh, F.: Grid of the future. In: *IEEE Power and Energy Magazine* (2009)
5. Hernandez, S.S., Galindo, P. P., Lopez, A.Q.: EPV PROJECT. Technology to integrate EV inside smart grids. In: *IEEE Conference on the European Energy Market* (2010)
6. Gomez, J.C., Morcos, M.M.: Impact of EV battery chargers on the power quality of distributed systems. *IEEE Trans. Power Deliv.* **18**(3), 975 (2003)
7. Lambert, F.: Secondary distribution impacts of residential electric vehicle charging. In: *California Energy Commission* (2000)
8. Morcos, M.M., Dillman, N.G., Mersman, C.R.: Battery chargers for electric vehicles. *IEEE Power Eng. Rev.* **20**(11), 8–11 (2002)
9. Khaligh, A., Zhihao, L.: Battery, ultracapacitor, fuel cell, and hybrid energy storage systems for electric, hybrid electric, fuel cell, and plug-in hybrid electric vehicles: state of the art. *IEEE Trans. Veh. Technol.* **59**, 2806–2814 (2010)
10. Monteiro, V., Gonçalves, H., Afonso, J.L.: Impact of electric vehicles on power quality in a smart grid context. In: *IEEE EPQU International Conference on Electrical Power Quality and Utilization*, Portugal (2011)
11. Joos, G., Dubois, M.R.: Integration of PHEVs and EVs experience from Canada. In: *IEEE PES Power and Energy Society General Meeting*, pp. 1–5 (2010)
12. Bertling, L., Carlson, O., Lundmark, S., Steen, D.: Integration of plug-in hybrid electric vehicles and electric vehicles—experience from Sweden. In: *IEEE PES Power and Energy Society General Meeting*, pp. 1–3 (2010)
13. Song, Y., Yang, X., Lu, Z., Integration of plug-in hybrid and electric vehicles experience from China. In: *IEEE PES Power and Energy Society General Meeting*, pp. 1–6 (2010)
14. Electra SARL, “Empresa”. <http://www.electra.cv/index.php/Empresa.html>. Accessed 21 Oct 2013
15. Samira dos Santos Andrade, “Qualidade de Energia Elétrica e Impacto das Energias Renováveis em Cabo Verde,” M.Sc. Dissertation, University of Minho, Portugal (2012)
16. Battery Charger, “Piktronik KOP1001,”. http://www.piktronik.com/index.php?option=com_content&view=article&id=33&Itemid=105&lang=en. Accessed 16 Oct 2013
17. Renault Fluence. <http://www.renault.pt/gama/veiculos-de-passageiros/fluence/novo-fluence/apresentacao/>. Accessed 16 Oct 2013

OpenADR—Intelligent Electrical Energy Consumption Towards Internet-of-Things

João Ferreira, Hugo Martins, Manuel Barata, Vítor Monteiro
and João L. Afonso

Abstract With the growing of irregular renewable energy sources, such as wind and solar, are required energy backup solutions to establish an advantageous compromise between the energy production and consumption. Typically, these renewable energy sources are not installed at the end-users level, which can create the problem of uncontrolled distributed energy sources. In this research work we propose a solution based on the standard OpenADR to handle this problem, creating a platform based on internet-of-things capable to turn-on or off electrical devices based on a central decision process that meets the requirements of energy producers and consumers. Producers can provide energy according to the consumer's requirements and take part of energy production and costs fluctuations. Based on an OpenADR standard for energy data exchange and a central cloud server, a list of services are provided to handle this transactions, with georeferenced information to minimize energy losses in the distribution process.

Keywords Openadr · Decision process · Smart grid · Distributed energy sources

J. Ferreira (✉) · V. Monteiro · J.L. Afonso
Centro ALGORITMI, University of Minho, 4800-058 Guimarães, Portugal
e-mail: jferreira@deetc.isel.ipl.pt

V. Monteiro
e-mail: vmonteiro@dei.uminho.pt

J.L. Afonso
e-mail: jla@dei.uminho.pt

J. Ferreira · H. Martins · M. Barata
ADEETC at ISEL, Lisbon, Portugal

J. Ferreira
ISCTE, Lisbon, Portugal

1 Introduction

Distribution Generation (DG) penetration into Distribution Network (DN) has been growing quickly due to the introduction of home production based on renewable energy sources. This DG raises concerns about the matching between production and consumption. Thus, it is in best awareness of all players involved to distribute them optimally (energy production and consumption) such that it will rise reliability, reduce system losses, and progress the voltage outline while serving the primary goal of demand supply [1]. System losses can also be reduced through capacitor banks to locally supply a portion of the reactive power [2, 3]. Most of literature is based on the assumptions that load is fixed and that the output of DG units is dispatchable and controllable [4]. These assumptions are inaccurate, because the uncertainties related to load and renewable based generation (wind and solar) are not considered. The available power from renewable based generation can ensure the restoration of some of customers affected in case of fault, improving overall system reliability. DN are normally meshed in design but operated radially. In on first step we transform this DN into a georeferenced graph in a process that we are able to calculate the distribution distance among several points in the distribution network. This approach allows us to decide based on a minimum losses process supplying loads at the minimum cost, growing system security and reliability and improving power quality [5]. Significant research concerning losses minimization in the field of network reconfiguration of distribution systems has been done [6–9]. DN reconfiguration and optimal power flow problems have been talked and studied separately by several studies performed in the literature, but they have hardly been studied at the same period applied with the same model and using in the calculation process a deterministic optimization and decomposition optimization technique [10]. This DN is transforming and evolving into a potentially more controllable grid than in the past, the so-called “Smart Grid” (SG) [11–13]. DN reliability in SG context is one of the major areas for DN design and operation. In this context and using the available standard openADR2.0 delivered by the OpenADR Alliance to create an open source Virtual End Node (VEN) client to retrieve Demand Request (DR) signals from a central point based on production availability. This approach allows to control remotely client equipment at users home to adjust real time production to consumption. Users define equipment that can work on this condition based on a defined profile, examples of these VENs are: electric vehicle, washing machines, heating systems, and air-condition. From this approach, two main benefits could be achieved. The first, in the client side, are defined the equipment that can reply to signals from the energy provider to minimize their energy consumption at periods of the power grid is low demand, or even to change some of their power consumption to periods where energy is commercialized at a lower cost. This appliances will also be able to react to signals from your energy provider to escape using energy during times of peak demand. Users can benefit from lower prices, using this approach. The second, in the production side, adjustment of production offer without big investments to store production excess.

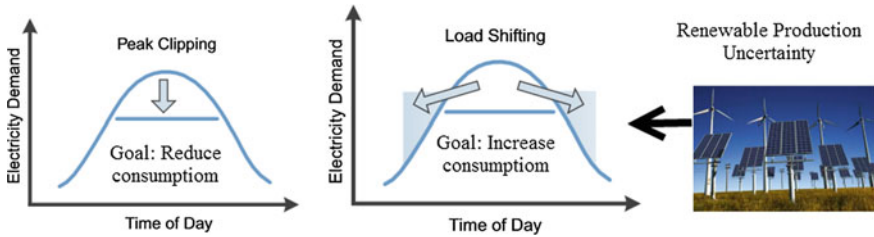


Fig. 1 Comparison between peak clipping and load shifting considering the intermittent energy production from renewable sources

DR program aims to reduce the peak hour consumption and the shift demand to off-peak hours, through the two-way IP communication stream between suppliers and consumers (offer vs demand), the grids can also adapt faster to allow the penetration of renewable energy sources and inspire users' participation in energy savings and collaboration through the DR mechanism. Actual DR is based on the demand management and the variable of price, load and renewable energy forecasting production, which call for complexity signal handling and optimization techniques. In Fig. 1, we show two faces of DR: (1) while the total electricity demand rests unpredictable and a financial encouragement reduces peak load, this is named peak clipping; and (2) on other side, load shifting features a fixed total demand, and the demand can be tuned forward or backward in time to off-peak hours. In additional to this renewable energy sources introduces production uncertainty which changes periodically this behavior.

2 OpenADR

Automated Demand Response (ADR) is a web interface control system that initiates DR events automatically by signaling other pre-programmed control systems and with the available production resources.

OpenADR2.0, an open communication protocol specifically designed for DR, is gaining momentum in the U.S., Asia and Europe. Initially developed by Lawrence Berkeley Nat. Lab OpenADR2.0 is now supported by an influential Alliance while more and more vendors integrate it into their technical products. Some vendors acting in the building energy management business start implementing OpenADR2.0 from design phases. OpenADR is certified by OASIS and has recently been approved as a Publicly Available Specification (PAS) by the International Electrotechnical Commission (IEC). A working group is also working on a harmonization between OpenADR2.0 and Common Information Model (CIM) [14].

The OpenADR protocol is a communication IP network to handle energy consumption requests based on production availability. Based on the Demand Response we centralize all transitions process between Virtual Top Node (VTN),

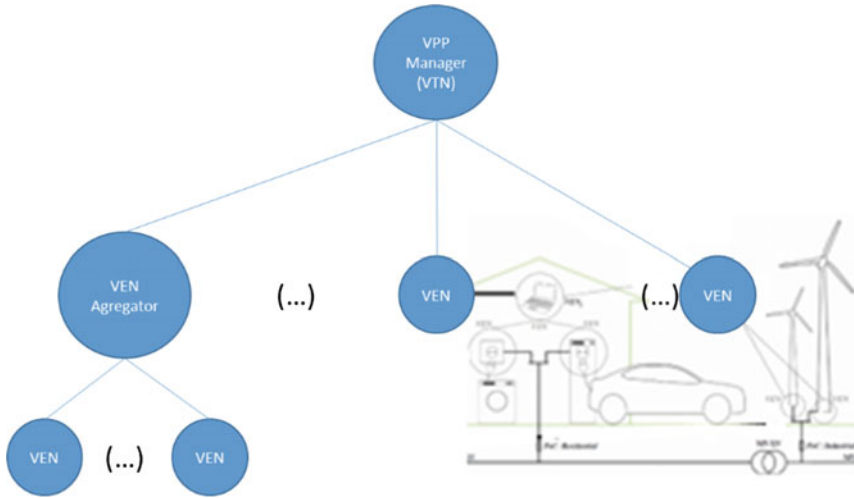


Fig. 2 VEN and VTN interaction with georeferenced position. VTN centralize information in a hierarchical process

identifies the entity that manage VENs) and Virtual End Node (VEN, client energy consumer or producer). Based on the graph of distribution network, a hierarchical relation is performed between VTN and VEN, see Fig. 2. VTN performs the role of Virtual Power Plant (VPP) manager. A VPP consists of an aggregation of Distributed Energy Resources (DERs). The VPP Manager centralize transitions from VEN with load resources that they interact and performed decision about loads ON/OFF based on distribution distance, previous calculated in georeferenced graph. This VPP receive information about production resource available and based on the demand response try to fit the resources do VEN needs with the goal of minimization power losses and non-supplied energy. All local Micro Generation (MG) can be handled as a VEN with a report service based on a metric device.

2.1 Functionalities Available for Stakeholders Interaction

OpenADR 2.0 supports several services from OASIS EI Version 1.0 standard with extensions for these services includes market requirements and DR stakeholder. A list of central available services is described at OpenADR (<http://www.openadr.org>), like logical request-response services. We create a new service, the distance distribution calculation, which output is the distance of VEN to other energy resource based on a georeference graph for the electrical DN. The main concern of this approach is the labour involved in the georeference process of each of these DN. Main idea for decision process of electrical distribution is the real distance on the DN. In Fig. 2, the area of the distribution network is transformed in a graph,

with georeferenced information and power limitations between the nodes. Each node is identified the distance and the distance is calculated between geographic coordinates of VTN and VEN matching to this nodes. Figure 2 shows this distribution network transformed to a georeferenced graph with dependencies. When a VEN is registered a distance calculation is performed to other VEN. For that we need all distribution nodes georeference.

2.2 Security

Network security measurement were performed based on networks standards at Transport Layer Security (TLS) with client. We are able to assure message integrity and confidentiality protection. Based on the OpenADR 2.0 specification requires that all nodes (both VTNs and VENs) uses public and private key with digital certificates issued by a trusted Certificate Authority (CA). VTN and VEN communication is authenticated using the digital certificates. VEN, based on the identification (venID) and VEN's digital certificate, based on a hashing using SHA algorithm. VTN certifies the VEN whose venID is claimed in the payload, that a sender of an incoming message is the trusted VEN. This is operation one-to-one mapping between the venID and the digital certificate.

2.3 VEN—Virtual End Node

The VEN has working control of a set of assets and processes and is able to control the electrical energy demand of these in response to an implicit set of messages (i.e., DR signals). The VEN performs a two way communication with a VPP receiving and transmitting messages that relate to power grid situations, conditions, or events.

Consumers define the number and type of electrical appliances of the house from a pre-defined class list. Three main operation classes are defined based on operation's needs:

- Class 1: Schedule-Based Appliances—Concerns with the electrical appliances time periods of operation. Since in the houses there are appliances with flexible operation time, like washing machines, dryers and dishwashers, users can define their operation time according to the best options in terms of energy availability.
- Class 2: Range Temperature Based Appliances—For equipment with temperature range, like refrigerators, heating systems or air conditioners, users can define the ranges, and the VPP manager will try to fit it based on energy availability.
- Class 3: Battery-Assisted Smart Appliances—The electric vehicle charging processes can be scheduled and controlled to adapt to energy availability.

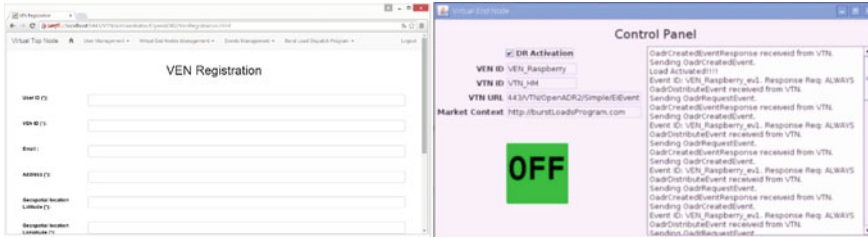


Fig. 3 Example of a web interface for VEN registration processes and VEN Web client interface where all information about this VEN transaction is displayed

VENs can also be energy producers that integrate a diversity of players: conventional electricity producers, renewable energy producers and home users with MG. Wind and the sun are the main renewable sources and the MG the electrical energy is obtained through micro wind turbines and solar photovoltaic panels. Today, this MG is provided to the electrical power grid without any concern about the Energy Market (EM) or the electrical power grid capability to receive energy (Fig. 3).

2.4 VTN—Virtual Top Node

Nodes in these networks are separated into two classes: (1) nodes that publish and transmit information about events to other nodes (e.g., utilities); (2) and nodes that receive the communications respond to that information (e.g., end-users). The upstream nodes that publish information about upcoming events are called Virtual Top Nodes (VTNs); the downstream nodes that receive this information are called Virtual End Nodes (VENs). In this context, the VTN manage the VEN’s resources based on geographic location of the generations resources look for nearest loads resources (based on electrical distribution distance) and activate loads consumption. Due to proximity between generation resources and loads we have less loss in transmission process.

The VENs with generation resources, send information about energy availability to VPP manager and establish communication between pre-defined VEN (main condition is the distribution distance). The OpenADR signals are transported via standards-based Internet Protocols (IP) such as Hyper Text Transfer Protocol (HTTP) or XML Messaging and Presence Protocol (XMPP).

2.5 *Electric Vehicle as a UPS*

The introduction of the Electric Vehicle (EV) into the power grid will also contribute to increase the energy consumption. However, the EV charging process can be controlled in collaboration with the energy production from renewables. Therefore, it can be useful to balance the energy production and consumption towards to reduce energy costs to power grid aggregator and to the end-user. Vehicle-Grid-Integration (VGI) technologies encompass this approach. At the University of Minho was developed a new operation mode that consists in the detection of a power outage in the power grid and the change of the EV battery charger control to operate as an off-line UPS [15]. This charging system with the introduction of VEN concept since the EV can handle more electric power. At user home, the EV can be charge with different profiles from the power grid of 240 V–15 A. There is already a diversity of EV, such as Nissan Leaf (with a battery capable to store a maximum energy of 24 kWh) and the Chevrolet Volt (with a battery capable to store a maximum energy of 16 kWh). In both case, considering a careful drive style it is possible to reach autonomies higher than 100 km. Once there is a diversity of EV with different battery power, we assume that in average we have 15 kWh available and in a for the energy market. Also there is a diversity of hybrid vehicle with low batteries capacities so we will assume the value of 10 kWh with a market penetration of 10 %. So our simulation handles a local VPP of 300 end-users with 30 EVs, each of them with 10 kWh. With the EV market penetration, the goal of flat power consumption (Fig. 1) is possible to be achieved at night periods (when the majority of EVs are at home plugged in at charging process). Consumption variations, as well as intermittent production due to renewable sources, can be dealt by the central control process, with production excess being used in the charging of EVs, and during production deficit the energy can be taken from EVs (operation in V2G—Vehicle-to-Grid mode). EVs can act as controlled load or generation resource, using a smart charging process, as explained and exemplified in [16, 17].

3 **Implementation of an OpenADR Infrastructure with RaspberryPi(S) Towards Internet of Things**

Since most fabricant do not provide an OpenADR yet or because the existence of old equipment, we developed a cheap solution around \$25. Figure 4, shows the product developed to create the VEN for a load or MG. RaspberryPi was configure to act as a VEN. In the Fig. 4, we simulated on/off operation through a LED but in real VEN operation this command is used to put on/off equipment or to slow \increase heat or cooling process. Also this can be used as a VEN with a generation resource where we add metering capability, display information is optional because information is stored as local HEMS (Home Energy Management System) and can

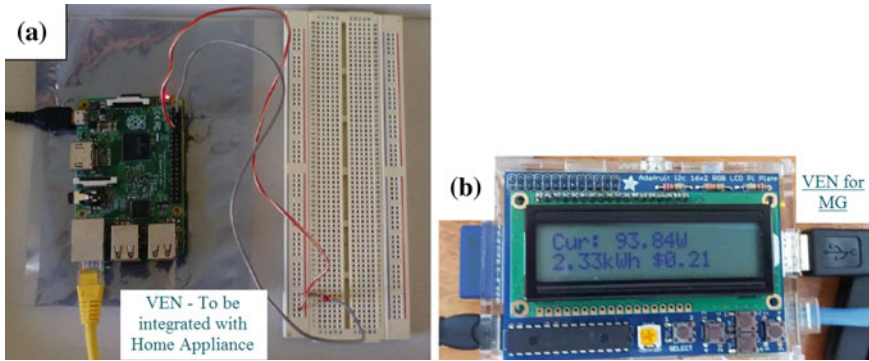


Fig. 4 Developed RaspberryPi VEN (a) and VTN for MG (b)

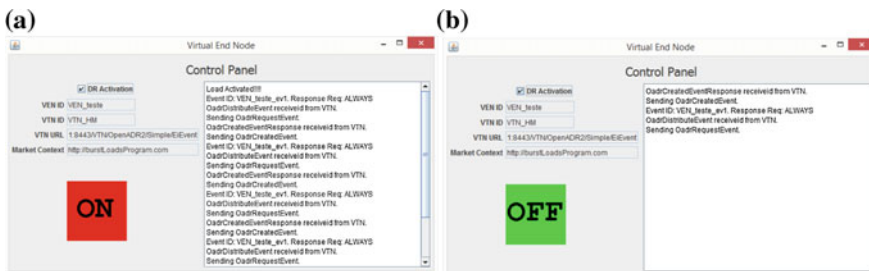


Fig. 5 VEN interface and associated transactions: a Turned on; b Turned off

be presented through a web application. Since most electrical appliances are not compliant with OpenADR a VEN of Fig. 5 should be integrated. All resources send information to local HEMS (Home Energy Management System) that was developed for VENs configuration interfaces and visualization of energy exchanges. Based on VENs definition a consumption profile is created where we add non OpenADR consumptions. This is basically a web interface application that interacts with local VENs. This consumption profile are important information to apply in a future work data mining approach to extract knowledge related with energy consumption.

Since is not easy to have a real scenario for testing, we simulated our approach creating several VENs and multiply the effect to have impact in electricity consumption. Regarding production we use real data from 3 days (28 a 30 April 1015) from Portuguese REN [18]. Also consumption patterns were available and a dynamic approach were performed to match production to consumption based on a central commands performed remotely at the VEN. We introduce a small scale VEN (ten) distributed geographic.

The first step is the VEN registration through a web application (Fig. 4a). In this register process the user defines the VEN class, working hours, consumption and

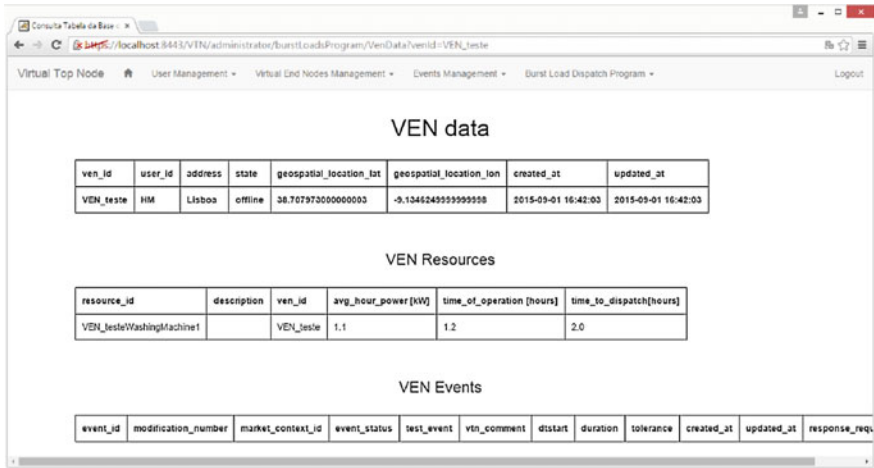
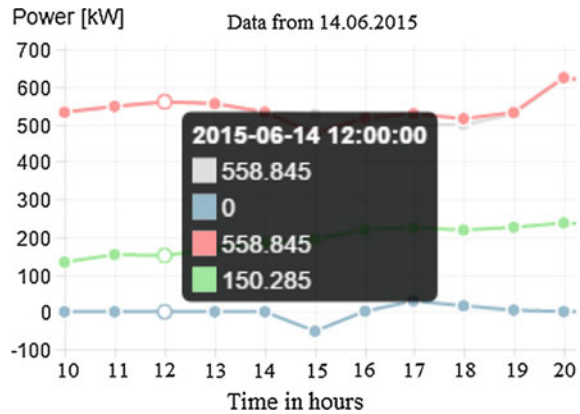


Fig. 6 VEN’s available reports with information stored at local VPP

geographic position. The simulation tool loads a request from the local VPP server, using the production and consumption data. If the consumption is above a predefined value, then an off remote command is performed, and if the production is high enough a remote on command is given. We perform small scale tests, with ten VEN, and with a simulation of production and consumption based on historical data. From these tests, several procedures of remote turn on/off of VEN were performed. We also have tested with success the decision of VEN on/off based on distribution distance of the VEN to the energy source and priority VEN class (see Sect. 2.3). The case of class 2 (for example, range temperature in a heating system), when temperatures goes down the value defined by the user, it assumes maximum priority, were also tested. Figure 5 shows the VEN interface and associated transactions when it is turned on and when it is remotely turned off, because there was no need to take electricity production excess. Figure 6 shows a web interface to local HEMS, where the user can check all actions and consumption performed by the VEN that he is the owner.

For MG, owners register the VEN, defining the renewable capacity, geographic localization and the report service poll interval with the energy produced and/or average power. Local device informs about the MG production that was not consumed. In our test environment we simulated VPP manager (VTN) based on historical energy production available from [18]. All the energy production is collected at central VPP manager for main producers and local MG production. Based on this information, the VPP manager takes the decision for the VEN being on/off, or for the VEN increasing or decreasing the power consumption. This decision is based on VEN class and distribution distance between VEN’s generation resources and VEN’s loads resources. So, based on production data and consumption data available from [18], a simulation process was taken.

Fig. 7 Home consumption stored at local VPP with graphic web interface for user presentation, each line represents different power consumption



It is possible to check the power consumption per house. Figure 7 shows an example where, at 12 h, one of the houses is not taking the energy produced (blue line), and therefore, this energy is delivered to the power grid. In this case, a nearest VEN with a load in off position was turned on automatically in order to consume energy. Also, it can be seen that at 15 h the consumption is negative (the house is injecting energy in the grid). This information is send to a local VPP manager, and a decision process takes place in other that a VEN or a set of VENs need to be turned on.

4 Conclusions

Distributed Energy Resources (DER), MG close to energy loads, are expected to grow into an important part of the future electrical power system [17]. OpenADR plays a vital part in this process, allowing consumption events based on external events, like production availability, that is reflected in energy price. The systems losses is higher in the distribution systems than in the transmission systems, therefore, once the DER are installed in the distribution systems (near of the electrical appliances) it is expected an increase of the efficiency at the distribution level. However, DER has the problem to handle with the changeability of the electrical appliances (according to the end-user) and the unpredictable energy production from renewables. In this context, Demand Response (DR) contributes to establish a collaborative process according to the use of the electrical appliances (schedules to start and stop) and the energy production information.

DR introduction is growing as system operators rely on to maintain the reliability of the electrical power grid. Market liberalization, economic value, and environmental regulations are all moving toward a path of fewer traditional central power plants and more DER to address future energy requirements. Information technologies can help speed up this transition and make it more reliable. In order to automate the DR dispatch process, an Automated Demand Response (ADR) is

used, which consists in manage the energy production and consumption, and the associated costs, according to the benefits of the grid operator, the aggregator and the end-user. According to a forecast established by Navigant Research, it is predictable that the global spending on ADR will increase from \$13 million to \$185 million, from 2014 to 2013 [19].

The upcoming reality of Smart Grids will need to join efforts from different fields of knowledge. In this research work we have joined two groups with different expertise, one at ISEL in Informatics and Telecommunication, and the other at the University of Minho in Energy and Power Electronics, with previous works on power quality, renewable energy and electric vehicle charging systems.

References

1. Hung, D.Q., Mithulanathan, N.: Multiple distributed generator placement in primary distribution networks for loss reduction. *Ind. Electron. IEEE Trans.* **60**, 1700–1708 (2013). doi:[10.1109/TIE.2011.2112316](https://doi.org/10.1109/TIE.2011.2112316)
2. Baran, M.E., Wu, F.F.: Optimal capacitor placement on radial distribution systems. *IEEE Trans. Power Deliv.* **4**, 725–734 (1989)
3. Abdel-Salam, T.S., Chikhani, A.Y., Hackam, R.: New technique for loss reduction using compensating capacitors applied to distribution systems with varying load condition. *IEEE Trans. Power Deliv.* **9**, 819–827 (1994). doi:[10.1109/61.296262](https://doi.org/10.1109/61.296262)
4. Wu, Y.K., Lee, C.Y., Liu, L.C., Tsai, S.H.: Study of reconfiguration for the distribution system with distributed generators. *IEEE Trans. Power Deliv.* **25**, 1678–1685 (2010). doi:[10.1109/TPWRD.2010.2046339](https://doi.org/10.1109/TPWRD.2010.2046339)
5. Das, D.: Reconfiguration of distribution system using fuzzy multi-objective approach. *Int. J. Electr. Power Energ. Syst.* **28**, 331–338 (2006). doi:[10.1016/j.ijepes.2005.08.018](https://doi.org/10.1016/j.ijepes.2005.08.018)
6. Bianzino, A.P., et al.: A survey of green networking research. *Commun. Surv. Tutorials IEEE* **14.1**, 3–20 (2012)
7. Baran, M.E., Wu, F.F.: Network reconfiguration in distribution systems for loss reduction and load balancing. *Power Deliv. IEEE Trans.* **4**, 1401–1407 (1989). doi:[10.1109/61.25627](https://doi.org/10.1109/61.25627)
8. Ababei, C., Kavasseri, R.: Efficient network reconfiguration using minimum cost maximum flow-based branch exchanges and random walks-based loss estimations. *IEEE Trans. Power Syst.* **26**, 30–37 (2011). doi:[10.1109/TPWRS.2010.2052076](https://doi.org/10.1109/TPWRS.2010.2052076)
9. Dias, F.M., Canizes, B., Khodr, H., Cordeiro, M.: Distribution networks planning using decomposition optimisation technique. *IET Gener. Transm. Distrib.* (2015). doi:[10.1049/iet-gtd.2014.0860](https://doi.org/10.1049/iet-gtd.2014.0860)
10. Khodr, H.M., Martinez-Crespo, J., Matos, M.A., Pereira, J.: Distribution systems reconfiguration based on OPF using benders decomposition. *IEEE Trans. Power Deliv.* **24**, 2166–2176 (2009). doi:[10.1109/TPWRD.2009.2027510](https://doi.org/10.1109/TPWRD.2009.2027510)
11. Aquino-Lugo, A.A., Klump, R., Overbye, T.J.: A control framework for the smart grid for voltage support using agent-based technologies. *Smart Grid, IEEE Trans.* **2**, 173–180 (2011). doi:[10.1109/TSG.2010.2096238](https://doi.org/10.1109/TSG.2010.2096238)
12. Arnold, G.W.: Challenges and opportunities in smart grid: a position article. *Proc. IEEE* **99**, 922–927 (2011). doi:[10.1109/JPROC.2011.2125930](https://doi.org/10.1109/JPROC.2011.2125930)
13. Vale Z, Morais H, Pereira N. Energy resources scheduling in competitive environment. In: 21st International Conference on Electrical Distribution, Frankfurt—Germany (2011)
14. <http://cimug.ucauiug.org/Projects/CIM-OpenADR/default.aspx>

15. Monteiro, V., Exposto, B., Pinto, J.G., Almeida, R., Ferreira, J.C., Meléndez, A.A.N., Afonso, J.L.: On-board electric vehicle battery charger with enhanced V2H operation mode. In: IEEE IECON Industrial Electronics Conference, pp. 1636–1642. Dallas Texas USA (2014)
16. Monteiro, V., Ferreira, J.C., Pinto, G., Pedrosa, D., Afonso, J.L.: iV2G charging platform. In: IEEE-ITSC, 13th International IEEE Conference on Intelligent Transportation Systems, pp. 409–414, 19–22 Sept (2010)
17. Ferreira, J.C., Silva, A., Afonso, J.L.: Agent based approaches for Smart charging strategy for Electric Vehicle. In: EVTEC 11 (1st International Electric Vehicle Technology Conference), 17–19 May 2011, in Yokohama, Japan (2011)
18. Ren WebSite. <http://www.centrodeinformacao.ren.pt/PT/Paginas/CIHomePage.aspx>. Accessed 28 2015
19. Navigant Report about OpenADR. <https://www.navigantresearch.com/research/automated-demand-response>. Accessed 28 2015.

Part XII
General Applications

A Low-Cost ZigBee-Based Wireless Industrial Automation System

Pedro Castro, João L. Afonso and José A. Afonso

Abstract This paper describes the development of an industrial automation system based on a ZigBee wireless sensor network, designed for the monitoring and control of multiple refrigeration equipments in an industrial area, replacing the existing cabled network, which is based on the LonWorks platform. For this purpose, ZigBee routers were used to replace the local controllers at the refrigeration equipments, while the central management controller was replaced by a ZigBee coordinator and a PC. The proposed system was developed using a hardware platform based in the CC2530 integrated circuit and the Z-Stack software. Results from experimental field tests performed in an industrial environment are provided in order to assess the performance of the developed ZigBee network.

Keywords Zigbee · Monitoring and control · Wireless sensor networks

1 Introduction

The increasing development in the field of telecommunications enabled, in the last decades, a marked evolution and expansion of the market of wireless network technologies, which are everywhere nowadays, due to the convenience and reduction of costs that result from the elimination of cables.

Many wireless communication technologies, such as IEEE 802.11/Wi-Fi [1] aim to provide high data rates to the users. Others, such as ZigBee [2], were conceived to scenarios where high data rates are not relevant, but low cost, low energy

P. Castro · J.A. Afonso (✉)
CMEMS-UMinho R&D Center, University of Minho, 4800-058 Guimarães, Portugal
e-mail: jose.afonso@dei.uminho.pt

P. Castro
e-mail: a55615@alunos.uminho.pt

J.L. Afonso
Centro ALGORITMI, University of Minho, 4800-058 Guimarães, Portugal
e-mail: joao.l.afonso@algoritmi.uminho.pt

consumption and small device size are paramount, being applied in the context of the wireless sensor networks (WSN) [3].

The evolution of the WSNs in the last decade, along with the progress in the area of sensors and actuators, allowed the emergence of applications in several areas, such as medicine [4, 5], agriculture [6], industry [7], smart buildings [8], etc. The characteristics of WSNs are suitable to industrial environments, for monitoring and control of multiple equipments distributed in a given area. In such scenario, the network nodes are normally responsible to deliver the information acquired from the sensors to a central station, where relevant parameters can be monitored and controlled.

Besides the lower material and maintenance costs due to the elimination of cables, ZigBee allow more flexibility in the deployment and expansion of networks, even after they started operating, without requiring manual alterations to the network topology. Due to the low complexity, ZigBee devices normally have lower costs than their wired counterparts. Unlike analogous wireless technologies such as Bluetooth, ZigBee possesses multihop capabilities, which allows extending the wireless network coverage.

This paper presents a ZigBee-based wireless automation system designed to operate in industrial/commercial environments and replace the existing wired network and the respective controllers. The proposed system is applied to the monitoring and control of multiple refrigeration equipments installed in an industrial area.

The rest of this paper is organized as follows. Section 2 describes the architecture and components of the original cabled monitoring and control system. Section 3 presents the wireless industrial automation system that was developed to replace the cabled system. Section 4 presents experimental network performance results from tests performed in an industrial environment, and Sect. 5 presents the conclusions.

2 Legacy Wired System

The monitoring and control of refrigeration systems is based on a network that provides communication between the different devices. These refrigeration systems are installed in large areas such as supermarkets and hypermarkets, trading posts and factories, where there is a requirement for a large number of refrigerated places and equipments.

There are various types of refrigeration equipments, such as refrigeration chambers, display cabinets, shop windows, etc. Figure 1 presents the architecture of a generic refrigeration equipment and the associated components, which are mostly sensors and actuators that can vary according to the function of the equipment. This refrigeration equipment is composed by an expansion valve, a fan, two temperature probes, a door sensor, an evaporator and an electric panel.

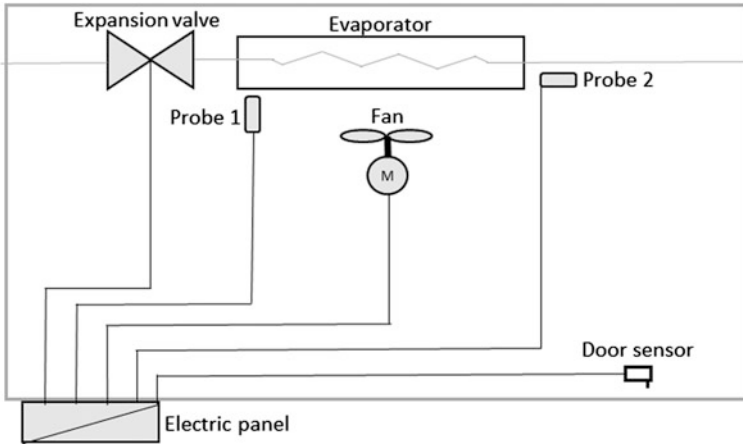


Fig. 1 Architecture of a generic refrigeration system

The electric panel serves as a support infrastructure for the operation of the sensors and actuators of the refrigeration system. For that purpose, it is composed by a controller and some electromechanical and thermal relays. Figure 2a shows a type of controller (AK-PC 530 [9]) that can be used. This component is responsible for the monitoring and control of the refrigeration equipment and also to communicate with a central management controller in order to send data from the sensors and the state of the actuators, as well as to receive commands from the central controller. The electromechanical relays are used on the power circuit to control the operation of the components that require currents higher than the controller is able to provide, such as the fan or the expansion valve, while the thermal relays are used to protect these power circuits.

Each refrigeration equipment includes two temperature probes (probe 1 and probe 2), at specific locations. Figure 2b shows a type of probe (EKS 111 [10]) that is used. These are PTC (Positive Temperature Coefficient) probes, which mean that

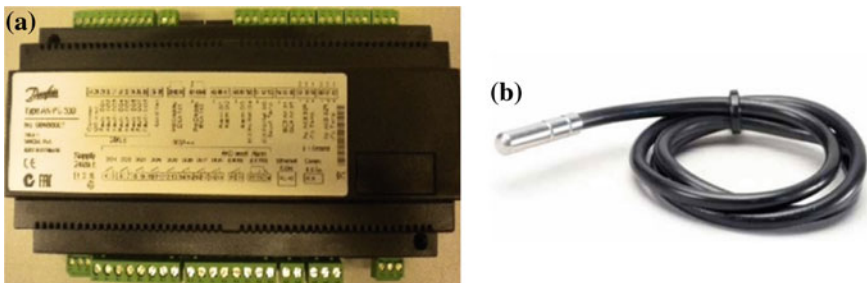


Fig. 2 Components of the original system: a AK-PC530 controller; b EKS 111 probe

their electric resistance increase with the temperature. These probes are directly connected to the controller, where their analog signal is converted to digital.

The door sensor is a miniature snap-action switch (also known as a micro switch) that is installed at the refrigeration equipment door. Its function is to provide information to the controller regarding the state of the door: open or closed.

The expansion valve controls the flux of the cooling fluid, which allows the evaporator to refrigerate the equipment through thermodynamic effects. The controller on the electric panel turns this valve on or off according to the readings from the probes and the temperature values defined for the refrigeration equipment. The expansion valves used in the original system are of type AKV 10 [11], and are powered with 230 V AC.

The fans control the flux of air that goes through the evaporator. They are connected to the power circuit and are commanded by the controller. As in the case of the valve, they can be turned on or off, and are powered with 230 V AC.

A central management controller is used to monitor and control all local refrigeration equipments. This controller receives data from the controllers of all the refrigeration equipments and sends commands back using network cables. It is also responsible for the user interface. The central management controller used in the original system (AK-SM 850 [12]) provides a display and access buttons to allow the user to monitor and configure the operation of the refrigeration equipments without requirement of any other external equipment. This controller is normally placed in the central electric panel in the machine room.

The communication between the devices of the original system is based on the LonWorks [13] network technology, and uses the standard RS-485 in the specification of the physical layer of the LonTalk protocol. The devices are connected in a bus topology using twisted pair cables. This topology allows a maximum transfer rate of 39.06 kbps and a maximum of 60 controllers. A repeater is required when the network cable length extends beyond the maximum length defined by this network technology (1200 m). The repeater used by the legacy system is the AKA 223.

3 Developed Wireless System

This work proposes the replacement of a cabled LonWorks network by a ZigBee-based wireless sensor network (WSN) satisfying similar operation requirements. The controllers are the main supporting devices for the operation of the LonWorks network. Therefore, the local controllers installed in the electric panels of the refrigeration equipments were replaced by ZigBee routers (ZR), while the central management controller was replaced by a ZigBee coordinator and a PC, which work as the central station. The cabled infrastructure between the controllers, based on a bus topology, was replaced by a ZigBee wireless network based on a mesh topology. The remaining components of the refrigeration equipments remained the same.

3.1 ZigBee Network

The ZigBee standard defines the upper layers of the ZigBee protocol stack, including the network layer (NWK) and the application layer (APL), while the IEEE 802.15.4 standard defines the physical (PHY) and the medium access control (MAC) layers. The devices used in this system operate in the 2.4 GHz frequency band with a PHY data rate of 250 kbps.

Since the ZigBee devices in this system have easy access to the mains power at the electric panels, it is not necessary to resort to batteries; therefore, there are no stringent restrictions in terms of energy consumption. Consequently, we decided to replace the local controllers by ZigBee routers, instead of using ZigBee end devices (ZED), which could potentially sleep during inactive periods in order to save energy. One advantage of the use of ZRs (which are distributed over the industrial facility) instead of ZEDs is that, thanks to the multihop mesh topology, they can seamlessly extend the coverage of the ZigBee network, relaying the packets of other ZRs that are out of the range of the ZigBee coordinator (ZC) and increasing the reliability of the network through the provision of alternative routes. Each ZR was physically connected to the sensors and actuators of the respective refrigeration equipment.

Besides the local monitoring and control of its sensors and actuators, each ZR sends data and receives the commands from the ZC located at the central electric panel, either directly or through other ZRs. It is also possible for a ZR to monitor sensors or control actuators from other refrigeration equipments through the wireless network if required.

After the network association process, a ZR can start to transfer data to the ZC. The first data frame sent by the ZR contains the identifier of the respective refrigeration equipment (the equipment number), as well as the characteristics of the sensors and actuators it has. After that, the subsequent data frames transport readings from the sensors and the state of the actuators connected to the ZR. These frames are sent periodically each one second. They have a payload of 20 bytes, and their total length, including the ZigBee headers and trailers, is 47 bytes.

3.2 Network Hardware and Software

The hardware platform used during the development of the code for the ZigBee devices and for the experimental evaluation of the wireless network performance was the CC2530 development kit, from Texas Instruments (TI). The main component of this kit is the CC2530 [14] SoC (System on Chip), which integrates a 8051-based microcontroller and a transceiver compliant with the IEEE 802.15.4 standard in the same chip. Each network device was composed by two boards that are connected together: a CC2530EM (Evaluation Module), which contains the CC2530 and other auxiliary components required for the operation of this chip and for wireless communication; and a SmartRF05 EB (Evaluation Board), which

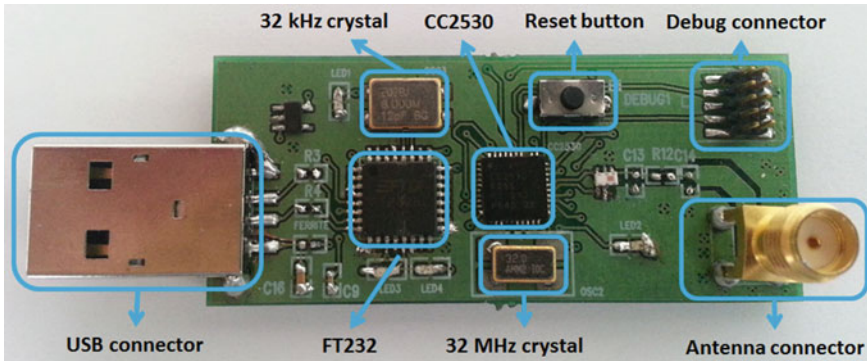


Fig. 3 Developed central station board

provides different alternatives to power the CC2530EM and contains several other components that are useful during the development phase, such as an LCD display, LEDs, buttons, and USB and RS-232 interfaces. After the development phase, these two boards can be replaced by smaller and lower cost alternatives.

Figure 3 presents the central station board that was developed to be connected to a PC and act as the ZigBee coordinator (ZC) of the wireless network, replacing the much larger boards of the development kit (this board measures 24 mm by 56 mm, while the SmartRF05 EB measures 114 mm by 128 mm). The CC2530 version used in this board is the CC2530F256, with 256 kB of flash memory. The FT232BL chip provides an USB to serial UART interface, allowing the ZC to send and receive data from the PC. The standard-A USB connector is used for data transfer and to power the ZC. This board also integrates an antenna connector, which is equal to the one used by the CC2530EM, and several other auxiliary components. The total cost of all the components of this board is around 33 euros.

Likewise, for the ZigBee routers (ZR), the TI development boards can be replaced by a much smaller and cheaper CC2530-based module and a power supply. For example, the ANAREN A2530R24CZ1GM module measures 19 mm by 11 mm and costs around 19 euros. The prices presented in this paper are retail prices for small quantities. Wholesale prices tend to be lower.

In terms of software, the development platform used for the WSN devices was the Z-Stack version Z-Stack-CC2530-2.5.0, supplied also by Texas Instruments, which supports the profiles ZigBee e ZigBee PRO of the ZigBee 2007 standard.

3.3 Refrigeration Equipments

Regarding the sensors, the analog probe 1 is used to monitor the evaporator temperature and the analog probe 2 monitors the ambient temperature at the refrigeration equipment. When the door is closed, the contact of the door sensor is closed and the

digital input P2.1 of the ZR reads a low logic level value, otherwise it reads a high level value.

The actuators of the refrigeration equipment that are controlled by the ZR are the expansion valve and the fan. The output ports of the ZR are not able to provide the voltage or the current required to control these actuators directly (the maximum output current for the P1 port is 20 mA). Therefore, the pins P1.0 and P1.1 are connected to relays that are used to control the expansion valve and the fan, respectively.

The refrigeration equipment operates between two predefined temperatures. The stopping temperature is the lower bound temperature desired for the system. When this temperature is reached, the refrigeration must stop. In contrast, the starting temperature is the maximum operating temperature specified for the system. When this temperature is reached, the refrigeration must start. The ZR controls the temperature of the refrigeration equipment through the monitoring of probe 2, which provides the ambient temperature. When its reading is equal or higher than the starting temperature, the expansion valve is switched on, in order to refrigerate the equipment, until it reaches the stopping temperature.

Once the refrigeration is turned on, the fan is also switched on, except in the following cases: the door sensor is on, which means that the door is open; or the system is defrosting. When the door is opened, both the fan and the expansion valve are switched off. The ZR controls the defrosting process through the monitoring of probe 1, which provides the evaporator temperature.

3.4 Central Station

The central station is composed by the ZC and a PC. The PC allows the visualization of the data collected by all the local refrigeration equipments, in real-time, as well as the remote control of their operation. The PC receives the readings and sends the commands to the ZC through a serial port.

The PC application, which provides the graphical user interface (GUI) to the user, was developed using Java and the NetBeans IDE v8.0.2. The data that can be monitored and/or configured on the PC application, for each one of the refrigeration equipments, are the following: equipment number; ambient temperature; evaporator temperature; state of the door sensor; state of the fan; state of the expansion valve; starting temperature; and stopping temperature.

4 Results and Discussion

This section presents results from experimental field tests performed in an industrial environment, with the purpose of evaluating the performance of the ZigBee network. Each network device was composed by two boards: a SmartRF05 EB and a

CC2530EM. One ZigBee device was programmed as ZC and the other devices were programmed as ZRs. These tests were performed in a meat processing factory where there was a constant movement of people and materials.

The placement of the ZC and the ZRs in the factory is shown in Fig. 4. In this configuration, it was noticed that, due to the distance and the propagation conditions, some of the ZRs (1, 2, 4 and 6) were not able to communicate directly with the ZC. Nevertheless, these ZRs were still able to exchange data with the ZC, by taking advantage of the ZigBee multihop capabilities. Therefore, in this deployment scenario, frames from/to ZRs 1 and 2 were routed through ZR 3, while frames from/to ZRs 4 and 6 were relayed by ZR 7.

The Wi-Spy 2.4x spectrum analyzer was used to assess the presence of other RF sources in the same spectrum used by the ZigBee devices (the 2.4 GHz frequency band), which may potentially cause interference. This analyzer has shown that the spectrum was being used by two Wi-Fi networks, in channels 4 and 12. The tests presented in this paper were performed using two different ZigBee channels, 11 and 26, which are located at the extremities of the available 2.4 GHz band. The carrier frequencies for these channels are 2405 and 2480 MHz, respectively. Regarding the co-located Wi-Fi networks, channels 4 and 12 have carrier frequencies of 2427 and 2467 MHz, respectively. Taking into account that the bandwidth of Wi-Fi signals is 22 MHz and that ZigBee signals occupy a bandwidth of 3 MHz, it can be concluded that these Wi-Fi and ZigBee signals do not overlap and, consequently, there were no significant interference from Wi-Fi networks during the tests.

In the first test, 1000 data frames with a payload of 90 bytes were sent consecutively with an interval of 200 ms. One goal of this test was to evaluate the worst-case scenario where large packets (close to the maximum length) are transmitted (large packets are more susceptible to channel errors). Figure 5 shows the packet loss rate (PLR) for each ZR and ZigBee channel in this test. The results for the two channels are very similar. The main differences are related to the location of the ZRs. ZRs 2 and 6, which were more distant from the ZC and had to send data

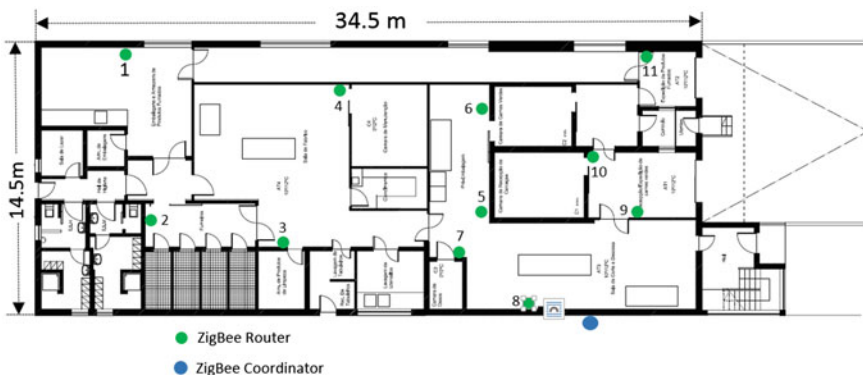


Fig. 4 Distribution of the ZigBee devices in the factory for the tests

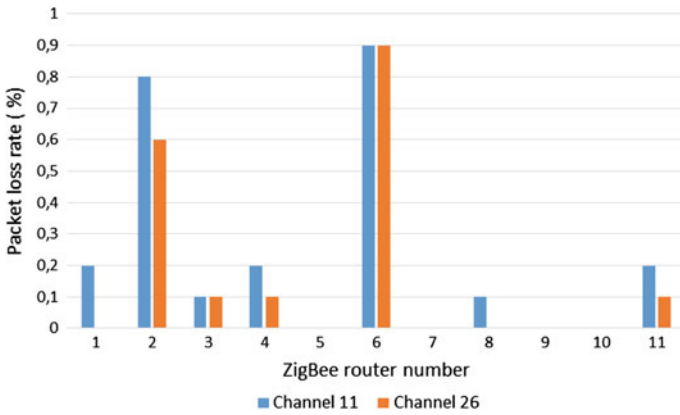


Fig. 5 PLR results with 90-byte payload in different channels

through other ZRs, presented the worse performance, although still acceptable, while other ZRs routers closer to the ZC were able to send all their packets without errors.

The second test was performed using the same traffic parameters of the final implementation of the wireless system that is being applied to monitoring and control of refrigeration equipments, which are referred in Sect. 3.1. Therefore, in this test, 1000 data frames with a payload of 20 bytes were sent consecutively with an interval of one second. The test was performed using the channel 26. Figure 6 presents a comparison between the packet loss rate (PLR) at channel 26, for each ZR, with payload of 90 bytes (first test) and 20 bytes (this second test). From the first to the second test, it can be observed that there is a small decrease in the PLR, on average, which is justified by the smaller payload, which decreases the probability of corruption of the packets.

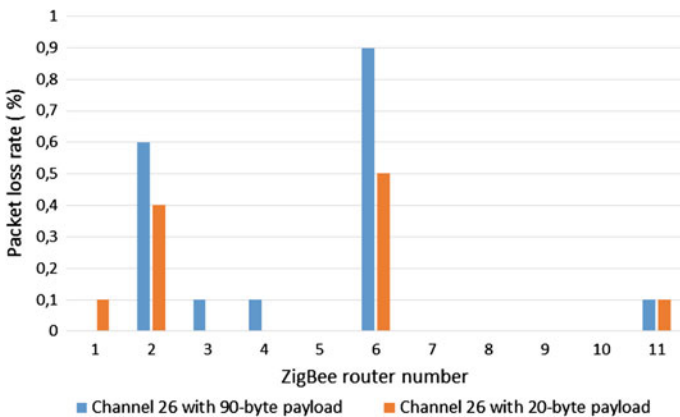


Fig. 6 PLR results with different payload lengths in channel 26

5 Conclusions

This work presents the development of a ZigBee wireless sensor network for monitoring and control of an industrial process, replacing the existing cabled network, based on the LonWorks networking platform. ZigBee routers replaced the local controllers at the refrigeration equipments, while the central management controller was replaced by a ZigBee coordinator and a PC.

The number of industrial/commercial facilities that use refrigeration equipments, namely medium and large commercial areas, has been growing in the last decades. The lifetime of this type of equipments is relatively short, between 10 and 15 years. The consequent required maintenance tasks create an opportunity to replace the legacy wired systems by wireless ones, which presents advantages in terms of deployment and maintenance costs.

Future works may include the provision of more functionalities in the developed system, to allow a more refined control and, consequently, to achieve higher efficiency in the operation of the refrigeration equipments. In this sense, a possible functionality to include is related to the control of the expansion valve, which could have more than two operation levels, being more opened when the temperature of the refrigeration equipment is higher, thus allowing the passing of more refrigeration fluid, or almost closed when the temperature of the refrigeration equipment is near to the stopping temperature.

Acknowledgments This work is supported by FCT (Fundação para a Ciência e Tecnologia) with the reference project UID/EEA/04436/2013, and by FEDER funds through the COMPETE 2020—Programa Operacional Competitividade e Internacionalização (POCI) with the reference project POCI-01-0145-FEDER-006941.

References

1. IEEE Std 802.11-2012: Part 11: Wireless LAN Medium Access Control (MAC) and Physical Layer (PHY) Specifications (2012)
2. Kinney, P.: ZigBee Technology: Wireless Control that Simply Works. Communications Design Conference (2003)
3. Borges, L.M., Velez, F.J., Lebres, A.S.: Survey on the characterization and classification of wireless sensor network applications. *IEEE Commun. Surv. Tutorials* **16**(4), 1860–1890 (2014)
4. López, H.F., Afonso, J.A., Correia, J.H., Simões, R.: HM4All: a vital signs monitoring system based in spatially distributed zigbee networks. In: 4th International Conference on Pervasive Computing Technologies for Healthcare (PervasiveHealth 2010), Munich, Germany (2010)
5. Gama, O., Carvalho, P., Afonso, J.A., Mendes, P.M.: Quality of service in wireless e-emergency: main issues and a case-study. In: 3rd Symposium of Ubiquitous Computing and Ambient Intelligence, pp. 95–102 (2009)
6. Zhou, Y., et al.: A design of greenhouse monitoring and control system based on ZigBee wireless sensor network. In: IEEE International Conference on Wireless Communications, Networking and Mobile Computing (WiCom 2007), Shanghai, China, pp. 2563–2567 (2007)

7. Gungor, V.C., Hancke, G.P.: Industrial wireless sensor networks: challenges, design principles, and technical approaches. *IEEE Trans. Ind. Electron.* **56**(10), 4258–4265 (2009)
8. Afonso, J.A., Rodrigues, F., Pereira, P., Gonçalves, H., Afonso, J.L.: Wireless Monitoring and Management of Energy Consumption and Power Quality Events. *World Congress on Engineering (WCE 2015)*, London, United Kingdom, pp. 338–343 (2015)
9. Danfoss: Capacity Controller AK-PC 530. Manual (2010)
10. Danfoss: Temperature Sensor type EKS 111. Technical Brochure (2012)
11. Danfoss: Electrically Operated Expansion Valve Types AKV 10. Datasheet (2012)
12. Danfoss: System Manager AK-SM 850. Quick Setup Guide (2013)
13. Echelon Corporation: Introduction to the LonWorks Platform. Version 2.0 (2009)
14. Texas Instruments: CC253x System-on-Chip Solution for 2.4-GHz IEEE 802.15.4 and ZigBee Applications. Datasheet (2010)

Comparative Analysis of Gain-Scheduled Wheel Slip Reset Controllers with Different Reset Strategies in Automotive Brake Systems

Miguel Cerdeira-Corujo, Adriana Costas, Emma Delgado and Antonio Barreiro

Abstract Wheel slip control bases its effectiveness on operating in the maximum adherence zone, guaranteeing the correct handling of the vehicle. The use of brake-by-wire systems and electromechanical actuators, make possible the control of each wheel slip independently, improving the performance of braking systems. Several controllers are proposed to enhance the overall effectiveness of the braking maneuver. To do this, several reset strategies are compared: reset control with zero crossing, fixed reset band and variable reset band. The improvements achieved proceed from the betterment of the outputs of the system such as the transient time and the overshooting. The robustness of the system to changes in the friction conditions is also improved by reset control and reset bands.

Keywords Automotive brake systems · Wheel slip control · Reset control · Traction control · Reset band

M. Cerdeira-Corujo (✉) · A. Costas · E. Delgado · A. Barreiro
Departamento de Enxeñaría de Sistemas e Automática,
Universidade de Vigo, Escola de Enxeñaría Industrial, Rúa Maxwell,
s/n. Campus Universitario Lagoas-Marcosende, 36310 Vigo, Galicia, Spain
e-mail: mcerdeira@uvigo.es
URL: <http://www.uvigo.gal/>

A. Costas
e-mail: adcostas@uvigo.es

E. Delgado
e-mail: emmad@uvigo.es

A. Barreiro
e-mail: abarreiro@uvigo.es

1 Introduction

The Anti-lock Braking System has been used for decades in order to avoid the locking of the wheels, in case of a sudden brake maneuver. In this article, the anti-lock mechanism is implemented by means of a control strategy based on the tracking of an input reference. It will be necessary to know the slip of each of the wheels in order to control it. This is possible in cars equipped with break-by-wire systems and electromechanical actuators, which make possible the control of each wheel slip individually. The use of electromechanical actuators redounds to high performance control modules such as ABS, TC (Traction Control), VSC (Vehicle Stability Control) among others.

There are several works which address the wheel slip control. In [1], Johansen et al. developed a wheel slip controller with gain-scheduling, based on a LQR approach. In [2] by means of a sliding mode controller, the wheel slip of an electric vehicle is regulated. Other contributions to model-based wheel slip control can be found in [3–7].

A reset controller is just a standard controller endowed with a reset mechanism which is a strategy that resets to zero (or to a certain percentage) one or several of the controller states, whenever a certain condition holds. The first application existent in the state of the art, about reset control, is encompassed on the seminal work of Clegg [8]. In this work, Clegg demonstrated the advantages of reset control compared to a classic control. The study of reset control was discontinued until the early 70s, when it was tackled by Horowitz's research group [9, 10]. In these articles, he highlighted how reset control helps to overcome fundamental limitations which affect linear systems [11, 12]. From the publication of these articles to the late 90s its study was once again discontinued. From that moment, the number of research groups interested in this kind of control has increased considerably. An interesting recent proposal is the PI+CI [13] which combines the advantages of a PI controller with those provided by a Clegg Integrator. Over the last years, reset control has been employed in different applications as reported in [14].

In recent years several authors have analyzed the behavior of systems with different reset strategies. One of the first modifications studied was the addition of a reset fixed band. This strategy comprises a reset mechanism that resets the state/s of the controller whenever the error signal enters a fixed band. This technique result especially beneficial in systems with time-delays [15]. The main problem with a fixed band is that the controller has been especially designed for a particular reference (or disturbance). The use of a variable reset band was also studied, being this used for overcoming the influence of dominant time delays over the reset action as reported in [16].

There are several works on the technical literature which cover the topic of reset control applied to wheel slip control such as [17]. The main goal of this work is to go a step forward by demonstrating how the use of reset control combined with different band strategies can result in a high-performance controller. In order to do

that, the performance of several controllers will be compared, i.e., variable reset band, fixed reset band, zero crossing reset and a PI controller.

This article is organized as follows. In Sect. 2 problem statement is introduced. Then, Sect. 3 presents the dynamic model of the braking maneuver. Section 4 contains all the considerations taken into account for the design of the controllers. After, some simulation results are included in Sect. 5 and finally, the conclusions are presented in Sect. 6.

2 Problem Statement

The wheel slip control is not easy at all, on the contrary, diverse uncertain parameters have to be considered. Wheel slip can be modelled, under certain conditions, by a first order differential equation which relates slip with braking torque and which is $\frac{\partial x}{\partial t} = F(s_x(t), T_b(t))$. The main issue resides in the fact that this relation is highly non-linear and undetermined.

Figure 1 shows a family of friction curves given for different conditions of the road surface. There are two clearly distinct zones. The one to the left of the maximum point and the one to the right of this maximum. The first zone, can be approximated by a linear relation. In order to yield good results, wheel slip control works on the propinquity of the maximum adherence area in the curve i.e., the linear zone. As long as the system is in the linear zone without reaching the top of the curve, more slip, implies greater adherence and as a consequence, better performance. This is only applicable to the linear zone since once a certain threshold has been exceeded, it would lead to the destabilization of the vehicle. Considering this, the developed controller is meant to be working the closer to the maximum adherence zone as possible. In any case, a conservative perspective has been adopted in

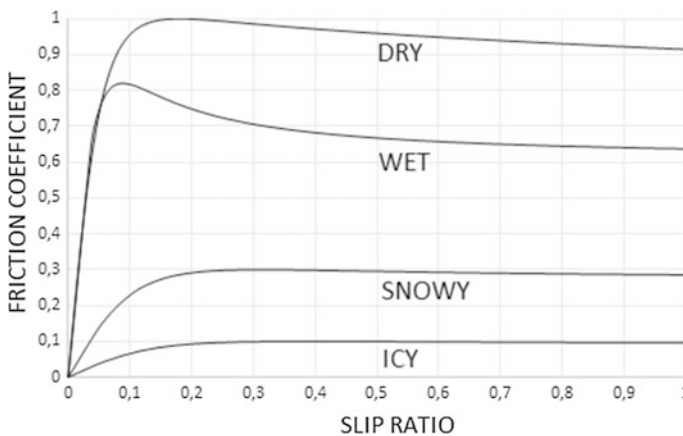


Fig. 1 Wheel slip ratio versus friction coefficient

order not to push the system to the limits of stability and consequently, the controller operates a little bit to the left of the maximum. In this way, the reference signals, have been selected ad hoc for each road condition, maximizing consequently the adherence provided by the controller and avoiding a destabilizing state.

The arduous issue on this regard, is obtaining the right operating point for each friction condition. This can be achieved by means of an estimator as reflected in [18, 19]. In this case, an estimator has not been used but in its place, several adherence curves have been studied particularized for the vehicle subject of study. It has been considered the hypothesis that the information of the friction coefficients is known immediately after a change in the conditions of the surface. These curves have been obtained for four different weather conditions (Dry, wet, snowy, icy).

Other issue that has been considered is the predominant relevance of the velocity and the existence of delays owing to communications [20]. There is a dependence between the velocity and bandwidth of the system due to the fact that the dynamic of the wheel slip is inversely proportional to velocity of the vehicle. Concerning the time delay issue, it has to be taken into consideration when designing the controllers, being this a particularly delicate topic for its implications for the stability of the system.

3 Brake Dynamic Model

3.1 Vehicle Model

The quarter car model has been used to define the dynamics of the braking maneuver. This model consists of a single wheel attached to a mass [1, 20]. As the wheel moves, a friction force arises from the tire-road contact, generating a rotation which propels the car forward. The equations of motion for a braking maneuver are given by (1) and (2).

$$M\dot{V} = -F_x. \quad (1)$$

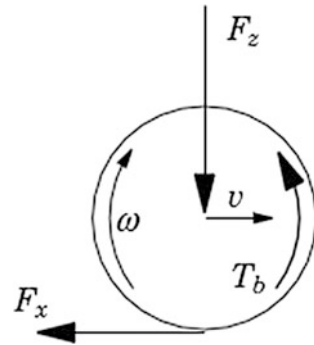
$$J\dot{\omega} = rF_x - T_b \quad (2)$$

where M is the mass of the quarter car, V is the velocity over the ground of the car, ω is the angular velocity of the wheel, F_x is the tire friction force, F_z is the vertical force, T_b is the brake torque, r is the wheel radius and J is the wheel inertia. Figure 2 shows a representation of the quarter car model with the whole set of parameters.

The longitudinal tire slip is defined as follows (3):

$$s_x = \frac{v - r\omega}{v} \quad (3)$$

Fig. 2 Quarter car model



Any of the wheels is locked if its slip is equal to 1 ($\omega = 0$). If the slip is equal to zero, it is what is called free motion ($\omega r = v$). The tire friction force F_x is defined by Eq. (4) which describes a force depending on the vertical force and the friction coefficient which is depicted as a function depending on various parameters.

$$F_x = F_z \mu(s_x, \mu_h, \alpha) \tag{4}$$

where μ_h is the maximum friction coefficient and α is the steering angle. After neglecting α for being in a longitudinal braking scenario, and consequently longitudinal slip is much more prevailing than the lateral slip, we have that the two most significant factors are s_x and μ_h . The resulting equation is:

$$F_x = F_z \mu(s_x, \mu_h) \tag{5}$$

3.2 Tire-Road Interaction

Professor Emeritus Pacejka developed what is called “The Magic Formula” which gives a mathematical approximation for curves as the ones in Fig. 1 [21, 22]. The simplified formula for the longitudinal case for constant coefficients:

$$F_x = F_z D(\mu_h) \sin[C \tan^{-1}(Bs_x - E(Bs_x - \tan^{-1}(Bs_x)))]] \tag{6}$$

where B , C , D and E are coefficients dependent on the tire characteristics, the velocity of the car, the vertical load and the road characteristics. Table 1 contains average value for the peak factor, B , C and E for different road conditions at a velocity of 50 km/h.

For this article, the friction curves have been obtained for four possible conditions as it was mentioned in the Problem Statement section. The slope of the linear zone as well as the limit of stability were used for tuning the controller parameters and for obtaining the reference applicable to each condition. Table 1 contains the

Table 1 Average value of peak factor B, C, E, D (μ_h) = $D\mu_h$ and reference signal

Road surface	D = μ_h	B	C	E	Ref
Dry asphalt	1	10	1.9	0.97	0.1
Wet asphalt	0.82	12	2.3	1	0.08
Snow	0.3	5	2	1	0.14
Ice	0.1	4	2	1	0.11

four different references that have to be applied to the input of the controller in order not to destabilize the vehicle. These values are typical sets of constant Magic Formula coefficients for common road conditions.

3.3 Model Characteristics

For the sake of concreteness, here are presented only the end equations of the model after all the simplifications considered. In [20] the whole explanation of the model can be examined.

$$\dot{V} = \frac{-F_z \mu_h}{m} \tag{7}$$

$$\dot{s}_x = \frac{-\beta m_i s_x + \alpha T_b(t - T)}{v} \tag{8}$$

where $\alpha = r/J$, $\beta = F_z r^2/J$ are constant coefficients and T is the communication delay set to 7 ms. If the systems operates in the linear zone, a linearization can be applied to the model. That will be achieved by selecting a good reference input.

$$G(s) = \frac{s_x(s)}{T_b(s)} = \frac{\alpha e^{-Ts}}{vs + \beta m_i} = \frac{\frac{\alpha}{v} e^{-Ts}}{s + \frac{\beta m_i}{v}} = \frac{\frac{\alpha}{v} e^{-Ts}}{s + p} \tag{9}$$

p is the pole of the transfer function, so whenever the system operates in the area to the right of the maximum of the curve, the slope will be negative which implies the existence of a positive pole and therefore, an unstable scenario. This is due to the fact that m_i is the slope of the curve in the linear zone.

The bandwidth of the linear model directly depends on the velocity. The higher the velocity, the narrower the bandwidth will be. To get a constant bandwidth regardless of the velocity, the error is multiplied by the velocity before being introduced to the controller. In this way, the bandwidth can be kept to 45° [20].

$$\omega_c = p \sqrt{\frac{2}{pT}} - 1 \quad pT \leq 0.3 \rightarrow MF = 45^\circ \tag{10}$$

The data used for this article are $J = 1.5 \text{ kg m}^2$, $r = 0.34 \text{ m}$, $\alpha = 0.2267 \text{ kg/m}$, $M = 433.75 \text{ kg}$, $F_z = 4463.6 \text{ N}$, $\beta = 293.3927 \text{ m/s}^2$, $T_b = 1500 \text{ Nm}$, $m_i(\text{dry}) = 9.5419$, $m_i(\text{wet}) = 14.7941$, $m_i(\text{snow}) = 1.8373$ and $m_i(\text{ice}) = 0.6270$. These are average values for an Audi A8 and for common road conditions.

4 Controllers and Design Criteria

A zero-crossing reset controller, a fixed-band reset controller, a variable band reset controller and a PI controller have been tested. The layout of the different elements of the simulation chain is exactly the same for all the controllers.

The PID (proportional-integral-derivative) are certainly the most utilized method of regulation, to the extent of meaning 90 % of all the control loops, as reported in [23]. Usually, the derivative action is not taken into consideration and as a result, the most typical controller structure is a PI.

The PI+CI controller combines the advantages of a PI controller with those derived from the use of reset control [13]. PI+CI is a particular case of a PI controller with an extra degree of freedom. So that, the right tuning of the PI+CI can yield better results than those produced by a PI. The equations of a PI+CI can be seen in (11).

$$PI + CI = \begin{cases} \dot{x}(t) = \begin{pmatrix} 0 & 0 \\ 0 & 0 \end{pmatrix} x(t) + \begin{pmatrix} 1 \\ 1 \end{pmatrix} e(t) & \text{if } e(t) \neq 0 \\ x(t^+) = \begin{pmatrix} 1 & 0 \\ 0 & 0 \end{pmatrix} x(t) & \text{if } e(t) = 0 \\ u(t) = K_I(1 - p_r \quad p_r)x(t) + K_P e(t) & \end{cases} \quad (11)$$

where $e(t)$ and $u(t)$ are the input and output signals, respectively, and $x(t) \in \mathbb{IR}_2$ is the state vector. An entire definition and description of the PI+CI can be found in [14] in Chap. 5 where the whole set of equations of a PI+CI can be revised.

The layout of the whole control loop (plant+controller) can be seen Fig. 3. As it can be observed, there are five different blocks which are, from left to right, the product block that scales the error signal, the controller block, which includes the control algorithm, a saturation block, which models the limits of the electromechanical actuators, the time delay block and the non-linear plant model (7), (8). The product block compares the reference input to the output signal and multiplies this difference by the velocity of the car over the ground. Once this has been calculated its result is introduced into the controller. Reset controllers work like regular PI controller but with a mechanism triggered whenever the error holds a certain condition. Depending on the type of reset implementation there will be three reset strategies.

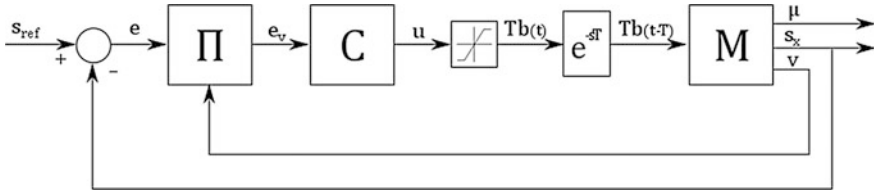


Fig. 3 Control loop blocks

The PI has a single set of parameters for the whole range of operation. The different PI+CI implementations, have exactly the same set of parameters for the base PI (K_P and K_I). All reset controllers have different reset ratios (p_r) for each operating condition. The change of the reset ratio, shared for all the reset controllers implemented, responds to a gain-scheduling strategy which uses an optimum value for each individual condition. The only thing that varies from PI+CI to another is the reset band. PI+CI 1 uses zero crossing band, PI+CI 2 uses a fixed band and PI+CI 3, a variable reset band.

For the PI tuning, the linear model represented by (9) has taken on board and the parameters for the different friction conditions have been calculated based on the curves in Fig. 1. A root locus and frequency domain analysis have been performed for the tuning of the PI. This process was repeated for all the different road surfaces collected in Table 1 as well as for different velocities. Once the different PI parameters were calculated, the next step was finding a unique combination of parameters that equally stabilizes all the operating conditions.

Although there are different works on the literature which tackle the tuning of the reset ratio [24–26] they focus their interests on linear systems so that, they cannot be applied straightforwardly, even if for the PI controller tuning a linear approximation was used, for the reset ratio, they are not suitable. So, for the tuning of the reset ratio, the flatter the response signal can be achieved, the better. The principle consists of getting that the error signal gets to zero as fast as possible once it has first crossed the reset band. Considering that no analytical expression yields good results, this has been done by means of simulation. So for the different road surfaces and velocities, an optimum reset ratio has been obtained.

The band selected for the comparative it is that works better within all the working limits. Regardless of the band chosen, the use of advance reset fits clearly with the system features, i.e., changing reference and time delay. Equation (12) presents the reset condition for an advanced band reset controller where only the time delay must be estimated:

$$h \frac{de}{dt} + e(t) = 0 \tag{12}$$

5 Simulation Results

The vehicle subjected to study is an Audi A8, whose technical data were used for the design and implementation of the controllers. The brake maneuver that is presented on this paper consists of a straight road segment with changing friction. The car starts with a velocity of 45 m/s and as time goes by and the car starts braking, the road conditions change twice. First, from a dry to a snowy segment to be followed for a new change to a wet segment. This sequence, despite the fact that this maneuver is not likely to happen in reality, it has been chosen to be presented here as a strong evidence of the effectiveness of the reset control with a variable band because of the severity of the conditions, being the most critical in terms of control. Table 2 collects the different parameters for the controllers. p_{r1} refers to the first conditions (dry asphalt and 45 m/s), p_{r2} refers to the second conditions (icy road and 35 m/s) and p_{r3} has to do with the final conditions (wet road and 10 m/s). Table 2 also contains the braking distances, braking times and IAE for the same maneuver and for the four separate controllers. Although a slight improvement is perceptible in the braking distances, the main enhancements can be seen in the following figures. Figure 4a–c presents the wheel slip for the whole course of the braking maneuver. As it can be noticed, the advanced reset controller is the one which yields the best result just like the overshooting and the rise time for a

Table 2 K_p , K_I and p_r for the four controllers

Controller	K_p	K_I	p_{r1}	p_{r2}	p_{r3}	Distance (m)	Time (s)	IAE
PI	240	20,000	0	0	0	264.9854	11.8822	1.4884
PI+CI 1	240	20,000	0.46	0.65	0.01	264.6053	11.71	1.2419
PI+CI 2	240	20,000	0.46	0.65	0.01	264.6027	11.8541	1.2432
PI+CI 3	240	20,000	0.46	0.65	0.01	264.6018	11.8539	1.2222

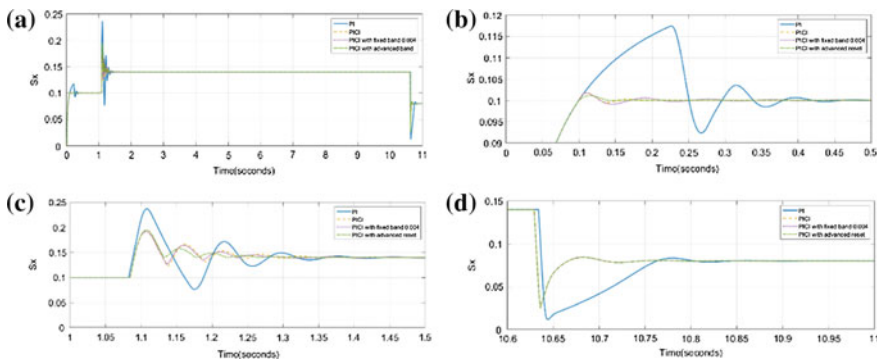


Fig. 4 Wheel slip for a longitudinal braking maneuver. **a** Wheel slip versus Time. **b** Reference change to 0.1. **c** Reference change to 0.14. **d** Reference change to 0.08

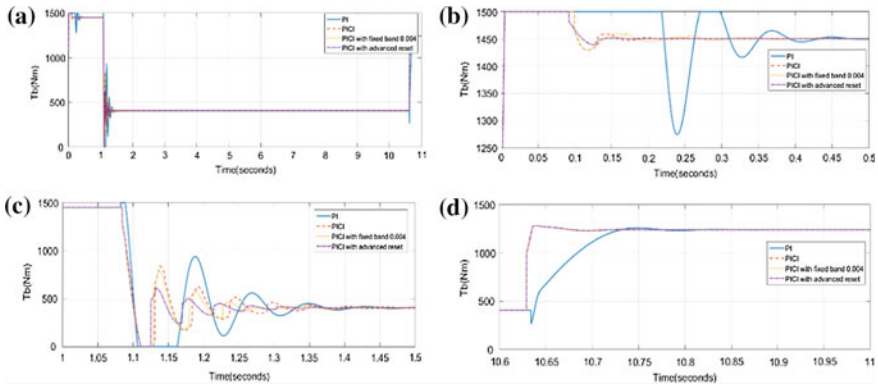


Fig. 5 Braking torque for a longitudinal braking maneuver. **a** Braking torque versus Time. **b** Reference change to 0.1. **c** Reference change to 0.14. **d** Reference change to 0.08

reference change proves. For a detailed view of each reference change have a look at figures b, c and d. The braking torque can be observed in Fig. 5. As it can be seen, the transient state is also improved since the overshooting is less prominent.

6 Conclusion

The objective of this work has been outperforming the prior state-of-the-art works on wheel slip control with reset control by using different reset bands. This has been achieved by implementing three gain-scheduled wheel slip controllers (comparing all of them to a conventional PI controller). The improvements originate in the fact that a gain-scheduled strategy, for the reset ratio, is considered as well as the use of reset bands which fits better for a system like this due to the changing references and the presence of a time delay. The preceding works on the topic, only employed one single reset ratio for the controller. This makes the tuning much more difficult since with one set of PI parameters and just one reset ratio, the controller has to be fully operational for all the possible situations, so that it will be difficult to set a trade-off between the different cases. On the contrary, with the addition of a different reset ratios and a reset band, a fine adjustment is achieved for each braking condition what leads to better responses. Undoubtedly, the most effective control strategy is the use of a variable reset band. Although the use of a fixed reset band can also yield good results, finding one band that fits for all the operating range is much more intricate since there will be some operating conditions for which the band will be better optimized than others.

Acknowledgments This work is supported by MINECO, Spain, under Project DPI2013-47100-C2-P.

Bibliography

1. Johansen, T.A., Petersen, I., Kalkkuhl, J., Lüdemann, J.: Gain-scheduled wheel slip control in automotive brake systems. *IEEE Trans. Control Syst. Technol.* **11**(6), 799–811 (2003)
2. De Castro, R., Araujo, R.E., Freitas, D.: Wheel slip control of EVs based on sliding mode technique with conditional integrators. *IEEE Trans. Ind. Electron.* **60**(8), 3256–3271 (2013)
3. Freeman, R.: *Robust Slip Control for a Single Wheel*. University of California, Santa Barbara (1995)
4. Yu, J.: A robust adaptive wheel-slip controller for antilock brake system. In: *Proceedings of the 36th IEEE Conference on Decision and Control* (1997)
5. Yi, J., Álvarez, L., Horowitz, R., De Wit, C.C.: Adaptive emergency braking control using a dynamic tire/road friction model. In: *Proceedings of the 39th IEEE Conference on Decision and Control* (2000)
6. Lüdemann, J.: *Heterogeneous and Hybrid Control with Application in Automotive Systems*, University of Glasgow (2002)
7. Liu, Y., Sun, J.: Target slip tracking using gain-scheduling for antilock braking systems. In: *Proceedings of the 1995 American Control Conference* (1995)
8. Clegg, J.: A nonlinear integrator for servomechanisms. *Trans. Am. Inst. Electr. Eng. Part II: Appl. Ind.* **77**(1), 41–42 (1958)
9. Horowitz, I.: *Quantitative feedback theory*. In: *IEE Proceedings D Control Theory and Applications* (1982)
10. Horowitz, I., Rosebaum, P.: Non-linear design for cost of feedback reduction in systems with large parameter uncertainty. *Int. J. Control* **21**(6), 977–1001 (1975)
11. Seron, M.M., Braslavsky, J.H., Goodwin, G.C.: *Fundamental Limitations in Filtering and Control*. Springer Science & Business Media (2012)
12. Åström, K.J.: Limitations on control system performance. *Eur. J. Control* **6**(1), 2–20 (2000)
13. Baños, A., Vidal, A.: Definition and tuning of a PI+CI reset controller. In: *Control Conference (ECC), 2007 European* (2007)
14. Baños, A., Barreiro, A.: *Reset Control Systems*. Springer Science & Business Media (2011)
15. Vidal, A., Baños, A.: QFT-based design of PI+CI reset compensators: application in process control. In: *16th Mediterranean Conference on Control and Automation* (2008)
16. Vidal, A., Baños, A.: Reset compensation for temperature control: experimental application on heat exchangers. *Chem. Eng. J.* **159**(1), 170–181 (2010)
17. Delgado, E., Barreiro, A., Díaz-Cacho, M., Falcón, P.: Wheel slip reset controller in automotive brake systems. In: *International Electric Vehicle Conference (IEVC)*. IEEE, Florence, Italy (2014)
18. Lee, C., Hedrick, K., Yi, K.: Real-time slip-based estimation of maximum tire-road friction coefficient. *IEEE/ASME Trans. Mechatron.* **9**(2), 454–458 (2004)
19. Rajamani, R., Phanomchoeng, G., Piyabongkarn, D., Lew, J.Y.: Algorithms for real-time estimation of individual wheel tire-road friction coefficients. *IEEE/ASME Trans. Mechatron.* **17**(6), 1183–1195 (2012)
20. Solyom, S., Rantzer, A., Lüdemann, J.: Synthesis of a model-based tire slip controller. *Veh. Syst. Dyn.* **41**(6), 475–499 (2004)
21. Pacejka, H.B., Bakker, E.: The magic formula tyre model. *Veh. Syst. Dyn.* 1–18 (1992)
22. Pacejka, H.B.: *Tire and Vehicle Dynamics*. Elsevier (2005)
23. Åström, K.J., Hägglund, T.: The future of PID control. *Control Eng. Pract.* **9**(11), 1163–1175 (2001)
24. Baños, A., Vidal, A.: Design of PI+CI Reset Compensators for second order plants. In: *IEEE International Symposium on Industrial Electronics* (2007)
25. Mercader, P., Baños, A.: Robust PI compensators design for FOPDT systems with large uncertainty. In: *14th International Conference on Control, Automation and Systems (ICCAS)* (2014)
26. Davó Navarro, M.: *Analysis and Design of Reset Control Systems* (2015)

Design and Development of Control System for Railway Cable Laying

Valentín Cañas, Andrés García, Javier de las Morenas
and Jesús Blanco

Abstract In this work is studied the automation of a railway cable laying system using a PLC as regulator, where the objective is to keep as stable as possible the stress of the cable being laid. As the system was completely manual, a previous work has been needed in order to set both sensors and actuators so that the system can be electrically controlled. Different tests were done in order to find out the relationship between the different variables, and to propose a regulator algorithm according to these. The obtained results show that the system is properly automated via PLC using the designed regulator.

Keywords Railway · Cable · Laying · Regulator · Control · PLC · PID

1 Introduction

Railway cable laying is the process by which catenary cables are arranged and stressed between anchor points. This process can be performed using different techniques, the most common being based in the use of winch or braking systems.

V. Cañas (✉) · A. García
AutoLog Group, School of Industrial Engineering, University of Castilla-La Mancha,
Ciudad Real, Spain
e-mail: valentin.canas@uclm.es

A. García
e-mail: andres.garcia@uclm.es

J. de las Morenas
AutoLog Group, Mining and Industrial Engineering School of Almadén,
University of Castilla-La Mancha, Almadén, Spain
e-mail: javier.delasmorenas@uclm.es

J. Blanco
AutoLog Group, Polytechnic School of Cuenca, University of Castilla-La Mancha,
Cuenca, Spain
e-mail: jesus.blanco@uclm.es

In the process of laying by winch, a winch is responsible for tightening the wire to achieve the required stress. This is a rather slow process since it is necessary to anchor the winch in each span of lying, but it allows operation in areas of difficult access. It is therefore mainly used in overhead electric power grids and high voltage lines in rural and mountainous areas.

The process of laying by braking is based on a different philosophy. A vehicle carries a cable braking system responsible for stressing the wire while it is moved by the vehicle. This method of cable laying is noticeably faster than the previous one but requires flat and accessible surfaces in order to be carried out correctly. That is why the laying by braking is usual in the electrification of railway lines, and is also easily exportable to tram and trolley lines. The latter method is more flexible and competitive for companies that perform aerial laying of railway catenaries. However, the braking laying process is more complex than the winch laying method, since it is necessary to control more parameters simultaneously, where several of them are related. Thus, a variation in the train speed causes a change in the cable stress.

To summarize, the main objective is to make the stress cable laying to be stable and close to a reference value, enhancing performance [1]. The braking is responsible for stressing the cable, but the variation in the speed of the train that is responsible for transporting the braking and the coil also causes variations in the stress of the cables being laid.

The way in which the problem was temporary solved, before the Autolog Group agreed to develop a method based in PLC (Programmable Logic Controller) to automate the process, was completely manual. It was therefore necessary for an operator to manually regulate the hydraulic valve of the braking system to try to remain laying stress as close as possible to the reference stress value. However, when the pressure was modified by the brake, the stress of the cable had a tendency to exceed the nominal values. Additionally, these oscillations showed to be considerably faster than the responsiveness of operators while trying to mitigate it. Automating the plant solves these problems [1].

Another important aspect to be known is whether the use of a PLC as controller that automates the process of cable laying is valid, as its performance level does not fit well with certain control applications where high speeds are required [2–4]. As mentioned, it is known that the process is difficult to control manually; and meanwhile, the partner company provided a PLC that offers minimum cycle times of 0.1 s while acting as regulator. Knowing that human reaction capacity is estimated to be in a similar order magnitude of a tenth of a second, it will be interesting to find out how the cycle time performance of the controller affects to its ability to dampen the overshoots of the system. This will allow to determine whether this PLC is suitable for the automation of the cable laying system, or instead, it is necessary to propose a different controller.

Furthermore, it is interesting to analyze not only the action of the braking, but also how the train speed affects the stress cable laying. It will be necessary to determine if there is a substantial difference in the results considering the variations due to changes in the speed. It has been assumed that the speed variations affect the

output of the system at a degree that can be accepted by the regulator as mere disturbances, but it should also be considered that the performance of the controller could not be enough to correct this effect adequately without taking account of the speed value. This fact will be analyzed.

2 Problem Statement

This section shows in detail the railway cable laying system in its initial state. It also shows the initial steps carried out in order to physically implement a controller with the ability to control the plant. The railway cable laying system is housed on a train, as shown in Figs. 1 and 2. The laying system consists of a hydraulic braking, several coils of catenary cable, and an arm that sets the cable to the required laying height.



Fig. 1 Train with braking machine and cable coils

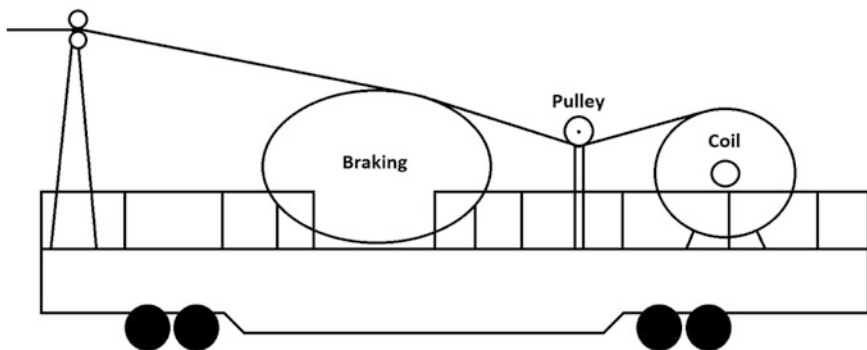


Fig. 2 Diagram of main elements in train

The hydraulic braking is responsible for fixing the cable stress through the laying operation. The control of the pressure that is exerted on the cable is carried out by a manual proportional valve, which modifies the pressure of the hydraulic circuit of the braking.

The resulting operating process for the laying cable results hard to manage. As all control operations must be made by the workers in charge of the train through the valve of the hydraulic braking. They have to constantly visually check, through pressure gauges, that the force exerted on the cable laying is constant and within specifications. This laying force may be different in each case, according to specifications, and values can be located between 10 and 25 kN depending on various factors such as the distance between supports, the cable section and the deflection of the catenary. As mentioned, the greatest difficulties in the process of laying are: the inter-dependence of the variation in the speed of the train with the stress of the cable laying, and the fast transient overshoot produced at each change in the position of the valve.

The laying speed of to the train, peaks at 4 km/h. Higher laying speeds make the process unnecessarily fast and hard to control by operators. The train has an approximate mass of 11,000 kg and the maximum acceleration in laying operation is 0.15 m/s^2 . In order to carry out the implementation of a controller, the plant was prepared so that it could be electrically controlled. That is, the regulator can read the required information from the system through the required sensors and can regulate it through actuators/valves. For this purpose, various modifications were performed.

The initial hydraulic valve used to act on the brake was replaced by a proportional solenoid valve, which controls the pressure of the system electrically so as to have an electrically controlled hydraulic braking system.

A rotation sensor with 200 pulses per revolution at a 10 cm diameter pulley was also installed between the coil of wire and the brake. This pulley was responsible for keeping stressed the wire between both devices at all times, absorbing the vibrations due to the inertia of the coil. At the output of this rotation sensor a conversion step from frequency to voltage based on LM2907N chip was set, so that a voltage signal proportional to the wire speed was available.

The braking has a gauge in order to visually provide information of the force applied on the cable by directly measuring the output pressure of the hydraulic braking system, since force and pressure are proportionally related. In order to have an electrical measure of the pressure, a pressure sensor with proportional voltage output was installed in the hydraulic circuit of the brake.

Additionally, a board based on the TDA2030 chip with adjustable gains by potentiometers was installed. Thus the signals of the plant can be adapted to the required levels of work on the implemented controller.

As it can be appreciated, through this series of actions a plant with electrical interface for both detecting the state thereof (cable stress and speed) and for acting upon it (control on the opening of the valve) was obtained. Therefore, this interface offers to any regulator that is able to work with analogue voltage signals, hardware capacity to carry out the control of this railway cable laying system.

3 Design and Implementation of the Regulator

The regulator, which closes the open loop of the system, is implemented in a PLC Siemens S7-1200 mounted in a control cabinet. This PLC has a PID control library, which allows implementing a PID regulator following the transfer function showed in the expression 1 [5].

$$y(s) = K_p \left[(b w(s) - x(s)) + \frac{w(s) - x(s)}{T_I s} + \frac{T_D s}{a T_D s + 1} (c w(s) - x(s)) \right] \quad (1)$$

- y* Output value of PID
- x* Output value of the process
- w* Setpoint
- s* Laplace operator
- K_p* Proportional gain
- a* Derivative delay coefficient
- T_I* Integral time
- b* Proportional weight
- T_D* Derivative time
- c* Derivative weight.

3.1 System Identification

In order to perform a theoretical controller design of the system, the first step was to analyze its real behavior in order to develop a model. Therefore, the unitary step response of the plant in open loop was obtained [6] (Fig. 3).

The input signal corresponds to the voltage applied to the hydraulic proportional valve, before the adjustable gains board, and the output signal gives the measure of the pressure of the hydraulic system, after the adjustable gains board. Both gains were adjusted in that board in order to have the same voltages in steady state. The measure was taken with a Tektronix MSO 4032 oscilloscope. The open loop tests were performed at a constant laying speed of 1 km/h.

In Fig. 4 it is possible to see how the plant behavior (in red) resembles that of a delayed standard second order system with overshooting. The delay was estimated to be 0.096 s. The non-delayed part of the response was estimated using the nonlinear least squares Gauss-Newton method to determine the best fitting second

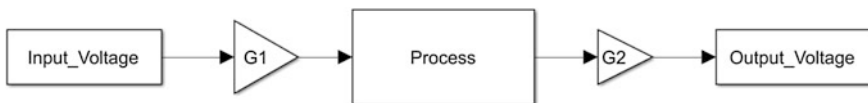


Fig. 3 Open loop tests diagram block

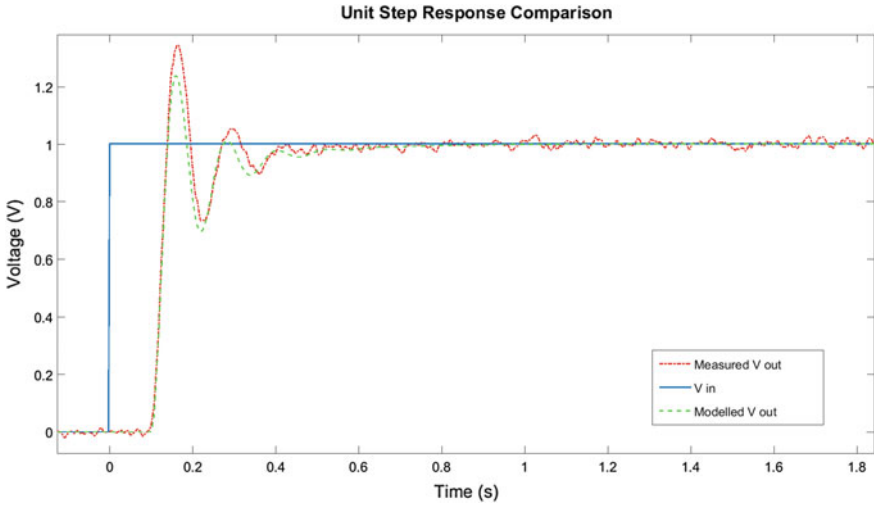


Fig. 4 Open loop step responses comparison

order transfer function. The obtained transfer function is shown in expression 2, which got a normalized root mean square error (NRMSE) value of 90.5 %.

$$TF(s) = \frac{1}{0.0343 s^2 + 0.0912 s + 1} \tag{2}$$

Given the symmetrical shape of the oscillations, it makes sense to consider an additional pole and zero pair such that the model fits better to the behavior of the real system. This leads to a more accurate regulator design. Using the same algorithm considering a transfer function with three poles and one zero, the NRMSE obtained is 93.45 %. Therefore, the transfer function corresponding to the identification of the plant model, including an estimated delay of 0.096 s, is shown in expression 3.

$$TF(s) = e^{-0.096s} \frac{1.598 s + 1}{0.06852 s^3 + 0.2167 s^2 + 2.091 s + 1} \tag{3}$$

In Fig. 4 is shown a comparison of the step response of the real plant. The red curve corresponds to the real behavior and the green to the model shown in expression 3. It can be appreciated that both systems have a similar response.

3.2 Regulator Design

Having defined the transfer function model of the system, a PID controller was designed. A PID regulator with derivative filter is calculated following the formula

for Ziegler-Nichols step response. This results in the PID controller whose transfer function is shown in expression 4.

$$PID(s) = 5.56 K_p \frac{1 + 0.18 s + (0.09 s)^2}{s(1 + 0.0043 s)} \quad (4)$$

The last step in designing the PID controller is calculating the value of K_p critical for stability. Here it is important to remember that the implementation of the PID in the PLC runs discretely with a period fixed in 0.1 s. Treatment of the entire system as continuous-time to find the values of the PID controller is sometimes feasible, but this approximation cannot be made when it comes to analyzing the stability of the closed loop system.

Thus, the limit value of K_p for system stability and the gain value, which set the system poles in the Z plane within the unit circle, are obtained. This results in a value of the proportional gain of PID limited to 0.554. Therefore, adjusting K_p to a lower value allows obtaining a stable system avoiding the problem of lack of damp typical of the Ziegler-Nichols formula. After some empirical experiences a value of $K_p = 0.31$ was finally chosen.

3.3 Implementation of a PID in the PLC

The expression of the PID controller provided by the manufacturer of the PLC (see expression 1) can be written as shown in expression 5.

$$\frac{y(s)}{w(s) - x(s)} = K \left[1 + \frac{1}{T_I s} + \frac{T_D s}{a T_D s + 1} \right] \quad (5)$$

supposing $b = c = 1$

As a result of expressions 4 and 5, it is possible to obtain the value of the two remaining parameters in expression 5, whose values are shown in 6.

$$a = 0.1, T_D = 0.045, T_I = 0.18 \quad (6)$$

Therefore, the values that have to be introduced in the PLC to tune the PID controller corresponding to this design are as follows in (7) (Fig. 5).

$$K = 0.31, T_D = 0.045, T_I = 0.18, a = 0.1, b = 1, c = 1 \quad (7)$$

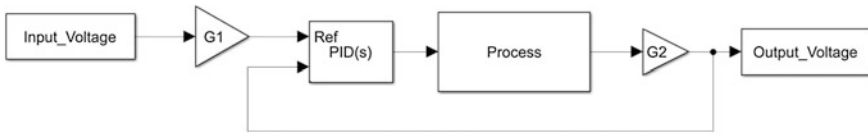


Fig. 5 Regulated system diagram block

4 Results

Once the regulator set in the system and programmed the PID, the response of the system was measured via oscilloscope. Figure 6 shows the measured output (red) for a cycle time of operation (T_{cycle}) of 0.3 s for the regulator output.

The same test was repeated for a cycle time of operation of 0.1 s for the regulator output (see Fig. 7). As can be observed, in both cases the calculated model allows us to predict in an accurate way the response of the real system. The response in the case of a time of operation of 0.1 s shows to be clearly better than in the case of 0.3 s, as overshoot is much lower and the response is faster.

Another test was done in order to determinate how the speed variation affects the system output. The results are shown in Fig. 8.

The regulator is able to correct the error induced by the speed variation so that the maximum error of the output is lower than 10 %. As can be noticed, the correction of the regulator corresponds to the same shape than the acceleration of the train.

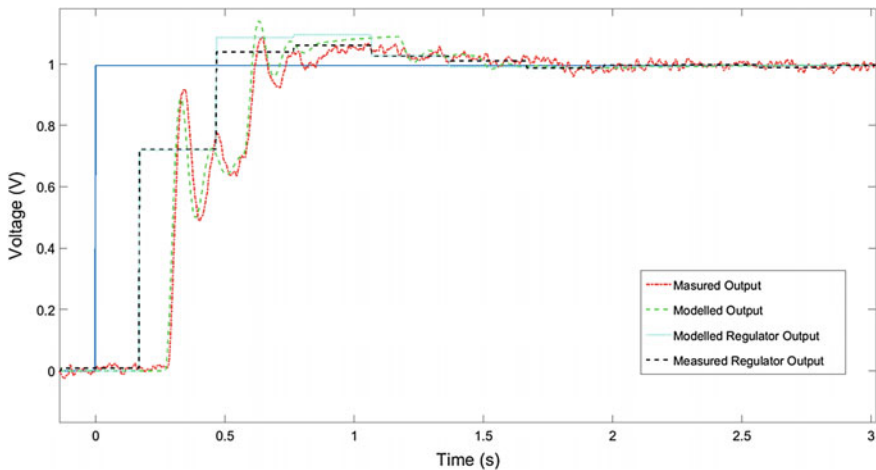


Fig. 6 Closed loop step response for $T_{cycle} = 0.3$ s

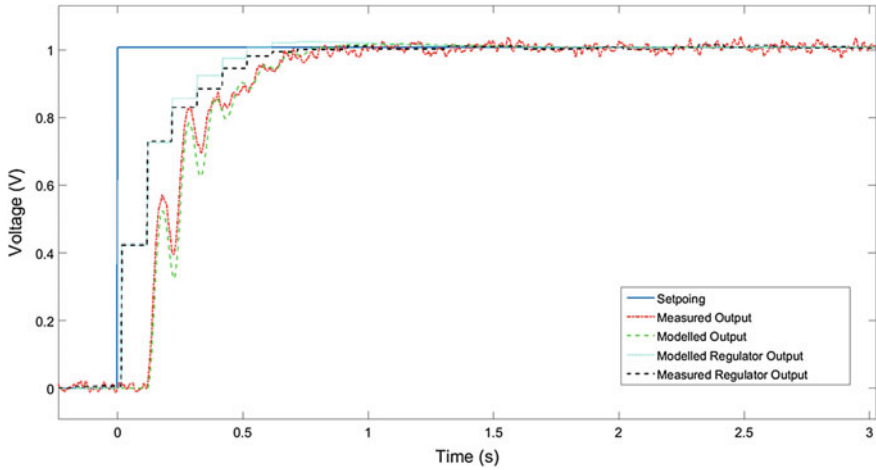


Fig. 7 Closed loop step response for $T_{cycle} = 0.1$ s

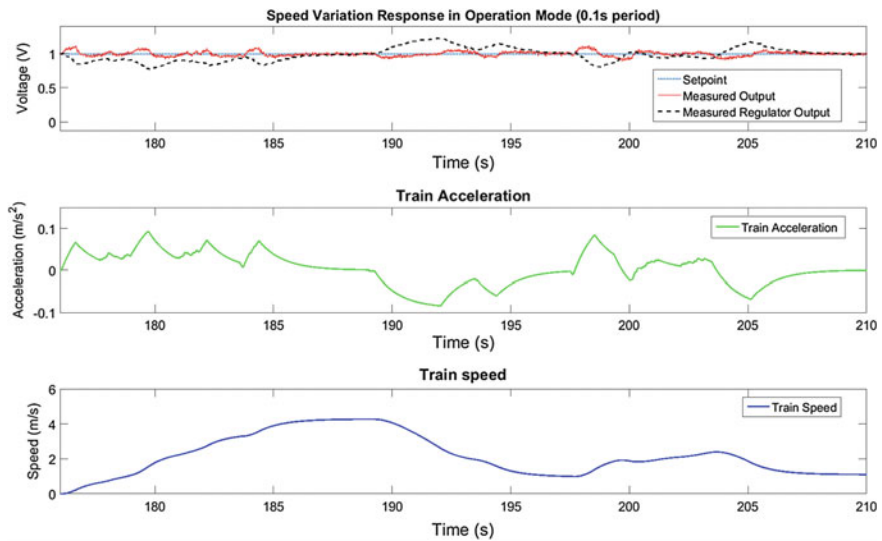


Fig. 8 Speed variation response in operation mode ($T_{cycle} = 0.1$ s)

5 Conclusion

In this work, the automation of a railway cable laying system has been achieved. The operating requirements have been met using a PID regulator via PLC.

When the system is set to work with a time of operation of 0.1 s, the output of the system does not show overshoot and has a settling time lower than 1 s, which

improves the minimum operating requirements. However, if the regulator is set to work at 0.3 s, there is an overshoot near to 15 % and settling time is bigger than 1 s. This shows why operators had problems to manually control the system without overshoots, as the time of reaction lays within that order of magnitude.

The regulator is also able to work in conditions of variable speed. As tested, maximum acceleration of train in laying operating mode allows the regulator to avoid errors bigger than 10 %, which fit the minimum operating requirements.

In spite of this good results, the following improvements have been proposed as possible in future works in order to enhance the automatic railway cable laying system as it is being considered to be exported to the building of large high speed railways in Saudi Arabia: considering different options than PLC, like industrial PC or embedded solutions, analyzing different regulator algorithms and developing a remote wireless control.

Acknowledgments This work is supported by the resolution of 31/07/2014, published by the University of Castilla-La Mancha, which establishes the regulatory bases and the call for pre-doctoral contracts for the training of researchers under the Plan Propio de I+D+i, co-financed by the European Social Fund. [2014/10340]

References

1. Choi, J.K., Nishida, S., Yokobiki, T., et al.: Automated cable-laying system for thin optical-fiber submarine cable installation. *IEEE J. Oceanic Eng.* **40**(4), 981–992 (2015)
2. Liu, X.M., Wang, S.Q.: Application of the PID control in mine calorific value regulating system based on PLC. *Adv. Des. Res. Manuf.* **605–607**(Pts 1–3), 1806–1809 (2013)
3. Mu, X.M., Wu, L., Sun, Y.F., et al.: The PID control system of flow measuring based on PLC. In: *Discovery, Innovation and Communication—5th CSAA Science and Technique Youth Forum*, pp. 76–79 (2012)
4. Wei, Y.H., Xu, C., Wang, G.R., et al.: The design of control system for motion platform based PLC. *Intell. Mater. Mechatron.* **464**, 222–228 (2014)
5. Xing, M.R., Zhang, J., Zhang, X.D.: The design of constant pressure water supply control system based on S7-200 PLC. *Mater. Process. Manuf III* **753–755**(Pts 1–4), 1665–1669 (2013)
6. Piquereau, J.Y., Trigessou, J.C.: Transfer-function identification through an examination of unit step response. *Automatisme* **21**(8–9), 263–267 (1976)

Mobile Sensing System for Cycling Power Output Control

José A. Afonso, Filipe J. Rodrigues, Delfim Pedrosa
and João L. Afonso

Abstract This paper describes the development of a novel cycling effort control system that contributes to promote the users' physical health and mobility. This system controls the motor assistance level of an electric bicycle in order to ensure that the cyclist's power output remains inside the desired limits, regardless of changes in variables such as the speed of the bicycle or the slope of the terrain. The power output is monitored using a sensor device that provides raw torque and cadence data, whereas a smartphone application processes these data, implements the effort control algorithm and provides the user interface. Modules on the bicycle handle the data acquisition, wireless communication with the smartphone and driving of the motor assistance level. Experimental results validate the effectiveness of the implemented power output control system.

Keywords Effort control · Power output · Mobile sensing · Electric bicycle

1 Introduction

Mobile sensing is an emerging R&D area focused on the collection and processing of data from sensors located inside and/or around mobile devices [1–3]. One of the potential applications of these systems is the cycling effort control. Cyclists frequently exercise at different intensity levels depending on the intended goals.

J.A. Afonso (✉) · F.J. Rodrigues
CMEMS-UMinho R&D Center, University of Minho, 4800-058 Guimarães, Portugal
e-mail: jose.afonso@dei.uminho.pt

F.J. Rodrigues
e-mail: a58664@alunos.uminho.pt

D. Pedrosa · J.L. Afonso
Centro ALGORITMI, University of Minho, 4800-058 Guimarães, Portugal
e-mail: delfim.pedrosa@algoritmi.uminho.pt

J.L. Afonso
e-mail: joao.l.afonso@algoritmi.uminho.pt

A common approach is to divide the exercise into different intensity zones, for example, below the lactate threshold (LT), between LT and the onset of blood lactate accumulation (OBLA4), and above OBLA4. These zones are usually calculated based on the measurement of the power output or heart rate [4, 5].

Mobile sensing systems applied to cycling include the Copenhagen Wheel project [6], the Biketastic platform [7] and the BikeNet project [8]. These systems use different sensors (accelerometer, magnetometer, microphone, thermistor, CO₂, CO, NO_x, torque, etc.), mobile operating systems (Android and iOS) and wireless networks for communication between the smartphone and the external sensors (IEEE 802.15.4, Bluetooth, etc.).

In [9], the authors present a cyclist's heart rate control system for a bicycle equipped with a Continuously Varying Transmission (CTV), composed by a heart rate monitor, a smartphone and an Electronic Control Unit (ECU), which communicate with each other via Bluetooth. The smartphone is responsible for the heart rate control algorithm, whereas the ECU executes the low level CTV control. In [10], the authors describe a system designed to maintain a continuous level of exercise intensity around the aerobic threshold, through the control of the motor assistance of an electric bicycle. This system is based on the monitoring of pedaling rate and the oxygen uptake (using an oxygen mask). Unlike these systems, this work proposes a novel effort control system for control of the cyclist's power output, based on the measurement of the torque and cadence.

The system proposed in this paper allows the provision of automatic effort control, based on the use of an electric bicycle and a smartphone, in order to assure that the cyclist's power output remains inside the desired limits, regardless of changes in variables such as the slope of the terrain or the speed of the bicycle, contributing to promote the users' physical health and mobility.

This paper is organized as follows. Section 2 presents an overview of the components of the developed system and their interaction. Section 3 describes the smartphone application. Section 4 presents results from the experimental tests and the corresponding discussion. Finally, Sect. 5 presents the conclusions and future work.

2 System Overview

The main components of the proposed system are an Electric Bicycle (EB) and a smartphone. The EB used for the implementation and evaluation of this system is a prototype developed at the University of Minho (Fig. 1). In addition to the original EB components, this system introduces a torque and cadence sensor, a central processing module and a Bluetooth gateway. The rear wheel support was used during the laboratory tests.

Figure 2 presents a detailed view of the interaction between the different blocks of the system. The microcontroller of the central processing module uses one ADC to read the torque signal and another one to read the battery level. A GPIO pin was configured to trigger an interrupt each time a pulse is generated by the cadence signal. These values are pre-processed in the microcontroller and aggregated into a

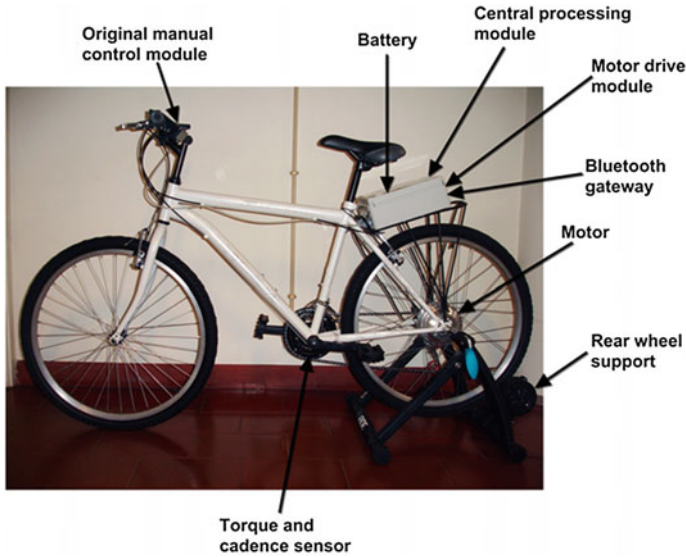


Fig. 1 Electric bicycle used in this work with the installed components

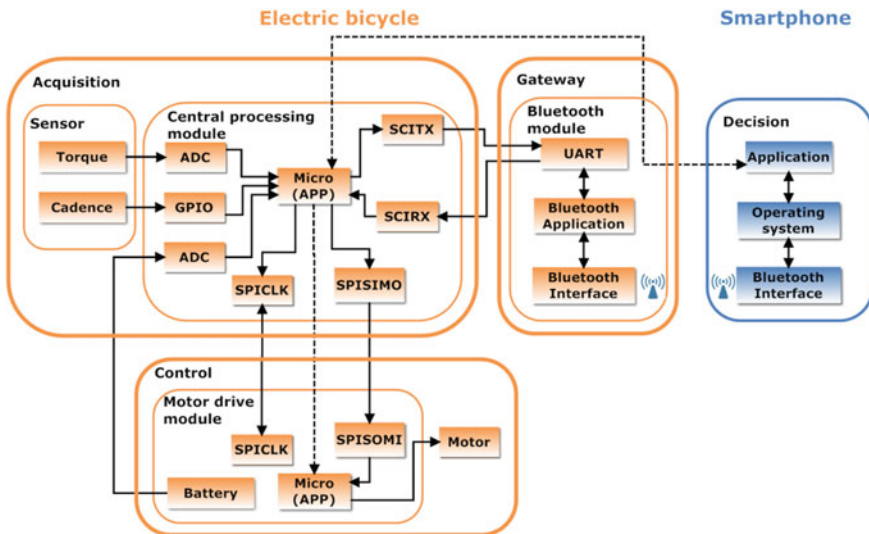


Fig. 2 Block diagram of the implemented system

data frame, which is sent to the Bluetooth gateway. This microcontroller uses its Serial Communication Interface (SCI) to communicate with the gateway, and its Serial Peripheral Interface (SPI) to communicate with the motor drive module. The Bluetooth gateway communicates with the smartphone using its radio interface.

The torque and cadence sensor was placed inside of the crankset, which ensures protection against external environment factors, and its standard dimensions allow compatibility with most types of bicycles. This device generates a linear analog torque signal in the range from -200 to $+200$ Nm. It also generates pulses as the pedal is rotated, which enable the calculation of the cadence.

The smartphone application processes the received data and implements the power output control algorithm, which decides the required motor assistance level in real-time, based on the measured power output and the thresholds specified by the user.

Figure 3 represents the information flow between the components of the system. After the authentication with central processing module of the bicycle, the

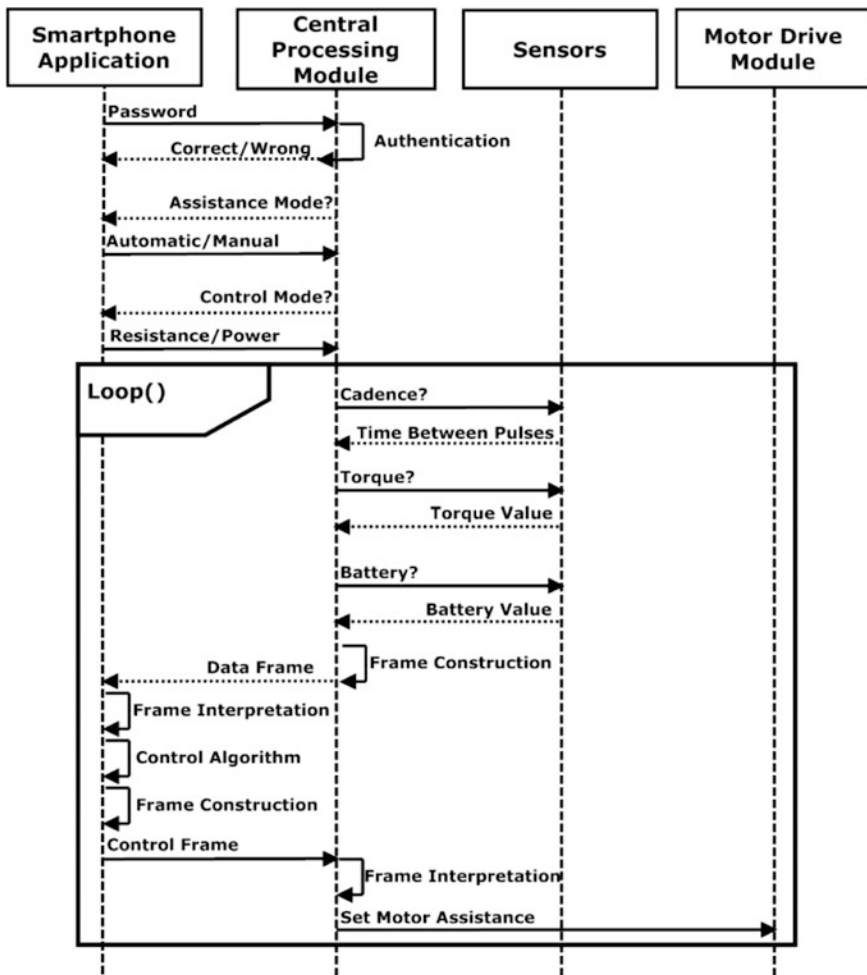


Fig. 3 Sequence diagram of information flow in the developed system

smartphone application gives the user the choice of the assistance mode: Manual mode, which allows the user to increase/decrease the motor assistance level through two buttons on the display; or Automatic mode, which allows the user then chooses the control mode: resistance mode, which considers only the measured torque; or power mode, which considers the power output calculated using both the cadence and the torque.

When the automatic mode is chosen, the application executes a loop code periodically. During this phase, the central processing module measures the time between pulses generated by the sensor, the torque and the EB battery level, and sends these data to the smartphone application, which calculates the cycling cadence, executes the effort control algorithm, and sends the decision back to the central processing module, which finally transmits it to the motor drive module to adjust the assistance level.

3 Smartphone Application

The smartphone application was developed and tested using an HTC Sensation Android smartphone. This application processes the data generated by the torque and cadence sensor and executes the power output control algorithm.

Taking into account that the sensor generates 8 pulses per full rotation of the pedal, the cadence, in rpm, may be calculated by counting the number of pulses (N_p) during a given sampling period (T_s), through the use of the following equation:

$$C = \frac{60 N_p}{8 T_s} \quad (1)$$

This procedure works well when T_s is relatively large (more than 1 s). However, when this value is small (as in the case of this work, where a sampling period of 200 ms was used), the resulting resolution is too low, due to the small number of samples collected, as shown in Fig. 6.

In order to solve this problem, we replaced the procedure of counting the number of pulses over the sampling period by the measurement of the time elapsed between consecutive pulses (T_p). With this new procedure, the cadence is calculated using the following equation:

$$C = \frac{60}{8 T_p} \quad (2)$$

The power output (P), in watts, can be obtained from the multiplication of the torque (τ), in Nm, and the angular velocity (ω) of the pedaling, in rad/s:

$$P = \tau \omega \quad (3)$$

where the angular velocity is obtained using the following equation:

$$\omega = \frac{2\pi C}{60} \tag{4}$$

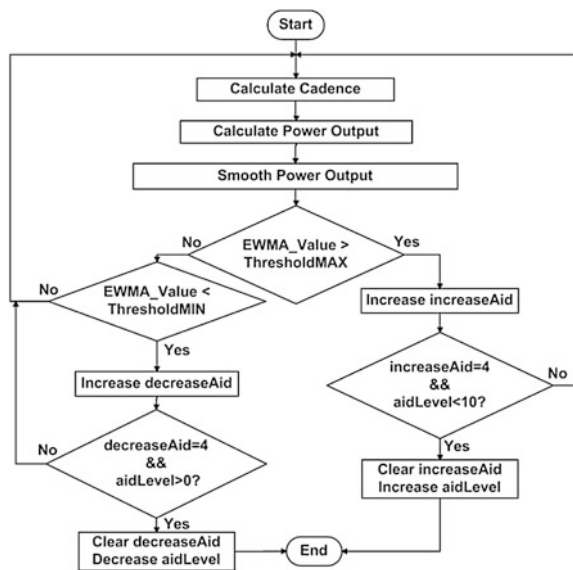
Another problem encountered during the development of the effort control system is that the signal provided by the torque sensor presents very large variations as the cyclist presses and releases the pedal. Since the power output depends on the torque, its value presents large variations as well (see the lower part of Fig. 7). Therefore, it was necessary to smooth the abrupt changes in the power output, to provide a more stable input to the control algorithm, in order to avoid undesired changes on the motor assistance level. To that purpose, we used the Exponentially Weighted Moving Average (EWMA), which is based on the following equations, where $0 \leq \alpha \leq 1$. Smaller values of α increase the smoothing but make the output less responsive to changes in the input, and vice versa.

$$S_k = X_k, k = 0 \tag{5}$$

$$S_k = \alpha X_k + (1 - \alpha) S_{k-1}, k > 0 \tag{6}$$

Figure 4 presents the implemented power output control algorithm. After receiving the sensor data, the smartphone application calculates the cadence and the power output, and then it applies the EWMA to smooth the power output. If the

Fig. 4 Flowchart of the power output control algorithm



resulting value exceeds the maximum threshold defined by the user, the variable `increaseAid` is incremented, and, if both the motor assistance level (`aidLevel`) is lower than the maximum level and `increaseAid` is equal to 4, the variable `increaseAid` is cleared and the motor assistance level (`aidLevel`) is incremented; otherwise, the processing returns to the start of the algorithm. A similar procedure is performed when the EWMA value decreases below the minimum threshold.

The variables `increaseAid` and `decreaseAid` store pre-defined values that can be adjusted to guarantee that the motor assistance level is not prematurely changed in response to transitory changes in the effort.

4 Results and Discussion

The first tests performed aimed to characterize the end-to-end delay, from the moment the sensor data is collected until the motor assistance is applied. The rationale was to determine a suitable value for the sampling time in order to guarantee that a new sample is only acquired after the feedback from the previous sample was processed. The information flows from the bicycle to the smartphone and back, and the delay includes data processing times at the smartphone and the microcontrollers, as well as Bluetooth wireless transmission and medium access times. This test collected 3000 samples. Through the CCDF (Complementary Cumulative Distribution Function) of the end-to-end delay, presented in Fig. 5, it can be concluded that any value above 120 ms assures that the sampling time is higher than the delay. In the following tests, a sampling time of 200 ms was used.

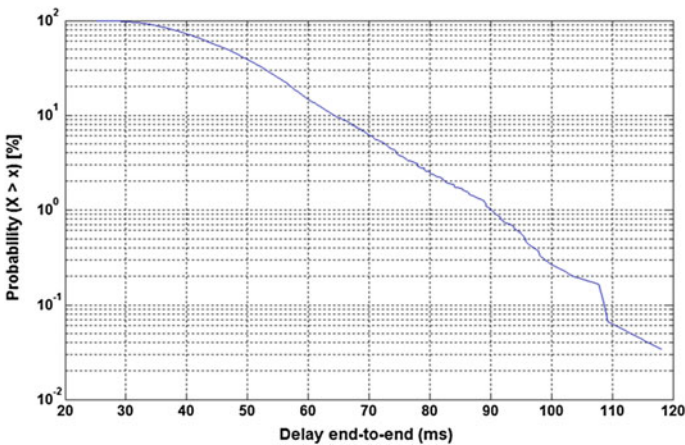


Fig. 5 Delay end-to-end complementary cumulative distribution function

The cadence value obtained through (1) provides low resolution, because, for normal values of cadence, the number of pulses generated during a short period of time is too low. Figure 6 reflects this situation, where the measured cadence oscillates among a small number of levels. As referred in Sect. 3, this problem was solved by counting the time between consecutive pulses provided by the cadence sensor and using Eq. (2). The upper part of Fig. 7 shows that a much higher cadence resolution can be obtained through this method.

Two types of experimental tests were made to compare the measured power output without/with the control algorithm: (1) variable resistance with constant cadence; (2) variable cadence with constant resistance. These tests were performed with the rear wheel placed on a support that allows the adjustment of the resistance applied to the bicycle, and with the EWMA parameter set to $\alpha = 0.1$. Results from type 1 tests were similar to those presented previously in [11], whereas results from type 2 tests are presented in Fig. 7 (without control) and Fig. 8 (with control).

At the beginning of these tests, the cadence was kept around 30 rpm during the time interval from 5 to 25 s, and was increased to 40 rpm between 25 and 45 s. After 45 s, the cadence was decreased again to 30 rpm. Figure 7 presents the behavior of the cadence and the power output for this scenario, without the use of the power output control algorithm. As the figure shows, the power output exceeds significantly, and during large periods, the maximum threshold defined.

In the case with the power output control algorithm enabled, shown in Fig. 8, the cadence pattern is similar to the previous one. As the figure shows, this effort control algorithm increases/decreases the motor assistance level when necessary,

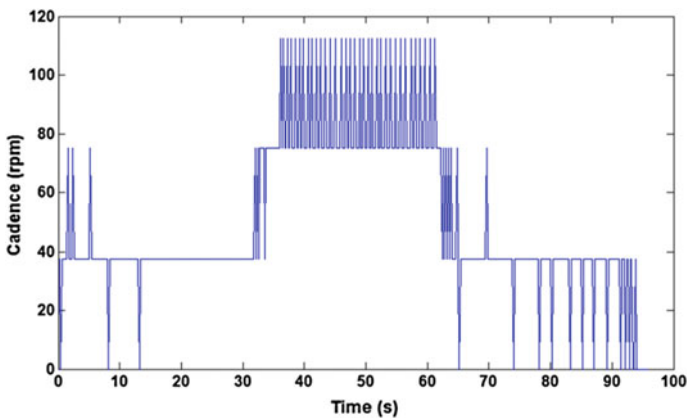


Fig. 6 Cadence measurement based on the number of pulses

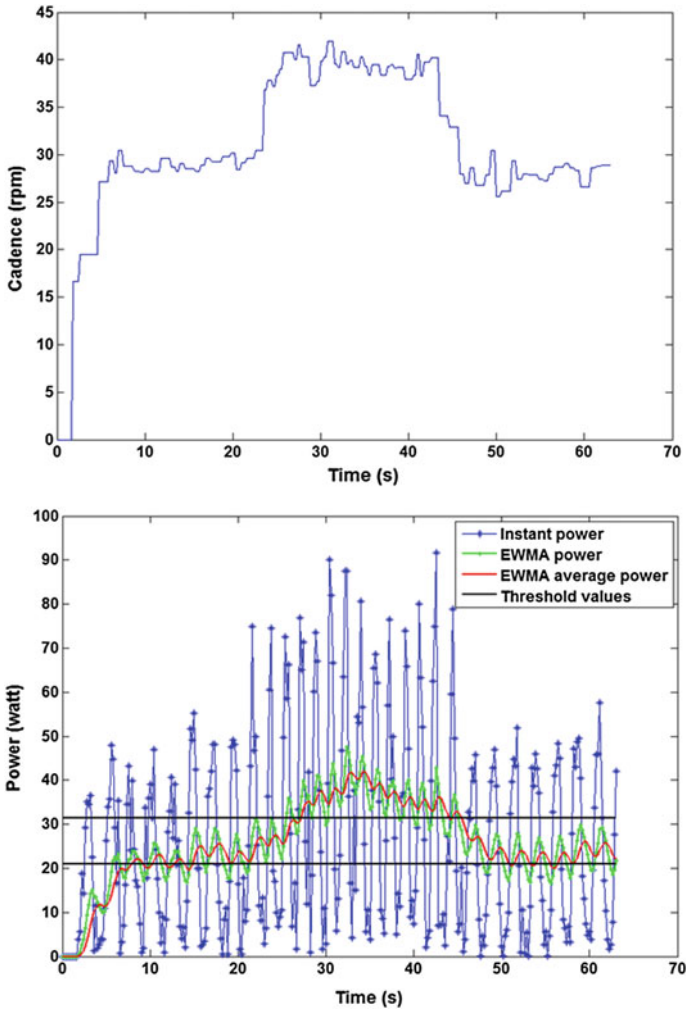


Fig. 7 Power output with variation of the cadence and without control

with the aim to maintain the average power output inside the defined thresholds. Due to limitations on the motor drive module of the electric bicycle, it was not possible to exceed the motor assistance level 4 (out of 10 defined levels), which imposed a constraint on the operation of the effort control algorithm, resulting in periods where the power output briefly exceeded the maximum threshold, because the algorithm was not able to increase the motor assistance as required anymore.

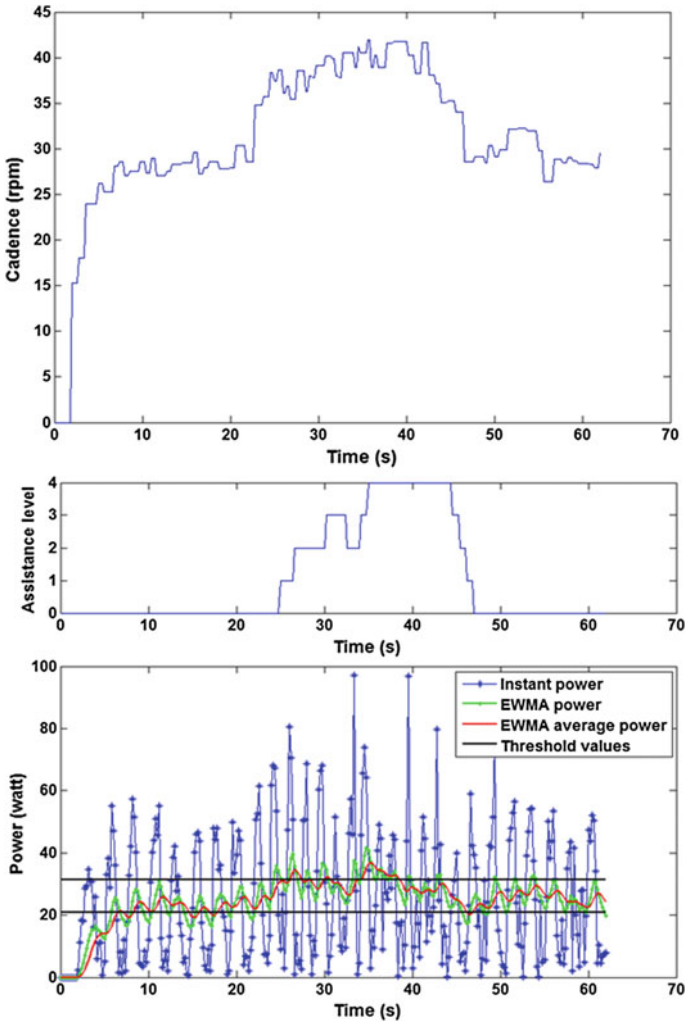


Fig. 8 Power output with variation of the cadence and with control

5 Conclusions

This paper describes a system that enables cycling power output control through the use of a smartphone and an Electric Bicycle (EB). Experimental results validate the proposed system, which has applications on fitness, healthcare and transportation.

In the future it is intended to integrate functionalities of three other mobile sensing systems, which were developed in parallel, into this system. The first one provides a georeferenced database, which can be accessed online, with measurements of several relevant cycling parameters, and offers the functionalities of

visualization of current and past routes in a map, sharing data with friends, joining or creating events, and locating friends [12]. The second one allows the monitoring of the posture of cyclists in real-time, using wireless motion capture sensors [13]. The third one provides personalized information to the cyclist, including EB range prediction and information regarding locally available public transport [14].

Future work includes also the integration in the same system of an effort control method based on the heart rate.

Acknowledgments This work is supported by FCT (Fundação para a Ciência e Tecnologia) with the reference project UID/EEA/04436/2013, and by FEDER funds through the COMPETE 2020 – Programa Operacional Competitividade e Internacionalização (POCI) with the reference project POCI-01-0145-FEDER-006941.

References

1. Khan, W.Z., Xiang, Y., Aalsalem, M.Y., Arshad, Q.: Mobile phone sensing: A survey. *IEEE Commun. Surv. Tutorials* **15**(1), 402–427 (2013)
2. Lane, N.D., et al.: A survey of mobile phone sensing. *IEEE Commun. Mag.* **48**(9), 140–150 (2010)
3. Campbell, A.T., et al.: The rise of people-centric sensing. *IEEE Internet Comput.* **12**(4), 12–21 (2008)
4. Pussieldi, G.A., et al.: Effort control through heart rate in an off road cross country bicycle race. *Fitness Perform. J.* **5**, 299–305 (2005)
5. Impellizzeri, F., et al.: Exercise intensity during off-road cycling competitions. *Med. Sci. Sports Exerc.* **34**(11), 1808–1813 (2002)
6. Outram, C., Ratti, C., Biderman, A.: The Copenhagen Wheel: An innovative electric bicycle system that harnesses the power of real-time information and crowd sourcing. In: *Proceedings EVER'2010*, Monaco (2010)
7. Reddy, S., et al.: Biketastic: sensing and mapping for better biking. In: *Proceedings of the SIGCHI Conference on Human Factors in Computing Systems*, Florence, Italy, pp. 1817–1820 (2010)
8. Eisenman, S.B., et al.: BikeNet: a mobile sensing system for cyclist experience mapping. *ACM Trans. Sensor Netw.* **6**(1), 1–39 (2009)
9. Corno, M., Giani, P., Tanelli, M., Savaresi, S.M.: Human-in-the-loop bicycle control via active heart rate regulation. *IEEE Trans. Control Syst. Technol.* **23**(3), 1029–1040 (2014)
10. Nagata, T., Okada, S., Makikawa, M.: Electric motor assisted bicycle as an aerobic exercise machine. In: *Proceedings of the 34th Annual International Conference of the IEEE EMBS*, San Diego, California, pp. 1933–1935 (2012)
11. Afonso, J.A., Rodrigues, F.J., Pedrosa, D., Afonso, J.L.: Automatic control of cycling effort using electric bicycles and mobile devices. In: *Proceedings of the World Congress on Engineering 2015*, London, U.K., pp. 381–386 (2015)
12. Oliveira, D., Afonso, J.A.: Mobile sensing system for georeferenced performance monitoring in cycling. In: *Proceedings of the World Congress on Engineering 2015*, London, U.K., pp. 269–273 (2015)
13. Maio, A.F., Afonso, J.A.: Wireless cycling posture monitoring based on Smartphones and Bluetooth low energy. In: *Proceedings of the World Congress on Engineering 2015*, London, U.K., pp. 653–657 (2015)
14. Ferreira, J.C., Monteiro, V., Afonso, J.A., Afonso, J.L.: Mobile cockpit system for enhanced electric bicycle use. *IEEE Trans. Ind. Inf.* **11**(5), 1017–1027 (2015)

Automatic Control of Madeira Wine Aging Process

Carlos M. Faria, Darío Baptista, José Carlos Marques
and Fernando Morgado-Dias

Abstract Madeira wine aging processes are slow and costly. Besides, the value invested, the storage space, the energy costs and temperature control must also be considered. It has been shown that the aging process can include a heating step under controlled conditions, which can decrease the time necessary to achieve the characteristics of a typical fortified wine. The temperature control inside the tanks in the Madeira wine storage, mostly carried out manually, is the most important step to achieve a high quality wine. This work describes the procedure developed to implement, at low cost, an automatic temperature control inside the tanks in a pilot scale unit. Five different controllers were tested, where the Direct Inverse Control was the one that shows the best performance.

Keywords Madeira wine aging process · Automatic control · Artificial Neural Networks · Direct Inverse Control

1 Introduction

Madeira wine is an important product for the economy of Madeira. An important step to achieve Madeira wine quality is aging, which improves quality and general characteristics, but it requires monitoring during storage, mainly the temperature inside the tanks. This process is costly both due to the investment that can only be recovered after 3, 5, 10 or more years, the storage space and temperature requirements. It has been shown that similar characteristics can be achieved in shorter time if the wine is heated at specific and well controlled temperature. Based on exper-

C.M. Faria · J.C. Marques · F. Morgado-Dias (✉)
University of Madeira, Funchal, Portugal
e-mail: morgado@uma.pt

D. Baptista · F. Morgado-Dias
Madeira Interactive Technologies Institute, Funchal, Portugal

J.C. Marques
I3N - Institute of Nanostructures, Nanomodelling and Nanofabrication, Aveiro, Portugal

Fig. 1 Image of the system with 10 tanks



iments introduced in the process since the XVIII century, the heating step must be carried out at about 45 °C for at least 3 months.

For this purpose a pilot scale unit equipped with 10 stainless steel tanks (maximum capacity of 200 L each) and a tap water heater (maximum capacity of 150 L) was designed and installed at the University of Madeira. In the system, heating is achieved through opening a set of valves allowing the passage of hot water in a loop circuit, which meanders inside the tanks (on-off valves). The maximum temperature of the heating system is 60 °C. The cooling is done through ambient heat dissipation keeping the valve closed. Figure 1 shows an image of this system.

The implementation of an automatic control system will allow a careful and efficient management and, consequently, a decrease of cost of this process.

2 Selection of the Sampling Period

To identify and control the system, an appropriate sampling period needs to be defined based on the rise time. By a rule of thumb, a relation between the rise time and the sampling period can be established [1] and is given by:

$$N_r = \frac{T_r}{h} \approx 4 \text{ to } 10 \quad (1)$$

where T_r is the time between the 10 % up to 90 % of the rise time, h is the sampling period and N_r is the number of samples that the rise time should include.

Applying a step input in the system and taking into account the maximum number of samples that the time rise should include according rule of thumb (i.e. $N_r = 10$), the sampling period is approximately 30 min. However, it was verified

that within 30 min, the temperature variation can be too high. In consequence, in order to avoid the risk of losing important information, it was decided decrease the sampling period to 15 min (the half-value obtained by rule of thumb).

3 Development of ARX Models for System Identification

Two types of samples are used in this work namely the valve opening time that allows the passage of hot water and the temperature inside of tanks. The models will be tested against real data to verify the accuracy of prediction. For that, the dataset was divided into two sets: the train dataset and the validation dataset. 70 % of the data for training, i.e. it was used to identify the physical system, (750 samples) and the next 25 % of the data for test (250 samples). This method allows capturing enough information to develop models with a good performance to predict the behavior of the system.

Also, two different types of models were developed: linear and non-linear. On the one hand, the linear least squares was used to estimate the parameters of a linear model. Mathematically, the linear least squares is an approach fitting solution to model data. The best approximation is defined by the minimum value of sum of squared difference between the data values and their corresponding modeled values [2].

On the other hand, a non-linear model was developed, using an artificial neural network (ANN). ANNs are organized with layers and, inside it, there are elements called artificial neurons which process the information [3]. The Levenberg-Marquardt [4] and Backpropagation [5] algorithms were used to train the ANN. To evaluate these two training algorithms, ANNs with 4 and 7 hidden neurons were developed.

Several class models were tested. However, only the AutoRegressive with eXogenous class model (ARX) results are presented because it was the one, which presents best performance. The ARX models consists in inserting past values of input and output signals [6].

3.1 Order of the Models

To develop a model ARX, for a specific problem, it is necessary to know the number of inputs that the model should have. The main difficulty is to know how many past inputs are need without increasing the complexity unnecessarily. There is not an exact answer to solve this problem, but there are solutions that attempt to solve it [6].

A study about the order of system was performed to identify the best solution with less cost to implement but it allows the model to represent the system with high level of confidence. Figure 2 presents graphically the loss function (also known as cost

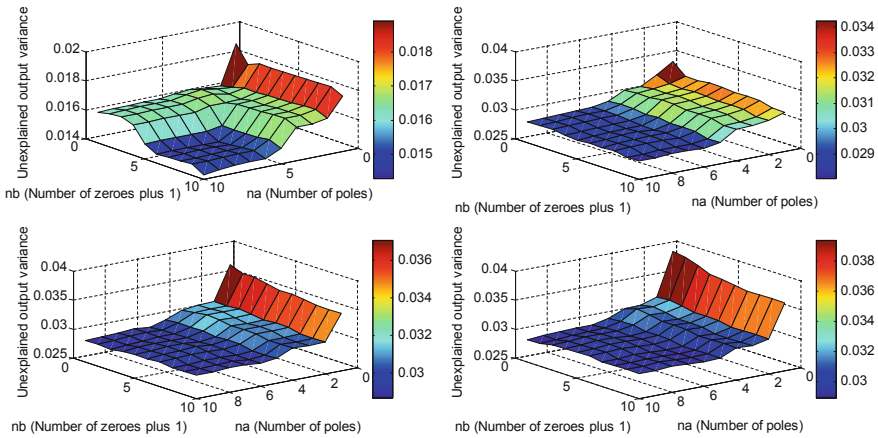


Fig. 2 Loss function to identify the order

function) of 1000 different combinations. This function represents the price to pay for inaccuracy of predictions. The parameters na and nb are the orders of the ARX model (na is number of past output terms and nb is the number of past input terms), nk is the delay (also called the dead time in the system).

To select the best order, it should take into account the equilibrium between the complexity and the accuracy [6]. The way to select the order, without increase unnecessarily the complexity, is where the loss function begins to decrease slowly. So, looking the Fig. 2, the best choice is $na = 2$, $nb = 1$ e $nk = 1$.

3.2 Analysis of the Developed Models

Table 1 shows the percentage of matching between the output target and the output predicted by the models, the following equation was used:

$$Best\ Fit\ (\%) = 100 \times \frac{1 - \frac{\|Y_{target} - Y_{predict}\|}{\|Y_{target} - \bar{Y}_{target}\|}}{\|Y_{target} - \bar{Y}_{target}\|} \tag{2}$$

Table 1 Best Fit (%) of all models developed for different algorithms

			Best Fit (%)
Linear model ARX			95.87
Non-linear model ARX (ANN)	4 neurons	Levenberg-Marquardt	89.01
		Backpropagation	87.23
	7 neurons	Levenberg-Marquardt	80.71
		Backpropagation	81.20

where the Y_{target} is the output target and $Y_{predict}$ is the output predicted by the model and \bar{Y}_{target} is the output target mean.

ANNs with different hidden neuron were developed. Here, it is presented only the two ANNs that had best performance. Comparing all models developed (linear and non-linear), it is concluded that the best options to represent the system is the linear model.

4 Development of the Control Structure

Different kinds of controllers were developed and tested, namely the Direct Inverse Control (DIC), the Internal Model Control (IMC), the Proportional-Integral-Derivative controller (PID), the Proportional-Integral-Derivative controller with Filter (PIDF) and the Model Predictive Control (MPC).

The DIC controller is an easy method to make control. It consists in connecting in series the inverse model and the process, as can be seen in Fig. 3. If the inverse model is of order superior to one, delayed samples of control and output are feedback to the inverse model input [7].

The IMC controller consists in a serial connection of the inverse model and the process. However, the inverse model received, as input, a signal. This signal reflects the perturbations that affect the system and the differences between the model and the process. Figure 4 shows a schematic of IMC controller [8].

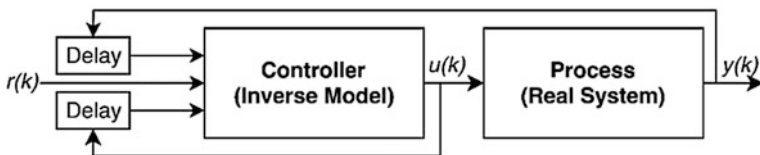


Fig. 3 Structure for direct inverse control. The signal $r(k)$ is the temperature set point inserted into the controller, $u(k)$ is the valve opening time that allows the passage of hot water, $y(k)$ is the temperature inside of tanks

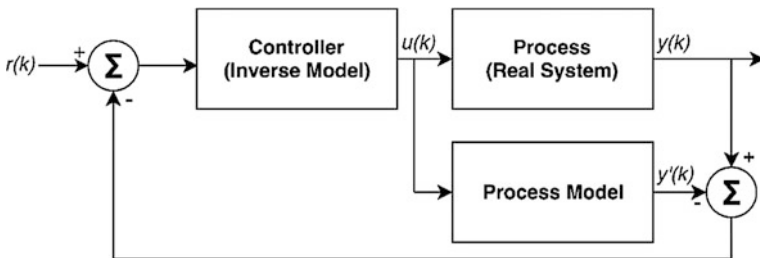


Fig. 4 Structure for internal model control. The signal $y^{\wedge}(k)$ is an estimative of the process

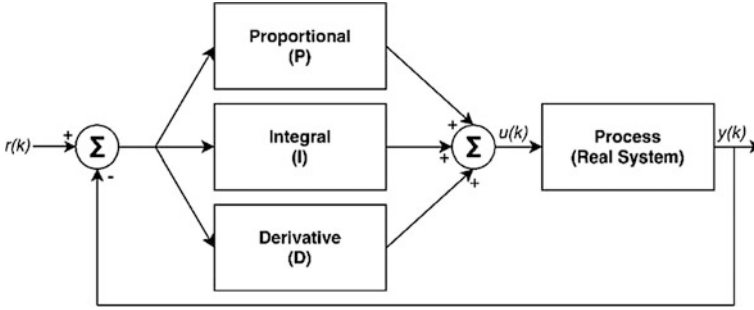


Fig. 5 Structure for PID control

The PID is named after its three correcting terms (proportional (K_p), integral (K_i), and derivative (K_d)) that are summed to calculate the output. Figure 5 shows a schematic of PID controller and Eq. 3 is its transfer function [9].

$$H_{PID}(s) = K_p + \frac{K_i}{s} + K_d s \tag{3}$$

The PIDF controller is the next generation to PID controller and the difference is a low pass filter to complement it [9]. Its transfer function, $H_{PIDF}(s)$ is given by:

$$H_{PIDF}(s) = \left(K_p + \frac{K_i}{s} + K_d s \right) \frac{1}{1 + T_f s} \tag{4}$$

where, T_f is a filter constant.

The MPC controller is used to predict the future evolution of the process to optimize the control signal. The output of the model combines with the output of the system to give a prediction of the future error of the system. This error is fed into an optimizer and it gives the predicted future inputs, which are fed back into the main model, restarting the cycle [10]. Figure 6 shows the basic structure of a MPC.

Fig. 6 Structure for MPC control

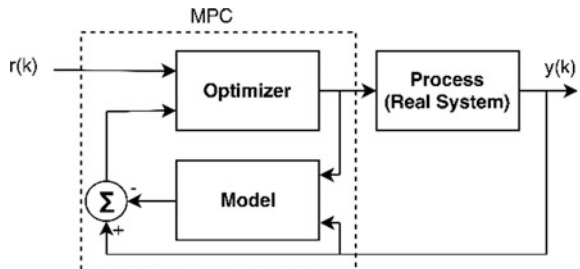


Table 2 Response step for the controllers PIDF, PID, IMC, MPC and DIC

Controller	PIDF	PID	IMC	MPC	DIC
Rise time (s)	7,20 e+04	7,20 e+04	7,20 e+04	7,20 e+04	7,20 e+04
Settling time (s)	2,38 e+05	2,49 e+05	1,24 e+05	3,60 e+05	1,28 e+05
Overshoot (%)	6,6	13,6	0,00364	1	0
Peak	1,07	1,14	1	1,01	1
Time occurrence of the peak (s)	1,55 e+05	1,51 e+05	2,00 e+05	1,48 e+05	1,80 e+05
Closed-loop stability	Stable	Stable	Stable	Stable	Stable

4.1 Response Step Analysis

The parameters to consider in the response step analysis are the rise time, settling time, overshoot and time occurrence of the peak. Table 2 presents all controllers used.

The controller was developed using ARX models with 95.87 % of matching with the real system. When the model is replaced by the real system, the control will be present some mismatches. So, to minimize this effect, the controller with lowest overshoot was chosen. As a second requirement, the controller with a small settling time was chosen to achieve faster the set point temperature. The main requisite for the system is a small settling time to achieve faster the set point temperature and small overshoot. So, analyzing Table 2, it was verified that IMC controller presents a small settling time. However, looking at the value of overshooting it was verified that IMC controller presents an overshoot (0.00364) and DIC controller do not present it. So, the controller DIC was chosen because it does not present overshoot and its settling time presents only a difference of 4000 s comparing with the IMC.

4.2 Simulation Analysis

A simulation with all controllers was done to verify and consolidate the decision about the best controller to choose. Figure 7 shows the simulations done with each controller where it was held a set point variation from 5 °C to 25 °C and vice versa.

To determine the best relationship between the simulations of the system response using each controller and the set point signal, the Mean Square Error (*MSE*) and the correlation coefficient (*R*) values are used. The *MSE* is a measure to estimate the average of the squares of the difference between the desired response and the set point [11]. It is defined by:

$$MSE = \frac{1}{N} \sum_{i=1}^N (Y_{target} - Y_{predict})^2 \quad (5)$$

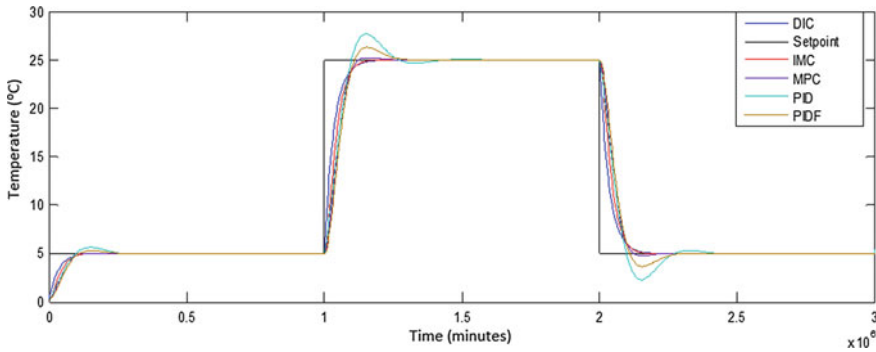


Fig. 7 Simulation for the controllers PIDF, PID, IMC, MPC and DIC

Table 3 MSE and R values between the set point signal and the simulations of system response using each controller

Controller	MSE of simulation	R of simulation
DIC	5,4135	0,9727
IMC	8,4797	0,9572
MPC	10,4711	0,9472
PID	10,0318	0,9500
PIDF	11,7054	0,9413

where N is the number of samples. However, it does not necessarily reflect whether a line fits the data tightly because the MSE depends on the magnitude of the data samples. The coefficient R solves that problem. R is a measure which indicates the linear relation between two variables [11]. By definition, the correlation coefficient is:

$$R = \frac{Cov(Y_{target}, Y_{predict})}{\sigma_{Y_{target}} \sigma_{Y_{predict}}} \tag{6}$$

where σ is the standard deviation and Cov the covariance. Table 3 shows the values of MSE and R between the set point signal and the simulations of system response using each controller.

5 Controller Implementation in the Real System

The controllers were tested with the real system. Table 3 shows the values of MSE and R between the set point signal and the response of physical system using DIC (Table 4).

Figures 8 and 9 show two different responses of the real system using DIC control. As expected, there are disturbances and the results are slightly worse than the simulation tests.

Table 4 MSE and R values between the set point signal and the response of physical system using DIC for the tank 10 and 7

	MSE	R
Tank 7	3,0528	0,9028
Tank 10	3,8748	0,8987

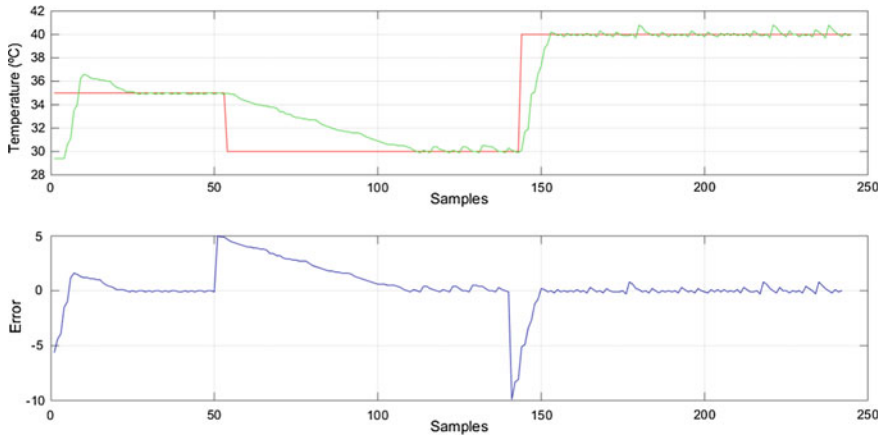


Fig. 8 Comparison between the set point temperature and the temperature inside the tank 10

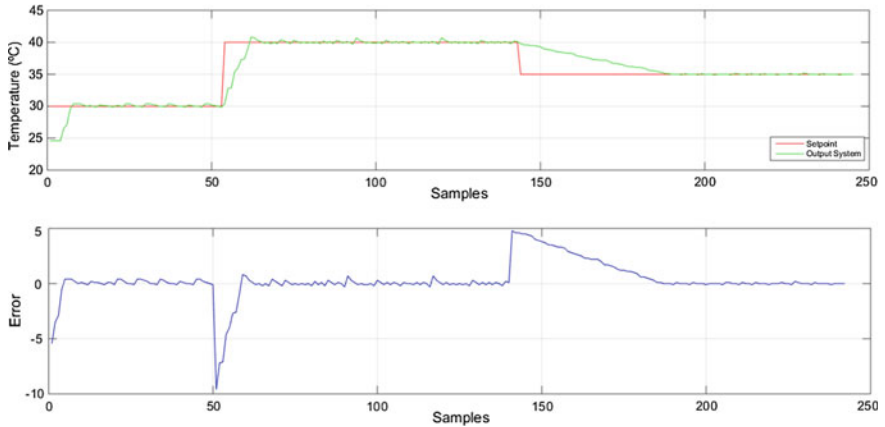


Fig. 9 Comparison between the set point temperature and the temperature inside the tank n° 7

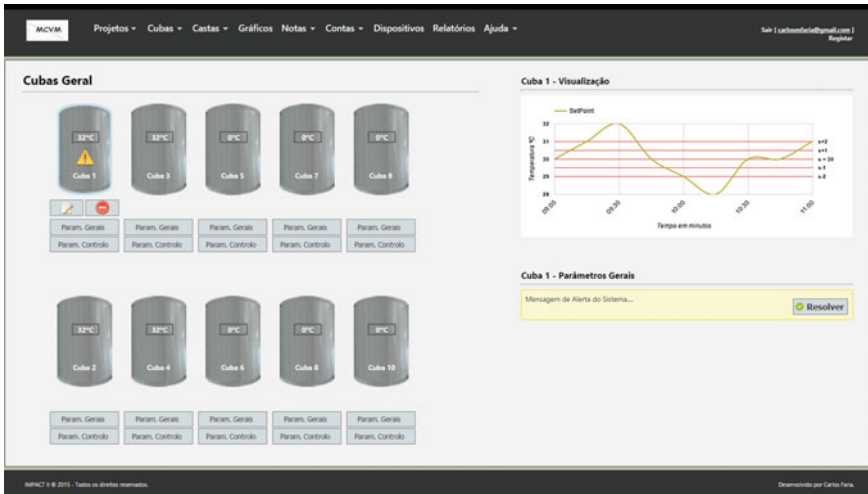


Fig. 10 General view of interface of tanks management interface

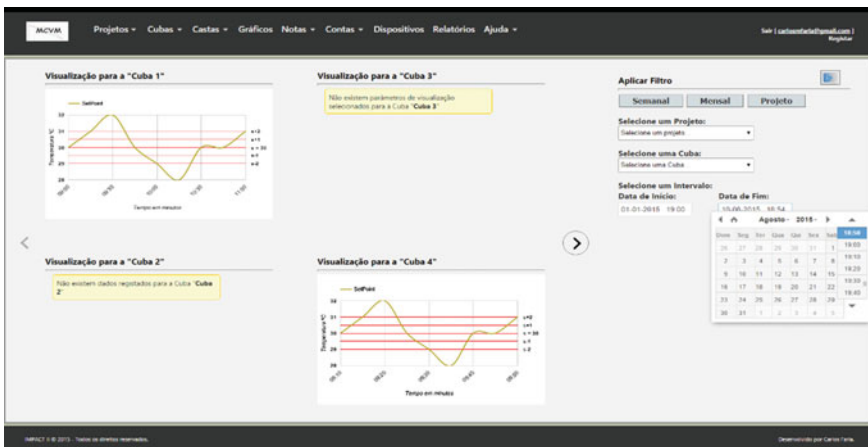


Fig. 11 General view of interface for a specific tanks management interface

A graphical interface was also developed for the users to easily monitor the temperature and set point. This interface can be seen in Figs. 10 and 11.

6 Conclusions

In this work a controller was developed to regulate the temperature inside of tanks to accelerate the aging process of Madeira wine. Two different kinds of models were developed with ARX class: linear and non-linear models. For this system, a

linear model presents a better result (95.87 %) and it was used to develop the controller. After that, several controllers were simulated. It was concluded that the controller DIC has a better performance because it presents a low settling time and a null overshoot. Besides, with this controller, there is a good matching between the response of physical system and the set point temperature (For tank 7: MSE = 3,0528 and R = 0,9028; For tank 10: MSE = 3,8748 and R = 0,8987).

Acknowledgments Acknowledgments to Portuguese Foundation for Science and Technology for their support through project PEst-OE/EEI/LA0009/2011.

Acknowledgments to ARDITI - Agência Regional para o Desenvolvimento da Investigação Tecnologia e Inovação through the support provided by the FSE—Madeira 14-20.

References

1. Åström, K., Wittenmark, B.: *Computer Controlled Systems*. Prentice Hall (1997)
2. Valença, M.R.: *Métodos Numéricos*, 3th edn. Ferreira e Salgado, Press LLC (1993)
3. Dias, F.M., Antunes, A., Vieira, J., Mota, A.: A sliding window solution for the on-line implementation of the Levenberg-Marquardt algorithm. *Eng. Appl. Artif. Intell.* **19/1**, 1–17 (2006). IFAC
4. Baptista, D., Morgado-Dias, F.: Comparing different implementations for the Levenberg-Marquardt algorithm. In: 10th Portuguese Conference on Automatic Control (2012)
5. Siddique, M.N.H., Tokhi, M.O.: Training neural networks: backpropagation vs. genetic algorithms. In: *Proceedings. IJCNN '01*, vol. 4, pp. 2673–2678. IEEE (2001)
6. Morgado Dias, F.M.: *Técnicas de controlo não-linear baseadas em Redes Neurais: do algoritmo à implementação*. Tese Universidade de Aveiro – Departamento de Electrónica e Telecomunicações (2005)
7. Morgado-Dias, F., Mota, A.M.: Direct inverse control of a Klin. In: 4th Portuguese Conference on Automatic Control. Guimaraes, Portugal (2000)
8. Gang, Q., Le, S., Ling, H.: A Practical application of IMC-PID controller in unmanned vehicle. *TELKOMNIKA Indonesian J. Electr. Eng.* **11(6)**, 3228–3235 (2013)
9. Hassaan, G.A., Al-Gamil, M.A., Lashin, M.M.: Tuning of a PIDF controller used with a highly oscillating second order process. *Int. J. Emerg. Technol. Adv. Eng.* **3(3)** (2013)
10. Wang, Y., Boyd, S.: Fast model predictive control using online optimization. *IEEE Trans. Control Syst. Technol.* **18(2)**, 267–278 (2010)
11. Principe, J.C., Euliano, N.R., Lefebvre, W.C.: *Neural and Adaptive System: Fundamentals Through Simulations*. Wiley, New York (1999)

Study of Quality Service in AIS Gateway System

Mário Assunção and Luis Mendonça

Abstract About 90 % of the volume of world trade is transported by sea via ships, this volume corresponds to about 70 % of world trade in value. Thus, maritime transport must be made on the basis of the highest rates of safety. Global distress communication systems, ship reporting systems, emergency radio beacons, and other technologies have greatly enhanced mariners' safety. Considering this, the paper presents a platform that enables the maritime access information from data provided by the Automatic Identification System (AIS) in a quick way only by using your mobile phone. The developed and made available platform intended as a complement to any existing technology that supports shipping with high safety indices. In this paper the proposed approach is used in two real situations. The results make it possible to understand that the quality of service is good and it can provide relevant information for shipping management.

Keywords Automatic identification system • Maritime transport • Quality of service • Safety of maritime transport

1 Introduction

Maritime transport has contributed effectively to the economic development of Europe, as it enables the business and exchanges between countries. This transport has as main features the cost the safety and the environmental protection. Maritime transport performs effectively and safely power supply as well as the transport of food and raw materials within Europe and worldwide [1]. The maritime transport in Europe and in the world is an important source of employment and income as

M. Assunção · L. Mendonça (✉)
Department of Marine Engineering, Escola Superior Náutica Infante D. Henrique,
Paço de Arcos, Portugal
e-mail: luismendonca@enautica.pt

M. Assunção
e-mail: marioassuncao@enautica.pt

enhances the participation of various stakeholders in several areas. Maritime transport provides globalization through made business, communications through the contacts between the various countries, the standardization of various entities because only in this way can make contacts and associations and diversification of trade result of contacts and committed business [2]. For all that shipping should be equipped with tools that improve the quality and safety available to its users, the crew and the environment. Maritime transport may involve several vessels with different products and different routes originating specialized transport networks. Specialized transport networks are composed by: ships, ports, factories, terminals and distribution centers. Considering the economic, environmental and safety features the shipping is a possible substitute for other cargo transport [3].

Maritime transport and trade made over the centuries for various locations around the world, have boosted the economic success of the countries involved. Maritime transport has a very high participation in internal and external trade of the European Union, respectively 90 % and 40 %. In terms of the quantities of goods loaded and unloaded values are about 3.5 billion tons each year [4]. The maritime labour is a very difficult profession, security of crews and the use of new technologies will be very important for the development of maritime transport. The sea routes involving Europe are the busiest in the world. So, for safety the monitoring of these routes and monitoring of ships are of great importance to prevent accidents. The development of new technologies and their use in maritime transport is essential for shipping, the trade and the economy can continue to evolve.

Maritime transport and its users can use a navigation protocol adopted internationally in the exchange of information related to navigation, the Automatic Identification System (AIS). This system has several possibilities among which facilitates the vessel traffic management, identifying the ship, its position, its course, its speed, navigation conditions as well as information related to security. AIS receive and shares the information automatically with other ships also equipped with the same system, as well as onshore facilities. The AIS database messages can be used to model the high density of vessel traffic zones for collision avoidance [5]. Also the AIS real time data can be used to aid the target detectors and radars sensors [6] or to help the maritime navigation, environment protection, ports operation [7]. Several AIS Web systems were developed, such AISLive-HIS, ShipAIS or Marine Traffic, to obtain AIS data, although these systems are paid, they present user-friendliness and with no real-time AIS data. Besides systems have been developed to increase the reliability of AIS data [8].

In this paper is proposed the development of AIS with the main objective of the improvement of maritime transport also in concerning safety. One developed and implemented a gateway mechanism that allows the connection of an Android mobile phone to a server that provides real time AIS information received from a VHF-AIS receptor. Hence the information provided by AIS can be used by a greater number of users and improve safety levels. The Quality of Service (QoS) is an issue to get accurate AIS real-time data, therefore is presented a QoS study of the developed AIS gateway system.

The paper is organized as follows. In Sect. 2, the safety of maritime transport is addressed. Section 3 presents the description of the Automatic Identification System and Sect. 4 gives a description of the developed NMEA-AIS gateway system. The measuring of the quality of service is addressed in Sect. 5. The QoS results obtained are shown and discussed in Sect. 6 and conclusions are drawn in Sect. 7.

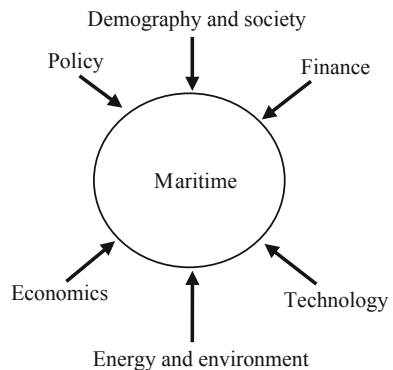
2 Maritime Transport

Considering freight the transportation systems can be done by land, by water or by air. These systems have distinct costs, capacity, speed and time delivery. The transportation system performed by land is normally performed by trucks with more flexibility and operating in many areas. By land the costs transportation for loading and unloading facilities and equipment are very low compared to other modes of transportation however with small capacity in regard to volume and weight. Other disadvantage is the use in some situations of only one driver per truck. Comparing transport by truck to transport by rail this has a more limited network but is more energy efficient. Transport by rail has also the advantage of fast transportation of bulk cargo on long distances however with the disadvantages of longer stops and cargo handling costs. The transportation by aircraft is the fastest however the higher speed implies higher transportation costs.

The maritime transport is slower than transport by land or by air but is cheaper when compared with those freight transport modes. Other advantages of maritime transportation are the ability of shipping bulk cargo and large volume cargo over long distances and the low emissivity gas by what are known as environmentally friendly as compared to other transport modes. Being comparatively favorable the maritime transport, will be important to assess how this transport mode can evolve. The development of maritime transport can be supported in six areas (Fig. 1): policy, demography and society, energy and the environment, technology, economics and finance [9].

The impacts of the technology and its innovation are difficult to quantify. However, the use of new technologies associated with maritime transport has

Fig. 1 Directions of maritime transport



associated advantages with regard to the safety of crew, passengers and cargo as well as the environment. It can thus be seen that technology and innovation make it possible to provide shipping with increasingly important features.

The AIS emerges in maritime transport in order to contribute to improving the quality of services provided based on the need for technological innovation and compliance with the laws that regulate it. In 2000 the International Maritime Organization (IMO) decided to adopt the use AIS on ships for Safety-of-Life-At-Sea (SOLAS), therefore it would be possible to provide information automatically about the ship to other ships and to onshore facilities. After the 31 December 2004 there is the requirement that AIS be installed on ships with the following characteristics: ships on international voyages with gross tonnage less than 300, ships in non-international voyages with gross tonnage less than 500, all passenger ships.

Thus the development of technology related to the AIS, as proposed in this article, may contribute to the improvement of service with regard to maritime transport.

3 Automatic Identification System

Operating AIS enhances communication and sending information from one ship to other ships and onshore facilities as well as receive information from other vessels and onshore facilities. Therefore reduces the risk of collision by providing vessels information allowing the shipping decisions with greater confidence [10]. This can be achieved through an AIS text message relating to security. AIS has enormous potential in many areas but the safety of ships is indeed improved when using this type of system. Some of the AIS features are: provide information, receive information, monitor and control the vessels, assisting in search and rescue and exchange information with onshore facilities. The users of AIS text messages should be aware that this information does not replace the use of other information, according to the rules of international navigation. The use of AIS messages during emergencies should consider that these messages cannot be received, recognized and put into practice by the entities that should receive as with posts Global Maritime Distress Safety Systems (GMDSS). The seafarer should be aware that AIS does not replace other systems should not be used in situations for which is not indicated. AIS should not be used when it is necessary to carry out urgent or instead of GMDSS communications. AIS provides the seafarer the potential to be seen and to be heard by other users of the AIS [11]. The AIS is considered as a complementary system with great features to enhance the quality of maritime transport, but should be used only as a security alert at the available information not eliminating any policy or national or international security procedure and any operational requirement or materials. The seafarer should be aware that the AIS must be in perfect working condition because only in this way the messages exchanged are reliable and can be used without prospects mislead [11]. The use of AIS messages enables the improvement of maritime security can additionally enable the relevant

navigation data storage that can certainly help to clarify the cause of some problems that may occur and hence contribute to its future resolution. AIS also has a high importance in the development of risk assessment models [9]. This importance is related to its ability to provide information on the speed and traffic distribution. The AIS information receptors on land are limited. Furthermore the AIS devices do not allow automatic repetitions of an alert. AIS safety messages are transmitted only once, and if the signal is corrupt or there is interference in the transmission, a situation that sometimes occurs with the AIS device, the message may not be received. The seafarer should know the AIS capabilities as well as its limitations [10]. They have been done some studies that enhance the determination of the risk profile of a ship based on the modeling of risk and information provided by AIS. Within the project European Marnis [9] was already set a risk index.

4 NMEA-AIS Gateway System

4.1 Hardware Implementation

AIS data is obtained with existing equipment in Escola Superior Náutica Infante D. Henrique and relate to vessels that move in the Tagus' river. This information is provided on mobile phones and only need to download and install the provided software application.

The National Marine Electronics Association - Automatic Identification System (NMEA-AIS) gateway system is implemented using several technical solutions in interconnected equipment's. The Fig. 2 shows the implemented block diagram. The entry block is the AIS receiver equipment (AIS-3R from Comar Systems) that reads and flood all AIS messages transmitted by AIS Class A and Class B transponders [12]. The digital messages are available in the USB equipment's port (NMEA 0183 format protocol). A server computer is connected to the AIS receiver by the USB port, and a running server application is listening all the incoming USB messages.

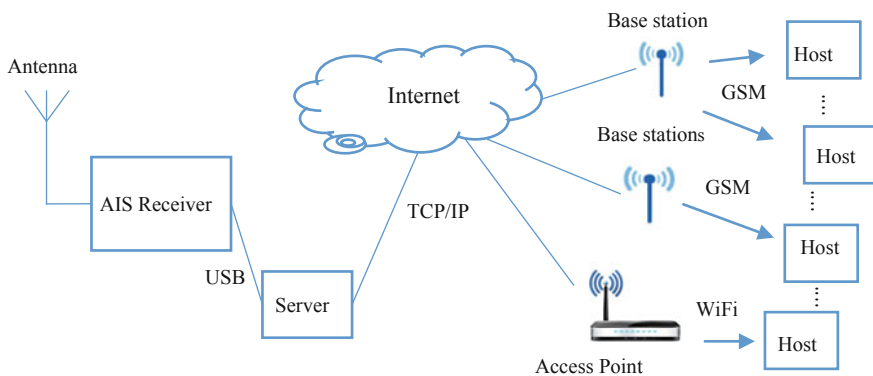


Fig. 2 Block diagram of AIS gateway system

The same application execute a parallel task for listening TCP/IP connections requested from internet by the host clients applications running in mobile equipment, such cell phone or tablet. In each client application the AIS messages are extracted and decoded from the NMEA messages. Additionally the NMEA messages and/or the AIS decoded are locally stored in the client host storage disk or card memory.

4.2 Software Development

In order to implement the NMEA-AIS gateway system two codes software were developed one to run in the server machine and the other to run in the host machine (Android based cell phone). The server software implements the tasks: read USB buffer incoming messages and save to local disk; listening and accept the TCP request connections; and relay the NMEA-AIS messages from USB buffer to the host using the TCP. The host software implements the functions: Establish a TCP connection to the server; save the NMEA-AIS messages in local file; decode the encapsulated AIS message; and show the geographical position of a vessel.

The AIS messages provide the information for traffic analyses and vessels' information. The host client applications are able to decode the AIS messages [13]. The position report messages, type 1, 2, 3, 18 and 19, give the geographical coordinates and the vessel Course Over Ground (COG), among others information. The host application uses the decoded information to map vessels polygon figures in a Google Map™ application window.

5 Measuring the Quality of Service

5.1 QoS System Performance

In order to achieve the overall AIS Gateway system performance a quality of service (QoS) measure has been performed. It is obvious the main goal of the system is to gateway the NEAM messages remotely, so the primary QoS merit figure, is the Packet Loss Rate (PLR) defined in Eq. (1). In this equation the N_{server} represents the number of USB messages transmitted by the AIS receiver and saved in the server, and the N_{host} represents number of the received messages and saved by the host application into the disk memory.

$$(PLR)_1 = \frac{N_{host}}{N_{server}}. \quad (1)$$

Many issues can cause the QoS degradation. In the implemented AIS gateway we identify the follow possible causes for data losses: Communication between AIS receiver and Server: An NMEA message in USB cable has checksum error and is

rejected by the server; An NMEA message is corrected buffered in server but the server does not have time to follow up before the next message is written in the buffer. And Communication between Server and Host(s): The TCP packet is sent but it takes a long time to reach the Host; The TCP packet is lost in Internet; The TCP packet had checksum error and was rejected by the Host; The Host take a long time process the received TCP packet compromising the next TCP packet; The Host (mobile) has a weak signal connection that affects the delivery time.

The overall QoS is depended on the two bridges communications, first the USB connection between AIS receiver and Server and second the TCP/IP connection between Server and Host(s) over the Internet system. The defined PLR in (1) can be split into two PLR, using the number of messages transmitted in TCP/IP connection, N_{TCP} . These messages are observed with Ethernet sniffer in the server local area network.

$$(PLR)_2 = \frac{N_{TCP}}{N_{server}}. \quad (2)$$

$$(PLR)_3 = \frac{N_{host}}{N_{TCP}}. \quad (3)$$

The subsystems PLRs proposed in (2) and (3) are partial performance indicators the implemented AIS gateway system. So it is possible to differentiate if the Packet Loss Rate is due to the server side or to the host side connections.

5.2 Measuring the QoS

The QoS measurement can be achieved by registering the traffic or the messages in system key points. To do that, text logger were implemented in server at USB buffer and in host applications at decoded TCP messages buffer. Additionally a traffic sniffer logs the TCP connection traffic between server and Internet. With logger text files one can compare the raw NMEA packets in server (N_{server}) with the storage NMEA packets in host (N_{host}). The Eq. (1) gives the overall QoS. Using the number of messages detected in the TCP connection (N_{TCP}) one can calculate subsystem QoS using the Eqs. (2) and (3). Plus the traffic analyser logs the retransmitted packets that occurs due to the traffic congestion, lost packet or host destination unreachable.

5.3 Measuring the Delay Time

The delay time although has not a directly influence in the QoS is somewhat another figure merit of the system. In the logger texts file it was also registered the

time for each NMEA packet. In server application it correspond to the instant of read USB buffer, in the host application it correspond to the instant when TCP message are received. The time delay is due mainly to the TCP connection. Although in some instants the Operation System, in server or in host, has to handle other running processes which can cause a significant contribution for the delay time.

6 QoS Results

Two scenarios for QoS measurement were tested for different conditions. In Table 1 is presented the test conditions for each scenario. The first test were short with favourable GSM network conditions. The second test was performed with instability.

GSM network conditions due to mobile movement or base station signal variation.

Using the text files logger for each test condition one obtain the statistical information of the NMEA packets in server (N_{server}) and the storage NMEA packets in host (N_{host}). The Table 2 presents the overall QoS using the Eq. (1). The first test condition has 100 % of QoS and the second test condition has 99.97 %. The USB incoming NMEA messages to the server are similar in the two case study, around 3.7 messages per second.

Notice that even the QoS of 100 % occurred in the first scenario, it was observed 4 retransmitted packets. Three of them are retransmitted once, and one has 3 retransmissions which caused a 2 s delay time. As can see this issue does not affect the overall QoS.

So that we could find the root cause of the 3 losses NMEA packets occurred in the second test scenario, it was observed in the TCP packets traffic analyser logger file that NMEA messages recorded in server logger haven't been sent through the TCP connection. That proves the server application does not gateway the NMEA message for unknown reasons. A possible error cause could be due to big data throughput in USB buffer. The Fig. 3 depicted the USB throughput when the particular instants of failure occur (instant of loss). No big data throughput was observed in the particular instant or the neighbour's instants.

Table 1 also presents the delay time for each scenario. As observed before the first scenario as less than 1 s of delay and a very uniform behaviour. In Fig. 4 is

Table 1 Two scenarios test conditions

Scenario	Mobile position	Move distance	Duration (min)
Fixed host mobile	Indoor	1 m	10
Moved host mobile	Indoor/Outdoor	15 km	97

Table 2 Two scenarios NMEA packets logged and overall QoS

Scenario	N_{server}	N_{host}	QoS (%)	Average delay time (s)	$\langle N_{server} \rangle / s$
Fixed host mobile	1287	1287	100	Less 1	3.77
Moved host mobile	13701	13697	99.97	1,43	3.72

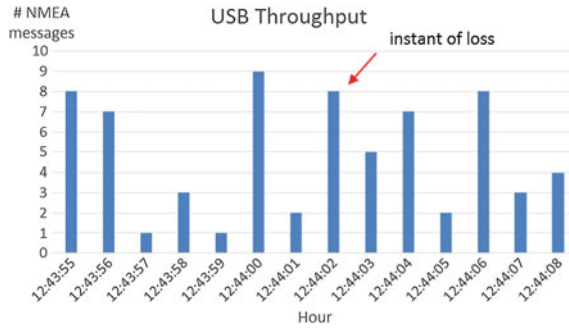


Fig. 3 USB throughput when 1 NMEA message was not sent by TCP (second scenario)

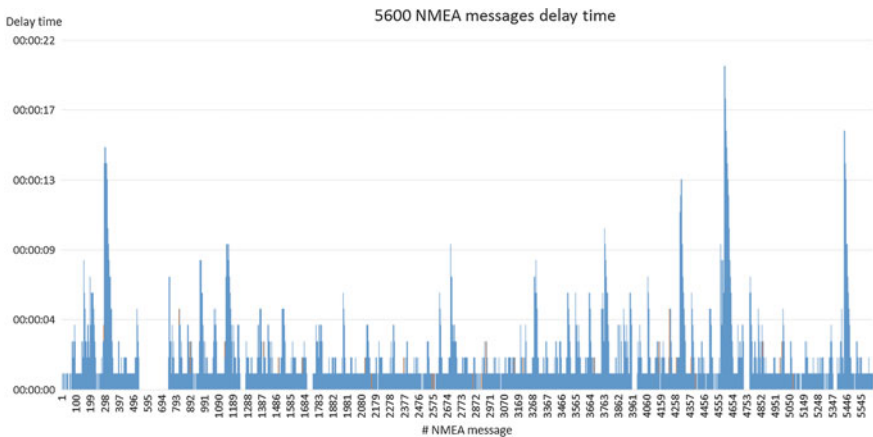


Fig. 4 Delay time for the second scenario test. Presented the first 5600 messages

depicted the delay time for the first 5600 NMEA messages in the second scenario case study. It is important to notice that the QoS in this extracted sample is 100 %. There are several instants where a high delay time occurs and one particular zone where a less than 1 s of delay is observed in the interval [#500, #700]. Since the overall QoS is 100 %, a possible explanation for the observed variation in the delay time is due to the poor network GSM signal conditions and the intermediated Internet equipment's queue.

7 Conclusions

A NMEA-AIS gateway system was implemented to aid the maritime vessel traffic. Technical solutions were developed to relay the NMEA-AIS messages from the VHF AIS receiver to the host mobile equipment connected to the GSM network. It is possible to implement this solution in different host Operation System platforms as long a TCP connection is available.

The developed system was measured in two different conditions scenario to determine its Quality of Service. Since the main connection issue is in the GSM network, the two scenarios are differentiated in cell phone movement characteristics. First it was measured in fixed position, second it was measured in movement condition. Both test conditions scenarios give an excellent QoS, 100 % in the first case and 99.97 % in the second case, which mean a few NMEA-AIS messages are not received in the cell phone.

Deeper analysis to check the root cause for loss NMEA messages allows us to conclude that the problem was in source of the TCP connection because the message wasn't sent. In conclusion the medium that supports the TCP connection over Internet and GSM networks are highly reliable. The AIS server design must be investigated to check the very small intermittent issue.

References

1. http://ec.europa.eu/transport/modes/maritime/index_en.htm. Accessed Dec 2015
2. Maritime Transport Policy, Improving the competitiveness, safety and security of European shipping, European Commission, European Commission, Directorate-General for Energy and Transport, B-1049 Brussels. http://ec.europa.eu/dgs/energy_transport/index_en.htm (2006). ISBN: 92-79-02947-9
3. United States Coast Guard, US Department of Homeland Security, Marine Safety Alert, Assistant Commandant for Marine Safety, Security and Stewardship (2010)
4. Annan, K.: The impacts of globalization on international maritime transport activity: past trends and future perspectives. In: Global Forum on Transport and Environment in a Globalising World. Guadalajara, Mexico, 10–12 Nov 2008
5. Mou, J.M., van der Tak, C., Ligterigen, H.: Study on collision avoidance in busy waterways by using AIS data. *J. Ocean Eng.* **31**, 483–490 (2010)
6. AIS-based evaluation of target detector and SAR sensors characteristics for maritime surveillance. *IEEE J. Sel. Top. Appl. Earth Obs. Remote Sens.* **8**(8), 3892–3901 (2015)
7. Riyadh, E., Jebali, C., Khaled, G., Ammar, K.: AIS data exchange protocol study and embedded software development for maritime navigation. In: Proceeding of IEEE 28th Canadian Conference on Electrical and Computer Engineering, pp. 1594–1599 (2015)
8. Hu, Q., Chen, J., Shi, C.: Bringing live AIS Information on the web sea charts by using Ajax. In: Proceeding of IEEE 7th International Conference on ITS Telecommunications, pp. 1–5 (2007)
9. Rodrigue, J.-P.: Maritime Transportation: Drivers for the Shipping and Port Industries, International Transport Forum 2010
10. Koldenhof, Y., Folbert, M.: Improving nautical risk modelling with the help of AIS, Marine Research Institute Netherlands Report 113, p. 13, Aug 2011

11. International Maritime Organization: AIS Safety-Related Messaging (2009)
12. Technical characteristics for an automatic identification system using time-division multiple access in the VHF maritime mobile band, ITU-R M1371, 04/2010
13. Maritime navigation and radio communication equipment and systems—Automatic identification systems (AIS)—Part 2: Class A shipborne equipment of the automatic identification system (AIS)—Operational and performance requirements, methods of test and required test results, International Electrotechnical Commission, IEC 61993-2:2012

Realization of PID Controllers in Analog Reconfigurable Hardware

Paulo J.R. Fonseca and Ramiro S. Barbosa

Abstract This paper describes the implementation of PID controllers using FPAA/dpASP devices. Two typical plants usually found in industrial applications are used to test the controllers and the results are compared with those obtained with the software MATLAB. For the tuning of the PID controllers it is adopted the well-known Ziegler-Nichols heuristic rules. The effectiveness of the proposed reconfigurable technology is demonstrated by the good accordance between the simulation results and the FPAA/dpASP circuit responses.

Keywords FPAA · dpASP · Z-N tuning rules · Reconfigurable · Analog design · PID controller

1 Introduction

PID control represents about 90 % of all industrial control loops. The PID has been thoroughly researched and is a well understood algorithm. We can mention numerous analysis tools, tuning techniques, and simulation tools available to analyze and design PID controllers [1–3].

The emergence of dynamically reconfigurable programmable analog circuits has been added to the options available to designers for implementing PID control loops. Field Programmable Analog Arrays (FPAAs) and dynamically programmed Analog Signal Processors (dpASPs) can be used for that purpose. These devices can be viewed as the analog equivalent of the well-established FPGAs (Field Programmable Gate Arrays), digital programmable devices. FPAA/dpASP device

P.J.R. Fonseca · R.S. Barbosa (✉)
Department of Electrical Engineering, GECAD – Knowledge Engineering
and Decision Support Research Center, Institute of Engineering/Polytechnic
of Porto (ISEP/IPP), Porto, Portugal
e-mail: rsb@isep.ipp.pt

P.J.R. Fonseca
e-mail: 1090038@isep.ipp.pt

technologies provide an easy way to implement analog circuits that can be reconfigurable by programming tools from manufactures, and in case of dpASPs are able to be dynamically reconfigurable “on the fly”. Their use increases the analog design integration and productivity, reducing the development time and facilitating future hardware reconfigurations reducing the costs. These technologies are very recent and are in rapid development to achieve a level of flexibility and integration to penetrate more easily the market. The applications of this technology are wide and include signal conditioning, filtering, data acquisition, and closed-loop control [4–14].

In this paper we design PID controllers using the FPAA/dpASP technology to control two typical plant transfer functions: a high-order transfer function and a first-order transfer function with time delay. The plant models are also implemented in a dpASP device. The PID controllers are tuned by using the Ziegler-Nichols (Z-N) heuristic rules. The performance of the PID controlled systems is assessed both in simulation with MATLAB and with the simulator of the development software tool of the FPAA/dpASP devices.

The paper is organized as follows. Section 2 gives the fundamentals of the reconfigurable analog hardware FPAA/dpASP devices. Section 3 presents the PID controller and the Z-N tuning rules. Section 4 shows two application examples and comparative results assessing the performance of the FPAA/dpASP technology. Finally, Sect. 5 gives the main conclusions.

2 FPAA/dpASP Technology

In this work we use the Anadigm QuadApex development board from Anadigm manufacturer [15]. It is a platform to get started for implementing and testing analog designs on the AnadigmApex AN231E04 dpASP devices. Furthermore, with its 32 bit PIC32 microcontroller and four dpASP devices, it provides a powerful platform to develop programmable analog designs [16].

The AnadigmApex represents the third generation of FPAA/dpASP devices from Anadigm company. Two members of the AnadigmApex family are AN131E04 and AN231E04 (Fig. 1). Both of these devices provide seven analog I/O Cells and four CABs (Configurable Analog Blocks). These structures are constructed from a combination of conventional Switched-Capacitor (SC) circuit elements and are programmed from off-chip non-volatile memory or by a host processor. Most of analog signal processing occurs within the CABs and is done with fully differential SC circuitry. The device processes analog signals in their I/O Cells and mainly on the CABs that share access to a single Look Up Table (LUT) which offers a method of adjusting any programmable element within the device in response to a signal or time base. The SRAM based dpASP AN23x devices are dynamically reconfigurable and their behavior can be modified partially or completely while operating. AN13X devices can be configured any number of times, but an intervening reset is required between each configuration load. AN23x

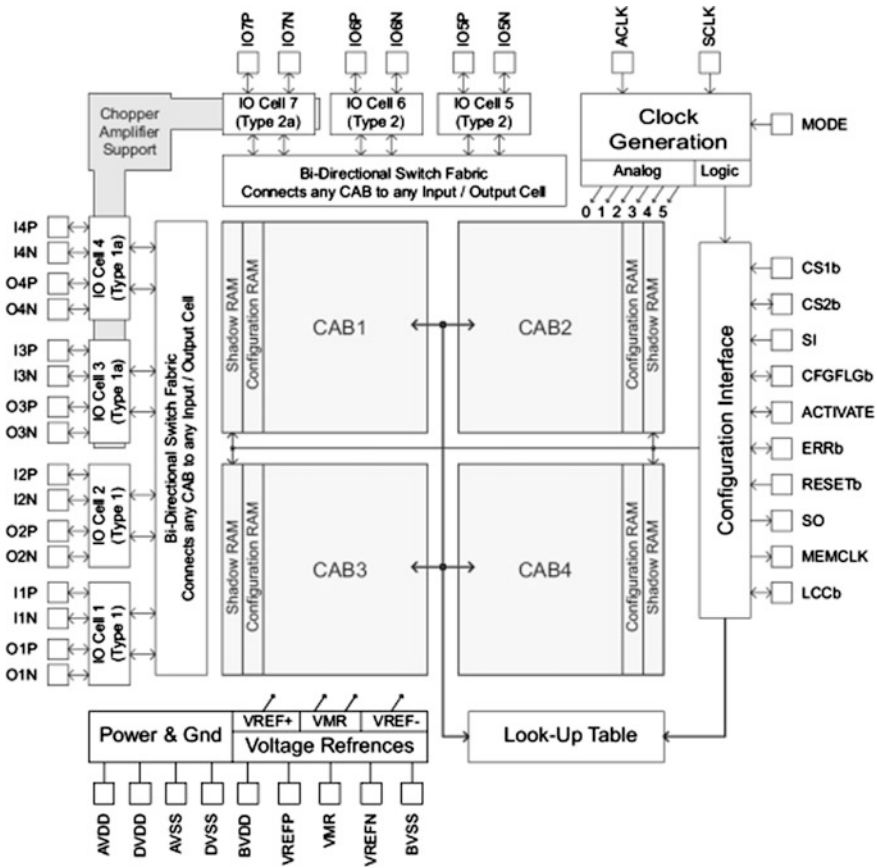


Fig. 1 Schematic of the FPAA AN13x and dpASP AN23x devices

devices are more flexible, allowing for on-the-fly reconfiguration any number of times after a reset [16, 17].

The software development tool is the AnadigmDesigner[®]2 (also provided by Anadigm), which makes it possible to design the desired circuit by using pre-defined blocks named CAMs (Configurable Analog Modules) [18]. One of the most important CAMs in our experiments is the bilinear filter CAM. Its transfer function is:

$$\frac{V_{out}(s)}{V_{in}(s)} = \pm \frac{2\pi f_0 G}{s + 2\pi f_0} \quad (1)$$

where f_0 is the corner frequency and G the pass-band gain. Figure 2 shows the circuit of the bilinear filter CAM.

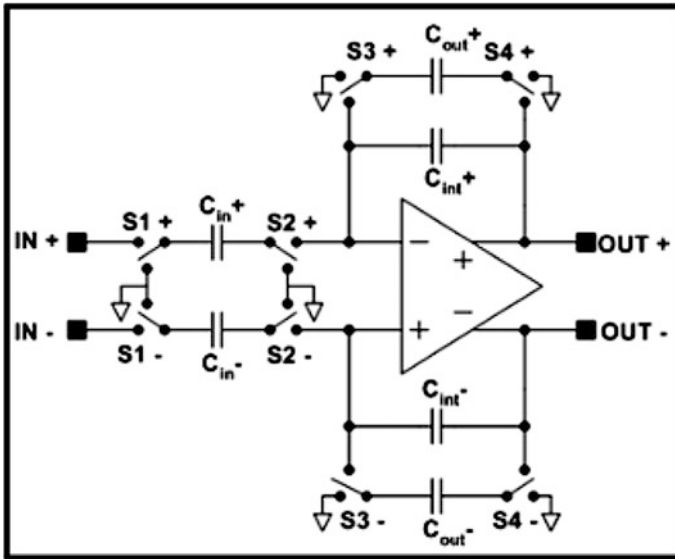


Fig. 2 Scheme of the bilinear filter CAM

3 PID Controller and Tuning

The block diagram of a typical PID controlled system is illustrated in Fig. 3. The transfer function of the PID controller is given by [1, 2]:

$$G_c(s) = \frac{U(s)}{E(s)} = K_p + \frac{K_i}{s} + \frac{K_d s}{T_f s + 1} \tag{2}$$

where K_p , K_i and K_d are correspondingly the proportional, integral and derivative gains to be tuned. The parameter T_f is the time constant of the first-order low-pass filter that limits the action of the differentiator.

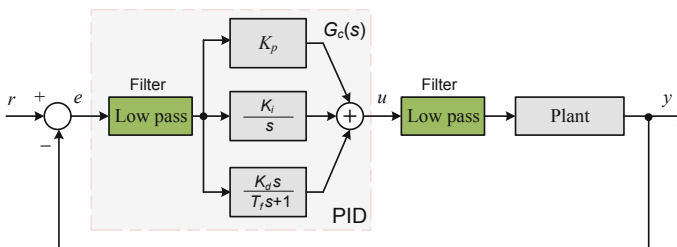


Fig. 3 Feedback control system with PID controller

The PID controller is implemented on third generation FPAA/dpASPs using CAM modules available on AnadigmDesigner[®]2 CAM library. The proportional, integral and differential actions of the PID controller are implemented by using the inverting gain, the integrator and the differentiator CAMs, respectively. The derivative bilinear filter CAM uses a corner frequency of 50 Hz while the corner frequency of the bilinear filters CAMs for the error and controller output is 2 kHz. The complete PID controller CAM scheme is reported in Fig. 4. Note that it was used two dpASPs (FPAA1-PID and FPAA2-PID) due to the limited resources of a single device to accommodate all necessary CAMs of the PID circuit. Usually different applications require different ranges to select the K_p , K_i and K_d parameters of the PID controller. However, the differential time constant from differential CAM and integration time constant from integration CAM are limited to a range selected on AnadigmDesigner[®]2. The implementation of the gain stages on separate P, I and D blocks gives more flexibility on the available settings for the PID gains. Some cautions in terms of noise and harmonics filtering are made, using bilinear CAMs, especially due to noise on output of differentiator and also harmonics on the sum/difference output CAMs. The output of the proportional and integrator blocks should be monitored using probes during simulation as saturation can occur easily after increase of K_p or K_i . The half sum/difference CAM on second dpASP (FPAA2-PID) has the function to sum the proportional, integral and differential actions. A small DC voltage can be programmed in conjunction in order to give a very small DC output value that in some circumstances can improve the response of the PID controller. In the third generation of Anadigm FPAA/dpASP, the saturation is internally achieved at amplitude of approximately 3 V and should be considered that internal ground signal reference (VMR) level is 1.5 V. These reference voltage levels should be considered during simulation to avoid response errors during implementation of the PID controllers.

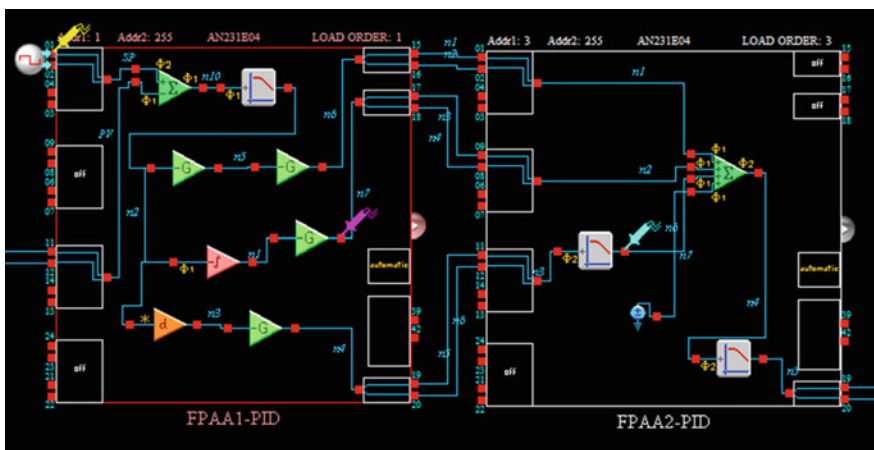


Fig. 4 PID controller implementation using two dpASPs AN231E04

In this work, the PID controllers are tuned by using the well-known Z-N heuristic rules. Ziegler and Nichols suggested two heuristic methods for the tuning of PID controllers [2, 3]. In the first method, the dynamics of the plant is described by a first-order transfer function with a time delay, $G_P(s) = Ke^{-sL}/(Ts + 1)$, where K is the gain, L the time delay and T the time constant. On the second method, the criteria for adjusting the parameters are based on evaluating the amplitude and frequency of the oscillations of the system at the limit of stability, yielding the ultimate gain K_u and the period of oscillation P_u . Then, the tuning parameters K_p , K_i and K_d are selected according controller type and plant parameters using tabulated formulas [2, 3].

4 Application Examples

In this section we design PID controllers using FPAA/dsASP devices to control two typical industrial plant transfer functions [19]. The adopted procedure is as follows:

- Model the system by a plant transfer function on MATLAB and AnadigmDesigner[®]2. Compare the results of the open-loop step responses with both methods.
- Test the PID controller in closed-loop with plant transfer function on MATLAB and AnadigmDesigner[®]2 using the Z-N tuning methods.
- Compare the results of the closed-loop step responses using the PID parameters from Z-N tuning rules.

For comparison purposes, the Integral of Absolute Error (IAE) between the closed-loop step response in MATLAB, $y_{MATLAB}(t)$, and the closed-loop step response in Anadigm Simulator, $y_{Simulator}(t)$, is computed as $IAE = \int_0^{T_{sim}} |y_{MATLAB}(t) - y_{Simulator}(t)| dt$, where T_{sim} is the time simulation corresponding to each of the experiments.

4.1 Example 1

Consider the plant model given by the third-order transfer function:

$$G_1(s) = \frac{1}{(s + 1)^3} \quad (3)$$

Figure 5 shows the entire PID control circuit using dpASPs. The first two dpASPs (FPAA1_PID and FPAA2_PID) are used to construct the PID controller in parallel form. The plant process $G_1(s)$ is implemented by the third dpASP (FPAA_PROCESS) using in cascade three bilinear filter CAMs.

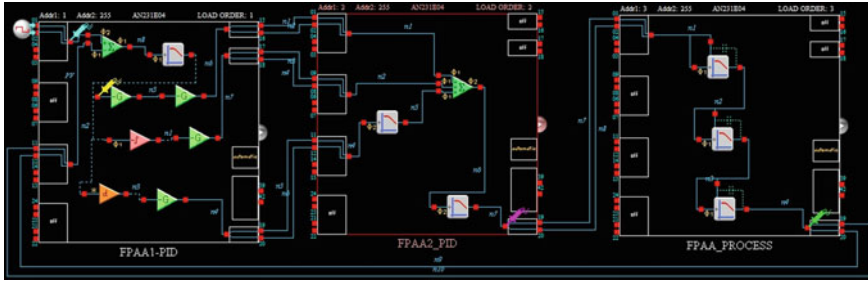


Fig. 5 Closed-loop PID controlled system with third-order plant transfer function $G_1(s)$

Figure 6 depicts the open-loop step response of $G_1(s)$ on MATLAB and Anadigm Simulator when applied a step input of amplitude of 1 V. The process parameters are determined as $(K, L, T) \equiv (1, 0.805, 3.69)$. Then, the PID gains obtained from Z-N process reaction curve method are $K_p = 1.2T/KL = 5.50$, $K_i = K_p/2L = 3.42$ and $K_d = 0.5K_pL = 2.22$. Figure 7 illustrates the closed-loop step responses on MATLAB and Anadigm Simulator when applied a step input of amplitude of 25 mV. As can be seen, the decay of oscillation is near a quarter amplitude which is in accordance with the Z-N rules. Also, both responses are very similar in terms of the steady-state and transient responses. The computed $IAE \cong 0.029$. These results validate the controller and the plant transfer function model implemented on dpASPs.

Next, we apply the Z-N ultimate sensitivity method as shown in Fig. 8. The corresponding ultimate gain is $K_u = 8$ and the period of oscillation is $P_u = 3.61$ s. Then, the calculated PID gains are $K_p = 0.6K_u = 4.8$, $K_i = 2K_p/P_u = 2.66$ and $K_d = K_pP_u/8 = 2.17$. Figure 9 illustrates the closed-loop step responses on MATLAB and Anadigm Simulator when applied a step input of amplitude of 25 mV. We observe again that the decay ratio of oscillation is near a quarter amplitude which is in accordance with the Z-N rules. Note once more that the step

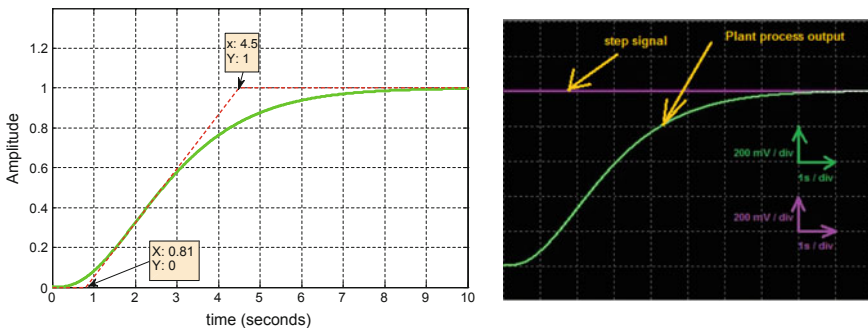


Fig. 6 Open-loop step response of $G_1(s)$ with MATLAB (left) and Anadigm Simulator (right)

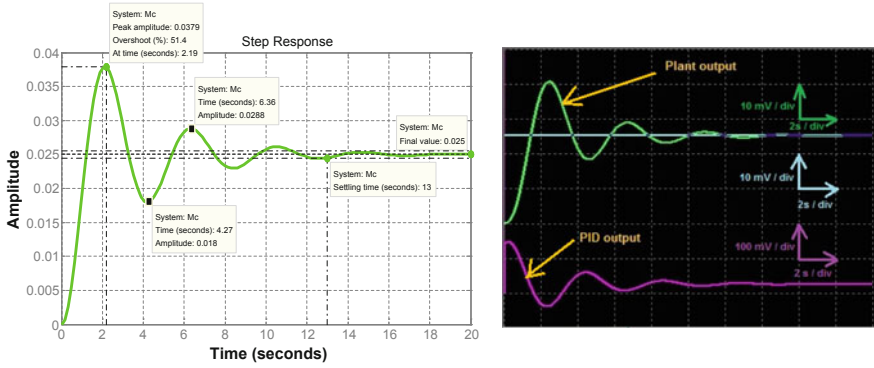


Fig. 7 Closed-loop step responses with $G_1(s)$ and PID controller tuned according to Z-N process reaction curve method in MATLAB (left) and Anadigm Simulator (right)

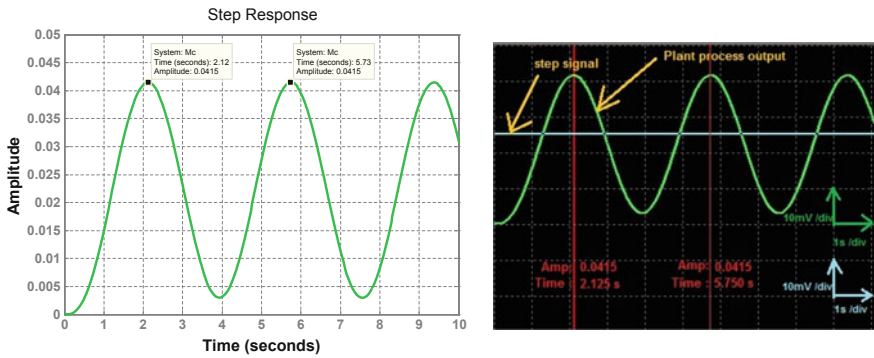


Fig. 8 Ultimate gain and period of oscillation of $G_1(s)$ in MATLAB (left) and Anadigm Simulator (right)

responses on Anadigm Simulator and MATLAB are very similar ($IAE \cong 0.024$) assessing the performance of the analog reconfigurable hardware technology.

4.2 Example 2

Consider now a first-order transfer function with a time delay:

$$G_2(s) = \frac{3.14}{s + 3.14} e^{-0.05s} \tag{4}$$

where the process parameters are $(K, L, T) \equiv (1, 0.05, 0.305)$.

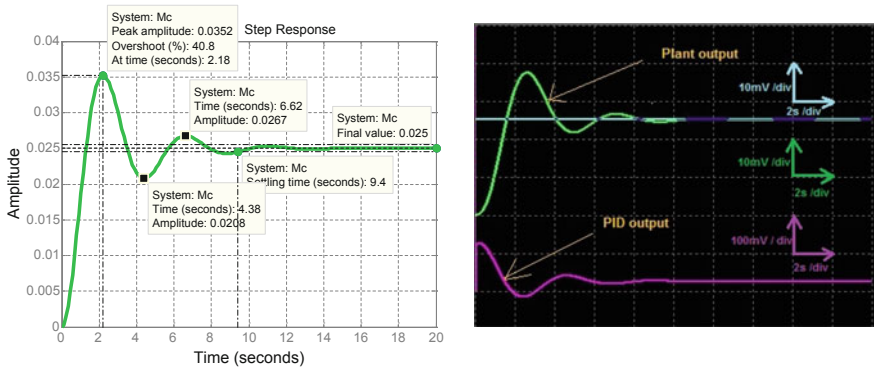


Fig. 9 Closed-loop step responses with $G_1(s)$ and PID controller tuned according to Z-N ultimate sensitivity method on MATLAB (left) and Anadigm Simulator (right)

Figure 10 shows the entire PID control circuit using dpASPs. The first two dpASPs (FPAA1_PID and FPAA2_PID) are used to construct the PID controller in parallel form. The plant process $G_2(s)$ is implemented by the third dpASP (FPAA_PROCESS) using in cascade a delay CAM and a bilinear filter CAM.

Figure 11 depicts the open-loop unit step response of $G_2(s)$ on MATLAB and Anadigm Simulator when applied a step input of amplitude of 1 V. The PID gains obtained from Z-N process reaction curve method are $K_p = 1.2T/KL = 7.64$, $K_i = K_p/2L = 76.4$ and $K_d = 0.5K_pL = 0.19$.

Figure 12 illustrates the closed-loop step responses on MATLAB and Anadigm Simulator when applied a step input of amplitude of 100 mV. The computed $IAE \cong 0.012$. It can be seen that the response shows a rather oscillatory system with a large overshoot corresponding to a low damping coefficient ($\zeta \cong 0.25$), as expected from a Z-N tuning methodology.

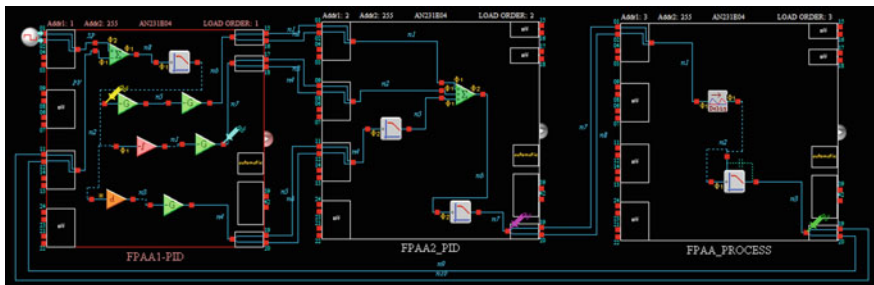


Fig. 10 Closed-loop PID controlled system with first-order plant process with time delay $G_2(s)$

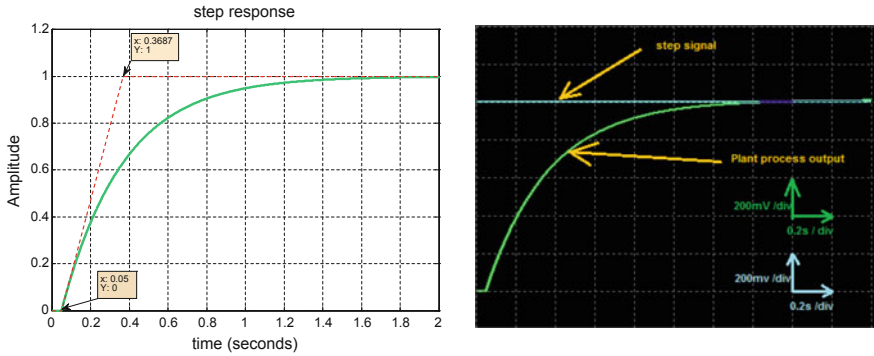


Fig. 11 Open-loop plant step responses of $G_2(s)$ in MATLAB (*left*) and Anadigm Simulator (*right*)

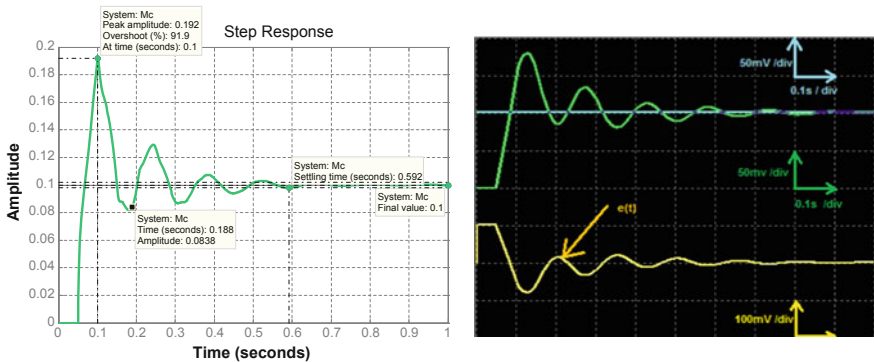


Fig. 12 Closed-loop step responses with $G_2(s)$ and PID controller tuned according Z-N open-loop method in MATLAB (*left*) and Anadigm Simulator (*right*)

5 Conclusions

The FPAA is a nice platform to design and implement PID controllers. In fact, the design of the PID controller can be done at a block level, and the simulation and test of each circuit takes only few minutes without the need to do complex mathematical calculations, choosing discrete components or focus on analog circuit details.

However, cautions in terms of filtering should be considered during design, especially due to noise on the output of differentiator block and also harmonics on the sum/difference output CAMs. Also, the output of the proportional and integrator blocks should be monitored using probes during simulation as saturation can occur easily after increase of proportional and integral gains.

It was described two examples of PID controller tuning using the Z-N heuristic methods. The obtained step responses using both methods show the quarter decay amplitude between the first and second oscillation which is in accordance with the Z-N methods. The obtained results on Anadigm simulator are very similar to those of MATLAB, revealing the good performance of dpASP circuits in implementing PID controllers.

Acknowledgments This work is supported by FEDER Funds through the “Programa Operacional Factores de Competitividade - COMPETE” program and by National Funds through FCT “Fundação para a Ciência e a Tecnologia”.

References

1. Åström, K.J., Häggglund, T.: PID Controllers: Theory, Design, and Tuning. Instrument Society of America, North Carolina (1995)
2. Franklin, G.F., Powell, J.D., Emami-Naeini, A.: Feedback Control of Dynamic Systems, 5th edn. Prentice-Hall, New Jersey (2006)
3. Ogata, K.: Modern Control Engineering, 4th edn. Prentice-Hall (2002)
4. Malcher, A., Pietraszek, S., Przybyla, T., Kidon, Z.: Real time QRS detection based on field programmable analog array. *J. Med. Inform. Technol.* **13**(2009), 183–188 (2009)
5. Zhang, W., Li, Y.: A self-adapted PID system based on intrinsic evolvable hardware. In: Proceedings of the International MultiConference on Engineers and Computers Scientists. Hong Kong, 19–21 Mar 2008
6. Falkowski, P., Malcher, A.: Dynamically programmable analog arrays in acoustic frequency range signal processing. *Metrol. Meas. Syst.* **XVIII** **1**, 77–90 (2011)
7. Malcher, A., Falkowski, P.: Analog reconfigurable circuits. *Int. J. Electron. Telecommun.* **60** (1), 15–26 (2014)
8. Visan, D.A., Lita, I., Cioc, I.B.: Temperature control system based on adaptive PID algorithm implemented in FPAA. In: 34th International Spring Seminar on Electronics Technology, pp. 501–504. Tratanska Lomnica, Slovakia, 11–15 May 2011
9. Wadikhaye, S.P., Yong, Y.K., Bhikkaji, B., Moheimani, S.O.R.: Control of a piezoelectrically actuated high-speed serial-kinematic AFM nanopositioner. *Smart Mater. Struct.* **23**, 1–12 (2014)
10. Chris, S.: Implementing process control with field programmable analog arrays. In: Embed Systems Conference. San Francisco (2004)
11. Mahji, S., Kotwal, V., Mehta, U.: FPAA-based PI controller for servo position control system. In: IFAC Conference on Advances in PID Control. Brescia, Italy, 28–30 Mar 2012
12. Dong, P., Bilbro, G.L., Chow, M.-Y.: Implementation of artificial neural network for real time applications using field programmable analog arrays. In: 2006 International Joint Conference on Neural Networks. Vancouver, BC, Canada, 16–21 Jul 2006
13. Schlottmann, C.R., Petre, C., Hasler, P.E.: A high-level Simulink-based tool for FPAA configuration. *IEEE Trans. Very Large Scale Integr. VLSI Syst.* **20**(1), 10–18 (2012)
14. Schlottmann, C.R., Hasler, P.E.: A high dense, low power, programmable analog vector-matrix multiplier: the FPAA implementation. *IEEE J. Emerg. Sel. Top. Circuits Syst.* **1**(3), 403–411 (2011)
15. Anadigm QuadApex Development Board, UM231004-K001, Anadigm Inc. <http://www.anadigm.com/>
16. AnadigmApex dpASP Family User Manual, AN13x series, AN23x series, UM000231-U001e, Anadigm Inc. <http://www.anadigm.com/>

17. AN231E04 Datasheet Rev 1.2, Anadigm Inc. <http://www.anadigm.com/an231e04.asp>
18. CAM documentation of AnadigmDesigner[®]2 development tool, Anadigm Inc. <http://www.anadigm.com/>
19. Åström, K.J., Hägglund, T.: Benchmark systems for PID control. In: Proceedings of IFAC Workshop on Digital Control, pp. 165–166. Terrassa, Spain (2000)

Speed Control of an Experimental Pneumatic Engine

João Pardelhas, Miguel Silva, Luis Mendonça and Luis Baptista

Abstract Speed control of an experimental pneumatic engine is used to implement and compare performance of different controllers. Firstly, the system static characteristics and transfer functions are identified so that controllers can be tuned and simulations can be done. Secondly, feedback, cascade and model free controllers are tuned, simulated and implemented. Finally, the controllers performances are compared and conclusions are drawn.

Keywords Speed control · Pneumatic engine · PID control · Cascade control · Model free control

1 Introduction

Speed control of rotating machinery is of great importance to the industry and has been under development for over 200 years [1]. Most controllers are Proportional and Integral (PI) or Proportional, Integral and Derivative (PID). Even more sophisticated control structures are, most of the times, proportional and integral or PID controllers at their lowest level [2].

PID control increasingly attracted the community interest for the past years, but improper tuning is still quite common and factory tuning is widely and inappropriately applied [3]. Even though PID controllers only have three parameters,

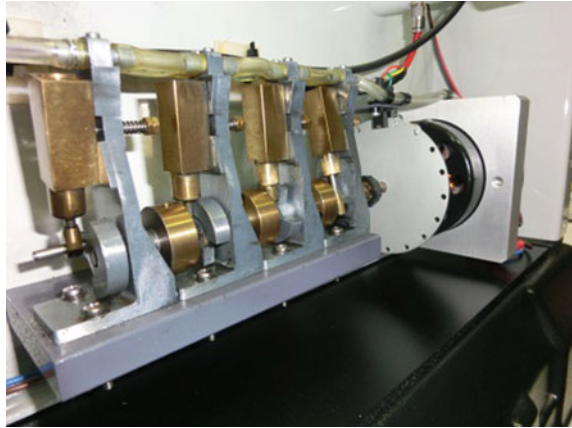
J. Pardelhas · M. Silva (✉) · L. Mendonça · L. Baptista
Department of Marine Engineering, Escola Superior Náutica Infante
D. Henrique, Paço de Arcos, Portugal
e-mail: miguelsilva@enautica.pt

J. Pardelhas
e-mail: joapardelhas@enautica.pt

L. Mendonça
e-mail: luismendonca@enautica.pt

L. Baptista
e-mail: luisbaptista@enautica.pt

Fig. 1 Engine speed control apparatus



finding their suitable values can be quite difficult. There are different approaches to PID tuning from which rise a wide variety of tuning rules.

A significant improvement on control structures has been developed in order to attenuate difficulties of different natures such as reduction of sensitivity of measurement noise, augment of model uncertainty robustness and better response to load disturbance and setpoint changes. The selected control structures to implement on the pneumatic engine are a PID controller in a typical feedback control loop, a Cascade Control (CC) loop and a Model Free Controller (MFC).

A pneumatic engine is used to obtain experimental results. The pneumatic engine is an apparatus, shown in Fig. 1, designed by TecQuipment, that models an internal combustion engine, where the speed and mechanical power are controlled by the amount of air supplied, instead of fuel. The dynamics of the CE107 are similar to an ignition compression engine in a dynamo-meter controlled test bed [4].

Its model is obtained and used to tune and simulate the response to a proposed setpoint following test.

Experimental results performance is quantified through the typical performance indices IAE, ISE, ITAE and ITSE.

The paper is organized as follows. The system modelling is addressed in Sects. 2 and 3 describes the control structures used in this paper. The results obtained are shown and discussed in Sect. 4 and conclusions are drawn in Sect. 5.

2 System Modelling

Both air supply valve and pneumatic engine modelling are achieved through experimental responses to step inputs. The basic principle is to control the position of the air supply valve, which is motorized by a d.c. motor, and so to regulate the engine speed under varying load conditions. The speed is controlled by the amount of air supplied to the system, which in turn depends on the air supply valve position.

2.1 Air Supply Valve

The air supply valve is a complex set of components. It is made of an electric motor that will move the shaft, a potentiometer used to estimate the valve position and the valve itself, where the air ow is controlled.

In order to reach the minimum pneumatic engine speed, 800 rpm, the air supply valve must be at approximately at 47 % of its position. Through the response to a step input of 100 % a First Order Plus Time Delay (FOPTD) approximation is carried out, Fig. 2. The transfer function is given by:

$$G_v(s) = \frac{X(s)}{V_{in}(s)} = \frac{1.38}{0.4s + 1} e^{-0.1s} \tag{1}$$

where $X(s)$ is the valve position and $V_{in}(s)$ is the input voltage on the air supply valve. The time constant was selected as the time it took the process to reach $T = 0.632$ kV. The dead time is smaller than a sampling period. It is assumed that it has the same magnitude, i.e. $L = 0.1$.

2.2 Pneumatic Engine

Pneumatic engine modelling is estimated through the complete system experimental response to a step input. The complete system includes the air supply valve, which model was already estimated has a FOPTD, and the pneumatic engine which is also approximated has a FOPTD. Estimation of a Second Order Plus Time Delay (SOPTD) is carried out using the Shinsky method [5] and method of moments [6]. In both methods, a single pole of the SOPTD is assumed know. Results are presented in Fig. 3 and transfer functions in Table 1.

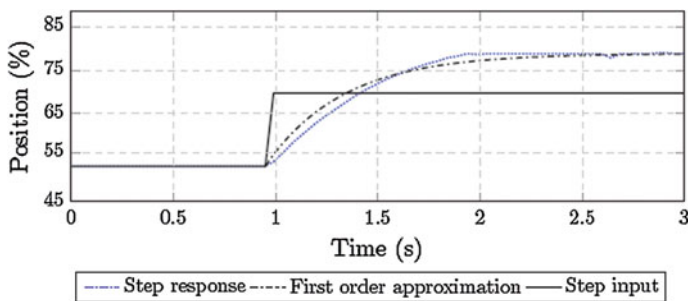


Fig. 2 Actuator response to a step input of 100 % on the working range

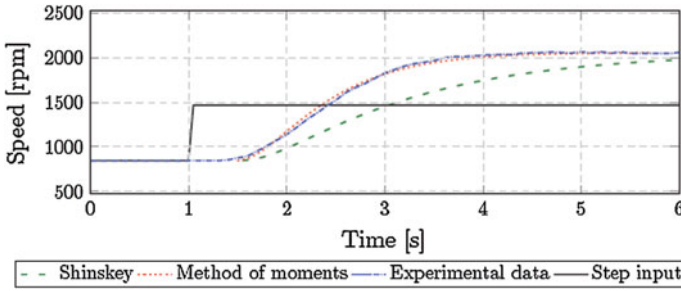


Fig. 3 Step input response and SOPTD approximations

Table 1 Air supply valve plus pneumatic engine SOPTD approximations

	Transfer function
Shinskey method	$\frac{1.95}{(1.47s + 1)(0.4s + 1)} e^{-0.52s}$
Method of moments	$\frac{1.95}{(0.6s + 1)(0.4s + 1)} e^{-0.52s}$

From the method of moments SOPTD approximation, and extracting the FOPTD air supply valve transfer function, the pneumatic engine FOPTD transfer function is given by:

$$G_e(s) = \frac{W(s)}{X(s)} = \frac{1.41}{0.6s + 1} e^{-0.42s} \tag{2}$$

where $W(s)$ is the pneumatic engine speed and $X(s)$ is the air supply valve position.

3 Control Structures

In this section the controllers are tuned, simulated and implemented. The performance is evaluated through the typical performance indices ISE, IAE, ITSE and ITAE.

A setpoint change response test is proposed. Simulations are carried out on SimuLink.

There are different anti-windup techniques and they can have a significant performance impact. A comparison is presented in [7] and results alert that even though some methods behave better than others under some conditions, they might not do so on different processes and controllers.

The back-calculation and tracking had a top overall performance for a batch of processes and tunings and for that reason was selected as the anti-windup structure in the controllers.

3.1 Feedback Control

Tuning rules are designed to adjust controller parameters for a specific control structure, a typical process model and a desired response.

For a SOPTD transfer function, that includes both air supply valve and pneumatic engine,

$$G(s) = \frac{K}{(T_1s + 1)(T_2s + 1)} e^{-sL} = \frac{1.95}{(0.6s + 1)(0.4s + 1)} e^{-0.52s} \tag{3}$$

the selected tuning rules for PID control to be simulated are the Ziegler and Nichols [8], Viteckova and Vitecek [9], Skogestad [10, 11]. All tuning rules are based on different tuning principles.

The best performance was obtained while using the Viteckova and Vitecek (VV) tuning rule, where the following gains for a parallel PID controller were obtained:

$$\begin{aligned} K_{cVV} &= 0.57 \\ K_{iVV} &= 0.57 \\ K_{dVV} &= 0.14 \end{aligned} \tag{4}$$

Both simulation and experiment are presented in Fig. 4.

Experimental results expose some process non-linearities, specially when the pneumatic engine is working on lower speeds. Response to an increase step input is different from the negative one, even though they have the same magnitude.

3.2 Cascade Control

Cascade control is known for reducing the process non-linearities [6]. Even though there are some developed approaches to tune cascade controllers tuning rules based on the process parameters are not so common [5].

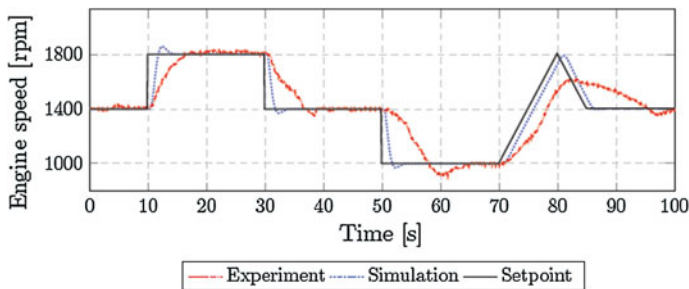


Fig. 4 Feedback control tuned with VV tuning rule

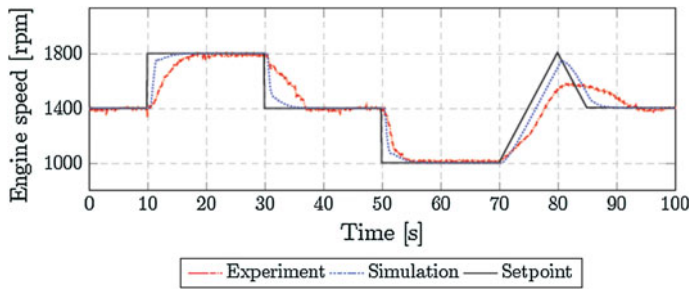


Fig. 5 CC experimental result

A tuning rule that fits the process, i.e., FOPTD and normalized time constants τ between 0.3 and 0.7, is presented in [7].

It yields the following gains for the inner loop controller

$$\begin{aligned} K_{c2} &= 2.09 \\ K_{i2} &= 4.83 \\ K_{d2} &= 0.06 \end{aligned} \quad (5)$$

and for the outer one

$$\begin{aligned} K_{c1} &= 0.75 \\ K_{i1} &= 0.91 \\ K_{d1} &= 0.13 \end{aligned} \quad (6)$$

Both simulation and experimental result are shown in Fig. 5.

Process response at lower working speeds is significantly closer to simulations, while using the CC, than VV. Still, it is quite different than higher ones and once again, revealing process non-linearities.

3.3 Model Free Control

The model-free control is a discrete time domain controller. Its output is obtained by estimating the process in real time. An ultra-local model and an intelligent PID controller, *i*PID, are used to eliminate the unknown parts of the process and possible disturbances, without any distinction between them [12].

Here an *i*P controller is used [12]. It is given by

$$u = - \frac{G_p - \dot{y} + k_p e}{\alpha} \quad (7)$$

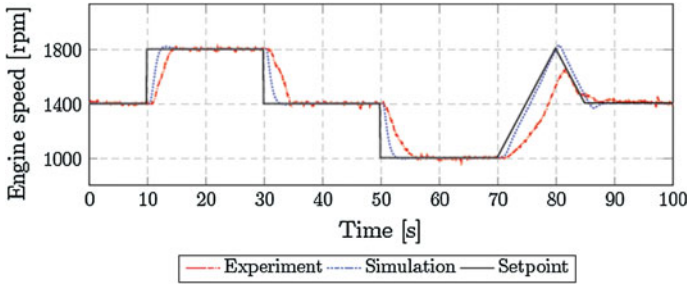


Fig. 6 MFC experimental results

where \dot{y} is derivative of y and α is a non-physical constant parameter obtained through trial and error. The controller output depends on a real time process estimation G_p [13]. An iP controller does not need anti-windup algorithms and it is here implemented, where $K_p = K_{pV} v = 0.57$ and $\alpha = 1$.

A good process estimation, from now on called G_{pest} , was already developed for an iP controller. It yields

$$G_{pest}(t) = \frac{1}{\psi} \left[\int_{t-\psi}^t (\dot{y} - \alpha u - k_p e) dt \right] \quad (8)$$

which is quite different from the traditional model identifications. The estimation is only valid for a short period of time and therefore ψ must be quite small when compared with the sampling period. Simulations and experiments use $\psi = 0.02$.

Simulation and experiment are presented in Fig. 6.

The response is very similar within all working ranges. The process reacts slower than simulations predicted, but in a stable manner. The ramp response could not eliminate the error as fast as expected, but still, it is better than VV and CC.

4 Results and Discussion

Performance quantification was carried out through the typical performance indices IAE, ISE, ITAE and ITSE.

Absolute performance indices for simulations are shown in Table 2 and for experiments in Table 3. MFC has the smaller difference between simulations and experiments.

Relative performance indices for simulations are shown in Table 4 and for experiments in Table 5. The feedback control loop performance indices were considered to be the starting values, and therefore set to one. The others are relative values. Performance indices higher than one are the translation of a worst performance and smaller than one represent a better performance.

Table 2 Simulation performance indices

	IAE	ISE	ITAE	ITSE
VV	4.92	1.62	252.85	63.89
CC	5.02	1.60	240.21	60.70
MFC	4.77	1.68	235.15	63.25

Table 3 Experimental performance indices

	IAE	ISE	ITAE	ITSE
VV	28.86	10.41	498.5	177.88
CC	25.22	7.34	419.80	118.46
MFC	15.31	5.62	324.15	140.52

Table 4 Simulation performance indices

	IAE	ISE	ITAE	ITSE
VV	1	1	1	1
CC	1.02	0.99	0.95	0.95
MFC	0.97	1.04	0.93	0.99

Table 5 Experimental performance indices

	IAE	ISE	ITAE	ITSE
VV	1	1	1	1
CC	0.87	0.71	0.84	0.67
MFC	0.53	0.54	0.65	0.79

Performance in simulations show that both CC and MFC are better than VV in most of performance indices, but not on all of them. However, MFC has the best experimental performance. Furthermore, the process response is similar in all working ranges, which contrasts with VV and CC.

5 Conclusions

Simulations are carried out on Matlab/Simulink. Performance is evaluated through the performance indices IAE, ISE, ITAE and ITSE. Feedback, cascade and MFC control structures are simulated and tuned based on proper tuning rules.

Simulation shows that MFC and CC have a better response than VV in 3 out of 4 performance indices.

The controllers are implemented on a dedicated hardware that includes a microcontroller and a motor drive. Together they are capable of moving the actuator based on the implemented control structure and tuning. MFC provides the best experimental performance. Furthermore, it has a smaller discrepancy between simulations and experiments. Cascade control has an overall better response than VV.

References

1. Bennett, S.: A History of Control Engineering 1800–1930. Peter Peregrinus Ltd, London (1979)
2. Astrom, K.J., Hagglund, Tore: Revisiting the Ziegler-Nichols step response method for PID control. *Process Control* **14**, 635–650 (2004)
3. Bialkowski, W.L.: Dream versus reality—a view from both sides of the gap. *Pulp Pap. Can.* **11**, 19–27 (1994)
4. CE107 Engine Speed Control User Guide. TecQuipment Ltd (2009)
5. O’Dwyer, A.: Handbook of PI and PID Controller Tuning Rules. Imperial College Press (2006)
6. Astrom, K.J., Hagglund, T.: Advanced PID control. ISA (2005)
7. Visioli, A.: Practical PID control. Springer Science (2006)
8. Ziegler, J.G., Nichols, N.B.: Optimum setting for automatic controllers. *Trans. ASME* **64**, 759–768 (1942)
9. Viteckova, M., Vitecek, A.: Controller tuning for controlled plants with time delay. In: Preprints of Proceedings of PID ‘00: IFAC Workshop on digital control, pp. 238–288 (2000)
10. Skogestad, S.: Probably the best simple PID tuning rules in the world. *J. Process Control* **13**, 291–309 (2003)
11. Hagglund, T., Astrom, K.J.: Revisiting the Ziegler-Nichols tuning rules for PI control. *Asian J. Control* **4**, 364–380 (2002)
12. Michel Fliess, Cedric Join. Model-free control 2 (2015). <http://arxiv.org/pdf/1305.7085.pdf>
13. Gédouin, P.-A., Delaleau, E., Bourgeot, J.-M., Join, C., Arbab-Chirani, S., Calloch, S.: Experimental comparison of classical pid and model-free control: position control of a shape memory alloy active spring 2 (2015). <https://hal.inria.fr/inria-00563941/document>

Design and Implementation of a PI Controller for a Metal Casting Machine

Bruno R. Mendes, Manuel F. Silva and Ramiro S. Barbosa

Abstract Control and monitoring systems capabilities are unavoidable to improve product quality, reduce production time, and to the rapid adaptation to changes in production. Therefore, it is advantageous to develop control and monitoring systems, and maximize the use of the resources already available in machine tools, without high additional costs and hard implementations. The use of Programmable Logic Controllers (PLC) on industries is growing. This sort of controller has been an election tool to attend present day requirements. It has the necessary resources to acquire and manage the information and control of the machines, and easily interacts with SCADA systems. The objective of the study described in this paper was to develop a solution for monitoring a metal casting machine, which could replace an outdated system installed on it, and find a solution to control a metal pouring process. All programs that allow the PLC to control the machine movements, and also perform the casting process, were developed during the project implementation. The results show that the developed solution is able to control the machine without the need to invest in a PC, which is a more expensive solution and with a more limited life time.

Keywords Control • PLC • HMI • Monitoring • Valve • Pouring process

B.R. Mendes · M.F. Silva (✉) · R.S. Barbosa
School of Engineering of the Polytechnic of Porto,
ISEP-IPP, Rua Dr. António Bernardino de Almeida, Porto, Portugal
e-mail: mss@isep.ipp.pt

B.R. Mendes
e-mail: bruno.roca.mendes@gmail.com

R.S. Barbosa
e-mail: rsb@isep.ipp.pt

M.F. Silva
INESC TEC, Rua Dr. Roberto Frias, Porto, Portugal

1 Introduction

This paper describes the control system update of a casting machine belonging to Grohe-Portugal [1], a faucet producing company, located in Albergaria-a-Velha. Grohe-Portugal contributes with a significant percentage to the total production of the Japanese LIXIL industrial group. Its main goals are high standards of quality, technology, design and sustainability, seeking to stand out from all others in the group.

In industry it is not viable to constantly update equipment, either hardware or software. Normally, this leads to problems when malfunctions and breakdowns appear due to discontinuation of some equipment by their manufacturers, leading to several problems, such as incompatibilities with the older ones [2]. Given these ideas, this project emerged by the need to optimize and update one of Grohe's production processes [1].

Grohe's production plant has a number of fully functional equipment, already with several years, that have never been updated or upgraded, and for which it is now difficult (if not impossible) to find spares. This creates difficulties for this company when breakdowns in these machines occur. Therefore, to surpass this problem, Grohe is trying to update the control and monitoring systems of some of its old equipment, changing the parts that are no longer available by others, that perform equivalently or even better, and for which it is foreseen a longer lifetime and easier replacement.

This was the case of the machine BP260 X (or Low Pressure), depicted in Fig. 1, which was the target of the intervention described [1]. This machine integrates the Foundry Department of Grohe's production process, being responsible for casting the raw material (brass and other copper molten metal alloy), into a faucet's metal body. The machine consists of a column, in which two heads with rotation capacity are mounted, and is designed to be operated by one operator, whose function is to place the sand cores, extract the permanent mold of the part and perform the quality supervision. The operator lies on a platform in front of the rotary motor. This machine is also equipped with a furnace that maintains the alloy at the desired temperature.

Fig. 1 Photograph of the BP260 X casting machine



Regarding its operation, the machine puts the molds in the furnace automatically, directing the metal alloy into the permanent mold (through a decrease in pressure on it, and therefore the name Low Pressure of the machine), from bottom to top through the spout, and waits until the molten metal is solid to open half of the investment shell to allow the operator extracting the product.

The machine old monitoring system run on a personal computer, whose hardware and software are no longer manufactured and supported. Therefore, in case of any failure it would be impossible to acquire spare parts for performing its maintenance and the only possible alternative would be to design a new control system for the same purpose, that does not need frequent updates and that is more robust.

Bearing these ideas in mind, the main objective of the work described in this paper was to develop a solution that would allow control and monitor the pouring process and upgrade some other parts. For its realization it was need to:

- Design the operator terminal or Human Machine Interface (HMI) that would interact with the PLC in order to allow viewing/adjusting—its variables, according to the user needs;
- Control and check the parameters of the pouring process. This is an operation that consists in injecting compressed air inside a furnace, bringing the liquid metal into the mold. As part of this system there was a pressure transducer to sense the pressure inside the furnace and an air valve controlled by the computer to inject the air.

2 Existing System Architecture

The old system architecture is presented in Fig. 2 (left). The machine movements are controlled by a controller (PLC) which, by means of actuators and sensors causes the machine to properly perform every move. Connected to the PLC there was a PC, running a program that controlled the pouring process and allowed the operator to monitor the process, through a HMI. The pressure valve is responsible for sending air to the Furnace, according to the predefined pressure value (for each faucet body the operators defined, through the HMI, a pressure curve over time to

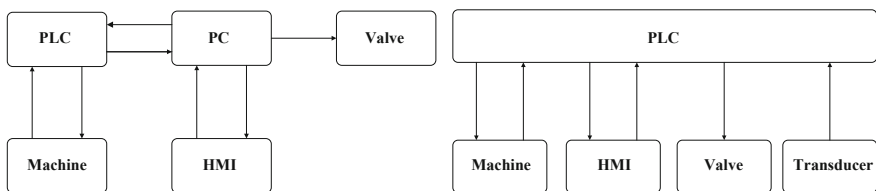


Fig. 2 Architecture of the existing system (left) and architecture designed to be implemented in the system (right)

be followed by the machine) that is entered into the HMI. The pressure values that the valve should provide change with time, in order for the curve specifications to be met. The valve is supplied at 24 V DC, with the output voltage between 0–10 V, leading to a pressure of 0–1 bar, and a maximum pressure of 2 bar.

During the analysis of the control system and machine monitoring, it was found that the control of the pouring process only used a database with values that are provided to the valve in order to fulfill the specifications over time without any sort of feedback (in open-loop).

Once the generic study regarding the machine functionalities finished, the next step was to analyze carefully the components to be replaced. In a first approach to the problem, the conclusion drawn was that the most viable, would be to find alternatives on the market to replace the older components, in particular the pressure regulating valve, and also find a solution to replace the whole monitoring system.

It was also set as an objective to convert the PLC program, which was in an older SIMATIC version V5.5 to the newer version available by Siemens, the TIA Portal V13 [3], and thereby circumventing future problems of maintenance or assistance. With this purpose it was used the CPU-314 1 for the new program, this one replacing the old CPU-315, with the old machine control program.

Furthermore, the integrated PC in the old system played a key role as it was responsible for controlling the pressure regulating valve, and also the link between the valve itself and the PLC that controlled the machine operation; in other words, the manufacturing process does not take place if the PC or PLC fail—which causes the system to have a major limitation.

Concerning the monitoring system, the operating system was quite old (Windows 98), having been discontinued, and the used HMI software also became obsolete, which lead to several compatibility issues with the operating systems used today. In short, with the increasing computational development and the current requirements of the computer itself, it would not be possible to update to a newer operating system. Even if the PC had the required capabilities, it would be completely unnecessary, since the hardware is so outdated that there are no longer drivers that could be installed in the new operating systems.

3 Architecture of the Developed System

Taking into account the above mentioned details, there were considered two possible solutions for the problem. One would be to use a high-level programming software, such as Visual Studio, and through a programming object-oriented language (such as Visual Basic or C#), develop a SCADA system capable of monitoring the machine, control the pressure regulation valve and serve as a link between the PLC and the new support hardware for the application. Another solution would be to resort to the PLC so that, in addition to control the machine

movements, it could also control the pouring process, and acquiring a SCADA system only for monitoring purposes.

The developed system (Fig. 2, right) eliminates the control of the casting process by the PC, being this done by the PLC. This way, the PLC becomes the central control unit, being all necessary equipment connected to the controller, which becomes responsible for all control aspects, namely for the machine and for the pouring process. It was also added a pressure transducer to the new architecture, used for reading the furnace pressure over time, so that these values could be applied to a new process control algorithm working in closed-loop. The furnace pressure is used as a feedback signal for a Proportional and Integrative (PI) controller, so that the furnace achieves and keeps the pressure levels necessary to comply with the specifications of the pouring process. The values received from the transducer will enter the PI controller as the feedback variable and, along with the P and I constants and the setpoints values assigned, will generate the value to be used for the valve. This transducer is powered at 24 V DC, with an output voltage between 0–10 V, corresponding to a pressure of 0–2 bar.

In order to overcome the problems of updates, drivers and operating systems found on computers, there was made a study around SCADA software applications that run in operator panels and can be connected to PLC. For this project it was used the iX Developer software provide by Beijer Electronics 5. This SCADA software contains all the basic functions needed to create an application. Functions have been developed keeping in mind the needs and preferences of users. The predefined objects in the developer's software can be used to create a complete process image, providing an overview of a complex application. Usually, in this software the programmer can customize the predefined objects or create their own objects.

Operator consoles can be connected to various types of automation equipment such as PLCs, servos and sensing units, either for control and performance assessment purposes. For information exchange are used tags, which belong to the system or may be internal. The tags have a symbolic name and may represent different types of data. Tags attached to objects can change values on the controller, and the tags values can be reflected to change the appearance of the object in several ways.

4 Implementation of the Proposed Solution

It was established that the proportional valve should receive pressure setpoints values at pre-set intervals of x seconds. According to the tables of the various pouring curves (internal to the company), all pressure values are set at 1 s intervals. Therefore, it was decided that in the new control system the valve will also receive the different values of setpoint every 1 s. Likewise, the transducer reads the pressure values in the furnace every 1 s. To be possible this type of control, it was used a PID function (function block already developed by Siemens), in which are used the setpoint values as an input parameter and the transducer reading as feedback

value. After the PI control is applied, it is calculated an output value which is sent to the valve analog address. The tuning of the PI controller is explained in detail below.

Regarding the PLC program were created functions that allow the interaction of the machine movements with the control of the pouring process. There were created two Data Blocks (DB): one for the pouring curve pressure values, and another as an output DB to storage all the values read by the transducer in real time.

In order to facilitate the manipulation of data, it was used the Instruction List (IL) programming language, also known as Statement List (STL), within the SIEMENS PLC. A function must be programmed to access different DBs, as the machine is in the furnace, and a timer must be set so that the reading of each value is processed at 1 s intervals. It is necessary to set the timer, also creating conditions that facilitate the program flow such as, for example, the creation of a coding sequence to ensure that the timer is reset each time a new value is read. As the reading of each pressure value is performed, the writing is also performed to other DB (the output DB). Analogously to what happens reading the values, writing is also performed through a pointer, with the write position being indicated by the present value of the pressure transducer to the DB address pointed output.

For the described programming, it was necessary to frame a PI controller to set the values to be sent to the regulator valve, depending on the setpoint values, and on the values of the pressure read by the pressure transducer.

Taking advantage of the tools provided by the TIA Portal, the application of this controller has become easier since this software provides a block, referred to as “CONT_C” which has an associated instance DB that contains all the variables needed to work correctly. This block must be called in a cyclic interrupt OB (OB 30–38), being typically used OB 35. A cyclical time should be established on the block so that it could be called to ensure that all calculations are performed correctly.

One of the parameters to be used is the “SP_INT” where it is entered the setpoint value. This value is introduced as a percentage, so it is necessary to associate the desired values, for example pressure, to a percentage scale. Similarly to the “SP_INT”, in the “PV_IN” is entered the input value read by the transducer. This can be introduced in a percentage format—however it is used the address “PV_PER” where the values read by the transducer can be sent directly to this variable without the need for scaling factors. The remaining values are input parameters to be set on the PID controller. There is assigned an external variable, which is responsible for sending the values obtained through the calculations of the controller to the analog address assigned to the regulating valve.

To complete one of the objectives of this project, a new HMI was developed to communicate with the PLC, based on the previous one, allowing to control and display a set of variables, as well as the graph of the pouring curve. Thus a new interface was created that does not differ much from the previously one, already used by Grohe’s machine operators. For this purpose it was decided to use the iX

Developer software with the properly configured functions that allow designing a simple but efficient HMI that could display all the parameters needed to a proper machine operation.

4.1 Controller Tuning Process

The PI controller tuning method adopted was the Cohen-Coon method, as this is a suitable method for systems that require a quick response. The Cohen-Coon tuning rules are adequate for use on self-regulating processes in case the control objective is to have a fast response. These tuning rules use three process characteristics (the process gain, the dead time, and the time constant), which are determined by performing a step test and analyzing the corresponding results.

The Cohen-Coon tuning rules aim for a quarter-amplitude decay response, just like the Ziegler-Nichols rules. Quarter-amplitude damping-type of tuning provides very fast disturbance rejection, but tends to be very oscillatory and frequently interacts with similarly-tuned loops. This type of tuning also leaves the loop vulnerable to instability in case the process gain, or the dead time, doubles in value. To fix both problems, the controller gain should be reduced by half (e.g. if the rule recommends using a controller gain of 2.0, is used only 1.0). This prevents the loop from oscillating around its setpoint as described above, and provides an acceptable stability margin.

To parameterize the PID controller, it was necessary to determine the constants to be framed in the TIA Portal block “CONT_C”, following the rules of the Cohen-Coon tuning method described in the next section.

5 Tests Performed and Results Achieved

Using the graphical tool available through the “CONT C” block, was applied a step corresponding to 10 % of the maximum capacity value of the valve and it was expected that the transducer follow this pressure value, allowing the system to stabilize [4]. Then, it was imposed a variation to 50 % of the total capacity of the valve, being obtained the graph depicted in Fig. 3.

Through the analysis of this graph were obtained various values which relate the time (in seconds) to the pressure (in percentage), i.e., values that describe the monitoring of the transducer over time to reach 50 % of its value, corresponding to 500 millibar (the requested pressure). Because there are leaks in the furnace, as can be seen in Fig. 3, the pressure in the oven does not reach the desired 500 millibar. Table 1 shows the various values obtained in this experiment.

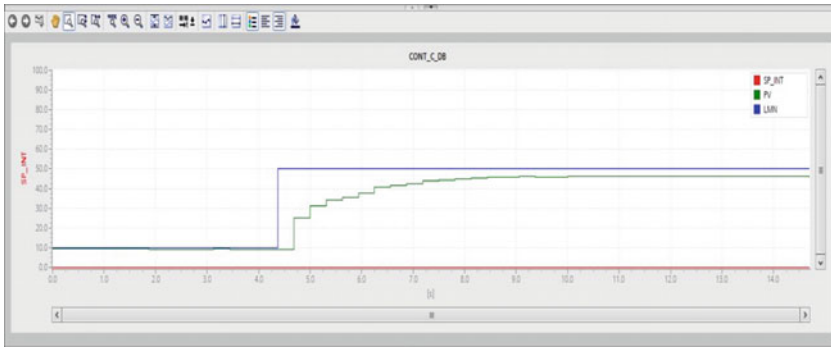


Fig. 3 Graph corresponding to 50 % variation of the total valve capacity

Table 1 Time versus pressure

Time (s)	Pressure (%)	$m = (y_2 - y_1)/(x_2 - x_1)$
4.688	9.13	∞
4.688	25.22	19.487
5	31.3	9.683
5.315	34.35	4.153
5.628	35.65	6.943
5.942	37.83	10.033
6.245	40.87	2.771
6.559	41.74	2.771
6.873	42.61	4.140
7.187	43.91	1.401
7.501	44.35	1.369
7.815	44.78	1.401
8.129	45.22	1.369
8.443	45.65	0.713
9.06	46.09	5.087

According to the results shown in Table 1, the gain computation process comes:

$$g_p = \frac{36.96}{40} = 0.924 \tag{1}$$

Given these results, it was calculated the maximum slope. The values in the first two columns of Table 1 were used to compute the slope (presented in the third column). According to the computed values, the slope is maximum at the point (4.688; 9.13) with the value $m = \infty$. Having an infinite slope, the line will be a vertical line at $x = 4.688$, tangent to the point where the slope is infinite (4.688; 9.13), as depicted in Fig. 4. The tangent line intersects the pressure curve at the 9.13 % point.

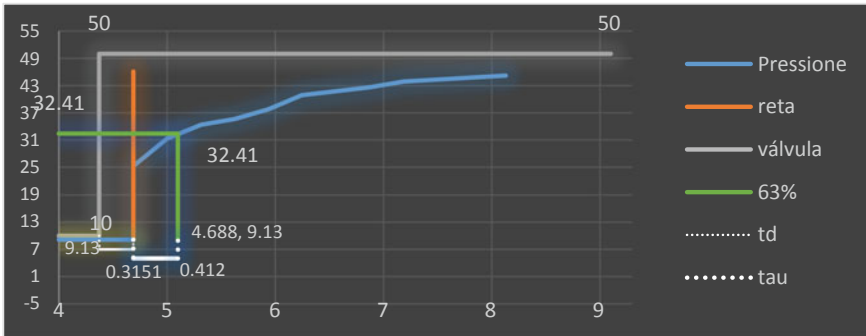


Fig. 4 Curve depicting the evolution of the pressure along time

It is necessary to calculate the point at which the pressure reaches 63 % of the total variation of the transducer, which varies from 9.13 % up to 46.09 %. Accordingly:

$$46.09 - 9.13 = 36.96 \% \tag{2}$$

$$36.96 * 0.63 = 23.28 \% \tag{3}$$

$$23.28 + 9.13 = 32.41 \% \tag{4}$$

Making this the intersection point with the initial curve, it is possible to obtain the time value and the point coordinates shown in Fig. 4.

Knowing this, it is possible to compute the dead time (t_d) and the time constant τ . The calculation of these values is given by:

$$t_d = 4.688 - 4.3729 = 0.315s \tag{5}$$

$$\tau = 5.1 - 4.688 = 0.412s \tag{6}$$

After being calculated these parameters, it is possible to compute the parameters for the Cohen-Coon algorithm [5]. Since the applied control algorithm is the PI, it comes:

$$K_c = \frac{0.9}{g_p} \left(\frac{\tau}{t_d} + 0.092 \right) = \frac{0.9}{0.924} \left(\frac{0.412}{0.3151} + 0.092 \right) = 1.36317 \tag{7}$$

$$\begin{aligned} T_i &= 3.33 \cdot t_d \cdot \frac{(\tau + 0.092 \cdot t_d)}{\tau + 2.22 \cdot t_d} \\ &= 3.33 \cdot 0.3151 \cdot \frac{(0.412 + 0.092 \cdot 0.3151)}{0.412 + 2.22 \cdot 0.3151} \\ &= 0.416296s \end{aligned} \tag{8}$$



Fig. 5 Values of the points for the first used curve (*left*) and response of the system to the curve defined (*right*)

As advised by the guide line, the values were divided by two, giving 6:

$$\frac{K_c}{2} = 0.681585; \frac{T_i}{2} = 0.20815s \quad (9)$$

Using the above calculated values for the Cohen-Coon control algorithm, new values were defined for the setup curve, to verify if the developed control system can follow different curves. Figure 5 (left) shows the values of the points for the first curve defined, with the corresponding response shown in Fig. 5 (right).

Compared to the control previously carried out, the new control system is designed to work with better prospects since it receives the feedback from the values read by the transducer, and its output will be adjusted according to the established setpoint.

After the systems being installed in the machine, several casting experiments were performed with distinct products. The results of these experiments allowed concluding that the parts being casted in this machine were being produced according to the quality requirements. Furthermore, the operators were able to easily adapt to the new HMI of the machine, without major learning difficulties.

6 Conclusions and Possible Future Developments

The work presented in this paper aimed to carry out the control and HMI development of a process for leaking parts of a metal casting machine. With this purpose in mind, was made the study of all involved components, both hardware and software.

Regarding the hardware, the outdated components that were replaced were a PLC with a S7-314 CPU and the SCADA system console. Regarding the software, two options were considered for solving the problem: the creation of a SCADA interface through object-oriented programming such as C#, which after its creation would be installed on a PC, and another that would be the PLC control unit, in

addition to controlling the machine, also controls the casting process, and then sending the information for a SCADA console acquired. It was considered as a better solution to have the control performed by the PLC, because according to the professional experience of the industrial area a PLC lasts longer than a computer when it comes to issues of upgrades and maintenance.

The obtained results were very positive, since all programming leading to the control system provided a pouring curve that fulfilled the desired specifications. Furthermore, the parts that are being presently casted in this machine are being produced according to Grohe's rigorous quality standards.

Acknowledgments This work is financed by the ERDF—European Regional Development Fund through the Operational Programme for Competitiveness and Internationalisation—COMPETE 2020 Programme within project «POCI-01-0145-FEDER-006961», and by National Funds through the FCT—Fundação para a Ciência e a Tecnologia (Portuguese Foundation for Science and Technology) as part of project UID/EEA/50014/2013.

References

1. Mendes, B.F.R.: Desenvolvimento de Aplicação para a Otimização de Processo Produtivo. Master Thesis. Instituto Superior de Engenharia do Porto (2015)
2. Gupta, B.P.: Modernization of Industrial Machines. <http://bin95.com/modernization-of-industrial-machinery.htm>. Accessed 30 May 2016
3. Romanholo: TIA Portal hands on—básico v11-v2. <http://pt.slideshare.net/marcosromanholo/01-tia-portal-hands-on-basico-v11v2?related=1>. Accessed 30 May 2016
4. Franklin, G.F., Powell, J.D.: Feedback Control of Dynamic Systems, 3rd edn. Addison-Wesley (1994)
5. Cohen, G.H., Coon, G.A: Theoretical consideration of retarded control. Trans. ASME. **75**, 827–834 (1953)
6. SIEMENS. CPU-314 DOC ON CD. 04/2000 Edition, electronic manual. [CD-ROM]
7. BEIJER ELECTRONICS. iX Developer User's Guide English. 10/2012 Edition, iX_Developer_MAEN832E_English. [PDF]

Part XIII
Education

Control Engineering Learning by Integrating App-Inventor Based Experiments

Filomena Soares, Paulo Moura Oliveira and Celina P. Leão

Abstract This paper presents a teaching/learning experiment on the use of MITAppI2 as a friendly tool in Automation courses. The goal was to assess if the up-to-date mobile applications can act as promoters in learning automation topics. The experiment took place in two Portuguese universities. The results achieved point towards a successful use of these tools in university classes.

Keywords Teaching/learning experiment • Automation • APP-inventor

1 Introduction

With the recent technological developments, the teaching/learning paradigm is prone to change in order to adapt both to these technologies and to twenty-one century students. Among the fast growing technologies are mobile devices, such as smart-phones and tablets. Indeed, currently the rate of use of smartphones by university students is quite high with the tendency to increase with time. The familiarity of today students with smartphones can be used advantageously by teachers as a way to motivate and enthusing students to learn specific lectures topics. Moreover, students want to learn how to develop mobile devices applica-

F. Soares (✉) · C.P. Leão

Centro Algoritmi, School of Engineering, Universidade do Minho, 4800-058 Guimarães, Portugal

e-mail: fsoares@dei.uminho.pt

C.P. Leão

e-mail: cpl@dps.uminho.pt

P.M. Oliveira

INESC TEC—INESC Technology and Science (Formerly INESC Porto), Department of Engineering, School of Sciences and Technology, Universidade de Trás-os-Montes e Alto Douro, UTAD, 5001-801 Vila Real, Portugal

e-mail: oliveira@utad.pt

© Springer International Publishing Switzerland 2017

P. Garrido et al. (eds.), *CONTROLO 2016*, Lecture Notes

in Electrical Engineering 402, DOI 10.1007/978-3-319-43671-5_71

tions. A tool that can be used to fulfill this need, for Android based devices, is the MIT App-Inventor 2 (MITAppI2) [1–4].

Why using the MITAppI2 [3]? This tool is quite easy to be used, it is freeware and it is based on a drag-and-drop technique, both for the graphical user interface design and well as for the block based programming. A major advantage of MITAppI2 is that it can be used by non-skilled programming students to develop Android based application in a fast and effective way. The time that goes by between student's first contact with MITAppI2 and testing an application in their mobile devices is very short, which can be used to challenge their curiosity.

The MITAppI2 was proposed in [5] as a tool to teach industrial automation and feedback control topics and [6, 7] to develop applications to bridge teachers and students. This paper reports a learning experience in which students were proposed to develop MITApp2 based applications involving topics of two curricular units: (i) Process Control and Automation, lectured in the third year of the Industrial and Management Engineering in UMinho University; and (ii) Industrial Automation, lectured in the fourth year of the Electrical and Computers Engineering in UTAD University.

The remaining of the paper is organized as follows: Sect. 2 revises selected topics regarding the MIT app inventor tool; Sect. 3 describes and contextualize the teaching/learning experiment; Sect. 4 presents some students' developed applications; Sect. 5 analyses the students' feedback and finally Sect. 6 completes with the final remarks and constrains of the study.

2 MIT App Inventor: Revision of Selected Topics

This section presents a review of some selected topics focused in: (i) review of research concerning App Inventor teaching/learning applications, particularly directed to university education; and (ii) the MITAppI2 basic characteristics and advantages of its use. Since its original development in 2008, the MIT App Inventor [1, 2] has been used to develop mobile applications either in and out of the classroom [3, 8]. The MIT AppI has been extensively used as a block based technique to serve as introductory programming language [4] as an alternative to Alice [9] and Scratch [10]. However, it can be also used to teach non-beginners programming as reported in [11–15]. The main advantages of MITAppI2 to develop Android applications is presented here through a simple illustrative example, considering an application (Math1). The purpose of Math1 consists in gathering a number inputted by the user and to display its square-root value. This toy problem can be used to state five steps for developing MITAppI2 applications:

1. Design the application user interface: as it can be visualized in the example shown in Fig. 1a, the MITAppI2 uses a drag-and-drop methodology. The user can select the graphical objects from several available libraries (User interface, Layout, Media, Drawing and Animation, Sensors, Social, among others).



Fig. 1 MITApp12 example: toy application to evaluate the square root of a user inputted number. Application user interface design and programming. **a** User interface design. **b** Blocks programming

2. Develop the program: this is accomplished changing to a block editor, also using a drag-and-drop technique. As it shown in the example presented in Fig. 1b, blocks are dragged from several available libraries, allowing defining program the behavior intended for each graphical object. In this case: when *Button1* is clicked, the input number is stored in a variable (*num1*), evaluates its square root keeping its value in the variable (*sqr_root*), and the result is displayed in *Textbox1*. The main advantages of using this block based programming methodology, is avoiding the tedious procedures involved with syntax based programming languages. The block programming provides high-level components [3] and it is more intuitive for non-experienced programmers.
3. Build the application. As any program design, the application can be built to be tested whenever the developer wants. The MITApp12 can be tested in several ways, such as: (i) generating a QR code (as illustrated in Fig. 2a for Math1) and then reading the code with the MIT App Inventor 2 companion [2]; (ii) downloading the application to the user computer and then installing it via USB connection; (iii) using an Android emulator such as [2].
4. Test the application. For the example provided a screenshot of a test is illustrated in Fig. 2b.
5. If the result is not satisfactory repeat de developing cycle from step 1.

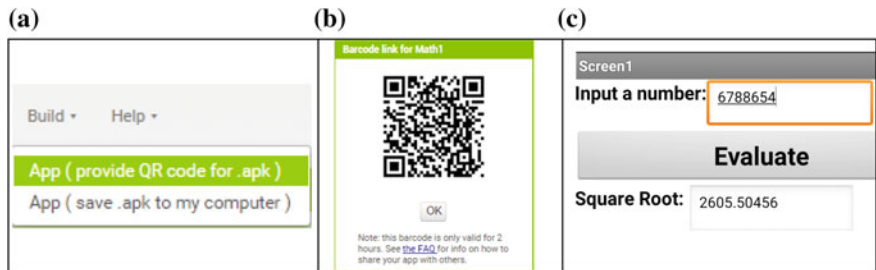


Fig. 2 MITApp12 example: toy application to evaluate the square root of a user inputted number. App key code generation and test. **a** QR code generation. **b** QR code. **c** Math1 screenshot test

3 Description and Contextualization of the Learning Experiment

This section presents the objective of the learning experiment, the courses characterization and the target group, as well as the methodology followed in the experiment.

3.1 Learning Experiment Goal

The goal of this teaching/learning experiment was to assess if MITAppI2 can be used as a friendly tool in Automation courses.

Following this trend, the aim was to find out answers to these research questions:

- May students easily acquire knowledge on a particular automation subject, while developing mobile applications using this software?
- Is MITAppI2 easy to use even for students that are not familiar with programming?
- Do students react positively to the introduction of new learning tools, in particular, mobile applications functionalities in their learning process in automation topic?

The experiment was performed in two different institutions in order to ascertain if students' perception differs with the course, university or school year.

3.2 Course Characterization

Course Syllabus and Target Group

This experiment took place in two universities at north of Portugal, UMinho and UTAD, in two different engineering courses.

In UMinho the Curricular Unit (CU) Process Control and Automation (PCA) was chosen, lectured in the 3rd year of the Industrial Engineering and Management Engineering in the 1st semester of the 2015–2016 curricular year. In this CU it is intended that students acquire knowledge necessary to explain and identify the main components and problems in control and industrial automation; to categorize and discriminate different sensors and actuators; to demonstrate and interpret the methods and techniques for modelling, formulating, designing, evaluating combinatorial controllers; to design and implement sequential controllers in different automation systems using Grafset; and to analyze and implement ladder diagrams in automation problems. 62 students were enrolled in the course, from which 55 regularly attended classes. It is worthwhile mention that class attendance was not mandatory.

In UTAD University the experiment took place in the Industrial Automation (IA) course of the 4th year of the Electrical and Computers Engineering in the 1st semester of the 2015–2016 curricular year. This course addresses industrial automation topics including logic control, discrete event based systems and process

control techniques. Students should acquire skills regarding programming of logic controller using ladder diagrams and Grafset (SFC). The course enrolled 25 students, from which 21 regularly attended classes.

Teaching/Learning Methodology

The PCA classes are mainly lead by the teacher as lectures and problem-solving exercises regarding combinational and sequential controllers. At the end of the semester, students have to present a project of an automatic system corresponding to a real-world problem. The case-study is freely chosen by students. Students must do the full project automation: specifications, requisites and associated controller in Grafset and Ladder Diagram. Also, and included in the overall assessment of the course, students have to develop a survey on a specific topic proposed by the teacher. The theoretical aspects concerning, for example, the control components, configuration and strategies, the functioning and constitution of on-off sensors, transducers, and actuators, among others, are topics for students' surveys. This year, this survey was performed in the form of quizzes developed in MITAppI2. The work was developed in groups of four elements each.

In IA course of UTAD, besides laboratory practical assignments concerning PLC programming and process control, students are also required to perform a synthesis written assignment concerning an industrial automation topic selected from a list provided by the lecturer or proposed by students. The objective of this synthesis assignment is to promote students self-learning regarding a specific topic, by searching related information from several sources: the Internet, digital scientific databases, and library, among others. This year, students were allowed to choose the synthesis assignment report format either as: (i) using a traditional approach, by writing a paper, (ii) developing an Android based mobile application, preferably developed with the MIT App-Inventor 2 tool. Students were allowed to perform this assignment individually or in groups of two.

Course Assessment

The evaluation of PCA course has three components: a written test with 60 % weight and the two team works (survey and project) each worth 20 %. The test has a minimum score of 7/20. The works are mandatory, even if the student does the CU at the examination period. In this case, the weight of the works remains at 40 %.

The evaluation of IA course is based in three components: a written test with 60 % weight and minimum score of 8.5/20, three laboratory practical assignments (groups of two students) with 30 % of weight and the survey or synthesis assignment with weight of 10 %.

3.3 Learning Experiment Planning and Procedure

The two curricular units' teachers met prior to the beginning of the semester in order to define the objective of the experiment, how to implement it in the two institutions, and how to assess the students' outcomes.

At the first classes day teachers launched to students the challenge to design applications in automation topics for mobile devices. All PCA students and some of IA students (16/21) accept the challenge. In the third week of classes, the IA teacher went to the University of Minho to give a talk on “How to develop MIT Inventor applications: a first guide”. Students were invited to send emails with doubts/questions regarding the use of the software. The goal was to provide students with a remote support. It is worth mentioning that only one student sent an email with doubts. The students were autonomous. Each group developed a quiz on the theoretical topic proposed by the teacher. The deadline to send the work was at middle of the semester and before Christmas holidays students present orally to class their application. By using an android emulator the students present their quiz and the functionalities of their work step by step. The executable files were available to all students in the Blackboard. They could install and test their knowledge on automation topics running the quizzes developed by the colleagues.

In UTAD the procedure was very similar to the one followed in UMinho. In the second semester week, students were invited to attend an extra class talk regarding a brief introduction about MITApp2. After students had selected the survey topic, they had until the last semester day with classes to deliver the teacher two APP files: the source (*.aia) and installation (*.apk). Two weeks before the semester end, students had to make an oral presentation to all the other students, showing the contents of their application demonstrating the developed application features.

4 Students’ Applications: Some Examples

This section presents some examples of the applications developed by students under this learning experiment. In the Fig. 3 screenshots taken from an application developed by UTAD students are presented. The topic addressed by this synthesis assignment is about the implications that the increase of automation will have in the nearby future. The application is organized in two main parts: theory and quiz. Figure 4 presents three of the developed quizzes applications by the students from UMinho.

5 Students’ Feedback

Nevertheless the positive tendency on the use of mobile technologies in the teaching/learning process, it is always suitable to understand and to know how students see this practice. In order to obtain feedback from students a questionnaire was applied to evaluate the use of the MITAppI2 as a friendly learning tool in Automation.

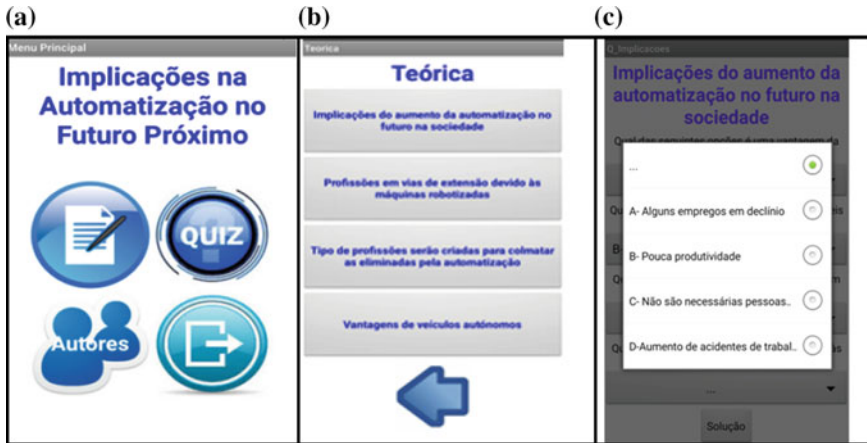


Fig. 3 Screenshots of application developed with MITAppI2 in IA course (in Portuguese). **a** Main screen. **b** Theory screen. **c** Quiz screen

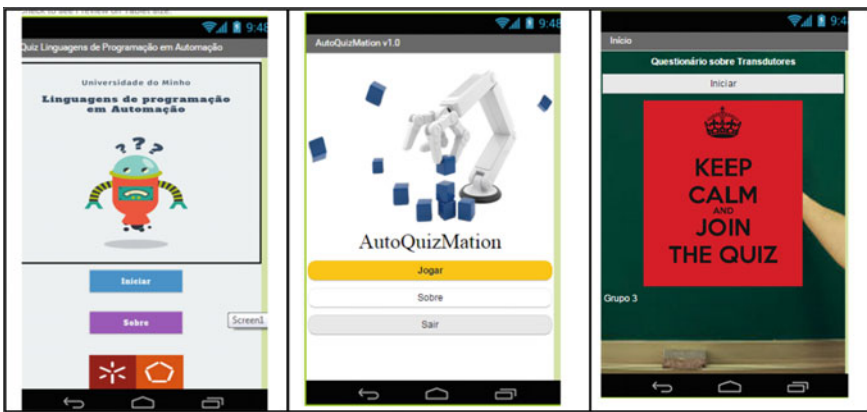


Fig. 4 Screenshots of application developed with MITAppI2 in PCA course (in Portuguese)

5.1 Material and Method

Students were asked to fulfil a questionnaire, after the oral presentation of the developed application, in order to obtain their perceptions regarding this experiment. The questionnaire fulfilment took around 10 min. The questionnaire was divided into five main parts: (1) student identification (number, course, sex, age, curricular year, mobile platform used, and previous experiences), (2) technical competences, (3) difficulties, (4) soft skills and (5) suggestions. In the followings subsections, each part is described and the data obtained analyzed in detail.

5.2 Questionnaire Results Analysis

After the students' characterization, the general experience evaluation is discussed taking into account the technical competencies acquired, the identification of the difficulties encountered during the development of the experience and the soft skills.

Students' Characterization

A total of 53 students accepted the challenge to respond to the questionnaire: 9 (17 %) from UTAD and 44 (83%) from UMinho. Most of the students are male (52.8 %) and their average age is 20.82 years old (SD = 1.77; interval range 19–28 years old). Unfolding per Course/University, 100 % of the students from UTAD are male and 43.2 % from UMinho. The majority of the students from UMinho have 19–20 years old (77.5 %) and 21–23 from UTAD (77.7 %). This difference in age was expected as both courses are taught in different academic years (3rd in UMINHO and 4th in UTAD).

Most of the students have and used Smartphone (88.9 %) for the experiment and the remaining 9.8 % Tablet. By Course/University, 90.5 % UMinho students use a Smartphone and 88.9 % from UTAD. These results show that there are no differences in the use of Smartphone between the two Courses/Universities ($\chi^2(1) = 1.00$, $p > 0.05$).

In total, 88.7 % refers not yet have performed experiments of this kind, or similar. There were, also, no differences between the two Courses/Universities (77.8 % from UTAD, and 90.9 % from UMinho; $\chi^2(1) = 0.31$, $p > 0.05$).

General Experience Evaluation

To evaluate the general experience, three main parts were considered: technical competences acquired, difficulties and soft skills. In this section, the analysis is made considering the whole (the 53 students).

To analyze the technical competences, a set of 8 sentences was considered: 2 evaluating the relevance of mobile application use (Relevance of the mobile application development; Relevance of mobile application development as a teaching/learning tool); 3 regarding the use of the MITAppI2 application (General opinion regarding MITAppI2; MITAppI2 usefulness as motivating element in learning; Ease of use of MITAppI2) and; 3 regarding the experiment general evaluation (How do you rate the experience; Rate the degree of innovation of the experience; Relevance of this experience in the development of interdisciplinary skills). These sentences were evaluated based on a 5-point Likert scale, in which 1-very poor and 5-very good, to characterize the level of satisfaction of each sentence. Figure 5 presents the students' satisfaction for these 8 sentences (in green the results regarding the three sentences related to the MITAppI2). According to the obtained results, the MITAppI2 is considered usefulness as motivating element in learning (50 % with 4 and higher) and easy to use (100 % rate with 3 and higher). The general opinion is positive, with 75 % with rate 3 and higher. The students appear receptive in use mobile applications as a tool in their learning process (75 % rate with 3 and higher).

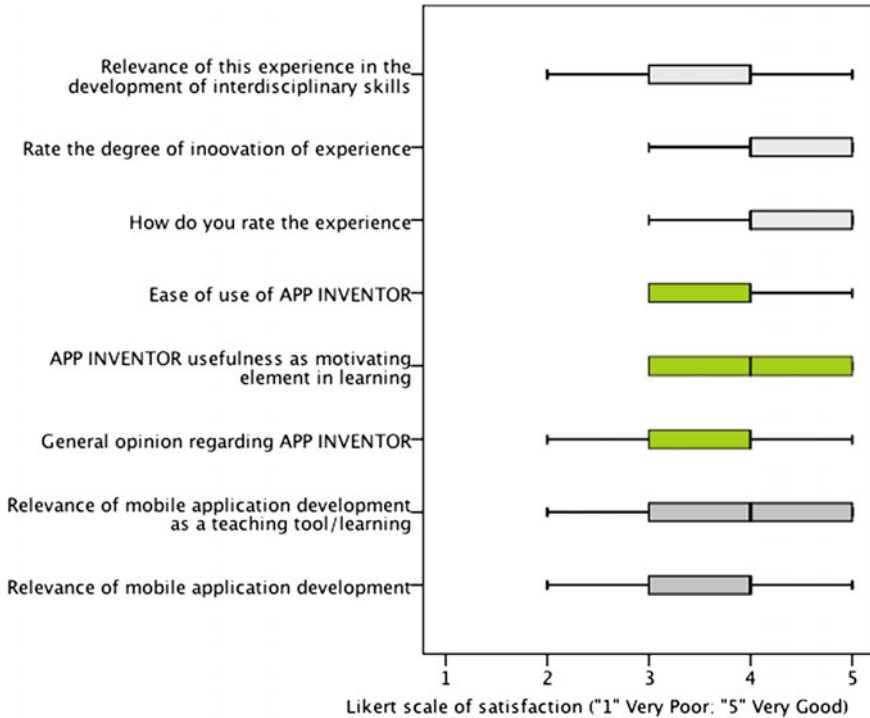


Fig. 5 Technical competences students' satisfaction evaluation

79.3 % of the students reported no difficulty using the application, and 86.6 % mentioned to be encouraged to learn Automation and Control contents by using MITAppI2. Two comments addressed by two students, can help to understand the negative percentage obtained (13.4 %) related to this topic:

By focusing on the application development, I didn't assimilate the fundamental concepts of the subject

Useful application, however, it doesn't help to consolidate the CU contents because we have to focus on the application development.

Interesting to observe that the positive rate (or negative) is independent if the student felt encouraged (or not) to learn Automation and Control contents ($\chi^2(1) = 0.42, p > 0.05$, after recoding the 5-point satisfaction scale into 2-point scale: negative (2 and 3) and positive (4 and 5)).

Regarding the evaluation of the soft skills acquired by using the MITAppI2, 50 % of students rate very positively (with 4 and 5), Fig. 6. The lower rank, as expected and in accordance with values obtained previously, was observed to the sentence related to if the experience provide material to study, with 25 % answered of 2.

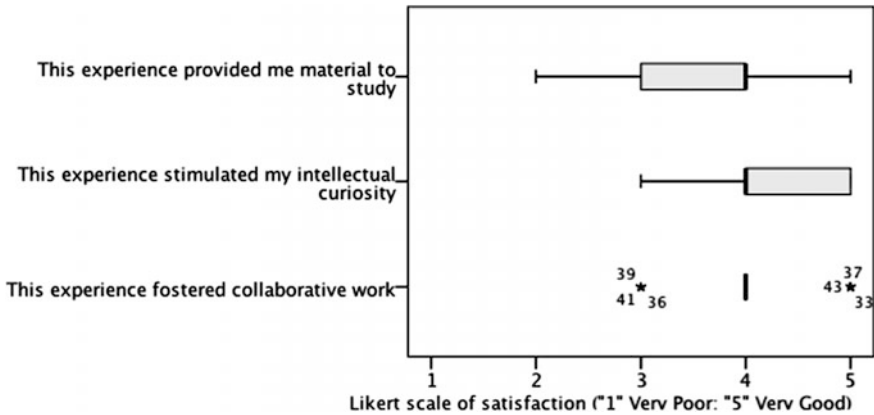


Fig. 6 Soft skills students’ satisfaction evaluation

6 Final Remarks and Constrains of the Study

The use of MITAppI2 as a friendly tool in Automation courses was studied in this learning experiment in two Portuguese universities: UTAD and UMinho. The results obtained through questionnaires allow inferring that students may acquire knowledge on a particular automation subject, while developing mobile applications using this software (although it is known that there are one or two students that considered this type of application may not help to consolidate the contents due to the necessary attention on the application development). In fact MITAppI2 is easy to use even for students that are not familiar with programming. Also, students reacted positively to the introduction of new learning tools, in particular, mobile applications functionalities. Somehow, the results of the described experiment foster not only the development of new applications but also the investigation of the benefits of mobile device applications in a larger scope of students centered learning and teaching areas (e.g. [16, 17]).

Since the institution is directly associated to the course and curricular year (one institution one curricular year), and for one of the institution the number of valid answers is relatively low, the analysis to ascertain if students’ perception differs with the course, university or school year is not consistent. So, future work includes to extent this study to more Automation courses within these two universities or others.

Acknowledgments The authors would like to express their acknowledgments to all students for their voluntary co-operation. This work has been supported by COMPETE: POCI-01-0145-FEDER-007043 and FCT – Fundação para a Ciência e Tecnologia within the Project Scope: UID/CEC/00319/2013.

References

1. Abelson, H.: App inventor pilot announcement (2009). <http://googleresearch.blogspot.com/2009/07/app-inventorfor-android.html>. Accessed 6 Dec 2010
2. MIT App Inventor page (2015). <http://appinventor.mit.edu/explore/>. Accessed 8 Dec
3. Wolber, D.: Democratizing computing with app inventor. *GetMobile* **18**(4) (2014)
4. Wolber, D.: App inventor and real-world motivation. In: SIGCSE'11, March 9–12, Dallas, Texas, USA, pp. 601–606 (2011)
5. De Moura Oliveira, P.B.: Teaching automation and control with app inventor applications. In: IEEE Global Engineering Education Conference (EDUCON), Tallinn University of Technology, Estonia, pp. 879–884 (2015)
6. Ramos, D., De Moura Oliveira, P.B., Solteiro Pires, E.J.: APP inventor as a tool to reach students, TEEM'15. ACM, Porto, Portugal, pp. 311–316 (2015)
7. Ramos, D.: App inventor android based m-learning based m-learning tool. MSc in Electrical and Computers Engineering, UTAD University, Portugal (2015)
8. Vázquez-Cano, E.: Mobile distance learning with smartphones and apps in higher education. *Educ. Sci.: Theory Pract.* **14**(4), 1505–1520 (2014). doi:[10.12738/estp.2014.4.2012](https://doi.org/10.12738/estp.2014.4.2012)
9. Scott, J., Bundy, A.: Viewpoint creating a new generation of computational thinkers, experiences with a successful school program in Scotland. *Commun. ACM* **58**(12), 37–40 (2015)
10. Cooper, S., Dann, W., Pausch, R.: Teaching objects-first in introductory computer science. In: Proceedings of the 34th SIGCSE Technical Symposium on Computer Science Education, Reno, NV (2003)
11. Malan, D., Leitner, H.: Scratch for budding computer scientists. In: Proceedings of the 38th SIGCSE Technical Symposium on Computer Science Education, Covington, KY, pp. 223–227 (2007)
12. Mahmoud, Q.H.: Integrating mobile devices into the computer science curriculum. In: 38th ASEE/IEEE Frontiers in Education Conference, pp. S3E17–S3E22 (2008)
13. Karakus, M., Uludag, S., Guler, E., Turner, S.W., Ugur, A.: Teaching computing and programming fundamentals via app inventor for android (2012). 978-1-4673-2334-5/12/\$31.00 ©2012 IEEE
14. Barbosa, J.L.V., Hahn, R., Barbosa, D.N.F., Segatto, W.: Intensive use of mobile technologies in a computer engineering course. *Computer Applications in Engineering Education*, pp. 686–698 (2012)
15. Soares, A.: Reflections on teaching app inventor for non-beginner programmers: issues, challenges and opportunities. In: Proceedings of the Information Systems Educators Conference, vol. 30, no. 2552, p. 11 (2013)
16. Potts, J., Moore, N., Sukittanon, S.: Developing mobile learning applications for electrical engineering courses. In: Proceedings of the IEEE Southeastcon, Nashville, TN, pp. 293–296 (2011)
17. Jou, M., Lin, Y.-T., Tsai, H.-C.: Mobile APP for motivation to learning: an engineering case. *Interact. Learn. Environ.* **10** (2015). doi:[10.1080/10494820.2015.1075136](https://doi.org/10.1080/10494820.2015.1075136)

Inverted Pendulum Controlled by an Analog PID Controller: A Framework for a Laboratorial Experiment

**Luís Dias, José Ferreira, Filomena Soares, Gil Lopes,
João Sena Esteves, M.J. Sepúlveda and Paulo Garrido**

Abstract This paper presents the design of a framework for a didactic kit for control studies based on a rotary inverted pendulum. One of the challenges was to involve students in the design of the platform. This first version of the kit was developed by students of the Integrated Master on Industrial Electronics and Computers Engineering at the University of Minho. It considers the design and implementation of the control of the angular position of an inverted pendulum through an analog Proportional, Integral and Derivative (PID) controller. This Single Input Single Output (SISO) control system allows retrieving the equilibrium position of the pendulum when it is subjected to disturbances.

Keywords Inverted pendulum · Analog PID controller · Laboratorial kit · SISO systems

L. Dias · J. Ferreira · F. Soares · G. Lopes · J.S. Esteves (✉) · M.J. Sepúlveda · P. Garrido

Industrial Electronics Department, School of Engineering, University of Minho, Guimarães, Portugal
e-mail: sena@dei.uminho.pt

L. Dias
e-mail: a61896@alunos.uminho.pt

J. Ferreira
e-mail: a41675@alunos.uminho.pt

F. Soares
e-mail: fsoares@dei.uminho.pt

G. Lopes
e-mail: gil@dei.uminho.pt

M.J. Sepúlveda
e-mail: mjs@dei.uminho.pt

P. Garrido
e-mail: pgarrido@dei.uminho.pt

F. Soares · J.S. Esteves · M.J. Sepúlveda · P. Garrido
R&D Algorithmi, School of Engineering, University of Minho, Guimarães, Portugal

1 Introduction

The relevance of developing and providing students real world experiments is, without argue, well accepted in the academic community. Real-world experimental case-studies are particularly important in engineering courses [1, 2].

Several studies have been reported in the literature regarding the control of the inverted pendulum system, rotary or fixed in a car or in a two-wheel configuration. Proportional, Integral and Derivative (PID), Linear Quadratic Regulator (LQR), Full State Feedback (FSF, also known by pole placement), and H_∞ controllers, among others, have been tested both in simulation using mathematical models and in real-world experiments (in commercial or own made didactic kits or in commercial products, where *Segway* is an example) [3–11].

Regarding Rotary Inverted Pendulum (RIP) control, Akhtaruzzaman and Shafie [10] described the steps to design three controllers for the *Quanser* system. The RIP system consists of a vertical pendulum, a horizontal arm, a gear chain, and a servomotor which drives the pendulum through the gear transmission system. The rotating arm is mounted on the output gear of the gear chain. An encoder is attached to the arm shaft to measure the rotating angle of the arm. At the end of the rotating arm there is a hinge instrumented with an encoder. The pendulum is attached to the hinge. The system is interfaced by a data acquisition board and controlled by *Matlab/Simulink* software. PID, LQR, and FSF controllers were compared in simulation and in the experimental kit. Based on the results, the classical PID method is capable of controlling the nonlinear system but it is not robust. In simulation, LQR is more robust, reliable, and faster than the FSF controller in successfully swinging the pendulum to the upright position. From the experimental results, however, both FSF and LQR can be effective in maintaining the RIP stable.

In [11], the authors also present a comparative study of four controllers on the *Quanser* RIP: PID, LQR, Fuzzy Logic and H_∞ controllers. The controllers were tested and tuned by trial and error in *MatLab/Simulink* based on a mathematical model of the RIP. In simulation, the Fuzzy controller shows smaller values of the overshoot peak and rise time on the closed loop response. The algorithms were then tested and compared on the physical RIP. LQR shows higher performance in the *Quanser* kit.

The work presented in this paper is focused on the development of a framework for a laboratorial experiment based on a rotary inverted pendulum. The first version of this didactic kit was designed and implemented by students in the curricular unit Project I from the 4th year of the Integrated Master on Industrial Electronics and Computers Engineering at the University of Minho. It is worth pointing out that the PID control implementation was performed using analog electronics, an objective proposed by the students.

The paper is organized in four sections. Section 2 details the developed system; Sect. 3 shows the results obtained. The conclusions and future perspectives of the work are addressed in Sect. 4.

2 Proposed System

In this section, the learning outcomes of the curricular unit and the project goal are presented. It is also described the proposed system that allows testing the pendulum equilibrium by implementing the three terms PID controller.

2.1 Learning Outcomes and Project Goal

Project I curricular unit runs in the 1st semester of the 4th year of the Integrated Master on Industrial Electronics and Computers Engineering at the University of Minho. It is a compulsory 5 h per week laboratorial class running in parallel in three laboratories. The students, working in pairs, are challenged to conceive a real-world project from the design to the implementation. The learning outcomes of the curricular unit are:

- Implement a robust and solid structure;
- Apply knowledge acquired at other, but related, curricular units;
- Develop a modular electronics design;
- Acquire real-time data for monitoring the system behaviour.

In this particular case, the project goal was to design and implement the first version of a framework for teaching/learning Control topics, from basic concepts to more advanced laws. The first version of this framework was the control of the angular position of an inverted pendulum by using an analog PID controller. This control acted to compensate for disturbances in order to maintain the equilibrium of the angular position of the pendulum. A Single Input Single Output (SISO) system was designed.

2.2 Mathematical Model

The system was first simulated in *Matlab/Simulink* using the mathematical model adapted from [10]. Figure 1 shows the results for the profile of the angular position of the pendulum when a pulse was introduced as an input reference. The controller parameters employed were: $K_p = 55$, $K_i = 1$, and $K_d = 0.4$.

2.3 Experimental Setup

The system developed in this work is presented in Fig. 2. Figure 2a illustrates the possible rotation movements, around the motor axis and the rotary potentiometer

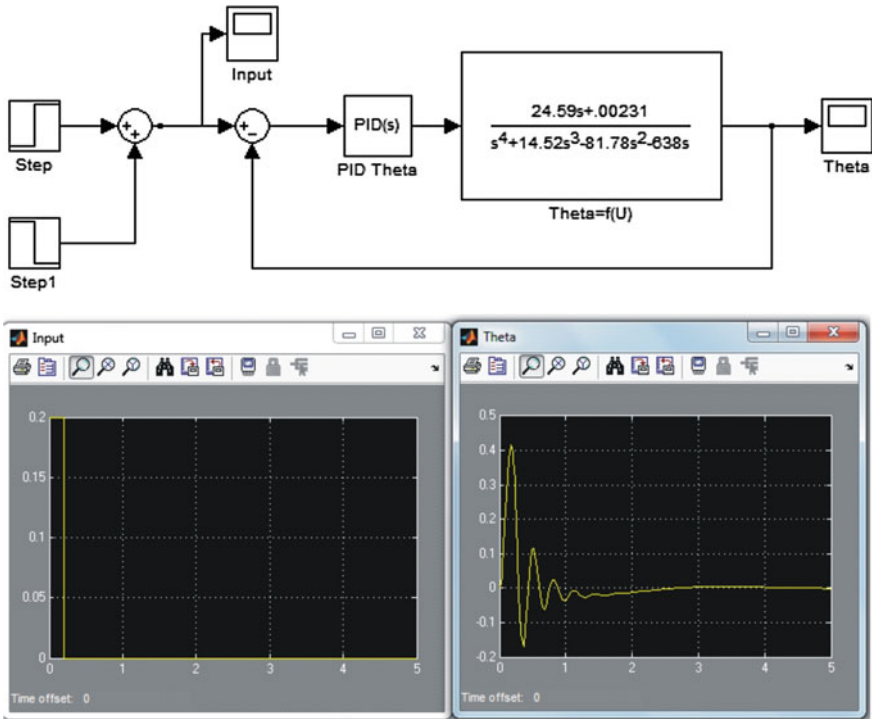


Fig. 1 Matlab/Simulink simulation based on the mathematical model adapted from [10]

axis. The potentiometer shaft is used as the inverted pendulum pivot. Thus, this component works as the sensor which provides the feedback signal to the PID controller. The real setup is shown in Fig. 2b. The system consists of a 35 cm length pendulum (Fig. 3a), a 23 cm long arm coupled to a motor (Fig. 3b), the

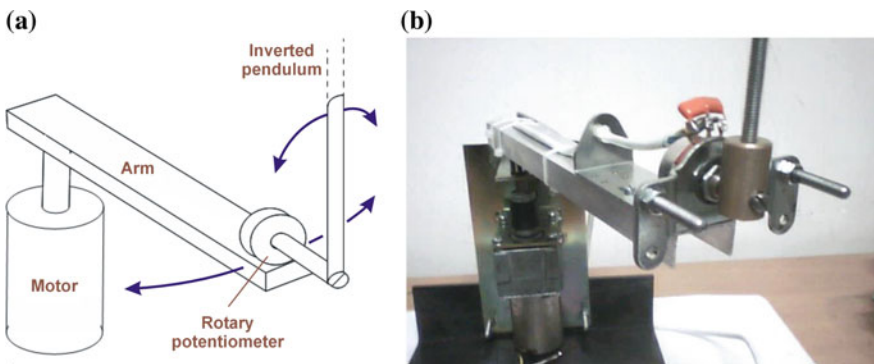


Fig. 2 Inverted pendulum kit: a system diagram; b real setup

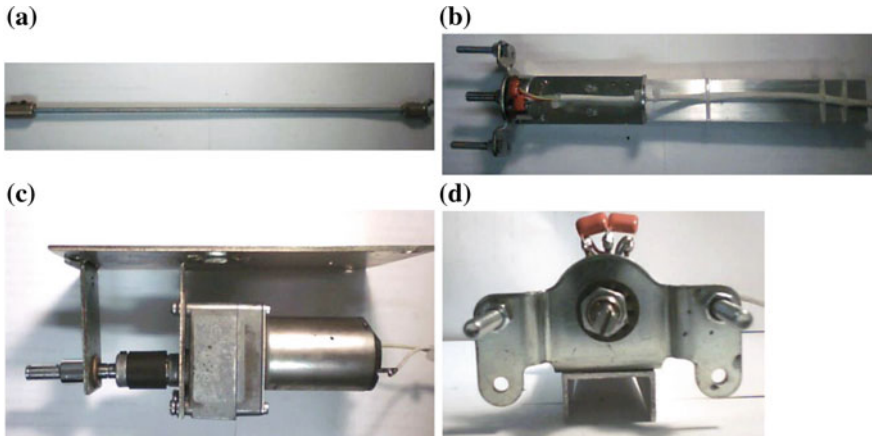


Fig. 3 The system constituents: **a** pendulum, **b** arm coupled to the motor, **c** motor, and **d** rotary potentiometer

motor (Fig. 3c), and the rotary potentiometer as the sensor positioned in the pendulum axis (Fig. 3d). All the parts were designed and built by the students. As previously referred, the design goal was to control the angular position of the pendulum and not the arm position.

2.4 System Description

Figure 4 shows the schematic block diagram of the developed system. Next, each module of the block diagram is described in detail.

Sensor

A rotary potentiometer is used as a sensor because the load (pendulum) is applied radially to its shaft. It establishes the relationship between the pendulum angle (controlled variable θ) and a voltage value. The output voltage Y_{sens} varies

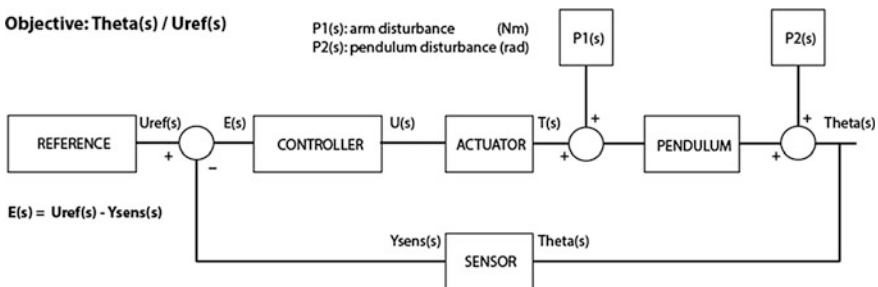


Fig. 4 Block diagram of the schematic of the control system

between +5 V ($\theta = +90^\circ$) and -5 V ($\theta = -90^\circ$) and the pendulum verticality was defined at 0 V ($\theta = 0^\circ$). The transfer function is defined as a gain of (1/18) V/°.

Reference

The reference is the voltage value U_{ref} obtained by a resistive voltage divider that defines the precise value of the pendulum equilibrium point. It establishes a maximum variation between +2 V (+36°) and -2 V (-36°).

Sum Point

The sum point is where the error of the system, defined in the Laplace domain as $E(s) = U_{ref}(s) - Y_{sens}(s)$, is calculated (in Volt). This circuit is implemented by a unitary gain differential amplifier (Fig. 5) with buffered inputs for isolation.

Controller

The analog PID controller [12] implementation (Fig. 6) is based on three operational amplifiers, each implementing one of the controller parameters, and a fourth amplifier used as adder of the values. Being an educational kit, it was developed with a simple design in order to provide, on each block, a focus on the components responsible for the parameter definition. Table 1 summarizes the components used to obtain the different PID parameter gains.

Actuator

The actuator provides motion to the arm that oscillates horizontally in order to maintain the pendulum equilibrium. It consists of three modules:

1. **PWM generator**—It converts the output signal of the PID controller into a pulse width modulation (PWM) value that defines the motor rotation speed and direction. It uses three operational amplifier circuits (integrator, threshold comparator and a simple comparator). The RC values of the integrator define the PWM frequency (20 kHz, in this project). Direction is obtained from the polarity of the signal (positive—clockwise, negative—counter-clockwise).

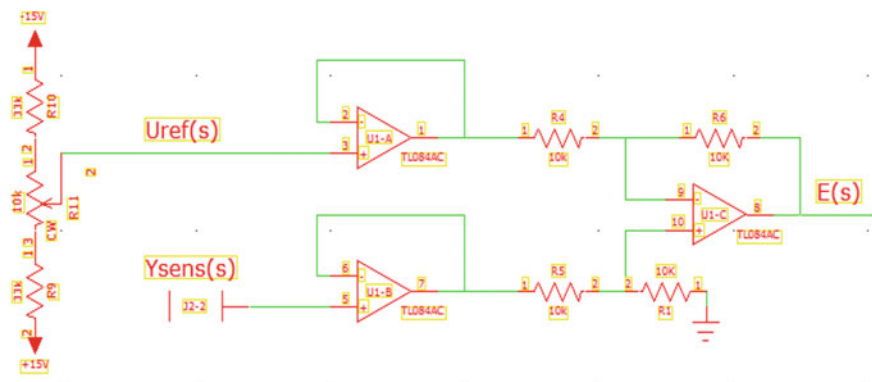


Fig. 5 Sum point circuit implemented with a unitary gain differential amplifier with buffered inputs

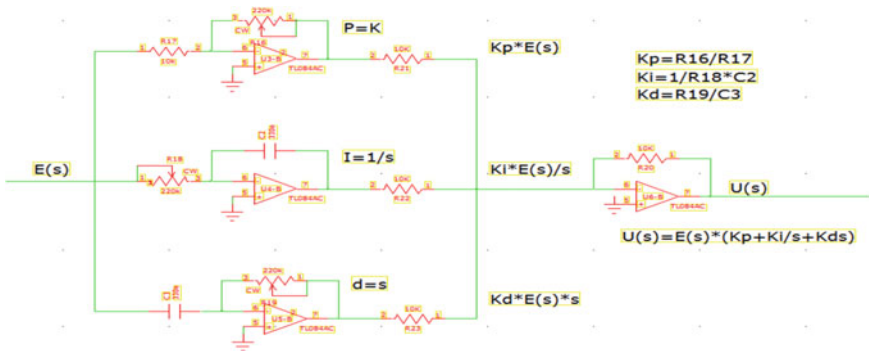


Fig. 6 PID controller circuit implemented with four operational amplifiers

Table 1 Component values and respective PID parameter gains

Parameter	Gain	Component values	
Kp	1–30	R17 = 10 kΩ	R16 = 220 kΩ
Ki	0–20	C2 = 470 nF	R18 = 220 kΩ
Kd	0–5	C3 = 22 μF	R19 = 220 kΩ

2. **DC/DC converter**—It converts the generated PWM signal into a signal that is suitable for the motor, based on an H-bridge solution implemented with N-type MOSFET transistors. In order to provide electrical isolation to the control circuit, this power circuit uses opto-couplers.
3. **Motor**—This is an important part of the system since it has to provide fast and accurate movements to the arm in order to balance the pendulum. It must have low inertia in the motion start and enough torque to move the arm and pendulum. A DC 12 V motor was used. It produces 300 revolutions per minute (RPM) at the rated voltage.

System Monitoring

A real-time acquisition system was developed in order to monitor the system behaviour and performance. It was based on the STM32F4 developer board, using two analog-to-digital (ADC) ports connected to $Y_{sens}(s)$ and $U(s)$. This board has a serial connection to a computer, where a program was developed with the Simulink[®] software. This, in turn, provides graphical output and data logging of the values read from the ADC ports of the STM32F4 board. Figure 7. shows a screen capture of the graphical output of the two signals, generated by the program developed in Simulink[®].

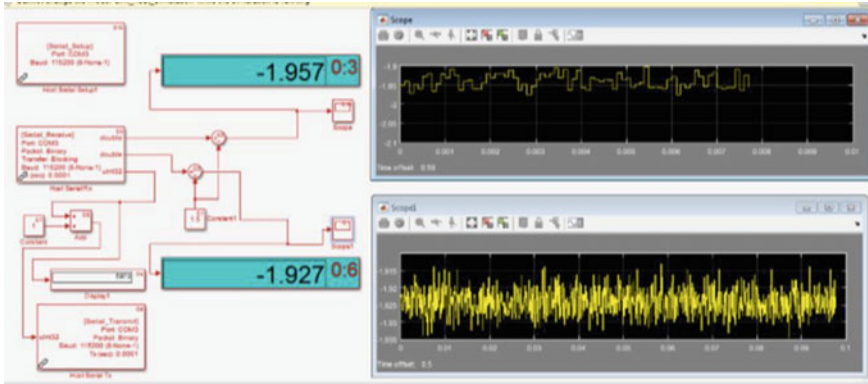


Fig. 7 Graphical output of $Y_{sens}(s)$ and $U(s)$ generated by the program developed in simulink®

3 Results

The first version of the framework, SISO control system, was tested in a laboratory environment. The results were analyzed in terms of the profiles of the error E and the control voltage of the PWM generator.

Figure 8 shows the results obtained using a proportional controller ($K_p = 12$) where four external changes were registered (stroke in the upper part of the pendulum). The pendulum successfully responds to a change of 10° in the angular position within 4 ms.

In Fig. 9, a Proportional, Integral (PI) controller is used ($K_p = 25$ and $K_i = 10$). The system shows a rapid recovery after the perturbation but there is an increase in the number of oscillations until equilibrium is restored. A 10° change in the pendulum position (tap in the upper part) is corrected in 8 ms.

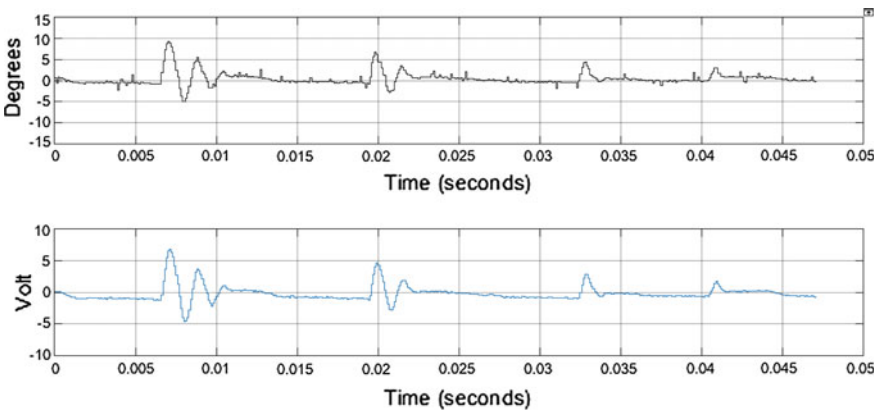


Fig. 8 Profiles of the error E and the control voltage of the PWM generator with $K_p = 12$

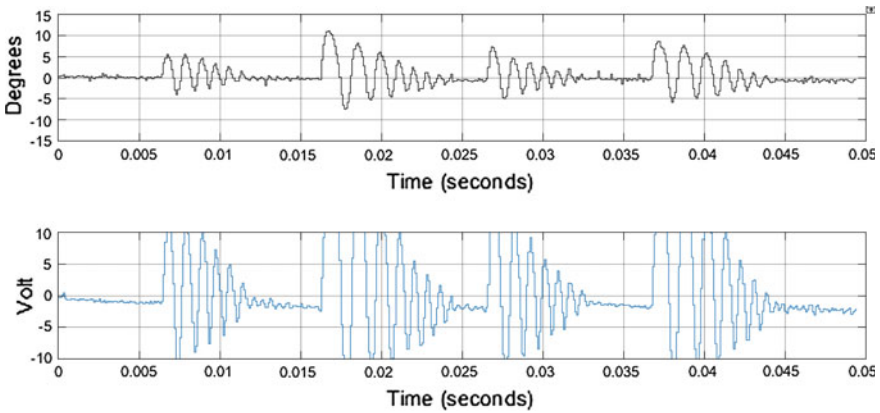


Fig. 9 Profiles of the error E and the control voltage of the PWM generator with $K_p = 25$ and $K_i = 10$

A Proportional, Derivative controller was tested ($K_p = 15$ and $K_d = 0.3$) and the results are shown in Fig. 10. The system presents good stability and recovery towards perturbations. A change of 5° in the pendulum position (tap in the upper part) is corrected in 3 ms.

Finally, a Proportional, Integral and Derivative (PID) algorithm was tested. Figure 11 shows the results obtained using the controller gains $K_p = 15$, $K_i = 10$ and $K_d = 0.3$. A change of 7° in the pendulum position (tap in the upper part) is corrected in 3 ms.

In https://www.youtube.com/watch?v=f87DM37r_Dw it is possible to see a video of the system performance while recovering from perturbations of the angular position.

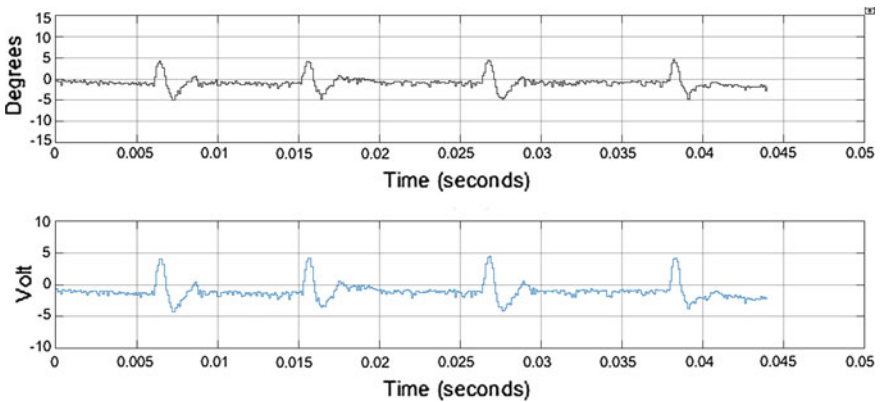


Fig. 10 Profiles of the error E and the control voltage of the PWM generator with $K_p = 15$ and $K_d = 0.3$

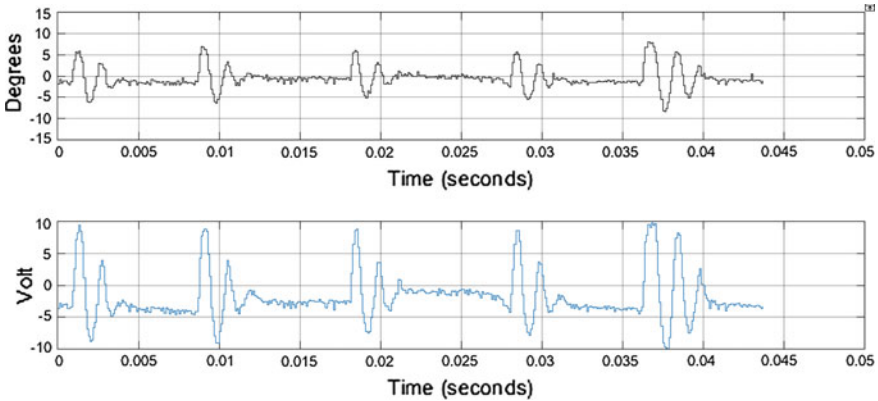


Fig. 11 Profiles of the error E and the control voltage of the PWM generator with $K_p = 15$, $K_i = 10$ and $K_d = 0.3$

4 Conclusions

Several works in the literature are focused on the importance of having practical tools to test real-world case-studies. These kits are particularly important in control engineering courses, where accessing real experiments, besides simulations, is considered fundamental.

This paper presented the first version of a framework for Control teaching/learning purposes based on a rotary inverted pendulum. This kit was developed by two students of the Integrated Master on Industrial Electronics and Computers Engineering at the University of Minho. The students designed and implemented the control of the angular position of an inverted pendulum by a PID controller. Analog electronics was used to build the system and to implement the controller. Students are familiar with—and, in some cases, particularly fond of—using digital electronics and, also, implementing control laws by software. The use of analog electronics was proposed by the students and considered a challenge. The kit allowed testing separately the three terms of the controller (proportional, integral and derivative actions).

So far, a SISO control system where the angular position of the pendulum is controlled has been developed. Future work considers optimizing the system through the inclusion of arm position control, wireless communications for monitoring purposes and other control algorithms. The goal is that the platform is designed and optimized by students, considered as a learning experience and, in the future, made available for students so that they may learn the basics and advanced topics of process control.

Acknowledgments This work has been supported by COMPETE: POCI-01-0145-FEDER-007043 and FCT—Fundação para a Ciência e Tecnologia within the Project Scope: UID/CEC/00319/2013.

References

1. Soares, F., Leão, C.P., Machado, J., Carvalho, V.H.: Experiences in automation and control in engineering education with real-world based educational kits. *Sensors Transducer J.* **193**(10) (2015)
2. de Souza, I.D.T., Silva, S.N., Teles, R.M., Fernandes, M.A.C.: Platform for real-time simulation of dynamic systems and hardware-in-the-loop for control. *Sensors* **14**, 19176–19199 (2014)
3. Yusuf, L.A., Magaji, N.: Performance comparison of position control of inverted pendulum using PID and fuzzy logic controllers. *J. Eng. Technol. (JET)* **9**(2) (2014)
4. Nasir, A.N.K., Ahmad, M.A., Rahmat, M.F.: Performance comparison between LQR and PID controller for an inverted pendulum system. In: *International Conference on Power Control and Optimization*, Chiang Mai, Thailand, July 2008
5. El-Nagar, A.M., El-Bardini, M., EL-Rabaie, N.M.: Intelligent control for nonlinear inverted pendulum based on interval type-2 fuzzy PD controller. *Alexandria Eng. J.* **53**, 23–32 (2014)
6. Jain, N., Gupta, R., Parmar, G.: Intelligent controlling of an inverted pendulum using PSO-PID controller. *Int. J. Eng. Res. Technol. (IJERT)* **2**(12) (2013)
7. Prasad, L.B., Tyagi, B., Gupta, H.O.: optimal control of nonlinear inverted pendulum system using PID controller and LQR: performance analysis without and with disturbance input. *Int. J. Autom. Comput.* **1**(6), 661–670 (2014)
8. Chakraborty, K., Mahato, J., Mukherjee, R.R.: Tuning of PID controller of inverted pendulum using genetic algorithm. *IJECT* **4**(1) (2013)
9. Jung, S., Ahn, J.K.: Remote control of an inverted pendulum system for intelligent control education. *Syst. Cybern. Inform.* **9**(4) (2011)
10. Akhtaruzzaman, Md., Shafie, A.A.: Modeling and control of a rotary inverted pendulum using various methods. In: *Comparative Assessment and Result Analysis, Proceedings of the 2010 IEEE International Conference on Mechatronics and Automation*, Xi'an, China, August 4–7, 2010
11. Sirisha, V., Junghare, A.S.: A comparative study of controllers for stabilizing a rotary inverted pendulum. *Int. J. Chaos Control Modell. Simul. (IJCCMS)* **3**(1/2) (2014)
12. Astrom, K., Hagglund, T.: *PID Controllers: Theory, Design, and Tuning*. Instrument Society of America (1995). ISBN 1-55617-516-7

Online Control of TOS1A Thermo-Optical Plant Using OpenModelica

Katarína Žáková

Abstract The paper describes remote approach to the control of thermo-optical plant. The attention is devoted to the open solution that is based on the OpenModelica simulation environment. The plant enables to control two variables: temperature and light intensity. Both of them can be influenced by the user, using a graphical user interface via a web browser. The user can run both the open and the closed loop experiment, as well. In the second case the predefined PI controller and the own control algorithm can be used. The graphical presentation of plant variables is constantly updated via server-sent events.

1 Introduction

Education at technical universities in the field of automation, industrial informatics, mechatronics and similar areas often requires the use of different calculation and simulation environments. These include for example Matlab, LabView, SciLab or OpenModelica software. In this paper the attention is devoted to the last mentioned. It is used as an engine for remote experiment that can be available online for all interested users. The concept of remotely running experimentation is no longer rare. The number of published examples presented at different international conferences and in scientific journals is constantly growing. Some of them can be found e.g. in [1–6].

Modelica language and/or OpenModelica simulation environment can be found in several solutions. Ferreti et al. [7] described a remote interface for simulation of robotic arms whose models are described in some descriptive language like Modelica.

The web-based teaching environment based on OpenModelica platform is presented in [8]. It provides a programming environment running within a web browser that after the task specification by a teacher is available for students. The presented

K. Žáková (✉)

Faculty of Electrical Engineering and Information Technology,
Slovak University of Technology, Ilkovičova 3, 81219 Bratislava, Slovakia
e-mail: katarina.zakova@stuba.sk

OMWeb environment is also compared to some other existing web-based and interactive platforms.

Similar solution—a learning environment aiming to support teaching in engineering education—is presented also in [9]. In comparison to the previous paper the described Modelica based virtual laboratory software enables not only text based modeling of the system but it also presents a graphical modeling in the Java remote application prototype.

Another platform supporting visual modeling in a web browser is presented in [10]. It is called WebMWorks and it was developed mainly for collaborative design and simulation based on Modelica. The platform was verified on the example of a pure electric vehicle in [11].

UN-VirtualLab solution [12] offers free web simulation environment that enables to perform experiments on precompiled OpenModelica based software models.

In [13] a web service based on SOAP is developed to compile and simulate remotely Modelica based models. The web service to OpenModelica engine using XML-RPC and JSON-RPC technology is described in [14].

As it is evident the web oriented solutions offering Modelica and OpenModelica functionality to online users are already available and can be used. It is more difficult to find remote experiment solutions that are based on this software environment. This paper tries to offer one possible way of such application. It is devoted to the remote control of the thermo-optical plant presented in the next section.

2 Thermo-Optical Plant

The presented online experiment was realised using the new laboratory thermo-optical plant TOS1A (Fig. 1).

The considered device was developed on the base of previous realisation of the plant called uDAQ28/LT [15] used for remote experimentation e.g. in [16, 17]. The new plant brought mainly the small change in the construction [18]. It has 3 inputs influencing

Fig. 1 Thermo-optical plant TOS1A



- bulb performance (the light and the heat source),
- system cooling (by fan),
- LED light (another light source)

and several outputs that enable user to measure actual value e.g. of

- light intensity,
- system temperature,
- fan speed.

The plant includes the built in filters of the first order for filtering the above mentioned outputs. The user has the possibility to set time constants of these filters. Derivatives of output variables are also available.

The TOS1A device is built using the programmable Arduino Due R3 board and it uses USB port for communication with a PC. The plant is easily usable in basic control courses and can be used for testing different control structures (e.g. PID, PI, pole assignment, etc.).

3 OpenModelica Environment

OpenModelica [19] is an open-source modeling, simulation and programming environment. It is based on Modelica modeling language that enables to describe various dynamical systems and processes and is aimed to be used both in industrial and academic area, as well. OpenModelica offers users several tools:

- (a) OpenModelica compiler (OMC) that compiles Modelica code in C. It can also be used interactively from the terminal as a CORBA object.
- (b) OpenModelica interactive terminal (OMShell) that provides an interactive interface to work with OMC.
- (c) OpenModelica NoteBook (OMNotebook) that enables Modelica language learning through the built-in graphical interface.
- (d) OpenModelica development environment (OMEdit) that is a graphical interface for creating simulation models and functions.

OpenModelica enables calling external functions. This fact plays a significant advantage in the programming environment and enables to design more advanced applications. OpenModelica currently supports external function calls from C language, Java and Python. OpenModelica has two main ways to run a simulation from a terminal:

- through OM compiler using .mos file,
- by sending commands to the executed OMC server via CORBA interface.

OpenModelica is primarily used for local computations. However, it can also be installed on the network server and used online via Internet.

4 Communication with USB Based Plant

As it was already told the considered plant is attached to the computer via USB port. There exist several third-party libraries that enable USB communication with the device. Let us introduce at least some of them.

4.1 *Arduino—Serial*

The library [20] was designed directly for Arduino mainboard. It is also included in the thermo-optical plant. The library is implemented in C language and it does not require any additional programs. It has open source code that is available in GitHub repository (Table 1).

It is run in the same way as C executable program:

```
$ ./arduino-serial -b 115200 -p /dev/ttyACM0 -S 'command' r
```

whereby the command options are explained in the table.

4.2 *PySerial*

The library [21] is written in Python language and it enables access to USB serial port. It is able to run on majority of operating systems (Windows, OSX, Linux, BSD) and is released under a free software license. The library offers same class based interface for all supported platforms; access to the port settings via Python properties and many other features.

The use of library is quite trivial. On the Unix based systems reading from and writing to the serial interface is realised in similar manner as reading from and writing to a file.

After loading the library it is possible to use all library components, i.e. to create new object for serial port that can be used for data reading and writing:

Table 1 Selected options for Arduino-serial command

Option	Explanation
-b	Set baud rate (bps) of Arduino (default 9600)
-p	Serial port Arduino is connected to
-S	Send string with newline to Arduino
-r	Receive string from Arduino and print it out

```
>> import serial
>> ser = serial.Serial('/dev/ttyACM0', 115200)
>> ser.read();
>> ser.write();
```

4.3 *Libusb*

It is a C library providing generic access to USB based devices [22]. It can be used by developers to facilitate their development of applications communicating with USB hardware on many different operating systems (Linux, OS X, Windows, Android, OpenBSD, etc.).

The library is often used as background for other tools that communicate with USB port (e.g. PyUSB).

4.4 *PyUSB*

The library [23] is written as Python module that enables easy access to USB devices. PyUSB relies on a native system library for USB access. PyUSB brings builtin back-ends for libusb 0.1, libusb 1.0 and OpenUSB.

The initial use of the library is a little bit more complicated. After importing PyUSB packages modules and determining the instance of the USB device

```
>> import usb.core
>> dev = usb.core.find(idVendor=0x2341, idProduct=0x003e)
```

it is needed to set the configuration and to define endpoint descriptor. Only then one can start the communication with the plant.

4.5 *Library Selection*

For the presented implementation the PySerial library was used. The advantage is that the library is included directly in OS Ubuntu (i.e. no additional installation is needed). In addition, it is based on interpreted Python language that does not require the compilation of the source code after each its change as it would necessary e.g. in the case of libusb library. In similar way it would be possible to use also PyUSB library but its implementation is more complicated. The solution based on Arduino USB support is slower and has longer responses than pySerial library.

4.6 Realization

The application was developed as Single Page Application (SPA). According to the Wikipedia’s definition [24] it is a web application or web site that fits on a single web page with the goal of providing a more fluent user experience similar to a desktop application.

Figure 2 shows the basic architecture of the developed application.

The aim is to control the thermo-optical plant on the base of parameters entered by user via web based graphical user interface. After their submitting the client application sends a request to the server where it is processed by the server application core. In this step the AJAX technology is used. The application core functions take care about the interactive communication between the plant and the client side. For this purpose two types of functions are used:

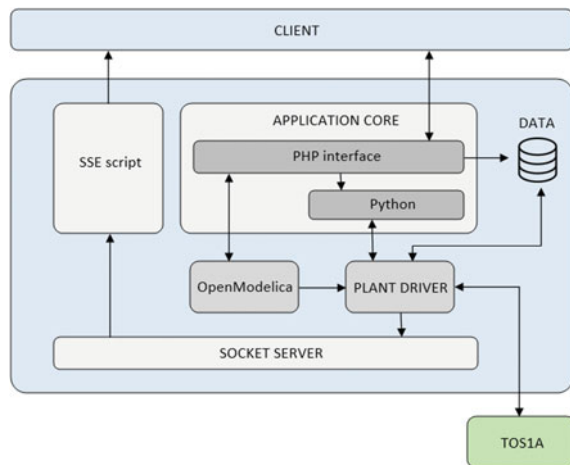
- php functions that create layer for processing experiment parameters, storing values, direct communication with the client and running the simulation environment (OpenModelica).
- python functions for the communication with the hardware. The python language was used because of its ability to cooperate with operating system on the low level.

The application core influences the plant using the plant driver. The data from the plant are sent to the server socket again via the plant driver. Server Sent Event script (SSE script) reads data from the socket and send them back to the user on the client side. They are visualised in the form of graphical dependencies.

SSE is one-way type of communication where script running on the server side sends data to the client. It is executed from the web browser and runs in a loop till the connection with client is closed. The client application receives following data

- measure data from the plant (received from the socket server),

Fig. 2 Basic architecture of the developed application



- information about the execution of the experiment,
- actual reference value,
- index of the controlled variable,
- boolean value describing whether OpenModelica process runs or not and if appropriate the process ID

that are sent in JSON format.

For the same purpose WebSocket could be used. It enables two-way communication. However, since in this case it was not necessary to establish a connection from a client side, the SSE communication was sufficient.

5 Graphical User Interface

Figure 3 illustrates the graphical layout of the developed client application. The middle part of the upper bar shows actual measured values from the plant. The displayed checkboxes enable to switch on or off visualisation of the corresponding variable in the graph. The gray color denotes the controlled variable (it can be changed by clicking on the name of other variable). The actual values of control variables are shown above the LED diodes in the virtual plant model in the right top part of the screen.

Experimental results are demonstrated using graphical dependencies. The present checkbox enables to turn on and off visualisation of the reference value that can also be changed during the experiment running. The plot can be zoomed using the mouse pointer.

The experiment can run both in open and closed loop, as well. The type of experiment is chosen on the left side of the application GUI (emphasized by the red box).

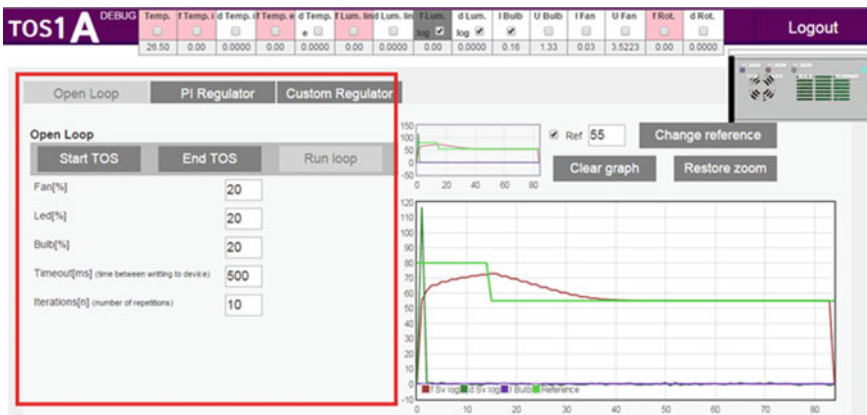


Fig. 3 Application graphical user interface

The open loop enables to measure step responses for the identification purposes. In this way it is possible to construct model of the plant that can be later used for the design of the controller.

The control in the closed loop can be realised using the predefined structure of PI controller or by defining own custom control algorithm. Controller parameters can also be changed during the simulation running.

In the case of custom controller it is necessary to define the control algorithm using Modelica syntax. Its example is shown in the following code.

```
model modelica_ExternalLibraries
parameter Real Ts = 0.01;
parameter Real Ref = 70;
Real Tos_in;
Real Tos_out;
Real error;
equation
when sample(0, Ts) then
error = Ref - Tos_in;
Tos_out = pre(Tos_out) + error/5;
end when;
annotation(experiment(StartTime = 0, StopTime = 1, Interval = 1));
end modelica_ExternalLibraries;
```

To reduce the probability of making syntax errors in the code a graphical environment that facilitates the definition of the algorithm was prepared (Fig. 4).

The user can define the type of each parameter, its name and the value. The type of the parameter is chosen from combo box where all OpenModelica data types are included (Real, Integer, String, Boolean, discrete Real, discrete Integer, discrete String, discrete Boolean). The user can add to the control structure so many param-

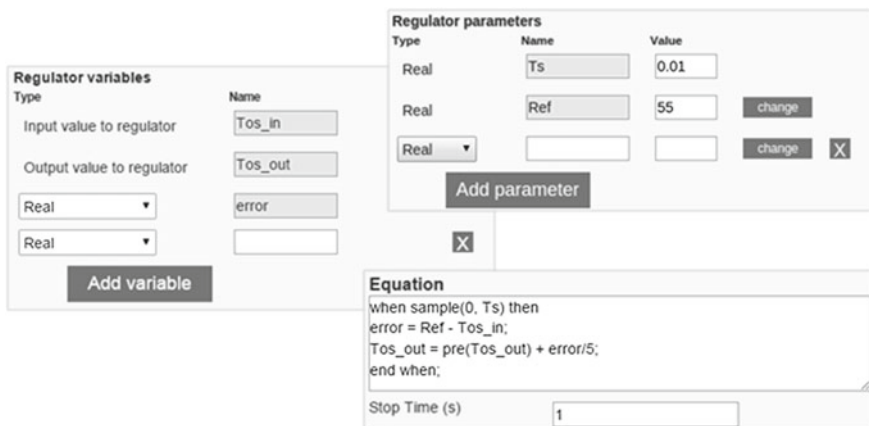


Fig. 4 Setting of custom control algorithm

ters as it is needed. Two parameters: sampling period (T_s) and reference value (Ref) are predefined from the beginning of the custom controller building.

The next part enables to specify variables of controller. Their definition is realized in similar way as it was done before. The only difference consists in the fact that in this case the user does not define the value of the variable. The name of the input and output variable (Tos_in , Tos_out) of the system cannot be changed.

The last part enables to define control algorithm. For its definition the text area is used and the user can use names of all parameters and variables that he or she defined before. The user needs to define the algorithm for calculation the controller output value (Tos_out) on the base of the variable that enters to the controller (Tos_in), i.e. the measured system output.

6 Conclusions

The designed application enables to control the thermo-optical system remotely. The advantage consists in the fact that the user can use not only the predefined PI controller but also own custom control algorithm.

The whole application was developed in frame of diploma thesis [25] and after incorporating the reservation system and multilingual support it could be included to the set of experiments that are offered to students for their experimentation.

Acknowledgments Author thanks to František Maras for his help with application implementation, fruitful discussions and critical reading of this paper. His help is very gratefully acknowledged. This work was supported by the Slovak Grant Agency, Grant VEGA No. 1/0937/14 and APVV-0343-12.

References

1. Bisták, P.: Advanced remote laboratory for control systems based on Matlab and .NET platform. In: 11th IEEE International Conference on Emerging eLearning Technologies and Applications (ICETA 2013), pp. 35–39 (2013)
2. Costa, R.J., Alves, G.R., Zenha-Rela, M.: Embedding instruments and modules into an IEEE1451-FPGA-Based weblab infrastructure. *Int J Online Eng* **3** (2012)
3. Kaluz, M., Garcia-Zubia, J., Fikar, M., Cirka, L.: A flexible and configurable architecture for automatic control remote laboratories. *IEEE Trans. Learn. Technol.* (2015). In Press
4. Leva, A., Donida, F.: Multifunctional remote laboratory for education in automatic control: the CrAutoLab experience. *IEEE Trans. Ind. Electron.* **55**(6) (2008)
5. Lojka, T., Miskuf, M., Zolotova, I.: Service oriented architecture for remote machine control in ICS. In: Proceedings of SAMI 2014—IEEE 12th International Symposium on Applied Machine Intelligence and Informatics, pp. 327–330 (2014)
6. Restivo, M.T., Mendes, J., Lopes, A.M., Silva, C.M., Chouzal, F.: A remote lab in engineering measurement. *IEEE Trans. Ind. Electron.* **56**(12), 4436–4843 (2009)
7. Ferretti, G., Gritti, M., Magnani, G., Rocco, P.: A remote user interface to modelica robot models. In: 3rd International Modelica Conference, Linköping, Sweden (2003)

8. Torabzadeh-Tari, M., Hossain, Z.M., Fritzson, P., Richter, T.: "OMWeb" virtual web-based remote laboratory for modelica in engineering courses. In: 8th International Modelica Conference, Dresden, Germany (2011)
9. Bouillon, P., Frochte, J.: Simulation- and web-based e-learning in engineering (Open source architecture and didactic issues). In: Proceedings of the 16th International Conference on Research and Education in Mechatronics, Bochum, Germany, pp. 127–134 (2015)
10. Liu, Q., Xiong, T., Liu, Q., Chen, L.: WebMWorks: a general web-based modeling and simulation environment for modelica. In: Proceedings of the 9th International Modelica Conference, Munich, Germany (2012)
11. Yin, X., Wu, Y., Liu, Q., Wang, S.: A web-based, collaborative modeling, simulation, and parallel computing environment for electromechanical systems. *Adv. Mech. Eng.* **7**(3) (2015)
12. Duarte, O.G.: UN-virtuallab: a web simulation environment of OpenModelica models for educational purposes. In: 8th International Modelica Conference, Dresden, Germany (2011)
13. Meyer zu Eissen: S., Stein, B.: Realization of web-based simulation services. *Comput. Ind.* **57**(3), 261–271 (2006)
14. Zakova, K.: Online use of OpenModelica via web service. In: 12th International Conference on Remote Engineering and Virtual Instrumentation (REV), Bangkok, pp. 152–156 (2015)
15. Huba, M.: Thermo-optical laboratory plant uDAQ28/LT (2008). <http://www.eas.sk/mod/product/show.php?ID=5>
16. Kaluz, M., Cirka, L., Fikar, M.: Remote control software for thermo-optical plant. In: 18th International Conference on Process Control, Tatransk Lomnica, Slovakia (2011)
17. Szolík, L., Zakova, K.: OpenModelica based remote control of thermo-optical plant. In: 9th International Conference on Remote Engineering and Virtual Instrumentation (REV) (2012)
18. Huba, T., Huba, M., Tapak, P.: Thermo-optical plant TOS1A. Technical User Guide, Bratislava: Slovenska e-akademia, no. 2014. 49 s v0.02. (in Slovak)
19. OpenModelica Users Guide, available at: https://openmodelica.org/images/docs/OpenModelicaUserGuide.htm#_Toc382076020 [10.5.2015]
20. Arduino-serial: C code to talk to Arduino (2015). <http://todbot.com/blog/2006/12/06/arduino-serial-c-code-to-talk-to-arduino>
21. pySerial (2016). <http://pythonhosted.org/pyserial/pyserial.html>
22. libusb (2016). <http://libusb.info/>
23. PyUSB (2016). <https://github.com/walac/pyusb/blob/master/docs/tutorial.rst>
24. Single-page application (2016). https://en.wikipedia.org/wiki/Single-page_application
25. Maras, F.: Control of laboratory experiment in the Internet environment, Diploma thesis, Slovak University of Technology, Bratislava, Slovakia (2014) (in Slovak)

DC Motor Educational Kit: A Teaching Aid in Control Theory

António Paulo Moreira, Paulo Costa, José Gonçalves
and Brígida M. Faria

Abstract This paper describes a laboratory control theory experiment supported by the use of a DC Motor Educational Kit. The impact, as a teaching aid, of the proposed laboratory control experiment is evaluated, having in mind the student's feedback. The DC motor that is used in the developed educational Kit is the EMG30, being a low cost 12 V motor equipped with encoders and a 30:1 reduction gearbox. The experiment is based on real hardware and on simulation, using the SimTwo realistic simulation software. In order to implement the realistic simulation the EMG30 model was obtained. Students' feedback was acquired using a questionnaire and the results confirmed the importance given to these practical experiments.

Keywords Control education · Laboratory experiment · DC motor

A.P. Moreira · P. Costa
Faculty of Engineering, Department of Electrical Engineering and Computers,
University of Porto, Porto, Portugal
e-mail: amoreira@fe.up.pt

P. Costa
e-mail: paco@fe.up.pt

J. Gonçalves (✉)
Department of Electrical Engineering, Polytechnic Institute of Bragança,
Bragança, Portugal
e-mail: gonalves@ipp.pt

B.M. Faria
School of Applied Health Technology, Polytechnic Institute of Porto,
Porto, Portugal
e-mail: btf@estsp.ipp.pt

A.P. Moreira · P. Costa · J. Gonçalves · B.M. Faria
INESC TEC, Institute for Systems and Computer Engineering, Technology and Science,
Porto, Portugal

B.M. Faria
LIACC - Artificial Intelligence and Computer Science Laboratory, Porto, Portugal

1 Introduction

This paper describes a laboratory control theory experiment supported by the use of a DC Motor Educational Kit. The DC motor that is used in the developed educational Kit is the EMG30, being a low cost 12 V motor equipped with encoders and a 30:1 reduction gearbox. DC motors have been used in research and education intensively over the past years [1–3], being also available many commercial educational DC motor Kits [4, 5].

The experiment is based on real hardware and simulation (using the SimTwo realistic simulation software). SimTwo is a realistic simulation software that can support several types of robots. Its main purpose is the simulation of mobile robots that can have wheels or legs, although industrial robots, conveyor belts and lighter-than-air vehicles can also be defined. Basically any type of terrestrial robot definable with revolute joints and/or wheels can be simulated in this software [6].

The motivation to use the EMG30 is the fact that it is an actuator worldwide popular, being a low cost 12 V motor equipped with encoders and a 30:1 reduction gearbox [7]. In order to implement the simulation, the EMG30 accurate model was obtained.

The paper is organized as follows: After a brief introduction it is described the developed setup applied to obtain the experimental data and the actuator parameters estimation. Then the laboratory control theory experiment is presented. Then the impact, as a teaching aid, of the proposed laboratory control experiment is evaluated, having in mind the student's feedback. Finally to round up the paper some conclusions are presented.

2 Modeling of the EMG30 Geared Motor

The EMG30 is an actuator worldwide popular, being a low cost 12 V motor equipped with encoders and a 30:1 reduction gearbox. The fact that it is equipped with encoders is an important feature because it provides important data to obtain the closed-loop velocity control.

The EMG30 model can be defined by the following equations, where U_a is the converter output, i_a is the DC Motor current, R_a is the equivalent resistor, L_a is the equivalent inductance and e is the back EMF (electromotive force) voltage as expressed by Eq. (1).

$$U_a = e + R_a i_a + L_a \frac{\partial i_a}{\partial t} \quad (1)$$

The motor can provide a torque T_L that will be applied to the load, being the developed torque (T_d) subtracted by the friction torque, which is the sum of the static friction (T_c) and viscous friction ($B\omega$), as shown in Eq. 2.

$$T_L = T_d - T_c - B\omega \quad (2)$$

Current i_a can be correlated with the developed torque T_d through Eq. 3, the back EMF voltage can be correlated with angular velocity through Eq. 4 and the load torque T_L can be correlated with the moment of inertia J and the angular acceleration through Eq. 5 [8].

$$T_d = K_s i_a \quad (3)$$

$$e = K_s \omega \quad (4)$$

$$T_L = J\dot{\omega} \quad (5)$$

In order to obtain experimental data, a setup, shown in Fig. 1, was implemented. The experimental setup is based on the Arduino micro-controller, the L6207 Drive, a DC Power source, an EMG30 actuator and the motor Load. The obtained data is the load angular velocity as a function of the input voltage. Two tests were performed, the first was to obtain the step response for a 12 V input (transitory response data) and the second test was the steady-state response for several input voltages (steady-state data).

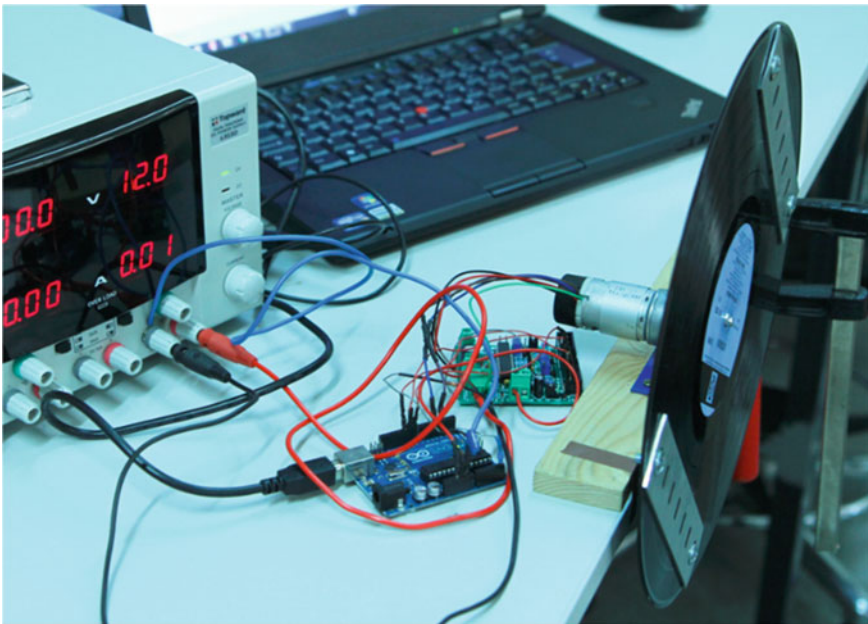


Fig. 1 Experimental setup

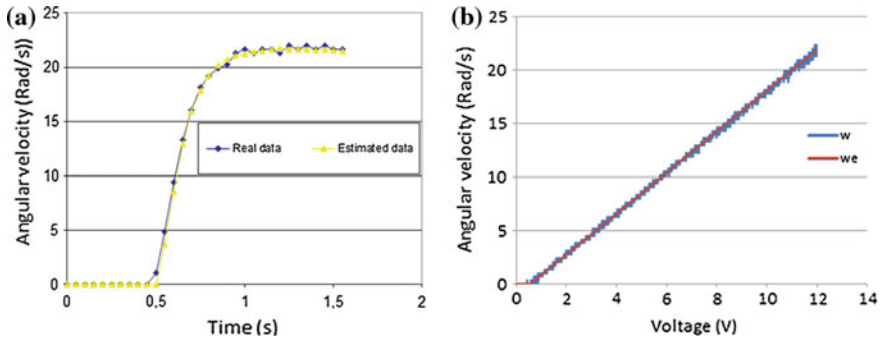


Fig. 2 Real and estimated actuator experiments. **a** Motor transitory response data. **b** Motor steady-state response data

It was obtained an electro-mechanical dynamical model that describes the motor, its gear box and the encoder. The estimated and the real transitory and steady-state responses are shown in Fig. 2. Details of the parameters estimation procedure and the EMG30 simulation in SimTwo can be found in [9].

The load has a known moment of inertia, given by the sum of three moments of inertia. A moment of inertia of a vinyl record $J_d = \frac{1}{2}m_d r_d^2$ (where m_d is the record mass and r_d is its radius) summed with the moments of inertia of two planar rectangles, each one given by the equation $J_r = m \frac{a^2+b^2}{12}$ (where a and b are the planar rectangles sides dimensions and m is the planar rectangles mass). Having in mind that the *Parallel axis theorem* has to be used in order to calculate the moment of inertia of the planar rectangles, mr_p^2 has to be summed to the previous calculated moment of inertia (where m is the rectangular plane mass and r_p is the perpendicular distance between the axis of rotation and the axis that would pass through the centre of mass of each rectangular plane) [10]. In order to estimate the motor moment of inertia it is subtracted to the estimated value J the calculated moment of inertia, being J_L the load moment of inertia and J_m the moment of inertia for the DC motor. The estimated parameters, previously presented in [9], were reviewed, being shown, in SI units, in Table 1. The presented equivalent inductance was directly measured.

Table 1 EMG30 estimated parameters

Parameters	Value
K_s	0.509
L_a	3.4E-3
R_a	7.101
B	0.000931
T_c	0.0400
J	0.00567
J_m	0.0019
J_L	0.00377

3 Laboratory Control Experiment

The proposed laboratory control experiment has as goal the study, by the students, of PID controllers design [11]. For that purpose it was conducted a DC motor closed-loop velocity control experiment, applying PID controllers. Initially the students worked with a realistic simulation of the DC Motor Educational Kit (Fig. 3a) and finally tested their controllers with real hardware (Fig. 3b). The experiment was simulated in the SimTwo realistic simulator, where the parameters that were described in Sect. 2 were applied, with the difference that for this experiment the load has a different moment of inertia and the used drive is the Pololu Dual MC33926 Motor Driver Shield for Arduino [12].

Students applied tuning control loops based on the Internal Model Control (IMC) tuning method [13]. This method has many advantages, such as its robustness and the ability for the user to specify the closed-loop time constant, being its major drawback the fact that when the process has a very long time constant the error will be integrated for a very long time (Fig. 5).

The IMC tuning method was developed for use on self-regulating processes. A self-regulating process stabilizes at some point of equilibrium, which depends on the process design and the controller output. If the controller output is set to a different value, the process will respond and stabilize at a new point of equilibrium, as shown in Fig. 4a.

The first step that students must do is to apply a step change in the controller output (CO), as shown in the example of Fig. 4a. The observed process output provides the parameters that allow an approximate estimate of the process as a first order system with time delay, as shown in Eq. 6, where $C(s)$ is the process output and $R(s)$ is the process input.

$$\frac{C(s)}{R(s)} = \frac{K}{\tau s + 1} e^{-t_d s} \quad (6)$$

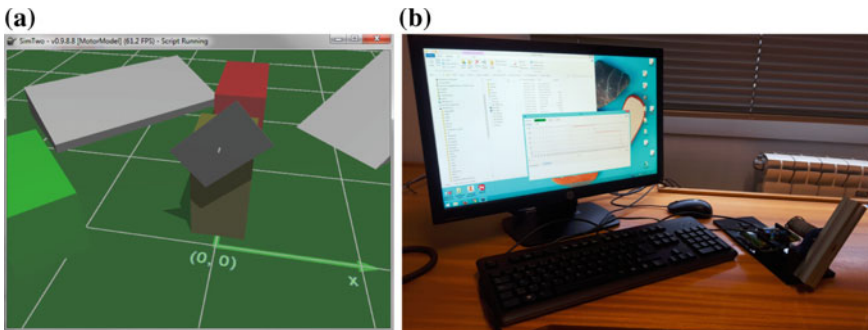


Fig. 3 DC motor educational kit. **a** Simulated experiment in SimTwo. **b** Experiment with real hardware

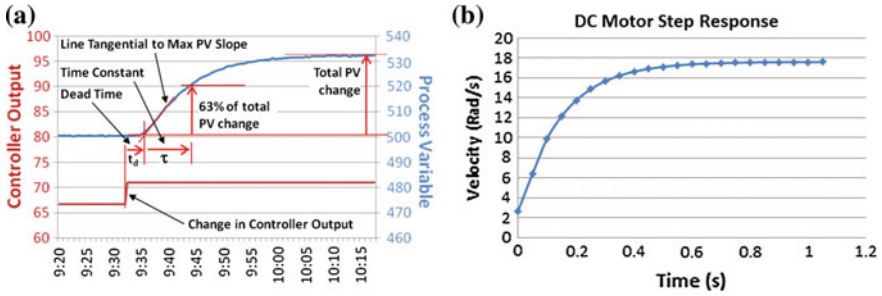


Fig. 4 Systems step response. a Self-regulating process step response [14]. b DC motor step response

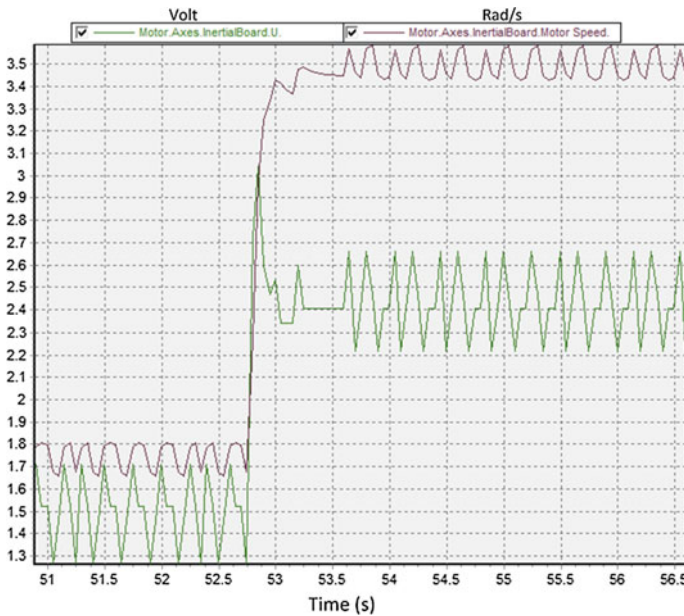


Fig. 5 Closed-loop response for low velocities

where: t_d is the dead time, τ is the time constant and K is the process gain, given by the total change in PV (Process Variable) (in %) divided by change in CO (in %). From the EMG30 DC motor step response (Fig. 4b), changing the controller output from 2 to 10 V, the process gain and time constant are estimated, being the dead time considered null. The process parameters are shown in Table 2.

Then students calculate the PID controller, based on the IMC tuning method, where the derivative time is null, the integral time is given by τ and the controller gain is given by Eq. 7, where τ_{cl} parameter allows to choose the desired closed-loop response time. Students applied $\tau_{cl} = \tau$, in order to the closed-loop system dynamics remains similar as its open loop response.

Table 2 Process parameters

Parameters	Value
K	5.25
τ	0.15
t_d	0

$$K_c = \frac{\tau}{K(\tau_{cl} + t_d)} \quad (7)$$

The chosen sample time was 50 ms which is high, when compared with the system time constant 150 ms, but low having in mind the low number of encoder transitions, especially for low velocities, as show in Fig. 5, so a compromise between these two aspects was made.

The problem with this controller is that the controller input, shown in green, can saturate, being the error integrated for a long time, which can generate an undesirable overshoot in the closed-loop response (Wind-Up), as it can be observed in Fig. 6a. That problem can be solved by stop integrating the error whenever the controller output saturates, giving the result seen in Fig. 6b.

Finally students test their controllers with real hardware, being shown an example of a DC motor closed-loop response in Fig. 7.

4 Laboratory Control Experiment Evaluation

In order to understand the best way to provide the information to students using the DC Motor Educational Kit, a sample of 67 individuals participate in an empirical study. The sample is composed by students of the fifth grade of Master in Electrical and Computer Engineering and these students have a mean age of 22 years old, where 15 % are females. Students' feedback was collected using a questionnaire with 7 questions related with the themes lectured in classes. Therefore it was asked the importance given to:

- 1: Axis control in the course;
- 2: Laboratory work for learning the axis control concepts;
- 3: Representativity of the laboratory work in the course content about axes motion control;
- 4: Representativity of the laboratory work regarding to potential skills acquired by students;
- 5: Testing hardware algorithms developed for the study of axes motion control;
- 6: Realistic simulation before testing the hardware;

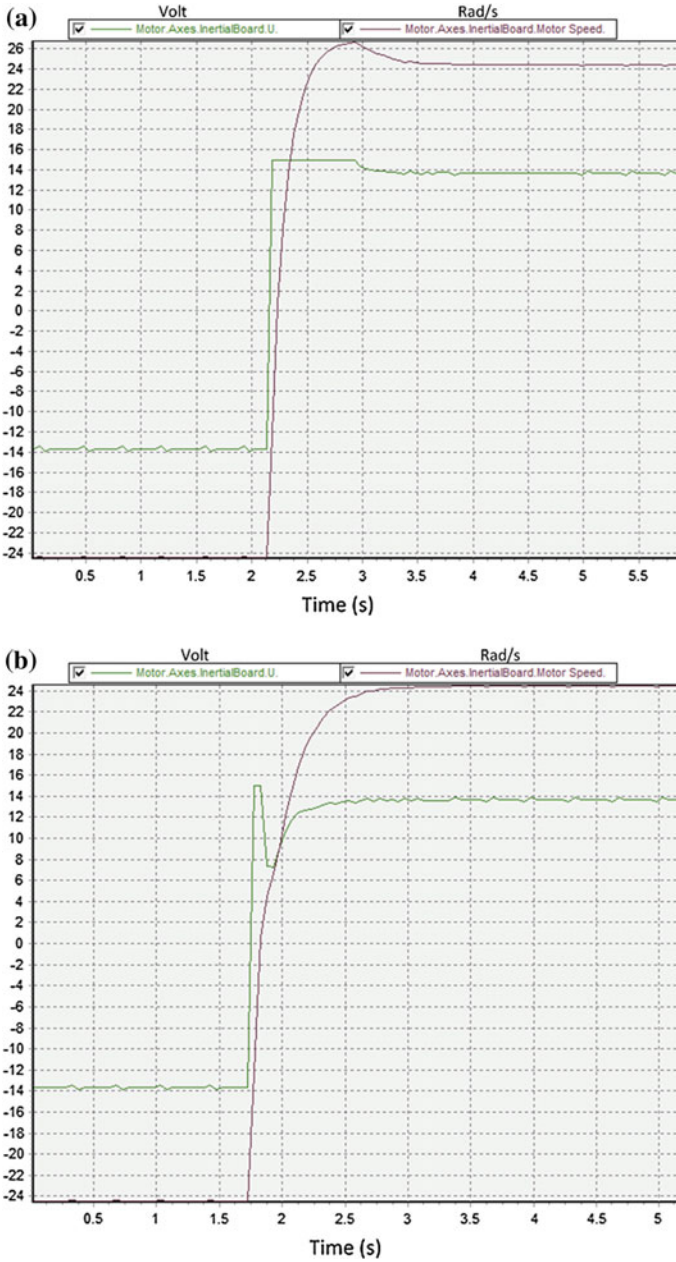


Fig. 6 Closed-loop DC motor response. **a** Closed-loop without anti wind-UP, **b** closed-loop with anti wind-Up

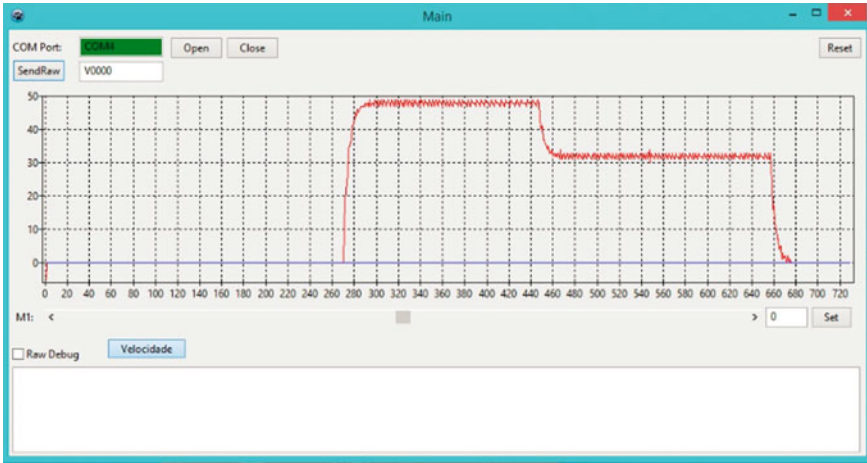


Fig. 7 Closed-loop response with real hardware

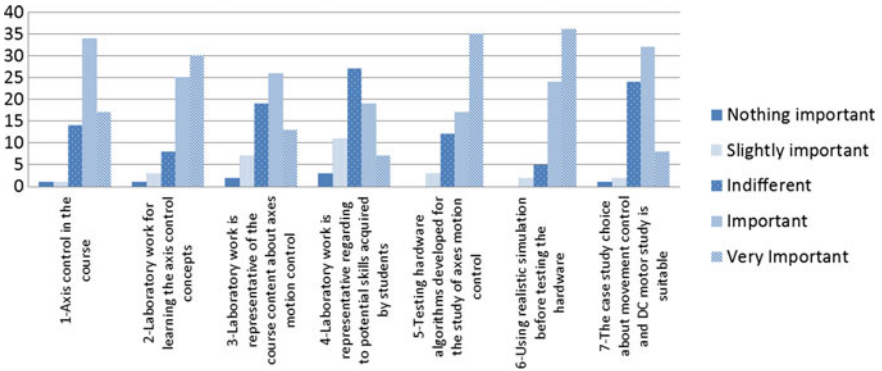


Fig. 8 Students' feedback

- 7: The choice of the case study about movement control and if the DC motor study was suitable.

Opinions were measured with a 5 Likert scale [15] from 1—*Nothing Important* to 5—*Very Important*. Figure 8 shows the results distribution and Table 3 presents the statistical measures median, mean, mode, minimum and maximum of the responses by question.

All questions have a median of responses classified as at least *Important*, except the question regarding the representativity of the laboratory work regarding to potential skills acquired by students in which the classification was *Indifferent*.

Table 3 Students' feedback

Questions	1	2	3	4	5	6	7
Median	4	4	4	3	5	5	4
Mean	3.97	4.19	3.61	3.24	4.25	4.4	3.66
Mode	4	5	4	3	5	5	4
Minimum	1	1	1	1	2	2	1
Maximum	5	5	5	5	5	5	5

These results confirm the importance given by students of using these laboratory control experiments. Moreover it is possible to conclude the great importance of using realistic simulation before testing the hardware.

5 Conclusions

This paper described a laboratory control theory experiment supported by the use of a DC Motor Educational Kit. The DC motor that is used in the developed educational Kit is the EMG30, being a low cost 12 V motor equipped with encoders and a 30:1 reduction gearbox. The experiment is based on real hardware and simulation (using the SimTwo realistic simulation software). In order to implement the simulation, the EMG30 accurate model was obtained.

The proposed laboratory control experiment has as goal the study, by the students, of PID controllers design. For that purpose it was conducted a DC motor closed-loop velocity control experiment, applying PID controllers. Initially the students worked with a realistic simulation of the DC Motor Educational Kit and finally tested their controllers with real hardware. Students applied tuning control loops based on the Internal Model Control (IMC) tuning method. This method has many advantages such as its robustness and the ability for the user to specify the closed-loop time constant, being its major drawback the fact that when the process has a very long time constant the error will be integrated for a very long time.

Students' feedback confirm the importance of testing hardware algorithms developed for the axes motion control study, the importance of using realistic simulation before testing the hardware and also the overall theme of axis control in the course of their Master in Electrical and Computer Engineering.

Acknowledgments This work is financed by the “Project TEC4Growth—Pervasive Intelligence, Enhancers and Proofs of Concept with Industrial Impact/NORTE-01-0145-FEDER-000020”, which is financed by the North Portugal Regional Operational Programme (NORTE 2020), under the PORTUGAL 2020 Partnership Agreement, and through the European Regional Development Fund (ERDF).

References

1. Srisertpol, J., Khajontraidet, C.: Estimation of DC motor variable torque using adaptive compensation. In: Control and Decision Conference, 2009. CCDC '09 (2009)
2. Kanojiya, R.G., Meshram, P.M.: Optimal tuning of PI controller for speed control of DC motor drive using particle swarm optimization. In: 2012 International Conference on Advances in Power Conversion and Energy Technologies (APCET) (2012)
3. Agung, I.G.A.P.R., Huda, S., Wijaya: Speed control for DC motor with pulse width modulation (PWM) method using infrared remote control based on ATmega16 microcontroller In: 2014 International Conference on I.W.A. Smart Green Technology in Electrical and Information Systems (ICSGTEIS) (2014)
4. DC Motor kit (2016). <http://www.hometrainingtools.com/dc-motor-kit>
5. Scientifics Educational Kits: Motor—ScientificsOnline.com (2016). <https://www.scientificsonline.com/product/scientifics-educational-kits-motor>
6. Costa, P., Gonçalves, J., Lima, J., Malheiros, P.: Simtwo realistic simulator: a tool for the development and validation of robot software. Int. J. Theory Appl. Math. Comput. Sci. (2011)
7. Gear motor with encoder (2016). <http://www.robotshop.com/en/devantech-12v-30-1-gear-motor-encoder.html>
8. Bishop, R.: The Mechatronics Handbook. CRC Press, New York (2002)
9. Gonçalves, J., Lima, J., Costa, P., Moreira, A.: Modeling and simulation of the EMG30 geared motor with encoder resorting to simtwo: the official robot@factory simulator. In: Flexible Automation Intelligent Manufacturing 2013, Porto (2013)
10. Ramsey, A.: Dynamics. Cambridge Library Collection—Mathematics (2009)
11. Åström, K.J., Häggglund, T.: Advanced PID control, ISA—The Instrumentation, Systems, and Automation Society; Research Triangle Park, NC 27709 (2006)
12. Pololu dual MC33926 motor driver shield for Arduino (2016). <https://www.pololu.com/product/2503>
13. Rivera, D., Morari, M., Skogestad, S.: Internal model control: PID controller design. Ind. Eng. Chem. Process Des. Dev. (1986)
14. Dataforth Corporation. Tuning control loops with the IMC tuning method, Application note AN124 (2016). <http://www.dataforth.com>
15. Likert, R.: A technique for the measurement of attitudes. Arch. Psychol. **140**, 1–55 (1932)